Learning Resources – Website Content CSCR Exam 3

Purpose: This document is intended to capture the website content of those sites referenced as learning resources for CSCR Exam 3. Note that only virtual resources are captured. Additional textbook study resources have not been included but are available for purchase as detailed on-line and in this document. If the "Initial Link" for a given assignment is still active, it can be leveraged. Otherwise, the contents that had previously been available at the "Initial Link" can be found later within this document by using the first link in each row.

Note that some materials can be listed multiple times within the Learning Objectives. In such instances, they will often appear only once in the below links. Additional materials, such as reference textbooks, are also further detailed within the Learning Objectives for this exam but may not be included in the following list. Candidates are encouraged to fully review both sets of resources.

1. Assignment 1, Module 1 and Module 2: Reference Sections 1.4, 1.5, 1.8, 1.9, 1.10, 2, 2.16, 4.3.1, 4.4, 4.5, of the book available for purchase: Initial Link
2. Assignment 1, Module 1 and Module 2: Monte Carlo Simulation: Initial Link
3. Assignment 1, Module 3: Reference Section 3 of the book available for purchase: Initial Link
4. Assignment 1, Module 3: List of Disasters by Cost: Initial Link
5. Assignment 2, Module 1: Tropical Cyclone Definition: Initial Link
6. Assignment 2, Module 1: South Atlantic Formation: Initial Link
7. Assignment 2, Module 1: South Atlantic Formation (2): Initial Link
8. Assignment 2, Module 1: Hurricane vs. Typhoon: Initial Link
9. Assignment 2, Module 2: Hurricane Season: Initial Link
10. Assignment 2, Module 2: Tropical Cyclone Climatology: Initial Link
11. Assignment 2, Module 2: Hurricane Records: Initial Link
12. Assignment 2, Module 2: Hurricanes by Decade: Initial Link
13. Assignment 2, Module 2: Hurricane Genesis: Initial Link
14. Assignment 2, Module 2: Hurricanes, Typhoons, and Cyclones: Initial Link
15. Assignment 2, Module 3: Hurricane Structure: Initial Link
16. Assignment 2, Module 3: Tropical Cyclone Structure: Initial Link
17. Assignment 2, Module 3: How Hurricanes Form: Initial Link
18. Assignment 2, Module 3: Video on Hurricane Formation (site contents are not pasted in document as they are a video): https://www.youtube.com/watch?v=1f-dT2yRXpk
19. Assignment 2, Module 4 and Assignment 2, Module 11: State of FL Loss Projection Model: Initial Link
20. Assignment 2, Module 4: NOAA Technical Report 23: Initial Link
21. Assignment 2, Module 4: Prediction of Hurricane Wind Speeds: Initial Link
22. Assignment 2, Module 4: Wind-Field and Filling Models: Initial Link
23. Assignment 2, Module 4: Statistical Models of Holland Pressure: Initial Link
24. Assignment 2, Module 4: NHC Terms: Initial Link
25. Assignment 2, Module 4: Guidelines for Converting Winds: Initial Link
26. Assignment 2, Module 5: Saffir-Simpson Scale: Initial Link
27. Assignment 2, Module 5: Saffir-Simpson Scale #2: Initial Link
28. Assignment 2, Module 5: Tools to Measure Hurricanes: Initial Link

29. Assignment 2, Module 6: Tropical Cyclone Formation: Initial Link
30. Assignment 2, Module 6: Tropical Cyclone Formation 2: Initial Link
31. Assignment 2, Modules 6 and 7: Saharan Air Layer Impact: Initial Link
32. Assignment 2, Modules 6 and 7: Wind Shear: Initial Link
33. Assignment 2, Module 6: Hurricane Formation: Initial Link
34. Assignment 2, Module 6: Hurricane Enhancers and Inhibitors: https://www.wcbi.com/weather-whys-hurricane-inhibitors/ *This link includes an embedded video. It is not included in this document for that reason.*
35. Assignment 2, Modules 6 and 7: Hurricane Decay: Initial Link
36. Assignment 2, Module 7: Factors that Hinder Development: Initial Link
37. Assignment 2, Module 7: Hurricane Development: Initial Link
38. Assignment 2, Module 7: Factors that Strengthen and Weaken Hurricanes: Initial Link
39. Assignment 2, Module 7: Empirical Model for Predicting Decay: Initial Link
40. Assignment 2, Module 7: Hurricane and Land Interaction: Initial Link
41. Assignment 2, Module 8: Movement of Hurricanes: Initial Link
42. Assignment 2, Module 8: Hurricane Forecasts (Chapter 4): Initial Link
43. Assignment 2, Module 9: Hurricanes Spawn Tornadoes: Initial Link
44. Assignment 2, Modules 9 and 10: Storm Surge: Initial Link
45. Assignment 2, Module 9: Hurricanes and Extreme Rainfall: Initial Link
46. Assignment 2, Module 9: Hurricanes and Mudslide: Initial Link
47. Assignment 2, Module 10: Storm Surge #2: Initial Link
48. Assignment 2, Module 10: SLOSH: Initial Link
49. Assignment 2, Module 10: Storm Surge Impacts: Initial Link
50. Assignment 2, Module 10: Effect of Coastal Erosion on Storm Surge: Initial Link
51. Assignment 2, Module 10: Storm Size on Surge: Initial Link
52. Assignment 2, Module 11: Storm Data: Initial Link
53. Assignment 2, Module 11: NOAA Technical Memo 22: Initial Link
54. Assignment 2, Module 12: Reference Sections 3.2.1 and 3.2.2 of book available for purchase: here
55. Assignment 2, Module 12: Modeling of Storm Tracks: Initial Link
56. Assignment 2, Module 13: Stochastic Modeling of Storm Tracks: Initial LInk
57. Assignment 2, Module 13: Using Statistical Models: Initial Link
58. Assignment 2, Module 13: Commission Standards Section M-2 Question 1: Initial Link
59. Assignment 2, Module 14: Human Influence and Harvey: Initial Link
60. Assignment 2, Module 14: Negative AMO Index: Initial Link
61. Assignment 2, Module 14: ENSO Teleconnections: Initial Link
62. Assignment 2, Module 14: ENSO and AMO Impact on Atlantic Hurricanes: Initial Link
63. Assignment 2, Module 14: El Nino and La Nina: Initial Link
64. Assignment 2, Module 14: ENSO Impact around the globe: Initial Link
65. Assignment 2, Module 14: Impacts of ENSO on Hurricane Season: Initial Link
66. Assignment 2, Module 14: ENSO Impact on Regional Hurricane Activity: Initial Link
67. Assignment 2, Module 14: AMO and AMV: Initial Link
68. Assignment 2, Module 14: NAO: Initial Link
69. Assignment 2, Module 14: NAO and Climate Variability: Initial Link

70. Assignment 2, Module 14: NAO Impacts: Initial Link
71. Assignment 2, Module 15: Wind Profile: Initial Link
72. Assignment 2, Module 16: Extra-tropical Cyclones: Initial Link
73. Assignment 2, Module 16: Difference between Hurricane and Typhoon: Initial Link
74. Assignment 2, Module 16: Hurricane and Typhoon: Initial Link
75. Assignment 2, Module 16: Extratropical Transition: Initial Link
76. Assignment 2, Module 16: Extratropical Hermine: Initial Link
77. Assignment 3, Module 1: Reference Books available for purchase
78. Assignment 3, Module 1: FEMA 454: Initial Link
79. Assignment 3, Module 1: Plate Tectonics: Initial Link
80. Assignment 3, Module 1: Plate Tectonics; Includes a video which is not included in this document: https://www.iris.edu/hq/inclass/animation/what_are_the_forces_that_drive_plate_tectonics
81. Assignment 3, Module 1: Understanding Earthquakes: Initial Link
82. Assignment 3, Module 1: Australia Earthquakes: Initial Link
83. Assignment 3, Module 1: Plate Boundaries: Initial Link
84. Assignment 3, Module 1: New Zealand Faults: Initial Link
85. Assignment 3, Module 2: FEMA 454, Section 2.2.2: Initial Link
86. Assignment 3, Module 2: USGS Fault Types: Initial Link
87. Assignment 3, Module 2: Normal Fault: Initial Link
88. Assignment 3, Module 2: Reverse Fault: Initial Link
89. Assignment 3, Module 2: Strike Slip Fault: Initial Link
90. Assignment 3, Module 2: Oblique: Initial Link
91. Assignment 3, Module 2: Pacific Northwest EQs: Initial Link
92. Assignment 3, Module 2: Tectonic Boundaries: Initial Link
93. Assignment 3, Module 2: Convergent Margin: Initial Link
94. Assignment 3, Module 2: Divergent Fast-Spreading Ridge: Initial Link
95. Assignment 3, Module 2: Transform: Initial Link
96. Assignment 3, Module 3: FEMA 454, Section 2.4.1: Initial Link
97. Assignment 3, Module 3: Magnitude and EQ Components: Initial Link
98. Assignment 3, Module 3: EQ Intensity: Initial Link
99. Assignment 3, Module 3: Moment Magnitude: Initial Link
100. Assignment 3, Module 3: Energy Release: Initial Link
101. Assignment 3, Module 4: FEMA 454, Sections 2.3.1 and 2.3.2: Initial Link
102. Assignment 3, Module 4: Seismogram: Initial Link
103. Assignment 3, Module 4: Seismic Waves: Initial Link
104. Assignment 3, Module 5: FEMA 454, Section 2.2.3: Initial Link
105. Assignment 3, Module 5: MMI: Initial Link
106. Assignment 3, Module 5: EQ Hazards Q&A: Initial Link
107. Assignment 3, Module 5: Spectral Acceleration: Initial Link
108. Assignment 3, Module 5: Seismic Waves on Buildings: Initial Link
109. Assignment 3, Module 5: JMA Intensity: Initial Link
110. Assignment 3, Module 5: Macroseismic Intensity: Initial Link
111. Assignment 3, Module 6: FEMA 454, Sections 2.6.1 and 2.6.2: Initial Link
112. Assignment 3, Module 6: Seismic Hazard Maps: Initial Link

113. Assignment 3, Module 6: Earthquake Hazards: Initial Link
114. Assignment 3, Module 6: Earthquake Scenarios: Initial Link
115. Assignment 3, Module 6: Earthquake Recurrence: Initial Link
116. Assignment 3, Module 6: Global Earthquake Model: Initial Link
117. Assignment 3, Module 7: FEMA 454, Section 3.6.3: Initial Link
118. Assignment 3, Module 7: San Francisco Liquefaction Maps: Initial Link
119. Assignment 3, Module 7: Amplification and Liquefaction: includes a video which is not included in this document: https://www.youtube.com/watch?v=536xSZ_XkSs
120. Assignment 3, Module 8: FEMA 454, Sections 2.2.3 and 3.6.2: Initial Link
121. Assignment 3, Module 8: 1906 Liquefaction: Initial Link
122. Assignment 3, Module 8: Sand Boils, Loma Prieta: Initial Link
123. Assignment 3, Module 8: Liquefaction: Initial Link
124. Assignment 3, Module 8: FEMA 454, Section 3.6.4: Initial Link
125. Assignment 3, Module 8: Landslides: Initial Link
126. Assignment 3, Module 8: Coseismic Landslide: Initial Link
127. Assignment 3, Module 8: Landslide Handbook Parts A and D: Initial Link
128. Assignment 3, Module 8: Tsunami Basics: Initial Link
129. Assignment 3, Module 8: Megathrust Tsunamis: Initial Link
130. Assignment 3, Module 8: Tsunami: Initial Link
131. Assignment 3, Module 8: Tsunami Ultimate Guide: Initial Link
132. Assignment 3, Module 9: EQ ShakeMaps: Initial Link
133. Assignment 3, Module 9: Induced Seismicity: Initial Link
134. Assignment 3, Module 9: EQ Early Warning Basics: Initial Link
135. Assignment 3, Module 9: EQ Early Warning USGS: Initial Link
136. Assignment 3, Module 9: Tsunami Warnings: Initial Link
137. Assignment 3, Module 10: FEMA 454, Section 2.10: Initial Link
138. Assignment 3, Module 10: HERP: Initial Link
139. Assignment 3, Module 10: EQ Hazard Basics: Initial Link
140. Assignment 3, Module 10: EQ Hazard Education: Initial Link
141. Assignment 3, Module 10: EQ Hazards Animation: Initial Link
142. Assignment 3, Module 10: Design Maps: Initial Link
143. Assignment 3, Module 10: Earthquake Risk: Initial Link
144. Assignment 3, Module 10: Exploring Natural Hazards: Initial Link
145. Assignment 5, Module 1: Occupancy Study Note: Initial Link
146. Assignment 5, Module 1: FEMA 454, Sections 4.5.2, 4.9, and 5.2: Initial Link
147. Assignment 5, Module 1: Building Height Study Note: Initial Link
148. Assignment 5, Module 1: Building Codes Study Note: Initial Link
149. Assignment 6, Module 1: FEMA 454, Sections 1.4.1: Initial Link
150. Assignment 6, Module 1: ARA Mitigation Study, Sections 5.2 and 5.3: Initial Link

2. Assignment 1, Module 1: Monte Carlo Simulation: https://www.riskamp.com/files/RiskAMP%20-%20Monte%20Carlo%20Simulation.pdf

Content of Website:

What is Monte Carlo Simulation?

Monte Carlo simulation, or probability simulation, is a technique used to understand the impact of risk and uncertainty in financial, project management, cost, and other forecasting models.

Uncertainty in Forecasting Models

When you develop a forecasting model – any model that plans ahead for the future – you make certain assumptions. These might be assumptions about the investment return on a portfolio, the cost of a construction project, or how long it will take to complete a certain task. Because these are projections into the future, the best you can do is estimate the expected value.

You can't know with certainty what the actual value will be, but based on historical data, or expertise in the field, or past experience, you can draw an estimate. While this estimate is useful for developing a model, it contains some inherent uncertainty and risk, because it's an estimate of an unknown value.

Estimating Ranges of Values

In some cases, it's possible to estimate a range of values. In a construction project, you might estimate the time it will take to complete a particular job; based on some expert knowledge, you can also estimate the absolute maximum time it might take, in the worst possible case, and the absolute minimum time, in the best possible case. The same could be done for project costs. In a financial market, you might know the distribution of possible values through the *mean* and *standard deviation* of returns.

By using a range of possible values, instead of a single guess, you can create a more realistic picture of what might happen in the future. When a model is based on ranges of estimates, the output of the model will also be a range.

This is different from a normal forecasting model, in which you start with some fixed estimates – say the time it will take to complete each of three parts of a project – and end up with another value – the total time for the project. If the same model were based on ranges of estimates for each of the three parts of the project, the result would be a range of times it might take to complete the project. When each part has a minimum and maximum estimate, we can use those values to estimate the total minimum and maximum time for the project.

What Monte Carlo Simulation can Tell You

When you have a range of values as a result, you are beginning to understand the risk and uncertainty in the model. The key feature of a Monte Carlo simulation is that it can tell you – based on how you create the ranges of estimates – how *likely* the resulting outcomes are.

How It Works

In a Monte Carlo simulation, a random value is selected for each of the tasks, based on the range of estimates. The model is calculated based on this random value. The result of the model is recorded, and the process is repeated. A typical Monte Carlo simulation calculates the model hundreds or thousands of times, each time using different randomly-selected values.

When the simulation is complete, we have a large number of results from the model, each based on random input values. These results are used to describe the likelihood, or probability, of reaching various results in the model.

For Example

For example, consider the model described above: we are estimating the total time it will take to complete a particular project. In this case, it's a construction project, with three parts. The parts have to be done one after the other, so the total time for the project will be the sum of the three parts. All the times are in months.

Task	Time Estimate			
Job 1	5 Months			
Job 2	4 Months			
Job 3	5 Months			
Total	14 Months			

Table 1: Basic Forecasting Model

In the simplest case, we create a single estimate for each of the three parts of the project. This model gives us a result for the total time: 14 months. But this value is based on three estimates, each of which is an unknown value. It might be a good estimate, but this model can't tell us anything about risk. How likely is it that the project will be completed on time?

To create a model we can use in a Monte Carlo simulation, we create three estimates for each part of the project. For each task, we estimate the minimum and maximum expected time (based on our experience, or expertise, or historical information). We use these with the "most likely" estimate, the one that we used above:

Task	Minimum	Most Likely	Maximum	
Job 1	4 Months	5 Months	7 Months	
Job 2	3 Months	4 Months	6 Months	
Job 3	4 Months	5 Months	6 Months	
Total	11 Months	14 Months	19 Months	

Table 2: Forecasting Model Using Range Estimates

This model contains a bit more information. Now there is a range of possible outcomes. The project might be completed in as little as 11 months, or as long as 19 months.

In the Monte Carlo simulation, we will randomly generate values for each of the tasks, then calculate the total time to completion[1]. The simulation will be run 500 times. Based on the results of the simulation, we will be able to describe some of the characteristics of the risk in the model.

To test the likelihood of a particular result, we count how many times the model returned that result in the simulation. In this case, we want to know how many times the result was less than or equal to a particular number of months.

Time	Number of Times (Out of 500)	Percent of Total (Rounded)	
12 Months	1	0%	
13 Months	31	6%	
14 Months	171	34%	
15 Months	394	79%	
16 Months	482	96%	
17 Months	499	100%	
18 Months	500	100%	

Table 3: Results of a Monte Carlo Simulation

The original estimate for the "most likely", or expected case, was 14 months. From the Monte Carlo simulation, however, we can see that out of 500 trials using random values, the total time was 14 months or less in only 34% of the cases.

Put another way, in the simulation there is only a 34% chance – about 1 out of 3 – that any individual trial will result in a total time of 14 months or less. On the other hand, there is a 79% chance that the project will be completed within 15 months. Further, the model demonstrates that it is extremely unlikely, in the simulation, that we will ever fall at the absolute minimum or maximum total values.

This demonstrates the risk in the model. Based on this information, we might make different choices when planning the project. In construction, for example, this information might have an impact on our financing, insurance, permits, and hiring needs. Having more information about risk at the beginning means we can make a better plan for going forward.

1 In this example, we use the beta-PERT distribution to generate random values based on a minimum, most likely, and maximum value. The PERT distribution is often used to model estimates of expert data. For more information on this and other probability distributions, see the documentation on our website.

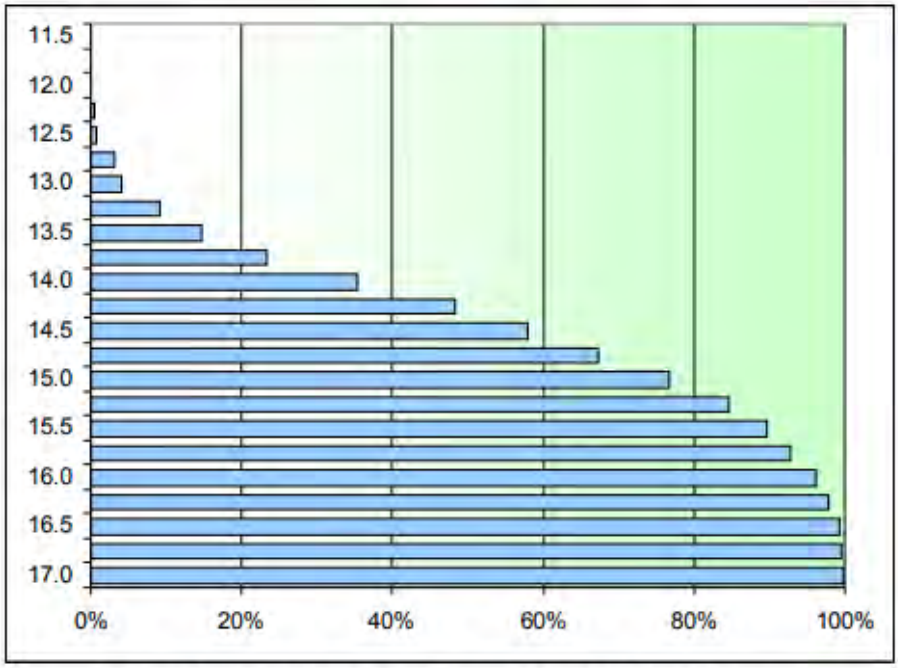

Figure 1: Probability of Completion Within Specified Time (Months)

How Reliable Is It?

Like any forecasting model, the simulation will only be as good as the estimates you make. It's important to remember that the simulation only represents probabilities and not certainty. Nevertheless, Monte Carlo simulation can be a valuable tool when forecasting an unknown future.

About RiskAMP

RiskAMP is a Monte Carlo simulation engine that works with Microsoft Excel®. The RiskAMP Add-in adds comprehensive probability simulation to spreadsheet models and Excel® applications. The Add-in includes 22 random distributions, 17 statistical analysis functions, a wizard for creating charts and graphs, and VBA® support – all for a fraction of the price of competing packages.

For more information, visit our website at http://www.riskAMP.com.

4. Assignment 1, Module 3: List of Disasters by Cost:
   https://en.wikipedia.org/wiki/List_of_disasters_by_cost

List of disasters by cost

1 language

Article Talk | Read Edit View history Tools

From Wikipedia, the free encyclopedia

> *This is a dynamic list and may never be able to satisfy particular standards for completeness. You can help by editing the page to add missing items, with references to reliable sources.*

Disasters can have high costs associated with responding to and recovering from them. This page lists the estimated economic costs of relatively recent disasters.

The costs of disasters vary considerably depending on a range of factors, such as the geographical location where they occur. When a large disaster occurs in a wealthy country, the financial damage may be large, but when a comparable disaster occurs in a poorer country, the actual financial damage may appear to be relatively small. This is in part due to the difficulty of measuring the financial damage in areas that lack insurance. For example, the 2004 Indian Ocean earthquake and tsunami, with a death toll of around 230,000 people, cost a "mere" $15 billion,[1] whereas in the Deepwater Horizon oil spill, in which 11 people died, the damage was six times higher.

The most expensive disaster in human history is the Chernobyl disaster, costing an estimated $700 billion.[2] Chernobyl's circumstances make it a unique but particularly devastating situation that is unlikely to ever happen again. Estimations have only increased over time, with the recent figure coming from the release of new government data up to 2016.[3] Furthermore, the cost is expected to perpetually increase for several thousand years as cleanup operations and the economic impact of the Chernobyl Exclusion Zone continue indefinitely.[4] The most expensive natural disaster is the 2011 Tōhoku earthquake and tsunami, costing an estimated $360 billion.[5]

Over $1 billion [edit]

This table lists disasters which are estimated to have an economic cost of at least 1 billion United States dollars without taking inflation into account.

List of disasters by cost. Over $1 billion. Actual, and inflated to 2024 (unless otherwise stated)

Event	Cost ($ billion)		Fatalities	Type	Year	Nation(s)
	Actual	Inflated				
Chernobyl disaster	$700[6]	$917.1	30–16,000	Contamination (Radioactive)	1986	Soviet Union (, ,)
2011 Tōhoku earthquake and tsunami + Fukushima nuclear disaster	$360[7][8][5]	$503.2	19,759	Undersea Megathrust Earthquake, Tsunami, Contamination (Radioactive)	2011	Japan
Great Hanshin earthquake	$200[9]	$412.7	5,502 – 6,434	Earthquake	1995	Japan
2023 Turkey–Syria earthquakes	$157.8[10][11]	$162.8	59,488 – 62,013	Earthquake	2023	West Asia (Turkey, Syria)
2008 Sichuan earthquake	$130[12]	$189.9	87,587	Earthquake	2008	China
Hurricane Katrina	$125[13]	$201.2	1,392	Tropical cyclone	2005	United States, Bahamas
Hurricane Harvey	$125[13]	$160.3	107	Tropical cyclone	2017	Americas (, , , , others)
Hurricane Ian	$112[13]	$120.3	161	Tropical cyclone	2022	North America (, , , others)
2020 South Asian floods	$105[14][15]	$127.6	6,511	Flood	2020	South Asia (, , , others)
Hurricane Maria	$91.6[13]	$117.5	3,059[16]	Tropical cyclone	2017	North America (, , , others)
						North America and

Event	Cost ($ billion)		Fatalities	Type	Year	Nation(s)
	Actual	Inflated				
Hurricane Milton	$85[17]	$85	35	Tropical cyclone	2024	North America and the Antiles (, , , others)
Hurricane Helene	$81.6[18]	$81.6	225	Tropical cyclone	2024	North America (, , , others)
Hurricane Ida	$75[19]	$87	107	Tropical cyclone	2021	North America (, , , others)
2019–20 Australian bushfire season	$69[20]	$83.8	451	Wildfire	2019-20	Australia
Hurricane Sandy	$68.7[13]	$94.1	254	Tropical cyclone	2012	North America (, , , others)
Hurricane Irma	$64.8[13]	$83.1	134	Tropical cyclone	2017	North America (, , , others)
Deepwater Horizon oil spill	$60 – $100[21]	$86.5 – $144.2	11	Contamination (Oil)	2010	United States
January 2025 Southern California wildfires	$57[22]	$57	30	Wildfire	2025	United States
2021 European floods	$54[23]	$62.7	243	Flood	2021	Europe (, , , others)
1988–1990 North American drought	$53.25[24]	$135.1	5,000+	Drought	1988-89	United States, Canada
2012–2013 North American drought	$49.6 – $56.1[25]	$67 – $75.7	104	Drought	2012-13	United States, Canada
2010 China floods	$51.4[26]	$74.1	3,189	Flood	2010	China, North Korea

Event	Cost ($ billion)		Fatalities	Type	Year	Nation(s)
	Actual	Inflated				
1994 Northridge earthquake	$49[27]	$104	57	Earthquake	1994	United States
2015 Southeast Asian haze	$47[28]	$62.3	100,300[29]	Wildfire, subsequent haze	2015	Southeast Asia (, , , others)
2016 Kumamoto earthquakes	$46[30]	$60.3	273	Earthquake	2016	Japan
2011 Thailand floods	$45.7[31]	$63.9	815	Flood	2011	Thailand
2023 South Asian floods	$41.6[32]	$42.9	2,309	Flood	2023	South Asia (, , , others)
2022 European heatwaves	$40.2[33]	$43.2	24,501	Heatwave	2022	Europe (, , , others)
2011 Christchurch earthquake	$40[34]	$55.9	185	Earthquake	2011	New Zealand
2022 Pakistan floods	$40[35]	$43	1,700	Flood	2022	Pakistan
Hurricane Ike	$38[13]	$55.5	214	Tropical cyclone	2008	North America (, , , others)
2020 China floods	$32[36][37]	$38.9	278[36]	Flood	2020	China
Typhoon Doksuri	$28.5[*citation needed*]	$29.4	137	Tropical cyclone	2023	Southeast Asia (, , , others)
2004 Chūetsu earthquake	$28[38][39]	$46.6	68	Earthquake	2004	Japan
Hurricane Wilma	$27.4[13]	$44.1	87	Tropical cyclone	2005	North America (, , others)

Event	Cost ($ billion)		Fatalities	Type	Year	Nation(s)
	Actual	Inflated				
Hurricane Andrew	$27.3[13]	$61.2	65	Tropical cyclone	1992	United States
February 13–17, 2021 North American winter storm	$26.5[40]	$30.8	237[41][42][43][44]	Winter storm, Infrastructure failure (electric)	2021	North America (, ,)
Hurricane Ivan	$26.1[13]	$43.4	124	Tropical cyclone	2004	North America (, , , others)
Hurricane Michael	$25.1[45]	$31.4	74	Tropical cyclone	2018	North America (, , , others)
2018 California wildfires	$24.0[25]	$30.1	103	Wildfire	2018	United States
2011 Sikkim earthquake	$22.3[46]	$31.2	111	Earthquake	2011	Southern Asia (, , , others)
2016 China floods	$22[47]	$28.8	449	Flood	2016	China
September 11 terrorist attacks	$21.8 – $135[48]	$38.7 – $239.7	2,996	Terror attack	2001	United States
Storm Daniel	$21.1[49]	$21.8	5,951 – 20,000	Tropical cyclone, Dam failure	2023	Libya, Greece
2021 Henan floods	$20.9[50]	$24.3	398 (official confirmed)	Flood	2021	China
1980 Irpinia earthquake	$20[51]	$76.3	4,900	Earthquake	1980	Italy
2024 Central European floods	$20[52]	$20	27	Flood	2024	Central Europe (, , , others)
2002 European floods	$19.2	$33.6	232	Flood	2002	Central Europe (, , , others)

Event	Cost ($ billion)		Fatalities	Type	Year	Nation(s)
	Actual	Inflated				
Hurricane Laura	$19.1[36][53]	$23.2	77	Tropical cyclone	2020	North America (, , , others)
Hurricane Rita	$18.5[13]	$29.8	97 – 125	Tropical cyclone	2005	United States
Cyclone Lothar	$17.6[54]	$33.2	140	European windstorm	1999	Western Europe (, , , others)
Typhoon Hagibis	$17.3[55]	$21.3	139	Tropical cyclone	2019	Japan
Hurricane Charley	$16.9[13]	$28.1	35	Tropical cyclone	2004	North America (, ,)
2012 Nigeria floods	$16.9[56]	$23.1	363	Flood	2012	Nigeria
2006 European heatwave	$16.3[57]	$23.9	3,418	Heatwave	2006	Europe (, , , others)
2009 L'Aquila earthquake	$16.0[58]	$23.5	308	Earthquake	2009	Italy
Hurricane Otis	$16.0[59]	$17	52 or more	Tropical cyclone	2023	Mexico
Typhoon Yagi	$15.8[citation needed]	$15.8	815	Tropical cyclone	2024	Southeast Asia (, , , , others)
2012 Northern Italy earthquakes	$15.8[60]	$21.6	27	Earthquake	2012	Italy
2013 European floods	$15.6[61]	$21.1	25	Flood	2013	Europe (, , , others)
Cyclone Amphan	$15.5[62][63]	$18.8	128[64]	Tropical cyclone	2020	Eastern South Asia (, , , others)
Hurricane Matthew	$15.1[65][66]	$19.8	731	Tropical cyclone	2016	North America (, , others)

Event	Cost ($ billion)		Fatalities	Type	Year	Nation(s)
	Actual	Inflated				
Great Flood of 1993	$15 – $20[67]	$32.7 – $43.5	47	Flood	1993	United States
Cyclones Daria, Vivian, and Wiebke	$15[68]	$36.1	197	European windstorm	1990	Western Europe (, , , others)
2004 Indian Ocean earthquake and tsunami	$15[1]	$25	230,000 – 280,000	Earthquake, Tsunami	2004	Southeast Asia (, , , others)
2010 Russian heat wave	$15[69]	$21.6	56,000	Wildfire, Heatwave	2010	Russia
October 2017 Northern California wildfires	$15[70][71] [*better source needed*]	$19.2	44	Wildfire	2017	United States
2010 Chile earthquake	$15 – $30[72]	$21.6 – $43.3	525	Earthquake	2010	Chile
2020 Beirut explosion	$15[73]	$18.2	218	Ammonium nitrate explosion	2020	Lebanon
2024 European floods	$14.9[74]	$14.9	337+	Flood	2024	Europe (, , , others)
2023 Western North America heat wave	$14.8[75]	$15.3	995	Heatwave	2023	North America (, ,)
2003 European heatwave	$14.5[76]	$24.8	72,000	Heatwave	2003	Europe (, , , others)
1988 Armenian earthquake	$14.2[77]	$37.8	38,000	Earthquake	1988	Armenia (Soviet Union)
Hurricane Irene	$14.2[13]	$19.8	58	Tropical cyclone	2011	North America (, , , others)

Event	Cost ($ billion)		Fatalities	Type	Year	Nation(s)
	Actual	Inflated				
Typhoon Jebi	$13[78]	$16.3	21	Tropical cyclone	2018	East Asia (, , , others)
Cyclone Nargis	$12.9[79]	$18.8	138,366	Tropical cyclone	2008	Myanmar
November 2015 Paris attacks	$12.7[80]	$16.8	130	Terror attack	2015	France
2015 South India floods	$12[81]	$15.9	506	Flood	2015	India
2020 Zagreb earthquake	$11.7[82]	$14.2	1	Earthquake	2020	Croatia, Slovenia
August 2020 Midwest derecho	$11.5[83]	$14	4[83]	Derecho	2020	United States
August 2016 Central Italy earthquake	$11[84]	$14.4	299	Earthquake	2016	Italy
2023 Emilia-Romagna floods	$11[85]	$11.4	17	Flood	2023	Italy
2024 Spanish floods	$11[86]	$11	232	Flood	2024	Spain
2025 Myanmar earthquake	$11[87]	$11	5,456	Earthquake	2025	Indochina (, , , others)
Typhoon Fitow	$10.4[88]	$14	12	Tropical cyclone	2013	China
2011 Super Outbreak + Hackleburg–Phil Campbell and Tuscaloosa–Birmingham tornadoes	$10.2[25]	$14.3	348	Tornado outbreak	2011	United States

Event	Cost ($ billion)		Fatalities	Type	Year	Nation(s)
	Actual	Inflated				
2021 Western North America heat wave	$10.1[75]	$11.7	1,400	Heat Wave	2021	Canada, United States
2016 Louisiana floods	$10 – $15[89]	$13.1 – $19.7	13	Flood	2016	United States
1980 United States heat wave	$10[25]	$38.2	1,700 – 10,000	Drought	1980	United States
Typhoon Mireille	$10[90]	$23.1	64	Tropical cyclone	1991	Japan
1999 Jiji earthquake	$10[91]	$18.9	2,415	Earthquake	1999	Taiwan
2007 Chūetsu earthquake	$10[92]	$15.2	11	Earthquake	2007	Japan
April 2015 Nepal earthquake	$10[93]	$13.3	8,964	Earthquake	2015	Southern Asia (, , , others)
Cyclone Kyrill	$10[68]	$15.2	44	European windstorm	2007	Western Europe (, , , others)
June 2008 Midwest floods	$10[25]	$14.6	16	Flood	2008	United States
1976 Tangshan earthquake	$10[25]	$55.3	242,419 – 655,000	Earthquake	1976	China
Typhoon Faxai	$10[94]	$12.3	3	Tropical cylone	2019	Japan, Wake Island
2014 Ludian earthquake	$9.91[95]	$13.2	615 – 727	Earthquake	2014	China
2018 Japan floods	$9.86 (official estimated) *[citation needed]*	$12.1	238 (official confirmed)	Flood	2018	Japan

Event	Cost ($ billion)		Fatalities	Type	Year	Nation(s)
	Actual	Inflated				
	[*citation needed*]		confirmed)			
Hurricane Frances	$9.8[13][96][97][98]	$16.3	50	Tropical cyclone	2004	North America (,)
Hurricane Hugo	$9.5[13]	$24.1	60	Tropical cyclone	1989	North America (, , , others)
Hurricane Georges	$9.4[13]	$18.1	604	Tropical cyclone	1998	North America (, , , others)
Typhoon Lekima	$9.28[99]	$11.4	105	Tropical cyclone	2019	Southeast Asia (, , , others)
Cyclone Gabrielle	$9.2[100]	$9.5	11	Tropical cyclone	2023	New Zealand
2022 Nigeria floods	$9.12[101]	$9.8	612	Flood	2022	Nigeria
Tropical Storm Allison	$9[102]	$16	55	Tropical cyclone	2001	United States, Canada
Typhoon Songda	$9[103]	$15	28	Tropical cyclone	2004	Japan
2022 Fukushima earthquake	$8.8[104]	$9.5	4	Earthquake	2022	Japan
1999 İzmit earthquake	$8.5[105]	$16	17,127 – 18,373	Earthquake	1999	Turkey
Tropical Storm Allison	$8.5[13]	$15.1	55	Tropical cyclone	2001	United States
Hurricane Gustav	$8.3[13]	$12.1	153	Tropical cyclone	2008	North America (, , , others)
Hurricane Eta	$8.3[36]	$10.1	189	Tropical cyclone	2020	Caribbean basin (, , , , others)
2010 Haiti earthquake	$8.1 – $14[106][107]	$11.7 – $20.2	100,000 – 220,000	Earthquake	2010	Haiti

Event	Cost ($ billion)		Fatalities	Type	Year	Nation(s)
	Actual	Inflated				
		$20.2	220,000			
Cyclone Fani	$8.1[108]	$10	89	Tropical cyclone	2019	India, Bangladesh
1990 Manjil–Rudbar earthquake	$8[109]	$19.3	45,000	Earthquake	1990	Iran
2017 Puebla earthquake	$8[110]	$10.3	370	Earthquake	2017	Mexico
Hurricane Jeanne	$7.9[13]	$13.2	3,035	Tropical cyclone	2004	North America (, , , others)
2016 Fort McMurray wildfire	$7.61[111][112]	$10	2	Wildfire	2016	Canada
2022 China heat wave	$7.6[113]	$8.2	50,900[114]	Heatwave	2022	China
2023 Slovenia floods	$7.6[115]	$7.8	7	Flood	2023	Julian Alps (, ,)
2001 Gujarat earthquake	$7.5[116]	$13.3	20,023	Earthquake	2001	India, Pakistan
2021 Pacific Northwest floods	$7.5[117]	$8.7	5	Flood	2021	Canada, United States
2024 Noto earthquake	>$7.4 (estimated)[118]	>$7.4	570	Earthquake	2024	Japan
Hurricane Sally	$7.3[83]	$8.9	5[83]	Tropical cyclone	2020	United States
Tornado outbreak sequence of May 19–27, 2024	$7.3[119]	$7.3	31	Tornado outbreak	2024	United States
Typhoon Rammasun	$7.13[120]	$9.5	196	Tropical cyclone	2014	Southeast Asia (, others)

Event	Cost ($ billion)		Fatalities	Type	Year	Nation(s)
	Actual	Inflated				
Typhoon Kammasun	$7.13[...]	$9.5	196	Tropical cyclone	2014	, , others)
2023 Al Haouz earthquake	$7[121]	$7.2	2,960	Earthquake	2023	Morocco
Exxon Valdez oil spill	$7[122]	$17.8	0	Contamination (Oil)	1989	North America (,)
Typhoon Nina + 1975 Banqiao Dam failure	$6.7[123]	$39.2	229,000	Tropical cyclone, Dam failure	1975	China, Taiwan
Hurricane Floyd	$6.5[13]	$12.3	74	Tropical cyclone	1999	North America (, ,)
2007 United Kingdom floods	$6.5[124]	$9.9	13	Flood	2007	United Kingdom
Typhoon Hato	$6.41[125][126][127]	$8.2	24	Tropical cyclone	2017	Southeast Asia (, , , others)
Space Shuttle Columbia disaster	$6.4[128]	$10.9	7	Space flight accident	2003	United States
Typhoon Saomai-Osang	$6.3[129]	$11.2	28	Tropical cyclone	2000	East Asia (, ,)
Black Saturday bushfires	$6.3[20]	$9.2	173	Wildfire	2009	Australia
2017 Iran–Iraq earthquake	$6.2[130]	$8	630	Earthquake	2017	Iran, Iraq
Typhoon Morakot	$6.2[131]	$9.1	789	Tropical cyclone	2009	Southeast Asia (, , , others)

Event	Cost ($ billion)		Fatalities	Type	Year	Nation(s)
	Actual	Inflated				
Hurricane Beryl	$6.2[132]	$6.2	70	Tropical cyclone	2024	, , , others)
Hurricane Mitch	$6.1[13]	$11.8	11,374+	Tropical cyclone	1998	North America (, , , others)
Cyclone Xynthia	$6.1[68]	$8.8	75	European windstorm	2010	Western Europe (, , , others)
2020 Petrinja earthquake	$6.1[133]	$7.4	7	Earthquake	2020	Balkans (, , , others)
Tornado outbreak of May 6–10, 2024	$6.1[119]	$6.1	6	Tornado outbreak	2024	United States
1989 Loma Prieta earthquake	$6[134]	$15.2	63	Earthquake	1989	United States
Typhoon Prapiroon	$6[135]	$11	75	Tropical cyclone	2000	Northeast Asia (, , , others)
Northeast blackout of 2003	$6[136]	$10.3	11	Infrastructure failure (electric)	2003	United States, Canada
Cyclone Klaus	$6[68]	$8.8	26	European windstorm	2009	Southeastern Europe (, , , others)
2013 Alberta floods	$6[137]	$8.1	5	Flood	2013	Canada
Typhoon Shanshan	$6[138]	$6	8	Tropical cyclone	2024	Japan, South Korea
Tornado outbreak of March 31–April 1, 2023	$5.7[139]	$5.9	33	Tornado outbreak	2023	United States

Event	Cost ($ billion)		Fatalities	Type	Year	Nation(s)
	Actual	Inflated				
2020 Kyushu floods	$5.67[...]	$6.9	77	Flood	2020	Japan
Cyclone Gudrun	$5.5[68]	$8.9	24	European windstorm	2005	North Europe (, , , others)
Hurricane Isabel	$5.5[13]	$9.4	51	Tropical cyclone	2003	United States
1993 Storm of the Century	$5.5[141]	$12	270[141]	Winter storm	1993	United States
2023 Hawaii wildfires	$5.5[119]	$5.7	102	Wildfire	2023	United States
2005 Kashmir earthquake	$5.2[142]	$8.4	86,000 – 87,351	Earthquake	2005	Pakistan , India
1980 El Asnam earthquake	$5.2[143]	$19.8	5,000	Earthquake	1980	Algeria
Hurricane Dorian	$5.1[144][145][146]	$6.3	84[145][146]	Tropical cyclone	2019	North America (, , , others)
1931 China floods	$5.07[147]	$104.8	422,499 – 4,000,000	Flood	1931	China
1985 Mexico City earthquake	$5[148]	$14.6	10,000 – 35,000	Earthquake	1985	Mexico
Typhoon Herb	$5[149]	$10	284 – 590	Tropical cyclone	1996	East Asia (, ,)
2003 Boumerdès earthquake	$5[51]	$8.5	2,266	Earthquake	2003	Algeria
2010 eruptions of Eyjafjallajökull	$5[150]	$7.2	0	Volcanic eruption	2010	Iceland, Northern Hemisphere (ash cloud only)

Event	Cost ($ billion)		Fatalities	Type	Year	Nation(s)
	Actual	Inflated				
						cloud only)
Tropical Storm Imelda	$5[151]	$6.1	5[151]	Tropical cyclone	2019	United States
2025 Tibet earthquake	$5[152]	$5	126	Earthquake	2025	Southern Asia (, ,)
2019 Karnataka floods	$4.95[153]	$6.1	61	Flood	2019	India
2014 Southeast Europe floods	$4.8[154]	$6.4	86	Flood	2014	Southeast Europe (, , , others)
2018 Kerala floods	$4.8[155]	$6	483	Flood	2018	India
2021–2022 Malaysian floods	$4.77[156]	$5.1	54	Flood	2022	Malaysia
Hurricane Opal	$4.7[13]	$9.7	63	Tropical cyclone	1995	North America (, , , others)
1997 Umbria and Marche earthquake	$4.67[157]	$9.1	11	Earthquake	1997	Italy
Typhoon Haiyan	$4.6[158][159][160]	$6.2	6,329 – 7,403	Tropical cyclone	2013	Southeast Asia (, , , others)
2022–2023 California floods	$4.6[161]	$4.7	22	Flood	2022-23	United States
1979 Montenegro earthquake	$4.5[162]	$19.5	136	Earthquake	1979	Yugoslavia (, ,)
1997 Central European flood	$4.5[163]	$8.8	114	Flood	1997	Central Europe (, ,)

Event	Cost ($ billion)		Fatalities	Type	Year	Nation(s)
	Actual	Inflated				
1997 Indonesian forest fires + 1997 Southeast Asian haze + Garuda Indonesia Flight 152	$4.47[164]	$8.8	240	Wildfire, subsequent haze and plane crash	1997	Southeast Asia (, , , others)
1999 Odisha cyclone	$4.44[165]	$8.4	9,887	Tropical cyclone	1999	South Asia (, , , others)
2020 Sudan floods	$4.43[166]	$5.4	100	Flood	2020	Sudan
Cyclone Gonu	$4.42[167]	$6.7	78	Tropical cyclone	2007	Oman, Iran
Hurricane Zeta	$4.4[168]	$5.3	9	Tropical cyclone	2020	North America and the Antiles (, , , others)
Typhoon Mawar	$4.3[169]	$4.4	6	Tropical cyclone	2023	West Pacific basin (, , , others)
Cyclone Phailin	$4.26[170]	$5.8	46	Tropical cyclone	2013	South Asia (, , , others)
1999 Athens earthquake	$4.2[171]	$7.9	143	Earthquake	1999	Greece
Typhoon Rusa	$4.2[172]	$7.3	238	Tropical cyclone	2002	East Asia (, , , others)
Hurricane Manuel	$4.2[173]	$5.7	123	Tropical cyclone	2013	Mexico
Tornado outbreak sequence of May 2003	$4.1[25]	$7	42	Tornado	2003	United States
2019 Iran floods	$4.1[174]	$5	77	Flood	2019	Iran

Event (Sort ascending)	Cost ($ billion)		Fatalities	Type	Year	Nation(s)
	Actual	Inflated				
2019 Iran floods	$4.1[174]	$5	77	Flood	2019	Iran
Great Storm of 1987	$4[68]	$11.1	22	European windstorm	1987	Western Europe (, , , others)
2017 Chiapas earthquake	$4[175]	$5.1	98	Earthquake	2017	Mexico, Guatemala
Hurricane Dennis	$3.98[176][177]	$6.4	88	Tropical cyclone	2005	North America and the Antiles (, , , others)
1983 Spanish floods	$3.9[178]	$12.3	34	Flood	1983	Spain
Hurricane Stan	$3.9[179]	$6.3	1,673	Tropical cyclone	2005	Central America (, , , others)
Hurricane Karl	$3.9[180]	$5.6	22	Tropical cyclone	2010	Mexico, Belize
Tornado outbreak of December 10–11, 2021	$3.9[181]	$4.5	90	Tornado	2021	United States
Cyclone Chido	$3.9[182]	$3.9	172+	Cyclone	2024	South-west Africa (, , , others)
Typhoon Mangkhut	$3.74[183]	$4.7	134	Tropical cyclone	2018	Southeast Asia (, , , others)
2024 Rio Grande do Sul floods	$3.7[184]	$3.7	181	Flood	2024	Brazil, Uruguay
Hurricane Isabel	$3.6[185]	$6.2	51	Tropical cyclone	2003	North America and the Antiles (, , , others)

Event	Cost ($ billion)		Fatalities	Type	Year	Nation(s)
	Actual	Inflated				
Cyclone Yasi	$3.6[186]	$4.6	7	Tropical cyclone	2011	Australia
Cyclone Hudhud	$3.58[187]	$4.8	124	Tropical cyclone	2014	India, Nepal
Typhoon Utor	$3.55[188]	$4.8	97	Tropical cyclone	2013	China, Philippines
Cyclone Matmo–Bulbul	$3.54[189]	$4.4	43	Tropical cyclone	2019	South Asia (, , , others)
Vargas tragedy	$3.5[190]	$6.6	10,000 – 30,000	Flood, landslide and mudflow	1999	Venezuela
2016 Kaikōura earthquake	$3.5[191]	$4.6	2	Earthquake	2016	New Zealand
Hurricane Idalia	$3.5[192]	$3.6	12	Tropical cyclone	2023	North America (, , , others)
Cyclone Vardah	$3.37[193]	$4.4	47	Tropical cyclone	2016	Indian Ocean basin (, , , others)
2022 eastern Australia floods	$3.33[194]	$3.6	27	Flood	2022	Australia
Hurricane Luis	$3.3[195]	$6.8	19	Tropical cyclone	1995	North America and the Antiles (, , , others)
2018 Hokkaido Eastern Iburi earthquake	$3.3[196]	$4.1	41	Earthquake	2018	Japan
1976 Çaldıran–Muradiye earthquake	$3.2[197]	$17.7	5,000	Earthquake	1976	Turkey, Iran

Sort ascending	Cost ($ billion)		Fatalities	Type	Year	Nation(s)
	Actual	Inflated				
Muradiye earthquake						
Space Shuttle Challenger disaster	$3.2[198]	$9.2	7[199]	Space flight accident	1986	United States
Typhoon Winnie	$3.2[200]	$6.3	372	Tropical cyclone	1997	East Asia (, , , others)
2010 Central European floods	$3.14[201]	$4.5	37	Flood	2010	Central Europe (, , , others)
Hurricane Isaac	$3.11[202][203]	$4.3	41	Tropical cyclone	2012	North America and the Antiles (, , , others)
1976 Moro Gulf earthquake	$3.1[204]	$17.1	8,000	Earthquake	1976	Philippines
Hurricane Iniki	$3.1[13]	$6.9	6	Tropical cyclone	1992	United States
2006 Yogyakarta earthquake	$3.1[205]	$4.8	5,749	Earthquake	2006	Indonesia
2019–20 Puerto Rico earthquakes	$3.1[206]	$3.8	4	Earthquake	2020	Puerto Rico
2023 Canadian wildfires	$3.1[207]	$3.2	8	Wildfire	2023	Canada, United States
Hurricane Delta	$3.09[208]	$3.8	6	Tropical cyclone	2020	North and Central America (, , , others)
Hurricane Fiona	$3.09[209][210]	$3.3	29	Tropical cyclone	2022	North America (, , , others)

Event	Cost ($ billion)		Fatalities	Type	Year	Nation(s)
	Actual	Inflated				
1964 Niigata earthquake	$3.0[211]	$30.4	36	Earthquake	1964	Japan
Hurricane Alicia	$3.0[212]	$9.5	21	Tropical cyclone	1983	United States
Hurricane Gilbert	$3.0[13]	$8	318	Tropical cyclone	1988	North America (, , , others)
2016 Ecuador earthquake	$3.0[213]	$3.9	676	Earthquake	2016	Latin America (, ,)
2019 Arkansas River floods	$3.0[214]	$3.7	5	Flood	2019	United States
Cyclone Yaas	$2.99[215]	$3.5	20	Tropical cyclone	2021	South Asia (, , , others)
June 2012 North American derecho	$2.9[25]	$4	22	Derecho	2012	United States
2019 Midwestern U.S. floods	$2.9[25]	$3.6	3	Flood	2019	United States
Tropical Storm Lee	$2.8[216]	$3.9	18	Tropical cyclone	2011	United States
2011 Joplin tornado	$2.8[217]	$3.9	158	Tornado	2011	United States
Cyclone Debbie	$2.73[218]	$3.5	14	Tropical cyclone	2017	Australia, New Zealand
AZF chemical plant explosion	$2.68[219]	$4.8	29	Explosion	2001	France
2010 Canterbury earthquake	$2.63[220]	$3.8	2	Earthquake	2010	New Zealand
1989 Newcastle earthquake	$2.6[221]	$6.6	13	Earthquake	1989	Australia

Event	Cost ($ billion)		Fatalities	Type	Year	Nation(s)
	Actual	Inflated				
Tornado outbreak sequence of May 2019	$2.5[25]	$3.1	8	Tornado	2019	United States
2017 Montana wildfires	$2.5[25]	$3.2	2	Drought, Wildfire	2017	United States
2017 Minneapolis hailstorm	$2.5[25]	$3.2	0	Hailstorm	2017	United States
Hurricane John	$2.5[222]	$2.5	29	Tropical cyclone	2024	Mexico
2024 Hualien earthquake	$2.5[223]	$2.5	19	Earthquake	2024	Eastern Asia (, ,)
Hurricane Michelle	$2.43[224]	$4.3	48	Tropical cyclone	2001	North and Central America (, , , others)
Severe weather sequence of July 13–16, 2024	$2.4[119]	$2.4	5	Derecho, tornado outbreak, flood	2024	United States
Typhoon Gaemi	$2.31[225][226]	$2.3	126	Tropical cyclone	2024	Southeast Asia (, , , others)
Cyclone Sidr	$2.3[227]	$3.5	15,000	Tropical cyclone	2007	Southern Asia (, , , others)
2009 Sumatra earthquakes	$2.3[228]	$3.4	1,115	Earthquake	2009	Indonesia
Typhoon Matsa	$2.23[229]	$3.6	25	Tropical cyclone	2005	East Asia (, , , others)
2022 Luding earthquake	$2.23[230]	$2.4	93	Earthquake	2022	China

Event	Cost ($ billion)		Fatalities	Type	Year	Nation(s)
	Actual	Inflated				
2017 Denver hailstorm	$2.2[25]	$2.8	0	Hailstorm	2017	United States
2011 Van earthquakes	$2.2[232]	$3.1	642	Earthquake	2011	Turkey
Cyclone Mocha	$2.2[233]	$2.3	463 – 564	Tropical cyclone	2023	Southern Asia (, , , , others)
Cyclone Roanu	$2.13[234]	$2.8	135	Tropical cyclone	2016	South Asia (, , , others)
Hurricane Agnes	$2.1[235]	$15.8	128	Tropical cyclone	1972	North America and the Antiles (, , , others)
Cyclones BOB 03 and Yemyin	$2.1[236][237]	$3.2	983	Tropical cyclone	2007	South Asia (, ,)
Tornado outbreak of March 6–7, 2017	$2.1[25]	$2.7	0	Tornado	2017	United States
Cyclone Komen	$2.06[238][239]	$2.7	167	Tropical cyclone	2015	South Asia (, ,)
2023 Jishishan earthquake	$2.05[240]	$2.1	151	Earthquake	2023	China
Typhoon In-fa	$2.04[241]	$2.4	6	Tropical cyclone	2021	East Asia (, , , others)
Teton Dam disaster	$2[242]	$11.1	11	Dam failure	1976	United States
1977 Vrancea earthquake	$2[243]	$10.4	1,700	Earthquake	1977	Black Sea basin (, , , others)

Event	Cost ($ billion)		Fatalities	Type	Year	Nation(s)
	Actual	Inflated				
Hurricane Joan–Miriam	$2[244]	$5.3	337	Tropical cyclone	1988	Central and South America (, , , others)
1999 Colombia earthquake	$2[245]	$3.8	1,900 – 5,800	Earthquake	1999	Colombia
December Storm	$2[246]	$3.8	20	European windstorm	1999	Central Europe (, ,)
2001 Nisqually earthquake	$2[247]	$3.6	1	Earthquake	2001	United States
Costa Concordia disaster	$2[248]	$2.7	33	Maritime disaster	2012	Italy
2013 Moore tornado	$2[249]	$2.7	26	Tornado	2013	United States
2022 Afghanistan floods	$2[250]	$2.1	670	Flood	2022	Afghanistan
2024 Persian Gulf floods	$2[251]	$2	46	Flood	2024	Persian Gulf basin (, , , others)
Hurricane Debby	$2[252]	$2	10	Tropical cyclone	2024	North America and Antiles (, , , others)
2003 Tokachi earthquake	$1.9[253]	$3.2	1	Earthquake	2003	Japan
Francis Scott Key Bridge collapse	$1.9[254]	$1.9	6	Bridge collapse	2024	United States
Cyclone Aila	$1.83[255]	$2.7	339	Tropical cyclone	2009	Bangladesh,

Event	Cost ($ billion)		Fatalities	Type	Year	Nation(s)
	Actual	Inflated				
Typhoon Hinnamnor	$1.81[256]	$1.9	20	Tropical cyclone	2022	East Asia (, , , others)
Hurricane Fifi–Orlene	$1.8[257]	$11.5	8,210	Tropical cyclone	1974	Central America (, , , others)
2011 Groundhog Day blizzard	$1.8[258]	$2.5	36[258]	Winter storm	2011	North America (, , ,)
2023 North India floods	$1.8[259]	$1.9	422	Flood	2023	India
Hurricane David	$1.79[260]	$7.8	2,078	Tropical cyclone	1979	North America and the Antiles (, , , others)
Hurricane Frederic	$1.77[261]	$7.7	12	Tropical cyclone	1979	North America and the Antiles (, , , others)
Cyclone Jal	$1.73[262]	$2.5	118	Tropical cyclone	2010	South and Southeast Asia (, , , others)
2018 Sulawesi earthquake and tsunami	$1.71[263]	$2.1	4,340 (confirmed)	Earthquake and tsunami	2018	Indonesia
Piper Alpha explosion	$1.7[264]	$5.8	165	Explosion (oil rig)	1988	United Kingdom
1991 Bangladesh cyclone	$1.7[265]	$3.9	138,866	Tropical cyclone	1991	Southern Asia (, , , others)
Deep Depression ARB 02	$1.64[266]	$2.4	180	Tropical cyclone	2008	Yemen
Typhoon Man-yi	$1.62[267]	$2.2	6	Tropical cyclone	2013	Japan

Event	Cost ($ billion)		Fatalities	Type	Year	Nation(s)
	Actual	Inflated				
2001 El Salvador earthquakes	$1.6[269]	$2.8	1,259	Earthquake	2001	Latin America (, ,)
Hurricane Dolly	$1.6[270][271]	$2.3	22	Tropical cyclone	2008	North and Central America (, , , others)
2013 Lushan earthquake	$1.6[272]	$2.2	216	Earthquake	2013	China
2021 Haiti earthquake	$1.6[273]	$1.9	2,248	Earthquake	2021	Haiti
Hurricane Allen	$1.57	$6	269	Tropical cyclone	1980	North America (, , , , others)
2020 Central Vietnam floods	$1.57[274]	$1.9	233	Flood	2020	Indochina (, ,)
Cyclone Tauktae	$1.57[275]	$1.8	174	Tropical cyclone	2021	South Asia (, , , others)
2022 KwaZulu-Natal floods	$1.57[276]	$1.7	436	Flood	2022	South Africa
2020 Elazığ earthquake	$1.56[277]	$1.9	41	Earthquake	2020	Turkey
2019 Dallas tornado	$1.55[278]	$1.9	0	Tornado	2019	United States
Cyclone Freddy	$1.53[279]	$1.6	1,434	Tropical cyclone	2023	Southern Africa (, , , others)
Autumn 2000 Western Europe floods	$1.52[280]	$2.8	20	Flood	2000	Western Europe (, , , others)
Hurricane Juan	$1.5[281]	$4.4	12	Tropical cyclone	1985	United States, Canada

Event	Cost ($ billion)		Fatalities	Type	Year	Nation(s)
	Actual	Inflated				
Hurricane Bob	$1.5[282]	$3.5	17	Tropical cyclone	1991	(, ,)
2003 Bam earthquake	$1.5[283]	$2.6	34,000	Earthquake	2003	Iran
Typhoon Talim	$1.5[284]	$2.4	172	Tropical cyclone	2005	Southeast Asia (, ,)
Hurricane Ingrid	$1.5[285]	$2	32	Tropical cyclone	2013	Mexico, United States
Cyclone Mekunu	$1.5[286]	$1.9	31	Tropical cyclone	2018	Arabian Peninsula (, ,)
Brumadinho dam disaster	$1.5[287]	$1.8	270	Dam failure	2019	Brazil
Typhoon Hagupit	$1.5[288]	$1.8	17	Tropical cyclone	2020	East Asia (, , , others)
Hurricane Francine	$1.5[289]	$1.5	0	Tropical cyclone	2024	United States, Mexico
Typhoon Jongdari	$1.48[290][291]	$1.9	0	Tropical cyclone	2018	Japan, China
Tropical Storm Etau (2009)	$1.44[292]	$2.1	28	Tropical cyclone	2009	Japan
2023 Auckland Anniversary Weekend floods	$1.43[293]	$1.5	4	Flood	2023	New Zealand
Hurricane Camille	$1.42[3]	$12.2	259	Tropical cyclone	1969	North America and the Antiles (, , , others)

Sort ascending	Cost ($ billion)		Fatalities	Type	Year	Nation(s)
	Actual	Inflated				
2020 Nashville tornado	$1.418[294][295]	$1.7	5	Tornado	2020	United States
Cyclone Winston	$1.4[296]	$1.8	44	Tropical cyclone	2016	Fiji
Cyclone Idai	$1.4[297]	$1.7	1,593	Tropical cyclone	2019	Southern Africa (, , , others)
Hurricane Iota	$1.4[36]	$1.7	84	Tropical cyclone	2020	Latin America (, , others)
2021 Cumbre Vieja volcanic eruption	$1.4[298]	$1.6	1	Volcanic eruption	2021	Spain
2009 Messina floods and mudslides	$1.39[299]	$2	31	Flood and mudslides	2009	Italy
Hurricane Elena	$1.3[300]	$3.8	9	Tropical cyclone	1985	United States, Cuba
Tropical Storm Fred	$1.3[258]	$1.5	7	Tropical cyclone	2021	North America and the Antiles (, , , others)
2021 Fukushima earthquake	$1.3[301]	$1.5	1	Earthquake	2021	Japan
1993 Latur earthquake	$1.3[105]	$2.8	9,748	Earthquake	1993	India
Hurricane Isidore	$1.28[302][303]	$2.2	22	Tropical cyclone	2002	North and Central America (, , , others)
2011 European floods	$1.25[304][305]	$1.7	17	Flood	2011	Europe and North Africa (, , , , others)

Event	Cost ($ billion)		Fatalities	Type	Year	Nation(s)
	Actual	Inflated				
Hurricane Odile	$1.25[306]	$1.7	18	Tropical cyclone	2014	Mexico, United States
Cedar Fire	$1.24 – $2[307]	$2.1 – $3.4	15	Wildfire	2003	United States
2020 Hyderabad floods	$1.23[308]	$1.5	98	Flood	2020	India
2020 Calgary hailstorm	$1.2 – $1.4[36][309][310]	$1.5 – $1.7	0	Hailstorm	2020	Canada
1965 Palm Sunday tornado outbreak	$1.217[311]	$12.1	266	Tornado outbreak	1965	United States
1996 Oman cyclone	$1.2[312]	$2.4	341	Tropical cyclone	1996	Arabian Sea basin (, ,)
January 2011 Rio de Janeiro floods and mudslides	$1.2[313]	$1.7	916	Flood, mudslides	2011	Brazil
Cyclone Veronica	$1.2[314]	$1.5	0	Tropical cyclone	2019	Australia, East Timor
Hurricane Elsa	$1.2[258]	$1.4	13	Tropical cyclone	2021	North America and the Antiles (, , , others)
July–August 2022 United States floods	$1.2[315]	$1.3	44	Flood	2022	United States
2023 São Paulo floods and landslides	$1.2[316]	$1.2	65	Flood, landslide	2023	Brazil
2024 Houston derecho	$1.2[119]	$1.2	8	Derecho	2024	United States

	Cost ($ billion)		Fatalities	Type	Year	Nation(s)
	Actual	Inflated				
Typhoon Fred	$1.18[317]	$2.5	3,063	Tropical cyclone	1994	East Asia (, ,)
Typhoon Haitang	$1.17[318]	$1.9	20	Tropical cyclone	2005	East Asia (, ,)
2010 Baja California earthquake	$1.15[319]	$1.7	4	Earthquake	2010	Mexico, United States
Cyclone Ita	$1.15[320][321]	$1.5	40	Tropical cyclone	2014	Oceania (, , , others)
Typhoon Bopha	$1.1[322]	$1.5	1,901	Tropical cyclone	2012	Philippines
Three Mile Island accident	$1.1[323]	$4.8	0	Contamination (Radiation)	1979	United States
1980 eruption of Mount St. Helens	$1.1[324]	$4.2	57	Volcanic eruption, Subsequent landslides and mudslides	1980	United States
Tropical Storm Agatha	$1.1[325]	$1.6	204	Tropical cyclone	2010	Central America (, , , others)
2013 North India floods	$1.1[326]	$1.5	6,054	Flood	2013	India, Nepal
May 2021 South Central United States flooding	$1.1[327]	$1.3	5	Flood	2021	United States
Hurricane Nicholas	$1.1[328]	$1.3	4	Tropical cyclone	2021	United States, Mexico
East Palestine, Ohio, train derailment	$1.1[329]	$1.1	0	Contamination (Hazardous materials)	2023	United States

Event	Cost ($ billion)		Fatalities	Type	Year	Nation(s)
	Actual	Inflated				
train derailment	$1.1[329]	$1.1	0	(Hazardous materials)	2023	United States
2019 Albania earthquake	$1.09[330]	$1.3	51	Earthquake	2019	Albania
2015 Tianjin explosions	$1.08 (official estimated) [*citation needed*]	$1.4	173 (official confirmed)	Explosion	2015	China
Typhoon Vamco	$1.06[331]	$1.3	102	Tropical cyclone	2020	Southeast Asia (, , others)
Cyclone Garance	$1.05[332]	$1.1	5	Tropical cyclone	2025	Southwest Indian Ocean (, ,)
Tropical Storm Alberto	$1.03[333]	$2.2	33	Tropical cyclone	1994	United States
Typhoon Damrey	$1.03[334]	$1.3	142	Tropical cyclone	2017	Southeast Asia (, , , others)
1923 Great Kantō earthquake	$1[335]	$18.5	142,800	Earthquake	1923	Japan
1948 Fukui earthquake	$1[336]	$13.1	3,769	Earthquake	1948	Japan
Vajont Dam disaster	$1[337]	$10.3	2,500	Landslide, subsequent Megatsunami and dam failure	1963	Italy
1963 Skopje earthquake	$1[338]	$10.3	1,100	Earthquake	1963	North Macedonia (Yugoslavia)
1972 Nicaragua earthquake	$1[339]	$7.5	10,000	Earthquake	1972	Nicaragua

Sort ascending	Cost ($ billion)		Fatalities	Type	Year	Nation(s)
	Actual	Inflated				
earthquake						
1976 Guatemala earthquake	$1[340]	$5.5	23,000	Earthquake	1976	Guatemala, Belize
Typhoon Ketsana	$1[341]	$1.5	921	Tropical cyclone	2009	Southeast Asia (, , ,)
Armero tragedy	$1[342]	$2.9	22,540	Volcano eruption, Mudslides	1985	Colombia
Surfside condominium collapse	$1	$1.2	98	Structure failure	2021	United States
1978 Thessaloniki earthquake	$1[109]	$4.8	50	Earthquake	1978	Greece, Yugoslavia, Bulgaria
1983 Sea of Japan earthquake	$1[343]	$3.2	104	Earthquake	1983	Japan
1985 Algarrobo earthquake	$1[344]	$2.9	177	Earthquake	1985	Chile
1987 Ecuador earthquakes	$1[345]	$2.8	1,000 – 5,000	Earthquake	1987	Ecuador
1988 Nepal earthquake	$1[346]	$2.7	709	Earthquake	1988	Nepal, India
1992 Cairo earthquake	$1[347]	$2.2	561	Earthquake	1992	Egypt
1994 Páez River earthquake	$1[348]	$2.1	1,100	Earthquake	1994	Colombia
1998 Adana–Ceyhan earthquake	$1[349]	$1.9	145	Earthquake	1998	Turkey

1999 Düzce earthquake	$1[350]	$1.9	845 – 894	Earthquake	1999	Turkey
1999 Bridge Creek–Moore tornado	$1[249]	$1.9	41	Tornado	1999	United States
2014 South Napa earthquake	$1[351]	$1.3	1	Earthquake	2014	United States
Cyclone Luban	$1[352]	$1.3	14	Tropical cyclone	2018	Arabian Sea basin (, ,)
Hurricane Nicole	$1[353]	$1.1	11	Tropical cyclone	2022	North America and the Antiles (, , , others)
2024 Chile wildfires	$1[354]	$1	137-507	Wildfire	2024	Chile

Under $1 billion [edit]

This table lists notable disasters which are estimated to have an economic cost of less than 1 billion United States dollars without taking inflation into account. This includes historical disasters, such as the Great Chicago Fire, which would surpass the value of $1 billion in modern currency.

Note: All damage figures are listed in millions of United States dollars.

List of disasters by cost. Under $1 billion. Actual, and inflated to 2024 (unless otherwise stated)

Event	Cost ($ millions)		Fatalities	Type	Year	Nation(s)
	Actual	Inflated				
Cyclone Akash	$982[355]	$1489	14	Tropical cyclone	2007	South Asia (, ,)
2013 Washington, Illinois tornado	$935[356][357]	$1262	3	Tornado	2013	United States
2016 Great Smoky Mountains wildfires	$922[358]	$1208	14	Wildfire	2016	United States
Daulatpur–Saturia tornado	$1.5-900[359][360]	$3.8 - $2283	1,300	Tornado	1989	Bangladesh
2020 Korea floods	$875[361]	$1063	32	Flood	2020	South Korea
1981 Gulf of Corinth earthquakes	$812[362]	$2808	22	Earthquake	1981	Greece
2019 Sichuan earthquake	$812[363]	$999	13	Earthquake	2019	China

5. Assignment 2, Module 1: Tropical Cyclone Definition: https://www.aoml.noaa.gov/hrd-faq/#what-is-a-hurricane

What Is a Tropical Cyclone, Tropical Disturbance, Tropical Depression, Tropical Storm, Hurricane, and Typhoon?

A ***tropical cyclone*** is a generic term for a low-pressure system that formed over tropical waters (25°S to 25°N) with thunderstorm activity near the center of its closed, cyclonic winds. Tropical cyclones derive their energy from vertical temperature differences, are symmetrical, and have a warm core.

If it lacks a closed circulation it is called a ***tropical disturbance***. If it has a closed circulation but under 39 mph (34 knots, or 17 meters per second) maximum sustained surface winds, it is called a ***tropical depression***. When winds exceed that threshold, it becomes a ***tropical storm*** and is given a name. Once winds exceed 74 mph (64 knots, 33 meters per second) it will be designated a ***hurricane*** (in the Atlantic or East Pacific Oceans) or a ***typhoon*** (in the northern West Pacific).

Tropical Disturbances -> Tropical Depressions -> Tropical Storms -> Hurricane or Typhoon.

What Is the Difference Between a Sub-tropical Cyclone, an Extra-tropical Cyclone, and a Post-tropical Cyclone?

The "**sub-tropical**" in sub-tropical cyclone refers to the latitudes 25°N to 35°N (or °S). However, the term refers to cyclones whose characteristics are neither fully tropical nor extratropical. They are either asymmetrical with a warm core or symmetrical with a cold core. Sub-tropical cyclones can transform into tropical or extra-tropical storms depending on conditions.

The "**extra-tropical**" in extra-tropical cyclone refers to the latitudes 35°N to 65°N (or °S). However, the term refers to cyclones that get their energy from the horizontal temperature contrasts that exist in the atmosphere. Extra-tropical cyclones are low-pressure systems generally associated with cold fronts, warm fronts, and occluded fronts. They are asymmetrical and have a cold core.

A **post-tropical cyclone** is a former tropical cyclone that no longer possesses sufficient characteristics to be considered a tropical cyclone, such as convection at its center. Post-tropical cyclones can continue producing heavy rains and high winds. Former tropical cyclones that have become fully **extra-tropical, sub-tropical, or remnant lows**, are three classes of post-tropical cyclones.

Neutercane is a term no longer in use. It referred to small (<100 miles in diameter) sub-tropical low-pressure systems that are short-lived.

6. Assignment 2, Module 1: South Atlantic Formation:https://www.aoml.noaa.gov/hrd-faq/#south-atlantic-and-tcs

Content of Website:

Why Doesn't the South Atlantic Ocean Experience Tropical Cyclones?

What never? Well, hardly ever.

In March, 2004 a hurricane DID form in the South Atlantic Ocean and made landfall in Brazil. But this still leaves the question of why hurricanes are so rare in the South Atlantic. Though many people might speculate that the sea surface temperatures are too cold, the primary reasons that the South Atlantic Ocean gets few tropical cyclones are that the tropospheric (near surface to 200mb) vertical wind shear is much too strong and there is typically no inter-tropical convergence zone (ITCZ) over the ocean (Gray 1968). Without an ITCZ to provide synoptic vorticity and convergence (i.e. large scale spin and thunderstorm activity) as well as having strong wind shear, it becomes very difficult to nearly impossible to have genesis of tropical cyclones.

In addition, McAdie and Rappaport (1991) documented the occurrence of a strong tropical depression/weak tropical storm that formed off the coast of Congo in mid-April of 1991. This storm lasted about five days and drifted toward the west-southwest into the central South Atlantic. So far, there has not been a systematic study as to the conditions that accompanied this rare event.

7. Assignment 2, Module 1: South Atlantic Formation (2): https://www.wral.com/why-don-t-hurricanes-form-in-the-south-atlantic-/1672862/

Content of Website:

Are there hurricanes or cyclones in the southern hemisphere near South America?

Mike Moss: The most proximate reasons for the lack of activity in the South Atlantic are sea surface temperatures that tend to run a shade cooler than ideal for tropical cyclone formation even in the southern summer, climatologically high values of vertical wind shear across that basin throughout the year, and a lack of pre-existing centers of rotation (vorticity) in that area. This last point is due both to the absence of tropical waves similar to those generated over west Africa in the northern hemisphere and to the fact the the Intertropical Convergence Zone (ITZC), which shifts toward the north in our summer and toward the south in the southern summer, usually stays at or north of the equator in the Atlantic Ocean (this zone of convergence, thunderstorms, horizontal wind shear and periodic low level rotation, and its cousin the Monsoon Trough in the Indian and Australian basins, are often formation regions in those basins and the central and eastern Pacific). A broad convergence zone like this need to reach about 5 degrees of latitude away from the equator in order for the Coriolis Force to have sufficient intensity to organize a full-fledged tropical cyclone, and the Atlantic ITCZ almost never shifts that far south, while the Monsoon trough in the Indian and Australian basins, and the western South Pacific, regularly does so.

The eastern South Pacific is just about as void of activity as the South Atlantic, due largely to the ITCZ also having a tendency to stay near or north of the equator, and to climatologically cool sea surface temperatures. Of course, one can then ask why are these factors aligned in such a way, which would make for a very long answer - the short version is they are all the result of the shapes, sizes, and distribution of continents and ocean basins, together with the character of the landform surfaces, and the Earth's tilted rotation axis and not quite circular orbit around the sun.

three possible such systems have been observed there since satellite monitoring began. The first was off Angola just west of Africa in 1991, another in January 2004 off Brazil, and most famously what has come to be named Cyclone Catarina, which reached apparent category 2 intensity before making landfall in southern Brazil on March 28, 2004.

Full question from Michael: Why don't hurricanes/cyclones regularly form in the South Atlantic ocean? What makes the South Atlantic different from the South Pacific and South Indian oceans in that regard? Thanks!

8. Assignment 2, Module 1: Hurricane vs. Typhoon: https://oceanservice.noaa.gov/facts/cyclone.html

Content of Website:

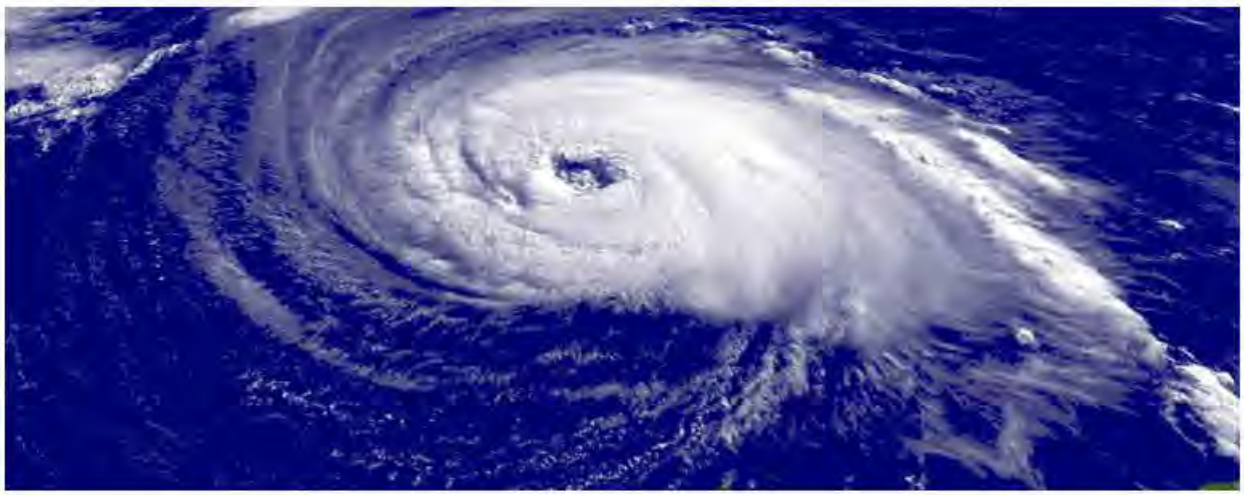

A close-up satellite image of Hurricane Isabel taken on Sept. 15, 2003. The National Ocean Service helps coastal communities prepare for and recover from major coastal storms such as hurricanes.

Hurricanes and typhoons are the same weather phenomenon: tropical cyclones. A tropical cyclone is a generic term used by meteorologists to describe a rotating, organized system of clouds and thunderstorms that originates over tropical or subtropical waters and has closed, low-level circulation.

The weakest tropical cyclones are called *tropical depressions* . If a depression intensifies such that its maximum sustained winds reach 39 miles per hour, the tropical cyclone becomes a *tropical storm.* Once a tropical cyclone reaches maximum sustained winds of 74 miles per hour or higher, it is then classified as a hurricane, typhoon, or tropical cyclone, depending upon where the storm originates in the world. In the North Atlantic, central North Pacific, and eastern North Pacific, the term *hurricane* is used. The same type of disturbance in the Northwest Pacific is called a *typhoon* . Meanwhile, in the South Pacific and Indian Ocean, the generic term *tropical cyclone* is used, regardless of the strength of the wind associated with the weather system.

The ingredients for tropical cyclones include a pre-existing weather disturbance, warm tropical oceans, moisture, and relatively light winds. If the right conditions persist long enough, they can combine to produce the violent winds, large waves, torrential rains, and floods we associate with this phenomenon. At times, when a weather system does not meet all of these conditions, but is forecast to bring tropical storm or hurricane force winds to land in the next day or two, it is called a *potential tropical cyclone* in the Atlantic basin and the central and eastern North Pacific basins.

In the Atlantic, hurricane season officially runs from June 1 to November 30. Ninety-seven percent of tropical cyclone activity occurs during this time period. However, there is nothing magical about these dates. Hurricanes can and do occur outside of this six month period.

9. Assignment 2, Module 2: Hurricane Season:https://www.aoml.noaa.gov/hrd-faq/#when-is-hurricane-season

When Is Hurricane Season?

The Atlantic hurricane season is **June 1st to November 30th**. In the East Pacific, it runs from **May 15th to November 30th**. Hurricane Awareness week runs from May 25th through May 31st and is a great time to get your hurricane kit and plans up to date.

NOAA's seasonal outlook is released in late May and revised in early August. You can find the latest version here: NOAA Seasonal Outlook

Hurricanes have occurred outside of the official six month season , but these dates were selected to encompass the majority of Atlantic tropical cyclone activity (over 97%). When the Weather Bureau organized its new hurricane warning network in 1935 it scheduled a special telegraph line to connect the various centers to run from June 15th through November 15th. Those remained the start and end dates of the 'official' season until 1964, when it was decided to end the season on November 30th, and in 1965, when the start was moved to the beginning of June. These changes made the Atlantic hurricane season six months long and easier for people to remember.

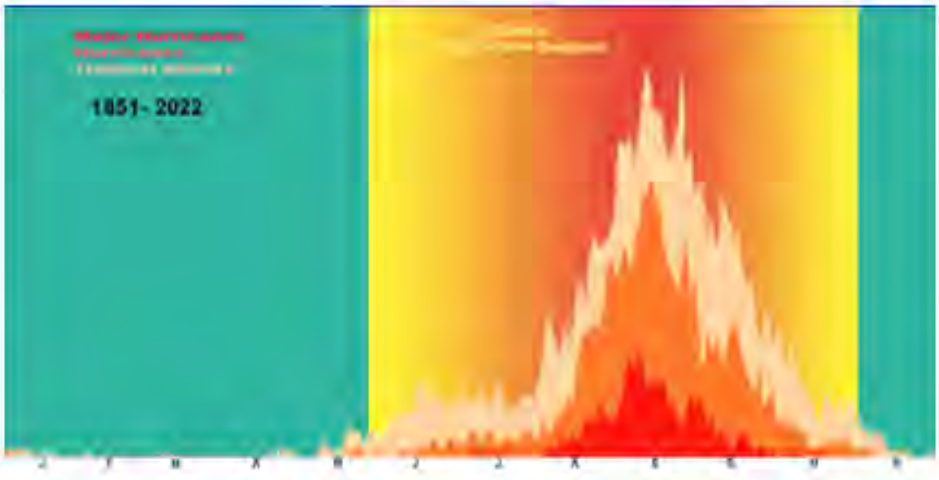

Atlantic Ocean tropical cyclone activity over a year

The Atlantic basin shows a very peaked season from August through October, with 78% of the tropical storm days, 87% of the minor hurricane days, and 96% of the major hurricane days occurring then (*Landsea (NHC)* 1993). Maximum activity occurs in early to mid September. "Out of season" tropical cyclones primarily occur in May or December.

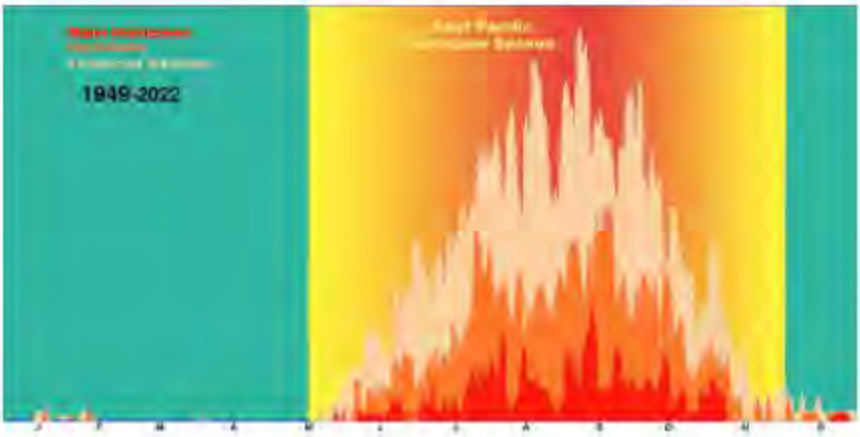

East Pacific Ocean tropical cyclone activity over a year

The Northeast Pacific basin has a broader peak with activity beginning in late May or early June and going until late October or early November with a peak in storminess in late August/early September. The National Hurricane Center's official dates for this basin are from May 15th to November 30th.

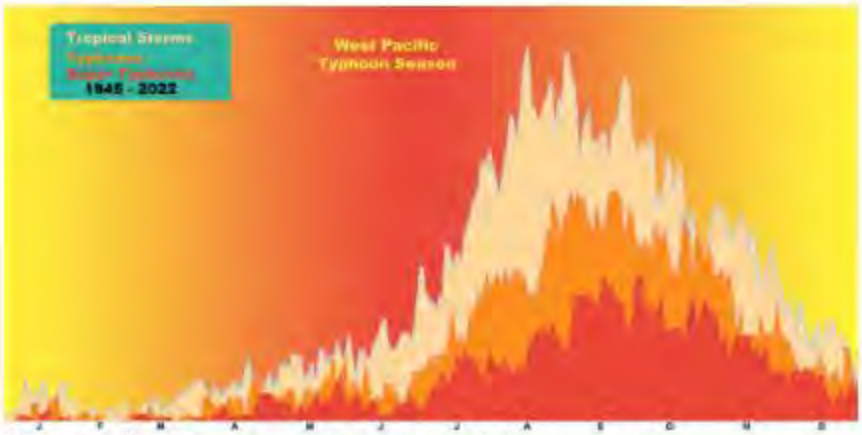

West Pacific Ocean tropical cyclone activity over a year

The Northwest Pacific basin has tropical cyclones occurring all year round regularly. There is no official definition of typhoon season for this reason. There is a distinct minimum in February and the first half of March, and the main season goes from July to November with a peak in late August/early September.

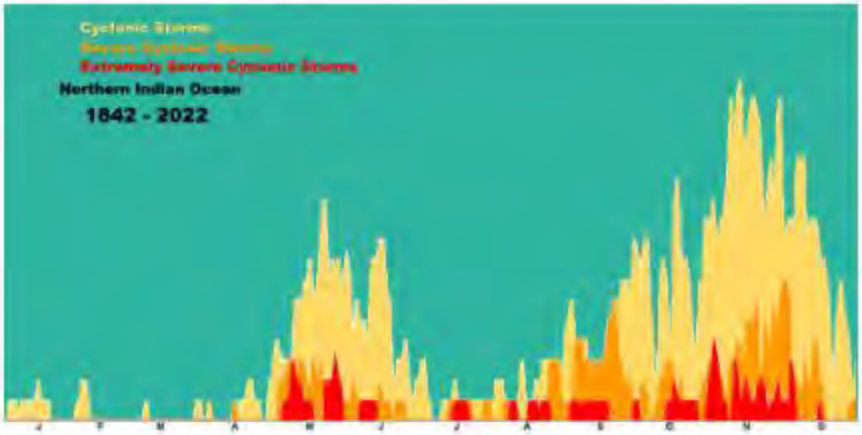

Northern Indian Ocean tropical cyclone activity over a year

The North Indian basin has a double peak of activity in May and November though tropical cyclones are seen from April to December. The severe cyclonic storms (>33 m/s winds [76 mph]) occur almost exclusively from April to June and late September to early December.

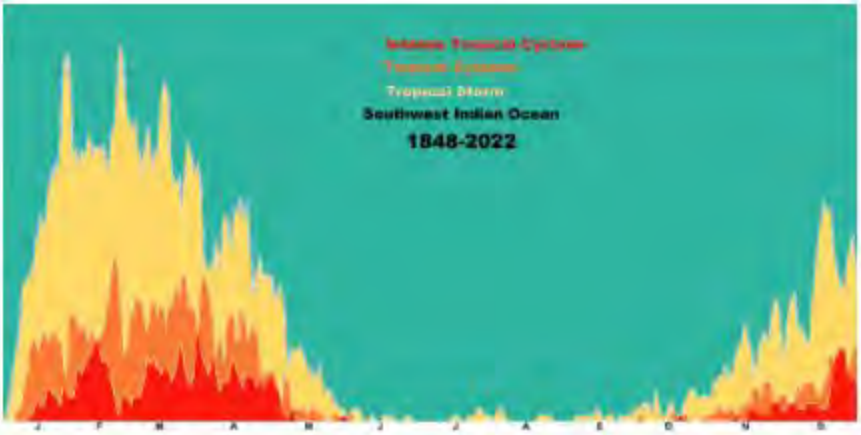

Southern Indian Ocean tropical cyclone activityn over a year

The Southwest Indian and Australian/Southeast Indian basins have very similar annual cycles with tropical cyclones beginning in late October/early November, reaching a peak in activity from mid-January to early May. The Australian/Southeast Indian basin February lull in activity is a bit more pronounced than the Southwest Indian basin's lull.

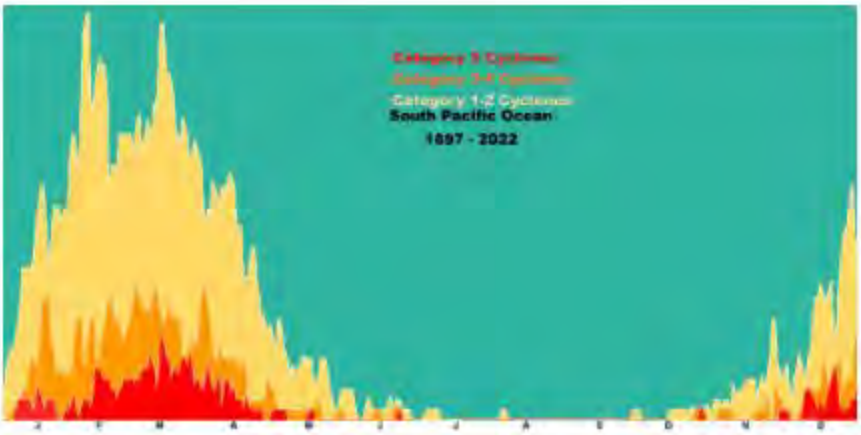

Southwestern Pacific Ocean tropical cyclone activity over a year

The Australian/Southwest Pacific basin begin with tropical cyclone activity in late October/early November, reaches a single peak in March, and then fades out in early May.

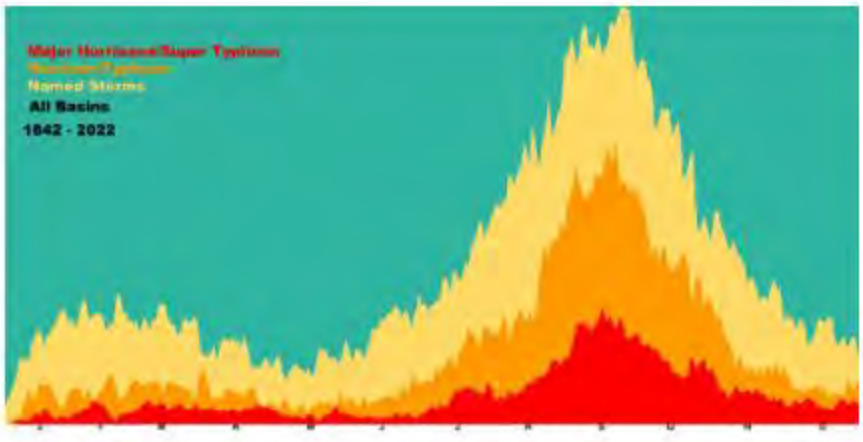

Global tropical cyclone activity over a year

Globally, September is the most active month and May is the least active month. (Neumann 1993)

10. Assignment 2, Module 2: Tropical Cyclone Climatology: https://www.nhc.noaa.gov/climo/

Overview

A tropical cyclone is a rotating, organized system of clouds and thunderstorms that originates over tropical or subtropical waters and has a closed low-level circulation. Tropical cyclones rotate counterclockwise in the Northern Hemisphere. They are classified as follows:

- **Tropical Depression:** A tropical cyclone with maximum sustained winds of 38 mph (33 knots) or less.
- **Tropical Storm:** A tropical cyclone with maximum sustained winds of 39 to 73 mph (34 to 63 knots).
- **Hurricane:** A tropical cyclone with maximum sustained winds of 74 mph (64 knots) or higher. In the western North Pacific, hurricanes are called typhoons; similar storms in the Indian Ocean and South Pacific Ocean are called cyclones.
- **Major Hurricane:** A tropical cyclone with maximum sustained winds of 111 mph (96 knots) or higher, corresponding to a Category 3, 4 or 5 on the Saffir-Simpson Hurricane Wind Scale.

Tropical cyclones forming between 5 and 30 degrees North latitude typically move toward the west. Sometimes the winds in the middle and upper levels of the atmosphere change and steer the cyclone toward the north and northwest. When tropical cyclones reach latitudes near 30 degrees North, they often move northeast.

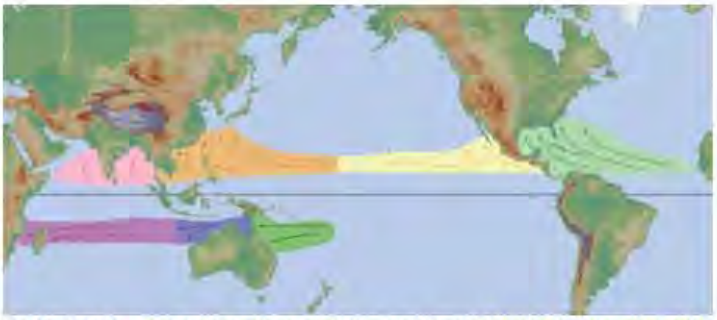

Tropical Cyclone formation regions with mean tracks (courtesy of the NWS JetStream Online School)

Atlantic and Eastern Pacific Hurricane Season Normal Activity

The Atlantic hurricane season runs from June 1 to November 30. The Atlantic basin includes the Atlantic Ocean, Caribbean Sea, and Gulf of America. Based on a 30-year climate period from 1991 to 2020, an average Atlantic hurricane season has 14 named storms, 7 hurricanes, and 3 major hurricanes (Category 3, 4, or 5 on the Saffir-Simpson Hurricane Wind Scale). The first named storm typically forms in mid to late June, the first hurricane tends to form in early to mid-August, and the first major hurricane forms in late August or early September.

The eastern Pacific hurricane season runs from May 15 to November 30. The eastern Pacific basin extends from Mexico and Central America westward to 140°W. Based on a 30-year climate period from 1991 to 2020, an average eastern Pacific hurricane season has 15 named storms, 8 hurricanes, and 4 major hurricanes. The first named storm typically forms in early to mid-June, the first hurricane tends to form in late June, and the first major hurricane forms in mid-July.

The following tables describe the progress of typical hurricane seasons in the Atlantic and eastern Pacific basins by showing benchmark dates when a given number of named storms, hurricanes, and major hurricanes typically forms. **It is important to note, however, that formation dates in individual hurricane seasons could vary considerably from these average dates.**

Table 1. Progress of the average Atlantic season (1991-2020). Date upon which the following number of events would normally have occurred.

Number	Named systems	Hurricanes	Major Hurricanes
1	Jun 20	Aug 11	Sep 1
2	Jul 17	Aug 26	Sep 19
3	Aug 3	Sep 7	Oct 28
4	Aug 15	Sep 16	-
5	Aug 22	Sep 28	-
6	Aug 29	Oct 15	-
7	Sep 3	Nov 15	-
8	Sep 9	-	-
9	Sep 16	-	-
10	Sep 22	-	-
11	Oct 2	-	-
12	Oct 11	-	-
13	Oct 25	-	-
14	Nov 19	-	-

Table 2. Progress of the average eastern Pacific season (1991-2020). Date upon which the following number of events would normally have occurred.

Number	Named systems	Hurricanes	Major Hurricanes
1	Jun 10	Jun 26	Jul 15
2	Jun 24	Jul 15	Aug 15
3	Jul 6	Jul 31	Sep 13
4	Jul 15	Aug 16	Oct 22
5	Jul 23	Aug 31	-
6	Aug 3	Sep 15	-
7	Aug 11	Sep 28	-
8	Aug 21	Oct 23	-
9	Aug 28	-	-
10	Sep 4	-	-
11	Sep 14	-	-
12	Sep 21	-	-
13	Oct 2	-	-
14	Oct 15	-	-
15	Nov 5	-	-

Seasonal Tropical Cyclone Activity

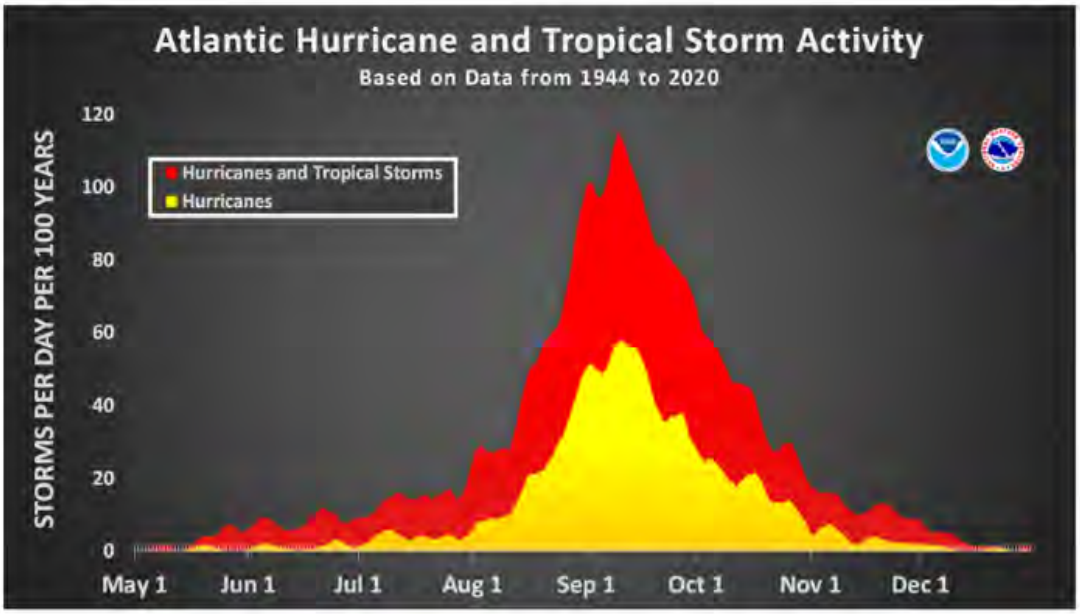

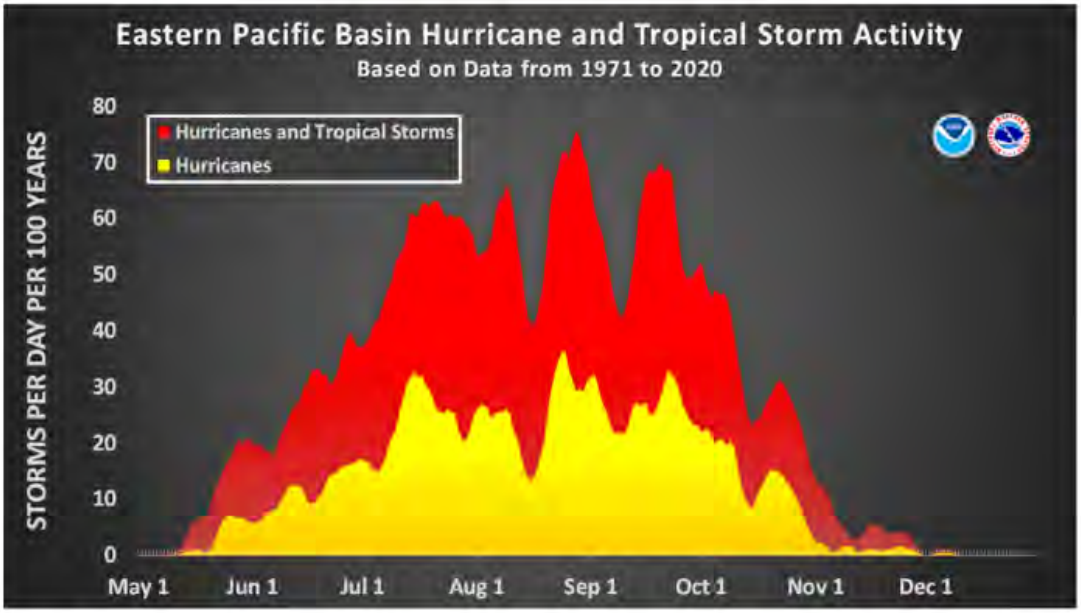

These charts show the amount of tropical cyclone activity, in terms of named storms and hurricanes, that occurs in the Atlantic and east Pacific basins on each calendar day between May 1 and December 31. Specifically, they show the number of hurricanes (yellow area), and combined named storms and hurricanes (red area) that occur on each calendar day over a 100-year period. The data have been smoothed using a 5-day running average centered on each calendar day. For the Atlantic basin (the Atlantic Ocean, the Caribbean Sea, and the Gulf of America), the chart is based on data from the 77-year period from 1944 to 2020 (starting at the beginning of the aircraft reconnaissance era) but normalized to 100 years. The official hurricane season for the Atlantic basin is from June 1 to November 30, but tropical cyclone activity sometimes occurs before and after these dates, respectively. The peak of the Atlantic hurricane season is September 10, with most activity occurring between mid-August and mid-October. For the eastern Pacific basin, the analyses are based on data from the 50-year period from 1971 to 2020 (starting when there was reliable satellite imagery) but also normalized to 100 years. The official hurricane season for the eastern Pacific basin is from May 15 to November 30, but tropical cyclones occasionally occur before and after these dates, respectively. A peak in activity is noted in late August, but this peak is less pronounced than the peak in Atlantic activity. Relatively high levels of activity in the eastern Pacific tend to be spread out over a longer portion of the season than in the Atlantic, with most tropical cyclones occurring between late June and early October.

Points of Origin by 10-Day Period

The figures below show the points of tropical cyclone genesis by 10-day periods during the hurricane season. The source years include 1851-2024 for the Atlantic and 1949-2024 for the Eastern Pacific from the HURDAT database.


March 1-10 Tropical and Subtropical Cyclone Points of Origin
50°N
45°N
40°N
35°N
30°N
25°N
20°N
15°N
10°N
5°N
130°W
120°W
110°W
100°W
90°W
80°W
70°W
60°W
50°W
40°W
30°W
20°W
Pacific points from 1949-2024
Atlantic points from 1851-2024

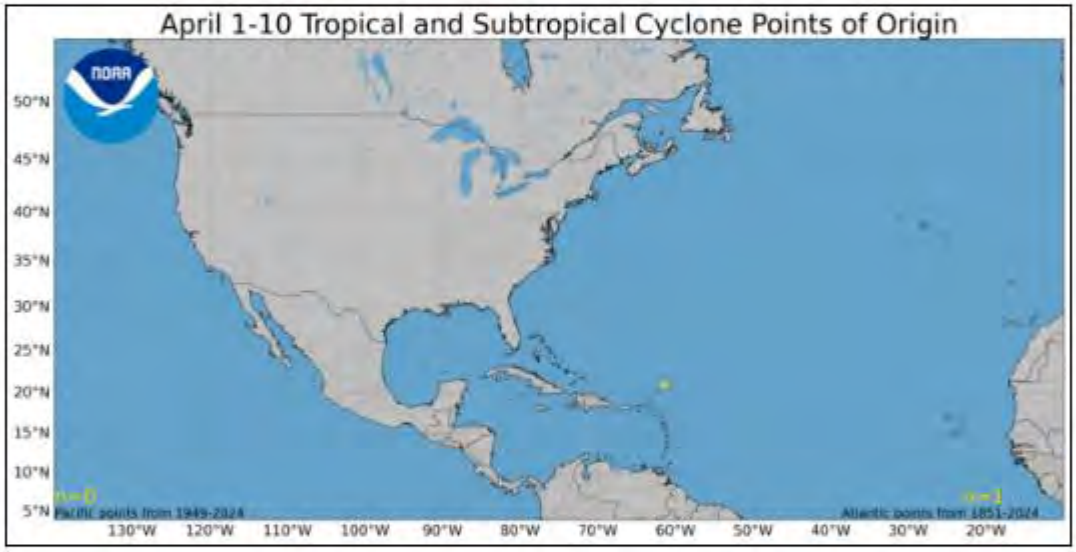
April 1-10 Tropical and Subtropical Cyclone Points of Origin
50°N
45°N
40°N
35°N
30°N
25°N
20°N
15°N
10°N
5°N
130°W
120°W
110°W
100°W
90°W
80°W
70°W
60°W
50°W
40°W
30°W
20°W
Pacific points from 1949-2024
Atlantic points from 1851-2024


April 11-20 Tropical and Subtropical Cyclone Points of Origin
50°N
45°N
40°N
35°N
30°N
25°N
20°N
15°N
10°N
5°N
130°W
120°W
110°W
100°W
90°W
80°W
70°W
60°W
50°W
40°W
30°W
20°W
Pacific points from 1949-2024
Atlantic points from 1851-2024

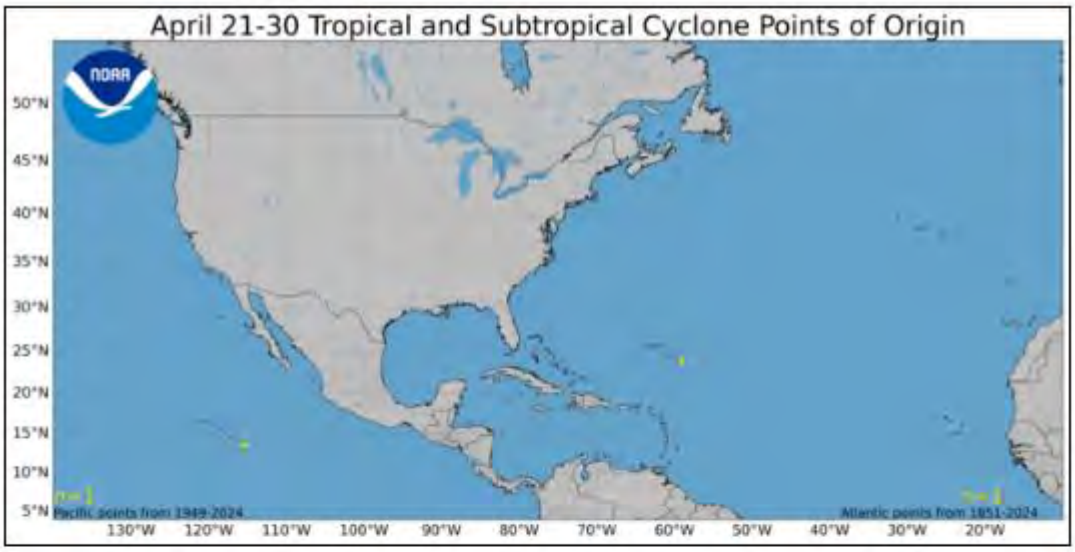
April 21-30 Tropical and Subtropical Cyclone Points of Origin
NOAA
50°N
45°N
40°N
35°N
30°N
25°N
20°N
15°N
10°N
5°N
n=1
Pacific points from 1949-2024
n=4
Atlantic points from 1851-2024
130°W
120°W
110°W
100°W
90°W
80°W
70°W
60°W
50°W
40°W
30°W
20°W

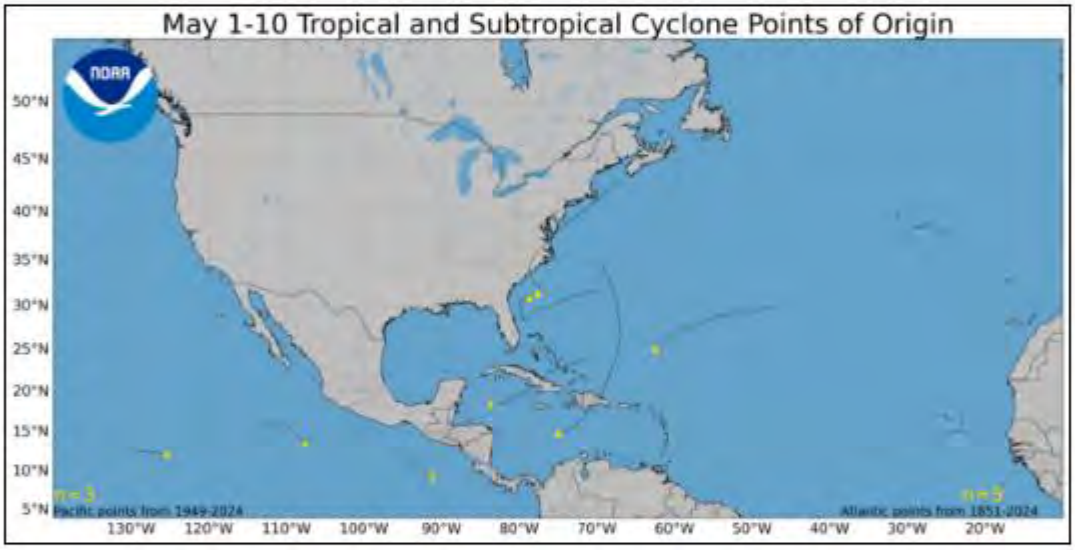
May 1-10 Tropical and Subtropical Cyclone Points of Origin
NOAA
50°N
45°N
40°N
35°N
30°N
25°N
20°N
15°N
10°N
5°N
n=3
Pacific points from 1949-2024
n=5
Atlantic points from 1851-2024
130°W
120°W
110°W
100°W
90°W
80°W
70°W
60°W
50°W
40°W
30°W
20°W

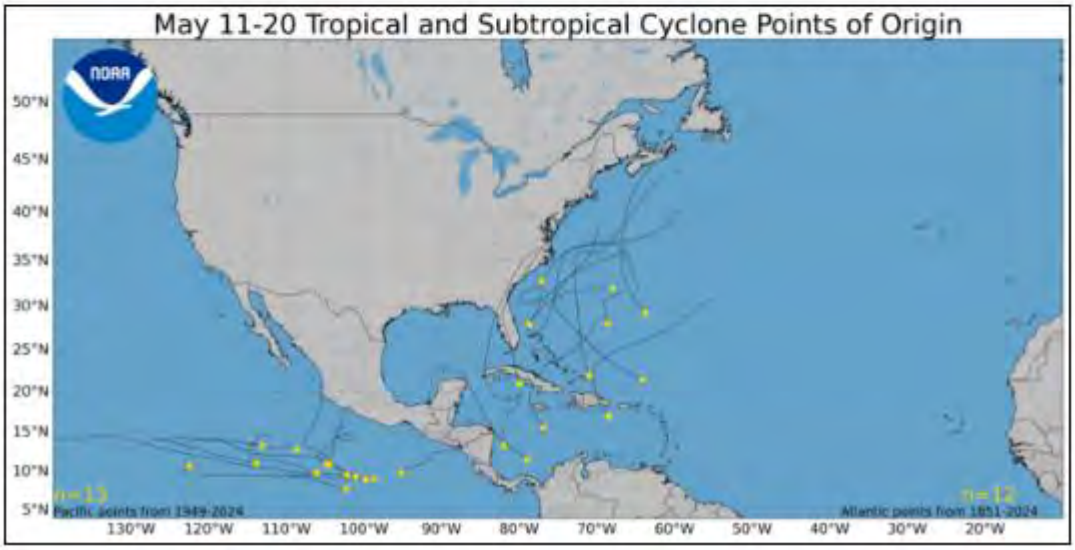
May 11-20 Tropical and Subtropical Cyclone Points of Origin
NOAA
50°N
45°N
40°N
35°N
30°N
25°N
20°N
15°N
10°N
5°N
n=13
Pacific points from 1949-2024
n=12
Atlantic points from 1851-2024
130°W
120°W
110°W
100°W
90°W
80°W
70°W
60°W
50°W
40°W
30°W
20°W


May 21-31 Tropical and Subtropical Cyclone Points of Origin
NOAA
50°N
45°N
40°N
35°N
30°N
25°N
20°N
15°N
10°N
5°N
n=31
Pacific points from 1949-2024
n=21
Atlantic points from 1851-2024
130°W
120°W
110°W
100°W
90°W
80°W
70°W
60°W
50°W
40°W
30°W
20°W

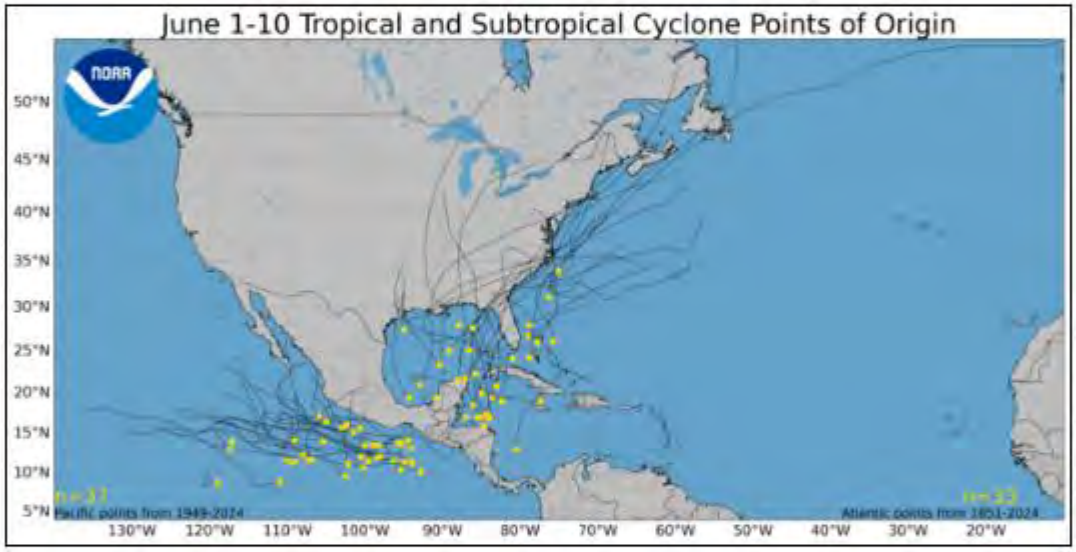
June 1-10 Tropical and Subtropical Cyclone Points of Origin
NOAA
50°N
45°N
40°N
35°N
30°N
25°N
20°N
15°N
10°N
5°N
n=37
Pacific points from 1949-2024
n=33
Atlantic points from 1851-2024
130°W
120°W
110°W
100°W
90°W
80°W
70°W
60°W
50°W
40°W
30°W
20°W

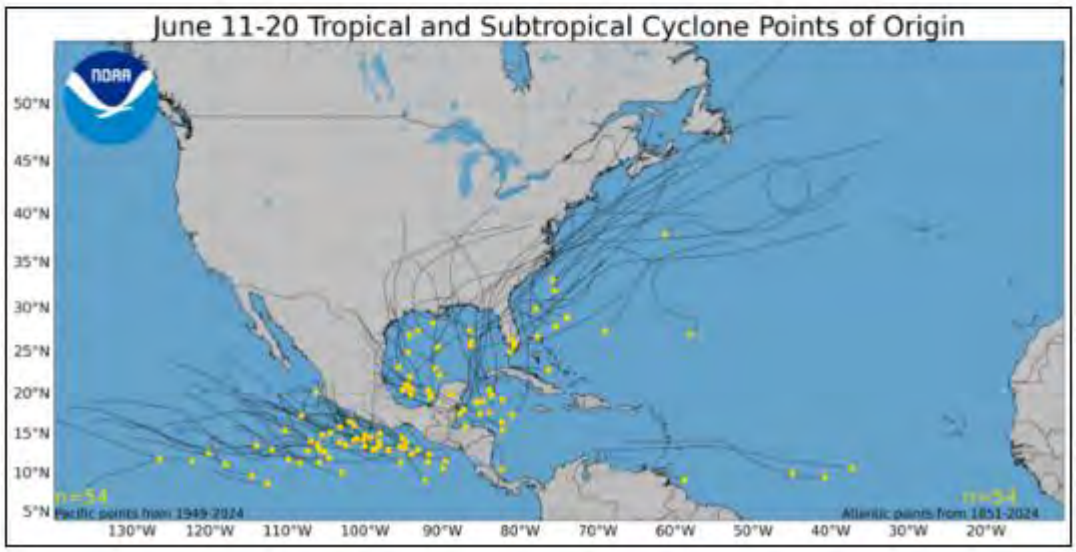
June 11-20 Tropical and Subtropical Cyclone Points of Origin
NOAA
50°N
45°N
40°N
35°N
30°N
25°N
20°N
15°N
10°N
5°N
n=54
Pacific points from 1949-2024
n=54
Atlantic points from 1851-2024
130°W
120°W
110°W
100°W
90°W
80°W
70°W
60°W
50°W
40°W
30°W
20°W

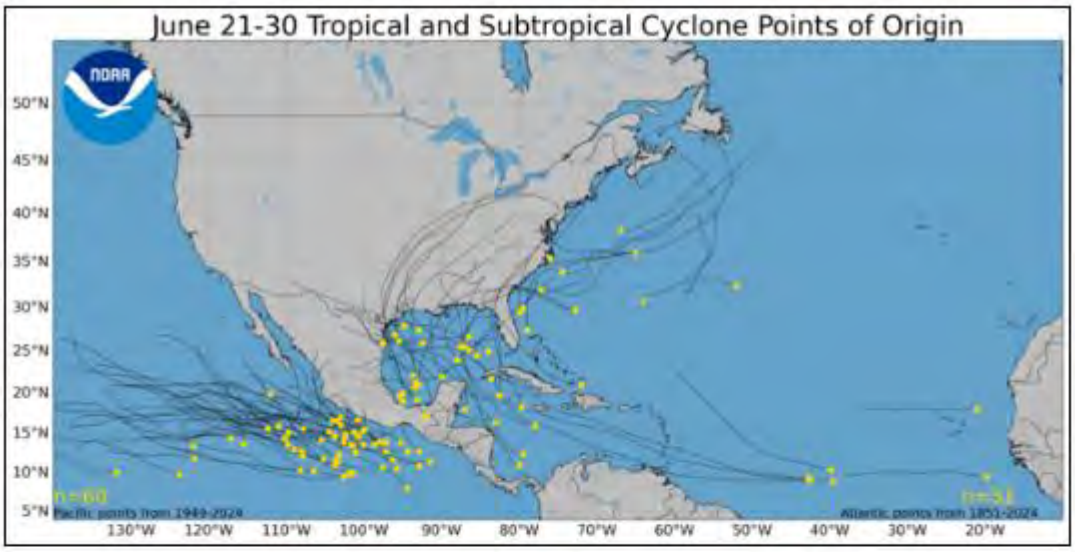
June 21-30 Tropical and Subtropical Cyclone Points of Origin
NOAA
50°N
45°N
40°N
35°N
30°N
25°N
20°N
15°N
10°N
5°N
130°W
120°W
110°W
100°W
90°W
80°W
70°W
60°W
50°W
40°W
30°W
20°W
n=60
Pacific points from 1949-2024
n=31
Atlantic points from 1851-2024


July 1-10 Tropical and Subtropical Cyclone Points of Origin
NOAA
50°N
45°N
40°N
35°N
30°N
25°N
20°N
15°N
10°N
5°N
130°W
120°W
110°W
100°W
90°W
80°W
70°W
60°W
50°W
40°W
30°W
20°W
n=39
Pacific points from 1949-2024
n=52
Atlantic points from 1851-2024

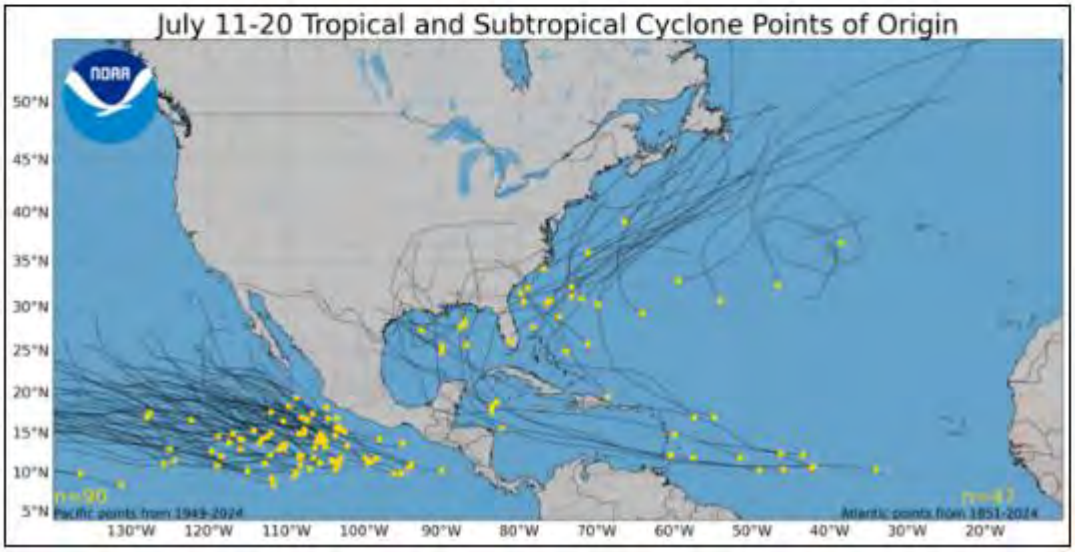
July 11-20 Tropical and Subtropical Cyclone Points of Origin
NOAA
50°N
45°N
40°N
35°N
30°N
25°N
20°N
15°N
10°N
5°N
130°W
120°W
110°W
100°W
90°W
80°W
70°W
60°W
50°W
40°W
30°W
20°W
n=90
Pacific points from 1949-2024
n=47
Atlantic points from 1851-2024

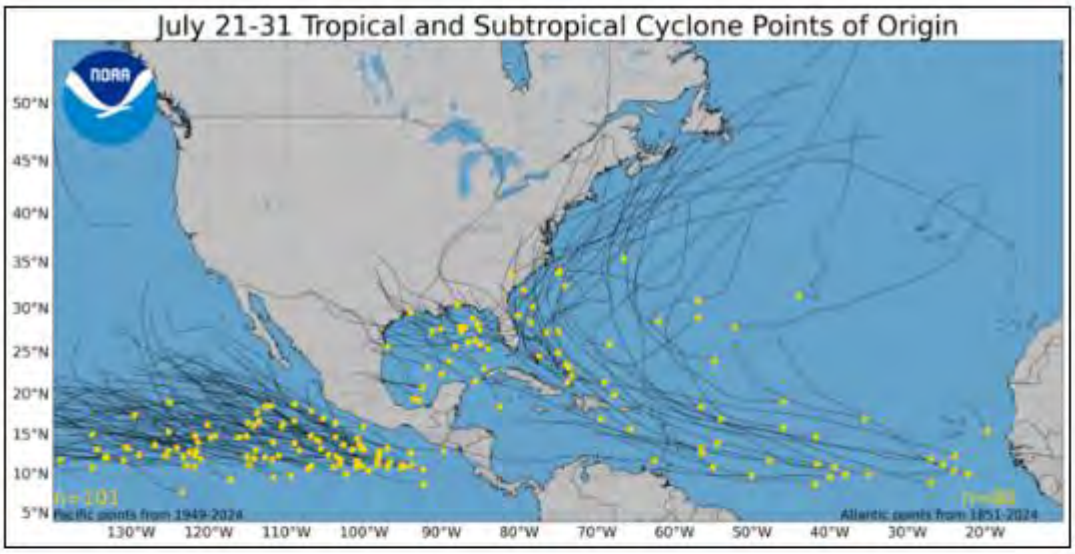
July 21-31 Tropical and Subtropical Cyclone Points of Origin
NOAA
50°N
45°N
40°N
35°N
30°N
25°N
20°N
15°N
10°N
5°N
130°W
120°W
110°W
100°W
90°W
80°W
70°W
60°W
50°W
40°W
30°W
20°W
n=101
Pacific points from 1949-2024
Atlantic points from 1851-2024

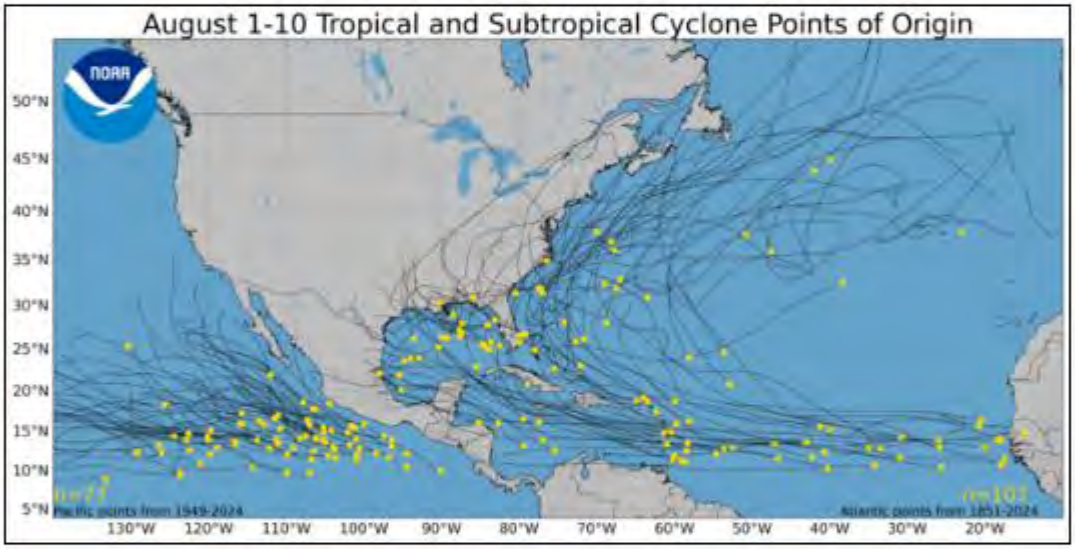
August 1-10 Tropical and Subtropical Cyclone Points of Origin
NOAA
50°N
45°N
40°N
35°N
30°N
25°N
20°N
15°N
10°N
5°N
130°W
120°W
110°W
100°W
90°W
80°W
70°W
60°W
50°W
40°W
30°W
20°W
Pacific points from 1949-2024
Atlantic points from 1851-2024

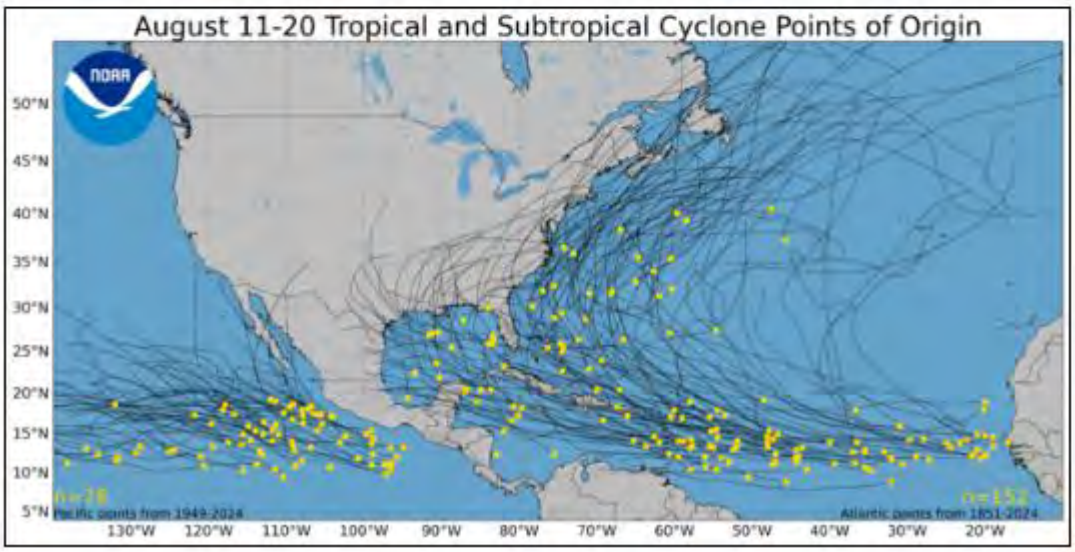
August 11-20 Tropical and Subtropical Cyclone Points of Origin
NOAA
50°N
45°N
40°N
35°N
30°N
25°N
20°N
15°N
10°N
5°N
130°W
120°W
110°W
100°W
90°W
80°W
70°W
60°W
50°W
40°W
30°W
20°W
Pacific points from 1949-2024
Atlantic points from 1851-2024

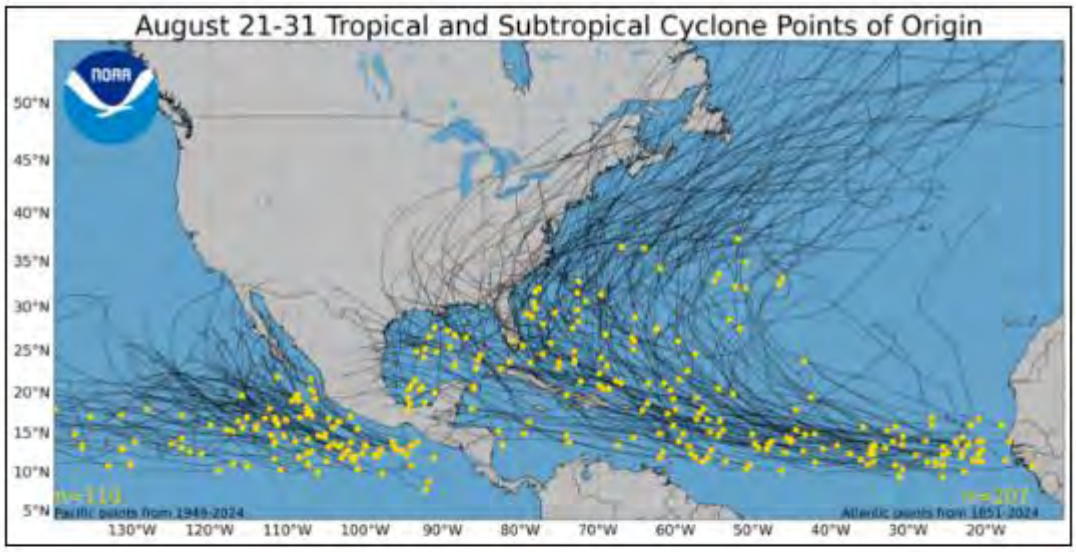
August 21-31 Tropical and Subtropical Cyclone Points of Origin
NOAA
50°N
45°N
40°N
35°N
30°N
25°N
20°N
15°N
10°N
5°N
130°W
120°W
110°W
100°W
90°W
80°W
70°W
60°W
50°W
40°W
30°W
20°W
n=110
Pacific points from 1949-2024
n=207
Atlantic points from 1851-2024

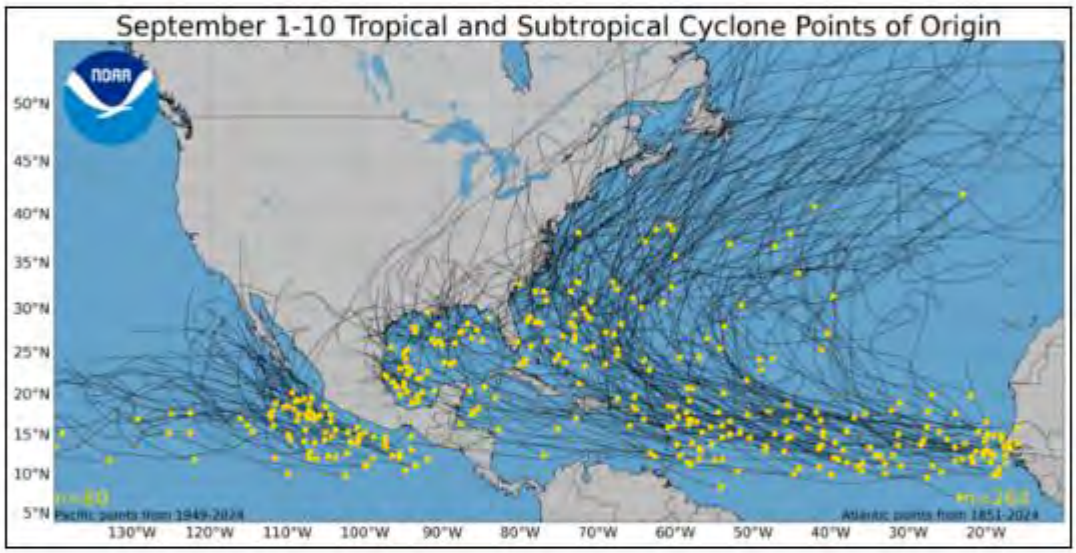
September 1-10 Tropical and Subtropical Cyclone Points of Origin
NOAA
50°N
45°N
40°N
35°N
30°N
25°N
20°N
15°N
10°N
5°N
130°W
120°W
110°W
100°W
90°W
80°W
70°W
60°W
50°W
40°W
30°W
20°W
n=80
Pacific points from 1949-2024
n=263
Atlantic points from 1851-2024

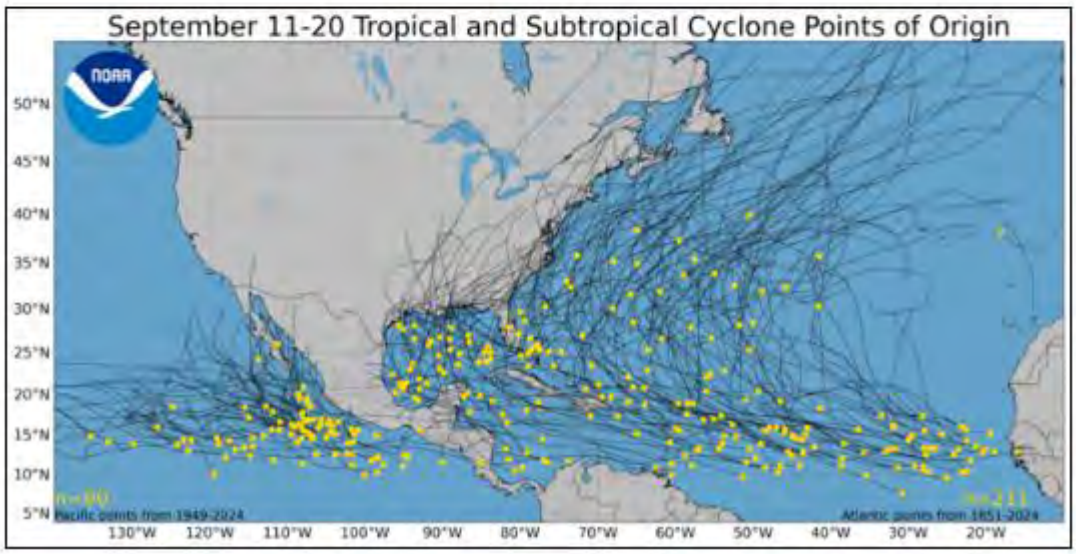
September 11-20 Tropical and Subtropical Cyclone Points of Origin
NOAA
50°N
45°N
40°N
35°N
30°N
25°N
20°N
15°N
10°N
5°N
130°W
120°W
110°W
100°W
90°W
80°W
70°W
60°W
50°W
40°W
30°W
20°W
n=80
Pacific points from 1949-2024
n=211
Atlantic points from 1851-2024


September 21-30 Tropical and Subtropical Cyclone Points of Origin
NOAA
50°N
45°N
40°N
35°N
30°N
25°N
20°N
15°N
10°N
5°N
130°W
120°W
110°W
100°W
90°W
80°W
70°W
60°W
50°W
40°W
30°W
20°W
n=73
Pacific points from 1949-2024
n=160
Atlantic points from 1851-2024

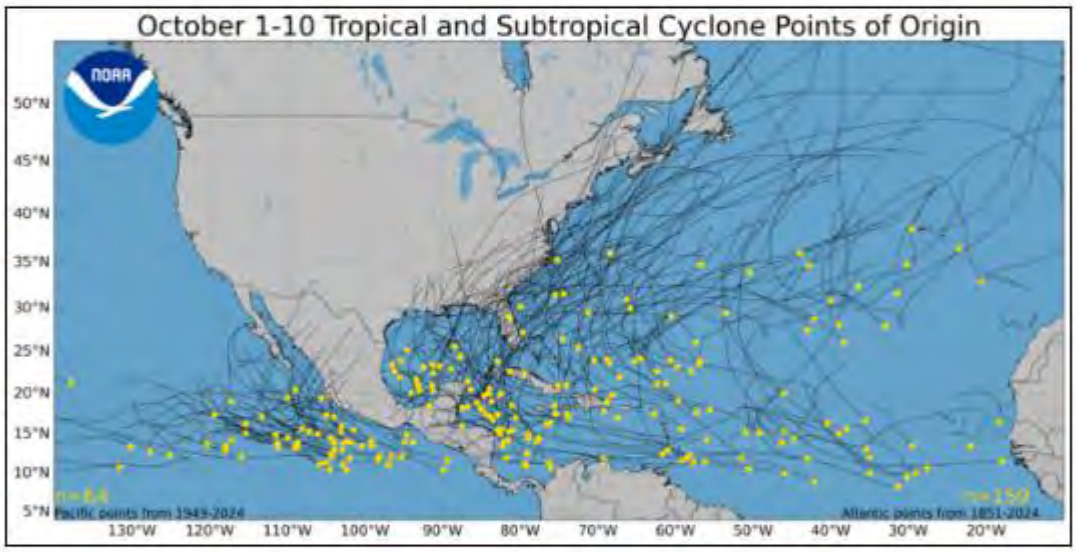
October 1-10 Tropical and Subtropical Cyclone Points of Origin
NOAA
50°N
45°N
40°N
35°N
30°N
25°N
20°N
15°N
10°N
5°N
130°W
120°W
110°W
100°W
90°W
80°W
70°W
60°W
50°W
40°W
30°W
20°W
n=84
Pacific points from 1949-2024
n=150
Atlantic points from 1851-2024


October 11-20 Tropical and Subtropical Cyclone Points of Origin
NOAA
50°N
45°N
40°N
35°N
30°N
25°N
20°N
15°N
10°N
5°N
130°W
120°W
110°W
100°W
90°W
80°W
70°W
60°W
50°W
40°W
30°W
20°W
n=52
Pacific points from 1949-2024
n=129
Atlantic points from 1851-2024

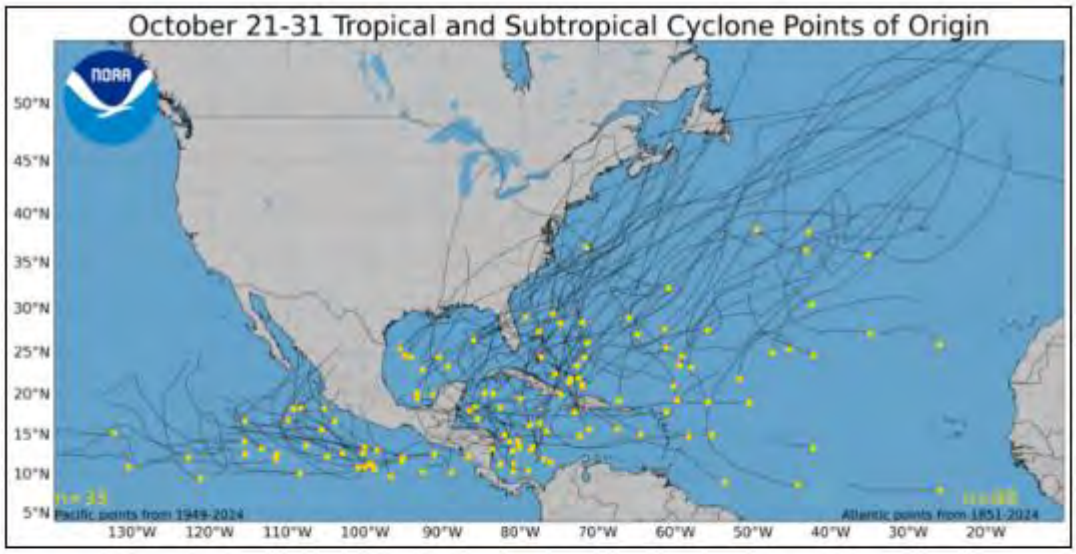
October 21-31 Tropical and Subtropical Cyclone Points of Origin
NOAA
50°N
45°N
40°N
35°N
30°N
25°N
20°N
15°N
10°N
5°N
130°W
120°W
110°W
100°W
90°W
80°W
70°W
60°W
50°W
40°W
30°W
20°W
n= 23
Pacific points from 1949-2024
n=68
Atlantic points from 1851-2024

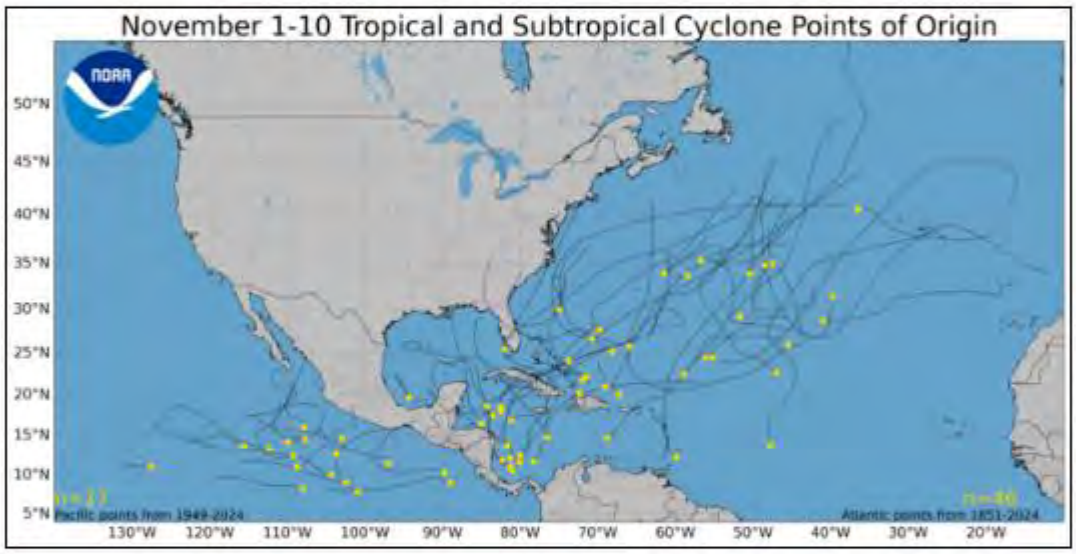
November 1-10 Tropical and Subtropical Cyclone Points of Origin
NOAA
50°N
45°N
40°N
35°N
30°N
25°N
20°N
15°N
10°N
5°N
130°W
120°W
110°W
100°W
90°W
80°W
70°W
60°W
50°W
40°W
30°W
20°W
n= 17
Pacific points from 1949-2024
n=40
Atlantic points from 1851-2024

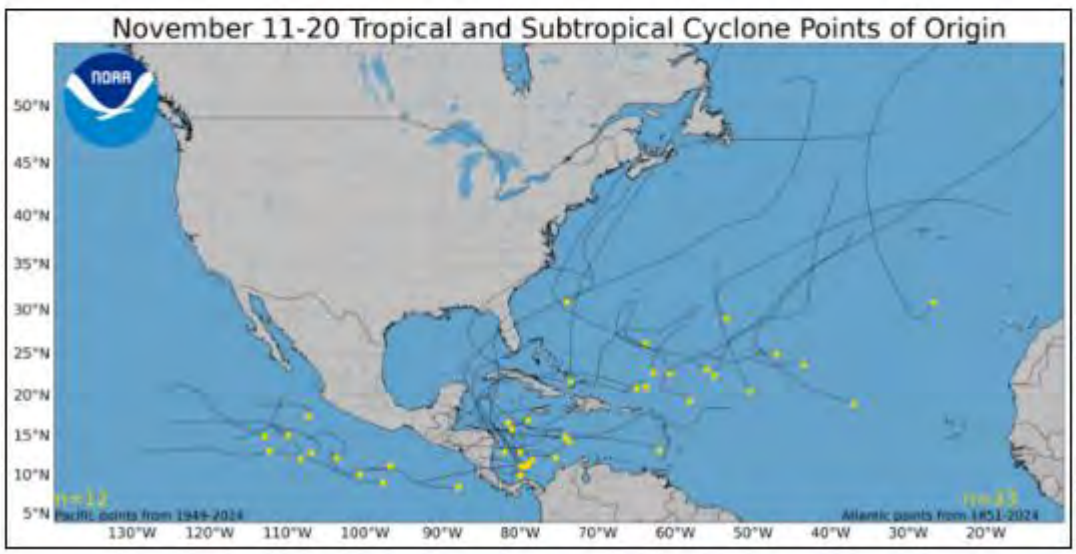
November 11-20 Tropical and Subtropical Cyclone Points of Origin
NOAA
50°N
45°N
40°N
35°N
30°N
25°N
20°N
15°N
10°N
5°N
130°W
120°W
110°W
100°W
90°W
80°W
70°W
60°W
50°W
40°W
30°W
20°W
n= 12
Pacific points from 1949-2024
n=43
Atlantic points from 1851-2024

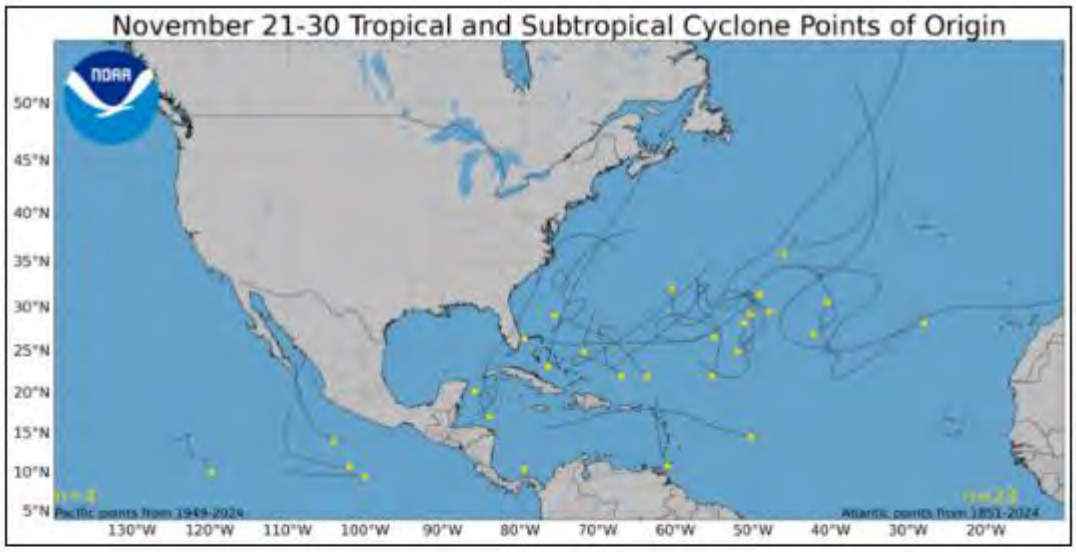
November 21-30 Tropical and Subtropical Cyclone Points of Origin
NOAA
50°N
45°N
40°N
35°N
30°N
25°N
20°N
15°N
10°N
5°N
130°W
120°W
110°W
100°W
90°W
80°W
70°W
60°W
50°W
40°W
30°W
20°W
n=8
Pacific points from 1949-2024
n=23
Atlantic points from 1851-2024

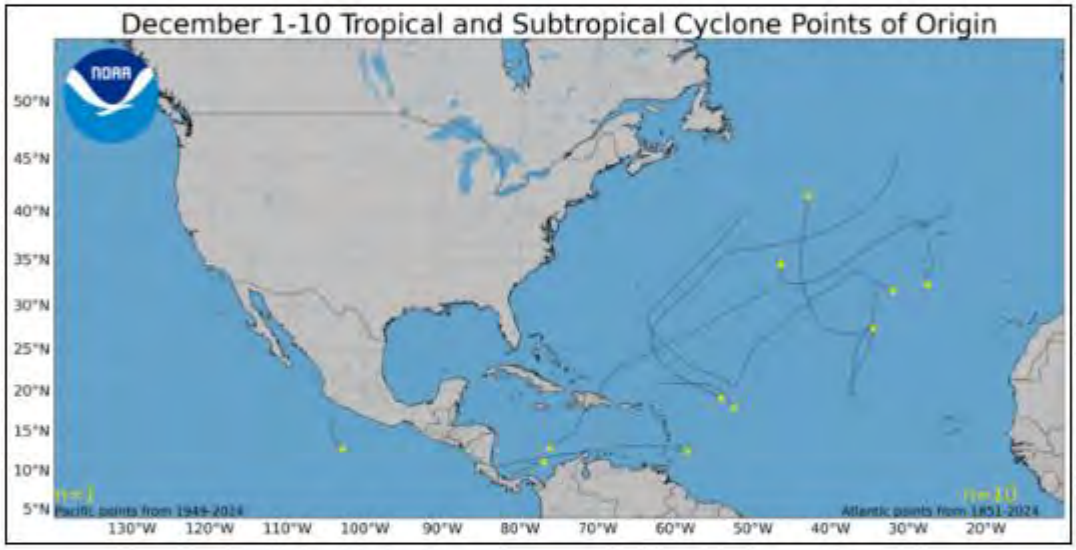
December 1-10 Tropical and Subtropical Cyclone Points of Origin
NOAA
50°N
45°N
40°N
35°N
30°N
25°N
20°N
15°N
10°N
5°N
130°W
120°W
110°W
100°W
90°W
80°W
70°W
60°W
50°W
40°W
30°W
20°W
n=1
Pacific points from 1949-2024
n=10
Atlantic points from 1851-2024


December 11-20 Tropical and Subtropical Cyclone Points of Origin
NOAA
50°N
45°N
40°N
35°N
30°N
25°N
20°N
15°N
10°N
5°N
130°W
120°W
110°W
100°W
90°W
80°W
70°W
60°W
50°W
40°W
30°W
20°W
n=0
Pacific points from 1949-2024
n=2
Atlantic points from 1851-2024

Typical Tropical Cyclone Occurrence Areas by Month

These maps show where tropical cyclones (named storms and hurricanes) tend to occur during each month of the hurricane season. The data are shown as the number of named storms or hurricanes whose centers pass within 150 nautical miles of a point on the map during a 100-year period. For the Atlantic basin, the analyses are based on data from the 77-year period from 1944 to 2020 (starting at the beginning of the aircraft reconnaissance era) but normalized to 100 years. For the eastern and central Pacific basins, the analyses are based on data from the 50-year period from 1971 to 2020 (starting when there was reliable satellite imagery) but also normalized to 100 years. Please note that the map legends vary from basin to basin and between named storms and hurricanes (but not between months) in order to make climatological patterns more apparent.

Atlantic Named Storms

Atlantic Hurricanes

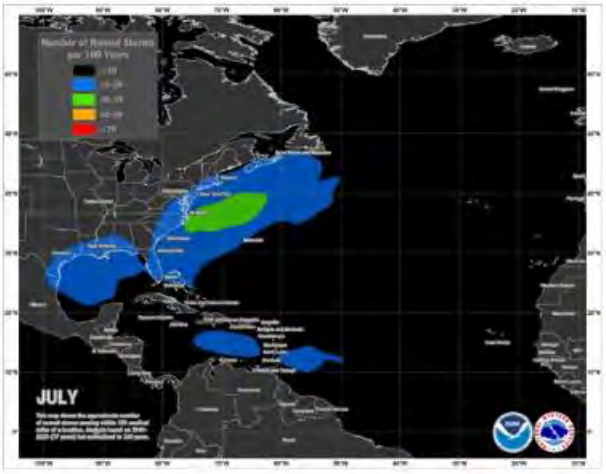
JULY


JULY

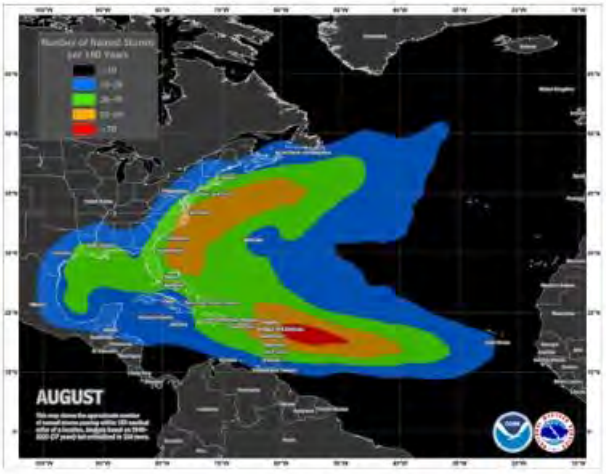
AUGUST

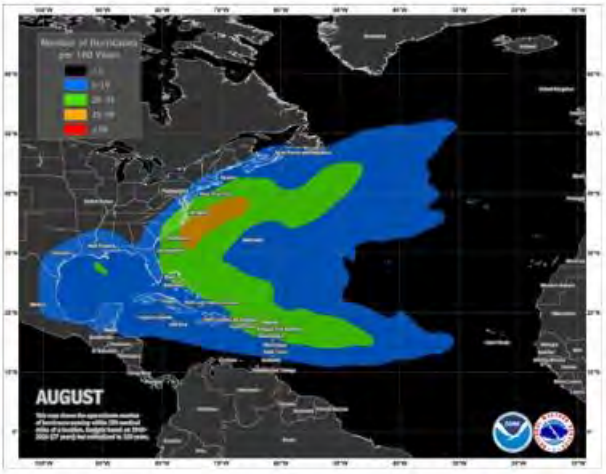
AUGUST

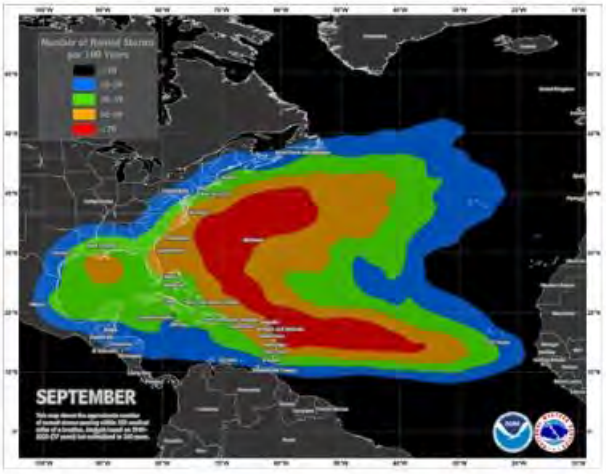
SEPTEMBER

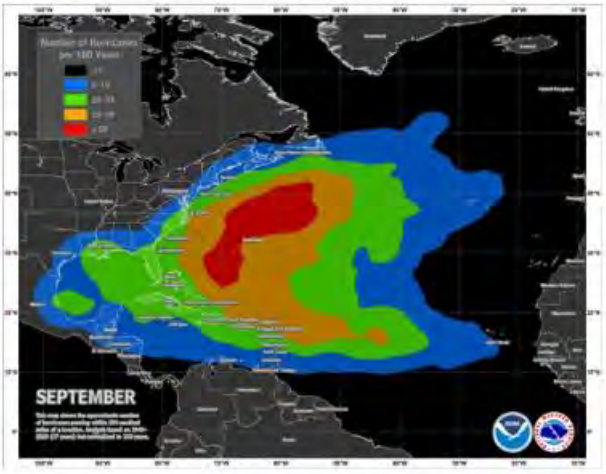
SEPTEMBER

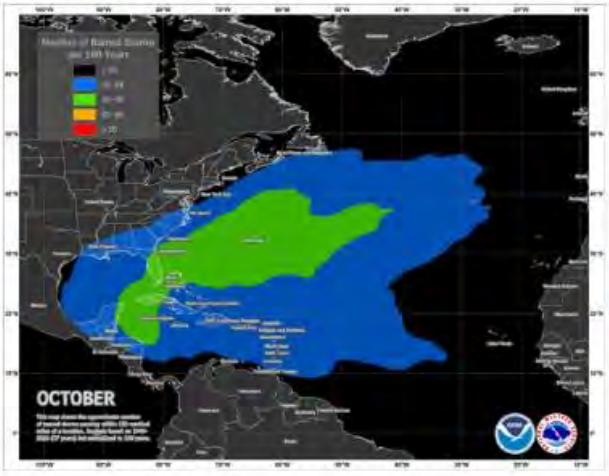

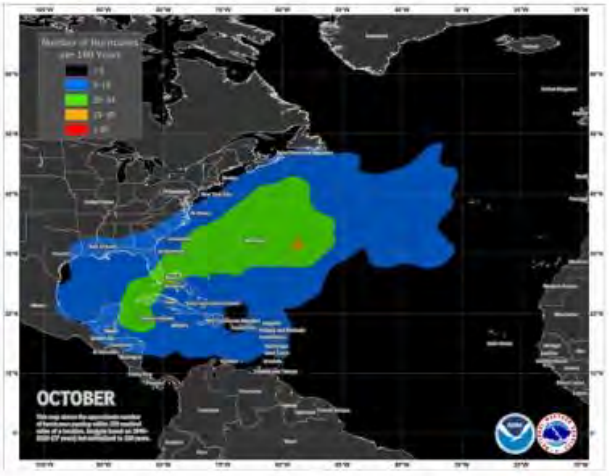

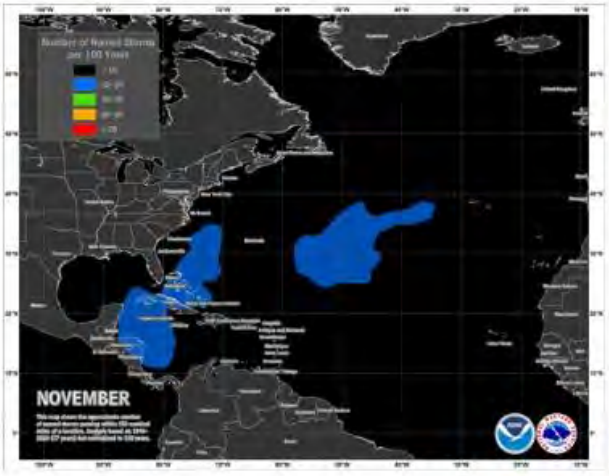

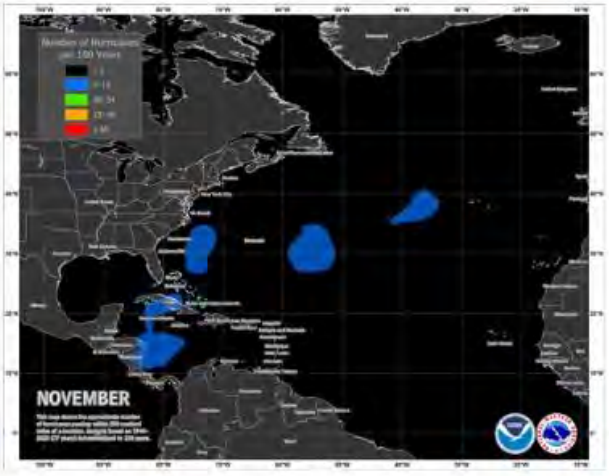

Eastern and Central Pacific Named Storms

Eastern and Central Pacific Hurricanes

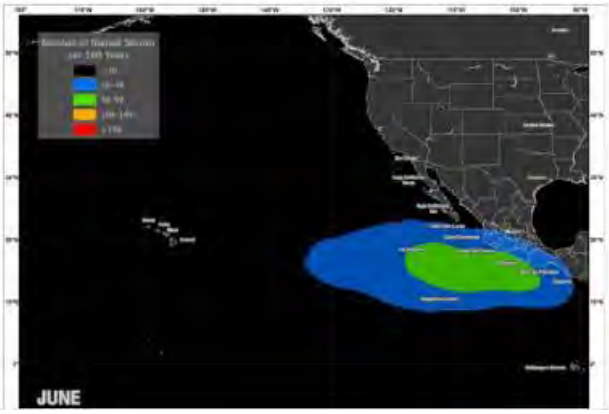

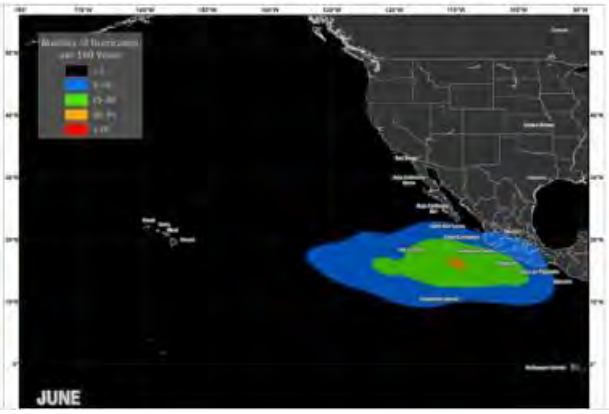

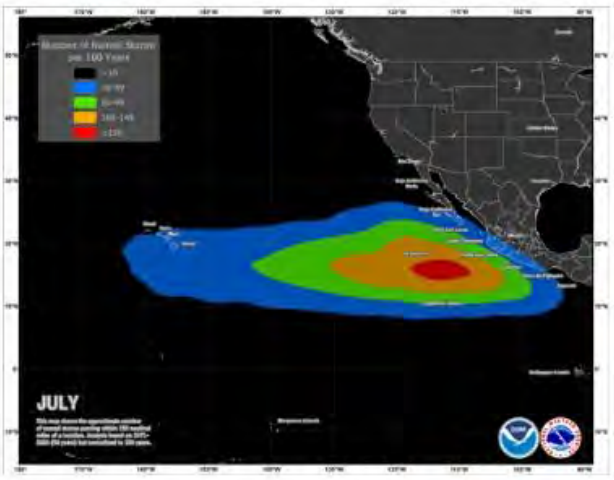
JULY

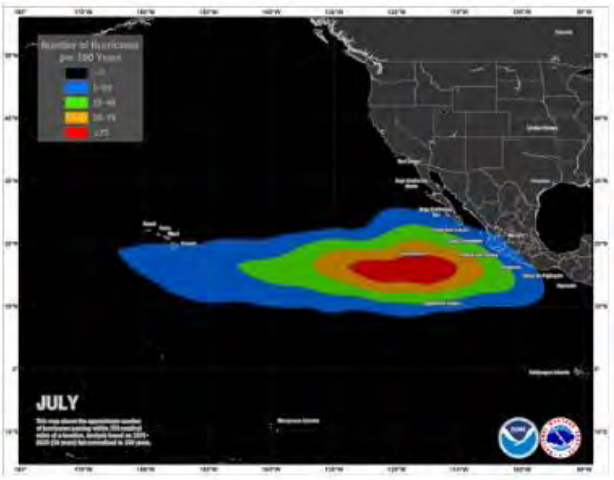
JULY

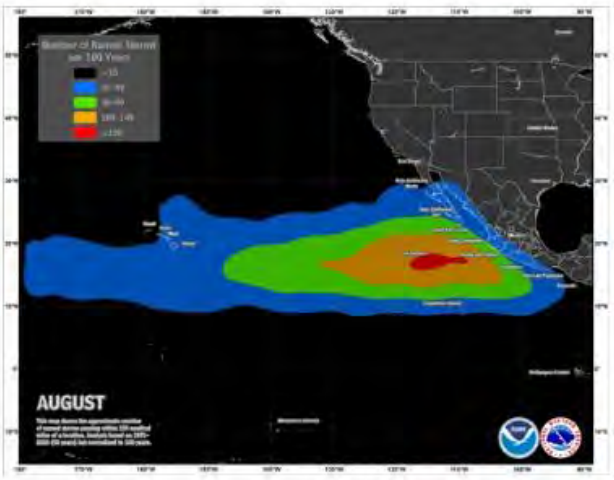
AUGUST

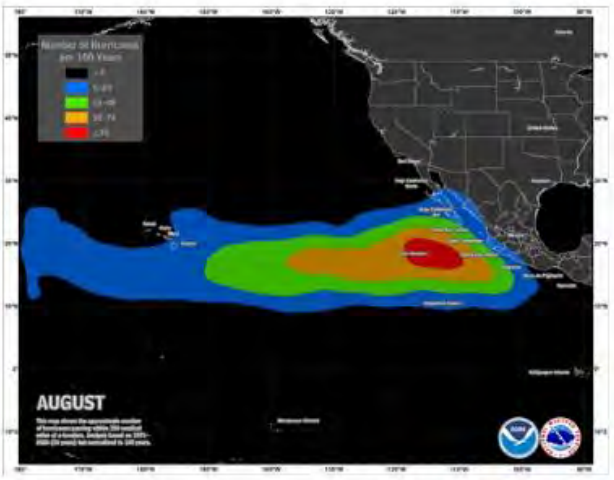
AUGUST

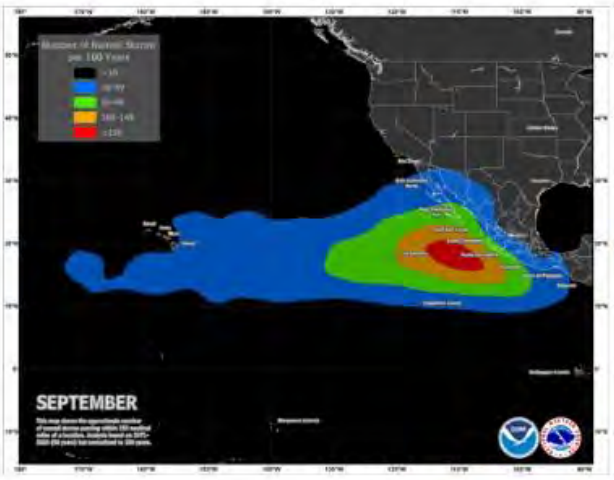
SEPTEMBER

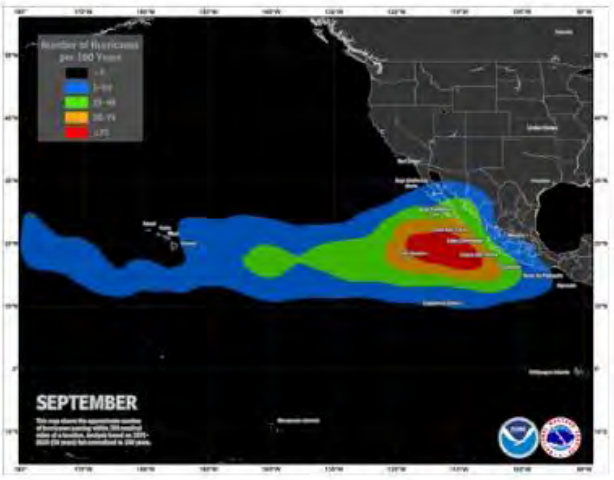
SEPTEMBER

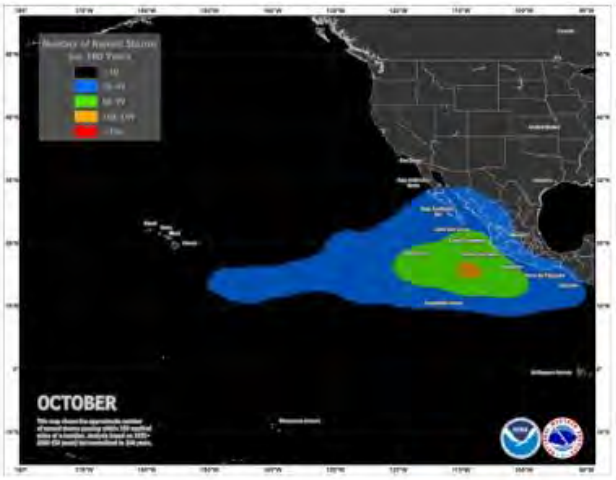

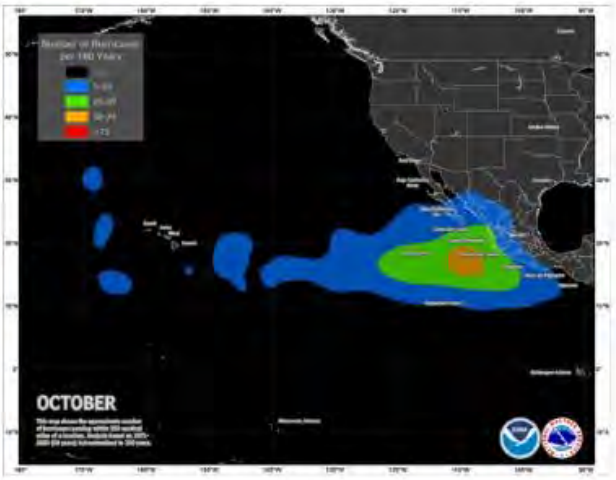

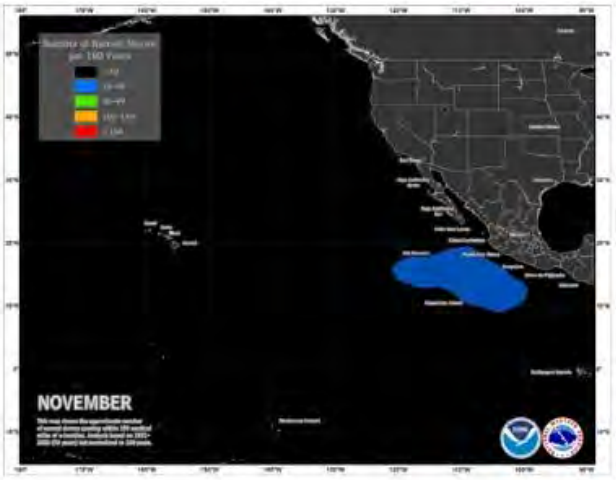

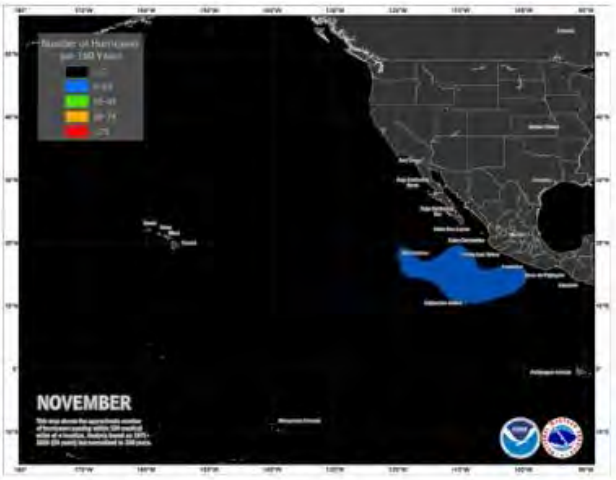

Central Pacific Named Storms

Central Pacific Hurricanes


JUNE


JUNE

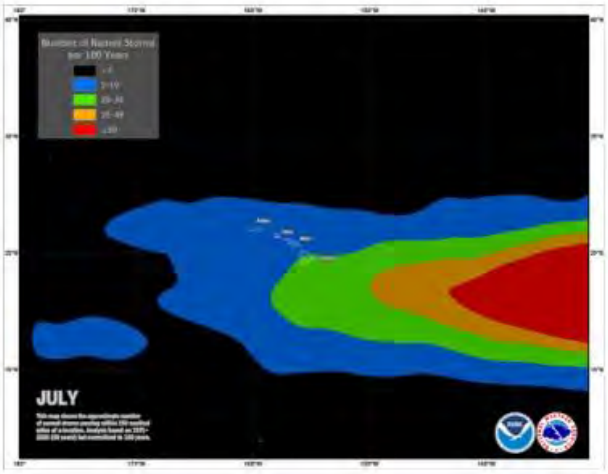
JULY

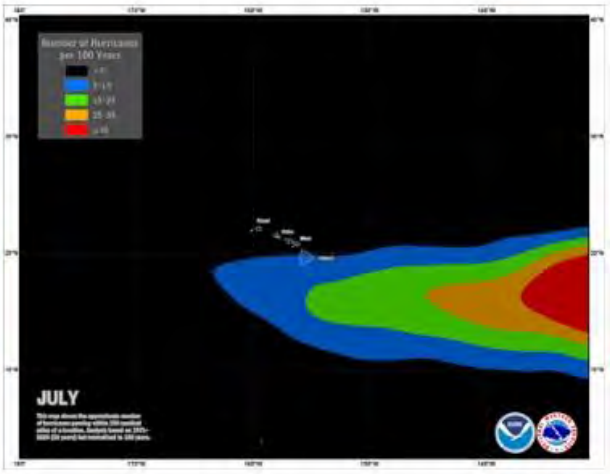
JULY

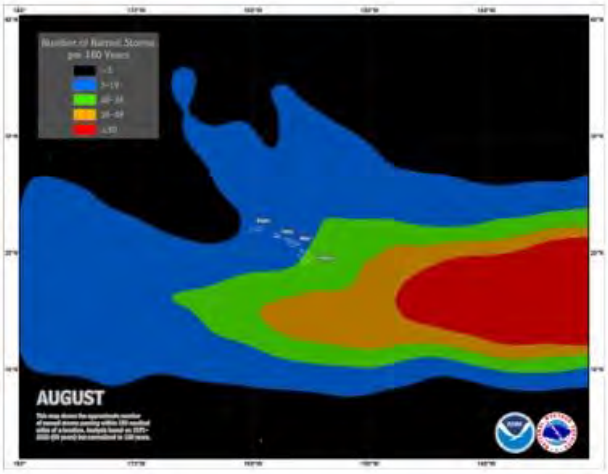
AUGUST

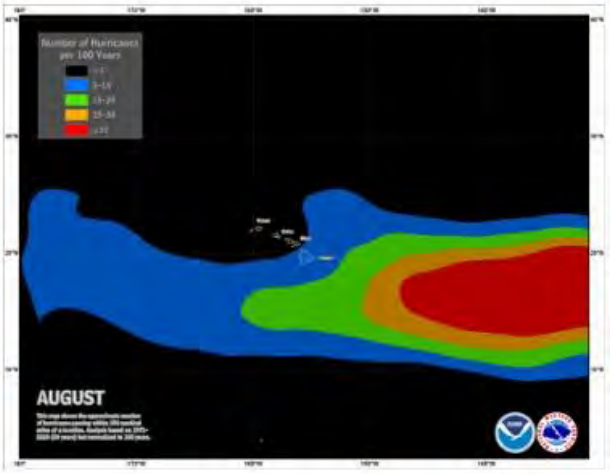
AUGUST

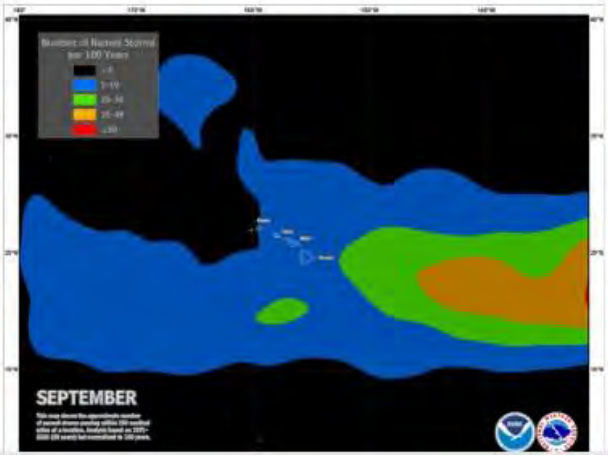
SEPTEMBER

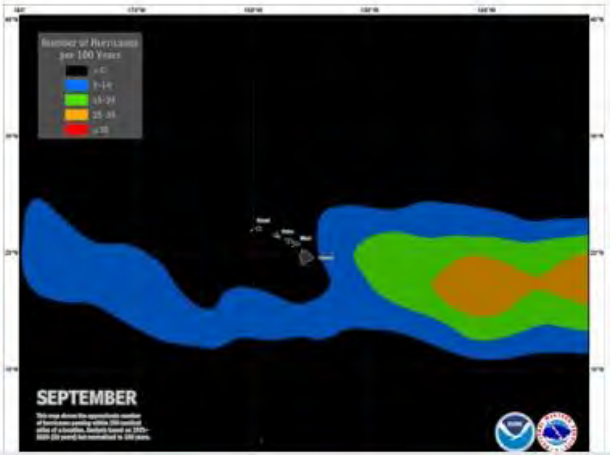
SEPTEMBER

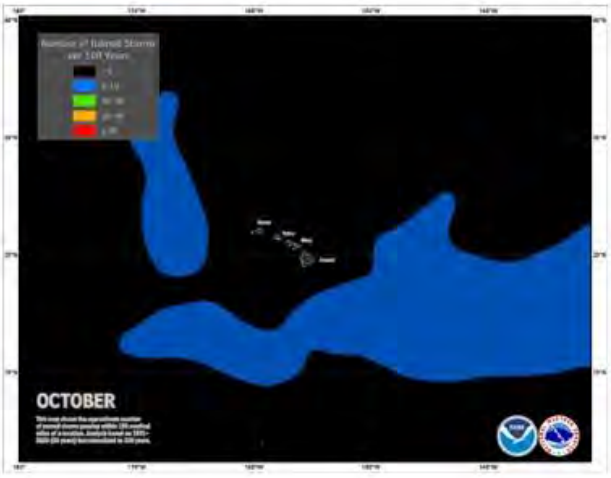
OCTOBER

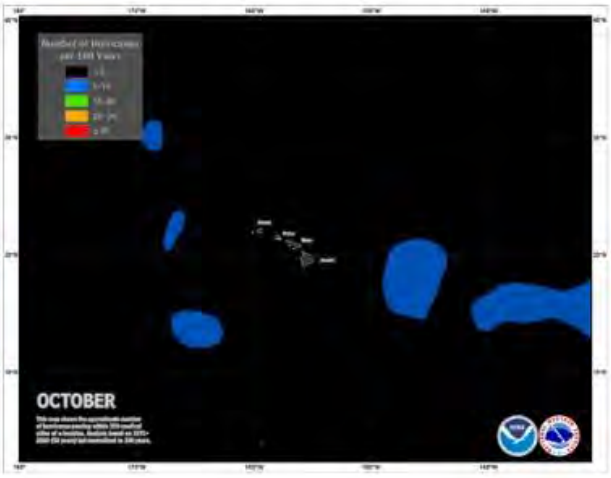
OCTOBER

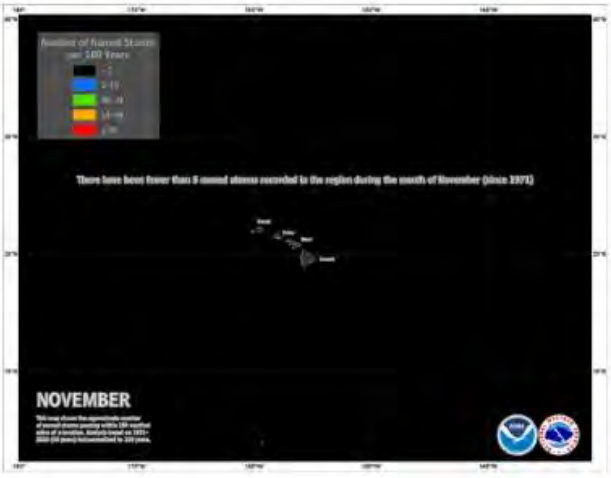
There have been fewer than 5 named storms recorded in the region during the month of November (since 1971)
NOVEMBER

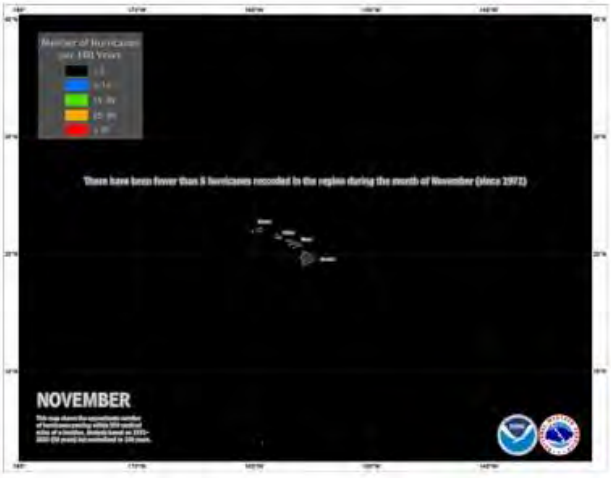
There have been fewer than 5 hurricanes recorded in the region during the month of November (since 1971)
NOVEMBER

High Resolution History Maps

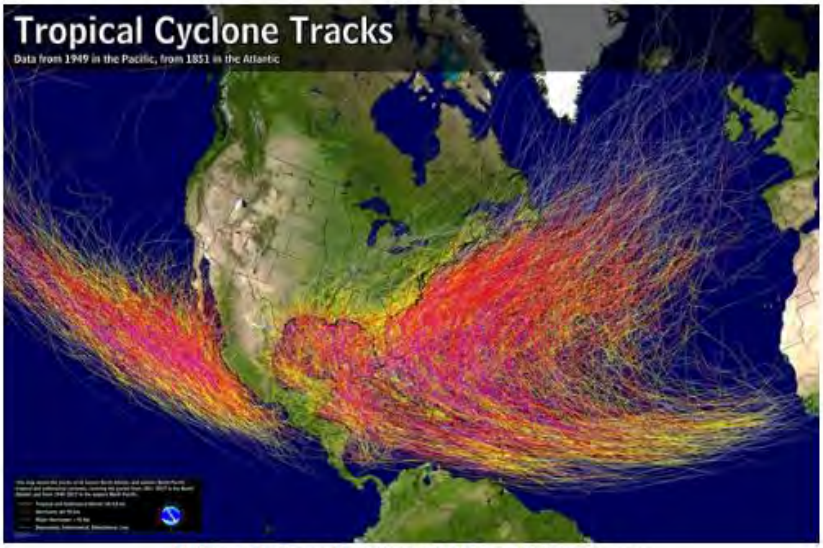

All North Atlantic and Eastern North Pacific tropical cyclones

Named Cyclones by Year

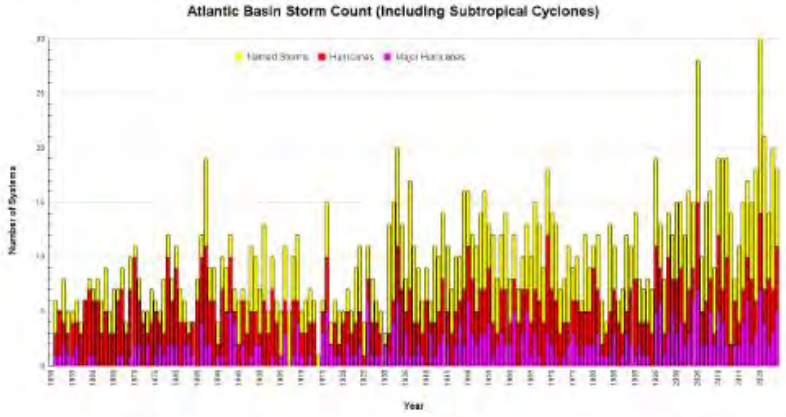

Bars depict number of named systems (yellow), hurricanes (red), and category 3 or greater (purple), 1850-2024

Download hires image

Download table of data (PDF)

Hurricane Return Periods

Hurricane return periods are the frequency at which a certain intensity of hurricane can be expected within a given distance of a given location (for the below images 50 nm or 58 statute miles). In simpler terms, a return period of 20 years for a major hurricane means that *on average* during the previous 100 years, a Category 3 or greater hurricane passed within 50 nm (58 miles) of that location about five times. We would then expect, *on average*, an additional five Category 3 or greater hurricanes within that radius over the next 100 years.

More information on return periods can be found from NOAA Technical Memorandum NWS NHC 38 (pdf) on the NHC Risk Analysis Program (HURISK).

Note: *The information on return period is generated with the 1987 HURISK program, but uses data through 2010.*

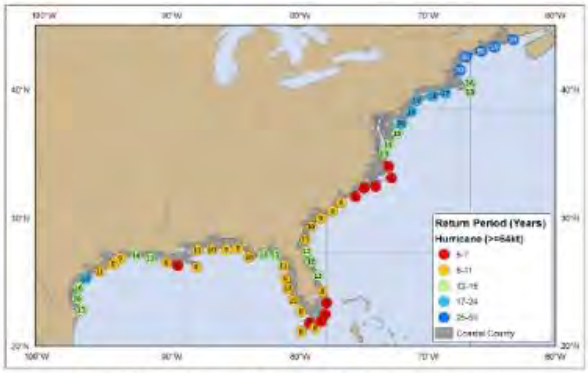

Estimated return period in years for hurricanes passing
within 50 nautical miles of various locations on the U.S. Coast

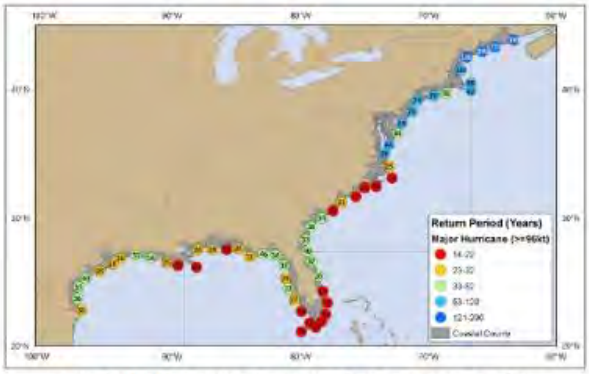

Estimated return period in years for major hurricanes passing
within 50 nautical miles of various locations on the U.S. Coast

CONUS Hurricane Strikes

1950-2023 CONUS Hurricane Strikes (Courtesy of NCEI)

CONUS Hurricane Strike Density (county maps)

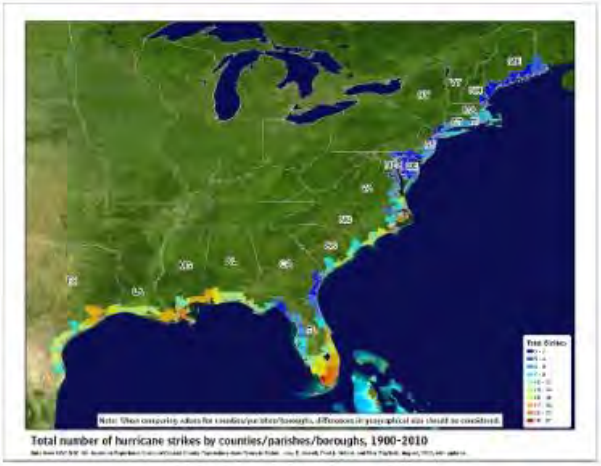

1900-2010 U.S. Hurricane Strikes

1900-2010 U.S. Hurricane Strikes - West Gulf

1900-2010 U.S. Hurricane Strikes - East Gulf

1900-2010 U.S. Hurricane Strikes - Southeast

1900-2010 U.S. Hurricane Strikes - Northeast

1900-2010 U.S. Major Hurricane Strikes

1900-2010 U.S. Major Hurricane Strikes - West Gulf

1900-2010 U.S. Major Hurricane Strikes - East Gulf

1900-2010 U.S. Major Hurricane Strikes - Southeast

1900-2010 U.S. Major Hurricane Strikes - Northeast

Central Pacific Climatology

The following graphs and charts describe some of the climatology of tropical cyclone activity in the area served by the Central Pacific Hurricane Center, between 140 degrees West longitude and the International Date Line and north of the equator.

Many factors affect the level of tropical cyclone activity from year to year. Among them are the state of the El Nino Southern Oscillation in the Pacific. Moderate to strong El Nino years are correlated with increased tropical cyclone activity in the Central Pacific and the occurrence of late season storms.

Continuous satellite coverage has been available in the Central Pacific since 1971 so many climatologies start with that date.Earlier accounts of tropical cyclone activity are based on land, ship, and aircraft observations as well as some non-continuous satellite data.

Hurricane Season Climatology Central Pacific (1971-2008)

	Hurricanes	Tropical Storms	Tropical Depressions	Total
Total Number	58	46	59	163
Percent of All Systems	36%	28%	36%	

Tropical Cyclones in the Central Pacific By Year

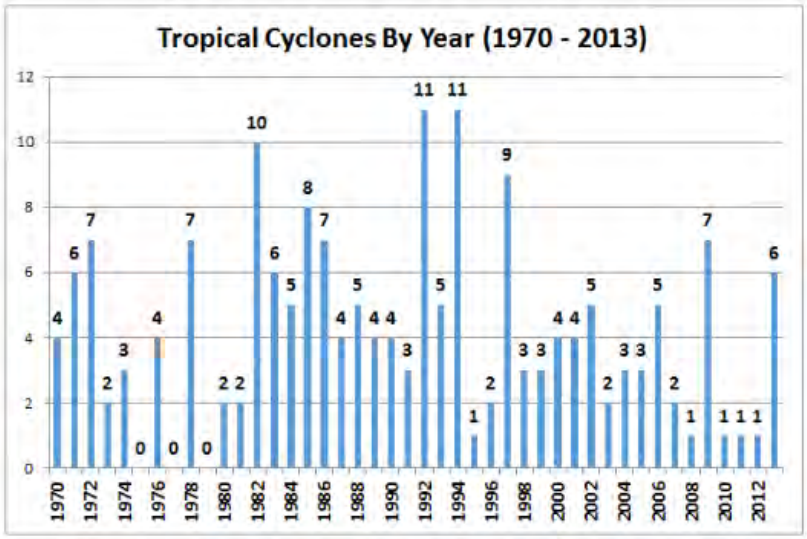

Tropical Cyclones in the Central Pacific By Month

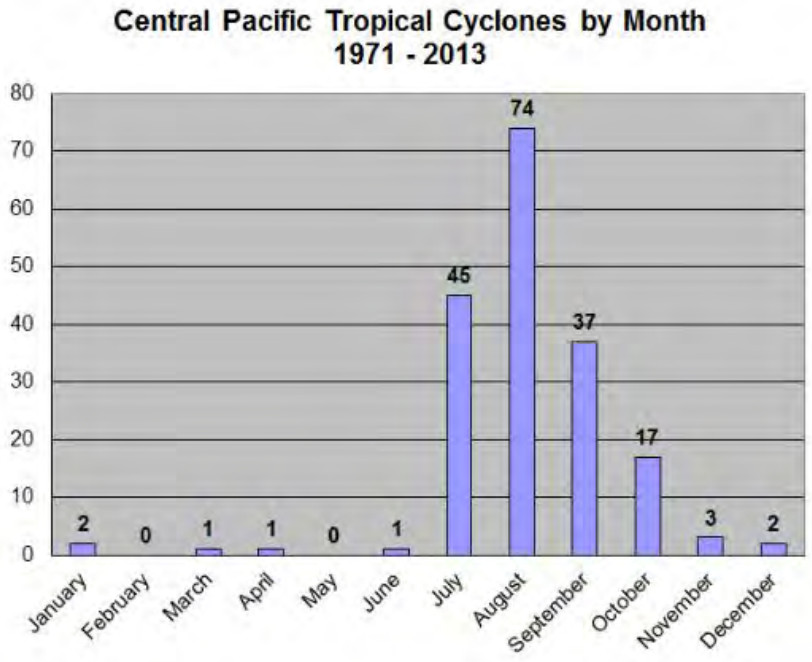

The following charts show the storms that have come within 200 miles and 75 miles of Hawaii. Storms that do not make landfall in Hawaii can still cause considerable damage, mostly from winds and surf.

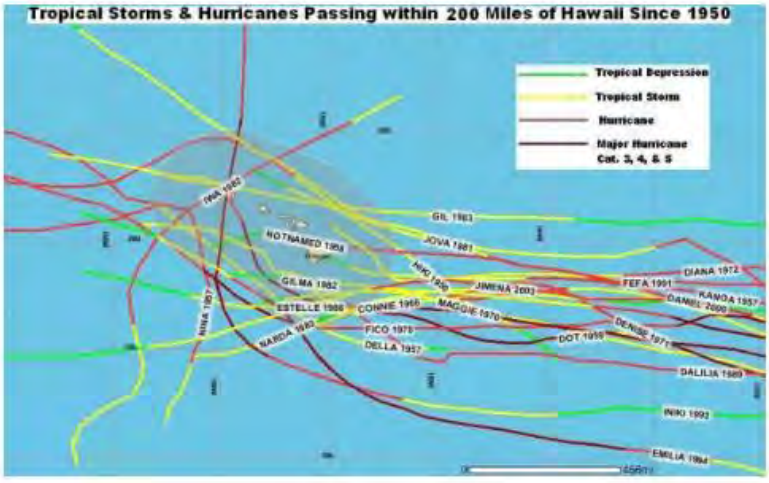

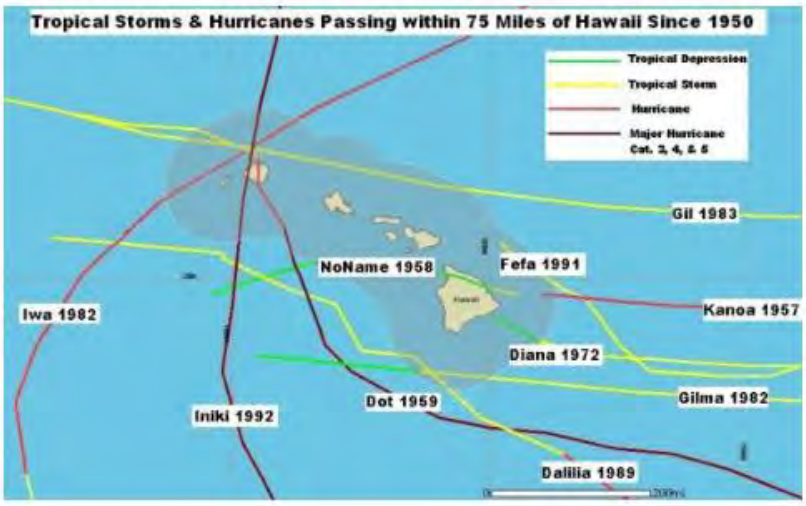
Tropical Storms & Hurricanes Passing within 75 Miles of Hawaii Since 1950
Tropical Depression
Tropical Storm
Hurricane
Major Hurricane
Cat. 3, 4, & 5
Gil 1983
NoName 1958
Fefa 1991
Iwa 1982
Kanoa 1957
Diana 1972
Gilma 1982
Dot 1959
Iniki 1992
Dalilia 1989

11. Assignment 2, Module 2: Hurricane Records: https://www.aoml.noaa.gov/hrd-faq/#record-storms-per-year-by-basin

Worldwide				
Lowest Central Pressure	1979	Typhoon Tip	Northwestern Pacific Basin	870 mb
Fastest 1-minute Sustained Wind	2015	Hurricane Patricia	Northeast Pacific Basin	96.2 m/s (185 kt, 215 mph)
Fastest Measured Wind Gust	1996	Tropical Cyclone Olivia	Australia	113 m/s (220 kt, 253 mph)
Most Rapid Intensification 24 hours	2019	Typhoon Hagibis	Northwest Pacific Basin	98 mb (988 to 890 mb) in 24 hr
Longest running	2023	Tropical Cyclone Freddy	South Indian Ocean	36 days
Farthest travelling	1994	Hurricane/Typhoon John	Pacific Basin	13180 km, 8190 miles
Longest at category 5	1961	Typhoon Nancy	Northwest Pacific Basin	5.50 Days
Highest Storm Surge	1899	Tropical Cyclone Mahina	Bathurst Bay, Australia	Est. 9m (30 feet)
Most Rainfall	1980	Tropical Cyclone Hyacinthe	La Rèunion, Madagascar	6083 mm (239.5")
Deadliest Tropical Cyclone	1970	"Bhola" Cyclone	Bangladesh	300,000+ deaths
Largest Area	1979	Typhoon Tip	Northwest Pacific Basin	1100 km [675 mi], ~3.8 million square kilometers
Smallest Area	2008	Tropical Storm Marco	Misantla, Veracruz, Mexico	19 km [12 miles]

What Are the Record Number of Tropical Storms in a Given Year by Basin?

Based on data from 1980-2024
(1980/81 to 2023/2024 for the Southern Hemisphere):

	Tropical Depression or stronger (closed circulation)			Tropical Storm or stronger (greater than 17 m/s sustained winds)			Hurricane/Typhoon/Severe Tropical Cyclone (greater than 33 m/s sustained winds)		
Basin	**Most**	**Least**	**Average**	**Most**	**Least**	**Average**	**Most**	**Least**	**Average**
Atlantic*	31	7	16.1	30	4	13.6	15	2	6.9
NE/Central Pacific**	31	11	20.5	27	8	17.1	16	3	9.0
NW Pacific	57	25	41.7	36	12	25.3	20	3	13.5
N Indian	20	3	9.0	8	0	4.0	6	0	1.4
SW Indian	20	4	12.4	15	3	9.1	11	1	4.5
Australia	30	8	15.5	17	4	10.1	12	0	5.1
South Pacific	24	1	12.9	16	1	6.7	9	0	3.3
Globally	150	97	124.1	105	62	84.3	56	13	42.5

What is the Total Number of Hurricanes and Average Number of Hurricanes in Each Month?

This table shows the total and average number of tropical storms, and those which became hurricanes, by month, for the period 1851-2020. It also shows the monthly total and average number of hurricanes to strike the U.S. since 1851.

Total and Average Number of Atlantic Tropical Cyclones by Month (1851-2024)

Month	Tropical Storms		Hurricanes		Major Hurricanes		U.S. Landfalling Hurricanes	
	Total	Average	Total	Average	Total	Average	Total	Average
JANUARY	7	0.40	3	0.02	0	0.00	0	0.00
FEBRUARY	1	0.01	0	0.00	0	0.00	0	0.00
MARCH	1	0.01	1	0.01	0	0.00	0	0.00
APRIL	3	0.02	0	0.00	0	0.00	0	0.00
MAY	32	0.19	5	0.03	0	0.00	0	0.00
JUNE	118	0.68	35	0.20	3	0.02	2	0.01
JULY	148	0.86	65	0.38	10	0.06	7	0.04
AUGUST	447	2.56	256	1.48	96	0.56	46	0.26
SEPTEMBER	726	4.20	434	2.51	168	0.97	65	0.37
OCTOBER	442	2.55	238	1.38	70	0.40	29	0.17
NOVEMBER	125	0.72	57	0.33	11	0.06	2	0.01
DECEMBER	24	0.14	8	0.05	0	0.00	0	0.00
YEAR	2074	11.98	1102	6.37	358	2.07	151	0.87

What Was the Most (Largest Number) of Hurricanes in the Atlantic Ocean at the Same Time?

Four hurricanes occurred simultaneously on two occasions. The first occasion was August 22, 1893, and one of these eventually killed 1,000- 2,000 people in Georgia and South Carolina. The second occurrence was September 25, 1998, when Georges, Ivan, Jeanne and Karl persisted into September 27, 1998 as hurricanes. Georges ended up taking the lives of thousands in Haiti. In 1971 from September 10 to 12, there were five tropical cyclones at the same time; however, while most of these ultimately achieved hurricane intensity, there were never more than two hurricanes at any one time.

This table ranks the top ten countries by most tropical cyclone strikes. These numbers are approximated from the IBTrACS database and include only those storm tracks that intersected the coastline at hurricane intensity (≥ 65 kt) and does NOT include storms that remained just offshore but may have affected the country.

Total number of tropical cyclone hits by country

Rank	Nation	Hits
1	United States of America	268
2	China	230
3	Philippines	176
4	Mexico	134
5	Japan	133
6	Cuba	79
7	Australia	66
8	Bahamas	61
9	Vietnam	45
10	Madagascar	30

However, it should be noted that some basins have longer histories of such activity and this might bias these counts. So the following is the ranking if we only look at storms since 1970, when world-wide satellite coverage became available.

Ranking of tropical cyclone hits by country since 1970

Rank	Nation
1	China
2	Philippines
3	Japan
4	Mexico
5	United States of America
6	Australia
7	Taiwan
8	Vietnam
9	Madagascar
10	Cuba

— **When was the earliest and latest Atlantic hurricane?**

Year	Name	Record Type	Attribution
1908	Unnamed	Earliest Hurricane in the Season	Earliest observed hurricane for the season in the Atlantic was on March 7, 1908
1954	Hurricane Alice	Latest Hurricane in the Season	December 31, 1954, the second 'Alice' of that year which persisted as a hurricane until January 5, 1955.
1966	Alma	Earliest Hurricane landfall in the United States	Northwest Florida on June 9, 1966
1985	Kate	Latest Hurricane landfall in the United States	November 22, 1985 near Mexico Beach, Florida

What have been the Most Intense Hurricanes to Strike the United States?

The most intense mainland United States hurricanes by central pressure (1851-2018)

RANK	HURRICANE	YEAR	CATEGORY (at landfall)	MINIMUM PRESSURE	
				Millibars	Inches
1	FL (Keys)	1935	5	892	26.35
2	CAMILLE (MS/SE LA/VA)	1969	5	900	26.58
3	MICHAEL (NW FL)	2018	5	920	27.17
4	KATRINA (LA)	2005	3	920	27.17
5	ANDREW (SE FL/SE LA)	1992	5	922	27.23
6	TX (Indianola)	1886	4	925	27.31
7	FL (Keys)/STX	1919	4	927	27.37
8	FL (Lake Okeechobee)	1928	4	929	27.43
9	DONNA (FL/Eastern U.S.)	1960	4	930	27.46
	Great Miami (FL)	1926	4	930	27.46

What have been the Deadliest Hurricanes for the United States?

RANK	HURRICANE	YEAR	CAT	DEATHS	COMMENTS
1	TX (Galveston)	1900	4	8000-12,000	
2	FL (SE/Lake Okeechobee)	1928	4	2500-3000	Same storm as #13 ADDENDUM
3	KATRINA (LA,MS, AL,FL,GA)	2005	3	1500	Deaths directly attributed
4	LA (Chenier e Caminanda)	1893	4	1100-1400	2000 including offshore deaths August
5	SC/GA (Sea Islands)	1893	3	1000-2000	
6	GA/SC	1881	2	700	
7	AUDREY (SW LA/N TX)	1957	4	>416	
8	FL (Keys)	1935	5	408	
9	LA (Last Island)	1856	4	400	With offshore deaths total is ~600
10	FL (Miami)/ MS/AL/Pensacola	1926	4	372	

12. Assignment 2, Module 2: Hurricanes by Decade: https://www.nhc.noaa.gov/pastdec.shtml

Content of Website:

U.S. Hurricane Strikes by Decade

Number of hurricanes by Saffir-Simpson Category to strike the mainland U.S. each decade.

Decade	Saffir-Simpson Category					All	Major
	1	2	3	4	5	1,2,3,4,5	3,4,5
1851-1860	7	6	5	1	0	19	6
1861-1870	8	6	1	0	0	15	1
1871-1880	7	6	7	0	0	20	7
1881-1890	9	8	3	1	0	21	4
1891-1900	8	5	5	3	0	21	8
1901-1910	10	4	4	0	0	18	4
1911-1920	8	5	4	3	0	20	7
1921-1930	7	2	3	2	0	14	5
1931-1940	9	6	3	1	1	20	5
1941-1950	8	6	5	5	0	24	10
1951-1960	7	4	3	3	0	17	6
1961-1970	0	6	2	3	1	12	6
1971-1980	6	2	4	0	0	12	4
1981-1990	9	2	3	1	0	15	4
1991-2000	2	7	4	0	1	14	5
2001-2010	8	4	6	1	0	19	7
2011-2020	9	5	1	3	1	19	5
2021-2024	3	2	1	3	0	9	4
1901-2024	86	55	43	25	4	213	72
Average Per Decade	6.9	4.4	3.5	2.0	0.3	17.2	5.8

Note: The number and intensities of U.S. hurricane is underestimated here before 1901 because of the sparsely populated U.S. coastline, particularly along part of Florida, Louisiana, and Texas.

13. Assignment 2, Module 2: Hurricane Genesis:
    https://www.hurricanescience.org/science/science/hurricanegenesis/

Content of Website:

Hurricane Genesis: Birth of a Hurricane

The beginning of life for any hurricane is a **pre-existing disturbance**, an area of low pressure, over the tropical ocean. However, several other ingredients are also required for a system to become a hurricane. In this section, the formation of a tropical depression, which is the weakest type of tropical cyclone, is discussed. The formation of a tropical depression can lead to the birth of a hurricane. In Hurricane Development: From Birth to Maturity, the maturation of a tropical depression into a hurricane is described. In Hurricane Decay: Demise of a Hurricane, the causes of hurricane decay are reviewed.

Setting the Stage for Hurricane Formation

Having a pre-existing disturbance is not the only ingredient necessary for a hurricane to form. This disturbance must be located in an environment that is favorable for development. Favorable conditions include:

- A sea surface temperature (SST) of at least ~26.5°C (80°F). The importance of warm ocean water for hurricane development and maintenance is discussed in Hurricane Development: From Birth to Maturity, and the same applies to the initial formation of a tropical depression.
- A vertical temperature profile in the atmosphere that cools enough with height to support thunderstorm activity. The development of thunderstorms, an example of atmospheric convection, is discussed in Hurricane Development: From Birth to Maturity.
- Sufficient water vapor in the middle of the troposphere. Even over the tropical oceans, dry air sometimes exists in the middle of the troposphere, and this dry air suppresses thunderstorms, preventing tropical depression formation. The more humid the air in the troposphere, the less the disturbance will have to moisten the air (via evaporation from the sea surface) in order for genesis to occur.
- Sufficient distance from the equator for the Coriolis Force to be significant, usually at least 483 km (300 miles). Closer to the equator, the Coriolis Force is weak, therefore, it is difficult to establish cyclonic rotation here (see Hurricane Structure and Primary Circulation).
- Low values of vertical wind shear from the surface of the earth to the upper troposphere (about 8 miles up). For reasons that remain unclear, wind shear inhibits the development of tropical depressions. Some research shows this may be due to the injection of dry air into the storm system.

Formation of a Tropical Depression

Schematic of tropical storms. Although best described in terms of its wavelike characteristics in the wind field, it also consists of a weak trough of low pressure. The presence of a disturbance like this indicates atmospheric instability and is often associated with tropical cyclone development.')" onmouseout="UnTip()">easterly waves (dashed lines) propagating westward from the West African coast towards the Caribbean Sea in the trade winds on the southern side of the subtropical ridge. The subtropical ridge is one of the main sources of environmental wind that steers both easterly waves and tropical cyclones westward across the tropical North Atlantic. Image credit: NOAA (http://www.aoml.noaa.gov/hrd/tcfaq/A4.html)

Even when favorable conditions are present, a tropical depression still may not form. For this reason, understanding and forecasting the **genesis** of a tropical depression is a difficult challenge. The leading theory for tropical depression formation begins with a pre-existing disturbance. This disturbance consists of an array of thunderstorms in an atmosphere where sufficient moisture or **water vapor** is present. In the North Atlantic and Northeast Pacific Oceans, most of the atmospheric disturbances that eventually form a hurricane are associated with an **African easterly wave**. An African easterly wave is an area of low atmospheric **pressure** that is embedded in the easterly **trade winds** and generally forms over Africa within the **intertropical convergence zone (ITCZ)**. The details of how an African easterly wave forms are complex, but ultimately, development is due to the strong temperature contrast between the hot and dry Sahara Desert and the much cooler and wetter Gulf of Guinea coast.

In other ocean basins, different kinds of atmospheric disturbances become tropical depressions. For example, many Northwest Pacific **typhoons** originate from a disturbance in a **monsoon trough**. Tropical cyclone activity over the North Indian Ocean is also typically related to monsoon depressions.

As the disturbance evolves, persistent converging winds in the lower and middle part of the troposphere associated with an organized group of thunderstorms, called a **mesoscale convective complex (MCC)**, produce a rotating column of air called a **mesoscale convective vortex (MCV)**. In the Northern Hemisphere, this rotation is caused by deflection of the converging winds by the Coriolis Force (see Hurricane Structure and Primary Circulation). At first, the MCV is usually displaced horizontally from the strongest thunderstorms, but then a second burst of thunderstorms at the MCV initiates the **intensification** process. As long as the conditions remain favorable, this MCV and the associated thunderstorms can begin to tap into the heat energy from the sea surface, leading to development of a tropical depression and perhaps, a hurricane Hurricane Development: From Birth to Maturity.

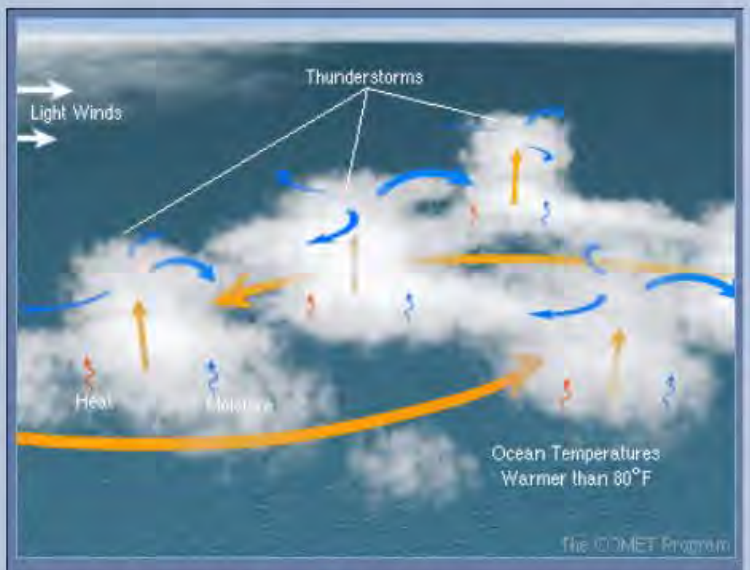

The birth of a tropical cyclone. This illustration shows a loosely organized group of storms, and within each storm, the arrows show heat and moisture rising into the atmosphere over the ocean. The big orange arrows indicate general counterclockwise (cyclonic) rotation, while the blue arrows indicate wind divergence in the upper troposphere. The sea surface temperature is warmer than 80° Fahrenheit, and the environmental winds are light with low vertical shear. The source of this material is the COMET® Website at http://meted.ucar.edu/ of the University Corporation for Atmospheric Research (UCAR) pursuant to a Cooperative Agreements with the National Oceanic and Atmospheric Administration, U.S. Department of Commerce.

Although less common, an **extratropical cyclone** from the **mid-latitudes** may act as a pre-existing disturbance that can form a tropical depression, assuming conditions are favorable for the disturbance to undergo **tropical transition**. During this transition, the disturbance begins to obtain its energy from the ocean instead of from horizontal temperature gradients in the atmosphere and the environmental wind field (see Hurricane Development: From Birth to Maturity). Sometimes, tropical transition occurs when the **maximum surface wind speed** is already stronger than 61kph (38 mph). In this case, the storm would be immediately classified as a tropical storm instead of a tropical depression. If the storm has characteristics of both an extratropical cyclone and a tropical storm, it is classified as a **subtropical storm**. Like a tropical storm, a subtropical storm may become a hurricane if it completes tropical transition and obtains a maximum surface wind speed of at least 119 kph (74 mph) (see Hurricane Life Cycle).

14. Assignment 2, Module 2: Hurricanes, Typhoons, and Cyclones: https://www.livescience.com/22177-hurricanes-typhoons-cyclones.html

Hurricanes, typhoons and cyclones: Earth's tropical windstorms

References By Tiffany Means published October 1, 2020

These whirling windstorms are one of Mother Nature's most destructive natural disasters.

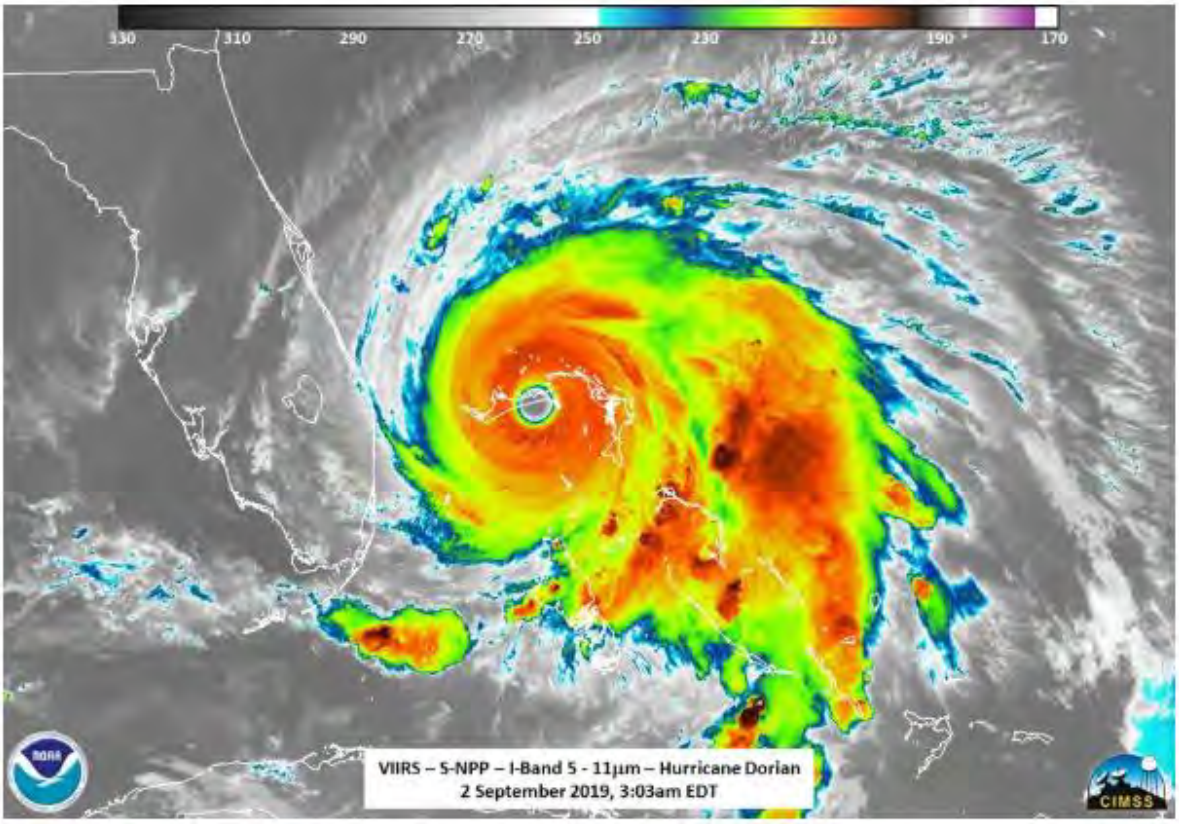

Infrared satellite imagery of Hurricane Dorian as it made landfall as a Category 5 hurricane over three islands in the Bahamas on the morning of Sep. 2, 2019. (Image credit: NOAA/CIMSS)

If you live or like to vacation along the world's coastlines, chances are good you've been affected by a tropical storm or hurricane.

Hurricanes, which are more broadly called "tropical cyclones" because they originate over Earth's tropical oceans, are some of nature's largest and fiercest storms. They get their name from Hurican, the Carib god of evil, according to the National Oceanic and Atmospheric Administration (NOAA).

Worldly windstorms

Tropical cyclones form in most of the world's tropical oceans, but always at least 300 miles (480 kilometers) north or south of the equator. Any closer to the equator than this, and the inertial force that causes storms to spin to the right in the Northern Hemisphere and to the left in the Southern Hemisphere, called the coriolis force, won't cause the storm system to spin.

When they form in the Atlantic or Eastern Pacific Oceans, tropical cyclones are called hurricanes. In the western North Pacific, the same type of storms are called typhoons. And in the South Pacific and Indian Oceans, they are called cyclones.

The Atlantic hurricane season lasts from June through November. The Eastern Pacific hurricane season runs from mid-May through November. Typhoons in the North Pacific occur year-round but peak in late August. And in the South Pacific, the cyclone season begins in October and ends in May.

In the Atlantic, hurricanes typically follow one of three paths, according to NOAA's National Hurricane Center:

- Originating off the West Coast of Africa near the Cape Verde Islands and traveling west toward the Caribbean and the East Coast of the United States.
- Originating in the western Caribbean, and moving into the U.S. Gulf Coast, or along the U.S. East Coast.
- Originating in the Gulf of Mexico and crashing into the Gulf Coast states, anywhere between Texas and Florida.

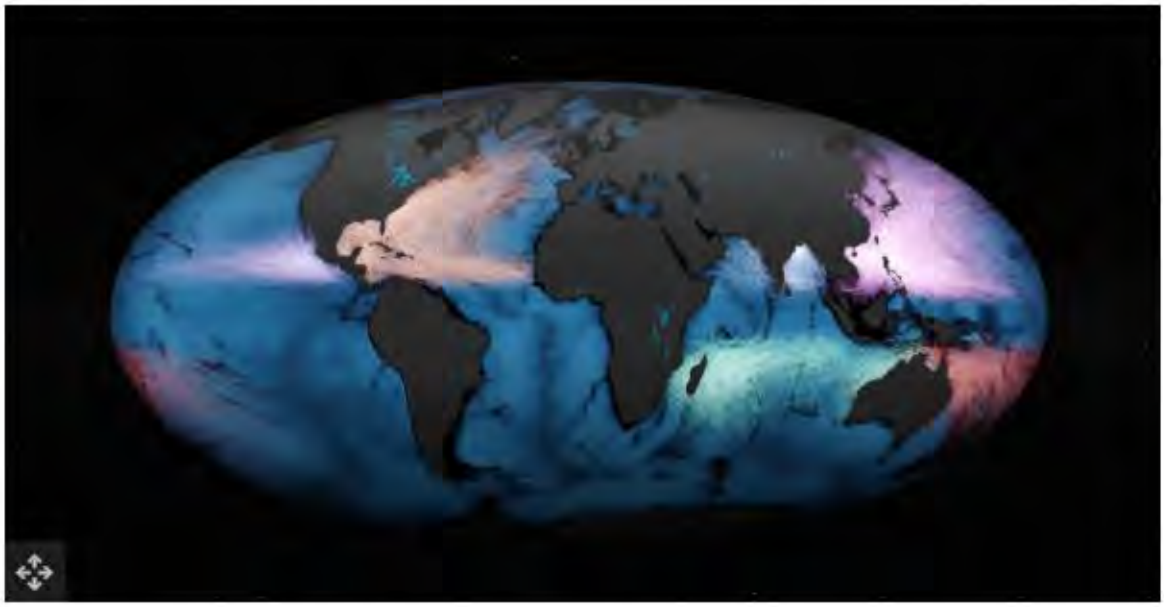

Graphic representation on world map of the activity in the world's major ocean tropical cyclones basins between 1842 - 2017. (Image credit: Shutterstock)

How hurricanes form

As with any weather event, certain atmospheric ingredients must be in place for a hurricane to cook up over the open ocean. According to NOAA's National Weather Service, these include:

- Warm ocean waters of at least 80 degrees Fahrenheit (27 Celsius) extending from the sea surface to a depth of 150 feet (46 meters) underwater.
- A moist and unstable atmosphere. In other words, an atmosphere with high humidity at upper levels and one in which air has a tendency to rise.
- A pre-existing disturbance near surface levels, such as a complex of thunderstorms, which meteorologists call tropical easterly waves.
- Sufficient distance (at least 300 miles, or 480 km) from the equator.
- Little to no wind shear, meaning wind speed and direction varies little between the surface and the troposphere, the lowest level of Earth's atmosphere, which stretches tens of thousands of feet above the surface.

When a storm forms under these minimum criteria, it is deemed a tropical cyclone, or more specifically, a tropical disturbance. At this initial stage, the disturbance is essentially a cluster of marine clouds and thunderstorms, but if ocean temperatures remain sufficiently balmy, the disturbance will continue to strengthen. And as the system becomes slightly more organized it may start to circulate. When the storm system's winds begin to circulate around a well-defined center, but its maximum sustained wind speeds have not exceeded 38 mph (61 km/h), the storm becomes categorized as a "tropical depression." It's at this stage that the storm earns a name.

Once maximum sustained winds reach between 39 and 73 mph (63 to 117 km/h), the cyclone is classified as a "tropical storm." And when a storm's sustained winds reach 74 mph (119 km/h) or greater, the cyclone is classified as a hurricane — or typhoon if it's in the North Pacific, and cyclone if in the South Pacific.

How hurricanes are categorized

Hurricanes are categorized according to the speed of their maximum sustained winds. The scale used for this purpose, called the Saffir-Simpson Hurricane Wind Scale, was developed in 1971 by civil engineer Herbert Saffir and by meteorologist and then-director of the U.S. National Hurricane Center, Bob Simpson. The Saffir-Simpson scale rates a hurricane's severity from 1 (very dangerous) to 5 (catastrophic), based on the following wind speeds:

- Category 1: Winds of 74-95 mph (119-153 km/h)
- Category 2: Winds of 96-110 mph (154-177 km/h)
- Category 3: Winds of 111-129 mph (178-208 km/h)
- Category 4: Winds of 130-156 mph (209-251 km/h)
- Category 5: Winds exceeding 157 mph (252 km/h)

Hurricanes that reach Category 3 or higher are considered "major hurricanes" because of their potential to cause significant damage and loss of life. Similarly, typhoons with winds exceeding 150 mph (241 km/h) earn the title of "super typhoon."

Although winds are the most common way to measure how intense a tropical cyclone is, central barometric pressure, which is the air pressure exerted by Earth's atmosphere on the storm's geographical center, is another way meteorologists measure a storm's intensity. In general, the lower a storm's central pressure, the stronger the storm. While lower pressure and higher winds tend to go hand-in-hand, one isn't necessarily indicative of the other. For example, as of 2019, Hurricane Wilma (2005), a Category 5 hurricane, held the record for the lowest central pressure (882 millibars) of any Atlantic hurricane, but Hurricane Allen (1980), also a Category 5 hurricane, ranks as the Atlantic hurricane with the strongest winds (its sustained winds reached 190 mph, or 306 km/h).

Beware of these features and hazards

The main physical features of a hurricane are its rainbands, eye and eyewall. These features take shape as surface air from all directions spirals in toward the center of the storm in a counter-clockwise pattern (or clockwise in the Southern Hemisphere).

Because this converging air has nowhere else to go it rises, creating a column of forceful rising air at the storm's center known as the eyewall. Rising air encourages clouds and thunderstorms to develop, which is why the eyewall is surrounded by a ring of towering thunderstorms that inflict some of the cylone's most severe punishment. Curved bands of clouds and thunderstorms trail away from the eyewall in a spiral fashion. These rainbands, which typically extend outward 50 to 300 miles (80 to 483 km) from the cyclone's center, can produce heavy bursts of rain and wind, as well as tornadoes.

Related: Hurricane preparation: What to do

The eyewall's strong rotation of air creates an empty vortex at its center. This empty area is the eye of the storm, and spans a distance about 20 to 40 miles (32 to 64 km) in diameter on average, according to NOAA. Inside the eye, air from the top of the cyclone sinks back down toward the surface to fill the void of the air that was pulled into the storm. Sinking air inhibits cloud formation, which is why the eye has calm winds and clear skies. A tropical cyclone is said to have made landfall when its eye hits the shoreline.

Violent winds are not the only hazard of hurricanes or cyclones. Storm surges — walls of seawater that are pushed toward shore by the sheer force of a storm's winds — can increase water levels by 15 feet (4.5 m) or more above the predicted astronomical tide. In 2017, the National Weather Service began issuing storm surge watches and warnings to alert areas along the U.S. Gulf and Atlantic coasts of the unique risk for life-threatening inundation from approaching tropical cyclones.

Flooding caused by storm surges and by heavy rainfall is a major hazard of hurricanes. According to a 2014 study published in The Bulletin of the American Meteorology Society, storm surge flooding has been the leading cause of hurricane-related fatalities for the past 50 years.

Related: **The costliest hurricanes in history**

Who picks hurricane names?

Hurricane names are determined by the World Meteorological Organization (WMO), an intergovernmental organization headquartered in Geneva, Switzerland, that serves as the international authority on weather, climate and hydrology. The WMO maintains six lists of alphabetical names that are recycled and reused every six years for the Atlantic and eastern Pacific Ocean basins. It also composes separate lists for the globe's five other cyclone zones, including the western Pacific, northern Indian, southwestern Indian, southeastern Indian, and Australian Ocean basins.

According to the National Hurricane Center, the current practice of assigning male and female names to hurricanes wasn't put into place until 1979. Before this, only female names were used. And for hundreds of years before that, storms often took the name of the holiday or saint's day on which they occurred.

Names are preferred to numbers because they're easier to remember. The one exception to this no-numbering rule is tropical depressions; because they aren't named, they take the title of whatever number cyclone they are within a particular season-year, that is, "Tropical Depression Three," or "Tropical Depression Fifteen," etc.

If a storm is ever so deadly or destructive that the future use of its name would be insensitive, that name is retired and a replacement name is chosen. For example, the names Katrina and Sandy have been removed from the list of Atlantic cyclone names because of the astounding amount of destruction and death that resulted from Hurricanes Katrina (2005) and Sandy (2012). More recently, Matthew (2016), Maria (2017), Florence (2018), and Michael (2018) were retired.

During extremely busy Atlantic hurricane seasons, all the names on the names list may be used up. When this happens, subsequent storms receive a name from the Greek alphabet (Alpha, Beta, Gamma and so on). This has only ever happened twice, according to NOAA: in 2005 and again in 2020.

Tropical Storm Beta nears the Texas coast on Sept. 21.
(Image credit: NOAA/NESDIS/STAR GOES-East Geocolor)

Hurricanes and climate change

Hurricanes feed off of heat energy, so as Earth's global temperatures continue to rise, hurricanes are bound to be affected. So far, it's not evident that hurricanes are necessarily forming more often because of rising temperatures, although scientists do predict that hurricane activity and intensity will likely increase in future years.

There is, however, a clear link between global warming and an increase in the number of Category 4 and 5 hurricanes. Climate change also appears to be causing hurricanes to intensify more rapidly than ever before, and to produce far more rain, according to Yale Climate Connections. These trends are likely a result of higher ocean temperatures and higher water vapor content in the atmosphere as the air heats up, according to NOAA's Geophysical Fluid Dynamics Laboratory.

Warmer-than-average ocean temperatures in the tropical Atlantic and Caribbean Sea are already contributing to the active 2020 Atlantic hurricane season, NOAA reported. Similar conditions have been producing busier-than-normal hurricane seasons since 1995. Scientists predict the annual trend of more frequent extreme storms and record-breaking hurricane seasons to continue as long as climate change persists.

15. Assignment 2, Module 3: Hurricane Structure:
    https://www.hurricanescience.org/science/science/hurricanestructure/

Hurricane Structure

Hurricane Structure

A mature hurricane is nearly circular in shape. The winds of a hurricane are very light in the center of the storm (blue circle in the image below) but increase rapidly to a maximum 10-50 km (6-31 miles) from the center (red) and then fall off slowly toward the outer extent of the storm (yellow).

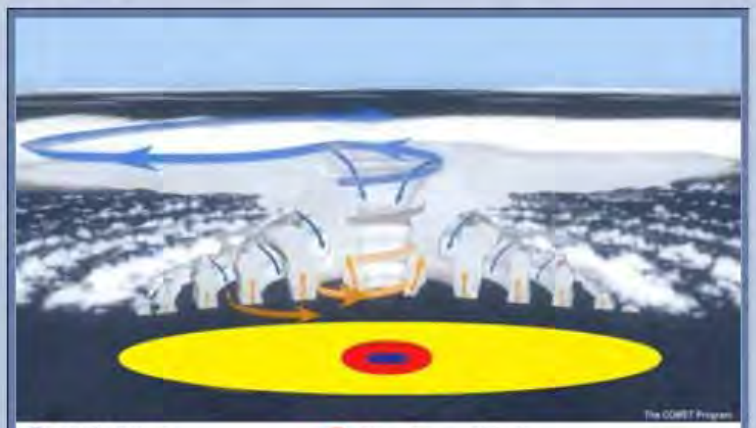

Vertical slice through the center of a mature hurricane. The winds of a hurricane are very light in the center of the storm (blue circle) but increase rapidly to a maximum 10-50 km (6-31 miles) from the center (red ring) and then fall off slowly toward the outer extent of the storm (yellow ring).

The size of a hurricane's wind field is usually a few hundred miles across, although the size of the hurricane-force wind field (with wind speed > 117.5 km/h [73 mph]) is typically much smaller, averaging about 161 km (100 miles) across. The area over which tropical storm-force winds occur is greater, ranging as far out as almost 500km (300 miles) from the eye of a large hurricane.

One of the largest tropical cyclones ever measured was Typhoon Tip (Northwest Pacific Ocean, October 12, 1979), which at one point had a diameter of about 2100 km (~1350 miles). One of the smallest tropical cyclones ever measured was Cyclone Tracy (Darwin, Australia, December 24, 1974), which had a wind field of only 60 miles (~ 100 km) across at landfall.

Relative sizes of the largest and smallest tropical cyclones on record, shown in comparison to the size of the United States. Image credit NOAA/NWS Jetstream- Online School for Weather.

A mature hurricane can be broken down into three main parts: the **eye**, **eyewall**, and outer region.

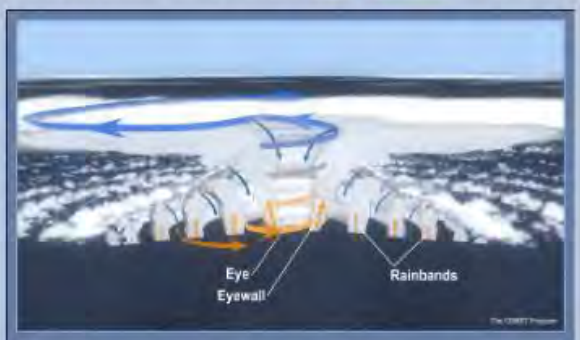

Vertical slice through the center of a mature hurricane. In the lower troposphere, air spiraling inward forms the outer rainbands. In the center is the eye, with nearly clear skies, surrounded by the violent eyewall, with the strongest winds and very heavy rain. Image credit: The COMET Program.

In mature hurricanes, strong surface winds move inward towards the center of the storm and encircle a column of relatively calm air. This nearly **cloud**-free area of light winds is called the eye of a hurricane and is generally 20-50 km (12-30 miles) in diameter. From the ground, looking up through the eye, skies may be so clear that you might see the stars at night or the sun during the day. Surrounding the eye is a violent, stormy eyewall, formed as inward-moving, warm air turns upward into the storm (see Hurricane Development: From Birth to Maturity). Usually, the strongest winds and heaviest **precipitation** are found in this area.

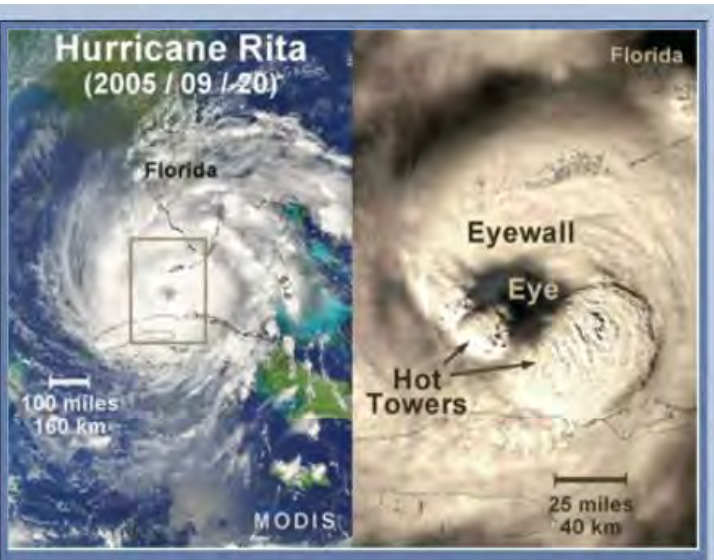

Satellite view (MODIS) and detailed imagery of Hurricane Rita as she intensified on September 20, 2005. The area contained in the square on the left is depicted to the right. The cloud-free eye and surrounding eyewall are clearly visible. "Hot towers" are the towering high clouds in a hurricane's eyewall that can generate very heavy rainfall and reach the top of the troposphere. These towers are called "hot" because a large quantity of heat is released inside them by water vapor condensing to form rain. Image credit: NASA.

In the Northern Hemisphere, the most destructive section of the storm is usually in the eyewall area to the right of the eye, known as the right-front quadrant. Based on the direction of movement of a hurricane during landfall, this section of the storm tends to have higher winds, seas, and storm surge.

The "right side of the storm" is defined with respect to the storm's motion: if the hurricane is moving to the west, the right side would be to the north of the storm; if the hurricane is moving to the north, the right side would be to the east of the storm, etc. In general, the strongest winds in a hurricane are found on the right side of the storm because the propagation of the hurricane also contributes to its winds. A hurricane with 145 km/h (90 mph) winds while stationary would have winds up to 160 km/r (100 mph) on the right side and only 130 km/h (80 mph) on the left side if it began propagating at 16 km/hr (10 mph). Image adapted from AOML FAQ D6 (www.aoml.noaa.gov/hrd/tcfaq/D6.html)

Outside the eyewall of a hurricane, rainbands spiral inwards towards the eyewall. These rain bands are capable of producing heavy rain and wind (and occasionally tornadoes). Sometimes, there are gaps between the bands where no rain is found. In fact, if one were to travel from the outer edge of a hurricane to its center, one would typically experience a progression from light rain to no rain back to slightly more intense rain many times with each period of rainfall being more intense and lasting longer until reaching the eye.

An In-Depth Look at Hurricane Eyes and Eyewalls

Not all hurricane eyewalls look the same. Compare three different hurricanes, Hurricanes Karl, Igor and Julia, seen left to right in this satellite image taken on on September 16, 2010. Image credit: NOAA

Not all hurricane eyewalls look the same, and the size and shape of a particular hurricane's eyewall often changes during the hurricane's lifetime. In what may be considered a "typical" hurricane, a single eyewall surrounds a nearly circular eye that is mostly cloud-free. However, eyewalls of strong, long-lived hurricanes sometimes contract over time, during which the maximum wind speed in the hurricane typically increases. Then, a new eyewall may begin to form outside of the original contracting eyewall, often from one of the innermost spiral bands. When a hurricane has more than one eyewall at once, it is said to have concentric eyewalls. After the outer eyewall forms, the inner (original) eyewall may decay, during which the maximum wind speed in the hurricane typically decreases. Eventually, the outer eyewall may become the only one left. The new outer eyewall may then begin to contract, leading to another period of hurricane strengthening. This cycle, which may repeat multiple times, is called an eyewall replacement cycle.

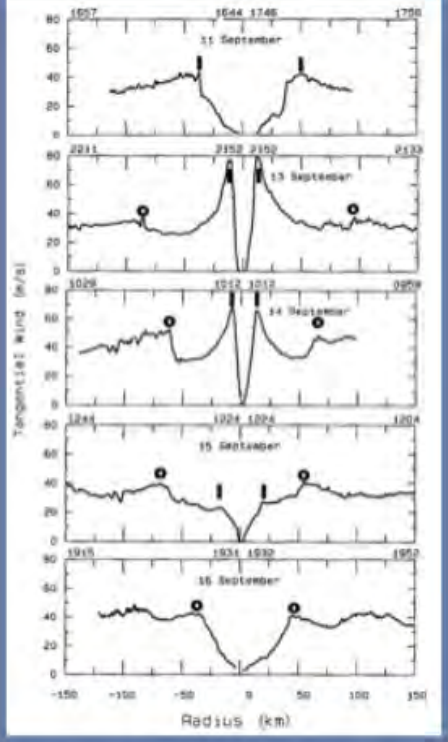

Wind speed in the primary circulation of Hurricane Gilbert (1988) at the altitude of an aircraft's flight-level (700 mb). The aircraft flew from south to north five times through the eye of Gilbert, and the wind speed along each flight leg is shown from left to right in the five images. **Bold I's** denote the locations of the wind maxima associated with the inner eyewall. **Bold O's** denote the locations of the wind maxima associated with the outer eyewall. Note how the inner eyewall contracts from the first image to the second image as the outer eyewall develops. From the second image through the fifth image, the inner and outer eyewalls both contract, with the inner eyewall completely dissipating by the fifth image. This series of five images shows one eyewall replacement cycle. Image adapted from Black and Willoughby (1992).

Eyewall replacement cycles can have very serious consequences, especially when they occur just before landfall. At great cost to life and property, Hurricane Andrew (1992) unexpectedly strengthened to a Category 5 hurricane while making landfall in southeastern Florida immediately following an eyewall replacement cycle. In addition to large and rapid intensity swings, eyewall replacement cycles usually cause hurricanes to grow larger. This occurred as Hurricane Katrina moved through the Gulf of Mexico, resulting in a much larger and more dangerous storm threatening New Orleans. During landfall, larger hurricanes do more wind damage, but they are also accompanied by greater storm surge and wave heights due to increased wind **fetch**. When multiple eyewall replacement cycles occur, the hurricane can continue to grow larger with each cycle. Hurricane Igor (2010) went through multiple cycles and became one of the larger Atlantic hurricanes on record, causing significant waves and rip currents along the U.S. east coast, even while staying far out to sea.

Hurricane eyes are not always circular. Oblong, elliptical eyes are sometimes observed, especially in weaker hurricanes. A strong hurricane may have a polygonal eyewall, where the eye takes the shape of a triangle, square, pentagon, or hexagon. Polygonal eyewalls are often associated with eyewall mesovortices, which are smaller-scale atmospheric swirls that can form within the eye and which can produce extremely strong winds. Eyewall mesovortices may remain nearly stationary relative to the hurricane's center, or they may rotate around the center within the eye or even pass through the hurricane's center.

Defense Meteorological Satellite Program (DMSP) image of Hurricane Isabel at 1315 UTC 12 Sep 2003. The ``starfish' pattern in the eye is caused by the presence of six mesovortices - one near the eye center and five surrounding it. Image credit: University of Wisconsin-Madison, Space Science Engineering Center, Cooperative Institute for Meteorological Satellite Studies (CIMSS)

16. Assignment 2, Module 3: Tropical Cyclone Structure: https://www.noaa.gov/jetstream/tropical/tropical-cyclone-introduction/tropical-cyclone-structure

Tropical Cyclone Structure

The main parts of a tropical cyclone are the rainbands, the eye, and the eyewall. Air spirals in toward the center in a counter-clockwise pattern in the northern hemisphere (clockwise in the southern hemisphere) and out the top in the opposite direction.

In the very center of the storm, air sinks, forming an "eye" that is mostly cloud-free.

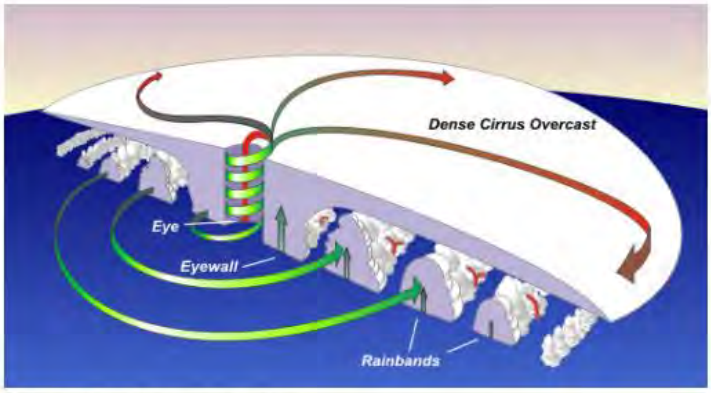

Cross section of a typical hurricane.
Download Image

The Eye

The hurricane's center is a relatively calm, generally clear area of sinking air and light winds that usually do not exceed 15 mph (24 km/h) and is typically 20-40 miles (32-64 km) across. An eye will usually develop when the maximum sustained wind speeds go above 74 mph (119 km/h) and is the calmest part of the storm.

The cause of eye formation is still not fully understood. It is probably related to the combination of "the conservation of angular momentum" and centrifugal force. The conservation of angular momentum means that objects will spin faster as they move toward the center of circulation. In other words, air increases its speed as it heads toward the center of the tropical cyclone.

One way of looking at this is watching figure skaters spin. The closer they hold their hands to the body, the faster they spin. Conversely, the farther the hands are from the body the slower they spin. In tropical cyclones, as the air moves toward the center, the speed must increase.

However, as the speed increases, an outward-directed force, called the centrifugal force, occurs because the wind's momentum directs the wind in a straight line. This straight line momentum leads to an outward pull against the curve of the wind moving around the center of the tropical cyclone. The sharper the curvature and/or the faster the rotation, the stronger the centrifugal force.

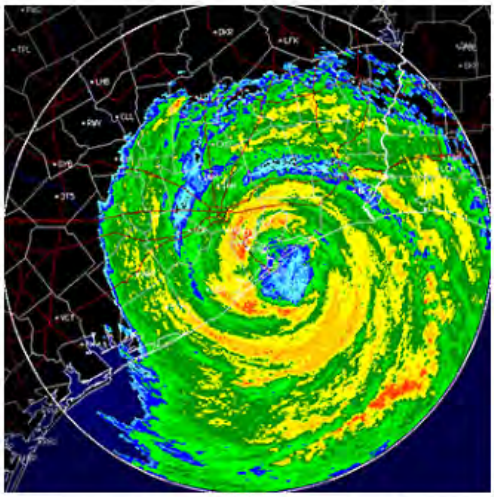

Radar image of hurricane Ike, September 13, 2008.
Download Image

Around 74 mph (119 km/h), the strong rotation of air around the cyclone balances inflow to the center, causing air to ascend about 10-20 miles (16-32 km) from the center, forming the eyewall. This strong rotation also creates a vacuum of air at the center, causing some of the air flowing out the top of the eyewall to turn inward and sink, replacing the loss of air mass near the center.

This sinking air suppresses cloud formation, creating a pocket of generally clear air in the center. People experiencing an eye passage at night often see stars.

Trapped birds are sometimes seen circling in the eye, and ships trapped in a hurricane report hundreds of exhausted birds resting on their decks. The landfall of **Hurricane Gloria** (1985) on southern New England was accompanied by thousands of birds in the eye.

The sudden change of very strong winds to a near calm state is a dangerous situation for people ignorant about a hurricane's structure.

Some people experiencing light wind and fair weather of an eye may think the hurricane has passed when actually, the storm is only half over, with dangerous eyewall winds returning shortly, this time from the opposite direction.

The Eyewall

Where the strong wind gets as close as it can is the eyewall. The eyewall consists of a ring of tall thunderstorms that produce heavy rains and usually the strongest winds. Changes in the structure of the eye and eyewall can cause changes in the wind speed, which is an indicator of the storm's intensity. The eye can grow or shrink in size, and double (concentric) eyewalls can form.

In intense tropical cyclones, some of the outer rainbands may organize into an outer ring of thunderstorms that slowly moves inward and robs the inner eyewall of its needed moisture and momentum. During this phase, the tropical cyclone is weakening.

Eventually the outer eyewall replaces the inner one completely and the storm can be the same intensity as it was previously or, in some cases, even stronger.

Rainbands

Curved bands of clouds and thunderstorms that trail away from the eye wall in a spiral fashion. These bands are capable of producing heavy bursts of rain and wind, as well as tornadoes. There are sometimes gaps in between spiral rain bands where no rain or wind is found.

In fact, if one were to travel between the outer edge of a hurricane to its center, one would normally progress from light rain and wind, to dry and weak breeze, then back to increasingly heavier rainfall and stronger wind, over and over again with each period of rainfall and wind being more intense and lasting longer.

Tropical Cyclone Size

Typical hurricane strength tropical cyclones are about 300 miles (483 km) wide although they can vary considerably.

Size is not necessarily an indication of hurricane intensity. Hurricane Andrew (1992), the second most devastating hurricane to hit the United States, next to Katrina in 2005, was a relatively small hurricane.

On record, **Typhoon Tip** (1979) was the largest storms with gale force winds (39 mph/63 km/h) that extended out for 675 miles (1087 km) in radius in the Northwest Pacific on 12 October, 1979. The smallest storm was **Tropical Storm Marco** with gale force winds that only extended 11.5 miles (18.5 km) radius when it struck Misantla, Mexico, on October 7, 2008.

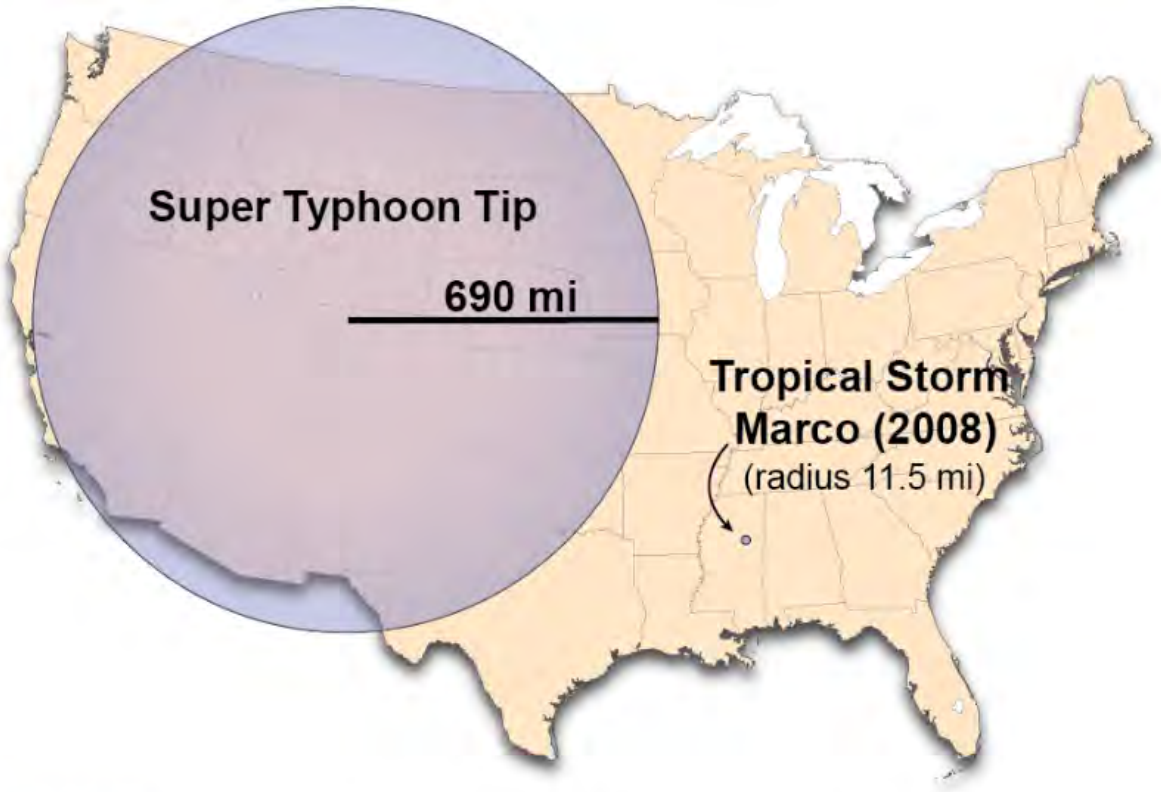

The relative sizes of the largest and smallest tropical cyclones on record as compared to the United States.
Download Image

However, the hurricane's destructive winds and rains cover a wide swath. Hurricane-force winds can extend outward more than 150 miles (242 km) for a large one. The area over which tropical storm-force winds occur is even greater, ranging as far out as almost 300 miles (483 km) from the eye of a large hurricane.

The strongest hurricane on record for the Atlantic Basin is Hurricane Wilma (pdf) (2005). With a central pressure of 882 mb (26.05") Wilma produced sustained winds of 184 mph (160 kt / 280 km/h). Air Force reconnaissance observations indicated that the eye of the hurricane had contracted to as small as 2 n mi (3.7 km) in diameter.

With an estimated sustained wind speed of 213 mph (185 kt / 325 km/h), the strongest hurricane in the Western Hemisphere was Hurricane Patricia (pdf) (2015). However, Patricia's hurricane force winds only extended out 20-25 miles (32-40 kilometers) from the compact, 7-mile (11 kilometer) diameter eye.

17. Assignment 2, Module 3: How Hurricanes Form: https://scied.ucar.edu/image/how-hurricanes-form

How Hurricanes Form

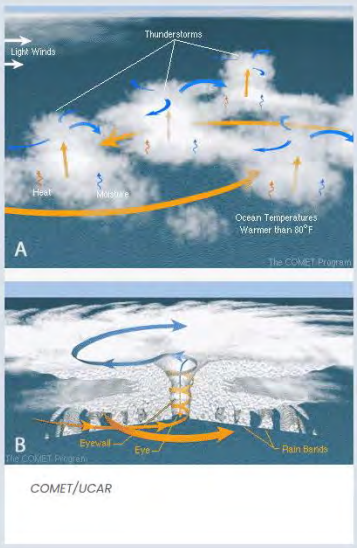

COMET/UCAR

The conditions needed to form a hurricane (tropical cyclone) include thunderstorms, warm ocean temperatures and light winds (A). Once formed, a hurricane consists of a huge rotating spiral of rain bands with a center of clear skies called the eye which is surrounded by the fastest winds of the storm in the eyewall (B).

19. Assignment 2, Module 4: State of FL Loss Projection Model:
https://www.aoml.noaa.gov/hrd/Powell/JWEIA_8_28.pdf

State of Florida Hurricane Loss Projection Model: Atmospheric Science Component

Mark Powell[a*], Steve Cocke[b], George Soukup[a], Sneh Gulati[c], Nirva Morisseau-Leroy[d], Chris Landsea[a], Neal Dorst[a] and Liza Axe[b]

[a]NOAA Hurricane Research Division, Miami FL USA

[b]Florida State University, Tallahassee, FL USA

[c]Florida International University, Miami FL USA

[d]University of Miami, Miami, FL USA

Abstract

The State of Florida is in the process of developing an open, public model for the purpose of probabilistic assessment of risk to insured residential property associated with wind damage from hurricanes. The model comprises atmospheric science, engineering, and financial/actuarial components and is planned for 2004 submission to the Florida Commission on Hurricane Loss Projection Methodology. The atmospheric component includes modeling the track and intensity life cycle of each simulated hurricane within the Florida threat area. When a storm approaches within 200 km of the Florida coast line, the wind field is computed by a slab model of the hurricane boundary layer coupled with a surface layer model based on the results of recent GPS sonde research. A time series of open terrain surface winds is then computed for each zip code in the threatened area. Depending on wind direction, an effective roughness length is assigned to each zip code based on the upstream roughness as determined from land cover/ land use products. Thousands of storms are simulated allowing determination of the wind risk for all zip codes in Florida. The wind risk information is then provided to the engineering and loss models to assess damage and average annual loss, respectively.

Keywords: Hurricane, risk, loss, catastrophe

1. Introduction

The historical record for establishing the risk of hurricanes throughout the coastal United States is limited to a period of about 100 years. Unfortunately this period is not sufficient to establish risk without large errors so alternative methods have been used since the 1970's (Ref [1]). Hurricane risk models are currently used to conduct simulations of thousands of years of storms based on statistical probability distributions of important historically observed parameters. This method is often referred to as the joint probability method since the probability of having an event is coupled with the probability that the event is of a given intensity. Commercial modeling interests have developed several versions of these which are used to advise the insurance industry for ratemaking. Unfortunately the models are proprietary so customers whose rates have increased on the basis of model calculations have no way of of examining or questioning the

results. The State of Florida is developing a public model to provide an understandable baseline for comparison to the commercial models. The model will be open and transparent, in which results can be examined in great detail. This paper will describe the atmospheric component of the model.

2. Threat area

To focus on storms capable of causing residential property damage in Florida, a threat area is defined to best capture the statistical characteristics of historical tropical cyclones that have affected the state. The area within 1000 km of a location (26.0 N, 82.0W) off the southwest coast of Florida (Fig. 1) was chosen since this captures storms that can affect the panhandle and northeast coasts of Florida, as well as storms that approach South Florida from the vicinity of Cuba and the Bahamas.

3. Annual occurrence and storm genesis

The model has the capability of simulating climate cycles and tropical cyclone activity according to different periods of the historical record (Ref[2]). The period 1851-2002 is the latest available but the period 1900-2002 is frequently used due to uncertainties about 19th century storms, especially for Florida. There are also uncertainties about the first half of the 20th century since aircraft reconnaissance only began in the 1940's so another choice in the period of record is the period 1944-2002. Four additional choices are available which simulate the warm (El Nino, fewer hurricanes) and neutral or cold (La Nina, more hurricanes) inter annual climate cycles in tropical cyclone activity, as well as the cold or warm phases of the Multi-decadal climate cycles. These choices constrain the historical record from which the fit of annual tropical cyclone occurrence is made. Two fits are tested, the negative binomial and the Poisson model. Goodness of fit tests determine which fit is used for the subsequent simulations. Once the number of tropical cyclones within the threat area for a given year is determined, the historical seasonal genesis frequency is empirically fit to determine the date and time of genesis for each storm.

4. Storm movement and intensity

The threat area is divided which into regions which contain the historical and seasonal characteristics of storm motion and intensity change. Initial location, intensity, and motion for each storm are based on the geographic probability distributions of each quantity for a given time within the season. We use a stochastic approach to model the storm genesis location and track and intensity evolution. A PDF for the initial storm position is derived from the historical "genesis" data, where by genesis we mean the time when the storm forms in or first appears in the threat area. The PDF is a derived for 0.5 degree latitude/longitude box regions, as well as time of season (month). A (uniform) random error term is added so that the storm may form anywhere within the 0.5 degree box. Figure 2 shows a plot of the spatial PDF for storm genesis location for the month of August.

We derive discrete PDFs based on historical data to provide the initial and subsequent motion and intensity of the storm. A storm is simulated by repeatedly sampling from these PDFs via a Monte Carlo approach. These PDFs are derived for variable-sized regions centered at every 0.5 degree latitude and longitude in the hurricane basin. The size of these regions is determined to be that which gives a robust probability density function (PDF) for the quantities of interest (speed, direction, and intensity), up to some maximum size. Once the storm has been given an initial condition, its subsequent evolution is governed by sampling the PDFs for change in intensity, change in translation speed, and change in heading angle in 6 hour increments. The time step is reduced to 1 hour when the storm is close to the coastline.

Intensity change is modeled by using the observed geographic probability distribution of six-hour changes of central pressure through modeling the potential intensity (Ref [3]). The potential intensity takes into account the concept of the hurricane as a heat engine constrained by the input (sea surface) and outflow (stratosphere) temperatures. Intensity change is limited so as to not exceed the maximum observed change for a particular geographic region. When a storm center crosses the coastline (landfall) the intensity change follows a pressure decay model (discussed below). If the storm moves back over the sea, the former intensity change model is reinstated.

The PDFs for change in speed and direction depend on the current speed and direction (binned in discrete intervals), as well as geographic location (0.5 degree lat-lon location) and time of season (month). Figure 3 shows a PDF for change in direction for 8 possible direction intervals (45 degree intervals). The PDF indicates that the storm has a high probability for maintaining current direction, except for westward traveling storms which tend to turn right (northward) somewhat.

This approach has a great advantage over early models that considered a circular approach region surrounding coastal cities. Storms that parallel the coast or make several landfalls can be properly simulated with this method.

5. Storm decay

The tropical ocean is typically warmer than the air above it, enabling a transfer of heat and moisture to the air. Inflow towards the center of the tropical cyclone transports this energy toward the eyewall, where it can help sustain convection, leading to a positive feedback of warming in the eye, lower minimum central pressure, stronger inflow, and more energy transport (Ref [4], [5]). Over the ocean this positive feedback loop may be slowed or reversed by ocean cooling, advection of relatively cold dry air with a history of travel over land, or strong wind shear that prevents the storm center from focusing heating in the eye (Refs. [6], [7]). As a hurricane make landfall, more and more of the circulation traverses land, and the storm loses it's source of energy (Ref. [8]). More and more dry and relatively cool air flows towards the center, and the air cools even more as it expands adiabatically while approaching lower pressures (Ref. [9]). The result is that the eye heating gradually decreases and the central pressure begins to increase or "fill".

Since the wind model depends on the specification of the pressure gradient, a method was needed to estimate the central pressure over land. The central pressure is modeled using the filling model of Vickery and Twisdale [10].

The HURDAT database and Ho et al. [11] contains documentation of storm decay and pressure filling for many hurricane landfall cases in the historical record. As a starting point for a simple decay model we will use the exponential decay as a function of time after landfall. Vickery and Twisdale [10] developed and tested a model for the Florida peninsula based on nine landfalling hurricanes and found the model to be slightly conservative within 3 h of landfall and slightly non conservative beyond 3 h after landfall. The form of the model is:

$$\Delta p(t) = \Delta p_o \exp(-at) \qquad (1)$$

where $\Delta p(t)$ is the time dependent central pressure deficit and t represents the time after landfall. The filling rate constant is given as:

$$a = a_o + a_1 \Delta p_o + \varepsilon \qquad (2)$$

where ε is a random error term with a normal distribution. The dependence of the filling rate constant on Δp allows stronger storms to decay faster than weak storms; a characteristic observed in hurricane landfalls (Ref. [12]). The random error term allows for the possibility that some storms will decay slower or faster than average. For the Florida peninsula Vickery and Twisdale (1995) use a_0=0.006, a_1= 0.00046, and the standard deviation of ε = 0.0025.

The Kaplan and DeMaria [13] model is also pertinent but it deals with wind decay rather than pressure decay and there is no well established method to convert inland-decayed peak winds to central pressure. The advantage of the filling model is that it provides a starting point to invoke an intensity redevelopment for storms that exit the coastline and reintensify over water. When a storm reemerges over water, the intensity is modeled along the track the same way it was before landfall using the decayed pressure as an initial value.

6. Wind field model

Once a simulated hurricane moves to within 200 km of the Florida coastline, the wind field model is turned on. The model is based on the slab boundary layer concept originally conceived by Ooyama [14] and implemented by Shapiro [15]. Similar models based on this concept have been developed by Thompson and Cardone [16] and Vickery et al. [16, 17]. As in Ref. [15] the model is initialized by a vortex in gradient balance with the pressure above the boundary layer. Gradient balance represents a circular flow caused by balance of forces on the flow whereby the inward directed pressure gradient force is balanced by an outward directed Coriolis and centripetal accelerations. The coordinate system translates with the hurricane vortex moving at velocity **c**. The vortex translation is assumed to equal the geostrophic flow associated with the large scale pressure gradient. As a possible future enhancement the large scale flow in which the vortex is embedded may be treated independently of the vortex motion as in Ref. [16]. In cylindrical coordinates that translate with the moving vortex, equations for a slab hurricane boundary layer under a prescribed pressure gradient (Ref. [15]} are:

$$\frac{u\partial u}{\partial r} - \frac{v^2}{r} - fv + \frac{v}{r}\frac{\partial u}{\partial \theta} + \frac{\partial p}{\partial r} - K\left[\nabla^2 u - \frac{u}{r^2} - \frac{2}{r^2}\frac{\partial u}{\partial \theta}\right] + F(\vec{c},u) = 0 = \frac{\partial v}{\partial t} \quad (3)$$

$$u\left[\frac{\partial v}{\partial r} + \frac{v}{r}\right] + fu + \frac{v}{r}\frac{\partial v}{\partial \theta} - K\left[\nabla^2 v - \frac{v}{r^2} + \frac{2}{r^2}\frac{\partial u}{\partial \theta}\right] + F(\vec{c},v) = 0 = \frac{\partial u}{\partial t} \quad (4)$$

where u and v are the respective radial and tangential wind components relative to the moving storm, p is pressure which varies with radius (r), f is the Coriolis parameter which varies with latitude, θ is the azimuthal coordinate, K is the eddy diffusion coefficient, and F(c,u), F(c,v) are frictional drag terms (discussed below). All terms are assumed to be representative of means through the boundary layer. The motion of the vortex is determined by the modeled storm track.

Note that equations (3) and (4) represent a steady state solution. In order to solve the equations they must be integrated until the steady state assumption is satisfied either through time integration (e.g. Ref. [16]) or numerical method (see model integration section below and appendix). More sophisticated multiple level models (e. g. Kurihara et al., [19]) include equations describing the thermodynamic processes including convection, cloud and precipitation microphysics, evaporation of sea spray, exchange of heat and moisture with the sea, etc. These processes interact to change the pressure and wind fields over time, but the computational requirements of such models make them poorly suited for risk assessment. An advantage of our approach is that the solution to (3) and (4) is straightforward and we do not have the computationally costly requirement to run the model to "steady state" each time we desire a solution. A limitation of our model (and all other Hurricane risk models) is the lack of physical representation of processes that may also contribute to the wind field of a tropical cyclone.

6.1 *Surface pressure field*

The symmetric pressure field p(r) is specified as:

$$p(r) = p_o + \Delta p e^{-\left[\frac{R_{max}}{r}\right]^B} \quad (5)$$

where p_o is the central minimum sea level pressure, B is the Holland [20] pressure profile shape parameter, Rmax is the radius of maximum gradient wind speed, and Δp is the pressure deficit or difference between p_o and the peripheral pressure at the location of the outermost curved pressure contour on a surface synoptic weather map. The central pressure is modeled according to the intensity modeling in concert with the storm track. The peripheral pressure is held constant at 1013 kPa in accordance with the mean global atmospheric surface pressure.

The mean tangential gradient wind is determined primarily by (5). In the development of the

HAZUS model for FEMA, the contractor demonstrated that the azimuthal location and radial extent of peak winds is very sensitive to *B*. Vickery et al. [18] used a NOAA-HRD database of research and reconnaissance aircraft measurements to study the dependence of *B* on po and Rmax observed by the aircraft at altitudes < 1.5 km, which Dunion et al. [21] have shown are representative of the mean boundary layer. The resulting Ref. [18] expression for B is:

$$B = 1.38 + 0.00184\Delta p - 0.00309 R_{\max} \qquad (6)$$

Expression (6) is used at present but a new method of pressure profile specification is under development by Willoughby [22].

6.2 *Radius of maximum wind*

The radius of maximum wind is determined from a distribution of values as a function of Pmin and latitude. As in Ref. [18], a log normal distribution is assumed for Rmax with a mean value determined as a function of Δp and Latitude. In developing the models for Rmax, we used the data from Ref. [11] for storms from 1900-1983, NOAA-HRD archives of realtime surface wind analyses from 1995-2002, an archive of the National Hurricane Center that was maintained by Dr. Mark DeMaria (now with NOAA's NESDIS at Colorado State University) for the years 1988-1999, and an HRD archive of aircraft observations for the years 1984-1987. The State of Florida model considers U. S. Atlantic coast hurricane landfalls with latitudes as high as 34 degrees north in order to help fill a dearth of information on storms affecting the Northeast Florida coastline. A generalized linear model for the natural log of Rmax ($r^2 = 0.212$) is

$$\ln R_{\max} = 2.0633 + 0.0182\Delta p - 0.00019008\Delta p^2 + 0.0007336 Lat^2 + \Delta \qquad (7)$$

where Δ is a normal random variable with a mean of zero and a variance of 0.169. Equation (7) describes the mean of the log normal distribution in nm. When a simulated storm is close enough to land to become a threat, an Rmax value is randomly chosen given the Δp and Latitude.

6.3 *Friction terms*

The frictional drag is in the direction opposite the total wind relative to the earth at the surface and represents the mean momentum flux from the atmosphere to the surface. The frictional terms in (3) and (4) may be specified in terms of the vertical gradient of stress:

$$F(\vec{c},u) = \frac{\partial \tau}{\partial z} \qquad (8)$$

The variation of τ with height over the depth of the slab boundary layer may be described by a function with properties supported by observations in the surface layer of tropical cyclones. Here we invoke the concept of a surface layer as the lower region of the boundary layer estimated at 200m in which stress is approximately constant. In reality the stress is greatest close to the surface, and is zero at the top of the boundary layer. By assuming stress as near constant over the surface layer we satisfy conditions for applying the logarithmic wind profile to describe the

vertical variation of the mean wind speed with height. The fact that a mean logarithmic wind profile has been observed in tropical cyclone eyewalls (Ref. [23]) provides justification for the surface layer concept. The evaluation of (8) may be approximated as 0.25 (τ_{sfc} / h), where τ_{sfc} is the surface stress and h represents the top of the boundary layer, taken to be 500 m. The factor 0.25 takes into account the fact that the average stress in the slab boundary layer is less than the mean stress of the surface layer. The 0.25 value is an estimate based on meteorological judgment. At the surface, the stress may be expressed in terms of the earth relative surface wind velocity U10 at a height of 10 m or 32 ft above the surface, and the neutral stability surface drag coefficient, Cd :

$$\tau_{sfc} = C_d \left|\vec{U}_{10} + \vec{c}\right| \left(\vec{U}_{10} + \vec{c}\right) \qquad (9)$$

where

$$C_d = \left(0.49 + 0.065 \left|\vec{U}_{10} + \vec{c}\right|\right) x 10^{-3} \qquad (10)$$

as specified by Large and Pond [24] and U_{10} is the surface (10 m, 32 ft) wind speed relative to the moving storm. Recent research by Powell et al., [23] has indicated that (10) may not apply in the open ocean but at present we believe it is appropriate near the coast where shoaling conditions would be expected and where the wind model is applied to assess risk.

As described below, U_{10} may be expressed in terms of the mean boundary layer wind, as supported by recent GPS sonde measurements in hurricanes:

$$\left|\vec{U}_{10}\right| = 0.8 \left|\vec{u}\right| \qquad (11)$$

6.4 *Eddy Diffusion*

The wind model describes the effects of horizontal turbulence following Shapiro [15] using a constant eddy diffusion coefficient, $k = 5 \times 10^4$ $m^2 s^{-1}$. In theory the role of eddy diffusion is to represent the effect of turbulence in mixing air horizontally in the radial and tangential directions. Vertical mixing (contained in the friction terms discussed earlier) is typically much larger in magnitude and is associated with a large body of research based on numerous field investigations. Horizontal mixing is most prominent in regions with strong horizontal gradients. Hence the greatest impact of eddy mixing will be in the eyewall where radial gradients are strong. In practice, this term primarily serves as a way to smooth out computational noise in the model results.

6.5 *Model integration*

The Hurricane wind field model includes a fully two dimensional, time-independent, numerical integration of the tangential and radial momentum equations for the mean boundary layer wind components (see Appendix for a complete description). The actual integration procedure is an iterative one, which makes use of a polar coordinate integration grid (Fig. 4) centered on the moving storm. The nested circles are separated from their inscribed and circumscribed neighbors by a radial separation of $R_{max}/10$, where R_{max} is the prescribed radius of maximum winds.

The integration proceeds in two separate but interlocking steps: The "ring" integration treats each concentric ring of grid points as if the radial derivatives in the momentum equations for the tangential and radial wind components are precisely known. Hence, the "ring" equations determine the tangential and radial wind components at each grid point on one of the concentric rings by solving two nonlinear coupled ordinary differential equations in the azimuthal variable with periodic boundary conditions. This integration is performed on each one of the concentric rings covering the domain of integration out to a distance of 20 R_{max}. The "spoke" integration treats each radial spoke of grid points as if the azimuthal derivatives are precisely known. Therefore, the "spoke" equations determine the tangential and radial wind components at each grid point on one of the "spokes" emanating outward from the origin by solving two coupled nonlinear ordinary differential equations in the radial variable measured in units of the RMW.

Since the "ring" process needs radial derivatives and the "spoke" process requires azimuthal derivatives, both of these processes can be started simultaneously by computing the requisite radial derivatives from an initial approximate wind field, which is computed for a stationary storm, and setting the azimuthal derivatives to zero. The asymmetry in the final wind field arises primarily from the fact that the friction terms are both proportional to the term:

$$\left|\vec{W}\right|\vec{W} - \left|\vec{c}\right|\vec{c} = \left|\vec{V}+\vec{c}\right|\left(\vec{V}+\vec{c}\right) - \left|\vec{c}\right|\vec{c} \qquad (12)$$

where $\vec{W}$ is the earth-relative total vector wind, $\vec{V}$ is the storm-relative total vector wind and $\vec{c}$ is the constant translational velocity. Thus, the asymmetry in the final result arises explicitly through the dependence on $\vec{c}$ as well as implicitly through induced asymmetry in $\vec{V}$. At the outset of the iteration, $\vec{V}$ has no azimuthal dependence since it was computed for a stationary storm. Hence the results of the first iteration yield "ring" and "spoke" wind fields (Fig. 5) which exhibit asymmetry solely due to the explicit dependence of the friction terms on the translation velocity. The friction terms computed from the initial wind field are used to provide the "given" terms in both the "ring" and spoke" equations which, separately, upon integration, furnish an improved version of the complete vector wind field, which is asymmetric. An optimum linear combination of the "ring" and "spoke" wind fields is then determined to

minimize the residuals of the complete set of fully two dimensional momentum equations. This optimum mixture of the "ring" and "spoke" wind fields, which is asymmetric, replaces the initial storm-relative wind field and the integration cycle can be repeated as often as needed. After a few iterations, the process converges such that there is very little difference between the "ring" and "spoke" wind fields or successive instances of the optimized composite wind field. The latest instance of the composite wind field (Fig. 6) is the model solution for the wind components in the translating coordinate system. A simple coordinate transformation then produces the earth-relative wind field based on the known translation velocity. Our methodology directly determines a "steady state" wind field describing a uniformly translating cyclone moving over a uniform surface with given frictional characteristics.

6.6 *Asymmetries in the wind field*

The solution of (3) and (4) exhibits a shift of the radius of maximum winds toward the center when compared with the gradient wind profile. The tangential winds are also super gradient due to the advection inward of angular momentum due to the radial flow induced by the frictional convergence. Besides vortex translation motion, radial advection of tangential momentum, and differential friction, other factors affecting the asymmetric distribution of winds in a tropical cyclone include wind shear, synoptic scale weather features, rainband convection, concentric eyewall cycles, and tertiary circulations associated organized linear flow features and turbulent eddies. In the simple model described here, only the motion and differential friction influences are taken into account. The remaining features are difficult to model but play an important role in determining the azimuthal location of the peak wind. A future version of the model will attempt to include the effects of wind shear.

6.7 *Marine surface layer*

Once the mean PBL motion field is determined, the surface wind is estimated through surface layer modeling. A neutral stability surface layer is assumed to exist. Monin-Obukov heights provide an estimate of the importance of shear or mechanically produced turbulence to buoyancy-produced turbulence. The large values of Monin-Obukov heights computed in tropical cyclones by Moss and Rosenthal [25] and Powell [26] are consistent with shear induced turbulence associated with neutral, well-mixed surface layers. In these conditions we can specify the surface stress and friction velocity in terms of a drag coefficient, and use the well known log profile to describe the variation of wind speed with height. The mean boundary layer (MBL) depth is assumed to be 500 m, and the MBL wind speed is assumed to apply to the midpoint of this layer or 250m. A log profile for neutral stability is assumed to apply from the surface (10 m) to 250 m. Recent research on marine boundary layer wind profiles in tropical cyclones (Ref. [23]) support this assumption. The mean surface wind for marine exposure is assumed to be 78% of the slab boundary layer wind, in accordance with recent results from over 300 boundary layer wind profiles observed in tropical cyclones (Ref. [23]). The height and exposure of the model surface wind is 10 m and "open" in accordance with standard ASTM 1996 and is assumed to represent a mean over a 3600 s time period. A gust factor (Ref. [27]) is used to

convert the mean wind to a maximum sustained one min wind as required by the State of Florida Commission on Hurricane Loss Projection, and to a peak 3s gust as required for the engineering component damage calculations. An example of the model wind field for Hurricane Andrew compared to a published observation-based wind field (Ref. [6]) is shown in Fig. 6.

Considering the wind shears present in tropical cyclones and the lack of cold sea surface temperatures in the vicinity of the Florida coastline, the neutral boundary layer assumption is justified. The marine roughness is modeled using the Large and Pond [24] drag coefficient to compute friction velocity given the mean surface wind speed, and then solving the neutral stability log law for for Zo. The Ref. [24] expression for drag coefficient was found to compare well with open ocean measurements in hurricanes for wind speeds up to hurricane force. For higher wind speeds, recent hurricane measurements (Ref. 23) suggest that the drag coefficient and roughness decrease with wind speed over the open ocean. However, since the use of the hurricane model for loss projection will apply to the landfall of the tropical cyclone where conditions are very different than those over the open ocean. Anctil and Donelan [28] suggest that shoaling conditions in the shallow water adjacent to the coastline cause increased roughness and drag coefficient. The Large and Pond expression dependence on wind speed estimates larger values that we assume are relevant to shoaling conditions. Sufficient measurements to improve the modeling of drag and roughness near the coast will not be available for several more years.

7. Land friction influences

To standardize observations for a common terrain (Ref. [27]), the mean surface wind for marine conditions is converted to "open terrain" conditions over land using the expression given in Simiu and Scanlan [29]. For each 10 min segment of storm motion, the open terrain exposure surface wind speed and direction is determined for all population-weighted zip code centroid locations within 200 km of the storm center. The open terrain wind at each zip code centroid is corrected to the observed terrain using a fetch-dependent virtual roughness for that particular direction and zip code. The virtual roughness takes into account the flow over upstream changes in roughness and assumes that internal boundary layer development prevents the flow from reaching complete equilibrium with its surroundings (Refs. [27, 30]). The flow is most influenced by the roughness of the terrain 3 km upstream of the zip code centroid, but the flow is still influenced by terrain further upstream. The approach we use is based on the Source Area Model (SAM) described in Schmidt and Oke [31]. SAM takes into account turbulence created by patchy terrain and determines the relative importance of the turbulence source area to a downstream wind sensor located at the zip code centroid. This approach is an improvement over current models that consider zip code roughness constant for all wind directions. Our method is especially advantageous for coastal zip code locations since flow with an upstream fetch over the sea can be significantly stronger than flow over a constant land roughness. The geographic distribution of roughness (Fig. 7) is associated with a classification of the land use / land cover in a particular region according to LANDSAT imagery used to develop the National Multi-Resolution Land Cover database (Ref. [32]). Determination of the roughness for each LU/LC classification was developed by the National Institute for Building Sciences for FEMA's multi

hazard damage mitigation model (HAZUS).

The maximum sustained 1 min surface wind and peak 3 s gust are computed by applying a gust factor (Ref. [27]) to the the mean surface wind. At the end of a simulation, time series of wind speed and direction exist for all zip codes in Florida for which hurricanes (or hurricanes that have decayed to a weaker status) have passed within 200 km. Landfalling tropical storms and hurricanes that have decayed post-landfall to a tropical storm with maximum winds of <18 m/s are are not considered. The great advantage of our approach over other models is that the full time series of the wind are retained at high resolution. Retaining this information makes possible the determination of additional damage-relevant parameters such as duration of winds exceeding hurricane force and wind steadiness. Powell et al [33] showed that damage to the building envelope was associated with small values of wind direction steadiness and large values of duration. These parameters capture the physical torque effects of thousands of gust-lull cycles as well as the fact that, given the susceptibility of residential buildings to damage at roof corners and gables, the more the wind direction changes during a strong wind event, the greater the chance that a given wind direction will occur for which a structure is susceptible.

8. Conclusions

In order to achieve stable results, a very large simulation of ~100,000 years of activity is prescribed. It is expected that the model would be run once per year to take advantage of the latest historical data to assess average annual loss to residential properties due hurricane wind damage. The primary user will be the Department of Financial Services and homeowners in the state of Florida, although there are many other research uses for the model and it is expected that the model will undergo periodic enhancements to attempt to keep up with the state of the art. The model will reside at Florida International University's International Hurricane Research Center in Miami. Complete documentation of the model algorithms and code will be available for public examination. Given that there may be one Florida hurricane landfall per year, this large number of storms will be contained in our database. Each storm may effect as many as 40 zip codes so it is expected that the database could contain several million time series instances, as well as track, intensity, and landfall wind field information on each storm. The database could then be queried for details on simulated storms and probability distributions relevant to a given zip code or county in Florida. The model is scheduled for submission in 2004 to the State of Florida Commission on Hurricane Wind Loss Projection (Ref. [34]).

Acknowledgements

This research is supported by the State of Florida through a Department of Financial Services grant to the Florida International University International Hurricane Research Center. We thank the Department of Homeland Security (Federal Emergency Management Agency) and the National Institute for Building Sciences for their assistance with the roughness classifications.

Appendix: Hurricane Model Equations and Integration

1. Definitions

R = Radius of maximum surface wind speed, specified

c_t = storm translation speed, specified

c_{dir} = storm translation direction compass heading , specified

Δp = Central pressure deficit, specified

$p(r) = p_o + \Delta p e^{-\left(\frac{R_{max}}{r}\right)^B}$ = sea level pressure

$B = 1.38 + 0.00184\Delta p - 0.00309R$ = Holland profile parameter

θ = Azimuthal coordinate, measured from north

$s = \frac{r}{R}$ = normalized radial coordinate

$v_g(s)$ = Gradient wind: $\frac{v_g^2}{r} + fv_g = \frac{1}{\rho}\frac{\partial p}{\partial r}$

$f = 2\Omega \sin\phi$ =Coriolis parameter

ϕ = latitude of storm center

$v_{o(s)}$ = normalized gradient wind (symmetric) = $v_{g(s)} / v_{gmax}$ where V_{gmax} is the maximum gradient wind in the radial profile

$\tilde{f} = \frac{Rf}{V_{g\,max}}$ = normalized Coriolis parameter

$v(s,\theta) = \frac{v}{v_g}$ = normalized storm-relative tangential wind component

$u(s,\theta) = \frac{u}{v_g}$ = normalized storm-relative radial wind component

μ = friction coefficient= $\frac{RC_d}{h}$

h= mean boundary layer height

C_d = Drag Coefficient

$c = \frac{c_t}{v_{g\,max}}$ = normalized translation speed

$g(s) - 2v_o(s)s^{-1} + \tilde{f}$ (A1)

$d(s) = \dot{v}_o + v_o s^{-1} + \tilde{f}$ (A2)

where a "dot" represents a derivative with respect to s, $g(s)$ and $d(s)$ depend only on V_0 and $\tilde{f}$

$\chi(s,\chi) = v(s,\chi) - v_o(s)$ = normalized departure from gradient balance

2. Equations of motion for a stationary storm

Substituting the terms from the definitions into (1) and (2) for a steady state, stationary storm (hence no azimuthal dependence: u = u(s) and / /= / /(s)) leads to the following normalized equations of motion:

$u\dot{u} - \mu\left(g + \mu s^{-1}\right) + \mu uw = 0$ (A3)

$u\left(\mu + \mu s^{-1} + d\right) + \mu\left(v_o + \mu\right)w = 0$ (A4)

$w = \sqrt{u^2 + (vo + \mu)^2}$ (A5)

w is the total normalized storm-relative wind vector.

3. Complete equations for a storm moving *northward* with translation speed c_t:

$u\partial_s u + s^{-1}\left(v_o + \mu\right)\partial_\mu u - \mu\left(g + \mu s^{-1}\right) + \mu\left(uw + c\left(w - c\right)\sin\mu\right) = 0$ (A6)

$u\partial_s \mu + s^{-1}\left(vo + \mu\right)\partial_\mu \mu + u\left(d + \mu s^{-1}\right) + \mu\left(\left(v_o + \mu\right)w + c\left(w - c\right)\cos\mu\right) = 0$ (A7)

$w = \sqrt{(u + c\sin\mu)^2 + \left(\left(vo + \mu\right) + c\cos\mu\right)^2}$ (A8)

4. Solve Spoke equations

Let $\square = v_o + \square$ (A9)

$$u^* \partial_s u + \square u w^* \square \left(g + \square s^{\square 1}\right)^* \square + \left[s^{\square 1} \square \partial_{\square} u + \square \left(c\left(w \square c\right) \sin \square\right)\right]^* = 0 \quad \text{(A10)}$$

$$u^* \partial_s \square + \square \square w^* + \left(d + \square s^{\square 1}\right)^* u + \left[s^{\square 1} \square \partial_{\square} \square + \square \left(w v_o + c\left(w \square c\right) \cos \square\right)\right]^* = 0 \quad \text{(A11)}$$

These are linear in u and $\square$ if * terms are evaluated with fields from the previous iteration.

5. Solve Ring equations

$$\left(s^{\square 1} \square\right)^* \partial_{\square} u + \left(\partial_s u + \square w\right)^* u \square \left(g + s^{\square 1} \square\right)^* \square + \square \left(c\left(w \square c\right) \sin \square\right)^* = 0 \quad \text{(A12)}$$

$$\left(s^{\square 1} \square\right)^* \partial_{\square} \square + \left(\partial_s \square + s^{\square 1} \square + d\right)^* u + \square w^* \square + \square \left(v_o w + c\left(w \square c\right) \cos \square\right)^* = 0 \quad \text{(A13)}$$

These are linear in u and $\square$ if * terms are evaluated with fields from the previous iteration.

6. Substitute a linear combination of each solution back into the complete equations (Item 3 above) such that

$u = Au_S + Bu_I$ (A14)

and

$\Pi = A\Pi_s + B\Pi_I$ (A15)

7. Compute the residuals (or "non zeroness" of the solutions to the complete equations) at points in the core of the storm near the peak wind area and select the values for A and B that minimize the residuals throughout this region such that the value of J is as small as possible.

$$J = \max\left(\text{ABS (Res u)} + \text{ABS (Res}\square\text{)}\right) \quad \text{(A16)}$$

8. The sequence (Items 4-7) is repeated until the solution converges. Equations (14) and (15) are used to evaluate the * terms in items 4 and 5 for the next iteration.

9. Once the wind field is determined, it is rotated such that zero in the azimuthal coordinate matches the specified storm translation direction compass heading.

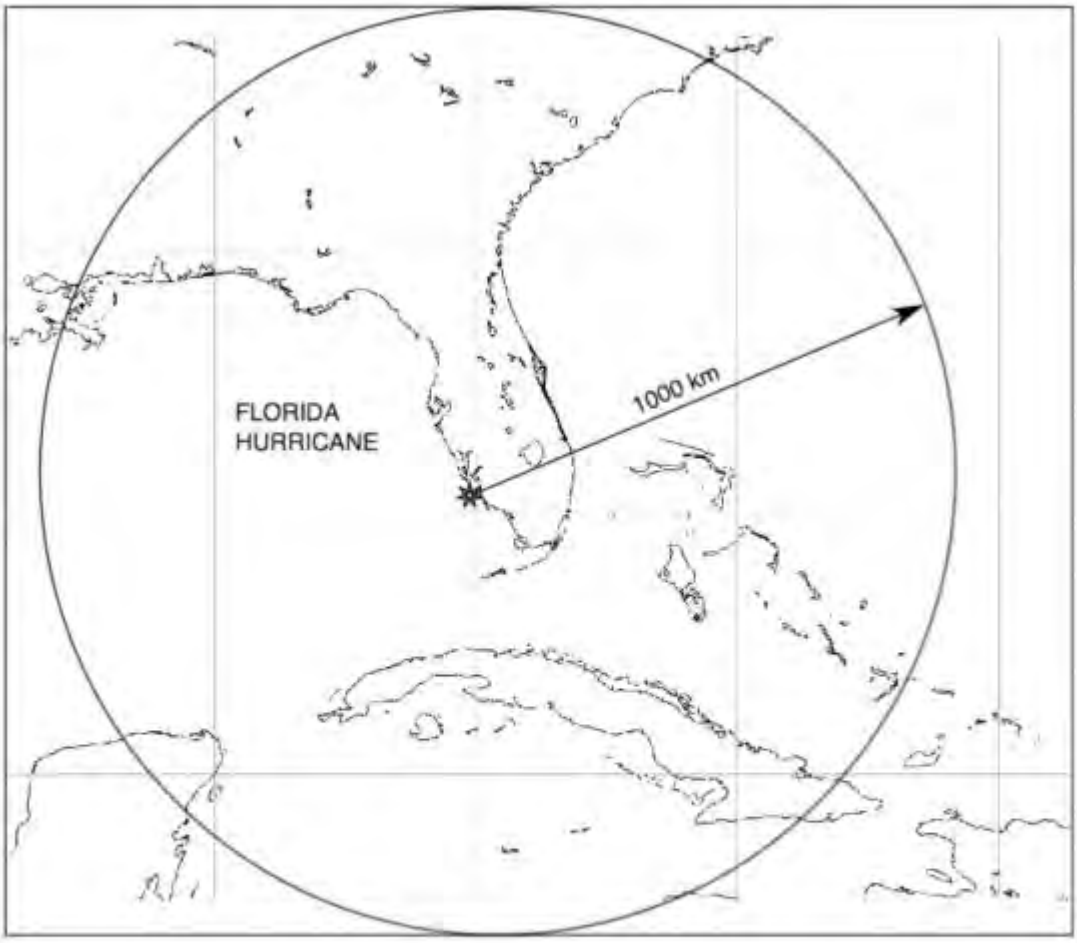

Figure 1. Threat area map. All storms entering or developing within the threat area are considered for characteristics relating to formation, movement, and intensity.

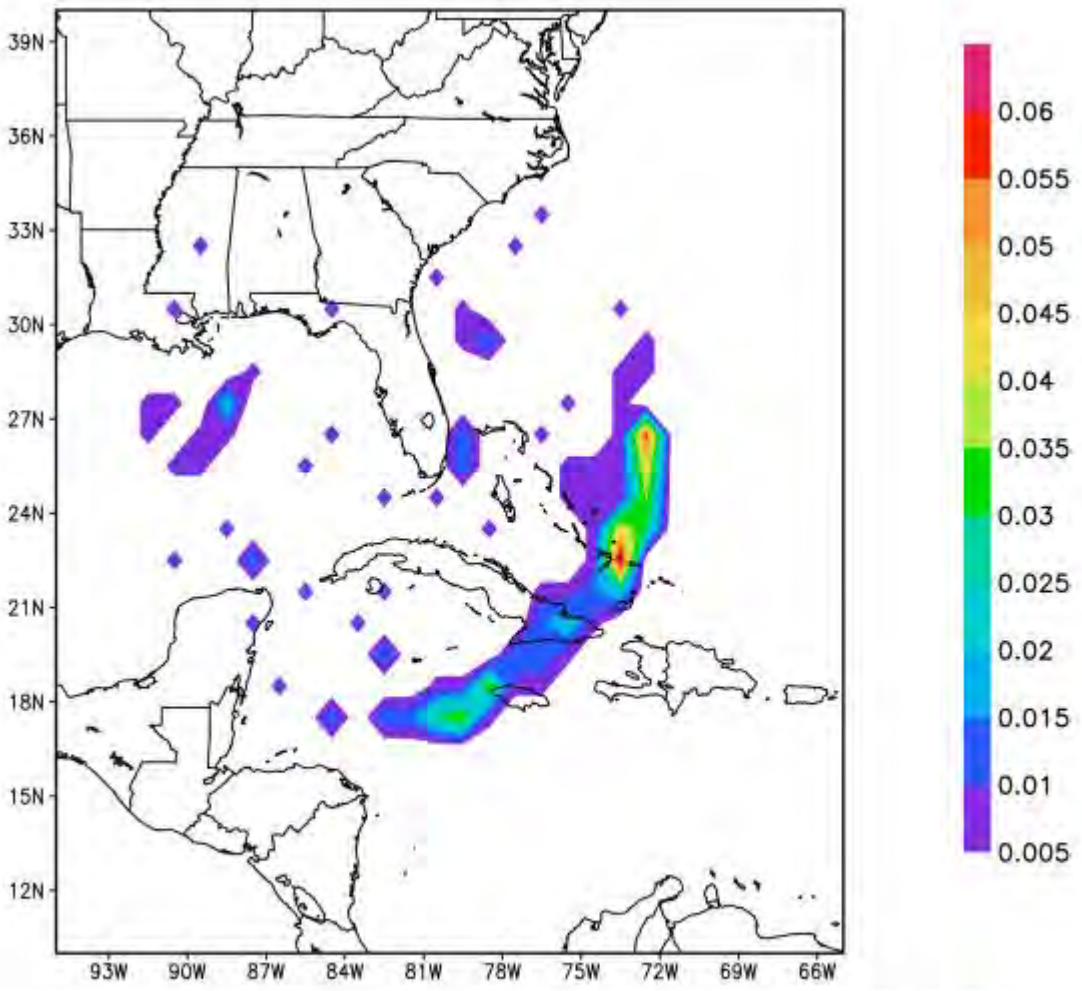

2. Geographic distribution of probability of a storm entering or developing within the threat area.

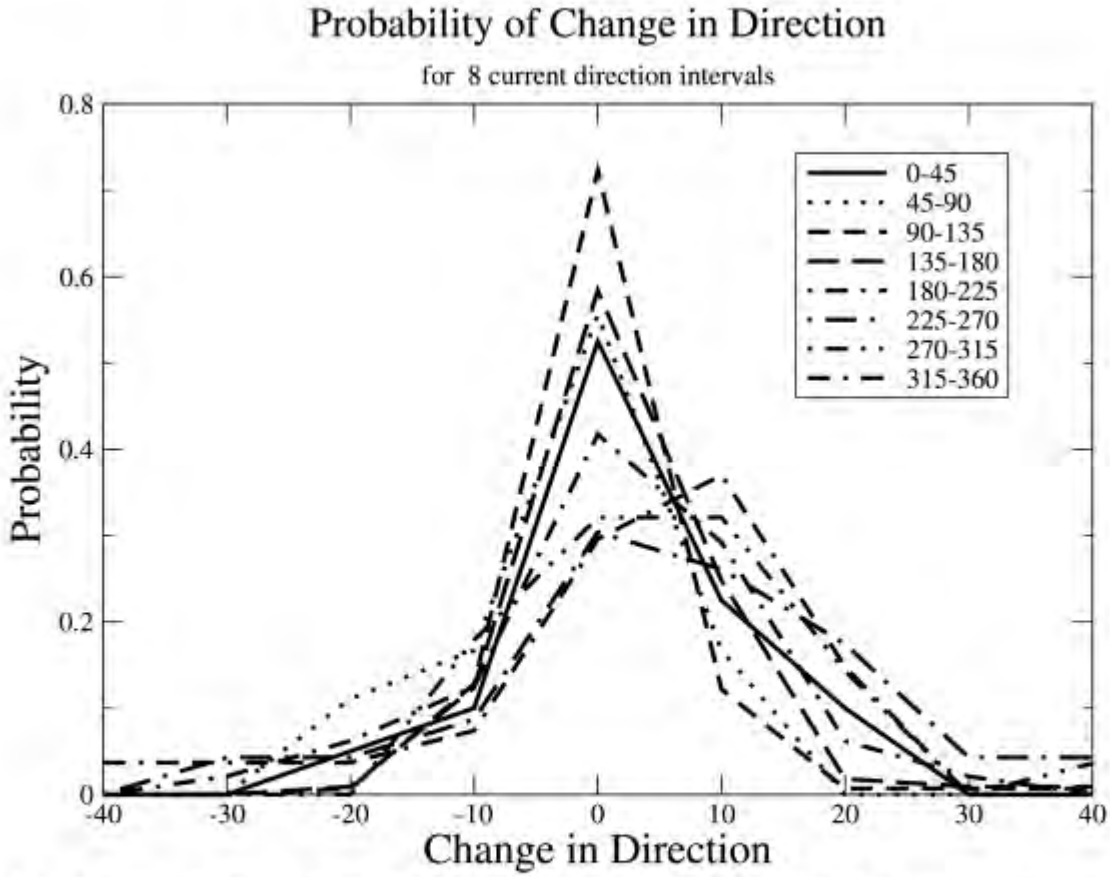

3. Probability of a change in direction of storm motion to the left or right of the current motion as a function of the current storm heading (in degrees from north).

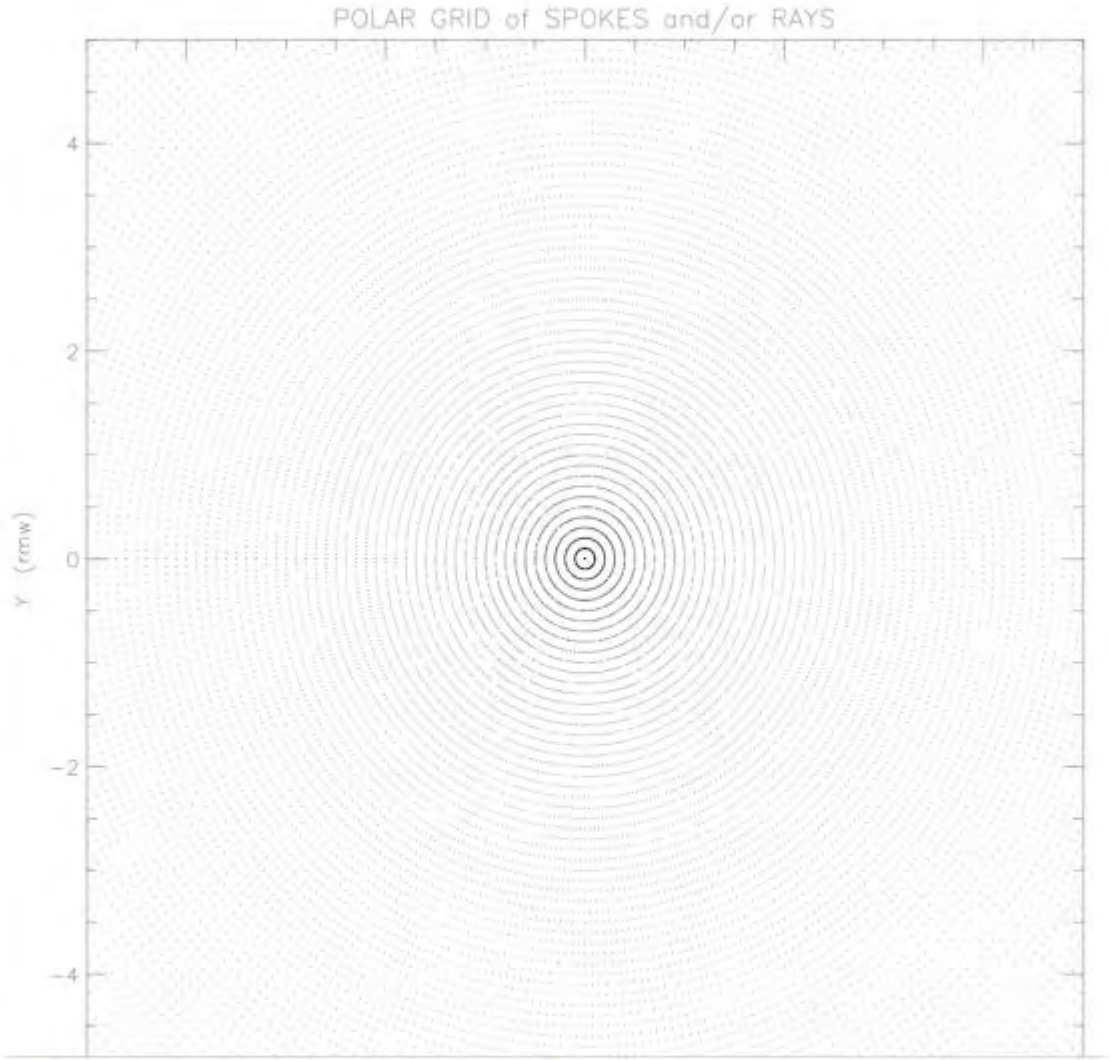

4. Polar coordinate ring and spoke system for solving equations of motion.

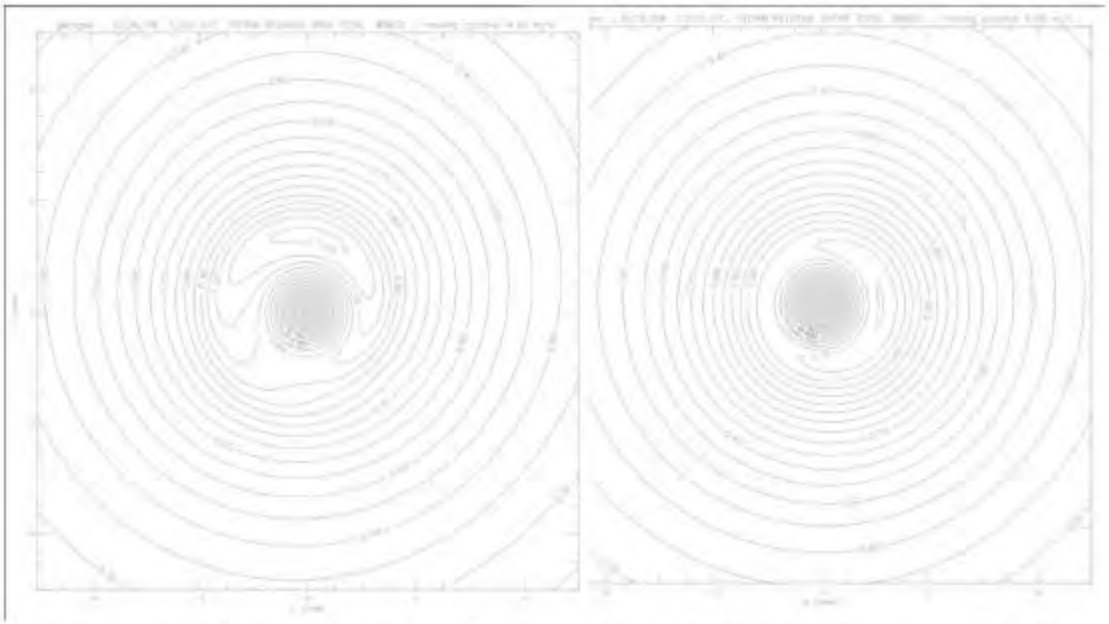

5. Horizontal distribution of mean boundary layer wind speed, relative to the moving storm for a simulation of Hurricane Georges. a) Ring solution, b) Spoke solution. Storm moving northward at 4.65 m/s. Horizontal coordinates are scaled by the radius of maximum wind, wind speed is scaled by the maximum gradient wind speed.

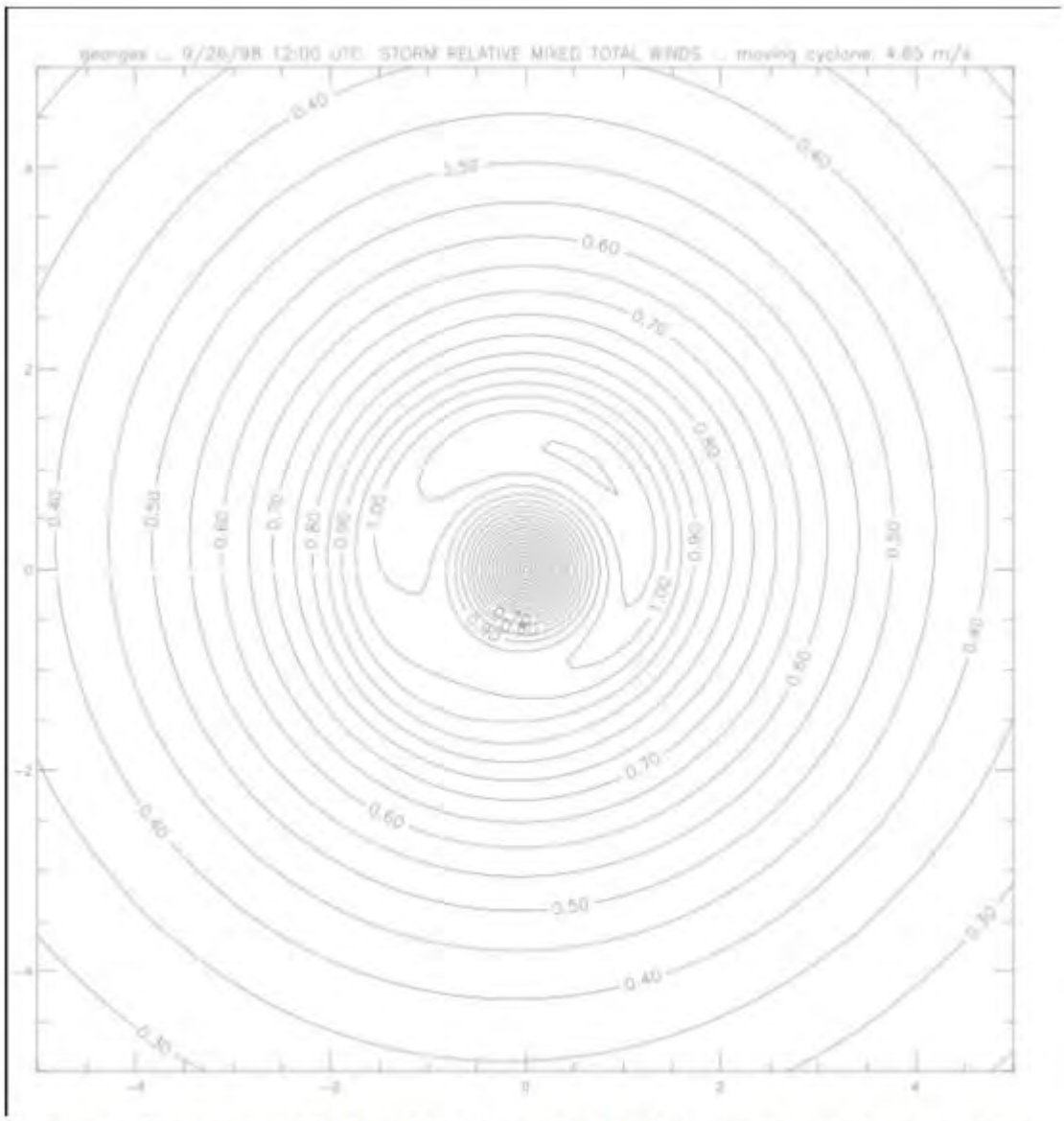

6. Same as Fig. 5 but wind field resulting from optimal combination of ring and spoke solutions to best solve the scaled versions of equations (1) and (2).

Model

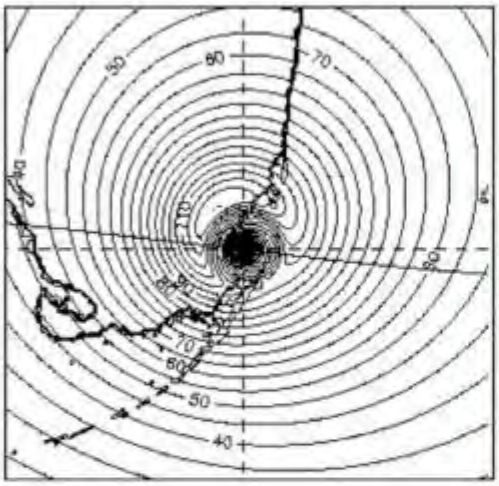

Observed

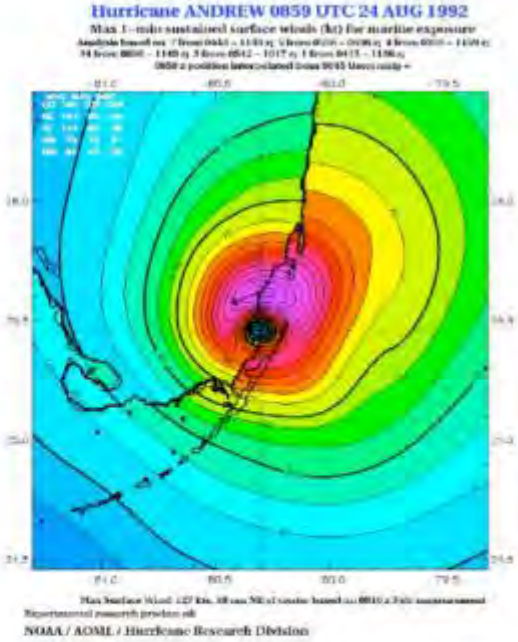

7. Comparisons of model surface wind field to observation based analysis of Hurricane Andrew (1992). Wind fields represent maximum sustained (1 min) wind speeds in knots. To convert to meters per second multiply by 2.23.

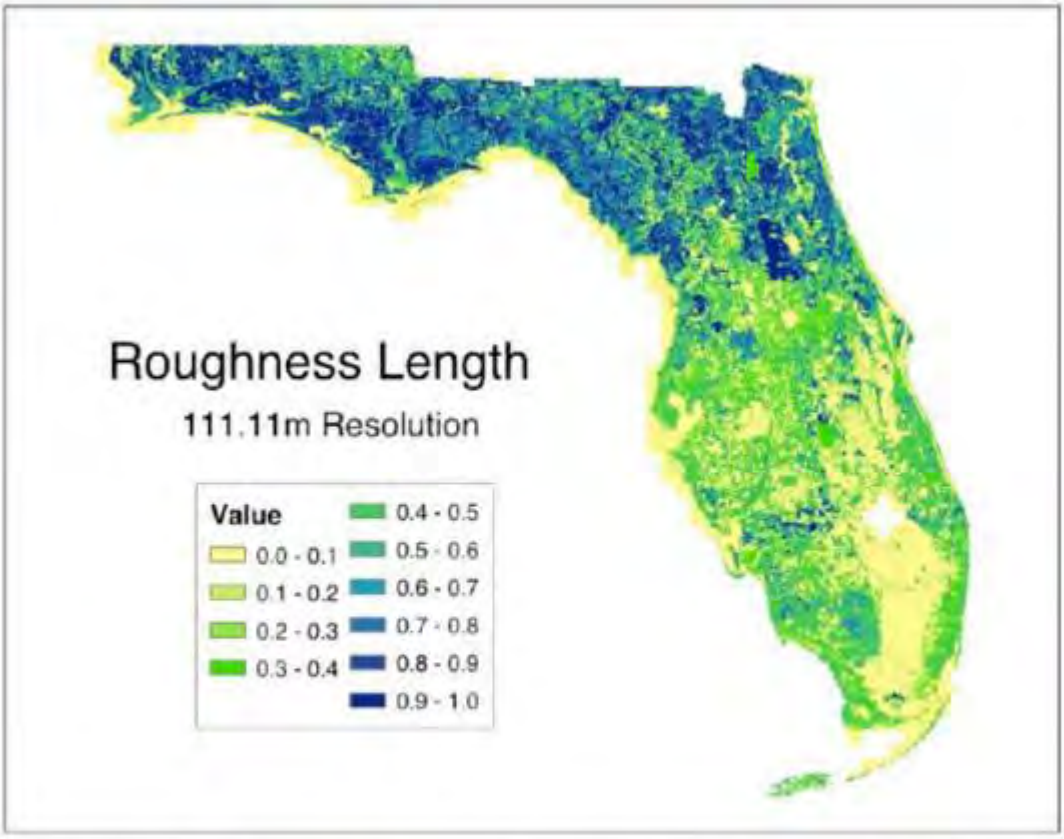

7. Distribution of aerodynamic roughness for the State of Florida determined from multi-resolution land-use land-cover classifications.

20. Assignment 2, Module 4: NOAA Technical Report 23: https://www.weather.gov/media/owp/oh/hdsc/docs/TR23.pdf

John F. Miller
Chief, Water Management Information
Division
Office of Hydrology, NWS

NOAA Technical Report NWS 23

Meteorological Criteria for Standard Project Hurricane and Probable Maximum Hurricane Windfields, Gulf and East Coasts of the United States

Washington, D.C.
September 1979

2.2.3 Central Pressure (Chapter 8)

Central pressure (p_o) is simply the lowest sea-level pressure at the hurricane center. Figures 2.1 and 2.2, respectively, show the adopted coastal variation of p_o for the SPH and for the PMH.

In general, p_o increases with latitude for both the SPH and the PMH. Coastal orientation relative to possible hurricane tracks results in the sharp rise in p_o between the southern New England coast and the Boston area.

Figure 2.3 shows Δp or $p_w - p_o$ for the SPH and the PMH. It compares the relative magnitude of the most important parameter used in computing hurricane wind speeds.

2.2.4 Radius of Maximum Winds (Chapter 9)

The radius of maximum winds (R) is the radial distance from the hurricane center to the band of strongest winds within the hurricane wall cloud, just outside the hurricane eye. Figures 2.4 and 2.5 show the adopted coastal variation of the permissible range in R for the SPH and the PMH, respectively.

R generally increases with latitude for both the SPH and the PMH. R is also somewhat dependent on p_o. The PMH is envisioned as a fully developed, tightly wound hurricane whose R for any particular coastal point is less than the R of the SPH at that location.

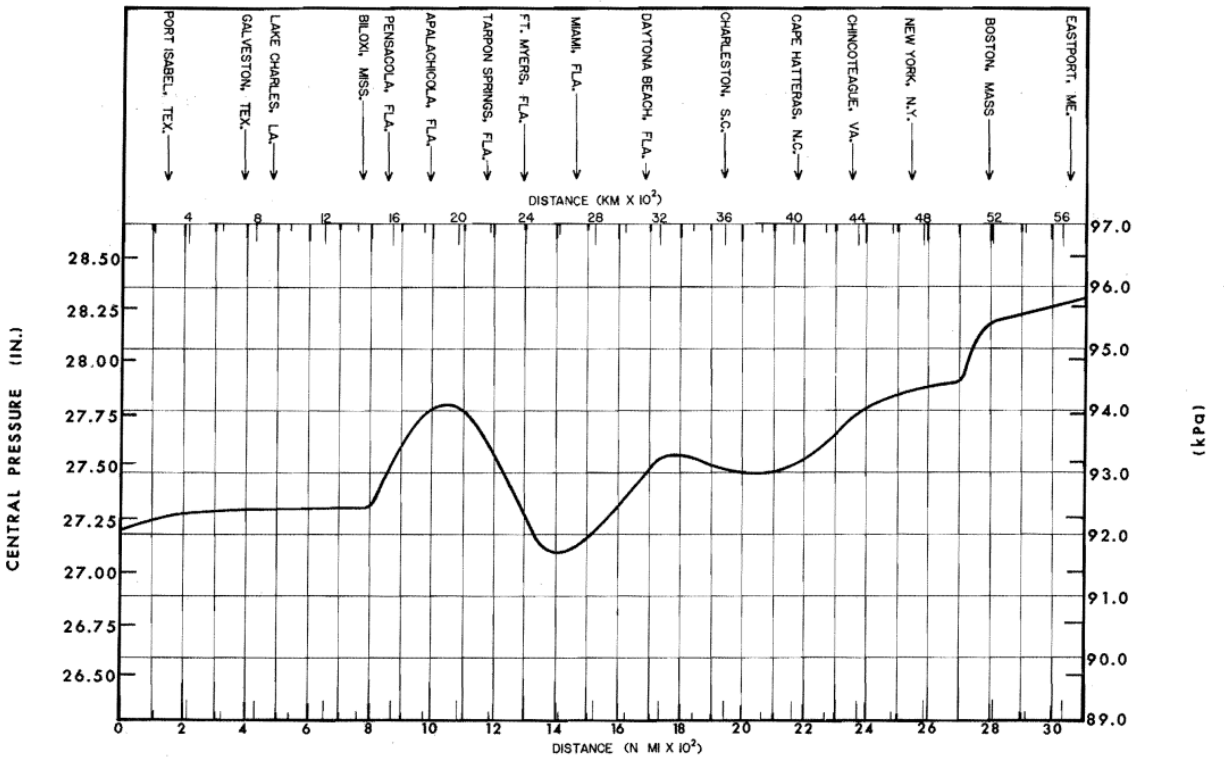

Figure 2.1.--Plot showing the adopted SPH p_o.

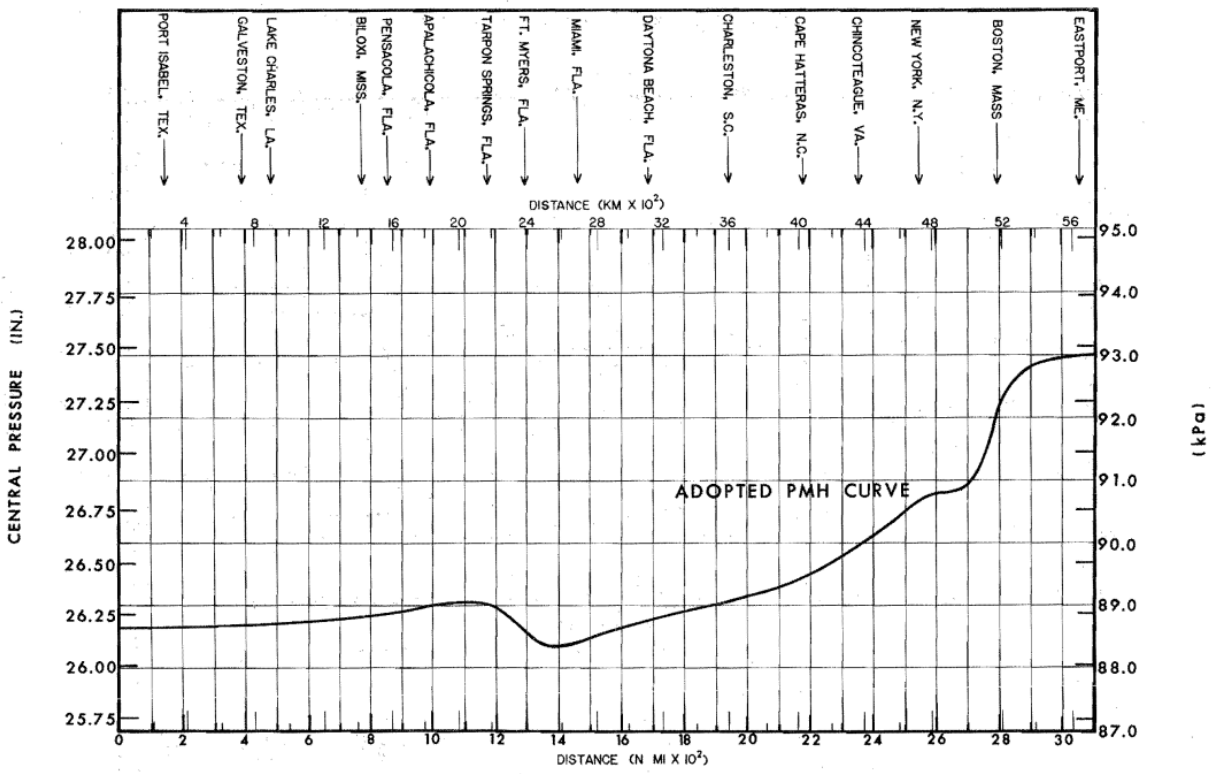

Figure 2.2.--Plot showing the adopted PMH p_o.

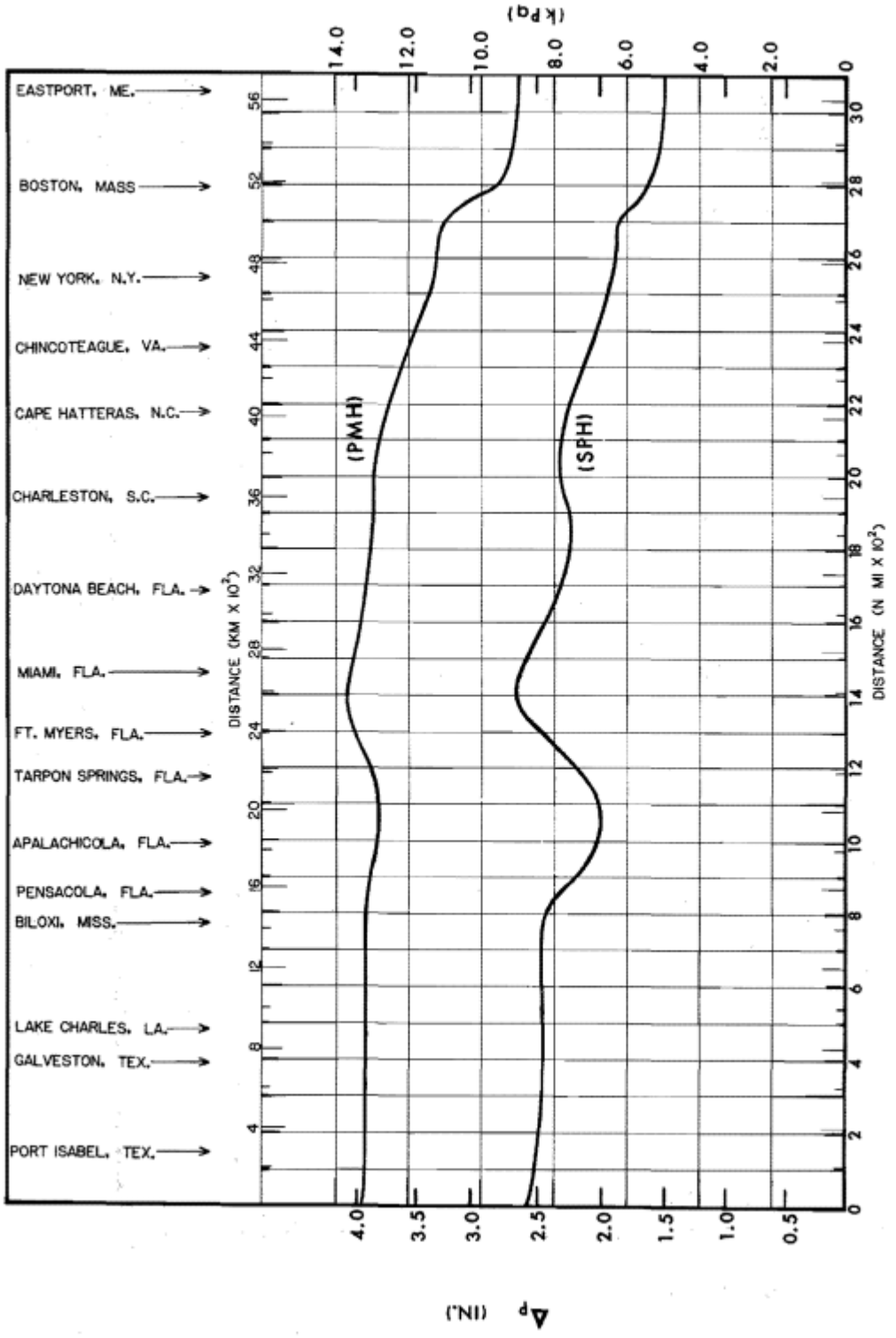

Figure 2.3.--Comparison of pressure drop (Δp) for the PMH and SPH

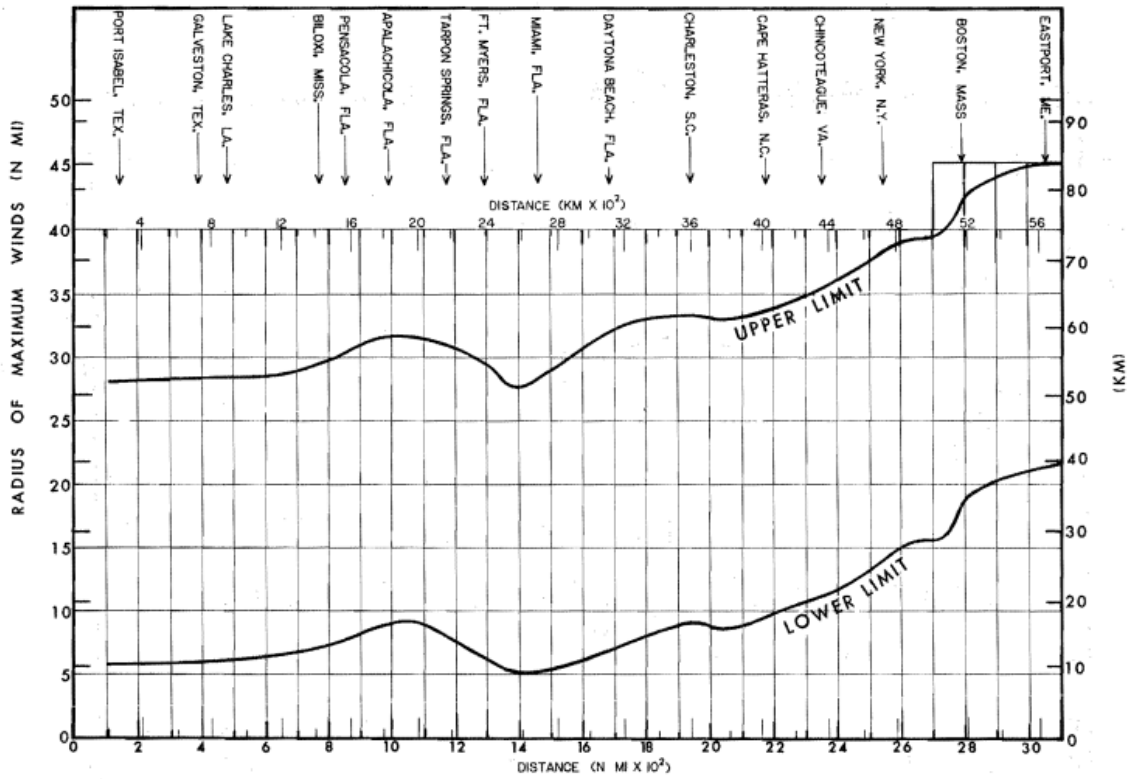

Figure 2.4.--Adopted upper and lower limits of radius of maximum winds for the SPH.

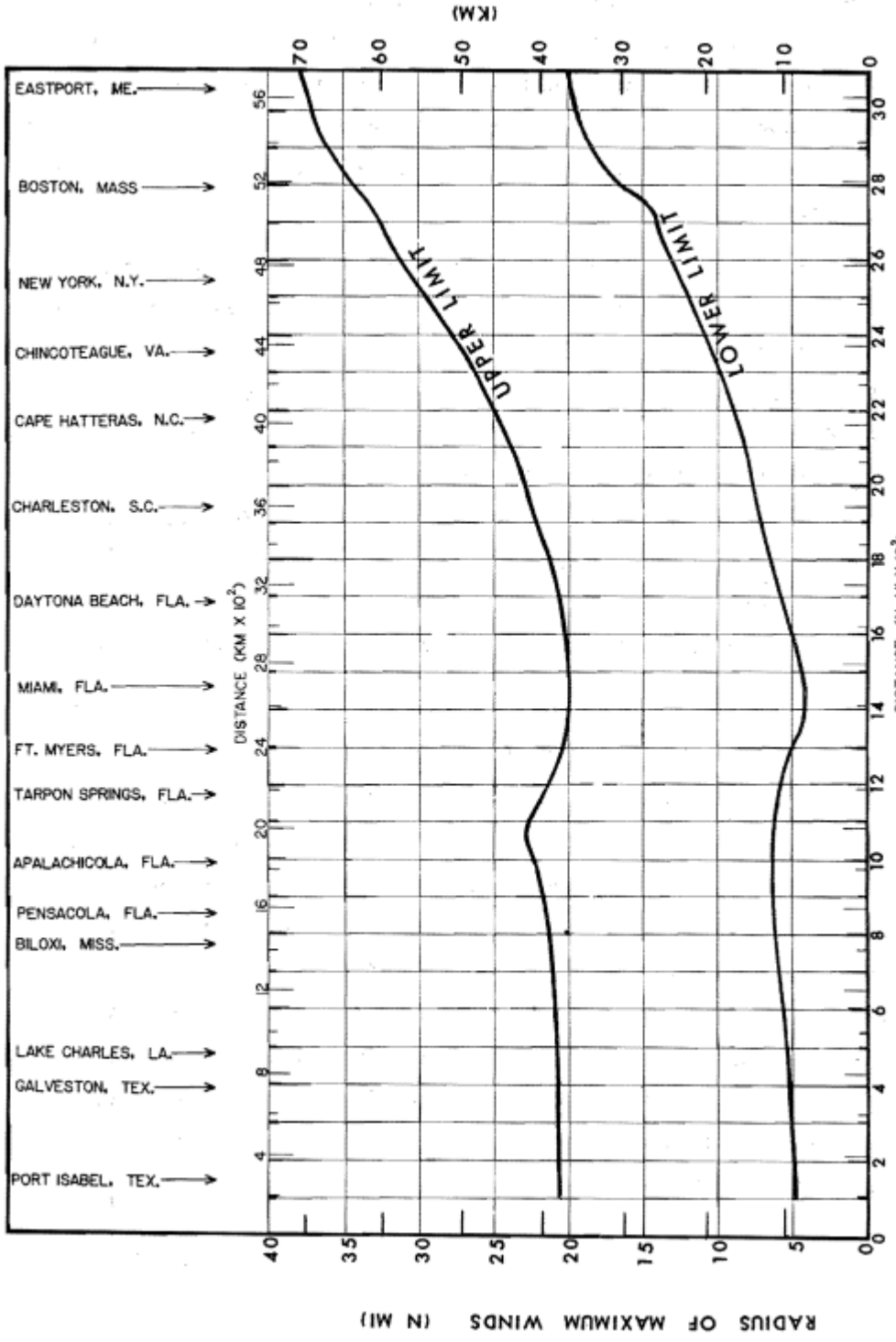

Figure 2.5.--Adopted upper and lower limits of radius of maximum winds for the PMH.

2.2.5 Forward Speed (Chapter 10)

Forward speed (T) refers to the rate of translation of the hurricane center from one geographical point to another. It is one component of the wind field of a moving storm and results in higher winds on the right side of the storm and lower on the left. Figure 2.6 shows the adopted coastal variation of the permissible range in T for the SPH and figure 2.7 shows this variation for the PMH.

Available data indicate that the upper limit of T for severe storms should be held constant with latitude to about milepost 1800. Similarly, the lower limit is constant for the PMH except for the northeastern Gulf, where the PMH is defined as a recurving, faster-moving hurricane. The lower limit for the SPH is constant to Cape Hatteras. North of Cape Hatteras, the lower and upper limits of both the PMH and SPH increase with latitude, although the increase is only slight north of Cape Cod. The range of PMH forward speeds is less than that for the SPH. Very slow speeds weaken a hurricane (see chapters 10 and 16). Very fast speeds result in a very asymmetrical wind field which is considered more possible with an SPH than a PMH.

2.2.6 Track Direction (Chapter 11)

The track direction (θ), or the path of forward movement along which the hurricane is coming (measured clockwise from north), is considered to be noninstantaneous in this report, i.e., the SPH and the PMH are not allowed to change course during the last several hours before striking the coast. Figures 2.8 and 2.9 show the permissible range of θ for the SPH and the PMH, respectively. Limiting θ's are based on possible directions over the open ocean, further constrained by sea-surface temperatures and other meteorological features. The permissible range is also a function of forward speed (T). As the angle between the coastal orientation and θ decreases, the slower hurricane weakens more than the faster-moving hurricane. Table 2.1 gives the T, by category, required for using figures 2.8 and 2.9.

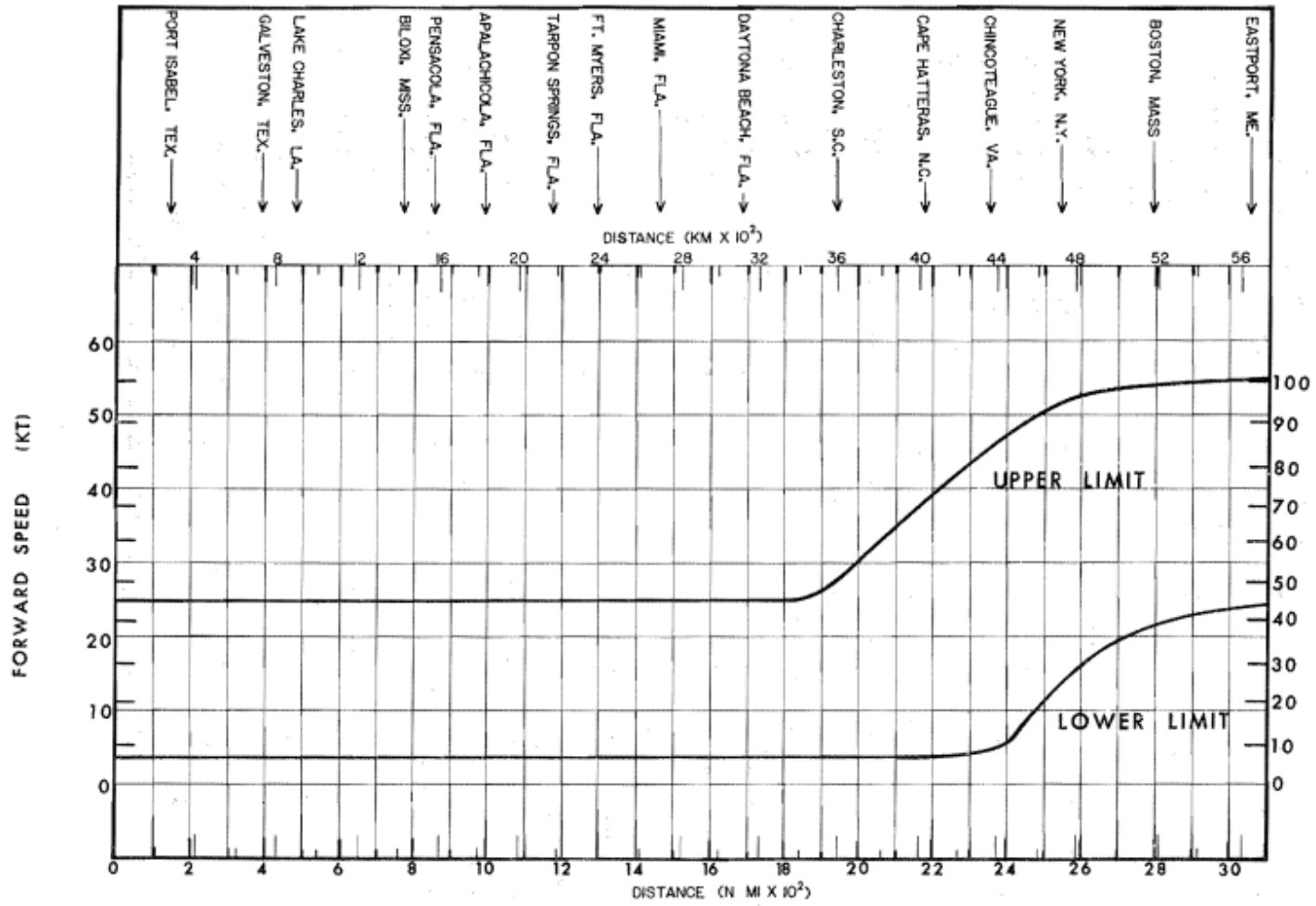

Figure 2.6.--Adopted SPH upper and lower limits of T.

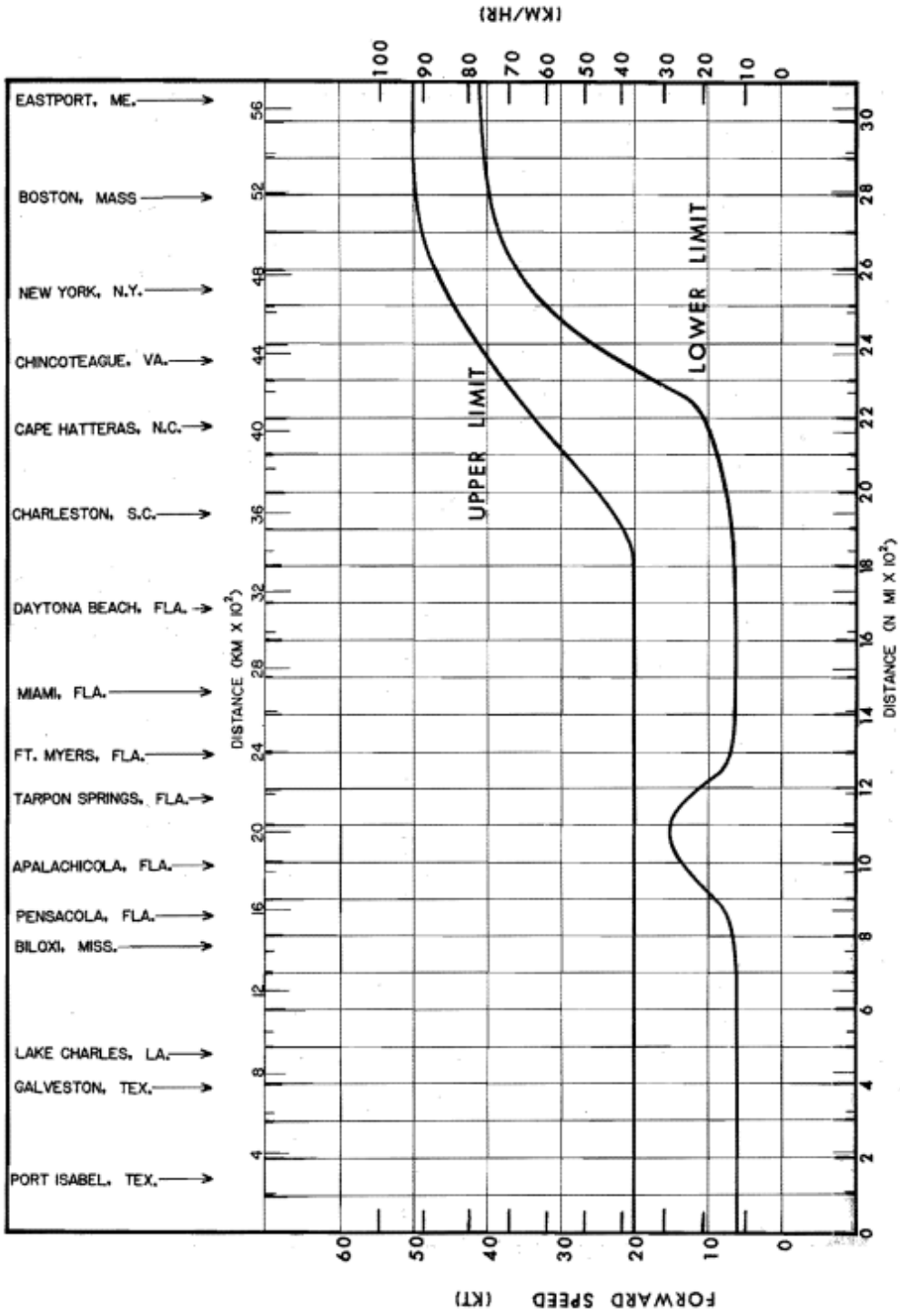

Figure 2.7.--Adopted PMH upper and lower limits of T.

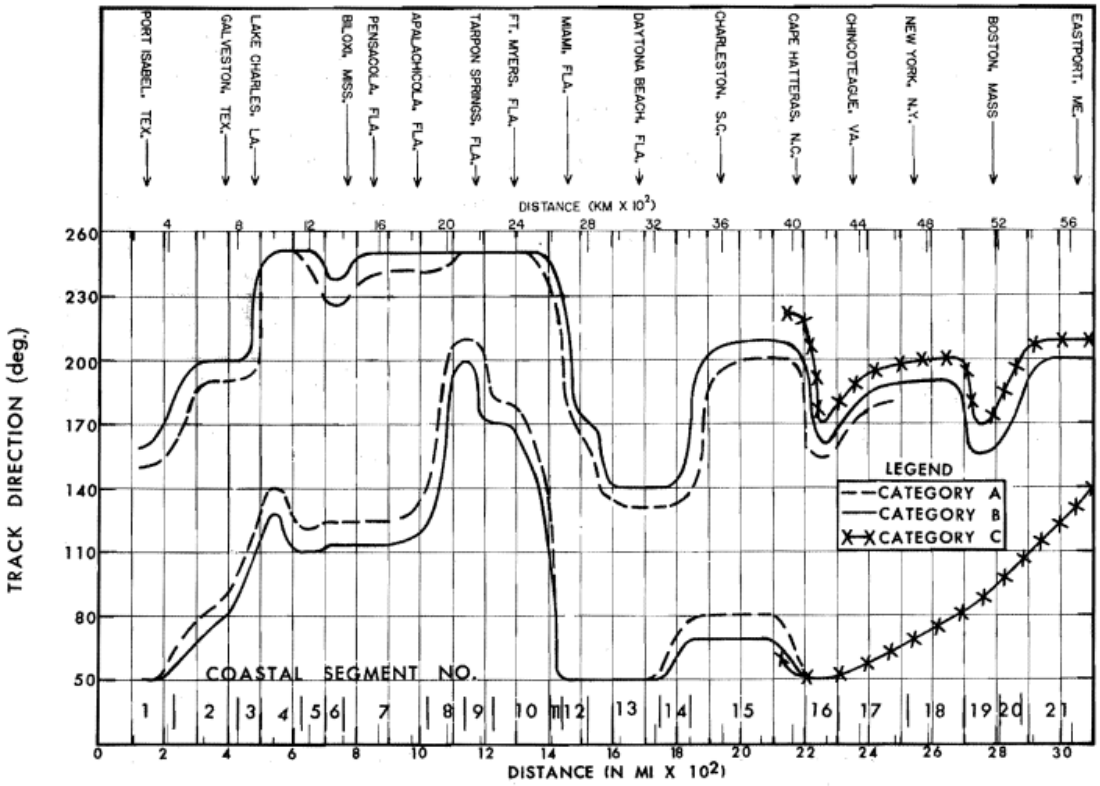

Figure 2.8.--Maximum allowable range of SPH θ after smoothing is represented by the area between the outermost curves.

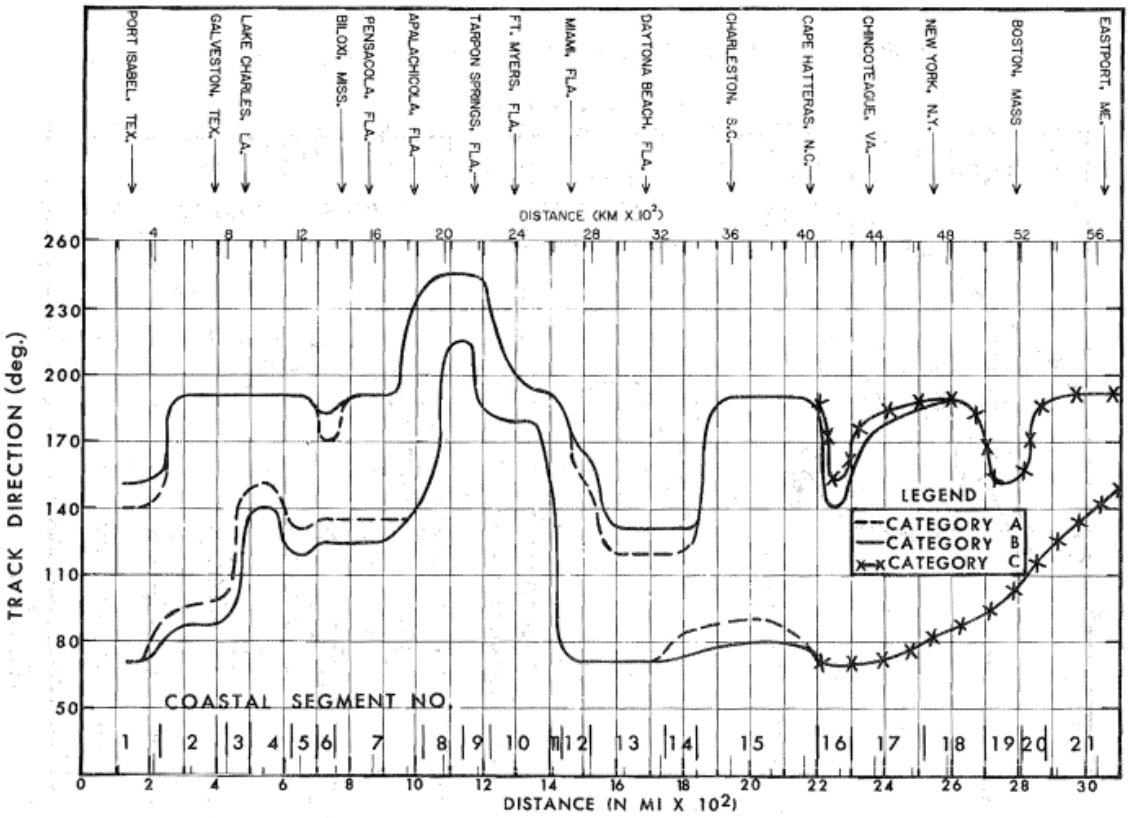

Figure 2.9.--Maximum allowable range of PMH θ after smoothing is represented by the area between the outermost curves.

Table 2.1.--Relation between forward speed (T) and track direction (θ)

a. For the PMH	
Speed category	Forward speeds (T)
A	6 kt $\leq$ T $\leq$ 10 kt (11 km/hr $\leq$ T $\leq$ 19 km/hr)
B	10 kt < T $\leq$ 36 kt (19 km/hr < T $\leq$ 67 km/hr)
C	T > 36 kt (T > 67 km/hr)
b. For the SPH	
Speed category	Forward speeds (T)
A	4 kt $\leq$ T $\leq$ 10 kt (7 km/hr $\leq$ T $\leq$ 19 km/hr)
B	10 kt < T $\leq$ 36 kt (19 km/hr < T $\leq$ 67 km/hr)
C	T > 36 kt (T > 67 km/hr)

5. METEOROLOGICAL AND OTHER PARAMETERS AND THEIR INTERRELATIONS

5.1 INTRODUCTION

This chapter focuses on the interrelations of parameters which influence the strength and regional variation of hurricane wind fields. This is preceded by brief definitions of the meteorological parameters used in this study: peripheral pressure (p_w), central pressure (p_o), radius of maximum winds (R), forward speed (T), track direction (θ), and wind inflow angle (ϕ). Two other parameters, latitude (ψ) and longitude (λ), were also considered.

To what extent parameters important to extreme hurricane wind fields are interrelated is of interest from two standpoints. One is from a broad aspect, in that a detailed study should show interrelations, even though they may not be sufficient to use in the SPH/PMH criteria. The other is to make use in this study of clear-cut relations shown in the tropical cyclone data.

5.2 DEFINITION OF METEOROLOGICAL PARAMETERS

Peripheral pressure (p_w) - the sea-level pressure at the outer limits of the hurricane circulation. p_w in this study is the average pressure for the first anticyclonically turning isobar outward from the storm center. We averaged the pressure north, east, south, and west of the hurricane center.

Central pressure (p_o) - the lowest sea-level pressure in a hurricane.

Radius of maximum winds (R) - the radial distance from the hurricane center to the band of strongest winds within the hurricane wall cloud.

Forward speed (T) - the rate of translation of the hurricane center from one geographical point to another.

Track direction (θ) - the path of forward movement along which the hurricane is coming measured in degrees clockwise from the north.

Wind inflow angle (ϕ) - the angle between true wind direction and a tangent to a circle concentric with the hurricane center.

5.3 Interrelations Between Pairs of Parameters

Interrelations between pairs of parameters were examined using linear correlation analyses. In most cases, these relations are curvilinear. However, from plots of the data we determined that these curvilinear relations closely approximated linear relations. Differences between curvilinear and linear relations are *least* for more intense cyclones, our primary area of interest. In addition, statistical relations between pairs of parameters cannot be used to estimate SPH and PMH wind fields directly (we would be extrapolating beyond the data). Also, more than two parameters are involved in the development of wind fields. The developed linear relations and graphical plots were considered adequate for general guidance.

Interrelations with p_w and ϕ were not considered. p_w varies slowly with time. ϕ (a function of the other parameters) is difficult to measure with any precision.

5.3.1 Zero-order Linear Correlation Coefficients

Linear correlation studies are based upon the assumption that the distribution of values (x, y) is a two-variable normal distribution. If the assumption of normality is satisfied, it is possible to use the observed value of the sample zero-order linear correlation coefficient (r) to test for independence. If the two variables are independent, regression curves take the form of horizontal or vertical straight lines. This implies that the population correlation coefficient (ρ) is equal to zero. If r (which is an estimate of ρ) is near zero, we shall say that we do not have sufficient reason to doubt the independence between x and y. However, if r is far from zero as determined by tests of significance, we shall reject the hypothesis that the two variables are independent (Dixon and Massey, Jr. 1957). Independence signifies that there is no relation between the variables, meaning that any conclusions drawn regarding one parameter in this report do not necessarily affect another parameter.

Table 5.1 summarizes the r's and standard errors of estimate ($s_{y \cdot x}$)* between pairs of the five parameters (p_o, R, T, θ and ψ, λ) for tropical cyclone data from each of three regions (east coast, gulf coast, and western North Pacific) and for three combinations of these regions (east and gulf coast, east coast and western North Pacific, and east and gulf coast and Western North Pacific). A storm is included for each region only when values were available for all parameters. Thus, some storms were not used, e.g., the gulf coast storm of September 20, 1909 for which R could not be determined; (see table 4.1). The table also indicates if the r is significant at the 1% or 5% level. The 5% level gives the values that would occur on the average once in 20 times in random sampling from uncorrelated material. The 1 % level is a more severe test.

Four of the r's between the pairs of parameters shown in table 5.1 are >0.50. (The table shows eight but half of these are mirror images of the other half.) These four are significant at the 1% level. All have latitude as one of the pair. The highest r (0.68) is T for east coast hurricanes. The next highest (0.52) is the θ for typhoons and with R for east coast hurricanes. The last (0.51) is with R for the combined set of east coast hurricanes and typhoons. These interrelations are guidance for establishing SPH and PMH criteria along the east coast (see chapters 9 to 11).

5.3.2 Plots of Data

Trend lines are drawn on all seven figures discussed in this subsection. These lines are drawn through the data by eye and are shown for illustrative purposes. The linear regression lines are not shown because most of the interrelations shown in the seven figures are somewhat curvilinear. r and $s_{y \cdot x}$† from table 5.1 are indicated in figures 5.1 to 5.7 for convenience.

---

*For both r and $s_{y \cdot x}$ we are assuming in a gross sense that all relations are linear. For a loose definition of $s_{y \cdot x}$ see section 5.4.

†Here again we are assuming in a gross sense that all relations are linear.

NOTES FOR TABLES 5.1 AND 5.2

p_o	:	central pressure
R	:	radius of maximum winds
θ	:	track direction
T	:	forward speed
ψ	:	latitude (east coast hurricanes and typhoons)
λ	:	longitude (gulf coast hurricanes)
r	:	linear correlation coefficient
r'	:	multiple correlation coefficient
r'^2	:	reduction of variance (square of the multiple correlation coefficient)
$s_{y.x}$	:	standard error of estimate
r sig, r' sig	:	r, r' is significant at the 5 % level /*
	:	r, r' is significant at the 1 % level */*
	:	r, r' is neither significant at the 1% nor 5 % levels /
N	:	sample size
vs.	:	versus
N/A	:	not applicable

Table 5.1.--Linear correlation coefficients between pairs of meteorological and other parameters.

Dependent Variable (y) \ Independent Variable (x)	p_o			R			θ			T			ψ, λ		
	r	$s_{y\cdot x}$	r sig	r	$s_{y\cdot x}$	r sig	r	$s_{y\cdot x}$	r sig	r	$s_{y\cdot x}$	r sig	r	$s_{y\cdot x}$	r sig
EAST COAST HURRICANES N = 49															
p_o in. (kPa)	-	-	-	.39	.49(1.7)	*/*	.02	.53(1.8)	/	-.10	.53(1.8)	/	.27	.51(1.8)	/
R n.mi. (km)	.39	12.2(22.6)	*/*	-	-	-	.30	12.6(23.4)	/*	.32	12.5(23.2)	/*	.52	11.3(20.9)	*/*
θ deg.	.02	55.3	/	.30	52.9	/*	-	-	-	.35	51.8	/*	.35	51.9	/*
T kt (km/hr)	-.10	9.2(17.0)	/	.32	8.7(16.1)	/*	.35	8.6(15.9)	/*	-	-	-	.68	6.7(12.4)	*/*
ψ deg.	.27	5.4	/	.52	4.8	*/*	.35	5.3	/*	.68	4.1	*/*	-	-	-
GULF COAST HURRICANES N = 67															
p_o in. (kPa)	-	-	-	.33	.51(1.7)	*/*	.14	.53(1.8)	/	.09	.53(1.8)	/	-.02	.54(1.8)	/
R n.mi. (km)	.33	8.3(15.4)	*/*	-	-	-	.19	8.7(16.1)	/	.15	8.7(16.1)	/	-.06	8.8(16.3)	/
θ deg.	.14	50.2	/	.19	49.8	/	-	-	-	.02	50.7	/	-.32	48.0	/
T kt(km/hr)	.09	4.6(8.5)	/	.15	4.6(8.5)	/	.02	4.6(8.5)	/	-	-	-	.02	4.6(8.5)	/
λ deg.	-.02	6.1	/	-.06	6.1	/	-.32	5.8	/	.02	6.1	/	-	-	-
WESTERN NORTH PACIFIC TYPHOONS N = 178															
p_o in. (kPa)	-	-	-	.20	.68(2.3)	*/*	.18	.68(2.3)	/*	-.07	.69(2.3)	/	.18	.68(2.3)	/*
R n.mi. (km)	.20	8.2(15.2)	*/*	-	-	-	.22	8.1(15.0)	*/*	-.02	15.4(8.3)	/	.26	8.0(14.8)	*/*
θ deg.	.18	44.5	/*	.22	44.1	*/*	-	-	-	± 0	N/A	/	.52		*/*
T kt (km/hr)	-.07	5.0(9.3)	/	-.02	5.0(9.3)	/	± 0	N/A	/	-	-	-	.10	5.0(9.3)	-
ψ deg.	.18	6.4	/*	.26	6.3	*/*	.52	5.5	*/*	.10	6.5	/	-	-	-

Table 5.1.--Linear correlation coefficients between pairs of meteorological and other parameters, continued.

Dependent Variable (y) \ Independent Variable (x)	p_o			R			θ			T			ψ, λ		
	r	$s_{y\cdot x}$	r sig	r	$s_{y\cdot x}$	r sig	r	$s_{y\cdot x}$	r sig	r	$s_{y\cdot x}$	r sig	r	$s_{y\cdot x}$	r sig
EAST AND GULF COAST HURRICANES N = 116															
p_o in. (kPa)	-	-	-	.34	.50(1.7)	*/*	.09	.53(1.8)	/	-.02	.53(1.8)	/			
R n.mi. (km)	.34	10.6(19.6)	*/*	-	-	-	.23	11.0(20.4)	/*	.32	10.7(19.8)	*/*			
θ deg.	.09	52.5	/	.23	51.3	/*	-	-	-	.20	51.6	/*			
T kt (km/hr)	-.02	7.3(13.5)	/	.32	6.9(12.8)	*/*	.20	7.1(13.2)	/*	-	-	-			
EAST COAST HURRICANES AND WESTERN NORTH PACIFIC TYPHOONS N = 227															
p_o in. (kPa)	-	-	-	.26	.64(2.2)	*/*	.16	.66(2.2)	/*	-.03	.66(2.2)	/	.22	.65(2.2)	*/*
R n.mi. (km)	.26	10.7(19.8)	*/*	-	-	-	.30	10.5(19.5)	*/*	.27	10.6(19.6)	*/*	.51	9.5(17.6)	*/*
θ deg.	.16	47.9	/*	.30	46.2	*/*	-	-	-	.19	47.6	*/*	.50	42.1	*/*
T kt (km/hr)	-.03	6.6(12.2)	/	.27	6.3(11.7)	*/*	.19	6.4(11.9)	*/*	-	-	-	.39	6.0(11.1)	*/*
ψ deg.	.22	7.4	*/*	.51	6.6	*/*	.50	6.6	*/*	.39	7.1	*/*	-	-	-
EAST AND GULF COAST HURRICANES AND WESTERN NORTH PACIFIC TYPHOONS N = 294															
p_o in. (kPa)	-	-	-	.28	.61(2.1)	*/*	.17	.63(2.1)	*/*	-.02	.64(2.2)	/			
R n.mi. (km)	.28	10.3(19.1)	*/*	-	-	-	.30	10.3(19.1)	*/*	.24	10.4(19.3)	*/*			
θ deg.	.17	49.0	*/*	.30	47.4	*/*	-	-	-	.15	49.1	/*			
T kt (km/hr)	-.02	6.2(11.5)	/	.24	6.0(11.1)	*/*	.15	6.1(11.3)	/*	-	-	-			

Table 5.2.--Multiple correlation coefficients involving meteorological and other parameters†

	r'	r'sig	r'^2	$s_{y \cdot x}$
EAST COAST HURRICANES N = 49				
p_o vs. R	.39	*/*	.15	0.49 in. (1.7 kPa)
p_o vs. R, T	.45	*/*	.20	0.48 in. (1.6 kPa)
p_o vs. R, T, ψ	.54	*/*	.30	0.45 in. (1.5 kPa)
R vs. ψ	.52	*/*	.27	11.3 n.mi. (20.4 km)
R vs. ψ, p_o	.58	*/*	.33	10.8 n.mi. (20.0 km)
θ vs. T	.35	/*	.12	51.8°
T vs. ψ	.68	*/*	.46	6.8 kt (12.5 km/hr)
T vs. ψ, p_o	.74	*/*	.55	6.2 kt (11.5 km/hr)
ψ vs. T	.68	*/*	.46	4.1°
ψ vs. T, p_o	.76	*/*	.58	3.6°
WESTERN NORTH PACIFIC TYPHOONS N = 178				
p_o vs. R	.20	*/*	.04	0.68 in. (2.3 kPa)
p_o vs. R, θ	.24	*/*	.06	0.67 in. (2.3 kPa)
R vs. ψ	.26	*/*	.07	8.0 n.mi. (14.9 km)
R vs. ψ, p_o	.30	*/*	.09	7.9 n.mi. (14.7 km)
θ vs. ψ	.52	*/*	.27	38.5°
T vs. ψ	.10	/	.01	5.0 kt (9.3 km/hr)
T vs. ψ, p_o	.13	/	.02	5.0 kt (9.3 km/hr)
ψ vs. θ	.52	*/*	.27	5.6°

†Only ordinary zero-order correlation coefficients are listed where additional combinations of parameters did not yield significant increases in r'.

5.3.2.1 INTERRELATIONS WITH CENTRAL PRESSURE (P_0). Figure 5.1 is a composite plot of p_o and R data for all hurricanes (tables 4.1-4.4) and typhoons (tables 4.5-4.6). The three data regions (east coast, gulf coast and western North Pacific) are distinguished by different plotting symbols. The conclusion from this plot is that R tends to be smaller and has a smaller range for lower p_o. This conclusion is supported by Myers (1954), Colon (1963), Sheets (1967), Shea and Gray (1972) and others. We also observe that the typhoon sample has nearly all R's $\leq$31 n.mi. (58 km) whereas quite a few hurricanes have R > 31 n.mi. Part of this may be explained by the hurricane sample extending into more northerly latitudes, where R's are generally larger, than the typhoon sample selected (see sec. 5.3.2.2).

A plot of p_o vs θ for all three regions (fig. 5.2) indicates that for the

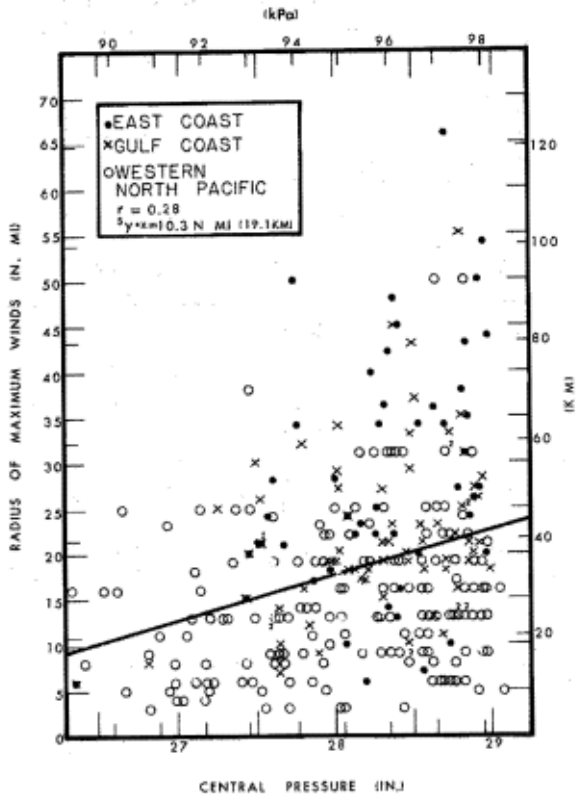

Figure 5.1.--Central pressure (p_o) vs. radius of maximum winds (R).

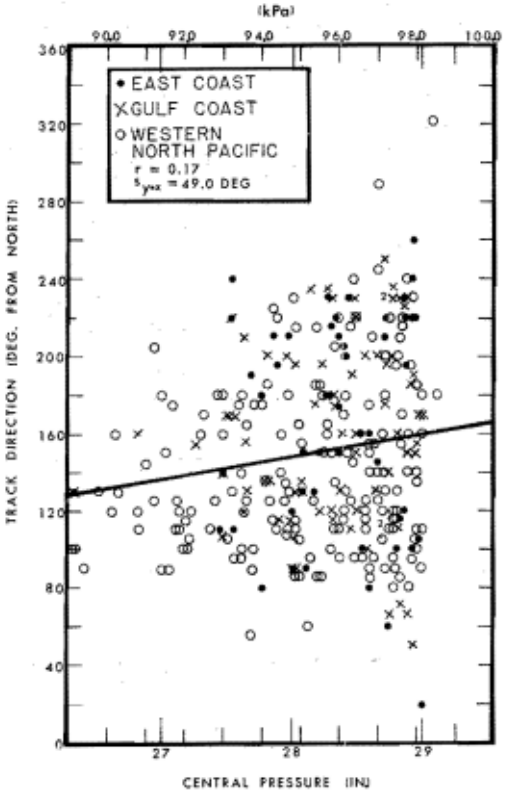

Figure 5.2.--Central pressure (p_o) vs. track direction (θ).

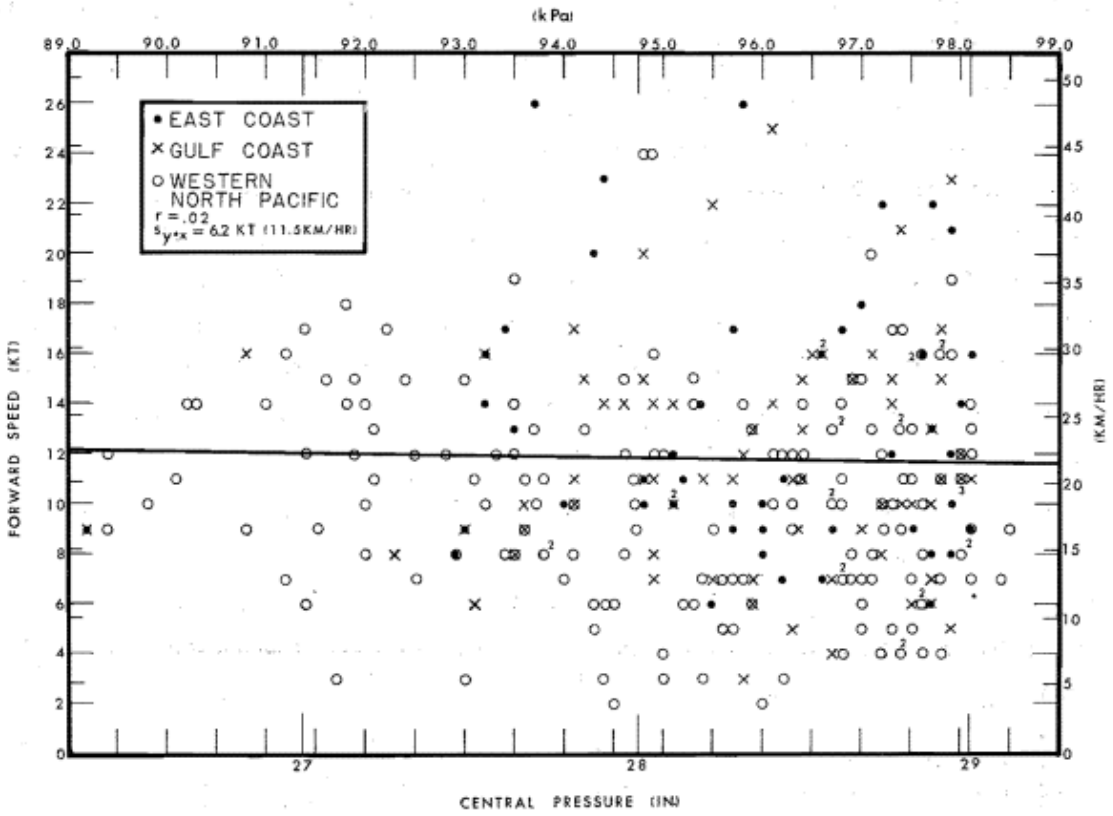

Figure 5.3.--Central pressure (p_o) vs. forward speed (T).

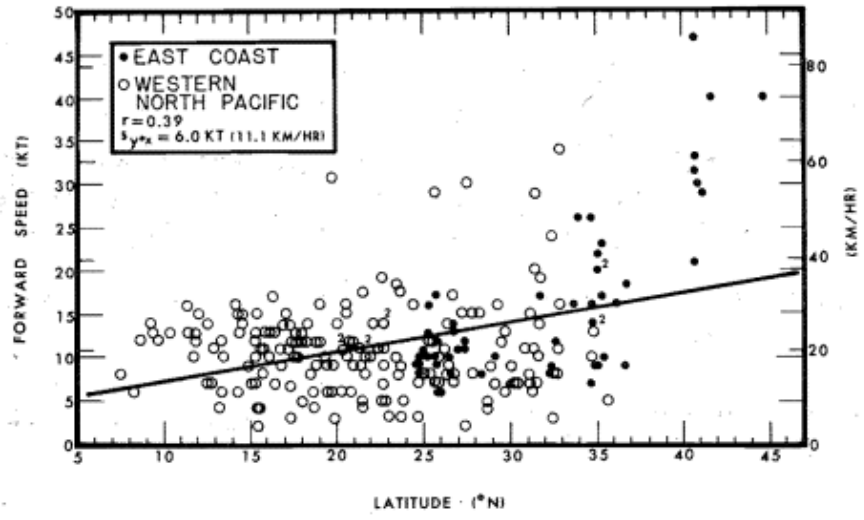

Figure 5.4.--Latitude (ψ) vs. forward speed (T).

more extreme tropical cyclones [$\leq$27.46 in. (93.0 kPa)] the range of θ is more restricted than it is for weaker storms. This indication supports restrictions on the entry direction of extreme storms at the coast.

Investigation of the interrelation between p_o and T (fig. 5.3) shows that storms with lower p_o move at slower speeds. Higher T's occur outside of tropical latitudes. Along the gulf coast, the most extreme storms ($p_o \leq 27.46$ in., 93.0 kPa) have moved between 8 and 16 kt (15 and 30 km/hr). Along the east coast, storms with p_o <27.75 in. (94.0 kPa) have traveled at T between 8 and 26 kt (15 and 48 km/hr). Western North Pacific typhoons have T between 3 and 18 kt (6 and 33 km/hr) for $p_o \leq 27.46$ in. (93.0 kPa). Weaker hurricanes and typhoons have a larger range of T.

5.3.2.2 INTERRELATIONS WITH LATITUDE (ψ). A composite plot of ψ vs. T data is shown in figure 5.4 for east coast hurricanes and typhoons of the western North Pacific. The general conclusion from this plot is that T tends to be lower and has a smaller range with lower ψ. The storms with higher T's north of 25°N have recurved and have consequently accelerated.

p_o is higher at temperate latitudes than at tropical latitudes, partly because of warmer sea-surface temperatures to the south. Higher p_o at temperature latitudes is shown by a plot of ψ vs. p_o data (fig. 5.5), a trend line, and the enveloping minimum p_o curve for east coast hurricanes and western North Pacific typhoons.

A plot of ψ vs. θ is shown in figure 5.6 for east coast hurricanes and western North Pacific typhoons. r has a relatively high value of 0.50. This plot shows the well-known pattern of tropical cyclones moving from the east at lower ψ and changing to directions from the south and southwest as they move clockwise around the outer edge of the subtropical high.

Figure 5.7 is a plot of ψ vs. R for east coast hurricanes and western North Pacific typhoons. r is again relatively high at 0.51. This plot supports what many meteorologists have observed as a characteristic of hurricanes and typhoons, i.e., storms expand in size as they move northward out of the tropics.

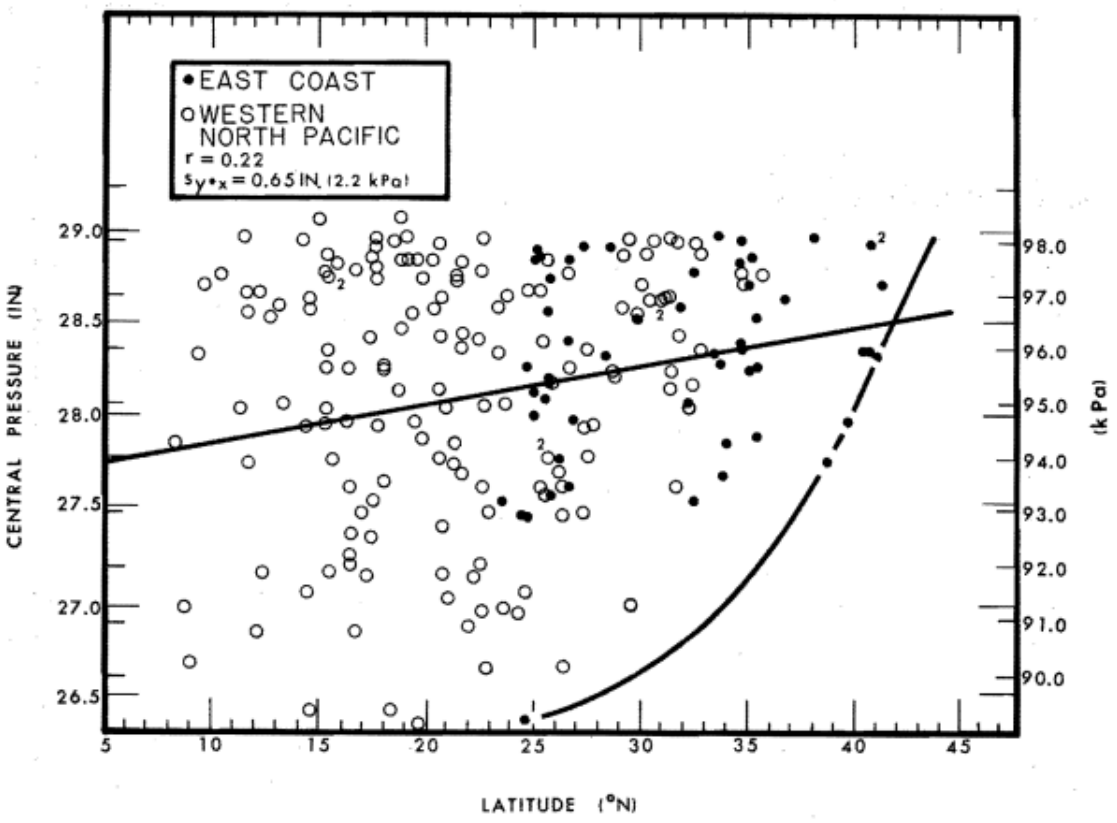

Figure 5.5.--Latitude (ψ) vs. central pressure (p_o)

5.4 Multiple Interrelations Between Sets of Parameters

Multiple correlation coefficients (r'), using the same parameters as in table 5.1, were calculated for east and gulf coast hurricanes, and for typhoon data (table 5.2). In cases where only an ordinary zero-order correlation coefficient is listed for a pair of parameters, e.g., θ vs. T (east coast), additional combinations of parameters did not yield significant increases in r'. For gulf coast hurricanes, the addition of a second parameter failed to yield significant increases in r' for all cases studied. Table VII of Mills (1955) was used to estimate significance. A screening technique selects the second, third, and fourth parameters which give the greatest increase in r' as each is added. A discussion of r' follows.

If Y denotes the regression function of a random variable y with respect to certain other variables x_1, x_2, ..., x_n, then the coefficient of multiple

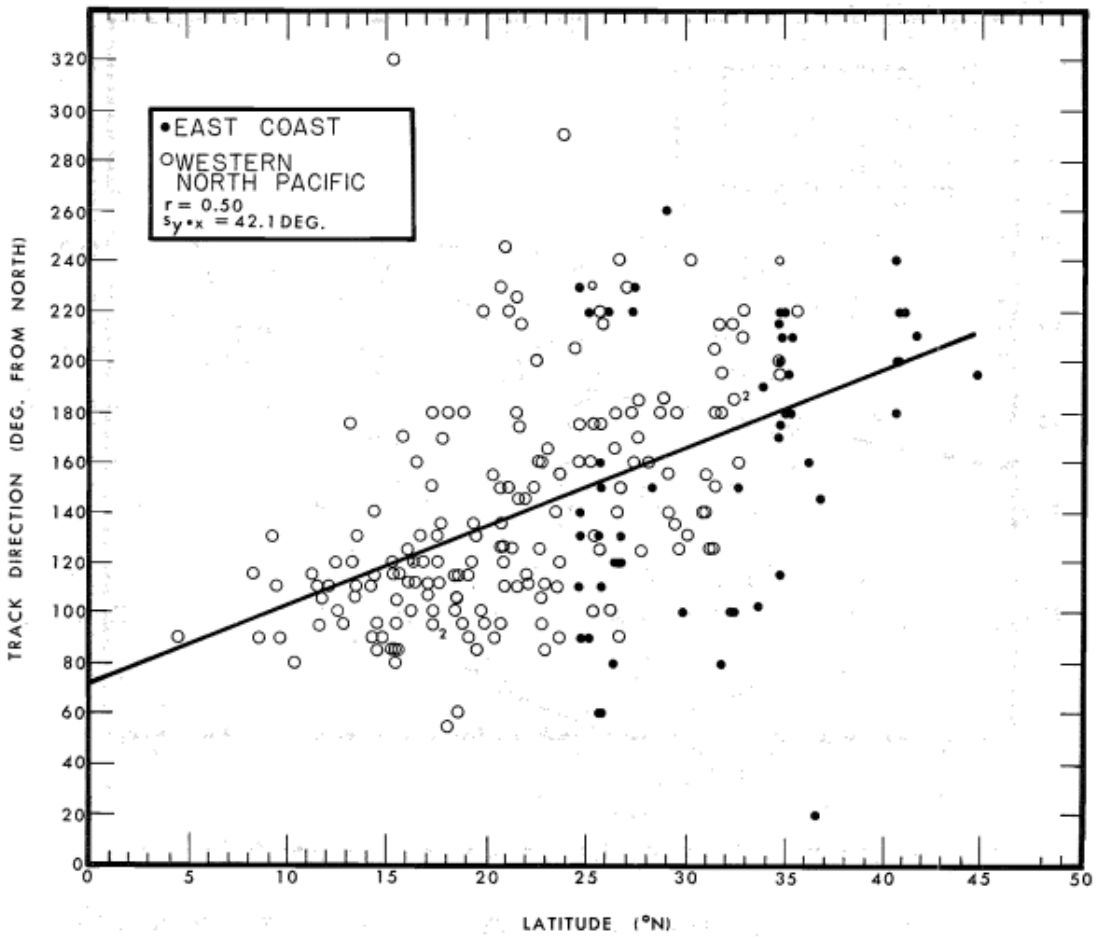

Figure 5.6.--Latitude (ψ) vs. track direction (θ).

correlation (r') between y and the x's is defined as the coefficient of simple linear correlation (r) between y and Y. However, the constants of the regression function automatically adjust the algebraic sign, with the result that the coefficient of correlation (r') between y and Y cannot be negative; in fact, its value is precisely equal to the ratio of their two standard deviations, i.e; $\sigma(Y)/\sigma(y)$. Therefore, r' ranges from 0 to 1, and the square of r' is equal to the relative reduction, i.e., the ratio of explained variance to total variance (Huschke 1959). Table 5.2 lists the coefficient of multiple correlation (r'), significance tests on r' at the 5 and 1 percent levels (Mills 1955), the reduction of variance (r'^2) and the standard error of estimate ($s_{y.x}$).

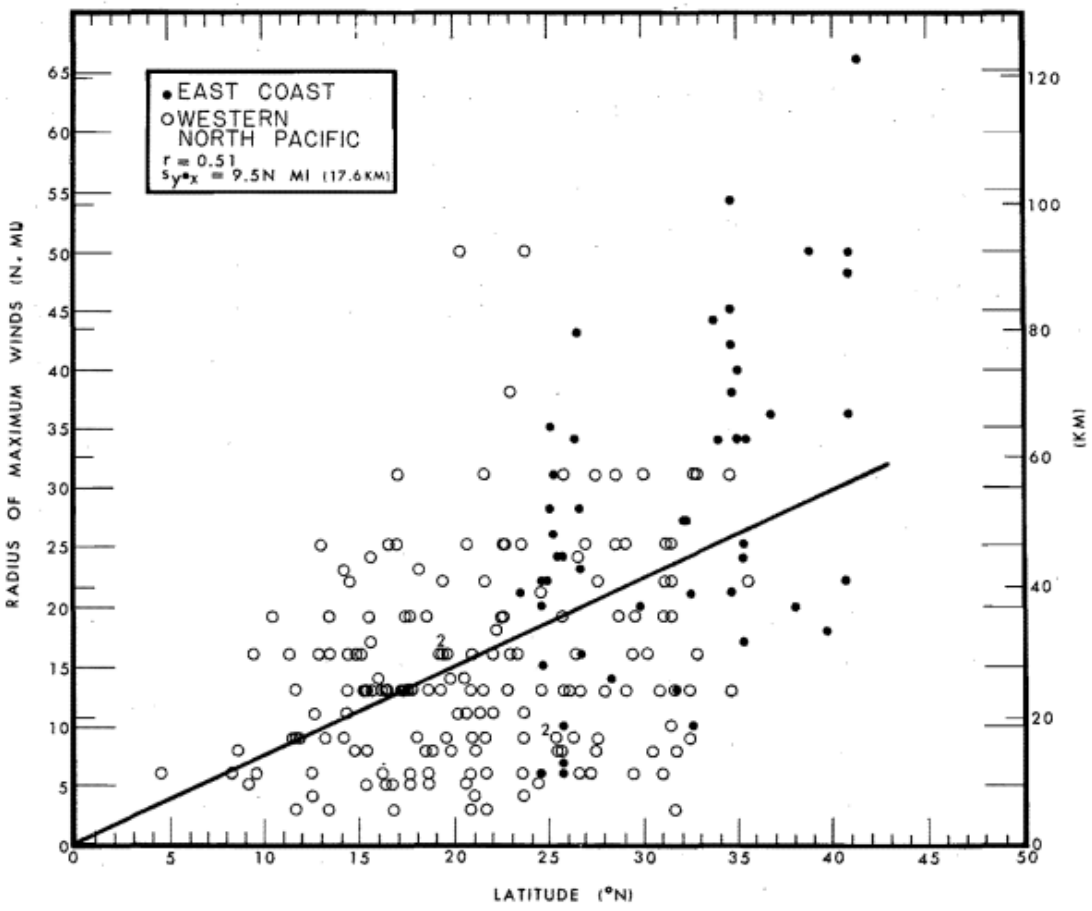

Figure 5.7.--Latitude (ψ) vs. radius of maximum winds (R).

The relation between reduction of variance (r'^2), standard deviation (σ), and standard error of estimate ($s_{y \cdot x}$) is given by:

$$r'^2 = 1 - s_{y \cdot x}^2/\sigma^2 = (\sigma^2 - s_{y \cdot x}^2)/\sigma^2 \qquad (5.1)$$

where

r'^2 = reduction in variance

σ = standard deviation, or the positive square root of the variance about the mean of the data.

$s_{y \cdot x}$ = standard deviation about the regression line.

Multiple correlations for the east coast hurricanes are higher than for the other two regions except for those involving θ. The highest $r' = 0.76$ [between ψ and T, p_o] occurs with east coast data.

5.5 Summary

The zero-order linear and multiple correlation coefficients, although often significant at the 1 % level, could not be used directly in developing criteria throughout this report. There are two reasons for this. First, the coefficients are derived from data for all hurricanes and typhoons from our period of record--not just the most extreme ones, which are too few in number to develop meaningful interrelations. Second, though the results are significant they explain only about one quarter of the variance and the standard error of estimates are large in relation to the magnitude of the individual variables.

The interrelations, however, were important guides in setting the along-coast variation of values for the SPH and PMH. Extrapolation beyond the data (especially for the PMH) was based primarily on theory and experience, taking into account trends shown in extrapolation of the data.

Meteorological parameters for western North Pacific typhoons blend in well with those of the east and gulf coast hurricanes for the common latitude span (25° to 35°N) in many of the interrelations shown (figs. 5.5, 5.6, and 5.7, for example). Some typhoon data fall out of the general limits of the hurricane data (fig. 5.1, for example). This is due to latitudinal and possibly other effects. Values of the typhoon parameters are less reliable than those of the hurricanes because of approximations, less detailed analyses, and fewer observations, particularly in earlier years. In general, however, the typhoon data support trends shown by the hurricane data; it is most helpful in supplementing data sparse areas on the plotted diagrams (for example, lower p_o and smaller R on fig. 5.1).

21. Assignment 2, Module 4: Prediction of Hurricane Wind Speeds: https://www.catriskcredentials.org/wp-content/uploads/2022/10/Prediction-of-hurricane-wind-speeds.pdf

PREDICTION OF HURRICANE WIND SPEEDS IN THE UNITED STATES

By Peter J. Vickery[1] and Lawrence A. Twisdale,[2] Members, ASCE

ABSTRACT: Prediction of hurricane wind speeds using a simulation approach is the most universally accepted methodology for estimating design wind speeds in hurricane-prone regions of the world. An updated hurricane simulation methodology incorporating newly developed wind-field and filling models is used to obtain hurricane wind speeds associated with various return periods along the hurricane-prone coastline of the United States. Simulation results using the new hurricane simulation methodology indicate that design wind speeds given in ASCE-7-88 for the inland portion of the hurricane-prone coastline are excessive, and that the long-return-period wind speeds given in 1980 by Batts et al. are low. The simulation approach is extended to illustrate areawide hurricane area risk versus single-point risk by comparing hurricane risk for Dade County, Fla., to a single-point risk of a building in Miami, Fla.

INTRODUCTION

The use of mathematical simulation methods to estimate hurricane wind speeds was first implemented by Russell (1968, 1971) for the Texas coast. Others have used this approach for portions of the United States coastline (Russell and Schueller 1974; Tryggvason et al. 1976; Batts et al. 1980; Georgiou et al. 1983; Twisdale and Dunn 1983; Georgiou 1985). The study by Batts et al. (1980) was a milestone, being the first study to examine the entire United States coastline, and it provided a rational means to determine design wind speeds associated with the Gulf and Atlantic coasts of the United States. At the time the Batts study was being carried out, there was relatively little good quality, full-scale data available with which to evaluate the physical models used in the simulation. Although the Monte Carlo simulation methods used by Batts et al. (1980) and other investigators are similar, there are significant differences in the physical models, methods of analysis, and critical hurricane wind-field modeling details. This paper summarizes results from a recent National Science Foundation project funded to develop an improved prediction methodology for hurricane wind speeds (Twisdale and Vickery 1992) with an emphasis placed on the importance of the hurricane wind-field models and filling models used in the methodology. The wind-field model, based on the work of Shapiro (1983), and the filling models are described in detail in Vickery and Twisdale (1995).

Simulation results indicate that hurricane wind speeds at inland locations are significantly overestimated in the study performed by Batts et al. (1980) and consequently, the design wind speeds given in ASCE-7-88 ("Minimum" 1990) for most inland stations (less than 200 km from the hurricane coastline) are excessive.

SIMULATION METHODOLOGY

At any given location on the hurricane-prone coastline of the United States, there are insufficient direct wind-speed measurements to enable estimates of hurricane wind speeds as a function of return period to be determined using traditional methods. To overcome this limitation, an indirect method first developed by Russell (1968) is used. With this approach, statistical distributions are developed of the central pressure difference (Δp), translation speed (c), size of the hurricane (R_{max}), and storm track and occurrence rate for a circular subregion centered on the site. The circular subregion approach was also used by Georgiou (1985) and Neumann (1991). Russell (1968), Russell and Schueller (1974), Tryggravson et al. (1976), Batts et al. (1980), and Twisdale and Dunn (1983) used a coast-crossing technique to derive the basic statistical distributions for Δp, c, θ, etc. Using the coast-crossing technique, straight-line segments radiating from the site are used, where storms crossing a given line segment are used to derive the basic input statistics. Neither approach (coast crossing or circular subregion) has an advantage over the other, and both are subject to the limitation that the selection of the subregion size or coastline segment length is arbitrary and requires subjective judgement. The effect of the subregion size selection on predicted hurricane wind speeds is discussed later.

The minimum basic parameters required to estimate wind speeds within a hurricane are the central pressure difference, Δp; the translation speed of the hurricane, c; and the size of the hurricane as defined by the radius to maximum winds, R_{max}. These data are then used in a hurricane wind-field model to estimate wind speeds within the hurricane. Information on the direction of storm travel θ (defined as the direction of motion measured clockwise from true north), and the minimum distance from the site of interest, d_{min} (defined as positive if the site is located to the right of the storm), are also used to simulate the effects of the hurricane. In the study described here, the site-specific statistical distribution of central pressure difference, storm speed, etc., are obtained for storms passing within a prescribed distance of the site under examination.

The statistical distributions of the central pressure difference, the translation velocity of the hurricane, the angle of approach of the hurricane, and the distance from the center of the hurricane to site are derived from data given on the HURDAT diskettes obtained from the National Climatic Data Center in Asheville, N.C. The statistics of Δp, c, θ, and d_{min} are determined from information on all tropical storms passing within a certain distance of the site of interest (sample circle), between the years 1886 and 1991. These statistics are site-specific and vary significantly with location along the Gulf and Atlantic coastlines.

Using the site-specific probability distributions of Δp, c, θ, and d_{min} in conjunction with a hurricane wind-field model, thousands of hurricanes are simulated. Each simulated storm travels along a straight line path, defined using the sampled values of d_{min} and θ, through the simulation subregion. The sampled value of Δp is held constant until landfall, after which time the storm is decayed using the filling models described in Vickery and Twisdale (1995). The storm translation speed is held constant for each simulated storm. The maximum

[1]Sr. Engr., Applied Research Associates, Inc., Raleigh, NC 27615.
[2]Prin. Engr., Applied Research Associates, Inc., Raleigh, NC.

Note. Associate Editor: Ahsan Kareem. Discussion open until April 1, 1996. Separate discussions should be submitted for the individual papers in this symposium. To extend the closing date one month, a written request must be filed with the ASCE Manager of Journals. The manuscript for this paper was submitted for review and possible publication on December 3, 1993. This paper is part of the ***Journal of Structural Engineering***, Vol. 121, No. 11, November, 1995. ©ASCE, ISSN 0733-9445/95/0011-1691–1699/$2.00 + $.25 per page. Paper No. 7006.

fastest-mile wind speeds at the site under investigation produced by each synthesized storm independent of direction and in each of 16 compass directions are recorded. The probability that the tropical storm wind speed (independent of direction) is exceeded during the time period, t, is

$$P(v > V) = \sum_{x=0}^{\infty} P(v > V|x)p_t(x) \quad (1)$$

where $P(v > V|x)$ = probability of the velocity, v, exceeding V given the occurrence of x storms; and $p_t(x)$ = probability of x tropical cyclones occurring during the time periods t. A uniform Poisson distribution is used to model the arrival rate statistics.

The probability that the tropical storm wind speed is exceeded during the time period, t, within the directional sector $\theta \pm \Delta\theta/2$ is

$$P(v > V, \theta) = [n(\theta)/N] \sum_{x=0}^{\infty} P_\theta(v > V|x)p_t(x) \quad (2)$$

where $P_\theta(v > V|x)$ = probability of the velocity v exceeding V given that x storms occur and produce a wind speed with a direction $\theta \pm \Delta\theta/2$; $n(\theta)$ = number of simulated storms producing a wind speed within the direction $\theta \pm \Delta\theta/2$; and N = total number of storms simulated.

The simulation methodology uses site-specific statistical models defining Δp, c, θ, d_{min}, and R_{max}, a physical model defining the hurricane wind field, and region-specific statistical models for the rate of decay of hurricanes after reaching land. The site-specific models for statistical models described in the following sections, and the filling rate models and windfield models are described in Vickery and Twisdale (1994).

STATISTICAL MODELS

Translation Velocity

The translation velocity of the tropical storm, c, is modeled using a lognormal distribution. The translation velocity is determined using the 6-h position data given in the HURDAT database. Along the Gulf Coast and South Atlantic coasts, a positive correlation between the translation velocity and the storm direction, θ, is observed. This correlation exists because storms that have recurved toward the north, on average, travel faster than those that have not yet recurved. Along the North Atlantic coast, virtually all storms have recurved and no correlation between heading and speed was observed. To take into account the correlation between the translation velocity, c, and heading, θ, the logarithmic mean of the translation velocity is modeled in the following form:

$$m_{lnc} = a_0 + a_1\theta \quad (3)$$

where m_{lnc} = logarithmic mean of the translation speed; and a_0 and a_1 = constants determined using the method of maximum likelihood. The logarithmic standard deviation, σ_{lnc}, is treated as a constant. Fig. 1 shows the modeled and observed relationship between heading and translation speed for storms in the Miami region and in the Galveston, Tex., region.

Approach Angle

The characteristics of the approach angle θ vary significantly along the coastline. We examined the von Mises distribution and a normal distribution, and with few exceptions, these distributions were rejected. The approach angle at all locations examined was found to be best modeled using a binormal distribution. Fig. 2 shows the fitted and observed distribution of the approach angle at Key West, Fla., and Wilmington, N.C. Note that for Key West, the bimodal char-

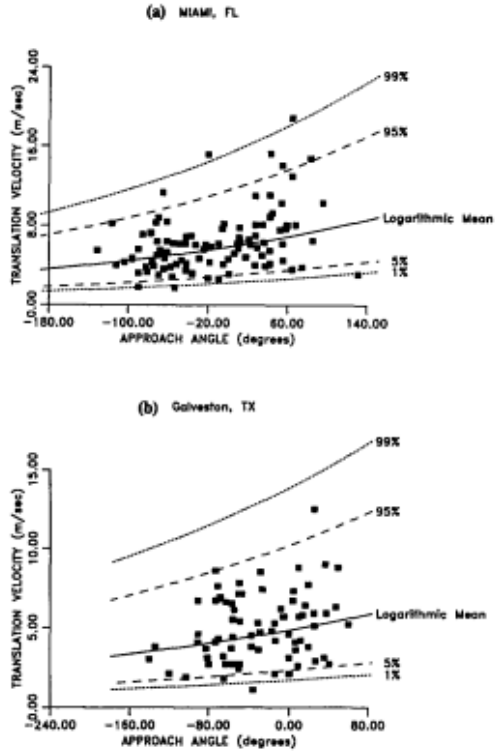

FIG. 1. Modeled and Observed Relationships between Storm Translation Speed and Approach Angle: (a) Miami; (b) Galveston, Tex.

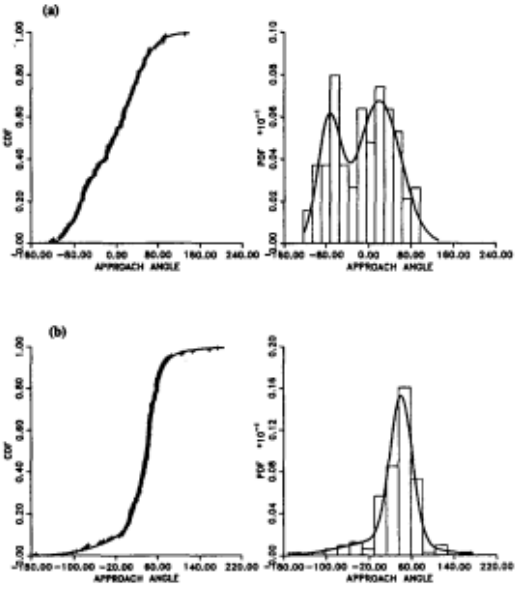

FIG. 2. Modeled and Observed Statistical Distributions of Approach Angle: (a) Key West, Fla.; (b) Wilmington, N.C.

acteristics of approaching hurricanes is clearly evident. This bimodal characteristic in the Key West region is produced by separate tropical cyclone populations, the first of which originate in the Atlantic and approach from easterly directions ($\theta = -90°$), and the second of which originate in the Gulf of Mexico and approach from westerly directions. This distinct bimodal approach angle characteristic is evident at all locations in South Florida and is noted in Ho et al. (1987).

Distance of Closest Approach

The distance of closest approach d_{min} is modeled at all stations examined using either a uniform or trapezoidal distribution.

Central Pressure Difference

The central pressure difference, Δp, is modeled using a Weibull distribution. To convert the central pressure data given in the HURDAT diskettes to a central pressure difference, a periphery pressure of 1,013 millibar (mbar) is used. The choice of a Weibull distribution was first suggested by Georgiou (1985) and was validated in this investigation. The lognormal distribution used by others (Russell 1968; Tryggvason et al. 1976; Batts et al. 1980; Twisdale and Dunn 1983) was found to be a poor model for the central pressure difference for all tropical cyclones; however, the lognormal distribution is suitable if only hurricanes ($\Delta p > 28$ mbar) are used in the simulation procedure. At some of the locations examined (South Florida, New York City area, South Carolina), there is a statistically significant correlation between Δp and the approach angle. In the South Florida region this correlation is attributed to the fact that storms generated in the Atlantic Ocean, which approach from the east, are usually more intense than those generated in the Gulf of Mexico, which approach from westerly directions. In the New York and South Carolina regions, the correlation between Δp and θ is attributed to the fact that storms with northeasterly direction components have, in general, during their history, passed over land and have weakened. The effect of the correlation between Δp and θ was included by modeling the scale parameter in the Weibull distribution as a linear function of the storm heading. The parameters describing the linear relationship between Δp and θ are determined using the maximum likelihood technique.

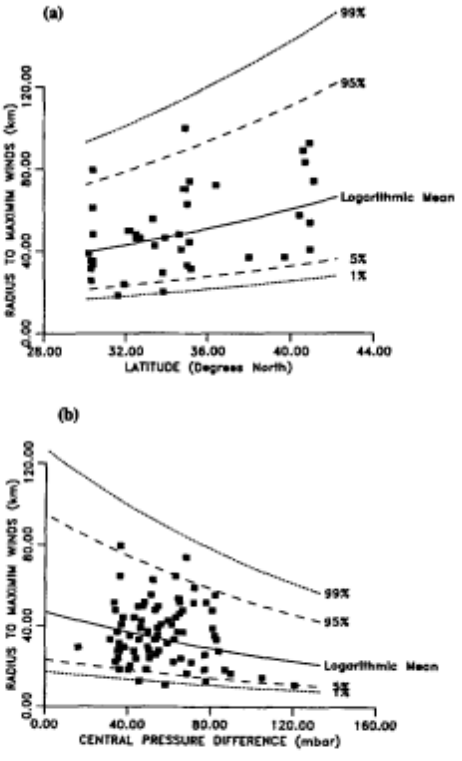

FIG. 3. Statistical Distributions for R_{max} Used in Simulation Methodology: (a) North of 30°N; (b) Between 22°N and 30°N

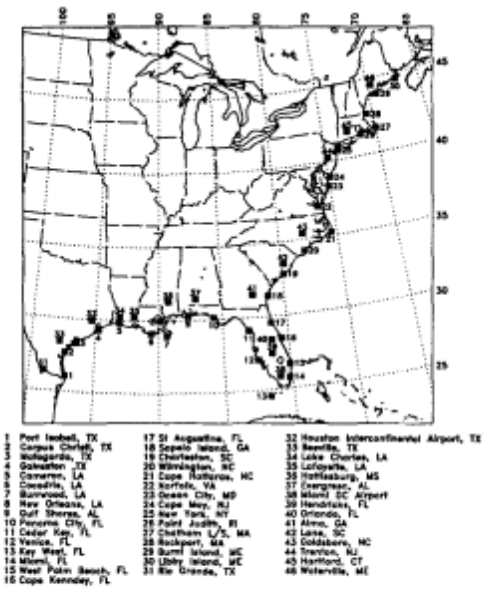

FIG. 4. Locations of Sites Examined for Predictions of Hurricane Wind Speeds

Radius to Maximum Winds

Using the R_{max} and Δp data given in Ho et al. (1987), relationships between R_{max} and Δp and R_{max} and latitude, ψ, were developed. Using all the R_{max} and Δp data yields a correlation coefficient of -0.23 between R_{max} and Δp, and a positive correlation coefficient of 0.47 between R_{max} and latitude. Both correlation coefficients are significant at the 5% level of confidence. The R_{max}-Δp information was separated into two groups, one for storms located between 22°N and 30°N (Florida and Gulf Coast region) and the other for storms north of 30°N (Atlantic Coast). Within the first latitude group, a correlation coefficient -0.18 exists between Δp and R_{max} (significant at the 10% level); and a smaller correlation of 0.14 between R_{max} and latitude is not significant. Within the second latitude group a correlation coefficient of 0.4 (significant at the 1% level) exists between Δp and latitude, and the negative correlation between R_{max} and Δp is not statistically significant.

In the simulation procedure, for locations south of 30°N, R_{max} is modeled using a lognormal distribution with the lognormal parameters given as

$$m_{\ln R_{max}} = 3.853 - 0.0061\Delta p; \quad \sigma_{\ln R_{max}} = 0.427 \quad (4a,b)$$

For storms north of 30°N the lognormal parameters are modeled using

$$m_{\ln R_{max}} = 2.395 + 0.0426\psi;\ \sigma_{\ln R_{max}} = 0.369 \quad (5a,b)$$

where ψ = latitude of the site.

The observed and modeled relationships between R_{max} and Δp, and R_{max} and ψ are shown in Fig. 3.

SIMULATIONS FOR COASTAL AND INLAND STATIONS

Coastal Stations

Simulations were performed at the 30 coastal and 16 inland stations shown in Fig. 4. Predicted 50- and 100-yr return period wind speeds are given in Tables 1 and 2 for coastal stations. All simulations were performed for site subregions that had a diameter of 500 km, with 10,000 storms simulated at each site. Results are given for the Shapiro-based (Vickery and Twisdale 1995) wind-field model coupled with the new filling-rate model, and with the Batts wind-field model coupled with both the new filling-rate model and the filling-rate model used by Batts et al. (1980). Comparing the results obtained using the different wind-field/filling models shows the effect of these components on the final predictions. Comparisons to the results obtained from Batts et al. (1980) are given for both the 50-yr and 100-yr return period wind speeds. Comparison of the predicted 100-yr return period wind speeds with those obtained by Georgiou (1985) are also presented. Table 1 also presents the recommended design wind speeds given in ASCE-7-88 ("Minimum" 1990), which are based principally on the results given in Batts et al. (1980). Fig. 5 compares the 50-, 100-, and 2,000-yr return period wind speeds versus the milepost obtained using the Shapiro-based wind-field model, new filling-rate models, and site-specific statistical distributions for Δp, c, d_{min}, and θ (here referred to as HURSIM), to the results given in Batts et al. (1980). The results clearly indicate that for rarer events (direct strikes by the eyewall), the Shapiro-based results exceed those given in Batts et al. (1980) and are more consistent with the maximum wind speeds in severe hurricanes.

The predicted 50- and 100-yr return period wind speeds derived in this study (using either wind-field/filling model combination) vary more rapidly with changes in position along the coastline than do those presented in Batts et al. (1980). This more rapid change with location is attributed to a combination of the modeling of the central pressure (using all tropical cyclones and a Weibull distribution) and the size of the sample subregion. In the study performed by Batts et al. (1980) all hurricanes making landfall 470 km to the left of the site (downcoast) and 370 km to the right of the site (upcoast) were used to derive statistics for Δp, etc. This large sample region smears any local climatological features that may exist at a particular site, decreasing wind speeds in regions subject to high hurricane activity, which are near those regions having relatively low hurricane activity, and conversely increasing wind speeds in adjacent regions experiencing reduced hurricane activity.

The most notable differences between the results obtained in this study and the results presented in Batts et al. (1980) are the lower predicted wind speeds (50- and 100-yr return period) obtained here along the Texas coast between Corpus Christi and Galveston, and the increase in predicted wind speeds along the New Orleans, Alabama, Mississippi, and Florida panhandle coastlines. We were unable to resolve differences in the wind speeds given in Batts et al. (1980) along the Texas coast between Corpus Christi and Galveston, which are much higher than the wind speeds obtained in this investigation using the HURSIM models. It is noted that these lower wind speeds are also evident in investigations per-

TABLE 1. 50-yr Return Period Fastest-Mile Wind Speeds at Coastal Locations

		PREDICTED FASTEST-MILE WIND SPEEDS									
		Vickery and Twisdale (1995)		Batts Wind New Filling		Batts Wind Batts Filling		Batts et al. (1980)		ASCE-7-88	
Location (1)	Milepost (2)	m/s (3)	mi/hr (4)	m/s (5)	mi/hr (6)	m/s (7)	mi/hr (8)	m/s (9)	mi/hr (10)	m/s (11)	mi/hr (12)
Port Isabell, Tex.	150	44	98	42	94	42	93	44	98	45	100
Corpus Christie, Tex.	250	39	87	36	81	36	80	43	96	42	95
Matagorda, Tex.	320	40	90	38	85	38	85	42	93	42	95
Galveston, Tex.	400	43	96	40	90	39	87	41	92	44	98
Cameron, La.	480	41	93	37	82	37	83	41	91	43	97
Cocodrie, La.	620	47	105	42	93	42	94	41	91	47	105
Burrwood, La.	700	49	109	45	101	45	100	41	92	47	105
New Orleans, La.	720	45	101	40	90	42	93	41	92	45	100
Gulf Shores, Ala.	820	48	107	43	96	43	96	41	91	45	100
Panama City, Fla.	920	45	102	40	90	40	90	39	87	44	99
Cedar Key, Fla.	1,120	43	96	37	83	38	85	40	89	43	97
Venice, Fla.	1,280	44	98	40	90	42	95	46	102	45	100
Key West, Fla.	—	50	111	45	101	45	100	—	—	51	115
Miami, Fla.	1,460	51	114	47	105	47	105	48	107	49	115
West Palm Beach, Fla.	1,510	50	112	44	99	45	100	46	104	46	102
Cape Canaveral, Fla.	1,610	43	95	38	85	40	89	44	99	43	97
St. Augustine, Fla.	1,700	43	96	38	85	42	95	41	92	42	95
Sapelo Island, Ga.	1,800	40	89	35	79	38	84	38	86	41	92
Charleston, S.C.	1,920	45	101	41	92	39	88	42	95	43	97
Wilmington, N.C.	2,050	48	107	41	92	42	94	43	96	45	100
Cape Hatteras, N.C.	2,180	46	103	42	94	44	98	44	98	49	110
Norfolk, Va.	2,280	40	90	35	79	41	92	42	93	40	90
Ocean City, Md.	2,380	41	93	38	85	41	92	36	81	40	90
Cape May, N.J.	2,450	41	92	38	86	42	93	37	81	37	83
New York, N.Y.	2,530	40	89	36	81	37	83	41	91	37	82
Port Judith, R.I.	2,650	42	94	36	81	38	85	43	96	39	88
Chatham L/S, Mass.	2,720	44	98	37	83	39	86	42	93	42	95
Rockport, Mass.	2,800	41	92	35	85	38	86	38	85	38	85
Burnt Island, Me.	2,910	39	87	32	72	33	75	33	74	34	88
Libby Island, Me.	3,050	39	87	32	72	32	72	—	—	—	—

TABLE 2. 100-yr Return Period Fastest-Mile Wind Speeds at Coastal Locations

Location (1)	Milepost (2)	PREDICTED FASTEST-MILE WIND SPEEDS									
		Vickery and Twisdale (1995)		Batts Wind New Filling		Batts Wind Batts Filling		Batts et al. (1980)		Georgiou (1985)	
		m/s (3)	mi/hr (4)	m/s (5)	mi/hr (6)	m/s (7)	mi/hr (8)	m/s (9)	mi/hr (10)	m/s (11)	mi/hr (12)
Port Isabell, Tex.	150	50	112	45	101	46	102	48	107	58	129
Corpus Christie, Tex.	250	45	100	40	90	40	90	48	107	55	122
Matagorda, Tex.	320	45	101	41	91	41	93	47	105	55	122
Galveston, Tex.	400	48	108	42	94	42	95	46	102	57	126
Cameron, La.	480	46	102	40	90	40	90	45	101	59	132
Cocodrie, La.	620	52	116	47	105	45	102	45	101	61	136
Burrwood, La.	700	54	121	47	106	47	106	45	100	61	137
New Orleans, La.	720	50	112	43	96	45	100	45	101	61	137
Gulf Shores, Ala.	820	53	119	46	102	46	104	45	101	60	135
Panama City, Fla.	920	50	111	43	96	43	96	43	96	58	129
Cedar Key, Fla.	1,120	47	106	41	92	41	92	42	95	53	118
Venice, Fla.	1,280	49	110	43	96	47	106	50	111	59	131
Key West, Fla.	—	55	124	51	114	49	109	—	—	—	—
Miami, Fla.	1,460	57	127	52	116	52	116	51	114	66	148
West Palm Beach, Fla.	1,510	56	125	48	107	49	110	51	113	66	148
Cape Canaveral, Fla.	1,610	48	108	42	94	46	103	48	108	63	140
St. Augustine, Fla.	1,700	48	107	42	94	48	107	44	99	56	125
Sapelo Island, Ga.	1,800	45	102	38	85	42	95	42	93	53	118
Charleston, S.C.	1,920	52	116	45	101	44	99	47	105	56	125
Wilmington, N.C.	2,050	53	119	48	107	45	100	47	105	56	126
Cape Hatteras, N.C.	2,180	52	116	48	107	49	110	48	107	55	122
Norfolk, Va.	2,280	44	99	38	85	45	101	44	99	51	114
Ocean City, Md.	2,380	46	104	40	89	47	105	41	92	46	102
Cape May, N.J.	2,450	46	104	42	94	46	102	42	93	50	112
New York, N.Y.	2,530	45	102	41	92	42	94	45	101	53	119
Port Judith, R.I.	2,650	46	103	39	87	41	91	47	105	54	120
Chatham L/S, Mass.	2,720	48	108	40	89	42	94	46	103	54	121
Rockport, Mass.	2,800	46	103	39	87	42	94	43	96	49	110
Burnt Island, Me.	2,910	43	96	35	78	37	83	38	86	44	99
Libby Island, Me.	3,050	43	96	34	76	35	79	—	—	—	—

formed by Georgiou et al. (1983) and Sanchez-Sezma et al. (1988), suggesting that the predicted wind speeds given in Batts et al. (1980) are excessive in this region. A reduction in predicted wind speeds on the west coast of the Florida peninsula is attributed to the new filling-rate model reducing the intensity of hurricanes approaching from the Atlantic Ocean and crossing the Florida peninsula. The predicted wind speeds on the west coast of Florida presented here are considered to be conservative because in this region the most intense hurricanes approach from an easterly direction, thus the strongest winds also approach from approximately easterly directions and will be reduced because of frictional effects, not included in the study for coastal locations (Vickery and Twisdale 1995) because the wind field treats coastal locations for onshore winds. At most other coastal locations examined here, the dominant wind direction associated with the simulated storms approaches from over water, indicating that the coastal exposure (onshore winds) assumption used in the wind-field model is appropriate. For locations along the Atlantic Coast, north of the South Carolina–North Carolina border, differences between results obtained in this study and those given in Batts et al. (1980) are not significantly different, and both results are believed to be conservative as a result of the wind-field model limitations associated with water temperature discussed in Vickery and Twisdale (1995).

Table 2 compares the 100-yr return period fastest-mile wind speeds obtained here to those given in Georgiou (1985) and Batts et al. (1980). The fastest-mile wind speeds, given in Georgiou (1985) as mean hourly values, were converted to fastest-mile wind speeds using the gust factor curve derived by Krayer and Marshall (1992). The Georgiou (1985) results appear high in comparison to the results of this investigation and other studies. The wind speeds given in Georgiou et al. (1983) agree reasonably well with those obtained here.

Inland Stations

Predicted 50- and 100-yr return period fastest-mile winds at the 16 inland stations examined are given in Tables 3 and 4. Simulations were performed using the HURSIM models, the Batts wind-field model coupled with both the HURSIM filling models, and the filling rate model used by Batts et al. (1980). The distance from the coastline for the stations examined varies between 40 and 100 km. The wind speeds obtained using the Shapiro-based models are significantly lower than those predicted using the Batts wind-field model coupled with the Batts filling model. The majority of the reduction in wind speeds is associated with the new wind-field model, rather than the new filling model. The relative contribution to the reduction in wind speed associated with the wind-field model and the filling model varies from site to site, and is a function of the local geography and the heading of the tropical cyclones. The results obtained using HURSIM models, which are shown in Vickery and Twisdale (1995) to be significant improvements over the models used in Batts et al. (1980), suggest that with the exception of the Florida peninsula, for locations 100 km or farther from the coast, the influence of hurricanes on the 50- and 100-yr return period wind speeds can be ignored. For locations less than 100 km from the coast, the combined influence of both hurricanes and nonhurricane winds needs to be considered, and for return periods of longer than approximately 100 yr, the influence of hurricanes may need to be considered. Comparisons of the 50-, 100-, and 2,000-yr predicted wind speeds derived using HURSIM models and those given in Batts et al. (1980) for the 16 inland stations

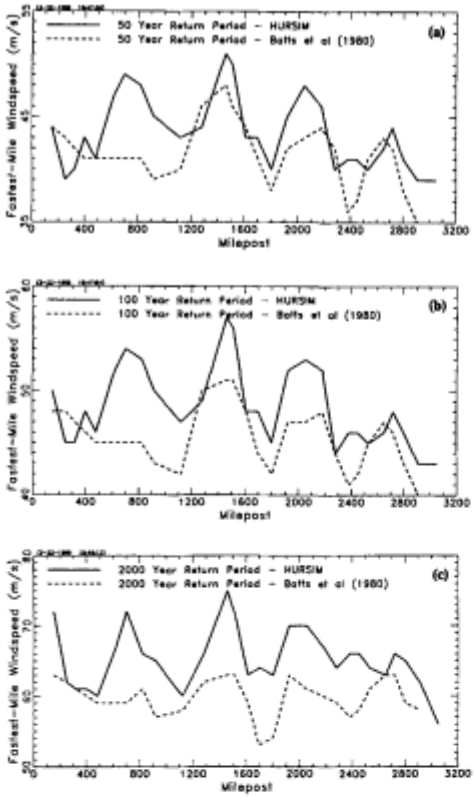

FIG. 5. Comparisons of Predicted Wind Speeds Obtained Using HURSIM Models and those Derived by Batts et al. (1980) for Coastal Stations

are plotted versus approximate milepost in Fig. 6. The HURSIM wind speeds are consistently lower than those of Batts et al. (1980) for all locations and all return periods. It is noteworthy that the results given in Batts et al. (1980) indicate that the 100-yr return period wind speeds 200 km inland from the coast at mileposts 500–600 and milepost 1,450 are identical to those wind speeds at the coast, raising questions as to the validity of the results of Batts et al. (1980) for inland locations.

SENSITIVITY STUDIES FOR MIAMI AND NEW YORK

Miami

Statistical distributions of the location dependent parameters (d_{min}, Δp, θ, and c) for storms centered around Miami were derived for sample circles having diameters ranging between 200 and 1,000 km. Sensitivity studies examining the effects of parameter correlation, storm decay models, etc., were performed for a 500-km diameter sample subregion. Table 5 presents the values of each of the input statistical distribution parameters used in the Miami simulation for the 500-km diameter subregion.

Correlation

Table 6 shows the results of a correlation analysis of the four variables (Δp, c, d_{min}, and θ) and the year of observation. As eluded to earlier, the correlation between Δp and θ is consistent with the observation that storms approaching from the east (generated off the African coast) are generally more intense than those generated in the Gulf of Mexico; and the correlation between the translation velocity, c, and the heading of the storm is consistent with the observation that storms that have recurved towards the north move faster than the easterly storms that have not recurved.

The negative correlation between Δp and year was observed at most stations examined. This negative correlation is primarily attributed to the fact that prior to the 1960s, there is a significant bias in recorded central pressures, where data are available only for the more significant storms. During the 1970s and later, central pressure data is given for all storms at each of the 6-h position on the HURDAT diskettes. This bias in the central pressure records suggests that there may be some conservatism in the statistical distributions of Δp.

Using statistics derived from the 500-km-diameter sample subregion and the Batts wind-field model, sensitivity studies examining the effect of correlated sampling and distribution censoring showed that including the correlation between Δp and θ, and θ and c produced changes in the 50- and 100-yr return period wind speeds of less than 2%. If the correlation between Δp and R_{max} is ignored, the predicted wind speeds are increased by 10% to 20%, depending on the return period. The effects of censoring the sampled values of the cen-

TABLE 3. 50-yr Return Period Fastest-Mile Wind Speeds at Inland Locations

Location (1)	Distance inland (2)	PREDICTED FASTEST-MILE WIND SPEEDS							
		Vickery and Twisdale		Batts Wind New Filling		Batts Wind Batts Filling		ASCE-7-88	
		m/s (3)	mi/hr (4)	m/s (5)	mi/hr (6)	m/s (7)	mi/hr (8)	m/s (9)	mi/hr (10)
Rio Grande, Tex.	100	22	49	30	67	31	69	36	80
Houston IAH, Tex.	60	33	74	37	83	37	83	38	85
Beeville, Tex.	60	27	60	31	70	32	72	37	92
Lake Charles, La.	50	34	77	47	83	37	83	41	92
Lafayette, La.	40	34	76	36	81	36	81	42	95
Hattiesburg, Miss.	100	32	72	40	90	42	93	39	87
Evergreen, Ala.	100	28	63	34	75	36	80	37	83
Miami DC Airport, Fla.	70	40	90	44	99	44	98	47	105
Hendricks, Fla.	90	32	72	37	83	41	92	43	97
Orlando, Fla.	60	35	78	34	77	39	87	42	95
Alma, Ga.	100	25	57	29	65	33	74	34	75
Lane, S.C.	60	35	77	37	83	41	92	39	88
Goldsboro, N.C.	100	29	64	32	72	39	87	35	78
Trenton, N.J.	60	36	80	36	81	39	87	34	75
Hartford, Conn.	60	34	77	35	78	37	83	34	75
Waterville, Me.	70	32	72	30	68	31	70	38	85

TABLE 4. 100-yr Return Period Fastest-Mile Wind Speeds at Inland Locations

Location (1)	Distance inland (2)	PREDICTED FASTEST-MILE WIND SPEEDS: Vickery and Twisdale m/s (3)	Vickery and Twisdale mi/hr (4)	Batts Wind New Filling m/s (5)	Batts Wind New Filling mi/hr (6)	Batts Wind Batts Filling m/s (7)	Batts Wind Batts Filling mi/hr (8)
Rio Grande, Tex.	100	25	57	33	74	35	79
Houston IAH, Tex.	60	37	82	35	78	39	88
Beeville, Tex.	60	32	71	34	77	36	81
Lake Charles, La.	50	39	87	39	87	40	90
Lafayette, La.	40	38	85	39	88	39	87
Hattiesburg, Miss.	100	36	81	43	96	46	103
Evergreen, Ala.	100	31	70	37	83	39	87
Miami DC Airport, Fla.	70	45	100	47	105	48	108
Hendricks, Fla.	90	36	80	42	94	45	101
Orlando, Fla.	60	39	87	38	85	41	92
Alma, Ga.	100	29	65	32	72	36	80
Lane, S.C.	60	38	86	40	90	45	100
Goldsboro, N.C.	100	33	73	37	83	43	96
Trenton, N.J.	60	40	90	39	87	44	99
Hartford, Conn.	60	38	85	37	83	41	92
Waterville, Me.	70	35	79	33	74	35	78

tral pressure difference to be less than 150 mbar and forcing R_{max} to be greater than 5 km and less than 150 km were both negligible, changing predicted wind speeds by less than 1/2%.

Subregion Size

The effect of diameter of the subregion circle was examined using the Shapiro-based representation of the hurricane wind field. Ten thousand storms were simulated for subregions of 300 km in diameter through to 1,000 km in diameter. The investigation showed that the predicted 50-yr return period wind speed ranged between a maximum of 55 m/s (124 mi/hr) for a sample subregion diameter of 300 km to a minimum of only 47 m/s (106 mi/hr) for a sample subregion diameter of 1,000 km. This 15% reduction in wind speed is reflected in predictions for other return periods as well. Most of the difference in the predicted wind speeds is caused by changes in the central pressure statistics with increasing circle diameter.

Return Period and Direction

Fig. 7 shows the resulting predicted wind speeds as a function of return period and direction for Miami obtained using both the Batts windfield model and the Shapiro-based windfield model. It is particularly noteworthy that the predicted wind speeds for long return periods are much greater when the Shapiro-based wind-field model is used to model the hurricane wind field. These larger wind speeds arise because the model more accurately represents the radial distribution of wind speed within the storm, where it does not underestimate the wind speeds within the eyewall region at the coastline. The directional characteristics of the predicted wind speeds obtained using the two different wind-field models exhibit some differences. The major difference is evident for westerly winds, where the Batts wind-field model yields higher wind speeds than the Shapiro-based wind-field model. The higher westerly winds predicted using the Batts model are caused by an overestimate in the magnitude of wind speeds modeled on the left side of the hurricane, and not because of the modeling of the wind direction itself.

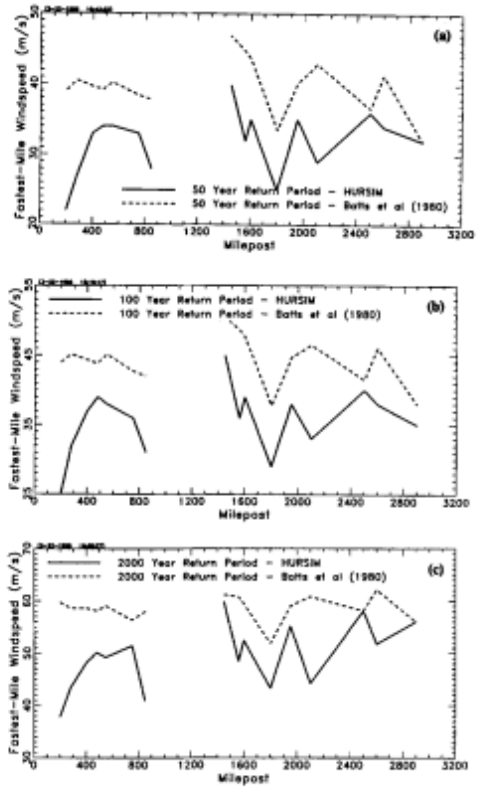

FIG. 6. Comparisons of Predicted Wind Speeds Obtained Using HURSIM Models and those Derived by Batts et al. (1980) for Inland Stations

Area versus Point Windspeed Exceedance Events

In addition to the point simulation for Miami used in this investigation and most others, a simulation was performed in which the maximum wind speeds produced by each storm at Miami were recorded, as were the maximum wind speeds at any point on the Dade County coastline. Fig. 8 shows a comparison of the predicted wind speeds for both a single-point location (of a few kilometers in length) in Miami and at any location on the Dade County coastline. The results indicate that the 100-yr return period fastest-mile wind speed at a single location in the Miami area is about 57 m/s (127 mi/hr), however the 100-yr return period fastest-mile wind speed for any location along the Dade County coastline is about 66 m/s (147 mi/hr). The wind speed predictions for the Dade County area indicate that on average, somewhere in Dade County, a fastest-mile wind speed of 45 m/s (100 mi/hr) will be exceeded once every 15 yrs. Although this result is not important for specifying the design wind speed for any single structure, it provides a better means to estimate the expected annual losses associated with hurricanes in a particular region. Clearly, if the heavily populated Broward County coastline had been included in this simulation, the predicted wind speeds for a given return period for this longer coastline segment would be higher, or conversely, the return period associated with a 45 m/s (100 mi/hr) fastest-mile wind speed would be lower. Examining hurricane wind speeds with a regional approach enables the frequency of intense storms that make landfall in the United States to be examined in a more rational manner. For example, in the case of Hurricane Andrew in

TABLE 5. Distributions and Distribution Parameters Used for Simulation of Hurricanes in Miami Region

Parameter (1)	Distribution (2)	Probability-density function $f_x(x)$ (3)	Distribution parameters (4)
d_{min} (km)	Uniform	a_2	$a_2 = 0.002$; $-R \le x \le R$
θ	Bi-Normal	$\frac{a_1}{\sqrt{2\pi}\sigma_{x1}} \exp\left[-\frac{1}{2}\left(\frac{x - m_{x1}}{\sigma_{x1}}\right)^2\right]$	$m_{x1} = -51.6$; $\sigma_{x1} = 38.1$; $m_{x2} = 37.3$
		$+ \frac{(1 - a_1)}{\sqrt{2\pi}\sigma_{x2}} \exp\left[-\frac{1}{2}\left(\frac{x - m_{x2}}{\sigma_{x2}}\right)^2\right]$	$\sigma_{x2} = 33.0$; $a_1 = 0.55$
c (m/s)	Lognormal	$\frac{1}{x\sqrt{2\pi}\sigma_{\ln x}} \exp\left[-\frac{1}{2}\left(\frac{\ln x - m_{\ln x}}{\sigma_{\ln x}}\right)^2\right]$	$m_{\ln x} = 1.768 - 0.002758$; $\sigma_{\ln x} = 0.413$
Δp (mbar)	Weibull	$\frac{k}{C}\left(\frac{x}{C}\right)^{k-1} \exp\left[-\left(\frac{x}{C}\right)^k\right]$	$C = 33.68 - 0.13348$; $k = 1.15$
R_{max} (km)	Lognormal	$\frac{1}{x\sqrt{2\pi}\sigma_{\ln x}} \exp\left[-\frac{1}{2}\left(\frac{\ln x - m_{\ln x}}{\sigma_{\ln x}}\right)^2\right]$	$m_{\ln x} = 3.85 - 0.00607\Delta p$; $\sigma_{\ln x} = 0.427$
λ	Poisson	$\frac{\lambda^x e^{-\lambda}}{x!}$	$\lambda = 1.22$

Note: m_x = mean of x; σ_x = standard deviation of x; $m_{\ln x}$ = mean of the logarithm of x; $\sigma_{\ln x}$ = standard deviation of the logarithm of x; and R = radius of the simulation subregion.

TABLE 6. Results of Correlation Analysis for Miami

	Year	d_{min}	θ	c (m/s)	Δp (mbar)
Year	1	0	0	0	−0.71
d_{min}		1	0	0	0
θ			1	0.33	−0.29
c				1	0
Δp (mbar)					1

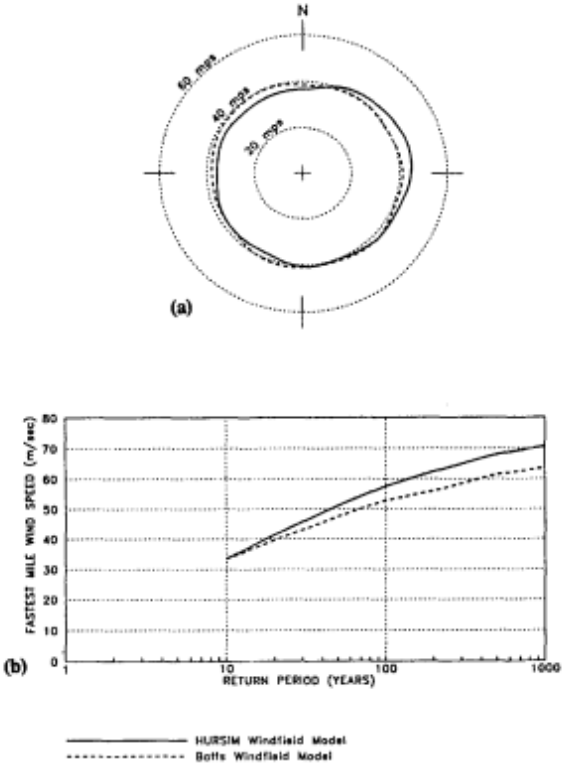

FIG. 7. Comparisons of Predicted Wind Speeds for Miami Showing Effect of Wind-Field Model on Predicted Wind Speeds

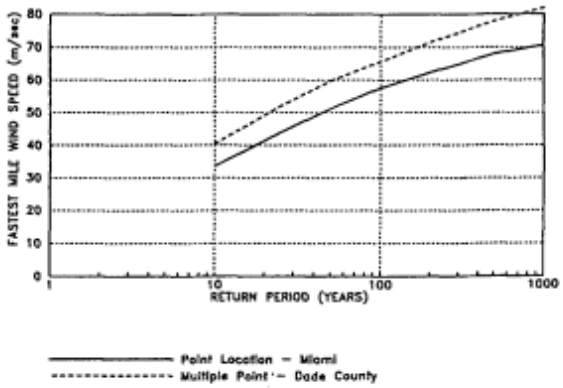

FIG. 8. Comparison of Predicted Wind Speeds for Miami (Point Location) and Dade County, Fla.

1992, the maximum fastest-mile wind speeds were on the order of 65 m/s (145 mi/hr) (Reinhold et al. 1993), and when considering a single point in the Miami region, this wind speed is associated with a return period of about 300 yr; however, the return period of this wind speed anywhere in Dade County, Florida is only about 100 yr. Using the results of Batts et al. (1980), the 65 m/s (145 mi/h) fastest-mile wind speed produced by Hurricane Andrew corresponds to a return period well in excess of 2,000 yr.

New York

Statistical distributions of the location-dependent parameters (d_{min}, Δp, θ, and c) for storms centered on New York City were derived for subregion diameters ranging from 200 to 800 km. The distribution defining d_{min}, Δp, θ, and c were all markedly influenced by changes in the sample subregion size (unlike Miami, where only the probability distribution of the central pressure difference was markedly influenced by the subregion size). Correlations between variables were found to change significantly with subregion size.

The predicted wind speeds given in Fig. 9 present results obtained using both the Batts and the Shapiro-based wind-field models combined with the HURSIM filling model for a 500-km-diameter subregion, so that the differences in results are the effect of different wind-field models only. Using the Batts wind-field model, the strongest winds are predicted to

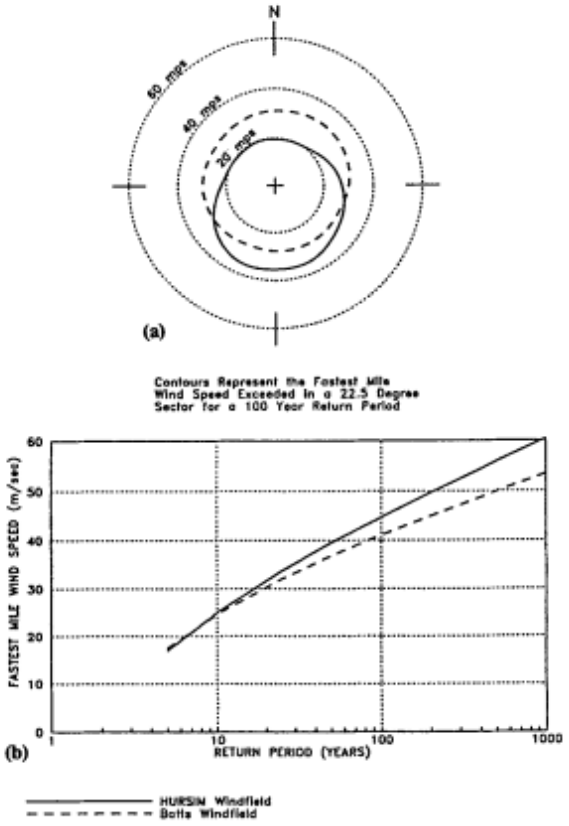

FIG. 9. Predicted Wind Speeds versus Return Period for New York Showing Effect of Wind-Field Model on Predicted Wind Speeds

approach from the north; whereas those predicted using the Shapiro-based wind-field model are easterly though southerly. The difference in directionality is again produced by the manner in which the translation speed of the storm is modeled. The empirical Batts wind-field model adds (subtracts) one-half of the translation speed to the right (left) side of the storm. The Shapiro-based wind-field model properly includes the full value of the storm motion, resulting in a more asymmetric storm. Along the northeast Atlantic coast, where hurricanes translate much faster than they do in the south Atlantic and Gulf regions, the impact of the translation speed on the wind-field is more pronounced than it is in the lower latitudes.

SUMMARY AND CONCLUSIONS

The Shapiro-based methodology incorporates significant improvements in filling models and wind-field models, and improved modeling of the correlations between key parameters used in the simulation procedure. The comparison of predicted wind speeds for return periods of 50, 100, and 2,000 yr shown in Fig. 5 reflects wind-field model differences where for rare events, wind speeds predicted using a Shapiro-based method are significantly higher than those given in Batts et al. (1980).

These new results suggest that for locations 100 km or farther from the coast, hurricanes contribute little to the design wind speeds for return periods of 100 yr or less. Hurricane winds may need to be considered when designing for less frequent events, and in such cases a site-specific study is recommended.

The results indicate that subregion identification is an important part of the simulation process. At this time a subregion diameter on the order of 500 km is recommended; however, improvements in the simulation methodology that will eliminate the subregion difficulties need to be examined in future research efforts.

The choice of the wind-field model has a significant impact on predicted wind speeds. This impact is particularly noteworthy where estimates of wind speed as a function of direction are required and it is felt that the directional data given in Batts et al. (1980) should not be used. Further comparisons between simulated and measured wind speeds in hurricanes are essential for improving the reliability of predicted windspeeds. These comparisons are particularly important for hurricanes along the North Atlantic coast, where not only is the colder water expected to influence results, but many of the hurricanes move at much higher speeds than those used to evaluate the wind-field models.

APPENDIX. REFERENCES

Batts, M. E., Cordes, M. R., Russell, C. R., Shaver, J. R., and Simiu, E. (1980). "Hurricane windspeeds in the United States." *Nat. Bureau of Standards Rep. No. BSS-124*, U.S. Dept. of Commerce, Washington, D.C.

Georgiou, P. N. (1985). "Design windspeeds in tropical cyclone-prone regions," PhD thesis, Fac. of Engrg. Sci., Univ. of Western Ontario, London, Ont., Canada.

Georgiou, P. N., Davenport, A. G., and Vickery, B. J. (1983). "Design wind speeds in regions dominated by tropical cyclones." *J. Wind Engrg. and Industrial Aerodynamics*, 13(1–3), 139–152.

Ho, F. P., et al. (1987). "Hurricane climatology for the Atlantic and Gulf coasts of the United States." *NOAA Tech. Rep. NWS38*, Federal Emergency Mgmt. Agency, Nat. Oceanic and Atmospheric Admin. (NOAA), Washington, D.C.

Krayer, W. R., and Marshall, R. D. (1992). "Gust factors applied to hurricane winds." *Bull. Am. Meteorological Soc.*, 73(5), 613–617.

"Minimum design loads for buildings and other structures." (1990). *ASCE-7-88*, ASCE, New York, N.Y.

Neumann, C. J. (1991). "The national hurricane center risk analysis program (HURISK)." *NOAA Tech. Memo. NWS NHC 38*, Nat. Oceanic and Atmospheric Admin. (NOAA), Washington, D.C.

Reinhold, T. A., Vickery, P. J., and Powell, M. D. (1993). "Windspeeds in Hurricane Andrew: myths and reality." *7th U.S. Nat. Conf. on Wind Engrg.*, Univ. of California, Los Angeles, Calif., 553–562.

Russell, L. R. (1968). "Probability distributions for Texas Gulf Coast hurricane effects of engineering interest," PhD thesis, Stanford Univ., Stanford, Calif.

Russell, L. R. (1971). "Probability distributions for hurricane effects." *J. Wtrwy., Harbors, and Coast. Engrg. Div.*, ASCE, 97(1), 139–154.

Russell, L. R., and Schueller, G. F. (1974). "Probabilistic models for Texas Gulf Coast hurricane occurrences." *J. Petroleum Technol.*, 279–288.

Sanchez-Sesma, J., Aguirre, J., and Sen, M. (1988). "Simple modeling procedure for estimation of cyclonic wind speeds." *J. Struct. Engrg.*, ASCE, 114(2), 352–370.

Shapiro, L. J. (1983). "The asymmetric boundary layer flow under a translating hurricane." *J. Atmospheric Sci., AMS*, 40(8), 1984–1998.

Tryggvason, B. V., Surry, D., and Davenport, A. G. (1976). "Predicting wind-induced response in hurricane zones." *J. Struct. Div.*, ASCE, 102(12), 2333–2350.

Twisdale, L. A., and Vickery, P. J. (1992). "Predictive methods for hurricane winds in the United States." *Final Rep. Small Business Innovation Grant ISI 916035*, Nat. Sci. Found., Washington, D.C.

Twisdale, L. A., and Dunn, W. L. (1983). "Extreme wind risk analysis of the Indian Point Nuclear Generation Station." *Final Rep. 44T-2491, Addendum to Rep. 44T-2171*, Res. Triangle Inst. Research Triangle Park, N.C.

Vickery, P. J., and Twisdale, L. A. (1995). "Wind-field and filling models for hurricane wind speed predictions." *J. Struct. Engrg.*, ASCE, 121(11), 1700–1709.

22. Assignment 2, Module 4: Wind-Field and Filling Models: https://www.catriskcredentials.org/wp-content/uploads/2022/10/Wind-Field-and-Filling-Models.pdf

WIND-FIELD AND FILLING MODELS FOR HURRICANE WIND-SPEED PREDICTIONS

By Peter J. Vickery[1] and Lawrence A. Twisdale,[2] Members, ASCE

ABSTRACT: Two key modeling components in the hurricane simulation process are the wind-field model, and the filling model, which describes the rate of decay of the hurricane after landfall is made. In the investigation described here, new wind-field and filling-rate models are developed for use in hurricane simulation routines. Detailed evaluations of the wind-field and filling models used in 1980 by Batts et al., which are used to develop the hurricane wind speeds given in ASCE-7-88, and the new wind-field and filling models are performed. Results indicate that the combination of wind-field and filling models employed in the original study used to derive hurricane wind speeds given in ASCE-7-88 yield significant overestimates of hurricane wind speeds at inland locations, and their wind-field model is unable to reproduce the high surface-level wind speeds evident in very intense storms. The deficiencies in the models used by Batts et al. are carried through to the recommended design wind speeds given in ASCE-7-88.

INTRODUCTION

This paper describes a new wind-field model and new filling-rate models developed for use in hurricane simulations. The new wind-field model described here incorporates the most recent information on hurricane gust factors, and the model is validated through comparisons to over 20 full-scale records of hurricane wind speeds. The wind-field model is based on the numerical model described in Shapiro (1983). New hurricane filling models are developed for three different regions of the United States. The new filling models reproduce the observations that more intense storms fill more rapidly than weak storms. The filling-rate models are evaluated with results of detailed filling-rate studies performed by Ho et al. (1987). The wind-field and filling-rate models used by Batts et al. (1980) are also evaluated through comparisons to full-scale data. The wind-field and filling models used by Batts et al. (1980) are examined because the results obtained from their study form the basis for the design wind speeds given in ASCE-7-88 ("Minimum" 1990). Results indicate that the filling-rate model used by Batts et al. (1980) produces simulated storms that decay much too slowly when compared to actual decay rates, and the Batts wind-field model overestimates wind speeds away from the coast and underestimates wind speeds within the eye wall of hurricanes at the coast.

WIND-FIELD MODELS

Shapiro-Based Wind-Field Model

The wind-field model described here employs the numerical solution of the equations of motion of a hurricane developed by Shapiro (1983). The numerical model developed by Shapiro (1983) is very similar to that originally developed by Chow (1971); however, Shapiro (1983) used a truncated spectral analysis to diagnose the boundary-layer flow field instead of solving the full nonlinear model as was done in Chow (1971). The original work of Shapiro (1983) was directed towards examining the effect of surface friction on the asymmetries in hurricane windfields. Georgiou (1985) also used the Shapiro wind-field model in his investigation of hurricane winds along the Gulf and Atlantic Coasts of the United States; however, the implementation of the Shapiro model in this study differs from that used by Georgiou. In Shapiro (1983), the momentum equations for a slab boundary layer of constant depth under an imposed symmetric pressure distribution are solved. The coordinate system moves with the hurricane vortex, which is in gradient balance with the pressure field above the boundary layer. The radial and tangential momentum equations in cylindrical coordinates (r, λ) are

$$u\frac{\partial u}{\partial r} - \frac{v^2}{r} - fv + \frac{v}{r}\frac{\partial u}{\partial \lambda} + \frac{\partial \phi}{\partial r} - K\left(\nabla^2 u - \frac{u}{r^2} - \frac{2}{r^2}\frac{\partial v}{\partial \lambda}\right) + F(c, u) = 0 \quad (1a)$$

$$u\left(\frac{\partial v}{\partial r} + \frac{v}{r}\right) + fu + \frac{v}{r}\frac{\partial v}{\partial \lambda} - K\left(\nabla^2 v - \frac{v}{r^2} + \frac{2}{r^2}\frac{\partial u}{\partial \lambda}\right) + F(c, v) = 0 \quad (1b)$$

where u and v = vertically integrated average values of the radial and tangential components of the velocity; ϕ = pressure distribution within the storm; c = translation speed of the hurricane; f = Coriolis parameter; K = a constant coefficient of eddy diffusion; r = radial distance from the storm center; λ = angle measured counterclockwise from an easterly direction; and F = frictional drag force. The frictional drag force acts parallel to the total velocity vector and is given as

$$F(\mathbf{c}, \mathbf{u}) = (C_D/h)|\mathbf{u} + \mathbf{c}|(\mathbf{u} + \mathbf{c}) \quad (2)$$

where $\mathbf{u}$ and $\mathbf{c}$ = vector components of the circulation-induced wind speed and the storm translation speed, respectively; and h = boundary-layer depth assumed to be a constant value of 1 km over the domain of the storm. The drag coefficient, C_D, used by Shapiro (1983) is based on the model developed by Deacon (Roll 1965) and varies linearly with velocity in the following form:

$$C_D = (1.1 + 0.04|\mathbf{u} + \mathbf{c}|) \times 10^{-3} \quad (3)$$

The drag coefficient expressed in (3) was originally developed for surface-level winds (10 m above the sea surface); consequently, for consistency, when used with upper-level (or vertically averaged) winds, C_D should be reduced by the ratio $(V_{10}/V_u)^2$ where V_u = value of the vertically integrated wind speed and V_{10} = wind speed 10 m above the water surface, suggesting that C_D should be reduced to between 50% and 70% of the 10-m value. In this study, a value of C_D reduced to 50% of that given in (3) is used. The modeling of the sea-surface drag coefficient as linearly dependent on wind

[1]Sr. Engr., Applied Research Associates, Inc., Raleigh, NC 27615.
[2]Prin. Engr., Applied Research Associates, Inc., Raleigh, NC.

Note. Associate Editor: Ahsan Kareem. Discussion open until April 1, 1996. Separate discussions should be submitted for the individual papers in this symposium. To extend the closing date one month, a written request must be filed with the ASCE Manager of Journals. The manuscript for this paper was submitted for review and possible publication on December 3, 1993. This paper is part of the ***Journal of Structural Engineering***, Vol. 121, No. 11, November, 1995. ©ASCE, ISSN 0733-9445/95/0011-1700–1709/$2.00 + $.25 per page. Paper No. 7458.

speed is considered by some researchers [e.g., Amorocho and Devries (1980) and Donelan (1982)] to be too simplistic. These researchers suggest a drag-coefficient model should recognize the existence of breaking waves. The results of Amorocho and Devries (1980) indicate that for mean wind speeds (at 10 m above sea level) greater than 20 m/s, a full breaker saturation state exists and the drag coefficient (based on the 10-m wind speed) is constant and equal to 0.0254, in which case modeling the geostrophic drag coefficient as a constant in the range of 0.02–0.03 would be more appropriate. The studies by Donelan (1982) indicate that the drag coefficient may be influenced by the direction of the waves with respect to the mean wind, with waves traveling in a direction opposite that of the wind yielding the higher values of C_D, resulting in a drag coefficient varying over the domain of the storm. The effect of varying the surface drag coefficient on the windfield is discussed in more detail in Twisdale and Vickery (1992).

The pressure distribution of $\phi = \phi_0(r)$ is assumed to be symmetric and in gradient balance with a specified vortex with a gradient wind $v_{gb}(r)$ so that

$$\frac{\partial \phi}{\partial r} = \frac{v_{gb}^2}{r} + f v_{gr} \tag{4}$$

The vortex is defined with a 30-km wide cubic spline transition region connecting a solid body rotation in the inner core in the form (r/R_{max}), to a profile in the form of $(r/R_{max})^{-n}$ in the outer vortex. R_{max} is the radial distance from the center of the storm to the location where the maximum wind speeds occur. In Shapiro (1983), the profile exponent, n, is assigned a value of 0.62; however, we examined other values of n in this investigation. Shapiro (1983) solves the momentum equations with the relative wind decomposed into a spectral representation where

$$u = u_0(r) + u_{c_1}(r)\cos\lambda + u_{s_1}(r)\sin\lambda + u_{c_2}(r)\cos 2\lambda + u_{s_2}(r)\sin 2\lambda \tag{5a}$$

$$v = v_0(r) + v_{c_1}(r)\cos\lambda + v_{s_1}(r)\sin\lambda + v_{c_2}(r)\cos 2\lambda + v_{s_2}(r)\sin 2\lambda \tag{5b}$$

where the subscripts c and s refer to the sine and cosine portions of the expansion.

The grid spacing used to solve (1) is variable, with a uniform grid of $\Delta r = 5$ km for $r < 2R_{max}$. For $r > 2R_{max}$, the grid spacing increases linearly out to a radius of 1,300 km. The output from the Shapiro model consists of 91 coefficients of each u_0, u_{c_1}, u_{s_1}, etc. Solving the momentum equations in spectral form does not produce a solution as accurate as the full nonlinear solution; but, because the entire tropical cyclone windfield is represented with relatively few parameters, the technique has advantages for employment in Monte Carlo simulations, as discussed in Twisdale and Vickery (1992). To cover the full range and combinations of Δp (the difference in pressure between the center of the storm and the ambient pressure), R_{max}, c, and f expected, we simulated 968 storms for each of a number of latitudes along the hurricane coastline of the United States. The coefficients generated for each storm are stored on disk and recalled as needed. Using the spectral modeling approach employed by Shapiro, 910 coefficients are read from disk for each storm. For each simulated storm the velocities u and v are found by interpolating from the Δp, R_{max}, c, and f results stored on disk.

The wind speeds produced by the numerical model are vertically averaged values defined as

$$V_u = \frac{1}{h}\int_0^h V(z)\,dz \tag{6}$$

where h = boundary-layer depth. The boundary-layer depth used by Shapiro (1983) and used here is 1 km. Assuming a neutral logarithmic boundary layer model in which

$$V(z) = V_h[\ln(z/z_0)/\ln(h/z_0)] \tag{7}$$

where V_h = wind speed at height h, yields values of V_u that are similar in magnitude to the wind speed of a height of 500 m for a wide range of roughness lengths z_0. For typical values of z_0, the difference between the vertically averaged wind speed and the wind speed at 500 m is about 2%. As a result, the vertically average wind speeds are taken as being equivalent to the upper-level wind speed at a height of about 500 m.

The upper-level winds are adjusted to surface level (10 m, over water) by applying a 17.5% reduction for $r < 2R_{max}$ and a 25% reduction for $R > 4R_{max}$, with a smooth transition curve used for intermediate values of r. This reduction in wind speed to surface level (over water) is similar to that used in Georgiou (1985), where wind speed data given in Myers (1954) was used in his model development. The reduction in wind speed to the surface (with respect to upper-level wind speeds) is also consistent with the 0.8 rule as described and evaluated in Powell (1980).

As discussed in Shapiro (1983), the use of a vertically averaged boundary-layer model leads to excessive estimates of radial velocities (and thus inflow angles) compared to those obtained in a more sophisticated multilevel model. In this study it is assumed that the inflow angles computed using the reduced drag coefficient are consistent with those at the surface level, rather than upper-level values, thus compensating for the overestimate of the inflow angles associated with the use of a vertically averaged boundary-layer model.

No reference to an averaging time is given in Shapiro (1983); however, results are applicable to a long period (nonturbulent) average assumed to be about 1 h. During the model development and comparisons to full-scale data, other long-period averaging times were examined (e.g., 10 min, etc.). The assumption of a 1-h averaging time provided the best comparisons to full-scale data, and these comparisons are shown later.

The hourly surface-level wind speeds (i.e., wind speeds averaged over 1 h) are converted to fastest-mile values using the gust-factor curve developed by Krayer and Marshall (1992) specifically for hurricane winds. The estimated fastest-mile wind speeds are considered to be representative of hurricane winds at the coastline (i.e., over water wind speeds). To account for the effects of surface friction, these coastal surface-level winds are linearly decayed to standard exposure C conditions ($V_s/V_u = 0.62$) over a distance of 30 to 50 km from the coastline (50 km for $R < 2R_{max}$ and 30 km for $R > 4R_{max}$), to enable estimates of wind speeds away from the coastline to be produced. The wind speed at a location x km from the coast, V_{sx} is given as

$$V_{sx}/V_u = (V_{sw}/V_u) - 0.004x; \quad V_{sx}/V_u \geq 0.62 \tag{8a,b}$$

where V_{sw} = surface wind speed at the coastline; V_u = upper-level, or vertically averaged, wind speed; and V_{sx} = surface wind speed x km from the coast. This linear reduction in wind speed with distance from the coast is more gradual than implied in some other investigations [e.g., Batts et al. (1980), Georgiou (1985), and Powell (1987)], however the comparisons between modeled and observed hurricane wind speeds tend to support the assumption for the case of onshore winds. This linear reduction in wind speed with distance from the coastline will lead to an overestimate of wind speeds near the coast when the wind is blowing from the land to the ocean (i.e., offshore winds). This overestimation of wind speeds for offshore winds is seen in comparisons of modeled and observed wind speeds for Hurricane Hugo, as discussed later.

Batts Wind-Field Model

The wind-field model used by Batts et al. (1980) (referred to here as the Batts model) is a modification of the Standard Project Hurricane Windfield Model where the maximum gradient wind speed, V_{gx}, is given as

$$V_{gx} = K\sqrt{\Delta p} - (R_{max}/2)f \quad (9)$$

where Δp = central pressure difference and K = a constant. The maximum 10-min wind speed at a height of 10 m over the ocean is given as

$$V(10, R_{max}) = 0.865V_{gx} + 0.5c \quad (10)$$

where c = translation speed of the storm. The 10-min wind speed over the ocean at any point in the storm (r, θ) is

$$V(10, r, \theta) = V(10, R_{max})V_r(r) - 0.5c(1 - \cos\theta) \quad (11)$$

where $V_r(r)$ = ratio of the maximum 10-min wind speed at the radius of maximum winds to the 10-min mean at a distance r from the center of circulation. The ratio $V_r(r)$ is given in Batts et al. (1980) in nomograph form. The angle θ in (11) is measured from a line making an angle of 115° (clockwise) from the direction of motion of the storm so that the region of maximum winds (relative to the earth) is always in the right rear quadrant of the storm. The 10-min mean overland wind speed is obtained by multiplying the overwater wind speed by 0.85, implying an immediate reduction in wind speed at the ocean-coastline interface. No further reduction in wind speed produced by surface friction for locations further inland is allowed for. The 10-min mean wind speeds are converted to fastest mile values using the results of Durst (1960), which have been shown to be inappropriate in the case of hurricane winds (Krayer and Marshall 1992).

Storm-by-Storm Comparisons

Because of the assumptions and empirical model components used in both the Shapiro-based wind-field model (e.g., drag coefficients, averaging time, inflow angles, etc.) and the Batts wind-field model, evaluation of the wind-field models through comparison to full-scale measurements is of critical importance, and provides the only means to evaluate the impact of the assumptions. Wind speeds estimated using both the Shapiro-based wind-field model and the Batts wind-field model were evaluated through comparisons to wind speeds measured in Hurricane Frederic (1979), Alicia (1983), Elena (1985), Hugo (1989), and Andrew (1992). In total, 26 detailed, full-scale wind-speed records were examined.

In all comparisons except Hurricane Andrew, information on Δp, storm position, direction, and translation speed used to evaluate the wind-field models was obtained from the 6-h position data given on the HURDAT diskettes. In the case of Hurricane Andrew, storm position and central pressure data were obtained from the National Hurricane Center (NHC) preliminary report on Hurricane Andrew. For Hurricane Hugo, additional information on Δp and position just before the time of landfall was obtained from Powell et al. (1991). A linear variation in central pressure with time was assumed between the known values. Radius to maximum wind data for each of the hurricanes were obtained from various sources. Given the information on Δp, storm position, and R_{max} as a function of time for each storm, we simulated the hurricane winds at a particular site as a function of time by moving the mathematical models of the hurricane windfield along the path of the storm. The translation speed of the hurricane is determined from the position and time information. The simulated wind speeds determined at 15-min intervals were adjusted to fastest mile values and compared to full-scale (measured) values.

In the case of Hurricane Alicia (1983), there is some controversy as to the value of R_{max}. Ho et al. (1987), Golden (1984) and Willoughby (1990) suggest that near the time of the landfall, R_{max} changed from about 28 km to near 58 km. Powell (1987) suggests that the apparent larger value of R_{max} is associated with outer rain-band activity, rather than a change in R_{max}. For the comparisons of simulated and observed wind speeds presented here, we found (using either wind-field model) that R_{max} of 28 km best reproduced wind speeds at locations near the center of the hurricane track, but the larger value of R_{max} reproduced wind speeds better at locations further removed from the center of the storm. Ho et al. (1987) indicated that the larger value of R_{max} should be used for storm surge computations near Galveston. In the case of Hurricane Frederic, a constant value of R_{max} of 35 km was used (Kaplan and Frank 1993; Powell 1982). R_{max} for Hurricane Elena was set equal to 22 km (Willoughby 1990). For Hurricane Hugo, R_{max} information was provided by Mark Powell of the National Oceanic and Atmospheric Administration/Hurricane Research Division (NOAA/HRD), and a constant value of 40 km was used in the simulations. For Hurricane Andrew in South Florida, R_{max}, was assigned a value of 18.5 km (Powell and Houston 1993).

Full-scale measurements of wind speed and direction for Hurricanes Alicia, Frederic, Elena, and Hugo, in the form of peak gust and/or 1-, 10-, 15-, or 30-min mean wind speeds, were provided by R. D. Marshall of the National Institute of Standards and Technology. Peak gust and/or mean wind-speed data were converted to fastest-mile equivalents using the gust-factor data given in Krayer and Marshall (1992). Information on anemometer heights and the surface roughness, z_0, was provided by R. D. Marshall. In the case of Hurricane Hugo, additional information on anemometer height and roughness length was provided by P. R. Sparks of Clemson University. All wind speeds, except those near the coast, were converted to equivalent exposure C conditions (z_0 = 0.03 m) using the procedure outlined in Marshall (1984). For coastal and offshore locations [U.S. Coast Guard Cutter (USCGC) Buttonwood for Hurricane Alicia, Data Buoy 42007 and Dauphin Island for Hurricane Elena, and the Molasses Reef and Fowey Rocks C-MAN stations for Hurricane Andrew] wind speeds are adjusted to the 10-m level using the local value of z_0, assumed to be 0.005 m. If the true value of z_0 differs from the assumed value of 0.005 to between 0.001 and 0.02 m, and for anemometer heights in the range of 5–50 m, this assumption leads to maximum errors for mean wind speeds corrected to 10 m of less than ±4%. In the case of the C-MAN stations when adjusting wind speeds to the 10-m level, no allowance for a change of the sea-surface roughness with wind speed is allowed for; however, the effective roughness length z_0 varies relatively little over a relatively wide wind-speed range. For example, defining C_D using (3) and computing z_0 from the following expression:

$$z_0 = 10\exp(-k/\sqrt{C_{D10}}) \quad (12)$$

where k = von Karman constant (k = 0.4) and is the drag coefficient based on the 10-m mean wind speed, leads to estimates of z_0 ranging between 0.0024 and 0.0076 m for mean wind speeds at 10 m ranging between 30 and 50 m/s. These values of z_0 support the assumed value of z_0 equal to 0.005 for coastal locations, and the assumption results in little error when the wind speeds are converted to 10-m values.

Detailed comparisons of the observed and simulated wind speeds of 12 of the 26 records examined (6 near coastal and 6 inland locations) are given in Figs. 1 and 2. For all of the near-coast locations examined here, the simulated wind speeds

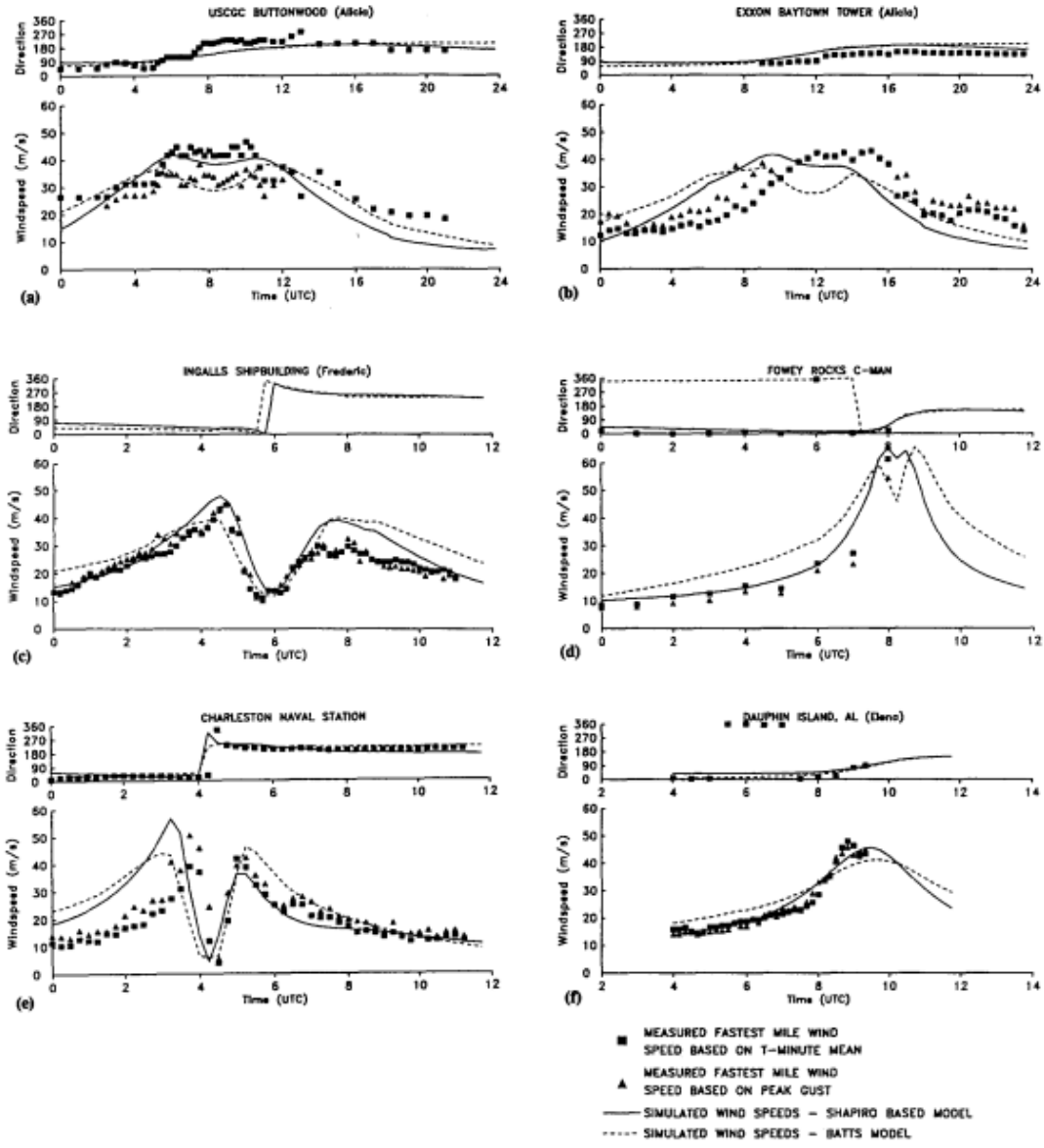

FIG. 1. Comparisons of Simulated and Observed Fastest-Mile Wind Speeds at Coastal Locations

derived using the Shapiro-based model are reduced as a linear function of the shortest distance to the coast. Fig. 1 shows comparisons of the Shapiro-based simulated fastest-mile wind speeds and measured fastest mile wind speeds obtained from the USCGC Buttonwood and the Exxon Baytown anemometer for Hurricane Alicia, Ingalls Shipyard for Hurricane Frederic, Dauphin Island for Hurricane Elena, Charleston Naval Base for Hurricane Hugo, and the Fowey Rocks C-MAN station for Hurricane Andrew. All of these stations are located within a few kilometers of the coast or just offshore, near the location of maximum winds. The comparison of the simulated and measured fastest-mile wind speeds at Dauphin Island, Ingalls Shipyard, and the USCGC Buttonwood all indicate that the Shapiro-based wind-field model provides a better representation of the measured wind speeds. At USCGC Buttonwood, the wind speeds obtained using the Shapiro-based model agree well with the full-scale fastest-mile wind speeds derived from the 10-min averaged data, whereas the wind speeds predicted using the Batts model agree well with the lower fastest-mile wind-speed data derived from measured peak gusts. At Dauphin Island, the Batts wind-field model underpredicts the peak wind speeds by about 10%, whereas the Shapiro-based model underestimates the peak winds by about 2%. At Ingalls Shipyard, the Shapiro-based model overestimates the peak wind speeds by about 10%, whereas the Batts model again underestimates the peak winds by about 8%; both wind-field models overestimate wind speeds recorded after the passing of the eye of the storm, but this overestimation is greater with the Batts model. In the case of Charleston Naval Base (Hurricane Hugo), the fastest-mile wind speeds simulated using the Shapiro-based model before the passing of the eye are significantly higher than those de-

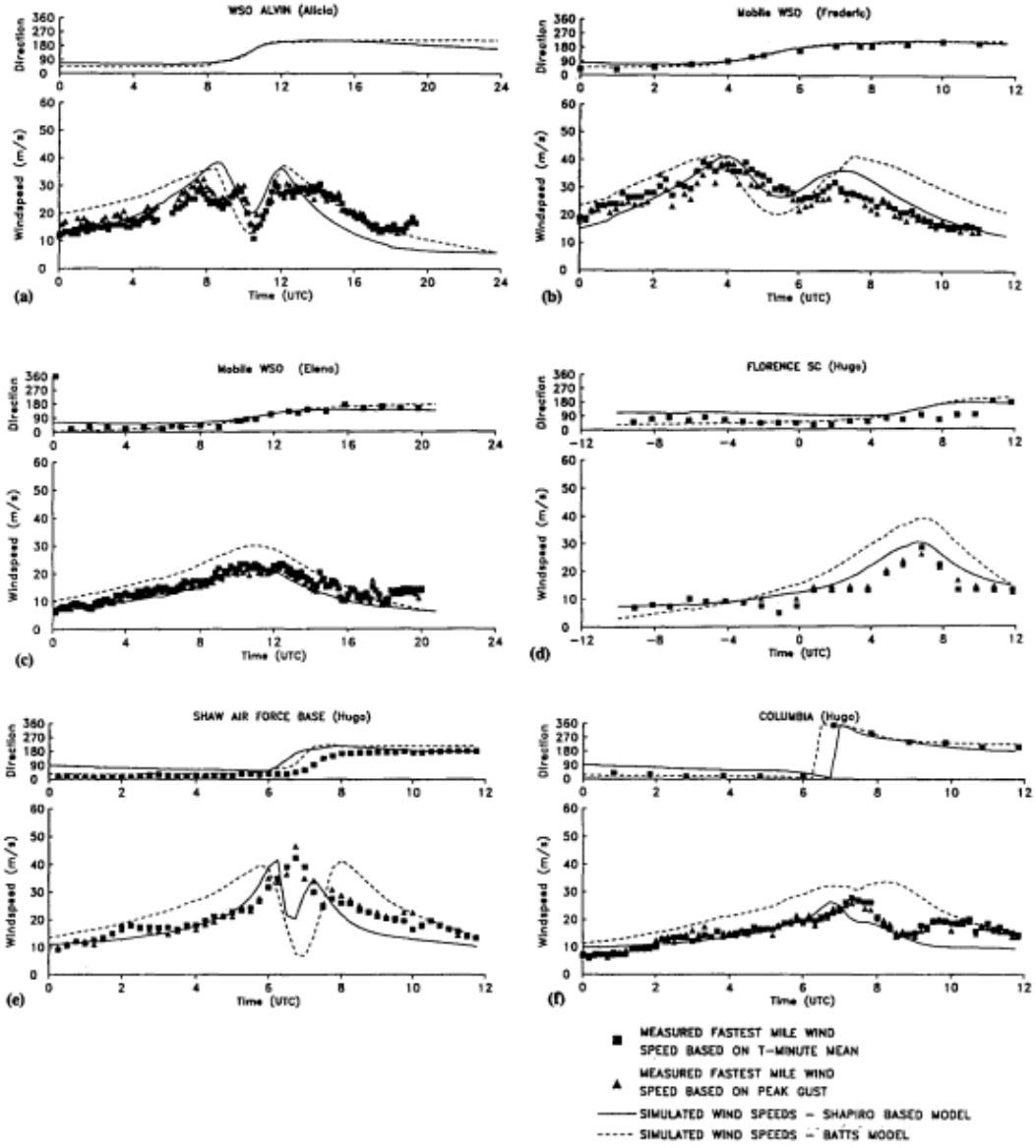

FIG. 2. Comparisons of Simulated and Observed Fastest-Mile Wind Speeds at Inland Stations

rived from either the measured peak gust or 10-min mean data, whereas after the passing of the eye the agreement is good. The peak wind speeds predicted by the Batts model before the passing of the eye wall agree well with the measured values, and slightly overestimate those occurring after the passing of the eye. At the two Charleston locations examined (Charleston Airport not shown), the Shapiro-based model overestimates the maximum wind speeds. This overestimation is thought to be a result of the winds approaching the anemometer sites having passed a much larger land fetch than at the other coastal locations examined (i.e., offshore winds in the Hugo case versus nearly onshore winds for other cases). This reduction in wind speed associated with frictional effects for the two Charleston locations is not treated in the implementation of the Shapiro-based wind-field model, where for an inland location, onshore winds are assumed (i.e., the wind speeds are reduced as a linear function of the minimum distance to the coastline, without considering the fact that the wind may have blown over a longer land fetch if the station is located on the left hand side of a landfalling storm). No full-scale measurements of wind speed were obtained for Hurricane Hugo at locations experiencing the maximum onshore winds within the eye wall. Comparisons of the predicted and measured wind speeds recorded during Hurricane Andrew at the Fowey Rocks C-MAN station (located to the north of the track, on the right side of the storm, near the region of maximum winds) show the maximum fastest-mile wind speeds simulated using either model are approximately equal, but the shape of the wind-speed trace is better reproduced using the Shapiro-based model. Because the Fowey Rocks C-MAN station is located offshore, the 15% wind-speed reduction required for land-based stations is not used in the Batts model in this comparison.

Fig. 2 shows comparisons of simulated and measured wind speeds at six inland stations [the National Weather Service (NWS) Station at Alvin for Hurricane Alicia; Mobile, Ala., for Hurricanes Frederic and Elena; and Shaw Air Force Base, Florence Airport Station, and Columbia Airport for Hurricane Hugo]. The figure clearly indicates the Shapiro-based model best reproduces hurricane winds at inland locations. As discussed in Twisdale and Vickery (1992), further improvements in the comparison of observed and simulated wind speeds for inland stations can be obtained by adjusting the surface drag coefficient used in the numerical model to be consistent with local terrain conditions.

Wind-Speed Prediction Error Analysis

Table 1 presents a summary of the percentage difference between the maximum measured and maximum simulated wind speeds obtained using the Shapiro-based model for 25 of the 26 records examined. The Fowey Rocks C-MAN measurement from Hurricane Andrew is not included in Table 1 because the anemometer system failed during the storm and it is not known whether the maximum wind speed was recorded. In Table 1, a negative percentage difference indicates that the maximum modeled wind speeds are lower than the maximum observed wind speeds.

Table 2 presents a summary of the percentage differences between simulated and measured wind speeds within a wind speed group. Fastest-mile wind speeds derived from either the peak gust or the mean wind-speed data are equally weighted. The results given in Table 2 indicate that the Shapiro-based wind-field model with a radial profile exponent, n, equal to 0.5 provides the best overall representation of the hurricane wind-field. The Batts model clearly underestimates the maximum fastest mile wind speeds (V_{fm}) near the eye wall ($V_{fm} > 40$ m/s) and overestimates the lower wind-speed values away from the eye wall.

For inland stations, the Batts wind-field model overestimates the measured wind speeds. The mean and standard deviation of the ratio of observed to predicted fastest-mile wind speed obtained using the Batts wind-field model for the nine inland stations (Charlotte comparisons are not included) are 1.18 and 0.16, respectively. Using the Shapiro-based model (with $n = 0.5$), the mean and standard deviation of the ratio of observed to predicted wind speeds are 1.03 and 0.09. The overestimation of wind speeds obtained using the Batts model is attributed to an underestimate or the reduction in the surface-level wind speed due to friction after the hurricane has moved inland. The minimum ratio of the surface-level wind speed to the upper-level wind speed in the Batts model is 0.73, which is notably higher than the value of 0.62 used in the implementation of the Shapiro-based model, or the value of 0.6 suggested by Powell (1987). At coastal land-based stations, positioned near the region of maximum winds, for Hurricanes Frederic, Alicia, and Elena, the Shapiro-based wind-field model performs better than the Batts wind-field model. The maximum wind speeds predicted by the Batts wind-field model at coastal locations, near the region of maximum winds, are generally lower than the measured values; the maximum wind speeds obtained from the Shapiro-based model agree well with the measured values, neither consistently overestimating or underestimating the peak wind speeds. The overall characteristics of the 12 to 24 h time series of wind speeds at these coastal locations are better modeled using the Sha-

TABLE 1. Percentage Difference between Peak Measured and Simulated Fastest-Mile Wind Speeds

Hurricane (1)	Measured Fastest-Mile Wind Speed (mi/hr) A (2)	Measured Fastest-Mile Wind Speed (mi/hr) B (3)	Batts Model (%) A (4)	Batts Model (%) B (5)	Shapiro-Based Model $n = 0.40$ (%) A (6)	Shapiro-Based Model $n = 0.40$ (%) B (7)	Shapiro-Based Model $n = 0.50$ (%) A (8)	Shapiro-Based Model $n = 0.50$ (%) B (9)	Shapiro-Based Model $n = 0.62$ (%) A (10)	Shapiro-Based Model $n = 0.62$ (%) B (11)
Frederic										
Ingalls Shipyard	95	100	−5	−10	+13	+7	+13	+7	+12	+6
Mobile WSO	86	88	+9	+7	+9	+7	+8	+6	+5	+2
Pensacola Airport	68	70	+7	+4	+9	+6	−4	−7	−18	−20
Pensacola NAS	78	66	+3	+22	+6	+25	−3	+14	−16	−1
Elena										
Buoy 42007	65	—	+32	—	+2	—	−2	—	−6	—
Dauphin Island	102	107	−9	−14	+6	+1	+1	−5	+1	−5
Mobile WSO	50	52	+34	+28	+14	+8	+1	−3	−12	−17
Pensacola Airport	55	55	+13	+13	+11	+11	−4	−3	−18	−8
Pensacola NAS	68	64	+1	+6	+6	+11	−7	−3	−19	−16
Alicia										
Alvin	72	68	+12	+18	+9	+15	+9	+14	+8	+14
Buttonwood	85	104	+0	−17	+9	−10	+8	−11	+8	−11
Exxon Baytown	—	100	—	−18	—	−6	—	−6	—	−7
Dow "A"	70	77	+12	+1	+14	+6	+18	+7	+17	+9
WSO Galveston	85	80	+0	+5	−4	+1	−5	+0	−5	+0
Houston IAH	73	78	+9	+1	−5	−11	−7	−13	−7	−13
Ellington AFB	84	83	+2	+3	+4	+6	+3	+4	+2	+3
USCGC Clamp	—	84	—	+1	—	+1	—	−1	—	−3
Hugo										
Myrtle Beach AFB	71	78	−4	−5	+10	+9	+6	+5	−15	−16
Charleston NAS	112	94	−12	+6	+14	+37	+13	+36	+11	+33
Charleston Airport	85	82	+16	+21	+34	+39	+31	+37	+22	+27
Columbia Airport	60	62	+27	+21	+3	+0	+0	−5	−2	−6
Shaw AFB	104	95	−11	−2	−10	−3	−10	−3	−15	−7
Charlotte Airport	70	46	+31	+98	+30	+96	+27	+91	+24	+87
McEntire Airport	71	67	+17	+23	+6	+13	+7	+14	+6	+13
Florence	57	63	+52	+36	+27	+15	+18	+7	+6	−4
Andrew										
Molasses Reef	48	55	+73	+46	+24	+8	+5	−9	−18	−29

Note: A = derived from peak gust; B = derived from mean wind speed (1-, 2-, 10-, 15-, or 30-minute average).

TABLE 2. Percentage Difference between Measured and Simulated Wind Speeds as Function of Wind-Speed Range

Fastest-mile wind-speed range (mi/hr) (1)	Stations[a] (2)	Batts Model		Shapiro-Based Model $n = 0.40$		Shapiro-Based Model $n = 0.50$		Shapiro-Based Model $n = 0.62$	
		Mean (3)	SD (4)	Mean (5)	SD (6)	Mean (7)	SD (8)	Mean (9)	SD (10)
$V > 90$[b]	1, 2, 3, 4, 16, 17	−8	7	5	14	4	14	2	14
$80 < V < 90$	5, 6, 18, 24, 25	7	8	12	15	10	14	8	10
$70 < V < 80$	7, 8, 9, 10, 19	6	7	8	5	6	9	−4	14
$60 < V < 70$	11, 12, 13, 20, 21, 22	21	16	9	8	2	9	−6	11
$V < 60$	14, 15, 23	25	14	13	6	−2	5	−19	6
All	All	12	23	11	17	6	17	0	19

Note: SD = standard deviation, WSO = Weather Service Office, NAS = Naval Air Station, and AFB = Air Force Base.

[a]1 = Ingalls Shipyard, 2 = Dauphin Island, 3 = USCGC Buttonwood, 4 = Exxon Baytown, 5 = Mobile WSO (Frederic), 6 = WSO Galveston, 7 = Pensacola NAS (Frederic), 8 = WSO Alvin, 9 = DOW Chemical Plant "A", 10 = Houston Intercontinental Airport, 11 = Pensacola Regional Airport, 12 = Data Buoy 42007, 13 = Pensacola NAS (Elena), 14 = Mobile WSO (Elena), 15 = Pensacola Airport (Elena), 16 = Charleston NAS, 17 = Shaw AFB, 18 = Charleston Airport, 19 = Myrtle Beach AFB, 20 = Columbia Airport, 21 = McEntire AFB, 22 = Florence, 23 = Molasses Reef C-MAN, 24 = Ellington AFB, and 25 = USCGC Clamp.

[b]Hurricane Andrew data not included because maximum wind speed was not recorded.

piro-based model. At near-coastal locations, away from the maximum winds, both models perform approximately equally well. At the overwater stations, wind speeds estimated using the Shapiro-based model agree well with the measured values, whereas the Batts wind-field model significantly overestimates the measured wind speeds when the overwater stations are on the left side of the storm (Buoy 42007 and Molasses Reef). This overestimate of the overwater wind speeds and slight underestimate of the near coastal wind speeds from the Batts model indicates that the sudden wind-speed reduction used in the Batts model is questionable. The good agreement for both the overwater and overland stations obtained using the Shapiro-based model indicates that the simple, gradual wind-speed decay is more realistic. Wind directions are modeled equally well using either wind-field models at or near the time the maximum wind speeds are measured.

Overall, the Shapiro-based wind-field model, with a radial profile exponent of 0.5, provides a good representation of the hurricane windfield. The two key points to note regarding the Batts wind-field model are the underestimation of the maximum winds near the eye wall, and the significant overestimation of wind speeds at inland stations. Neither of these deficiencies appear in the Shapiro-based wind-field model. It should be noted that all comparisons are for hurricanes making landfall in the southern portion of the United States. As described in Powell and Black (1990), in more northern regions, where the water temperature is lower than in the Gulf of Mexico and the South Florida Peninsula, the ratio of surface-level winds to upper-level winds is lower, suggesting that the surface-level, overwater wind speeds may be overestimated using either of the wind-field models described here for the North Atlantic Coast.

FILLING-RATE MODELS

Once a tropical cyclone makes landfall it weakens as the central pressure rises. This rate of weakening varies with storm, location of landfall, and the central pressure difference at the time of landfall (Δp_0). Proper modeling of the filling of the storms is important for the prediction of hurricane winds at inland locations. Schwerdt et al. (1979) studied 16 landfalling hurricanes and subdivided the filling rates into three different geographic regions (Gulf Coast, Florida peninsula, and Atlantic Coast). They found that hurricanes making landfall on the Florida peninsula filled the slowest and storms making landfall on the Gulf Coast filled fastest. Ho et al. (1987) used the same three geographic regions used by Schwerdt et al. (1979) to define the filling rates. Along the Gulf Coast and the Florida peninsula they represent three filling-rate curves [for storms with values of Δp_0 of 110, 100, and 85 millibar (mbar), with the more intense storms filling more rapidly than the weak ones]. Along the Atlantic Coast they present only one filling-rate curve.

Georgiou (1985) developed filling models for four geographic regions (western Gulf Coast, central Gulf Coast, Florida Peninsula, and the Atlantic Coast). He departed from the commonly used models, where filling is dependent on the time since landfall, and developed models based on the distance traveled since making landfall, with no dependence of the storm filling rate as a function of intensity.

The filling-rate model used by Batts et al. (1980) is independent of location and intensity at landfall. The filling rate used by Batts et al. (1980) is given as

$$\Delta p(t) = \Delta p_0 - 0.675(1 + \sin \phi)t \tag{13}$$

where $\Delta p(t)$ = central pressure difference (mbar) at t h after landfall; and ϕ = angle between the storm direction and the coastline at the point of landfall.

In this study, three different filling-rate models were developed using central pressure and position data given in HURDAT. For storms making landfall on the Gulf Coast, 20 storms were used. Nine storms were used to develop filling-rate models in each of the Atlantic Coast and Florida Peninsula regions. The filling rates were modeled in the following form:

$$\Delta p(t) = \Delta p_0 \exp(-at) \tag{14}$$

The filling constant a is given as

$$a = a_0 + a_1 \Delta p_0 + \varepsilon \tag{15}$$

where ε = a normally distributed error term with a mean of zero. The constants a_0 and a_1 and the standard deviation of the error term, σ_ε, for each of the three geographic regions are given in Table 3. Fig. 3 shows the fitted values of the decay constant, a, plotted versus the central pressure difference at the time of landfall for each of the three geographic regions. In the case of the Gulf Coast storms, the exponential decay model was found to reproduce observed filling rates better when a 2-h delay was incorporated into the model.

TABLE 3. Exponential Filling-Rate Constants

Region (1)	a_0 (2)	a_1 (3)	σ_ε (4)	r^2 (5)
Florida Peninsula	0.006	0.00046	0.0025	0.8
Gulf Coast	0.035	0.00050	0.0355	0.07
Atlantic Coast	0.038	0.00029	0.0093	0.16

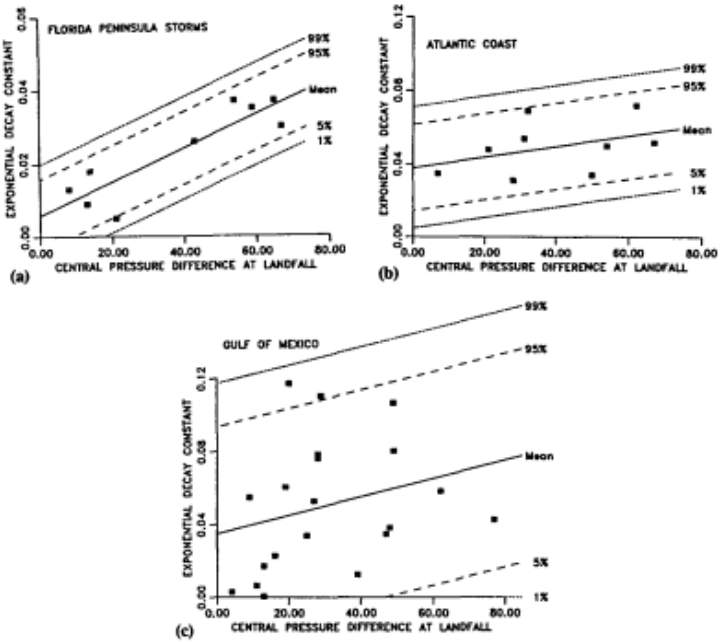

FIG. 3. Filling Constant *a* versus Central Pressure Difference at Landfall

The filling-rate models developed here and the filling-rate model used by Batts et al. (1980) were evaluated through comparisons of detailed filling studies presented in Ho et al. (1987). Tables 4–6 show the mean and standard deviation of the difference (in mbar) between the predicted and observed increase in central pressure with time after landfall for the three regions. All of the hurricanes used in the comparison had central pressure differences at landfall of 25 mbar or more. A positive difference indicates that the modeled results are conservative. The data given in Tables 4–6 indicate that the new filling model is slightly conservative for Gulf Coast storms, slightly nonconservative for Florida storms, and approximately mean-centered for Atlantic Coast storms. The filling-rate model used by Batts et al. (1980) is conservative in all regions, and on average this conservatism increases with time after landfall.

TABLE 4. Difference between Modeled and Observed Increase in Central Pressure (mbar) after Landfall Using New and Batts Filling Models for Gulf Coast

Filling-rate model	Time after landfall (h)						Unweighted composite average
	2	4	6	8	10	12	
New filling model							
Mean (mbar)	6.3	3.8	2.5	0.9	2.6	3.2	3.2
SD (mbar)	8.7	11.5	11.7	11.3	10.6	8.8	10.4
Batts filling model							
Mean (mbar)	4.3	7.1	10.3	14.4	17.9	20.5	12.4
SD (mbar)	8.6	13.7	15.6	17.4	16.4	16.2	14.4

Note: SD = standard deviation.

TABLE 5. Difference between Modeled and Observed Increase in Central Pressure (mbar) after Landfall Using New and Batts Filling Models for Florida Peninsula

Filling-rate model	Time after landfall (h)			Unweighted composite average
	3	6	9	
New filling model				
Mean (mbar)	2.9	−2.3	−4.3	−1.2
SD (mbar)	9.2	3.9	4.4	5.8
Batts filling model				
Mean (mbar)	7.4	3.3	2.8	4.5
SD (mbar)	11.2	3.8	2.8	5.9

Note: SD = standard deviation.

TABLE 6. Difference between Modeled and Observed Increase in Central Pressure (mbar) after Landfall Using New and Batts Filling Models for Atlantic Coast

Filling-rate model	Time after landfall (h)						Unweighted composite average
	2	4	6	8	10	12	
New filling model							
Mean (mbar)	−0.9	−0.1	0.1	0.4	2.6	−0.8	0.2
SD (mbar)	1.6	2.7	4	5.1	3.7	2.7	3.3
Batts filling model							
Mean (mbar)	2.5	7.9	8.3	10.2	14.2	9.6	8.8
SD (mbar)	1.9	4.8	6.9	9	11.2	9.6	7.2

Note: SD = standard deviation.

The filling-rate models developed here reproduce the observation that intense storms fill more rapidly than weak storms, as noted in Tuleya et al. (1984) in their investigation examining both historical storms and simulated storms. The introduction of a random error term allows for the simulation of storms that fill much more slowly or rapidly than average.

EFFECT OF COMBINED WIND-FIELD AND FILLING MODELS ON WIND SPEEDS AT INLAND LOCATIONS

To examine the combined effect of the filling models and wind-field models on wind-speed estimates, simulations of hurricane wind speeds at 9 of the 10 inland stations examined

TABLE 7. Comparison of Simulated and Observed Wind Speeds at Inland Locations Showing Combined Effect of Filling Models and Windfield Models

Hurricane (1)	Location (2)	Distance inland (km) (3)	Simulated fastest-mile wind speed divided by observed fastest-mile wind speed (Shapiro-based wind-field and new filling model)[a]		Simulated fastest-mile wind speed divided by observed fastest-mile wind speed (Batts wind-field and Batts filling models)[b]	
			A (4)	B (5)	A (6)	B (7)
Frederic	Mobile	17[c]	1.09	1.06	1.18	1.15
Alicia	Alvin	30	1.09	1.14	1.13	1.19
Alicia	Houston (IAH)	50[d]	0.88	0.82	1.14	1.07
Alicia	USCGC Clamp	20[d]				1
Hugo	Columbia	180	1.13	1.1	1.58	1.53
Hugo	Shaw AFB	130	0.91	1	1.07	1.17
Hugo	McEntire AFB	140	1.1	1.16	1.44	1.52
Hugo	Florence	100	1.14	1.03	1.75	1.59
Hugo	Charlotte	290	1.33	2.02	1.6	2.43

Note: A = based on peak gust; B = based on mean wind speed; and SD = standard deviation.
[a]With Charlotte measurement, mean = 1.12 and SD = 0.26; without Charlotte measurement, mean = 1.04 and SD = 0.1.
[b]With Charlotte measurement, mean = 1.38 and SD = 0.36; without Charlotte measurement, mean = 1.3 and SD = 0.24.
[c]Distance from Mobile Bay.
[d]Distance from Galveston Bay.

earlier were performed. The Mobile, Ala., wind speeds recorded during Hurricane Elena are not included in this comparison because the maximum wind speeds were observed before the hurricane made landfall. In these storm-specific simulations, the central pressure difference at landfall is used to initiate the simulation and is then decreased once landfall is made using the filling models described earlier. This simulation approach reproduces wind speeds at inland locations similar to those that would be obtained in an actual simulation. The results of the simulations are given in Table 7, where it is clearly seen that the combination of the Batts filling model and Batts wind-field model yield conservative estimates of wind speeds at inland locations, with a mean overestimate of 38%. The overestimate of wind speeds produced by the Batts models increases with distance from the coast. The combination of the Shapiro-based wind-field model and new filling models, though still yielding conservative results, overestimates the observed wind speeds by only 12%. When the anomalous Charlotte wind-speed measurement is removed from the comparisons, the mean overestimate of the observed wind speeds obtained using the Shapiro-based wind-field model and the filling models is 4%, whereas if the Batts models are used the overestimate is 30%.

SUMMARY AND CONCLUSIONS

Extensive evaluation of the wind-field models clearly indicates that the model used by Batts et al. (1980) underestimates the maximum wind speeds in intense hurricanes near the eye wall at coastal locations, and overestimates wind speeds at inland locations. These deficiencies are not evident in the Shapiro-based wind-field model. The evaluation of the filling models indicates that the model used in Batts et al. (1980) is conservative, and the combined deficiencies in the Batts filling model and wind-field model result in a significant overestimate of wind speeds for inland locations. The Shapiro-based wind-field model combined with the new filling models are believed to provide better predictions of hurricane wind speeds at both near-coastal locations and inland locations than do the results of earlier studies; however, further research into the rate of reduction of wind speeds near the surface after a hurricane makes landfall is required. Further comparisons between modeled and observed wind speeds for storms making landfall in the northern United States are also required to improve the reliability of the model to estimate wind speeds in fast moving hurricanes traveling over cold water.

APPENDIX. REFERENCES

Amorocho, J., and Devries, J. J. (1980). "A new evaluation of wind stress coefficient over water surfaces." *J. Geophys. Res.*, 85, 433–442.

Batts, M. E., Cordes, M. R., Russell, C. R., Shaver, J. R., and Simiu, E. (1980). "Hurricane wind speeds in the United States." *Nat. Bureau of Standards Rep. No. BSS-124*, U.S. Dept. of Commerce, Washington, D.C.

Chow, S. H. (1971). "A study of windfield in the planetary boundary layer of a moving tropical cyclone," MS thesis in Meteorology, School of Engrg. and Sci., New York Univ., New York, N.Y.

Donelan, M. A. (1982). "The dependence of the aerodynamic drag coefficient on wave parameters." *Proc., 1st Int. Conf. on Meteorology and Air/Sea Interaction of the Coast. Zone*, 351–367.

Durst, C. (1960). "Wind speeds over short periods of time." *The Meteorological Mag.*, 89(1056), 181–187.

Georgiou, P. N. (1985). "Design wind speeds in tropical cyclone-prone regions," PhD thesis, Fac. of Engrg. Sci., Univ. of Western Ontario, London, Ont., Canada.

Golden, J. H. (1984). "Meteorological overview of Hurricane Alicia." *Proc., Spec. Conf., Hurricane Alicia: One Year Later*, ASCE, New York, N.Y., 1–20.

Ho, F. P., et al. (1987). "Hurricane climatology for the Atlantic and Gulf Coasts of the United States." *NOAA Tech. Rep. NWS38*, Federal Emergency Mgmt. Agency, Nat. Oceanic and Atmospheric Admin. (NOAA), Washington, D.C.

Kaplan, J., and Frank, W. M. (1993). "The large-scale, inflow-layer structure of Hurricane Frederic (1979)." *Monthly Weather Rev.*, 121(1), 3–20.

Krayer, W. R., and Marshall, R. D. (1992). "Gust factors applied to hurricane winds." *Bull. Am. Meteorological Soc.*, 73(5), 613–617.

Marshall, R. D. (1984). "Fastest-mile wind speeds in Hurricane Alicia." *Nat. Bureau of Standards Tech. Note No. 1197*, U.S. Dept. of Commerce, Washington, D.C.

"Minimum design loads for buildings and other structures." (1990). ASCE-7-88, ASCE, New York, N.Y.

Myers, V. A. (1954). "Characteristics of United States hurricanes pertinent to levee design for Lake Okeechobee, Florida." *Hydrometeorological Rep. No. 32*, U.S. Dept. of Commerce, Washington, D.C.

Powell, M. D. (1980). "Evaluations of diagnostic marine boundary-layer models applied to hurricanes." *Monthly Weather Rev.*, 108, 757–766.

Powell, M. D. (1982). "The transition of Hurricane Frederic (1979), boundary-layer wind field from the open Gulf of Mexico to landfall." *Monthly Weather Rev.*, 110, 1912–1932.

Powell, M. D. (1987). "Changes in the low-level kinematic and thermodynamic structure of Hurricane Alicia (1983) of landfall." *Monthly Weather Rev.*, 115(1), 75–99.

Powell, M. D., and Black, P. G. (1990). "The relationship of hurricane reconnaissance flight-level wind measurements to winds measured by

NOAA's oceanic platforms." *J. Wind Engrg. and Industrial Aerodynamics*, 36, 381–392.
Powell, M. D., Dodge, P. P., and Black, M. L. (1991). "The landfall of Hurricane Hugo in the Carolinas: surface wind distribution." *Weather and Forecasting*, 6, 379–399.
Powell, M. D., and Houston, S. (1993). "Surface wind field analyses in Hurricane Andrew." *Proc., 20th Conf. on Hurricanes and Tropical Meteorology*, Am. Meteorological Soc., Boston, Mass.
Roll, H. U. (1965). *Physics of the marine atmosphere*. Academic Press, New York, N.Y.
Schwerdt, R. W., Ho, F. P., and Watkins, R. R. (1979). "Meteorological criteria for standard project hurricane and probable maximum hurricane windfields, Gulf and Atlantic Coasts of the United States." *NOAA Tech. Rep. NWS23*, U.S. Dept. of Commerce, Washington, D.C.
Shapiro, L. J. (1983). "The asymmetric boundary layer flow under a translating hurricane." *J. Atmospheric Sci., AMS*, 40(8), 1984–1998.
Tuleya, R. E., Bender, M. A., and Kurihara, Y. (1984). "A simulation study of the landfall of tropical cyclones using a moveable-mesh model." *Monthly Weather Rev.*, 112(1), 124–136.
Twisdale, L. A., and Vickery, P. J. (1992). "Predictive methods for hurricane winds in the United States." *Final Rep., Small Business Innovation Res. Grant ISI 916035*, Nat. Sci. Found., Washington, D.C.
Willoughby, H. E. (1990). "Temporal changes of the primary circulation in tropical cyclones." *J. Atmospheric Sci.*, 47(2), 242–264.

23. Assignment 2, Module 4: Statistical Models of Holland Pressure: https://journals.ametsoc.org/view/journals/apme/47/10/2008jamc1837.1.xml

Statistical Models of Holland Pressure Profile Parameter and Radius to Maximum Winds of Hurricanes from Flight-Level Pressure and H*Wind Data

PETER J. VICKERY AND DHIRAJ WADHERA

Applied Research Associates, Inc., Raleigh, North Carolina

(Manuscript received 24 July 2007, in final form 8 March 2008)

ABSTRACT

In many hurricane risk models the inclusion of the Holland B parameter plays an important role in the risk prediction methodology. This paper presents an analysis of the relationship between B and a nondimensional intensity parameter. The nondimensional parameter includes the strong negative correlation of B with increasing hurricane size [as defined by the radius to maximum winds (RMW)] and latitude as well as a positive correlation with sea surface temperature. A weak positive correlation between central pressure deficit and B is also included in the single parameter term. Alternate statistical models relating B to RMW and latitude are also developed. Estimates of B are derived using pressure data collected during hurricane reconnaissance flights, coupled with additional information derived from the Hurricane Research Division's H*Wind snapshots of hurricane wind fields. The reconnaissance data incorporate flights encompassing the time period 1977 through 2001, but the analysis was limited to include only those data collected at the 700-hPa-or-higher level. Statistical models relating RMW to latitude and central pressure derived from the dataset are compared to those derived for U.S. landfalling storms during the period 1900–2005. The authors find that for the Gulf of Mexico, using only the landfall hurricanes, the data suggest that there is no inverse relationship between RMW and the central pressure deficit. The RMW data also demonstrate that Gulf of Mexico hurricanes are, on average, smaller than Atlantic Ocean hurricanes. A qualitative examination of the variation of B, central pressure, and radius to maximum winds as a function of time suggests that along the Gulf of Mexico coastline (excluding southwest Florida), during the final 6–24 h before landfall, the hurricanes weaken as characterized by both an increase in central pressure and the radius to maximum winds and a decrease in B. This weakening characteristic of landfalling storms is not evident for hurricanes making landfall elsewhere along the U.S. coastline.

1. Introduction

Hurricane risk models are commonly used for estimating insurance risk (e.g., Powell et al. 2005; Vickery et al. 2006), for providing information on wind speeds for the design of buildings in the United States (American National Standards Institute 1982; American Society of Civil Engineers 1990, through to the present), the Caribbean (Caribbean Community Secretariat 1986), and Australia (Standards Association of Australia 1989), or for use in estimating design storm surge values. The simulation methodologies are described in detail in reports and in the peer-reviewed literature (e.g., Batts et al. 1980; Georgiou 1985; Vickery et al. 2000; Powell et al. 2005; James and Mason 2005; Lee and Rosowsky 2007). One of the components used within a hurricane risk model is a hurricane wind field model. In most hurricane risk applications the primary inputs to the hurricane wind field model include a representation of surface pressure field (defined using a minimum of a radius and a central pressure deficit) and a system translation speed. The surface level pressure field is used to drive a wind field model to obtain estimates of the wind speeds at the top of the boundary layer (assumed to be about 500 m in most cases), and then coupled with a boundary layer model to finally arrive at estimates of the surface level wind field, as defined by wind speeds and directions at any location within the model hurricane. These wind field model inputs are simulated using statistical models derived from historical data to develop thousands of years of simulated hurricanes. Historical information on central pressure is usually obtained from sources including the National Hurricane Center (NHC) database (HURDAT; Jar-

Corresponding author address: Peter J. Vickery, 8540 Colonnade Center Drive, Ste. 307, Raleigh, NC 27615.
E-mail: pvickery@ara.com

DOI: 10.1175/2008JAMC1837.1

vinen et al. 1984) and the Tropical Prediction Center publication (Blake et al. 2007 and predecessors). Information for the storm radius [usually defined by the radius to maximum winds (RMW)] is usually derived from the National Weather Service (NWS) 38 publication (Ho et al. 1987), supplemented with additional information derived from the Hurricane Research Division's H*Wind (Powell et al. 1998) snapshots of hurricane wind fields.

In some hurricane risk models an additional term, commonly referred to as the Holland B parameter, is used to define the pressure field and plays an important role in the risk prediction methodology (e.g., Vickery et al. 2000; Powell et al. 2005).

Holland (1980) describes the radial distribution of surface pressure in a hurricane in the form

$$p(r) = p_0 + \Delta p \exp - \left(\frac{A}{r^B}\right), \tag{1}$$

where $p(r)$ is the surface pressure at a distance r from the storm center, p_0 is the central pressure, Δp is the difference between the peripheral pressure and the central pressure, A is the location parameter, and B is Holland's pressure profile parameter. Holland (1980) showed that RMW $= A^{1/B}$, and thus (1) can be expressed as

$$p(r) = p_0 + \Delta p \exp - \left(\frac{\text{RMW}}{r}\right)^B. \tag{2}$$

The gradient balance velocity V_G for a stationary storm is thus

$$V_G = \left\{ \left(\frac{\text{RMW}}{r}\right)^B \frac{B\Delta p \exp\left[-\left(\frac{\text{RMW}}{r}\right)^B\right]}{\rho} + \frac{r^2 f^2}{4} \right\}^{1/2} - \frac{fr}{2}, \tag{3}$$

where ρ is the density of air and f is the Coriolis parameter. The maximum wind speed at the RMW is

$$V_{G\max} \approx \sqrt{\frac{B\Delta p}{e\rho}}. \tag{4}$$

In parametric hurricane wind field models where the input surface pressure field is defined by two parameters (Δp and a radius), the maximum wind speed in the simulated hurricane is proportional to $\sqrt{\Delta p}$, whereas with the introduction of the additional term, B, the maximum wind speed in the simulated hurricane is proportional to $\sqrt{B\Delta p}$. Figure 1 presents example pressure profiles and gradient speed wind profiles associated with (1)–(3).

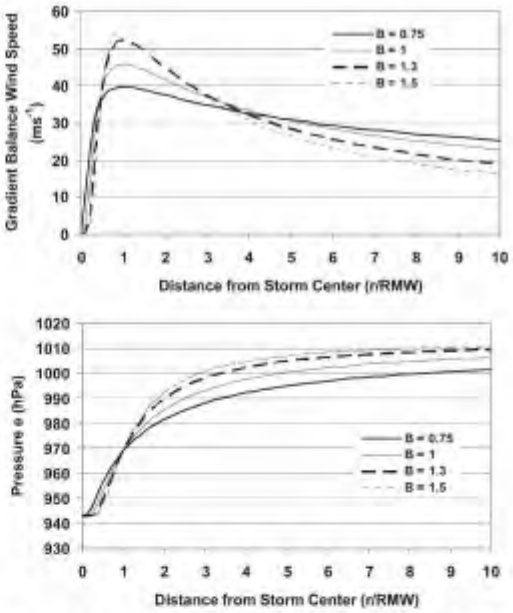

FIG. 1. Effect of B on (top) gradient balance wind speed and (bottom) pressure vs distance from storm center.

It is noteworthy that modeling the surface pressure field using an equation in the form of (2) is a significant improvement over modeling the pressure field with empirical models described by only two parameters. The approach still has limitations, as discussed for example in Thompson and Cardone (1996), Willoughby and Rahn (2004), Willoughby et al. (2006), and Vickery et al. (2008); the use of a single value of B (or RMW) does not reproduce the azimuthal and radial variations in the pressure fields (and hence wind fields) that are often found in real hurricanes.

Thus, while the use of (2) has limitations, when incorporated within a hurricane simulation model, the approach allows for the modeling of both Hurricane Katrina–like storms ($p_0 \sim 920$ hPa, $V_{\max} \sim 110$ kt) and Hurricane Charley–like storms, ($p_0 \sim 942$ hPa, $V_{\max} \sim 125$ kt), where $V_{\max}$ is the estimated maximum 1-min average wind speed at a height of 10 m over water as defined by the NHC. The omission of B does not allow for the variation in the maximum wind speed observed in real hurricanes for a given Δp (all else being equal).

Modeling B as a random variable within a hurricane simulation model was first introduced by Vickery et al. (2000). They estimated B using a subset of the reconnaissance aircraft dataset used here, by fitting a variation of (4) to the wind speeds from flights flown at heights of 3000 m and less and 1500 m and less and

settled on a model based on the 1500 m and less estimates of B. Their fits were performed over the range [0.5RMW, 1.5RMW], and they modeled B as a function of RMW and Δp using

$$B = 1.38 - 0.001\,84\Delta p + 0.003\,09\text{RMW}; \quad r^2 = 0.026. \tag{5}$$

Willoughby and Rahn (2004) used the same flight-level dataset used here to estimate B, deriving their estimates of B by minimizing a cost function incorporating both wind speed and pressure (as defined by geopotential height). Willoughby and Rahn (2004) developed statistical models for B and RMW in the form

$$B = 1.0036 + 0.0173V_{F\max} + 0.0313\ln(\text{RMW}) + 0.0087\psi; \quad r^2 = 0.51, \quad \sigma_B = 0.25 \quad \text{and} \tag{6}$$

$$\ln(\text{RMW}) = 3.94 - 0.0223V_{F\max} + 0.0281\psi; \quad r^2 = 0.297; \quad \sigma_{\ln\text{RMW}} = 0.441, \tag{7}$$

where $V_{F\max}$ is the maximum flight-level wind speed and ψ is latitude. Unfortunately, an equation in the form of (6) cannot be used in hurricane risk models where wind speeds are outputs of the models, not inputs. Powell et al. (2005) obtained the B values computed by Willoughby and Rahn (2004) and developed a model for B in the form

$$B = 1.881 - 0.005\,57\text{RMW} - 0.010\,97\psi; \quad r^2 = 0.2; \quad \sigma_B = 0.286. \tag{8}$$

The importance of B in hurricane wind speed risk modeling is demonstrated in Fig. 2 where, using the hurricane simulation model described by Vickery and Twisdale (1995) coupled with the wind field model described in Vickery et al. (2008), we estimate the magnitude of the peak (3 s) gust wind speed (10 m above ground in open terrain) at two locations using two different models describing B. The first model for B is that given in Vickery et al. (2000) and reproduced here as (5), and the second model is presented later in this paper as (22). The comparisons indicate that changing the statistical model for B from that described using (5) to that described using (22) results in a reduction in the estimated 100-yr return period wind speed of −6% at Biloxi and −9% at Cape Hatteras. These 6% and 9% reductions in wind speed correspond to 12% and 18% reductions of the wind loads needed to design building components, suggesting a possible significant economic penalty (or savings) associated with the modeling of B.

The RMW also plays an important role in hurricane

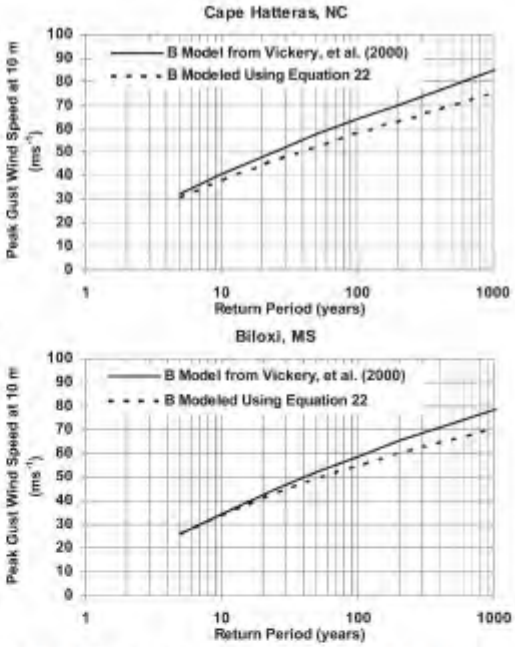

FIG. 2. Effect of changes in statistical models for B on predicted peak gust wind speed vs return period: (top) Cape Hatteras, NC and (bottom) Biloxi, MS.

risk prediction, particularly for storm surge and wave modeling. The RMW data provided in the NWS 38 publication constitute a primary reference for developing RMW models, as it provides information of the RMW for almost all hurricanes making landfall along the U.S. coastline between 1900 and 1985. Here we use the flight-level and H*Wind data to develop statistical models of the RMW (relating the RMW to other parameters that are usually modeled in a risk model) and compare these models with models developed using the more traditional approach that includes landfalling hurricane RMW data only. The models (both open ocean and landfall) are presented for all hurricanes, and separately for Gulf of Mexico (GoM) hurricanes and Atlantic Ocean hurricanes.

Analysis approach and findings

To obtain information on both B and RMW we use pressure data collected during hurricane reconnaissance flights, coupled with additional information derived from the Hurricane Research Division's H*Wind (Powell et al. 1998) snapshots of hurricane wind fields. We examine the correlation of RMW with latitude and central pressure as well as region (Gulf of Mexico ver-

sus Atlantic Ocean). We compare statistical models developed using the reconnaissance and H*Wind data with those derived using landfall-only data and show that in the case of Gulf of Mexico storms the limited landfall dataset does not exhibit the negative RMW–Δp relationship included in most risk models and the reconnaissance and H*Wind data.

We find that B is inversely correlated with both the size and latitude of a hurricane. A weak positive correlation of B with central pressure deficit and sea surface temperature is also evident. A statistical relationship between B and a nondimensional parameter incorporating central pressure, radius to maximum winds, sea surface temperature, and latitude is introduced. A separate assessment of B obtained by modeling the surface level wind speeds of landfalling hurricanes is used in a comparison with the characteristics of B deduced using the reconnaissance and H*Wind data.

2. Datasets and estimation of B and RMW

The primary dataset used to develop a database of B and RMW was the upper-level reconnaissance data (available at ftp://ftp.aoml.noaa.gov/hrd/pub/data/flightlevel/). This dataset is described in more detail in Willoughby and Rahn (2004), and includes 606 "logical" sorties taken during the period 1977 through 2004. All data have been processed as described in Willoughby and Chelmow (1982). This dataset was supplemented with additional information on B and RMW derived from H*Wind snapshots of hurricane wind fields.

a. *Estimation of B and RMW using reconnaissance data*

The upper-level aircraft dataset used here contains a total of 4546 radial profiles from 62 Atlantic tropical cyclones. These data are the same as those used by Willoughby and Rahn (2004) in their analysis of B. For each storm in the database, data have been organized based on the different flights that passed through the storm. For each flight, the airplane traversed through the hurricane a number of times in different directions. For every pass the data were collected from the center of the storm to a certain radius (usually 150 km). The data are then organized according to radial distance from the center of the storm. For each bin (based on the radius from the center of the storm), flight-level pressure, flight altitude, dewpoint temperature, wind speed, and air temperature are available.

A quality control (QC) criterion was used to filter out profiles. Each of the filtered profiles has at least one of the following characteristics associated with it: (i) flight-level pressure is not equal to 700 hPa, (ii) Δp is less than 25 hPa, (iii) the RMW is greater than two-thirds of the sampling domain, (iv) the distance of the aircraft closest approach to the center is greater than half of the RMW, (v) data are available for less than one-third of the sampling range (i.e., less than 50 km), and (vi) visual inspection that involved eliminating profiles with a considerable amount of data missing in the range of interest [0.5RMW, 1.5RMW]. The rationale for using criterion i is that the pressure fields derived from flight-level surfaces of less than 700 hPa are likely to be less representative measurements of the surface observations. Criterion ii results in the data associated with more intense storms. The rationale for using criteria iii–vi is to ensure that there are a sufficient number of measurements on both sides of the RMW to have a clear representation of the shape of the profile (Willoughby and Rahn 2004). In the case of criterion ii, we note that category 1 hurricane winds can occur when Δp is less than 25 hPa; however, we attempt to limit the data to be biased toward the more intense storms, which govern wind risk studies. As will be noted later, we further truncate the data to include only storms with central pressures less that 980 hPa, or $\Delta p - 33$ hPa.

TABLE 1. Distribution of filtered pressure profiles based on filtering criteria.

Filter criteria	No. of profiles eliminated
i	459
ii	1180
iii	121
iv + v + vi	531
Total No. of filtered profiles	2291

The use of the quality control criteria eliminated a total of 2291 profiles from a set of 4556 profiles. Table 1 presents the count of the eliminated pressure profiles based on the QC criteria. It is clear that criteria i and ii are the most common reasons for profile elimination. The storm by storm percentage of the retained profiles is given in Table 2. For some storms, no profiles were retained as all the profiles either had Δp of less than 25 hPa (e.g., Chantal in 1995) or a flight-level pressure of less than 700 hPa (e.g., Hugo in 1989).

The geographical distribution of the profiles that passed the QC criteria is shown in Fig. 3.

Figure 4 presents a few examples of pressure profiles that were eliminated from the analysis. Both the measured pressure data and the corresponding fit to Holland's equation are shown. It is observed that each of the subplots in Fig. 4 is compromised by at least one of the above-mentioned quality control criteria.

TABLE 2. Percentage of flight-level pressure profiles retained.

Storm	Year	Total	Retained	Percent retained	Comments
No name	1938	5	5	100.00	Data extracted manually from Myers and Jordan (1956)
Anita	1977	20	20	100.00	
David	1979	24	17	70.83	
Frederic	1979	62	38	61.29	
Allen	1980	125	43	34.40	
Gert	1981	78	1	1.28	$\Delta p < 25$ hPa for all the cases, except one
Alicia	1983	50	39	78.00	
Arthur	1984	22	0	0.00	$\Delta p < 25$ hPa for all the cases
Diana	1984	128	67	52.34	
Danny	1985	26	0	0.00	$\Delta p < 25$ hPa for all the cases
Elena	1985	122	99	81.15	
Gloria	1985	42	24	57.14	
Isabel	1985	48	0	0.00	$\Delta p < 25$ hPa for all the cases
Juan	1985	36	6	16.67	
Charley	1986	28	0	0.00	$\Delta p < 25$ hPa for all the cases
Emily	1987	56	1	1.79	40 out of 56 profiles have flight-level pressure < 700 hPa
Floyd	1987	22	0	0.00	$\Delta p < 25$ hPa for all the cases
Florence	1988	20	11	55.00	
Gilbert	1988	50	39	78.00	
Joan	1988	6	5	83.33	
Dean	1989	12	1	8.33	
Gabrielle	1989	12	10	83.33	
Hugo	1989	40	0	0.00	Flight-level pressure < 700 hPa for all the cases
Jerry	1989	17	5	29.41	
Gustav	1990	84	82	97.62	
Bob	1991	92	34	36.96	
Claudette	1991	73	71	97.26	
Andrew	1992	141	95	67.38	
Debby	1994	10	0	0.00	$\Delta p < 25$ hPa for all the cases
Gordon	1994	83	8	9.64	57 out of 83 profiles have $\Delta p < 25$ hPa
Allison	1995	39	3	7.69	35 out of 39 profiles have $\Delta p < 25$ hPa
Chantal	1995	72	0	0.00	$\Delta p < 25$ hPa for all the cases
Erin	1995	97	66	68.04	
Felix	1995	130	59	45.38	
Gabrielle	1995	16	0	0.00	$\Delta p < 25$ hPa for all the cases
Iris	1995	132	41	31.06	
Luis	1995	130	77	59.23	
Marilyn	1995	116	96	82.76	
Opal	1995	76	21	27.63	
Roxanne	1995	141	52	36.88	
Bertha	1996	78	56	71.79	
Cesar	1996	34	0	0.00	$\Delta p < 25$ hPa for all the cases
Edouard	1996	178	135	75.84	
Fran	1996	143	102	71.33	
Hortense	1996	109	59	54.13	
Josephine	1996	23	1	4.35	
Kyle	1996	8	0	0.00	$\Delta p < 25$ hPa for all the cases
Lili	1996	68	28	41.18	
Marco	1996	67	1	1.49	$\Delta p < 25$ hPa for all the cases, except two
Erika	1997	56	36	64.29	
Bonnie	1998	193	113	58.55	
Danielle	1998	133	48	36.09	
Earl	1998	32	3	9.38	
Georges	1998	202	125	61.88	
Mitch	1998	86	57	66.28	
Bret	1999	102	49	48.04	
Dennis	1999	158	83	52.53	
Floyd	1999	163	103	63.19	
Keith	2000	50	40	80.00	
Leslie	2000	29	0	0.00	$\Delta p < 25$ hPa for all the cases
Michael	2000	21	11	52.38	
Humberto	2001	46	13	28.26	
Michelle	2001	89	61	68.54	

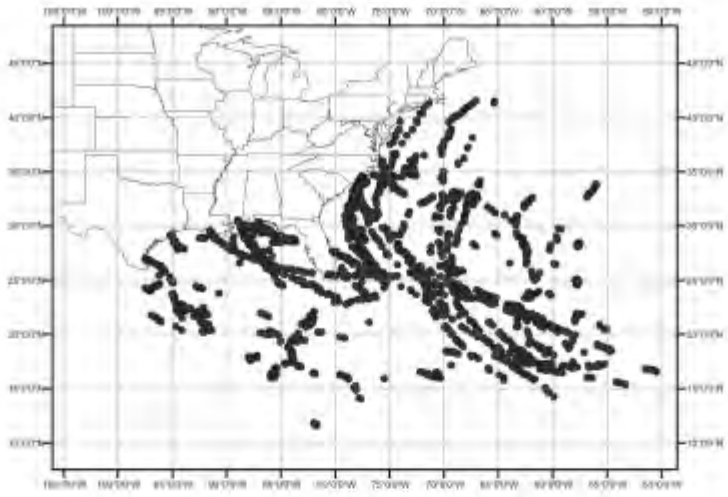

FIG. 3. Geographical distribution of the profiles passing the QC criteria.

To estimate the values of B and RMW that best represent the pressure field using (2), we first estimate RMW using the radius to the measured maximum wind speed. We then vary the values of RMW and B over the range [0.5RMW, 1.5RMW] and [0.5, 2.5], respectively, and retain the values that minimize the mean of the square difference between the measured and modeled surface pressure over the range [0.5RMW, 1.5RMW]. The mean square error is defined as

$$\varepsilon^2 = \frac{\sum_{i=0.5\mathrm{RMW}}^{1.5\mathrm{RMW}} (P_{\mathrm{obs}_i} - P_{\mathrm{theo}_i})^2}{n}, \tag{9}$$

where P_{obs_i} is the measured pressure, P_{theo_i} is the theoretical pressure calculated using (2), and n is the number of data points in the range [0.5RMW, 1.5RMW]. The corresponding r^2 value for the fit is given by

$$r^2 = 1 - \frac{\varepsilon^2}{\sigma^2}, \tag{10}$$

where σ is the standard deviation of the measured pressure data in the range of [0.5RMW, 1.5RMW]. Minimizing the error over the range [0.5RMW, 1.5RMW] ensures that the estimate of B is associated with the

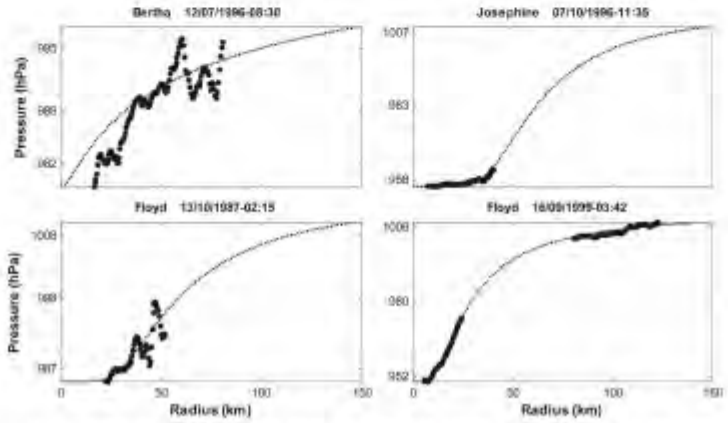

FIG. 4. Examples of the eliminated profiles: (top left) Bertha (1996), (top right) Josephine (1996), (bottom left) Floyd (1987), and (bottom right) Floyd (1999).

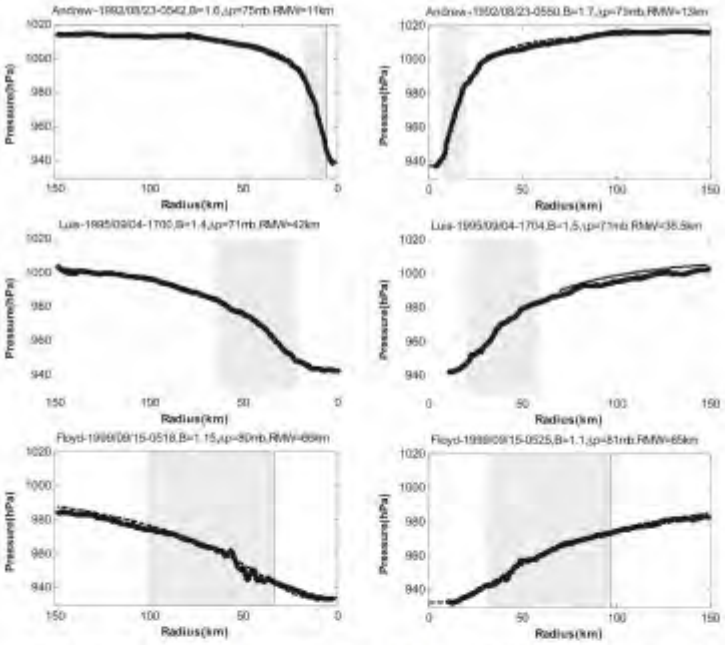

FIG. 5. Examples of surface pressure profiles for a traverse across a given hurricane: (top) Andrew at (left) 0542 and (right) 0550 UTC; (middle) Luis at (left) 1700 and (right) 1704 UTC; and (bottom) Floyd at (left) 0518 and (right) 0525 UTC.

area of a hurricane producing the maximum wind speeds, which is most important when using the results to derive design-wind speeds.

Figure 5 presents examples of model and measured surface pressure profiles, where each row corresponds to a complete airplane traverse in one direction. The shaded regions in Fig. 5 represent the error-minimizing range of [0.5RMW, 1.5RMW]. The fit parameters (i.e., the B, Δp, and RMW) are also provided in the title of each profile. For a given traverse through a hurricane, the differences in B and RMW arise from real asymmetries that exist in storms (i.e., both B and RMW vary with azimuth), errors in parameter estimation, and differences brought about by temporal changes of the hurricane as a whole. The average RMW is 46 km (standard deviation of 22 km), and the mean and standard deviation of Δp are 51 and 18 hPa, respectively. The mean and standard deviation of B are 1.25 and 0.32, respectively. The mean B value of 1.25 is slightly less than the value of 1.31 computed by Willoughby and Rahn (2004) in their analysis, and the standard deviation, 0.32, is slightly less than their value of 0.36. Seventy-one percent of the fits yield r^2 values greater than 0.95 and 80% of the fits have rms errors less than 2.5 hPa. The maximum rms error was 24.6 hPa, which occurred for one of Hurricane Opal's profiles where Holland's equation overestimated the pressures at all points.

The approach for analyzing the B and RMW data involved the estimation of RMW and B from each single pass of a flight through the storm, and then smoothing the variations in B and RMW as a function of time. The smoothing procedure used was a five-point moving average. The approach taken here to smooth the estimates of B obtained from a single pass through the storm differs from that used in Willoughby and Rahn (2004), where they used B estimated from an azimuthal average. Both approaches are flawed in that they eliminate the azimuthal variation in B that exists in real hurricanes; however, as will be shown later, the statistical models resulting from the two sets of data are remarkably similar to one another. Furthermore, when applied in real-world problems, the modeled input pressure or wind field is assumed to be axisymmetric, consistent with the analysis assumptions.

Figure 6 presents 10 examples of both the single flight (point estimates) and the smoothed estimates of B and RMW plotted versus time, for landfalling hurri-

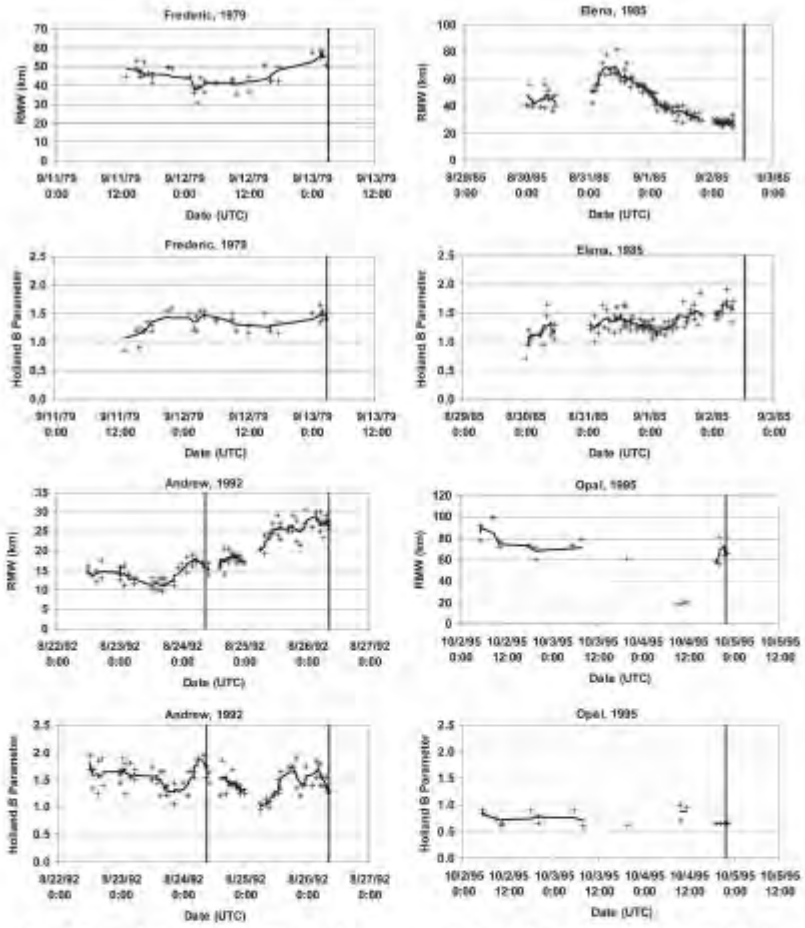

FIG. 6. Examples of smoothed (line) and point estimates (symbols) of RMW and B derived from 700-hPa-level pressure data. The vertical lines represent time of landfall.

canes. The landfall time is indicated with a vertical line in each plot. Using the smoothed data, values of B and RMW were extracted at intervals of approximately 3 h and retained for use in the statistical analyses. The mean values of B and RMW for the smoothed dataset are 1.21 and 47 km, respectively. The corresponding standard deviations are 0.29 and 21 km, respectively.

*b. Estimation of B and RMW using H*WIND data*

The flight-level data encompass storms through 2001, and thus to supplement the dataset with more recent storms, some additional storms analyzed using the H*Wind methodology were added. The only storms added were the intense storms from the 2004 and 2005 seasons that had been reanalyzed using the most recent stepped frequency microwave radiometer (SFMR) calibrations. The intense storms that have been reanalyzed include Hurricane Katrina (2005) and Hurricane Ivan (2004). Hurricane Rita was added to the dataset even though it had not been reanalyzed, because at its most intense, the storm had a minimum central pressure of less than 900 hPa.

Since the pressure field is not available with H*Wind data, a more simplistic approach is taken to estimate the value of B associated with a given H*Wind snapshot. Using the wind field model described in Vickery et al. (2008) and the values of central pressure, RMW, storm translation speed, and the maximum sustained

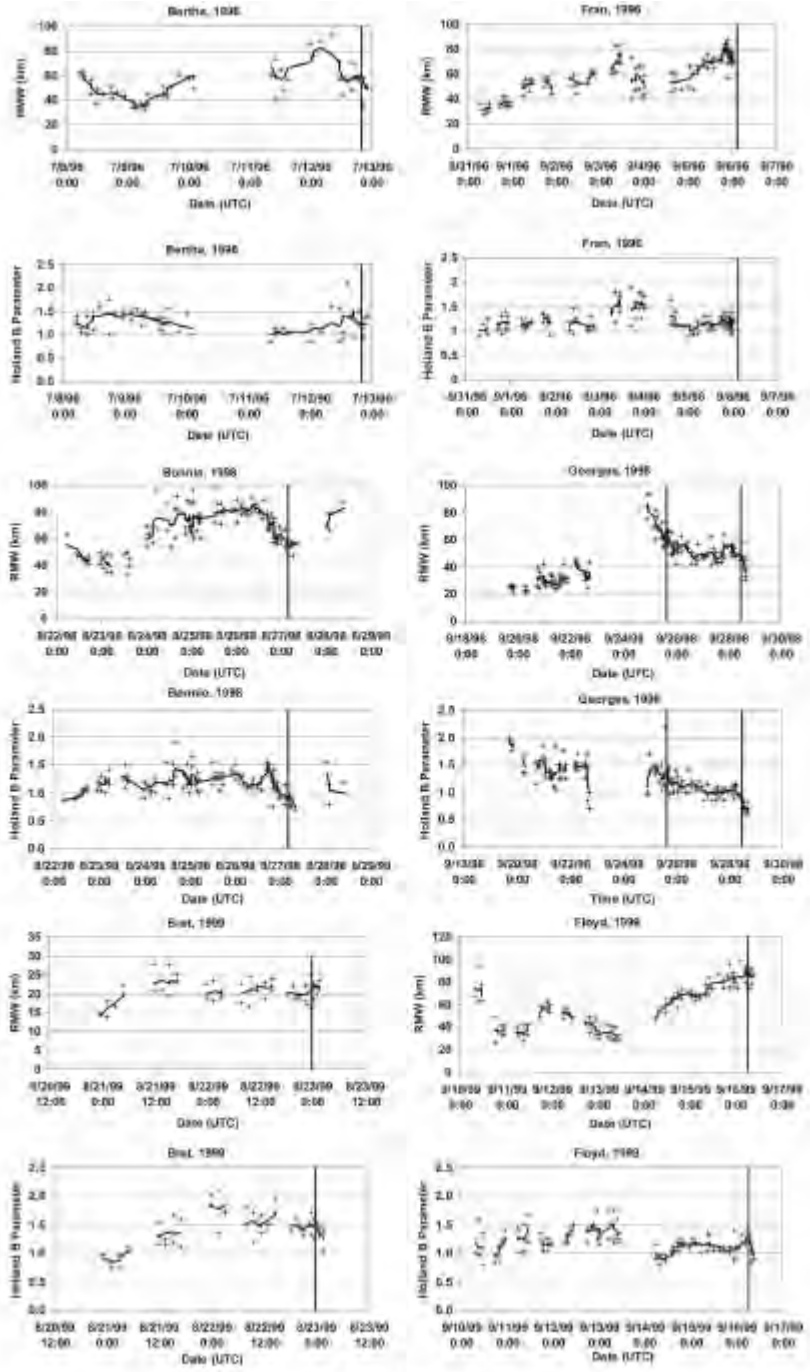

FIG. 6. (*Continued*)

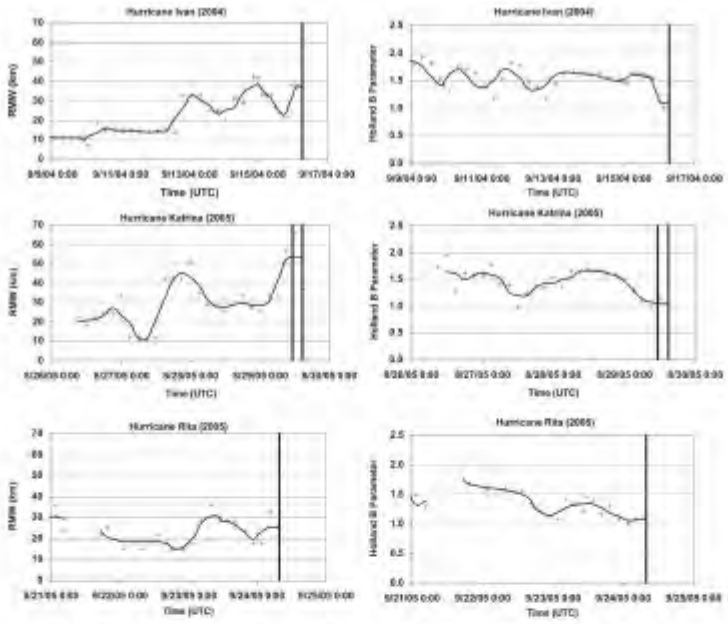

FIG. 7. Smoothed (line) and point estimates (symbols) of (left) RMW and (right) B derived from H*Wind data. Vertical line(s) represents time of landfall: (top) Ivan, (middle) Katrina, and (bottom) Rita.

wind speed, a B value is chosen so that the maximum surface level wind speed (1-min sustained value) obtained from the model matches the H*Wind estimate of the maximum wind speed. Thus the estimated values of B are obtained through an indirect measure, matching the maximum wind speed rather than the shape of the entire wind field. Matching the peak wind rather than the shape of the wind field ensures that the estimate of B is associated with the maximum sustained wind speed in the hurricane, which is most important when using the results to derive design wind speeds. Figure 7 presents plots of RMW and B as a function of time for the three aforementioned hurricanes.

3. Statistical models of radius to maximum winds

The RMW plays an important role in hurricane risk prediction, with the RMW data provided in the NWS 38 publication being a primary source for developing RMW models since they provide information of the RMW for almost all hurricanes making landfall along the U.S. coastline between 1900 and 1985. Here we use the flight-level and H*Wind data to develop statistical models for the RMW (relating RMW to other parameters that are usually modeled in a risk model) and compare these models with models developed using the more traditional approach that includes landfalling hurricane RMW data only. The models (both open water and landfall) are presented for all hurricanes, and separately for Gulf of Mexico hurricanes and Atlantic Ocean hurricanes. Unless noted otherwise, in the statistical analyses that follow, all model parameters are statistically significant at the 95% confidence level.

a. All-, Gulf of Mexico, and Atlantic Ocean hurricane RMW models

1) ALL HURRICANES

The RMW for all points (flight-level data plus H*Wind data) in the dataset having a central pressure of less than 980 hPa was modeled as a function of Δp and latitude, ψ, in the form

$$\ln(\mathrm{RMW}) = 3.015 - 6.291 \times 10^{-5}\Delta p^2 + 0.0337\Psi;$$
$$r^2 = 0.297, \quad \sigma_{\ln \mathrm{RMW}} = 0.441. \tag{11}$$

An analysis of the errors (difference between the regression model estimates and the data) indicates that

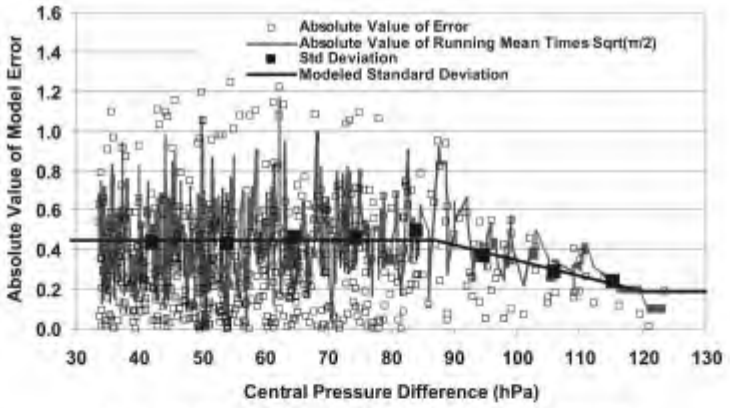

FIG. 8. Absolute value of RMW model error vs Δp for all hurricanes.

the model error reduces with increasing Δp, as indicated in Fig. 8.

The error, $\sigma_{\ln RMW}$, is modeled in the form

$$\sigma_{\ln RMW} = 0.448, \quad \Delta p \le 87, \tag{12a}$$

$$\sigma_{\ln RMW} = 1.137 - 0.007\,92\Delta p, \; 87\ \text{hPa} \le \Delta p \le 120\ \text{hPa}, \tag{12b}$$

and

$$\sigma_{\ln RMW} = 0.186, \quad \Delta p > 120\ \text{hPa}. \tag{12c}$$

Figure 9 presents the modeled and observed values of RMW plotted versus Δp. The modeled data are given as the median and the range is defined by $\pm 2\sigma_{\ln RMW}$. The modeled range reflects the reduction in $\sigma_{\ln RMW}$ as a function of Δp.

2) Gulf of Mexico hurricanes

To determine if the characteristics of the RMW associated with the Gulf of Mexico storms differed from those obtained using the all-storm data, the RMW–Δp and RMW–ψ relationships were reexamined. For this analysis the Gulf of Mexico storms included all hurricanes west of 81°W and north of 18°N. The RMW for all storms (flight-level data plus H*Wind data) in the Gulf of Mexico dataset with central pressures less than 980 hPa were modeled as a function of Δp in the form

$$\ln(\text{RMW}) = 3.858 - 7.700 \times 10^{-5}\Delta p^2;$$

$$r^2 = 0.290, \quad \sigma_{\ln RMW} = 0.390. \tag{13}$$

The RMW was found to be independent of latitude. As in the all-storm case, the model error reduces with increasing Δp, as indicated in Fig. 10.

The error, $\sigma_{\ln RMW}$, for Gulf of Mexico hurricanes is modeled in the form

$$\sigma_{\ln RMW} = 0.396, \; \Delta p \le 100\ \text{hPa}, \tag{14a}$$

$$\sigma_{\ln RMW} = 1.424 - 0.010\,29\Delta p, \; 100\ \text{hPa} \le \Delta p \le 120\ \text{hPa}, \tag{14b}$$

and

$$\sigma_{\ln RMW} = 0.19, \; \Delta p > 120\ \text{hPa}. \tag{14c}$$

Figure 11 presents the modeled and observed values of RMW plotted versus Δp for the Gulf of Mexico hurricanes. The modeled data are given as the median estimates and the range defined by $\pm 2\sigma_{\ln RMW}$. The modeled range reflects the reduction in $\sigma_{\ln RMW}$ as a function of Δp.

Figure 12 presents the median values of the RMW computed using (11) (all-hurricane RMW model) computed for latitudes of 25°N (southern Gulf of Mexico) and 30°N (northern Gulf of Mexico), where it is seen that for the northern Gulf of Mexico storms, the all-hurricane RMW model overestimates the size of the Gulf of Mexico hurricanes.

3) Atlantic Ocean hurricanes

In the case of Atlantic Ocean hurricanes, defined as all hurricanes east of 80°W, the RMW for all storms (flight-level data plus H*Wind data) are best modeled as a function of Δp and ψ in the form

$$\ln(\text{RMW}) = 3.421 - 4.600 \times 10^{-5}\Delta p^2 + 0.000\,62\psi^2;$$

$$r^2 = 0.236, \quad \sigma_{\ln RMW} = 0.466. \tag{15}$$

The error, $\sigma_{\ln RMW}$, for Atlantic Ocean hurricanes is independent of central pressure.

b. Comparisons of open-water RMW models with landfalling RMW models and data

The statistical models for RMW derived from the flight-level and H*Wind data are representative of re-

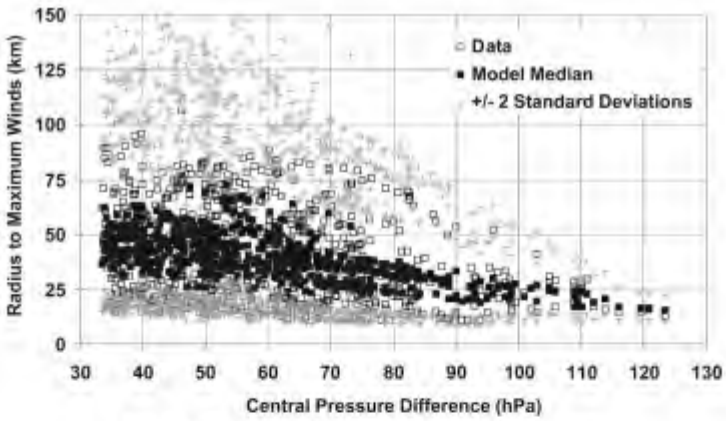

FIG. 9. Modeled and observed RMW vs Δp for all hurricanes.

lationships between the RMW, Δp, and so on for hurricanes located primarily in the open water. Here we compare these models with the RMW models derived using the more traditional approach of including only landfalling hurricane data. The landfall RMW data are given in Vickery (2005), which presents a summary of RMW, Δp, and landfall location data compiled primarily from a combination of RMW data given in NWS 38 (Ho et al. 1987) and RMW data obtained from H*Wind snapshots for hurricanes valid at or near the time of landfall.

Figure 13 presents the RMW for storms making landfall along the Gulf and Atlantic coasts of the United States plotted as a function of Δp. In the case of Gulf Coast landfalling hurricanes, no statistically significant correlation exists between the RMW and either latitude or Δp. In the case of hurricanes making landfall along the Atlantic coast, the RMW is positively correlated with latitude, and negatively correlated with Δp^2. (The negative correlation between RMW and Δp^2 is significant at the 94% confidence level.) As a group (i.e., both Atlantic and Gulf Coast landfalling hurricanes), the RMW is also positively correlated with latitude and negatively correlated with Δp^2.

Using only landfall values of RMW, the following statistical models best define the relationship among RMW, Δp, and latitude:

(i) Gulf of Mexico landfalling hurricanes:

$$\ln(\mathrm{RMW}) = 3.558; \quad \sigma_{\ln\mathrm{RMW}} = 0.457, \tag{16}$$

(ii) Atlantic coast landfalling hurricanes:

$$\ln(\mathrm{RMW}) = 2.556 - 5.963 \times 10^{-5}\Delta p^2 + 0.0458\psi;$$
$$r^2 = 0.336, \quad \sigma_{\ln\mathrm{RMW}} = 0.456, \quad \text{and} \tag{17}$$

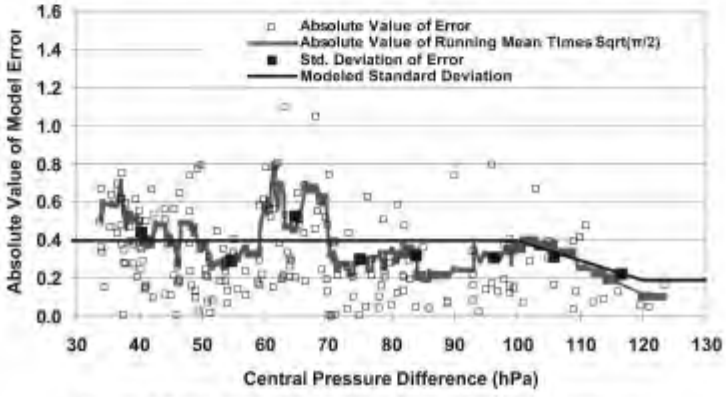

FIG. 10. Absolute value of RMW model error vs Δp for GoM hurricanes.

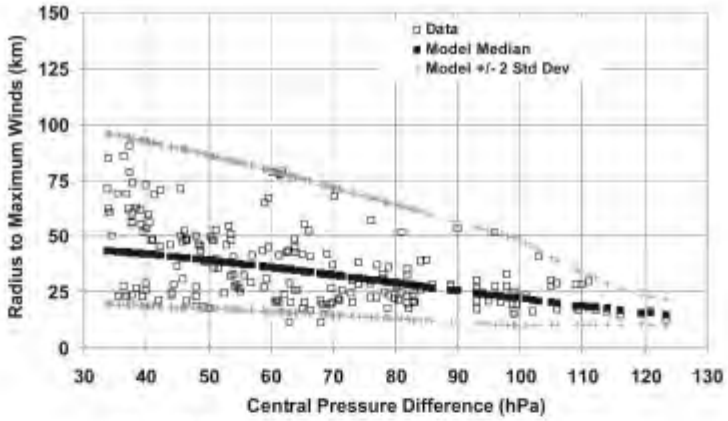

FIG. 11. Modeled and observed RMW vs Δp for GoM hurricanes.

(iii) Gulf and Atlantic coast landfalling hurricanes:

$$\ln(\mathrm{RMW}) = 2.377 - 4.825 \times 10^{-5}\Delta p^2 + 0.0483\phi;$$
$$r^2 = 0.203, \quad \sigma_{\ln\mathrm{RMW}} = 0.457. \tag{18}$$

The ability of the RMW models developed using the flight-level and H*Wind data (primarily open-ocean data) to model the landfalling hurricane RMW was tested by computing the mean and root-mean-square errors (in both logarithmic and linear space) and r^2 values resulting from using (11)–(15) (open-ocean models) with the landfall RMW data. The results are summarized in Table 3 (errors in log space) and Table 4 (errors in linear space). Tables 3 and 4 also present the errors associated with the statistical models for the landfall RMW developed with the landfall RMW data. The mean error, $\mu_{\ln\mathrm{RMW}}$, is defined as modeled RMW minus the observed RMW; thus a mean positive error indicates that the model overestimates observed RMW. A comparison of the model errors given in Tables 3 and 4 with those resulting from the statistical analyses of the landfalling storms alone indicates that the models derived from the flight-level and H*Wind data can be used to define the characteristics of landfalling hurricanes. In the case of landfalling Gulf of Mexico hurricanes, the use of the GoM RMW model, which contains the negative correlation between RMW and Δp^2, is not statistically significantly different from the uncorrelated RMW–Δp relationship derived from the landfalling hurricanes alone. This observation suggests that

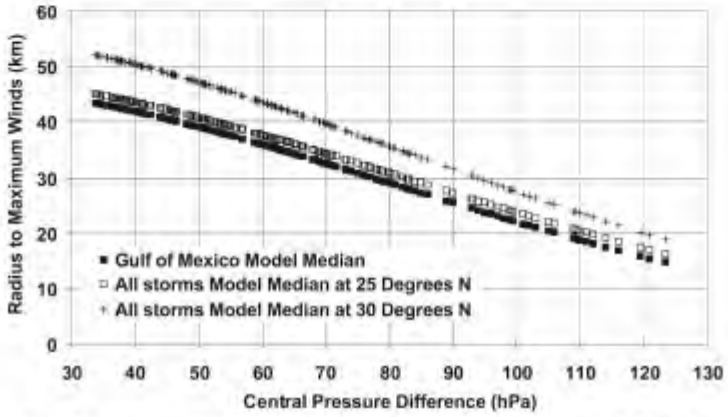

FIG. 12. Comparison of all hurricanes' model-predicted median RMW with GoM model median RMW vs Δp.

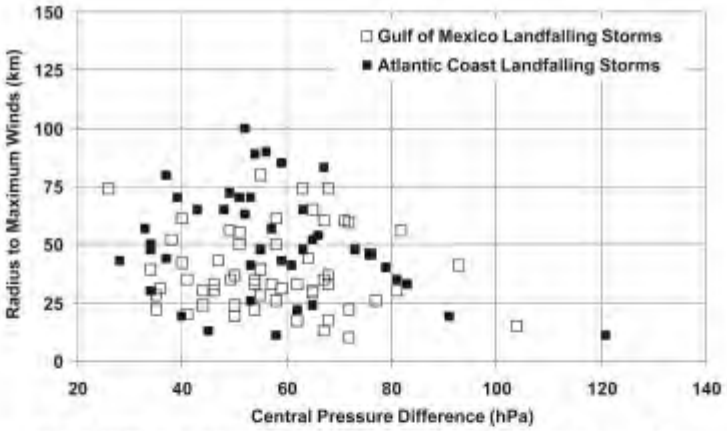

FIG. 13. RMW vs Δp for landfalling storms along the Gulf and Atlantic coasts of the United States.

there are an insufficient number of intense landfalling hurricanes in the historical landfall data to discern the RMW–Δp correlation, and a model developed using the GoM landfall data alone would not include this important negative RMW–Δp relationship. The recommended statistical models are shown in boldface type in Tables 3 and 4.

4. Analysis and behavior of B

In this section we use the time series of B, RMW, Δp, and so on derived from the H*Wind and reconnaissance data to develop a statistical model (or models) for B that can be used to estimate B given other parameters that are usually used in hurricane risk models. We also examine an apparent reduction in B as hurricanes approach the northern Gulf of Mexico coastline, and compare B values estimated from the H*Wind and reconnaissance data with those estimated using a wind field model and surface level wind speed measurements.

a. Statistical model for B

The B values computed as discussed in section 2 were found to be correlated to the radius to maximum winds, Δp, latitude, and sea surface temperature. Only points associated with central pressures less than 980 hPa are included in the analysis. The analysis was performed with the "smoothed" time series of B, with samples taken approximately every 3 h along the track of each hurricane. Figure 14 presents the variation of B as separate linear functions of the RMW, Δp, latitude (ψ), and the mean sea surface temperature T_s. It is clear from the data presented in Fig. 14 that B decreases with increasing RMW and increasing latitude. A weak positive correlation with both Δp and sea surface tempera-

TABLE 3. RMW model errors. Errors are computed in natural log space.

RMW data	Model	Error (natural log km)		Mean significantly different from 0?	r^2
		Mean	Std dev		
Gulf-landfall	Mean (Gulf-landfall) [Eq. (16)]	0.00	0.46		0.00
Gulf-landfall	**Gulf-ocean [Eq. (13)]**	0.03	0.46		−0.01
Gulf-landfall	All–open water [Eq. (11)]	0.21	0.45	Yes	0.00
Gulf-landfall	All-landfall [Eq. (18)]	0.05	0.46		0.00
Atlantic-landfall	Mean	0.00	0.56		0.00
Atlantic-landfall	Atlantic-landfall [Eq. (17)]	0.00	0.44		0.37
Atlantic-landfall	All-landfall [Eq. (18)]	−0.06	0.44		0.37
Atlantic-landfall	Atlantic–open water [Eq. (15)]	0.11	0.45		0.35
Atlantic-landfall	**All–open water [Eq. (11)]**	0.06	0.45		0.35
All-landfall	Mean	0.00	0.51		0.00
All-landfall	All-landfall [Eq. (18)]	0.00	0.45		0.22
All-landfall	All–open water [Eq. (11)]	0.15	0.46	Yes	0.20

TABLE 4. RMW model errors. Errors are computed in linear space.

RMW data	Model	Error (km) Mean	Error (km) Std dev	Mean significantly different from 0?	r^2
Gulf-landfall	Mean (Gulf-landfall) [Eq. (16)]	0.0	16.8		0.00
Gulf-landfall	**Gulf–open water [Eq. (13)]**	**−2.1**	**17.2**		**−0.04**
Gulf-landfall	All–open water [Eq. (11)]	5.0	17.4	Yes	−0.07
Gulf-landfall	All-landfall [Eq. (18)]	−1.7	17.2		−0.05
Atlantic-landfall	Mean	0.0	22.8		0.00
Atlantic-landfall	Atlantic-landfall [Eq. (17)]	−3.6	19.1		0.29
Atlantic-landfall	All-landfall [Eq. (18)]	−6.3	19.0	Yes	0.30
Atlantic-landfall	Atlantic–open water [Eq. (15)]	0.9	19.2		0.29
Atlantic-landfall	**All hurricane–ocean [Eq. (11)]**	**−1.3**	**19.0**		**0.30**
All-landfall	Mean	0.0	20.3		0.00
All-landfall	All-landfall [Eq. (18)]	−3.7	18.1	Yes	0.21
All-landfall	All–open water [Eq. (11)]	2.4	18.2		0.19

ture is also evident. We know that T_s is correlated with latitude, RMW is positively correlated with latitude, and RMW is negatively correlated with Δp; hence we also look at partial correlations. Figure 15 presents partial correlations of B adjusted for RMW, Δp, latitude (ϕ), and the mean sea surface temperature T_s. The partial correlation for adjusted B with adjusted RMW, T_s, and latitude (ϕ) cases is significant at a 95% confidence level. For Δp partial correlation is insignificant at a 95% confidence level.

To incorporate the effects of RMW, Δp, latitude (ϕ), and T_s into a single model, a new nondimensional variable A was developed, defined as

$$A = \frac{\text{RMW} f_c}{\sqrt{2R_d(T_s - 273)\ln\left(1 + \dfrac{\Delta p}{p_c e}\right)}}. \tag{19}$$

Equation (19) was derived with the intent to model B as a function of a nondimensional parameter. The parameter A was developed considering

(i) as RMW increases B decreases,
(ii) as latitude increases B decreases, and
(iii) maximum wind speed in a hurricane is proportional to $\sqrt{B}$ and has an upper theoretical limit (e.g., Emanuel 1988).

To include the maximum wind speed in the model we use the relationship (Emanuel 1988) that the maximum wind speed in a tropical cyclone is

$$V_{\max} = \sqrt{2R_d T_s \ln\left(\frac{p_{\max}}{p_c}\right)}, \tag{20}$$

where $V_{\max}$ is the maximum wind speed, R_d is the gas constant for dry air (N m kg^{-1} K^{-1}), $p_{\max}$ is the pressure at r = RMW, T_s is the sea surface temperature (K), and p_c is the pressure at the storm center.

This expression was simplified using Holland's (1980) pressure profile equation [(2)] from which it can be shown that at r = RMW,

$$\frac{p_{\max}}{p_c} = 1 + \frac{\Delta p}{p_c e}. \tag{21}$$

Equation (21) was substituted into (20) to obtain the denominator in (19). A value of 273° was subtracted from the SST in (20) because the regression model performed better using SST in degrees Celsius rather than Kelvin. The numerator of A is the product of the RMW (in meters) and the Coriolis force, defined as $2\Omega \sin\phi$, and represents the contribution to angular velocity associated with the Coriolis force. Hence, both the numerator and denominator of A have the units of velocity, and thus A is nondimensional.

Modeling B as a function of $\sqrt{A}$ yields a linear model (Fig. 16) with B negatively correlated with $\sqrt{A}$ and has an r^2 of 0.34, with a standard deviation of the error equal to 0.225. The relationship between B and $\sqrt{A}$ is expressed as

$$B = 1.7642 - 1.2098\sqrt{A}; \quad r^2 = 0.345, \quad \sigma_B = 0.226. \tag{22}$$

To determine if the relationship between B and A is valid for intense storms, the observed and model values of B were plotted as a function of RMW for strong hurricanes (i.e., storms with a central pressure of <930 hPa), as shown in Fig. 17. The data presented in Fig. 17 indicate that in the case of strong storms with large RMW (RMW > 40 km), the relationship between B and A described earlier breaks down, with the values of B being less than those predicted by the model. Although only two storms with large RMW and low central pressures exist in the data analyzed (Hurricane Katrina in the Gulf of Mexico and Hurricane Floyd in the

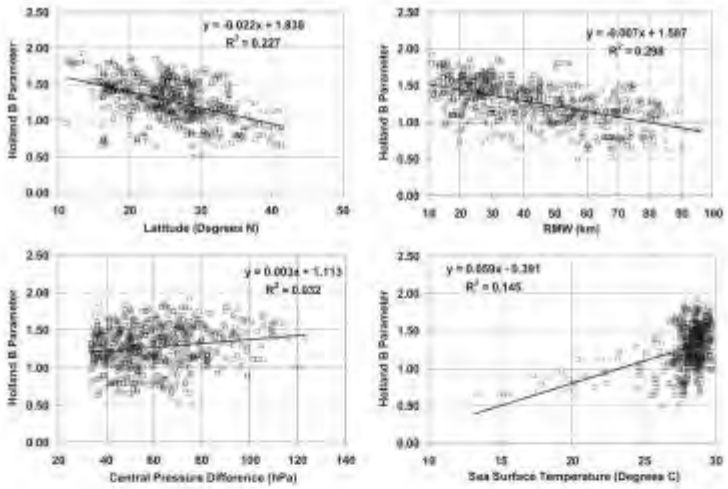

FIG. 14. Relationships between B and (top left) latitude, (top right) RMW, (bottom left) Δp, and (bottom right) T_s.

Atlantic), the data indicate that the likelihood of a storm with a central pressure less than −930 hPa and an RMW greater than 40 km, combined with a B value greater than about 1.1, is remote. The mean value of B for these large, intense hurricanes is 1.01, and the standard deviation is 0.082. In cases in which these strong storms are simulated, B is constrained to lie within the range of the mean $\pm 3\sigma$.

As in the case of the analysis of Gulf of Mexico hurricanes with respect to the behavior of RMW with Δp and latitude, B values for all hurricanes within the Gulf of Mexico were extracted and analyzed alone. Unlike the results seen for the RMW in which the GoM hurricanes were found to be smaller than the other hurricanes, the variation of B with A for the GoM hurricanes is essentially identical to that seen in the all-hurricane case. Figure 18 presents the individual B values for the GoM and Atlantic hurricanes along with the model-

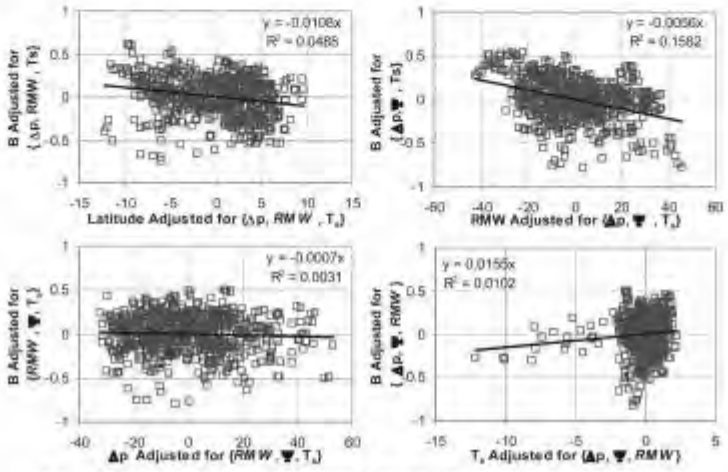

FIG. 15. Partial correlations for B adjusted for (top left) latitude, (top right) RMW, (bottom left) Δp, and (bottom right) T_s.

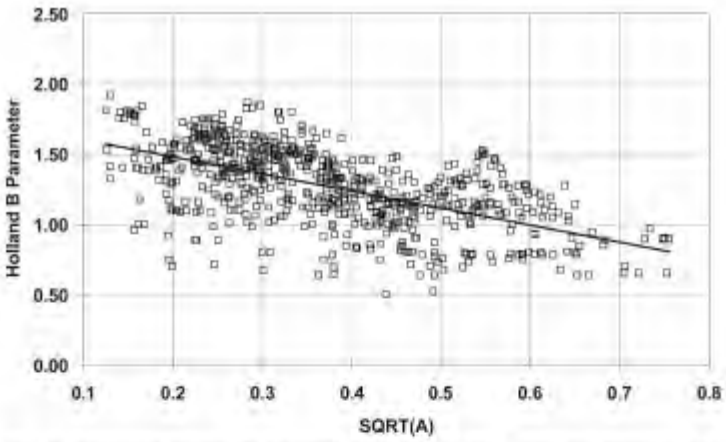

FIG. 16. Relationship between the Holland B parameter and the dimensionless parameter $A^{1/2}$.

predicted mean values of B, where it is clearly evident that there is, for practical purposes, no difference in the variation of B with A between the two regions.

An alternate model relating B to the product of f_c and RMW is given in the form

$$B = 1.833 - 0.326\sqrt{f_c \mathrm{RMW}};$$
$$r^2 = 0.357, \quad \sigma_B = 0.221. \tag{23}$$

A statistical model relating B to RMW (km) and ψ in the same form as that developed by Powell et al. (2005) is

$$B = 1.881 - 0.005\,57\mathrm{RMW} - 0.012\,95\psi;$$
$$r^2 = 0.356, \quad \sigma_B 0.221. \tag{24}$$

Equation (24) is similar to the model given in Powell et al. (2005) presented earlier in (8).

For practical purposes, any of the three linear regression models given in (22), (23), or (24) can be used to model B. Again, note that the units of RMW used in (22) and (23) are meters, but (24) uses RMW in kilometers.

b. *Changes in B near land*

During the 2004 and 2005 storm season, it was noted that the four storms that made landfall along the Gulf of Mexico coastline (Ivan in 2004, and Dennis, Katrina, and Rita in 2005) all weakened over a 12–24-h period before making landfall, with this weakening (increasing

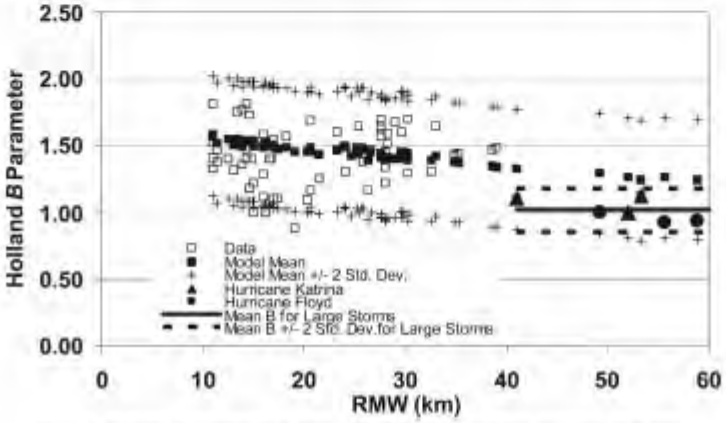

FIG. 17. Holland B parameter vs RMW for storms with central pressure <930 hPa.

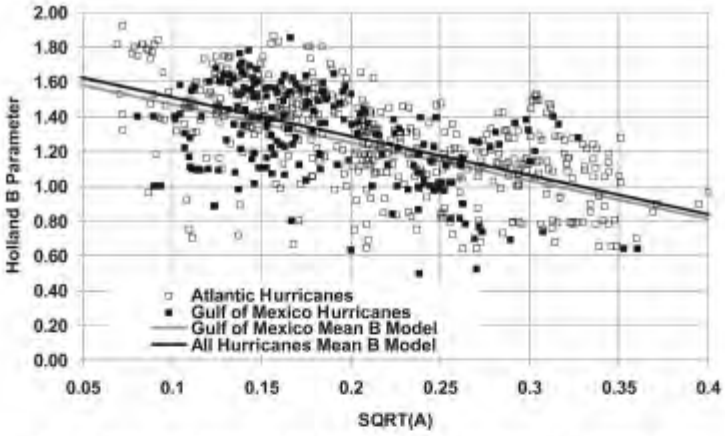

FIG. 18. Relationship between B and the dimensionless parameter $A^{1/2}$, comparing the all-hurricane data with the GoM hurricane data.

central pressure) accompanied by a decrease in B and an increase in the RMW. The magnitude of the decrease in B is larger than the decrease expected to be brought about by the increase in RMW alone as estimated through any of (22), (23), or (24). This observed decrease in B was included in the modeling of the coastal flood risk for both coastal Louisiana and Mississippi. In the Louisiana and Mississippi studies, B was reduced from a mean value of 1.27 (open water) to 1.0 at the time of landfall for all hurricanes with RMW less than 8 nm, where for these smaller storms B at landfall remained at 1.27. The reduction in B from 1.27 to 1.0 was implemented over the last 6–12 h before landfall (varying with storm translation speed). Using the reconnaissance and H*Wind derived times series of B we examine whether these data also support a consistent decrease in B as hurricanes approach land. Qualitatively the time series of B presented in Fig. 6 (reconnaissance data) and also in Fig. 7 (H*wind data) show a reduction in B as hurricanes approach the Gulf of Mexico coastline. Table 5 presents the change in B during the 12 h prior to landfall derived from both the H*Wind data and the reconnaissance data. Gulf of Mexico storms are treated separately from the Florida

TABLE 5. Change in B during the last 12 h before U.S. landfall.

Gulf of Mexico storms		Change in B during last 12 h prior to landfall		Atlantic coast and Florida Peninsula hurricanes		Change in B during last 12 h prior to landfall	
Year	Hurricane name	ReCon	H*Wind	Year	Hurricane name	ReCon	H*Wind
1979	Frederic	0.19		1984	Diana	0.08	
1985	Elena	0.04		1985	Gloria	0.02	
1992	Andrew	−0.24		1991	Bob	−0.14	
1995	Opal	−0.23		1992	Andrew	0.27	
1998	Georges	−0.24		1996	Fran	0.06	
1999	Bret	−0.23	−0.03	1998	Bonnie	−0.43	
2002	Lili		−0.37	1996	Bertha	0.04	
2004	Ivan		−0.46	1999	Floyd	0.23	0.24
2005	Dennis		−0.53	2004	Frances		−0.10
2005	Katrina		−0.26	2004	Jeanne		0.19
2005	Rita		−0.11	2003	Isabel		0.00
				2004	Charley		0.00
				2004	Wilma		0.04
Mean			−0.21	Mean		0.04	
Std dev			0.20	Std dev		0.18	
Std error in mean			0.06	Std error in mean		0.05	

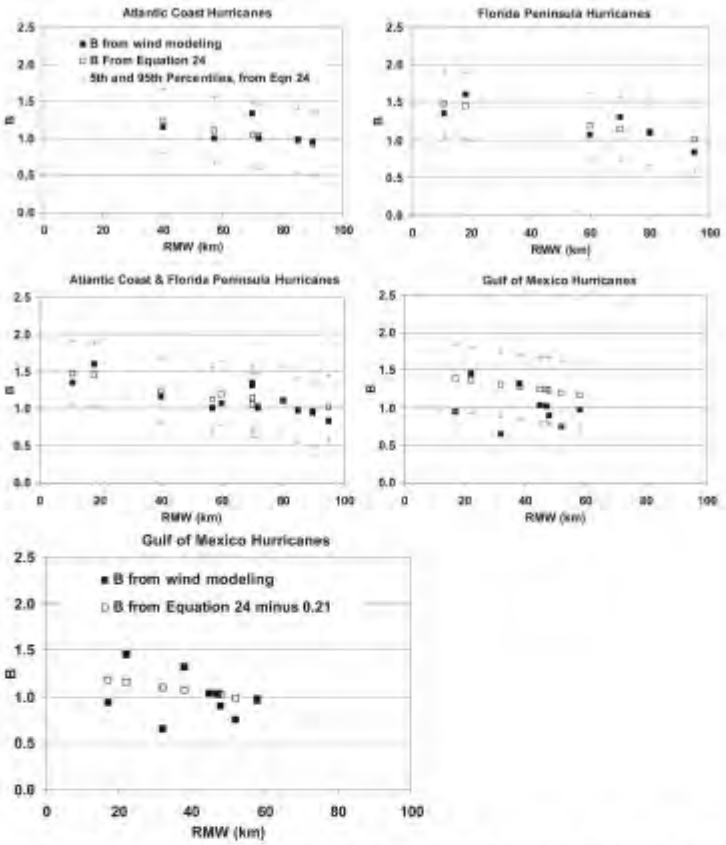

FIG. 19. Comparison of modeled [(24)] and independently observed values of B for landfalling hurricanes: (top left) Atlantic coast, (top right) Florida Peninsula, (middle left) Atlantic coast and Florida Peninsula, (middle right) GoM, and (bottom) GoM with B from wind modeling and from (24) minus 0.21.

Peninsula and Atlantic coast landfalling hurricanes. In the case of hurricanes making landfall along the Gulf of Mexico coastline, a mean reduction of 0.21 in B over the last 12 h is evident. The reduction of 0.21 is significantly different from zero at a 95% confidence level. In the case of Atlantic and Florida Peninsula landfalling hurricanes a mean increase in B of 0.04 over the past 12 h is evident, but this difference (from zero) is not statistically significant. Thus, the limited dataset supports a reduction in B as hurricanes approach the Gulf of Mexico. In the case of the 2004 and 2005 hurricanes, with B estimated from the maximum wind speeds estimated using H*Wind, there is some concern as to the possibility that a nonhomogeneous input wind speed dataset may yield variations (in this case reductions) of wind speed that are caused by the H*Wind analysis methodology rather than true variations of the wind speed within the hurricane. For example, if a series of reconnaissance aircraft were not equipped with the SFMR, then the estimates of the surface level winds rely heavily on the algorithm used in H*Wind to convert the aircraft winds to surface winds. Similarly, if a subsequent series of reconnaissance aircraft were equipped with the SFMR, then H*Wind will rely on the SFMR wind speed estimates to estimate the surface wind speeds rather than adjusting flight-level wind speeds to surface values. If there were a bias in either of the approaches for estimating wind speeds, then H*Wind would produce artificial changes in the maximum wind speed in a hurricane. As indicated in Table 5, the reduction in B over the last 12 h deduced from the H*Wind wind speed estimates appears only in the

Gulf of Mexico hurricanes and not the Florida hurricanes, suggesting that the variation of B as a hurricane approaches the Gulf of Mexico coastline is not an artifact of the H*Wind wind speed estimates.

Comparison of flight-level B values with landfall analysis B values

An independent analysis of the behavior of B using estimates of B derived from comparisons of modeled and surface wind fields using the hurricane boundary layer model described in Vickery et al. (2008) was performed and is discussed here. In Vickery et al., estimates of B are obtained by changing estimated values of B and RMW for a model hurricane near the time of landfall to match time series of measured and modeled surface level wind speeds, wind directions, and pressures. Recalling that the primary use of the statistical models for B is as an input to a hurricane wind field, demonstrating that the values of B used in a wind field model are consistent with those derived from the aircraft, is a critical and important step. Figure 19 presents a comparison of B values computed using (24) with those derived from the landfall analyses for the Atlantic coast, Florida Peninsula, Atlantic and Florida Peninsula combined, and Gulf Coast (excluding the Florida Peninsula). In the case of the Atlantic coast and the Florida Peninsula hurricanes, it is clear that the estimates of B derived from (24) are consistent with those estimated independently using the analyses of landfalling wind fields, with the B values derived from the landfall analyses falling well within the 95% confidence bounds. In the case of the Gulf of Mexico landfalling storms, (24) overestimates the mean value of B by 0.21, consistent with a reduction in B for the majority of the sample hurricanes approaching and making landfall along the Gulf of Mexico coast.

Figure 20 presents a comparison of B values derived from the flight-level data to those used in the wind field model described in Vickery et al. (2008) used for estimating the wind speeds associated with landfalling storms. Although there are only 11 cases for which both flight-level data and poststorm wind analyses are available, the comparison indicates that the B values used within the hurricane wind field model to match the surface observations of wind speeds and pressures are about 7% less than those derived from the flight-level data, but is not a statistically significant difference.

The limited comparisons of B derived from surface-level wind speed analyses with those derived from the reconnaissance data provide additional confidence to the statistical models developed using the reconnaissance data. The comparisons also demonstrate that there is consistency between the B values estimated from the aircraft data and the wind field model that subsequently uses the B values in probabilistic modeling.

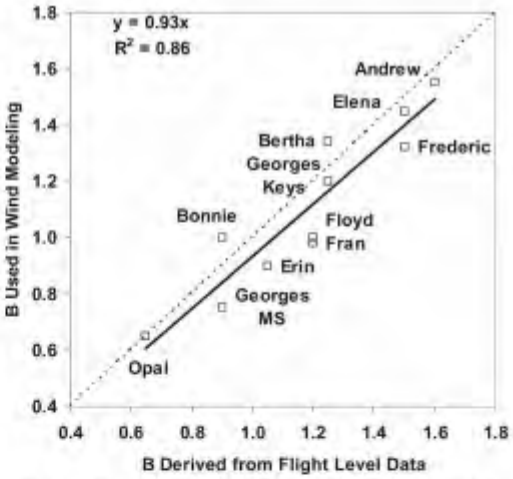

FIG. 20. Comparison of Holland B parameters derived from flight-level data with those derived using a postlandfall wind field analysis.

5. Summary

Statistical models relating RMW to latitude and central pressure derived from the reconnaissance and H*Wind dataset are compared to those derived for U.S. landfalling storms during the period 1900–2005. The analysis indicates that using RMW data comprising only landfalling Gulf of Mexico hurricanes suggests that there is no inverse relationship between RMW and the central pressure deficit. The RMW data also demonstrate that Gulf of Mexico hurricanes are, on average, smaller than Atlantic Ocean hurricanes.

The Holland pressure profile parameter B was found to decrease with increasing latitude and increase with decreasing RMW. A weak positive correlation between B and both Δp and sea surface temperature was also observed. The effect of all four of these parameters was accounted for by defining a nondimensional parameter A, defined by (19); however, a two-parameter model (with dimensions) relating B to the RMW and the Coriolis parameter is an equally good predictor of B. The relationship between B and A was found to be the same in the Atlantic Basin and in the Gulf of Mexico. The limited data for large (as defined by RMW) hurricanes, having low central pressures ($p_c < 930$ hPa), indicate that B has an upper limit of approximately 1.2–1.3.

The few cases for which flight-level data were available up to the time a hurricane made landfall along the Gulf of Mexico coastline indicate that in most cases B tends to decrease as the hurricane approaches land. Recognizing that the dataset is limited, this observation suggests that using the statistical model for B derived using open-water data may result in an overestimate of B for landfalling storms along the Gulf of Mexico.

Acknowledgments. The research described herein was partially funded under a contract with the Federal Emergency Management Agency and by the U.S. Army Corps of Engineers under Contract W912-HZ-06-P0193. The authors are solely responsible for the accuracy of the statements and the interpretations contained in this publication.

REFERENCES

American National Standards Institute, 1982: Minimum design loads for buildings and other structures. ANSI Rep. A58.1, 109 pp.

American Society of Civil Engineers, 1990: Minimum design loads for buildings and other structures. ASCI Rep. 7-88, 110 pp.

Batts, M. E., M. R. Cordes, L. R. Russell, J. R. Shaver, and E. Simiu, 1980: Hurricane wind speeds in the United States. National Bureau of Standards Rep. BSS-124, U.S. Department of Commerce, 50 pp.

Blake, E. S., E. N. Rappaport, J. D. Jarrell, and C. W. Landsea, 2007: The deadliest, costliest, and most intense United States hurricanes from 1851 to 2006 (and other frequently requested hurricane facts). NOAA Tech. Memo. NWS-TPC-5, 43 pp.

Caribbean Community Secretariat, 1986: Caribbean Uniform Building Code (CUBiC), Part 2, section 2: Structural design requirements wind load. Caribbean Community Secretariat, Georgetown, Guyana, 58 pp.

Emanuel, K. A., 1988: The maximum intensity of hurricanes. *J. Atmos. Sci.*, **45,** 1143–1155.

Georgiou, P. N., 1985: Design windspeeds in tropical cyclone-prone regions. Ph.D. thesis, Faculty of Engineering Science, University of Western Ontario, 295 pp.

Ho, F. P., J. C. Su, K. L. Hanavich, R. J. Smith, and F. P. Richards, 1987: Hurricane climatology for the Atlantic and Gulf Coasts of the United States. NOAA Tech. Rep. NWS38, Federal Emergency Management Agency, Washington, DC, 195 pp.

Holland, G. J., 1980: An analytical model of the wind and pressure profiles in hurricanes. *Mon. Wea. Rev.*, **108,** 1212–1218.

James, M. K., and L. B. Mason, 2005: Synthetic tropical cyclone database. *J. Waterw. Port Coastal Ocean Eng.*, **131,** 181–192.

Jarvinen, B. R., C. J. Neumann, and M. A. S. Davis, 1984: A tropical cyclone data tape for the North Atlantic Basin 1886-1983: Contents, limitations and uses. NOAA Tech. Memo. NWS NHC 22, U.S. Department of Commerce, 21 pp.

Lee, K. H., and D. V. Rosowsky, 2007: Synthetic hurricane wind speed records: Development of a database for hazard analyses and risk studies. *Nat. Hazards Rev.*, **8,** 23–34.

Myers, V. A., and E. E. Jordan, 1956: Wind and pressure over the sea in the hurricane of September 1938. *Mon. Wea. Rev.*, **84,** 261–270.

Powell, M. D., S. H. Houston, L. R. Amat, and N. Morisseau-Leroy, 1998: The HRD real-time hurricane wind analysis system. *J. Wind Eng. Ind. Aerodyn.*, **77-78,** 53–64.

——, G. Soukup, S. Cocke, S. Gulati, N. Morisseau-Leroy, S. Hamid, N. Dorst, and L. Axe, 2005: State of Florida hurricane loss prediction model: Atmospheric science component. *J. Wind Eng. Ind. Aerodyn.*, **93,** 651–674.

Standards Association of Australia, 1989: Loading code, Part 2—Wind forces. SAA Rep. AS1170, Sydney, Australia, 96 pp.

Thompson, E. F., and V. J. Cardone, 1996: Practical modeling of hurricane surface wind fields. *J. Waterw. Port Coastal Ocean Eng.*, **122,** 195–205.

Vickery, P. J., 2005: Simple empirical models for estimating the increase in the central pressure of tropical cyclones after landfall along the coastline of the United States. *J. Appl. Meteor.*, **44,** 1807–1826.

——, and L. A. Twisdale Jr., 1995: Prediction of hurricane wind speeds in the United States. *J. Struct. Eng.*, **121,** 1691–1699.

——, P. F. Skerlj, A. C. Steckley, and L. A. Twisdale, 2000: Hurricane wind field model for use in hurricane simulations. *J. Struct. Eng.*, **126,** 1203–1221.

——, ——, J. X. Lin, L. A. Twisdale Jr., M. A. Young, and F. M. Lavelle, 2006: The HAZUS-MH hurricane model methodology part II: Damage and loss estimation. *Nat. Hazards Rev.*, **7,** 82–93.

——, D. Wadhera, M. D. Powell, and Y. Chen, 2008: A hurricane boundary layer and wind field model for use in engineering applications. *J. Appl. Meteor.*, in press.

Willoughby, H. E., and M. B. Chelmow, 1982: Objective determination of hurricane tracks from aircraft observations. *Mon. Wea. Rev.*, **110,** 1298–1305.

——, and M. E. Rahn, 2004: Parametric representation of the primary hurricane vortex. Part I: Observations and evaluation of the Holland (1980) model. *Mon. Wea. Rev.*, **132,** 3033–3048.

——, R. W. R. Darling, and M. E. Rahn, 2006: Parametric representation of the primary hurricane vortex. Part II: A new family of sectional continuous profiles. *Mon. Wea. Rev.*, **134,** 1102–1120.

24. Assignment 2, Module 4: NHC Terms: https://www.nhc.noaa.gov/aboutgloss.shtml

Glossary of NHC Terms

See also: NWS Glossary

Jump to: a - b - c - d - e - f - g - h - i - j - k - l - m - n - o - p - q - r - s - t - u - v - w - x - y - z

Advisory:
Official information issued by tropical cyclone warning centers describing all tropical cyclone watches and warnings in effect along with details concerning tropical cyclone locations, intensity and movement, and precautions that should be taken. Advisories are also issued to describe: (a) tropical cyclones prior to issuance of watches and warnings and (b) subtropical cyclones.

Best Track:
A subjectively-smoothed representation of a tropical cyclone's location, intensity, type, and size over its lifetime. The best track contains the cyclone's latitude, longitude, maximum sustained surface winds, minimum sea-level pressure, stage (e.g., tropical, extratropical, remnant low, etc.), and size (e.g., radius of maximum winds, hurricane-force winds, 50-kt winds, and tropical storm-force winds) at 6-hourly intervals and at landfall for tropical storms and hurricanes. These best track attributes, based on a post-storm assessment of all available data, may differ from values contained in system advisories. The best track locations also generally will not reflect the erratic motion implied by connecting individual center fix positions.

Center:
Generally speaking, the vertical axis of a tropical cyclone, usually defined by the location of minimum wind or minimum pressure. The cyclone center position can vary with altitude. In advisory products, refers to the center position at the surface.

Center / Vortex Fix:
The location of the center of a tropical or subtropical cyclone obtained by reconnaissance aircraft penetration, satellite, radar, or synoptic data.

Central Dense Overcast:
A dense mass of clouds that covers the eyewall or the most tightly curved inner bands of a tropical cyclone.

Central North Pacific Basin:
The region north of the Equator between 140W and the International Dateline. The Central Pacific Hurricane Center (CPHC) in Honolulu, Hawaii is responsible for tracking tropical cyclones in this region.

Cyclone:
An atmospheric closed circulation rotating counter-clockwise in the Northern Hemisphere and clockwise in the Southern Hemisphere.

Direct Hit:
A close approach of a tropical cyclone to a particular location. For locations on the left-hand side of a tropical cyclone's track (looking in the direction of motion), a direct hit occurs when the cyclone passes to within a distance equal to the cyclone's radius of maximum wind. For locations on the right-hand side of the track, a direct hit occurs when the cyclone passes to within a distance equal to twice the radius of maximum wind. Compare indirect hit, strike.

Eastern North Pacific Basin:
The portion of the North Pacific Ocean east of 140W. The National Hurricane Center in Miami, Florida is responsible for tracking tropical cyclones in this region.

Eye:
The roughly circular area of comparatively light winds that encompasses the center of a severe tropical cyclone. The eye is either completely or partially surrounded by the eyewall cloud.

Eyewall / Wall Cloud:
An organized band or ring of cumulonimbus clouds that surround the eye, or light-wind center of a tropical cyclone. Eyewall and wall cloud are used synonymously.

Extratropical:
A term used in advisories and tropical summaries to indicate that a cyclone has lost its "tropical" characteristics. The term implies both poleward displacement of the cyclone and the conversion of the cyclone's primary energy source from the release of latent heat of condensation to baroclinic (the temperature contrast between warm and cold air masses) processes. It is important to note that cyclones can become extratropical and still retain winds of hurricane or tropical storm force.

Extratropical Cyclone:
A cyclone of any intensity for which the primary energy source is baroclinic, that is, results from the temperature contrast between warm and cold air masses.

Fujiwhara Effect:
The tendency of two nearby tropical cyclones to rotate cyclonically about each other.

Gale Warning:
A warning of 1-minute sustained surface winds in the range 34 kt (39 mph or 63 km/hr) to 47 kt (54 mph or 87 km/hr) inclusive, either predicted or occurring and not directly associated with tropical cyclones.

High Wind Warning:
A high wind warning is defined as 1-minute average surface winds of 35 kt (40 mph or 64 km/hr) or greater lasting for 1 hour or longer, or winds gusting to 50 kt (58 mph or 93 km/hr) or greater regardless of duration that are either expected or observed over land.

Hurricane / Typhoon:
A tropical cyclone in which the maximum sustained surface wind (using the U.S. 1-minute average) is 64 kt (74 mph or 119 km/hr) or more. The term hurricane is used for Northern Hemisphere tropical cyclones east of the International Dateline to the Greenwich Meridian. The term typhoon is used for Pacific tropical cyclones north of the Equator west of the International Dateline.

Hurricane Local Statement:
A public release prepared by local National Weather Service offices in or near a threatened area giving specific details for its county/parish warning area on (1) weather conditions, (2) evacuation decisions made by local officials, and (3) other precautions necessary to protect life and property.

Hurricane Season:
The portion of the year having a relatively high incidence of hurricanes. The hurricane season in the Atlantic, Caribbean, and Gulf of America runs from June 1 to November 30. The hurricane season in the Eastern Pacific basin runs from May 15 to November 30. The hurricane season in the Central Pacific basin runs from June 1 to November 30.

Hurricane Warning:
An announcement that sustained winds of 64 knots (74 mph or 119 km/hr) or higher are *expected* somewhere within the specified area in association with a tropical, subtropical, or post-tropical cyclone. Because hurricane preparedness activities become difficult once winds reach tropical storm force, the warning is issued 36 hours in advance of the anticipated onset of tropical-storm-force winds. The warning can remain in effect when dangerously high water or a combination of dangerously high water and waves continue, even though winds may be less than hurricane force.

Hurricane Watch:
An announcement that sustained winds of 64 knots (74 mph or 119 km/hr) or higher are *possible* within the specified area in association with a tropical, subtropical, or post-tropical cyclone. Because hurricane preparedness activities become difficult once winds reach tropical storm force, the hurricane watch is issued 48 hours in advance of the anticipated onset of tropical storm force winds.

Indirect Hit:
Generally refers to locations that do not experience a direct hit from a tropical cyclone, but do experience hurricane force winds (either sustained or gusts) or tides of at least 4 feet above normal.

Inter-Tropical Convergence Zone:
A zonally elongated axis of surface wind confluence of northeasterly and southeasterly trade winds in the tropics.

Invest:
A weather system for which a tropical cyclone forecast center (NHC, CPHC, or JTWC) is interested in collecting specialized data sets (e.g., microwave imagery) and/or running model guidance. Once a system has been designated as an invest, data collection and processing is initiated on a number of government and academic web sites, including the Naval Research Laboratory (NRL) and the University of Wisconsin Cooperative Institute for Meteorological Satellite Studies (UW-CIMSS). The designation of a system as an invest does not correspond to any particular likelihood of development of the system into a tropical cyclone; operational products such as the Tropical Weather Outlook or the JTWC/TCFA should be consulted for this purpose.

Inundation:
The flooding of normally dry land, primarily caused by severe weather events along the coasts, estuaries, and adjoining rivers. These storms, which include hurricanes and nor'easters, bring strong winds and heavy rains. The winds drive large waves and storm surge on shore, and heavy rains raise rivers. (A tsunami — a giant wave caused by earthquakes or volcanic eruptions under the sea or landslides into the sea — is another kind of coastal inundation, but should not be confused with storm surge.)

Landfall:
The intersection of the surface center of a tropical cyclone with a coastline. Because the strongest winds in a tropical cyclone are not located precisely at the center, it is possible for a cyclone's strongest winds to be experienced over land even if landfall does not occur. Similarly, it is possible for a tropical cyclone to make landfall and have its strongest winds remain over the water. Compare direct hit, indirect hit, and strike.

Major Hurricane:
A hurricane that is classified as Category 3 or higher.

Maximum Sustained Surface Wind:
The standard measure of a tropical cyclone's intensity. When the term is applied to a particular weather system, it refers to the highest one-minute average wind (at an elevation of 10 meters with an unobstructed exposure) associated with that weather system at a particular point in time.

Monsoon:
A large-scale, seasonally-reversing surface wind circulation in the tropics accompanied by large amplitude seasonal changes in precipitation.

Monsoon Trough:
A surface trough in association with a monsoon circulation. This is depicted by a line on a weather map showing the location of minimum sea level pressure coinciding with the maximum cyclonic turning of the surface winds, with southwesterly or northwesterly flow prevailing equatorward and northeasterly flow prevailing poleward of the typically zonally oriented trough axis.

National Geodetic Vertical Datum of 1929 [NGVD 1929]:
A fixed reference adopted as a standard geodetic datum for elevations determined by leveling. The datum was derived for surveys from a general adjustment of the first-order leveling nets of both the United States and Canada. In the adjustment, mean sea level was held fixed as observed at 21 tide stations in the United States and 5 in Canada. The year indicates the time of the general adjustment. A synonym for Sea-level Datum of 1929. The geodetic datum is fixed and does not take into account the changing stands of sea level. Because there are many variables affecting sea level, and because the geodetic datum represents a best fit over a broad area, the relationship between the geodetic datum and local mean sea level is not consistent from one location to another in either time or space. For this reason, the National Geodetic Vertical Datum should not be confused with mean sea level.

Post-storm Report:
A report issued by a local National Weather Service office summarizing the impact of a tropical cyclone on its forecast area. These reports include information on observed winds, pressures, storm surges, rainfall, tornadoes, damage and casualties.

Post-tropical Cyclone:
A former tropical cyclone. This generic term describes a cyclone that no longer possesses sufficient tropical characteristics to be considered a tropical cyclone. Post-tropical cyclones can continue carrying heavy rains and high winds. Note that former tropical cyclones that have become fully extratropical...as well as remnant lows...are two classes of post-tropical cyclones.

Potential Tropical Cyclone:
A term used in NWS advisory products to describe a disturbance that is not yet a tropical cyclone, but which poses the threat of bringing tropical storm or hurricane conditions to land areas within 72 hours.

Preliminary Report:
Now known as the "Tropical Cyclone Report". A report summarizing the life history and effects of an Atlantic or eastern Pacific tropical cyclone. It contains a summary of the cyclone life cycle and pertinent meteorological data, including the post-analysis best track (six-hourly positions and intensities) and other meteorological statistics. It also contains a description of damage and casualties the system produced, as well as information on forecasts and warnings associated with the cyclone. NHC writes a report on every tropical cyclone in its area of responsibility.

Present Movement:
The best estimate of the movement of the center of a tropical cyclone at a given time and given position. This estimate does not reflect the short-period, small scale oscillations of the cyclone center.

Radius of Maximum Winds:
The distance from the center of a tropical cyclone to the location of the cyclone's maximum winds. In well-developed hurricanes, the radius of maximum winds is generally found at the inner edge of the eyewall.

Rapid Intensification:
An increase in the maximum sustained winds of a tropical cyclone of at least 30 kt in a 24-h period.

Relocated:
A term used in an advisory to indicate that a vector drawn from the preceding advisory position to the latest known position is not necessarily a reasonable representation of the cyclone's movement.

Remnant Low:
A post-tropical cyclone that no longer possesses the convective organization required of a tropical cyclone...and has maximum sustained winds of less than 34 knots. The term is most commonly applied to the nearly deep-convection-free swirls of stratocumulus in the eastern North Pacific.

Saffir-Simpson Hurricane Wind Scale:
The Saffir-Simpson Hurricane Wind Scale is a 1 to 5 categorization based on the hurricane's intensity at the indicated time. The scale provides examples of the type of damage and impacts in the United States associated with winds of the indicated intensity. The following table shows the scale broken down by winds:

Category	Wind Speed (mph)	Damage
1	74 - 95	Very dangerous winds will produce some damage
2	96 - 110	Extremely dangerous winds will cause extensive damage
3	111 - 129	Devastating damage will occur
4	130 - 156	Catastrophic damage will occur
5	> 156	Catastrophic damage will occur

A detailed description of the Saffir-Simpson Hurricane Wind Scale is available at http://www.nhc.noaa.gov/aboutsshws.php.

Storm Surge:
An abnormal rise in sea level accompanying a hurricane or other intense storm, and whose height is the difference between the observed level of the sea surface and the level that would have occurred in the absence of the cyclone. Storm surge is usually estimated by subtracting the normal or astronomic high tide from the observed storm tide.

Storm Surge Warning:
The danger of life-threatening inundation from rising water moving inland from the shoreline somewhere within the specified area, generally within 36 hours, in association with an ongoing or potential tropical cyclones, a subtropical cyclone or a post-tropical cyclone. The warning may be issued earlier when other conditions, such as the onset of tropical-storm-force winds are expected to limit the time available to take protective actions for surge (e.g., evacuations). The warning may also be issued for locations not expected to receive life-threatening inundation but which could potentially be isolated by inundation in adjacent areas.

Storm Surge Watch:
The possibility of life-threatening inundation from rising water moving inland from the shoreline somewhere within the specified area, generally within 48 hours, in association with an ongoing or potential tropical cyclones, a subtropical cyclone or a post-tropical cyclone. The watch may be issued earlier when other conditions, such as the onset of tropical-storm-force winds are expected to limit the time available to take protective actions for surge (e.g., evacuations). The warning may also be issued for locations not expected to receive life-threatening inundation but which could potentially be isolated by inundation in adjacent areas.

Storm Tide:
The actual level of sea water resulting from the astronomic tide combined with the storm surge.

Storm Warning:
A warning of 1-minute sustained surface winds of 48 kt (55 mph or 88 km/hr) or greater, either predicted or occurring, not directly associated with tropical cyclones.

Strike:
For any particular location, a hurricane strike occurs if that location passes within the hurricane's strike circle, a circle of 125 n mi diameter, centered 12.5 n mi to the right of the hurricane center (looking in the direction of motion). This circle is meant to depict the typical extent of hurricane force winds, which are approximately 75 n mi to the right of the center and 50 n mi to the left.

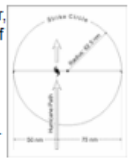

Subtropical Cyclone:
A non-frontal low-pressure system that has characteristics of both tropical and extratropical cyclones. Like tropical cyclones, they are non-frontal, synoptic-scale cyclones that originate over tropical or subtropical waters, and have a closed surface wind circulation about a well-defined center. In addition, they have organized moderate to deep convection, but lack a central dense overcast. Unlike tropical cyclones, subtropical cyclones derive a significant proportion of their energy from baroclinic sources, and are generally cold-core in the upper troposphere, often being associated with an upper-level low or trough. In comparison to tropical cyclones, these systems generally have a radius of maximum winds occurring relatively far from the center (usually greater than 60 n mi), and generally have a less symmetric wind field and distribution of convection.

Subtropical Depression:
A subtropical cyclone in which the maximum sustained surface wind speed (using the U.S. 1-minute average) is 33 kt (38 mph or 62 km/hr) or less.

Subtropical Storm:
A subtropical cyclone in which the maximum sustained surface wind speed (using the U.S. 1-minute average) is 34 kt (39 mph or 63 km/hr) or more.

Synoptic Track:
Weather reconnaissance mission flown to provide vital meteorological information in data sparse ocean areas as a supplement to existing surface, radar, and satellite data. Synoptic flights better define the upper atmosphere and aid in the prediction of tropical cyclone development and movement.

Tropical Cyclone:
A warm-core non-frontal synoptic-scale cyclone, originating over tropical or subtropical waters, with organized deep convection and a closed surface wind circulation about a well-defined center. Once formed, a tropical cyclone is maintained by the extraction of heat energy from the ocean at high temperature and heat export at the low temperatures of the upper troposphere. In this they differ from extratropical cyclones, which derive their energy from horizontal temperature contrasts in the atmosphere (baroclinic effects).

Tropical Cyclone Plan of the Day:
A coordinated mission plan that tasks operational weather reconnaissance requirements during the next 1100 to 1100 UTC day or as required, describes reconnaissance flights committed to satisfy both operational and research requirements, and identifies possible reconnaissance requirements for the succeeding 24-hour period.

Tropical Depression:
A tropical cyclone in which the maximum sustained surface wind speed (using the U.S. 1-minute average) is 33 kt (38 mph or 62 km/hr) or less.

Tropical Disturbance:
A discrete tropical weather system of apparently organized convection -- generally 100 to 300 nmi in diameter -- originating in the tropics or subtropics, having a nonfrontal migratory character, and maintaining its identity for 24 hours or more. It may or may not be associated with a detectable perturbation of the wind field.

Tropical Storm:
A tropical cyclone in which the maximum sustained surface wind speed (using the U.S. 1-minute average) ranges from 34 kt (39 mph or 63 km/hr) to 63 kt (73 mph or 118 km/hr).

Tropical Storm Warning:
An announcement that sustained winds of 34 to 63 knots (39 to 73 mph or 63 to 118 km/hr) are *expected* somewhere within the specified area within 36 hours in association with a tropical, subtropical, or post-tropical cyclone.

Tropical Storm Watch:
An announcement that sustained winds of 34 to 63 knots (39 to 73 mph or 63 to 118 km/hr) are *possible* within the specified area within 48 hours in association with a tropical, subtropical, or post-tropical cyclone.

Tropical Wave:
A trough or cyclonic curvature maximum in the trade-wind easterlies. The wave may reach maximum amplitude in the lower middle troposphere.

25. Assignment 2, Module 4: Guidelines for Converting Winds: https://library.wmo.int/viewer/48652/download?file=wmo-td_1555_en.pdf&type=pdf&navigator=1

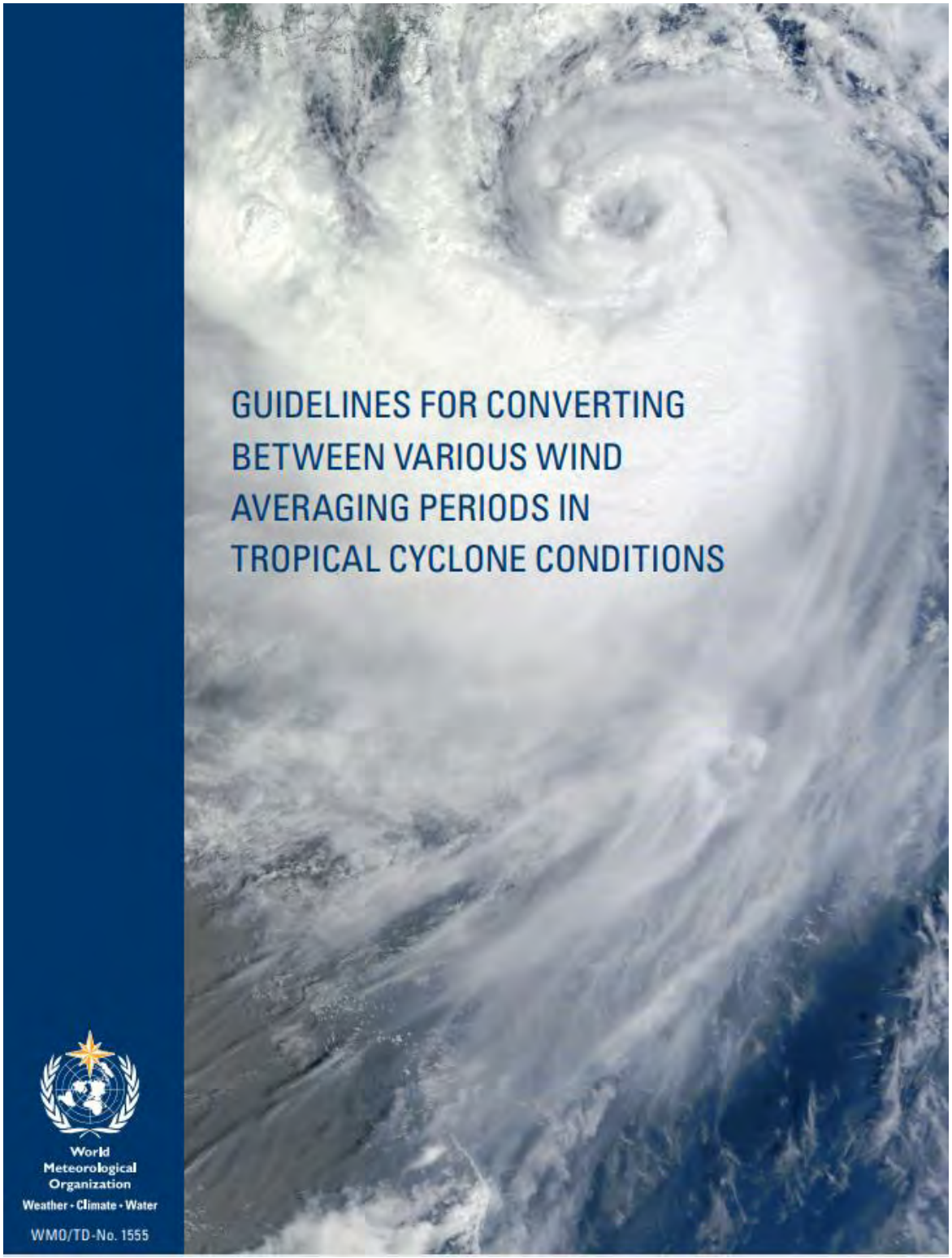

GUIDELINES FOR CONVERTING BETWEEN VARIOUS WIND AVERAGING PERIODS IN TROPICAL CYCLONE CONDITIONS

by

B. A. Harper[1], J. D. Kepert[2] and J. D. Ginger[3]

August 2010

[1]BE (Hons), PhD (James Cook), Systems Engineering Australia Pty Ltd, Brisbane, Australia.
[2]BSc (Hons) (Western Australia), MSc, PhD (Monash), Bureau of Meteorology, Centre for Australian Weather and Climate Research, Melbourne, Australia.
[3]BSc Eng (Peradeniya-Sri Lanka), MEngSc (Monash), PhD (Queensland), Cyclone Testing Station, James Cook University, Townsville, Australia.

Chairperson, Publications Board
World Meteorological Organization (WMO)
7 bis, avenue de la Paix
P.O. Box 2300
CH-1211 Geneva 2, Switzerland

Tel.: +41 (0) 22 730 84 03
Fax: +41 (0) 22 730 80 40
E-mail: Publications@wmo.int

Acknowledgements:

The authors wish to thank Woodside Energy Ltd (Stan Stroud) and its project participants for permission to present detailed Tropical Cyclone *Orson* wind data, the photograph of North Rankin 'A' and to quote example wind gust factor results. The Tropical Cyclone *Orson* track plot is shown courtesy Australian Bureau of Meteorology. Thanks also to John Holmes (JDH Consulting) for valuable suggestions.

Detailed comments on an earlier version of this report by Peter Black (NOAA/HRD), James Franklin (NOAA/NHC), Chris Letchford (TTU), Craig Miller (UWO) and Mark Powell (NOAA/HRD) were important in improving the study and are gratefully acknowledged.

Comments received from three WMO-appointed reviewers were also valuable in finalising the document.

Contents

Appendices

Tables

Figures

Executive Summary

This report documents the basis of recommendations for converting between wind speeds having different time averaging periods under tropical cyclone conditions. The report was commissioned in response to a request arising from the Fourth Tropical Cyclone RSMC's Technical Coordination Meeting in Nadi (Fiji), November 2002. Accordingly, a review has been undertaken of past and contemporary theory and data relevant to the issue of wind averaging periods and conversions under tropical cyclone conditions both over the open ocean and in coastal situations. The important physical and statistical aspects of the problem are identified and an example from a severe tropical cyclone is used to demonstrate the practical manifestation of those matters.

It is concluded that the accurate measurement of wind speed fluctuations, especially under tropical cyclone conditions, is a difficult and demanding activity that will always result in scatter from even the most careful analyses, and the available data and some theories show many inconsistencies. Clearly there are still significant gaps in our understanding of atmospheric turbulence characteristics under strong wind conditions. However, because the forecasting of tropical cyclones is an already difficult task, a simplified approach has been recommended that should nevertheless lead to an increase in consistency of quoted and forecast winds. An existing mathematical model of wind over-land in extra-tropical conditions has been adapted for this purpose and nominally calibrated against a wide range of assembled tropical cyclone data. The recommended procedure is seen as a practical interim solution until such time as increased data collection and analysis provides a more definitive description of the near-surface wind turbulent energy spectrum in various situations under tropical cyclone conditions.

The review has specifically highlighted the need to distinguish clearly between randomly sampled estimates of the mean wind speed based on any chosen averaging period and the peak gust wind speed of a given duration within a particular observation period. It is particularly noted that mean wind speed estimates should not be converted between different averaging periods using gust factors – only gust wind speeds.

Differences between the recommended conversion factors specified here and those previously specified in the WMO (1993) Global Guide are reasonably significant in a number of ways. Firstly, the present analysis considers a wider range of averaging periods and exposures, focusing on cases of specific concern for tropical cyclone forecasting. Secondly, the magnitudes of the equivalent conversion factors are different from those in the present Global Guide. Also, converting between agency estimates of storm-wide maximum wind speed (*Vmax*) is seen to require special considerations and the recommendation provided here is necessarily a function of the exposure. Accordingly, the review recommends an at-sea conversion between the so-called 1-min "sustained" estimate of peak storm intensity and the 10-min average wind speed estimate of 0.93, rather than the "traditional" value of 0.88, which has been shown here to be associated more with an off-land exposure. This implies that current practice has underestimated the at-sea 10-min average *Vmax* by about 5%, relative to an equivalent 1-min value. However, it is also strongly recommended that the "Dvorak-related" intensity estimation techniques be re-calibrated based on a more rigorous and consistent treatment of wind-averaging issues.

It is recommended that the WMO regional associations and panels work towards revising and standardising their wind terminology, definitions and associated use of averaging periods in the various operational plans and in accordance with WMO (2008). This will assist in ensuring that the historical record contains more consistent measurements and/or estimates that can be reliably transformed or converted for assisting in further development of the science.

The continued expansion and improvement of quality automatic weather station (AWS) surface networks and research-standard specialist facilities is strongly encouraged in order to gather the necessary information for future reviews.

1 Introduction

This guideline has been prepared to provide a technical reference for best practice application of wind averaging conversion factors under tropical cyclone conditions. This issue arose from an IWTC-IV recommendation in 1998 (4th International Workshop on Tropical Cyclones) and a Working Group was formed at the Fourth Tropical Cyclone Regional Specialised Meteorological Centre's (RSMC) Technical Coordination Meeting in Nadi (Fiji), November 2002, to coordinate the present study. It is expected that the recommendations here will be incorporated into an update of the Global Guide for Tropical Cyclone Forecasting (WMO 1993) scheduled for 2010.

1.1 Scope

The present study scope[1] was to: *Undertake reviews and assessments leading to the recommendation of suitable conversion factors between the WMO over-water +10 m standard 10 min average wind and 1 min, 2 min and 3 min "sustained" winds in tropical cyclone conditions.*

The study does not consider matters relating to the choice of wind speed thresholds used by various agencies when defining tropical cyclone intensities, nor does it consider the vertical structure of the wind within tropical cyclones, other than where such structure is especially relevant to the issue of wind speed conversion factors. However, some agency-specific definitions and usage are discussed within the context of a desire for increased standardisation of nomenclature and technical clarity. In support of this, Appendix A provides a summary of existing practice as documented in the five WMO tropical cyclone regional associations.

1.2 Approach

The report firstly addresses the theoretical background to a simple statistical model of the near-surface wind environment. This provides a review of the fundamental issues needing consideration, leading then to the specific case of tropical cyclones. The development is supported by reference to numerous case studies and an example tropical cyclone wind dataset is included to assist in practical application. Only basic mathematical developments have been included and the interested reader is referred to the relevant texts for further detail.

Using a variety of existing methods and data, recommendations are then made as to the appropriate method to be used for deriving wind averaging conversion factors for tropical cyclone conditions. The aim has been to provide a broad-brush guidance that will be most useful to the forecast environment rather than a detailed analytical methodology. Notwithstanding this, accurate wind prediction and measurement under all conditions (not just tropical cyclones) is a very difficult and challenging problem that requires careful consideration of a number of important matters. It is therefore not the intention of this review to discourage in any way the positive and increasing move towards better and more extensive insitu measurement of tropical cyclone winds in all types of environments. In particular, post analysis of tropical cyclone events should seek to use the highest possible site-specific analytical accuracy for estimating local wind speeds. This would include consideration of local surface roughness, exposure and topographic effects when undertaking quantitative assessments of storm impacts.

An extensive bibliography on the subject of wind measurement and conversion is included to assist with future research efforts. For the interested reader, Appendix B provides an overview of the historical development of scientific studies of the wind with special reference to tropical cyclones.

[1] While the study scope did not specifically address the issue of near-instantaneous wind "gusts", the authors considered it necessary to include the full range of wind variability in the assessment. Also, the scope was later extended by the client in requesting some nominal "in-land" exposure guidance.

1.3 Wind Averaging Conventions and Gust Factors

The WMO standard for estimating the mean wind is the 10-min average. This has the advantage of averaging over a period that is typically sufficiently long to incorporate most of the shorter period fluctuations in natural wind (turbulence) but is sufficiently short to be normally regarded as representing a period of near-constant background mean wind. Dobson (1981), for example, provides background and a practical guide for marine conditions from the WMO perspective.

Although any period of time can be chosen for averaging the wind speed, shorter periods of averaging will typically produce more erratic values than the 10-min average. For example, ten 1-min averages taken during a 10-min period will produce values that lie both above and below the 10-min mean value. Any single 1-min random sample is an equally valid (unbiased) estimate of the mean wind but it is likely to be higher or lower than the true mean wind. Hence, while one estimate of the mean wind is (statistically) as good as another, in practice, mean winds measured over shorter periods will possess greater variance and will therefore be "less reliable". Alternatively, if there was no turbulence in the wind, then all averaging periods would yield the same true mean wind speed.

The practice of "converting" between wind speeds that are obtained from different wind averaging periods (e.g. 10-min, 1-min, 2-min, 3-min etc) is only applicable if the shorter averaging period wind is regarded as a "gust", i.e. the highest average wind speed of that duration within some longer period of observation. This results in a high-biased estimate of the mean wind. For example, while the 3-sec average is typically acknowledged as a "gust", this is only true if it is the highest 3-sec average within a period. If the 3-sec average is effectively a random sample, then it is an estimate of the true mean. The lowest 3-sec average is conversely a "lull" (low-biased). The "maximum 1-min sustained" wind, as used in some WMO regions, refers to the highest 1-min average within a period of observation and is therefore also a gust relative to the estimated mean wind over that same period. Even a 10-min average wind can be a gust if it is the highest 10-min average observed within, say an hour, assuming that the mean wind is constant over that one hour period. It is important that all wind speed values be correctly identified as a mean or a gust.

Hence, wind speed conversions to account for varying averaging periods are only applicable in the context of a maximum (gust) wind speed of a given duration observed within some longer interval. Furthermore, the conversions are always relative to the mean wind speed and only applicable if the wind flow is steady (or stationary). Accordingly, there is no basis for converting any estimate of the mean wind speed (based on randomly sampled 1-min, 2-min, 3-min, etc averages) to any other estimate of the mean wind speed (e.g. based on a 10-min average). Mean wind speed estimates cannot be converted as they are all equivalent measures of the true mean wind but with differing variance. Section 2 specifically addresses this issue. Simply measuring the wind for a shorter period at random will not ensure that it is always higher than the mean wind. Hence, a visually estimated wind, taken for practical reasons over a short period, is statistically equivalent to an instrumented measure over the same or a longer period. The mean wind estimate is therefore always of critical importance and should be based on the longest practical interval that can be regarded as stationary. In practice, the 10-min average generally satisfies this requirement. Once the mean wind is reliably measured or estimated, the effects of turbulence in typically producing higher but shorter-acting winds of greater significance for causing damage can be estimated using a "gust factor".

The "gust factor" is then a theoretical conversion between an estimate of the mean wind speed and the expected highest gust wind speed of a given duration within a stated observation period. In order for a gust factor to be representative, certain conditions must be met, many of which may not be exactly satisfied during a specific weather event or at a specific location. Hence, isolated comparisons of measured mean winds and their associated gusts may show differences from the theoretical values. Theoretical gust factors are applicable only in a statistical sense and the semi-empirical theories available are based on many sets of observations. However, theoretical gust

factors are still extremely useful for making forecasts of the most likely gust wind speed that will accompany the forecast mean wind speed within a specific period of observation, and at the same height above the surface. From the observational perspective, the aim is to process measurements of the wind so as to extract an estimate of the mean wind and its turbulence properties. From the forecasting viewpoint, the aim is, given a specific wind speed metric derived from a process or product, to usefully predict other metrics of the wind.

There are two specific assumptions that apply for the theoretical estimation of gust factors:

(a) Turbulent Flow with a Steady Mean Wind Speed

If the mean wind is not steady within the period of the observation, then the observed gust is likely to deviate from the expected gust obtained from the statistical theory. In fact, if the mean wind trends either upward or downward during the period, then the observed gust is likely to yield a gust factor higher than predicted by theory. Non-steadiness in the mean wind over the observation period is one typical reason why there will likely be scatter in observed gust factors during actual events. In statistical terms we require the wind record to be "stationary".

(b) Constant Surface Features

The statistical theory of gust factors assumes that the turbulent boundary layer is in equilibrium with the underlying surface roughness. This equilibrium assumption requires an extended constant roughness fetch for many kilometres and so if there are varying roughness conditions on a fetch, or if the direction of winds is changing during the observation period, then this will also potentially alter the expected gust factors. Likewise wind gusts measured on hills and slopes are likely to deviate from the theory.

Also, as gust factors are normally expected to increase towards the surface as a result of increasing mixing, the nominated factor is only applicable between the mean wind speed and the gust wind speed at the same height (e.g. +10 m) above the surface.

1.4 Recommended Procedure for Wind Speed Conversion

Wind speed conversions are possible only in the context of a maximum (gust) wind speed of a given duration observed within some longer interval, relative to the true mean wind speed. To ensure clarity in the description of wind speed, a nomenclature is introduced that will clearly describe and differentiate a gust from a mean, as follows:

It is proposed that an estimate of the true mean wind V should be explicitly identified by its averaging period T_o in seconds, described as V_{To}, e.g.

V_{600} is a 10-min averaged mean wind estimate;

V_{60} is a 1-min averaged mean wind estimate;

V_{3} is a 3-sec averaged mean wind estimate.

Likewise, it is proposed that a gust wind should be additionally prefixed by the gust averaging period τ and be described as $V_{\tau,To}$, e.g.

$V_{60,600}$ is the highest 1-min mean (gust) within a 10-min observation period;

$V_{3,60}$ is the highest 3-sec mean (gust) within a 1-min observation period.

The "gust factor" $G_{\tau,To}$ then relates as follows to the mean and the gust:

$$V_{\tau,To} = G_{\tau,To}\, V$$

where the true mean wind V is estimated on the basis of a suitable sample, e.g. V_{600} or V_{3600}.

On this basis, Table 1.1 provides the recommended near-surface (+10 m) conversion factors $G_{\tau,To}$ between different wind averaging periods, where the duration τ of the gust observation is referred to a base reference observation period T_o and there is an estimate available of the true mean wind V.

Table 1.1 Recommended wind speed conversion factors for tropical cyclone conditions.

Exposure at +10 m		Reference Period	Gust Factor $G_{\tau,To}$				
			Gust Duration τ (s)				
Class	Description	T_o (s)	3	60	120	180	600
In-Land	Roughly open terrain	3600	1.75	1.28	1.19	1.15	1.08
		600	1.66	1.21	1.12	1.09	1.00
		180	1.58	1.15	1.07	1.00	
		120	1.55	1.13	1.00		
		60	1.49	1.00			
Off-Land	Offshore winds at a coastline	3600	1.60	1.22	1.15	1.12	1.06
		600	1.52	1.16	1.09	1.06	1.00
		180	1.44	1.10	1.04	1.00	
		120	1.42	1.08	1.00		
		60	1.36	1.00			
Off-Sea	Onshore winds at a coastline	3600	1.45	1.17	1.11	1.09	1.05
		600	1.38	1.11	1.05	1.03	1.00
		180	1.31	1.05	1.00	1.00	
		120	1.28	1.03	1.00		
		60	1.23	1.00			
At-Sea	> 20 km offshore	3600	1.30	1.11	1.07	1.06	1.03
		600	1.23	1.05	1.02	1.00	1.00
		180	1.17	1.00	1.00	1.00	
		120	1.15	1.00	1.00		
		60	1.11	1.00			

Some example applications of the above recommendations (see also Harper et al. 2008) are as follows:

- To estimate the expected "off-land" 3-s peak gust in a 1-min period, multiply the estimated "off-land" mean wind speed by 1.36
- To estimate the expected "off-sea" 3-s peak gust in a 10-min period, multiply the estimated "off-sea" mean wind speed by 1.38
- To estimate an "at-sea" 1-min peak gust in a 10-min period, multiply the estimated "at-sea" mean wind speed by 1.05

Note that the above examples deliberately do not distinguish between estimates of the mean wind speed based on different durations of observation. Similarly, it is not possible to convert from a measured gust back to a specific time-averaged mean wind – only to the estimated true mean speed. Hence:

- To estimate the "off-sea" mean wind speed given only a peak observed gust of 1-min duration (τ = 60 s) measured in a 10-min period (T_o = 600 s), multiply the observed 1-min gust by (1/1.11) = 0.90

Also, it is not appropriate to use particular ratios of the $G_{\tau,To}$ values to infer relationships between different reference periods, e.g. $G_{3,600} / G_{3,60}$ is not equal to $G_{60,600}$. All conversions between gusts

must be referenced via the estimate of the applicable mean wind speed, which in stationary conditions does not depend upon the observation period.

1.5 Converting Between Agency Estimates of Storm Maximum Wind Speed

The concept of a storm-wide maximum wind speed *Vmax* is a metric of tropical cyclone intensity[2] used by all agencies and is often used to classify storms according to a simplified intensity scale (e.g. the Saffir-Simpson scale in the USA context). Such a metric conceptually has an associated spatial context (i.e. anywhere within or associated with the storm) and a temporal fix context (at this moment in time or during a specific period of time). While it may be expressed in terms of any wind averaging period it remains important that it be unambiguous in terms of representing a mean wind or a gust.

Because the development of tropical cyclone intensity estimation methodologies has been dominated by the Dvorak (1975, 1984) method and associated Atkinson and Holliday (1977) pressure-wind relationship for the past 30 years, the so-called maximum 1-min "sustained" wind has become the *de facto* standard in terms of obtaining an initial estimate of the storm maximum wind speed. Accordingly, agencies that prefer the standard 10-min averaged wind have traditionally applied a wind-averaging conversion (refer Appendix A) to reduce the maximum 1-min wind value. Leaving aside that Dvorak is silent on the issue of wind averaging and only refers to the "maximum wind speed" or MWS, Atkinson and Holliday (1977) does represent an intention to recommend a peak 1-min gust via the use of the Sissenwine et al. (1973) methodology, which is referenced to a 5-min observation period. Technically, this implies a gust wind speed of $V_{60,300}$. Recently the original analysis of the Atkinson and Holliday data has also been questioned (Harper 2002; Knaff and Zehr 2007), which relates to the overall accuracy of the wind speed estimates themselves.

Assuming that one is satisfied that the starting estimate of the storm maximum wind speed is accurate for the intended purposes, it may be converted to other wind speed metrics in accordance with the recommendations presented here. However, in practice this typically involves converting from the maximum 1-min "sustained" wind (a gust but without a stated observation period) to the highest 10-min wind speed in the storm. As noted in the previous section, it is technically not possible to convert from a gust back to a specific time-averaged mean wind – only to the estimated true mean speed. Accordingly, in Appendix E, a practical argument is made for nominal conversion between, for example, $Vmax_{60}$ and $Vmax_{600}$ values via the hourly mean wind speed reference, and the recommendations are summarised in Table 1.2. This approach should be regarded as an interim measure until a more robust and recoverable process is developed for estimating the storm maximum wind speed metric. It can be noted that the recommended conversion for at-sea exposure is about 5% higher than the "traditional" value of 0.88, which is seen to be more appropriate to an off-land exposure.

Table 1.2 Recommended conversion factors between agency estimates of maximum tropical cyclone wind speed *Vmax*.

$Vmax_{600}=K\ Vmax_{60}$	At-Sea	Off-Sea	Off-land	In-Land
K	0.93	0.90	0.87	0.84

[2] Existing practice seems to be that this metric is often subjectively assigned according to agency-specific interpretations. An assessment of those practices is outside of the present scope and the reader is referred to agency documentation.

1.6 The Impact of Modelled Winds and New Instrumentation

This study deals primarily with "conventionally" measured wind estimates from a fixed height near the surface. However, winds derived from numerical models, remote sensing instruments (SFMR, Doppler radar) and moving platforms (aircraft, GPS dropwindsondes) also need to be correctly assimilated into the framework of mean and turbulent components. While the detail of this is outside of the present scope it is noted that winds from numerical models, unless including an explicit eddy representation, should be regarded as mean wind estimates over space and time.

2 The Nature of the Near-Surface Wind

This chapter introduces the essential concepts of variability in the surface winds, explains the importance of the true mean wind and how to interpret and estimate winds that are obtained from different samplings of the mean wind over different periods of time.

2.1 The Mean Wind

While the term "wind speed" in common or colloquial use can occasionally be misused, it is generally accepted to be the *mean* or *average* wind, with reasonably widespread public recognition of, and respect for, the co-existence of the temporarily higher "gust" and lower "lull" winds. Additionally, only the longitudinal or along-wind component is normally acknowledged in the common-usage framework. However, in professional usage, it is well understood that the presence of turbulence over a range of time and space scales causes a degree of unsteadiness in any wind sample and, depending on how that is measured, the wind magnitude will present as a fluctuating time history. In addressing the basic concepts it is useful to consider only the longitudinal component and ignore for the moment that the fluctuating component is actually a vector quantity in the three independent spatial dimensions.

For the purpose of this review, it is assumed that the mean near-surface (< 100 m) wind speed V over land and sea in "strong" wind conditions (> 17 m s^{-1}) typical of tropical cyclones can be well approximated by an equilibrium form of the logarithmic boundary layer profile under neutral stability conditions (e.g. Lumley and Panofsky 1964, Powell et al. 2003):

$$V(z) = \frac{u_*}{k} \ln\left(\frac{z}{z_0}\right) \approx V_{To}(z) \qquad (1)$$

where V_{To} = the mean wind speed (m s^{-1}) averaged over a period of T_o (s)
u_* = a scale parameter, the so-called friction velocity (m s^{-1}) $= \sqrt{\tau_s / \rho_a}$
τ_s = the surface shear stress (N m^{-2})
ρ_a = air density (kg m^{-3})
k = von Karman's "constant" (≈ 0.41)
z_0 = a scale parameter, the representative surface roughness length (m)
z = elevation above land or mean sea level (m); for $z > z_0$
(this term is sometimes replaced by $(z - d)$ where d is a displacement height above a rough wall boundary layer such as a dense forest.)

The form of Eqn 1 is shown graphed in Figure 2.1 as the "mean wind". This is a steady-state simplification of the real condition that extensive observational and theoretical work has demonstrated to be a very good approximation under neutral stability conditions, suitable to enable development of a practical model of the near-surface wind. The theoretical basis is that the profile is formed and maintained by a process of frictional dissipation and mechanical mixing between the wind in the free atmosphere and the land or sea surface. The boundary layer is often subdivided into the surface or constant stress layer, in which the logarithmic profile applies, and the outer or mixed layer. Buoyancy forces in the surface layer are typically assumed negligible on the basis that the mechanical mixing in the strong winds typical of tropical cyclones is sufficiently vigorous to overcome density differences[3]. Also, convectively-driven phenomena such as downbursts or gust fronts and flow instabilities such as boundary layer rolls are excluded (a later section addresses the

[3] This remains a reasonable yet not wholly justifiable assumption that in time may be superceded as more near-surface data becomes available.

potential significance of this in the context of tropical cyclones). In particular, effective changes in actual surface roughness will vary continuously in many land environments due to directional wind shifts, and rarely be constant for more than a few kilometres. Although a constant upwind roughness domain (fetch) of many tens of kilometres is required to ensure that the profile is in equilibrium over its full height, response to roughness changes is achieved much more quickly at lower elevations, e.g. at the standard reference height of 10 m above ground level (AGL). Also, it is assumed here that the surface is essentially flat and that the flow is therefore free of topographic influences that would lead to local accelerations. Many texts describe procedures suitable for adequately adjusting the above theoretical wind profile for specific situations (e.g. Cook 1985; Wieringa 1986; ESDU 2002a,b; Holmes 2001; ANSI 1996; Verkaik 2000; Standards Australia 2002a; WMO 2008), which are essential when comparing readings between differently sited anemometers. Powell et al. (1996) provides specific advice in regard to landfalling tropical cyclone conditions.

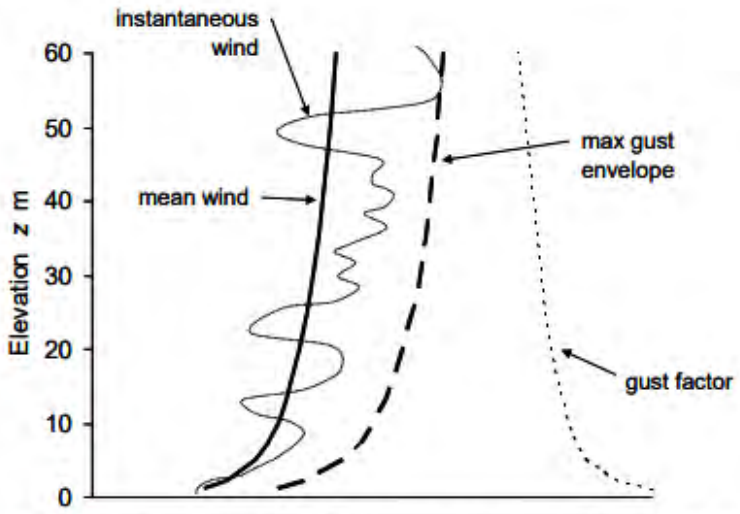

Figure 2.1 A traditional schematic view of the near-surface vertical profile of strong winds.

The application of Eqn 1 then requires the specification of u_* and z_o, which are used to scale the speed and the height respectively. In practice, u_* can be expressed in terms of a surface drag coefficient C_{10} referenced to the standard reference height of +10 m for neutral stability conditions, e.g.

$$C_{10} = \frac{\tau_s}{\rho_a V_{To}^2(10)} = \frac{u_*^2}{V_{To}^2(10)} \qquad \text{for large } T_o\text{, typically 10 min} \qquad (2)$$

Combining Eqn 1 and 2 allows u_* to be eliminated, leaving:

$$C(z) = \left[\frac{k}{\ln(z/z_o)}\right]^2 \qquad (3)$$

noting that the drag coefficient is a function of height.

To complete the above simplified model of the near surface wind we require an estimate of the surface roughness length z_o. In the case of winds over water, the surface roughness is clearly dependent on the wind speed, whereby ripples and then increasingly larger surface waves will be

generated, subject to depth, fetch and wave age considerations. The exact dependence of wind speed and the effective surface roughness over the ocean has been subject to much investigation (e.g. Large and Pond 1981, Fairall et al. 2003) but always limited by difficulties in obtaining reliable data, especially at high wind speeds typical of tropical cyclones. Notwithstanding significant advances in understanding and amassing of much improved data sets over the open ocean, the dimensionally-based Charnock (1955) hypothesis that was originally based on lake data is still widely applied, namely:

$$z_o = \frac{\alpha u_*^2}{g} \tag{4}$$

with α being an empirical coefficient derived from measurements, typically found to be in the range 0.01 to 0.03 (e.g. Garratt 1977). The drag coefficient determined by combining the Charnock relation with (3) is quite consistent with empirical estimates of the surface drag coefficient over the ocean, for example after Large and Pond (1981):

$$10^3\, C_{10} = 0.49 + 0.065\, V_{To}^2 \qquad \text{for} \quad 11\,\mathrm{m\,s^{-1}} \le V_{To} \le 26\,\mathrm{m\,s^{-1}} \tag{5}$$

However, there has long been speculation that under more extreme wind conditions the drag coefficient and the surface roughness may reach some type of limiting condition due to wave breaking, flow separation and the like. A number of recent studies present strong evidence for this effect, e.g. Powell et al. (2003) analysed GPS sonde data within hurricane eyewall regions, Donelan et al. (2004) undertook laboratory wind-wave experiments and French et al. (2007) performed direct flux measurements from low flying aircraft within hurricanes. The extent to which the surface waves themselves might modify the lower logarithmic surface layer remains open (e.g. Jansen 1989, Large et al. 1995) until more full scale data becomes available.

To illustrate the range of sea surface roughness descriptions that has emerged over time, Figure 2.2(a) presents surface drag coefficients and Figure 2.2(b) the equivalent roughness relationships. Garratt (1977), Large and Pond (1981), Andersen and Løvseth (1992) represent typical fixed-Charnock α forms that have been extrapolated here to higher wind speeds, while Fairall et al. (2003) incorporates a variable α. In contrast to these trends, the latest investigations targeting tropical cyclone conditions in the open ocean suggest significantly lower overall roughness values are applicable. In respect of conditions closer to land in shoaling wave environments it is likely that the roughness is greater, as suggested by Andersen and Løvseth (1992), but there has been little detailed analysis of wind-wave interaction in this environment.

The appropriate z_o for application over the ocean or on land therefore needs to be estimated for specific conditions, typically over space and time. On land, a number of guideline roughness classifications have been devised based on detailed site specific measurements and calibrations (e.g. Wieringa (1992) and Wieringa et al. (2001)). Table 2.1 presents a modified version of these that has been further interpreted here to describe features more likely in tropical cyclone regions and also made consistent with the oceanic conditions noted above.

In the developments and discussion that follow, attention is focused on the "smooth to open" classification over nearly flat land or coastal sea with a surface roughness length z_0 of nominally 0.03 m. This is almost universally acknowledged as "standard exposure" on the basis that the vast majority of all land wind measurements have been obtained from airports and it is also deemed representative of rough coastal seas (e.g. Standards Australia 2002a[4]; Vickery and Skerlj 2000). Also, only the standard reference height of +10 m is now considered. For conversion of the subsequent recommendations to other roughness regimes and elevations, the interested reader is referred to the nominated texts.

[4] The Australian/New Zealand wind loading standard uses 0.02 m but this is functionally similar.

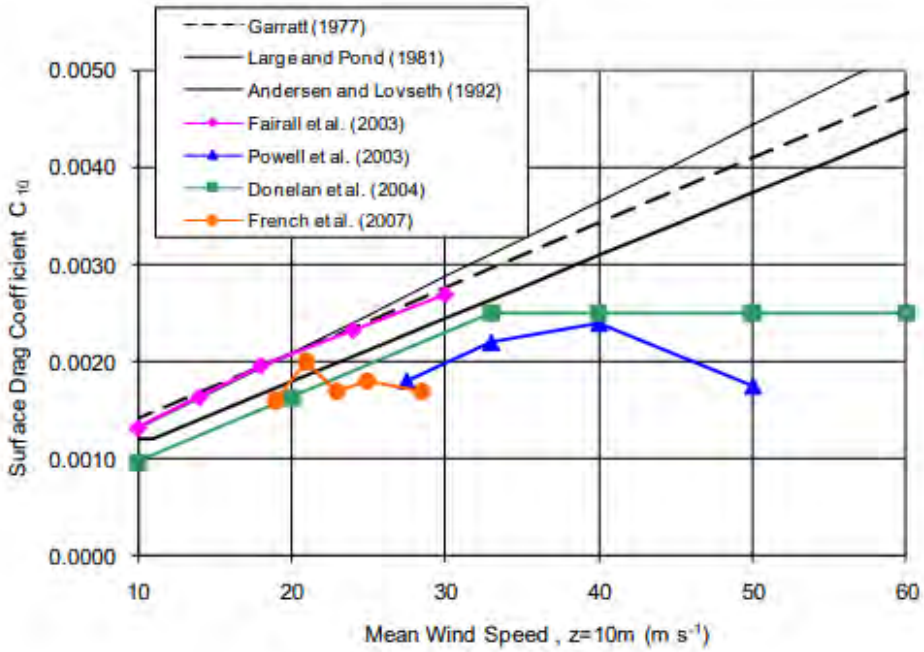

(a) Surface Drag Coefficient

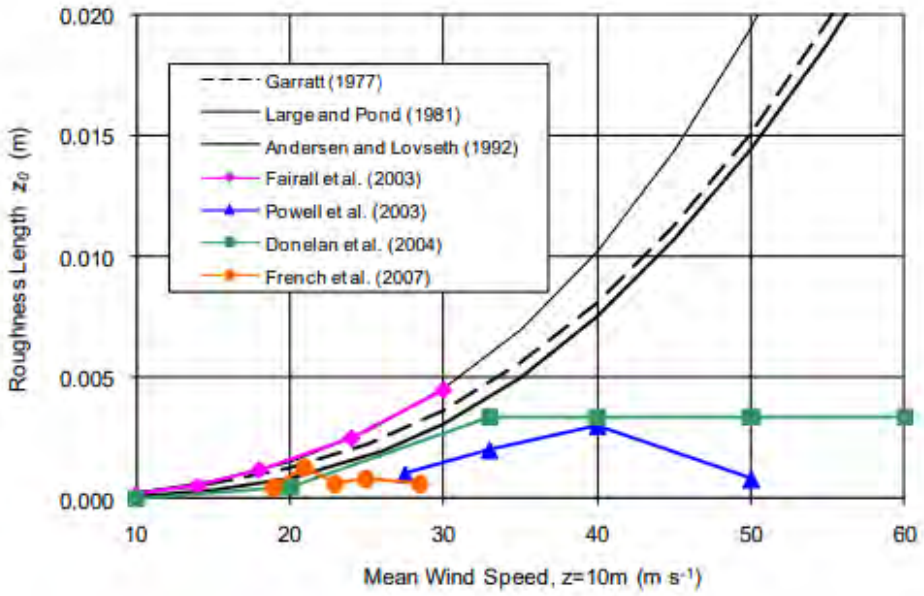

(b) Roughness Length

Figure 2.2 Example oceanic surface drag coefficients and roughness lengths.

Table 2.1 Representative terrain classes and roughness classifications for tropical cyclone applications (adapted from Wieringa et al. 2001).

Terrain Class	Terrain Description	Roughness Length z_0 (m)	Surface Drag Coefficient C_{10}
Sea	Open sea conditions for all wind speeds, exposed tidal flats, featureless desert, and tarmac.	0.0002 – 0.005	0.001 – 0.003
Smooth	Featureless land with negligible vegetation such as wide beaches and cays, exposed reefs.	0.005 – 0.03	0.003 – 0.005
Open	Nearshore water for winds > 30 m s^{-1}, level country with low grass, some isolated trees, airport surrounds.	0.03 – 0.10	0.005 – 0.008
Roughly Open	Low crops, few trees, occasional bushes.	0.10 – 0.25	0.008 – 0.012
Rough	Lightly wooded country, high crops, centres of small towns.	0.25 – 0.5	0.012 – 0.019
Very Rough	Mangrove forests, palm plantations, metropolitan areas.	0.5 – 1.0	0.019 – 0.032
Closed	Mature regular rainforests, inner city buildings (CBD).	1.0 – 2.0	0.032 – 0.065
Skimming	Mixture of large high and low-rise buildings, irregular large forests with many clearings.	> 2.0	> 0.065

2.2 Measuring the Mean Wind

Here, we briefly consider some of the statistical issues in measuring the mean wind. We assume that the actual wind is the sum of a mean wind and some turbulence, and the aim is to process measurements of the wind so as to extract an estimate of the mean wind. The emphasis is on issues associated with this averaging, rather than with the positioning and logging of anemometers, although these are of importance also. For simplicity, we assume that the instruments in use are free from systematic biases, or at least, that any such biases are removed.

To begin with, assume an ideal anemometer that provides instantaneous point measurement of the wind, and an unchanging synoptic situation. If the anemometer was interrogated at a suitable frequency and these data collected over some period, then their mean over that averaging period could be calculated. Assuming that the wind sampled during the averaging period was effectively a random sample, then the sample mean would be an unbiased estimate of the true mean wind at that point. "Unbiased" is meant in the statistical sense; that is, the expected value of the sample mean is equal to the true mean. In practice, a random sample can be achieved by choosing the averaging period before the measurements are taken; e.g. the last 5 minutes of the hour.

The finite sample implies that there is inevitably a degree of uncertainty in the sample mean. The variance of the sample mean is (Lumley and Panofsky 1964):

$$\sigma_{\bar{u}}^2 = 2\sigma_u^2 \frac{T_u}{T_o} \tag{6}$$

where σ_u is the wind variance, T_u is the integral time scale for that wind component, and T_o is the averaging period. Turbulence is correlated in space and time, so increasing the frequency of measurement does not result in a proportional increase in the amount of independent information. The spatial and temporal correlation scales of turbulence may be measured by the turbulence integral length and time scales, which typically depend upon the wind speed, surface roughness, height above the surface, and stability. If we interpret samples taken at an interval of $2T_u$ as being effectively independent, giving $T_o/(2T_u)$ independent samples, then this formula reduces to the well-known result that the variance of the sample mean for independent samples is inversely proportional

to the sample size. The rate at which the anemometer is sampled is assumed to be at least as frequent as $2T_u$, but does not otherwise enter into consideration.

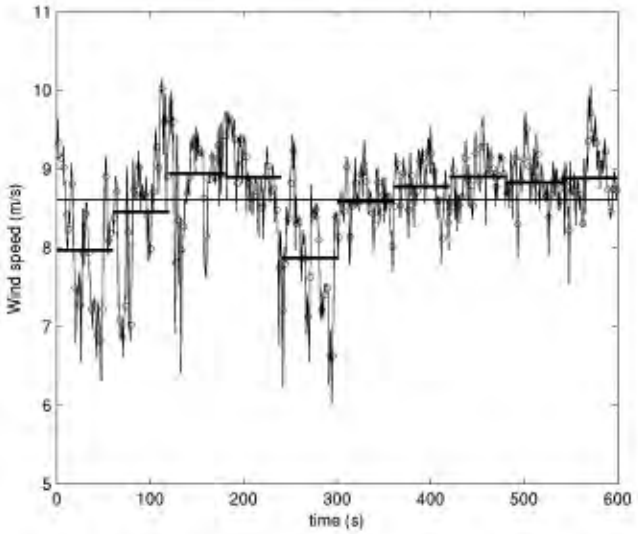

Figure 2.3 Measuring the mean wind.

By way of illustration, Figure 2.3 presents 10 minutes of sonic anemometer data measured at North West Cape, Western Australia, at 42 m height. The thin curve is the 1-s mean wind derived from sonic 10 Hz measurements, the open circles are the 3-s mean wind speeds. Thick horizontal bars show the 1-min mean wind speed and the thin horizontal line is the 10-min mean wind speed.

Thus the difference between 1-s, 3-s, 1-min and 10-min observed means is solely that the longer averaging period leads to the sample mean being a more accurate estimate of the true mean. Provided that the sampling is random, the expected values for each averaging period are equal, and individual realisations will be both greater and less than the true mean. Note however that if a 10-min sample is subdivided into ten 1-min samples, the mean of each calculated, and the largest of these 1-min means is chosen, then this is no longer an unbiased estimate of the true mean, since the sampling is not random. Such a measurement is, in fact, termed a gust (refer 2.4 for definition).

We have so far assumed an ideal, instantaneous response anemometer. Real anemometers implicitly apply some averaging, due to e.g. the mechanical inertia of cups, or the finite signal path length in a sonic anemometer. While there are numerous historical references dealing with the filtering effects of anemometers (e.g. Deacon 1955; Wieringa 1973; Greenway 1979; Beljaars 1987a,b; Wieringa 1996; Miller 2007; WMO 2008) it seems rare for manufacturers to publish instrument response characteristics. It can be shown that the best way to describe a cup anemometer's response is in terms of a distance constant, which represents the wind-sample required to respond to a stepped change in speed (e.g. Kristensen 1993). A typical cup anemometer may have a distance constant of the order of a few to a few 10's of metres, which implies that information on smaller space scales is filtered out. The corresponding time constant may be found by dividing the distance constant by the mean wind speed, so such anemometers have an inherently faster response in high winds. If the averaging period is much longer than the filter time scale, then the filtering provided by the anemometer can be ignored, but it has to be considered when the two are comparable. This topic will not be further discussed here, but should be of significant concern where long-term climatological measurements are interrupted by inevitable changes in instrumentation. The Dines pitot-tube recorder, for example, which has been in worldwide use throughout the 20th century, and

is widely credited with the ability to accurately measure a "2 to 3 s" gust (Sanuki 1952; Whittingham 1964; Deaves and Harris 1978), is rapidly being replaced by more compact self-contained cup and propeller anemometer systems that have different response characteristics.

Our other key assumption is that the true mean wind is in fact steady. If this is not the case, then more sophisticated processing will be necessary to remove the turbulent part of the signal, as otherwise the trend in the mean wind may bias the sample mean away from the true mean. For example, a 10-min mean measured during the passage of a sharp eyewall wind maximum of a fast-moving storm may reduce the amplitude of the true mean wind maximum. In practice, averaging periods are chosen as a compromise between minimising sampling errors, reducing the errors due to non-stationarity, and (for non-electronically logged systems) observer patience. Values of the order of 10 minutes are typically many times the integral time scale, but short enough that nearly all meteorological phenomena of operational interest can be considered stationary.

We close with two remarks. Firstly, the interaction between a mechanical anemometer and turbulence is nonlinear, which may lead to upward biases of the order of a few percent in measured mean winds. This phenomenon is known as "overspeeding" and is analysed in significant detail for cup anemometers by Kristensen (1993). Secondly, remotely-sensed wind measurements often involve 2-dimensional averaging rather than the 1-dimensional averaging of an anemometer. For example, scatterometer data might be representative of a nominal 25-km square of the ocean surface. Such measurements almost always sample many more integral scale's worth of wind than a line average, not least because the integral length scale perpendicular to the wind direction is several times less than that parallel to it. Thus such wind measurements may have relatively low variance, although they may also contain significant biases due to factors not taken into account in the retrieval, such as heavy rain in the case of a scatterometer.

2.3 Representing the Fluctuating Wind

Following Reynolds (1895) (see also e.g. Garratt 1992; Kaimal and Finnigan 1994; Holmes 2001), the instantaneous (longitudinal) wind $V(t)$ can be simply represented as the sum of the mean wind V_{To} and a fluctuating component $u(t)$ about the mean such that:

$$V(t) = V_{To} + u(t) \tag{7}$$

and the variability can be summarised by calculating the standard deviation (or root-mean-square) of the fluctuating component about the mean:

$$\sigma_u = \sqrt{\frac{1}{T_0}\int_0^{To}\left(V(t) - V_{To}\right)^2 dt} \tag{8}$$

A non-dimensional form of this variability relative to the mean is simply the coefficient of variation, which is termed the turbulence intensity in this context:

$$I_u = \frac{\sigma_u}{V_{To}} \tag{9}$$

Based on the many detailed measurements made over land in high latitudes from large scale depression systems, a common simplifying approximation to the magnitude of turbulence fluctuation for land-based wind engineering applications is given by:

$$\sigma_u = 2.5u_* \tag{10}$$

This provides an order of magnitude estimate only of this complex relationship (e.g. refer Lumley and Panofsky (1964) for more detail) that conveniently removes u_* and k when combining with Eqn 1. This then provides an approximate indication of the variation in turbulence intensity with surface roughness and height, namely:

$$I_u = \frac{1}{\ln(z/z_o)} \tag{11}$$

which it should be noted, implicitly assumes that σ_u, the standard deviation of the wind speed fluctuation about the mean, is actually constant with height[5] at least near the surface.

The accurate measurement of turbulence intensity requires high response instrumentation, reasonably high speed sampling (> 5 Hz depending on height and wind speed etc) and is also sensitive to the choice of T_o (e.g. refer Schroeder and Smith 2003), which can make inter-comparisons more difficult. Normally, T_o is chosen to be hourly in synoptic environments and usually not less than 10 min (refer Section 2.5 also). Hence reference here to I_u implies a base reference $T_o \geq 600$ s.

The capability to accurately measure I_u is normally only available at purpose-built research-grade facilities but, following WMO endorsement (e.g. Beljaars 1987a, WMO 2008) arguably should now be routine. Accordingly, due to the sparse occurrences of tropical cyclones, there are relatively few estimates available of the turbulence intensity in those conditions. Recently, the development of mobile instrumented towers in the USA (e.g. Schroeder et al. 2002; Masters et al. 2005) has lead to a greater capture rate of tropical cyclone conditions. Partly due to this lack of comparative data, there has been much debate about the possible differences between tropical and extra-tropical turbulence intensities (e.g. Wilson 1979a; Melbourne and Blackman 1982; Ishizaki 1983; Krayer and Marshall 1992; Black 1993; Sharma and Richards 1999; Paulsen and Schroeder 2005; Vickery and Skerlj 2005).

Acknowledging for the moment that there may be reasons for differences between tropical and extra-tropical conditions, the collective I_u values near the earth's surface appear similar in order-of-magnitude terms for equivalent exposures. However, even small differences of the order of 10% could be important in structural assessments. In closing, it is noted that Eqn 11 yields a typical value for I_u of about 0.17 for z = 10 m and for standard exposure with a z_0 of 0.03 m.

2.4 The Concept of the Gust Wind Speed and the Gust Factor

Extending the preceding discussion, the instantaneous wind can, in simple terms, be considered as the superposition of a range of eddy sizes and speeds within the air flow, moving along at the mean speed. Hence, assuming that the scale and strength of these eddies are largely independent and random, the Gaussian statistical distribution is typically used to describe the expected variation in sampled speeds, namely:

$$f_u(u) = \frac{1}{\sigma_u\sqrt{2\pi}} e^{\left[-0.5\left(\frac{u-V_{To}}{\sigma_u}\right)^2\right]} \tag{12}$$

gives the probability *density* of the instantaneous wind based solely on the specified mean speed V_{To} and the standard deviation σ_u ; whereby $f_u(u).du$ is the probability that $V(t)$ will lie in the interval u_o+du for $u=u_o$ (Holmes 2001).

The statistical variability of the natural wind has been shown by numerous studies to be reasonably well modelled by the Gaussian assumption. Some examples of this under tropical cyclone

[5] This is an assumption of convenience here to illustrate the principal observation that turbulence intensity is expected to decrease with height but it is far from certain that σ_u does not also reduce with height in tropical cyclone conditions.

conditions include Powell et al. (1996) during Hurricane *Bob* and Schroeder and Smith (2003) during Hurricane *Bonnie*, while Paulsen and Schroeder (2005) compares some limited tropical and extra-tropical datasets.

While the measurement of a gust is seemingly straightforward, being the highest average speed recorded within a specified period, a statistical definition is required for predictive purposes. Following Kristensen et al. (1991) we define the expected maximum gust V_τ as:

The wind speed averaged over a duration of τ seconds which, on average, is exceeded once during the reference period T_o.

Kristensen et al. (1991) discuss some consequences of this definition:

- the expected gust is the mode (the most probable value) of the probability distribution,
- the probability of not exceeding the expected gust is $e^{-1} = 0.37$,
- the probability of exceeding the expected gust exactly once is $e^{-1} = 0.37$, and
- the probability of exceeding the expected gust twice or more is $1 - 2/e = 0.26$.

The expected gust wind speed is then typically modelled as:

$$V_\tau = V_{To} + g_{\tau,To}\,\sigma_u \tag{13}$$

where $g_{\tau,To}$ is termed the peak factor, representing the number of standard deviations that the maximum gust speed's magnitude is statistically expected to lie above the mean speed over the period T_o, consistent with the selected gust duration τ. This is often expressed relative to the mean wind reference magnitude in terms of a gust factor G and the turbulence intensity:

$$G_{\tau,To} \;=\; \frac{V_\tau}{V_{To}} \;=\; 1 + g_{\tau,To}\,I_u \tag{14}$$

Using this approach, it remains to select appropriate values for turbulence intensity I_u and obtain a statistically based estimate of $g_{\tau,To}$ to arrive at recommended values for $G_{\tau,To}$ for tropical cyclone conditions. However, there still remain a number of issues that need consideration, and the determination of g has been subject to some historical debate. A number of slightly different formula for g have been proposed (e.g. Davenport 1964; Wieringa 1973; Forristall 1988; Mitsuta and Tsukamoto 1989) and some alternate statistical theories offered (e.g. Bergstrom 1987; Kristensen et al. 1991; Boettcher et al. 2003), which can be shown to be approximately equivalent within a range of assumptions (Kristensen 1993).

The most complete theoretical description available that satisfies the present scope requirements is summarised by ESDU (2002b), which is based on the original statistical approach by Davenport (1964) as augmented by the analyses of Greenway (1979, 1980) and Wood (1983). This approach considers the sampling of independent gust episodes from a pre-determined spectrum of the natural wind (the von Karman form), which relies on estimating the mean zero-crossing frequency associated with the spectra relevant to the chosen averaging period and gust duration. Then, with the assumption of a Gaussian parent distribution, this can be shown to produce an Extreme Value Type I (or Gumbel) distribution for the maximum gusts and the mean of this distribution is then taken as the expected value. As noted above, Kristensen et al. (1991) takes a slightly different view and chooses the mode of the distribution, which will always be less than the mean due to the positive skewness, but the results are almost indistinguishable. Because of the probabilistic nature of the gust, gust measurements will always have some scatter about the expected gust value, even if the forecast is perfect and all the assumptions are justified.

2.5 The Relevance of the Spectral Gap and the Need for Stationarity

If we wish to accurately know the expected deviation of wind speed from a time-averaged mean condition, then it is important that the reference used for the mean is stable, well defined and not

subject to trends that would otherwise interfere with, for example, the ergodic hypothesis (Lumley and Panofsky 1964). This is achieved by focussing on the relevant subset of eddy time and space scales and choosing a reference position that is sufficiently homogeneous and stationary to be suitable for this purpose.

One of the earliest investigations into the range of naturally occurring turbulent wind scales was documented by Van der Hoven (1957), who constructed a broad energy spectra based on almost one year of wind measurements, using varying averaging periods, obtained from a 125 m tower at Brookhaven National Laboratory. The data was pieced together in as consistent a manner possible for the times and spectrally analysed, including some high frequency data collected during the passage of Hurricane *Connie*. A schematised reproduction of this original spectrum is given in Figure 2.4, which showed that the measured wind energy was not equally distributed across all frequencies but rather indicated preferences for certain scales. Spectral energy peaks were clearly identified at periods of 4 days, 12 h and near 1 min. between these prominent energy peaks, a "spectral gap" was identified with a minimum energy occurring around about 1 h. The spectral peaks indicate time scales at which most energy is being generated, which are then transferred to other scales by a cascade process. Frequencies where there is little or no energy present are known as "spectral gaps". It was found that the spectral gap was independent of the magnitude of the mean wind speed and was quite flat over the range from about 3 h to 20 min. This broadscale spectral behaviour has been identified at other sites around the world both on land and at sea, although the details vary (e.g. Smedman-Högström and Högström 1974; Gomes and Vickery 1977; Wieringa 1989) depending on stability, height, the locally dominant processes and their energetics (the energy scale might vary). The most significant peak at 4 days is considered typically representative of the passage of weather systems at the synoptic scale, with the near 1-min peak, the second highest, attributed to mechanical and convective turbulence in the micrometeorological scale, with the intermediate peak representing the mesoscale range (e.g. Fiedler and Panofsky 1970; Pierson 1983) where diurnal and semi-diurnal processes also contribute. As described by Jensen (1999) the concept of a spectral gap offers an attractive separation of the atmospheric motions into a deterministic low-frequency part and the unpredictable turbulent part.

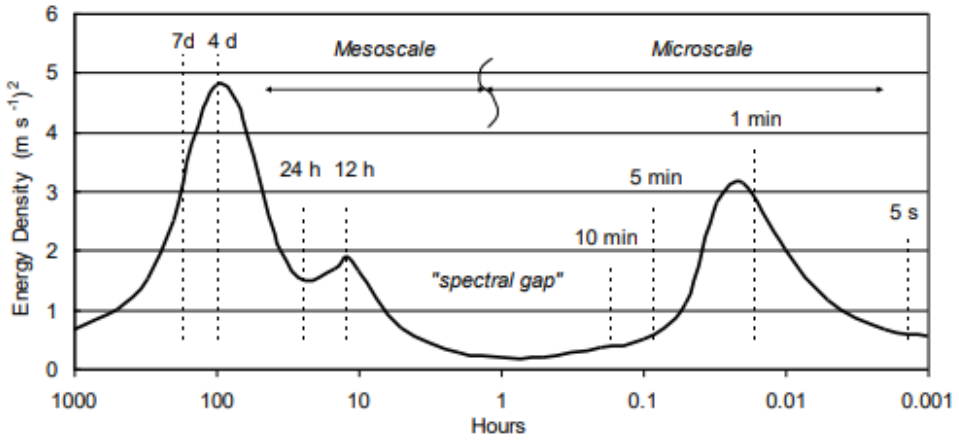

Figure 2.4 Schematic energy spectrum of near-ground wind speed after Van der Hoven (1957).

The presence of a spectral gap between the mesoscale and the microscale is therefore conceptually appealing as the averaging period over which a generally practical "mean" wind would be best calculated, as there is clearly much less variability (variance being the area under the curve in Figure 2.4) in measurements taken from that region of the spectrum. Any random sample averaged over such periods (say 3 h to 20 min) could be expected to have a relatively sharp probability density function when compared with a similarly sampled set of random values using (say) 1-min averaged speeds. This results in the mean value being largely independent of the actual length of

the record. Averaging over such periods is therefore also consistent with the desire to have a statistically stationary sample free from longer scale trends. Wieringa (1973) for example, highlights the ready potential for overestimation of gust factors that occurs if stationarity is not adequately considered and data is not correctly de-trended.

Fordham (1985) however notes that the presence of a spectral gap does not necessarily guarantee quasi-stationary conditions but does indicate a higher probability than otherwise of finding data records which will pass some statistical test for stationarity. Also, the spectral gap may not always reliably occur in a specific situation, as noted by Dobson (1981). Ishida (1989), for example, found some intermittent energy peaks (15 min to 1 h) in high latitude buoy data which appear to be related to convective events. It might also be expected that similar intermittent energy features might be found in a tropical cyclone and Naito (1988) shows a significant peak near 1 h for various strong wind over-ocean datasets, including a typhoon, but a gap nearer 10 min. Powell et al. (1996) shows that a near-coast spectrum from Hurricane *Bob* at least displays similar microscale behaviour to the Van der Hoven example, with a broad energy peak around 1 min and various sharper peaks at 30 s or less. Schroeder and Smith (2003) have identified more low frequency energy than expected in Hurricane *Bonnie* data but concede that this may be due to difficulties in obtaining good stationarity of records, without which low frequency energy artificially accumulates in the spectra. Some recent studies also highlight the likelihood of boundary layer roll-vortices in tropical cyclones (e.g. Wurman and Winslow 1998; Foster 2005; Morrison et al. 2005) with periodicity of 5 to 10 min, suggesting averaging periods in excess of this might be desirable. The measured 1-min wind record shown later in Figure 3.2 is perhaps evidence of such variability.

The likely presence of a spectral gap at or near the hourly averaged wind speed resulted in its broad adoption as the reference period of choice for statistical studies of smaller scale near-ground atmospheric turbulence. However, as more homogeneous data has become available over time, it has become increasingly clear that the large energy gap first identified by Van der Hoven is simply not as great as suggested in Figure 2.4 and may typically only be about a factor of two lower than the higher frequency peak energy level (e.g. Jensen 1999).

In situations such as tropical cyclones, where the phenomena of interest typically presents with relatively high space and time gradients near its centre, retreat to a slightly lower averaging period of about 10 min is desirable to avoid non-stationarity of the record. Even more transient atmospheric events such as thunderstorm downbursts or tornados naturally require suitably downscaled mean wind averaging periods (e.g. Orwig and Schroeder 2007). Figure 2.5 presents an example wind energy spectrum from Powell et al. (1996), annotated here to indicate the principal averaging times of interest and the nominal spectral gap. This specific example shows a sharp peak in variability near 30 s, before the high frequency tail decay commences at about 10 s. The energy present at 10-min cycling can be seen to have less than half the variability of that at 1-min cycling.

2.6 Convective Features, Convergence and Instabilities

Whether convective processes might play a more significant role in the tropical cyclone boundary layer than the more extensively sampled extra-tropical wind environments has been the subject of much conjecture (Melbourne and Blackman 1982; Ishizaki 1983; Krayer and Marshall 1992; Black 1993; Sharma and Richards 1999; Sparks and Huang 2001; Paulsen and Schroeder 2005; Vickery and Skerlj 2005).

In the extra-tropics, the role of convective versus mechanical sources has also been explored (e.g. Bradbury et al. 1994) but found to be sufficiently and identifiably separate as to not interfere with the traditional UK approach to building design, although it is noted that extreme gust factors are always caused by convection but extreme gusts might be due to either process. Young and Kristensen (1992) demonstrate quantitatively how the surface layer would be gustier in unstable than in stable conditions. Meanwhile, Brasseur (2001) has recently advocated a direct transport-of-momentum-from-gradient approach to forecasting of gusts but this theory has previously met with

limited support relative to the purely mechanical approach (e.g. Baran 1992; Mahrt and Gibson 1992). In Australia, the convective event has always been known to dominate design wind speeds outside of cyclonic regions, but turbulence intensity has been based largely on UK approaches (Standards Australia 2002b).

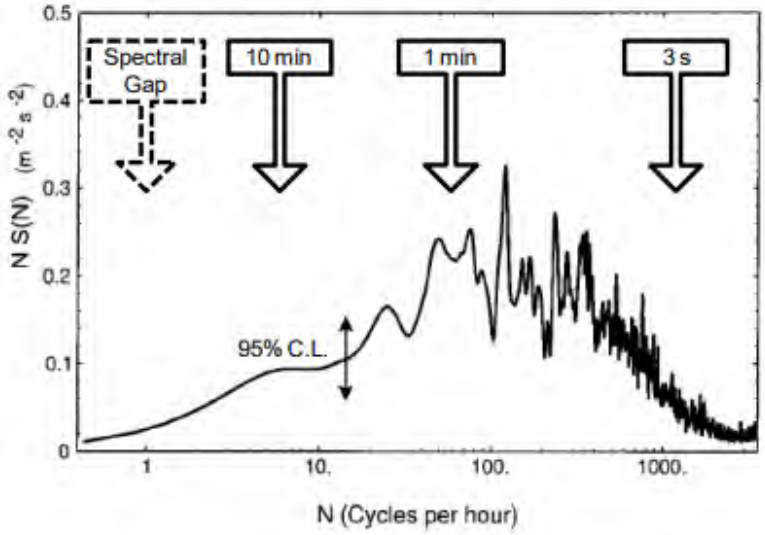

Figure 2.5 Example tropical cyclone wind energy spectrum after Powell et al. (1996).[6]

Clearly tropical cyclones are the result of the large-scale integration of convective processes and exhibit evidence of local convection (e.g. Powell et al. 1991). However, the separation of mechanical and convective processes from any near-surface wind record, at least in strong winds, is likely a difficult if not impossible process even with sensitive instrumentation. While there is no doubt that mechanical mixing near the ground is the dominant and pervasive process, the extent to which tropical convection acts to increase the vertical transport of momentum and enhance the turbulence intensity is yet to be fully quantified. Detailed measurements by Schroeder and Smith (2003) during *Bonnie* reported the possible signature of convection when some integral scales seemed to increase without changes in roughness and Paulsen and Schroeder (2005) reported up to a 6% increase in turbulence intensity between some equivalent tropical and extra-tropical exposures, the difference increasing with increasing roughness.

One of the first insights into the possible role of convective processes in tropical cyclones was provided by the coastal tower measurements of Wilson (1979ab) on the Western Australian coastline during the close approach of several storms. The vertical profiles of time history winds obtained from five anemometers (9 m to 390 m height) indicated a low level wind maximum near 60 m with a profile exhibiting shear levels higher than logarithmic. Above 60 m the profile showed clear evidence of longer period, apparently convective events associated with rainbands, which presented in the form of jets. After stratification into likely convective and non-convective subsets, the gust factor $G_{3,600}$ was found to decrease above the surface from a mean of about 1.4 at 9 m to 1.1 at 200 m for the mechanical case, but above 200 m the likely convective processes averaged 1.2 to

[6] Powell Houston and Reinhold (1996): §FIG. 3. Spectral density plot of detrended fluctuations of the streamwise component of the wind at 20 m height measured at the USACE Duck, North Carolina, pier for alongshore flow in 23 m s^{-1} mean winds during Hurricane Bob on 19 August 1991. Spectral estimates have been smoothed with a 20-point Hanning filter. Vertical axis is the product of frequency and spectral density, which has units of variance; horizontal axis is frequency expressed in cycles per hour on a logarithmic scale. The vertical line with arrows refers to the 95% confidence interval applied to an estimate of 0.1 $m^2 s^{-2}$. The area beneath the curve is proportional to the contribution of a given frequency band to the total variance.

1.5. Wilson also noted that the surface wind gust consistently underestimated the mean wind at 390 m. Also, the surface gust was always less than the mean winds at 60 m, suggesting the mechanical mixing depth near the surface was small. It seems possible that the increased shear near the surface was influenced to some extent by the higher level transports.

Analytical and numerical modelling of the tropical cyclone boundary layer by Kepert (2001, 2002c) and Kepert and Wang (2001) has shown that a marked wind speed maximum is often present in the upper boundary layer. The boundary-layer depth is about 500 m at the radius of maximum winds (RMW), increasing to about 1.5 - 2 km at larger radii. These models do not include the effects of moist convection, demonstrating that this is not necessary for the generation of steady low-level jets. Examination of the near-surface wind profile in the numerical model shows that it is close to logarithmic up to at least 100 m height. Observational studies (Franklin et al. 2003; Powell et al. 2003; Kepert 2002b,c; Kepert 2006a,b; Bell and Montgomery 2008; Schwendike and Kepert 2008) have confirmed the presence of both the low-level wind maximum, and the near-surface logarithmic layer.

Black and Marks (1991) identified the presence of mesoscale vortices (e.g. Figure 2.6) circulating within the tropical cyclone eyewall region and later Willoughby and Black (1996) proposed that incursions into the boundary layer from such features could be responsible for locally high strips of damage in the landfall of Hurricane *Andrew*. Subsequently, Black et al. (1999) was able to document a possible example of such a feature recorded at Barrow Island, Western Australia, during the eyewall passage of Tropical Cyclone *Olivia* (925 hPa). In this case several unusually large surface gusts were recorded, the highest 3 s peak of 113 m s^{-1} being registered within a single record when the +10 m 5-min mean was 41 m s^{-1}, yielding $G_{3,300} = 2.75$. The other unusual $G_{3,300}$ gusts ranged from 1.6 to 2.6 within an overall storm mean of about 1.3. Section 3 here presents evidence of a potentially similar feature from the same region recorded in 1989 during Tropical Cyclone *Orson* (905 hPa). Other recent gust factor studies have reported little or no direct evidence of convective downdraft features in the vicinity of the eyewall (e.g. Sparks and Huang 2001; Vickery and Skerlj 2005) but these instances typically represent less energetic encounters. There is far too little data to make any firm recommendations, but there seems to be some limited and incomplete evidence showing that transient winds, not due to turbulence *per se*, may occur in tropical cyclone eyewalls with magnitudes in excess of double the otherwise prevailing mean wind.

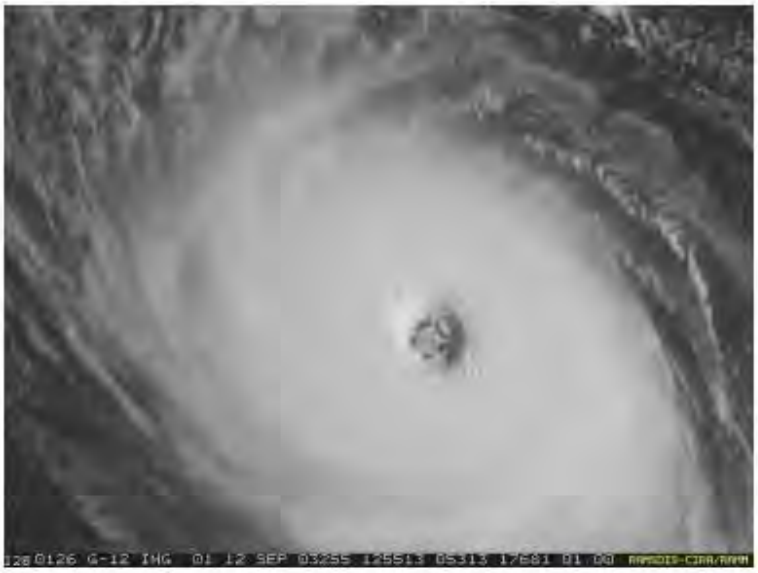

Figure 2.6 Mesovortices within the eye of Hurricane Isabel (2003).

Whether such features are simply isolated or form part of a deterministic framework, possibly even related to 2-D eyewall instability (e.g. Kossin et al. 2004) is yet to be determined. Certainly, highly energetic features are known to exist (Marks et al. 2008) and may penetrate to the surface.

The approach of tropical cyclones near elevated land has long been known to result in increased convergence of the low-level flows and undoubtedly leads to enhanced vertical transport of momentum, which is likely to enhance near-surface turbulence levels (e.g. Yeh and Elsberry 1993). However, Kepert (2002a, 2006b) and May et al. (2008) also show that the process of landfall even over flat and relatively featureless land may lead to a substantial change in the near-surface winds due to changes in surface roughness interacting with the vortex boundary layer dynamics.

Taking the above arguments into account, and based on the evidence suggested from a number of near-coast measurements presented later, it is concluded that convective or at least non-mechanical turbulence processes probably play a more significant role in tropical cyclone turbulence intensities than in extra-tropical conditions. In respect of non-turbulent transients such as eyewall instabilities, these features are not presently considered in operational forecasts and warnings but the situation may change in the future as more data becomes available.

3 An Example Extreme Oceanic tropical Cyclone Wind Record

For illustrating some of the foregoing discussions on wind characteristics and averaging times it is instructive to examine a specific tropical cyclone wind record, which not only has a variety of parameters recorded but also shows how stationarity can be compromised during an eyewall passage.

Severe Tropical Cyclone *Orson* (BoM 1992; 905 hPa) passed directly over the North Rankin 'A' (NRA) natural gas production platform (19.5856°S, 116.1368°E) operated by Woodside Energy Ltd in March 1989 (refer Figure 3.1), 130 km offshore of the Western Australian coastline. Peak recorded winds were 62.3 m s^{-1} (10-min) and 66.4 m s^{-1} (1-min) at a level of +36.4 m above sea level. Two identically exposed anemometers[7] were automatically logged and the following wind speed parameters were electronically calculated and stored:

- Averaged 1-min wind speed every minute, V_{60}
- Averaged 10-min wind speed every 10 minutes, V_{600}
- Highest 3-s gust in each 10 minutes, $V_{3,600}$
- Highest 3-s gust in each hour and its time of occurrence, $V_{3,3600}$

Figure 3.1 Location map and NRA facility during TC *Orson*.

Unfortunately both anemometers were destroyed during the eye passage, most likely due to the impact of lightweight debris that was stripped from the main structure. One anemometer failed at the time of the first eyewall encounter, the second instrument failed during the second, and the record of $V_{3,600}$ is incomplete due to transmission problems, thus illustrating the difficulty of reliably recording under such extreme conditions. The record here is from the eastern anemometer, which survived the longest and has the better exposure through the first eyewall passage. A nearby moored Waverider™ buoy also failed at a recorded significant wave height (H_s) of about 10 m and estimated single maximum wave heights were of the order of 20 m (Harper et al. 1993).

Figure 3.2(a) shows the time history variation of the indicated winds over a three hour period that includes the eye passage, where the more variable solid line is the continuously available V_{60}, which is lagged by the V_{600} dotted line reported each 10 minutes. The heavy stepped lines are the gust wind speeds $V_{60,600}$ (solid black) and $V_{3,600}$ (dashed red). The solid triangles are time-aligned $V_{3,3600}$ and considered suspect on either side of the eyewall. The only identifiable measure of the turbulence in the mean wind in this case is from V_{60}, being the highest frequency that was continuously recorded. As expected, any instantaneous value of V_{60} might be above or below the 10

[7] The sensors were propeller-vane Qualimetrics Skyvane instruments, separated by about 30 m horizontally either side of a central cable-stayed flare tower on a cantilevered structure extending out over the ocean.

minute averaged V_{600} value for that interval and, although any single V_{60} is an unbiased estimate of the mean wind, it clearly will have a higher variance than any single V_{600} value and is therefore likely to have a greater associated error as an estimate of the true mean wind. Use of an hourly wind speed reference here would also clearly be unsuitable due to the rapid trends on that timescale. The observed gust $V_{60,600}$ can be seen to follow the peaks of V_{60} within each 10 minute interval. Note however the influence of non-stationary conditions on $V_{60,600}$ and $V_{3,600}$ whereby the peak gust is typically registered at the end of the interval when mean speeds are increasing, and at the beginning of the interval when mean speeds are decreasing. As previously mentioned, it can be speculated that the observed periodicity in the V_{60} record is perhaps partly due to the influence of boundary layer roll-vortices.

$V_{60,600}$ is then plotted relative to the contemporaneous V_{600} as the gust factor $G_{60,600}$ in Figure 3.2(b). $G_{60,600}$ is relatively constant until the eyewall passage, averaging around 1.08, but then increases and becomes more erratic in the rapidly changing but lower speeds within the eye. Through the eyewall and eye regions, V_{600} clearly suffers extreme stationarity problems that result in the erratic $G_{60,600}$ values being of no specific consequence. Likewise, the observed gust $V_{3,600}$ in Figure 3.2(a) (when available) has been converted to the gust factor $G_{3,600}$ in Figure 3.2(b) and shows a similar behaviour, initially near-constant at about 1.23.

The extreme spike of $G_{3,600}$ within the eye is associated with a V_{600} of only 9 m s^{-1} and is not of practical interest, again because of non-stationarity. However, two of the three values of $V_{3,3600}$ shown (solid triangles), that are separately recorded by the data logging system, convert to equivalent $G_{3,600}$ values in excess of 2.0. The peak $V_{3,3600}$ of 132.6 m s^{-1} and its later companion of 91 m s^{-1} were originally discarded in the post-storm analysis as likely erroneous data spikes. However, the seemingly well-behaved values of V_{60} during the same period suggest that the logging system was functioning normally. Whether these data are valid or not cannot be determined. They are presented here only as increasing potential evidence for the transient phenomena discussed in Section 2.6. It can be noted that there were also two significant $G_{60,600}$ events for V_{600} values of 10 and 22 m s^{-1} probably associated with convective rainbands.

In Figure 3.3, a summary of the gust factor behaviour is presented for the period of about 2 days when V_{600} exceeded 10 m s^{-1} at the sensor height[8]. Figure 3.3(a) plots $G_{60,600}$ and the two values of $G_{3,600}$ as a function of V_{600}, showing that the mean values given by the superimposed lines (using a 5 m s^{-1} banding) do not vary appreciably but the scatter reduces as mean speed increases. The reason for this may relate directly to Eqn 6 whereby, assuming a constant eddy integral length scale, a larger number of samples at the higher wind speed improves the accuracy of the estimate. Note that this example analysis does not include a check for stationarity as the high frequency data was not recoverable, and all analyses are at sensor height.

Figure 3.3(b) then presents the same information but in the form of sample histograms and cumulative distributions (binned at 0.025 intervals for V_{600} > 10 m s^{-1}) for $G_{60,600}$ and $G_{3,600}$, where the modal values are 1.075 and 1.200 respectively, the medians are 1.08 and 1.22 and the means (s.d.) are 1.094 (0.097) and 1.237 (0.067).

This single example of extreme winds during a tropical cyclone serves to illustrate many of the principal theoretical wind averaging issues regarding stationarity, filtering, non-mechanical or convectively-generated turbulence, potential structure-related transients and the clear difference between measures of the mean wind and measures of gusts. It also demonstrates that interpreting gust factors measured under non-stationary conditions can be difficult.

[8] While the present discussion seeks to avoid the equally complex issue of the vertical profile of wind speed, the adjustment factor from +36.4 m to +10 m would be of the order of 0.85 based on ISO (2003) or API (2002).

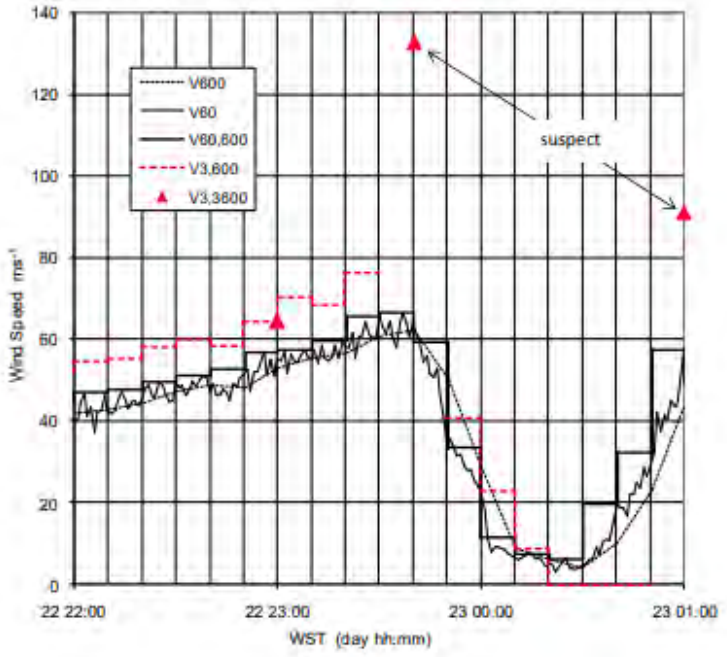

(a) Wind Speeds

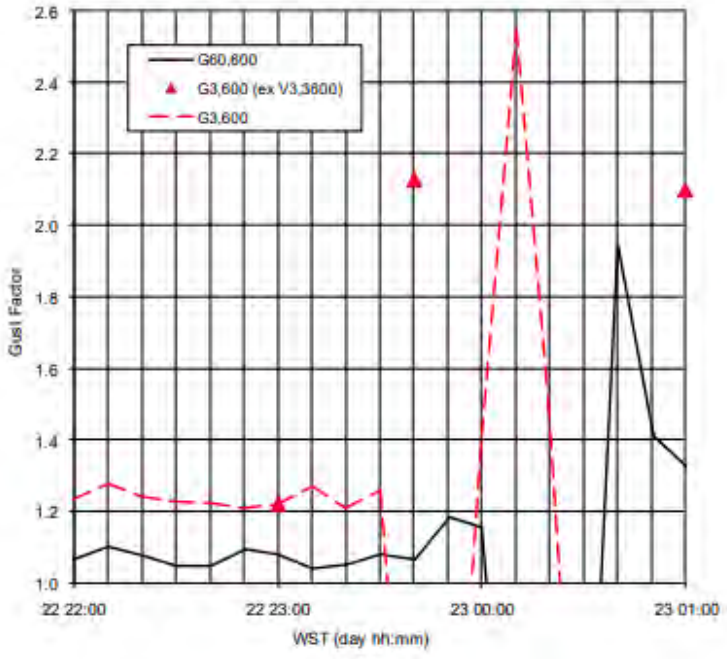

(b) Gust Factors

Figure 3.2 Time history of wind speed and gust factors during TC *Orson* (1989).

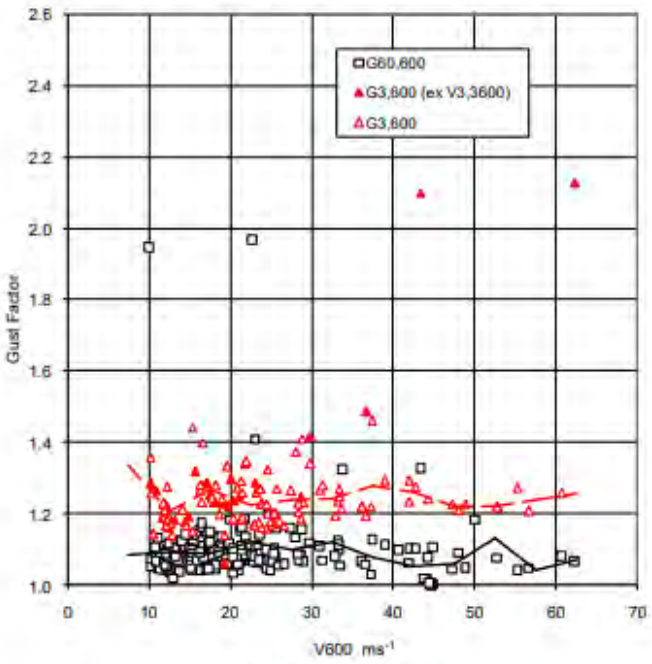

(a) Gust Factor Variability

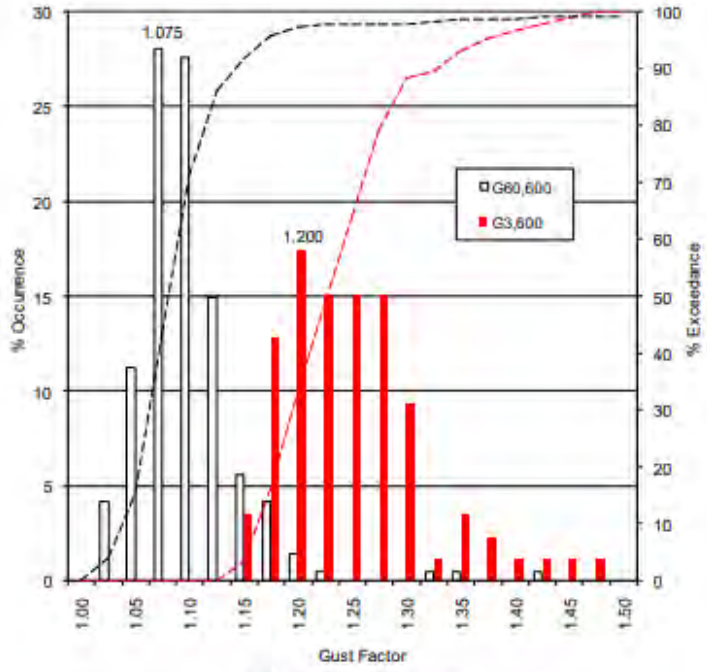

(b) Gust Factor Distribution

Figure 3.3 Summary gust factor variability during TC *Orson* (1989).

4 A Compendium of Data and Theories

The approach taken here now is to begin to compare the available (limited) evidence from measurements of tropical cyclone conditions with the established gust theories that are derived from largely land-based extra-tropical conditions. As mentioned previously, the nominal land context is strong winds, typically $V_{To} > 17$ m s^{-1}, standard exposure with roughness length $z_0 = 0.03$ m and height $z = +10$ m. However, there are instances where the available data do not exactly represent this situation – some for obviously practical reasons – and some is reported within specific wind speed bands. Also, some information presented here is based on very extensive datasets that have been smoothed, while some is derived from only a few situations or is simply a recommendation in common usage. Some data is derived from high frequency studies and other data is mean and gust only from AWS sites, some strip-chart based. Attempts have also been made to present original data and thereby avoid simply repeating previous recommendations. Rather than attempt to individually correct each of the published values, which itself requires model assumptions and the like, the data has been logically grouped and clearly identified to hopefully illustrate the emerging trends.

Mindful of the need to provide broad guidance, the presentation of data and theory has been grouped here into three characteristic over-water wind-relative regimes or exposures that are likely to be of most interest to tropical cyclone forecasters and should capture what are believed to be the critical differences, namely:

- "off-land" - any land-based near-coastal exposure with offshore wind;
- "off-sea" - any land-based near-coastal exposure with onshore wind;
- "at-sea" - nominally > 20 km offshore.

Figure 4.1 a to d shows a summary of data and theories collected during this review, presented here in the context of gust factors relative to the "effective" hourly reference period, i.e. values of $G_{\tau,3600}$. Not all of the data collected (refer Appendix C for details and author cross-references) could be objectively presented in an hourly reference context but is used in the subsequent comparisons in Section 4.4. Figure 4.1a is a combination of all the information collected, unstratified by the above exposure classes and provided simply for completeness and comparison. By way of example, the uppermost curve presents the results by Schroeder and Smith (2003), where a peak 3-s gust duration ($\tau = 3$) within an hour yields a gust factor for $G_{3,3600}$ of about 1.72. The symbols and lines on the figures offer some consistency, the principal features being that open symbols and lighter-weight lines normally represent non-land exposures. Curves are indicated on the basis of complete analyses or theories, while points represent less comprehensive studies, recommendations or single events. The legends are alphabetical and also indicate either the approximate mean speed range associated with the dataset that formed the theory or the mean speed value used in a speed-dependent theory.

The remaining Figure 4.1 *b* to *d* present data in terms of the nominated exposure classes, as detailed below.

4.1 "Off-Land" Exposure

A brief explanation of each of the datasets follows. AS/NZS 1170.2 is the implicit $G_{3,3600}$ of 1.67 embodied in the Australia/New Zealand design standard (Standards Australia 2002a) for tropical cyclone regions. Ashcroft (1994) is an extract of tabulated gust factors from a reasonably comprehensive study of UK hourly, 1-min and 3-s gust data that considered different methods of analysis, effects of stationarity and roughness, and appears to be the most recent UK study. Cook (1985) is a simplified form based on the Wieringa (1973) approach used as the basis of a structural design procedure in the UK. Durst (1960) was the earliest reasonably complete description of gust factor variation based on UK data and assumed a simple Gaussian gust model, which yields a

characteristic "S-shaped" curve in this presentation. It can be seen that Ashcroft, and Durst form a reasonably consistent grouping, while Cook gives higher G values for $\tau > 20$ s. Next is ESDU (2002b), which was initially published in 1983 in its present form, based on the Davenport (1964) statistical approach as discussed in Section 2.4, combined with extensive datasets and boundary layer models from previous UK wind engineering analyses (e.g. Deaves and Harris 1978). The ESDU formulation is only very slightly sensitive to mean speed and latitude ($\lambda = 50°$ here). The shapes of the ESDU and Durst curves are similar although ESDU has higher G for $\tau < 4$ s and much lower G for $30 < \tau < 600$ s, which is the lowest of all the theories shown here.

K&M (Krayer and Marshall 1992) was the first widely adopted USA hurricane-specific investigation and was later adopted by ANSI (1996) for building design in the USA. It follows the Durst approach based on the analysis of 10-min data (strip chart only) from mostly airport AWS sites during four USA hurricanes. It has some event sets in common with Powell (1982, 1987) but recommends higher G values. It can also be seen to predict much higher G values than the UK-based formulations. M&T (Mitsuta and Tsukamoto 1989) is based on detailed measurements from the very small Tarama Island near Japan in a typhoon region. However, the dataset is described as based only on overland fetch situations (approx. 4 km sugar cane and coconut palm), which suggests that the boundary layer may have been in transition rather than equilibrium. Powell (1987) analysed surface winds from Hurricane Alicia and found significant variability depending on the location of rainbands. His recommended $G_{3,600}$ values are interpreted here as probably being most representative of the "off land" exposure and are nominally adjusted by 1.05 to represent $G_{3,3600}$ (a reasonable estimate based on ESDU (2002b)).

S&H (Sparks and Huang 2001) was essentially a follow-up analysis to K&M but considered separate digital airport and near-coastal AWS data during recent USA hurricanes. The indicated data point here has been taken as representative of their broad conclusions for an "off-land" condition. S&S (Schroeder and Smith 2003) can be seen to provide the highest of all G values (ignoring Cook at high τ) and is based on high frequency data collected during Hurricane *Bonnie* from a WEMITE mobile tower located at an airport site about 10 km from the coast. It can be seen to estimate higher G than K&M for $\tau <$ 10s. The Sissenwine et al. (1973) relationship is shown next, which although difficult to classify, has been included here under both the "off-land" and "off-sea" categories mainly because it is implicitly used in that context by virtue of its use in the Atkinson and Holliday (1977) wind-pressure relationship. Some interpretation has been needed to display it in this context as it is referenced to a 5-min wind and is speed dependent. Here the average gust factors for 20 to 40 m s^{-1} are used and a nominal value of 1.09 is assumed for $G_{300,3600}$. The relationship in this case lies below the other candidate forms, consistent with comments by Black (1993). Two separate mean speed results are also shown based on the Wieringa (1973) recommendations that were derived from 12 m s^{-1} mean wind data from a tower on a lake in Holland, with the results compared with other European datasets. While the examples shown here are outside the original data range, it can be seen that the Wieringa analysis suggests a decreasing G for increasing mean speed. Finally, two speed-specific results applicable to the "off-land" case from the recent V&S (Vickery and Skerlj 2005) review are shown. V&S is essentially a further follow-up to the K&M study but includes more (digital) AWS data from a variety of exposures and chooses to reject some data used by K&M as being unsuitable for gust factor analysis. V&S conclude that the ESDU theoretical approach is applicable to hurricane conditions and contradicts the recommendations of K&M and the example from S&S. There is no data shared by V&S and S&H.

In summary, while there is a broad consistency between the analyses based on extra-tropical conditions over land, which mainly derive from UK measurements, there is more inconsistency between studies derived from tropical cyclone conditions, albeit all suggesting increased G values. In regard to the tropical cyclone estimates; Powell (1987) is an averaged value from a number of land stations having varying exposures; S&S is high quality data but only for a single event at a fixed location; M&T is also high quality data but for multiple (unspecified) events at a fixed location, the exposure of which is somewhat unclear.

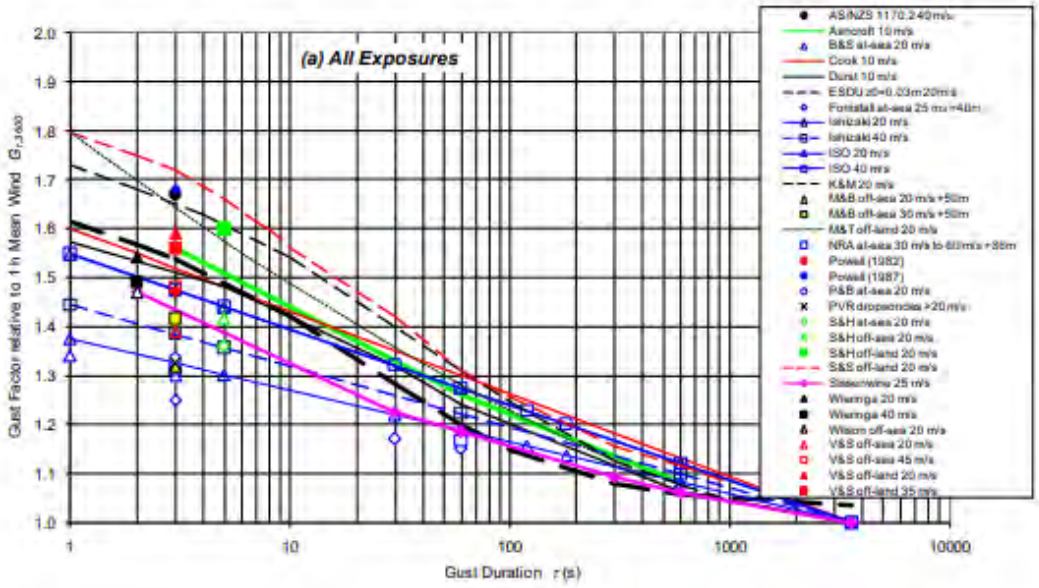

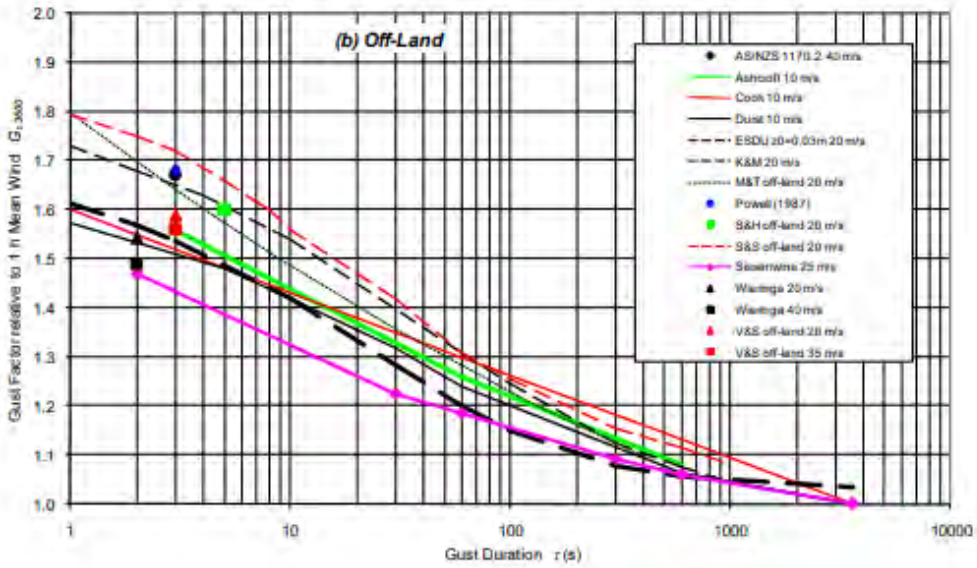

Figure 4.1 Comparison of available gust factors relative to an hourly mean wind.

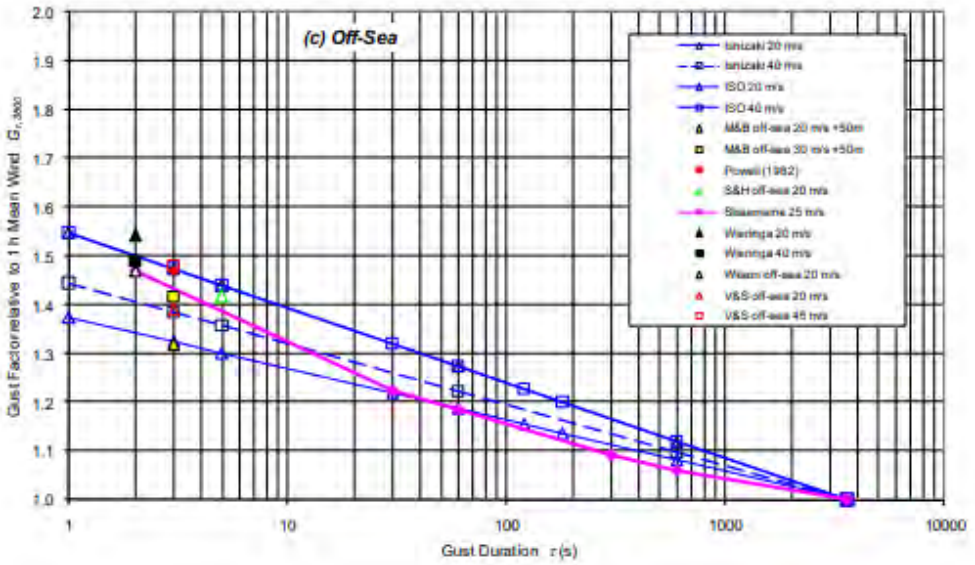

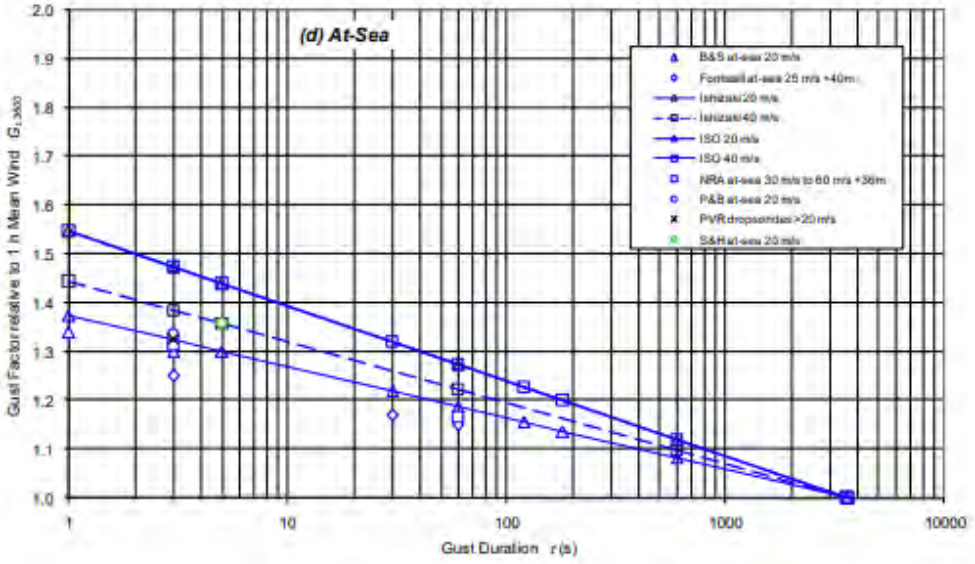

Figure 4.1 Comparison of available gust factors relative to an hourly mean wind. (contd.)

S&H's single point shown here is not a clear recommendation from that study but has been based on their discussion and seems contrary to their thesis that hurricane winds are similar to extra-tropical; V&S have attempted arguably the most consistent analysis of AWS data from a variety of sites and storms. Conclusions based on this information are that tropical cyclone gust factors "off-land" are probably higher than extra-tropical gust factors and that gust factors in general appear to decrease with increasing mean speed.

4.2 "Off-Sea" Exposure

Immediately the available dataset is diminished as the majority of European land-based studies are removed, although Wieringa (1973) is retained from the "off-land" classification as the theory was largely based on data from a lake and may be more applicable to this exposure category.

Working through the available relationships once more, the first considered is Ishizaki (1983), where two speed-specific ranges are shown, illustrating the theory that G decreases with increasing mean speed. The Ishizaki proposal is largely empirically-based and derives from consideration of nine typhoon datasets in and around Japan and, while not exclusively considering "off-sea" conditions, would appear to mainly consider that case (e.g. includes Tarama Island data). The context of the Ishizaki recommendations was to provide structural design gust factors for typhoon conditions and it has been widely used in Australia within that context with reasonable success (e.g. Holmes 2001; Harper 1989, 1993, 1999, 2001). The Ishizaki curves shown here use that author's recommended mean non-dimensional turbulence parameter of 0.4. As noted previously the Ishizaki curves tend to follow the envelope of the peak gust and hence may simply be reflecting the effect of improved sample averaging at higher wind speeds, rather than a real reduction in gust factor. Also worth noting is the straightline character of the relationship, similar to the time averaging approximation of Cook (1985).

The next proposal considered is from the draft ISO (2003) standard for offshore structural design, based on the analysis of extensive marine-aspect data from the Island of Frøya on the Norwegian coast by Anderson et al. (1991) and Andersen and Løvseth (1992, 1993, 2006). This study was commissioned as a Joint Industry Project for the offshore oil and gas industry in the North Sea and remained under technical embargo for some years. However, the same recommendations, including spectral descriptions, have now been adopted by API (2002), which provides design standards for offshore structures in the Gulf of Mexico, thus apparently endorsing this approach for hurricane conditions. There is a strong wind speed dependency in the ISO proposals that can be seen to be contrary to Ishizaki; for example the ISO 20 m s^{-1} starts from a low base and the ISO 40 m s^{-1} curve overlies the Ishizaki 20 m s^{-1} curve. Notwithstanding that the instrumented towers were located close to the sea, some of the Frøya data may have been affected by an internal boundary layer and this might be reflected in the increased low frequency energy seen in spectra. The ISO lines are also straightline, unlike the "S-shaped" Durst and ESDU formulations, and inspection of the detailed supporting reports shows little evidence for curvature in this context.

Data analysed by Melbourne and Blackman (1982) from Waglan Island near Hong Kong is presented here (M&B) as two speed ranges, showing an increase in G with mean wind (s.d. 0.13 in each case). The M&B analyses are based on Dines data from 39 typhoon episodes over the period 1953 to 1980 but suffer from a number of measurement and siting issues on this rugged and steep site. Firstly the data was strip-chart based and had to be corrected for the (significant) local topographic effects. The +75 m anemometer data was adjusted to a free-stream +50 m over the sea by the application of wind tunnel modelling and a peak factor g of 3.7 was assumed to provide representative mean winds, based on the Deaves and Harris (1978) recommendation for Dines gust response. M&B were amongst the first to suggest that the near-shore sea surface roughness was higher than previously expected in strong wind conditions and this thinking underpinned recommendations in Standards Australia (1989, 2002a) that a z_0 of 0.02 m was representative of tropical cyclone "off-sea" conditions. Notwithstanding this, Sharma and Richards (1999) have

pointed to apparent inconsistencies in the AS/NZS 1170.2 turbulence intensities and gust factor approach, claiming higher values should be used.

Powell (1982) analysed surface winds from Hurricane Frederic and his recommended $G_{3,600}$ values are interpreted here as probably being representative of the "off sea" exposure and are also nominally adjusted by 1.05 to represent $G_{3,3600}$. Sissenwine (1973) is again shown and in this context appears somewhat closer to the consensus. A single indicative value from Sparks and Huang (2001) is next, based again on their general discussion, although lower values around 1.3 were individually reported, say, for Hurricane *Bonnie* from the Cape Lookout CMAN station. A single mean value from Wilson (1979a) is indicated for North West Cape coastal tower data but this has been adjusted here from his original $G_{3,600}$ of 1.40 by the 1.05 factor. Finally two examples from Vickery and Skerlj (2005) for marine and near-shore coastal exposure are indicated (V&S).

In summary, for the "off sea" exposure there appears to be some support for the extra-tropically based ISO proposals amongst the tropical cyclone experience, but with the distinct exception of the Ishizaki approach (which was a mixture of offshore island and coastal data).

4.3 "At-Sea" Exposure

The ISO and Ishizaki 20 and 40 m s^{-1} cases have been carried forward here to provide a background to the remaining very limited data for the "at sea" exposure class. The first new data points (B&S) are from Brown and Swail (1991), showing their $G_{1,3600}$ and $G_{3,3600}$ recommendations based on extra-tropical data from West Sole platform in the North Sea and Bedford Tower near Nova Scotia. Also shown are values interpreted from Forristall (1988) for Hurricane *Eloise* in the Gulf of Mexico. Black (1993) has dismissed the B&S and Forristall data previously as being too low and unsuitable for tropical cyclone conditions because of stability issues arising from relatively cool air being swept into the storms. However, for comparison, some composite estimates for $G_{3,3600}$ and $G_{60,3600}$ based on four tropical cyclones (including *Orson* from Section 3) measured at +36m on North Rankin 'A' platform (NRA) show that the B&S values at least may not be unusually low. The NRA values are all in winds of order 30 m s^{-1} or greater but have been adjusted here by 1.05 from their 600 s T_o base reference period.

Searching for more data in this offshore context, Powell and Black (1990) data from buoys on the USA Atlantic coast during hurricanes is shown as P&B, taking their nominal $G_{5,510}$ as approximately equivalent to $G_{3,600}$ and then multiplying also by 1.05. Next is Powell et al. (2003), providing the first indication of gust factors in hurricanes as measured by GPS dropwindsondes (shown as PVR). Their mean nominal +10 m mean gust factor value of 1.25 has been interpreted here as a $G_{3,600}$ and adjusted by 1.05, although it is noted that the authors comment on not being entirely certain at this stage as to the likely applicable τ value because of loss of high frequency components in the analysis. Indeed, because of the quasi-Lagrangian reference of the 10 to 15 m s^{-1} fall rate of GPS dropwindsondes, there remains some doubt at this time as to the applicable T_o reference period. Finally, the Sparks and Huang (2001) broad recommendation for offshore situations is included.

In summary, all available "at sea" gust factors are significantly lower than the "off-sea" case and are closely approximated by the ISO 20 m s^{-1} curve. However, many of the data represent mean winds well in excess of 20 m s^{-1} and are therefore at significant variance with (say) the ISO 40 m s^{-1} curve, even allowing for some elevation differences. Meanwhile, the empirical Ishizaki curve would converge onto the data at about 65 m s^{-1}. It is concluded that the ISO curve may be too sensitive to the mean wind in this situation and that this may relate to its formulation based on the near-shore wave shoaling and breaking environment rather than in the open ocean. It is also worth noting that the NRA data are a particularly valuable reference in these circumstances, especially since the data have been collected from several types of instrumentation in winds up to 30 m s^{-1}.

4.4 A Simplified Gust Model for Tropical Cyclone Forecasting

The accurate measurement of wind speed fluctuations, especially under tropical cyclone conditions, is a demanding activity that will always result in scatter from even the most careful analyses. There are significant gaps in our understanding of atmospheric turbulence characteristics and with necessarily complex empirical descriptors, many degrees of freedom result.

The forecasting of tropical cyclones is an already difficult task. In consideration of the apparently wide range of observational data presented, and the problem of ensuring consistent analysis, a sensible approach in the context of recommending wind averaging formula would therefore seem to be one of applying consistency within a suitable theoretical framework. This section therefore proposes a simplified approach to achieve that goal, which can be readily updated as further information comes to hand. Based on the foregoing review of theoretical studies of the relationship between different wind averaging periods and the assessment of available data, the approach recommended by ESDU (2002b) is deemed currently the most appropriate basis for conversion and comparison purposes. In this regard the present review supports Vickery and Skerlj (2005), which also proposes the ESDU method. However, not all aspects of this approach are necessarily of interest here with regard to tropical cyclones. In particular, the full method relies on largely UK datasets for estimating turbulence intensities, their variation with height and also changes in terrain roughness and the like.

For the present forecasting purposes the standard (nominal) observational elevation of +10 m only is of interest and it will be assumed that the terrain/sea is of constant form and roughness and that mean winds are in excess of 17 m s^{-1}. Under these limitations, it is considered appropriate to replace the complex ESDU formulations with suitable *a priori* estimates of the longitudinal turbulence intensity I_u. This specifically permits adjustment of turbulence values to better represent the apparently enhanced conditions observed near and on land during tropical cyclones, and also conveniently avoids any determination of actual z_o values at this time. Appendix D presents a summary of the recommended method, which also requires some extension of the ESDU procedures for the shorter τ values of interest to this study.

The way forward here is therefore to use only the available tropical cyclone specific data, suitably grouped into the previous exposure classes, to calibrate the recommended ESDU method for a range of I_u values. This also permits the use of some data from Appendix C that was not used in Section 4 because of T_o reference periods less than 600 s, and therefore deemed unreliable for converting to an hourly reference. Only 3600 s, 600 s and 60 s reference period data are available for this procedure and the best-fit condition was arrived at objectively based on least squared error.

Figure 4.2 presents the final calibrations in terms of the three previously defined "over water" exposure classes and Table 4.1 summarises the adopted values for longitudinal turbulence intensity and roughness length, which also includes a nominal "in-land" class based on the "roughly open" classification of Table 2.1. By way of explanation, each set of data points in the figure refers to a different wind averaging period of the mean wind, which is overlaid by the proposed equivalent ESDU analytical form. From Appendix C it can be noted that the standard deviation of the gust factors, where available, is of order 0.1 and this is indicated by the nominal error bars.

Table 4.1 Recommended turbulence intensities and associated roughness lengths for tropical cyclone forecasting purposes.

Exposure Class	Turbulence Intensity I_u	Roughness Length z_o (m)
"in-land"	0.250	0.18
"off-land"	0.200	0.07
"off-sea"	0.150	0.013
"at-sea"	0.100	0.0005

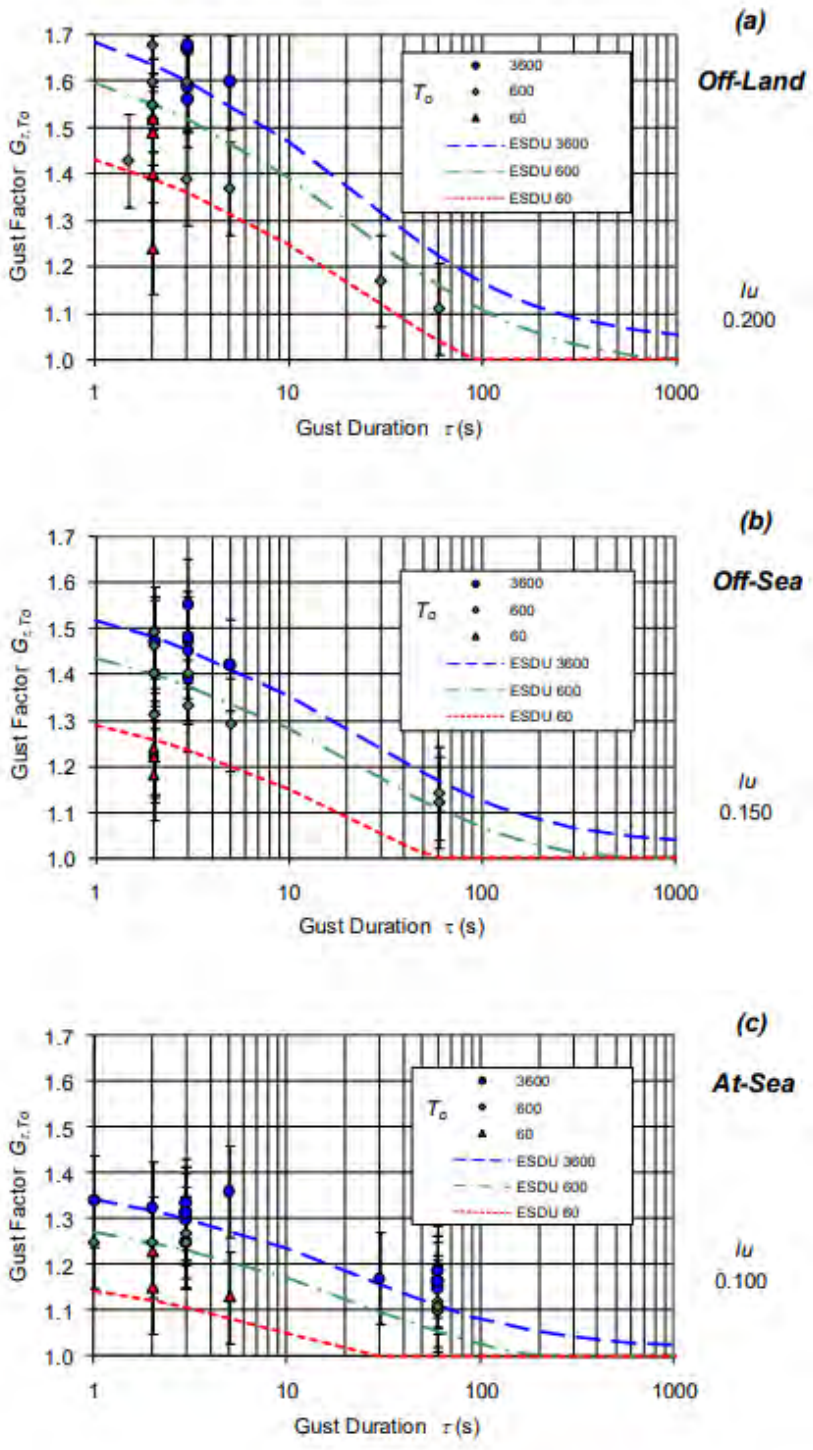

Figure 4.2 Calibration of the modified ESDU method for tropical cyclone forecasting purposes.

5 Conclusions and Recommendations

A review has been undertaken of past and contemporary theory and data relevant to the issue of wind averaging periods and wind speed conversions under tropical cyclone conditions focusing on the open ocean and coastal situations. The recommended conversions are given in Table 1.1.

It is concluded that the accurate measurement of wind speed fluctuations, especially under tropical cyclone conditions, is a difficult and demanding activity that will always result in scatter from even the most careful analyses, and the available data and some theories show many inconsistencies. Clearly there are still significant gaps in our understanding of near-surface atmospheric turbulence characteristics under strong wind conditions. However, because the forecasting of tropical cyclones is an already difficult task, a simplified approach has been recommended that should nevertheless lead to an increase in consistency of quoted and forecast winds. An existing mathematical description of wind over-land in extra-tropical conditions has been adapted for this purpose and nominally calibrated against a wide range of assembled tropical cyclone wind data. The recommended procedure is seen as a practical interim solution until such time as increased data collection and analysis provides a more definitive description of the wind turbulent energy spectrum in various situations under tropical cyclone conditions.

The review has specifically highlighted the need to distinguish clearly between randomly sampled estimates of the mean wind speed based on any chosen averaging period and the peak gust wind speed within a particular observation period. It is particularly noted that mean wind speed estimates should not be converted between different averaging periods – only gust wind speeds.

It is recommended that the WMO regional associations and panels work towards revising and standardising their wind terminology, definitions and associated use of averaging periods in the various operational plans (e.g. as summarised here in Appendix A) and in accordance with WMO (2008). This will assist in ensuring that the historical record contains more consistent measurements and/or estimates that can be reliably transformed or converted for assisting in further development of the science.

The review has also identified the need for special considerations in regard to converting between agency estimates of storm-wide maximum wind speed (*Vmax*) that are based on different wind averaging periods (refer Table 1.2). This is because such estimates imply both space and time contexts and the past practice of associating the so-called 1-min "sustained" wind with the Dvorak (1984) intensity estimation method has been done without regard to a stated observation period.

Accordingly, the review recommends an at-sea conversion between the $Vmax_{60}$ estimate of peak storm intensity and the $Vmax_{600}$ estimate of 0.93, rather than the "traditional" value of 0.88, which has been shown here to be associated more with an off-land exposure. This implies that current practice has underestimated the $Vmax_{600}$ by about 5%, relative to an equivalent $Vmax_{60}$ value.

It is also strongly recommended that the WMO work towards a re-calibration of the "Dvorak-related" intensity estimation techniques, based on a more rigorous treatment of wind-averaging issues.

The continued expansion of quality automatic weather station (AWS) networks and research-standard specialist facilities is strongly encouraged in order to gather the necessary information for future reviews and revised recommendations. Forecasters and researchers are also urged to ensure that AWS siting, instrument selection, sampling, processing, documentation and archiving of wind data is carried out in a manner that will ensure accurate estimation of the mean wind and its associated turbulence properties. As a minimum, this should include the 10-min averaged wind (V_{600}) and the 3-sec peak gust in each 10 minutes ($V_{3,600}$), with the 1-min average wind also desirable (V_{60}) because of its adopted usage in the TC context. Where possible, episodes of high wind (say >17ms^{-1}) should be recorded continuously at 10Hz sampling to provide research-grade datasets.

Appendix A A Critique of Existing WMO Practice

The current practices of the five tropical cyclone regional association panels and committees in regard to wind averaging periods are contained in WMO (2002abc) and WMO (2003ab). There are three stated wind speed types and associated averaging periods currently in use. The three declared "surface" wind types found in the WMO regional operational plans are:

- Average (or mean) wind speed
- Wind gust speed
- Maximum sustained wind speed

Table A-1 below summarises the critical points of difference in terms of the stated averaging periods used, while the literal definitions of these wind types are presented overleaf in Table A-2 for reference. It is important to note that these definitions serve two distinct purposes: (i) for the taking of observations (the Average Wind Speed column), and (ii) for describing the intensity of tropical cyclones (the Maximum Sustained Wind Speed column). It is noted that only RA IV HC defines "surface" winds as being measured at a height of 10 m and none of the plans specify the actual exposure of the wind measurement or estimate, although "at sea" is implied in the general tropical cyclone context.

Table A-1 Defined surface wind averaging periods in current WMO operational plans.

Committee	Region	Average Wind Speed	Gust Wind Speed	Maximum Sustained Wind Speed
RA I TCC (Tropical Cyclone Committee)	SW Indian Ocean	10-min	Not defined	1-min
WMO/ESCAP Panel on Tropical Cyclones	N Indian Ocean	10-min (recording) 3-min (non-recording)	Not defined	Maximum value of the average; either 10-min, 3-min or 1-min at the surface.
RA IV HC (Hurricane Committee)	Americas and the Caribbean	1-min (recording and non-recording)[9]	Not defined	*Not defined but average is implied.*
RA V TCC (Tropical Cyclone Committee)	S Pacific Ocean and SE Indian Ocean	10-min (1min for USA territories)	Not defined	Maximum value of the average.
ESCAP/WMO Typhoon Committee	NW Pacific, South China Sea	10-min (recording) 3-min (non-recording)	Not defined	Maximum value of the average; either 10-min, 3-min or 1-min.

In addition to the above WMO affiliates, the US Department of Defense Joint Typhoon Warning Center (JTWC) based in Hawaii, which covers certain Western Pacific and Indian Ocean areas, uses nomenclature similar to RA IV HC. It is also understood that a 2-min average wind may be in use in China, possibly for non-recording situations, but this is not described in the ESCAP/WMO Typhoon Committee documentation. The operational plans define neither the averaging period nor the reference period for a wind gust. Also, while all of the associations recommend archiving the averaging period used for the average wind estimate, only three (RA IV HC, V TCC, ESCAP/WMO Typhoon) recommend archiving the applicable gust averaging period. RA I TCC provides guidance on converting the average 10-min wind speed to a gust speed (1.41) and to a 1-min sustained speed (1.14) for over-water conditions.

Table A-2 Literal definitions of the various wind speed types in the glossary of current regional WMO tropical cyclone, typhoon and hurricane operational plans.

Committee	Region	Average Wind Speed	Gust Wind Speed	Maximum Sustained Wind Speed
RA I TCC (Tropical Cyclone Committee)	SW Indian Ocean	Speed of the wind averaged over the previous 10 minutes.	Instantaneous peak value of surface wind speed.	Surface wind speed averaged over the previous 1 minute.
WMO/ESCAP Panel on Tropical Cyclones	N Indian Ocean	Speed of the wind averaged over the previous 10 minutes (mean surface wind) as read from the anemogram or the 3 minutes mean determined with the non-recording anemometer or estimated wind at sea by the mariners using the Beaufort scale.	Instantaneous peak value of surface wind speed, recorded or expected.	Maximum value of the average wind speed at the surface.
RA IV HC (Hurricane Committee)	Americas and Caribbean	Determined by averaging observed values from a direct-reading instrument or a recorder over a 1 minute period. The standard height of the wind measuring instrument is 10 meters.	Fluctuation in a short time of wind speed with a variation of 10 knots or more between peaks and lowest speeds.	(Not defined but average is implied.)
RA V TCC (Tropical Cyclone Committee)	S Pacific Ocean and SE Indian Ocean	Speed of the wind averaged over the previous 1 or 10 minutes.	Sudden, brief increase of the wind speed over its average value	Same meaning as average.
ESCAP/WMO Typhoon Committee	NW Pacific, South China Sea	Speed of the wind averaged over the previous 10 minutes (mean surface wind) as read from the anemogram or the 3 minutes mean determined with the nonrecording anemometer or estimated wind at sea by mariners using the Beaufort scale.	Instantaneous peak value of surface wind speed.	Maximum value of the average wind speed at the surface.

The Global Guide to Tropical Cyclone Forecasting (WMO 1993), which arose as an initiative from the International Workshop on Tropical Cyclones, includes wind gust factors within its wide range of technical recommendations. While none of the WMO operational plans reference the Global Guide it is understood that the guidelines therein are widely used by forecasters.

The Global Guide does not provide background into the various issues that specifically relate to the selection of wind averaging periods, but it does define a gust averaging period as 2-s and also identifies some of the key associated observational issues. The recommendations are summarised within its §Section 9.5.2 and derive from its §Table 4.2, introduced as follows:

Gust factors defined by the ratio of peak 2-s wind to the mean wind at 10 m elevation for various exposures and averaging times and in wind speeds of at least hurricane force. Parenthesis give an indication of the range in gust factors.

Table A-3 Existing Global Guide advice ***(NB: Superceded here)***

	Ocean	Flat Grassland	Woods/City
1-min Mean	1.25 (1.17-1.29)	1.35 (1.29-1.45)	1.65 (1.61-1.77)
10-min Mean	1.41 (1.37-1.51)	1.56 (1.51-1.70)	2.14 (1.89-2.14)
10-min Mean over Ocean	1.41	1.31	1.11

The data used to prepare the above is attributed to studies by Atkinson (1974), Spillane and Dexter (1976) and Padya (1975) and is a simplified form of §Table 7.3 in BoM (1978). The factors provided in the final row of Table A-3 are from Spillane and Dexter (1976) and are relative to the mean over-ocean speed, combining an allowance for an expected reduction in mean winds with increasing surface roughness but offset by an increase in gustiness.

It should be noted that the above table does not explicitly provide a conversion between a 1-min peak gust and a 10-min mean wind, although §Table 7.4 in BoM (1978) recommends 1/0.88 (=1.14), apparently based directly on the recommendation by Atkinson (1974). Meanwhile, §Section 1.3.3 of WMO (1993) does recommend a conversion of 1/0.871 (=1.15), with linkage to Simiu and Scanlon (1978) and Durst (1960) (see also Appendix E). It appears that ratios of the factors in Table A-3 may have also been commonly used to infer that a $G_{2,600}/G_{2,60}$ factor of 1.41/1.25 (= 1.13) is applicable over the ocean for converting from 10-min to 1-min "means". Use of gust factor ratios in this way, however, is not correct.

Either way, there is confusion or ambiguity in Table A-3 between the wind averaging time and the reference or observing time of the wind speed sample. For example, the labelled "1-min Mean" is not an unbiased estimate of the mean wind in this context and should be referred to as a "gust", in exactly the same context as the 2-sec gust, which forms the basis of the table recommendations.

It is concluded that the existing WMO regional association definitions of mean winds, "sustained" winds and wind gusts leads to uncertainty and ambiguity with regard to how specific metrics of the wind can be inter-compared. This reflects a lack of rigor generally in describing near-surface winds within the forecasting environment that can lead to misinterpretation and result in unintentional biases (high and low) of forecast winds. In particular, there is a tendency to misuse the term "mean" wind amongst the tropical cyclone community where the maximum 1-min "sustained" wind is involved. Also, it is noted that only RA IV HC defines the "surface" wind height as being 10 m and no plans explicitly state the wind exposure, although the typical context is "at sea".

Appendix B History of Scientific Studies of the Wind with Special Reference to Tropical Cyclones

According to Greenway (1979), possibly the earliest scientific consideration of the impact of wind forces was that following the Tay Bridge disaster in 1880 Britain, which resulted in a seven year study of wind pressures on four different sized sensing boards at the location of the Firth of Forth Railway Bridge in Scotland. The resulting differences in maximum wind pressures painstakingly measured over this time not only yielded a level of critical insight into wind turbulence scales that we now appreciate, but also highlights the continuing need for rigour and persistence when attempting to describe local properties of the near-surface wind. The production of the first Dines pressure tube anemometer followed in 1892 and quickly became a worldwide standard for measuring the wind that is still in widespread use today. Its oft-quoted nominal peak response to a "2 to 3 s" gust has underpinned much of the world's thinking about characterising the force of the wind for structural design purposes (e.g. Sanuki 1952; Whittingham 1964).

Some of the earliest identified comprehensive wind studies in the 20th century appear to be that of Sherlock and Stout (1932) in the USA at Ann Arbor and Giblett (1932) in the UK at Cardington, all understandingly limited to the land environment at that time. However it was not until the mid 1950s that the need for statistical guidance gained prominence and early spectral measurements by Panofsky and McCormick (1954), for example, set the scene for the future study of atmospheric turbulence. Around the same time, tower-based measurements by Deacon (1955) at Sale in Australia were valuable additions to the topic and also addressed the issue of anemometer response and filtering effects in the analysis of peak gusts.

Charnock (1955) used a modest set of measurements made over a UK water supply reservoir to propose a simple yet profound non-dimensional scaling of the surface wind stress over water with wind speed. Perhaps surprisingly, Charnock's proposal survives to this day as one of the central empirical postulates governing turbulent wind structures over the ocean.

Building on the Panofsky work, Van der Hoven (1957) illustrated the broadband spectral character of the near surface wind and identified the possibility of a near-universal wind energy gap around 1 h, a concept desirable for building a practical statistical description of the wind. Using this concept, a relatively simple analysis by Durst (1960) using Giblett's UK data (specifically 16 high frequency 10 minute records combined with 44 days of data run) has survived as a useful resource to this day (e.g. Krayer and Marshall 1992; ANSI 1996; Powell et al. 1996) in spite of its simplified statistical approach that assumed Gaussian rather than extreme value gust statistics.

Some of the earliest references to studies of tropical cyclone winds and associated gust factors appear due to Bell (1961), who studied typhoons in the Hong Kong area, and the summary by Tanigutchi (1962), which considers storms near Japan from 1955 to 1962.

In the 1960s, demands for more slender structures and increasingly light-weight construction materials, lead to the structural design specialisation of *wind engineering*. Davenport (1961, 1964) is widely regarded as the father of this science and his development of a spectral form for near-surface winds paved the way for many detailed studies during the 1960s and 1970s. His 1964 treatment of the statistical estimation of short period gusts within a given averaging time is still widely regarded as the method of choice (e.g. ESDU 2002b). Whittingham (1964) provided a solid summary of much work to that time, including an assessment of the peak gust response of the Dines anemometer, and was the first to summarise the significant Australian experience with extreme wind gusts from tropical cyclones. Deacon (1965) presented similar relationships to Durst for the effect of different averaging times on estimating a 2-s gust using data from Sale, Cardington and Shellard's (1958) UK data. Brook and Spillane (1968) also proposed a variant to the Davenport spectrum, which included a gust profile approach with apparently similar predictive skill.

The 1970s represented a rapid period of growth in knowledge. Wieringa (1973) extended the Durst methodology in combination with the Davenport (1961) roughness scaling concepts and produced an analytical approximation to the gust formula, which was compared with a variety of datasets. Counihan (1975) also provides an extensive review of boundary layer studies of special relevance to UK structural design challenges of the time. Sissenwine et al. (1973) undertook a wide-ranging investigation into the characteristics of extreme winds for use worldwide by the US Air Force. Although their available datasets were somewhat disparate and the analyses highly empirical, they proposed a series of nomograms for gustiness as a function of speed and height, and considered averaging intervals appropriate for specific length scales. A contemporary review by Atkinson (1974) for the Joint Typhoon Warning Center (JTWC) appears to offer the earliest review and recommendation of gust factors for tropical cyclone conditions, highlighting the difficulties of such measurements and lamenting the lack of reliable data – a situation that is not much changed 30 years later. The review drew upon a range of discrete observations (many as summarised by Tanigutchi 1962), combined with several years of Navy ship reports and other isolated data. Unfortunately however, both Sissenwine et al. (1973) and Atkinson (1974) began a trend of incorrectly referring to ratios of average wind speeds. The former considers 5 min and 1 min averages, while the latter considers 10 min and 1 min averages, while both additionally accept the concept of a peak gust. Implicit in each development is that the estimated 1-min winds are indeed the highest 1-min winds within either the 5-min or 10-min reference period and hence are not random averages of wind speed but rather gusts.

In the mid-1970s Simpson (1974) and Saffir (1975) were influential in proposing a "hurricane disaster-potential scale" that extended the Beaufort scale ranges, and remains in prominent use today in the USA. In the present context it is worth noting that while Saffir (1975) clearly labelled the proposed index wind speeds as "2 or 3 s gusts", there is no similar confirmation in Simpson (1974) as to the applicable averaging period. Subsequently, it appears that a popular assumption was made to associate the Saffir-Simpson wind speed ranges with the so-called "1-min sustained" wind. Potential consequences of this sequence of assumptions were recently raised by Sparks (2003).

During the latter part of the 1970s the development of UK wind engineering structural design codes was rapid, moving from earlier power law representations of the boundary layer vertical wind speed profile (e.g. Newbury and Eaton, 1974) to the more theoretically-based logarithmic profile (e.g. Deaves and Harris, 1978). Increasingly, attempts to better describe tropical cyclone conditions were made (Mackey and Ko 1975; Choi 1978; Spillane and Dexter 1976) and some important case studies were presented (Padya 1975; Wilson 1979a,b). Atkinson and Holliday (1977) developed a wind-pressure relationship for typhoons in the Western North Pacific based on adjusting measured peak wind gusts to a 1-min average wind using recommendations from Sissenwine et al. (1973). This relationship is still used extensively worldwide by tropical cyclone forecasters (Velden et al. 2006) as a part of the Dvorak (1984) intensity estimation technique.

In the 1980s the emerging discipline of wind energy fostered further theoretical study (e.g. Fordham 1985; Beljaars 1987a,b; Kristensen et al. 1989) while tropical cyclone related studies increased in the North West Pacific region (Melbourne and Blackman 1982; Choi 1983; Ishizaki 1983; Naito 1988; Ishida 1989; Mitsuta and Tsukamoto 1989). Many of these studies involved nearshore towers or island-based measurements, although the results sometimes showed large variations in the estimated gust factors, likely due to the wide range of exposures. In the Atlantic (Powell 1982, 1987) provided detailed analyses of landfalling Gulf of Mexico Hurricanes *Frederic* and *Alicia*, comparing aircraft observations adjusted using the Powell (1980) boundary layer model with surface measurements and determining representative surface gust factors for forecasting purposes.

In the offshore zone, some of the earliest reliable data on gust factors came from oceanographic studies in the North West Atlantic (e.g. Wu 1982; Tieleman 1985; Smith and Chandler 1987) and Dobson (1981), on behalf of the WMO, comprehensively considered the many issues concerning

reliable mean wind measurements at sea. Forristall (1988) was one of the first to propose a specific gust factor model for tropical cyclones, using offshore platform data in the Gulf of Mexico.

In the Australian region, where design codes had traditionally followed UK practice, the devastating impact of *Tracy* at Darwin in 1974 had already prompted a special allowance for tropical cyclone conditions. Standards Australia (1989) further revised these recommendations to recognise an increased turbulence regime during tropical cyclone conditions, this being based largely on subsequently measured data (e.g. Wilson 1979ab; Melbourne and Blackman 1982).

In the 1990s, Brown and Swail (1991) presented a review of available methods for estimating strong wind gusts in general oceanic conditions but were unable to make comprehensive recommendations. Northern European studies (e.g. Kristensen et al. 1991; Mahrt and Gibson 1992; Ashcroft 1994) continued to explore detailed turbulent structures and gust factors, mainly over land. One exception to these was a joint oil industry project (Andersen et al. 1991, 1992, 1993) that specifically addressed marine exposure and has now become a recommended industrial standard for both extra-tropical and tropical conditions (ISO 2003; API 2002).

In Japan, Hayashi (1991, 1992) continued the tradition of high quality spatial analyses and in Europe, Wieringa (1992) provided a revised Davenport surface roughness classification system. In the USA, interpretation of the growing database of offshore tropical cyclone winds both at reconnaissance level and the surface became available (Powell and Black 1990) and a number of significant and influential case studies appeared (e.g. Powell et al. 1991; Krayer and Marshall 1992; Powell and Houston 1996; Powell et al. 1996; Schroeder et al. 1998).

Black (1993) provided insight to the historical use of gust factors in the NW Pacific and discounted some of the later gust factor data from extra-tropical systems as being stability-affected. Holmes (1997) proposed revised guidelines for estimating the wind averaging period that would critically affect structures of various scale. Sharma and Richards (1999) provided a review of contemporary practices for specification of turbulence intensities and gust factors in tropical cyclone conditions, suggesting that some present design allowances may be insufficient.

In the current decade, theoretical turbulence studies are still proceeding (e.g. Toriumi et al. 2000; Brasseur 2001; Boettcher et al. 2003) but the increasing availability of higher quality *insitu* tropical cyclone data in the USA from fixed CMAN and also mobile platforms has caused a sudden burst of analyses (e.g. Sparks and Huang 2001; Schroeder et al. 2002; Paulsen et al. 2003; Paulsen and Schroeder 2005; Vickery and Skerlj 2005; Masters et al. 2005).

Some of the latest insight into open ocean gust factors has now come from analysis of GPS dropwindsondes (Franklin et al. 2003, Powell et al. 2003) and increasing demands are being placed on agencies that provide community wind speed estimates (e.g. Sparks 2003, 2004) for more relevant and accurate advices.

In summary, the science of the natural wind has progressed significantly since its beginnings in the 1930s, with the 1960s and 1970s dominated by applications in wind engineering, and the 1980s onwards benefiting from better and more extensive datasets as a result of advances in computing and storage technology. In the 1990s, knowledge of tropical cyclone conditions in particular has increased markedly. Notwithstanding the increased data however, interpretation still relies on relatively robust concepts founded in the 1950s.

Appendix E Converting Between Agency Estimates of Tropical Cyclone Peak Wind Speeds

As detailed in Appendix A, operational centres define the tropical cyclone intensity as the strongest "surface" wind, averaged over some specified period, occurring anywhere within or nominally associated with the storm[10]. The exposure for the definition, although not stated, is implicitly taken to be sea before landfall and flat open terrain afterwards, with an observation height of 10 m. Defining intensity as the strongest wind implies that the intensity is dependent on the gustiness, and in turn that the numerical value will depend on the averaging period, since longer averaging periods will filter out more of the turbulence and have a lower maximum wind. The problem is to convert tropical cyclone intensity estimates based on one wind averaging period to those based on another. For convenience, we take the two averaging periods to be the commonly-used 1 and 10 minutes, but the arguments herein are applicable to other periods also.

Consider first an idealised situation with an infinite area exposed to a turbulent wind field in which the true mean wind V is everywhere the same. Suppose that the intensity of this weather system in terms of the maximum 1-min mean wind speed is $Vmax_{60}$ and that we wish to convert this intensity estimate to a different averaging period, that is, estimate the maximum 10-min mean in the storm, $Vmax_{600}$. We estimate the true mean wind V from $Vmax_{60}$ as

$$V = Vmax_{60}/G_{60,infinity} \tag{E-1}$$

where the *infinite* reference time for the gust factor is taken because the domain is assumed infinite.

We may then similarly estimate the maximum 10-min gust as

$$Vmax_{600} = V\,G_{600,infinity} = (Vmax_{60}/G_{60,infinity})\,G_{600,infinity} \tag{E-2}$$

So the conversion in this case is to multiply by $G_{600,infinity}/G_{60,infinity}$. In practice, gust factors for infinite reference periods are unavailable, but in expectation that the gust factor will asymptote as the reference period increases, we pragmatically use the longest period considered here, 1 hour, for practical computations.

The top row of Table E-1 shows these values for various exposures, taken from Table 1.1. They should be compared to the ratio of the 10-min mean to the 1-min mean from Appendix A, referred to as the "traditional" approach in Table E-1. For storms with at-sea exposure, the recommended conversion factor is closer to 1 than the traditional value, implying that conversions from 1-min to 10-min standards have in the past tended to underestimate the 10-min intensity of storms by about 5% (assuming that the 1-min estimate is unbiased). Note also that the differences between columns are significant, demonstrating that the conversion factor has a strong dependence on exposure, a variation that does not seem to have been applied in practice.

[10] The intensity metric may be subject to specific agency interpretations and may exclude processes or features that occur within the tropical cyclone and cause high wind speeds but are deemed by the analyst to not be representative of the storm's circulation, possibly because of their assumed transient nature. For example, in Hurricane Felix, an SFMR-observed wind of 163 kt in close proximity to a dropsonde observation of 195 kt at 120-m height (Beven 2008) were both deemed to have "sampled a small-scale feature unrepresentative of the intensity of Felix at the time" (Brennan et al. 2009, page 20) and the best-track intensity was set to 150 kt. This intensity estimate was noted to be conservative.

Table E-1 Comparison of recommended and traditional conversion factor approaches.

	Conversion	At-Sea	Off-Sea	Off-Land	In-Land
Recommended Method	$G_{600,3600}/G_{60,3600}$	1.03/1.11= 0.93	1.05/1.17 =0.90	1.06/1.22 =0.87	1.08/1.28 =0.84
Comparison	$1/G_{60,600}$	0.95	0.90	0.86	0.83
Traditional	See text	0.88			

The origins of the traditional 0.88 (or its reciprocal, 1.13) are not entirely clear. Some users (e.g. Kamahori et al. 2006) cite Simiu and Scanlon (1978), and indeed the ratio $G_{600,3600}/G_{60,3600}$ as calculated from their §Eqn 2.3.30, does equal 0.88 provided that the roughness length z_0 is taken to be 0.02 m. The WMO (1993, §Section 1.3.3) value of 0.871 similarly follows from z_0 = 0.05 m provided that a nonlinear interpolation of the data in Simiu and Scanlon is made (Charles Neumann, personal communication 2008). The ratio 0.88 can also be obtained from Durst (1960, §Table VII with modifications noted by the text), which was subsequently used in Simiu and Scanlon's derivation. However, we note that both z_0 = 0.02 m, z_0 = 0.05 m and Durst's data are all characteristic of open terrain land, and that the roughness length over the ocean is significantly less[11]. Thus the long-standing use of this factor for tropical cyclone intensity conversion over the sea appears incorrect. Indeed, applying Simiu and Scanlon (1978, §Eqn 2.3.30) to a typical high-wind marine z_0 = 0.002 m (e.g. Powell et al. 2003, Donelan et al. 2004, French et al. 2007) yields 0.91, which is closer to the at-sea ratio recommended here. Hence, while we have placed the traditional 0.88 in the at-sea column of Table E-1 to reflect its extensive past usage, properly it belongs in the at-land column.

Some have apparently noted that the factor 0.88 = $G_{2,60}/G_{2,600}$ with these gust factor values taken from the ocean values in WMO (1993, §Table 4.2) or BoM (1978, §Table 7.3). Possibly this association has arisen from the close proximity of the latter table with a statement that the appropriate conversion of intensity for averaging period over the ocean is 0.88, although no clear citation of the source of 0.88 is given there. We regard such a connection as fundamentally incorrect, since it implies a conversion via the maximum 2-s gust, which does not necessarily occur within either the maximum 1-min or 10-min reference periods, and nor is the maximum gust in a 1-min period necessarily equal to the maximum gust in a 10-min period, as can be seen, for instance, in Figure 2.3. Further, this line of argument inherently involves a confusion of reference and averaging periods.

Unlike the idealised situation discussed above, real storms do not have infinite uniform wind fields. One implication of this fact is that the averaging period should not be too long, due to the requirements for stationarity (Section 2.5) and to not smooth out the important strong gradients near the eyewall. A second is that an infinite reference period for the gust factors becomes inappropriate. Searching for the maximum gust in space within a storm is akin to searching in time within an anemometer record, and in principal at least, one could define a reference time equivalent T_{eq} to a given reference area. For instance, we might define T_{eq} so that in each case we are searching over the same number of integral-scale's worth of air for the maximum wind, remembering that one search is linear and the other over an area. Having done so, it is straightforward to extend the above reasoning and conclude that $G_{600,Teq}/G_{60,Teq}$ is the appropriate intensity conversion factor. A complication is that the size and shape of the maximum wind belt varies between tropical cyclones – narrow versus broad, confined to one quadrant versus quasi-axisymmetric, and small RMW vs large. Thus the equivalent reference time T_{eq} is in principal situation-dependent. The maximum

[11] We also caution the reader that these authors frequently say "mean" when in fact they mean "gust".

wind belt typically scales as 10's of km long and from a few to 10's of km wide. Noting that 10 km along-wind is equivalent to 200 s for a mean wind of 50 m/s, and that the cross-wind turbulence length scale is shorter than the long-wind one, we might reasonably expect that T_{eq} is typically of the order of an hour or more. If, in addition, the storm is in near steady state, then an intensity estimate should be valid for several hours, supporting an even longer T_{eq}. Noting that the gust factor asymptotes as the reference time increases, we therefore take T_{eq} = 3600 s for practical computations.

The lower limit for T_{eq} is 600 s, since it is impossible to have a 10-min gust within a shorter reference period. This limit might be approached, but not reached, in a storm with a short and narrow maximum wind belt, and noting that $G_{600,600} = 1$, would justify the intensity conversions contained in the middle row of Table E-1. This case should probably also be restricted to very rapidly intensifying storms, where the intensity estimate is valid for only a short time. Comparing the recommended $G_{600,3600}/G_{60,3600}$ to the limit $1/G_{60,600}$, the differences between these rows of the table are not large, of the order of anemometer instrument error under good conditions, and much less than intensity estimate error from Dvorak (1984) or aircraft-to-surface wind reduction calculations. Hence there is no practical need to make this distinction and we advocate the use of $G_{600,3600}/G_{60,3600}$. The main weakness in this extension of the argument is that the true mean wind speed is not uniform over the maximum wind belt, so the maximum gust might not coincide with the maximum true mean wind. However this weakness is deemed to be immaterial in practice, because the conversion factor is not very sensitive to T_{eq}.

One could note that the marine surface roughness, and hence the gust factor, depends on the wind speed, implying that the intensity conversion factor should likewise vary. However, varying the roughness length from 0.0005 m (fitted here via I_u for "at sea", and according to Eqn 11) to 0.003 m (the potential upper limit indicated by Powell et al. (2003) and others) changes $G_{600,3600}/G_{60,3600}$ from 0.928 to 0.913 according to the ESDU method. Such slight sensitivity of about 1.6% is negligible in the present context.

Thus we recommend that tropical cyclone intensity estimates in terms of the maximum 1-min mean wind are converted to a maximum 10-min mean wind equivalent by multiplying by $G_{600,3600}/G_{60,3600}$ which, over the ocean for the gust parameterisation herein, equals 0.93. We note that this conversion factor makes a smaller adjustment than has traditionally been used in the application of the Dvorak technique. This change is partly due to our use of an updated gust factor parameterisation from that of Simiu and Scanlon (1978), but more that the previous factor seems to have incorrectly applied open terrain, rather than marine, conditions. Our values thus imply a modest numerical increase of about 5% in the 10-min intensity estimate, relative to the equivalent 1-min value. We also emphasise that different conversion factors are necessary for different exposures, a point that seems overdue for reconsideration and implementation. It can be noted that in the extreme wind example of Section 3, that the ratio between the insitu directly measured $Vmax_{600}$ and the $Vmax_{60}$ for severe tropical cyclone *Orson* is 0.938, albeit at a higher elevation than 10 m.

In closing, we note that the above discussion is complex because of the long-standing practice of defining tropical cyclone maximum intensity in terms of a wind gust. A definition of storm intensity in terms of the mean wind speed would avoid such difficulties.

26. Assignment 2, Module 5: Saffir-Simpson Scale:
    https://www.nhc.noaa.gov/aboutsshws.php?large

Saffir-Simpson Hurricane Wind Scale

Climatology | Names | Wind Scale | Extremes | Models | Breakpoints

The Saffir-Simpson Hurricane Wind Scale is a 1 to 5 rating based only on a hurricane's maximum sustained wind speed. **This scale does not take into account other potentially deadly hazards such as storm surge, rainfall flooding, and tornadoes.**

The Saffir-Simpson Hurricane Wind Scale estimates potential property damage. While all hurricanes produce life-threatening winds, hurricanes rated Category 3 and higher are known as major hurricanes*. Major hurricanes can cause devastating to catastrophic wind damage and significant loss of life simply due to the strength of their winds. Hurricanes of all categories can produce deadly storm surge, rain-induced floods, and tornadoes. These hazards require people to take protective action, including evacuating from areas vulnerable to storm surge.

*In the western North Pacific, the term "super typhoon" is used for tropical cyclones with sustained winds exceeding 150 mph.

Category	Sustained Winds	Types of Damage Due to Hurricane Winds
1	74-95 mph 64-82 kt 119-153 km/h	**Very dangerous winds will produce some damage:** Well-constructed frame homes could have damage to roof, shingles, vinyl siding and gutters. Large branches of trees will snap and shallowly rooted trees may be toppled. Extensive damage to power lines and poles likely will result in power outages that could last a few to several days.
2	96-110 mph 83-95 kt 154-177 km/h	**Extremely dangerous winds will cause extensive damage:** Well-constructed frame homes could sustain major roof and siding damage. Many shallowly rooted trees will be snapped or uprooted and block numerous roads. Near-total power loss is expected with outages that could last from several days to weeks.
3 (major)	111-129 mph 96-112 kt 178-208 km/h	**Devastating damage will occur:** Well-built framed homes may incur major damage or removal of roof decking and gable ends. Many trees will be snapped or uprooted, blocking numerous roads. Electricity and water will be unavailable for several days to weeks after the storm passes.
4 (major)	130-156 mph 113-136 kt 209-251 km/h	**Catastrophic damage will occur:** Well-built framed homes can sustain severe damage with loss of most of the roof structure and/or some exterior walls. Most trees will be snapped or uprooted and power poles downed. Fallen trees and power poles will isolate residential areas. Power outages will last weeks to possibly months. Most of the area will be uninhabitable for weeks or months.
5 (major)	157 mph or higher 137 kt or higher 252 km/h or higher	**Catastrophic damage will occur:** A high percentage of framed homes will be destroyed, with total roof failure and wall collapse. Fallen trees and power poles will isolate residential areas. Power outages will last for weeks to possibly months. Most of the area will be uninhabitable for weeks or months.

Note: there is an embedded video at the above link which has not been included in this document.

27. Assignment 2, Module 5: Saffir-Simpson Scale #2:
https://www.nhc.noaa.gov/pdf/sshws.pdf

The Saffir-Simpson Hurricane Wind Scale

Updated May 2021

The Saffir-Simpson Hurricane Wind Scale is a 1 to 5 categorization based on the hurricane's intensity at the indicated time. The scale – originally developed by wind engineer Herb Saffir and meteorologist Bob Simpson – has been an excellent tool for alerting the public about the possible impacts of various intensity hurricanes[1]. The scale provides examples of the type of damage and impacts in the United States associated with winds of the indicated intensity. In general, damage rises by about a factor of four for every category increase[2]. The maximum sustained surface wind speed (peak 1-minute wind at the standard meteorological observation height of 10 m [33 ft] over unobstructed exposure) associated with the cyclone is the determining factor in the scale. (Note that sustained winds can be stronger in hilly or mountainous terrain – such as the over the Appalachians or over much of Puerto Rico - compared with that experienced over flat terrain[3].) The historical examples provided in each of the categories correspond with the observed or estimated maximum wind speeds from the hurricane experienced at the location indicated. These do not necessarily correspond with the peak intensity reached by the system during its lifetime. It is also important to note that peak 1-minute winds in hurricane are believed to diminish by one category within a short distance, perhaps a kilometer [~ half a mile] of the coastline[4]. For example, Hurricane Wilma made landfall in 2005 in southwest Florida as a Category 3 hurricane. Even though this hurricane only took four hours to traverse the peninsula, the winds experienced by most Miami-Dade, Broward, and Palm Beach County communities were Category 1 to Category 2 conditions. However, exceptions to this generalization are certainly possible.

The scale does not address the potential for other hurricane-related impacts, such as storm surge, rainfall-induced floods, and tornadoes. It should also be noted that these wind-caused damage general descriptions are to some degree dependent upon the local building codes in effect and how well and how long they have been enforced. For example, building codes enacted during the 2000s in Florida, North Carolina and South Carolina are likely to reduce the damage to newer structures from that described below. However, for a long time to come, the majority of the building stock in existence on the coast will not have been built to higher code. Hurricane wind damage is also very dependent upon other factors, such as duration of high winds, change of wind direction, and age of structures.

Earlier versions of this scale – known as the Saffir-Simpson Hurricane Scale – incorporated central pressure and storm surge as components of the categories. The central pressure was used during the 1970s and 1980s as a proxy for the winds as accurate wind speed intensity measurements from aircraft reconnaissance were not routinely available for hurricanes until 1990[5]. Storm surge was also quantified by category in the earliest published versions of the scale dating back to 1972[6]. However, hurricane size (extent of hurricane-force winds), local bathymetry (depth of near-shore waters), topography, the hurricane's forward speed and angle to

---

[1] H. S. Saffir, 1973 in *The Military Engineer*; and R. H. Simpson, 1974 in *Weatherwise*

[2] R. A. Pielke, Jr. and colleagues, 2008 in *Natural Hazard Review*.

[3] C. A. Miller, and A. G. Davenport, 1998 in *Journal of Wind Engineering and Industrial Aerodynamics*.

[4] P. J. Vickery and colleagues, 2009 in *Journal of Applied Meteorology and Climatology*.

[5] R. C. Sheets, 1990 in *Weather and Forecasting*.

[6] *National Hurricane Operations Plan*, 1972.

the coast also affect the surge that is produced[7,8]. For example, the very large Hurricane Ike (with hurricane force winds extending as much as 125 mi from the center) in 2008 made landfall in Texas as a Category 2 hurricane and had peak storm surge values of about 20 ft. In contrast, tiny Hurricane Charley (with hurricane force winds extending at most 25 mi from the center) struck Florida in 2004 as a Category 4 hurricane and produced a peak storm surge of only about 7 ft. These storm surge values were substantially outside of the ranges suggested in the original scale. Thus, to help reduce public confusion about the impacts associated with the various hurricane categories as well as to provide a more scientifically defensible scale, the storm surge ranges, flooding impact and central pressure statements are being removed from the scale and only peak winds are employed in this revised version – the Saffir-Simpson Hurricane **Wind** Scale. (The impact statements below were derived from recommendations graciously provided by experts [Bruce Harper, Forrest Masters, Mark Powell, Tim Marshall, Tim Reinhold, and Peter Vickery] in hurricane boundary layer winds and hurricane wind engineering fields[9,10].)

Category One Hurricane (Sustained winds 74-95 mph, 64-82 kt, or 119-153 km/h)
Very dangerous winds will produce some damage
People, livestock, and pets struck by flying or falling debris could be injured or killed. Older (mainly pre-1994 construction) mobile homes could be destroyed, especially if they are not anchored properly as they tend to shift or roll off their foundations. Newer mobile homes that are anchored properly can sustain damage involving the removal of shingle or metal roof coverings, and loss of vinyl siding, as well as damage to carports, sunrooms, or lanais. Some poorly constructed frame homes can experience major damage, involving loss of the roof covering and damage to gable ends as well as the removal of porch coverings and awnings. Unprotected windows may break if struck by flying debris. Masonry chimneys can be toppled. Well-constructed frame homes could have damage to roof shingles, vinyl siding, soffit panels, and gutters. Failure of aluminum, screened-in, swimming pool enclosures can occur. Some apartment building and shopping center roof coverings could be partially removed. Industrial buildings can lose roofing and siding especially from windward corners, rakes, and eaves. Failures to overhead doors and unprotected windows will be common. Windows in high-rise buildings can be broken by flying debris. Falling and broken glass will pose a significant danger even after the storm. There will be occasional damage to commercial signage, fences, and canopies. Large branches of trees will snap and shallow rooted trees can be toppled. Extensive damage to power lines and poles will likely result in power outages that could last a few to several days. Hurricane Dolly (2008) is an example of a hurricane that brought Category 1 winds and impacts to South Padre Island, Texas. Hurricane Iwa (passing just northwest of Kauai in 1982) and Hurricane Dot (landfall on Kauai in 1959) are examples of Category 1 hurricanes that directly impacted Hawaii.

Category Two Hurricane (Sustained winds 96-110 mph, 83-95 kt, or 154-177 km/h)
Extremely dangerous winds will cause extensive damage
There is a substantial risk of injury or death to people, livestock, and pets due to flying and falling debris. Older (mainly pre-1994 construction) manufactured homes have a very

---

[7] Jelesnianski, C. P., 1972 in *NOAA Technical Memorandum NWS 46*.

[8] J. L. Irish, D. T. Resio, and J. J. Ratcliff, 2008 in *Journal of Physical Oceanography*.

[9] F. Masters, P. Vickery, B. Harper, M. Powell, and T. Reinhold, 2009 in *Engineering Guidance Regarding WindCaused Damage Descriptors*.

[10] T. Marshall, 2009 in *On the Performance of Buildings in Hurricanes – A Study for the Saffir-Simpson Scale Committee*.

high chance of being destroyed and the flying debris generated can shred nearby manufactured homes. Newer manufactured homes can also be destroyed. Poorly constructed frame homes have a high chance of having their roof structures removed especially if they are not anchored properly. Unprotected windows will have a high probability of being broken by flying debris. Well-constructed frame homes could sustain major roof and siding damage. Failure of aluminum, screened-in, swimming pool enclosures will be common. There will be a substantial percentage of roof and siding damage to apartment buildings and industrial buildings. Unreinforced masonry walls can collapse. Windows in high-rise buildings can be broken by flying debris. Falling and broken glass will pose a significant danger even after the storm. Commercial signage, fences, and canopies will be damaged and often destroyed. Many shallowly rooted trees will be snapped or uprooted and block numerous roads. Near-total power loss is expected with outages that could last from several days to weeks. Potable water could become scarce as filtration systems begin to fail. Hurricane Frances (2004) is an example of a hurricane that brought Category 2 winds and impacts to coastal portions of Port St. Lucie, Florida with Category 1 conditions experienced elsewhere in the city.

Category Three Hurricane
(Sustained winds 111-129 mph, 96-112 kt, or 178-208 km/ h)
Devastating damage will occur
There is a high risk of injury or death to people, livestock, and pets due to flying and falling debris. Nearly all older (pre-1994) manufactured homes will be destroyed. Most newer manufactured homes will sustain severe damage with potential for complete roof failure and wall collapse. Poorly constructed frame homes can be destroyed by the removal of the roof and exterior walls. Unprotected windows will be broken by flying debris. Well-built frame homes can experience major damage involving the removal of roof decking and gable ends. There will be a high percentage of roof covering and siding damage to apartment buildings and industrial buildings. Isolated structural damage to wood or steel framing can occur. Complete failure of older metal buildings is possible, and older unreinforced masonry buildings can collapse. Numerous windows will be blown out of high-rise buildings resulting in falling glass, which will pose a threat for days to weeks after the storm. Most commercial signage, fences, and canopies will be destroyed. Many trees will be snapped or uprooted, blocking numerous roads. Electricity and water will be unavailable for several days to a few weeks after the storm passes. Hurricane Ivan (2004) is an example of a hurricane that brought Category 3 winds and impacts to coastal portions of Gulf Shores, Alabama with Category 2 conditions experienced elsewhere in this city.

Category Four Hurricane
(Sustained winds 130-156 mph, 113-136 kt, or 209-251 km/h)
Catastrophic damage will occur
There is a very high risk of injury or death to people, livestock, and pets due to flying and falling debris. Nearly all older (pre-1994) manufactured homes will be destroyed. A high percentage of newer manufactured homes also will be destroyed. Poorly constructed homes can sustain complete collapse of all walls as well as the loss of the roof structure. Well-built homes also can sustain severe damage with loss of most of the roof structure and/or some exterior walls. Extensive damage to roof coverings, windows, and doors will occur. Large amounts of windborne debris will be lofted into the air. Windborne debris damage will break most unprotected windows and penetrate some protected windows. There will be a high percentage of structural damage to the top floors of apartment buildings. Steel frames in older industrial buildings can collapse. There will be a high

percentage of collapse to older unreinforced masonry buildings. Most windows will be blown out of high-rise buildings resulting in falling glass, which will pose a threat for days to weeks after the storm. Nearly all commercial signage, fences, and canopies will be destroyed. Most trees will be snapped or uprooted and power poles downed. Fallen trees and power poles will isolate residential areas. Power outages will last for weeks to possibly months. Long-term water shortages will increase human suffering. Most of the area will be uninhabitable for weeks or months. Hurricane Charley (2004) is an example of a hurricane that brought Category 4 winds and impacts to coastal portions of Punta Gorda, Florida with Category 3 conditions experienced elsewhere in the city. Hurricane Iniki, which made landfall on Kauai in 1992, is an example of a Category 4 hurricane at landfall in Hawaii.

Category Five Hurricane

(Sustained winds 156 mph or higher, 136 kt or higher, or 251 km/h or higher)

Catastrophic damage will occur

People, livestock, and pets are at very high risk of injury or death from flying or falling debris, even if indoors in manufactured homes or framed homes. Almost complete destruction of all manufactured homes will occur, regardless of age or construction. A high percentage of frame homes will be destroyed, with total roof failure and wall collapse. Extensive damage to roof covers, windows, and doors will occur. Large amounts of windborne debris will be lofted into the air. Windborne debris damage will occur to nearly all unprotected windows and many protected windows. Significant damage to wood roof commercial buildings will occur due to loss of roof sheathing. Complete collapse of many older metal buildings can occur. Most unreinforced masonry walls will fail which can lead to the collapse of the buildings. A high percentage of industrial buildings and low-rise apartment buildings will be destroyed. Nearly all windows will be blown out of high-rise buildings resulting in falling glass, which will pose a threat for days to weeks after the storm. Nearly all commercial signage, fences, and canopies will be destroyed. Nearly all trees will be snapped or uprooted and power poles downed. Fallen trees and power poles will isolate residential areas. Power outages will last for weeks to possibly months. Long-term water shortages will increase human suffering. Most of the area will be uninhabitable for weeks or months. Hurricane Andrew (1992) is an example of a hurricane that brought Category 5 winds and impacts to coastal portions of Cutler Ridge, Florida with Category 4 conditions experienced elsewhere in south Miami-Dade County.

Note: A “major” hurricane is one classified as a Category 3 or higher.

28. Assignment 2, Module 5: Tools to Measure Hurricanes: https://sciencing.com/tools-used-measure-hurricanes-6862094.html

Tools Used To Measure Hurricanes

By Joan Whetzel | Updated Mar 24, 2022

The period from August through mid-September marks the height of a six-month hurricane season in the North Atlantic. When hurricanes occur, most ships disperse to safer locations, leaving a void in data-collecting ability for meteorologists. That's when NASA, the National Oceanic and Atmospheric Administration (NOAA) and the National Weather Service (NWS) step in to gather information. But to monitor these storms and the winds that cause so much damage, these organizations need specialized tools.

Saffir-Simpson Scale

Saffir-Simpson Scale

The Saffir-Simpson Hurricane Scale was developed as a tool for categorizing hurricanes according to sustained wind strength, measured for one minute, at approximately 10 meters (33 feet) above the water's surface. The categories consist of: Category One Hurricane: 74 to 95 mph sustained winds, which will deliver some damage. Category Two: 96 to 110 mph sustained winds, creating widespread damage. Category Three: 111 to 130 mph sustained winds, with overwhelming destruction. Category Four: 131 to 155 mph sustained winds, producing catastrophic destruction Category Five: Sustained winds 155 mph or greater, with catastrophic results

Ocean Temperature Measurement

Ocean Temperature Measurement

Tropical Rainfall Measuring Mission (TRMM) microwave imagers and Advanced Microwave Scanning Radiometers (AMSR-E) measure temperatures of ocean surface waters, which determine the direction a hurricane will travel and potential hurricane intensity. A floating buoy dropped from an airplane sends out a spool of wire to determine the water temperature and radios it back to the plane.

Satellites

Satellites

Scientist Vernon Dvorak developed a method for estimating hurricane strength by comparing satellite images with physical characteristics of the hurricane. This has become the basis for hurricane forecasting models used by meteorologists. NASA satellites collect hurricane data from space combined with computer-based climate mock-ups of sea surface temperatures, rain, wind and wave height.

Buoys

Buoys

Buoys remain the last manmade structure in the waters in and near hurricanes, and because they don't travel, buoys are suitable for the attachment of weather measuring instrumentation. Buoys can measure wind and air pressure, water and air temperatures as well as wind direction with anemometers, and they can measure sustained wind speeds in one-minute increments.

Reconnaissance Aircraft

Reconnaissance Aircraft

Hurricane reconnaissance airplanes fly into hurricanes to measure wind speeds and barometric pressure and visually inspect the ocean surface. Planes travel at altitudes of approximately 10,000 feet and calculate wind measured at 10 meters above sea level based on measurements at 10,000 feet. Dropsondes descend from the plane with a pint-sized parachute to measure wind speed, providing approximate wind readings closer to the water surface, but they only gather localized snapshots rather than sustained wind speed information.

29. Assignment 2, Module 6: Tropical Cyclone Formation: http://www.aoml.noaa.gov/hrd/tcfaq/A15.html

— How Do Tropical Cyclones Form?

In order for a tropical cyclone to form, several atmospheric and marine conditions must be met.

Temperature & Humidity: Ocean waters should be 80° Fahrenheit at the surface and warm for a depth of 150 feet, because warm ocean waters fuel the heat engines of tropical cyclones. They also need an atmosphere which cools fast enough with increasing height so that the difference between the top and bottom of the atmosphere can create thunderstorm conditions. A moist mid-troposphere (3 miles high) is also needed because dry air ingested into thunderstorms at mid-level can kill the convection.

Spin & Location: The Coriolis force is an apparent force that deflects movement of air to the right coming from the Northern hemisphere and to the left coming from the Southern hemisphere. The force is greatest at the poles and zero at the equator, so the storm must be at least 300 miles from the equator in order for the Coriolis force to create the spin. This force causes hurricanes in the Northern hemisphere to rotate counter-clockwise, and in the southern hemisphere to rotate clockwise. This spin may play some role in helping tropical cyclones to organize. (As a side note: the Coriolis force is not strong enough to affect small containers such as in sinks and toilets. The notion that the water flushes the other way in the opposite hemisphere is a myth.)

Wind: Low vertical wind shear (the change of wind speed and direction with height) between the surface and the upper troposphere favors the thunderstorm formation, which provides the energy for tropical cyclones. Too much wind shear will disrupt or weaken the convection.

Having these conditions met is necessary but not sufficient, as many disturbances that appear to have favorable conditions do not develop. Past work (Velasco and Fritsch 1987, Chen and Frank 1993, Emanuel 1993) has identified that large thunderstorm systems (called mesoscale convective complexes) often produce an inertially stable, warm core vortex in the trailing altostratus decks of the MCC. These mesovortices have a horizontal scale of approximately 100 to 200 km [75 to 150 mi], are strongest in the mid-troposphere (5 km [3 mi]) and have no appreciable signature at the surface. Zehr (1992) hypothesizes that genesis of the tropical cyclones occurs in two stages:

Stage 1 occurs when the convective cluster produces a mesoscale vortex. Stage 2 occurs when a second blow up of convection at the mesoscale vortex initiates the intensification process of lowering central pressure and increasing inflowing winds. Stage 3 is when bands of rainshowers form along the inflowing winds. Stage 4 then occurs when an eyewall and eye begin to form at the center of circulation.

30. Assignment 2, Module 6: Tropical Cyclone Formation 2:
https://www.noaa.gov/jetstream/tropical/tropical-cyclone-introduction

Tropical Cyclone Introduction

A tropical cyclone is a warm-core low pressure system, without any front attached, that develops over the tropical or subtropical waters and has an organized circulation. These include hurricanes and typhoons.

There are several favorable environmental conditions that must be in place before a tropical cyclone can form. They are:

Hurricane Isabel on September 15, 2003. NASA image.
Download Image

- Warm ocean waters (at least 80°F / 27°C) throughout a depth of about 150 ft. (46 m).
- An atmosphere which cools fast enough with height such that it is potentially unstable to moist convection.
- Relatively moist air near the mid-level of the troposphere (16,000 ft. / 4,900 m).
- Generally, a minimum distance of at least 300 miles (480 km) from the equator.
- A pre-existing near-surface disturbance.
- Low values (less than about 23 mph / 37 km/h) of vertical wind shear between the surface and the upper troposphere. Vertical wind shear is the change in wind speed with height.

Tropical cyclone formation basins

Given that sea surface temperatures need to be at least 80°F (27°C) for tropical cyclones to form, it is unsurprising that they form near the equator. However, with only the rarest exceptions, these storms do not form within 5° latitude of the equator.

This is due to the lack of sufficient *Coriolis force*, the force that causes the cyclone to spin. With the above criteria, there are seven regions around the world where tropical cyclones are likely to form.

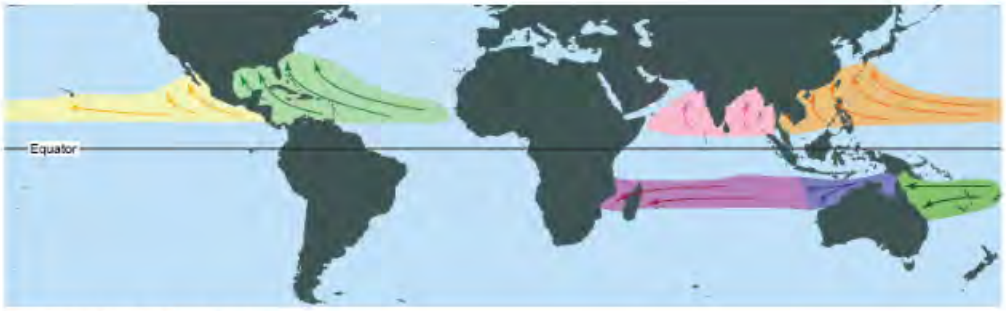

Global tropical cyclone formation basins.
Download Image

North Atlantic Ocean, the Gulf of America, and the Caribbean Sea

The hurricane season is officially from June 1 to November 30. Peak activity is in early to mid September. Occasionally, there may be a tropical cyclone that occurs in May or December.

Northeast Pacific basin (Mexico to about the dateline)

A broad peak with activity beginning in late May or early June and going until late October or early November, with a peak in storminess in late August/early September.

Northwest Pacific basin (From the dateline to Asia, including the South China Sea)

Occur regularly all year, although there is a distinct minimum in February and the first half of March. The main season goes from July to November with a peak in late August/early September.

North Indian basin (Including the Bay of Bengal and the Arabian Sea)

Tropical cyclones occur from April to December, with a double peak of activity in May and November. The severe cyclonic storms (>74 mph / 119 km/h winds) occur almost exclusively from April to June and again in late September to early December.

Southwest Indian basin (From Africa to about 100°E)

Late October/early November to May, with a double peak in activity in mid-January and mid-February/early March.

Southeast Indian/Australian basin (100°E to 142°E)

Late October/early November to May, with a double peak in activity in mid-January and mid-February/early March. A lull in activity in February is a bit more pronounced than the Southwest Indian basin's lull.

Australian/Southwest Pacific basin (142°E to about 120°W)

Begins in late October/early November, reaches a single peak in late February/early March, and then fades out in early May.

The need for warm water

Warm water powers the tropical cyclone and is the most important factor in its development. As water vapor (water in the gaseous state) rises, it cools.

This cooling causes the water vapor to condense into liquid, which we see as clouds. In the process of condensation, heat is released.

This heat warms the atmosphere, making the air lighter, which then continues to rise. As it does, more air moves in near the surface to take its place, which is the strong wind we feel from these storms.

Therefore, once the center of the storm (the "eye") moves over land, it will begin to weaken rapidly, not because of friction, but because the storm lacks the moisture and heat that the ocean provided.

This depletion of moisture and heat hurts the tropical cyclone's ability to produce thunderstorms near the storm center. Without this convection, the storm rapidly diminishes.

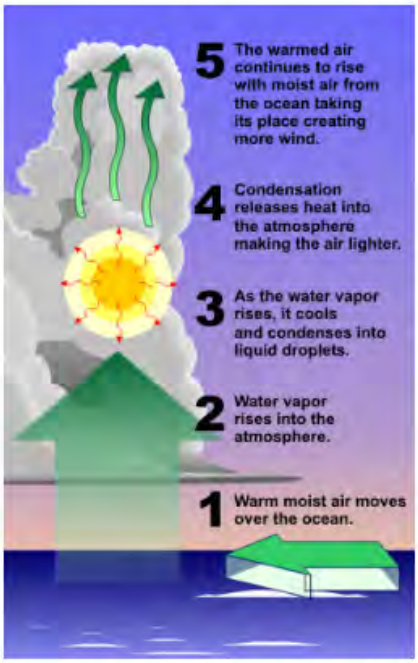

When water temperature is at least 80°F (27°C)...
Download Image

However, warm water alone is not enough for the formation of a tropical cyclone. There also needs to be a disturbance in the atmosphere, such as:

- **Easterly Waves:** Also called tropical waves, this is an inverted trough of low pressure moving generally westward in the tropical easterlies. A trough is defined as a region of relative low pressure. The majority of tropical cyclones form from easterly waves.
- **West African Disturbance Line (WADL):** This is a line of convection (similar to a squall line) which forms over West Africa and moves into the Atlantic Ocean. WADLs usually move faster than tropical waves.
- **TUTT:** A TUTT (Tropical Upper Tropospheric Trough) is a trough or cold core low in the upper atmosphere which produces convection. On occasion, one of these develops into a warm-core tropical cyclone.
- **Old Frontal Boundary:** Remnants of a polar front can become lines of convection and occasionally generate a tropical cyclone. For Atlantic Ocean storms, this will occur early or late in the hurricane season in the Gulf of America or Caribbean Sea.

Global heat transfer through tropical cyclones

This NASA movie is Hurricane Wilma in October, 2005, showing the life of the storm.

The color of the ocean represents sea surface temperature – orange and red indicate temperatures of 82°F (28°C) or greater.

As Wilma moves northwest, then eventually northeast, the water temperature decreases (indicated by the color change to light blue) after the storm passes a particular location. This is the result of the heat being removed from the ocean and provided to the storm.

This transfer of heat shows the global impact of tropical cyclones. They take heat stored in the ocean and transfer it to the upper atmosphere, where the upper level winds carry that heat to the poles. This keeps the polar regions from being as cold as they could be and the tropics a bit cooler.

There have sometimes been suggestions for mitigating tropical cyclones, such as "seeding" storms with chemicals to decrease their intensity or dropping water-absorbing material into the storm to soak up some of the moisture. Some have even suggested using nuclear weapons to disrupt the circulation, thereby decreasing the intensity.

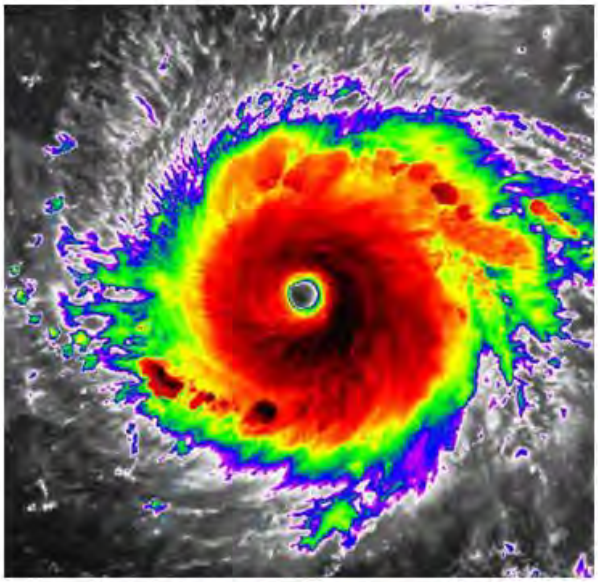

An infrared satellite image of Hurricane Irma, September 12, 2017. This type of image measures the temperature of the tops of clouds. The colder the cloud top, the higher it extends into the atmosphere. The colors from green to red to black help identify the higher cloud tops, with the darkest colors being the tallest clouds.
Download Image

While well meaning, these suggestions vastly underestimate the amount of energy generated and released by tropical cyclones.

Additionally, even if we could disrupt these storms, it would not be advisable. Since tropical cyclones help regulate the Earth's temperature, any decrease in tropical cyclone intensity would mean the oceans retain more heat.

Over time, the build-up of heat could possibly enhance subsequent storms and lead to more numerous and/or stronger events.

There has also been much discussion about the abnormally high number of storms for the 2005 Atlantic basin (27 named storms including 15 hurricanes). Compared to the age of the Earth, our knowledge about tropical cyclone history is only very recent.

Only since the advent of satellite imagery in the 1960's do we have any real ability to count, track, and observe these systems across the vast oceans. Therefore, we will never know the actual record number of tropical cyclones in the Atlantic Oceans.

Tropical Cyclone Structure

The main parts of a tropical cyclone are the rainbands, the eye, and the eyewall. Air spirals in toward the center in a counter-clockwise pattern in the northern hemisphere (clockwise in the southern hemisphere) and out the top in the opposite direction.

In the very center of the storm, air sinks, forming an "eye" that is mostly cloud-free.

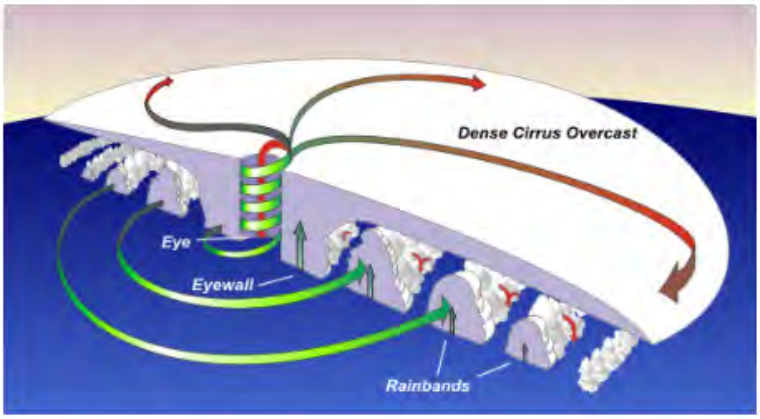

Cross section of a typical hurricane.
Download Image

The Eye

The hurricane's center is a relatively calm, generally clear area of sinking air and light winds that usually do not exceed 15 mph (24 km/h) and is typically 20-40 miles (32-64 km) across. An eye will usually develop when the maximum sustained wind speeds go above 74 mph (119 km/h) and is the calmest part of the storm.

The cause of eye formation is still not fully understood. It is probably related to the combination of "the conservation of angular momentum" and centrifugal force. The conservation of angular momentum means that objects will spin faster as they move toward the center of circulation. In other words, air increases its speed as it heads toward the center of the tropical cyclone.

One way of looking at this is watching figure skaters spin. The closer they hold their hands to the body, the faster they spin. Conversely, the farther the hands are from the body the slower they spin. In tropical cyclones, as the air moves toward the center, the speed must increase.

However, as the speed increases, an outward-directed force, called the centrifugal force, occurs because the wind's momentum directs the wind in a straight line. This straight line momentum leads to an outward pull against the curve of the wind moving around the center of the tropical cyclone. The sharper the curvature and/or the faster the rotation, the stronger the centrifugal force.

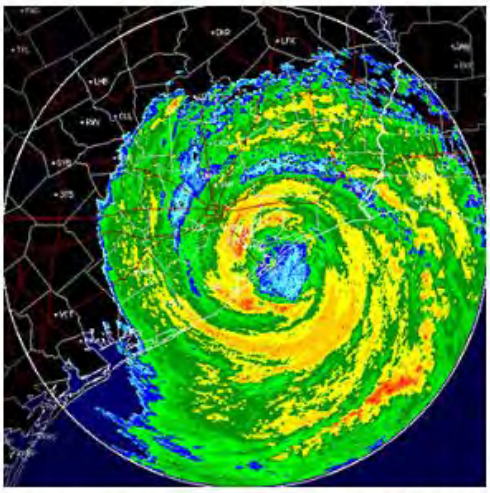

Radar image of hurricane Ike, September 13, 2008.
Download Image

Around 74 mph (119 km/h), the strong rotation of air around the cyclone balances inflow to the center, causing air to ascend about 10-20 miles (16-32 km) from the center, forming the eyewall. This strong rotation also creates a vacuum of air at the center, causing some of the air flowing out the top of the eyewall to turn inward and sink, replacing the loss of air mass near the center.

This sinking air suppresses cloud formation, creating a pocket of generally clear air in the center. People experiencing an eye passage at night often see stars.

Trapped birds are sometimes seen circling in the eye, and ships trapped in a hurricane report hundreds of exhausted birds resting on their decks. The landfall of **Hurricane Gloria** (1985) on southern New England was accompanied by thousands of birds in the eye.

The sudden change of very strong winds to a near calm state is a dangerous situation for people ignorant about a hurricane's structure.

Some people experiencing light wind and fair weather of an eye may think the hurricane has passed when actually, the storm is only half over, with dangerous eyewall winds returning shortly, this time from the opposite direction.

The Eyewall

Where the strong wind gets as close as it can is the eyewall. The eyewall consists of a ring of tall thunderstorms that produce heavy rains and usually the strongest winds. Changes in the structure of the eye and eyewall can cause changes in the wind speed, which is an indicator of the storm's intensity. The eye can grow or shrink in size, and double (concentric) eyewalls can form.

In intense tropical cyclones, some of the outer rainbands may organize into an outer ring of thunderstorms that slowly moves inward and robs the inner eyewall of its needed moisture and momentum. During this phase, the tropical cyclone is weakening.

Eventually the outer eyewall replaces the inner one completely and the storm can be the same intensity as it was previously or, in some cases, even stronger.

Rainbands

Curved bands of clouds and thunderstorms that trail away from the eye wall in a spiral fashion. These bands are capable of producing heavy bursts of rain and wind, as well as tornadoes. There are sometimes gaps in between spiral rain bands where no rain or wind is found.

In fact, if one were to travel between the outer edge of a hurricane to its center, one would normally progress from light rain and wind, to dry and weak breeze, then back to increasingly heavier rainfall and stronger wind, over and over again with each period of rainfall and wind being more intense and lasting longer.

Tropical Cyclone Size

Typical hurricane strength tropical cyclones are about 300 miles (483 km) wide although they can vary considerably.

Size is not necessarily an indication of hurricane intensity. Hurricane Andrew (1992), the second most devastating hurricane to hit the United States, next to Katrina in 2005, was a relatively small hurricane.

On record, **Typhoon Tip** (1979) was the largest storms with gale force winds (39 mph/63 km/h) that extended out for 675 miles (1087 km) in radius in the Northwest Pacific on 12 October, 1979. The smallest storm was **Tropical Storm Marco** with gale force winds that only extended 11.5 miles (18.5 km) radius when it struck Misantla, Mexico, on October 7, 2008.

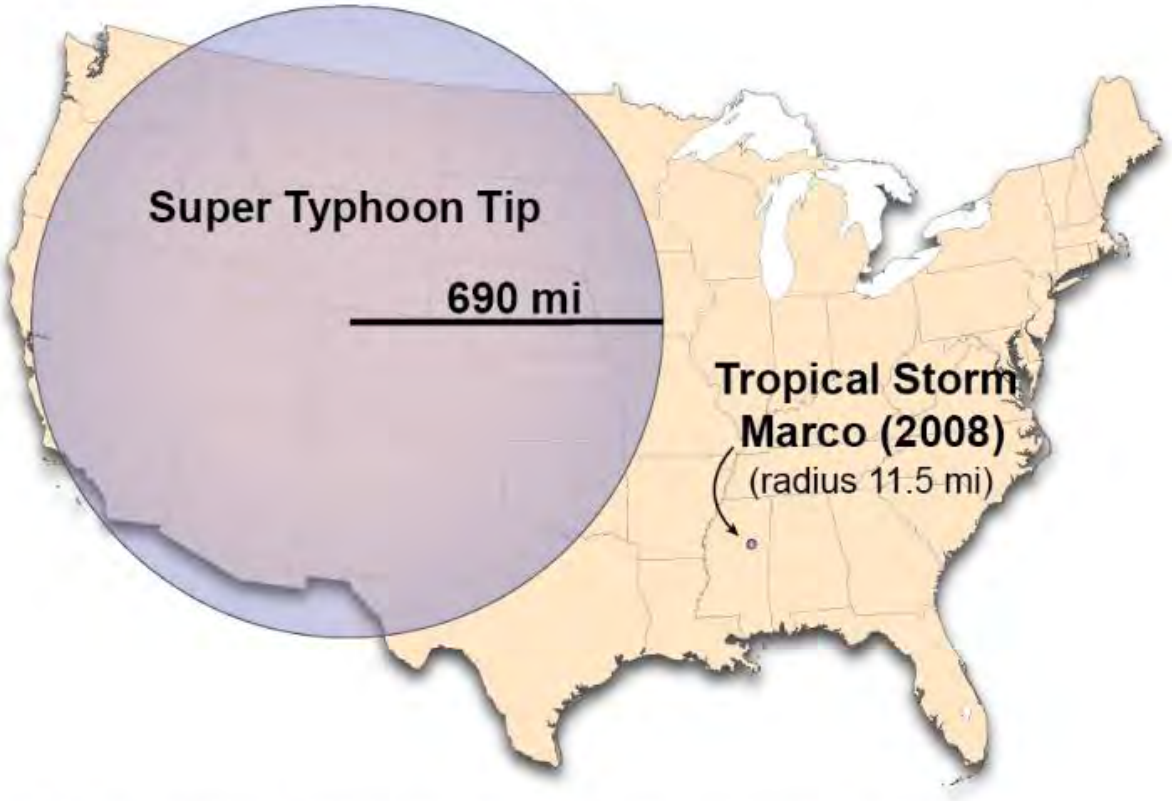

The relative sizes of the largest and smallest tropical cyclones on record as compared to the United States.
Download Image

The strongest hurricane on record for the Atlantic Basin is Hurricane Wilma (pdf) (2005). With a central pressure of 882 mb (26.05") Wilma produced sustained winds of 184 mph (160 kt / 280 km/h). Air Force reconnaissance observations indicated that the eye of the hurricane had contracted to as small as 2 n mi (3.7 km) in diameter.

With an estimated sustained wind speed of 213 mph (185 kt / 325 km/h), the strongest hurricane in the Western Hemisphere was Hurricane Patricia (pdf) (2015). However, Patricia's hurricane force winds only extended out 20-25 miles (32-40 kilometers) from the compact, 7-mile (11 kilometer) diameter eye.

31. Assignment 2, Module 6: Saharan Air Layer Impact:
https://journals.ametsoc.org/view/journals/bams/85/3/bams-85-3-353.xml

THE IMPACT OF THE SAHARAN AIR LAYER ON ATLANTIC TROPICAL CYCLONE ACTIVITY

BY JASON P. DUNION AND CHRISTOPHER S. VELDEN

The Saharan Air Layer may be yet another piece of the puzzle in advancing our understanding of tropical cyclone intensity change in the North Atlantic and Caribbean.

The Saharan air layer (SAL), an elevated layer of Saharan air and mineral dust, has been investigated for several decades, but its link to Atlantic tropical cyclone (TC) activity has never been fully examined. This work discusses recently developed Geostationary Operational Environmental Satellite (GOES) split-window satellite imagery that permits continuous tracking of the SAL across the North Atlantic, Caribbean, and Gulf of Mexico. This new type of satellite imagery reveals that the SAL may play a major role in suppressing TC activity in the North Atlantic. This paper presents documentation of these suppressing characteristics for a number of specific TC–SAL interactions that have occurred during several recent Atlantic hurricane seasons.

AFFILIATIONS: DUNION—CIMAS, University of Miami, and NOAA/AOML/Hurricane Research Division, Miami, Florida; VELDEN—CIMSS, University of Wisconsin—Madison, Madison, Wisconsin
CORRESPONDING AUTHOR: Jason P. Dunion, NOAA/AOML/Hurricane Research Division, 4301 Rickenbacker Causeway, Miami, FL 33149
E-mail: jason.dunion@noaa.gov
DOI: 10.1175/BAMS-85-3-353

In final form 17 October 2003

The SAL occurs during the late spring through early fall over extensive portions of the North Atlantic Ocean between the Sahara Desert, the West Indies (Prospero and Carlson 1972), and the United States (as documented by recent GOES satellite imagery). Carlson and Prospero (1972) proposed that a dry, well-mixed layer often extends to ~500 hPa over Africa during the summer months. As this air mass advances westward from the North African coast, often in association with African easterly waves (AEWs; Burpee 1972), it is undercut by cool, moist low-level marine air and becomes the SAL. Just offshore, the SAL's base is at ~900–1800 m and the top is usually below 5500 m (Diaz et al. 1976). Near its southern boundary, the SAL is also associated with the midlevel African easterly jet centered near 700 hPa, which can greatly increase the low-level vertical wind shear. The SAL appears to retain its Saharan characteristics of warm, stable air near its base, and dryness and dustiness throughout its depth as it is carried as far as the western Caribbean Sea (~7000 km from the northwest African coast). Previous work has suggested that the SAL is typically confined to an east–west wavelength of 2000–3000 km (Karyampudi and Carlson 1988). However, the SAL-tracking GOES imagery indicates that the SAL's wavelength can extend to 4000–5000 km and cover an area of the Atlantic slightly larger than the 48 contiguous United States.

Geostationary satellites reveal that the SAL often enhances convection along its western and southern boundaries (Chen 1985), but in its interior, the combination of embedded dry, stable air and strong easterly wind shear inhibits the occurrence of the deep convection that is essential for TC formation. During an average summer, about six named TCs form in the main development region (Goldenberg and Shapiro 1996) of the tropical Atlantic between 10° and 20°N, near the SAL's southern boundary. The GOES SAL-tracking imagery indicates that when both TCs and AEWs [the precursors for ~65% of Atlantic named TCs (Pasch et al. 1998)] are engulfed by the SAL, much of their deep convection dissipates. Consequently, these tropical circulations can lose a major portion of their strength while still over the warm tropical Atlantic.

A METHOD FOR TRACKING THE SAL WITH GOES SATELLITE IMAGERY. The SAL is not readily detectable with the individual visible and infrared (IR) channels on the GOES imager. Although visible satellite imagery can detect the SAL's suspended mineral dust in the eastern North Atlantic, the dust becomes more diffuse and difficult to monitor as the air in the SAL moves westward. Because of the SAL's limited vertical extent (~500–850 hPa), the dry air it contains can be difficult to detect with traditional water vapor imagery available from the 6.5- and 6.7-μm channels on the GOES satellites. These channels respond most sensitively to radiation emitted at approximately 400 hPa (Velden et al. 1998). Therefore, dry SAL air below ~500 hPa may be undetectable when the air above the SAL is relatively moist. Although the individual spectral channels on the GOES satellites were not designed to track the SAL, recent tests have shown that the position of the SAL's dust and lower-tropospheric dry air can be tracked most reliably with the split-window IR channels (10.7 and 12 μm) on the *GOES-8* imager (Prata 1989). These IR channels are unlike the water vapor channels because they have weighting functions in the lower troposphere. The SAL signal they detect is not affected by variations in upper-level moisture (in cloud-free areas).

The mineral dust and dry lower-tropospheric air in the SAL reduce the brightness temperature differences that typically exist between the 10.7- and 12-μm channels on *GOES-8*. These changes in brightness temperature differences allow the SAL to be tracked over time and space. Under typical cloud-free atmospheric conditions, the 10.7-μm IR emissions originate closer to the earth's surface than do those in the 12-μm IR channel, which is more sensitive to absorption by low-level water vapor. Because the 10.7-μm channel more effectively senses the near-surface atmosphere, its signal is usually warmer than the 12-μm channel. However, the SAL environment affects the 12-μm signal in two ways. First, the exceptionally dry air in the SAL results in a decrease in the amount of IR absorption by low-level moisture, thus, increasing the brightness temperatures in the 12-μm channel. This acts to reduce the brightness temperature difference between the 10.7- and 12-μm channels. Second, suspended mineral dust in the SAL absorbs some of the incident solar radiation it receives and reradiates it as longwave IR radiation. Dust emits this radiation more effectively at 12 μm than at 10.7 μm. Therefore, the dust further reduces the brightness temperature difference between the 10.7- and 12-μm channels and, in extreme dust events, can even reverse the sign of the difference. Image enhancements were developed to take advantage of these temperature anomalies measured by the GOES IR channels to track the SAL. Typical brightness temperature (BT) differences between the 12- and 10.7-μm channels ($BT_{12} - BT_{10.7}$) in the non-SAL tropical Atlantic range from +5° to 10°C. Brightness temperature differences between −4° and +4°C are enhanced to track the SAL in the *GOES-8* imagery. The ability of this satellite imagery to detect the SAL air mass was verified using moisture information from Global Positioning System (GPS) dropwindsondes (GPS sondes; Hock and Franklin 1999) and is discussed in the section titled "dry air intrusion into the TC circulation."

In early 2003, *GOES-8* was replaced by *GOES-12*. This new satellite does not have a 12-μm channel. Therefore, a similar SAL-tracking algorithm was developed for *GOES-12* that substitutes the 10.7- and 12-μm channels with 3.9- and 10.7-μm channels, respectively. The brightness temperature differences between the 10.7- and 3.9-μm channels ($BT_{10.7} - BT_{3.9}$) in the non-SAL tropical Atlantic typically range from +6° to 10°C. The *GOES-12* algorithm applies the same principles previously discussed for the *GOES-8* technique to track the dry, dusty air in the SAL. This slightly modified algorithm enhances brightness temperature differences ($BT_{10.7} - BT_{3.9}$) between −13° and +5°C to identify the SAL, and was calibrated using the original methods and imagery developed with *GOES-8*. However, because of solar contamination inherent with the 3.9-μm channel, this new algorithm is only useful for tracking the SAL during nighttime hours.

CHARACTERISTICS OF THE SAL AFFECTING TC FORMATION. *Enhanced low-level temperature inversion.* The temperature at the base of the

SAL (~800–900 hPa) is often 5°–10°C warmer than the Jordan (1958) mean tropical sounding (Diaz et al. 1976). While the warmth of the air above the SAL's base results from its origin over the Sahara, it is maintained by the absorption of solar radiation by the suspended mineral dust. This daytime heating can exceed the overall longwave cooling in the layer, thereby warming the SAL and reenforcing the temperature inversion at its base (Carlson and Benjamin 1980).

Climatologically, the base of the trade wind inversion is less than 500 m off the northwest African coast and rises westward and equatorward to above 2000 m (Hastenrath 1991). In the central tropical North Atlantic, temperature increases through the inversion are generally 1°–2°C. The level at which the SAL mineral dust warms the lower troposphere is approximately coincident with this inversion. Although the dust's effect on microphysical processes is not fully understood, the warming it induces enhances the trade wind inversion, which can limit vertical motions through the SAL (Carlson and Prospero 1972). This stronger inversion may inhibit the development of convection in weak AEWs, as well as allow the SAL to sustain its thermodynamic properties for thousands of kilometers across the Atlantic basin.

Dry air intrusion into the TC circulation. Though it can promote convection along its western and southern boundary (Chen 1985), the dry SAL air can act to suppress convection by enhancing evaporatively driven downdrafts (Emanuel 1989; Powell 1990). We hypothesize that AEWs simply propagate into the SAL, while the low- to-midlevel inflow of TCs advect the SAL's low humidity into the TC circulation. This dry air is also associated with reduced vales of convective available potential energy (CAPE), a measure of the stability of the atmosphere. Smaller values of CAPE imply greater atmospheric stability and, therefore, reduced convective activity.

Because of the SAL's limited vertical extent, its dry air can be difficult to quantify using the moisture channels on the GOES and Meteosat second-generation (MSG) satellites. The most effective way to study the SAL's low humidity is by first identifying it with the GOES SAL-tracking imagery and then directing aircraft to make in situ measurements of its thermodynamic structure. The National Oceanic and Atmospheric Administration (NOAA) G-IV hurricane surveillance aircraft dispensing GPS sondes (Aberson and Franklin 1999) is an ideal platform to gather complete kinematic and thermodynamic vertical profiles of the SAL and to provide insight into the processes by which the SAL air affects tropical disturbances.

SAL and non-SAL air masses were inadvertently sampled by GPS sondes during operational G-IV missions around Hurricanes Danielle and Georges of 1998 and Hurricanes Debby and Joyce of 2000. Composite vertical profiles of the relative humidity and mixing ratio were generated using the GOES SAL-tracking imagery to examine these air masses in detail. Only GPS sondes that were clearly in SAL or non-SAL tropical air, as indicated by the GOES SAL-tracking imagery (see, e.g., Fig. 1), were used in the composites (10-hPa vertical bins). Figure 2 shows the composite SAL and non-SAL soundings from these four TCs compared with the climatological mean Jordan vertical profiles (Jordan 1958) of the relative humidity and mixing ratio for the region of the West Indies from July to October. The Jordan sounding has lower relative humidities (~10%) and mixing ratios (~1.5 g kg^{-1}) in the 600–850-hPa layer than the non-SAL composite vertical profile computed from 24 soundings. By contrast, the composite SAL profile (29 soundings) is significantly (99% level determined from a Student's *t* test) different from both the Jordan mean sounding and the non-SAL composite. In the SAL, relative humidities are 25%–45% lower, and mixing ratios average 2.5–5.5 g kg^{-1} less between 600 and 850 hPa. For the Hurricane Danielle case, the SAL-targeted GPS sondes indicate that the SAL appears to have maintained its thermodynamic characteristics (Carlson and Prospero 1972) as it moved ~5000 km across the North Atlantic to a position < 500 km off the southeast U.S. coast. The 29 SAL profiles used to create Fig. 2 suggest that the variability of the moisture in the SAL is relatively low. The standard deviation of the 700-hPa relative humidity was < 8% for these 29 soundings. This figure also suggests that the tropical Atlantic is characterized by a multiple distribution of environmental moisture soundings that is not well represented by a single climatological sounding (e.g., Jordan 1958). Instead, a moist tropical environment exists that is periodically modified by the passage of dry SAL outbreaks. Also, because there was no means of tracking the SAL until recently, it is likely that the climatology originally compiled by Jordan included both SAL and non-SAL soundings. This suggests that the Jordan mean tropical moisture sounding (July–October) may be substantially drier than the typical non-SAL moist tropical sounding that exists in the North Atlantic during this time of year.

Vertical wind shear induced by the SAL midlevel easterly jet. The southern or southwestern edge of the SAL usually coincides with an easterly wind maximum

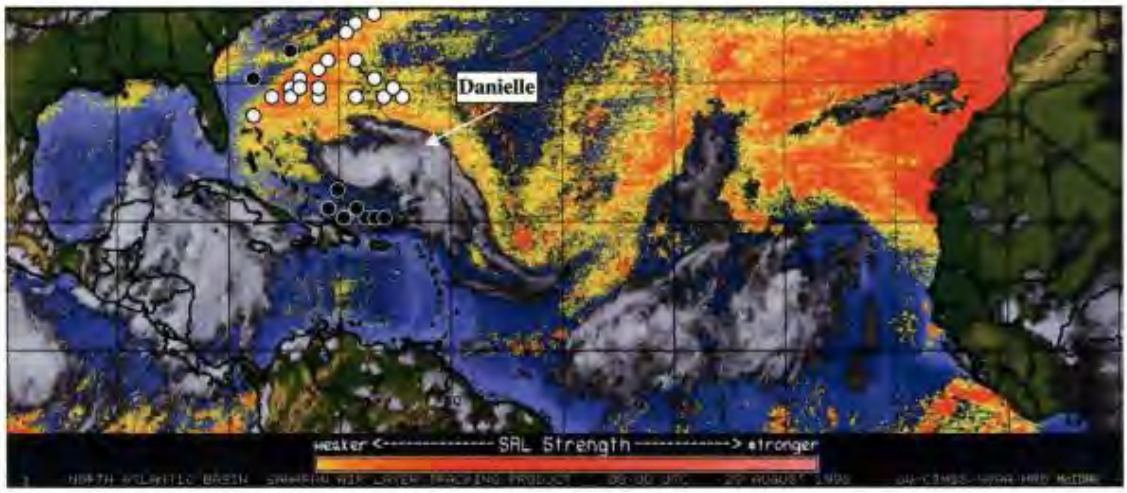

FIG. 1. GOES SAL-tracking satellite imagery with overlaid GPS dropsonde points for Hurricane Danielle on 0000 UTC 29 Aug 1998. The yellow–red shading indicates likely SAL regions with increasing amounts of dust content and dry lower-tropospheric air, as detected by the GOES imagery. Light circles indicate GPS sondes dropped in the SAL environment. Dark circles indicate GPS sondes dropped in non-SAL tropical environments.

near 700 hPa. It is a westward extension of the African easterly jet that is in thermal wind balance with the horizontal temperature gradients that exist between the warm air in the interior of the SAL and cooler tropical air to the south (Carlson and Prospero 1972). The wind speed at the maximum is often 10–17 m s^{-1} and can be as high as 25 m s^{-1}, which is generally 7–10 m s^{-1} faster than the typical trade wind flow. The easterly jet along the SAL's southern boundary can sometimes be tracked using GOES low-level cloud-drift winds and microwave satellite surface winds from QuikSCAT (Liu et al. 1998) and the Special Sensor Microwave Imager (SSM/I; Goodberlet et al. 1989).

GOES SAL-tracking imagery suggests that the SAL's midlevel wind maximum suppresses TC forma-

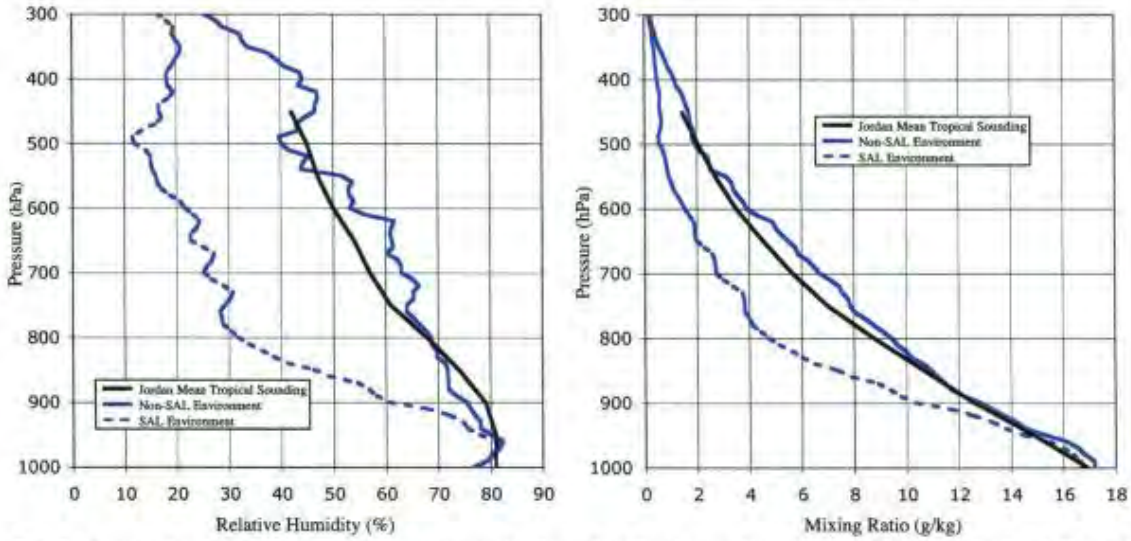

FIG. 2. Composite GPS sonde profiles from sondes launched in the environments of Hurricanes Danielle and Georges of 1998 and Hurricanes Debby and Joyce of 2000. SAL and non-SAL environments were determined using GOES SAL-tracking imagery (see, e.g., Fig. 1). The Jordan mean tropical sounding for the area of the West Indies for Jul–Oct is presented for reference.

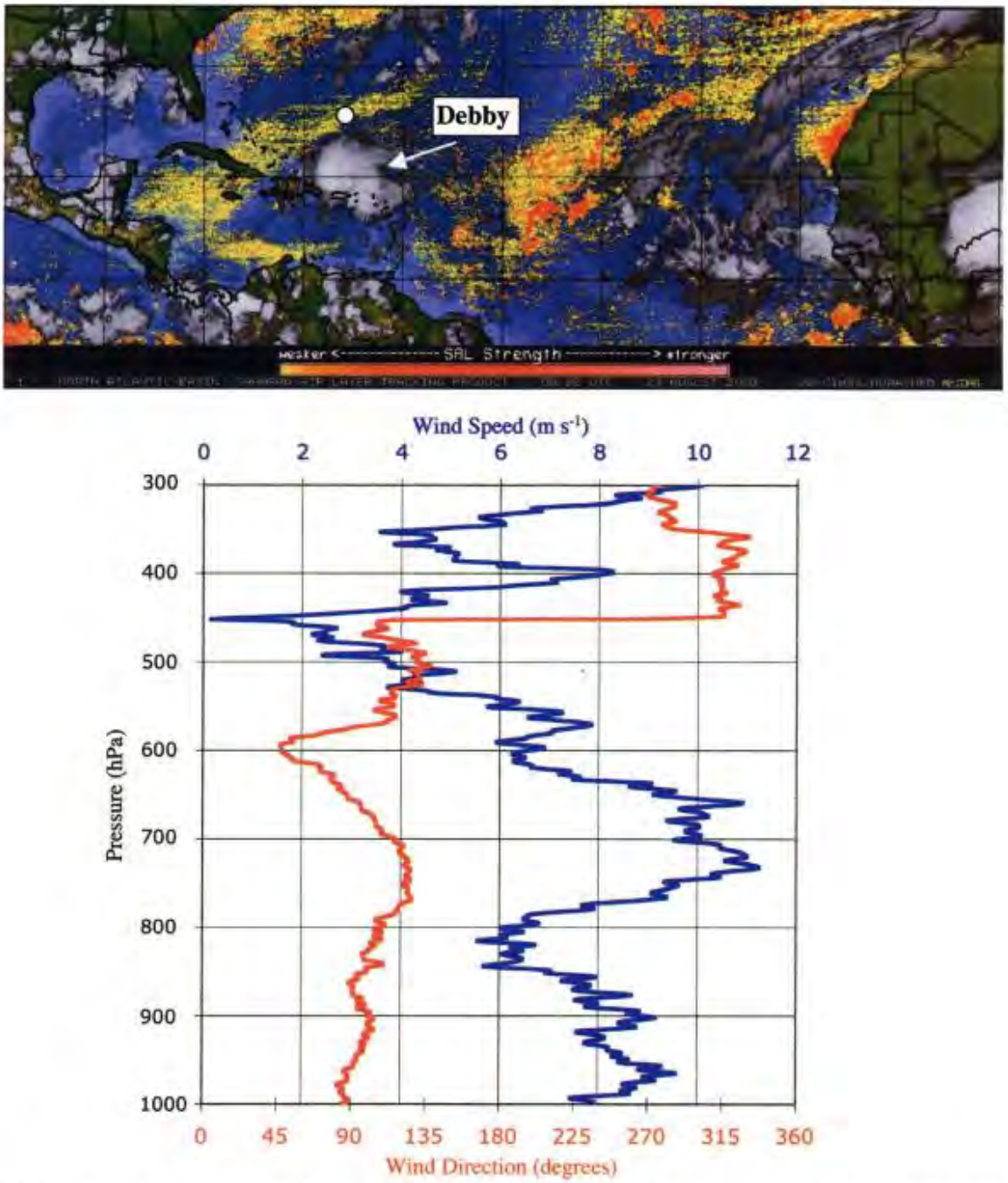

FIG. 3. (top) GOES SAL-tracking satellite imagery with an overlaid GPS dropsonde point ~700 km north-northeast of Hurricane Debby on 0000 UTC 23 Aug 2000. The yellow–red shading indicates likely SAL regions with increasing amounts of dust content and dry lower-tropospheric air, as detected by the GOES imagery. The light circle indicates a GPS sonde dropped in the SAL environment. (bottom) The vertical profiles of wind speed and direction observed by this GPS sonde are plotted.

tion. These embedded strong winds significantly increase the local vertical wind shear by increasing the low- to-midlevel easterly flow. In fact, several of the TCs examined in this study that were embedded in the SAL (Hurricanes Debby and Joyce of 2000 and Tropical Storm Chantal of 2001) had low-level circu-

lations that raced ahead of their mid- and upper-level deep convection, due to the influence of the SAL's midlevel jet.

The vertical wind shear created by the SAL midlevel jet can be significant, but is often difficult to resolve. First, there is limited lower- and midtropospheric wind data available over the tropical Atlantic. Although GPS index sondes are capable of detecting the strong easterly wind surge often associated with the SAL (see Fig. 3), their use is typically limited spatially and temporally. Second, the SAL's shallow vertical extent (~500–850 hPa) makes it difficult to detect using most remote sensing platforms. For these reasons, the SAL's easterly jet may not be generally well represented in global models. Additionally, typical calculations of the vertical wind shear that use the 850-hPa level to represent the lower-tropospheric winds may produce underestimates in the presence of the SAL. Because the 850-hPa level is usually near the bottom of the SAL (and possibly below it), the true magnitude of the low-to-midlevel winds may be underestimated. The broader 700–925-hPa layer is more useful for representing the wind in the lower troposphere and helps to better resolve the strong vertical wind shear caused by the SAL's low- to midlevel easterly jet.

EFFECTS OF THE SAL ON SPECIFIC ATLANTIC TCS. *Hurricane Joyce: September 2000.* Hurricane Joyce formed from an AEW that was positioned several hundred kilometers ahead of a large SAL outbreak. Favorable environmental conditions allowed this AEW to develop from a weak tropical depression late on 25 September 2000 to an 80-kt (41 m s^{-1}) hurricane early on 28 September. The SAL was positioned ~500 km northeast of Joyce on 26 September. It overtook Joyce late on 27 September (SAL positioned < 2° from the TC circulation center) and soon began to suppress convection in the storm. Hurricane Isaac (located ~1500 km northwest of Joyce at this time) intensified into a category-4 hurricane as it recurved to the northwest and separated from the suppressing influence of the westward-advancing SAL. However, the SAL likely caused Joyce to weaken by imposing low humidity and strong vertical wind shear on the main circulation.[1] During the next 48 h, Joyce weakened to a moderate tropical storm, and within 96 h it became a disorganized tropical depression. The sequence described above is illustrated in Fig. 4's time series depiction of Joyce, Isaac, and the SAL from 26 to 30 September, and in Fig. 5's best-track intensity plot for Joyce.

Early on 28 September marked the beginning of Joyce's weakening trend. Prior to this, the Statistical Hurricane Intensity Prediction Scheme (SHIPS; DeMaria and Kaplan 1999) had been underforecasting the 24- and 48-h intensities for Joyce (Fig. 5). Figure 5 indicates that after the SAL reached Joyce, the SHIPS 24- and 48-h intensity forecasts were overestimated by as much as ~40–55 kt (~20–28 m s^{-1}), likely due to increased vertical wind shear and dry air entrainment, which were not effectively represented by the model data used in the SHIPS scheme. *GOES-8* low-level (600–925 hPa) cloud-drift winds indicated that the SAL wind-surge strength was 10–18 m s^{-1} just northeast of Joyce. Consequently, the vertical wind shear northeast of Joyce increased to 40–60 kt (20–30 m s^{-1}) by 0000 UTC on 28 September (Fig. 6). The University of Wisconsin—Madison (UW) Cooperative Institute for Meteorological Satellite Studies (CIMSS) wind shear calculation shown in Fig. 6 is calculated by differencing the winds in the 150–350-hPa and 700–925-hPa layers using data from the U.S. Navy Operational Global Atmospheric Prediction System (NOGAPS) model and GOES water vapor and cloud-drift satellite winds. This algorithm removes the circulation associated with the TC vortex from the grid field and uses bilinear interpolation to replace the vortex region with environmental values that surround the storm.

The UW CIMSS vortex extraction procedure may produce underestimates of vertical wind shear in cases like Hurricane Joyce, where the northeast SAL quadrant of the storm contains high wind shear (40–60 kt, 20–30 m s^{-1}) and the other non-SAL quadrants have much lower values of wind shear (0–10 kt, 0–5 m s^{-1}). SHIPS calculates vertical wind shear by averaging the shear values in the 200–800-km radius around the TC. This technique will also tend to underestimate the

[1] Although it is uncertain exactly how long it will take the SAL's dry air and enhanced vertical wind shear to weaken a TC, the time delay and extent of weakening are likely proportional to the size and strength of the TC's circulation. This aspect of the SAL requires further research.

FIG. 4. (facing page) GOES SAL-tracking satellite imagery time series showing Hurricane Joyce's interaction with the SAL (top) 1200 UTC 26 Sep 2000, (middle top) 1200 UTC 27 Sep 2000, (middle bottom) 0000 UTC 29 Sep 2000, and (bottom) 0000 UTC 30 Sep 2000. The yellow–red shading indicates likely SAL regions and increasing amounts of dust content and dry lower-tropospheric air, as detected by the GOES imagery. The dotted lines indicate the western and southern boundaries of the advancing SAL.

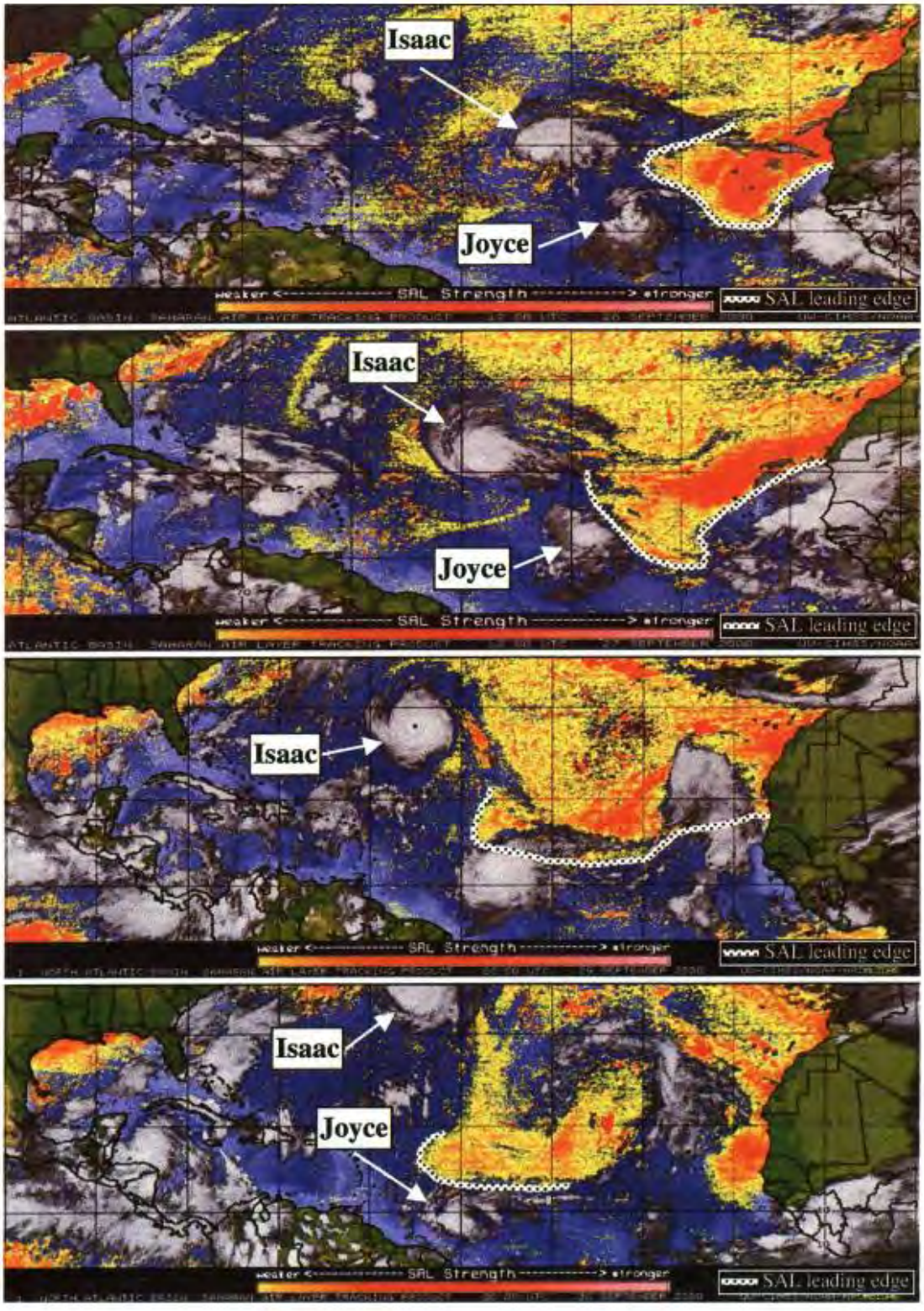

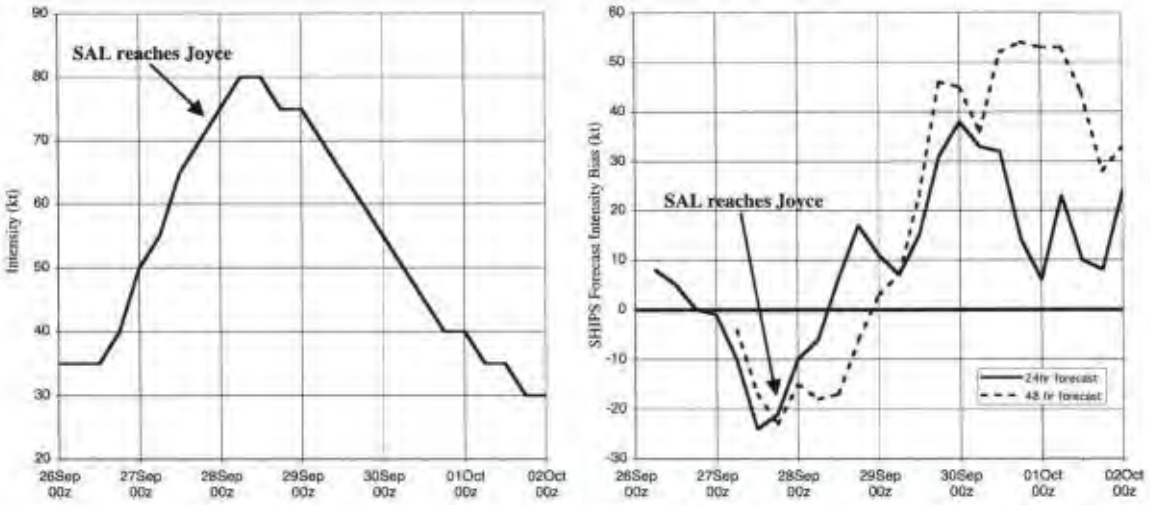

FIG. 5. (left) Hurricane Joyce best-track intensity and (right) SHIPS forecast intensity bias for the period from 26 Sep to 2 Oct 2000. The approximate time at which the SAL overtook the storm is indicated in both plots.

wind shear in cases such as Hurricane Joyce when the shear magnitude is asymmetrically distributed around the TC. Therefore, the vertical wind shear at Hurricane Joyce's location may have been higher than is being depicted for 0000 UTC 28 September by the UW CIMSS shear analysis (Fig. 6) and by SHIPS (16 kt, 8 m s^{-1}).

The presence of the SAL was also confirmed by a NOAA G-IV surveillance flight on 30 September. GPS sondes launched during this flight detected SAL air with relative humidities as low as 5% and mixing ratios as low as 1 g kg^{-1} in the 600–850-hPa layer 400–500 km north and west of Joyce.

1999–2002 Atlantic TCs. The best-track intensities for several 1999–2001 Atlantic TCs that interacted with SAL are shown in Fig. 7. GOES SAL-tracking imagery was used to determine if a TC's circulation center was in proximity (< 2°) to the SAL. Figure 8 is similar to Fig. 7 and shows the 24- and 48-h bias of the SHIPS intensity forecasts relative to National Hurricane Center best-track intensities.

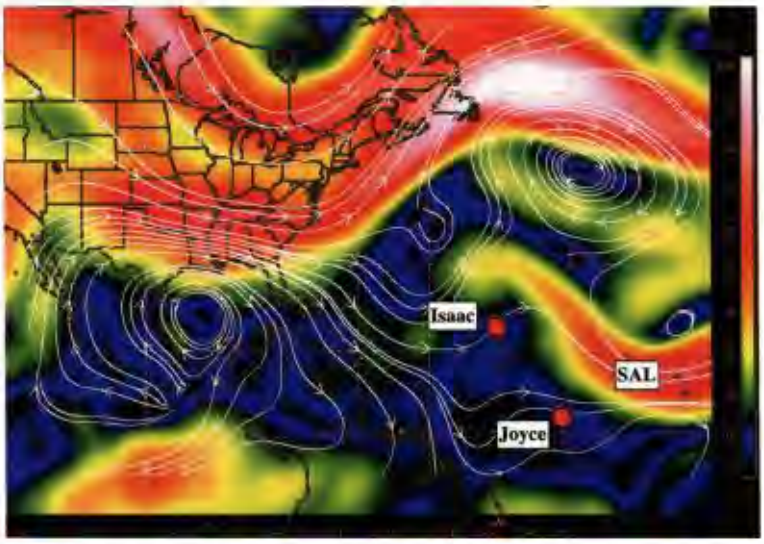

FIG. 6. Vertical wind shear (kt) for 0000 UTC 28 Sep 2000. Shear values are indicated by colored shading and were calculated by differencing the mean wind vectors of the 150–350- and 700–925-hPa layers. The shear vector is indicated by the white streamlines. Hurricanes Joyce and Isaac, as well as the strong vertical shear induced by the SAL, are indicated.

Hurricanes Cindy and Floyd of 1999 and Erin and Felix of 2001 represent TCs that were initially under the influence of the SAL (Fig. 7). All of these TCs eventually emerged from the SAL and attained major hurricane status. This scenario is depicted for Hurricane Erin in Fig. 9. Erin immediately began interacting with the SAL as it emerged from the North African coast. It became embedded in the SAL and struggled to maintain tropical storm intensity for the next several days. However, when Erin emerged from the SAL as a 35-kt (18 m s^{-1})

tropical storm at 0000 UTC 8 September, it rapidly intensified into a 105-kt (54 m s^{-1}) major hurricane within just 48 h (Fig. 7).[2] SHIPS overforecast Erin's intensity (up to 45 kt, 23 m s^{-1}) while it was in the SAL and underforecast its intensity (up to 50 kt, 26 m s^{-1}) as it began to emerge from the SAL (Fig. 8).

Hurricane Debby of 2000 and Tropical Storm Chantal of 2001 were never able to separate from the SAL. These systems struggled to maintain their intensities and were consistently overforecast by SHIPS (Figs. 7 and 8). Tropical Depression No. 7 of 2002 (not shown) was overrun by the SAL. This 30-kt (15.5 m s^{-1}) TC dissipated into a disorganized area of convection less than 24 h after the SAL engulfed it early on 8 September.

Figure 7 demonstrates the suppressing influence of the SAL on TC activity and indicates that TCs that are being affected by the SAL tend to weaken or have difficulty intensifying into mature hurricanes. Figure 8 indicates that SHIPS has difficulty predicting the intensities of TCs transitioning into or out of the SAL and tends to overestimate intensity forecasts of TCs that are interacting with the SAL.

SUMMARY AND CONCLUSIONS.

The GOES multispectral technique described here creates a unique kind of satellite image that allows tracking of the SAL across the North Atlantic basin and

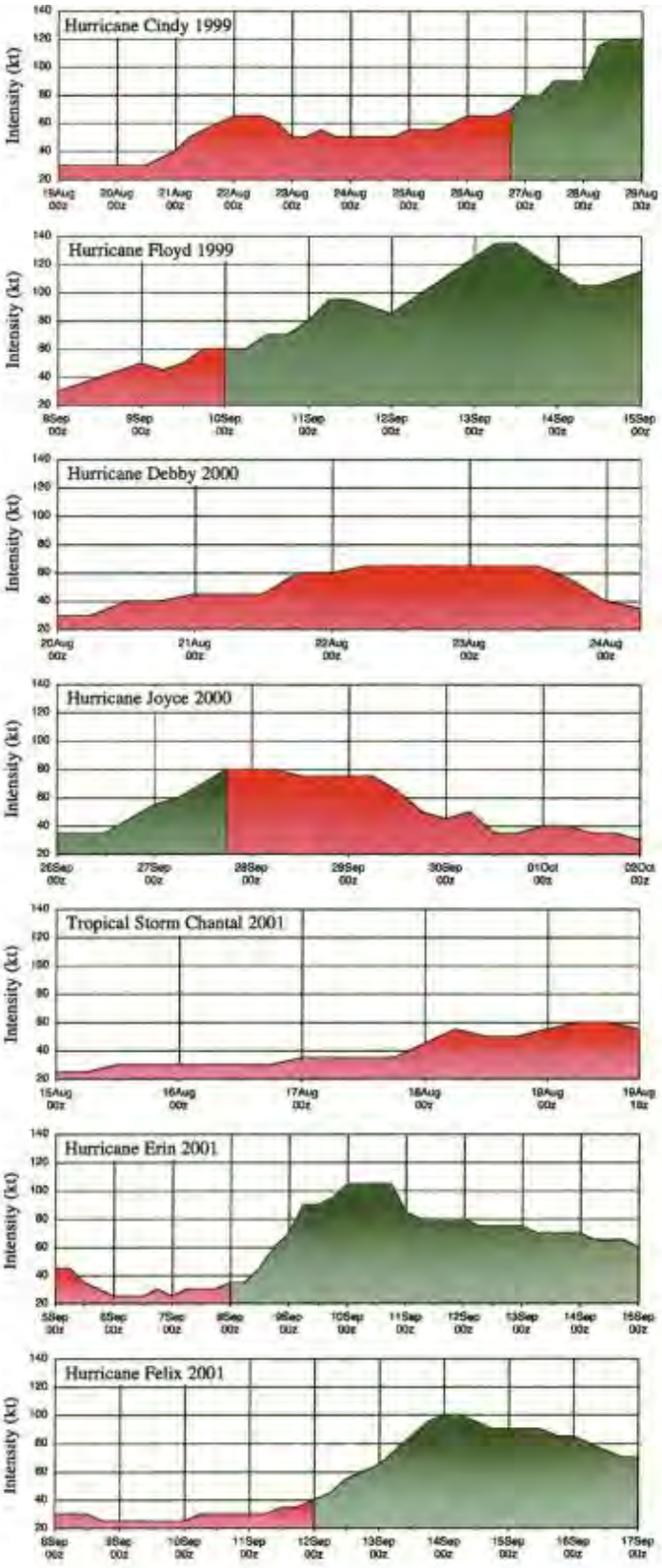

[2] The satellite imagery begins to detect what is likely polluted continental air north of Erin on 8 September (Fig. 9). This air mass is unrelated to the SAL air that is positioned south of Erin from the central Caribbean to the west coast of Africa and appears not to have significantly affected Erin's intensity.

FIG. 7. Time series of NHC best-track intensity for several Atlantic tropical cyclones in 1999 through 2001. Red shading indicates that the TC was under the suppressing influence of the SAL. Green shading indicates periods when the SAL was not impacting the TC.

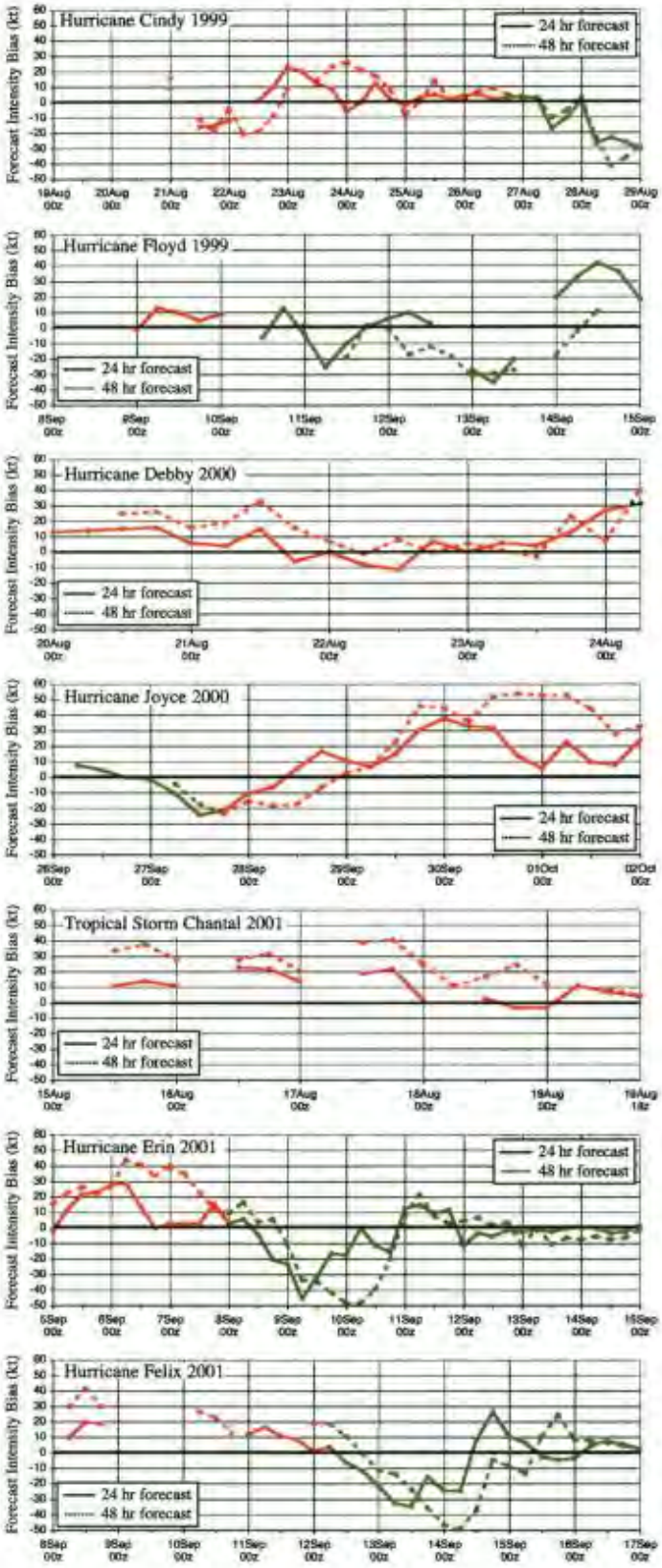

has provided some insight into the relationship between the SAL and North Atlantic TCs. The satellite imagery also reveals that the size of the SAL over the Atlantic, usually in the region of 15°–30°N, can exceed an area larger than the contiguous United States. Of more significance, the SAL appears to affect TC intensity change in the North Atlantic. It suppresses the intensity of TCs that it engulfs (Joyce 2000), while TCs that emerge from its influence (Erin 2001) can rapidly develop into strong hurricanes.

The GOES SAL-tracking satellite imagery also suggests that a possible link exists between the SAL and the overall TC activity that occurs in the North Atlantic. The North Atlantic basin averages about 10 named TCs per year. This represents ~40% and ~60% less annual TC activity than typically occurs in the eastern North Pacific (16.5 named storms) and western North Pacific (26 named storms) basins, respectively (Neumann 1993). There are climatological differences between Atlantic and Pacific basins that may account for some of the variation in TC activity between these ocean basins. However, the presence of the SAL and its ability to inhibit the growth of the North Atlantic's large number of seedlings (AEWs; Pasch et al. 1998) into named TCs may be a factor contributing to the relatively smaller number of TCs that typically occur in this basin each year. Several conclusions and recommendations can be drawn from this study:

- The SAL appears to suppress Atlantic TC activity in three main ways. First, it introduces dry, stable air into the storm, which promotes convectively driven downdrafts in the TC. Second, the SAL's midlevel easterly jet can dra-

FIG. 8. Time series of the SHIPS 24- and 48-h intensity bias relative to the NHC best track for the several Atlantic tropical cyclones shown in Fig. 7. Red lines indicate that the TC was under the suppressing influence of the SAL. Green lines indicate periods when the SAL was not impacting the TC.

matically enhance the local vertical wind shear. Third, the SAL enhances the preexisting trade wind inversion in the Atlantic, which acts to stabilize the environment.

- The extremely dry air that characterizes the SAL appears to undergo surprisingly little modification as it traverses the North Atlantic. The temperature inversion typically found at the SAL's base may contribute to the longevity of this dry air.
- The tropical North Atlantic is likely characterized by a multiple distribution of environmental moisture soundings that include moist tropical and SAL. This suggests that the mean Jordan tropical sounding (July–October) may be substantially drier than the typical non-SAL moist tropical soundings that exists in the North Atlantic during this time of year.
- Data from GPS sondes (that have inadvertently sampled the SAL) and GOES satellite-derived

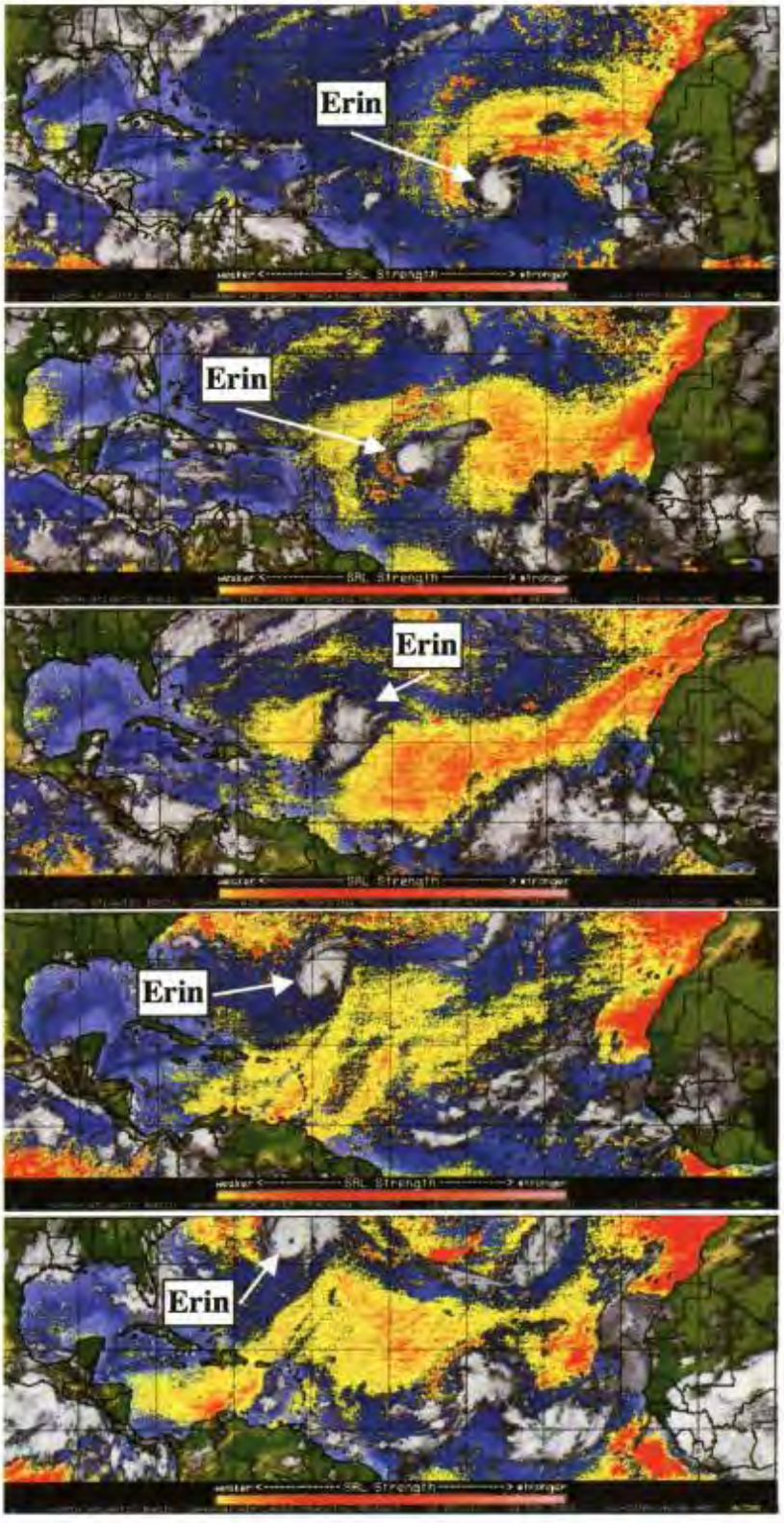

FIG. 9. GOES SAL-tracking imagery time series showing Hurricane Erin's interaction with the SAL at (top to bottom) 0000 UTC 2 Sep 2001, 0000 UTC 4 Sep 2001, 1800 UTC 5 Sep 2001, 1200 UTC 8 Sep 2001, and 1800 UTC 9 Sep 2001. The yellow–red shading indicates likely SAL regions with increasing amounts of dust content and dry lower-tropospheric air, as detected by the GOES imagery.

winds suggest the importance of assimilating the SAL-induced vertical wind shear and moisture information into forecast models.

- The intensity change of TCs influenced by the SAL may not be well predicted by the operational SHIPS model. SHIPS does not specifically consider the SAL in its methodology and relies on model data that may not effectively represent the SAL's thermodynamic properties.
- The presence of SAL signatures in the GOES SAL-tracking satellite imagery shows promise as a predictor for both TC nonintensification as well as rapid deepening.

Future work regarding the SAL will involve further validation of the GOES SAL-tracking imagery using GPS sondes. A more detailed understanding of SAL–TC interactions can be attained utilizing U.S. Air Force Reserve Command and NOAA aircraft that are able to collect measurements of the lower troposphere. This effort could be supplemented by improved SAL detection that uses high-resolution satellite imagery, such as the Moderate Resolution Imaging Spectroradiometer (MODIS) on the *Terra* and *Aqua* satellites, and total precipitable water estimates from the constellation of SSM/I satellites. This wide array of observations could also be used to assess how effectively forecast models capture the SAL's thermodynamics and how this information could be optimally utilized to improve model forecasts.

ACKNOWLEDGMENTS. This study was the result of collaborative efforts between the NOAA/AOML/Hurricane Research Division and the UW CIMSS. The authors would like to thank Dr. Robert Burpee for his insight and meticulous reviews of the various versions of this manuscript. Thanks to John Kaplan of HRD for his input into this work as it related to the SHIPS intensity forecast model, as well as Dr. Frank Marks of NOAA/HRD and Dr. Joseph Prospero of the University of Miami CIMAS for their insightful input and general knowledge of the Saharan air layer. Special thanks also to David Stettner of UW CIMSS for his assistance in retrieving the vast amount of archived GOES satellite imagery and UW CIMSS cloud-drift wind and wind shear data that were instrumental in carrying out this work. This paper benefited from reviews by Dr. Robert Burpee of the University of Miami CIMAS, Dr. Christopher Landsea and Dr. Frank Marks of NOAA/HRD, and Dr. Hugh Willoughby of Florida International University.

REFERENCES

Aberson, S. D., and J. L. Franklin, 1999: Impact on hurricane track and intensity forecasts of GPS dropwindsonde observations from the first-season flights of the NOAA Gulfstream-IV jet aircraft. *Bull. Amer. Meteor. Soc.*, **80,** 421–427.

Burpee, R. W., 1972: The origin and structure of easterly waves in the lower troposphere of North Africa. *J. Atmos. Sci.*, **29,** 77–90.

Carlson, T. N., and J. M. Prospero, 1972: The large-scale movement of Saharan air outbreaks over the northern equatorial Atlantic. *J. Appl. Meteor.*, **11,** 283–297.

——, and S. G. Benjamin, 1980: Radiative heating rates of Saharan dust. *J. Atmos. Sci.*, **37,** 193–213.

Chen, Y.-L., 1985: Tropical squall lines over the eastern Atlantic during GATE. *Mon. Wea. Rev.*, **113,** 2015–2022.

DeMaria, M., and J. Kaplan, 1999: An updated Statistical Hurricane Intensity Prediction Scheme (SHIPS) for the Atlantic and eastern North Pacific basins. *Wea. Forecasting*, **14,** 326–337.

Diaz, H. F., T. N. Carlson, and J. M. Prospero, 1976: A study of the structure and dynamics of the Saharan air layer over the northern equatorial Atlantic during BOMEX. National Hurricane and Experimental Meteorology Laboratory NOAA Tech. Memo. ERL WMPO-32, 61 pp.

Emanuel, K. A., 1989: The finite-amplitude nature of tropical cyclogenesis. *J. Atmos. Sci.*, **46,** 3431–3456.

Goldenberg, S. B., and L. J. Shapiro, 1996: Physical mechanisms for the association of El Niño and West African rainfall with Atlantic major hurricane activity. *J. Climate*, **9,** 1169–1187.

Goodberlet, M. A., C. T. Swift, and J. C. Wilkerson, 1989: Remote sensing of ocean surface winds with the Special Sensor Microwave/Imager. *J. Geophys. Res.*, **94,** 14 547–14 555.

Hastenrath, S., 1991: *Climate Dynamics of the Tropics*. Kluwer Academic, 488 pp.

Hock, T. F., and J. L. Franklin, 1999: The NCAR GPS dropwindsonde. *Bull. Amer. Meteor. Soc.*, **80,** 407–420.

Jordan, C. L., 1958: Mean soundings for the West Indies area. *J. Meteor.*, **15,** 91–97.

Karyampudi, V. M., and T. N. Carlson, 1988: Analysis and numerical simulations of the Saharan air layer and its effect on easterly wave disturbances. *J. Atmos. Sci.*, **45,** 3102–3136.

Liu, W. T., W. Tang, and P. S. Polito, 1998: NASA scatterometer provides global ocean surface wind

32. Assignment 2, Module 6: Wind Shear: https://www.aoml.noaa.gov/impact-of-wind-shear-on-tropical-cyclone-intensity/

Research Explores Impact of Wind Shear Direction on Tropical Cyclone Intensity

A recent study in the journal *Monthly Weather Review* is the first to examine how the direction of wind shear changes how much heat and moisture are available to a tropical cyclone and how these factors influence tropical cyclone intensity change.

The amount of wind shear, i.e., the change of the wind with height, is one of the most commonly used predictors of tropical cyclone intensity change, with large amounts of wind shear generally being unfavorable for intensification. Regardless of the direction of the wind shear, tropical cyclones in the North Atlantic basin usually have warm, moist air from the environment near the sea surface on their east side (solid red arrows in the images) and cool, dry air from the environment on their west side (solid blue arrows in images).

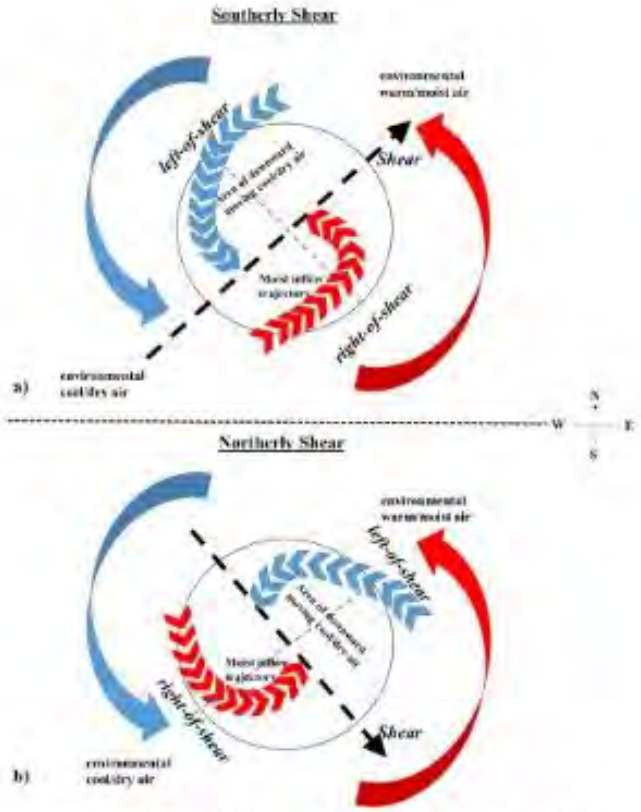

A schematic of the different environmental (solid arrows) and storm (dashed arrows) processes for tropical cyclones in the North Atlantic basin exposed to southerly wind shear (top image) and northerly wind shear (bottom image). Blue indicates cool, dry air, while red indicates warm, moist air.

In addition to environmental air, when tropical cyclones are experiencing wind shear, an area of warm, moist air moves inward toward the tropical cyclone center from right-of-shear (dashed red lines in images) and an area of cool, dry air moves inward from downward-moving air left-of-shear (blue dashed lines in images). Previous studies have shown that when a tropical cyclone has temperature and humidity evenly distributed around its eyewall, known as symmetry, conditions are favorable for intensification.

When wind shear is southerly (top image), the downward moving cool, dry air left-of-shear is in the same location (northwest quadrant) as the cool, dry air in the environment. Additionally, the area of environmental warm, moist air coincides with the area of inward moving warm, moist air (southeast quadrant).

This overlapping cool, dry air in the northwest quadrant and overlapping warm, moist air in the southeast quadrant leads to an asymmetric distribution of temperature and moisture around the storm, which is unfavorable for intensification because the warm, moist air that tropical cyclones require to sustain their strong thunderstorms and intensify is limited.

In contrast, when the wind shear is northerly (bottom image), the downward moving cool, dry air left-of-shear is in the northeast quadrant in a region of warm, moist environmental air. In this scenario, the inward moving warm, moist air coincides with the region of cool, dry environmental air.

Since these air masses partially cancel each other out, the temperature and moisture near the ocean surface in environments of northerly wind shear are more symmetrically distributed around the tropical cyclone, making these storms more likely to intensify. Conversely, tropical cyclones exposed to southerly wind shear environments have a more asymmetric distribution of temperature and moisture, making them less likely to intensify.

These relationships show that tropical cyclone structure and intensity are directly influenced by the surrounding environment and that knowledge of the wind environment provides tropical cyclone forecasters with another tool to predict intensity change, helping better protect both life and property.

33. Assignment 2, Module 6: Hurricane Formation: https://www.weather.gov/source/zhu/ZHU_Training_Page/tropical_stuff/hurricane_anatomy/hurricane_anatomy.html

Hurricane Facts

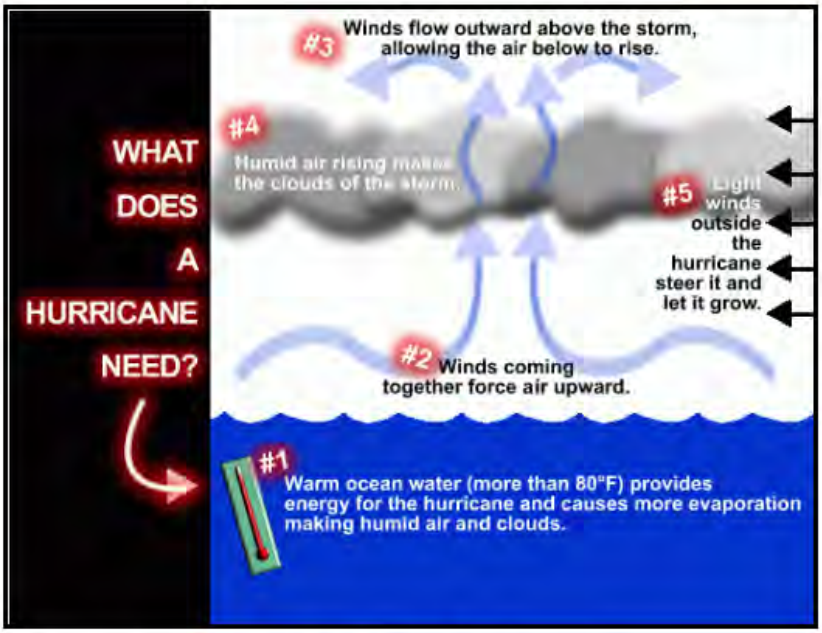

There are six widely accepted conditions for hurricane development:

1. The first condition is that ocean waters must be above 26 degrees Celsius (79 degrees Fahrenheit). Below this threshold temperature, hurricanes will not form or will weaken rapidly once they move over water below this threshold. Ocean temperatures in the tropical East Pacific and the tropical Atlantic routinely surpass this threshold.

2. The second ingredient is distance from the equator. Without the spin of the earth and the resulting Coriolis force, hurricanes would not form. Since the Coriolis force is at a maximum at the poles and a minimum at the equator, hurricanes can not form within 5 degrees latitude of the equator. The Coriolis force generates a counterclockwise spin to low pressure in the Northern Hemisphere and a clockwise spin to low pressure in the Southern Hemisphere.

3. The third ingredient is that of a saturated lapse rate gradient near the center of rotation of the storm. A saturated lapse rate insures latent heat will be released at a maximum rate. Hurricanes are warm core storms. The heat hurricanes generate is from the condensation of water vapor as it convectively rises around the eye wall. The lapse rate must be unstable around the eyewall to insure rising parcels of air will continue to rise and condense water vapor.

4. The fourth and one of the most important ingredients is that of a low vertical wind shear, especially in the upper level of the atmosphere. Wind shear is a change in wind speed with height. Strong upper level winds destroy the storms structure by displacing the warm temperatures above the eye and limiting the vertical accent of air parcels. Hurricanes will not form when the upper level winds are too strong.

5. The fifth ingredient is high relative humidity values from the surface to the mid levels of the atmosphere. Dry air in the mid levels of the atmosphere impedes hurricane development in two ways. First, dry air causes evaporation of liquid water. Since evaporation is a cooling process, it reduces the warm core structure of the hurricane and limits vertical development of convection. Second, dry air in the mid levels can create what is known as a trade wind inversion. This inversion is similar to sinking air in a high pressure system. The trade wind inversion produces a layer of warm temperatures and dryness in the mid levels of the atmosphere due to the sinking and adiabatic warming of the mid level air. This inhibits deep convection and produces a stable lapse rate.

6. The sixth ingredient is that of a tropical wave. Often hurricanes in the Atlantic begin as a thunderstorm complex that moves off the coast of Africa. It becomes what is known as a midtropospheric wave. If this wave encounters favorable conditions such as stated in the first five ingredients, it will amplify and evolve into a tropical storm or hurricane. Hurricanes in the East Pacific can develop by a midtropospheric wave or by what is known as a monsoonal trough.

Additional items...

- Each year, an average of ten tropical storms develop over the Atlantic Ocean, Carribean Sea, and Gulf of Mexico. Many of these remain over the ocean. Six of these storms become hurricanes each year. In an average 3-year period, roughly five hurricanes strike the United States coastline, killing approximately 50 to 100 people anywhere from Texas to Maine. Of these, two are typically major hurricanes (winds greater than 110 mph).

- Typical hurricanes are about 300 miles wide although they can vary considerably in size.

- The eye at a hurricane's center is a relatively calm, clear area approximately 20-40 miles across.

- The eyewall surrounding the eye is composed of dense clouds that contain the highest winds in the storm.

- The storm's outer rainbands (often with hurricane or tropical storm-force winds) are made up of dense bands of thunderstorms ranging from a few miles to tens of miles wide and 50 to 300 miles long.

- Hurricane-force winds can extend outward to about 25 miles in a small hurricane and to more than 150 miles for a large one. Tropical storm-force winds can stretch out as far as 300 miles from center of a large hurricane.

- Frequently, the right side of a hurricane is the most dangerous in terms of storm surge, winds, and tornadoes.

- A hurricane's speed and path depend on complex ocean and atmospheric interactions, including the presence or absence of other weather patterns. This complexity of the flow makes it very difficult to predict the speed and direction of a hurricane.

- Do not focus on the eye or the track-hurricanes are immense systems that can move in complex patterns that are difficult to predict. Be prepared for changes in size, intensity, speed and direction.

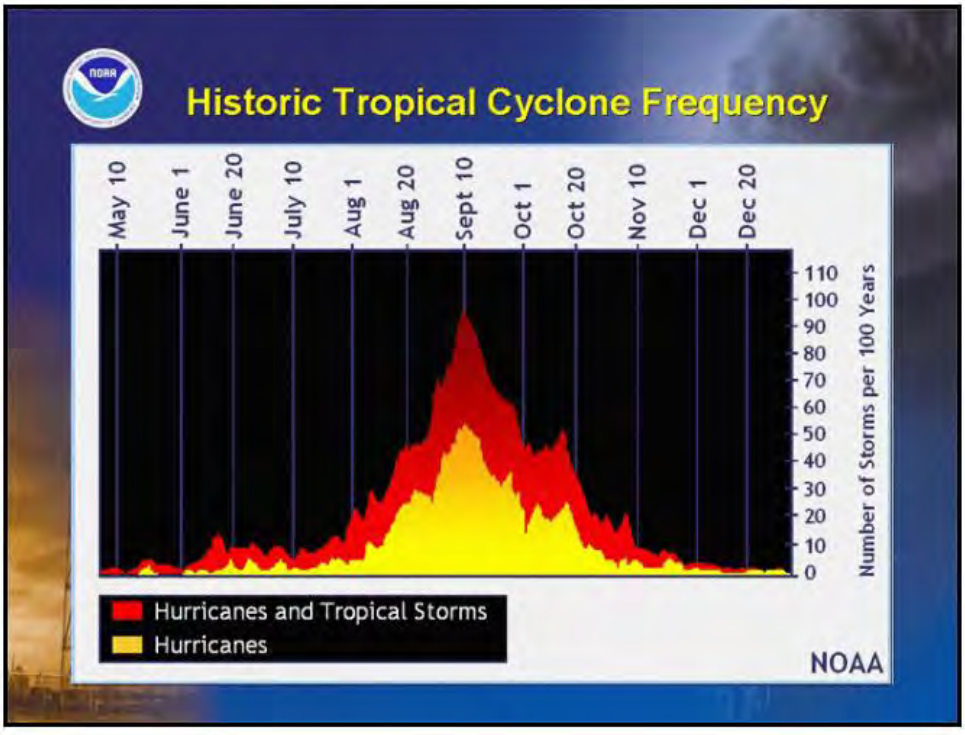

35. Assignment 2, Module 6: Hurricane Decay:
https://www.hurricanescience.org/science/science/hurricanedecay/

Hurricane Decay: Demise of a Hurricane

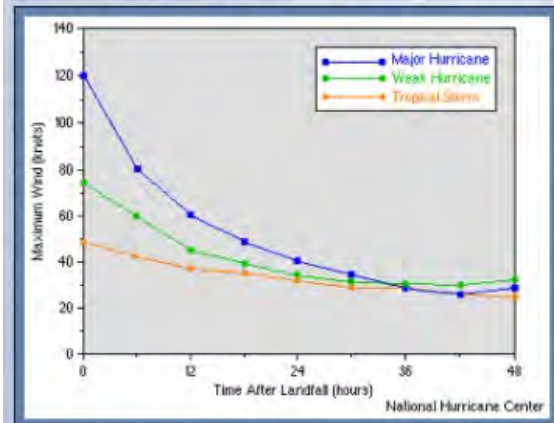

This graph shows how rapidly wind speed decreases once a hurricane reaches land. The roughness of the land terrain increases friction, but more critical, once over land, the system is cut off from its heat and moisture sources. Sustained winds in a hurricane will decrease at a relatively constant rate (approximately half the wind speed in the first 24 hours). Thus, the faster the forward speed of a landfalling hurricane, the further inland hurricane force winds may penetrate. Image credit the National Hurricane Center (NHC).

In Hurricane Genesis: Birth of a Hurricane, the formation of tropical depressions in the Earth's **atmosphere** is discussed. The formation of a **tropical depression** can become the birth of a **hurricane**. In Hurricane Development: From Birth to Maturity, the maturation of a tropical depression into a hurricane is described. In this section, the causes of hurricane decay or death are reviewed. Just as there are many factors that contribute to the birth and survival of a hurricane, there are also many causes for a hurricane to weaken and/or die.

Landfall usually causes a hurricane to quickly decay (for more detail see, Interaction between a Hurricane and Land). Hurricanes require **evaporation** from the warm ocean surface to survive (see Hurricane Development: From Birth to Maturity). Once a hurricane makes landfall, it is separated from its ocean energy source, and hence, can no longer extract heat from the ocean. Since the air masses over land are drier and contain more **aerosol particles** than over the ocean, less moisture is carried into the storm, **cloud** coverage lessens, and air is cooled and then sinks, disrupting the **hurricane's secondary circulation** and hindering critical **thunderstorm** development (see Hurricane Development: From Birth to Maturity). To a lesser extent, the increased roughness of the land surface also weakens a hurricane as increased **friction** causes a reduction in surface circulation.

Even if a hurricane remains over the ocean, once the storm moves northward (in the Northern Hemisphere) out of the **tropical ocean** and into the **mid-latitudes**, it begins to move over colder water, again losing the warm water source necessary to drive the hurricane. As less moisture is evaporated into the atmosphere to supply cloud formation, the storm weakens. Sometimes, even in the tropical oceans, colder water churned up from beneath the sea surface by the hurricane can cause the hurricane to weaken (see Interaction between a Hurricane and the Ocean). Even when the ocean conditions are favorable for the hurricane to be maintained, a hurricane may encounter an area of particularly dry and dusty air, such as the Saharan Air Layer (SAL), causing the hurricane to weaken, though the role of the SAL is being debated.

Hurricane decay can also be caused by strong **vertical wind shear**, a change in wind direction or speed with height. This change in wind speed or direction with height can enhance the mixing of drier environmental air into the storm **eyewall** leading to **downdrafts**, which inhibit **intensification**. Fast, upper-tropospheric winds can create very high values of wind shear and can separate cloud tops from their bases and cause the vertical circulation around a hurricane's eyewall to tilt. As heat and moisture at upper levels are advected away from the low-level circulation of the hurricane, its development is inhibited. Midlevel warming within the storm's center also reduces convective activity and inhibits intensification. Without a strong secondary circulation, a hurricane cannot be sustained (see Hurricane Development: From Birth to Maturity). The response to vertical shear partially depends on the storm circulation, so the response to similar values of vertical shear can vary from storm to storm. Vertical wind shear is common in the mid-latitudes, although it can also occur over the tropical oceans where it cannot only weaken a hurricane but also help to prevent one from forming in the first place (see Hurricane Genesis: Birth of a Hurricane).

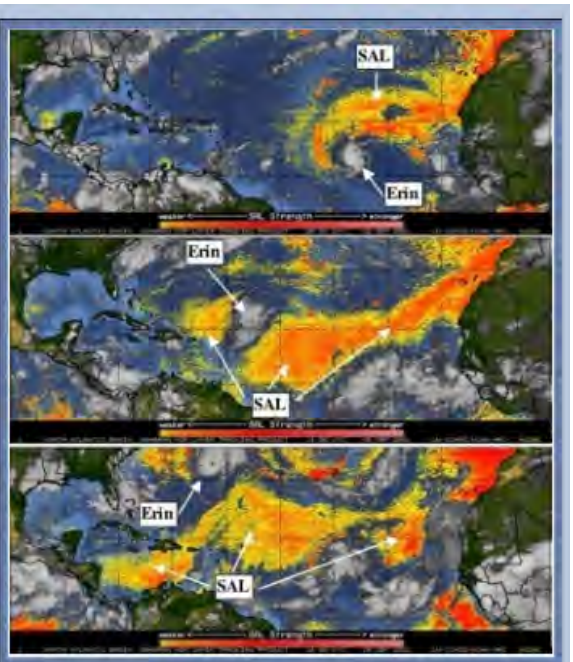

Hurricane Erin (2001) in the Saharan Air Layer (SAL). The SAL is indicated by the yellow and orange colors in each image. Erin's strength may have been negatively affected when it interacted with the SAL. Image credit: NOAA/AOML

When a hurricane moves into the mid-latitudes, it may be absorbed by a different kind of low-pressure weather system called an **extratropical cyclone**. Extratropical cyclones are responsible for much of the sensible weather (such as rain and snow) that people who live in the mid-latitudes experience, especially during the winter months. Unlike hurricanes, extratropical cyclones require areas of sharp horizontal temperature contrasts, called fronts, to form. Although the mechanisms for creating an extratropical cyclone are quite different than the mechanisms for creating a hurricane, the added moisture and energy from an absorbed hurricane can sometimes cause an extratropical cyclone to rapidly intensify, as in the case of the "Perfect Storm" in late-October 1991. Sometimes, a hurricane itself may transition into an extratropical cyclone when it moves into the mid-latitudes. This process, called **extratropical transition (ET)**, involves the hurricane losing its **warm core**, which weakens and becomes a **cold core low**, while the wind field and cloud field expand in size. Once extratropical transition is complete, the storm is sustained from energy that it extracts from the environmental wind field (in the presence of temperature fronts) instead of energy from the ocean.

During extratropical transition, a cyclone frequently produces intense rainfall and strong winds and has increased forward motion, so that such systems pose a serious threat to land and maritime activities. Hurricane Irene (1999) is a good example of a hurricane which underwent an explosive extratropical transition. The storm began in the Caribbean and then moved across Cuba and southern Florida. As it rapidly accelerated into the North Atlantic, the hurricane became an intense extratropical low over the maritime provinces of southeast Canada, actually exhibiting its strongest winds after its transition.

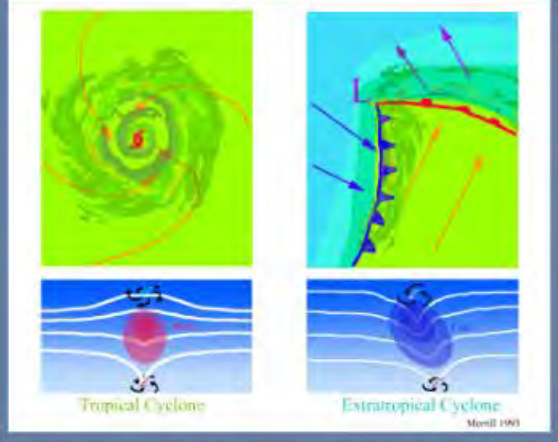

The top schematics show horizontal maps of the surface temperature and wind fields associated with a tropical cyclone (left) and an extratropical cyclone (right). Colors indicate temperature (blue: 15°C=59°F, blue-green: 20°C=68°F, green: 25°C=77°F). Solid lines indicate surface wind speeds (34 kt=39 mph and 64 kt=74 mph). The bottom schematics show vertical maps of the pressure surfaces and circulation at the surface and tropopause. It should be noted that the anticyclonic (clockwise in the Northern Hemisphere) circulation shown at the tropopause only exists outside of the eyewall; in the eyewall, the circulation is still cyclonic (counterclockwise in the Northern Hemisphere) like it is in the lower troposphere. Image credit: NOAA/AOML

Afternoon satellite image of Tropical Storm Ida (2009), showing the classic signature of a tropical storm undergoing transition to an extratropical cyclone. There is heavy thunderstorm activity near the center, but the long band of clouds to the east of Ida doesn't look much like a spiral band--it looks more like a front. Image courtesy of wunderground.com.

36. Assignment 2, Module 7: Factors that Hinder Development: https://hurricaneville.com/factors-that-hinder-development/#:~:text=Tropical%20cyclones%20such%20as%20tropical,or%20even%20dissipate%20them%20altogether.

What causes hurricanes to decay and dissipate? Hurricanes can become very powerful, but they're not immortal. Tropical cyclones such as tropical storms and hurricanes have a finite life span and their share of enemies. Factors that hinder development include cooler sea surface temperatures, hostile upper-level winds, land, and sinking air that all inhibit further strengthening, or even dissipate them altogether.

Colder sea surface temperatures – Warm water is the engine of all tropical cyclones. Sea surface temperatures must be at or above 80 degrees Fahrenheit in order for a tropical storm or hurricane to flourish. Anything colder than that will cause the storm to weaken or even dissipate.

Shearing winds aloft – Tropical storms and hurricanes are "vertically stacked systems." That means that clouds in the hurricane engine build vertically to great heights in the troposphere and lower stratosphere. In order for this to happen, these storms must have light winds aloft. Hostile upper-level wind conditions produce shearing, which blows off the high cloud tops of these storms and causes them to become disorganized.

Sinking air – Sinking air, or subsidence from high pressure such as the subtropical ridge can also inhibit development. Again, hurricanes are vertically stacked systems so they need to have air rise from the surface to the upper levels. Sinking air from high pressure hinders thunderstorm development, which is a critical element in hurricane strengthening.

Land, of course – The ultimate hindering factor to hurricanes is of course land. When hurricanes or tropical storms make landfall, the friction caused by a large land mass, and their terrain cuts off the hurricane's circulation, and squeezes out the storm's moisture. In some cases, rugged terrain such as mountains can squeeze out tons of moisture, which in turn produces heavy rainfall and flooding.

37. Assignment 2, Module 7: Hurricane Development: https://www.hurricanescience.org/science/science/development/

Hurricane Development: From Birth to Maturity

In Hurricane Genesis: Birth of a Hurricane, the formation of tropical depressions in the Earth's **atmosphere** is discussed. The formation of a **tropical depression** can lead to the birth of a **hurricane**. In this section, the maturation of a tropical depression into a hurricane and the survival of that hurricane are reviewed. In Hurricane Decay: Demise of a Hurricane, the causes of hurricane decay are described.

A Hurricane's Energy Source: The Ocean

Development of a tropical depression into a mature hurricane requires heat energy from the ocean surface. For this reason, hurricanes do not usually develop over land or outside of the warm **tropical oceans** where the **sea surface temperature (SST)** is colder than ~26.5°C (~80°F). In the image below, the orange areas indicate where the sea surface temperature was at least 26.5°C (79.7°F) on September 24, 2009. In the North Atlantic Ocean, this area extends westward along a narrow swath from the west coast of Africa to the northern tip of South America. At the western end of this swath, the warm water also extends northward through the **Caribbean Sea** and into both the Gulf of Mexico and **Sargasso Sea** (off the east coast of Florida). The size of the warm water area changes with the seasons. In the North Atlantic Ocean, September generally has the largest area of the warmest water; earlier or later in the year, the area of warm sea surface temperatures is smaller. It is not a coincidence that the peak of the Atlantic **hurricane season** also occurs in September.

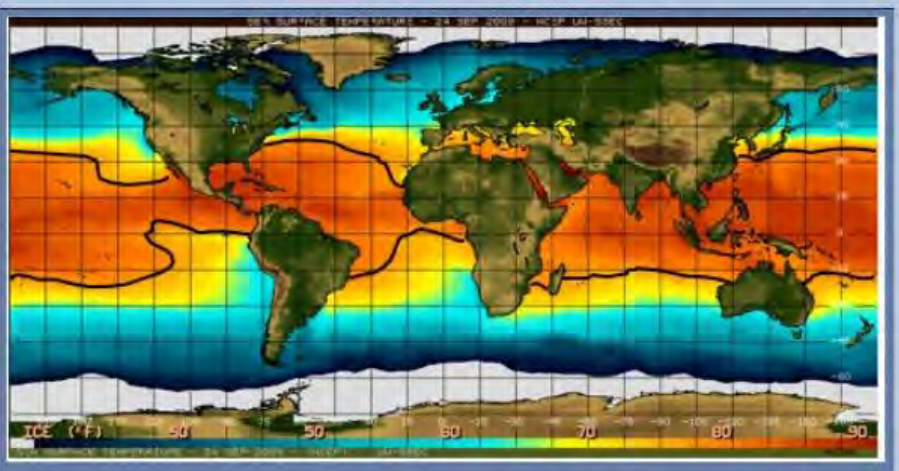

Sea Surface Temperature (SST) image for the global ocean, based on data gathered on September 24, 2009. Blue an green colors indicate cooler waters (less than 15.6°C [60°F]) while orange and red colors, outlined by the black curves, indicate warmer waters (at least 26.5°C [~80°F]). Image courtesy of the Space Science and Engineering Center, University of Wisconsin-Madison.

Heat is transferred from the ocean to the atmosphere when water at the ocean's surface evaporates to become **water vapor**. This causes the ocean to cool slightly. The heat transferred to the atmosphere from the ocean is stored in the water vapor as **latent heat**. To understand why **evaporation** of ocean water transfers heat from the ocean to the atmosphere, please see Basic Science. It is important to note, however, that underneath a hurricane, other processes within the ocean usually cause the sea surface to cool much more than evaporation does, as described in Interaction between a Hurricane and the Ocean.

Energy Cycle: A Hurricane's Secondary Circulation

In the lower **troposphere**, **air parcels** carry heat energy obtained from the ocean. These air parcels spiral inward towards the center of the developing hurricane. Once an air parcel reaches the hurricane's **eyewall**, it turns upward and rises due to a process called convection. The added heat from the ocean causes the air rising in the eyewall to be warmer than the surrounding environment, allowing it to continue to rise.

Once the air parcel reaches the tropopause, the boundary between the troposphere and the stratosphere, it begins to spiral outward. As the air parcel spirals outward, it loses heat to outer space by long wave radiation. At some point far away from the center of the hurricane, the cooled air parcel begins to sink back towards the lower troposphere. Then, this cycle, which is known as a hurricane's secondary circulation, is complete.

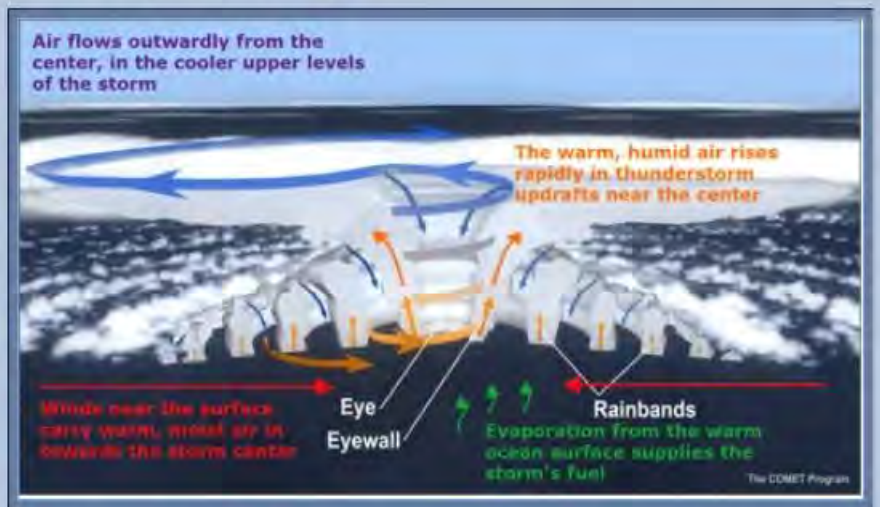

Vertical slice through the center of a mature hurricane showing the secondary circulation. In the lower troposphere, air spirals inward towards the center of the hurricane (red arrows), then upward in the eyewall (orange arrows), and then outward at the top of the troposphere (blue arrows). Eventually, the air sinks back towards the lower troposphere (smaller, blue arrows), and the circulation continues with new and/or recycled air spiraling inward towards the eyewall. The secondary circulation works like a heat engine. For heat energy to be converted to mechanical energy, air must flow into the hurricane (in the lower troposphere) at a higher temperature than it exits the hurricane (at the top of the troposphere).

Since the conversion of heat energy to mechanical energy drives the hurricane's secondary circulation, a hurricane can be treated as a **heat engine**. For the engine to continue working, air must flow into the system (the hurricane) at a higher temperature than it exits the system. As long as the air parcels can rise in the eyewall and then spiral outward at the tropopause faster than other air parcels can spiral inward towards the eyewall in the lower troposphere, the central pressure in the developing hurricane will fall. A falling central pressure is one way to measure how much a hurricane is intensifying. Increasing winds increase the transfer of heat from the ocean, creating a positive feedback. When the central pressure falls, air parcels begin to spiral inward towards the eyewall faster to fill the vacuum. If the air parcels spiral inward faster, then the maximum wind speed will increase. Increasing maximum wind speed is another way to measure how much a hurricane is intensifying (more intense hurricanes have faster maximum sustained wind s). Eventually, a hurricane may reach a near steady state (in theory), where the heat energy coming in from the ocean is balanced by the energy lost to frictional dissipation in the atmosphere. In this "quasi-steady state", neither the hurricane's central pressure nor its maximum wind speed changes much over time. In reality, though, a hurricane rarely remains in quasi-steady state for an extended period of time because changes in the surrounding atmosphere, the underlying ocean, or the hurricane's internal structure can cause the hurricane's intensity to change.

38. Assignment 2, Module 7: Factors that Strengthen and Weaken Hurricanes: https://blog.ucsusa.org/brenda-ekwurzel/hurricane-watch-checklist-four-factors-that-strengthen-and-four-that-weaken-tropical-cyclones

Hurricane Watch Checklist: Four Factors that Strengthen and Four that Weaken Tropical Cyclones

August 27, 2012 | 10:10 am

Brenda Ekwurzel
Former Staff

Whenever I see that a tropical storm is threatening to convert into a tropical cyclone – that's meteorology-speak for hurricanes in the Atlantic, typhoons in the Pacific or cyclones in the Indian Ocean – I consult my checklist. These are the factors that can nip that tropical storm in the bud or escalate it into a full blown hurricane.

Four Factors that Can Strengthen Tropical Cyclones

1. Sea surface temperatures warmer than 79 degrees Fahrenheit (26 degrees Celsius)
2. Low vertical wind shear
3. Warm moist air
4. Ocean area along the projected storm track

Four Factors that Can Weaken Tropical Cyclones

1. Cooler Sea surface temperatures less than 79 degrees Fahrenheit (26 degrees Celsius)
2. High vertical wind shear
3. Dry air
4. Land masses along the projected storm track

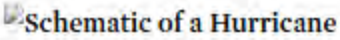

Figure 1: In a tropical cyclone, air rotates inward to the center (or "eye"), then rises to higher altitudes. As warm, moist air rises, the air cools and condenses to rain, releasing heat. This cycle of evaporation and condensation powers the storm. Adapted from a figure courtesy of NOAA.

How do these Factors Play a Role?

Here are a some figures and a brief overview of how these factors work in concert to influence hurricanes. For a little fuller description you can go to this two page summary that includes figure 1. It gives a quick glimpse into why these factors play a role in large part because warm moist air rising to upper levels helps fuel a hurricane. For a more technical description check out the Quick Study feature in *Physics Today* by Kerry Emanuel (Massachusetts Institute of Technology).

I first consult the NOAA sea surface temperature charts because warmer ocean waters evaporate and add moisture to the surface air at a greater pace than cold ocean water. Similar to when we see more tendrils of steam rise from a pot of water on the stove as it warms.

Figure 2: Sea Surface Temperature Map for August 23, 2012. I added a few labels to supplement the original tiny font in this NOAA figure. The left most end of the color bar scale is -2.0 degrees Celsius (28.4 degrees Fahrenheit) and the right most number is 34.3 degrees Celsius (93.7 degrees Fahrenheit). The color greater than the 26 degrees Celsius (critical for tropical cyclones) is also indicated in a few places.

Next it is worth checking on conditions for vertical wind shear – a change in wind speed or direction with altitude. If the shear is relatively weak, than warm moist air can rise and condense into rain releasing heat in a concentrated region helping to fuel the cycle shown in figure 1. If there is higher wind shear, the region where the heat is released is distributed over a larger area dissipating the energy compared to the more concentrated area in the low wind shear case. We can think of it as upper level winds blowing the upper level heat away.

Third look for dry air nearby to the tropical storm or hurricane that can be pulled in and deprive the hurricane of much needed moisture. If there are dry patches nearby or along the projected storm track this can give some solace. If moist air abounds, pay closer attention to the forecast. NOAA has made great progress in having more accurate hurricane storm tracking, leading to smaller land areas that need evacuation alerts. Hurricane intensity projections are still an active area of research.

Finally, given the important role that moist air plays, land area compared to ocean area really matters. Land, even with some lakes, hardly can compare to a vast ocean surface area ready to deliver moisture to a storm along the ocean portion of the storm track. That is if the water is warm enough. For example, even during hurricane season, vigorous winds from a prior storm can churn the waters bringing colder deeper waters to the surface putting the brakes on hurricane development.

As land dwellers we can breathe sigh of relief when the season slides toward fall and the ocean waters start to cool and the winds start blowing harder as the temperature difference between the tropics and the polar regions increases. Until next summer when I pull out my hurricane watch check list again.

39. Assignment 2, Module 7: Empirical Model for Predicting Decay: https://journals.ametsoc.org/view/journals/apme/34/11/1520-0450_1995_034_2499_asemfp_2_0_co_2.xml

A Simple Empirical Model for Predicting the Decay of Tropical Cyclone Winds after Landfall

JOHN KAPLAN AND MARK DEMARIA

Hurricane Research Division, NOAA/AOML, Miami, Florida

(Manuscript received 26 January 1995, in final form 8 May 1995)

ABSTRACT

An empirical model for predicting the maximum wind of landfalling tropical cyclones is developed. The model is based upon the observation that the wind speed decay rate after landfall is proportional to the wind speed. Observations also indicate that the wind speed decays to a small, but nonzero, background wind speed. With these assumptions, the wind speed is determined from a simple two-parameter exponential decay model, which is a function of the wind speed at landfall and the time since landfall. A correction can also be added that accounts for differences between storms that move inland slowly and storms that move inland rapidly. The model parameters are determined from the National Hurricane Center best track intensities of all U.S. landfalling tropical cyclones south of 37°N for the period 1967–93. Three storms that made landfall in Florida prior to 1967 were also included in the sample. Results show that the two-parameter model explains 91% of the variance of the best track intensity changes. When the correction that accounts for variations in the distance inland is added, the model explains 93% of the variance.

This model can be used for operational forecasting of the maximum winds of landfalling tropical cyclones. It can also be used to estimate the maximum inland penetration of hurricane force winds (or any wind speed threshold) for a given initial storm intensity. The maximum winds at an inland point will occur for a storm that moves inland perpendicular to the coastline. Under this assumption, the maximum wind at a fixed point becomes a function of the wind speed at landfall and the translational speed of motion. For planning purposes, maps of the maximum inland wind speed can be prepared for various initial storm intensities and speeds of motion. The model can also be applied to the entire wind field of an individual storm to provide a two-dimensional field of the maximum wind during a given storm. Examples of each of these applications are presented.

1. Introduction

The recent landfalls of Hurricanes Hugo (1989) and Andrew (1992) have illustrated the need for more accurate predictions of the inland effects of hurricane winds. Unlike most previous U.S. landfalling hurricanes, the majority of the 36 deaths and most of the estimated $30–$40 billion in damage directly attributed to these storms were due to the effects of wind rather than storm surge (U.S. Department of Commerce 1993; National Research Council 1994). At the time that Hugo and Andrew made landfall, forecasters at the National Hurricane Center (NHC) relied on past experience to make inland wind forecasts since none of the operational tropical cyclone (TC) prediction models provided intensity forecasts over land. Beginning in 1992, a three-dimensional TC prediction model developed at the Geophysical Fluid Dynamics Laboratory (GFDL) provided near-real-time overwater and overland track and intensity forecasts to the NHC (Bender et al. 1993). Lawrence and Gross (1993, 1994) have shown that the GFDL model overwater track forecasts had considerable skill compared to the other tropical cyclone track models that NHC employed during the 1992 and 1993 hurricane seasons. However, their results also indicated that the GFDL overwater intensity forecasts were somewhat worse, on average, than those produced by the other intensity models. To date, no comprehensive evaluation of the GFDL overland intensity forecasts has been performed.

In contrast to the rather sophisticated GFDL model, most previous attempts to model the decay of TCs over land have been empirical. In one of the earliest such studies, Hubert (1955) found that hurricanes making landfall along the Atlantic coast of the United States filled more rapidly than those that made landfall along either the Gulf of Mexico or Florida coastlines. Malkin (1959) performed a similar study and determined that there was a tendency for the most intense hurricanes to fill the most rapidly. He also found that the filling rate of hurricanes decreased as the percentage of the storm's underlying circulation that was over water increased. More recently, Schwerdt et al. (1979) and Ho et al. (1987) showed that hurricanes making landfall

Corresponding author address: John Kaplan, AOML/NOAA, Hurricane Research Division, 4301 Rickenbacker Causeway, Miami, FL 33149.

along the Gulf of Mexico coastline filled most rapidly, while those that made landfall along the Florida coastline filled the slowest.

The primary emphasis of the above studies was the evaluation of the decrease in the pressure gradient between the TC center and the surrounding environment as a function of time since landfall. In several of these studies, some form of the gradient or cyclostrophic wind equation was used to estimate the overland maximum wind speeds consistent with these pressure gradients. Batts et al. (1980) developed a slightly more sophisticated model for determining the maximum possible inland wind speeds. In their model, the decrease in the pressure gradient after landfall was obtained using an empirical equation that was a function of the time a TC was over land and the angle at which the storm crossed the coastline. The inland wind speeds of the TC were then computed as a function of the azimuthal and radial distance from the storm center using an approximate form of the gradient wind equation. Batts et al. assumed that the translational speed of the storm resulted in an asymmetric wind field where the strongest winds were always in the right rear quadrant. Also, the inland wind speeds were reduced to account for the sudden increase in surface roughness experienced immediately after a TC makes landfall. Georgiou (1985) used a similar approach but added a level of complexity by employing a modified version of Shapiro's (1983) hurricane planetary boundary layer model to predict both inland wind speeds and directions. The decrease in the pressure gradient after landfall required to run this model was determined by an empirical relationship developed for four separate regions of the United States. Unlike most previous studies, the filling rates obtained by Georgiou were a function of distance inland rather than time inland.

In this study, a simple empirical model for predicting TC wind speeds after landfall is described. This model directly predicts the decrease in wind speeds, rather than predicting the pressure increase and then inferring the winds from the pressure. A correction term that accounts for the distance a TC is inland is included in the model. This term is used to account for storms that move at some angle to the coastline rather than perpendicular to the coast at landfall. The dataset used to develop the model is described in section 2, and the derivation of the model is discussed in section 3. Applications of the decay model are presented in section 4. Conclusions and ideas for future research are discussed in section 5.

2. Data

The database used to derive the decay model consists of all named TCs that made landfall in the United States from 1967 to 1993, and a few additional TCs that made landfall along the Florida coastline prior to 1967. Tropical cyclone position and intensity estimates for the 1967–93 cases were obtained from the HURDAT file maintained by NHC (Jarvinen et al. 1988). The lone exception is for the intensity estimates of Hurricane Andrew (1992) over Florida, which were obtained from Powell and Houston (1995, unpublished manuscript). The HURDAT file consists of 6-h estimates of position, central pressure, and maximum sustained 1-min surface wind speed (MSSW) for all named Atlantic TCs from 1886 to 1993. Landfalling TCs prior to 1967 were not used in this study because Neumann (1994) found that the HURDAT file is less reliable for pre-1967 events. The problem with these earlier events is that TC position and intensity estimates were only archived once per day before 1931 or twice per day prior to the mid-1950s. From the mid-1950s to the mid-1960s, positions and intensities were determined every 6 h, although not all of the 6-h values were saved. Consequently, interpolation was necessary to obtain the intermediate 6-h position, central pressure, and wind estimates for many TCs during the pre-1967 era. This was accomplished by employing nonlinear interpolation to estimate the intermediate 6-h positions, while a simple linear interpolation between existing intensity estimates was used to obtain the intermediate wind speeds and pressure. Neumann found that while this technique worked fairly well when a TC was over water, serious problems were detected in some overland position and intensity estimates. He indicated that the problems with overland intensity estimates were especially troublesome because a linear interpolation scheme was used to obtain intensity estimates at intermediate times even though the decay of TCs has been shown to be nonlinear (Malkin 1959; Schwerdt et al. 1979; Ho et al. 1987). The errors in the overland positions, while not as serious as those for the overland intensities, did result in some storms crossing the coastline at incorrect locations. Thus, except for a few Florida landfalling cases that were hand analyzed, only TCs that made landfall from 1967 to 1993 are used in this study.

The sample was also restricted to TCs that made landfall from near the Texas–Mexico border to the North Carolina–Virginia border. Tropical cyclones making landfall outside the United States were excluded because fewer surface observations are routinely available for the poststorm analysis in these regions. Tropical cyclones making landfall north of the North Carolina–Virginia border were not used because they likely have different decay properties than those in other regions. These differences are probably due to more frequent interactions with extratropical systems as well as the comparatively large variations in the terrain type (i.e., forest, hills, etc.) encountered after landfall. Moreover, TCs in this region are typically weakening at landfall due to the effects of the cooler surface waters at these latitudes. Consequently, the assumption made later in this paper (section 3) that TCs exhibit little change in intensity just prior to landfall

is clearly not valid for this region. For these reasons, a separate study of the decay of TCs in this area is planned for the future.

Because relatively few hurricanes made landfall along the Florida coastline during the period 1967–93, it was desirable to include a few hurricanes that made landfall in this area prior to 1967. This is particularly important for evaluating the claim of previous authors (Malkin 1959; Schwerdt et al. 1979; Ho et al. 1987) that TCs making landfall along the Florida coastline fill less rapidly than TCs in other regions in the United States (e.g., Gulf Coast). As discussed above, the HURDAT file is less accurate prior to 1967. Therefore, surface data archived at the National Climatic Data Center (NCDC) in Asheville, North Carolina, were employed to aid in determining TC position and intensities for Hurricanes Donna (1960) and Cleo (1964). Wind data were also obtained for the unnamed 1949 Florida hurricane from a study by the U.S. Weather Bureau (1951). These storms were chosen because of the availability of surface observing stations along the path of these hurricanes. Details of the procedures used to obtain MSSW estimates for these Florida hurricanes are contained in the appendix.

The MSSW estimates that were obtained for the three Florida hurricanes by the procedures described in the appendix were, on average, approximately 20 kt lower than those in the HURDAT file. Since previous studies (i.e., Powell et al. 1991) indicate that wind speeds just a few kilometers inland are only about 80% as large as the winds on the coast, the higher wind speed values in the HURDAT file could, in part, be the result of estimating inland wind speeds by interpolating between the higher wind speeds observed on the east and west coasts of Florida. Whatever the reason for these differences, it is believed that the intensity estimates for the landfalling Florida hurricanes used in this study, while not perfect, are comparable in accuracy to those found in the HURDAT file commencing in 1967.

The tracks of the three landfalling Florida hurricanes as well as the other 64 landfalling TCs used to derive the decay model are depicted in Fig. 1. The sample includes 401 MSSW estimates (at 6-h intervals) from these 67 TCs. Nearly all of these TCs dissipated, became extratropical, or moved back over water within 48 h. The average postlandfall duration of each TC was 17 h, and the average decrease in the MSSW was 28 kt. In this paper, knots are used instead of meters per second because the MSSW values in the HURDAT file are specified in 5-kt increments. More important, this decision was made because the decay model is being developed for operational use by the NHC and the Federal Emergency Management Agency, both of whom provide wind forecasts and warnings in units of knots.

3. Model development

Previous observational (Miller 1964) and numerical modeling studies (Ooyama 1969; Rosenthal 1971; Tuleya et al. 1984) have shown that the primary mechanism responsible for the rapid decay of TCs after landfall is the greatly reduced latent and sensible heat fluxes over land. More recently, Tuleya (1994) demonstrated that the reductions in these fluxes were due to the decreased land temperature beneath the storm center. This reduction in surface land temperature was a result of the finite heat capacity and conductivity of the soil subsurface. The above modeling studies, as well as observational studies performed by Schwerdt et al. (1979) and Ho et al. (1987), have also shown that the rate of decay of TCs is largest just after landfall and that the decay rate is proportional to the landfall intensity.

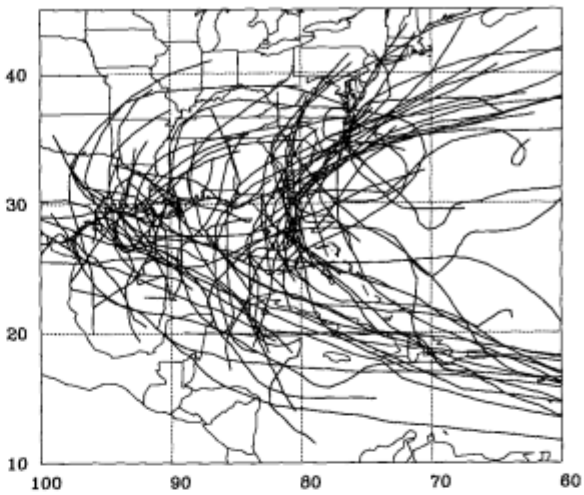

FIG. 1. Tracks of the 67 landfalling TCs used to develop the decay model.

The availability of the relatively large database obtained for the current study makes it possible to evaluate these findings by examining the decrease in the MSSW of all landfalling TCs in this data sample. In this study, the landfall intensity was assumed to be the MSSW at the time the TC crossed the coastline. Since the HURDAT file does not contain either the time or the intensity of the TC at landfall, it was necessary to estimate this information from the available data. The time of TC landfall was obtained by linearly interpolating the HURDAT positions to the landfall point. The intensity at landfall was assumed to be the MSSW at the time closest to but proceeding landfall. Thus, since the HURDAT file has 6-h resolution, this MSSW could be representative of the storm intensity up to 6 h prior to TC landfall. While these procedures could introduce some uncertainty, Merrill (1987) found that the median 12-h intensity change for Atlantic TCs within about 200 km of the coastline was nearly zero. Therefore, while the MSSW values at landfall may be inaccurate for some TCs, they should be reasonable for the majority of the cases employed in this study.

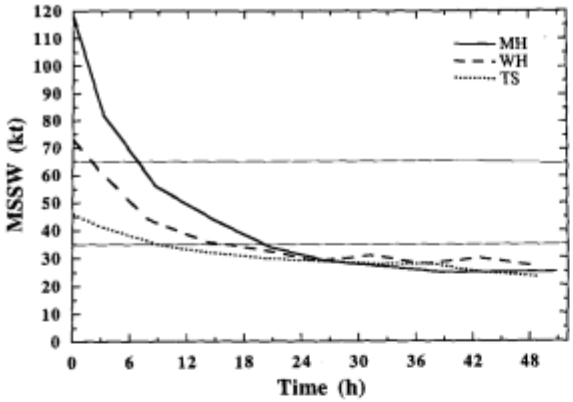

FIG. 2. The mean change in MSSW as a function of the elapsed time after landfall for the mean tropical storm (TS), weak hurricane (WH), and major hurricane (MH). The solid horizontal lines depict the threshold of hurricane- (65 kt) and tropical-storm- (35 kt) force MSSWs.

To illustrate the effect of initial intensity on decay rate, all TCs were placed into one of three stratifications—tropical storm ($35 \leqslant \text{MSSW} \leqslant 63$), weak hurricane ($64 \leqslant \text{MSSW} \leqslant 96$), and major hurricane ($\text{MSSW} \geqslant 97$)—based on their MSSW (kt) at landfall. Figure 2 shows the average intensity of each of these stratifications as a function of the elapsed time after landfall. This figure indicates that although the rate of decay of the MSSW of major hurricanes exceeds the decay rate for both weak hurricanes and tropical storms, the shapes of the decay curves are quite similar. Figure 2 also suggests that TCs decay to approximately the same MSSW after about 24–30 h regardless of their intensity at landfall. It is interesting to note that even the average major hurricane falls below hurricane intensity in about 7 h and below tropical storm strength in about 20 h.

a. Derivation of the decay model

The assumption that TCs decay at a rate that is proportional to their landfall intensity is the basis of our empirical inland wind decay model (IWDM) and can be expressed by the following differential equation:

$$\frac{dV}{dt} = -\alpha V, \tag{1}$$

where V (kt) is the MSSW, α is the decay constant (h^{-1}), and t (h) is the time after landfall. The solution to (1) is given by

$$V(t) = V_0 e^{-\alpha t}, \tag{2}$$

where V_0 is the MSSW at $t = 0$.

As shown in Fig. 2, the MSSW decays to some background wind speed V_b. This effect can be included by adding an extra term to (1) to give

$$\frac{dV}{dt} = -\alpha(V - V_b), \tag{3}$$

which has a solution given by

$$V(t) = V_b + (V_0 - V_b)e^{-\alpha t}. \tag{4}$$

The observational results of Myers (1954), Schwerdt et al. (1979), Powell (1982, 1987), and Powell et al. (1991) indicate that hurricane winds decrease abruptly as the landfalling storm crosses the coastline. Powell et al. (1991) noted that this rapid decrease in wind speed occurs within a few kilometers of the coastline as onshore winds quickly adjust to the increased roughness of the underlying land surface. Consequently, V_0 in (4) is multiplied by a reduction factor R to account for this rapid decrease to give

$$V(t) = V_b + (RV_0 - V_b)e^{-\alpha t}. \tag{5}$$

The parameters V_b and α in (5) were determined by minimizing the error between the predicted and observed values of V using the method of least squares for a range of R values. Table 1 indicates that the variance explained r^2 by the IWDM generally exceeds 90%. The relatively high r^2 values in the table demonstrate that the model does a good job of reproducing the decay rate of the landfalling cases. A slightly better fit was obtained with $R = 1.0$ or 0.9 than with 0.8 or 0.7. The slight increase in the mean absolute error (AE) and the root-mean-square error (rmse) with $R = 0.8$ or 0.7 resulted from underestimation of the MSSW for data points within 12 h of landfall. Table 1 also shows that the magnitude of α decreases as R decreases, but the magnitude of V_b is nearly the same for all R values. The relatively constant V_b value is consistent with Fig. 2, which shows that after landfall TCs decay to the same MSSW regardless of their initial intensity.

b. Correction for proximity to the coastline

The results of Malkin (1959) suggest that TCs whose circulations are partially over water decay less rapidly than those that are entirely over land. This result seems reasonable since a TC that remained partially over water would presumably experience larger fluxes of heat and moisture than a TC entirely over land. To determine if such a mechanism could be observed in the

TABLE 1. The variance explained r^2, mean absolute error AE, root-mean-square error rmse, and α and V_b coefficients obtained for a series of R values used in the IWDM.

R	r^2 (%)	AE (kt)	rmse (kt)	α (h^{-1})	V_b (kt)
1.0	91	6.4	8.8	0.115	27.0
0.9	91	6.5	8.8	0.095	26.7
0.8	91	7.0	9.2	0.080	26.9
0.7	89	8.0	10.4	0.069	28.0

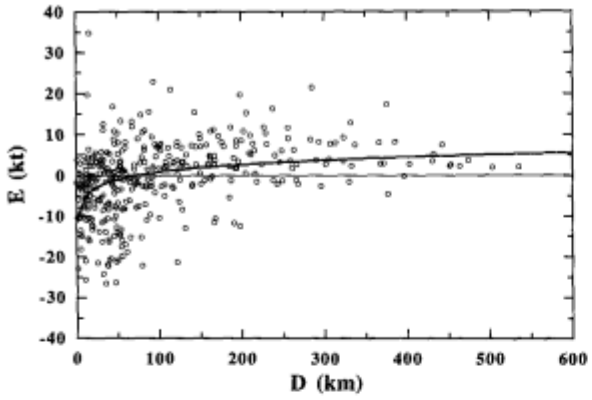

FIG. 3. The relationships between the IWDM error E and the mean distance inland D of a TC during the forecast period. The best-fit line for these points is also shown.

current dataset, the average distance inland D was calculated for each observation. Figure 3 is a scatter diagram where the y axis is the error E between the MSSW predicted using (5) (assuming $R = 0.9$) and the observed MSSW, and the x axis is D. Also shown in Fig. 3 is the best-fit line for these points. A logarithmic relationship was employed rather than a linear relationship because of the superior fit obtained when using such a technique.

Although the data points exhibit considerable scatter, Fig. 3 suggests that on average the IWDM tends to underpredict ($E < 0$) the MSSW of landfalling TCs closest to the coastline while overpredicting ($E > 0$) the MSSW of TCs farther inland. However, Fig. 3 also indicates that the average model bias is fairly small ($E \leqslant \sim 5$ kt), except very near the coastline where a more significant negative bias is evident. This negative bias suggests that storms nearer to the coastline decay less rapidly than those farther inland as suggested by Malkin (1959). Shea and Gray (1973) and Samsury and Zipser (1995) found that the mean radius of maximum wind of hurricanes is approximately 35 km. Moreover, Jorgensen (1984) and Black et al. (1995, unpublished manuscript) determined that the mean width of the eyewall of hurricanes is about 20–25 km. The results of Jorgensen (1984) also indicate that on average slightly more than 50% of the eyewall convection lies beyond the radius of maximum wind. These results indicate that, on average, the eyewall convection surrounding the mean TC extends 50 km from the TC center. Figure 3 indicates that on average the IWDM predicts too much decay for TCs with $D \leqslant 70$ km. This result is consistent with the above inner-core studies and suggests that when $D \leqslant 70$ the eyewall of many TCs remains partially over water, resulting in less decay than is observed for TCs for which D exceeds 70 km.

To include the effect of the distance inland, a correction term C was added to (5) to give

$$V(t) = V_b + (RV_0 - V_b)e^{-\alpha t} - C, \qquad (6)$$

where C is expressed by

$$C = m\left[\ln\left(\frac{D}{D_0}\right)\right] + b \qquad (7)$$

and D is restricted using $D \geqslant 1$. In (7), D is specified in units of kilometers, $D_0 = 1$ km, and the slope m and intercept b are constants determined by a least squares fit. Inspection of the size of the AE with time indicates that smaller model errors result when the values of m and b in (7) are allowed to vary with time. Figure 4 shows the values of m and b obtained for forecasts grouped in 6-h forecast periods assuming $R = 0.9$. Best-fit curves for m and b as quadratic functions of time are also shown in Fig. 4. These best-fit curves are used to determine m and b in (7) to obtain forecasts of $V(t)$, which are continuous in time. The best-fit curves for m and b for the $R = 0.9$ case are given by

$$m = c_1 t(t_0 - t) \qquad (8)$$

and

$$b = d_1 t(t_0 - t), \qquad (9)$$

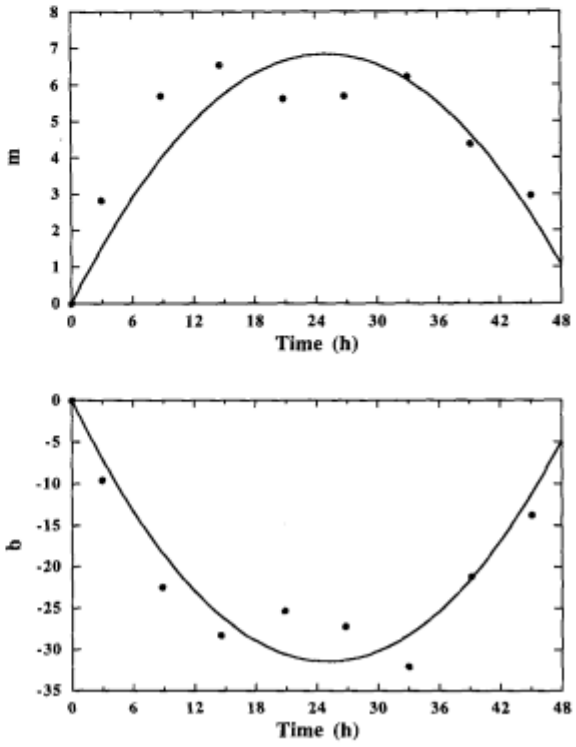

FIG. 4. The variation of the slope m (top) and intercept b (bottom) of the correction term employed in the IWDM as a function of forecast time. The quadratic best-fit lines for these points are also shown.

TABLE 2. As in Table 1 except for the version of the IWDM that includes a correction term that accounts for the mean distance inland D of a TC during the forecast period. The results from Table 1 are shown in parentheses to facilitate comparison between the two versions of the IWDM.

R	r^2 (%)	AE (kt)	rmse (kt)	α (h^{-1})	V_b (kt)
1.0	92 (91)	6.4 (6.4)	8.4 (8.8)	0.115 (0.115)	27.0 (27.0)
0.9	93 (91)	6.2 (6.5)	8.0 (8.8)	0.095 (0.095)	26.7 (26.7)
0.8	93 (91)	6.3 (7.0)	8.1 (9.2)	0.080 (0.080)	26.9 (26.9)
0.7	91 (89)	6.8 (8.0)	8.8 (10.4)	0.069 (0.069)	28.0 (28.0)

where $c_1 = 0.0109$ kt h^{-2}, $d_1 = -0.0503$ kt h^{-2}, and $t_0 = 50$ h.

Table 2 shows the error statistics for the IWDM using the values of C obtained from (7). This table indicates that the use of the correction term results in an increase in r^2 of about 1%–3% depending upon which R value was employed in the model. The table also shows that the size of the AE and the rmse are reduced by approximately 0%–15% and 5%–15%, respectively, when the correction term is included. While these improvements are not particularly large, they do suggest that correcting for the distance inland of a TC during the forecast period adds some skill to the the basic version of the IWDM model. No changes are observed in the values of α and V_b since the correction term simply fits the residual error of the basic decay model.

The results in Table 2 indicate that the use of an R of 0.9 yields the smallest errors (AE and rmse) for the case when the correction term is included in the IWDM model. More importantly, most of the improvement was for cases within the first 12 h after landfall (not shown). This is significant since Fig. 2 indicates that most TC decay occurs within this first 12 h. Although Table 2 shows that the use of $R = 0.8$ yielded nearly as good a prediction, it was decided that a conservative approach should be taken, and consequently the larger R value of 0.9 was employed in the model.

Equation (10) shows the final version of the IWDM used in the remainder of this paper:

$$V(t) = V_b + (RV_0 - V_b)e^{-\alpha t} - C, \qquad (10)$$

where $R = 0.9$, $V_b = 26.7$ kt, and $\alpha = 0.095$ h^{-1}. If included, the correction factor C is given by (7) with m and b determined from (8) and (9).

Figure 5 shows a scatter diagram of the observed versus model-predicted changes in MSSW. This figure indicates that there is generally good agreement between the predicted and observed changes although the model does not perform quite as well during the first 12 h after landfall as it does for for predictions made for $t \geq 12$ h. The increased difficulty in the first 12 h is likely due to the uncertainty both in the time of TC landfall and in the landfall intensity.

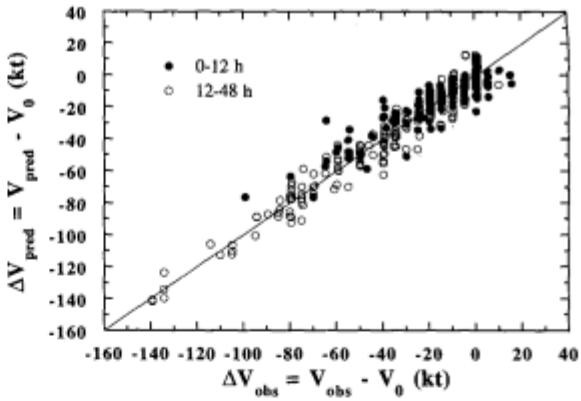

FIG. 5. The observed ($\Delta V_{obs} = V_{obs} - V_0$) versus the model-predicted ($\Delta V_{pred} = V_{pred} - V_0$) change in MSSW for the 401 landfall cases used to develop the IWDM. The solid circles denote forecasts made within the first 12 h after landfall, while the open circles indicate forecasts for the period from 12 to 48 h after landfall.

c. *Regional variations in decay rates*

As discussed in section 1, several previous studies (e.g., Schwerdt et al. 1979; Ho et al. 1987) have suggested that there are regional differences in the decay rates of landfalling TCs. To investigate whether such differences could be detected in the current dataset, the U.S. coastline was divided into three geographical regions (Gulf Coast, East Coast, and Florida) as shown in Fig. 6. These regions were chosen for consistency with previous studies. Four versions of the model will be compared. The first version is the same as the one described previously, using all 401 landfalling TC cases [i.e., Eq. (10)]. This version will be referred to as the USIWDM in the remainder of this section. The other

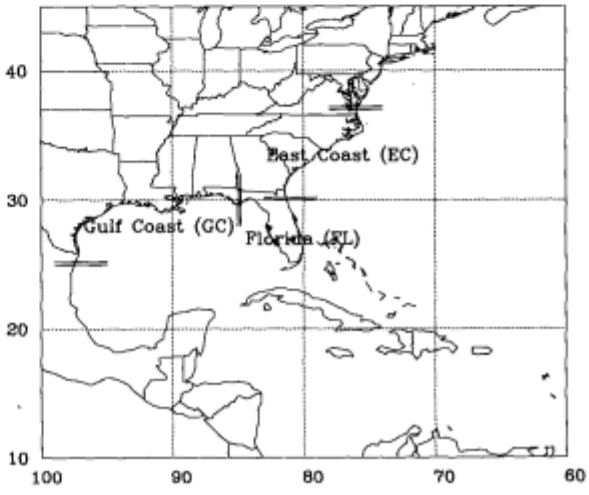

FIG. 6. The three different geographic regions (Gulf Coast, East Coast, and Florida) for which the IWDM was derived.

three versions of the model were obtained by rederiving the model (new values of α, V_b, and the correction term coefficients were computed) separately for each region employing only those TCs that made landfall in that particular region. These new versions of the model are referred to as the GCIWDM, ECIWDM, and FLIWDM for the Gulf Coast, East Coast, and Florida region, respectively. An R value of 0.9 was employed in all versions of the model since this value yielded the smallest model errors for all regions.

The results for the three regional versions of the model are shown in Table 3. The errors obtained without the correction term (not shown) were similar to, although somewhat larger than, those in Table 3. The results in Table 3 indicate that the AE and rmse obtained using the GCIWDM and ECIWDM models are only a few percent smaller than those obtained using the USIWDM. Moreover, there is no significant improvement in r^2 in these two regional models, relative to the USIWDM. This lack of improvement is true even though the α values differ by 9%–27% for the Gulf Coast and East Coast regions, respectively. Unlike the results obtained for the other two regions, Table 3 indicates that the use of the regional Florida model (FLIWDM) did not result in improvement over the USIWDM. This lack of improvement is due to the difficulties encountered when evaluating the correction term used in the FLIWDM. For reasons described in succeeding paragraphs, the relatively small number of cases combined with the low average MSSW of the Florida landfalling sample made accurate evaluation of the correction term more difficult for Florida than it was for the other two regions.

The differences in the error statistics of the regional versions of the IWDM relative to the USIWDM are smaller than might be expected given the magnitude of the differences in α and V_b. This result is due to the more significant improvement in model performance that occurs when the correction term is included in the USIWDM, relative to the regional models. The smaller number of landfall cases in the regional samples increased the noise in the estimates of m and b for each 6-h forecast interval. This noise made it more difficult to fit the quadratic time variation, as shown in Fig. 4 for the total sample.

Although Table 3 suggests that α varies from region to region, it is unclear whether these variations are due to actual differences in the meteorological conditions or are the result of other nonmeteorological factors. One possible nonmeteorological factor is the effect of data errors on the estimation of α. To see this effect, consider (10) without the small correction term C. If $RV_0 - V_b$ is small relative to V_b (weak storms at landfall), α can be varied significantly without much change in $V(t)$. This result indicates that when α is estimated using observations, small errors in $V(t)$ will lead to large errors in α. Conversely, if $RV_0 - V_b$ is large relative to V_b (strong storms at landfall), α cannot be varied very much without significantly affecting $V(t)$. Therefore, when estimating α from observations, small errors in $V(t)$ will not lead to large errors in α, relative to the case when $RV_0 - V_b$ is small. To illustrate this principle, first assume that (10) is exactly valid for the case with $C = 0$. Then, consider a storm with a landfall intensity of 41 kt (the average for the Florida sample in Table 3). After 6 h, the intensity will be reduced to 32.5 kt. Now, suppose there was a 5-kt error in the intensity estimate at 6 h ($V = 37.5$ or 27.5 kt), and these values were used to estimate α. If these values of V are substituted into (10) and it is assumed that V_b is fixed (since V_b in Table 3 did not vary very much from region to region), (10) can be solved for α yielding α values of -0.010 and $0.424\ \text{h}^{-1}$ when $V = 37.5$ and $V = 27.5$ kt, respectively. If the initial intensity of a storm at landfall was 72 kt (the average for the Gulf Coast sample), then the intensity at 6 h from (10) would be 48.2 kt. A 5-kt error at 6 h would imply $V = 53.2$ or 43.2 kt, which gives α values of 0.061 or $0.140\ \text{h}^{-1}$. Thus, for a 5-kt error in V at 6 h, α would range from -0.010 to $0.424\ \text{h}^{-1}$ when $V_0 = 41$ kt, compared with a range of only 0.061–$0.140\ \text{h}^{-1}$ when $V_0 = 72$ kt.

The above discussion indicates that the uncertainty in the estimate of α is greater for the case when the landfall intensity of the storm is lower. The smaller values of α in Table 3 for the Florida cases might then be due to this effect since the average landfall intensity

TABLE 3. IWDM statistics for the three separate geographic regions (i.e., Gulf Coast, East Coast, and Florida). Statistics are also presented for the USIWDM applied to the regional model samples. The results shown are for the version of the IWDM that corrects for the mean distance inland D of a TC during the forecast period and that employs a reduction factor R of 0.9. The number of cases N, the mean landfall MSSW $\overline{V_0}$, the average forecast duration $\bar{T}$, and the mean change in MSSW during the forecast period $\overline{\Delta V}$ are also shown for each region.

Region	Model version	r^2 (%)	AE (kt)	rmse (kt)	α (h^{-1})	V_b (kt)	N	$\overline{V_0}$ (kt)	$\bar{T}$ (h)	$\overline{\Delta V}$ (kt)
Gulf Coast	GCIWDM	94	5.6	7.7	0.104	25.5	246	72	19.1	37.5
	USIWDM	94	5.8	7.8	0.095	26.7				
East Coast	ECIWDM	78	6.2	7.7	0.069	28.5	68	58	15.7	19.5
	USIWDM	76	6.6	8.1	0.095	26.7				
Florida	FLIWDM	39	7.4	9.1	0.038	30.0	87	41	13.8	5.8
	USIWDM	46	7.1	8.6	0.095	26.7				

was less than in other regions. Of course, α was not determined from a single observation but was estimated by a least squares fit to multiple observations. However, if the intensity estimates were biased, the same analysis would apply. A small positive bias in the estimates of the storm intensity after landfall, or negative bias in the intensity estimate at landfall, could account for the low value of α in Table 3 for the Florida sample. Also, since the effect of this bias is less for stronger storms, the estimate of α might be expected to increase as the average intensity increases. This increase can be seen in Table 3 where $\alpha = 0.038$, 0.069, and 0.104 for the Florida, East Coast, and Gulf Coast samples, which have average landfall intensities of 41, 58, and 72 kt, respectively.

The above results suggest that the regional differences in the decay model can be accounted for by differences in the landfall intensities combined with a small intensity bias and so are not considered reliable. Therefore, the USIWDM [Eq. (10)] developed with the total sample should be used in all three regions. The lack of strong regional differences in the storm decay rate is consistent with the modeling study of Tuleya (1994), which shows that TC decay after landfall results from the significant reduction in sensible and latent heat fluxes due to the reduced land temperature beneath the storm. This reduction in land temperature is due to the low heat capacity and conductivity of the soil subsurface. Although the heat capacity and conductivity have regional variations, these variations are small relative to ocean–land differences.

The rejection of the regional differences in the decay rate in Table 3 contradicts results from previous studies. Schwerdt et al. (1979) and Ho et al. (1987) indicated that the decay rate (as measured by minimum sea level pressure deficit) is largest for Gulf storms, slightly smaller for East Coast storms, and much smaller for Florida storms. However, similar to the results in Table 3, the Gulf Coast sample in these two studies contained the most intense storms. Thus, small biases in the intensity estimates may have contributed to regional differences in their decay rates. In addition, the Florida sample in these two studies included only four hurricanes, where the data for three of these storms were obtained from Malkin (1959). The main weakness of the Malkin study was the uncertainty in the pressure at landfall. The absence of aircraft reconnaissance data made it necessary for Malkin to rely primarily on pressure observations collected at the synoptic map times when computing the filling rate for each of these hurricanes. These synoptic maps were available every 3 h for the latter two hurricanes but only every 12 h for the earliest one. Moreover, since these hurricanes did not make landfall at precisely the synoptic map times, Malkin was forced to estimate the landfall pressures of these hurricanes by various means, including interpolating backward in time using the decay rate observed at the first available synoptic time. Since previous studies have shown that the rate of decay of TCs decreases with increasing time after landfall, the decay rate that was applied backward in time was probably too small. The use of such a technique would likely yield a landfall pressure that was too high, resulting in underestimation of the decay rate computed for these hurricanes.

Further support for the hypothesis that the decay rates for Florida cited by Schwerdt et al. (1979) and Ho et al. (1987) are too low can be found in the recent landfall of Hurricane Andrew (1992). Mayfield et al. (1994), using aircraft reconnaissance observations as well as numerous surface observations, determined that Andrew made landfall just south of Miami, with a central pressure of approximately 922 mb and exited the west coast of Florida with a pressure of 951 mb. By the procedures outlined in section 2, Andrew required about 3.2 h to traverse the Florida peninsula. Following the methodology of Ho et al. (1987), it is possible to compute the filling rate FR using

$$\mathrm{FR} = \frac{\Delta P_t}{\Delta P_0}, \tag{11}$$

where ΔP_0 is the pressure deficit at the time of landfall and ΔP_t is the pressure deficit at some time t after landfall. The pressure deficit after landfall ΔP_t is defined by:

$$\Delta P_t = P_n - P_t, \tag{12}$$

where P_n is the mean pressure around a TC and P_t is the central pressure of the TC at some specified time t after landfall. Both of these quantities are specified in units of millibars.

Ho et al. (1987) used a climatological value of 1013 mb for P_n. Substituting $P_n = 1013$ mb and $P_0 = 922$ mb (Andrew's landfall pressure) into (12) yields $\Delta P_0 = 91$ mb. Following the same procedures yields $\Delta P_{3.2} = 62$ mb. From (11), the observed FR for Andrew at $t = 3.2$ h is then 0.68. This observed FR can be compared with the results of Schwerdt et al. (1979) and Ho et al. (1987). Linear interpolation of the temporal changes in ΔP_t for the Florida region listed in Table 20b of Ho et al. (1987) yields $\Delta P_t \sim 82$ mb at $t = 3.2$ h, which corresponds to a P_t of ~931 mb. Substituting $\Delta P_t = 82$ mb into (11) yields an FR of 0.90. Thus, the filling rates computed for Andrew based on the results of Ho et al. (1987) are too small to explain the observed rate of decay of Andrew. However, if the changes in ΔP_t computed by Ho et al. (1987) for the Gulf of Mexico region are employed instead of those obtained for Florida, the agreement is much better. Linear interpolation of the temporal changes in ΔP_t obtained for the Gulf of Mexico region by Ho et al. (1987, Table 20a) yields $\Delta P_t \sim 70$ mb ($P_t \sim 943$ mb) at $t = 3.2$ h. Substituting this value into (11) yields an FR of 0.77, which is in much better agreement with the observed FR of 0.68 than the 0.90 value obtained

using the Florida decay curves of Ho et al. (1987). This example supports the hypothesis that filling rates of hurricanes making landfall along the Florida coastline are probably not significantly different than those in other regions.

4. Applications

The IWDM can be used in a number of applications. The most obvious use is for operational forecasting of the maximum winds associated with landfalling hurricanes. Given a forecast track, the time of landfall and the distance inland as a function of time can be estimated. The storm intensity at landfall is also required for the forecast. DeMaria and Kaplan (1994) have shown that the average 12-h intensity forecast error for storms over the water is about 7 kt, so a reasonable estimate of the landfall intensity could be obtained for storms that are not too far from land. Given this information, (10) could be used to estimate the storm intensity along the inland part of the forecast track.

As an example of the above application, consider the landfall of Hurricane Andrew (1992) in Louisiana. According to the NHC best track, this storm made landfall approximately 150 km west of New Orleans between 0600 and 1200 UTC 26 August 1992 with an intensity of 115 kt and dissipated just after 0600 on 28 August near the Tennessee–North Carolina border. Figure 7 shows the NHC best track intensities at 6-h intervals and the intensity prediction from the IWDM with and without the correction for distance inland [C in Eq. (10)]. The forecast intensities were calculated every half hour, and the intensity was assumed to be constant (115 kt) from 0600 UTC 26 August ($t = 0$) to the landfall point ($t = 2.5$ h). The rapid decrease in intensity at landfall is due to the application of the reduction factor [R in Eq. (10)]. In this example, the best track storm positions (rather than a forecast track) were used to determine the landfall time (by linear interpolation between the 6-h positions) and the distance to the coast after landfall. This figure shows that the model does a reasonable job of predicting the intensity of Andrew after landfall. The maximum error is about 10 kt at 18 h. When the distance inland correction is included, the model predicts slightly lower intensities than without the correction after 18 h. The average of the intensity errors at the eight best track positions after landfall is about the same with and without the distance inland correction (average error about 7 kt).

Although the IWDM was developed from a sample of the maximum winds of landfalling tropical cyclones, it can also be applied to a wind field to provide a crude estimate of the swath of inland winds. For this application, it is necessary to estimate the two-dimensional surface wind field of a storm just prior to landfall. The IWDM can then be applied to every point of this wind field to provide

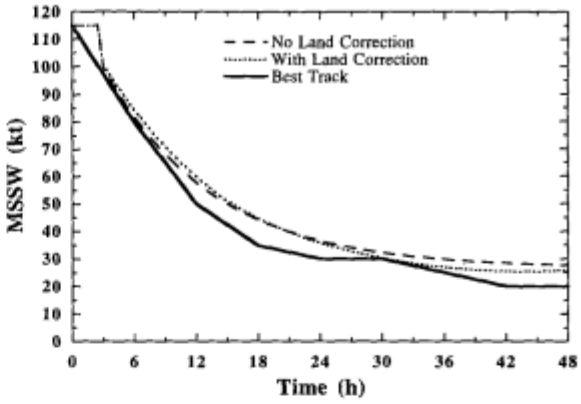

FIG. 7. The observed (6-h interval) and predicted (0.5-h interval) MSSW (kt) for the Louisiana landfall of Hurricane Andrew (1992). The prediction was made with and without the correction for distance inland.

a wind swath. Detailed real-time analyses of hurricane wind fields are being produced as an experimental product (Burpee et al. 1994) but are not yet operational. In the interim, a parametric model similar to that used in storm surge modeling (Hubbert et al. 1991) can be used to obtain a representative surface wind field prior to landfall. The parametric approach assumes that the wind field is the sum of an azimuthally symmetric vortex and a constant vector that represents the storm motion. With this assumption, the wind speed just prior to landfall can be determined by

$$V_0(r,\theta) = c_s[\cos(\theta)] + V_x\left(\frac{r}{r_x}\right)\exp\left\{\frac{1}{a}\left[1-\left(\frac{r}{r_x}\right)^a\right]\right\}. \quad (13)$$

In (13), r is the radial distance from the storm center, and θ is the angle measured counterclockwise from a line perpendicular and to the right of the direction of motion. The wind field in (13) requires the specification of the parameters c_s, V_x, r_x, and a. The parameter c_s is the amplitude of the right to left asymmetry due to the storm motion. The value of this parameter could be determined from an empirical relationship, as a function of the storm translational speed, as described in the appendix. However, as a first approximation, it will be assumed that c_s is equal to the storm translational speed. The parameter V_x is the symmetric part of the MSSW. Because the operational estimate of the MSSW (M_x) of a storm is for the total wind field, V_x is determined by

$$V_x = M_x - c_s. \quad (14)$$

The parameter r_x is the radius of maximum wind. This parameter could be estimated from aircraft data, if available, or from the estimate of the storm-eye diameter that

is routinely available on the tropical cyclone forecast/advisory issued by NHC. From an analysis of aircraft observations for several recent landfalling storms, it was found that a crude estimate of r_x can be obtained by taking 0.75 times the eye-diameter estimate. It should also be mentioned, however, that the eye-diameter estimate is not always reliable, especially for weaker storms. The final parameter to be specified is a, which determines the storm size. This parameter can be estimated from aircraft data, if available, or by a least squares fit of (13) to the radii of 65- and 50-kt winds reported on the tropical cyclone forecast/advisory.

Once the wind speed field just prior to landfall is determined, the IWDM model can be applied to every point of this field to estimate the wind field of the storm as it moves inland, where the time in (10) is the time since the storm center made landfall. Because the distance inland calculation is only valid for the storm center, this correction term is neglected when estimating the inland wind field. To provide a wind swath, the maximum wind at any time during the storm can be calculated.

As an example of the above application, consider the landfall of Hurricane Andrew (1992) in south Florida. This case was chosen because a detailed analysis of the maximum wind at any time during the storm has been prepared by Powell and Houston (1995, unpublished manuscript). Their study used all available aircraft and surface observations to produce wind analyses before and after Andrew made landfall in south Florida. According to the NHC best track, the MSSW of Andrew just prior to landfall in south Florida was 125 kt, and the speed of motion was 17 kt. Thus, c_s = 17 kt and V_x = 108 kt. The r_x was set to 17 km, as determined from the wind analysis prior to landfall shown in Powell and Houston (1995, unpublished manuscript). The radius of 50-kt winds in their analysis was used to estimate a, which was set to 0.45 for this case.

Figure 8 shows the observed wind swath and that predicted by the IWDM, where the observed positions were used in the model, rather than a forecast track. The model did a reasonable job of predicting the basic features of the observed wind field, such as the area covered by 35-kt winds and the extent of the inland penetration of the 95-kt wind contour. However, the details of the wind field such as the area covered by 95-kt winds near the landfall point were not well represented. This limitation is probably due to the fact that the simple parametric model cannot capture all of the details of the wind field at landfall, and the IWDM does not well represent the complex interactions that occur as a storm moves over the ocean–land boundary. Fujita (1978) and Wakimoto and Black (1994) provide examples of the complexities of the wind fields associated with landfalling Hurricanes Celia (1970) and Andrew (1992).

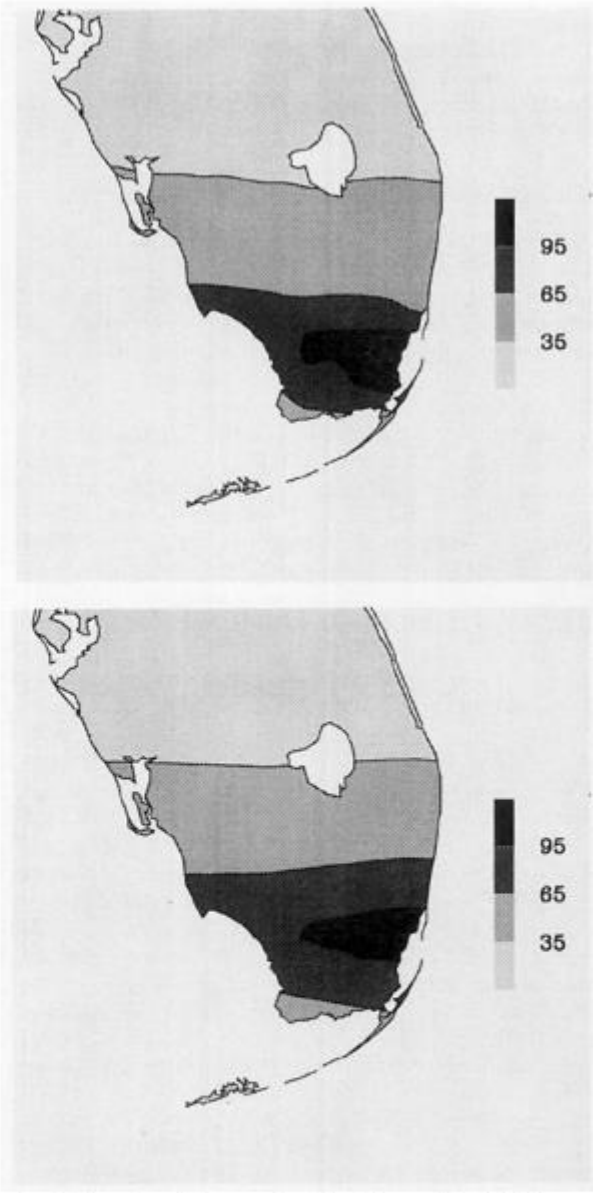

FIG. 8. The observed (top) and predicted (bottom) MSSW (kt) at any time during the south Florida landfall of Hurricane Andrew (1992).

In the above applications, the observed track was used to determine the landfall point and the storm positions over land. In an operational setting, it would be necessary to use a forecast track to run the IWDM. In this case, the uncertainties in the forecast track would probably lead to larger errors than those caused by errors in the IWDM. For example, during the 1993 Atlantic hurricane season, the average error of the official NHC 12-h track forecast was 85 km (Lawrence and Gross 1994). This distance is comparable to the width

of the area of hurricane force winds (65 kt) in Fig. 8. If the track used in the IWDM were shifted 85 km to the north or south, there would be almost no overlap between the predicted and observed swaths of hurricane-force winds. One possible solution to this problem is to determine the wind swath for an ensemble of track forecasts. A similar approach is used in storm surge modeling where the maximum envelope of waters (MEOWs) are determined by calculating the maximum level of high water for a set of possible storm tracks in a particular region (Jarvinen and Lawrence 1985).

If the small correction for distance inland is neglected in (10), the inland wind speed depends only on the storm intensity at landfall and the time since landfall. For an inland point, the highest winds will occur from a storm that moves inland perpendicular to the coastline and moves so that the radius of maximum wind passes directly over that point. For a storm moving at a constant speed, the time inland can be determined directly from the shortest distance from that point to the coast. Under these assumptions, maps of the maximum inland penetration of winds can be prepared, given the storm speed of motion and the intensity at landfall.

Figures 9–11 show the maximum possible sustained wind speeds for the Atlantic and Gulf Coasts for hurricanes with a range of landfall intensities and speeds of motion. The speeds of motion (8, 12, and 16 kt) represent slow-, medium-, and fast-moving hurricanes, as determined from the data sample used to develop the IWDM. The slow (fast) speed is the 10th (90th) percentile of the distribution of the hurricane speeds at landfall. The medium speed is the average of the sample. The range of intensities at landfall (75, 105, and 135 kt) represent category 1, 3, and 5 hurricanes. These figures show that all of Florida and a substantial fraction of the other coastal states from Texas to North Carolina are vulnerable to hurricane-force winds, although the probability of occurrence at any given location is, of course, quite low. These figures also show that for inland locations, the effect of the storm speed of motion is just as important as the storm intensity at landfall. For example, hurricane-force winds penetrate farther inland for a fast-moving category 3 storm (Fig. 10) than for a slow-moving category 5 storm (Fig. 11).

The data sample used to develop the IWDM is not long enough to accurately determine the distribution of storm speeds and intensities at landfall. However, by using a longer time period and more sophisticated statistical techniques such as those described by Darling (1991), the speed and intensity distributions could be determined. These distributions could then be combined with the IWDM to estimate the probability of hurricane force and other wind thresholds at inland locations.

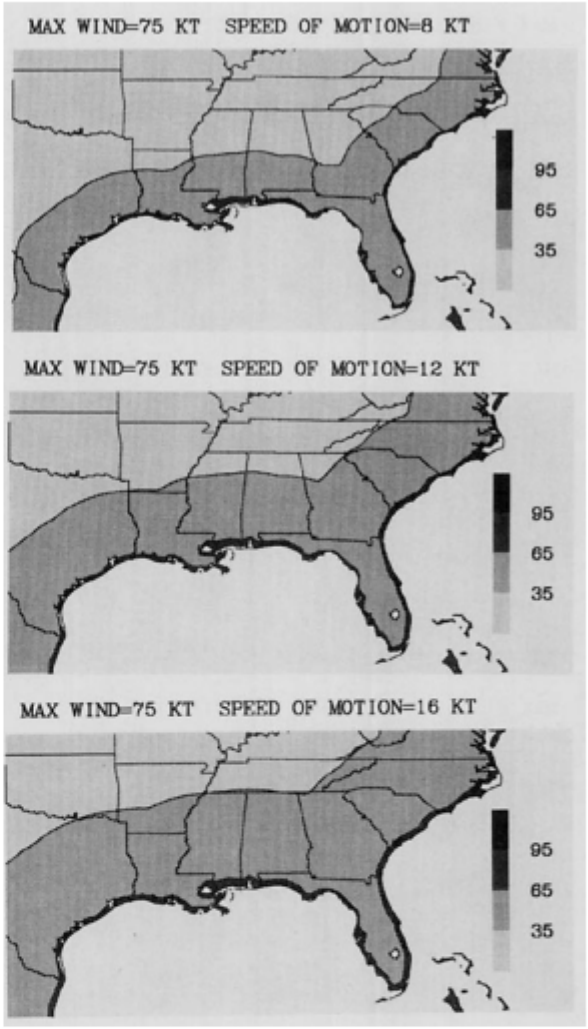

FIG. 9. The maximum possible sustained inland wind speed (kt) for any slow- (top), medium- (middle), or fast- (bottom) moving category 1 (75 kt at landfall) storm.

5. Summary and conclusions

An empirical model for predicting the decay of TC winds after landfall [referred to as the Inland Wind Decay Model (IWDM)] has been described. The IWDM is a simple two-parameter model that was derived based upon the assumption that TC winds decay exponentially with time after landfall. The database used to derive the model consisted of all named TCs that made landfall in the United States south of 37°N between 1967 and 1993. Three hurricanes that made landfall along the Florida coastline prior to 1967 were also included in the sample. Position and intensity estimates for these landfalling storms were obtained from the NHC HURDAT file, except for the intensity estimates for the Florida hurricanes that were derived

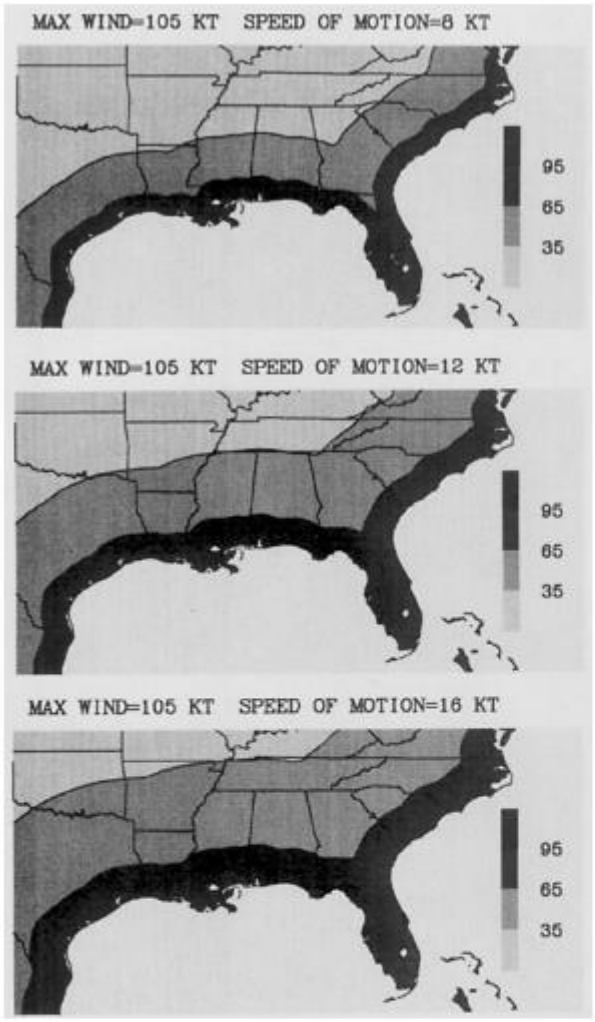

based upon data obtained from the NCDC and the U.S. Army Corps of Engineers.

This study shows that the basic version of the IWDM explains 91% of the variance of the decay of the MSSW for the 401 cases in the developmental database. When an additional term is included in the model to account for the mean distance inland of a TC during the forecast period, the variance explained increased to 93%. This term was added because several studies have shown that TCs that move parallel to the coastline decay less rapidly than TCs that move directly inland. The results of this study also suggest that there do not appear to be significant regional variations in the decay rates of landfalling TCs, in contrast to results from previous studies. It is possible that some minor regional differences in decay rates exist, but cannot be detected because of the limited accuracy of the wind speed estimates used to develop the IWDM. Further investigation of the regional differences in the decay rates of TCs is warranted.

Several applications of the IWDM were described. The IWDM can predict the maximum sustained surface winds as a function of time after landfall, as well as provide a swath of wind speeds produced by landfalling TCs. To provide the wind swath, the IWDM is applied to the tropical cyclone wind field at landfall. Perhaps most importantly, the IWDM can produce maps of the maximum possible sustained surface wind speeds that inland locations would experience for TCs of various landfall intensities and speeds of forward motion. These maps demonstrate that the speed of forward motion of a landfalling TC is just as important as the landfall intensity when assessing how far inland strong winds will penetrate.

Further research is required to refine the IWDM. Observational studies of the decay of TC winds over

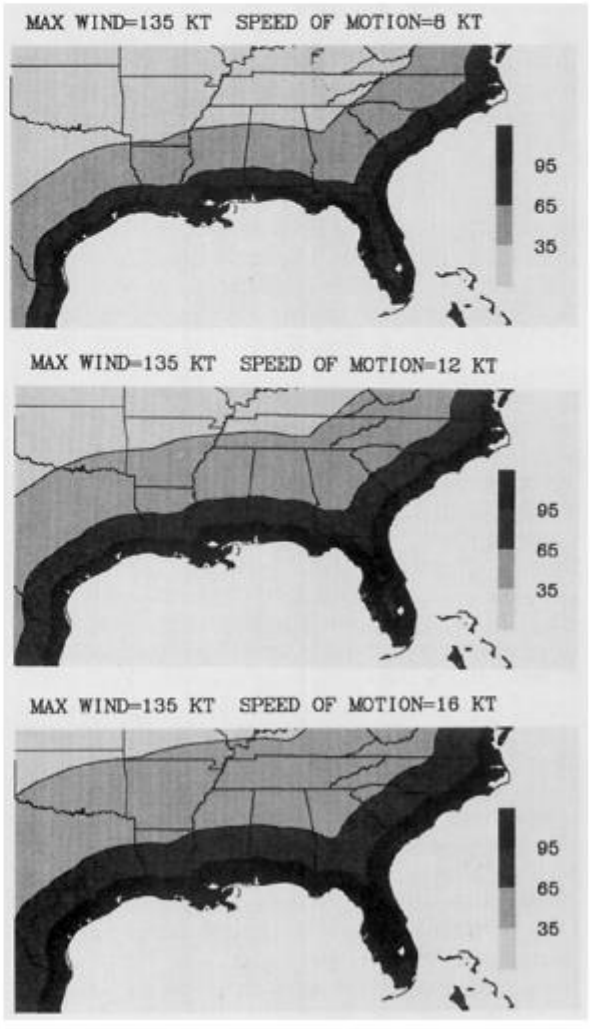

FIG. 11. Same as Fig. 9 for a category 5 (135 kt at landfall) storm.

land would be particularly useful for verifying the model, especially for the case where the entire wind field is predicted. Moreover, the IWDM could be improved by employing a boundary layer model to predict the wind direction as well as wind speed. Finally, a model similar to the IWDM described in this study could be developed for the New England region. These high-latitude storms were eliminated from the present study because topography and interaction with baroclinic weather systems might have significant effects on storm decay in this area.

Acknowledgments. We wish to thank Drs. R. B. Burpee and M. D. Powell, and S. H. Houston of HRD for their constructive reviews of an earlier version of this paper. The authors benefited from the helpful suggestions of Dr. M. D. Powell during the course of this research. Tom Ross of NCDC supplied the data for Hurricanes Donna (1960) and Cleo (1964), and Mark Powell and Sam Houston provided the wind fields that were used to develop the parametric wind model described in section 4. Dr. Robert Merrill of the Cooperative Institute for Meteorological Studies in Madison, Wisconsin, provided much of the computer code used to determine a storm's distance from the coastline, and Mike Black of HRD assisted with the preparation of several of the figures. This research was partially funded by the Federal Emergency Management Agency (FEMA).

APPENDIX

Estimating the MSSWs of Pre-1967 Landfalling Florida Hurricanes

Surface data archived at the National Climatic Data Center (NCDC) were used to obtain position and intensity estimates for Hurricanes Donna (1960) and Cleo (1964). The wind data employed to obtain intensity estimates for the unnamed 1949 Florida hurricane were obtained from a report by the U.S. Weather Bureau (1951). The NCDC data for Hurricanes Cleo and Donna consisted of hard copies of daily observation logs that contained wind direction, sustained wind speed, wind gusts, surface pressures, and other information typically found in surface aviation weather observations. Although the time resolution of the observations varied, the resolution of the wind observations was normally several minutes when a TC was closest to the particular observing site. The daily observation logs contained other important information, such as the magnitude and time of the maximum sustained wind and/or wind gust, the minimum surface pressure, and the timing of any observed eye passage. The wind data obtained from the U.S. Weather Bureau consisted of a series of sustained 10-min winds and surface pressures recorded within a few hours of the time of eye passage of the unnamed 1949 hurricane over Lake Okeechobee. These observations were obtained from a special observing array on Lake Okeechobee that was set up by the U.S. Army Corps of Engineers.

The tracks for the three additional Florida storms were obtained from the HURDAT file. Although the storm positions before 1967 are thought to be somewhat less accurate than those in succeeding years as described previously, the HURDAT tracks for these three storms are in good agreement with those presented in the detailed studies and meteorological accounts given in the U.S. Weather Bureau (1951), Miller (1964), and Dunn (1965). The storm positions are also consistent with the timing of the maximum wind observed for each of these storms. An observation was judged to be close enough to the storm center for the purpose of determining the MSSW if the observing site was at a distance comparable to the radius of maximum wind The radius of maximum wind values for these storms was obtained from Ho et al. (1987). Based on this criterion, a combined total of six observations for the three storms was close enough to the storm center to be used to estimate the MSSW at a specific time after landfall.

Because the above wind observations were representative of various anemometer heights and averaging times, it was necessary to standardize these observations to obtain winds consistent with those in the HURDAT file (i.e., the MSSW). The research of Powell et al. (1991, 1995, unpublished manuscript) has shown the importance of employing such standardization techniques when analyzing landfalling hurricanes. The first step in this process was to adjust the winds to the 10-m level using a neutral stability log wind law (Panofsky and Dutton 1984). The anemometer heights of the observing sites were obtained from the *National Wind Data Index* (Changery 1978). Unfortunately, the index does not provide a direct means of estimating the site roughness length required for use in the log wind law calculations. However, because nearly all of the sites were located at airports, a roughness length corresponding to open airport exposure (Panofsky and Dutton 1984) was assumed when adjusting winds to 10 m. Since the observations represented winds averaged over various time periods, gust factor relationships developed by Powell et al. (1995, unpublished manuscript) were used to convert these winds to 1-min average values. They developed these relationships based on the work of Durst (1960), Krayer and Marshal (1992), and from National Oceanic and Atmospheric Administration moored buoy data collected by the National Data Buoy Center and analyzed by the Hurricane Research Division of the Atlantic Oceanographic and Meteorological Laboratory since 1979. An asymmetry factor developed by Schwerdt et al. (1979) was then added to these wind speeds to obtain estimates of the storm's MSSW. This was done since the wind observations were rarely located in the right front quadrant of the TC where the strongest winds are typically observed (Shea and Gray 1973; Frank 1977). The

asymmetry factor was formulated such that a fraction of the storm speed of forward motion is added to winds on the right side of the TC and subtracted from winds on the left side. The relationship itself is somewhat conservative since the asymmetry factor is always less than the storm speed of motion. The average change in wind speed resulting from the above standardization procedures was about 20%.

REFERENCES

Batts, M. E., M. R. Cordes, L. R. Russell, J. R. Shaver, and E. Simiu, 1980: Hurricane wind speeds in the United States. National Bureau of Standards Building Science Series 124, U.S. Department of Commerce, 50 pp.

Bender, M. A., R. J. Ross, R. E. Tuleya, and Y. Kurihara, 1993: Improvements in tropical cyclone track and intensity forecasts using the GFDL initialization system. *Mon. Wea. Rev.*, **121,** 2046–2061.

Burpee, R. W., and Coauthors, 1994: Real-time guidance provided by NOAA's Hurricane Research Division to forecasters during Emily of 1993. *Bull. Amer. Meteor. Soc.*, **75,** 1765–1783.

Changery, M. J., 1978: *National Wind Data Index Final Report.* U.S. Department of Commerce, 245 pp.

Darling, R. W. R., 1991: Estimating probabilities of hurricane wind speeds using a large-scale empirical model. *J. Climate*, **4,** 1035–1046.

DeMaria, M., and J. Kaplan, 1994: A statistical hurricane intensity prediction scheme (SHIPS) for the Atlantic basin. *Wea. Forecasting*, **9,** 209–220.

Dunn, G. E., and Staff, 1965: The hurricane season of 1964. *Mon. Wea. Rev.*, **93,** 175–187.

Durst, C. S., 1960: Wind speeds over short periods of time. *Meteor. Mag.*, **89,** 181–186.

Frank, W. M., 1977: The structure and energetics of the tropical cyclone. Part I: Storm structure. *Mon. Wea. Rev.*, **105,** 1119–1135.

Fujita, T. T., 1978: Manual of downburst identification for Project NIMROD. SMRP Res. Paper 156, University of Chicago, 104 pp.

Georgiou, P. N., 1985: Design wind speeds in tropical cyclone-prone regions. Ph.D. dissertation, University of Western Ontario, 295 pp.

Ho, F. P., J. C. Su, K. L. Hanevich, R. J. Smith, and F. P. Richards, 1987: Hurricane climatology for the Atlantic and Gulf Coasts of the United States. NOAA Tech. Rep. NWS 38, 195 pp. [Available from NWS/NOAA, U.S. Dept. of Commerce, 8060 13th St., Silver Spring, MD 20910.]

Hubbert, G. D., G. J. Holland, L. M. Leslie, and M. J. Manton, 1991: A real-time system for forecasting tropical cyclone storm surges. *Wea. Forecasting*, **6,** 86–97.

Hubert, L. F., 1955: Frictional filling of hurricanes. *Bull. Amer. Meteor. Soc.*, **36,** 440–445.

Jarvinen, B. R., and M. B. Lawrence, 1985: An evaluation of the SLOSH storm surge model. *Bull. Amer. Meteor. Soc.*, **66,** 1408–1411.

——, C. J. Neumann, and M. A. S. Davis, 1988: A tropical cyclone data tape for the North Atlantic Basin, 1886–1983: Contents, limitations, and uses. NOAA Tech. Memo. NWS NHC 22, Miami, FL, 21 pp.

Jorgensen, D. P., 1984: Mesoscale and convective-scale characteristics of mature hurricanes. Part I: General observations by research aircraft. *J. Atmos. Sci.*, **41,** 1268–1285.

Krayer, W. R., and R. D. Marshal, 1992: Gust factors applied to hurricane winds. *Bull. Amer. Meteor. Soc.*, **73,** 613–617.

Lawrence, M. B., 1994: 1993 National Hurricane Center forecast verification. *Minutes of the 48th Interdepartmental Conf.*, Miami, FL, Office of Fed. Coord. for Meteor. Services and Supporting Research, NOAA, B-15–B-24.

——, and J. M. Gross, 1993: 1992 National Hurricane Center forecast verification. *Minutes of the 47th Interdepartmental Conf.*, Miami, FL, Office of Fed. Coord. for Meteor. Services and Supporting Research, NOAA, B-13–B-21.

Malkin, W., 1959: Filling and intensity changes in hurricanes over land. National Hurricane Research Project Rep. 34, U.S. Weather Bureau, Washington, DC, 18 pp.

Mayfield, M., M. L. Avila, and E. N. Rappaport, 1994: Atlantic hurricane season of 1992. *Mon. Wea. Rev.*, **122,** 517–538.

Merrill, R. T., 1987: An experiment in statistical prediction of tropical cyclone intensity change. NOAA Tech. Memo. NWS NHC-34, 34 pp.

Miller, B. I., 1964: A study on the filling of Hurricane Donna (1960) over land. *Mon. Wea. Rev.*, **92,** 389–406.

Myers, V. A., 1954: Characteristics of United States hurricanes pertinent to levee design for Lake Okeechobee, FL. Hydrometeorological Rep. 32, U.S. Department of Commerce, Washington, DC, 106 pp.

National Research Council, 1994: *Hurricane Hugo: Puerto Rico, The U.S. Virgin Islands, and South Carolina September 17–22, 1989.* National Academy Press, 276 pp.

Neumann, C. J., 1994: An update to the National Hurricane Center "Track Book." *Minutes of the 48th Interdepartmental Conf.*, Miami, FL, Office of Fed. Coord. for Meteor. Services and Supporting Research, NOAA, A-47–A-53.

Ooyama, K., 1969: Numerical simulation of the life cycle of tropical cyclones. *J. Atmos. Sci.*, **26,** 3–40.

Panofsky, H. A., and J. A. Dutton, 1984: *Atmospheric Turbulence.* Wiley-Interscience. 397 pp.

Powell, M. D., 1982: The transition of the Hurricane Frederic boundary layer wind fields from the open Gulf of Mexico to landfall. *Mon. Wea. Rev.*, **110,** 1912–1932.

——, 1987: Changes in the low-level kinematic and thermodynamic structure of Hurricane Alicia (1983) at landfall. *Mon. Wea. Rev.*, **115,** 75–99.

——, P. P. Dodge, and M. L. Black, 1991: The landfall of Hurricane Hugo in the Carolinas: Surface wind distribution. *Wea. Forecasting*, **6,** 379–399.

Rosenthal, S. L., 1971: The response of a tropical cyclone model to variations in boundary layer parameters, initial conditions, lateral boundary conditions, and domain size. *Mon. Wea. Rev.*, **99,** 767–777.

Samsury, C. E., and E. J. Zipser, 1995: Secondary wind maxima in hurricanes: Airflow and relationship to rainbands. *Mon. Wea. Rev.*, in press.

Schwerdt, R. W., F. P. Ho, and R. R. Watkins, 1979: Meteorological criteria for standard project hurricane and probable maximum hurricane windfields, Gulf and East Coasts of the United States, NOAA Tech. Rep. NWS 23, 317 pp. [Available from NWS NOAA, U.S. Department of Commerce, 8060 13th St. Silver Spring, MD 20910.]

Shapiro, L. J., 1983: The asymmetric boundary layer flow under a translating hurricane. *J. Atmos. Sci.*, **40,** 1984–1998.

Shea, D. J., and W. M. Gray, 1973: The hurricane's inner core region. Part I: Symmetric and asymmetric structure. *J. Atmos. Sci.*, **30,** 1544–1563.

Tuleya, R. E., 1994: Tropical storm development and decay: Sensitivity to surface boundary conditions. *Mon. Wea. Rev.*, **122,** 291–304.

——, M. A. Bender, and Y. Kurihara, 1984: A simulation study of the landfall of tropical cyclones using a movable nested-mesh model. *Mon. Wea. Rev.*, **112,** 124–136.

U.S. Department of Commerce, 1993: *Hurricane Andrew: South Florida and Louisiana August 23–26, 1992.* U.S. Department of Commerce, 131 pp.

U.S. Weather Bureau, 1951: Analysis of winds over Lake Okeechobee during tropical storm of August 26–27, 1949. Hydrometeorological Rep. 26., U.S. Department of Commerce, Washington, DC, 80 pp.

Wakimoto, R. M., and P. G. Black, 1994: Damage survey of Hurricane Andrew and its relationship to the eyewall. *Bull. Amer. Meteor. Soc.*, **75,** 189–200.

40. Assignment 2, Module 7: Hurricane and Land Interaction: http://www.hurricanescience.org/science/science/hurricaneandland/

Interaction between a Hurricane and the Land

As a **hurricane** approaches land, portions of the outer circulation start to include air originating over land. This land-based air is cooler and drier than the air in the hurricane that originated over water. This portion of the circulation over land is initially efficient in transporting the cooler, drier air towards the center of the hurricane because of the increased **friction** over land relative to over the ocean (see Primary Circulation). In the right-front quadrant of the hurricane, the variation in inflow can help create areas of strong air **convergence** in the lower **troposphere**. These convergence zones provide a favorable environment for outer rainbands that are capable of severe weather, including tornadoes, well before the storm center crosses the coast.

In the hours prior to **landfall**, hurricanes typically pass over cooler ocean shelf water, which can limit hurricane intensity relative to warmer ocean water further off the coast (see Hurricane Development: From Birth to Maturity). This temperature difference between ocean shelf water and ocean water further off the coast may be even larger below the sea surface than at the sea surface, which may further limit hurricane intensity near the coast but prior to landfall (see Interaction Between a Hurricane and the Ocean).

Atmospheric fronts and regions of strong **vertical wind shear** are often present near the coast. When a coastal front interacts with a hurricane prior to landfall, cooler, drier air may be transported into one side of the hurricane, leading to weakening. Enhanced vertical wind shear also typically weakens a hurricane.

When one or more of the processes described above leads to weakening of a hurricane in the hours before landfall, the hurricane's wind field is often observed to expand in size. This wind field expansion can be explained by a physical law called conservation of angular momentum. Sometimes, outer portions of the hurricane may experience increased wind speeds even though the maximum wind speed is decreasing, as in the case of Hurricane Katrina (2005). While the intensity reduction may be welcomed from the standpoint of anticipated wind damage at landfall, the wind field expansion may be equally or more dangerous because of increased risks from storm surge and waves. Wind field expansion increases the **fetch**, defined as the distance the wind travels over the sea surface, which allows increased wave development that can contribute to both **storm surge** and wave damage.

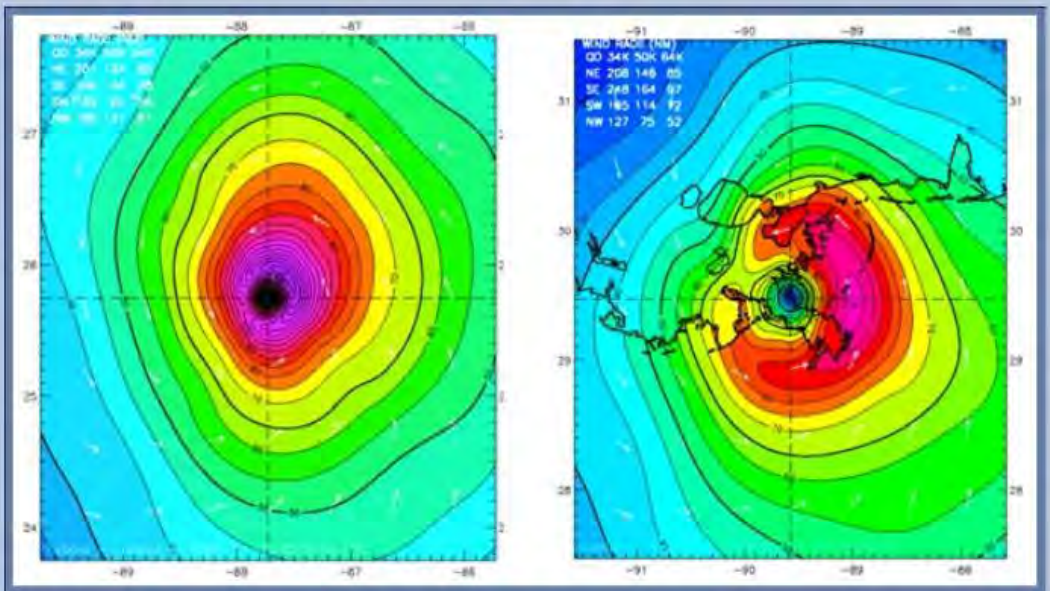

Comparison of Hurricane Katrina's wind field. On left, 24 hours before landfall with a peak sustained wind speed of 257 km/h (160 mph) and radius of maximum wind of 26 km (16 miles). On right, Katrina at landfall with a peak sustained wind speed of 189 km/h (117 mph) and radius of maximum wind of 65 km (40 miles). The integrated energy was maintained at about ~115 TJ (terajoule). Wind fields were analyzed from observations using H*Wind (Powell et al., 2010).

There are notable exceptions to the often-observed weakening of hurricanes in the hours prior to landfall, particularly in mid season and at lower **latitudes** when a hurricane can intensify while passing over a warm ocean feature that may be relatively close to land without the negative influence of strong vertical wind shear (e.g. Hurricanes Carla 1961, Celia 1971, Andrew 1992, and Katrina 2005). Such hurricanes may also undergo eyewall replacement cycles that can magnify their impacts if landfall occurs during the intensification part of the cycle.

During landfall, as the eyewall begins to cross the coast, differences between the air friction caused by the ocean and the land cause the wind field to become less symmetric around the hurricane's center, and lead to areas of enhanced air convergence and divergence in certain regions of the hurricane. The regions can affect the distribution of convection and rainfall, but primarily they contribute to a large variation in wind speed and **gustiness** over a small area (land causes the wind to be more gusty). As air in the hurricane crosses the coast from ocean to land, the air flow responds to the new underlying surface with about 80% of the adjustment occurring a few hundred meters inland but the remaining 20% taking tens of kilometers to occur. The gustiness over the ocean is on the order of 10% but may increase to 20-30% or more over land (where there is increased friction), depending on the roughness of the land surface. Therefore, steady winds over land may be lower than over the ocean due to higher roughness, but the winds over land may have higher gusts.. Flow over complex terrain is much more complicated, with localized wind maxima occurring on exposed hillsides where air flow may accelerate over bluff shaped hilltops to more than double the wind speed of the surrounding air.

By the time the hurricane's center crosses the coast, the inflowing wind speed has increased to over half the primary circulation's wind speed, so drier (and often cooler) air is fueling over half the eyewall, resulting in rapid weakening. The expansion of the wind field continues, but now much of the outer part of the hurricane's circulation is experiencing enhanced roughness over land, so the size of the **tropical storm** and hurricane strength wind fields begin to decrease and eventually dissipate.

41. Assignment 2, Module 8: Movement of Hurricanes: http://www.aoml.noaa.gov/h

What Determines the Movement of Tropical Cyclones?

Tropical cyclones – to a first approximation – can be thought of as being steered by the surrounding environmental flow throughout the depth of the troposphere (from the surface to about 12 km or 8 mi). Dr. Neil Frank, former director of the U.S. National Hurricane Center, used the analogy that the movement of hurricanes is like a leaf being steered by the currents in the stream, except that for with a hurricane the stream has no set boundaries.

Subtropical ridge and its relationship with Cape Verde hurricane tracks

In the tropical latitudes (typically equatorward of 20°-25°N or S), tropical cyclones usually move toward the west with a slight poleward component. This is because there exists an axis of high pressure called the subtropical ridge that extends east-west poleward of the storm. On the equatorward side of the subtropical ridge, general easterly winds prevail. However, if the subtropical ridge is weak – often times due to a trough in the jet stream – the tropical cyclone may turn poleward and then recurve back toward the east. On the poleward side of the subtropical ridge, westerly winds prevail thus steering the tropical cyclone back to the east. These westerly winds are the same ones that typically bring extratropical cyclones with their cold and warm fronts from west to east.

rd/tcfaq/G5.html

Divergent hurricane track due to trough

Many times it is difficult to tell whether a trough will allow the tropical cyclone to recurve back out to sea (for those folks on the eastern edges of continents) or whether the tropical cyclone will continue straight ahead and make landfall.

For more non-technical information on the movement of tropical cyclones, see Pielke and Pielke's "Hurricanes: Their Nature and Impacts on Society". For a more detailed, technical summary on the controls on tropical cyclone motion, see Elsberry's chapter in "Global Perspectives on Tropical Cyclones".

42. Assignment 2, Module 8: Hurricane Forecasts (Chapter 4): https://pielkeclimatesci.files.wordpress.com/2012/10/b-11.pdf

CHAPTER 4

Hurricane Forecasts

4.1 TROPICAL CYCLONE MOVEMENT

Tropical cyclones move because the storm is embedded in a larger-scale region of moving air, referred to as the steering current, which tends to move the low-level low pressure center, upper-level high pressure and associated cluster of thunderstorms in the direction of that flow (e.g. see Riehl and Burgner 1950; Riehl and Shafer 1946; Simpson 1946). Tropical cyclones of different intensity are steered by winds at different levels in the troposphere (Figure 4.1).[1] The cyclone itself, of course, is part of the large-scale flow, and its motion is also influenced by its own internal circulation. This sets up a complex process of interaction that is a challenge to predict. Yet accurate prediction of a hurricane's movement is central to short-term decisions to protect life and property.

4.2 EXTERNAL FLOW: THE STEERING CURRENT

If the steering flow were fixed in time, hurricane track forecasting would be comparatively simple. Unfortunately, this is not the case, as the orientation and strength of the steering current changes in response to the position of large-scale pressure features. Contrary to popular conception, however, in the Atlantic most tropical cyclones have fairly regular, well-defined tracks because the location and orientation of the Bermuda and Azores high pressure systems, which determine the track of most Atlantic tropical cyclones, usually change only slowly during the hurricane season. However, the difficulty in predicting a storm track occurs either when the typical climatological steering

[1] G.J. Holland of the Bureau of Meteorology in Melbourne, Australia suggests using the winds averaged within a concentric band of 125–250 miles (200–400 km) from the storm center. In another study, tropical cyclones were found to move about 2–4 miles per hour (1–2 meters per second) faster and 10 to 20 degrees to the left of the mean wind flow between about 5000 feet (~1.5 km) and 30 000 feet (~9 km) averaged over an area within a 5 to 7 degree of latitude radius centered on the storm (McElroy 1996).

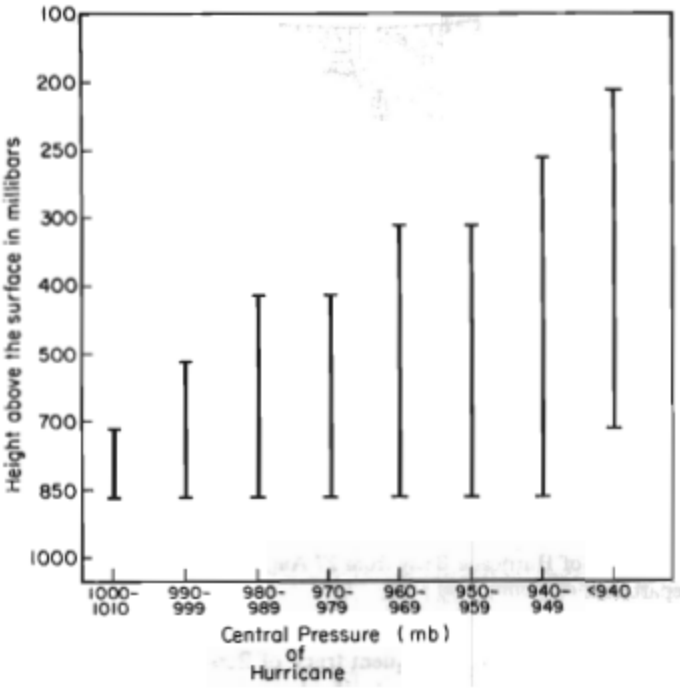

Figure 4.1 The layer of the atmosphere which steers storms of various intensities. Note that weaker storms are steered by a shallow layer of winds lower in the atmosphere and stronger storms are steered by a deeper layer of the atmosphere (adapted from Holland 1993b)

wind flow is replaced by a less common, large-scale flow or, even more importantly, when rapid changes in time occur in the strength and orientation of the steering current.

For example, on 4 September 1965, Hurricane Betsy was moving northwest around the southern rim of the large Bermuda High in the central Atlantic. The track of the storm is shown in Figure 4.2. As the storm was moving northward off the east coast of the United States in a climatologically expected direction and speed, a re-adjustment occurred in the steering current because of a low pressure system associated with a cold front over the central United States. This change resulted in the movement of the Bermuda High towards the west until it was centered north of the storm system. As a result, Hurricane Betsy was blocked from continuing its expected northward movement and became stationary. The Bermuda High center continued to build westward so that, after about a day, the steering currents became northerly and the storm began to move south towards the northern Bahamas. With the re-establishment of the

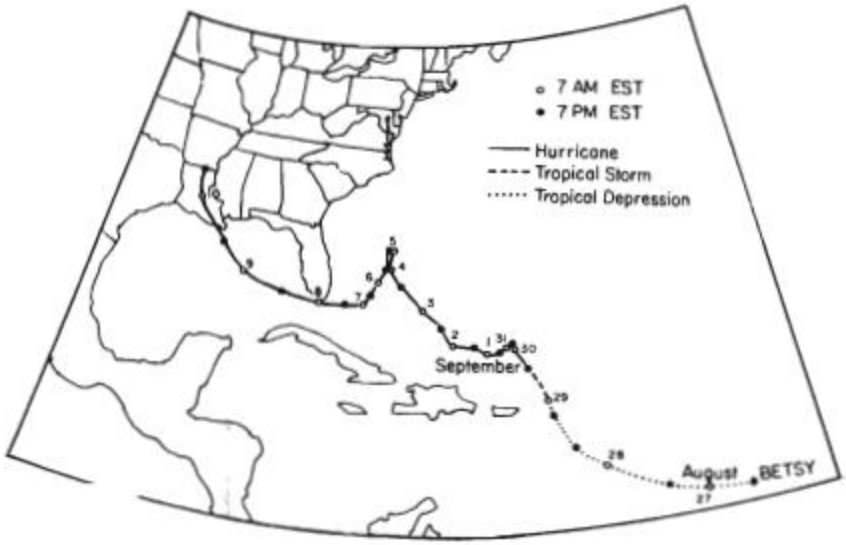

Figure 4.2 Track of Hurricane Betsy from 27 August to 10 September, 1965. Source: DOC (Department of Commerce) 1965

High center to the west, the subsequent track of Betsy traveled around the new position of the Bermuda High, eventually slamming into New Orleans when it finally began once more moving northward around the western flank of the Bermuda High. A major forecast problem associated with this storm was when it would begin its turn towards the west around the southern periphery of the High. An earlier turn would have brought Betsy onshore near Miami, with possible major devastation to that urbanized area. A later turn would have permitted the storm to pass through the Florida Straits. As it happened, the storm crossed over the Florida Keys.

The steering current associated with Hurricane Andrew is shown in Figure 4.3. Displayed in these figures are the wind speeds and directions averaged across the troposphere from a height of about 1 mile (850 mb) to about 7.5 miles (200 mb). The position of Andrew's center at each of the times is superimposed on the figures. The movement of Andrew by this steering current is evident in Figure 4.3 as it traveled westward across South Florida and then northwest into Louisiana.

Figure 4.3 (a-h) Steering current (defined as the average wind speed and direction between 850 millibars and 200 millibars) for Hurricane Andrew at 12-hour intervals starting at 7 am Eastern Standard Time on 22 August 1992. In the figure, the length of the arrows represents the speed of the steering current where a unit arrow of 5.6 miles per hour (~2.5 meters per second) is displayed. The position of Andrew's center is shown by the hurricane symbol. (Figure prepared by Joe Eastman, Colorado State University).

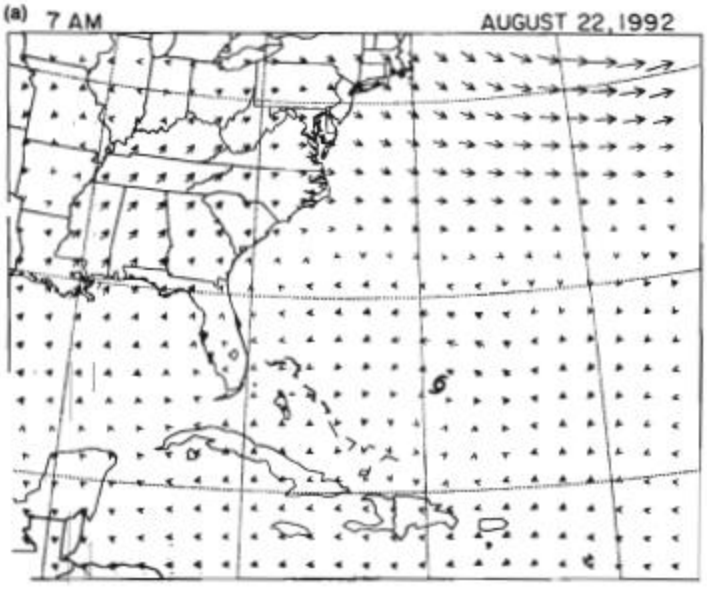
(a) 7 AM
AUGUST 22, 1992

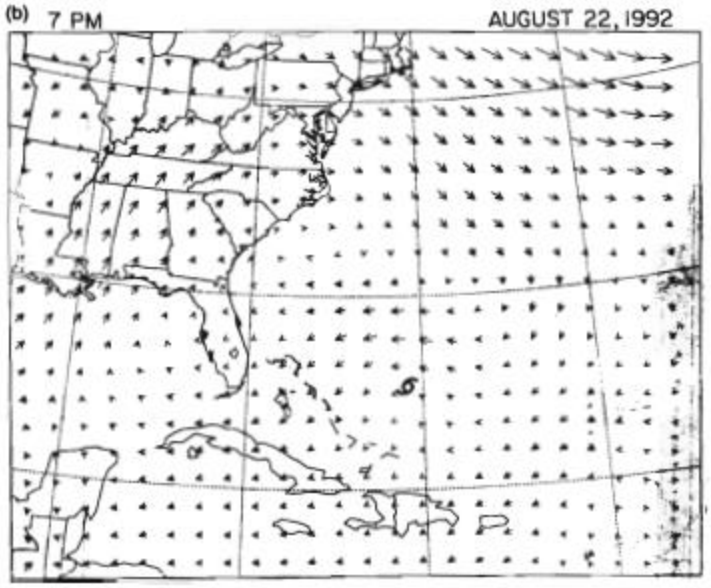
(b) 7 PM
AUGUST 22, 1992

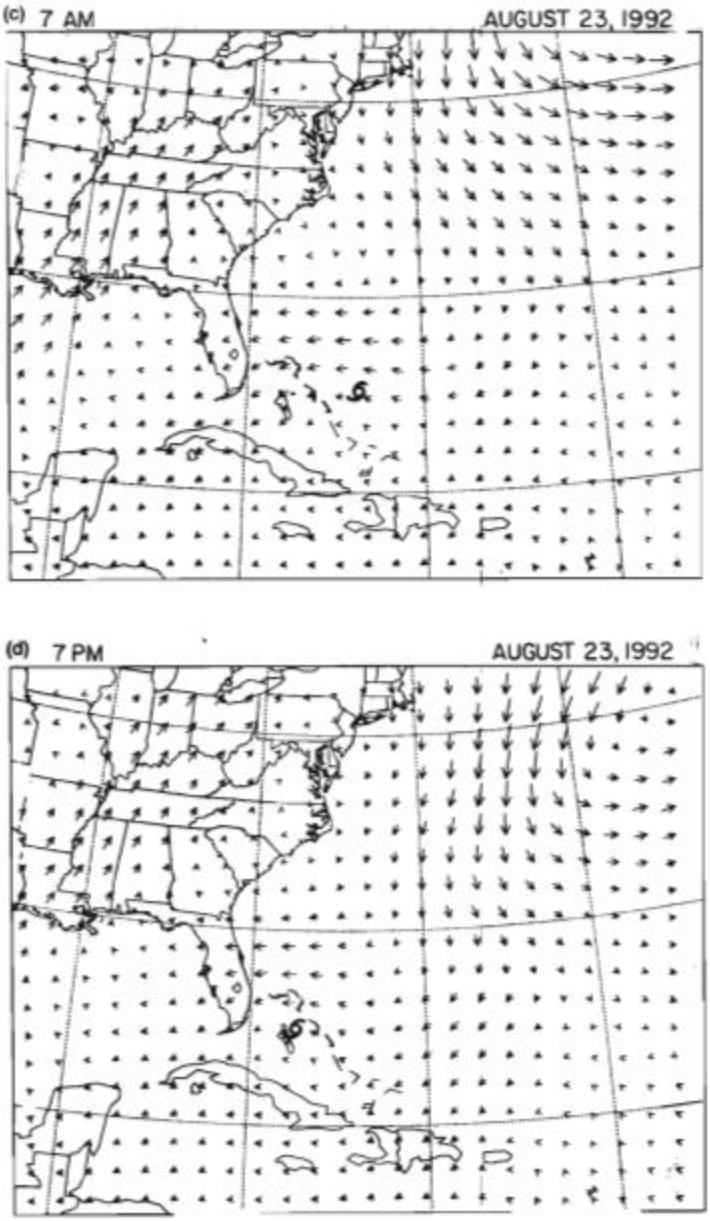

Figure 4.3 (*continued*)

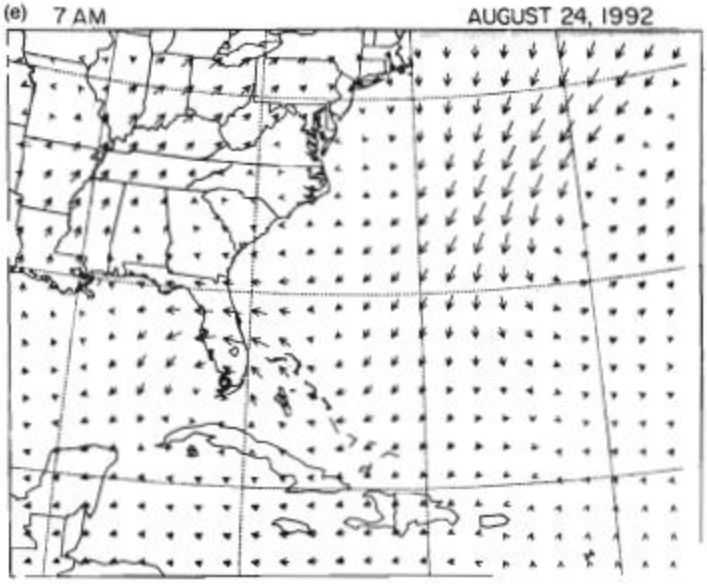

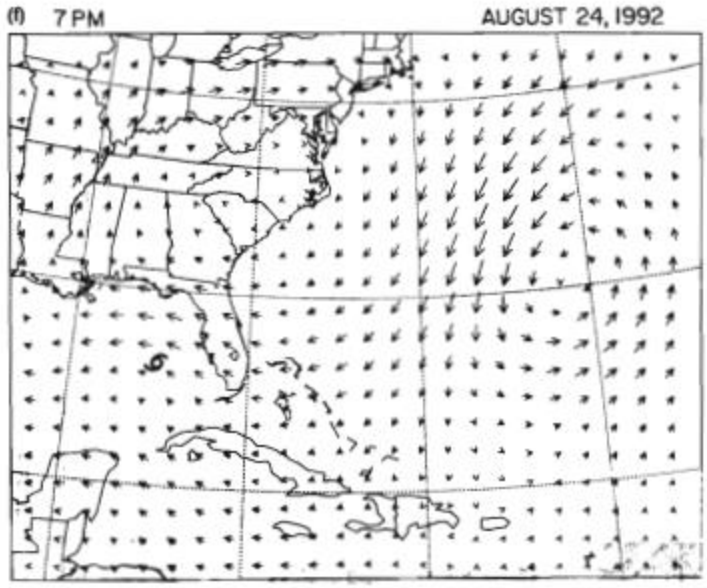

Figure 4.3 (*continued*)

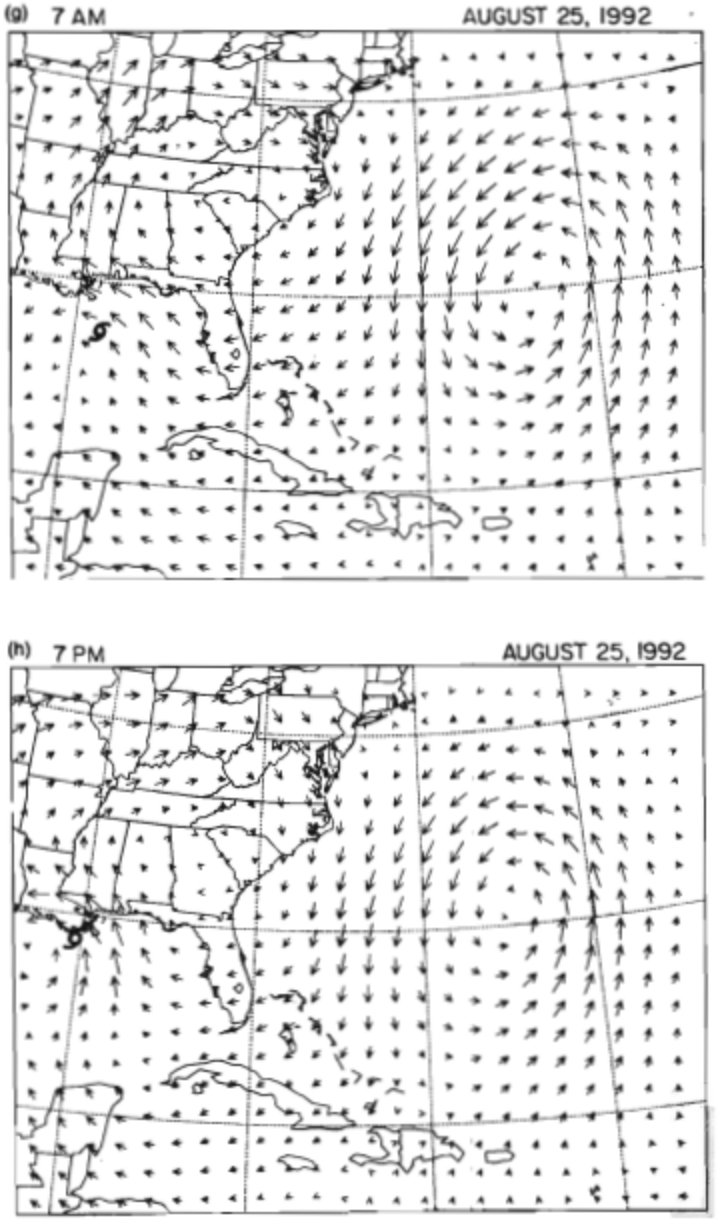

Figure 4.3 (*continued*)

While the news media often attribute hurricanes "with a life of their own", they are, of course, generally well-behaved natural phenomena and, to a large extent, their movement can be explained by the steering currents alone, as shown in the two examples discussed in the last two paragraphs. The difficulty in forecasting their motion occurs when the steering currents are weak and ill-defined and/or when the future state of the steering currents is uncertain. In addition, the need to forecast fairly precise points of landfall to aid emergency planning also contributes to the difficult task of hurricane forecasting.

Tropical cyclones occasionally undergo rapid acceleration in forward motion. This happens when the storm becomes linked to a strong mid-latitude weather system. In addition, tropical cyclones can become absorbed into developing mid-latitude storms thereby infusing added moisture and wind energy from the tropical cyclone and resulting in a more intense mid-latitude storm than otherwise would occur.

An example of a storm that accelerated rapidly out of the tropics was the New England hurricane of 1938. The development of strong, southwesterly winds to the west of this hurricane, associated with a developing mid-latitude storm, resulted in its rapid acceleration to the north at a forward speed of more than 60 mph (27 meters per second). The storm crossed Long Island, New York with little warning, resulting in more than 600 deaths in New England (see Chapter 2).

In 1954, Hurricane Hazel also underwent a similar rapid acceleration to a speed of 60 mph (27 meters per second), as strong south to southwesterly winds developed to the west of the storm. Hazel crossed the North Carolina coastline at 9:25 am on 15 October, and reached Toronto, Canada only 14 hours later where it resulted in 80 deaths (Joe et al. 1995). At that time, it was the most destructive hurricane to reach the North Carolina coast. Every fishing pier was destroyed over a distance of 170 miles (270 km) from Myrtle Beach, South Carolina to Cedar Island, North Carolina. All traces of civilization were practically annihilated at the immediate waterfront between Cape Fear and the South Carolina state line. In 1989, Hurricane Hugo accelerated onto the South Carolina coast at Charleston in association with southeasterly winds caused by a low pressure area in the northeastern Gulf of Mexico, in combination with the Bermuda High to the northeast.

4.3 INTERACTION OF THE STEERING CURRENT AND THE HURRICANE

If the steering current in the immediate vicinity of the storm was constant, its influence on storm motion would be relatively straightforward. Unfortunately, this is generally not the case. The steering current speed and direction are never constant and change both in location and time. If the steering current,

for example, becomes stronger towards the right of a hurricane, with respect to its motion, the tendency is for the storm to move towards the right and to slow down. If, however, the steering current becomes weaker towards the right of a moving hurricane, the tendency is for the storm to turn to the left. In addition, a downstream speed-up of the steering current would accelerate a storm, while a downstream deceleration would slow it down (Holland 1983).

The spatial structure of the steering flow directly influences storm motion because the hurricane and steering current are not separate, distinct features but are intertwined with one another. The hurricane is not like a spinning cork flowing down a stream but is more analogous to an eddy within a stream or cream poured into coffee. Just as with a hurricane, an eddy that is rotating counterclockwise tends to move toward a region in which the flow structure enhances the counterclockwise rotation.

The Earth's rotation (as represented by the Coriolis effect; see Figure 3.2) will also influence storm motion. Since the Coriolis effect is greater at higher latitudes, it contributes to the counterclockwise circulation on the west side of a storm (in the northern hemisphere) where northerly winds occur. The net result is a tendency for a poleward and slightly westerly drift with respect to the steering current.

The thunderstorms associated with the hurricane also modify the steering current (Wang and Holland 1996). The air in the upper tropospheric outflow (divergence) descends at some distance from the storm. If this outflow of air were uniform around the storm, there would be no direct effect on the steering current. Observational analysis, however, shows that this outflow is often concentrated in narrow regions in what are called "outflow jets", which can be observed from satellites. If, for instance, this accumulation of air occurred in the front right quadrant with respect to a storm's movement around the southwest side of the Bermuda High, the consequence would be a strengthening of the Bermuda High from what would occur in the absence of the storm (due to the introduction of air to the high pressure system which increases its pressure further). The net result is a movement of the storm to the left of the track that it would have in the absence of this effect. The neglect of this effect in the forecasting of the landfall location of Hurricane Gilbert in 1988 resulted in an erroneous storm track prediction by an independent forecast group of a landfall on the Texas coast. Hurricane Gilbert made final landfall on the northeast coast of Mexico (Sheets 1990). Correspondingly, an outflow jet which results in an accumulation of air in the right rear quadrant of a westward-moving hurricane would tend to accelerate the storm northward in the northern hemisphere.

The importance of outflow jets on storm motion becomes more significant for larger and more intense storms for which the quantity of air in the outflow is greater. It also becomes a more important component in determining the track of a hurricane or tropical storm when the steering currents are weak and ill-defined. Otherwise, when the steering current is strong, outflow jets from

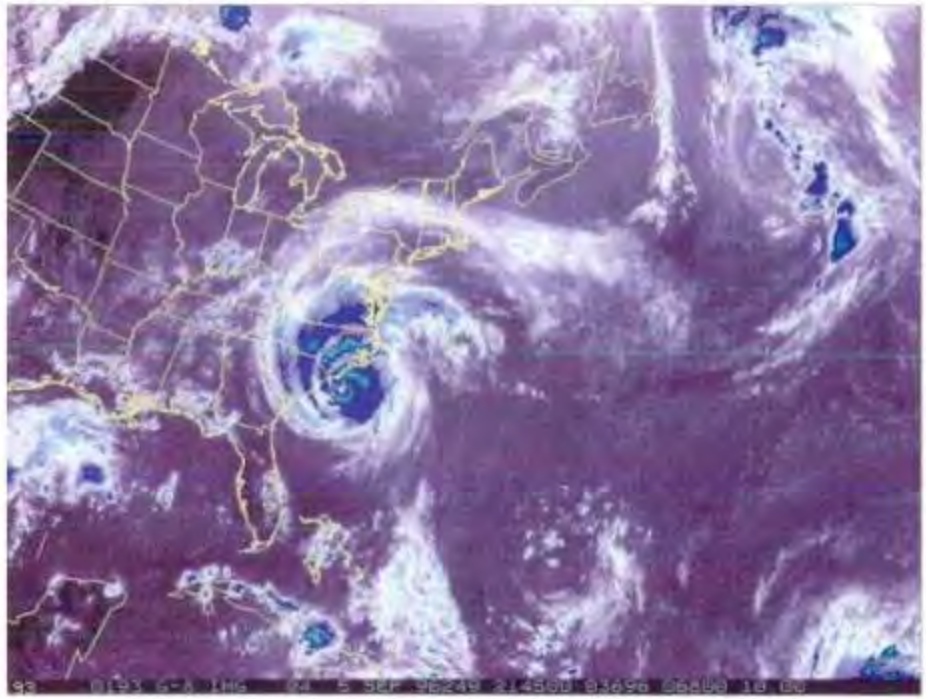

Figure 4.4 Infrared color image of Hurrican Fran taken by a geostationary satellite on 5 September 1996. The image illustrates the cirrus cloud outflow from the upper levels of the storm which appear as wispy white clouds. They are best seen to the north of the storm stretching from West Virginia over New York and east over the Atlantic. Image courtesy of Ray Zehr, NOAA

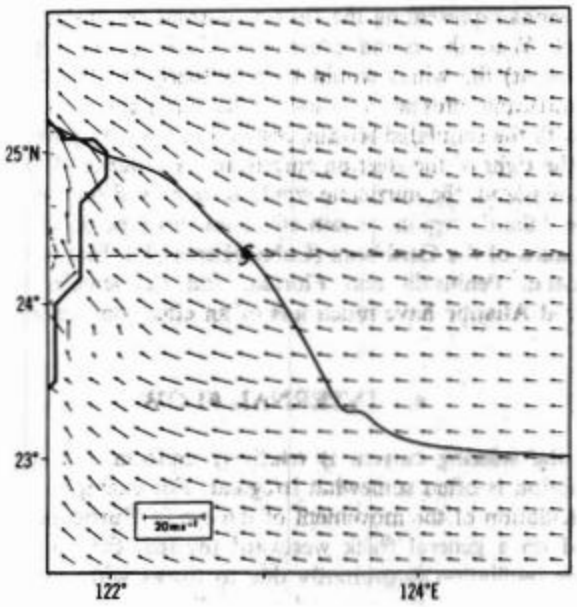

Figure 4.5 Model simulation of the influence of the island of Taiwan on a hurricane track (solid line). (North is to the top of the figure.) Without the presence of the island or the storm, the wind would be easterly at all locations. The island modifies the steering flow such that a southerly steering flow develops just to its east. Source: Bender, Tuleya and Kurihara (1987). Reproduced with permission of the American Meteorological Society

the tropical cyclone are only of secondary importance in terms of determining storm motion.

Figure 4.4 (see color plate) presents a satellite picture to illustrate an outflow jet (Hurricane Fran, 1996). The large avenue of bright clouds stretching to the north and northeast of the storm are cirrus clouds which were transported to that quadrant of the system by the outflow jet. These cirrus clouds are evidence of this air movement to the periphery of the storm through upper-level divergence as thunderstorms reach the upper troposphere. These cirrus clouds will continuously dissipate on their downward edge as the air sinks in this region. The outflow from a tropical cyclone can also counteract the destructive effect on the storm of a vertical shear of the larger-scale wind field, by deflecting those winds around this outflow (Elsberry and Jeffries 1996).

Mountainous islands also influence the movement of a hurricane through the alteration of the steering current. Figure 4.5 illustrates a numerical model simulation of the influence of a large mountainous island on the track of a

storm. The winds representing the steering current are easterly in the absence of the island. With the island present to block the flow (even without a hurricane present) the winds would turn southerly to the east of the island. With the hurricane present as shown, the circulation around the storm, interacting with the simulated terrain, resulted in the path plotted in the figure, which is to the right of the steering current in the absence of the storm. In the absence of the island, the hurricane would have moved on a general westward track. In the Atlantic region, terrain effects of this type occur associated with the larger islands of the Caribbean (Cuba, Hispañola). Flatter landscape, such as the Yucatan Peninsula and Florida, and the smaller islands of the Caribbean and Atlantic have much less of an effect on cyclone tracks.

4.4 INTERNAL FLOW

Even when the steering current is relatively uniform and steady, however, hurricane motion is often somewhat irregular. For example, Figure 4.6 illustrates the oscillation of the movement of the eye of Hurricane Dora (1964) as it progressed on a general track westward towards the upper east coast of Florida. This oscillation is primarily due to forces within the hurricane. In Hurricane Anita (1977), the eye and eye wall were observed by aircraft to have an oscillation around the mean track with an amplitude of 3 miles (5 km) and a period of 6 hours (Willoughby 1979). This small-scale irregular behavior of the center of the storm has been attributed to the thunderstorms and strong winds in the eye wall region, which causes the center to deviate short distances to the left or right of its track, similar to the motion of a spinning top. The larger circulation envelope of the hurricane, with its much greater inertia, more closely follows the steering current and tends to force the eye wall back towards the center of the larger circulation.

4.5 TROPICAL CYCLONE TRACK, INTENSITY, AND SEASONAL FORECASTING

Hurricane predictions in the United States are prepared at the National Hurricane Center in Miami, Florida for tropical cyclones in the Gulf of Mexico, the Caribbean and the Atlantic Ocean and the eastern Pacific (Figure 4.7). Other regions of responsibility are shown in Appendix D.

4.5.1 Tropical cyclone track predictions

The National Hurricane Center utilizes a suite of models to forecast tropical cyclone tracks (DeMaria 1995; Aberson and DeMaria 1994). They include one based on climatology and persistence (CLIPER), a statistical model which

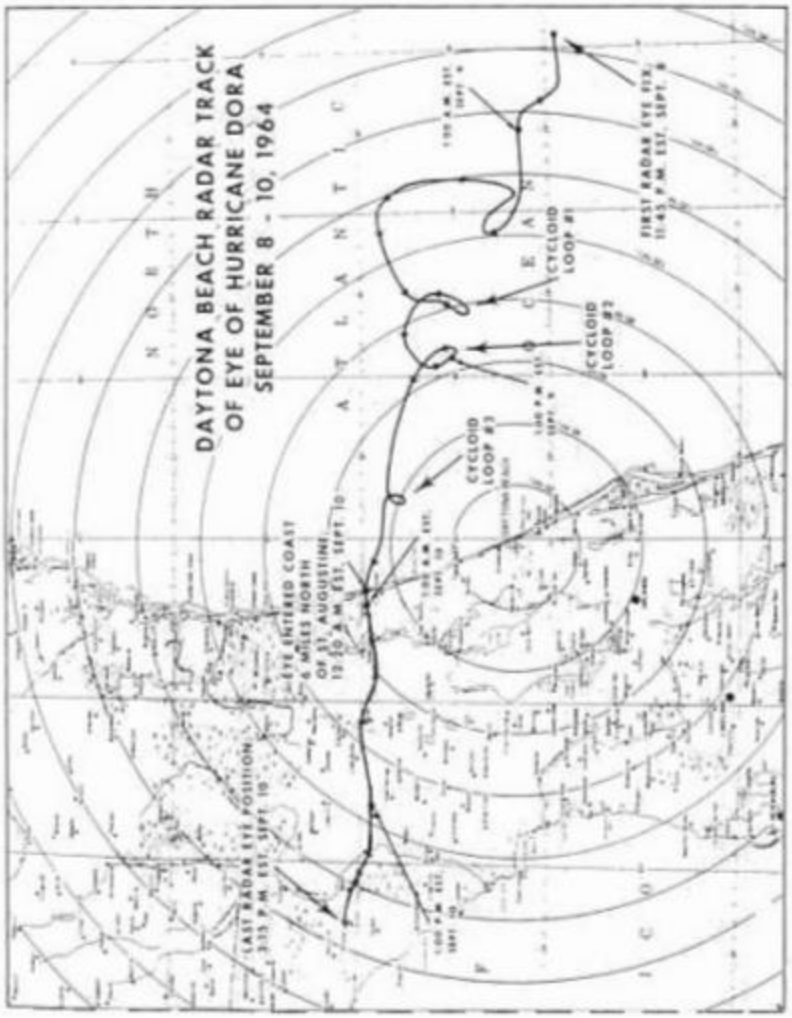

Figure 4.6 Daytona Beach radar track of eye of Hurricane Dora, 8–10 September 1964. The wobbles seen in the Hurricane's motion as it made landfall are not completely understood or predictable. Possible explanations include the influence of land on the storm's circulation, and resultant wobbling similar to a spinning top which is perturbed slightly from its path. Source: DOC (Department of Commerce) 1964

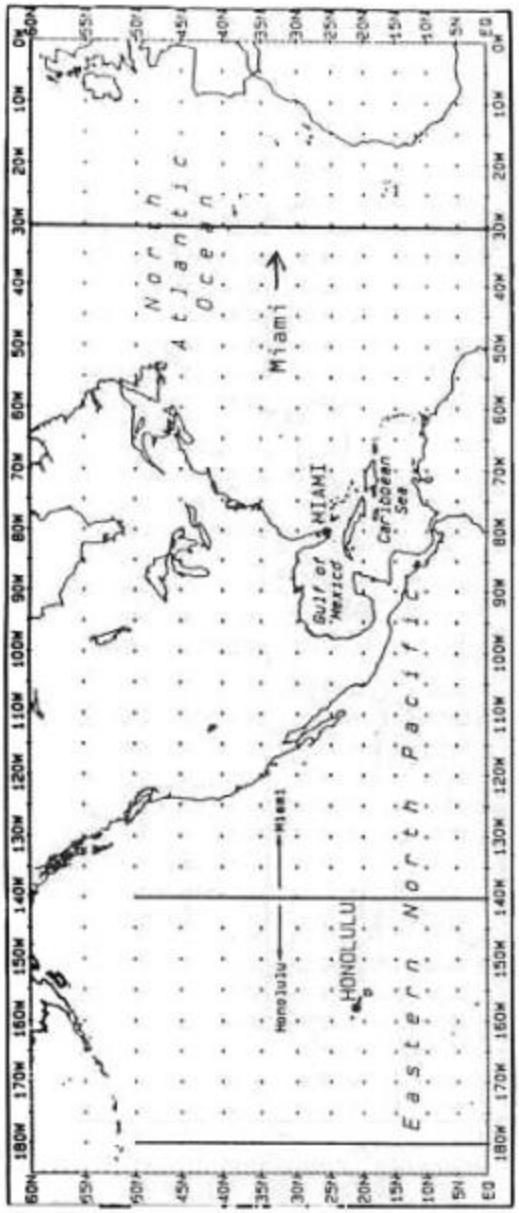

Figure 4.7 Hurricane responsibility area of the National Hurricane Center in Coral Gables, Florida

uses information from the National Weather Service (NWS) global prediction model (NHC 90; McAdie 1991), and several which solve mathematical equations for atmospheric flow including VICBAR (Aberson and DeMaria 1994), BAM (Marks 1992), the Geophysical Fluid Dynamics Lab (GFDL) model (Bender et al. 1993), and the National Meteorological Center (NMC) Aviation Medium Range Forecast (MRF) global forecast models (Lord 1993). During the 1992 and 1993 seasons, the GFDL model track forecasts were superior to the other track models (Aberson and DeMaria 1994); the improved forecasts of hurricane track using this model are also summarized by Sawyer (1995).

Track forecasts are very sensitive to how the actual hurricane is initially defined in the model (Leslie and Holland 1995). For instance, track predictions depend on the choice of hurricane radius and strength, and its initial location. Improved measurements of temperature, wind, and humidity in and around tropical cyclones have contributed to improved operational track forecasts (Burpee et al. 1996). An example of a 72-hour track forecast for Hurricane Hugo for different models is given in Figure 4.8. This figure illustrates that despite significant progress in hurricane forecasting, exact track prediction remains fraught with difficulties. Hugo actually made landfall near Charleston, South Carolina. Hurricane track models are also summarized in Puri and Holland (1993).*

Figure 4.9 illustrates the trend and accuracy of 24-hour, 48-hour, and 72-hour forecasts of storm position between 1970 and 1992. As of 1997, average forecast errors are on the order of 115 miles (185 km) for 24-hour forecasts, 230 miles (368 km) for 48-hour forecasts, and 345 miles (552 km) for 72-hour forecasts (C. Landsea, 1997, personal communication). Note that an improvement of only about 20 miles (42 km) has been achieved in 24-hour position forecasts over 23 years, despite the great advances both in monitoring these storms (e.g. radar, satellite, reconnaissance aircraft) and in computer power to process and analyze the data.

---

* Four criteria have been proposed for accurate track forecasts using models such as VICBAR, BAM, the GFDL model, and the Aviation global model (Elsberry 1995). These are: adequate initial specifications of the environmental wind field, the symmetric and asymmetric cyclone vortex structure, and the adequacy of the prediction models to forecast the time evolution of the vertical and horizontal wind field. An accurate representation of the diabatic heating of the atmosphere by the hurricane, and the prediction of winds and temperature in the upper troposphere are also essential to accurately characterize hurricane–environmental interactions (Wu and Kurihara 1996). When the large-scale weather pattern is changing with time, these requirements are difficult to achieve with sufficient accuracy.

The MRF model is used for general weather forecasting in addition to its application for tropical cyclone track prediction. VICBAR, BAM, NHC90 and the GFDL model use forecast fields from the MRF model for input. One version of NHC90 (referred to as UK90) uses output from the United Kingdom Meteorological Office global forecast model.

The GFDL model includes the most physical realism in its formulation, including moving nested grids which translate with the cyclone and a sophisticated vortex initialization scheme with the finest horizontal grid interval of 20 km (DeMaria 1995; Bender et al. 1993).

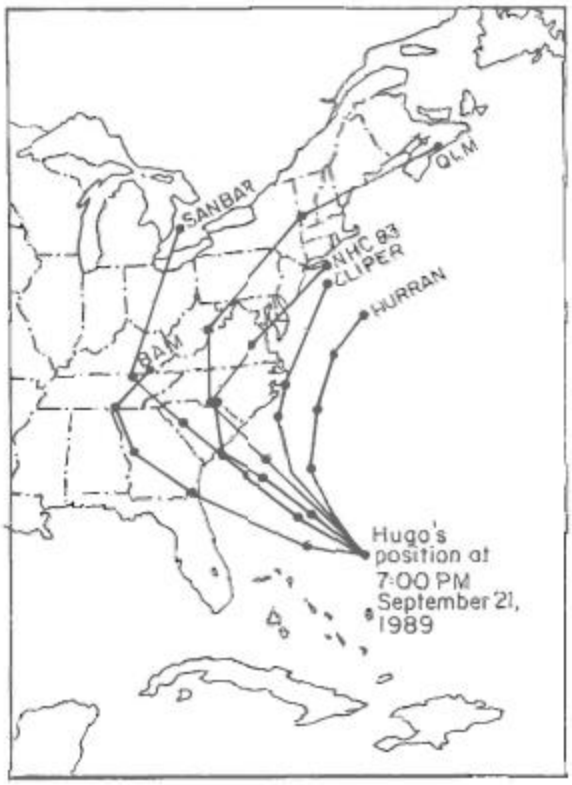

Figure 4.8 National Hurricane Center 72-hour forecast tracks for Hurricane Hugo 1989, starting from its position at 0 GMT on 21 September 1989. The forecast 12-hour positions for each of six forecast techniques are shown as black dots

Since 1983, probabilities of a tropical cyclone passing within 75 miles (121 km) of specific geographic locations have also been publicly distributed. An example of the format used in these probability forecasts is shown in Figure 4.10, in this case for Hurricane Erin in 1995.

4.5.2 Tropical cyclone intensity change predictions

Forecasting of changes in tropical cyclone intensity is a much more difficult task than forecasting tropical cyclone tracks. Several methods are used to predict changes in intensity. The simple climatology and persistence intensity technique (SHIFOR) and the statistical hurricane intensity prediction scheme

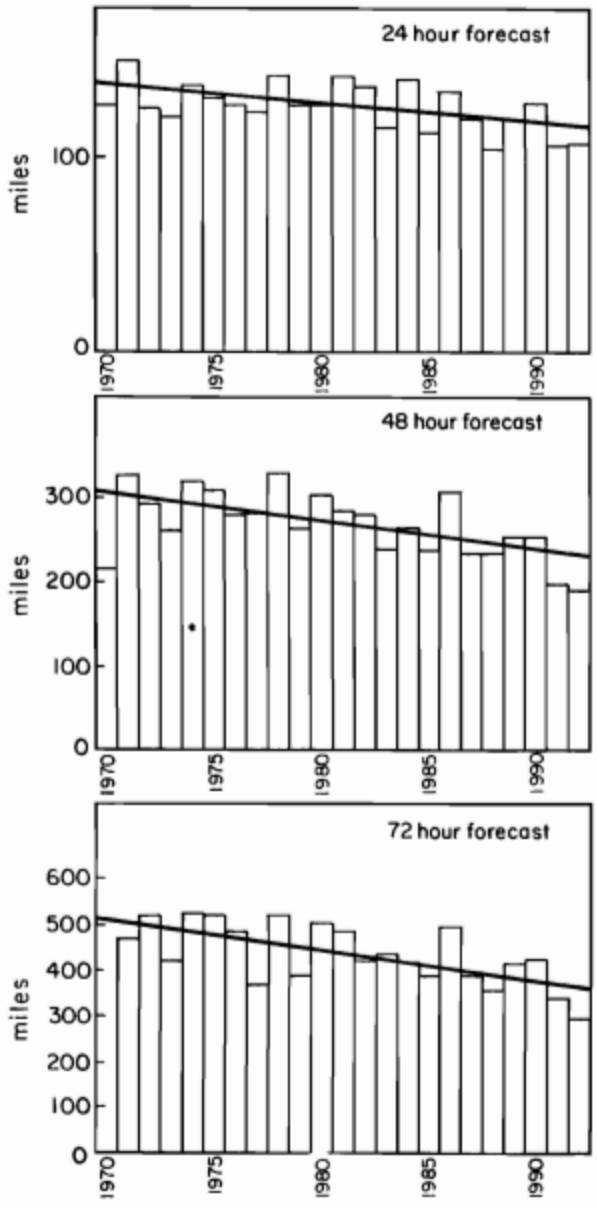

Figure 4.9 Annual average NHC official forecast errors for 24 hours, 48 hours, and 72 hours (1970–1992). The diagonal line shows the trend. Source: McAdie and Lawrence (1993)

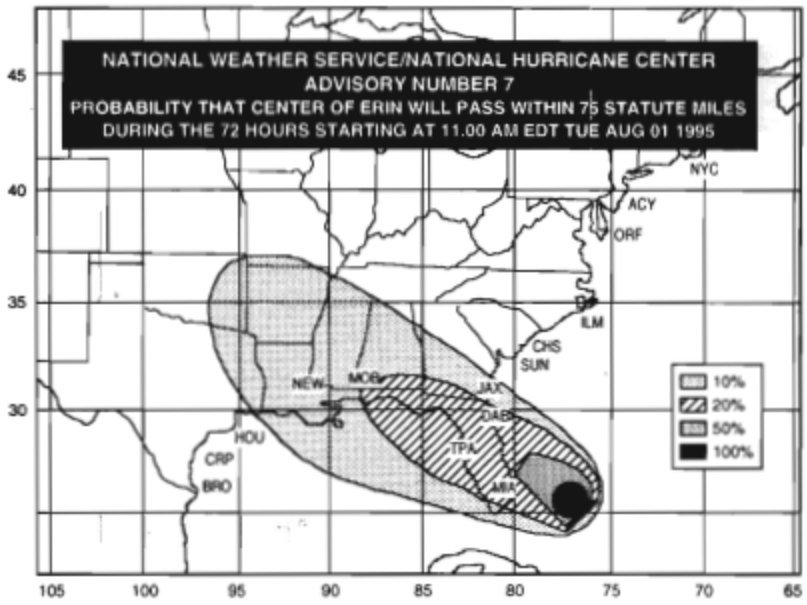

Figure 4.10 Forecast probability that the center of Erin will pass within 75 miles during the 72 hours starting at 11 am Eastern Daylight Time on 1 August 1995 (redrawn from the National Hurricane Center WWW page at http://www.nhc.noaa.gov)

(SHIPS) are used for tropical cyclone intensity forecasts. SHIFOR, analogous to the CLIPER track model, uses only climatology, persistence, and current storm characteristics to calculate statistically the most expected intensity change. SHIPS, in contrast, utilizes selected current meteorological and ocean data, including the difference between the current tropical cyclone intensity and its potential maximum based on sea surface temperature (DeMaria and Kaplan 1994). SHIPS has average intensity errors that are 10–15% smaller than those for SHIFOR. The GFDL model, briefly described in Section 4.3.1, also predicts intensity change. However, its horizontal resolution is insufficient to resolve the eye wall region, which is critically involved with the intensification process. Preliminary research modeling with finer spatial resolution for Hurricane Andrew suggests that the more detailed representation of the thunderstorms in the eye wall region and in the inflow to the hurricane can lead to improved intensity change forecasts (Eastman 1995, Liu et al. 1997). Operational techniques have so far shown little skill in intensity change prediction; thus forecasters primarily rely on empirical techniques.

Satellite imagery is often used to estimate the intensity of clusters of oceanic tropical thunderstorms, including tropical cyclones and hurricanes. This

approach is particularly useful when reconnaissance aircraft are unavailable to monitor the strength of such a thunderstorm cluster. The use of satellite images for this purpose is based on a pattern recognition decision tree (Dvorak 1975; 1984). The difference in the temperature of the eye of the hurricane, and the cloud top temperatures of the surrounding eye wall, based on infrared satellite images, is one example of the use of this technique.

When tropical systems move close enough to land, aircraft reconnaissance is also used to monitor their intensities (Neal Dorst in Landsea 1997). These flights are conducted by the US Air Force Reserve 53rd Weather Reconnaissance Squadron and the National Oceanographic and Atmospheric Administration (NOAA) Aircraft Operations Center. The 10 WC-130 Air Force planes of the squadron are based at Keesler Air Force Base in Mississippi, but, as needed, are positioned elsewhere, including islands in the the eastern Caribbean Sea. Measurements include wind, temperature and humidity at flight level, as well as data collected by dropping instruments along the flight path. The three NOAA aircraft (two P-3 Orions and a Gulfstream IV), based at MacDill Air Force Base in Florida have more sophisticated instrumentation, including on-board weather radar. These three aircraft are generally used only for hurricanes that are threatening landfall, or otherwise have specific scientific interest.

4.5.3 Seasonal predictions of tropical cyclone activity

Researchers also prepare forecasts for entire seasons. Professor William Gray of Colorado State University leads a team that forecasts tropical cyclone activity for upcoming seasons in the Atlantic, Gulf of Mexico and Caribbean (Gray et al. 1995). Table 4.1 summarizes Gray's forecasts from 1984 to mid-1997.

Their forecasts, also made in early August for the remainder of the tropical cyclone season, are based on a number of factors including (Gray 1995; Landsea et al. 1994):

1 The winds at a height of about 15 miles (about 24 kilometers) and about 13 miles (about 21 kilometers). There is increased hurricane activity when the winds are more westerly than average and where there are smaller differences in wind between the two levels. These winds fluctuate between east and west in a cycle that is slightly longer than two years and is called the "stratospheric quasibiennial oscillation". Thus this factor alone would tend to make seasons vary between active and quiet from one year to the next (Shapiro 1989).
2. The state of the El Niño–Southern Oscillation (ENSO) cycle. A warm event in the equatorial East Pacific is associated with reduced hurricane activity, while a cold event is associated with enhanced activity (on ENSO see Glantz 1996).

Table 4.1 Seasonal forecasts of Atlantic hurricane activity produced by Professor William Gray of Colorado State University, and actual hurricane incidence. Forecasts available at http://tropical.atmos.colostate.edu/forecasts/.

Forecast of	1950–1993 Mean	1984	1985	1986	1987	1988	1989	1990	1991	1992	1993	1994	1995	1996	1997
A. November (9 to 14 month)															
No. of hurricanes	5.7									**4** *4*	**6** *4*	**6** *3*	**8** *11*	**5** *9*	**6** –
No. of named storms	9.3									**8** *6*	**11** *8*	**10** *7*	**12** *19*	**8** *13*	**10** –
No. of hurricane days	23									**15** *16*	**25** *10*	**25** *7*	**35** *62*	**20** *45*	**24** –
No. of named storm days	46									**35** *38*	**55** *30*	**60** *28*	**65** *121*	**40** *78*	**50** –
Hurricane destruction potential	68									**35** *51*	**75** *23*	**85** *15*	**100** *173*	**50** *135*	**60** –
No. of Category 3-4-5 hurricanes	2.2									**1** *1*	**3** *1*	**2** *0*	**3** *5*	**2** *6*	**2** –
Category 3-4-4 hurricane days	4.5									**2** *3.25*	**7** *0.75*	**7** *0.0*	**8** *11.5*	**5** *13*	**4** –
B. Late May/early June (0 to 6 month)															
No. of hurricanes	5.7	**7** *5*	**8** *7*	**4** *4*	**5** *3*	**7** *5*	**4** *7*	**7** *8*	**4** *4*	**4** *4*	**7** *4*	**5** *3*	**8** *11*	**6** *9*	**7** –
No. of named storms	9.3	**10** *12*	**11** *11*	**8** *6*	**8** *7*	**11** *12*	**7** *11*	**11** *14*	**8** *8*	**8** *6*	**11** *8*	**9** *7*	**12** *19*	**10** *13*	**11** –
No. of hurricane days	23	**30** *18*	**35** *21*	**15** *10*	**20** *5*	**30** *24*	**15** *32*	**30** *27*	**15** *8*	**15** *16*	**25** *10*	**15** *7*	**35** *62*	**20** *45*	**25** –
No. of named storm days	46	**45** *51*	**55** *51*	**35** *23*	**40** *37*	**50** *47*	**30** *66*	**55** *68*	**35** *22*	**35** *38*	**55** *30*	**35** *28*	**65** *121*	**45** *78*	**55** –
Hurricane destruction potential	68					**75** *81*	**40** *108*	**90** *57*	**40** *23*	**35** *51*	**65** *23*	**40** *15*	**110** *173*	**60** *135*	**75** –
No. of Category 3-4-5 hurricanes	2.2							**3** *1*	**1** *2*	**1** *1*	**2** *1*	**1** *0*	**3** *5*	**2** *6*	**3** –
Category 3-4-5 hurricane days	4.5								**2** *1.25*	**2** *3.25*	**0** *0.75*	**1** *0.0*	**6** *11.5*	**5** *13*	**5** –
C. Late July/early August (0 to 4 month)															
No. of hurricanes	5.7		**7** *7*	**4** *4*	**4** *3*	**7** *5*	**4** *7*	**6** *8*	**3** *4*	**4** *4*	**6** *4*	**4** *3*	**9** *11*	**7** *9*	
No. of named storms	9.3		**10** *11*	**7** *6*	**77** *7*	**11** *12*	**9** *11*	**11** *14*	**7** *8*	**8** *6*	**10** *8*	**7** *7*	**16** *19*	**11** *13*	
No. of hurricane days	23		**30** *21*	**10** *10*	**15** *5*	**30** *24*	**15** *32*	**25** *27*	**10** *8*	**15** *16*	**25** *10*	**12** *7*	**30** *62*	**25** *45*	
No. of named storm days	46		**50** *51*	**25** *23*	**35** *37*	**50** *47*	**35** *66*	**50** *68*	**30** *22*	**35** *38*	**50** *30*	**30** *28*	**65** *121*	**50** *78*	
Hurricane destruction potential	68					**75** *81*	**40** *108*	**75** *57*	**25** *23*	**35** *51*	**55** *23*	**35** *15*	**90** *173*	**70** *135*	
No. of Category 3-4-5 hurricanes	2.2							**2** *1*	**0** *2*	**1** *1*	**2** *1*	**1** *0*	**3** *5*	**3** *6*	
Category 3-4-5 hurricane days	4.5							**5** *1.0*	**0** *1.25*	**2** *3.25*	**2** *0.75*	**1** *0.0*	**5** *11.5*	**4** *13*	

Blank areas in the table indicate that these forecasts were not made (Gray 1994; 1995). These forecasts are available at http://tropical.atmos.colostate.edu/forecasts/index.html.
Forecasts are given in bold type, actual values in italic.
Named storm: A tropical storm or hurricane.
Hurricane day: Four 6-hour periods during which a tropical cyclone is estimated to have hurricane-strength winds.
Named storm day: Four 6-hour periods during which a tropical cyclone is observed or estimated to have tropical storm or hurricane-strength winds.
Hurricane destruction potential: A measure of a hurricane's potential for wind and storm surge destruction defined as the sum of the square of a hurricane's maximum wind speed (in 10^4 knots^2) for each 6-hour period of its existence.
Category 3-4-5 hurricane day: Four 6-hour periods during which a tropical cyclone has intensity of Saffir/Simpson Category 3 or higher.

3. Prior rainfall in the western Sahel region of Africa. Wetter conditions are related to increased hurricane activity.
4. Spatial differences of surface pressure and surface temperature over western Africa during the previous February through May. Large differences correspond with more hurricane activity.
5. Average sea level pressure in the Caribbean in the previous spring and early summer. If the pressures are low, hurricane activity is generally enhanced.
6. Winds at a height of about 7.5 miles (about 12 km) for five low latitude sites in the Caribbean. Hurricane activity is increased if the easterly winds are stronger than average.
7. Warmer sea surface temperatures in the North Atlantic help create more Atlantic hurricanes. This factor has been used in the seasonal hurricane forecasts since August 1996 (C. Landsea, 1997, personal communication).

The seasonal forecast is for named tropical cyclones, hurricanes, intense hurricanes (Category 3 or stronger storms); the number of days with tropical cyclones, hurricanes, and intense hurricanes; hurricane destruction potential; and net tropical cyclone activity. Over a 45-year period (1950–1994), there were annual averages of 2.1 intense hurricanes and 4.5 intense hurricane days. During this period the maximum number of intense hurricanes was seven in 1950, while the largest number of intense hurricane days was 21 in 1961.

The seasonal forecasts indicate that above-average hurricane seasons occur when the Sahel region is wetter. In this situation, areas of thunderstorms that propagate across this area of Africa (and are a major source for tropical cyclones in the Atlantic, Gulf of Mexico, and Caribbean; Pasch and Avila 1994) are in a more favorable environment since transpiring vegetation, which has grown in response to the rains earlier in the year, provides a water vapor source to the clouds. Thus these systems are more likely to persist when they move westward off the African west coast. The rainfall in west Africa also directly relates to the vertical wind shear in the Atlantic Ocean tropical cyclone development region, with wetter years having lower shear (Goldenberg and Shapiro 1996).

Several of the other predictors relate to a reduction in the vertical shear of the wind as being associated with enhanced hurricane activity. As discussed in Chapter 3, weak shear is a favorable condition for tropical cyclone development. Lower surface pressures in the Caribbean, also an environmental condition that favors development, is associated with convergence of water vapor and heat into propagating thunderstorm cloud clusters, as well as tropical cyclones after they develop.

4.5.4 Attempts at tropical cyclone modification

There have been attempts by scientists to modify the intensity of tropical cyclones. The main hypothesis is that by seeding cumulus clouds with silver

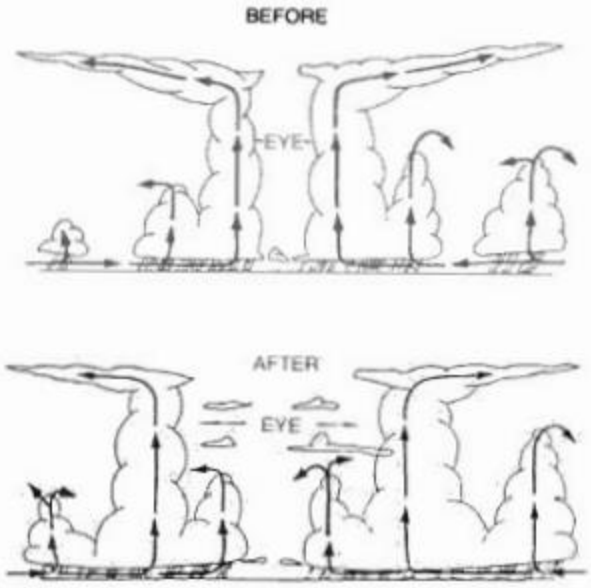

Figure 4.11 Hypothesized vertical cross-sections through a hurricane eye wall and rain bands before and after seeding. Dynamic growth of seeded clouds in the inner rain bands provides new conduits for conducting mass to the outflow layer and causes decay of the old eye wall. Source: Simpson et al. (1978)

iodide outside the eye wall, clouds with liquid water colder than 0°C (referred to as "supercooled water") could be converted to ice crystals. This change of phase of water would release the heat of fusion, thereby enhancing the growth of the cumulus clouds and establishing the eye wall at a greater radius from the center of the storm circulation. Without the silver iodide, it is hypothesized that the cloud droplets would remain liquid. Just as ice skaters slow their rotation when their arms are spread out, the hypothesis is that a larger radius of the eye wall will cause a reduction in wind strength. The hypothesis is sketched schematically in Figure 4.11.

This program of tropical storm modification was called Project Stormfury. Robert and Joanne Simpson were the original source of the Stormfury hypothesis in 1960. Their insight was inspired by an observation of Hurricane Donna (1960) by Professor Herbert Riehl, who noted that nearly all of the outflow cloudiness stemmed from an aggregation of thunderstorms in the front right quadrant of the eye wall. Hurricanes Esther (1961), Beulah (1963), and Debbie (1969) were seeded as part of this project, although only the Debbie experiments closely followed the most recent Stormfury hypotheses.

In an earlier experiment, a hurricane was seeded on 13 October 1947 off the southeast United States coast. Because it subsequently moved westward into the Georgia coast, questions were raised among critics of weather modification as to whether the seeding caused the abrupt change in storm track. More recent analysis strongly suggests that the alteration in direction would have occurred in any case. Hurricane Ginger was also seeded in 1971. However, it was an anomalous storm with an eye wall usually below 20 000 feet (6100 meters) and no significant quantities of supercooled water were found.

Hurricane modification ended because of equivocal research findings including evidence that hurricanes may only infrequently be amenable to modification because of their very large variability, questions of national and international legal issues, and a general loss of support for weather modification efforts (Cotton and Pielke 1995; Pielke and Glantz 1995). Currently, further seeding experiments are not being performed. Project Stormfury was terminated in 1983 (Willoughby et al. 1985). A policy consequence of the inability to control hurricanes is that impacts must be mitigated by reducing societal exposure and *not* by modifying event incidence.

4.5.5 Value to society of forecasts

The production of a hurricane forecast is only the first step in the process of its effective use by decision-makers. A hurricane forecast must also be communicated through a process of – hear, understand, believe, personalize, respond, and confirm (as described by Sorensen and Mileti 1988). A decision by an individual to act in response to the information about an approaching storm, or any other extreme event for that matter, is conditioned by a wide range of factors such as perceived risk, education, time to impact, and many more (Sorensen 1993). Social scientists have a well developed understanding of the process of natural hazards warnings and human response (see, e.g., Drabek 1986). The use of a forecast must be understood in the broad context of a process from production through communication through response.

The US National Weather Service (NWS) produces and issues a number of products related to hurricanes: hurricane watches and warnings, flash flood watches, flash flood warnings, flash flood statements, tornado watches and warnings, severe thunderstorm watches and warnings, severe weather statements, and special weather statements (NOAA 1994). Once a forecast or warning is produced it is typically distributed to a range of Federal, state, and local agencies, including FEMA, the Corps of Engineers, and state and local emergency management agencies. Similarly, the media – including print, television, and radio – also receive NHC weather products and are often a critical link in the communication process. Recently, the World Wide Web has provided a wide range of information resources in both text and graphic formats (http://www.nws.noaa.gov/).

A forecast is only useful if it can be incorporated into the decision process of a particular user. For this to happen, "it is vital that [official] personnel share knowledge of dissemination systems, procedures, capabilities, and response requirements with the media; Federal, state, and local agencies; and the general public involved in the total warning process" (NOAA 1994). Similarly, officials must also be aware of the information needs of and decision-making constraints on users of their information. Effective use of a forecast is *not* achieved simply by sending information from one party to another; it is the result of two-way interaction between the sender and receiver.

A focus on the process of decision-making is central to realistic determination of the opportunities for and limitations on use of forecasts to reduce societal vulnerabilities to hurricanes (Pielke 1994). To focus on process is to focus on the formulation, promulgation, and execution of particular decisions (Lasswell 1971). Often, both scientists and policy-makers alike behave as if the development of scientific information (such as a forecast) is sufficient to lead to better decisions. From a decision-maker's perspective, a call for better information from scientists can forestall the need to make difficult decisions while placing the burden of problem-solving upon the scientists (Clark and Majone 1985). From a scientist's perspective, a focus on information allows for relative autonomy from the "politics" of decision-making and a justification for continued funding. However, it is often the case that scientific information is misused or not used at all because of rigidities in and practicalities of decision-making processes (e.g. Feldman and March 1981).

Specific decisions are made in the context of a set of alternative courses of action. For example, in order to better prepare for the hurricane threat, citizens of New Orleans might desire a range of alternative responses to the following questions: How strictly shall we enforce our buildings codes? At what point in time before an approaching hurricane shall evacuation become mandatory? How much, if any, increase in insurance should citizens be required to carry in the face of a long-term forecast of increased hurricane incidence? Alternative actions in response to each question are embedded in a broader context of values, feasibility, and efficacy. For instance, building code enforcement cannot be separated from issues such as the costs (to the resident) of building a reinforced structure and the tax revenues necessary to hire a sufficient number of building inspectors. In many respects, decisions to which forecasts may be relevant are decisions about how a community wishes to move into the future.

Policy-makers require some sense of the usefulness of short- and long-term forecasts with respect to the hurricane problem in order to determine the amount of resources to be placed into their development versus alternative responses. However, demonstration of use or value of hurricane forecasts is a challenging analytical task. Glantz (1986) notes that "one could effectively argue that the value of climate-related forecasts will in most instances be at least as much a function of the political, economic, and social settings in

which they are issued than of the soundness of information in the forecast itself". Put another way, the solution to the hurricane problem is potentially very different in Dade County, Florida, from that in Worcester County, Maryland, and both of those may be significantly different from the solution in Nueces County, Texas as a result of economic, political, and civic differences between the various communities. Further, what works in the mainland United States may not work as effectively on islands or in other countries.

Apart from demonstrating the value of improved forecasts, accurate assessment of societal vulnerabilities to hurricanes is a very challenging task. An example of the difficulties in defining the extent and magnitude of the hurricane threat is provided by the response of the insurance industry to Hurricane Andrew. The 1992 event served as a "wake-up call" to the insurance industry. Prior to Andrew the insurance industry largely ignored hurricane climatology and instead kept records of hurricane-related deaths and economic damage, according to Russell Mulder, director of risk engineering at the Zurich-American Insurance group (Wamsted 1993). The insurance industry's records were accurate measures of their losses, but not of hurricanes: they neglected storms that did not make landfall and underestimated the potential impact of storms that made landfall in relatively unpopulated areas. Since Hurricane Andrew, the insurance industry has paid closer attention to the hurricane threat (e.g. Banham 1993; Noonan 1993; Wilson 1994). One would expect the insurance industry to be among the most sensitive to societal vulnerability to hurricanes; however, Hurricane Andrew demonstrated that even when concern exists, accurate definition of the hurricane problem is difficult.

One expert in the value of forecasts states that "forecasts possess no intrinsic value. They acquire value through their ability to influence the decisions made by the users of the forecasts" (Murphy 1993). Yet, because numerous factors contribute to any particular decision "assessing the economic value of forecasts is not a straightforward task" (Murphy 1994). That is, a forecast is, at best, only one of a multitude of factors which influence a particular (potential) user. It is often difficult to identify the signal of the forecast in the noise of the decision-making process. Factors external to the forecast may hinder its use.

Two complementary approaches to assessment of forecast value can be summarized as use-in-theory and use-in-practice Murphy (1994) calls these *prescriptive* and *descriptive* assessments of forecast value, while Glantz (1977) uses the terminology of "what ought to be" and "what is". Use-in-theory refers to efforts to estimate the "value of forecasts under the assumption that the decision maker follows an optimal strategy" (Stewart 1997). Generally, economists, statisticians, and decision theorists share expertise in assessment of use-in-theory (e.g. Winkler and Murphy 1985). Use-in-practice refers to efforts, including case studies, to understand how decisions are actually made in the real world and the value of forecast information therein (e.g. McNew

et al. 1991). Political scientists, sociologists, and psychologists are examples of those with expertise in assessment of use-in-practice.

It is likely that, as forecasts of hurricane incidence demonstrate increased skill, the value of such forecasts will not be self-evident to most users. Hence, it may be worthwhile for producers of both short- and long-term forecasts to conduct an ongoing parallel research effort targeted at actual and potential users. Such a parallel program could focus on assessments of use-in-theory and use-in-practice in order to identify opportunities for and constraints on improved and proper use of hurricane forecasts. Counties, states, and SLOSH basins would be appropriate levels of analysis for an assessment. Particular decisions could be identified from a decision process map, such as that created by Lee County Florida and reproduced as Appendix E. Such assessments may find that in some cases a particular decision process may constrain effective use of a forecast. Other assessments may find clear opportunities to leverage forecast information for reduced vulnerability. If public funding dedicated to the development of improved forecasts of hurricane activity are justified in terms of their value added to social processes, then the sustainability of support for such research may depend in large part upon demonstration of actual use or value.

Where society ought to spend its limited resources to best address the hurricane problem is not clear. The lessons of the weather modification experience provide a warning to the scientific community. Modification of hurricane incidence will remain impractical for the foreseeable future, in spite of the mid-century optimism following an intensive series of efforts to "tame" hurricanes in the 1950s and 1960s (Gentry 1974). Experience with hurricane modification does provide one very important lesson: Care must be taken not to "over-promise" expected benefits deriving from research (e.g. Tennekes 1990; Namias 1980).

Consider the following statement made in the late 1940s in a talk given by Nobel Laureate Irving Langmuir at the dawn of optimism about hurricane modification: "The stakes are large and with increased knowledge, *I think that we should be able to abolish the evil effects of these hurricanes*" (quoted in Byers 1974, emphasis added). On one level such claims reflect the eternal optimism of science and technology. But at another level, such claims are publicly irresponsible and potentially damaging to the institution of science (Changnon 1975). One can easily imagine a policy maker, excited by the possibilities of Langmuir's claim, making an argument that "preparedness plans for hurricanes would no longer be necessary because in weather modification scientists had discovered a magic bullet". Of course, taking the thought a step further, had a hurricane then hit a poorly prepared community, it is reasonable to expect that blame would have been laid at the feet of the scientist, and not the policy maker. In the context of forecasts of hurricane activity, credibility with the public will be difficult to gain, and easy to lose (Slovic 1993).

Weather modification is perhaps an extreme example of the risks involved with overselling science. However, in an era when science is increasingly called upon to contribute to the resolution of many difficult societal problems, demonstration of benefits may become central to sustained federal support of research to develop improved forecasting capabilities.

43. Assignment 2, Module 9: Hurricanes Spawn Tornadoes:
https://www.livescience.com/37235-how-hurricanes-spawn-tornadoes.html

How Do Hurricanes Spawn Tornadoes?

News By Douglas Main published September 10, 2017

Here, hurricanes Katia, Irma and Jose swirl in the Atlantic on Sept. 8, 2017. The raging trio was captured by the Visible Infrared Imaging Radiometer Suite (VIIRS) on the Suomi NPP satellite. The day-night band allowed the instrument to show both the city lights as well as the swirling hurricanes. (Image credit: NASA Earth Observatory)

As if Hurricane Irma — now a major Category 4 storm that's battering Key West with the west coast of the Florida Peninsula in its crosshairs — weren't enough to worry about: The monster storm could spawn tornadoes in parts of the Sunshine State.

Hurricanes and tornadoes are typically thought of as separate phenomena, with tornadoes conjuring up images of the flat prairie and hurricanes associated with the warm, coastal tropics. Hurricanes are much, much larger than tornadoes (Irma's innards stretch some 400 miles, or 644 kilometers, across), but tornadoes can generate much faster winds than hurricanes.

Sometimes, tropical storms and hurricanes, like Hurricane Irma, can spin out tornadoes.

But how do hurricanes and tropical storms create tornadoes?

Hurricanes and tropical storms, collectively known as tropical cyclones, provide all the necessary ingredients to form tornadoes. First, most hurricanes carry with them individual supercells, which are rotating, well-organized thunderstorms. These are typically the storms that spin up monster twisters in the Plains. All tornadoes need thunderstorms to form, said Brian McNoldy, a researcher at the University of Miami.

Second, hurricanes bring with them warm, moist air, which acts as their fuel. The result? An instability in the atmosphere — namely, a layer of warm air with slightly colder and less-moist air above it. This arrangement is unstable because the warm air wants to rise, since it is less dense than the cooler air. [50 Amazing Hurricane Facts]

Finally, hurricanes create wind shear, or an abrupt change in wind speed and direction over a short change in height. These alternating winds can create swirling air, called rolls. These vortices may then be flipped vertically — creating tornadoes — by thunderstorm updrafts, which are basically currents of warm, rising air, McNoldy told LiveScience in 2013.

Most hurricanes that make landfall create tornadoes, McNoldy said.

"It's pretty uncommon to not have tornadoes with these," he said. Tornadoes mostly form over land, instead of over water, because the land slows down surface-level winds, creating even more wind shear, McNoldy said. Tornadoes form wherever these pre-existing supercells happen to be, he added, but meteorologists are still unable to predict exactly where tornados will strike.

These twisters usually form in the swirling bands of rain outside the cyclone, typically in the "front-right quadrant" of the storm, McNoldy said. In other words, if the storm is moving north, you're most likely to find tornadoes to the northeast of the cyclone's eye, he said. In the case of Irma, which is moving currently in the north-northwest direction, the National Hurricane Center says tornadoes are a possibility in the southern, central and eastern portions of the Florida Peninsula.

Cyclone-spawned tornadoes are not fundamentally different from the tornadoes that form in the Great Plains. However, tornadoes born out of hurricanes tend to be less powerful, usually not exceeding a rating of EF2 on the Enhanced Fujita scale. Secondly, twisters that form in the Plains, like the tornado that struck Moore, Oklahoma, in 2013, get all of their ingredients from separate places. In the case of the Oklahoma tornado outbreak, for example, the warm air came north from the Gulf of Mexico, while the cold air came south from Canada. In the case of hurricanes, however, they provide all the required components for twisters themselves.

44. Assignment 2, Module 9: Storm Surge: https://www.nhc.noaa.gov/surge/

Storm Surge Overview

Contents

Introduction

Storm surge from tropical cyclones poses a significant threat to life and property along the coast and is currently the leading cause of fatalities from hurricanes. All locations along the U.S. East and Gulf coasts are vulnerable to storm surges. Storm surge can even travel up rivers and canals, reaching well inland from the coastline. The impacts from Hurricane Ian (2022) are a reminder of the widespread devastation storm surge can cause, attributing to 41 lives lost. Awareness of the destructive potential of storm surge is crucial for improving safety and resilience in coastal communities.

Aerial imagery from NOAA's National Geodetic Survey of damage in the Times Square district of Fort Myers Beach, FL, after Category 4 Ian struck the area.

What is Storm Surge?

Storm surge is an abnormal water level rise generated by a storm over and above the predicted astronomical tide. **Storm tide** is the water level rise due to the combination of storm surge and the astronomical tide. This rise in water level can cause extreme flooding in coastal areas, particularly when storm surge coincides with normal high tide, resulting in storm tides reaching up to 20 feet or more in some cases. However, to avoid confusion, "storm surge" is used interchangeably. Keep in mind neither definition includes wave action occurring on top of the surge, which can add additional feet to the overall water level.

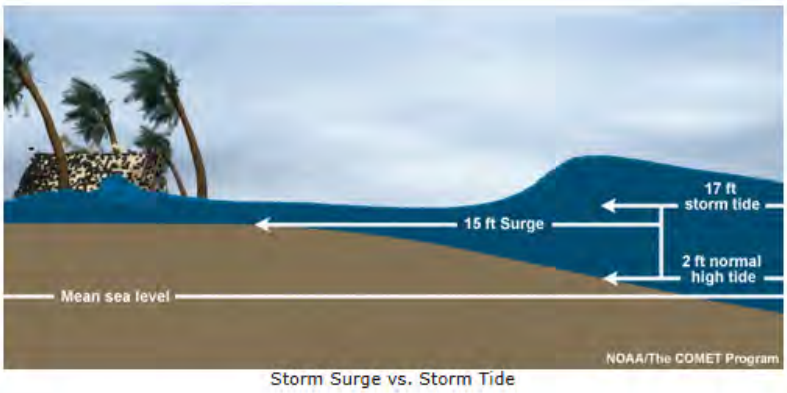

Storm Surge vs. Storm Tide

What Causes Storm Surge?

Storm surge is primarily caused by the strong onshore winds of a hurricane or tropical storm. The wind circulation around the eye of a hurricane causes a vertical circulation in the ocean. While in deep water, there is no indication of storm surge because there is nothing to interfere with this circulation. However, once the storm reaches the shallower waters near the coast, the vertical circulation is disrupted by the ocean bottom. The water can no longer move downward, so it begins to move upward and inland, resulting in storm surge.

Factors Impacting Surge

The maximum amount of storm surge for a particular location depends on several factors. Storm surge is a very complex phenomenon because it is sensitive to the slightest changes in **storm intensity, forward speed, size (radius of maximum winds), angle of approach to the coast, and the shape and characteristics of the coastline**. Below are examples of these factors and a hypothetical storm surge flooding graphic representing where inundation occurred and how high the water reached in the simulation.

- **Storm Intensity (Wind Speed)**

  Stronger winds will produce a higher storm surge. The two images below show potential storm surge inundation from two different storm intensities: A Category 2 storm on the left and a Category 3 storm on the right.

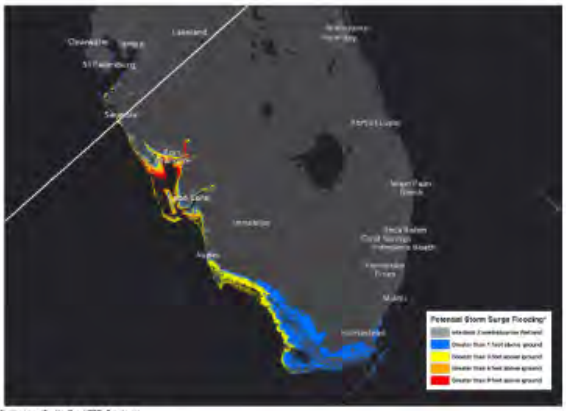

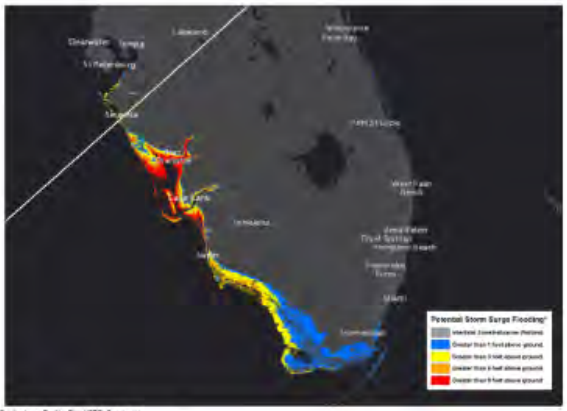

- **Forward Speed**

  While a faster storm will produce a higher surge at the immediate coastline, a slower storm will produce a surge that penetrates farther inland. The two images below show the surge generated by two hypothetical hurricanes hitting the western Louisiana coast: The faster storm is on the left, and the slower storm is on the right.

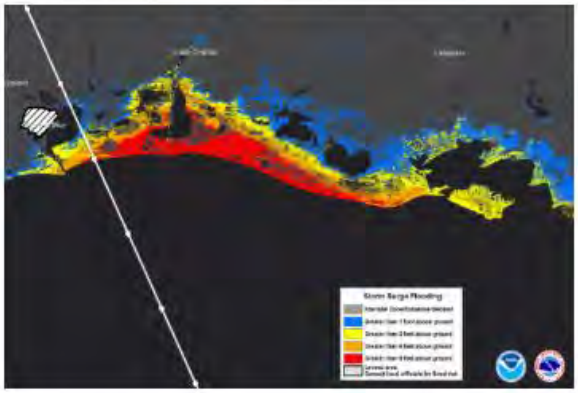

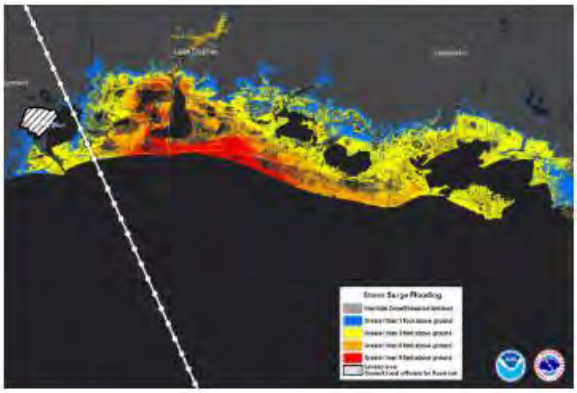

- **Size (Radius of Maximum Winds)**

  A larger storm will produce a higher surge. There are two reasons for this. First, the winds in a larger storm push on a larger ocean area. Second, the strong winds in a larger storm will tend to affect an area longer than in a smaller storm.

Surge animation of a small storm vs. a large storm pushing water (Click on image to play video)

- **Angle of Approach**

  The angle at which a storm approaches a coastline can affect the amount of storm surge pushed over land. A storm that moves onshore perpendicular to the coast is more likely to produce a higher storm surge than one that moves parallel to the coast or inland at an oblique angle. The image on the left shows a storm approaching at an angle; however, the image on the right shows a storm approaching nearly perpendicular to the coastline. Areas highlighted in red and orange increase around Staten Island and along the banks of the Hudson River between New Jersey and New York.

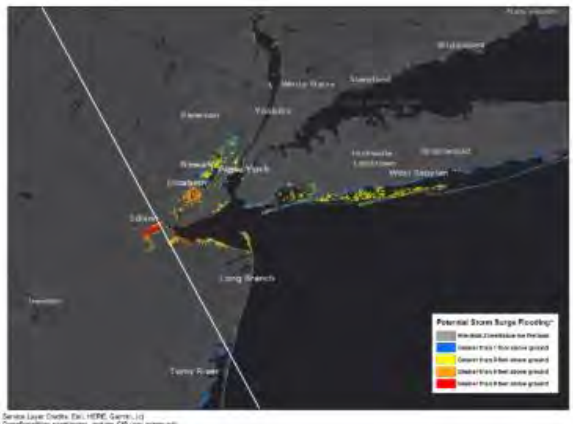

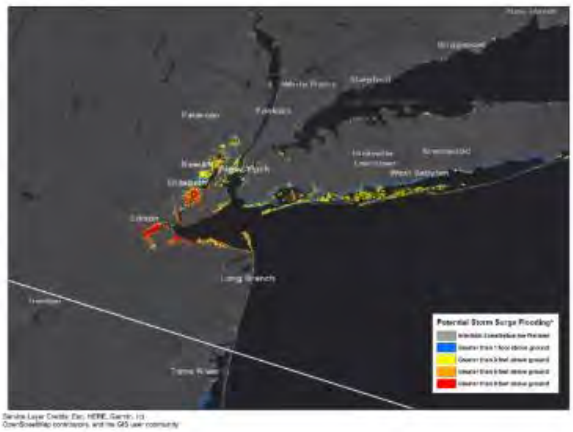

- **Width and Slope of the Ocean Bottom**

  A wide, gently sloping continental shelf will allow for a higher storm surge. In contrast, a narrow, steeply sloping shelf will allow more difficulty creating storm surge. Areas along the Gulf Coast, especially Louisiana and Mississippi, are particularly vulnerable to storm surge because the ocean floor gradually deepens offshore.

  Conversely, areas along Florida's southeast coast have a shelf that drops off very quickly, making it less vulnerable to storm surge.

Surge animation of a steep continental shelf vs a gently sloping continental shelf (Click on image to play video)

- **Shape of the Coastline and Local Features**

  Storm surge will be higher when a storm makes landfall on a concave coastline (curved inward, such as Apalachee Bay in Florida) than a convex coastline (curved outward, such as the Outer Banks of North Carolina). Storm surge is also highly dependent on local features and barriers that affect the flow of water. A good example is the coast of North Carolina, which has complex features such as barrier islands, inlets, sounds, bays, and rivers.

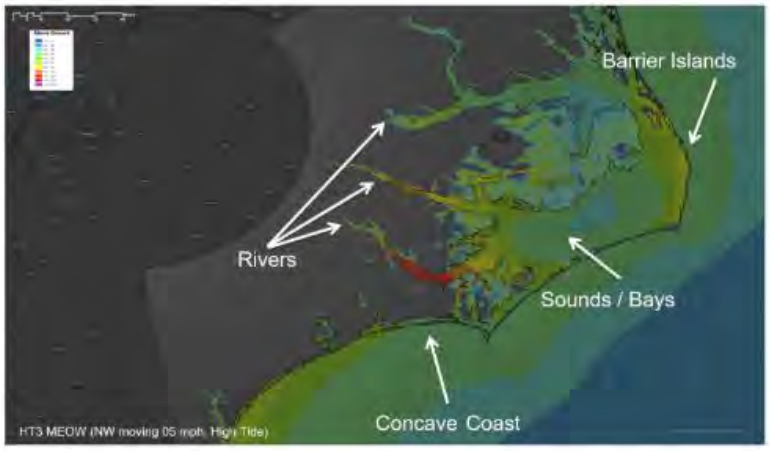

Total Water Level

In reality, storm surge only makes up a part of what causes water levels to rise along the coast during a hurricane. Tides, wave setup, and freshwater flow all contribute to the total water level rise.

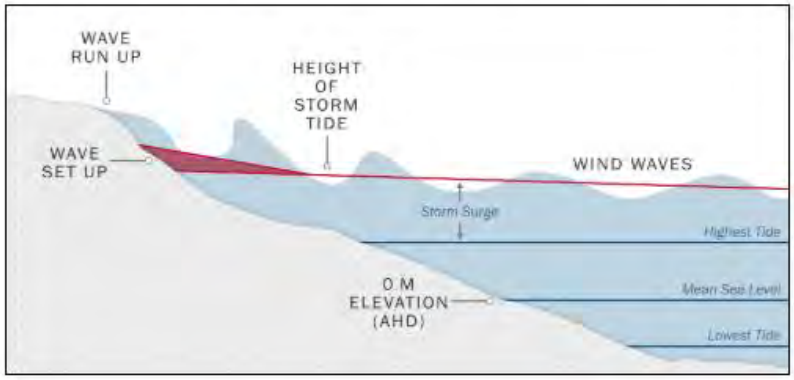

Storm Surge can be Dangerous or Life-Threatening

Adding to the destructive power of surge, battering waves may increase damage to buildings directly along the coast. Water weighs approximately 1,700 pounds per cubic yard; extended pounding by frequent waves can demolish any structure not specifically designed to withstand such forces. The two elements work together to increase the impact on land because the surge allows waves to extend inland.

Additionally, currents created by tides combine with the waves to severely erode beaches and coastal highways. Buildings that survive hurricane winds can be damaged if erosion undermines and weakens their foundations. In confined harbors, the combination of storm tides, waves, and currents can also severely damage marinas and boats. Saltwater intrusion in estuaries and bayous endangers public health, kills vegetation, and can send animals, such as snakes and alligators, fleeing from flooded areas.

Additionally, currents created by tides combine with the waves to severely erode beaches and coastal highways. Buildings that survive hurricane winds can be damaged if erosion undermines and weakens their foundations. In confined harbors, the combination of storm tides, waves, and currents can also severely damage marinas and boats. Saltwater intrusion in estuaries and bayous endangers public health, kills vegetation, and can send animals, such as snakes and alligators, fleeing from flooded areas.

45. Assignment 2, Module 9: Hurricanes and Extreme Rainfall: http://www.wpc.ncep.noaa.gov/research/mcs_web_test_test_files/Page1637.htm

Hurricanes and extreme rainfall.

Hurricanes, tropical systems and depressions pose a special forecast problem. Tropical storms and hurricanes or their remains are capable of producing extremely heavy rainfall and often produce serious flooding and flash flooding. A presentation by Rusty Pfost documented some of the more impressive rainfall associated with tropical cyclones. He notes that rainfall rates of up to 6 inches per hour have been reported and that 43 inches of rain was reported in 24 hours at Alvin, Texas as a result of the remains of Tropical Storm Claudette. Flooding resulting from the rainfall associated with tropical systems accounted for 292 deaths during the 1970-1999 which was 59% of the total deaths from tropical systems (Rappaport et al. 1999).

HPC quantitative precipitation forecasts are to a certain extent dependent of the track of the system provided by the Tropical Prediction Center. Forecasts are usually modeled to the NHC track with amounts to a certain extent dependent on the size of the storm and its speed. However, the amount of rainfall that a storm produces does not appear to be related to the intensity of the storm. The Rappaport et al. study suggests that there is no apparent relationship between the intensity of the tropical cyclone at landfall and the number of rainfall induced deaths that occur because of the storm.

The heaviest rainfall associated with tropical systems usually falls along or near the coast and typically occurs slightly to the right of the track of the storm. A 46 storm composite of the average 48 hr rainfall is offered below (Goodyear 1968). The same study indicates that there is about a 50% chance that the period of heaviest rainfall will occur in the 12-h period starting 6 hours prior to landfall and ending 6 hours after landfall. The 6 hour period just pri ly to receive the maximum 6 hourly

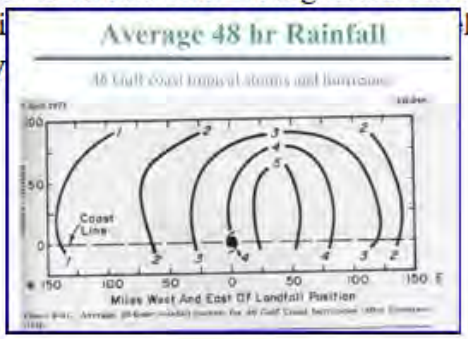

Another study, done more recently by Rusty Pfost, for hurricanes with a landfall in Florida, found that the maximum rainfall was usually a little to the east of the storm. However, Pfost found a few exceptions (see figure below). The maximum rainfall usually falls within the eyewall or with the spiral bands and occur where the frictional convergence is maximized on the east side of the storm. Unfortunately, some storms are highly asymmetric and have more convection on the west side of the storm than the east. Others may be highly sheared with most of their convection located well east of the center.

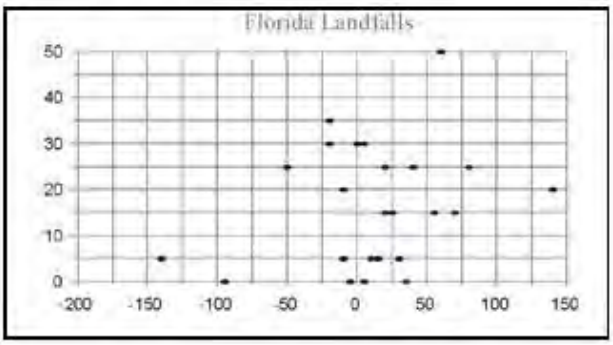

Forecasters in the in the 60s and 70s often used a rule of thumb (**the Kraft rule of thumb technique**) to estimate the rainfall associated with tropical systems.

Maximum rainfall (inches)=100/speed (in knots)

Northern Gulf coast storms

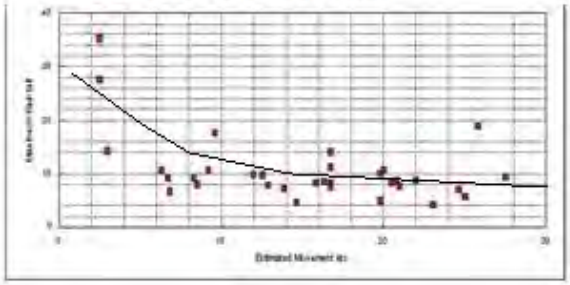

Florida landfall storms

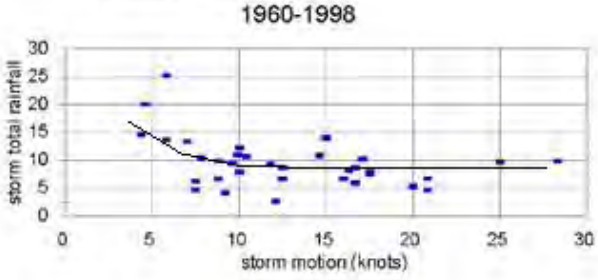

The two graphs above argue that forecasters should not wed themselves to the Kraft technique. The second fastest moving northern Gulf of Mexico landfall storm produced the third highest precipitation maximum of all northern Gulf storms. On both graphs above, a curve has been drawn to try to best fit the points. The slope of both curves is very flat except at speeds below 10 knots where the slope steepens. The lack of a well defined relationship between the speed of the cyclone and its associated precipitation maximum should come as no surprise since the Kraft method fails to take into account the following: 1)the size of the storm, 2) the amount of convection associated with it, 3) that some storms are asymmetric due to shear and 4) the impact of nearby fronts. The graphs suggest that the maximum storm total rainfall will be in the 5 to 10 inch range for storms moving between 6 and 30 knots. The rainfall maxima for storms moving slower than 6 knots was usually above 15 inches.

The Satellite Tropical Rainfall Potential (TRaP) technique provides another more scientifically based method of estimating the rainfall potential of a tropical cyclone as it makes landfall (Kidder et al. 2005). Equation used to determine the rainfall using the TRaP technique is provided in the figure below.

Images from Scofield, Kuligowski

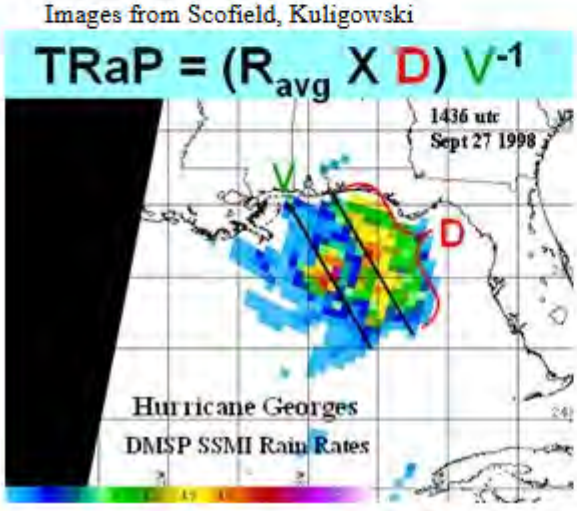

Where R_{avg} is the hourly rainfall rates measured by the satellite sensors, D is the measure length along the axis of the storms movement and V is the velocity of the storm. The speed and direction that TRaP uses for its rainfall predictions comes from the NHC forecast tracks.

TRaP rainfall forecast

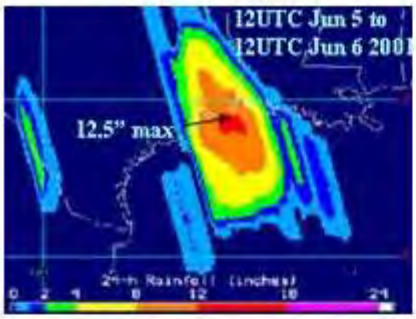

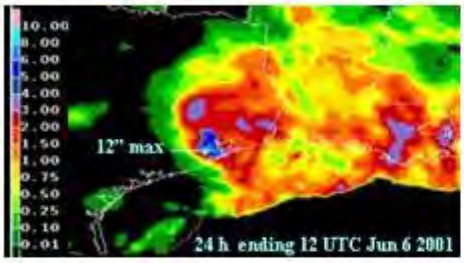

Multi-sensor observed rainfall analysis

Eta model forecast

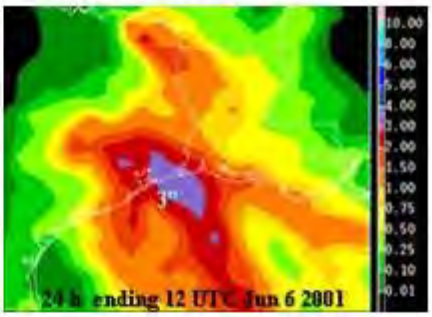

The technique's precipitation projections were quite a bit better than the Eta's. If a storm changes little in character and the NHC track is fairly accurate, the TRaP rainfall should provide a pretty good estimate of the system's rainfall potential at landfall.

TRaP assumes that the rainfall rates measured by the satellite sensors are accurate, that the precipitation rates and distribution of precipitation within and around the storm will remain the same with the same. It fails to take into account changes due to eyewall replacement, changes that are taking place in the environment around the storm that may impact it. For example, dry air being entrained into the storm or changes in the shear, both of which can impact the structure of the storm.

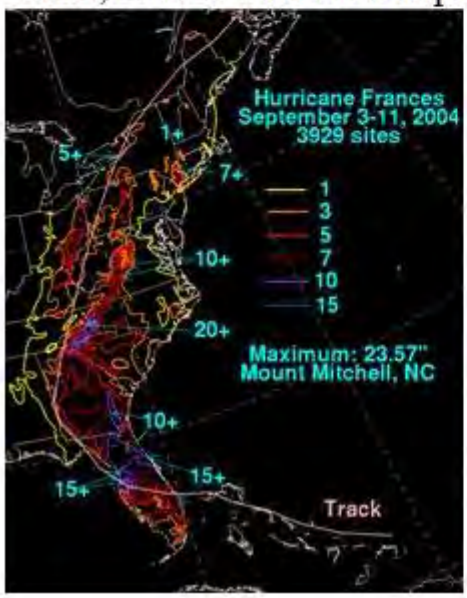

Roth (personal communication) has noted that there are a number of factors that modulate the distribution of rainfall associated with tropical cyclones. Storm size, morphology, track, interaction with synoptic and mesoscale features and even the time of day can impact the precipitation associated with the storm. He offered the figure at left to illustrate how complex the precipitation pattern can be. The heaviest rainfall remained on the east side of the storm as it moves across southern Georgia.

As it approached the Appalachains,[illegible] strong flow into mountains produced very heavy rainfall along their east slopes and a minimum on the west side of the mountains (this minimum was very pronounced over Virginia).[illegible] However,[illegible] as the remains turned northeastward another maximum formed along a weak front associated with the entrance region of an upper level jet streak.[illegible] Here, the maximum ended up to the west of the storm track.

As illustrated by the figure above,[illegible] how to forecast the distribution of rainfall associated with a tropical system becomes more difficult once it moves inland and turns towards the north or northeast and gains latitude.[illegible] The chances of entraining dry air into some quadrant of the storm increases as it moves away from the coast, which increases its chances of becoming asymmetric.[illegible] Also,[illegible] as a storm turns northward, it often starts to interact with a mid-level trough. When this occurs,[illegible] the axis of heaviest precipitation then often falls to the west of the track of the surface center.[illegible] The proximity to a mid-level trough and increase in latitude raise the chances that the storm might interact with a frontal boundary.

From Bosart and Dean 1991

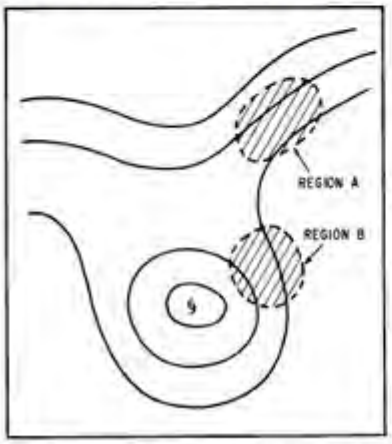

FIG. 2. Schematic of midtropospheric streamlines associated with possible tropical-storm-related flooding.

Bosart and Dean (1991) have offered a schematic of the mid-tropospheric streamlines associated with possible tropical storm related flooding.[illegible] The southern area is associated with the forcing of the storm itself,[illegible] while the northern area is usually associated with moisture interacting with a frontal boundary.[illegible] Strong frontogenesis is often occurring within this area.[illegible] Where the heaviest rainfall will be located relative to the[illegible] storm is strongly related to its structure.[illegible]

Precipitation primarily left of Track storms

A study by Atallah and his colleagues (2007) composited 14 cyclones that had the bulk of their rainfall occur to the west of the track of the cyclone circulation. Six of the storms made landfall along the Gulf of Mexico west of the Appalachians. Their composite argues strongly that storms that have most of their rainfall distributed on the west side of storm s track interact with upper level trough and potential vorticity maximum in a synergistic way.

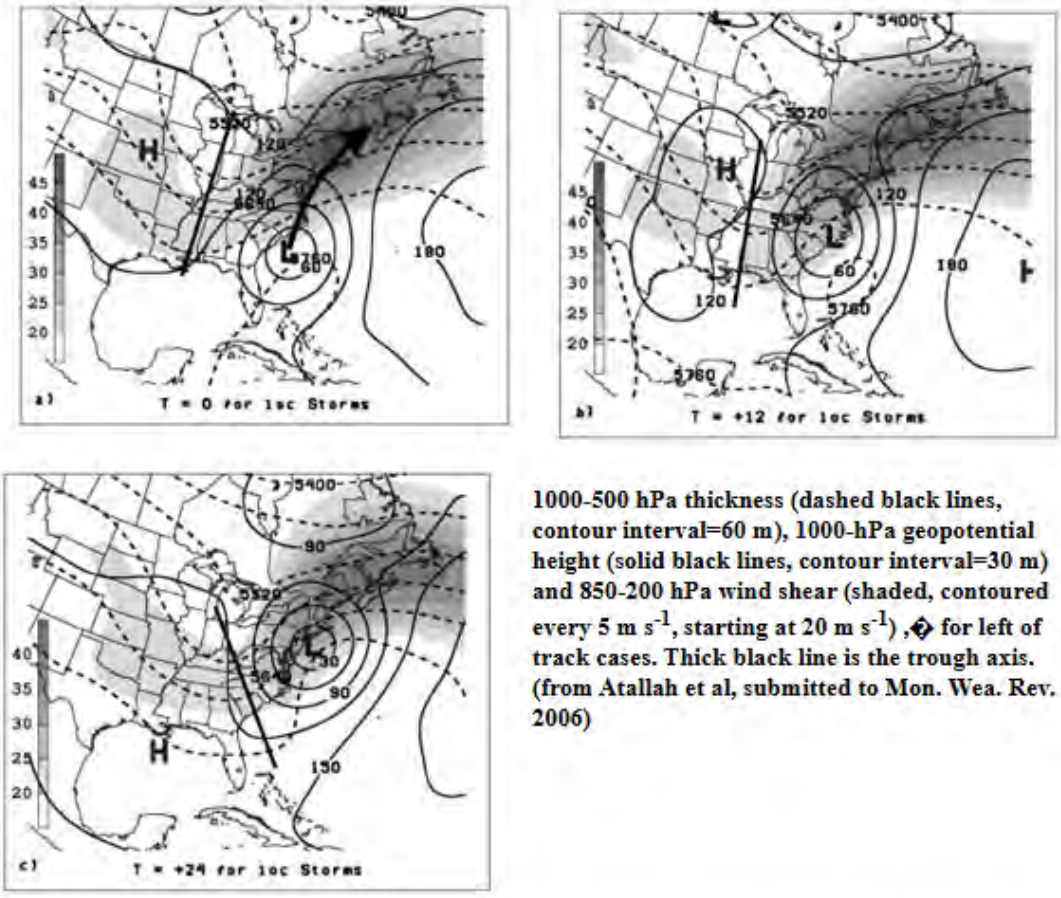

1000-500 hPa thickness (dashed black lines, contour interval=60 m), 1000-hPa geopotential height (solid black lines, contour interval=30 m) and 850-200 hPa wind shear (shaded, contoured every 5 m s^{-1}, starting at 20 m s^{-1}) , for left of track cases. Thick black line is the trough axis. (from Atallah et al, submitted to Mon. Wea. Rev. 2006)

Storms undergoing a transition to becoming extratropical typically have their heaviest rainfall to the west of the track. The 850-200 hPa shear suggests that there was a strong jet streak present to the north or northwest of the cyclone and implies that the storm was located near the right entrance region of a jet streak where frontogenesis is favored. The composite also suggests that the axis of the upper-level trough shifts from having a slight positive tilt or neutral one to having a negative tilt as the storm undergoes extratropical transition (ET).

Agnes illustrates one way in which a tropical storm or hurricane may interact with a trough.◆ If the upper-level trough has a pronounced negative tilt,◆ the hurricane circulation may phase with the trough and be absorbed by the deepening 500-hPa trough.◆ When this occurs,◆ the surface low may re-intensify through baroclinic processes. The surface low also may almost stall or loop as it is pulled into the 500-hPa circulation.◆◆ Note how the gradient of the isotherms tightens between 0000 UTC and 1200 UTC at 500-hPa and the surface.◆◆

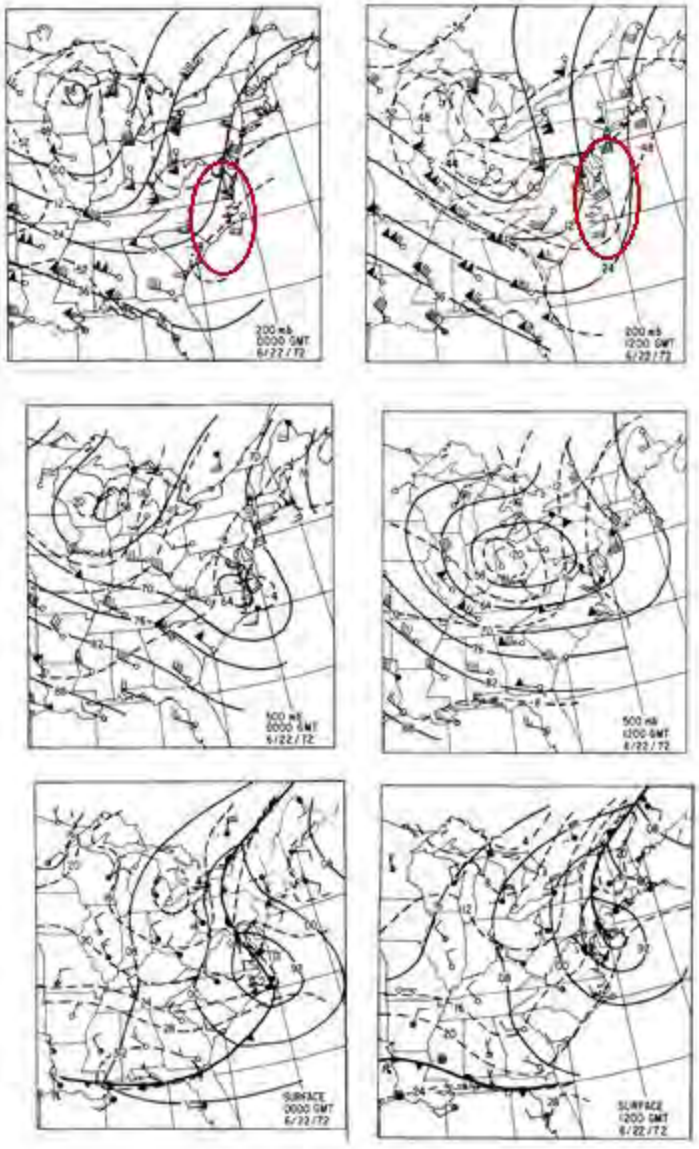

From Bosart and Dean, 1991

Strong frontogenesis was occurring with the heaviest rainfall located along and to the west of the surface trough associated with the front.◆ The front on the north side of the storm often becomes stationary for a period.◆ This adds to the systems potential to produce an extended period of heavy rainfall. The figure below shows the movement of the front. Note how slowly it moves over Pennsylvania.◆

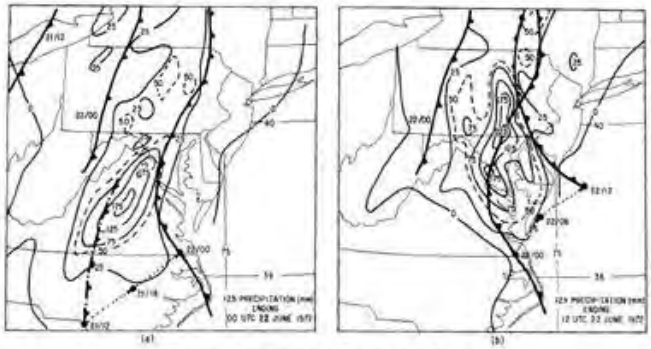

From Bosart and Dean, 1991

Such strong phasing between a tropical system and a strengthening negative tilted mid-level trough to its west is unusual.◆ The 200-hPa analyses above both have red ovals which roughly depict the area where the right rear quadrant of the north-south oriented jet streak is juxtaposed with the left exit region of another jet streak to the south.◆ Uccellini and Kocin (1987) have documented that similar jet streak configurations are conducive to the deepening of east coast snowstorms.◆◆

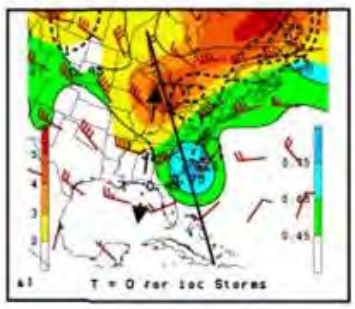

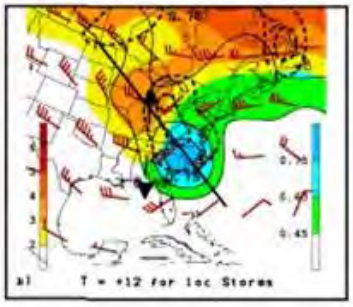

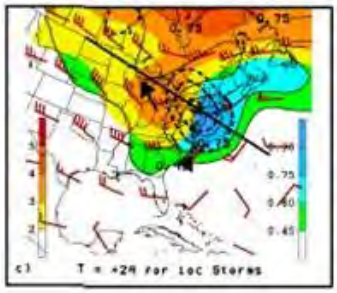

850-700-hPa PV (shaded in cool colors every 0.15 PVU starting at .45 PVU where 1 PVU=10^{-6}Kkg^{-1} m^2 s^{-1}) and 300-200-hPa PV (shaded in warm colors every 1 PVU starting at 2 PVU) and winds (barbs, knots convention).◆◆ Thick dashed contours indicate areas of positive PV advection in the 300-200 hPa layer.◆ The thick black line represents the axis of cross sections that except for at T+24 are not shown.◆ The arrows define the axis of the upper trough.◆ (from Atallah et al, submitted to Mon. Wea. Rev. 2006)

The potential vorticity (PV) structure for the LOT storms evolves very much like an east coast snowstorm. The upper level PV maximum approached a low level center with each center initially having their own area of PV advection. However, as the distance between them decreases, the advection areas merge together, generally to the north and northwest of the tropical cyclone center.

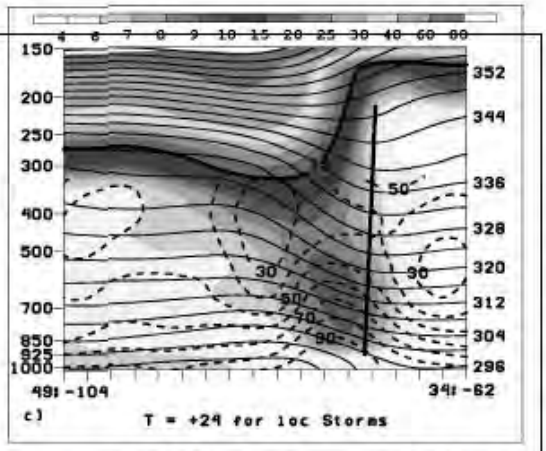

Cross section of PVU (shaded, starting at .4 PVU as given by the color bar), isentropes (thin solid lines, contoured every 3oK), relative humidity (dashed line contoured every 10%) for line onT+24 shown above . The thick solid line indicates the position of the warm core associated with the tropical system. from Atallah et al, submitted to Mon. Wea. Rev. 2006

Kocin and Uccellini (2004) have noted a similar evolution of the PV fields during many East coast snowstorms and note the synergistic interactions between the upper level dynamical processes (the PV and jet streak evolution) and the low level diabatic processes in the development of east coast snowstorms. A similar interaction and feedback takes place in tropical system undergoing extratropical transition (ET).

Hurricane Floyd is a classic case where ET is taking place, and not surprisingly, the bulk of its rainfall occurred to the left of the track.

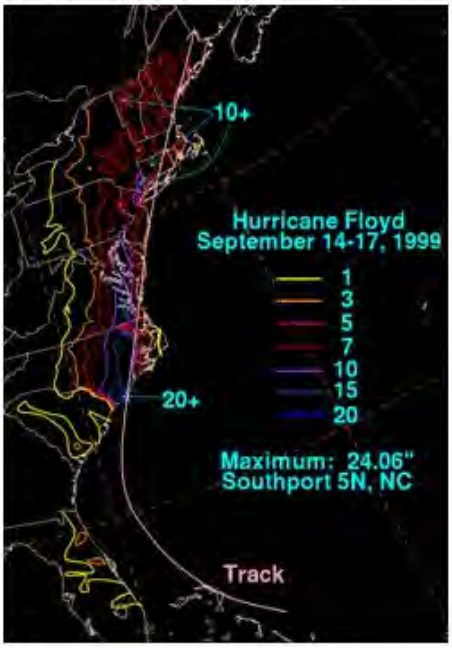

Storms interacting with fronts tend to be some of the wetter storms and can produce heavy rain even as though the remains of the storm may be fairly fast moving. Neither the Kraft rule of thumb or precipitation forecast based on TRaP will work well with transitioning storms. The operational models sometimes handle the precipitation well but at other times do not do a good job. They often have problems in handling the latent heating and associated ridging (Atallah et al, 2006).

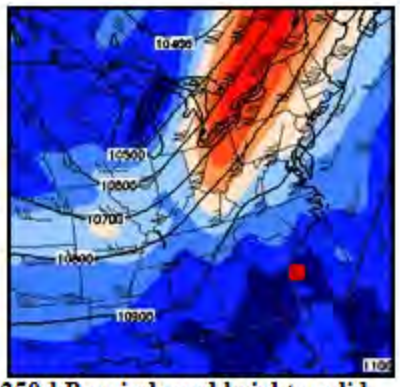

250-hPa winds and heights valid 0000 UTC 16 Sept 1999, the red dot indicates the positions of Floyd

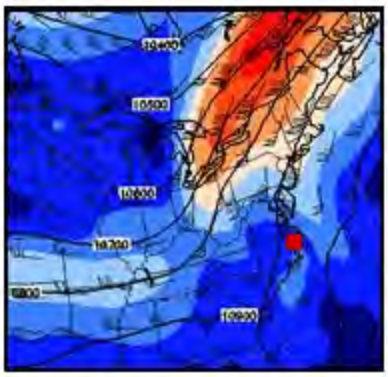

250-hPa winds and heights valid 1200 UTC 16 Sept 1999, the red dot indicates the positions of Floyd

At 0000 UTC, as Floyd moved northward (the red dot on the figure shows its position), a strong positively tilting upper level trough was moving eastward in the vicinity of the Great Lakes and associated upper level jet streak was located to its east. Note that as the upper trough shifted eastward and the distance between the trough and Floyd decreased, the geopotential heights across eastern New England actually rose and the flow across the region became anticyclonic suggesting that the latent heating associated with Floyd was feeding back and was altering the pattern. The half wavelength between the base of the trough and this shortwave ridge was shortening which increased the upper level divergence. This is a fairly common characteristic of storms undergoing extratropical transition.

Another important thing to note about the pattern is the location of Floyd along the right entrance region of the upper level jet streak, one that has a significant along stream variation. The strong along stream variation suggests two things: 1) that the lower branch of the associated transverse circulation will be acting in concert with the low level circulation associated with Floyd to enhance any thermal gradient across the region, 2) will act to increase the upper level divergence across the region.

Table of contents Next Page

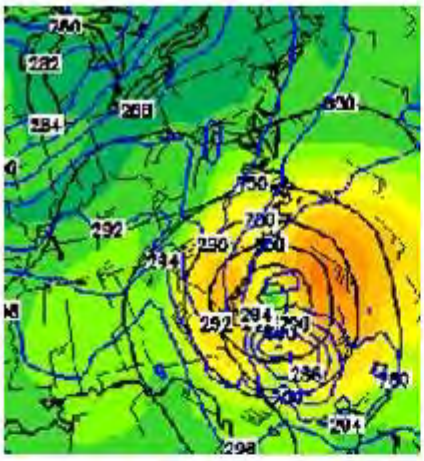

925-hPa height and winds (black), temperature (blue lines, °K),• valid 0000 UTC 16 Sept 1999

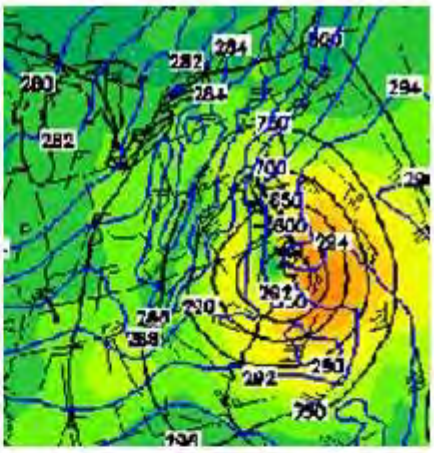

925-hPa height and winds (black), temperature (blue lines, °K),• valid 1200 UTC 16 Sept 1999

A pool of cooler drier air is usually associated with mid- and upper level troughs, especially the stronger ones.• Note the almost cold air damming look to the isotherms over Virginia and the Carolinas.• Clearly a front was present and showed up on the 925-hPa 0000 UTC Sept. 16 analysis.•• As the Floyd interacted with the trough and moved north,• the thermal gradient tightened to its north and east.• Strong frontogenesis and isentropic lift was taking place along the thermal boundary

Loop courtesy of Rod Scofield

The 4-panel GOES-8 loop shows water vapor imagery (top right) and three goes sounding channels.• The two bottom panels of the loop are sensitive to mid- (left) and low-level (right) moisture.• Note how the clouds increase to the west and northwest of the storm and that the heavy rainfall across North Carolina begins well in advance of Floyd.•

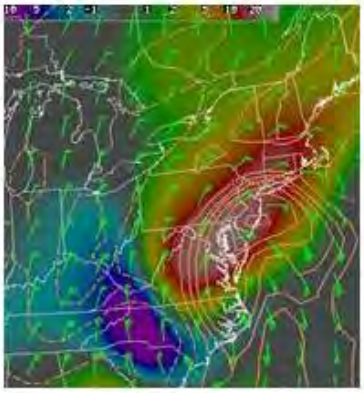

925-hPa winds, frontogenesis (orange contours) and 700-hPa omega (upward motion is red and white area) valid 1200 UTC 16 Sept

Image from Kelsch lecture

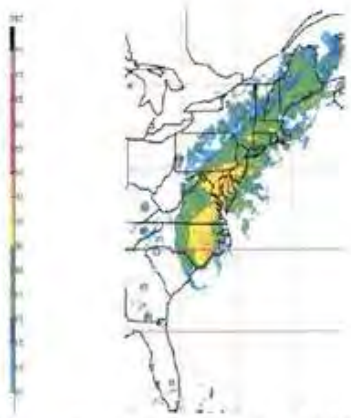

Composite radar reflectivity valid 1200 UTC 16 Sept. From Atallah and Bosart 2003.

The radar echoes and region of rainfall elongated along the frontal band. Such an elongation of the precipitation pattern is typical when a front is present. The axis of precipitation of left of track (LOT) storms often is aligned parallel to the movement of the storm which increases the period of heavy rainfall. Bosart (personal commuciation) believes that the LOT cases on average produce a larger total volume of rainfall than right of track (ROT) cases. The idea is supported by two six-case composites (shown below) that one of his students, Josh Darr, assembled for his M.S. thesis at SUNY Albany.

Strong extra-transition 6 case composite cases, precipitation contoured in mm.

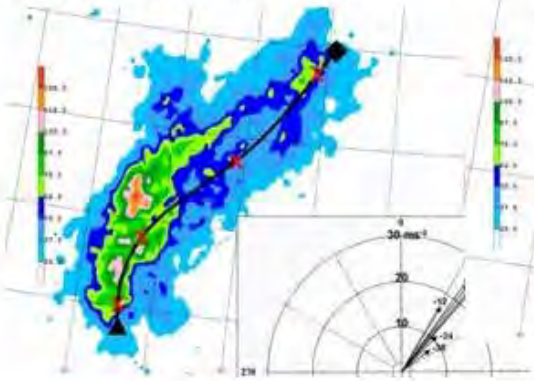

Composite of non-transition cases, precipitation contoured in mm.

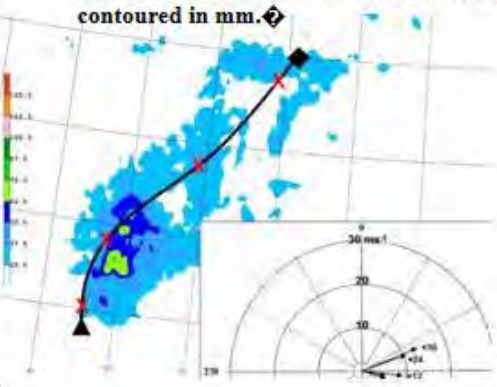

Precipitation primarily right of the track (ROT).storms.

The composites of storms with the bulk of their precipitation to the right of the track from the Atallah et al. study are shown below. There are several notable differences in the ROT composite from the pattern typically associated with LOT storms. The axis of the 850-200-hPa shear is typically oriented more westerly than the more north-south oriented axis associated with the approaching trough during LOT cases. Also, the location of the upper level jet streak is much farther removed for ROT cases than for LOT cases. The baroclinic zone as shown by the leading edge of the 1000-500 hPa thickness is also much farther removed from the storm. Also, implied 1000-hPa circulation is much weaker, especially on the northern and west side of the system where there is a much weaker gradient implying that the easterly low level winds are quite a big weaker for ROT storms than LOT. storms.

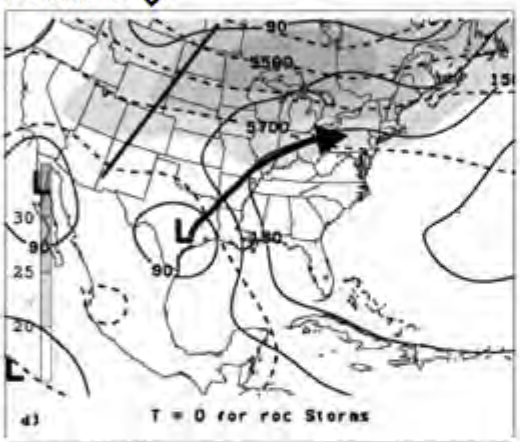

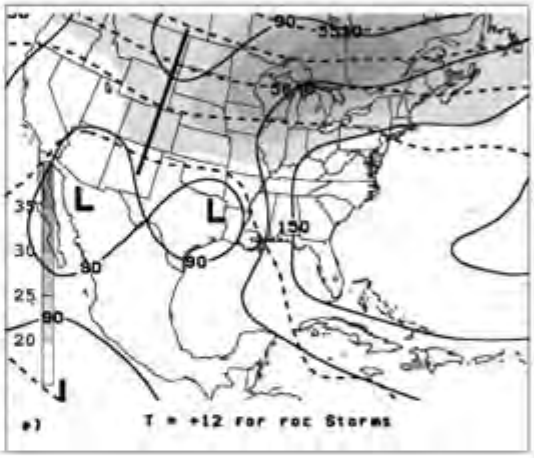

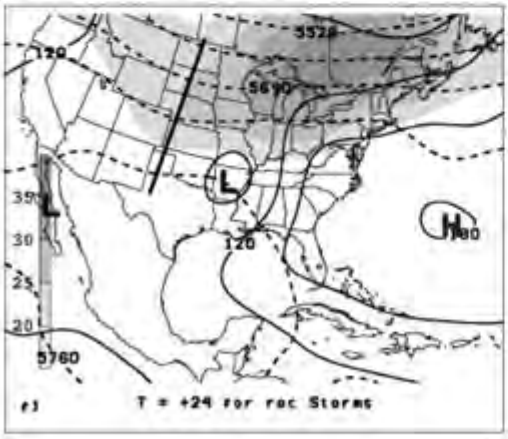

1000-500 hPa thickness (dashed black lines, contour interval=60 m), 1000-hPa geopotential height (solid black lines, contour interval=30 m) and 850-200 hPa wind shear (shaded, contoured every 5 m s^{-1}, starting at 20 m s^{-1}) , for right of track cases. Thick black line is the trough axis. (from Atallah et al, submitted to Mon. Wea. Rev. 2006)

The more zonal look to the pattern helps keep any northern stream PV anomaly well removed from the low level PV center associated with the tropical system. The right hand composites lack the negative tilt.

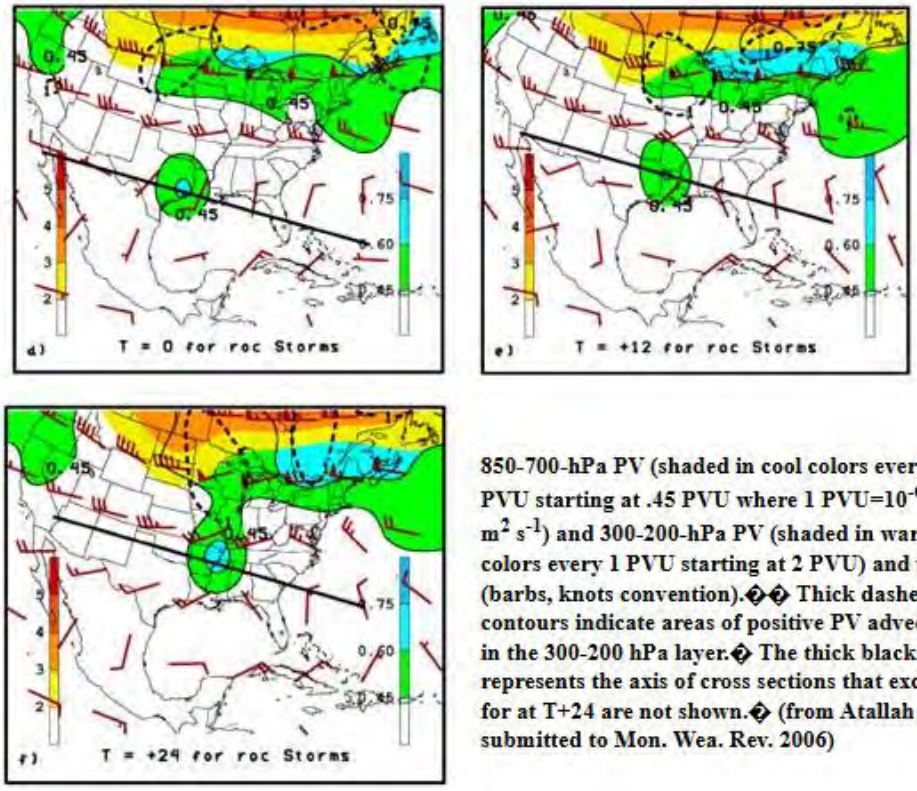

850-700-hPa PV (shaded in cool colors every 0.15 PVU starting at .45 PVU where 1 PVU=10^{-6}Kkg^{-1} m^2 s^{-1}) and 300-200-hPa PV (shaded in warm colors every 1 PVU starting at 2 PVU) and winds (barbs, knots convention).�� Thick dashed contours indicate areas of positive PV advection in the 300-200 hPa layer.� The thick black line represents the axis of cross sections that except for at T+24 are not shown.� (from Atallah et al, submitted to Mon. Wea. Rev. 2006)

Don't be fooled by the composite's location of either LOT or ROT cases. 11 of the 16 cases for the ROT composite made landfall over the Gulf of Mexico and 5 made landfall along the east coast, usually near the Georgia-South Carolina border.� 8 of the storms transitioned from a ROT storm to a LOT storm.�

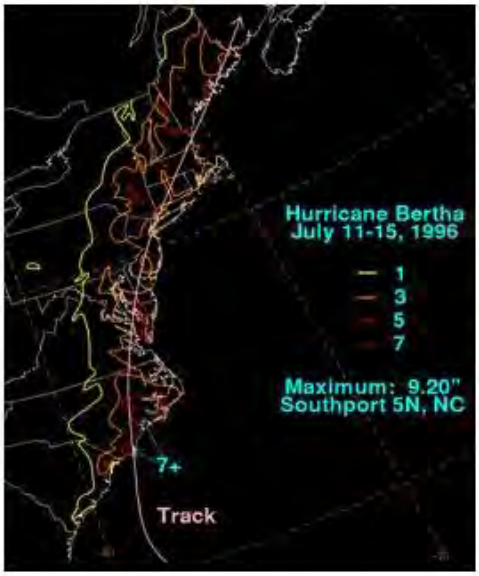

The track and speed of Hurricane Bertha were very similar to that of Floyd making it an interesting storm to study since it rainfall amounts and rainfall distribution were different than occurred during Bertha.� The axis of heaviest rainfall during Bertha was to the right of the track across the southern Middle Atlantic States but shifted to the west side from New Jersey northward.�

Bertha and Floyd were both Category 2 hurricanes at landfall. However, the circulation associated with Bertha was smaller. An even bigger difference between the systems was the thermal structure around the storm.

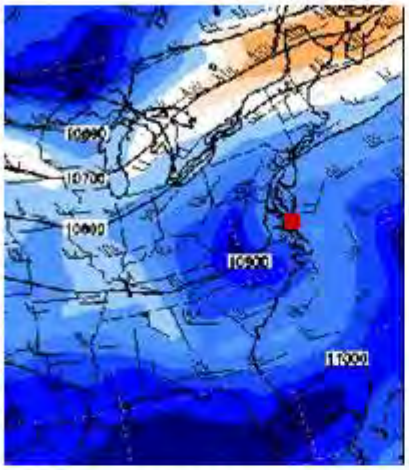

250-hPa winds and heights valid 0000 UTC 13 July 1996, the red dot indicates the positions of Bertha

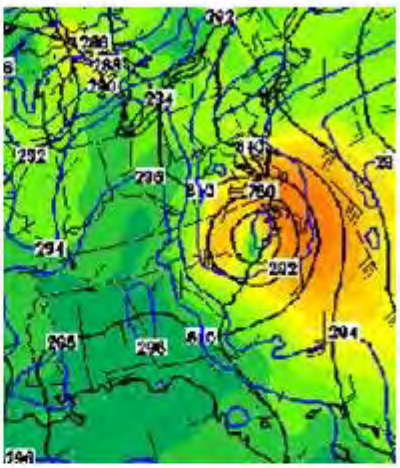

925-hPa height and winds (black), temperature (blue lines, ^{o}K), valid 0000 UTC 13 July 1999

During Bertha the 292^{o}K isotherm dipped southward around Bertha which helped make the isotherms almost parallel to the winds to the north and northeast of Bertha (see figure above). At 00 UTC 13 July, no frontal boundary was present near the storm. The lack of warm advection suggested that the heavy rainfall would be confined to near the center or to feeder bands on its east side. Also, the jet was well removed from the storm with generally westerly flow across the storm, the latter suggests that the storm may have been affected by shear. Also, the orientation of the upper level jet was more west to east than north to south when compared to Floyd. The implied shear would tend to keep the convection on the east side of the system and at that time, the heaviest rainfall was located to the east of storm. The structure of the storm is an important component in predicting the rainfall with a storm.

Rainfall maximum to right of track composite (ROT)

Rainfall maximum to left of track composite(LOT)

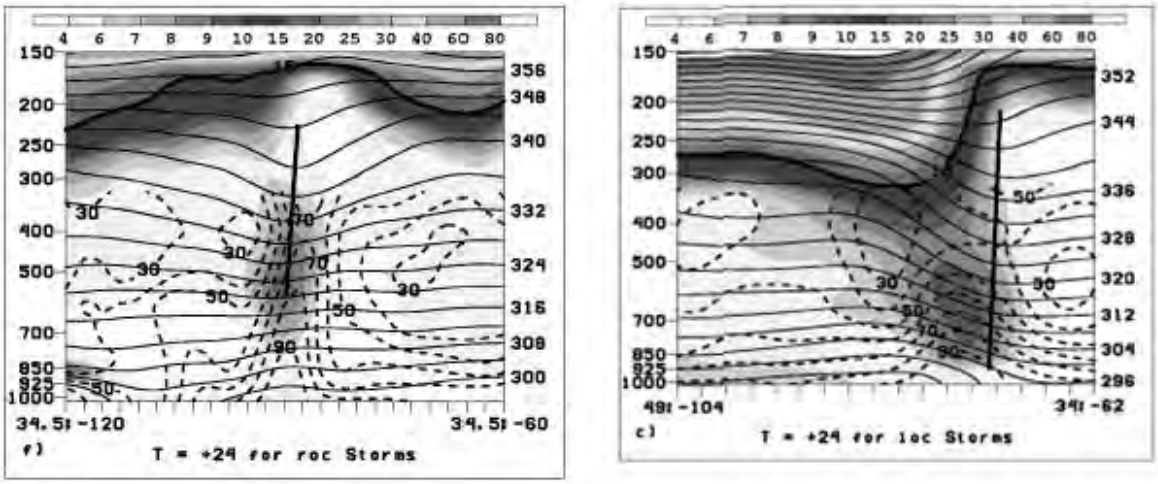

Cross section of PVU (shaded, starting at .4 PVU as given by the color bar), isentropes (thin solid lines, contoured every 3oK), relative humidity (dashed line contoured every 10%) for line onT+24 shown above .• The thick solid line indicates the position of the warm core associated with the tropical system.

The Atallah et al. composite cross section for ROT versus LOT shows several marked differences.• The area of high relative humidity on the ROT cases is deeper than on the LOT case composite suggesting upright convection might be the dominant type of precipitation.• The warm core (thick black line) on the ROT composite is not as well defined at lower layers as on the LOT composite and there is actually a weak cold pool at the lowest layers.• The authors caution that the cold pool may be a function of the lack of resolution of the reanalysis data.• However,• the same cold pool was present in the NARR data during the period when the bulk of the rainfall was located to the right of Bertha•s track so the cold pool is probably present during at least a portion of the ROT cases.

Back to Bertha,• the thermal structure of the system slowly changed during the next 15 hours and by 15 UTC July 13, a thermal boundary developed which promoted low level warm advection (the area enclosed by the thick back line).•• By then,• the 925-hPa absolute vorticity (red lines) looks like it is being captured by a weak negative tilted trough (axis is defined by magenta line).• The upper trough and low level thermal boundary are both much weaker than during Floyd.•

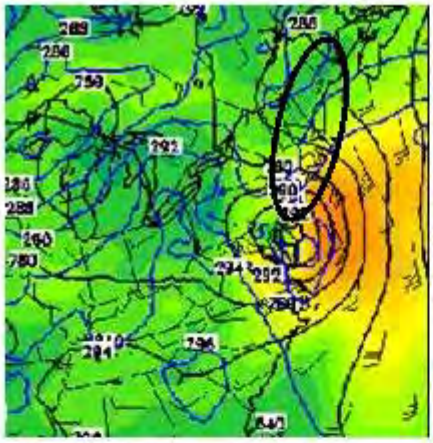

925-hPa height and winds (black), temperature (blue lines, °K),
valid 1500 UTC 13 July 1999

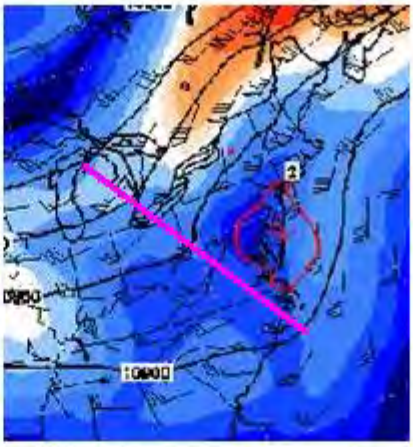

250-hPa winds and heights valid 1500 UTC 13 July 1999

In summary, the structure of a storm seems to determine whether the heaviest rainfall will occur to the left or right of the track. Storms interacting with upper level troughs, jet streaks and baroclinic zones tend to have their precipitation transition to the left side of the track. There is a deep frontal boundary clearly defined in the isentrope field on the LOT composite. No frontal structure is evident on the ROT composite.

Another possible useful tool is the cyclone phase space diagram developed by Hart (2003). The diagram provides a tool to objectively diagnose whether the system is warm or cold core and whether the thermal structure will promote asymmetry. A sample of the product is shown below. The ordinate measures the symmetry of the system while the abscissa measures the thermal structure and whether the system has warm or cold core structure. The location of the storm at various times is given at the upper right hand corner of the figure.

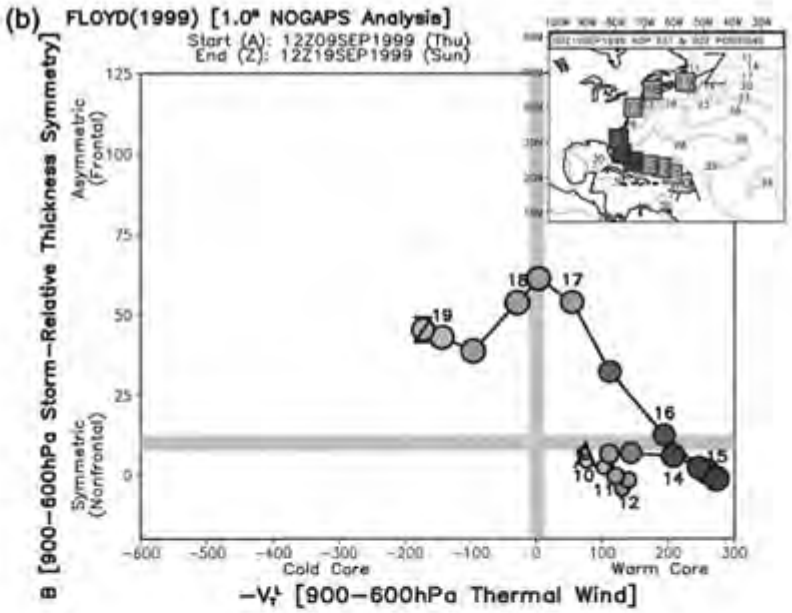

From Evans and Hart 2003

Note when Floyd was labeled with the number 16 it crossed the line between being a symmetric and asymmetric warm core system and that during the next 12 hours the storm became increasingly asymmetric.◆ This was also about the time when the bulk of the precipitation transitioned to the west side of the track.◆ The phase space diagrams provide a quick way to investigate the structure of a storm using model forecasts of the storm.◆◆ When the diagram starts indicating that a storm is starting to become asymmetric,◆ look closely at model diagnostic fields to see whether the storm is starting to transition.◆ Also look for fronts and jet streaks to that might help focus the precipitation to the left of the storms track.◆◆◆

46. Assignment 2, Module 9: Hurricanes and Mudslide:
https://www.sciencedaily.com/releases/2014/07/140721123922.htm

Storm-triggered landslides: Examining causes of devastating debris flow

Date: July 21, 2014

Source: Wiley

Summary: Storm-triggered landslides cause loss of life, property damage, and landscape alterations. For instance, the remnants of Hurricane Camille in 1969 caused 109 deaths in central Virginia, after 600 mm of rain fell in mountainous terrain in 6 hours. More recently, on 8 August 2010, a rainstorm-induced landslide devastated the Chinese county of Zhouqu, causing more than 1000 deaths. A new modeling study examines the multiple factors, both natural and human caused, that came together to produce this event.

Storm-triggered landslides cause loss of life, property damage, and landscape alterations. For instance, the remnants of Hurricane Camille in 1969 caused 109 deaths in central Virginia, after 600 mm of rain fell in mountainous terrain in 6 hours. More recently, on 8 August 2010, a rainstorm-induced landslide devastated the Chinese county of Zhouqu, causing more than 1000 deaths. A new modeling study by *Ren* examines the multiple factors, both natural and human caused, that came together to produce this event. The triad of storm-triggered landslides is geological condition, surface loading and vegetation roots, and extreme precipitation.

Extreme precipitation can be explained by three factors: low-level moisture buildup, conditional instability, and a lifting mechanism. When several factors (e.g., El Niño years, hurricane remnants, lifting mechanisms (e.g., orography, cold fronts, jets, and differential heating from land cover contrast), and weather pattern phase-lock) work in synergy in a region, extreme precipitation may occur.

Using a multiple-phase scalable and extensible geofluid model, the author considered geological features of the region, as well as an earthquake, drought, deforestation, and topsoil erosion before the triggering storm. Previously, drought conditions created cracks and crevices in the surface; these cracks and crevices were deepened by the 2008 *M*7.9 Wenchuan earthquake.

Another key factor in setting up the conditions for the landslide was human-induced deforestation and topsoil erosion, the study found. The results "underscore the urgency for a high priority program of re-vegetation of Zhouqu County, without which the region will remain exposed to future disastrous, progressive bulking type landslides," the author reports.

47. Assignment 2, Module 10: Storm Surge #2: https://www.sciencedirect.com/topics/earth-and-planetary-sciences/storm-surge

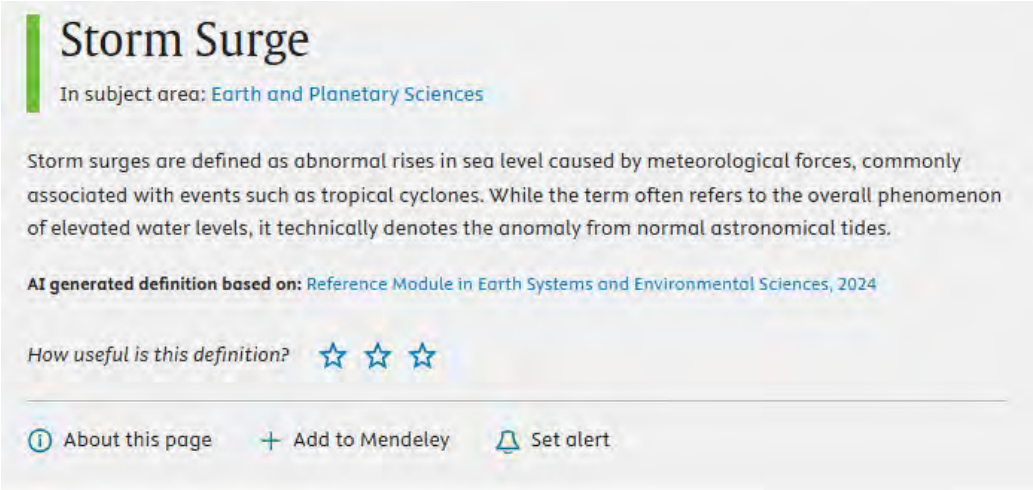

Storm Surge

In subject area: Earth and Planetary Sciences

Storm surges are defined as abnormal rises in sea level caused by meteorological forces, commonly associated with events such as tropical cyclones. While the term often refers to the overall phenomenon of elevated water levels, it technically denotes the anomaly from normal astronomical tides.

AI generated definition based on: Reference Module in Earth Systems and Environmental Sciences, 2024

How useful is this definition? ☆ ☆ ☆

About this page + Add to Mendeley Set alert

Chapters and Articles

You might find these chapters and articles relevant to this topic.

Chapter

Hazards

Storm surges

Storm surges, defined as masses of water that are pushed toward the shore by meteorologic forces, are a primary cause of the injuries, deaths, and structural damages associated with hurricanes, cyclones, northeasters, and other coastal storms. When the advancing surge of water coincides with high tides, the resulting rise in sea level is further exacerbated. Storm surges may reach several dozen feet under the right conditions, as was the case in Hurricane Katrina. Even moderate storm surges, such as the 12-foot surge caused by Hurricane Sandy that was pushed into New York and New Jersey, are capable of causing profound impacts when major metropolitan areas are affected. Storm surge impacts may be exacerbated by wind-driven turbulence, which becomes superimposed on the storm tide and further damages inundated structures by means of wave action (each cubic yard of water results in 1700lb of pressure on affected structures). The surge height at landfall is ultimately dictated by the expanse and intensity of the storm, the height of the tide at the time of landfall, and the slope of the seafloor approaching land. The longer and shallower the seafloor, the greater the storm surge will be. Because much of the United States' densely populated Atlantic and Gulf Coast coastlines lie less than 10ft above mean sea level, storm surge risk is extreme.

Storm surge is the increased sea surface elevation resulting from a tropical or extratropical cyclone moving toward the coast. Tropical storm intensity contributes to storm surge height, but it also related to forward speed, central pressure, and angle of approach (relative to the coast) of the storm and the local topography and bathymetry. Of all the geophysical risks to coastal regions, storm surges are the most severe (von Storch and Woth, 2008). The largest loss of life associated with tropical cyclones is caused by storm surge (Doocy et al., 2013).

Nott (in this volume) discusses the reconstruction of historic storm surges through the investigation of coral rubble, cheniers, sand beach ridges, shell ridges, gravel ridges, pumice ridges, sand splays, and washover deposits, with the oldest of the deposits being 7,000 years. Of these, only beach ridges are used to underpin modeling using Generalized Extreme Value theory and Bayesian analysis approach to statistically derive storm surge return periods (Nott and Jagger, 2013). Studies in the United States, Japan, and Australia reveal similar temporal patterns of quiescent and heightened tropical cyclone activity. Nott also summarizes the literature that discusses the relationship between El Niño and La Niña in the past 5,000 years to tropical cyclone activity in the southwest Pacific and Atlantic Oceans. Similar to Scheffers' chapter, understanding historical records aids our present-day efforts to futurecast.

Horn (in this volume) suggests that we have a substantial understanding of the physical components of storm surges, including modeling, and the warning systems are continually improving, yet there continues to be substantial loss of life. The reason for increased loss of life relates to inadequate mitigation, acting to reduce storm surge severity and number, and adaptation, living with storm surge risk, efforts. The majority of her chapter focuses on adaptation measures that, in turn, may reduce the vulnerability to storm surge: (1) storm surge barriers, with discussions on Delta Works in the Netherlands; recent efforts in the United Kingdom and the Thames Estuary; the Mose system in Venice, Italy; the Hurricane and Storm Damage Risk Reduction System in New Orleans, USA; and proposed storm surge barriers to protect New York and New Jersey post Hurricane Sandy (2012); (2) storm surge warning; and (3) storm surge disaster risk reduction by decreasing exposure and vulnerability to storm surges, which are now increasing.

von Storch et al. (in this volume) present case studies on storm surge to demonstrate the variability between storm surges and tropical and extratropical storm intensity, erosion extent, and loss of life and property. For example, they discuss tropical-cyclone-generated storm surges at Qingdao, China. This region, which is important to China's economy, has experienced nine events from 1949 to 2003 with sea levels in excess of 5.1 m. The periodicity of storm surge activity, likely related to anthropogenic climate change, is demonstrated using Hamburg and the Elbe estuary. The final case study is the southern Baltic Sea coast, which has experienced several extratropical storm surges, with the largest being in 1913.

Storm Surges

Storm surges are defined as masses of water pushed toward and onto the shore by meteorological forces. They are the primary cause of the injuries, deaths, and structural damages associated with hurricanes, cyclones, nor'easters, and other coastal storms. When an advancing surge of water coincides with a high tide, the resulting increases in coastal sea levels are further exacerbated. Storm surges can reach several dozen feet under the right conditions, most notably when they coincide with an astronomical high tide or when they interfere with river flow. In a surge, wind-driven turbulence becomes superimposed on the storm tide, thereby causing further damage to structures that are inundated through wave action (each cubic yard of water exerts 1700 lb of pressure on affected structures). The surge height at landfall is ultimately dictated by the expanse and intensity of the storm, the height of the tide at the time of landfall, and the slope of the sea floor approaching land. The longer and shallower the sea floor, the greater the storm surge will be.

Because much of the United States' densely populated Atlantic and Gulf Coast coastlines lie less than 10 feet above mean sea level, storm surge risk is extreme. Hurricane Katrina served as a reminder of the speed and intensity of the storm surge threat that persists in greater part due to increasing coastal development. After crossing southern Florida, Katrina followed a westward track across the Gulf of Mexico before turning northwest toward the Gulf Coast. The storm made its second landfall as a strong category 4 hurricane in Plaquemines Parish, Louisiana, on August 29, 2005. When the storm made its third and final landfall along the Mississippi/Louisiana border, its hurricane-force winds extended up to 190 miles from the center of the storm, and tropical storm-force winds extended for approximately 440 miles. The strength of and the wide geographical area affected by the storm resulted in a surge greater than anything previously recorded along the Gulf Coast. A 30-foot storm surge, combined with very strong wave action and constant high winds, resulted in a magnitude of destruction never before experienced in the United States. The enormous pressure by the force of the storm surge on the levee system that protected New Orleans caused several breaches that flooded the city with as much as 20 feet of water in some areas. The National Hurricane Center developed an animation showing how a hurricane causes a storm surge: http://bit.ly/2QUvVSr.

The National Hurricane Center operates a computerized model, called SLOSH (Sea, Lake, and Overland Surges from Hurricanes), to estimate storm surge heights and winds resulting from historical, hypothetical, or predicted hurricanes. When making calculations, SLOSH takes into account pressure, size, forward speed, track, and wind. The model's output is a color-coded map indicating storm surge heights for defined areas in feet above the model's reference level. These calculations are applied to a specific locale's shoreline, incorporating the unique bay and river configurations, water depths, bridges, roads, and other physical features. When SLOSH is used to estimate storm surge from predicted hurricanes, forecast data are entered every 6 hours over a 72-hour period and updated as new forecasts become available. SLOSH is accurate within a range of 20% plus or minus what is observed. The model accounts for astronomical tides, but it does not consider rainfall, river flow, or wind-driven waves. However, this information can be combined with the model's output to create a more accurate analysis of at-risk areas.

The National Weather Service also runs a storm surge model for extratropical storms called ET-SURGE (also known as ETSS). This model is a variation of SLOSH that works with nonhurricane systems.

48. Assignment 2, Module 10: SLOSH: https://slosh.nws.noaa.gov/sdp/SLOSH-Display-Training.pdf

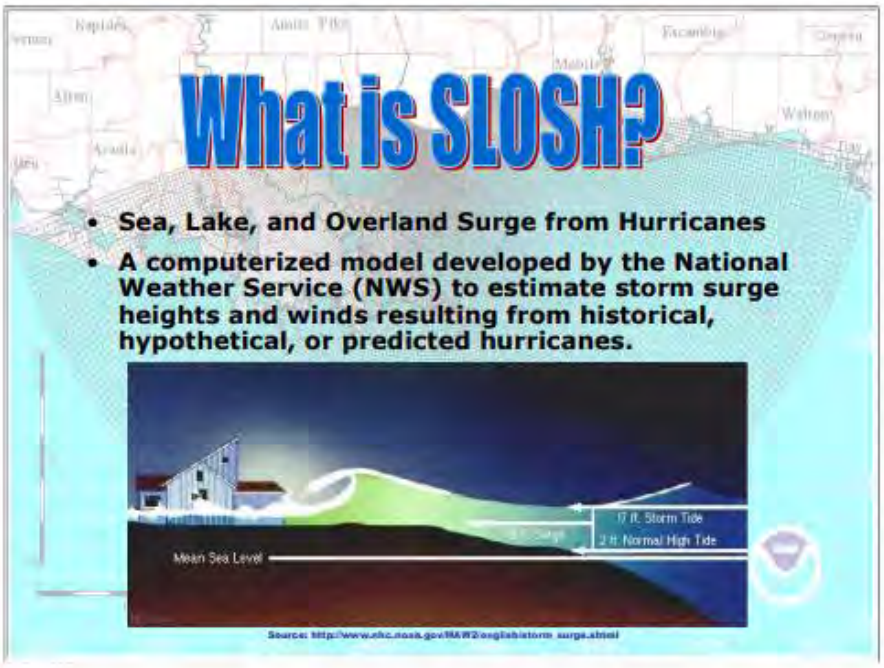

- SLOSH stands for Sea, Lake, and Overland Surge from Hurricanes. It is a computerized model developed by the National Weather Service (NWS) to estimate storm surge heights and winds resulting from historical, hypothetical, or predicted hurricanes.
- SLOSH is used by the National Hurricane Center (NHC) for the exclusive benefit of NWS, US Army Corps of Engineers (USACE), and Emergency Management personnel.
- There are several other storm surge models in use, including ADCIRC, however, SLOSH is the primary model used by the Federal Emergency Management Agency (FEMA), the National Oceanographic and Atmospheric Administration (NOAA), and USACE. It is also the basis for Hurricane Evacuation Studies (HES).

Definitions:

ADCIRC - Advanced Circulation model for oceanic, coastal, and estuarine waters
FEMA – Federal Emergency Management Agency
HES – Hurricane Evacuation Study
NHC – National Hurricane Center
NOAA – National Oceanographic and Atmospheric Administration
NWS – National Weather Service
SLOSH – Sea, Lake and Overland Surge from Hurricanes
USACE – United States Army Corps of Engineers

Storm Surge

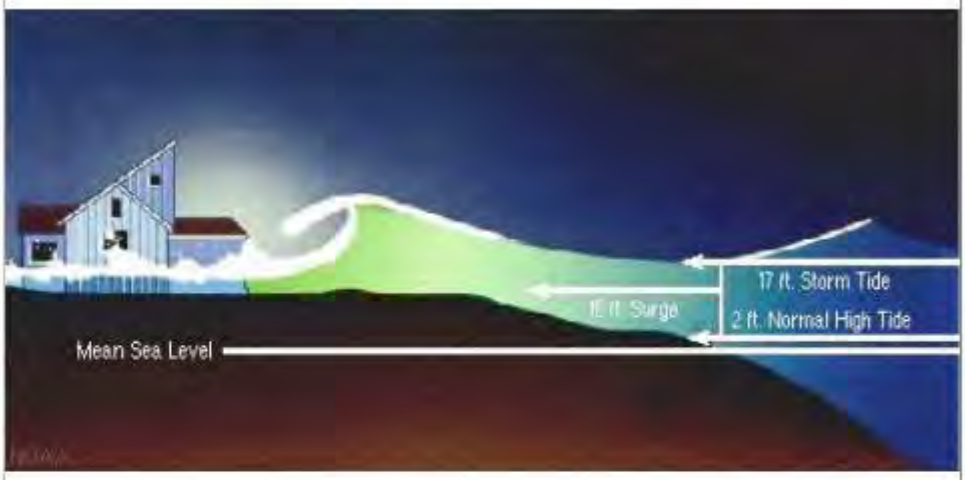

- This picture visually depicts the definition of a storm surge.
- Storm surge is water that is pushed toward the shore by the force of the winds swirling around the storm.
- This advancing surge combines with the normal tides to create the hurricane storm tide, which can increase the mean water level by 15 feet or more.

Definitions:

Storm Surge – water that is pushed toward the shore by the force of winds swirling around a storm.

Storm Tide – the combination of the normal tide and the storm surge to create the total increase in water level due to the storm.

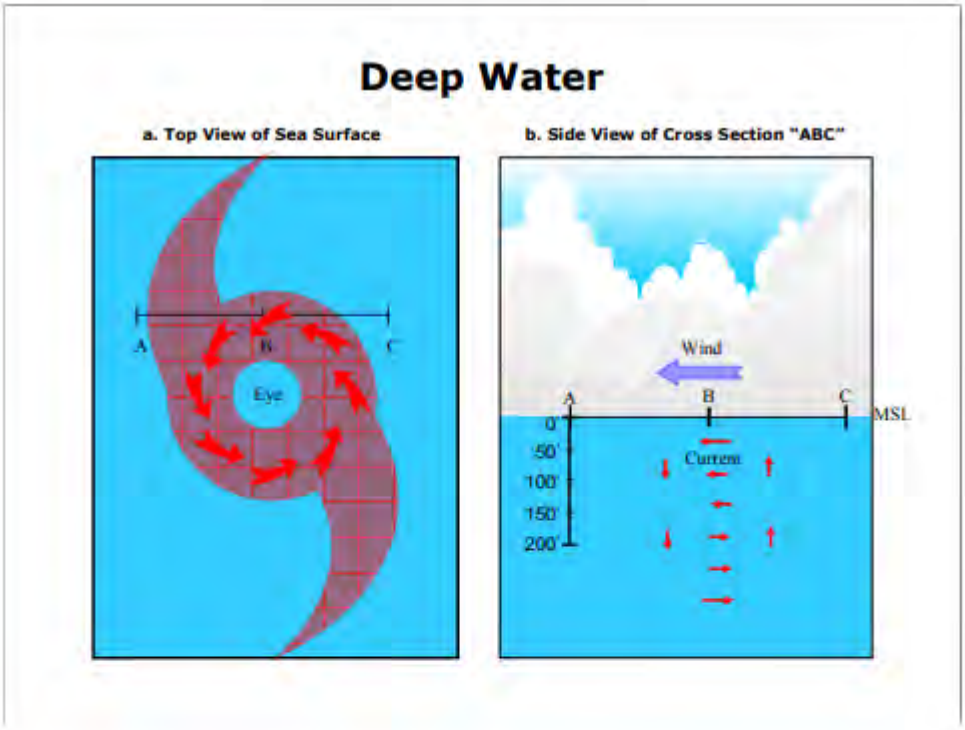

- This illustration shows how in deep water, the wind and current create a cycle of water which alleviates the build up of storm surge.
- Storm surge begins to build while the hurricane is still far out at sea over deep water. The low pressure near the center of the storm causes the water to rise. In deep water, a counter current develops well below the surface which counters an attempt by the wind to build up surges.

Note:

- There is some sea level rise due to the pressure change, but that is small compared to wind driven surge on a "shallow" continental shelf.

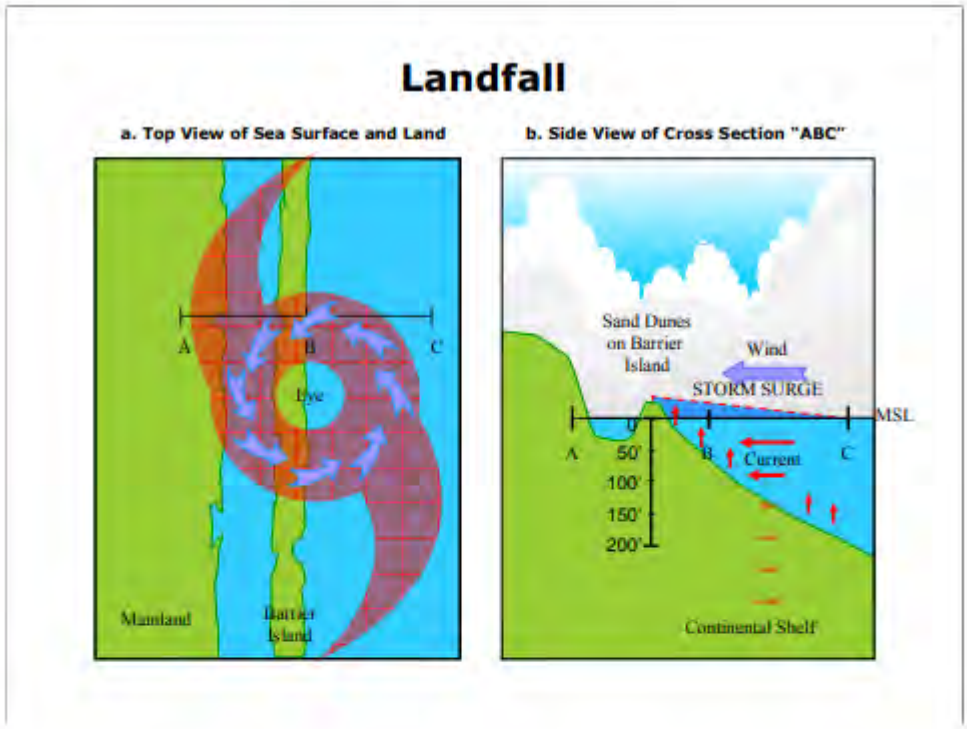

- As the water depth decreases closer to the shore, the excess water that is built up by the central pressure of the storm is not able to dissipate. The increased water has no place to go except up onto the shore. The force of winds swirling around the storm pushes the water toward the shore and creates storm surge.
- The level of storm surge in a particular area is also determined by the slope of the continental shelf. A shallow slope of the coast will allow a greater surge to inundate coastal communities. Areas with a steeper continental shelf will not see as much surge inundation, although large breaking waves can still present major problems.

Tide with Storm Surge

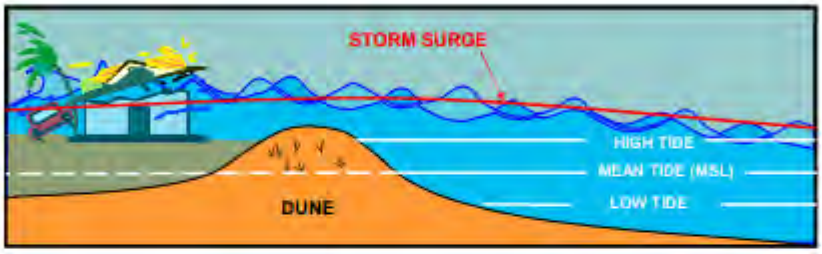

- The tide level when a hurricane makes landfall can have a major impact on the total water surface elevation caused by the storm (storm tide). If a storm makes landfall at high tide, the storm tide may be several feet higher than if a storm makes landfall at mean or low tide.
- This rise in water level can cause severe flooding in coastal areas.

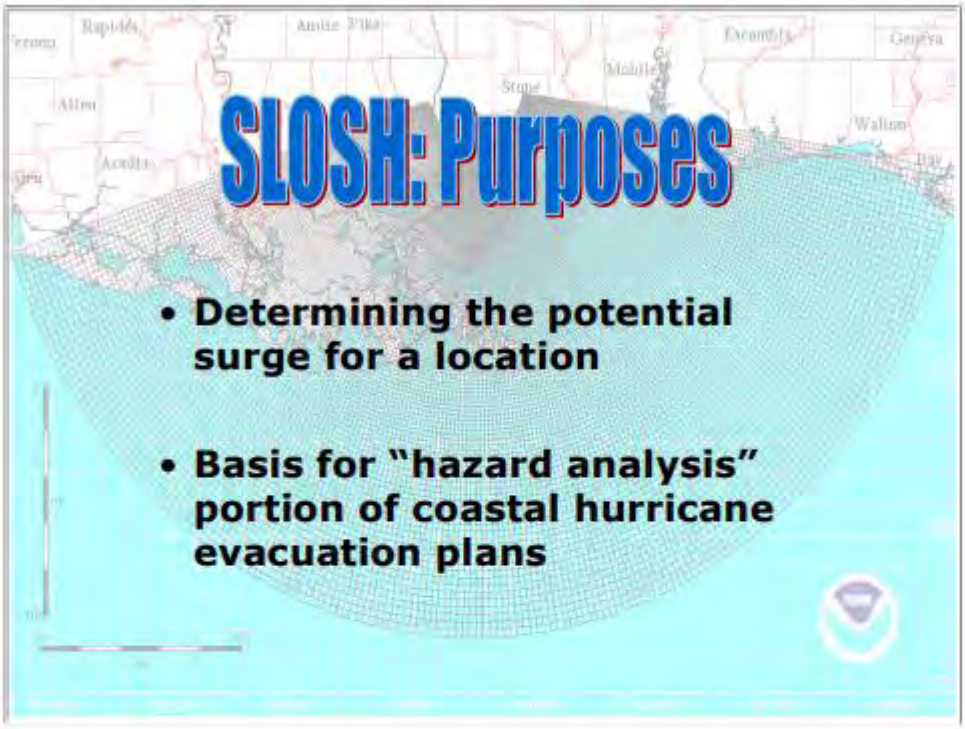

- SLOSH is best used for defining the potential flooding from storm surge for a location from a threatening hurricane, rather than as a predictor of the specific areas that will be inundated during a particular event.
- SLOSH output is used as the hazard analysis for hurricane evacuation plans. SLOSH model results are combined with traffic flow information for creating a HES and combined with rainfall amounts, river flow, or wind-driven waves to determine a final analysis of at-risk areas.

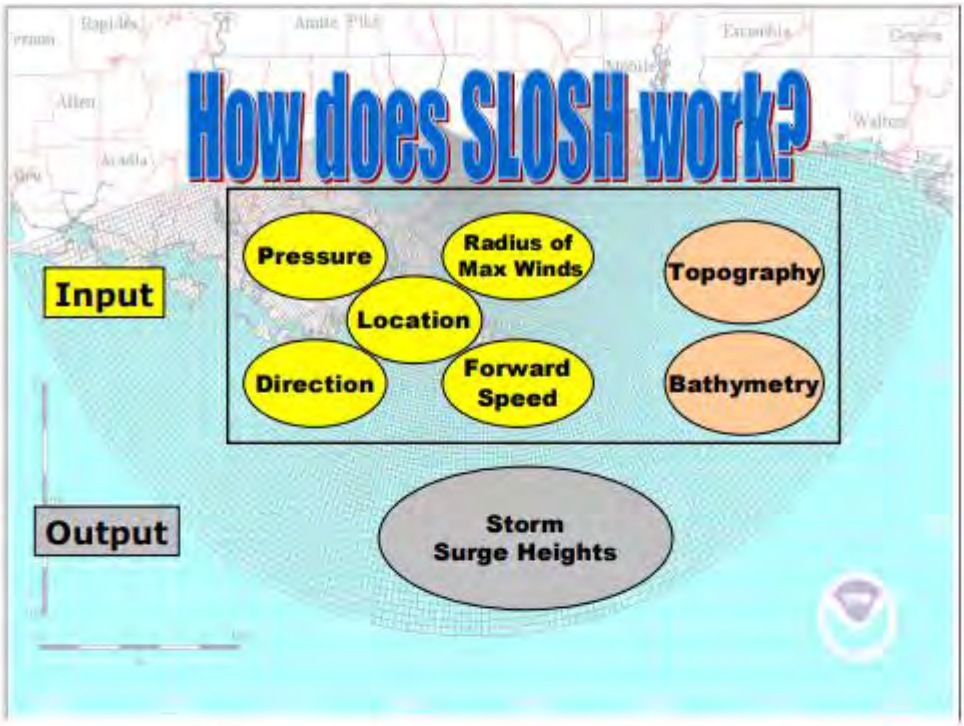

- Given a SLOSH Basin, which is a geographical region with known values of topography and bathymetry, and a hurricane track (identified by its pressure, radius of maximum winds, location, direction, and speed), the SLOSH model solves a complex set of equations and outputs data which are shown as color-coded storm surge in the SLOSH display.

Important Note:

- The point of a hurricane's landfall is crucial to determining which areas will be inundated by the storm surge. If the forecast hurricane track is not correct, the SLOSH model will be inaccurate.

Definitions:

Bathymetry – the water depth relative to mean sea level. It may be expressed as positive or negative, but should be understood to be negative.

SLOSH Basin – a geographical region with known values for topography and bathymetry.

Topography – the configuration of a surface, including the elevation and position of its natural and man-made features.

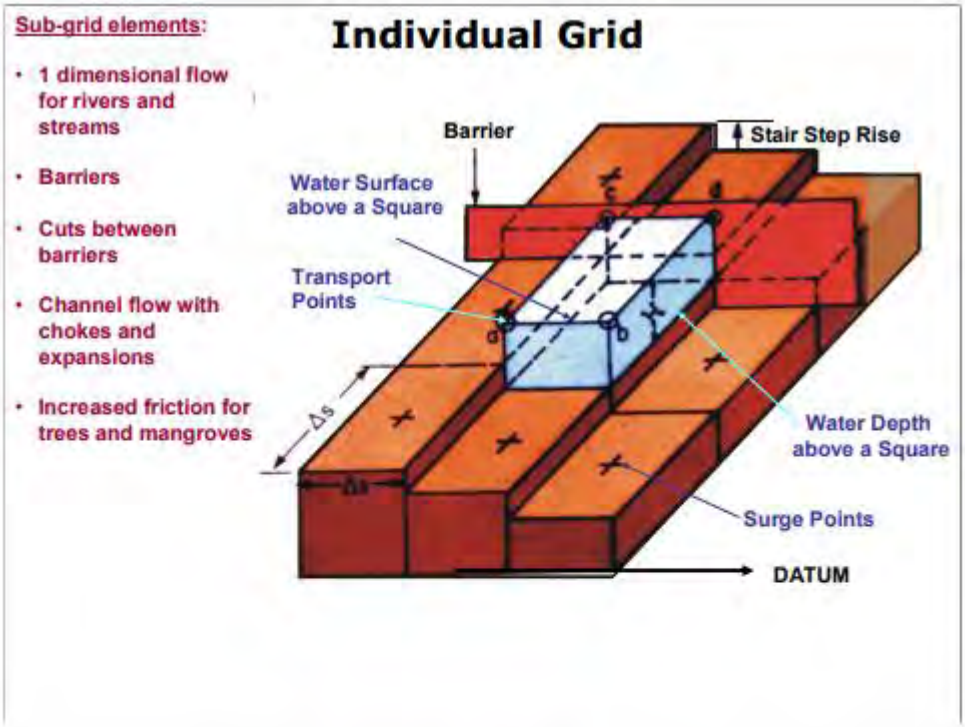

- The individual elements of the SLOSH grid are the basis for calculating water surface elevations caused by storm surge in a specific SLOSH basin.
- The grid allows for barriers to flow, cuts in barriers, one dimensional flow in rivers and streams, and increased friction for trees and mangroves in certain grid blocks to be taken into consideration in the calculations.
- Δs refers to the distance or length of each side of the grid element.
- The transport points are the points at which flow enters and exits the cell.
- The water depth is calculated based on the elevation of the grid cell and the amount of water that is able to flow into that cell. The water surface is found at the elevation of the water depth combined with the average ground elevation of the grid cell.

SLOSH Model grid with geographic data at full resolution

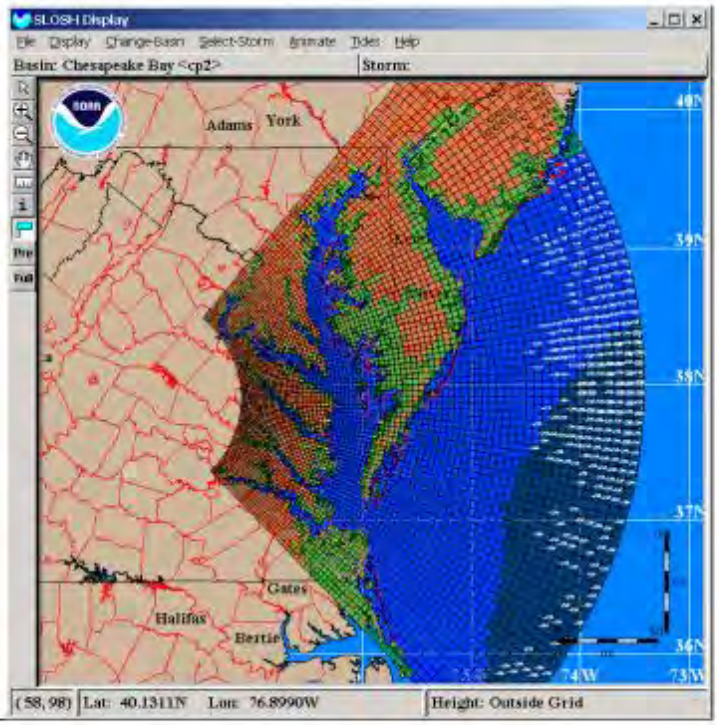

- The SLOSH model contains topographic information for each grid cell. This data is combined with the storm surge calculations based on the storm characteristics to determine the water surface elevations caused by storm surge.
- The majority of the topographic data is obtained from the U.S. Geological Survey (USGS). However, other data sources are utilized in small areas where available and necessary.
- Currently when SLOSH basins are updated, bathymetry is obtained from the National Geophysical Data Center (NGDC). Many basins have already been updated.

Definitions:
NGDC – National Geophysical Data Center.
USGS – U.S. Geological Survey

SLOSH Model grid with geographic data at finer resolution

Used by Basin Developer for quality control

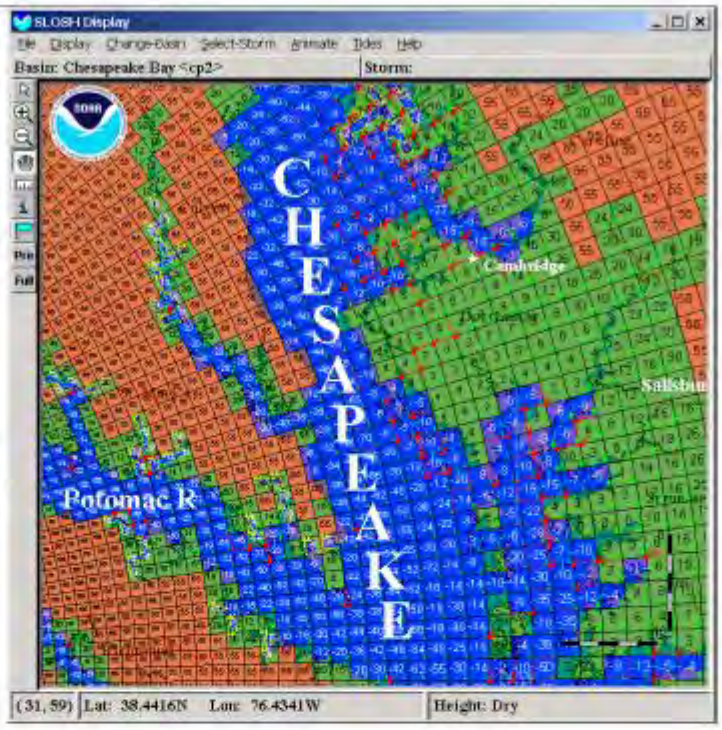

- The elevation for each grid cell is the average of the ground surface elevations found in that grid cell. The number shown in each cell is that average elevation. The water surface elevations are determined the same way. For each cell an average water surface elevation is found and assigned to that cell.
- The user of the SLOSH Display program does not have access to this detailed topography. This illustration shows an enhanced version of the SLOSH grid.

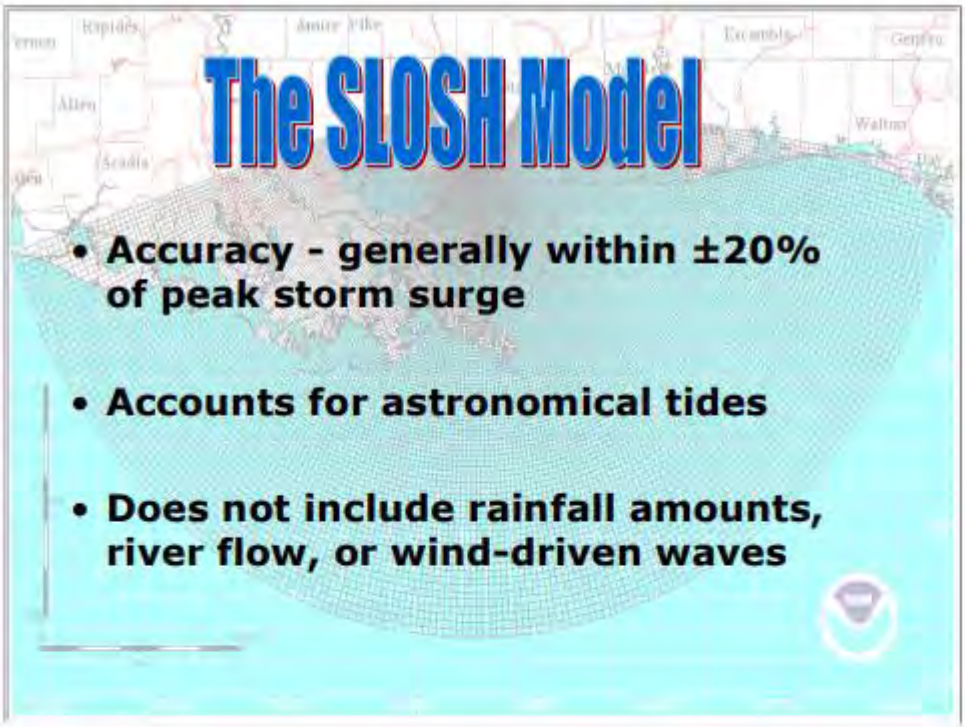

- Accuracy for the SLOSH model is generally within plus or minus 20% of the peak storm surge. If the model calculates a peak storm surge of 10 feet for the event, you can expect the observed peak to range from 8 to 12 feet.
- Post storm analyses are conducted to show how SLOSH model data compare to actual historical storm data.
- The accuracy of plus or minus 20% for the SLOSH model is for a KNOWN hurricane track, intensity, and size, based on looking at surge measurements (primarily high water marks) from past hurricanes.
- Astronomical tides can add significantly to the water height. The model accounts for tides by specifying the initial tide level.
- The SLOSH model does not include rainfall amounts, river flow, or wind-driven waves. These are combined with the model results in the final analysis of at-risk areas.

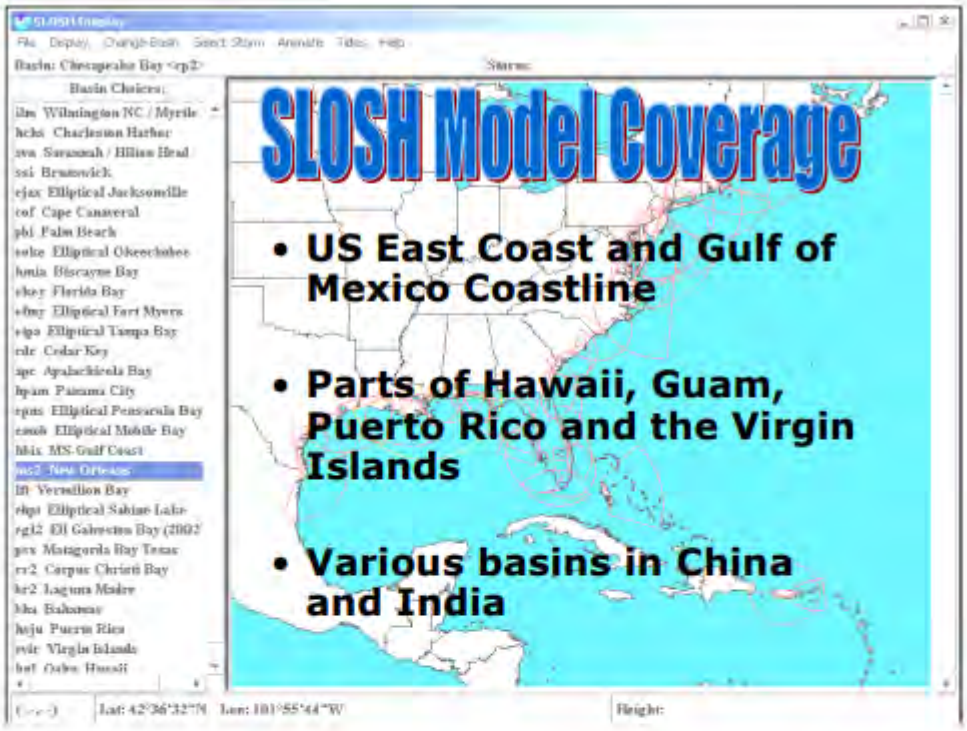

- The SLOSH model covers the U.S East Coast and the Gulf of Mexico coastline.
- Parts of Hawaii, Guam, Puerto Rico, and the Virgin Islands are included.
- Various basins in China and India are also available.
- Simulation studies have been conducted and data generated for the display program for all of the US East and Gulf coast basins. Even though basins are included for other areas, simulation studies may not have been conducted. For example, there are 5 basins in India and China but simulation studies were never performed for these areas.

Several generalizations can be drawn from SLOSH models.

- More intense storms cause higher surges.
- The highest surges usually occur to the right of the storm track (traveling with the storm) at approximately the radius of maximum wind.
- Fast moving storms cause high surges along open coast and lower surges in sheltered bays and estuaries.
- Slow moving storms usually result in greater flooding inside bays and estuaries, with smaller values along the open coast.

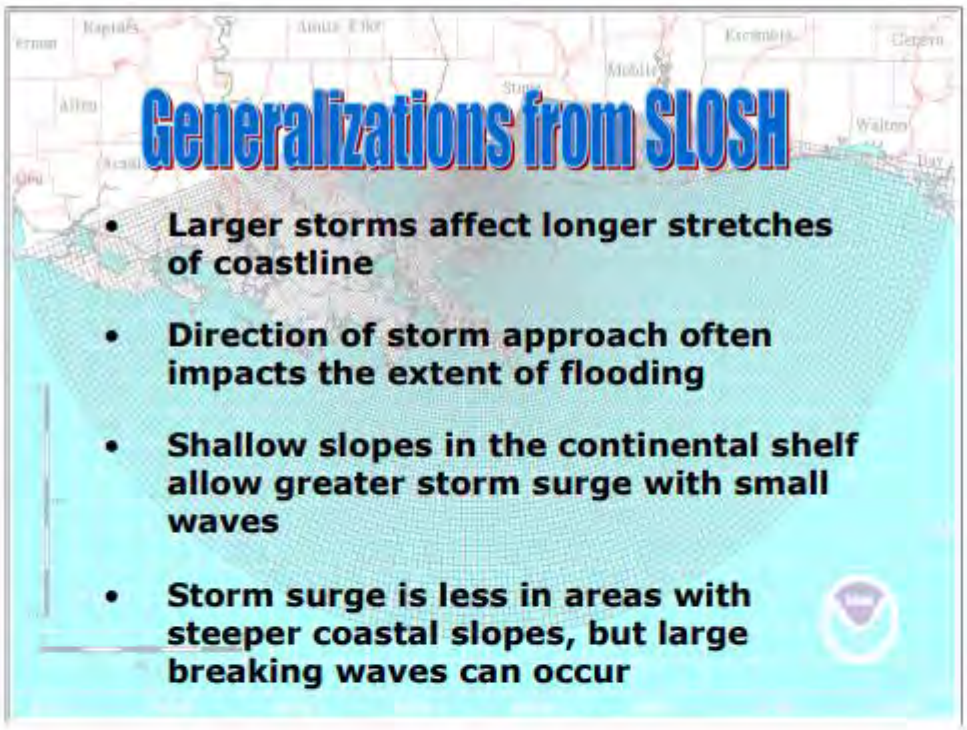

- Larger storms affect longer stretches of the coastline. A larger storm is defined as a storm having a greater radius of maximum wind.
- The direction of storm approach often impacts the extent of flooding. Depending on location, storms from one direction may cause inundation, while a storm of the same magnitude from a different direction may cause little flooding.
- The slope of the continental shelf will affect the level of surge in a particular area. Areas with shallow slopes of the continental shelf will allow a greater storm surge, but waves are small.
- Areas with deep water just offshore experience large waves, but little storm surge.

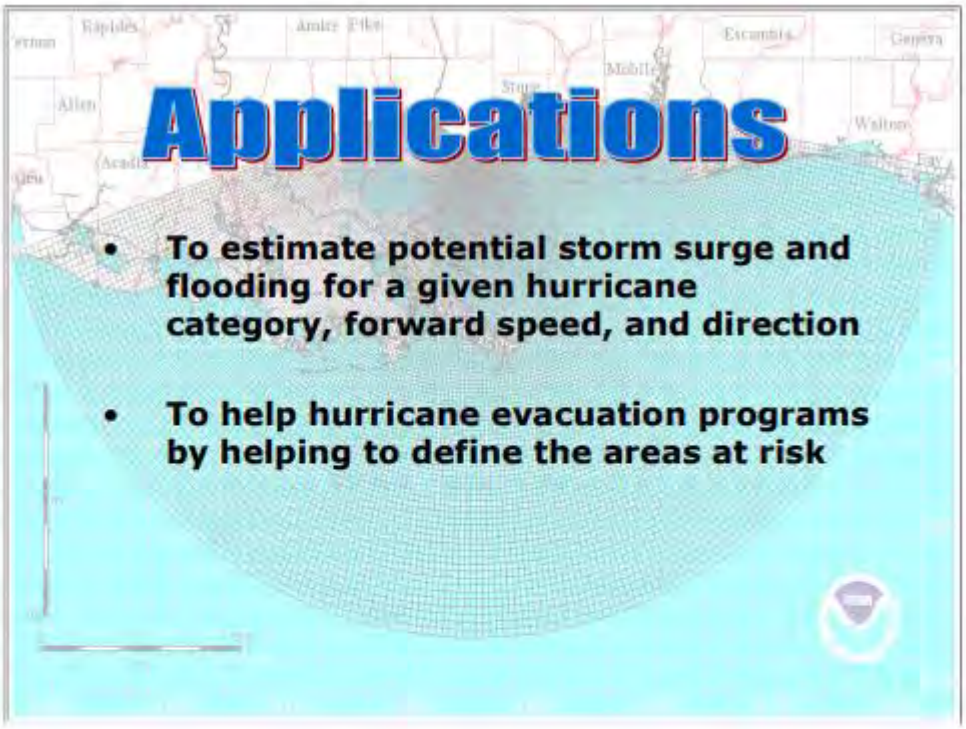

SLOSH output can be applied:

- To estimate potential storm surge and flooding for a given hurricane category, forward speed, and direction.
- To help hurricane evacuation programs by defining the areas at risk. From there, the threatened population, evacuation zones, and evacuation routes are determined, and the percentage of people evacuating and evacuation times are estimated.

49. Assignment 2, Module 10: Storm Surge Impacts:
http://www.hurricanescience.org/society/impacts/stormsurge/

Hurricane Impacts Due to Storm Surge, Wave, and Coastal Flooding

The coastal flooding triggered by hurricanes is as destructive as wind but can be even more deadly, and is by far the greatest threat to life and property along the coastline. Storm surge, wave, and tides are the greatest contributors to coastal flooding, while precipitation and river flow also contribute during some storms. Hurricane Katrina (2005) is a prime example of the damage and devastation that can be caused by surge: at least 1600 fatalities stemmed from Katrina and many of those deaths occurred directly, or indirectly, as a result of storm surge.

The storm surge of Hurricane Ivan (2004) pushed sand off of the shore of Pensacola Beach and into this Florida house. Image credit: FEMA/Mark Wolfe.

Storm surge is the bulge of water that washes onto shore during a storm, measured as the difference between the height of the storm tide and the predicted astronomical tide. It is driven by wind and the inverse barometric effect of low atmospheric pressure, and is influenced by waves, tides, and uneven bathymetric and topographic surfaces. The storm tide, which includes storm surge and the astronomical tide, is shown below.

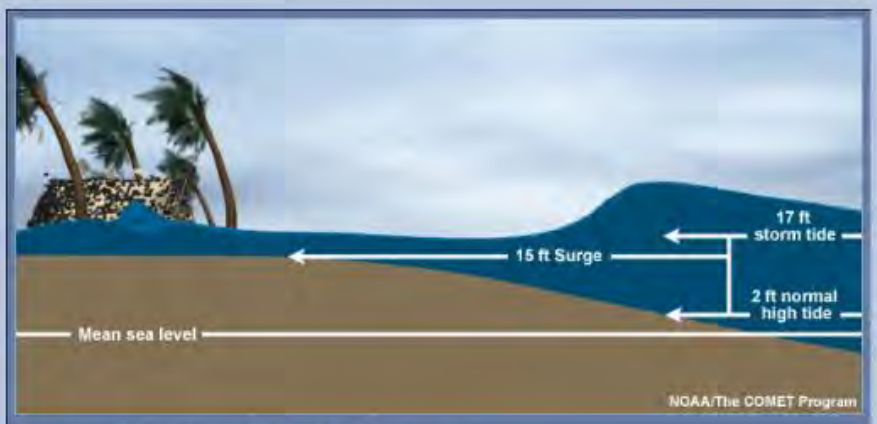

Image credit: NOAA/UCAR/The COMET Program.

Storm surge and coastal flooding depend on a number of factors. These factors include the intensity of a storm, its size, translational speed, angle of approach to the coast, landfall location, and the bottom slope at that location. It is well accepted that the most influential factor in storm surge generation is the central pressure deficit, which controls the intensity of a hurricane, i.e., wind velocity and stress over the ocean surface and inverse barometric effects. The influence of the other factors, such as the storm size (measured by the radius from the center of a hurricane to the location of maximum wind speed), the translational speed, and the angle of approach, became apparent after Hurricane Katrina's catastrophic storm surge in 2005 (Hurricane Katrina was a Category 3 storm). Lower atmospheric pressure (faster wind speeds) and larger storms create a greater storm surge potential. Slower and larger but weaker hurricanes (e.g., Category 3 storms such as Katrina) cause much higher storm surge and flooding (even to inland areas) when compared to faster and small but more intense hurricanes (e.g., Hurricane Charley in 2004). Storms that make a perpendicular approach toward the coastline will also cause a greater storm

Storm surge is produced by water being pushed toward the shore by the force of the winds moving cyclonically (counter clockwise) around the storm. Image credit: UCAR/The COMET Program.

Bathymetry and topography changes often occur as a result of storms and erosion, and also vary geographically. These geographic differences affect Base Flood Elevations (BFEs) and resultant coastal responses and flood hazard areas. For example, the Pacific coast is characterized by steep bathymetry and a narrow coastal shelf, and flooding is predominantly caused by large waves rushing up the shore (wave runup - the maximum extent of high-velocity uprush of individual waves above the average water level). In contrast, the Gulf and Atlantic coasts are characterized by wide, shallow coastal shelves, and flooding is dominated by storm surge and breaking waves. Water surface elevations at the shoreline are a combination of the average water level determined by wind setup (due to the direct action of wind stresses at the air-sea interface) and wave setup (due to breaking waves, see below), and a fluctuating water level caused by wave runup.

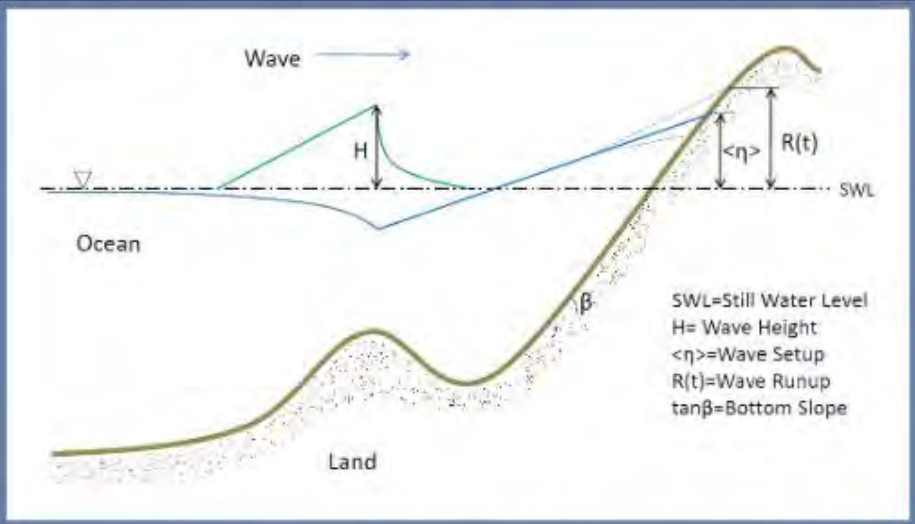

Hurricane winds generate waves in the ocean. As these waves propagate into shallow water, wave heights increase due to a process called "shoaling". As the wave heights increase, the waves eventually break and impart their momentum to the water, causing onshore flow near the surface and offshore flow or "undertow" near the bottom, and an overall elevation in water level at the coast ("wave setup" – the rise in the water surface caused by breaking waves, and "wave runup" - the rush of wave water up a slope or structure).

Storm surge and coastal flooding have both vertical and horizontal dimensions. Storm surge can reach heights of more than 12 m (40 ft) near the center of a Category 5 hurricane, and fan out across several hundred miles of coastline, gradually diminishing away from the hurricane's center. Coastal flooding can reach far inland, tens of miles from the shoreline. While the peak surge often occurs at the landfall of a storm along an open coastline, large surge has been found to occur hours before hurricane landfall as a "fore-runner" (e.g., during Hurricane Ike along the Texas coast in 2008) and/or after hurricane landfall as a "post-runner" (e.g, during Hurricane Wilma along SW Florida coast in 2005). These "fore-runner" and "post-runner" surges can actually cause unexpected coastal flooding, damage property, and endanger lives.

Local topographic features such as buildings, levees, wetlands, sand dunes, and barrier islands reduce storm surge, wave forces, and coastal flooding. At the same time, these topographic features may be reshaped or even removed during a severe storm (see Ecosystem Perspective: What can a hurricane do to the environment?. After the landfall and passage of Hurricane Katrina (2005), levees in New Orleans breached and catastrophic flooding followed shortly afterwards. Storm surge, wave, and coastal flooding are also complicated by the presence of estuaries. For example, a long and narrow estuary can significantly increase the storm surge due to a "funneling" effect. Storm surge can travel from the mouth to the head of an estuary, causing a delayed peak surge in that location when winds have already subsided. Diverse geographic variations in local bathymetry and topography result in very different responses of coastal regions to hurricanes. Hence, it is difficult to assign a uniform storm surge value for a hurricane of any given intensity. Due to this, the Saffir-Simpson Wind Scale no longer associates storm surge value to hurricane of any category.

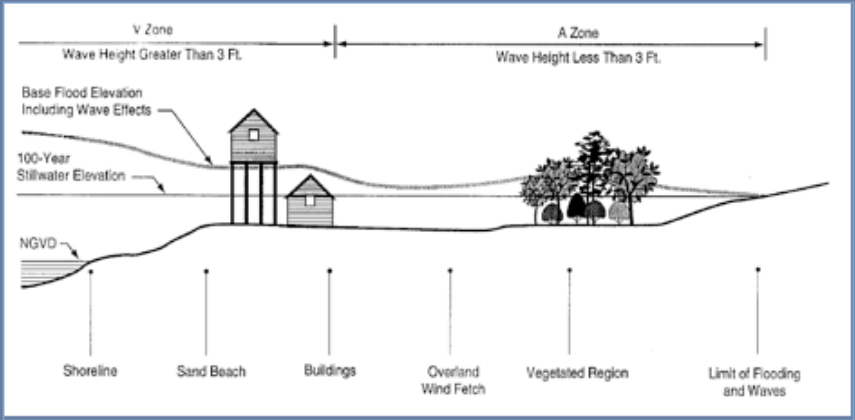

Coastal areas are subject to flood risks, especially those associated with tropical cyclones. As storm surge and waves propagate onto the coastal area, they can continue to grow and inundate the beaches, buildings and vegetation, while being dissipated at the same time. FEMA estimates the flood elevation due to storms surge and waves with a 1% annual chance of occurrence. The 100-year Stillwater Elevation does not include the effect of waves, while the Base Flood Elevation (BFE) includes both storm surge and wave effects (note the house that was built on stilts to meet the BFE and how projected flooding may impact that house, vs. the structure without the same mitigation measures in place). In the "V Zone", hurricane induced waves and currents can generate significant hydrodynamic forces to destroy flooded buildings. In the "A Zone", wave effects are less significant but buildings can still be flooded.

The combination of storm surge, battering waves, and high winds can be deadly. In the United States, the Atlantic and Gulf Coast coastlines are densely populated and many regions lie less than 3m (10 ft) above mean sea level. In August 1969, Hurricane Camille, the second most intense hurricane on record to hit the United States, produced a storm tide of 7.5 m (24.6 ft) at Pass Christian, MS. The combination of Camille's winds, surges, and rainfall caused 256 deaths (143 on the Gulf Coast and 113 in the Virginia floods) and $1.421 billion in damage.

Damage from Hurricane Camille (1969) along the Mississippi Gulf Coast. Image credit: NOAA.

Damage from Hurricane Camille (1969) along the Mississippi Gulf Coast. Image credit: NOAA.

In 2005, Hurricane Katrina impacted the same region of the Mississippi coast. Although Katrina was a Category 3 hurricane with 209 km/h (130 mph) sustained winds (Camille was a Category 5 hurricane with 306 km/h [190 mph] sustained winds), Katrina's storm surge exceeded Camille's at all locations, topping out at 8.5 m (27.8 ft) at Pass Christian, MS. Even though Camille was a much more intense hurricane, Katrina was a much larger storm, causing a higher storm surge that also covered a much larger area. Hurricane Camille was a small storm with a very tight eye, and, at landfall, hurricane-force winds only extended about 97 km (60 mi) to the east of the storm's center. Camille had an 18 km (11 mi) diameter eye and a radius of maximum winds of approximately 24 km (15 mi). In contrast, Hurricane Katrina, had a large, 60 km (37 mi) diameter eye, and hurricane-force winds extended out about 193 km (120 mi) to the east of the storm's center. Katrina's radius of maximum winds was about 48 km (30 mi), double that of Hurricane Camille. Katrina therefore set in motion a volume of water about four times greater than Camille, a U.S.-record storm surge that impacted a wide region from Grand Isle, LA, to Mobile Bay, AL, and killed over 1300 people.

Observation of Storm Surge, Wave, and Flooding

Observation data of storm surge, wave, and coastal flooding are needed for scientific understanding of the dynamics of surge, wave, and flooding, as well as for verification of numerical models.

Observation of storm surge relies on sparsely located tidal gages installed by NOAA and other agencies along the coastline. The continuously observed data at a tidal gage gives the total water elevation relative to a vertical datum (e.g., NAVD88 or NGVD25). The observed water elevation consists of storm surge, tide, and wave setup. While the tide contained in the data can be removed by applying a 32-hour filter to the data or by subtracting the NOAA-predicted tide at that location to give the storm surge value (see an example below), it is difficult to isolate the wave setup from the remaining data signal. The only way to determine the wave setup is by simulation of surge and wave during hurricanes, and comparison of simulated surge and wave with data.

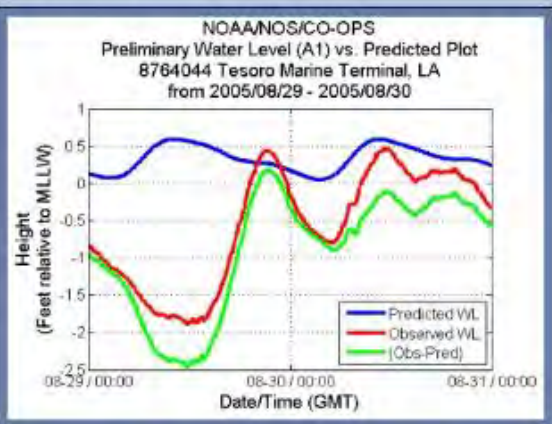

Observed water level, predicted tide, and storm surge (obs-pred) at Tesoro Marine Terminal, Louisiana, during Hurricane Katrina (2005). Source: NOAA/NOS/CO-OPS.

NOAA Tidal Station 8761305 at Shell Beach, LA. Image credit: NOAA.

Observation of coastal flooding is based on the so-called High Water Marks (HWMs) in flooded area during a hurricane. These HWMs, which supposedly record the highest water level during a hurricane, are often difficult to interpret due to the following problems: 1) it is difficult to know if waves are included in the HWMs; 2) the vertical datum of the HWMs is often missing; 3) the HWMs are often observed at locations near a major river; and 4) the HWMs only provide peak water elevation, without any information on when the peak occurred.

For hurricanes prior to Katrina, only limited tidal gage data and HMWs are available. Since Hurricane Katrina, the United States Geological Service (USGS) has deployed arrays of more than 40 pressure sensors in upland areas during hurricanes to measure the continuous coastal flooding data over a large upland area. These data during recent hurricanes (e.g., Rita, Wilma, and Ike) have been found to be very valuable in understanding and quantifying the dynamics of coastal flooding. They provide the time history and spatial extent of coastal flooding, which cannot be provided by conventional tidal gages in water.

Black/brown high water lines from floodwaters associated with Hurricane Katrina (2005) remain on this New Orleans, LA house. The red, spray-painted mark on the front of the house indicates that Urban Search and rescue teams checked this house for people. Image credit: Marvin Nauman/FEMA.

50. Assignment 2, Module 10: Effect of Coastal Erosion on Storm Surge: http://www.mdpi.com/2077-1312/4/4/85/pdf

Journal of *Marine Science and Engineering*

MDPI

Article

Effect of Coastal Erosion on Storm Surge: A Case Study in the Southern Coast of Rhode Island

Alex Shaw [1], Mohammad Reza Hashemi [1,*], Malcolm Spaulding [1], Bryan Oakley [2] and Chris Baxter [1]

[1] Department of Ocean Engineering, University of Rhode Island, Narragansett, RI 02882, USA; alex_shaw@my.uri.edu (A.S.); spaulding@egr.uri.edu (M.S.); baxter@egr.uri.edu (C.B.)

[2] Environmental Earth Science Department, Eastern Connecticut State University, Willimantic, CT 06226, USA; oakleyb@easternct.edu

* Correspondence: reza_hashemi@uri.edu; Tel.: +1-401-8746217

Academic Editor: Richard P. Signell
Received: 26 July 2016; Accepted: 22 November 2016; Published: 7 December 2016

Abstract: The objective of this study was to assess the effect of shoreline retreat and dune erosion on coastal flooding in a case study located in the southern coast of Rhode Island, USA. Using an extensive dataset collected during 2011, an ADCIRC model was developed to simulate the propagation of storm surge in the coastal areas, including coastal inlets and ponds. A simplified methodology, based on the geological assessment of historical trends of the shoreline retreat and dune erosion in this area, was incorporated in the model to represent coastal erosion. The results showed that for extreme storms (e.g., a 100-year event), where coastal dunes are overtopped and low-lying areas are flooded, the flooding extent is not significantly sensitive to coastal erosion. However, failure of the dunes leads to a significant increase of the flooding extent for smaller storms. Substantial dampening of the storm surge elevation in coastal ponds for moderate and small storms was associated with coastal inlets connecting to coastal ponds which are often not resolved in regional surge models. The shoreline change did not significantly affect the extent of flooding. It was also shown that the accuracy of a storm surge model highly depends on its ability to resolve coastal inlets, which is critical for reliable storm surge predictions in areas with inlet-basin systems.

Keywords: dune erosion; coastal ponds; storm surge; coastal flooding

1. Introduction

The northeast of the US, including the coastal regions of Rhode Island, have been impacted by hurricanes in the past, most recently Hurricane Sandy in 2012. Climate change is expected to change the strength and frequency of these events, putting more coastal areas at risk [1]. Further, it is estimated that sea level will rise between 0.2 and 2 m by 2100 in the northeast of the US, which also magnifies the impacts of coastal flooding [2]. As coastal flooding is sensitive to changes in bathymetry and topography of a region, coastal erosion can potentially affect the storm surge propagation. Storm surge and coastal erosion interact in two ways: (1) storm surges (and wave forces) lead to coastal erosion; (2) coastal erosion affects the propagation of storm surge and consequently alters the extent of flooding. While it is possible to examine the two-way interaction processes using morphodynamic models (e.g., [3,4]), which incorporate sediment transport and bed level changes, validating morphodynamic models is very challenging, and developing those models is costly. Alternatively, assuming worst case scenarios (complete dune erosion, shoreline retreat at specified rate, etc.) is an alternative method which allows understanding the effect of coastal erosion on flooding for extreme scenarios (e.g., [5]).

Our case study is located in the southern coast of Rhode Island (Figure 1), which consists of several coastal ponds and barriers. The shorelines are retreating at a rapid rate, in some areas up to

1.15 m per year [6]. The coastal dunes are also eroded during major storm events (Figure 2). The failure of dunes can affect the dynamics of the inlet-basin/pond system.

Figure 1. Overview of the the study area in the southern coast of Rhode Island. Other details include save points (blue crosses) from the North Atlantic Coast Comprehensive Study (NACCS) (see Section 2), Woods Hole Group Inc. water level gauge locations (orange dots), and a red box around the study area. Transects in the dark blue area were used to apply erosion scenarios (Figure 8).

Figure 2. Failure of dunes protecting Ninigret Pond after Hurricane Carol (1954); source: Rhode Island (RI) Coastal Resources Management Council.

The objective of this study is to investigate the effects of dune erosion and shoreline retreat (together and separately) on storm surge. The study was carried out using numerical modeling, and analysis of the field data.

Section 2 describes several sources of data (observed/hindcast) which have been used in this study; in particular, the hydrodynamic data, which have been collected during 2011, and other relevant storm surge modeling studies in the region are presented. Section 3 explains the simplified methodology which has been used to simulate shoreline retreat and dune erosion. Details of the ADCIRC (ADvanced CIRCulation) model of the study area are provided in Section 4. Several scenarios of coastal erosion and storm surge are discussed in Section 5. Discussions and summary of the results are presented at the end.

2. Data

From July 2010 to September 2011, Woods Hole Group carried out an extensive data collection program [7], for the US Army Corp of Engineers (USACE) New England District, entitled "Wave, Tide and Current Data Collection, Washington County, Rhode Island". The primary purpose of that work was to collect site-specific data to support a RI Regional Sediment Management Study, and included a collection of water elevation, currents, wave, and meteorological data. Their study included measurement of water elevations inside coastal ponds (Figure 1), as well as waves and currents offshore. This data provided a unique source for understanding the effect of inlet-pond systems on water elevation in this area. Hurricane Irene, which impacted this area during the observation period, was also used for model validation.

For simulation of synthetic storms (i.e., 100-year event), the North Atlantic Coast Comprehensive Study (NACCS; [8,9]) was used. NACCS is based on a system of numerical models including ADCIRC [10], WAve Model (WAM), and STeady state spectral WAVE model (STWAVE) [11]. It has simulated hydrodynamic and wave fields of 1050 synthetic tropical storms as well as 100 extratropical historical storms over the Atlantic Coast. The model was based on a relatively high resolution unstructured mesh (30 m–50 m near the coast). The synthetic storms were generated based on the statistical analysis of past storms. The NACCS provides model results at the save points (Figure 1), including time series of the wind, wave and water levels for the events and return period analyses for the tropical storms. These data were used to force the model at the boundary for a synthetic storm representing a 100-year event. It should be added that some of the save points of the NACCS are located inside the coastal ponds which may be inaccurate, as will be discussed later. For the 100-year event, all synthetic storms simulated in NACCS were examined, and a storm surge event which generated the water levels of around 100-year storm surge at Newport (8452660) and Providence (8454000) National Oceanic and Atmospheric Adminstration (NOAA) water level stations was selected. This storm had a maximum surge of 3.20 m (Mean Sea Level (MSL)) at Newport (Figure 3), which is close to 3.35 m (MSL) or 2.7 m (Mean Higher High Water (MHHW)) for the 100-year event, considering the 100-year event at the upper 95% confidence level.

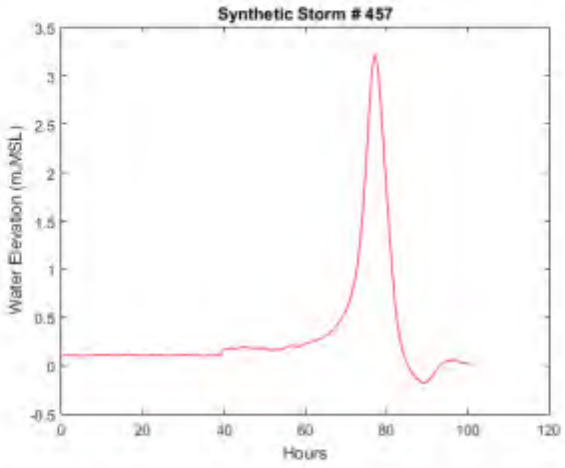

Figure 3. The time series of storm surge for synthetic storm 457—from NACCS—which approximately produces 100-year storm surge (at the upper 95% confidence level) near the Newport NOAA water level station.

Since coastal erosion occurs during major storms, several hurricanes were considered in this study. For validation, Hurricane Irene (late August 2011) was selected as observed data was available during this hurricane in several locations inside the model domain. A larger storm event, Hurricane Bob,

a strong tropical storm which occurred on 19 August 1991 was chosen. Hurricane Bob provides a good representation of large storms in the area, but it was not large enough to overtop the barriers. Also, two synthetic storms from NACCS including a storm representing the 100-year event (which is important for planning purposes) were simulated.

For the surge model, both bathymetry and topography of the domain (a digital elevation model: DEM) were necessary due to wetting and drying. A DEM with a resolution of 10 m was used based on the National Geography Data Center (NGDC) Bathymetry Data and the USACE 2010 coastal Light imaging, Detection, And Ranging (LiDAR) survey. The LiDAR survey focused on the south coast and extended about 1 km offshore (Figure 4).

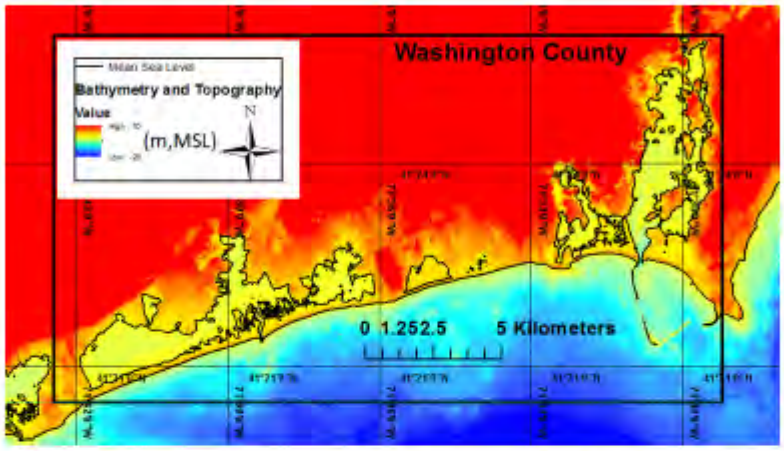

Figure 4. The Digital Elevation Model (DEM) around the study area.

Wind data (for forcing the ADCIRC model) were extracted from the USACE Wave Information Study (WIS) hindcasts near the domain. The WIS data covers a period from 1980 to 2012. For this study, the wind fields from large storm events were of interest. It should be mentioned, as the model domain covered just the southern coast of RI, the spatial variability of wind was considered negligible in this small area. For this 30-year period, Hurricane Bob which made land fall in RI on 19 August 1991, was chosen. Hurricane Bob gives a good representation of large storms in the area [9]. It is the fifth largest storm recorded at the NOAA tide gauge at Newport RI, and approximately corresponds to a 20-year event, according to the extremal analysis for the site (Figure 5). The Newport water elevation station is the closest station to the study area (71.33 W, 41.51 N) and has a long record including major hurricanes. The wind field for Hurricane Bob extracted from WIS is plotted in Figure 6.

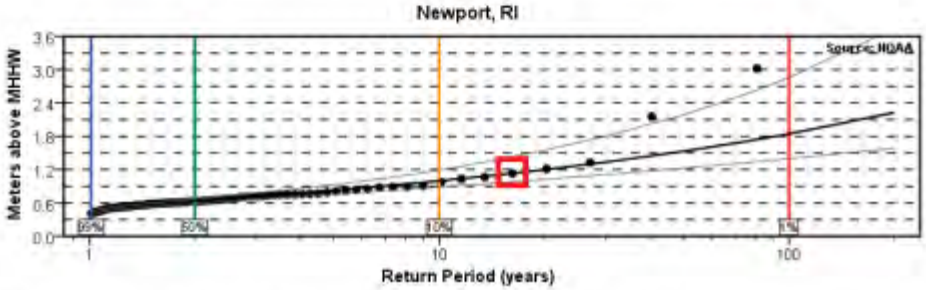

Figure 5. Extremal analysis of water elevation (MHHW = MSL + 0.65) for Newport NOAA station (8452660); the red box shows Hurricane Bob.

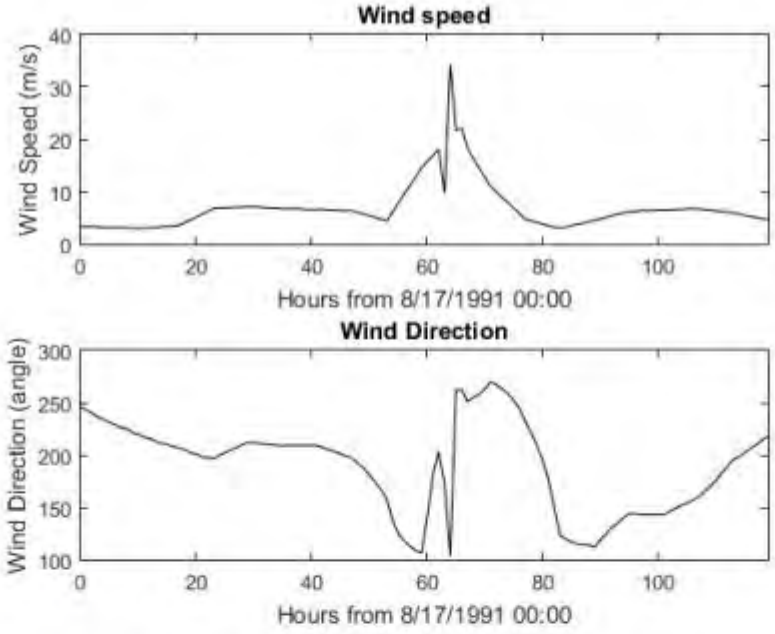

Figure 6. Plots of the wind speed and direction for Hurricane Bob at WIS station number 63079, which is located near the region (71.22 W, 41.25 N).

3. Coastal Erosion Scenarios

Coastal erosion scenarios were based on shoreline retreat and dune erosion during large storm events. The past shoreline retreat rates were used to estimate erosion rates for erosion scenarios, and the DEM was changed according to these rates. It should be mentioned that the rate of erosion is expected to rise due to Sea Level Rise (SLR); nevertheless, this assumption was made to simplify the analysis. Further research is necessary to include the effect of SLR on the rate of erosion. The shoreline retreat rates were calculated using aerial photographs from 1939 to 2014 (Figure 7; [6]). It should be added that shorelines retreat in severe storms and recover during fair weather; however, there is a consistent trend of shoreline retreat over past decades in this region.

Figure 7. A sample shoreline change map for a beach in the study area [6].

The projected shoreline retreat over the next 25 years was considered. The shoreline was divided into the cross-shore profiles shown in Figure 8. In the selected area, the beach profiles consist of an offshore beach slope, a near shore beach slope, and a dune system. The offshore beach slope was extended horizontally to the corresponding 25 years erosion (Figure 9). The same near shore profile and dune system was then assumed at the end of each profile. This method retreats the shoreline while keeping the same beach profile geometry. Once the transects were modified, they were linearly interpolated to modify the DEM of the model.

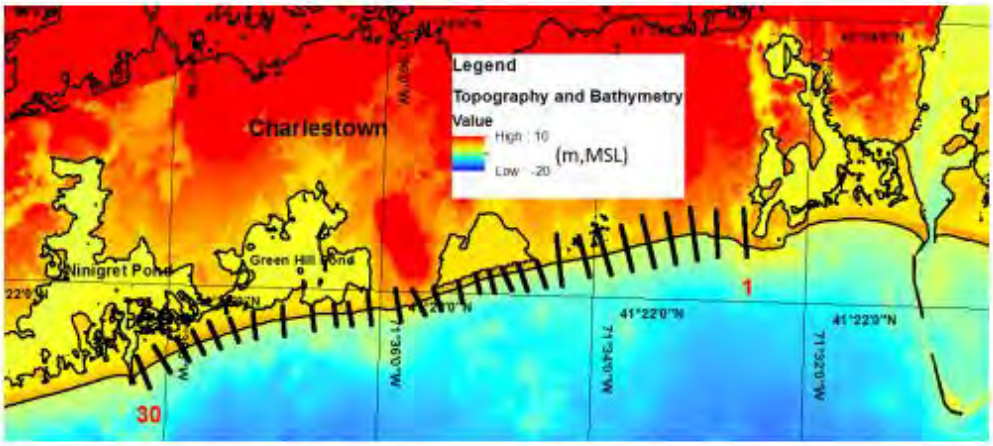

Figure 8. Crossshore transects made to implement coastal erosion between Charlestown Beach and Matunuck Beach (Numbered 1–30).

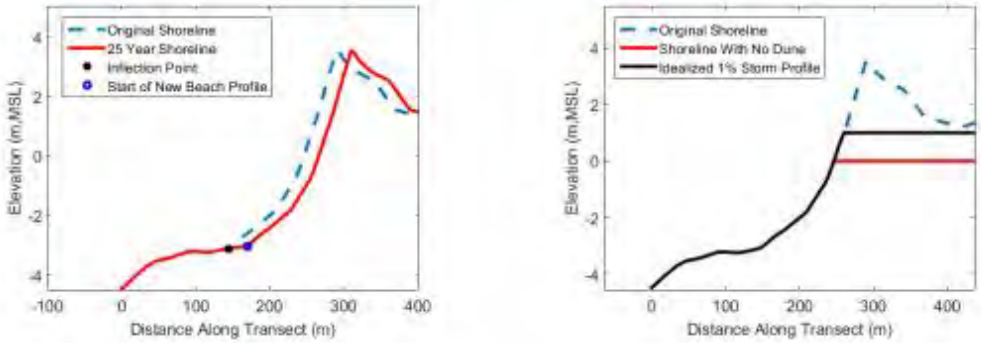

Figure 9. The simplified method which was used to estimate the shoreline geometry after erosion in future. Transect 30 (as an example; Figure 8), with the original shoreline (blue), 25-year shoreline (red), and intersection point (star) are shown. The vertical axis is exaggerated for better clarity. (**a**) shoreline geometry after erosion; (**b**) erosion of the dunes.

Coastal erosion during large storms can lead to failure of dunes as well as retreat of the shoreline. During storm events, the combined action of storm surge and waves erode the dune and create surge channels and wash-over fans (Figure 2). To implement dune erosion in the DEM, it was assumed that the dunes were eroded or simply cut off at an elevation Mean High Water (MHW) with a horizontal line (Figure 9). The elevation of the post storm profile was determined by examining the washover fans deposited after past hurricanes in this area, including 1938 Hurricane, the Ash Wednesday storm (1962), and Hurricane Sandy. The elevations of the washover fans were estimated using LiDAR; the slope of 0.003 cm/m was measured for washover fans after Hurricane Sandy, which can be assumed horizontal for the model resolution used in this study.

4. Numerical Modeling

For surge modeling, the ADCIRC model was used. ADCIRC is based on the finite element method and unstructured mesh discretization, allowing areas such as coastal inlets to be resolved with a reasonable computational cost. ADCIRC has been coupled with Simulating WAves Nearshore (SWAN), and can simulate the wave-surge interactions [12]. This model has been extensively used to predict storm surge flooding (e.g., [10,13]).

A mesh was created, resolving coastal inlets, using the Surface water Modeling System Software (SMS) with a resolution of 30 m near the coastline, 150 m farther offshore, and 2 km near the open boundaries. The mesh is plotted in Figure 10. The model was forced along the open boundaries by water elevation, and by wind stress/pressure over the domain. The model was run in the 2-D mode, with a Manning friction coefficient of 0.018 (below MSL), and up to 0.06 in land areas. For the tidal case, the model was forced using five harmonic constituents for tides including M2, N2, K1, S2, and O1 which can be extracted from tidal databases [14]. M4 and other overtide constituents were neglected. M4 is generated in shallower regions by friction, and causes tidal asymmetry. Neglecting the M4 component can change the water level by around 6 cm, which can be neglected during a major storm surge event. These constituents represent the main components of tide for this area (Table 1).

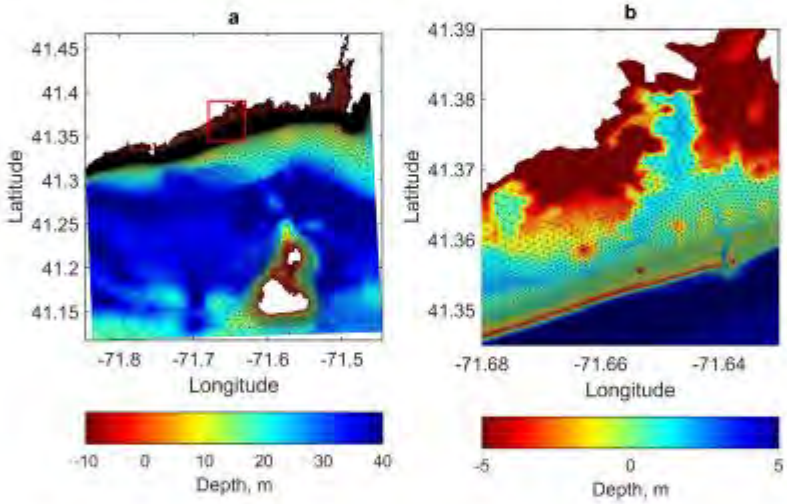

Figure 10. An overview of the mesh used for surge modeling in the southern coast of RI. The model domain is larger than the study area and includes Block Island near the southern boundary. Subfigure (**b**) shows a magnified view of the rectangular area in Subfigure (**a**) around Ninigret Pond.

Table 1. Harmonic constituents at the Newport and Providence NOAA water elevation stations.

Harmonics	Newport Amplitude (m)	Newport Phase (degrees)	Providence Amplitude (m)	Providence Phase (degrees)
M2	0.505	2.3	0.643	9.5
S2	0.108	25.0	0.138	33.6
N2	0.124	345.8	0.152	354.6
K1	0.062	166.1	0.073	169.4
M4	0.057	35.8	0.103	202.2
O1	0.047	202.0	0.027	312.7
M6	0.0005	220.1	0.027	312.7
MK3	0.0008	19.5	0.016	39.3
S4	0.0007	5.1	0.014	23.8
MN4	0.026	347.9	0.014	12.7

5. Results

5.1. Model Skill Assessment

To test the performance of the model for tides and storm surge, the Woods Hole Group Inc. data were used [7]. The observed data were compared with the model results during a spring-neap cycle (for tides), and during Hurricane Irene (for storm surge). For tides, the model was run for 30 days from 14 May 2011 until 13 June 2011 with a one day ramping period. This time period is within the duration of the Woods Hole Group data collection campaign. The model and observed water elevation data were analysed by `T_Tide` code to compute tidal constituents [15]. Table 2 shows the comparison between the modeled results and the observed data at the two stations inside Ninigred Pond. As this table shows, the modeled and observed data, in general, are in good agreement. In particular, the performance of the model for the phase and amplitude of the dominant M2 component is good. The model underpredicts the amplitude of S2, but as this component is very small, its effect is not that significant inside the pond. The overall RMSEs (Root Mean Square Error) for amplitude and phase are 0.015 m and 25°, respectively, which are convincing.

Table 2. Skill assessment of the numerical model for tidal predictions inside Ninigret Pond; see Figure 1 for location of the stations. RMSE for amplitude and phase are 0.015 m and 25°, respectively.

Constituents	NW				NN			
	Model		Observation		Model		Observation	
	amp (m)	Phase (deg)	amp (m)	Phase (deg)	amp (m)	Phase (deg)	amp (m)	Phase (deg)
O1	0.022	277	0.018	283	0.022	271	0.017	277
K1	0.024	217	0.019	223	0.024	210	0.019	216
N2	0.021	48	0.017	71	0.020	34	0.017	56
M2	0.083	82	0.081	89	0.075	69	0.077	75
S2	0.008	114	0.021	106	0.007	98	0.021	101

For the storm surge case, Hurricane Irene was simulated, a category 3 storm that occurred in late August 2011. The comparison of the model results and observations are depicted in Figure 11. The performance of the model for both stations is very good with an RMSE of 0.065 m and 0.041 m for NN and NW respectively; however, the model slightly overestimates the surge. Overall, given the magnitude of errors, the performance of the model was considered satisfactory.

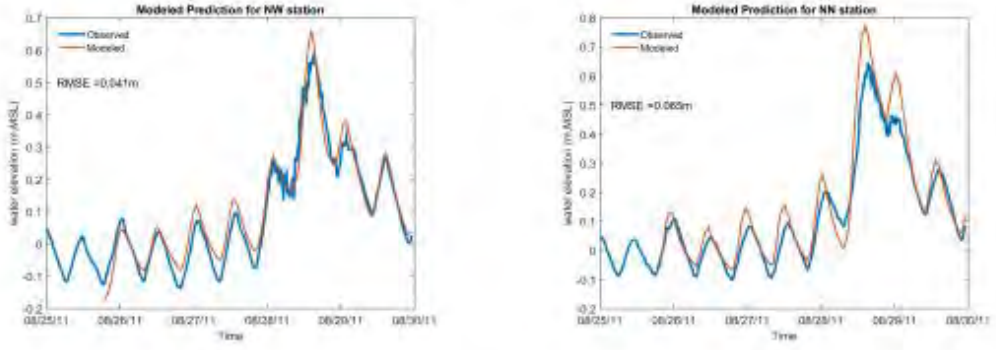

(a) (b)

Figure 11. Comparison between the model predictions and the observed data for Hurricane Irene (see Figure 1 for location of the stations). (**a**) NW station; (**b**) NN station.

5.2. Propagation of Tides/Storm Surge in Coastal Ponds; Effect of Coastal Inlets

As mentioned previously, the southern coast of RI consists of several coastal ponds and barriers, and the failure of dunes can affect the inlet-basin/pond system. At first, a simplified analysis was

carried out based on the previous research about the dynamics of inlet-basins, and the collected data in this area. This analysis helped interpret modeling results. Figure 12 shows the comparison of water elevation inside and outside Ninigret Pond using observed data for a duration of one month. A dramatic reduction of the amplitude can be observed in this figure. A coastal inlet, in general, causes a reduction of water elevation amplitude and a phase-lag or a delay inside coastal ponds relative to offshore. This is mainly associated with the energy dissipation by high velocity currents in an inlet. Simplified analytical methods have been introduced in the literature to compute the reduction of the amplitude, and the phase lag, based on the geometry and physical characteristics of the inlet-basin system. A detailed analytical analysis of inlet-basin hydrodynamics can be found in the Coastal Engineering Manual [16]. Considering a long wave (e.g., tide or surge), with an amplitude of a_o, and a period of T, the effect of a coastal inlet on tide/surge signal as it propagates from the ocean to the pond can be written as,

$$[R, \phi_l] = f(A_i/A_b, R_h, L, T, \mathbf{F}); \quad R = 1 - a_i/a_o \tag{1}$$

where R is the reduction in the amplitude, a_i is the amplitude inside the basin/pond, ϕ_l is the phase lag, A_i is the cross sectional area of the inlet, A_b is the area of a basin or a pond, R_h is the hydraulic radius of the inlet, L is the length of the inlet, and $\mathbf{F}$ represents the frictional coefficients for the entrance, exit and channel friction losses. For Ninigret Pond, $A_b = 7.5\ \text{km}^2$, $A_i = 45\ \text{m}^2$, $L = 1.7$ km, $R_h = 1.5$ m. Using these parameters, and assuming entrance, and exit loss coefficients of 0.1 and 1.0, respectively (recommended by the Coastal Engineering Manual [16]), leads to $R = 80\%$ and $\phi_l = 90^\circ$. The impact of inlets on tidal signal was also assessed using observed data. By performing a tidal analysis using `T_Tide` [15] inside (Wood Holes Group Station) and outside this pond (NOAA, Weekapaug Point 71.76 W, 41.33 N), R for the M2 tidal component was found to be 76% for the NW station (Figure 1), with phase lags of 90.5° or about 3 h and 6 min. These values which are based on the observations are very close to the analytical method predictions (i.e., $R = 80\%$ and $\phi_l = 90^\circ$). Considering that some storm surge events have similar (or longer) periods, if coastal barriers for this pond fail, this reduction of the amplitude no longer exist. Consequently, dune erosion can lead to a significant increase in the flooding area.

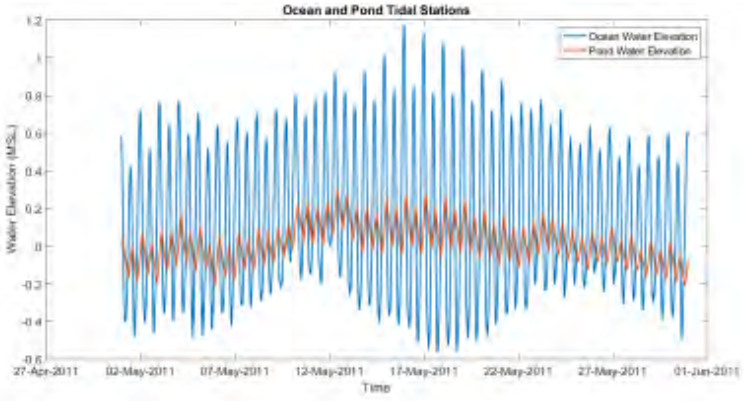

Figure 12. Comparison of observed water elevation data inside and outside Ninigret Pond (NW Gauge, Figure 1).

Further, the geometry of a coastal inlet has a controlling effect on the reduction of the amplitude of water elevation signal. Considering the three coastal ponds in this area (Figure 1; Ninigret Pond, Trustom Pond, and Point Judith Pond), the effect of coastal inlet geometry can be further examined. Point Judith Pond has a wide and deep inlet with a width of 80 m and a depth of around 7 m. Trustom Pond, on the contrary, has no permanent connection to the ocean for tides, but during

large storm events, part of its barrier is overtopped or breached (for example in Hurricane Sandy) causing some flooding. Ninigret Pond has a relatively narrow inlet (35 m), protected by hard structures. The water elevations in the three ponds are plotted for a tidal cycle, and for a storm event (Hurricane Bob) in Figure 13 using the ADCIRC model. As this figure shows, the water elevation signal for tide inside and outside of the Point Judith Pond is almost the same due to its wide inlet, but the peak of storm surge slightly attenuates during the storm event. For Trustom Pond, the barrier is not overtopped for tides or the storm surge scenario. Ninigret Pond shows a significant reduction for tides ($R = 80\%$) and for Hurricane Bob ($R = 68\%$) due to its narrower inlet. Therefore, if a storm surge does not overtop or erode coastal dunes, coastal inlets can significantly decrease the magnitude of a storm surge (inside a coastal pond).

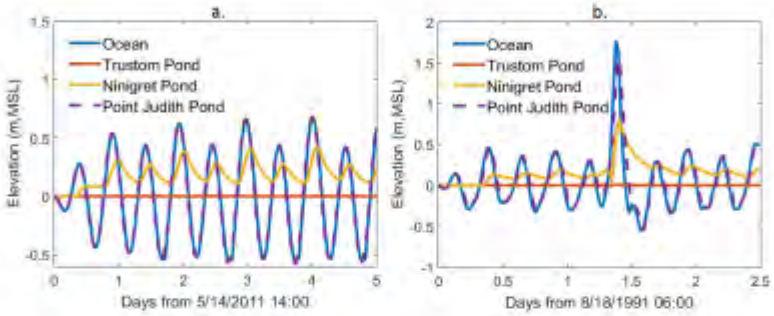

Figure 13. Effect of coastal inlet geometry on surge inside three coastal ponds in the study area; comparison of water elevation in Ninigret Pond, Trustom Pond, and Point Judith Pond for (**a**) Tides; (**b**) Hurricane Bob.

The above analysis shows a significant dampening of tide and surge signal caused by coastal inlets. However, the frequency/period of a water elevation signal and the geometry of an inlet are the two important factors which control this dampening [17–19]. Figure 14 shows the reduction of amplitudes of various water elevation signals assuming different periods for Ninigret Pond. The analysis was performed using the simplified analytical method mentioned earlier [16]. As this figure shows, frequencies of 1, 2, and 2.5 days lead to 0.65, 0.38, and 0.25 reductions, respectively. Therefore, a storm surge which has a long period (more than 2 days) will be less effected compared to a tidal signal with a period of 12 h. It should be added that the total water level during a storm surge is due to the combination of tide and surge signals. In addition, the geometry of an inlet, as discussed above, is another important factor, which should be always considered before generalizing these results.

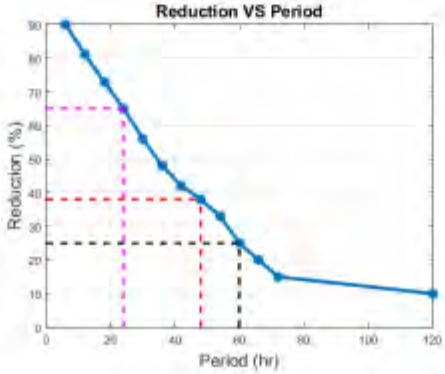

Figure 14. Effect of water elevation signal period on reduction of the amplitude for Ninigret Pond.

5.3. Effect of Erosion on Storm Surge

Two erosion scenarios were considered: shoreline change in 25 years, and dune erosion. As mentioned, the erosion of dunes is a common consequence of large hurricanes in the study area as can be seen in Figure 2, which shows the partial failure of the dune system of Ninigret Pond during Hurricane Carol in 1954. Several scenarios considering the two storm cases (100-year synthetic storm and Hurricane Bob) were considered.

For Hurricane Bob, the flooding areas assuming eroded (retreated) shoreline and the current shoreline were examined. Table 3 shows the summary of results. Considering a retreated shoreline in 25 years, the flooding extent slightly increases by 0.22 km^2, which is 20% of the original flooded area (1.12 km^2). This increased flooding area is approximately the advance of the sea (about 30 m) due to coastal erosion; therefore, the shoreline retreat does not significantly increase the extent of flooding. However, when the dunes are eroded, the flooding extent increased by 2.33 km^2, which is a 207% increase. When dunes erode, the coastal inlets of the ponds can no longer dampen the surge signal, and therefore a much larger area within coastal ponds are flooded. For this scenario, the flooding extent advanced up to 500 m in some areas. Figure 15 shows the flooding extent for existing dunes, and eroded dune profile scenarios.

Table 3. Differences in flooded areas near the eroded shoreline for Hurricane Bob assuming erosion scenarios.

Erosion Scenario	Current Flooded Area, km^2	Changed Flooded Area, km^2	Difference, km^2	Percentage Increase
Shoreline retreat in 25 years	1.13	1.35	0.22	19.7%
Eroded dunes	1.13	3.5	2.33	207%

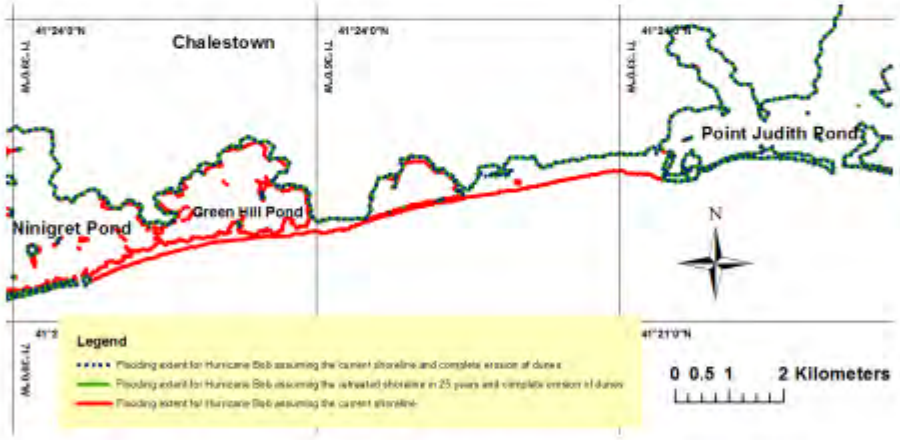

Figure 15. Comparison of Hurricane Bob flooding extent assuming current condition (red) and current shoreline with no dune system (blue), and the 25-year retreated shoreline as well as complete dune failure (black).

For the 100-year event, the erosion scenarios (shoreline retreat and dune erosion) did not lead to a significant change in flooded areas as shown in Figure 16. This is because for this event, the storm surge is large enough to overtop the dunes (the dune top elevation is about 3 m, MSL in this area); therefore, even if the dunes were solid structures and could resist the erosion during storm surge, they could not protect the coastal ponds. It should be noted that the failure of dunes may significantly affect wave propagation for the 100-year event (waves can break over dunes, due to decreased water depth).

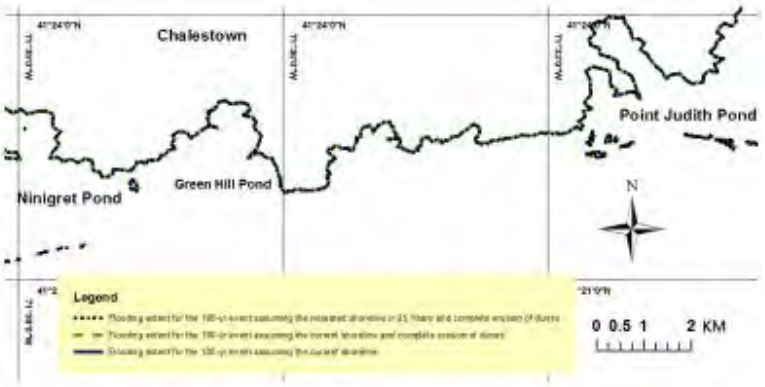

Figure 16. Comparison of 100-year flooding extent assuming the current shoreline (blue), current shoreline with eroded dune system (green), and the 25-year retreated shoreline plus complete dune failure (black). Lines overlap for this scenario.

SLR, in general, leads to an increase of the flooding extent [20]. A very simple way of investigating the impact of SLR on flooding is the bathtub approach or adding the magnitude of SLR to elevations predicted by a storm surge model; this methods neglects the nonlinearity of the storm surge propagation. A more accurate method includes changing the DEM, and simulating the storm surge assuming a SLR scenario. Consistent to our analysis which assumed a 25 years shoreline retreat, 30 cm or 1 foot SLR was assumed, corresponding to projected values by NOAA (High) for 25 years [21]. Figure 17 shows that the extent of flooding, as expected, increases in some areas. The flooding area increased from 4.72 km^2 to 6.80 km^2, leading to a 44% increase.

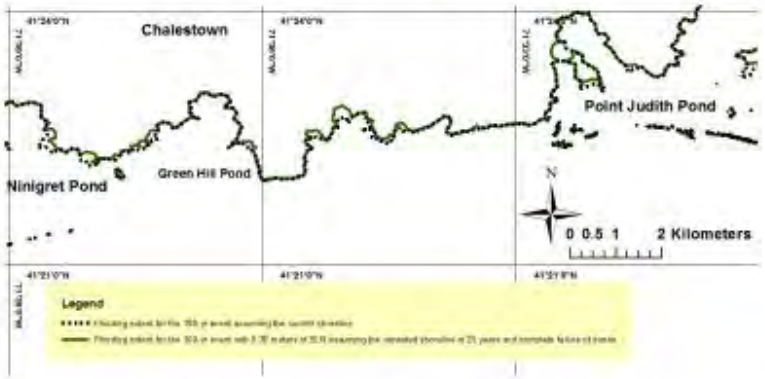

Figure 17. Comparison of flooding extend of the 100-year storm event, assuming 30 cm SLR, and coastal erosion.

6. Discussion

The geometry of coastal inlets controls the storm propagation for moderate storms in areas with inlet-basin systems. Some regional modeling studies such as NACCS have not resolved these inlets, and their predictions inside coastal ponds may not be reliable beyond barriers and inside ponds. Figure 18 is an example showing the poor resolution of the NACCS mesh around Ninigret Pond inlet. In Figure 19, the prediction of storm surge for a moderate synthetic storm (220, which has a peak elevation of 1.67 m, MSL in Newport [8]), near two save points (see Figure 18b) located inside and outside Ninigret Pond, has been compared with that from our model. The surge event was channeled through the inlet, but given the poor resolution of the NACCS model, water levels are overestimated. It should be noted that NACCS results, unlike the ADCIRC model developed in this study, have not

been validated inside coastal ponds and very near shore in RI. Also, waves for this storm are not that significant inside the pond; therefore, wave-surge interaction cannot be associated with higher storm prediction in the NACCS model. The results are identical at the boundary (Point A), as the ADCIRC model was forced by NACCS at the open boundary.

(a) NACCS model resolution around Ninigret inlet

(b) Comparison points: A, B, and C

Figure 18. Effect of model resolution on the results; Subfigure (**a**) shows an example of low resolution NACCS mesh in a coastal inlet; Subfigure (**b**) shows the locations of comparison for NACCS results and those obtained in this study.

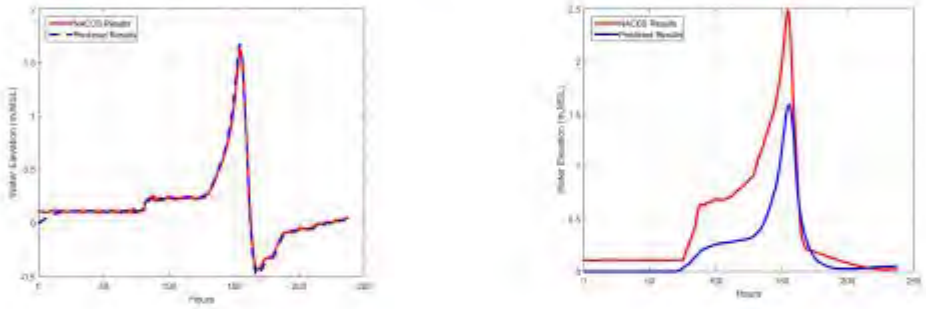

(a) **(b)**

Figure 19. Comparison of NACCS results and ADCIRC model of this study for synthetic Storm 220. See Figure 18b for locations of comparison. (**a**) Comparison at B: outside Ninigret Pond; (**b**) Comparison at C: inside Ninigret pond.

The dunes along the entire southern coast of RI have an average height of 3.39 m above MSL, but in some areas they are as low as 1.1 m. This means that a storm with a magnitude of 100-year (3.35 m, (MSL) considering the 100-year event at the upper confidence level curve) can potentially overtop all of the dunes. A hurricane such as Carol, which had a surge height of 2.7 m, MSL at Newport RI can breach the dunes (Figure 2), and have a similar but lesser effect on flooding (increasing the flooding extent). Various factors are associated with the erosion of dunes [22], including the geotechnical properties of dunes, the elevation of dunes compared to surge, wave-induced forces, and wave runup/overtopping. Therefore, it is a challenging task to specify a threshold for a storm which leads to dune failure. Morphological modeling (e.g., [4]) along with data collection during and after large storms around coastal dunes can improve our understanding of this process for this area, for future studies.

The analysis carried out in this study was based on two extreme scenarios: complete dune erosion, and no dune erosion. In reality, dunes are partially eroded during major storms (Figure 2), and gradually recover during calmer months. Therefore, a storm cluster can lead to more damage compared with isolated events. The effect of erosion on storm surge is overestimated by assuming complete erosion of dunes. However, the results show the significant impact of dune erosion on flooding, and quantify this impact for this extreme scenario.

7. Conclusions

We explored the effect of dune erosion and shoreline retreat on coastal flooding in an area which consists of coastal ponds protected by dunes and connected to the ocean by narrow inlets. A storm surge model was developed/validated with a unique dataset, which included water elevation data inside coastal ponds during 2011 and measurements during Hurricane Irene. The conclusions are summarized as follows:

1. The results showed that erosion of dunes has more effect on flooding extent compared with retreat of shorelines.
2. For storms which do not overtop or erode the coastal dunes, the inlets of coastal ponds can significantly decrease the storm surge elevation. This can be explained using the concepts of inlet-basin hydrodynamics. However, for very extreme storms such as a 100-year event where coastal dunes are overtopped, and low-lying areas are flooded, the flooding extent did not significantly change.
3. Assuming complete erosion of the dunes and for the scenario of Hurricane Bob, simulations showed a more than 200% increase in the flooding extent. Several sources of uncertainty can affect these estimations. For instance, in many cases, dunes are partially eroded. Coupled hydrodynamic and morphodynamic models which can simulate dunes erosion more accurately, can lead to more realistic estimations.
4. Numerical surge models which do not fully resolve coastal inlets (e.g., NACCS model in RI) lead to significant errors in the prediction of surge in coastal ponds. Accurate bathymetric and topographic measurement of coastal inlets is essential for storm surge modeling in areas with inlet-basin systems.

Acknowledgments: This work was under taken with funding support from a Rhode Island Community Development Block Grant (4712) from the U.S. Department of Housing and Urban Development and the State of Rhode Island Division of Planning Office of Housing and Community Development. Thanks to US Army Corps of Engineers (USACE) for sharing the North Atlantic Coastal Comprehensive Studies' dataset. Thanks to National Hurricane Center (NHC) and Center for Operational Oceanographic Products and Services from NOAA for supplying hurricane and water level data. Thanks to Woods Hole Group Inc. for providing the water elevation data. Thanks to Marissa Torres for her comments on the paper.

Author Contributions: Alex Shaw developed the numerical models, and analysed the results. Mohammad Reza Hashemi initiated and led the research, and helped in discussion of the results. Malcolm Spaulding advised the research in many aspects, including analysis of the results and development of the models. Bryan Oakley contributed in coastal erosion and general discussions. Chris Baxter helped in the discussion of the results.

Conflicts of Interest: The authors declare no conflict of interest.

References

1. Wahl, T.; Jain, S.; Bender, J.; Meyers, S.D.; Luther, M.E. Increasing risk of compound flooding from storm surge and rainfall for major US cities. *Nat. Clim. Chang.* **2015**, *5*, 1093–1097.
2. Parris, A.; Bromirski, P.; Burkett, V.; Cayan, D.R.; Culver, M.; Hall, J.; Horton, R.; Knuuti, K.; Moss, R.; Obeysekera, J.; et al. *Global Sea Level Rise Scenarios for the United States National Climate Assessment*; NOAA Technical Report OAR CPO-1; NOAA: Silver Spring, MD, USA, 2012
3. Roelvink, D.; Reniers, A.; van Dongeren, A.; de Vries, J.V.T.; McCall, R.; Lescinski, J. Modelling storm impacts on beaches, dunes and barrier islands. *Coast. Eng.* **2009**, *56*, 1133–1152.
4. McCall, R.T.; de Vries, J.V.T.; Plant, N.; van Dongeren, A.; Roelvink, J.; Thompson, D.; Reniers, A. Two-dimensional time dependent hurricane overwash and erosion modeling at Santa Rosa Island. *Coast. Eng.* **2010**, *57*, 668–683.
5. Kurum, M.O.; Edge, B.; Mitasova, H.; Overton, M. Effects of coastal landform changes on storm surge along the Hatteras Island breach area. *Coast. Eng. Proc.* **2011**, *1*, 25.
6. Boothroyd, J.; Hollis, R.; Oakley, B.; Henderson, R. *Shoreline Change from 1939–2014, Washington County, Rhode Island. 1:2,000 scale, 45 maps*; Technical Report; Rhode Island Geological Survey: Kingston, RI, USA, 2016.

7. Woods Hole Group. *Wave Tide and Current Data Collection Contract No. W912WJ-09-D-0001-0026*; US Army Corps of Engineers: New England District, MA, USA, 2012.
8. Cialone, M.A.; Massey, T.C.; Anderson, M.E.; Grzegorzewski, A.S.; Jensen, R.E.; Cialone, A.; Mark, D.J.; Pevey, K.C.; Gunkel, B.L.; McAlpin, T.O. *North Atlantic Coast Comprehensive Study (NACCS) Coastal Storm Model Simulations: Waves and Water Levels*; Technical Report, DTIC Document; The U.S. Army Engineer Research and Development Center: Vicksburg, MS, USA, 2015.
9. Hashemi, M.R.; Spaulding, M.L.; Shaw, A.; Farhadi, H.; Lewis, M. An efficient artificial intelligence model for prediction of tropical storm surge. *Nat. Hazards* **2016**, *82*, 471–491.
10. Luettich, R., Jr.; Westerink, J.; Scheffner, N.W. *ADCIRC: An Advanced Three-Dimensional Circulation Model for Shelves, Coasts, and Estuaries*; Report 1. Theory and Methodology of ADCIRC-2DDI and ADCIRC-3DL. Technical Report, DTIC Document; US Army Corps of Engineers : Washington DC, USA, 1992.
11. Smith, J.M.; Sherlock, A.R.; Resio, D.T. *STWAVE: Steady-State Spectral Wave Model User's Manual for STWAVE*, version 3.0; Technical Report, DTIC Document; US Army Corps of Engineers: Washington DC, USA, 2001.
12. Dietrich, J.C.; Tanaka, S.; Westerink, J.J.; Dawson, C.; Luettich, R., Jr.; Zijlema, M.; Holthuijsen, L.H.; Smith, J.; Westerink, L.; Westerink, H. Performance of the unstructured-mesh, SWAN + ADCIRC model in computing hurricane waves and surge. *J. Sci. Comput.* **2012**, *52*, 468–497.
13. Westerink, J.J.; Luettich, R.A.; Feyen, J.C.; Atkinson, J.H.; Dawson, C.; Roberts, H.J.; Powell, M.D.; Dunion, J.P.; Kubatko, E.J.; Pourtaheri, H. A basin-to channel-scale unstructured grid hurricane storm surge model applied to southern Louisiana. *Mon. Weather Rev.* **2008**, *136*, 833–864.
14. Mukai, A.Y.; Westerink, J.J.; Luettich, R.A., Jr.; Mark, D. *Eastcoast 2001, a Tidal Constituent Database for Western North Atlantic, Gulf of Mexico, and Caribbean Sea*; Technical Report, DTIC Document; US Army Corps of Engineers: Washington DC, USA, 2002.
15. Pawlowicz, R.; Beardsley, B.; Lentz, S. Classical tidal harmonic analysis including error estimates in MATLAB using T_TIDE. *Comput. Geosci.* **2002**, *28*, 929–937.
16. US Army Corps of Engineers. *Hydrodynamics of Tidal Inlets*; EM 1110-2-1100 ed.; US Army Corps of Engineers: Washington DC, USA, 2008.
17. Wong, K.C.; DiLorenzo, J. The response of Delaware's inland bays to ocean forcing. *J. Geophys. Res. Oceans* **1988**, *93*, 12525–12535.
18. Chuang, W.S.; Swenson, E.M. Subtidal water level variations in Lake Pontchartrain, Louisiana. *J. Geophys. Res. Oceans* **1981**, *86*, 4198–4204.
19. Aretxabaleta, A.L.; Butman, B.; Ganju, N.K. Water level response in back-barrier bays unchanged following Hurricane Sandy. *Geophys. Res. Lett.* **2014**, *41*, 3163–3171.
20. Woodruff, J.D.; Irish, J.L.; Camargo, S.J. Coastal flooding by tropical cyclones and sea-level rise. *Nature* **2013**, *504*, 44–52.
21. Sweet, W.V. *Sea Level Rise and Nuisance Flood Frequency Changes around the United States*; NOAA Technical Report NOS CO-OPS 073; National National Oceanic and Atmospheric Administration: Silver Spring, MD, USA, 2014.
22. Judge, E.K.; Overton, M.F.; Fisher, J.S. Vulnerability indicators for coastal dunes. *J. Waterw. Port Coast. Ocean Eng.* **2003**, *129*, 270–278.

51. Assignment 2, Module 10: Storm Size on Surge: https://www.academia.edu/11963487/The_Influence_of_Storm_Size_on_Hurricane_Surge#:~:text=SEPTEMBER%202008%20IRISH%20ET%20AL.%202003%20The%20Influence,might%20be%20estimated%20from%20the%20Saffir%E2%80%93Simpson%20hurricane%20scale.

The Influence of Storm Size on Hurricane Surge

JENNIFER L. IRISH

Zachry Department of Civil Engineering, Texas A&M University, College Station, Texas

DONALD T. RESIO

Coastal and Hydraulics Laboratory, U.S. Army Engineer Research and Development Center, Vicksburg, Mississippi

JAY J. RATCLIFF

New Orleans District, U.S. Army Corps of Engineers, New Orleans, Louisiana

(Manuscript received 20 November 2006, in final form 25 January 2008)

ABSTRACT

Over the last quarter-century, hurricane surge has been assumed to be primarily a function of maximum storm wind speed, as might be estimated from the Saffir–Simpson hurricane scale. However, Hurricane Katrina demonstrated that wind speed alone cannot reliably describe surge. Herein it is shown that storm size plays an important role in surge generation, particularly for very intense storms making landfall in mildly sloping regions. Prior to Hurricane Katrina, analysis of the historical hurricane record evidenced no clear correlation between surge and storm size, and consequently little attention was given to the role of size in surge generation. In contrast, it is found herein that, for a given intensity, surge varies by as much as 30% over a reasonable range of storm sizes. These findings demonstrate that storm size must be considered when estimating surge, particularly when predicting socioeconomic and flood risk.

1. Introduction

The Saffir–Simpson hurricane scale (Table 1) was developed in 1969 to provide weather forecasters and emergency planners with a simple method for estimating wind damage potential (e.g., Simpson 1974). This scale is based solely on estimated maximum wind speed within a hurricane, and in spite of its narrow perspective, has proven to be an adequate indicator of hurricane wind damage. However, reliance on this scale as an indicator of potential storm surge has led to serious misconceptions within the public and scientific communities alike. For example, the Saffir–Simpson scale cannot be used to answer why a storm like Hurricane Katrina, classified by the National Oceanographic and Atmospheric Administration (NOAA) as a category 3 storm at landfall (National Weather Service 2005; Blake et al. 2006), produced a much larger storm surge than that produced by Hurricane Camille, classified by NOAA as a category 5 storm at landfall (Blake et al. 2006; Neumann et al. 1999). As will be shown here, the primary reason for this discrepancy appears to be in storm size. The purpose of this paper is to investigate the general influence of hurricane size, in addition to wind speed (Saffir–Simpson scale), in generating surge at the coast.

As noted in an article on the rising death toll in Hurricane Katrina found in Biloxi, Mississippi's *Sun Herald* (Norman 2006), "an oft heard refrain . . . is Hurricane Camille killed more people in 2005 than it did in 1969. Many officials and locals believed those . . . who had survived what was then the strongest recorded hurricane were lulled into a false sense of security that kept them in harm's way." Even today, many people still echo the sentiment that it would have been much worse if a Saffir–Simpson category 5 storm had struck this area rather than Katrina. Evidence will be presented that shows the Saffir–Simpson scale is not a particularly good indicator of storm surge along the coast and that storm size, along with bottom slope, is also a critical factor in the generation of large coastal surges.

Corresponding author address: Jennifer L. Irish, Zachry Department of Civil Engineering, Texas A&M University, 3136 TAMU, College Station, TX 77843.
E-mail: jirish@civil.tamu.edu

DOI: 10.1175/2008JPO3727.1

ale.

TABLE 1. Saffir–Simpson hurricane scale (Simpson 1974; National Weather Service 2006).

Saffir–Simpson category	Max 1-min wind speed ($m\ s^{-1}$)	Storm surge (m)
1	33.0–42.5	1.2–1.5
2	42.9–49.2	1.8–2.4
3	49.6–58.1	2.7–3.7
4	58.6–69.3	4.0–5.5
5	>69.3	>5.5

Figure 1 shows a measure of storm intensity (far-field pressure, estimated as 1020 mb, less central pressure Δp) and a measure of size (radius to maximum wind speed R_{max}) for Hurricanes Camille (left side) and Katrina (right side) as a function of distance to landfall. As this figure shows, Hurricane Katrina was significantly larger than Hurricane Camille during its entire passage through the Gulf of Mexico, as well as during its final approach to land. In this paper we will examine the hypothesis that storm size significantly influences the potential for storm surge generation in hurricanes. As will be shown here, it is very likely that storm size is the dominant factor in surge generation for these two storms, and that this is the primary reason why surges in Hurricane Katrina [7.5–8.5 m; see U.S. Army Corps of Engineers (2006a)] were substantially higher than surges in Hurricane Camille [6.4–6.9 m; see U.S. Army Corps of Engineers (2006b)]. Furthermore, it appears that on all shallow coasts, the role of storm size in surge generation can be of the same magnitude as storm intensity, particularly for intense storms.

In this paper we will first provide a background on past efforts to characterize hurricane surge and an overview of hurricane surge generation. Next, we detail our approach for investigating the surge response to hurricane size, in addition to wind speed and continental shelf slope. Finally, we present our results and analyses with respect to historical observations.

2. Background

To appreciate the lack of focus on hurricane size and the emphasis on the Saffir–Simpson scale as an indicator of hurricane surge, it is useful to examine the history of storm surge response research. Earlier studies to correlate peak storm surge with hurricane meteorological conditions suggested that storm size is not well correlated with peak surge, and that the Saffir–Simpson scale may be a reasonable surge indicator by area (Hoover 1957; Conner et al. 1957; Harris 1959, 1963; Jelesnianski 1972). Building on initial analyses (Hoover 1957; Conner et al. 1957), Harris (1959, 1963) stated that peak surge was determined by a simple relationship to the central pressure and regional bottom slope. Jelesnianski (1972) used a numerical hydrodynamic model to develop a series of nomographs relating peak surge to central pressure, storm size, and a shoaling factor. Although accounting for storm size, he noted that peak surge was only weakly dependent on size.

Since the 1970s, the scientific and public communities alike have accepted that peak surge may largely be determined from either the central pressure deficit or the related maximum wind speed (Saffir–Simpson scale). Consequently, most hurricane surge studies, for both forecasting and coastal protection design, have relied heavily on intensity and wind speed as the determining factors for hurricane surge response (e.g., Berke et al. 1984). While both hurricane intensity and size are regularly included, along with local geometry, when simulating and predicting hurricane surge with the Sea, Lake, and Overland Surges from Hurricanes (SLOSH; Jelesnianski 1984, 1990) and other models (e.g., Westerink et al. 2007), the resulting surge from these prediction models has traditionally been attributed to intensity and presented with respect to the Saffir–Simpson category. Blain et al. (1998) did investigate storm size, but only in the context of optimizing grid resolution for numerical surge simulation. Most methods to characterize surge in the Atlantic and Gulf of Mexico, while considering storm size, have followed the earlier works reported in the 1950s through the 1970s and have not analyzed a large enough hurricane size range, particularly in conjunction with very shallow continental shelves, to fully capture the impact of hurricane size on surge generation (e.g., Taylor 1980; Russo 1998; Weisberg and Zheng 2006).

In the early 1990s, Dolan and Davis (1992) and Davis and Dolan (1993) recognized the shortcomings of the Saffir–Simpson scale for predicting storm damage, and they presented an intensity scale that additionally correlates storm duration and wave power for extratropical storm events with coastal erosion and overwash. However, this intensity scale, which was developed for very large weather systems, does not give an indication of expected peak storm surge as it relates to storm size. Almost all hurricane flood damage studies show that damage to communities along the Gulf of Mexico are primarily a function of flood elevation. For example, the extensive surveys conducted following Hurricane Katrina did not show a high correlation between flooding duration and damage, but they did demonstrate a high correlation between flood elevation and damage.

Weisberg and Zheng (2006) studied the influence of the Saffir–Simpson scale (hurricane intensity), landfall location, forward speed, and direction with respect to

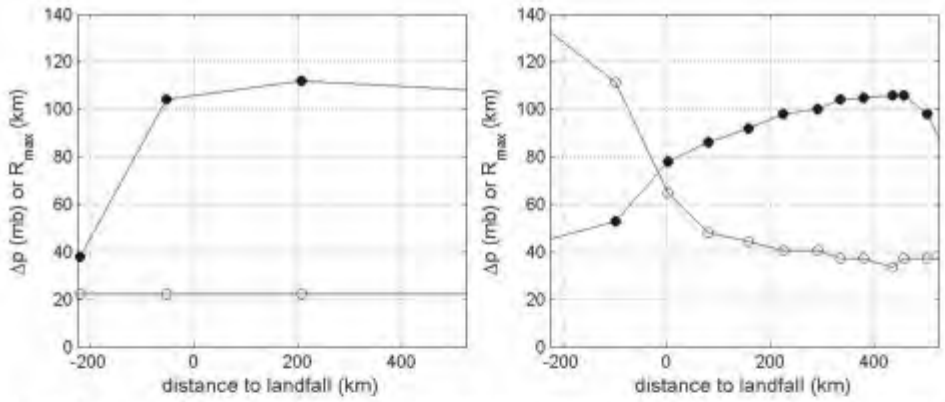

FIG. 1. Observed hurricane intensity (Δp, solid) and size (R_{max}, hollow) as Hurricanes (left) Camille and (right) Katrina move landward. Hurricanes track from right to left such that distances prior to landfall are positive.

the coast on simulated hurricane surge within a bay and concluded that the surge response was indeed sensitive to all of these parameters. While Weisberg and Zheng (2006) considered two different hurricane sizes in their analysis, only one size per Saffir–Simpson category was investigated; thus, no conclusions could be drawn in regard to the influence of hurricane size on surge for a given storm intensity.

Most recently, Powell and Reinhold (2007) presented a new approach for assessing wind damage by hurricanes by considering the integrated kinetic energy over the entire storm, thus inherently including storm size, rather than solely relying on maximum wind speed. However, such an approach has yet to be considered for hurricane surge estimation.

The above-mentioned hurricane studies emphasized storm intensity with limited consideration of storm size. The specific influence of hurricane size on storm surge has not yet been characterized largely because the influence of storm size has historically been considered insignificant, based upon those studies performed in the late 1950s through the early 1970s, which could not make use of data on very large hurricanes like Hurricane Katrina. However, the limited consideration given to hurricane size has lead to widespread misconceptions regarding surge generation by hurricanes, and in particular by Hurricane Katrina. In this paper, we seek to address this shortcoming in the state of knowledge regarding hurricane surge generation.

To newly investigate the role of storm size on hurricane surge potential, it is essential to appropriately represent the hurricane wind field and to use a high-quality numerical model, such as the Advanced Circulation (ADCIRC) model, for hurricane surge generation. The following gives a conceptual overview of hurricane wind field structure and hurricane surge generation. Although it is recognized that hurricanes can have very complex wind field structures (e.g., double eyewalls, eyewall replacement cycles, organized spiral bands, asymmetries resulting from proximity to land, etc.), a simple set of parameters has proven effective for estimating winds within hurricanes for the purpose of driving ocean response models (Thompson and Cardone 1996; Vickery et al. 2000). Primary parameters used in this context typically include

1) central pressure deficit as a measure of storm intensity,
2) a radius scale related to storm size,
3) the forward speed of the storm, and
4) the peakedness of the storm wind speed distribution (Holland's B; see Holland 1980).

Direct wind stress, wave radiation stresses, and barotropic water level adjustments represent the primary surge forcing mechanisms within a hurricane. In this paper, we neglect the effects of waves to simplify our analyses. The justification for this is twofold. First, this paper is not intended to improve the precise calculation of storm surge, but rather to isolate the effect of storm size on coastal surge levels. Second, because the size of a hurricane affects both the fetch and duration for generating waves, increasing storm size tends to increase wave heights, which would lead to higher wave setup along the coasts. Including this effect would, if anything, add to the hypothesized positive relationship between increasing storm size and coastal surges. Contributions to storm surge resulting from astronomical tide are also neglected in this paper, because these contributions are largely independent of hurricane size.

For the case of steady onshore wind acting uniformly on a water body with constant bottom slope (S_o), the storm surge (ζ) is of the form

$$\zeta \propto \frac{\tau}{S_o} \propto \frac{V^2}{S_o}, \tag{1}$$

where τ is the wind shear stress at the water surface and V is wind speed. In the more realistic case of space–time-varying hurricane wind fields, both storm size and its forward speed affect the duration of high winds at a given point. Close to the hurricane's center, the cyclostrophic approximation for wind speed [$V(r)$] as a function of distance from the storm eye (r), in the absence of storm forward motion, is given by (Holland 1980)

$$V(r) = \left[\left(\frac{r}{R_{\max}} \right)^B \left(\frac{B\Delta p}{\rho_{\text{air}}} \right) e^{-\left(\frac{R_{\max}}{r} \right)^B} \right]^{1/2}, \tag{2}$$

where B is Holland's dimensionless parameter that dictates the radial pressure profile shape and typically ranges from 0.9 to 1.9. Evaluating Eq. (2) at the point of maximum wind demonstrates that maximum wind speed is directly proportional to the square root of Δp, thus illustrating the well-accepted view that Δp is the primary scaling factor for the storm wind field, and thus storm surge. However, Eq. (2) also demonstrates that the radial size of the storm is important when considering the spatial distribution of hurricane winds, and suggests that storm size must also contribute to storm surge generation.

In nature, the cyclonic wind field distribution is modified by several factors. As the storm approaches the coast, the hurricane track angle relative to the coast and the hurricane forward speed both strongly influence the progression of the wind directions. Thus, in the more general case, storm intensity, size, track, and forward speed, and bottom slope are all expected to influence coastal hurricane surges. Other factors affecting total surge at the shoreline include attributes of the coastal landscape, such as the configuration of the land–sea interface, the bottom roughness in offshore and inundated areas, and the relative phase of astronomical tide and hurricane landfall. The influence of specific historical hurricanes on specific coastal landscapes along the Gulf of Mexico has been well studied by a number of investigators (e.g., Westerink et al. 2007; Signorini et al. 1992; Luettich et al. 1992; Westerink et al. 1992). It is our intent here to simplify the storm surge problem to more generally assess the influence and interaction of meteorological parameters like storm size with regional-scale topography, namely, continental shelf slope.

3. Approach

To investigate the influence of storm size on peak storm surge, a numerical investigation of idealized hurricanes was conducted. The assumptions made in our analysis are fairly simple, and we have done this on purpose to isolate surge scaling with storm size. Central pressure deficit, storm size, storm forward speed, and peakedness, in conjunction with information on the background pressure field, were used as input into a coupled hurricane vortex–planetary boundary layer (PBL) model (Thompson and Cardone 1996) to estimate sustained near-surface winds throughout the storm.

Storm wind and pressure fields were generated using the PBL model for 18 unique $R_{\max}$ and Δp pairs by incrementally varying $R_{\max}$ from 18.5 to 55.6 km, and Δp from 40 to 130 mb. For each field, the $R_{\max}$ and Δp values were held constant as the storm progressed due northward with a speed of 5.1 m s^{-1}. Additional wind and barometric pressure fields with alternate track angles and forward speeds were also generated to assess surge generation sensitivity to these parameters. In addition to this base set of simulations, a series of sensitivity simulations were carried out to assess the impact on peak surge by hurricane track variation (60° to the west through 45° to the east of due north) and forward speed (2.6–10.3 m s^{-1}).

Using the PBL-modeled wind fields, storm surges along the shoreline were computed from the finite-element longwave ADCIRC numerical model (Westerink et al. 1992; Luettich et al. 1992), with the coefficient of wind drag within the ADCIRC model "capped" to follow measured wind drag relationships (Powell et al. 2003).

For this experiment, the ADCIRC model domain included the entire Gulf of Mexico water body, with simplifications. In particular, the northern gulf boundary was represented by a straight coastline with an east–west orientation. The regional bathymetry within the model grid was further simplified by using shore-parallel contours with a constant bottom slope. Using this grid configuration, storm surge simulations were performed for eight different bottom slopes S_o, ranging from 1:10 000 to 1:250. These slopes represent very mild to very steep idealized continental shelf regions, with the mildest slope representative of conditions in the vicinity of New Orleans, Louisiana.

4. Numerical simulations

To quantify the influence of storm size on surge, peak storm surge for each storm and slope combination was

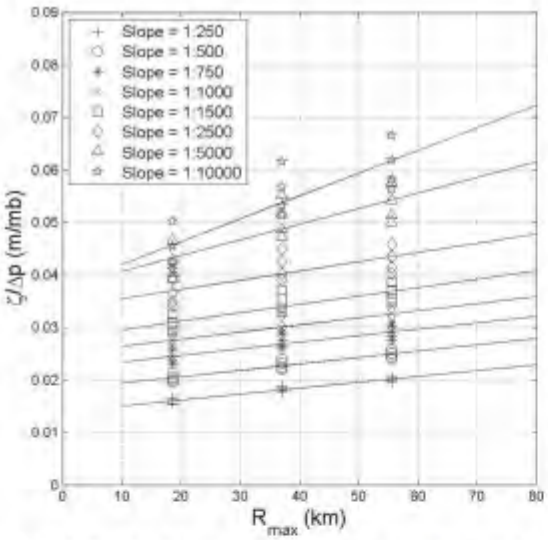

FIG. 2. Simulated hurricane surge (ζ) normalized by central pressure deficit (Δp) vs hurricane size (R_{max}) at landfall.

extracted from the ADCIRC simulation results. Figure 2 shows the relationship between peak surge at the coast and storm size for moderately intense to very intense storms ($\Delta p \geq 80$ mb). In this figure, the effect of hurricane intensity is removed from this comparison by dividing peak surge by intensity, where intensity is proportional to the square of the maximum wind speed, which translates to the Saffir–Simpson category [Eq. (2)]. As this figure demonstrates, for a given shelf slope the peak surge increases as storm size increases, indicating that storm size effectively increases the distance over which the wind acts. Furthermore, because the linear trend with storm size becomes steeper as shelf slope becomes milder, this figure also shows that the role of storm size in producing surge becomes increasingly important over mildly sloping bottoms. This trend with hurricane size or slope is not captured by the Saffir–Simpson scale.

Figure 3 shows that for bottom slopes of 1:1, 000 and 1:10 000, peak storm surge increases as expected with increasing Δp and with decreasing bottom slope. Yet this figure also shows that peak surge depends not only on storm intensity, but also on storm size. When S_o = 1:1000 and Δp = 100 mb, peak surge at the shoreline varies from 2.8 to 3.3 m as R_{max} varies from 18.5 to 55.6 km. This surge variation is much greater for the very mildly sloping case of S_o = 1:10 000, where peak surge at the shoreline varies from 4.5 to 6.2 m.

To assess the sensitivity of storm surge to storm track, additional numerical simulations were performed by varying the angle of storm approach, while holding storm forward speed constant at 5.1 m s^{-1}. As expected, all storm tracks with more westerly headings (positive angles) produced smaller surges than the due north track for both moderately and mildly sloping bottoms (Fig. 4). For the most mildly sloping bottom, those storms with a more easterly heading (negative angles) produced surges that were as large, or slightly larger (no more than 8%), than the due north track. Other tracks tend to reduce the storm surge, with a maximum reduction of approximately 25%. These simulations indicate that consideration of tracks perpendicular to the shoreline tend to overpredict peak surge produced by more oblique approach angles, on average by 8%.

Next, a series of simulations were performed by varying storm forward speed from 2.6 to 10.2 m s^{-1} to assess sensitivity to this parameter. The simulation results indicate a correlation between storm forward speed and peak storm surge for steep to moderate bottom slopes, primarily because the PBL model produces higher maximum wind speeds within faster-moving storms than slower storms (Fig. 5). When $S_o \leq$ 1:2500, a 50% increase in forward speed translates to a 15%–20% increase in peak surge. For more mildly sloping bottoms, only a minimal increase, if any, in the peak surge was predicted. This limited surge response predicted by the simulations on mildly sloping bottoms, like those near New Orleans, arises because the relative decrease in storm residence time offshore with increased storm forward speed dominates the surge response. Here, an equilibrium state is approached more quickly, even for fast-moving storms, because the mild slope creates a much larger shallow area (e.g., increased fetch) over which the hurricane winds act. On more steeply sloping bottoms the effective cross-shore area over which the winds act is smaller and thus less influential; therefore, the relative increase in hurricane wind speed with increasing forward speed dominates the simulated surge response.

5. Results

As was seen in Fig. 3, the numerical results indicate that, in addition to storm intensity and bottom slope, storm size is important in generating surge at the coast. For a given storm intensity, the figure plainly shows that simulated storm surge increases with storm size, and that this relationship holds for all bottom slopes. However, the numerical results indicate that the role of storm size in surge generation becomes much more important on mildly sloping bottoms and for intense storms. For example, given a value of Δp equal to 70 mb on a slope of 1:10 000, peak surge increases 0.4 m for

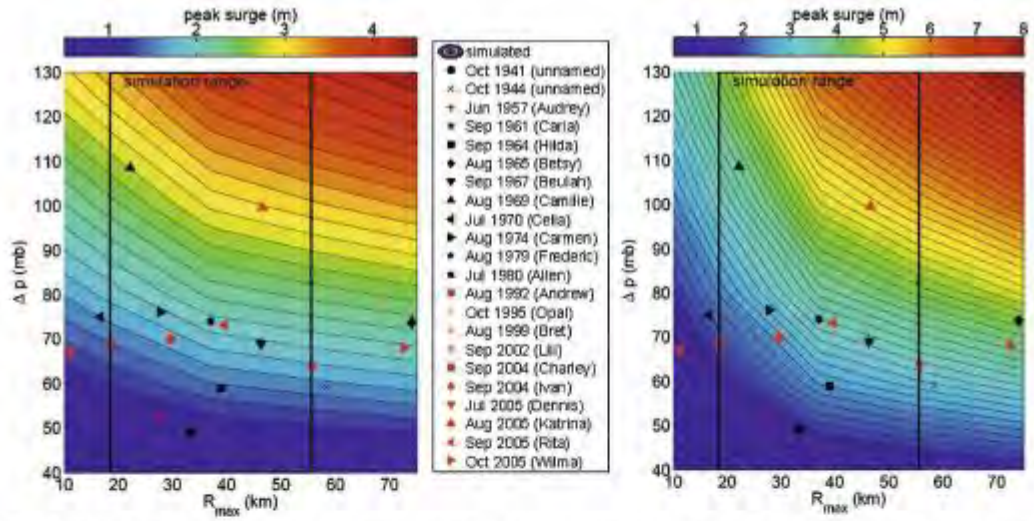

FIG. 3. Simulated peak surge as a function of hurricane size (R_{max}) and intensity (Δp) for the (left) 1:1000 bottom slope (S_o) case and the (right) 1:10 000 bottom slope (S_o) case. Historical R_{max} and Δp observations are superimposed on the numerical results to indicate peak surge potential if the historical storm made landfall in a region characterized by a bottom slope of either (a) 1:1000 or (b) 1:10 000.

every 10-km increase in R_{max}. The same storm on a 1:1000 slope produces only an increase of 0.15 m for every 10-km increase in R_{max}. Likewise, a horizontal cut through Fig. 3 at large values of Δp shows a much higher variability in surge levels than a cut at small values of Δp. Because older studies of storm surge primarily dealt with surges from moderate storms on moderate slopes (Hoover 1957; Conner et al. 1957; Harris 1959, 1963; Jelesnianski 1972), it is not too surprising that no strong relationship between storm size and peak surge at the coast was found.

Historical observations may also be used to support the contention that storm size is more important for surge generation on mildly sloping bottoms and for more intense hurricanes. Figure 6 shows observed peak surge versus storm size at landfall for the subset of

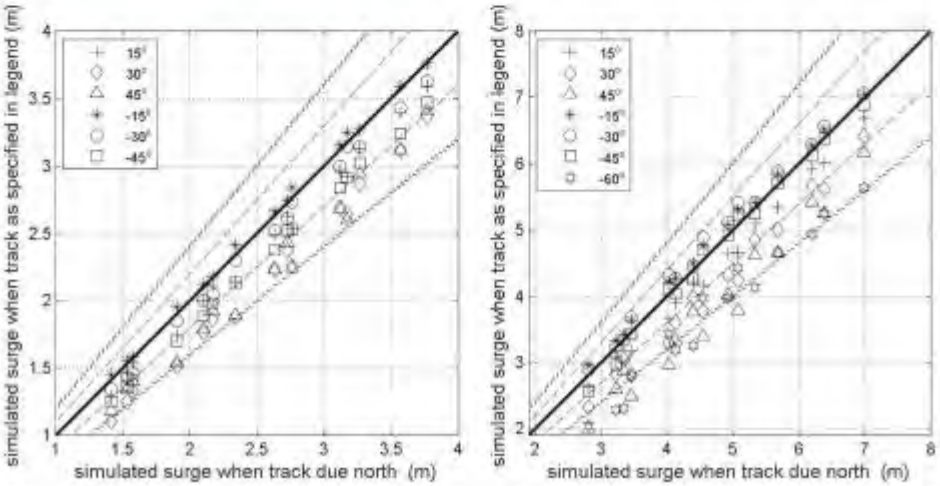

FIG. 4. Simulated peak surge as a function of hurricane track angle, measured counterclockwise from a due north approach for (left) S_o = 1:1000 and (right) S_o = 1:10 000. Plus or minus 0%, 10%, and 20% increases or decreases in value are marked by the solid, dashed, and dotted lines, respectively.

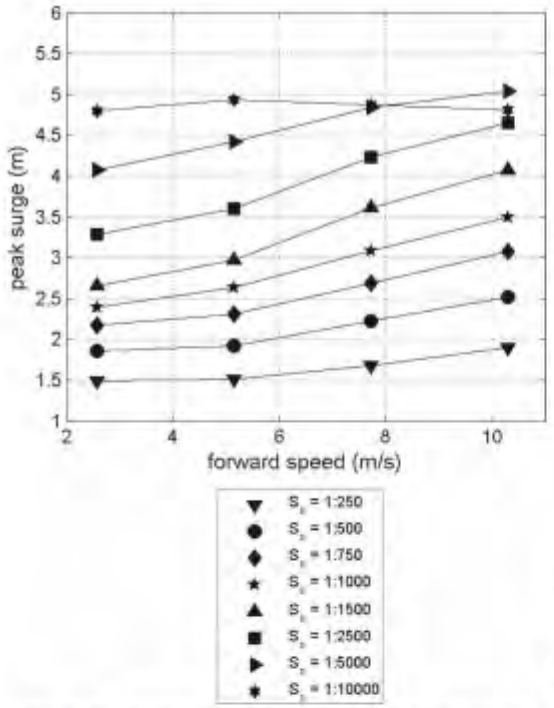

FIG. 5. Simulated peak surge as a function of storm forward speed and bottom slope.

historical hurricanes with intensities greater than Δp = 80 mb. As in Fig. 2, the effect of hurricane intensity is removed from the comparison presented in Fig. 6 by dividing peak surge by intensity, which correlates with the Saffir–Simpson category. Figure 6 demonstrates that the observed data support the numerical findings presented in Fig. 2. Specifically, Fig. 6 shows evidence that increases in storm size increase storm surge and that this relationship becomes more significant as shelf slope becomes milder. This figure and our numerical findings both support our claim that the Saffir–Simpson scale alone is not a good indicator of peak hurricane surge.

Superimposed on Fig. 3 are the Δp and R_{max} values at landfall for 22 major hurricanes (Table 2). On the figure, the R_{max} and Δp combination for Hurricane Katrina plots at a higher peak surge level than that for Hurricane Camille. When S_o = 1:1000, the R_{max} and Δp combination for Hurricane Betsy, also a major hurricane impacting the Mississippi and Louisiana coastlines, plots at a slightly lower peak surge level than that for Hurricane Camille. Illustrating the importance of bottom slope on surge prediction for the more mildly sloping S_o = 1:10 000 case, peak surge values for these

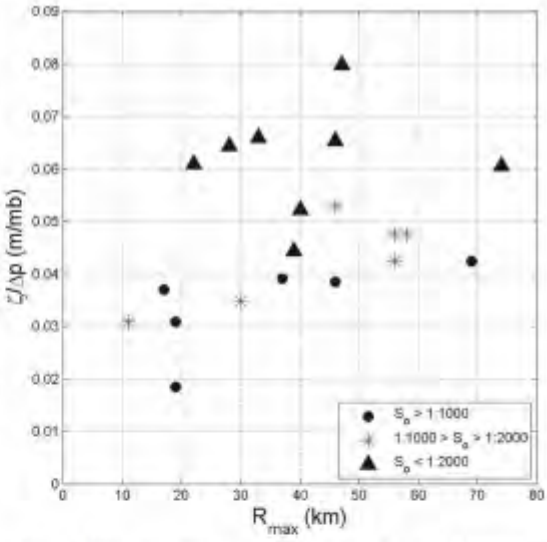

FIG. 6. Observed hurricane surge (ζ) normalized by observed central pressure deficit (Δp) vs hurricane size (R_{max}) at landfall.

two storms are reversed, with Hurricane Betsy associated with a slightly larger surge than Hurricane Camille. The actual slope along the coastline near New Orleans falls between the 1:1000 and 1:10 000 slope values, so these significantly different storms impacting New Orleans produce similar peak surges in our simulations.

Using the numerical results and following curve-fitting procedures, a parametric relationship between peak surge at the shoreline and Δp, R_{max}, and S_o was developed (see the appendix). Figure 7 plots this peak surge estimate versus the observed peak surge. While the relationship developed from the idealized simulations does not include wave setup, which is significant for most storms, astronomical tide, and impacts of local geometry, the observations match reasonably well. In particular, estimates for hurricanes of moderate intensity and size largely fall below the observed value by 10%–20%. Because wave setup was not included in the numerical analysis, it is logical that the estimate based on the numerical results is low. Furthermore, it is probable that wave setup contributes on the order of 10%–20% to the total hurricane water level along Gulf of Mexico coastlines (Dean and Bender 2006; U.S. Army Corps of Engineers 2006a).

The results for Hurricanes Ivan, Dennis, and Frederic, whose central pressure deficit were within 5 mb of one another, demonstrate that the surge estimates capture the relative influence of storm size on moderately sloping bottoms. Hurricanes Ivan and Dennis

TABLE 2. Historical hurricane characteristics at landfall.

Storm date (Name)	Central pressure (mb)[a]	Radius to maximum wind (km)[b]	Saffir–Simpson category[c]	Estimated influencing continental shelf slope	Observed open coast surge (m)
October 1941 (unnamed)	970	33	2	1:2, 000–1:3, 500	3.2[d]
October 1944 (unnamed)	960	58	3	1:1, 500–1:1, 700	2.3–3.4[e]
June 1957 (Audrey)	964	46	4	1:4, 000	3.4–3.8[g]
September 1961 (Carla)	936	56	4	1:1, 000–1:1, 700	3.3–3.7[c]
September 1964 (Hilda)	960	39	3	1:4, 000–1:7, 500	2.3–3.0[f]
August 1965 (Betsy)	945	74	3	1:5, 000–1:10, 000	4.1–4.8[g]
September 1967 (Beulah)	950	46	3	1:800–1:1, 100	2.4–2.9[g]
August 1969 (Camille)	910	22	5	1:5, 000–1:10, 000	6.4–6.9[g]
July 1970 (Celia)	944	17	3	1:800–1:1, 100	2.7–2.8[h]
August 1974 (Carmen)	943	28	3	1:2, 500	
August 1979 (Frederic)	950	46	3	1:1, 500–1:1, 900	3.5–3.8[i]
July 1980 (Allen)	945	37	3	1:800–1:1, 100	2.1–3.7[h]
August 1992 (Andrew)	949	30	5	1:750–1:1, 500	2.4[j]
October 1995 (Opal)	940	69	3	1:750–1:1, 000	3.1–3.7[k]
August 1999 (Bret)	953	19	3	1:800–1:1, 100	0.9–1.5[l]
September 2002 (Lili)	966	28	1	1:4, 000–1:7, 500	3.2–3.6[f]
September 2004 (Charley)	950	19	4	1:500–1:1, 000	2.1
September 2004 (Ivan)	955	56	3	1:1, 500–1:1, 900	3.0–3.1[m]
July 2005 (Dennis)	952	11	3	1:750–1:1, 500	1.7–2.5[n]
August 2005 (Katrina)	919	47	3	1:5, 000–1:10, 000	7.5–8.5[o]
September 2005 (Rita)	946	40	3	1:2, 500–1:3, 000	3.0–4.6[o]
October 2005 (Wilma)	951	73	3	1:500–1:1, 000	1.8–2.4[p]

[a] National Weather Service (2000)
[b] U.S. Army Corps of Engineers (2006a)
[c] Blake et al. (2006)
[d] Harris (1963)
[e] Ho and Miller (1982)
[f] U.S. Army Corps of Engineers (2006b)
[g] U.S. Army Corps of Engineers (1968)
[h] National Weather Service (2000)
[i] U.S. Army Corps of Engineers (1981)
[j] National Weather Service (1993)
[k] U.S. Army Corps of Engineers (1995)
[l] Lawrence and Kinberlain (2001)
[m] National Weather Service (2005)
[n] National Oceanic and Atmospheric Administration (2005)
[o] Knabb et al. (2006)
[p] Pasch et al. (2006)

both made landfall along the Alabama coastline, while Hurricane Frederic made landfall slightly to the east, along the western Florida Panhandle. Hurricanes Ivan and Frederic were large in size while Hurricane Dennis was the smallest in the considered historic record. Consequently, the observations and the surge estimate for Hurricane Dennis are about 1 m lower than those for Hurricanes Ivan and Frederic.

The three largest storms, in terms of peak surge, are Hurricanes Betsy, Camille, and Katrina, all making landfall in the vicinity of New Orleans. These three storms demonstrated that the surge estimates do also capture the relative influence of storm size and storm intensity on mildly sloping bottoms. A larger surge is estimated for Hurricane Katrina than for Hurricane Camille, which was a more intense but much smaller storm. Additionally, the surge estimate for Hurricane Betsy is smaller than that estimated for both Hurricanes Katrina and Camille, largely reflecting Betsy's significantly weaker intensity. However, it is interesting to note that Hurricane Betsy, both in terms of observed and estimated surge, generated the third largest surge of historical storms considered; thus, this storm demonstrates that the surge estimates also capture the influence of hurricane size, for which Betsy is the largest in the historical set, for weak storms passing over a mild continental shelf slope.

However, for both Hurricanes Katrina and Camille,

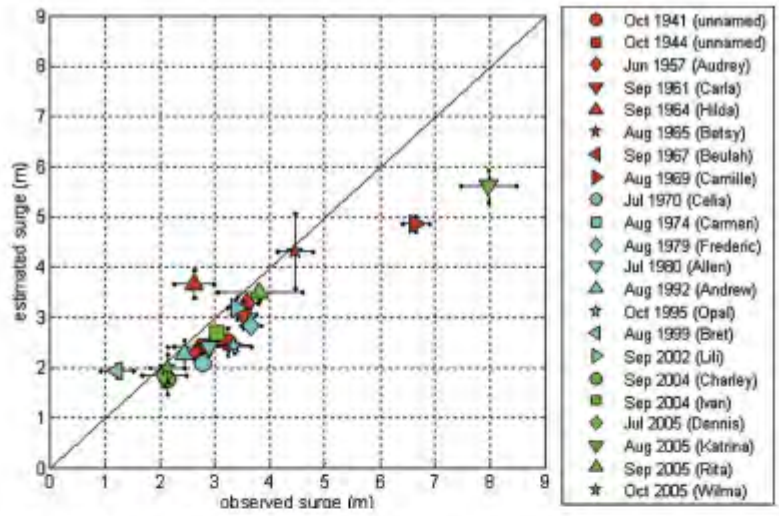

FIG. 7. Estimated vs observed peak surge. Horizontal error bars represent the range of observed peak surge in the vicinity of expected maximum alongshore surge to the east of the hurricane eye at landfall. Vertical error bars represent the range of estimated peak surge as it relates to the range of bottom slopes in the region of landfall.

the surge estimate is lower than that observed. There are a number of reasons why this occurs. First, the numerical simulations are idealized and do not represent the complex topography of the New Orleans area where the regional-scale Mississippi River Delta feature would result in additional surge levels to the east of this feature. Additionally, surge response to localized geographic features, particularly shallow back-bay areas, can also significantly influence localized wind setup. Indeed, the largest observed surge during Hurricane Katrina occurred inside Bay St. Louis, Mississippi, a localized feature not considered in this study. Second, wave setup is not included. For Hurricanes Camille and Katrina, wave setup was on the order of 1.5 m (U.S. Army Corps of Engineers 2006a). Third, both Hurricanes Camille and Katrina approached the coast from the southeast. While Hurricane Katrina turned due north during final approach, Hurricane Camille maintained an approach angle of 20°, measured counterclockwise from a due north approach. The surge estimate is based solely on storms following a due north track, and, as Fig. 4 demonstrates, a reduction in peak surge by about 8% is expected for more northwesterly tracks. Fourth, the storm forward speed at landfall for both Hurricanes Camille and Katrina was about 6.7 $m\,s^{-1}$ and is 30% higher than the uniform forward speed used in determining the surge estimates. As Fig. 5 illustrates, an increase in surge on the order of 5% can be expected for these two storms making landfall in the New Orleans area. Finally, the idealized wind and pressure fields for these storms may not capture all of the details of the surge generation process at the coast in these two storms. Nonetheless, the numerical simulations revealed that the physical phenomena governing surge generation does explain why the surge from Hurricane Katrina was larger than that from Hurricane Camille, and this is validated by the observations. Further, these two storms emphasize the importance of storm size on surge generation. Finally, our results indicate that a landfalling storm the size of Hurricane Camille, which is also characterized by the tropical cyclone maximum possible intensity (MPI) for the Gulf of Mexico, on the order of 880 mb (Tonkin et al. 2000), cannot produce a surge as large as that produced by a storm the size of Hurricane Katrina.

6. Conclusions

Research from the late 1950s through the 1970s concluded that, based on observations from historical hurricanes, the influence of storm size on surge was relatively small. At that time, the historical dataset included only hurricanes from small to moderate size and intensity. The data used for this conclusion were taken solely from high-water marks, which contain considerable scatter, making it difficult to distinguish possible storm size–related effects. Given the lack of observational motivation, no systematic study of the potential impact of storm size on coastal storm surges via either theoretical or numerical methods had been conducted prior

to Hurricane Katrina. The lack of clear observational evidence and theoretical studies on the impact of storm size led to the implicit neglect of the potentially catastrophic role that this could play in coastal surges.

Our analysis of observed recent and historical storm data along with idealized numerical simulation data demonstrate that storm size plays a key role in hurricane surge generation in coastal areas, particularly for the case of intense storms on very shallow slopes. Thus, while the Saffir–Simpson scale has historically provided an adequate categorization of hurricane wind damages, it does not provide a reliable estimate of expected hurricane flooding damages.

As a good example of the importance of this effect, our results indicate that a hurricane of Camille's size, even if that storm attained the maximum possible intensity (MPI) for the Gulf of Mexico (around 880 mb), could not produce a storm surge along the Mississippi coast of the same magnitude as that of Hurricane Katrina. Thus, although Hurricane Katrina was only a category 3 storm, it represents a much more serious coastal flooding threat than small category 5 storms.

Acknowledgments. The research presented herein was funded by the U.S. Army Engineer Research and Development Center. The authors would like to acknowledge Ms. Linda Lillycrop and Dr. David Levinson for their assistance in gathering information on historical hurricane surge observations and on the Saffir–Simpson scale, respectively. The data and results described herein, unless otherwise noted, were obtained from work funded by or performed by the U.S. Army Engineer Research and Development Center, Coastal and Hydraulics Laboratory. The use of trade names does not constitute an endorsement in the use of these products by the U.S. Government.

APPENDIX

Best-Fit Lines for Surge Relationship

While not recommended for use as a surge model, a best-fit relationship to our simulation results provides useful insight regarding the coupled impact of hurricane size along with hurricane intensity and shelf slope. A polynomial curve fit was developed using the numerical simulation data by considering, in order, 1) ζ versus R_{max}, where Δp and S_o are constant, and 2) the variation of ζ versus R_{max} as Δp varies. The resulting relationship is

$$\sqrt{\hat{\zeta}} = \left[\sqrt{\widehat{R_{max}}}\ 1\right]\left\{C(S_o)\begin{bmatrix}\widehat{\Delta p^2}\\ \widehat{\Delta p}\\ 1\end{bmatrix}\right\}, \quad \text{(A1)}$$

where $\widehat{\ }$ indicates a dimensionless quality and

$$\hat{\zeta} = \frac{\zeta g}{V_{max}^2}, \quad \text{(A2)}$$

$$\widehat{\Delta p} = \frac{\Delta p}{p_{atm}}, \quad \text{(A3)}$$

$$\widehat{R_{max}} = \frac{R_{max} g}{V_{max}^2}, \quad \text{(A4)}$$

$C(S_o)$ = 2 × 3 curve-fitting coefficient matrix: (A5)

$$S_o = 1{:}250\begin{pmatrix} -2.159\times10^{-2} & 1.593\times10^{-2} & 6.674\times10^{-4}\\ 4.211\times10^{-1} & -1.813\times10^{-1} & 7.242\times10^{-2}\end{pmatrix},$$

$$S_o = 1{:}500\begin{pmatrix} -3.585\times10^{-2} & 1.753\times10^{-2} & 6.767\times10^{-4}\\ 8.539\times10^{-1} & -2.877\times10^{-1} & 8.833\times10^{-2}\end{pmatrix},$$

$$S_o = 1{:}750\begin{pmatrix} -3.460\times10^{-2} & 1.751\times10^{-2} & 6.581\times10^{-4}\\ 1.176\times10^{0} & -3.880\times10^{-1} & 1.032\times10^{-1}\end{pmatrix},$$

$$S_o = 1{:}1000\begin{pmatrix} -1.329\times10^{-2} & 1.403\times10^{-2} & 8.424\times10^{-4}\\ 1.124\times10^{0} & -4.078\times10^{-1} & 1.111\times10^{-1}\end{pmatrix},$$

$$S_o = 1{:}2500\begin{pmatrix} -9.340\times10^{-2} & 3.072\times10^{-2} & 3.080\times10^{-4}\\ 2.888\times10^{0} & -8.063\times10^{-1} & 1.459\times10^{-1}\end{pmatrix},$$

$$S_o = 1{:}5000\begin{pmatrix} -1.078\times10^{-1} & 3.996\times10^{-2} & 4.444\times10^{-4}\\ 3.974\times10^{0} & -1.093\times10^{0} & 1.653\times10^{-1}\end{pmatrix}, \quad \text{and}$$

$$S_o = 1{:}10\,000\begin{pmatrix} -1.369\times10^{-1} & 4.937\times10^{-2} & 7.558\times10^{-4}\\ 4.845\times10^{0} & -1.301\times10^{0} & 1.731\times10^{-1}\end{pmatrix}.$$

REFERENCES

Berke, P., T. Larsen, and C. Ruch, 1984: A computer system for hurricane hazard assessment. *Comput. Environ. Urban Syst.*, **9,** 259–269.

Blain, C. A., J. J. Westerink, and R. A. Luettich Jr., 1998: Grid convergence studies for the prediction of hurricane storm surge. *Int. J. Numer. Methods Fluids,* **26,** 369–401.

Blake, E. S., E. N. Rappaport, J. D. Jarrell, and C. W. Landsea, 2006: The deadliest, costliest, and most intense United States tropical cyclones from 1851 to 2005 (and other frequently requested hurricane facts). NOAA Tech. Memo. NWS TPC-4, 48 pp.

Conner, W. C., R. H. Kraft, and D. L. Harris, 1957: Empirical methods for forecasting the maximum storm tide due to hurricanes and other tropical storms. *Mon. Wea. Rev.*, **85,** 113–116.

Davis, R. E., and R. Dolan, 1993: Nor'easters. *Amer. Sci.*, **81,** 428–439.

Dean, R. G., and C. J. Bender, 2006: Static wave setup with emphasis on damping effects by vegetation and bottom friction. *Coastal Eng.*, **53,** 149–156.

Dolan, R., and R. E. Davis, 1992: An intensity scale for Atlantic Coast northeast storms. *J. Coastal Res.*, **8,** 840–853.

Harris, D. L., 1959: An interim hurricane storm surge forecasting guide. U.S. Weather Bureau Rep. 32, 24 pp.

——, 1963: Characteristics of the hurricane storm surge. U.S. Weather Bureau Tech. Paper 48, 139 pp.

Ho, F. P., and J. F. Miller, 1982: Pertinent meteorological and hurricane tide data for Hurricane Carla. NOAA Tech. Rep. NWS 32, 111 pp.

Holland, G. J., 1980: An analytic model of the wind and pressure profiles in hurricanes. *Mon. Wea. Rev.*, **108,** 1212–1218.

Hoover, R. A., 1957: Empirical relationships of the central pressure in hurricanes to the maximum surge and storm tide. *Mon. Wea. Rev.*, **85,** 167–174.

Jelesnianski, C. P., 1972: SPLASH (Special Program to List Amplitudes of Surges from Hurricanes): I. Landfall storms. NOAA Tech. Memo. NWS TDL-46, 52 pp.

——, 1984: SLOSH—A hurricane storm surge forecasting model. Preprints, *Oceans '84 Conf.*, Washington, D.C., Marine Technology Society and IEEE/Oceanic Engineering Society, 314–317.

——, 1990: Storm surge modeling in the United States. NIST-SP-796, 66–76.

Knabb, R. D., D. P. Brown, and J. R. Rhome, 2006: Tropical cyclone report: Hurricane Rita 18-26 September 2005. National Hurricane Center Rep., 33 pp.

Lawrence, M. B., and T. B. Kinberlain, 2001: Preliminary report: Hurricane Bret 18-25 August 1999. National Hurricane Center Rep., 10 pp.

Luettich, R. A., J. J. Westerink, and N. W. Scheffner, 1992: Modeling 3-D circulation using computations for the western North Atlantic and Gulf of Mexico. *Estuarine and Coastal Modeling II,* M. Spaulding, Ed., ASCE, 632–643.

National Oceanic and Atmospheric Administration, 2005: Hurricane Dennis storm tide summary. NOAA Rep., 14 pp.

National Weather Service, cited 1993: Memorable Gulf coast hurricanes of the 20th century. [Available online at http://www.aoml.noaa.gov/general/lib/mgch.html.]

——, cited 2000: Hurricane history. [Available online at http://www.srh.noaa.gov/crp/docs/research/hurrhistory/.]

——, cited 2005: Powerful Hurricane Ivan slams the US central Gulf coast as an upper category-3 storm. [Available online at http://www.srh.noaa.gov/mob/ivan_age/.]

——, cited 2006: The Saffir–Simpson hurrican scale. [Available online at http://www.nhc.noaa.gov/aboutsshs.shtml.]

Neumann, C. J., B. R. Jarvinen, C. J. McAdie, and J. D. Elms, 1999: Tropical cyclones of the North Atlantic Ocean, 1871–1998. NOAA Historical Climatology Series 6-2, 43 pp.

Norman, J., 2006: Katrina's dead. *Sun Herald,* 17 February 2006 A1, A8–9.

Pasch, R. J., E. S. Blake, H. D. Cobb III, and D. P. Roberts, 2006: Tropical cyclone report Hurricane Wilma 15-25 October 2005. National Hurricane Center Rep., 27 pp.

Powell, M. D., and T. A. Reinhold, 2007: Tropical cyclone destructive potential by integrated kinetic energy. *Bull. Amer. Meteor. Soc.*, **88,** 513–526.

——, P. J. Vickery, and T. A. Reinhold, 2003: Reduced drag coefficient for high wind speeds in tropical cyclones. *Nature,* **422,** 279–283.

Russo, E., 1998: Estimating hurricane storm surge amplitudes for the Gulf of Mexico and Atlantic coastlines of the United States. *Proc. Oceans'98,* Vol. 3, Nice, France, IEEE, 1301–1305.

Signorini, S. R., J. S. Wei, and C. D. Miller, 1992: Hurricane-induced surge and currents on the Texas–Louisiana shelf. *J. Geophys. Res.*, **97** (C2), 2229–2242.

Simpson, R. H., 1974: The hurricane disaster-potential scale. *Weatherwise,* **27,** 169, 186.

Taylor, R. B., 1980: Simplified methods for prediction of hurricane surge and wave runup. *Mar. Technol. Soc. J.*, **14** (3), 20–26.

Thompson, E. F., and V. J. Cardone, 1996: Practical modeling of hurricane surface wind fields. *J. Waterw. Port Coastal ASCE,* **122** (4), 195–205.

Tonkin, H., G. J. Holland, N. Holbrook, and A. Herderson-Sellers, 2000: An evaluation of thermodynamic estimates of climatological maximum potential tropical cyclone intensity. *Mon. Wea. Rev.*, **135,** 746–762.

U.S. Army Corps of Engineers, 1968: Report on Hurricane Beulah 8-21 September 1967. Galveston District Rep., 143 pp.

——, 1981: Hurricane Frederic post disaster report. Mobile District Rep., 6 pp.

——, 1995: Hurricane Opal storm surge and wave runup. Mobile District Memo., 22 pp.

——, 2006a: Performance evaluation of the New Orleans and southeast Louisiana hurricane protection system. Interagency Performance Evaluation Task Force, Draft Final Rep., 259 pp.

——, 2006b: Appendix B: History of hurricane occurrences. Louisiana Coastal Protection and Restoration (LACPR) Preliminary Tech. Rep., New Orleans District Rep., 40 pp.

Vickery, P. J., P. F. Skerlj, A. C. Steckley, and L. A. Twisdale, 2000: Hurricane wind field model for use in hurricane simulations. *J. Struc. Eng. ASCE,* **126,** 1203–1222.

Weisberg, R. H., and L. Zheng, 2006: Hurricane storm surge simulations for Tampa Bay. *Estuaries Coasts,* **29** (6A), 899–913.

Westerink, J. J., R. A. Luettich, A. M. Baptista, N. W. Scheffner, and P. Farrar, 1992: Tide and storm surge predictions using finite element model. *J. Hydraul. Eng. ASCE,* **118** 373–1390.

——, and Coauthors, 2008: A basin- to channel-scale unstructured grid hurricane storm surge model as implemented for southern Louisiana. *Mon. Wea. Rev.*, **136,** 833–864.

52. Assignment 2, Module 11: Storm Data:
https://www.aoml.noaa.gov/hrd/hurdat/Data_Storm.html

The revised Atlantic hurricane database (HURDAT2) - Chris Landsea – April 2022

The National Hurricane Center (NHC) conducts a post-storm analysis of each tropical cyclone in its area of responsibility to determine the official assessment of the cyclone's history. This analysis makes use of all available observations, including those that may not have been available in real time. In addition, NHC conducts ongoing reviews of any retrospective tropical cyclone analyses brought to its attention, and on a regular basis updates the historical record to reflect changes introduced via the Best Track Change Committee (Landsea et al. 2004a, 2004b, 2008, 2012, Hagen et al. 2012, Kieper et al. 2016, and Delgado et al. 2018). NHC has traditionally disseminated the tropical cyclone historical database in a format known as HURDAT (short for HURricane DATabase – Jarvinen et al. 1984). This report updates the original HURDAT documentation to reflect significant changes since 2012 to both the format and content for the tropical cyclones and subtropical cyclones of the Atlantic basin (i.e., North Atlantic Ocean, Gulf of Mexico, and Caribbean Sea). *(Note for April 2022: Radius of Maximum Wind added into HURDAT2 for the first time beginning with the 2021 hurricane season.)*

The original HURDAT format substantially limited the type of best track information that could be conveyed. The format of this new version - HURDAT2 (HURricane DATa 2nd generation) - is based upon the "best tracks" available from the b-decks in the Automated Tropical Cyclone Forecast (ATCF – Sampson and Schrader 2000) system database and is described below. Reasons for the revised version include: 1) inclusion of non-synoptic (other than 00, 06, 12, and 18Z) best track times (mainly to indicate landfalls and intensity maxima); 2) inclusion of non-developing tropical depressions; and 3) inclusion of best track wind radii.

An example of the new HURDAT2 format for Hurricane Ida from 2021 follows:

```
AL092021,                IDA,     40,
20210826, 1200,  , TD, 16.5N,  78.9W,  30, 1006,    0,    0,    0,    0,    0,    0,    0,    0,    0,    0,    0,    0,   60
20210826, 1800,  , TS, 17.4N,  79.5W,  35, 1006,   60,    0,    0,    0,    0,    0,    0,    0,    0,    0,    0,    0,   50
20210827, 0000,  , TS, 18.3N,  80.2W,  40, 1004,   60,    0,    0,    0,    0,    0,    0,    0,    0,    0,    0,    0,   50
20210827, 0600,  , TS, 19.4N,  80.9W,  45, 1002,   70,    0,    0,    0,    0,    0,    0,    0,    0,    0,    0,    0,   40
20210827, 1200,  , TS, 20.4N,  81.7W,  55,  996,   80,   60,    0,   60,   30,    0,    0,    0,    0,    0,    0,    0,   30
20210827, 1800, L, HU, 21.5N,  82.6W,  70,  987,   80,   60,   40,   60,   40,   30,    0,   20,   20,    0,    0,    0,   20
20210827, 2325, L, HU, 22.4N,  83.2W,  70,  988,   80,   60,   40,   60,   40,   30,    0,   20,   20,    0,    0,    0,   20
20210828, 0000,  , HU, 22.6N,  83.5W,  70,  989,  100,   60,   40,   70,   50,   30,    0,   30,   20,    0,    0,    0,   20
20210828, 0600,  , HU, 23.5N,  84.7W,  70,  987,  100,   60,   40,   70,   50,   30,    0,   30,   20,    0,    0,    0,   20
20210828, 1200,  , HU, 24.4N,  85.7W,  70,  986,  110,   80,   60,  100,   50,   40,   20,   30,   25,   20,    0,    0,   20
20210828, 1800,  , HU, 25.6N,  86.6W,  80,  976,  110,  100,   70,  100,   50,   40,   20,   40,   25,   20,   10,   20,   20
20210829, 0000,  , HU, 26.7N,  87.6W,  90,  967,  120,  100,   80,  110,   70,   60,   40,   60,   35,   30,   20,   30,   20
20210829, 0600,  , HU, 27.6N,  88.7W, 115,  950,  120,  100,   80,  110,   70,   60,   40,   60,   35,   30,   20,   30,   15
20210829, 1200,  , HU, 28.5N,  89.6W, 130,  929,  130,  110,   80,  110,   70,   60,   40,   60,   45,   35,   20,   30,   10
20210829, 1655, L, HU, 29.1N,  90.2W, 130,  931,  130,  110,   80,  110,   70,   60,   40,   60,   45,   35,   20,   30,   10
20210829, 1800,  , HU, 29.2N,  90.4W, 125,  932,  130,  120,   80,   80,   70,   60,   40,   40,   45,   35,   20,   25,   10
20210830, 0000,  , HU, 29.9N,  90.6W, 105,  944,   80,  120,   80,   70,   50,   60,   40,   40,   30,   30,   20,   20,   10
20210830, 0600,  , HU, 30.6N,  90.8W,  65,  978,   80,  130,   80,   40,   50,   50,    0,    0,   30,   30,    0,    0,   30
20210830, 1200,  , TS, 31.5N,  90.9W,  40,  992,   50,  160,   60,   30,    0,    0,    0,    0,    0,    0,    0,    0,   40
20210830, 1800,  , TS, 32.2N,  90.5W,  35,  996,    0,  160,    0,    0,    0,    0,    0,    0,    0,    0,    0,    0,   80
20210831, 0000,  , TD, 33.0N,  90.0W,  30,  996,    0,    0,    0,    0,    0,    0,    0,    0,    0,    0,    0,    0,  250
20210831, 0600,  , TD, 33.8N,  89.4W,  25,  996,    0,    0,    0,    0,    0,    0,    0,    0,    0,    0,    0,    0,  210
```

```
20210831, 1200,  , TD, 34.4N,  88.4W,  25,  996,    0,    0,    0,    0,    0,    0,    0,    0,    0,    0,    0,    0,  250
20210831, 1800,  , TD, 35.1N,  87.1W,  20,  999,    0,    0,    0,    0,    0,    0,    0,    0,    0,    0,    0,    0,  250
20210901, 0000,  , TD, 35.8N,  85.5W,  20, 1000,    0,    0,    0,    0,    0,    0,    0,    0,    0,    0,    0,    0,  270
20210901, 0600,  , TD, 36.7N,  83.6W,  20, 1000,    0,    0,    0,    0,    0,    0,    0,    0,    0,    0,    0,    0,  270
20210901, 1200,  , EX, 37.7N,  81.5W,  25, 1000,    0,    0,    0,    0,    0,    0,    0,    0,    0,    0,    0,    0,  300
20210901, 1800,  , EX, 39.0N,  78.5W,  30,  999,    0,    0,    0,    0,    0,    0,    0,    0,    0,    0,    0,    0,  210
20210902, 0000,  , EX, 39.8N,  75.6W,  35,  997,    0,  150,    0,    0,    0,    0,    0,    0,    0,    0,    0,    0,  150
20210902, 0600,  , EX, 40.6N,  72.8W,  40,  997,    0,  150,  150,    0,    0,    0,    0,    0,    0,    0,    0,    0,  150
20210902, 1200,  , EX, 41.4N,  69.7W,  40,  997,  180,  150,    0,    0,    0,    0,    0,    0,    0,    0,    0,    0,  150
20210902, 1800,  , EX, 43.3N,  67.2W,  40,  996,    0,  150,    0,    0,    0,    0,    0,    0,    0,    0,    0,    0,  150
20210903, 0000,  , EX, 45.4N,  64.7W,  40,  995,  150,  150,    0,    0,    0,    0,    0,    0,    0,    0,    0,    0,  150
20210903, 0600,  , EX, 46.6N,  63.6W,  45,  992,  150,  150,   60,  150,    0,    0,    0,    0,    0,    0,    0,    0,  120
20210903, 1200,  , EX, 47.5N,  62.7W,  45,  991,  120,  150,   90,   90,    0,    0,    0,    0,    0,    0,    0,    0,   90
20210903, 1800,  , EX, 48.6N,  62.4W,  45,  992,  250,  150,  120,  120,    0,    0,    0,    0,    0,    0,    0,    0,   90
20210904, 0000,  , EX, 48.8N,  63.1W,  45,  992,  180,   90,   90,  120,    0,    0,    0,    0,    0,    0,    0,    0,   90
20210904, 0600,  , EX, 48.7N,  63.9W,  40,  992,  120,    0,    0,  120,    0,    0,    0,    0,    0,    0,    0,    0,   90
20210904, 1200,  , EX, 47.6N,  63.9W,  35,  996,  120,    0,    0,  120,    0,    0,    0,    0,    0,    0,    0,    0,   90
20210904, 1800,  , EX, 46.6N,  63.5W,  30,  999,    0,    0,    0,    0,    0,    0,    0,    0,    0,    0,    0,    0,   90
```

There are two types of lines of data in the new format: the header line and the data lines. The format is comma delimited to maximize its ease in use. The header line has the following format:

```
AL092021,                 IDA,     40,
123456789012345678901234568901234567
```

AL (Spaces 1 and 2) – Basin – Atlantic
09 (Spaces 3 and 4) – ATCF cyclone number for that year
2021 (Spaces 5-8, before first comma) – Year
IDA (Spaces 19-28, before second comma) – Name, if available, or else "UNNAMED"
40 (Spaces 34-36) – Number of best track entries – rows – to follow

Notes:

1) Cyclone number: In HURDAT2, the order cyclones appear in the file is determined by the date/time of the first tropical or subtropical cyclone record in the best track. This sequence may or may not correspond to the ATCF cyclone number. For example, the 2011 unnamed tropical storm AL20 which formed on 1 September, is sequenced here between AL12 (Katia – formed on 29 Aug) and AL13 (Lee – formed on 2 September). This mismatch between ATCF cyclone number and the HURDAT2 sequencing can occur if post-storm analysis alters the relative genesis times between two cyclones. In addition, in 2011 it became practice to assign operationally unnamed cyclones ATCF numbers from the end of the list, rather than insert them in sequence and alter the ATCF numbers of cyclones previously assigned.

2) Name: Tropical cyclones were not formally named before 1950 and are thus referred to as "UNNAMED" in the database. Systems that were added into the database after the season (such as AL20 in 2011) also are considered "UNNAMED". Non-developing tropical depressions formally

were given names (actually numbers, such as "TEN") that were included into the ATCF b-decks starting in 2003. Non-developing tropical depressions before this year are also referred to as "UNNAMED".

The remaining rows of data in the new format are the data lines. These have the following format:

```
20210829, 1655, L, HU, 29.1N,  90.2W, 130,  931,  130,  110,   80,  110,   70,   60,   40,   60,   45,   35,   20,   30,   10
12345678901234567890123456789012345678901234567890123456789012345678901234567890123456789012345678901234567890123456789012345
```

2021 (Spaces 1-4) – Year
08 (Spaces 5-6) – Month
29 (Spaces 7-8, before 1st comma) – Day
16 (Spaces 11-12) – Hours in UTC (Universal Time Coordinate)
55 (Spaces 13-14, before 2nd comma) – Minutes
L (Space 17, before 3rd comma) – Record identifier (see notes below)
- C – Closest approach to a coast, not followed by a landfall
- G – Genesis
- I – An intensity peak in terms of both pressure and wind
- L – Landfall (center of system crossing a coastline)
- P – Minimum in central pressure
- R – Provides additional detail on the intensity of the cyclone when rapid changes are underway
- S – Change of status of the system
- T – Provides additional detail on the track (position) of the cyclone
- W – Maximum sustained wind speed

HU (Spaces 20-21, before 4th comma) – Status of system. Options are:
- TD – Tropical cyclone of tropical depression intensity (< 34 knots)
- TS – Tropical cyclone of tropical storm intensity (34-63 knots)
- HU – Tropical cyclone of hurricane intensity (> 64 knots)
- EX – Extratropical cyclone (of any intensity)
- SD – Subtropical cyclone of subtropical depression intensity (< 34 knots)
- SS – Subtropical cyclone of subtropical storm intensity (> 34 knots)
- LO – A low that is neither a tropical cyclone, a subtropical cyclone, nor an extratropical cyclone (of any intensity)
- WV – Tropical Wave (of any intensity)
- DB – Disturbance (of any intensity)

29.1 (Spaces 24-27) – Latitude
N (Space 28, before 5th comma) – Hemisphere – North or South
90.2 (Spaces 31-35) – Longitude
W (Space 36, before 6th comma) – Hemisphere – West or East
130 (Spaces 39-41, before 7th comma) – Maximum sustained wind (in knots)

931 (Spaces 44-47, before 8th comma) – Minimum Pressure (in millibars)
130 (Spaces 50-53, before 9th comma) – 34 kt wind radii maximum extent in northeastern quadrant (in nautical miles)
110 (Spaces 56-59, before 10th comma) – 34 kt wind radii maximum extent in southeastern quadrant (in nautical miles)
70 (Spaces 62-65, before 11th comma) – 34 kt wind radii maximum extent in southwestern quadrant (in nautical miles)
60 (Spaces 68-71, before 12th comma) – 34 kt wind radii maximum extent in northwestern quadrant (in nautical miles)
40 (Spaces 74-77, before 13th comma) – 50 kt wind radii maximum extent in northeastern quadrant (in nautical miles)
60 (Spaces 80-83, before 14th comma) – 50 kt wind radii maximum extent in southeastern quadrant (in nautical miles)
80 (Spaces 86-89, before 15th comma) – 50 kt wind radii maximum extent in southwestern quadrant (in nautical miles)
30 (Spaces 92-95, before 16th comma) – 50 kt wind radii maximum extent in northwestern quadrant (in nautical miles)
45 (Spaces 98-101, before 17th comma) – 64 kt wind radii maximum extent in northeastern quadrant (in nautical miles)
25 (Spaces 104-107, before 18th comma) – 64 kt wind radii maximum extent in southeastern quadrant (in nautical miles)
35 (Spaces 110-113, before 19th comma) – 64 kt wind radii maximum extent in southwestern quadrant (in nautical miles)
20 (Spaces 116-119, before 20th comma) – 64 kt wind radii maximum extent in northwestern quadrant (in nautical miles)
15 (Spaces 122-125) – Radius of Maximum Wind (in nautical miles)

Notes:

1) Record identifier: This code is used to identify records that correspond to landfalls or to indicate the reason for inclusion of a record not at the standard synoptic times (0000, 0600, 1200, and 1800 UTC). For the years 1851-1970 and 1991 onward, all continental United States landfalls are marked, while international landfalls are only marked from 1951 to 1970 and 1991 onward. The landfall identifier (L) is the only identifier that will appear with a standard synoptic time record. The remaining identifiers (see table above) are only used with asynoptic records to indicate the reason for their inclusion. Inclusion of asynoptic data is at the discretion of the Hurricane Specialist who performed the post-storm analysis; standards for inclusion or non-inclusion have varied over time. Identification of asynoptic peaks in intensity (either wind or pressure) may represent either system's lifetime peak or a secondary peak.

2) Time: Nearly all HURDAT2 records correspond to the synoptic times of 0000, 0600, 1200, and 1800. Recording best track data to the nearest minute became available within the b-decks beginning in 1991 and some tropical cyclones since that year have the landfall best track to the nearest minute.

3) Status: Tropical cyclones with an ending tropical depression status (the dissipating stage) were first used in the best track beginning in 1871, primarily for systems weakening over land. Tropical cyclones with beginning tropical depression (the formation stage) were first included in the best track beginning in 1882. Subtropical depression and subtropical storm status were first used beginning in 1968 at the advent of routine satellite imagery for the Atlantic basin. The low status – first used in 1987 - is for cyclones that are not tropical cyclone or subtropical cyclones, nor extratropical cyclones. These typically are assigned at the beginning of a system's lifecycle and/or at the end of a system's lifecycle. The tropical wave status – first used in 1981 - is almost exclusively for cyclones that degenerate into an open trough for a time, but then redevelop later in time into a tropical cyclone (for example, AL10-DENNIS in 1981 between 13 and 15 August). The disturbance status is similar to tropical wave

and was first used in 1980. It should be noted that for tropical wave and disturbance status the location given is the approximate position of the lower tropospheric vorticity center, as the surface center no longer exists for these stages.

4) Maximum sustained surface wind: This is defined as the maximum 1-min average wind associated with the tropical cyclone at an elevation of 10 m with an unobstructed exposure. Values are given to the nearest 10 kt for the years 1851 through 1885 and to the nearest 5 kt from 1886 onward. A value is assigned for every cyclone at every best track time. Note that the non-developing tropical depressions of 1967 did not have intensities assigned to them in the b-decks. These are indicated as "-99" currently, but will be revised and assigned an intensity when the Atlantic hurricane database reanalysis project (Hagen et al. 2012) reaches that hurricane season.

5) Central Pressure: These values are given to the nearest millibar. Originally, central pressure best track values were only included if there was a specific observation that could be used explicitly. Missing central pressure values are noted as "-999". Beginning in 1979, central pressures have been analyzed and included for every best track entry, even if there was not a specific in-situ measurement available.

6) Wind Radii – These values have been best tracked since 2004 and are thus available here from that year forward with a resolution to the nearest 5 nm. Best tracks of the wind radii have not been done before 2004 and are listed as "-999" to denote missing data. Note that occasionally when there is a non-synoptic time best track entry included for either landfall or peak intensity, that the wind radii best tracks were not provided. These instances are also denoted with a "-999" in the database.

7) Radius of Maximum Wind: These values have been best tracked only starting in 2021. Before 2021, the missing data are denoted as "-999". Uncertainty in the RMW values – expressed as estimated absolute error in nautical miles – have been provided by a survey of the NHC Hurricane Specialists in 2022:

Tropical Storm/Subtropical Storm - Satellite/no scatterometer within 6 hr	27
Tropical Storm/Subtropical Storm - Satellite/with scatterometer within 6 hr	17
Tropical Storm/Subtropical Storm - Aircraft and satellite	13
Tropical Storm/Subtropical Storm - U.S. landfall	13
Category 1 or 2 Hurricane - Satellite/no scatterometer within 6 hr	16
Category 1 or 2 Hurricane - Satellite/with scatterometer within 6 hr	12
Category 1 or 2 Hurricane - Aircraft and satellite	9
Category 1 or 2 Hurricane - U.S. landfall:	8
Category 3, 4, or 5 Hurricane - Satellite/no scatterometer within 6 hr	11
Category 3, 4, or 5 Hurricane - Satellite/with scatterometer within 6 hr	9

Category 3, 4, or 5 Hurricane - Aircraft and satellite	5
Category 3, 4, or 5 Hurricane - U.S. landfall	5

General Notes:

The database goes back to 1851, but it is far from being complete and accurate for the entire century and a half. Uncertainty estimates of the best track parameters available for are available for various era in Landsea et al. (2012), Hagen et al. (2012), Torn and Snyder (2012), and Landsea and Franklin (2013). Moreover, as one goes back further in time in addition to larger uncertainties, biases become more pronounced as well with tropical cyclone frequencies being underreported and the tropical cyclone intensities being underanalyzed. That is, some storms were missed and many intensities are too low in the pre-aircraft reconnaissance era (1944 for the western half of the basin) and in the pre-satellite era (late-1960s for the entire basin). Even in the last decade or two, new technologies affect the best tracks in a non-trivial way because of our generally improving ability to observe the frequency, intensity, and size of tropical cyclones. See Vecchi and Knutson (2008), Landsea et al. (2010), Vecchi and Knutson (2012), Uhlhorn and Nolan (2012), Vecchi et al. (2021) on methods that have been determined to address some of the undersampling issues that arise in monitoring these mesoscale, oceanic phenomenon.

The only aspect of the original HURDAT database that is not contained in the new HURDAT2 is the state-by-state categorization of the Saffir Simpson Hurricane Wind Scale for continental U.S. hurricanes. This information is not a best track quantity and thus will not be included here. However, such U.S. Saffir Simpson Hurricane Wind Scale impact records will continue to be maintained, but within a separate database.

References:

Delgado, S., C. W. Landsea, and H. Willoughby, 2018: Reanalysis of the 1954-63 Atlantic hurricane seasons. *J. Climate*, **31**, 4177-4192. https://www.aoml.noaa.gov/hrd/Landsea/delgado-et-al-jclimate-2018.pdf

Hagen, A. B., D. Strahan-Sakoskie, and C. Luckett, 2012: A reanalysis of the 1944-53 Atlantic hurricane seasons - The first decade of aircraft reconnaissance. *J. Climate*, **25**, 4441-4460. http://www.aoml.noaa.gov/hrd/Landsea/1944-1953_Published_Paper.pdf

Jarvinen, B. R., C. J. Neumann, and M. A. S. Davis, 1984: A tropical cyclone data tape for the North Atlantic Basin, 1886-1983: Contents, limitations, and uses. *NOAA Technical Memorandum NWS NHC 22*, Coral Gables, Florida, 21 pp. http://www.nhc.noaa.gov/pdf/NWS-NHC-1988-22.pdf

Kieper, M. E., C. W. Landsea, and J. L. Beven, II, 2016: A reanalysis of Hurricane Camille. *Bull. Amer. Meteor. Soc.*, **97**, 367-384. https://www.aoml.noaa.gov/hrd/Landsea/kieper-landsea-beven-bams-2016.pdf

Landsea, C. W., and J. L. Franklin, 2013: Atlantic hurricane database uncertainty and presentation of a new database format. *Mon. Wea. Rev.,* **141**, 3576-3592. http://www.aoml.noaa.gov/hrd/Landsea/landsea-franklin-mwr2013.pdf

Landsea, C. W., C. Anderson, N. Charles, G. Clark, J. Dunion, J. Fernandez-Partagas, P. Hungerford, C. Neumann, and M. Zimmer, 2004a: The Atlantic hurricane database re-analysis project: Documentation for the 1851-1910 alterations and additions to the HURDAT database. *Hurricanes and Typhoons: Past, Present and Future*, R. J. Murname and K.-B. Liu, Eds., Columbia University Press, 177-221. http://www.aoml.noaa.gov/hrd/Landsea/rpibook-final04.pdf

Landsea, C. W. , D. A. Glenn, W. Bredemeyer, M. Chenoweth, R. Ellis J. Gamache, L. Hufstetler, C. Mock, R. Perez, R. Prieto, J. Sanchez-Sesma, D. Thomas, and L. Woolcock, 2008: A reanalysis of the 1911-20 Atlantic hurricane database. *J. Climate*, **21**, 2138-2168. http://www.aoml.noaa.gov/hrd/Landsea/reanal_1911-20.pdf

Landsea, C. W., S. Feuer, A. Hagen, D. A. Glenn, J. Sims, R. Perez, M. Chenoweth, and N. Anderson, 2012: A reanalysis of the 1921-1930 Atlantic hurricane database. *J. Climate*, **25**, 865-885. http://www.nhc.noaa.gov/pdf/landsea-et-al-jclimate2012.pdf

Landsea, C.W., J. L. Franklin, C. J. McAdie, J. L. Beven II, J. M. Gross, R. J. Pasch, E. N. Rappaport, J. P. Dunion, and P. P. Dodge, 2004b: A re-analysis of Hurricane Andrew's (1992) intensity. *Bull. Amer. Meteor. Soc.*, **85**, 1699-1712. http://www.aoml.noaa.gov/hrd/Landsea/landseabams2004.pdf

Landsea, C.W., G.A. Vecchi, L. Bengtsson, and T. R. Knutson, 2010: Impact of duration thresholds on Atlantic tropical cyclone counts. *J. Climate,* **23**, 2508-2519. http://www.aoml.noaa.gov/hrd/Landsea/landsea-et-al-jclim2010.pdf

Sampson, C. R., and A. J. Schrader, 2000: The Automated Tropical Cyclone Forecasting System (Version 3.2). *Bull. Amer. Meteor. Soc.*, **81**, 1231-1240. https://journals.ametsoc.org/doi/pdf/10.1175/1520-0477%282000%29081%3C1231%3ATATCFS%3E2.3.CO%3B2

Torn, R. D., and C. Snyder, 2012: Uncertainty of tropical cyclone best-track information. *Wea. Forecasting*, **27**, 715-729. https://journals.ametsoc.org/doi/pdf/10.1175/WAF-D-11-00085.1

Uhlhorn, E. W., and D. S. Nolan, 2012: Observational undersampling in tropical cyclones and implications for estimated intensity. *Mon. Wea. Rev.*, **140**, 825-840. https://journals.ametsoc.org/doi/pdf/10.1175/MWR-D-11-00073.1

Vecchi, G. A., and T. R. Knutson, 2008: On estimates of historical North Atlantic tropical cyclone activity. *J. Climate*, **21**, 3580-3600. https://journals.ametsoc.org/doi/pdf/10.1175/2008JCLI2178.1

Vecchi, G. A., and T. R. Knutson, 2011: Estimating annual numbers of Atlantic hurricanes missing from the HURDAT database (1878–1965) using ship track density. *J. Climate*, **24**, 1736-1746. https://journals.ametsoc.org/doi/pdf/10.1175/2010JCLI3810.1

Vecchi, G. A., C. Landsea, W. Zhang, G. Villarini, and T. Knutson, 2021: Changes in Atlantic major hurricane frequency since the late-19th century. *Nature Communications*. **12**, 1-9. https://www.aoml.noaa.gov/hrd/Landsea/Vecchi_et_al-2021-Nature_Communications.pdf

Most Intense (3, 4, 5) Continental United States Hurricanes: 1851 - 1970, and 1983-2023

(Revised in May 2024 to include the 2023 hurricane seasons' reanalyses)

Rank	#	Date	Time	Latitude	Longitude	Max Winds (kt)	SS HWS	RMW nm	Central Pressure (mb)	States Affected	Name
1	3	9/3/1935	0200Z	24.8N	80.8W	160	5	5	892	CFL5,BFL5	"Labor Day"
2	9	8/18/1969	0400Z	30.3N	89.4W	150	5	10	900	MS5,LA5,AL1	Camille
3	4	8/26/1992	0905Z	25.5N	80.3W	145	5	10	922	CFL5,BFL4	Andrew
4	14	10/10/2018	1730Z	30.0N	85.5W	140	5	10	919	AFL5,I-GA2	Michael
5	1	8/10/1856$	1800Z	29.2N	91.1W	130	4	10	934	LA4	"Last Island"
5	5	8/20/1886	1300Z	28.1N	96.8W	130	4	15	925	BTX4	"Indianola"
5	2	9/10/1919	0700Z	24.6N	82.9W	130	4	15	927	BFL4,CFL2	---
5	2	8/14/1932	0400Z	29.0N	95.2W	130	4	10	935	CTX4,BTX1	"Freeport"
5	3	8/13/2004	1945Z	26.6N	82.2W	130	4	5	941	BFL4,CFL1,DFL1	Charley
5	13	8/27/2020	0600Z	29.8N	93.3W	130	4	15	939	LA4,ATX1	Laura
5	9	8/29/2021	1655Z	29.1N	90.2W	130	4	10	931	LA4	Ida
5	9	9/28/2022	1905Z	26.7N	82.2W	130	4	20	941	BFL4,ICFL1,DFL1,SC1	Ian
6	7	9/18/1926	1200Z	25.7N	80.3W	125	4	20	930	CFL4,BFL3	"Great Miami"
6	4	9/17/1928	0000Z	26.7N	80.0W	125	4	30	929	CFL4,BFL3,AFL1,DFL1	"Lake Okeechobee"
6	5	9/10/1960	0700Z	24.8N	80.9W	125	4	20	930	BFL4,CFL4	Donna
6	3	9/11/1961	2000Z	28.3N	96.4W	125	4	20	931	BTX4, CTX3, ATX1	Carla
7	1	9/9/1900	0200Z	29.1N	95.1W	120	4	15	936	CTX4	"Galveston"
7	4	8/3/1970	2100Z	27.8N	97.1W	120	4	10	944	ATX4	Celia
7	11	9/22/1989	0400Z	32.8N	79.8W	120	4	20	934	SC4,INC1	Hugo
8	10	10/2/1893	0800Z	29.3N	89.8W	115	4	10	948	LA4	"Chenier Caminanda"
8	7	10/2/1898	1600Z	30.9N	81.4W	115	4	20	938	GA4,DFL2	---
8	2	8/17/1915	0700Z	29.2N	95.1W	115	4	25	940	CTX4,BTX1,LA1	"Galveston"
8	6	8/18/1916	2200Z	27.0N	97.4W	115	4	25	932	ATX4	---
8	9	9/15/1945	1930Z	25.3N	80.3W	115	4	10	949	CFL4,BFL2,DFL1	---
8	4	9/16/1947	1630Z	26.1N	80.1W	115	4	15	943	CFL4,BFL2	---
8	8	9/22/1948	0500Z	25.8N	81.3W	115	4	10	940	BFL4,CFL2	---
8	2	8/26/1949	2300Z	26.6N	80.0W	115	4	20	954	CFL4,BFL1,AFL1,DFL1,GA1	---
8	11	10/18/1950	0500Z	25.7N	80.2W	115	4	5	955	CFL4,DFL1	King
8	14	10/14/1954	1530Z	33.9N	78.6W	115	4	20	938	SC4,NC4	Hazel
8	8	9/29/1959	1700Z	32.5N	80.4W	115	4	10	951	SC4	Gracie
8	3	9/8/1965	0400Z	29.2N	90.1W	115	4	30	946	LA4	Betsy
8	9	8/25/2017	0300Z	28.0N	96.9W	115	4	10	937	BTX4	Harvey
8	11	9/10/2017	1300Z	24.7N	81.5W	115	4	10	931	BFL4,CFL1	Irma
9	6	9/16/1855$	0300Z	29.2N	89.5W	110	3	---	945	LA3,MS3	"Middle Gulf Shore"
9	1	8/11/1860$	2000Z	29.2N	90.0W	110	3	---	945	LA3,MS3,AL2	---
9	4	9/1/1879$	1600Z	29.5N	91.4W	110	3	---	945	LA3	---

9	2	8/13/1880#	0100Z	25.8N	97.0W	110	3	10	931	ATX3	----------
9	2	9/10/1882	0200Z	30.4N	86.8W	110	3	---	949	AFL3,AL1	----------
9	3	8/16/1888$	1900Z	25.8N	80.1W	110	3	---	945	CFL3,BFL1	----------
9	4	9/29/1896	1100Z	29.2N	83.1W	110	3	15	960	AFL3,DFL3,GA2,SC1,NC1,VA1	----------
9	6	9/29/1915	1800Z	29.1N	90.3W	110	3	20	944	LA3,MS2	"New Orleans"
9	10	9/5/1933	0400Z	26.1N	97.2W	110	3	20	940	ATX3	----------
9	11	9/4/1933	0500Z	26.9N	80.1W	110	3	15	948	CF3	----------
9	2	9/23/1941	2200Z	28.8N	95.6W	110	3	20	942	CTX3,BTX2	----------
9	2	6/27/1957	1330Z	29.8N	93.7W	110	3	15	946	LA3,CTX2	Audrey
9	8	9/27/1958*	1800Z	33.9N	77.6W	110	3	20	938	NC3	Helene
9	12	8/29/2005	1110Z	29.3N	89.6W	110	3	20	920	LA3,MS3,AL1	Katrina
10	10	10/12/1886	2200Z	29.8N	93.5W	105	3	---	950	LA3,CTX2	---------
10	9	10/13/1893	1300Z	33.0N	79.5W	105	3	15	955	SC3,NC2,VA1	---------
10	5	10/9/1894	0300Z	30.2N	85.5W	105	3	---	950	AFL3,GA1	---------
10	3	8/18/1899	0100Z	35.2N	75.8W	105	3	---	945	NC3	---------
10	8	10/18/1906	0900Z	24.7N	81.1W	105	3	10	953	BFL3,CFL3	---------
10	2	7/5/1916	2100Z	30.4N	88.4W	105	3	20	950	MS3,AL2,AFL2	---------
10	1	8/6/1918	1800Z	29.8N	93.2W	105	3	10	955	LA3,CTX1	---------
10	6	/9/21/1938	2000Z	40.7N	72.9W	105	3	40	941	NY3,CT3,RI3,MA2	"Great New England"
10	13	10/18/1944	2100Z	24.6N	82.9W	105	3	30	949	BFL3	---------
10	5	9/5/1950	1700Z	29.1N	82.8W	105	3	15	960	AFL3,BFL1	Easy
10	9	9/16/2004	0650Z	30.2N	87.9W	105	3	25	946	AL3,AFL3	Ivan
10	10	9/26/2004	0400Z	27.2N	80.2W	105	3	45	950	CFL3,BFL1,AFL1	Jeanne
10	4	7/10/2005	1930Z	30.4N	87.1W	105	3	5	946	AFL3,IAL1	Dennis
10	21	10/24/2005	1030Z	25.9N	81.7W	105	3	25	950	BFL3,CFL2	Wilma
11	4	8/23/1851$	2100Z	30.1N	85.7W	100	3	---	955	AFL3,GA1	"Great Middle Florida"
11	1	8/26/1852	0600Z	30.2N	88.6W	100	3	10	961	AL3,MS3,LA2,AFL1	"Great Mobile"
11	2	9/8/1854	2000Z	31.7N	81.1W	100	3	40	950	GA3,SC2,DFL1	"Great Carolina"
11	3	9/8/1965	1100Z	25.0N	80.5W	100	3	30	952	BFL3, CFL3	Betsy
11	6	9/8/1869	2200Z	41.4N	71.7W	100	3	30	965	RI3,MA3,CT1	"Eastern New England"
11	3	8/17/1871$	0200Z	27.1N	80.2W	100	3	30	955	CFL3,DFL1,AFL1	----------
11	5	10/7/1873$	0100Z	26.5N	82.2W	100	3	25	959	BFL3,CFL2,DFL1	----------
11	3	9/16/1875	2100Z	27.7N	97.2W	100	3	---	955	BTX3,ATX2	----------
11	4	10/3/1877$	0500Z	30.0N	85.5W	100	3	---	955	AFL3,GA1	----------
11	2	8/18/1879	1200Z	34.7N	76.7W	100	3	15	971	NC3,VA2	----------
11	6	8/28/1893	0500Z	31.7N	81.1W	100	3	25	954	GA3,SC3,NC1,DFL1	"Sea Island"
11	4	7/21/1909	1700Z	28.9N	95.3W	100	3	20	959	CTX3	"Velasco"
11	9	9/21/1909	0000Z	29.5N	91.3W	100	3	30	952	LA3,MS2	"Grand Isle"
11	11	10/11/1909	1800Z	24.7N	81.0W	100	3	20	957	BFL3,CFL3	----------
11	4	9/29/1917	0200Z	30.4N	86.6W	100	3	40	949	AFL3,LA2,AL1	----------
11	2	9/14/1919	2100Z	27.2N	97.3W	100	3	35	950	ATX3,BTX3	----------
11	6	10/25/1921	2000Z	28.1N	82.8W	100	3	20	958	BFL3,AFL2,DFL1	"Tampa Bay"

11	3	8/25/1926	2300Z	29.2N	90.9W	100	3	15	967	LA3	----------
11	7	9/20/1926	2200Z	30.3N	87.5W	100	3	15	955	AFL3,AL3,MS1	----------
11	2	9/28/1929	1300Z	25.0N	80.5W	100	3	30	948	BFL3,CFL3	----------
11	3	8/30/1942	0900Z	28.3N	96.6W	100	3	20	950	BTX3,CTX2	----------
11	5	8/27/1945	1200Z	28.2N	96.7W	100	3	10	963	BTX3,ATX1,CTX1	----------
11	6	8/31/1954	1400Z	40.9N	72.2W	100	3	20	955	NY3,CT3,RI3,MA2,NC1	Carol
11	1	6/8/1966	1900Z	24.6N	82.7W	100	3	---	962	BFL3,AFL1	Alma
11	13	9/20/1967	1200Z	25.9N	97.2W	100	3	10	940	ATX3	Beulah
11	3	8/18/1983	0700Z	29.1N	95.1W	100	3	10	962	CTX3	Alicia
11	5	9/2/1985	1300Z	30.4N	89.2W	100	3	10	959	AL3,MS3,AFL3	Elena
11	4	8/26/1992	0830Z	29.6N	91.5W	100	3	20	956	LA3	Andrew
11	5	8/31/1993	2100Z	35.2N	75.1W	100	3	30	961	NC3	Emily
11	17	10/4/1995	2200Z	30.3N	87.1W	100	3	50	942	AFL3,IAL1	Opal
11	6	9/6/1996	0030Z	33.9N	78.0W	100	3	40	954	NC3	Fran
11	3	8/23/1999	0000Z	26.9N	97.4W	100	3	10	951	ATX3	Bret
11	18	9/24/2005	0740Z	29.7N	93.7W	100	3	20	937	LA3,CTX2	Rita
11	28	10/28/2020	2100Z	29.2N	90.6W	100	3	20	970	LA3,MS2,I-AL1	Zeta
11	09	08/30/2023	1145Z	29.9N	83.6W	100	3	10	950	AFL3,I-GA1	Idalia

Notes:

Date/Time: Date and time when the circulation center crosses the U.S. coastline (including barrier islands). Time is estimated to the nearest hour.

Lat/Lon: Location is estimated to the nearest 0.1 degrees latitude and longitude (about 6 nm).

Max Winds: Estimated maximum sustained (1 min) surface (10 m) winds to occur along the U. S. coast.

SSHWS: The estimated Saffir-Simpson Hurricane Wind Scale at landfall based upon maximum 1-min surface winds.

RMW: The radius of maximum winds (primarily for the right front quadrant of the hurricane), if available.

Cent Press: The central pressure of the hurricane at landfall. Central pressure values in parentheses indicate that the value is a simple estimation (based upon a wind-pressure relationship), not directly measured or calculated.

States Affected: The impact of the hurricane upon individual U.S. states by Saffir-Simpson Scale (again through the estimate of the maximum 1-min surface winds at each state). (ATX-South Texas, BTX-Central Texas, CTX-North Texas, LA-Louisiana, MS-Mississippi, AL-Alabama, AFL-Northwest Florida, BFL-Southwest Florida, CFL-Southeast Florida, DFL-Northeast Florida, GA-Georgia, SC-South Carolina, NC-North Carolina, VA-Virginia, MD-Maryland, DE-Delaware, NJ-New Jersey, NY-New York, PA-Pennsylvania, CT-Connecticut, RI-Rhode Island, MA-Massachusetts, NH-New Hampshire, ME-Maine. In Texas, south is roughly from the Mexico border to Corpus Christi; central is from north of Corpus Christi to Matagorda Bay and north is from Matagorda Bay to the Louisiana border. In Florida, the north-south dividing line is from Cape Canaveral [28.45N] to Tarpon Springs [28.17N]. The dividing line between west-east Florida goes from 82.69W at the north Florida border with Georgia, to Lake Okeechobee and due south along longitude 80.85W.)

$ - Indicates that the hurricane may not have been reliably estimated for intensity (both central pressure and maximum 1-min windspeed) because of landfall in a relatively uninhabited region. Errors in intensity are likely to be underestimates of the true intensity.

- Indicates that hurricane made landfall first over Mexico, but caused hurricane winds in Texas. The position given is that of Mexican landfall. The strongest winds impacted Mexico. The winds indicated here are lower than in HURDAT and are lower than they were over Mexico. Central pressure given is that at Mexican landfall.

* - Indicates that the hurricane center did not make a U.S. landfall, but did produce the indicated hurricane-force winds over land. In this case, central pressure is given for the hurricane's point of closest approach.

53. Assignment 2, Module 11: NOAA Technical Memo 22:
https://repository.library.noaa.gov/view/noaa/7069

NOAA Technical Memorandum NWS NHC 22

A TROPICAL CYCLONE DATA TAPE FOR THE NORTH ATLANTIC BASIN, 1886-1983: CONTENTS, LIMITATIONS, AND USES

Brian R. Jarvinen, Charles J. Neumann, and Mary A. S. Davis
NHC, Miami, Florida

National Hurricane Center
Miami, Florida
March 1984
Second Printing, October 1988

UNITED STATES
DEPARTMENT OF COMMERCE
C. William Verity, Secretary

National Oceanic and Atmospheric Administration
William E. Evans
Under Secretary and Administrator

National Weather Service
Elbert W. Friday
Assistant Administrator

CONTENTS

DEFINITIONS

Cyclone: An atmospheric closed-circulation rotating counterclockwise in the Northern Hemisphere.

Extratropical Stage: In tropical meteorology this refers to the transformation of a tropical cyclone from a warm core to a cold core system. This process usually occurrs poleward from the belt of tropical easterlies.

GMT: Greenwich Mean Time. Also referred to as "Z" time or Zulu time. Mean solar time of the meridian at Greenwich, England, used as the basis for standard time throughout most of the world.

Hurricane: A warm-core tropical cyclone in which the maximum sustained surface wind (1-min mean) is $\geq$ 64 kt.

Knot: The unit of speed in the nautical system; 1 n.mi. h^{-1} It is equal to 1.1508 mi h^{-1} or 0.5144 m s^{-1}.

Millibar: A pressure unit of 1000 dyn cm^{-2}, convenient for reporting atmospheric pressures.

Subtropical Cyclones: Nonfrontal, low pressure systems that comprise initially baroclinic circulations developing over subtropical waters. There are two types: (1) A cold low with circulation extending to the surface layer and maximum sustained winds generally occurring at a radius of about 100 mi or more from the pressure center. These cyclones sometimes undergo a metamorphosis and become tropical storms or hurricanes. (2) A mesoscale cyclone originating in or near a frontolyzing zone of horizontal wind shear, with radius of maximum sustained winds generally less than 30 mi. The entire circulation sometimes encompasses an area initially no more than 100 mi in diameter. These marine cyclones may change in structure from cold to warm core. While generally short-lived, they may ultimately evolve into major hurricanes or into extra-tropical cyclones.

Subtropical cyclones are classed according to intensity as follows:

a. Subtropical Depression: A subtropical cyclone in which the maximum sustained surface wind (1-min mean) is $\leq$ 33 kt.
b. Subtropical Storm: A subtropical cyclone in which the maximum sustained surface wind (1-min mean) is $\geq$ 34 kt.

Tropical Cyclone: A nonfrontal low pressure system of synoptic scale developing over tropical or subtropical waters and having definite organized circulation.

Tropical Depression: A tropical cyclone in which the maximum sustained surface wind (1-min mean) is $\leq$ 33 kt.

Tropical Storm: A warm-core tropical cyclone in which the maximum sustained surface wind (1-min mean) ranges from 34 to 63 kt.

A TROPICAL CYCLONE DATA TAPE FOR THE NORTH ATLANTIC BASIN,[1] 1886-1982: CONTENTS, LIMITATIONS, AND USES

Brian R. Jarvinen, Charles J. Neumann, and Mary A. S. Davis
NWS, National Hurricane Center, Miami, Florida

ABSTRACT

The National Hurricane Center maintains a computer file on North Atlantic tropical cyclones. The file contains dates, tracks, wind speeds, and central pressure values (if available) for all tropical cyclones occurring over the 98-year period, 1886 through 1983 and is updated annually. The data organization, format, and limitations are discussed and several uses of the data are demonstrated.

INTRODUCTION

The National Hurricane Center (NHC) is essentially a forecasting, rather than a data collecting, agency of NOAA. However, pursuant to its operational responsibility in the detection, tracking, and forecasting of tropical cyclones, and its additional responsibility in the applied research and public service area, the Center maintains detailed computer files on North Atlantic tropical storms and hurricanes. This report describes the content, format, limitations, and uses of the data, hereafter referred to as the HURDAT (HURricane DATa) data set.

2. BACKGROUND OF DATA SET

The initial requirement for computerized tropical cyclone data at NHC can be traced to a requirement of the NASA Space Program in the mid-1960's. At the request of Space Program officials, Hope and Neumann (1968) of the Spaceflight Meteorology Group, formerly collocated with the National Hurricane Center, studied the climatological impact of tropical cyclones on launches of space vehicles from the Kennedy Space Center. An extension to the authors' studies led to the operational HURRAN (HURRicane ANalog) program (Hope and Neumann, 1970) for the prediction of tropical cyclone motion out through 72 hr.

Originally, Hope and Neumann based their studies on a now obsolete card deck 988 (CD 988) obtained from the National Climatic Center.

---

[1]The North Atlantic tropical cyclone basin includes most of the North Atlantic, Gulf of Mexico, Caribbean Sea, and adjacent land areas.

However, the original card deck has been extensively revised by NHC and tailored to its specific needs. Under the sponsorship of the U.S. Navy, the National Climatic Center has also revised card deck 988 and reissued it as card deck 993. The tropical cyclone tracks for the 1886 through 1963 portion of this latter deck correspond to those given by Cry (1965). The tropical cyclone tracks in HURDAT correspond to those given by Neumann, et al. (1981) in a revision to Cry, in which tracks are extended through the 1980 hurricane season. The revision also includes a few changes to some of Cry's original tracks. A copy of this data set may be purchased from NOAA/NESDIS, National Climatic Center, Federal Building, Asheville, NC, 28801. In requesting the tape, specific referrence should be made to the NHC edition.

3. THE HISTORY OF DATA OBSERVATIONS

The four basic pieces of information recorded on the computer file are the tropical cyclone's position (latitude and longitude), maximum sustained wind speed in knots, the central pressure in millibars (if available), and the time and date. The availability and accuracy of these parameters has by no means been constant throughout the years. Figure 1 indicates graphically the technical advances in observing systems that have occurred since the formation of the Hurricane Warning Service in 1871. This figure shows that, until organized reconnaissance began in 1944, the two major sources of information on tropical cyclones were land stations and ships at sea. Undoubtedly, during this early period some storms went undetected. However, ships encountered tropical cyclones more frequently in earlier years because they did not always have the benefit of forecasts. Many times a storm was detected and then "lost" for several days before it was encountered by another ship or observed from a land station. At other times a storm moved over land stations and through the major shipping lanes, thus allowing its track and intensity to be determined with a reasonable degree of accuracy. Therefore, during this early period of data the most useful information is track rather than wind data, although some of the tropical cyclones do have useful maximum wind information. Nevertheless, the user of the wind information is cautioned not to make an overly precise interpretation of this parameter for the entire period of record and especially before 1944. The reader is referred to Neumann, et al. (1981) for a list of additional references on tropical cyclone tracking.

Organized aircraft reconnaissance has allowed continuous monitoring of the storm's track, maximum sustained wind field, and central pressure. This is reflected in the increase of pressure data beginning in 1944. The coastal radar network has improved the track information mainly for landfalling storms.

The largest single advance in the detection and tracking of tropical cyclones has been the introduction of weather satellites with their associated visible and infrared sensors. With the initial position of a tropical cyclone determined from satellite a reconnaissance aircraft is dispatched to measure the more precise wind field, central pressure, and location of the center.

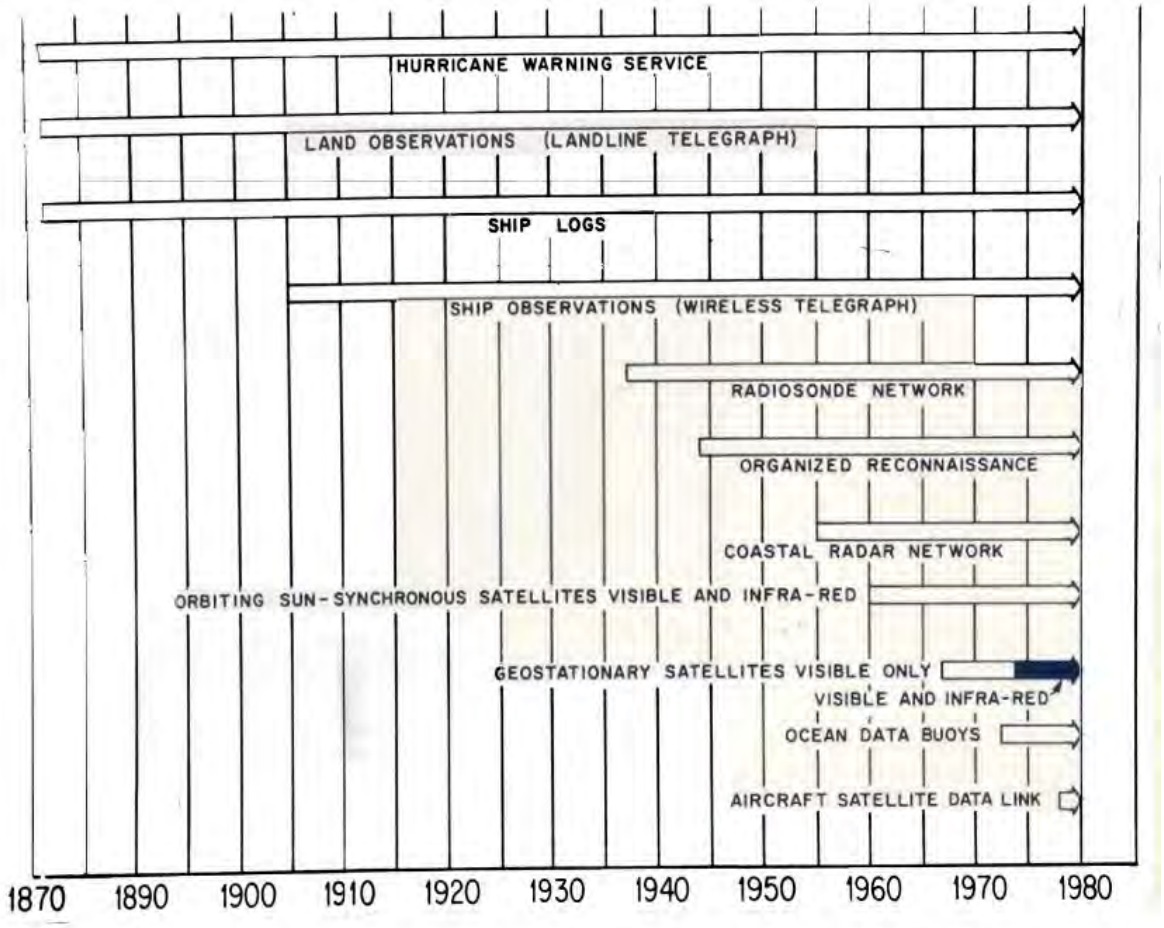

Figure 1. Technical advances in systems for observing tropical cyclones, 1871 through 1980.

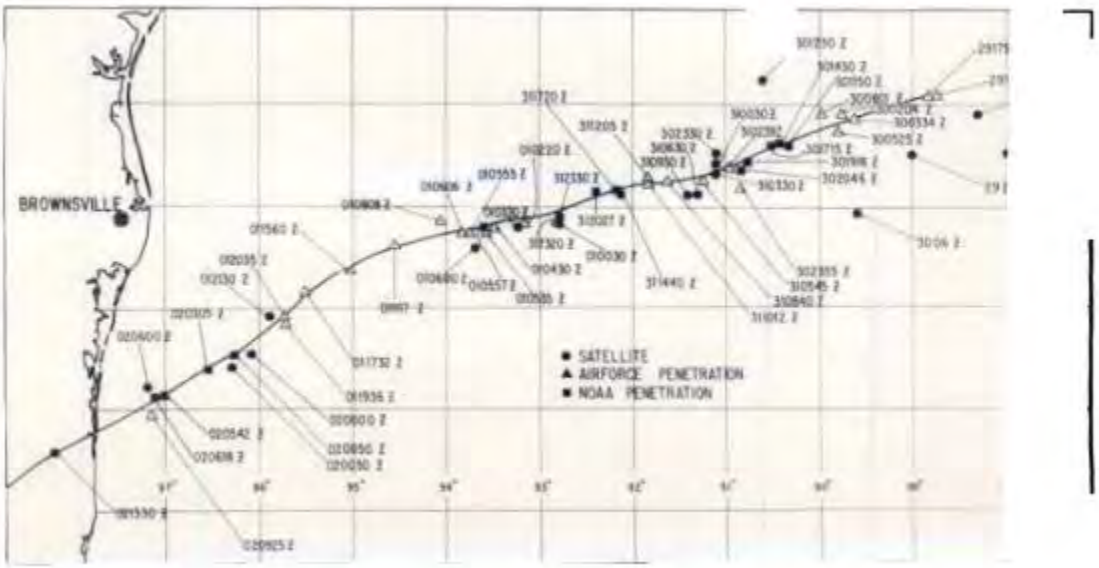

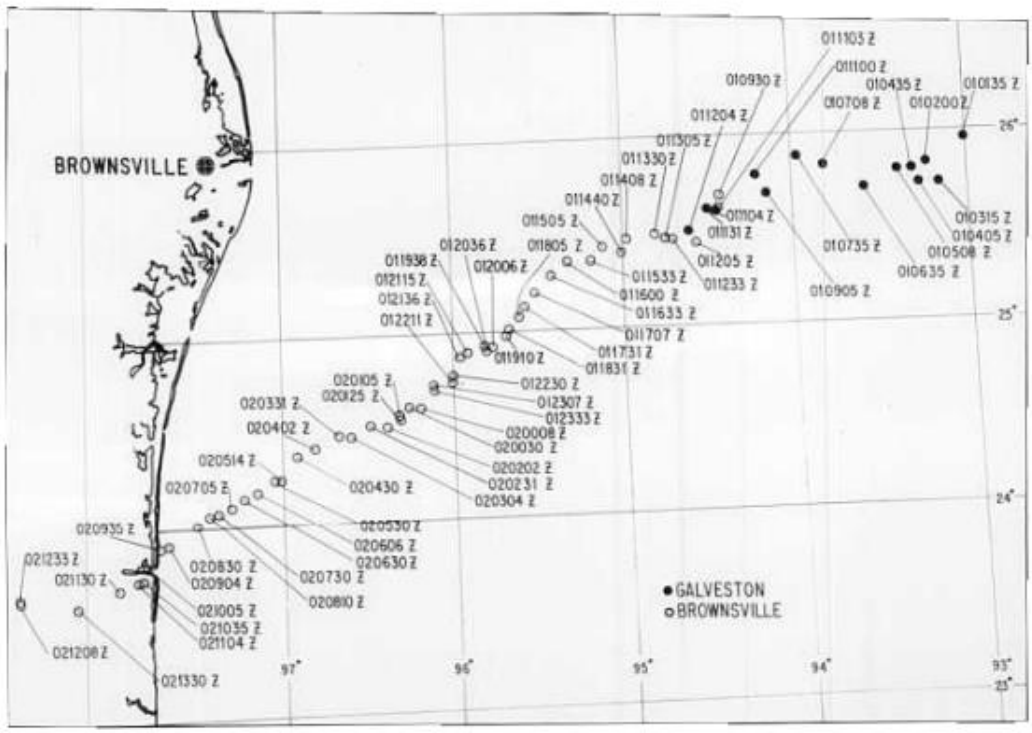

Figure 3. Radar center estimates for tropical cyclone Anita, 1977. The Galveston radar was able to make several estimates before the cyclone passed out of its range and into Brownsville's range. Note the small-scale oscillations in the track and compare this with the best track in Figure 2.

First, small-scale oscillatory (trochoidal) motions which are transitory in nature and not representative of the more conservative motion of the entire storm envelope must be considered. Smoothing is necessary to remove these small-scale motions, which are on the order of 5 to 20 n.mi. about some mean path. Radar documentation of these eye oscillations on tropical cyclone Carla, 1971, is presented in Figure 4. Recent evidence of similar motion based on satellite imagery of tropical cyclone Belle, 1976, is provided by Lawrence and Mayfield (1977). Therefore, final tracks should be considered as the best estimate of the larger scale storm motion, rather than precise locations of the eye.

Second, for a number of reasons, the pattern of wind, rainfall, and storm surge are typically higher in the right semicircle of a storm (looking towards the direction of motion) where the rotational and translational forces work in the same direction. Again, final tracks must take into account these asymmetries.

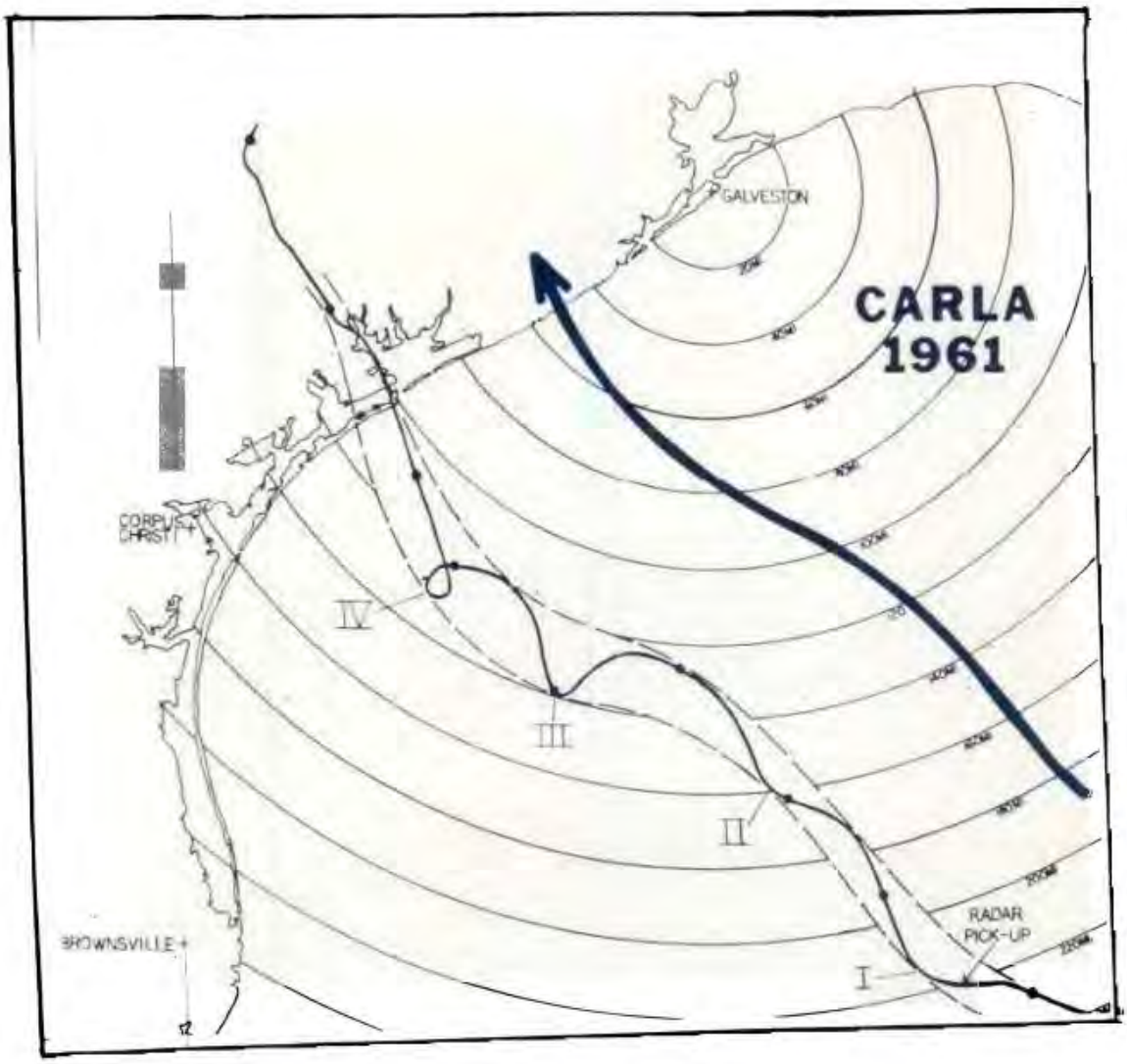

Figure 4. Portion of hurricane Carla track over Gulf of Mexico showing four smoothed trochoidal oscillations of storm center. Track is based on "fixes" from three coastal radars. Heavy track, offset to northeast, shows portion of smoothed "best track". Range markers are at 20-n.mi. intervals. (Figure adapted from Weatherwise, October, 1961.)

When an analyst has finished constructing a best track, storm positions at 6-hourly intervals are noted. The times for the four positions per day are (0000, 0600, 1200, and 1800) Greenwich Mean Time (GMT). These are the positions that are stored on the HURDAT tape.

Before 1931, only 1200 GMT positions were recorded on the original card deck 988 (see page 1). The three intermediate positions were interpolated from the 1200 GMT positions. From 1931 through 1956, although four positions per day were determined by the forecaster, only the 0000 and 1200 GMT positions were recorded. Here it was necessary to interpolate for the 0600 and 1800 GMT positions. A nonlinear interpolation scheme was used to obtain these intermediate positions. The polynomial interpolation described by Akima (1970) gave highly satisfactory results. However, each track interpolation was carefully checked to insure that important features, such as loops in the track, were retained.

Beginning in 1956, storm positions were recorded four times per day for verification of official forecasts which are also issued four times per day. The need for these positions increased during the 1960's with the coming of the computer age; they are required for many purposes, such as computer plotting of the tracks, implementation of the operational models, verification of the forecasts from the operational models, and verification of the official forecasts.

5. WIND SPEEDS

Each of the four daily storm positions has a corresponding wind speed. These wind values are specified in knots and rounded to the nearest 5-kt value, i.e., 68 kt becomes 70 kt while 67 kt becomes 65 kt. The wind values are estimated or measured averages over a 1-min period. Therefore, these values are not the peak winds or gusts. For further information on the relationship of gusts to average winds, the reader is referred to Dunn and Miller (1964), pp. 61-67; Padya (1975); and Atkinson and Holliday (1977).

To understand the limitations of the wind speed values, it is instructive to explore the various means by which the different observing platforms have actually measured the wind. First, for land stations, several types of wind recording devices have been used over the period of record. For example, in the 1890's, triple register instruments were introduced. The wind speed was one of the parameters measured and recorded by a counter device utilizing a 3-cup anemometer. In the 1950's, the present day recording device used by the National Weather Service was introduced. Known as the F-420 system, it measures wind speed and direction and also records wind gusts. Several other types of anemometers have been used in the recording of the maximum wind speed. These include 4-cup and 22-cup anemometers, it is felt that larger errors are introduced by the location and height of a particular anemometer.

The locations and heights of anemometers have varied at National Weather Service stations as the stations have been moved. The exposure of the anemometer to buildings can be very significant. For example, during the most destructive storm in the history of Miami, Florida, in 1926, the official recording anemometer was between several large buildings. It was estimated by the meteorologist in charge that the wind values recorded were approximately one-half of the actual value.

It should be noted that the chance of a tropical cyclone passing directly over a fully instrumented facility is remote. On many occasions, even when a storm passes over a populated area, the maximum wind must be inferred from indirect evidence, such as peripheral wind measurements or damage profiles.

Estimations of the wind over the ocean by ships are determined by the state of the sea and given in the Beaufort scale. Over the past 30 years some ships have been instrumented with anemometers. However, because the ship is a moving platform (in three directions), corrections are necessary to determine a wind value. The state-of-the-sea determination is a one-step observation and is thus favored by mariners. A study by Shinners (1963) found that anemometer-measured winds versus state-of-the-sea-determined winds were (1) lower up to about 20 kt, (2) approximately the same from 20 to 30 kt, and (3) greater above 30 kt. In other words, state-of-the-sea-determined winds are underestimates of the actual wind at higher speeds. The magnitudes of these underestimates are approximately 6 kt for the range 36 to 45 kt, 13 kt for the range 46 to 55 kt, and 15 kt for the range 56 to 65 kt. However, both types of wind values are received in ship reports today.

Likewise, although aircraft reconnaissance measures the flight-level winds anywhere from 500 to 10000 ft, the surface winds are a subjective estimate based upon observation of the sea state and/or tables relating flight-level winds to surface winds.(Black and Adams, 1983)

Finally, wind speed values were computed on occasions from pressure values using the formula (Kraft, 1961):

$$V_{max} = 14*(1013-P_{center})^{1/2}$$

where:

V_{max} = maximum sustained wind
and
P_{center} = pressure at center in millibars

Since the advent of weather satellites, techniques have been developed by Dvorak (1973 and 1975) and Hebert and Poteat (1975) to determine wind speed from the shape of a tropical and subtropical cyclone's cloud field, respectively. This estimation, along with those received from aircraft reconnaissance, forms the main nucleus of information to determine the final wind field. Figure 5 contains final surface wind and pressure profiles for tropical cyclone Anita, 1977. Also shown are the original surface wind and pressure information which was used to determine the profiles. Time increases to the right. The wind speed is specified in knots and pressure in millibars. The scatter and discrepancies in the various wind reports is quite evident. Here, again, as in the best track determination, the analyst subjectively determines the profiles. It is extremely important for the analyst to understand the weaknesses and strengths of the various measuring platforms.

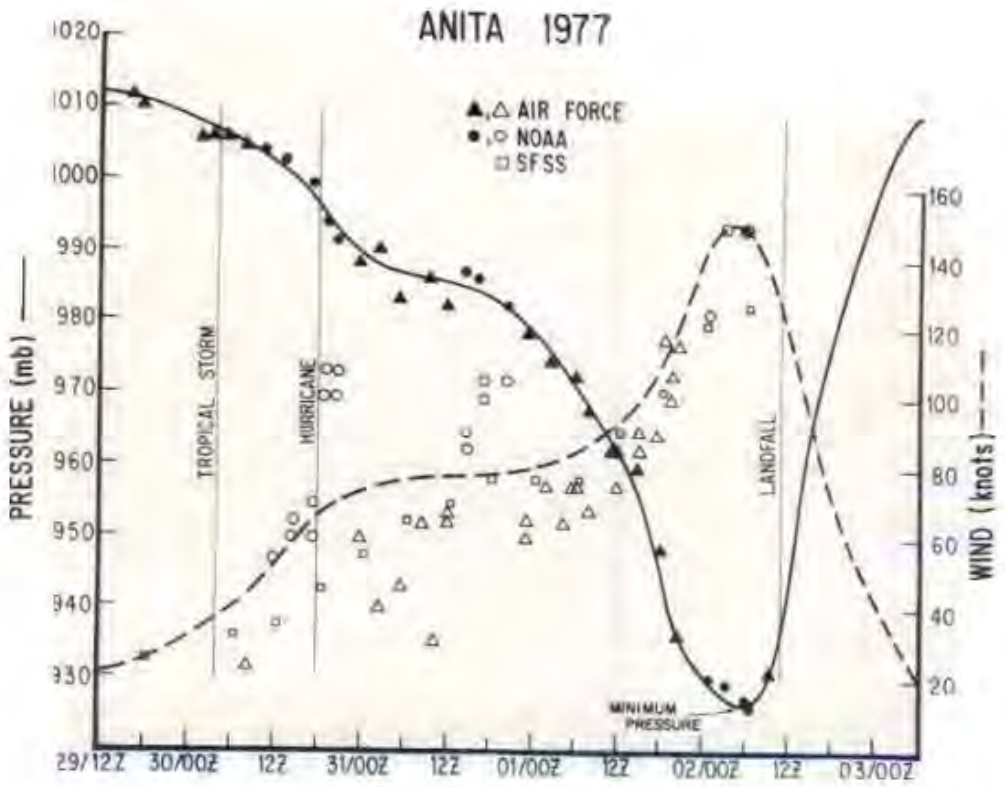

Figure 5. Final wind (dashed line) and pressure (solid line) profiles with actual data for tropical cyclone Anita, 1977.

6. PRESSURES

The tropical cyclone's central pressure on HURDAT is specified in millibars. Only reported central pressures within +2 hr of one of the four reporting times are included in the data. As discussed earlier, the frequency of pressure values decreases as one goes back in the period of record. Thus, unlike wind speeds, central pressures are often missing.

Pressures at populated centers affected by a storm may be well documented, even though the eye of the storm passed a good distance away. Those pressures <u>are not</u> part of this data set. It should be emphasized that all pressures on HURDAT are observed and that no pressures were determined from the winds.

Figure 5 shows a pressure profile and actual pressure data used to determine this profile. Since the satellite intensity classification determines the maximum sustained winds only, no pressure values are

given. It is clearly evident from the raw pressure data that the central pressure is a much more conservative property of the tropical cyclone than the wind field.

7. DATA FORMATS

The master deck that was used to generate the computer file consisted of three types of cards: Title, Data, and Classification. Each storm has one title card containing all required information to identify it. The first item on the card is the sequence number. The month, day, and year follow in that order. This is the first day on record for the storm. The next three numbers refer to the number of days the storm was in existence (M), the storm number for that year, and the cumulative storm number (SNBR), where the first storm in 1886 is 1 and the last storm in 1983 is 815. The next variable is the storm name. Before the naming of tropical storms in 1950, a "not named" message fills the space on the cards. The next item on the card is a storm crossing index (XING). The final item on the card is the Saffir/Simpson Hurricane Scale (SSS). In the present version this number should be ignored before 1899. To relate hurricane intensity to damage potential, the National Hurricane Center has adopted the Saffir/Simpson Hurricane Scale. This descriptive scale, over a range of categories 1 through 5, is shown in Table 4. Saffir/Simpson scale numbers are given only for hurricanes that crossed the continental United States. In a few instances, a Saffir/Simpson number of zero appears. This indicates that the storm, although classified as a hurricane over coastal waters, weakened to below hurricane strength before crossing the immediate coast line. On the title card, column 80 is used to denote the last storm of the year if punched with an L.

The single Title card is followed by two or more Data cards, one for each GMT day of the storm's existence. Each contains four sets of numbers where each set contains the storm type, the storm position (latitude in degrees north and longitude in degrees west), wind speed, and the central pressure. The sets correspond to the times 0000, 0600, 1200, and 1800 GMT. The storm types are *-Tropical Storm or Hurricane, D-Tropical Disturbance, S-Subtropical Storm, W-Tropical Wave, and E-Extratropical Storm.

The Classification card's purpose is to classify the maximum status attained during a storm's life. The index can take on one of three values: Tropical Storm (TS), Hurricane (HR), or Subtropical Storm (SS).

Tables 1 through 3 indicate the exact location of each parameter on the three types of cards. Copies of the computer cards for Anita, 1977, and an unnamed tropical storm, 1937, are shown in Figure 6. Note the difference in the amount of central pressure data.

The record size on the magnetic tape is 80 bytes, (i.e., each record is a card image.) This allows the user to read the tape as if it were a card deck. The user may then want to store certain information in larger records which will reduce input/output time. A fortran program to read and write the HURDAT tape, with formatted input and output statements, is given in Appendix I. The necessary physical parameters for reading the tape (i.e., density, parity, etc.) will be supplied by the National Climatic Center along with the tape.

Table 1. Title Card - Format and Contents

Computer Card Columns	Contents
1 - 5	Card sequence number
7 - 8	Month
10 - 11	Day (first day of storm on record)
13 - 16	Year
20 - 21	Value of M (M=number of days storm existed)
23 - 24	Storm number for that year
31 - 34	Cumulative storm number
36 - 47	Storm name
53	Crossing (1=hit U.S. coastline, 0=did not)
59	Saffir/Simpson Hurricane Scale number
80	Last storm of year if L

Table 2. Storm Data Card - Format and Contents

Latitudes and longitudes are rounded to the nearest tenth.
Wind speed is rounded to the nearest 5 kt.
Pressure is rounded to the nearest millibar.

Computer Card Columns	Contents
1 - 5	Card sequence number
7 - 8	Month
10 - 11	Day
12	Storm type at 0000Z
13 - 15	Latitude at 0000Z
16 - 19	Longitude at 0000Z
21 - 23	Wind speed at 0000Z
25 - 28	Central pressure at 0000Z
29	Storm type at 0600Z
30 - 32	Latitude at 0600Z
33 - 36	Longitude at 0600Z
38 - 40	Wind speed at 0600Z
42 - 45	Central pressure at 0600Z
46	Storm type at 1200Z
47 - 49	Latitude at 1200Z
50 - 53	Longitude at 1200Z
55 - 57	Wind speed at 1200Z
59 - 62	Central pressure at 1200Z
63	Storm type at 1800Z
64 - 66	Latitude at 1800Z
67 - 70	Longitude at 1800Z
72 - 74	Wind speed at 1800Z
76 - 79	Central pressure at 1800Z

Table 3. Classification Card - Format and Contents

Computer Card Column	Contents
1 - 5	Card sequence number
7 - 8	Maximum status of storm during its life

Table 4. Saffir/Simpson Hurricane Scale

Category Number	Definition
1	Winds of 74 to 95 miles per hour. Damage primarily to shrubbery, trees, foliage, and unanchored mobile homes. No real damage to other structures. Some damage to poorly constructed signs. And/or: storm surge 4 to 5 feet above normal. Low-lying coastal roads inundated, minor pier damage, some small craft in exposed anchorage torn from moorings.
2	Winds of 96 to 110 miles per hour. Considerable damage to shubbery and tree foliage; some trees blown down. Major damage to exposed mobile homes. Extensive damage to poorly constructed signs. Some damage to roofing materials of buildings; some window and door damage. No major damage to buildings. And/or: storm surge 6 to 8 feet above normal. Coastal roads and low-lying escape routes inland cut by rising water 2 to 4 hours before arrival of hurricane center. Considerable damage to piers. Marinas flooded. Small craft in unprotected anchorage torn from moorings. Evacuation of some shoreline residences and low-lying island areas required.
3	Winds of 111 to 130 miles per hour. Foliage torn from trees; large trees blown down. Practically all poorly constructed signs blown down. Some damage to roofing materials of buildings; some window and door damage. Some structural damage to small buildings. Mobile homes destroyed. And/or: storm surge 9 to 12 feet above normal. Serious flooding at coast and many smaller structures near coast destroyed; larger structures near coast damaged by battering waves and floating debris. Low-lying escape routes inland cut by rising water 3 to 5 hours before hurricane center arrives. Flat terrain 5 feet or less above sea level flooded inland 8 miles or more. Evacuation of low-lying residences within several blocks of shoreline possibly required.

Table 4. Saffir/Simpson Hurricane Scale continued

Category Number	Definition
4	Winds of 131 to 155 miles per hour. Shrubs and trees blown down; all signs down. Extensive damage to roofing materials, windows and doors. Complete failure of roofs on many small residences. Complete destruction of mobile homes. And/or: storm surge 13 to 18 feet above normal. Flat terrain 10 feet or less above sea level flooded as far as 6 miles. Major damage to lower floors of structures near shore due to flooding and battering waves and floating debris. Low-lying escape routes inland cut by rising water 3 to 5 hours before hurricane center arrives. Major erosion of beaches. Massive evacuation of all residences within 500 yards of shore possibly required, and of single-story residences on low ground within 2 miles of shore.
5	Winds greater than 155 miles per hour. Shrubs and trees blown down; considered damage to roofs of buildings; all signs down. Very severe and extensive damage to windows and doors. Complete failure of roofs on many residences and industrial buildings. Extensive shattering of glass in windows and doors. Some complete building failures. Small buildings overturned or blown away. Complete destruction of mobile homes. And/or: storm surge greater than 18 feet above normal. Major damage to lower floors of all structures less than 15 feet above sea level within 500 yards of shore. Low-lying escape routes inland cut by rising water 3 to 5 hours before hurricane center arrives. Massive evacuation of residential areas on low ground within 5 to 10 miles of shore possibly required.

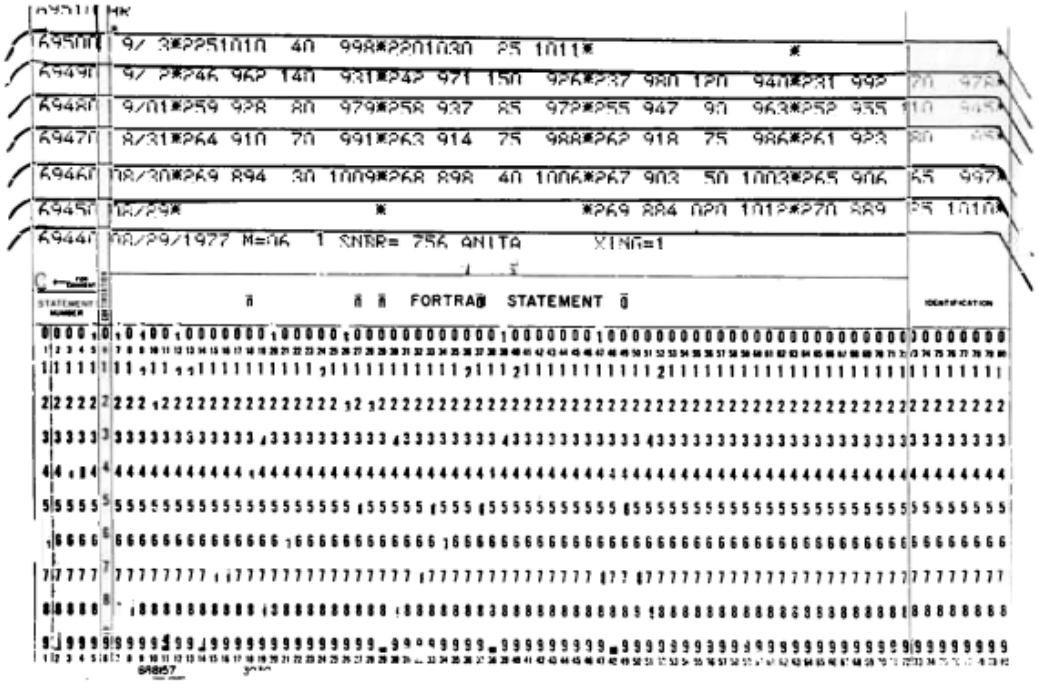

a.

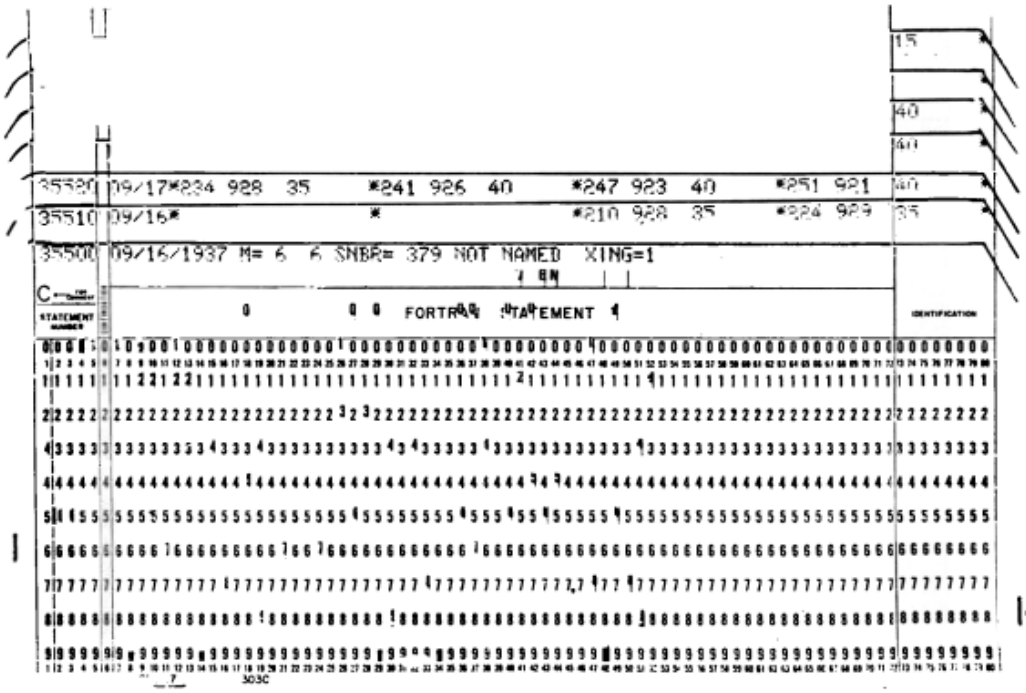

b.

Figure 6. Copies of computer cards giving the information for tropical cyclone Anita, 1977 (a.) and an unnamed tropical cyclone, 1937 (b.).

8. USES OF THE DATA

This section highlights some of the uses of the HURDAT tape at the National Hurricane Center. The thousands of requests received over the years indicate a much broader usage of the data than presented here.

The most requested products are the tracks. Figure 7 shows the tracks for all tropical cyclones beginning September 1 through 5, 1886 through 1977.

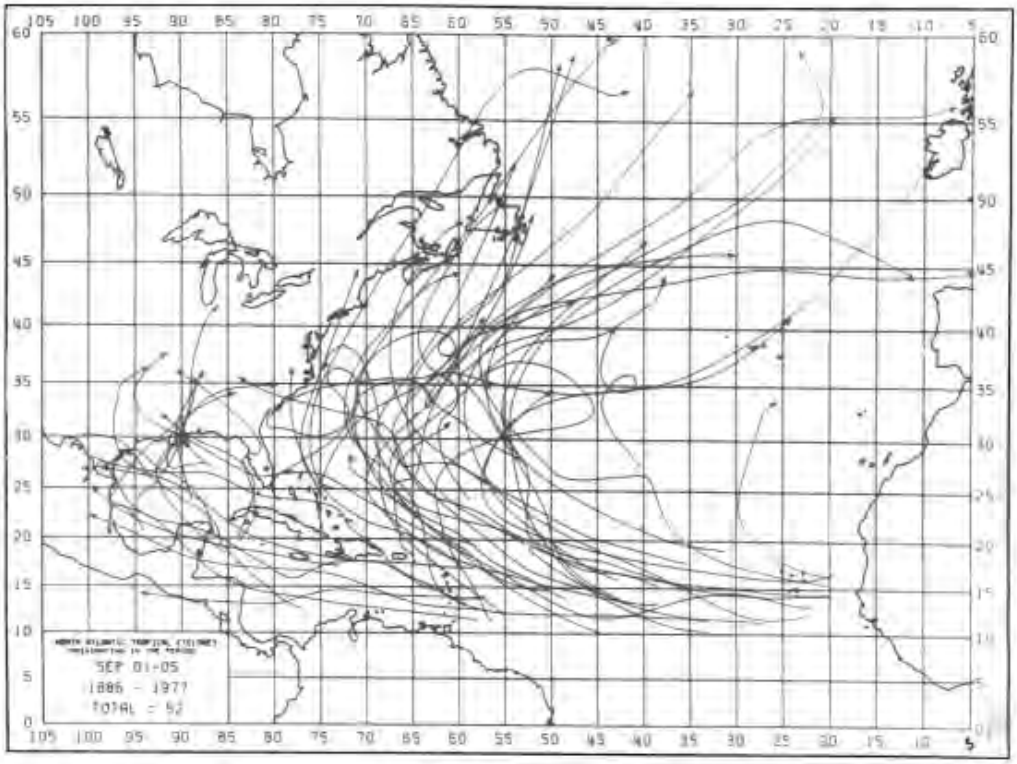

Figure 7. Tracks of tropical cyclones originating September 1 through 5, 1886 through 1977.

There are frequent requests for all tropical cyclones passing within a given distance from a particular location. Figure 8 shows all tracks of tropical cyclones of hurricane intensity when they were within 50 n.mi. of Miami, Florida, for 1886 through 1983. Table 5 is a copy of the printout giving additional information, such as the point and time of closet approach of the tropical cyclone to Miami and the maximum wind within the 50 n.mi. circle. A legend is included to explain each value in the table.

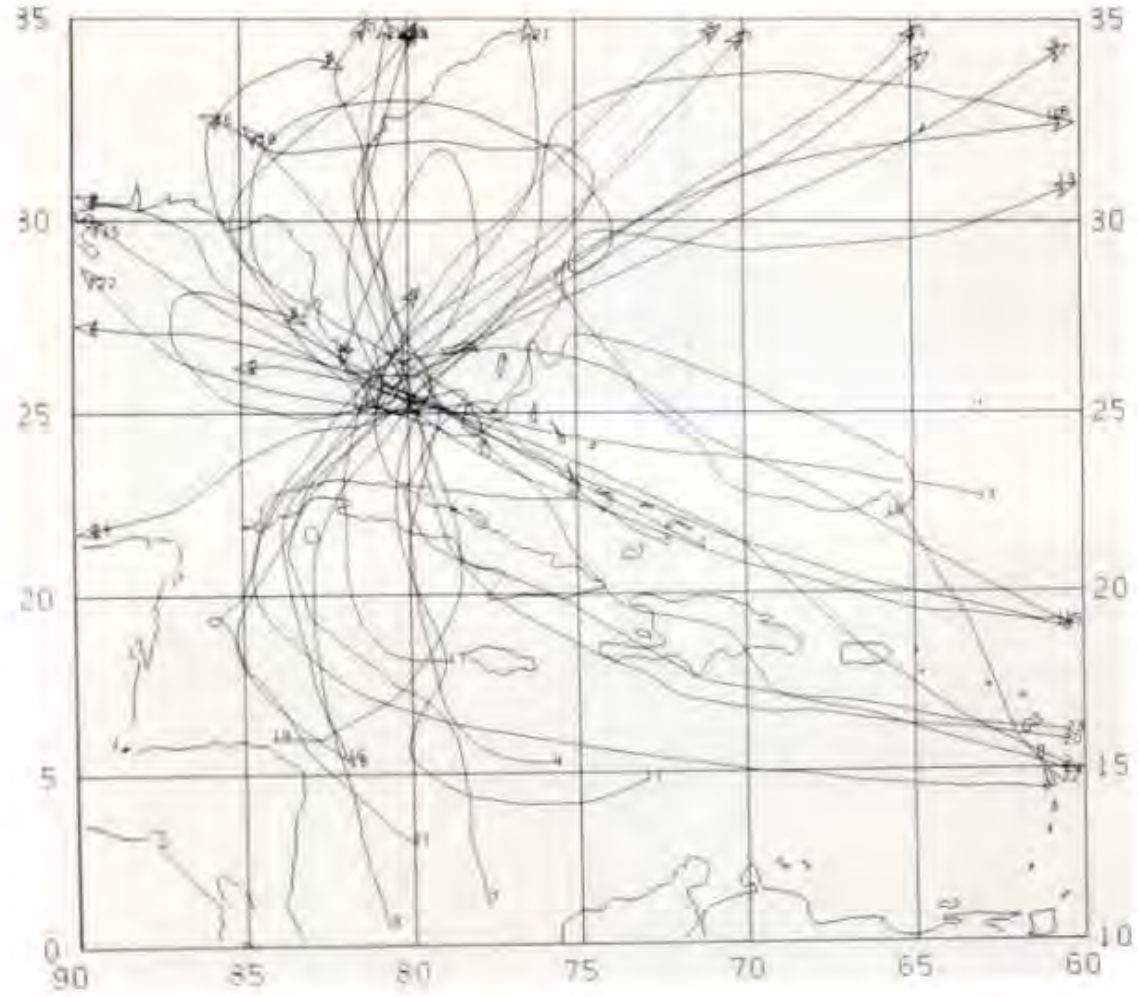

Figure 8. Tracks of all tropical cyclones of hurricane intensity passing within 50 n.mi. of Miami, Florida. The 50 n.mi. circle is also plotted. The numbers at the beginning and end of each track refer to column 1 of Table 4.

Standard statistical graphs showing frequency for various periods are often produced. Figure 9 gives an example of the annual tropical cyclone frequency, 1886 through 1982.

One of the many objective models in current operational usage at NHC is an analog model as described by Hope and Neumann (1970). This model scans the HURDAT tape and selects tropical cyclones that have characteristics similar to the current tropical cyclone in progress. These analog tropical cyclones are composited and a forecast track is generated. Figure 10 shows an example of an analog forecast for tropical cyclone Anita, 1977. Also included in the plot are the 50% probability elipses at the forecast intervals of 12, 24, and 36 hr.

Table 5 Computer Printout of All Hurricanes That Passed Within 50 n.mi. of Miami, Florida 1886 through 1983

MAP INDEX (1)	STARTING DATE (2)	LENGTH (DAYS) (3)	SEASONAL INDEX (4)	STORM'S NAME (5)	CLOSEST POINT OF APPROACH (CPA) (6)		DATE AT CPA (8)	TIME AT CPA (9)	DISTANCE TO CPA (10)	WIND (11)	REF # (12)
1	8/14/1888	11	1	NOT NAMED	25.6N	80.4W	8/16	1700Z	12.NM	94KT	30
2	8/18/1891	8	1	NOT NAMED	25.2N	80.3W	8/24	1600Z	25.NM	75KT	49
3	9/ 6/1903	8	1	NOT NAMED	26.2N	79.9W	9/11	2200Z	31.NM	83KT	141
4	10/12/1904	10	3	NOT NAMED	26.0N	80.3W	10/17	1600Z	12.NM	65KT	150
5	6/14/1906	10	2	NOT NAMED	25.9N	80.8W	6/17	0800Z	28.NM	70KT	159
6	10/11/1906	12	8	NOT NAMED	25.8N	80.3W	10/18	0900Z	2.NM	100KT	165
7	10/ 6/1909	8	8	NOT NAMED	25.4N	80.0W	10/11	2000Z	29.NM	84KT	189
8	9/11/1926	12	6	NOT NAMED	25.6N	80.3W	9/18	1200Z	12.NM	115KT	276
9	10/14/1926	11	10	NOT NAMED	25.4N	79.9W	10/21	0500Z	35.NM	95KT	280
10	9/22/1929	13	4	NOT NAMED	24.1N	80.6W	9/28	1700Z	47.NM	86KT	296
11	9/15/1935	10	6	NOT NAMED	25.8N	80.3W	9/ 4	1800Z	2.NM	85KT	357
12	10/30/1935	10	5	NOT NAMED	25.5N	80.5W	10/ 6	1100Z	23.NM	105KT	408
13	10/ 3/1941	12	5	NOT NAMED	25.5N	80.5W	9/15	2300Z	17.NM	110KT	469
14	9/12/1945	9	2	NOT NAMED	25.6N	80.4W	9/14	1500Z	31.NM	135KT	481
15	9/ 4/1947	13	4	NOT NAMED	25.5N	80.4W	9/ 4	1500Z	5.NM	95KT	461
16	10/ 9/1947	8	3	NOT NAMED	25.9N	80.5W	10/12	0700Z	13.NM	75KT	465
17	9/18/1948	8	2	NOT NAMED	26.1N	80.8W	9/22	0500Z	35.NM	97KT	473
18	10/ 3/1948	14	3	NOT NAMED	25.7N	80.1W	10/ 9	0000Z	11.NM	90KT	474
19	10/13/1950	7	11	KING	25.8N	80.2W	10/18	0600Z	4.NM	95KT	499
20	8/20/1964	17	5	CLEO	25.9N	80.0W	8/27	0900Z	13.NM	90KT	629
21	10/ 8/1964	10	11	ISBELL	26.2N	80.8W	10/14	2300Z	38.NM	110KT	630
22	8/27/1965	13	5	BETSY	25.1N	80.3W	9/ 8	1000Z	44.NM	110KT	652
23	9/21/1966	6	9	INEZ	25.2N	80.7W	10/ 4	1400Z	40.NM	75KT	651
24	8/25/1979	11	4	DAVID	26.1N	79.5W	9/ 3	1100Z	45.NM	85KT	777

NOTES:
(1) INDEX NUMBER CORRESPONDS TO INDICIES GIVEN ON MAP AT BEGINNING AND END OF STORM TRACK.
(2) INITIAL DETECTION DATE OF THIS TROPICAL CYCLONE.
(3) RECORDED DURATION OF STORM IN CALENDAR DAYS.
(4) STORM NUMBER FOR GIVEN YEAR CORRESPONDING TO THOSE GIVEN IN REFERENCE (1).
(5) STORMS WERE NOT FORMALLY NAMED PRIOR TO 1950.
(6) - (10) THESE COLUMNS GIVE LOCATION AND TIME OF CLOSEST APPROACH AND DISTANCE OF STORM CENTER TO SITE. THIS IS NOT NECESSARILY THE WIND RECORDED AT GIVEN SITE, SEE REFERENCE (2).
(11) MAXIMUM SUSTAINED WIND SPEED NEAR STORM CENTER WHILE STORM CENTER IS WITHIN SPECIFIED DISTANCE FROM SITE.
(12) CUMULATIVE STORM INDEX NUMBER BEGINNING WITH STORM 1 IN 1886.

REFERENCES

(1) JARVINEN, B. R., AND E. L. CASO, 'A TROPICAL CYCLONE DATA TAPE FOR THE NORTH ATLANTIC BASIN, 1886-1977: CONTENTS, LIMITATIONS, AND USES', NOAA TECHNICAL MEMORANDUM NWS NHC 6, JUNE 1978.
(2) NEUMANN, C. J., G. W. CRY, E. L. CASO AND B. R. JARVINEN, 'TROPICAL CYCLONES OF THE NORTH ATLANTIC OCEAN, 1871-1980', NOAA, NATIONAL CLIMATIC CENTER, ASHEVILLE, N. C., JULY 1981, PP. 174.

*CONSULT REFERENCES 1 AND 2 FOR DATA LIMITATIONS.

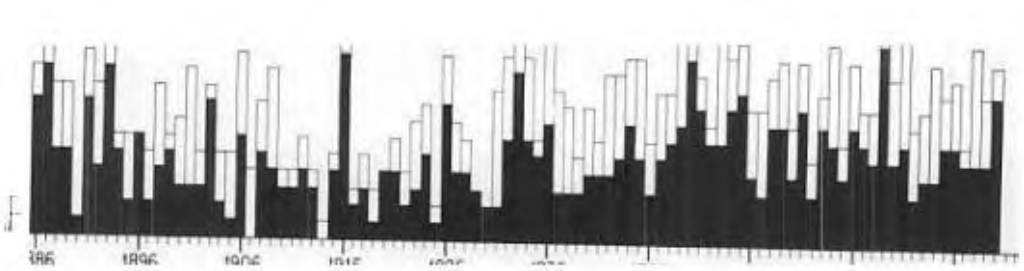
FREQUENCY

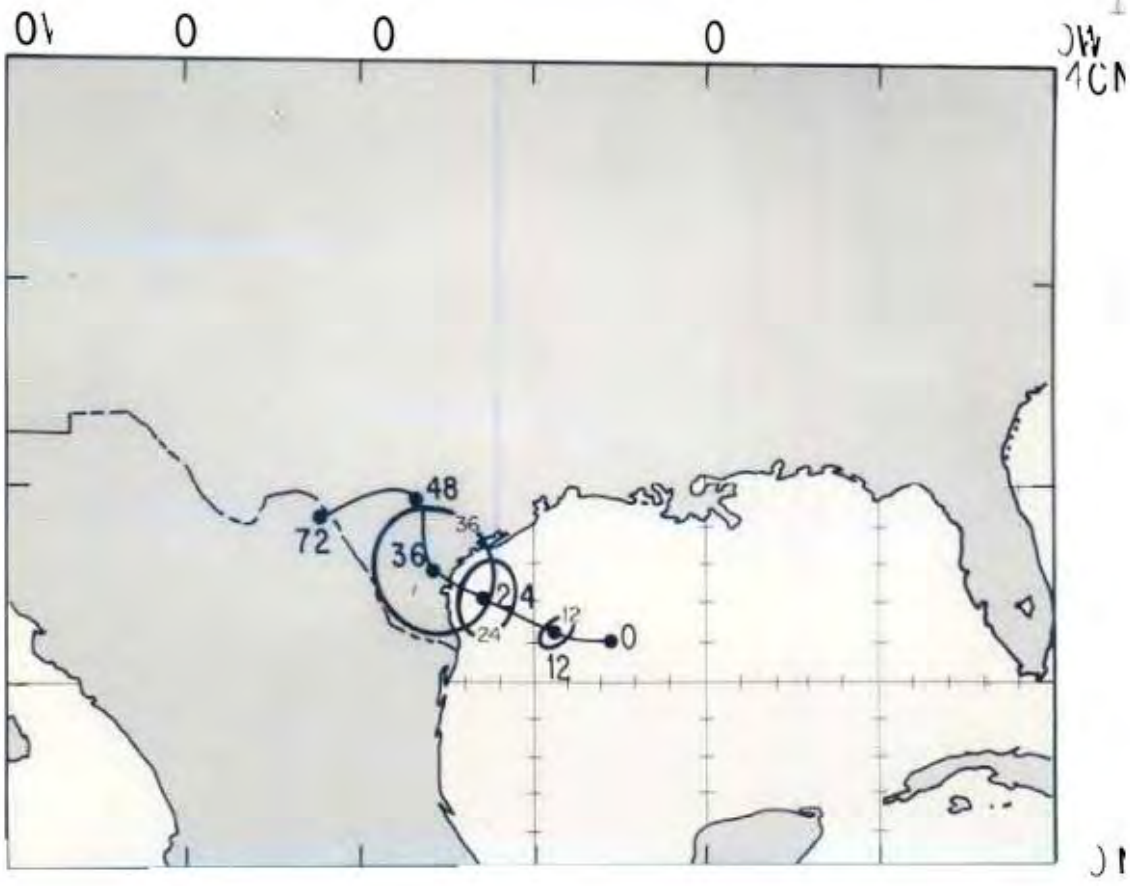
48
72
36
36
24
24
12
12
0

These are determined from the scatter of the analog composites at the respective forecast interval. Other forecast models use the climatological information as one of many pieces of information to determine a forecast track.

Uses of the data also include intensity forecasts from regression analyses of the wind data and determination of pressure wind relationships.

REFERENCES

Akima, H., 1970: A New Method of Interpolation and Smooth Curve Fitting Based on Local Procedures, Journal of the Association for Computing Machinery, Vol. 17, No. 4, pp. 589-602.

Atkinson, G. D. and C. R. Holliday, 1977: Tropical Cyclone Minimum Sea Level Pressure/Maximum Sustained Wind Relationship for the Western North Pacific, Monthly Weather Review, Vol. 105, No. 4, 421-427.

Black, P.G. and W.L. Adams, 1983: Guidance for Estimating Surface Winds Based on Sea State Observations from Aircraft and Sea State Catalog, Special Report from the Federal Coordinator for Meteorological Services and Supporting Research, FCM-G1-1983, Washington, D.C., 83 pp.

Cry, G. W., 1965: Tropical Cyclones of the North Atlantic Ocean, Technical Paper No. 55, U.S. Weather Bureau, Washington, D.C., pp.

Dunn, G. E. and B. I. Miller, 1964: Atlantic Hurricanes, Louisiana State University Press, Baton Rouge, LA, 377 pp.

Dvorak, V. F., 1973: A Technique for the Analysis and Forecasting of Tropical Cyclone Intensities from Satellite Pictures, NOAA Technical Memorandum NESS-45, Washington, D.C., 19 pp.

------, 1975: Tropical Cyclone Intensity Analysis and Forecasting from Satellite Imagery, Monthly Weather Review, Vol. 103, No. 5 pp. 420-430.

Hebert, P. J. and K. O. Poteat, 1975: A Satellite Classification Technique for Subtropical Cyclones, NOAA Technical Memorandum NWS SR-83, Fort Worth, Texas, 25 pp.

Hebert, P. J. and G. Taylor, 1975: Hurricane Experience Levels of Coastal County Populations - Texas to Maine, Special Report, 153 pp.

Hope, J. R. and C. J. Neumann, 1968: Probability of Tropical Cyclone Induced Winds at Cape Kennedy, Weather Bureau Technical Memorandum SOS-1, Silver Spring, MD, 67 pp.

------ and ------, 1970: An Operational Technique for Relating the Movement of Existing Tropical Cyclones to Past Tracks, Monthly Weather Review, Vol. 98, No. 12, pp. 925-933.

Kraft, R.H., 1961: The Hurricane's Central Pressure and Highest Wind, Mariners Weather Log, Vol. 5, No. 5, 157 pp.

Lawrence, M. B. and B. M. Mayfield, 1977: Satellite Observations of Trochoidal Motion During Hurricane Belle 1976, Monthly Weather Review, Vol. 105, No. 11, pp. 1458-1461.

Neumann, C. J., G. W. Cry, E. L. Caso, and B. R. Jarvinen, 1981: Tropical Cyclones of the North Atlantic Ocean, 1871-1980, 174 pp.

Padya, B. M., 1975: Spatial Variability and Gustiness of Cyclone Winds: Gervaise, Mauritius, February 1975, Australian Meteorological Magazine, Vol. 23, No. 3, pp. 61-69.

Saffir, H. S., 1977: Design and Construction Requirements for Hurricane Resistant Construction, American Society of Civil Engineers, New York, Preprint Number 2830, 20 pp.

Shinners, W., 1963: Comparison of Measured and Estimated Winds at Sea, U.S. Member Working Group, WMO, (unpublished manuscript).

U.S. DOC, NOAA, Federal Coordinator for Meteorological Services and Supporting Research, 1977: National Hurricane Operations Plan, FCM 77-2, 104 pp.

APPENDIX I A SAMPLE PROGRAM TO READ AND WRITE HURDAT

```
      DIMENSION IDATE(50,5),ALAT(50,4),ALON(50,4),IPED(50,4),IPRE(50,4)
      DIMENSION IA(19),IB(58),ICE(50,4)
      WRITE(6,1)
    1 FORMAT(1H1)
      DO 50 I=1,1000
C     EACH PASS THROUGH DO LOOP 50 READS ONE STORM
      READ(19,2,END=99) (IA(J),J=1,19),M,(IB(J),J=1,58),LSTORM
C     19=HURDAT TAPE.  READ TITLE CARD.  OBTAIN M WHICH GIVES THE
C     NUMBER OF GMT DAYS THAT THE STORM WAS IN EXISTENCE.
    2 FORMAT(19A1,I2,58A1,1X,A1)
      DO 7 II=1,M
C     DO LOOP 7 READS M DATA CARDS AND STORES VALUES IN ARRAYS.
      READ(19,5) (IDATE(II,J),J=1,5),((ICE(II,J),ALAT(II,J),ALON(II,J),
     1IPED(II,J),IPRE(II,J)),J=1,4)
    5 FORMAT(6X,5A1,4(A1,F3.1,F4.1,1X,I3,1X,I4))
    7 CONTINUE
      READ(19,8) IQ
C     READ IDENTIFICATION CARD
    8 FORMAT(6X,A2)
C
C     DATA FOR ONE STORM READ INTO STORAGE.  THE FOLLOWING STATEMENTS
C     WRITE THIS DATA OUT.
C
      WRITE(6,11)
      WRITE(6,12) (IA(J),J=7,19),M,(IB(J),J=1,59)
      DO 9 J=1,M
      WRITE(6,13) (IDATE(J,K),K=1,5),((ICE(J,K),ALAT(J,K),ALON(J,K),
     1IPED(J,K),IPRE(J,K)),K=1,4)
    9 CONTINUE
   11 FORMAT(1H0,/,/,/,2X,40H----------------------------------------)
   12 FORMAT(1H0,10x,13A1,I2,59A1,/,/,20X,5H0000Z,17X,5H0600Z,17x,
     15H1200Z,17X,5H1800Z,/,/,
     27X,4HDATE,2X,4(3HLAT,3X,3HLON,2X,3HVEL,1X,4HPRES,3X))
   13 FORMAT(1H ,5X,5A1,1X,4(A1,F4.1,1X,F5.1,1X,I3,1X,I4,2X))
   50 CONTINUE
   99 CONTINUE
      STOP
      END
```

55. Assignment 2, Module 12: Modeling of Storm Tracks:
https://www.giss.nasa.gov/pubs/docs/2007/2007_Hall_ha00310j.pdf

Tellus (2007), 59A, 486–498
Printed in Singapore. All rights reserved

TELLUS

Statistical modelling of North Atlantic tropical cyclone tracks

By TIMOTHY M. HALL[1]* and STEPHEN JEWSON[2], [1]*NASA GISS, New York, NY, USA;* [2]*Risk Management Solutions, London, UK*

(Manuscript received 15 August 2006; in final form 19 February 2007)

ABSTRACT

We present a statistical model of North Atlantic tropical cyclone tracks from genesis site through lysis. To propagate tracks we use the means and variances of latitudinal and longitudinal displacements and model the remaining anomalies as autoregressive. Coefficients are determined by averaging near-neighbour historical track data, with 'near' determined optimally by using jackknife out-of-sample validation to maximize the likelihood of the observations. The number of cyclones in a simulated year is sampled randomly from the historical record, and the cyclone genesis sites are simulated with a spatial probability density function using kernels with optimized bandwidths. Simulated cyclones suffer lysis with a probability again determined from optimal averaging of historical lysis rates. We evaluate the track model by comparing an ensemble of 1950–2003 simulations to the historical record using several diagnostics, including landfall rates. In most regions, but not all, the observations fall within the variability across the ensemble members, indicating that the simulations and observations are statistically indistinguishable. An intensity component to the TC model, necessary for risk assessment applications, is currently under development.

1. Introduction

Powerful tropical cyclones (TCs) are among the most devastating natural phenomena, and there has been great interest in estimating and forecasting the risk of wind, rainfall and flooding damage. Numerical weather forecast models, which integrate the fundamental equations of motion from observed initial conditions, form the basis for predicting the evolution of particular TCs days in advance. At seasonal and longer time scales, however, weather is unpredictable, and TCs must be treated stochastically, although ensemble simulations with numerical weather models may still be useful. Various approaches to statistical TC risk assessment have been developed over the past 20 yr by private sector and academic researchers. Generally, detailed descriptions of private-sector models are not publicly available, with only broad outlines published in conference abstracts. The models published with more detailed descriptions include Darling (1991), Chu and Wang (1998), Vickery et al. (2000), Casson and Coles (2000), James and Mason (2005), Emanuel et al. (2006) and Rumpf et al. (2007).

The characteristics of TCs at landfall are of primary interest in risk assessment, and a natural approach to modelling landfall statistically is to use historical data on TCs exclusively at landfall (e.g. Jagger et al., 2001). However, in many coastal regions there are few or no historical events, making assessment of the risk difficult. One way to overcome this limitation is to make use of entire historical TCs, from genesis to lysis, thereby enhancing by roughly two orders of magnitude the amount of data on which to construct a statistical model. Of course, the majority of the data is less relevant to landfall. Historical TC behaviour in the central Atlantic contains less information useful for assessing landfall rates than does TC behaviour at or near a coastal region. Nonetheless, in regions of rare landfall, historical TCs that merely pass within 100 s of kilometres of landfall provide constraints for risk assessment.

A crucial component of basin-wide TC modelling is the TC track, the geographic trajectory from genesis to lysis, and it is the modelling of this component that we focus on here. Basin-wide approaches have been taken by several researchers, for tracks as well as intensity. Vickery et al. (2000) use an autoregressive model for increments in track speed and direction, with a random error term acting as the innovation. Separate regression coefficients are fit and gridded for eastward and westward heading TCs. James and Mason (2005) also fit an autoregressive model for TCs in the Coral Sea near northeastern Australia, but they model the latitudinal and longitudinal increments, rather than the velocity increment. Their coefficients do not vary spatially, and an ad hoc term is added to the latitude model to inhibit tracks from propagating too near the equator. Emanuel et al. (2006)

*Corresponding author.
e-mail: thall@giss.nasa.gov
DOI: 10.1111/j.1600-0870.2007.00240.x

propagate tracks (in one of their two approaches) by sampling a transition matrix, populated from historical analysis, that relates prior track speed and direction to the new speed and direction. Casson and Coles (2000) simply draw from the set of complete historical tracks, translating the tracks by small random displacements. Rumpf et al. (2007) separate TCs into independent classes based on geographic characteristics, then sample kernel probability density functions (pdfs) build from historical speed and direction increments to propagate the simulated TCs.

Simulated TC genesis in these studies is performed in several ways. Emanuel et al. (2006) sample from a time- and space-dependent pdf constructed by binning historical genesis events and smoothing. James and Mason (2005) apply a scheme that interpolates historical genesis. Vickery et al. (2000) simply sample directly the historical genesis sites. Rumpf et al. (2007) use a near-neighbour approach similar to ours to develop and sample a genesis kernel pdf.

We also take a basin-wide approach to North-Atlantic TC track modelling. Our model is non-parametric, in the sense that simulations are derived by spatially averaging historical data, rather than fitting parametric forms to the data. We have strived to make maximal use of historical data, without over-fitting the model, by using out-of-sample validation to optimize data averaging. In contrast to many other studies, we document explicitly this objective procedure to average historical data. At a given location $\mathbf{r}$, we base the genesis, propagation, and lysis (death) of TCs on data near $\mathbf{r}$. For the tracks, mean six-hourly displacement increments are computed, as are variances about the mean and autocorrelations of the anomalies of track displacements. The magnitude of the random noise forcing (the 'innovation') depends on the variance and the autocorrelation, and is ultimately drawn from model residuals. Genesis and lysis rates are modelled by sampling pdfs built from historical events using kernel techniques. For all elements, the length scales over which historical data are averaged (the definition of 'near') are chosen to maximize the jackknife out-of-sample likelihood of the observations.

This paper summarizes are present state of model development. In contrast to many other published work on stochastic TC modelling no intensity is simulated here, nor is any intensity information used in the track modelling. Intensity modelling is clearly indispensable for TC risk assessment, and we are presently developing an intensity model to complement the track model. However, we believe it worthwhile first to describe and evaluate the TC track component of the model in detail.

After reviewing the historical data we outline our modelling procedure. We then describe in detail each of the modelling elements: mean displacements, variance, and autocorrelation for the propagation; and genesis and lysis. Subsequently, we compare simulated TCs to historical TCs using the large-scale diagnostics of track-point density, latitude and longitude crossing rates, and landfall rates.

2. Data

Following other North Atlantic TC modelling efforts (Vickery et al., 2000; Emanuel et al., 2006) we use the HURDAT 'best track' historical tropical cyclone data set compiled by NOAA's National Hurricane Center (Javinen et al., 1984; www.aoml.noaa.gov/hrd/hurdat). HURDAT provides date, time, longitude, latitude, central pressure and maximum wind speed every 6 h for TCs rated tropical disturbance and higher back to the 1800s. However, only from 1950 was aircraft reconnaissance used routinely to monitor TCs. Information on earlier cyclones is less reliable. In this study we use 524 HURDAT TCs from 1950 to 2003, inclusive. This represent all TCs in this period, except for a small number (order 10) that had spurious six-hourly displacements (e.g. 10s of degrees latitude or longitude).

Figure 1 shows these 524 historical TCs. Most North Atlantic TCs are born in the subtropical middle Atlantic and the Caribbean. Their trajectories follow a general sweep northwestward in the subtropics, then veer northeastward at mid-latitudes. Superposed on this average behaviour is considerable pseudo-randomness; many TCs move in directions opposing the average trajectory. The randomness makes a stochastic approach to simulation necessary.

3. Outline of the tropical cyclone track model

Our simulation of a TC track can be summarized by the following steps.

(i) Generate the first point on the track from the genesis model. This is the first 'current point' of the simulation.

(ii) Compute mean latitude and longitude displacements from the current point by averaging historical displacements with a weight that declines with distance from the current point.

(iii) Compute variances about the mean in directions parallel and perpendicular to the mean, again weighting historical data inversely with distance from the current point.

(iv) Simulate a displacement as $u = \overline{u} + \epsilon_u u_{\text{rms}}$ for the direction parallel to the mean track and $v = \epsilon_v v_{\text{rms}}$ for the direction perpendicular, where overline indicates mean quantities and the subscript 'rms' indicates root-mean-squared variances. The ϵ are innovations, that is, random forcing drawn from a standard normal distribution of zero mean and unit variance (or, subsequently, from model residuals).

(v) Use u and v to propagate the TC to the second point. For the second point onward the simulation is summarized by the following steps.

(vi) Find the local mean and variances as above and store.

(vii) Find autocorrelation coefficients in the parallel direction (ϕ_u) and perpendicular direction (ϕ_v) by regressing all historical displacements against their previous displacements. The historical elements in the regression are weighed inversely with distance from the current point.

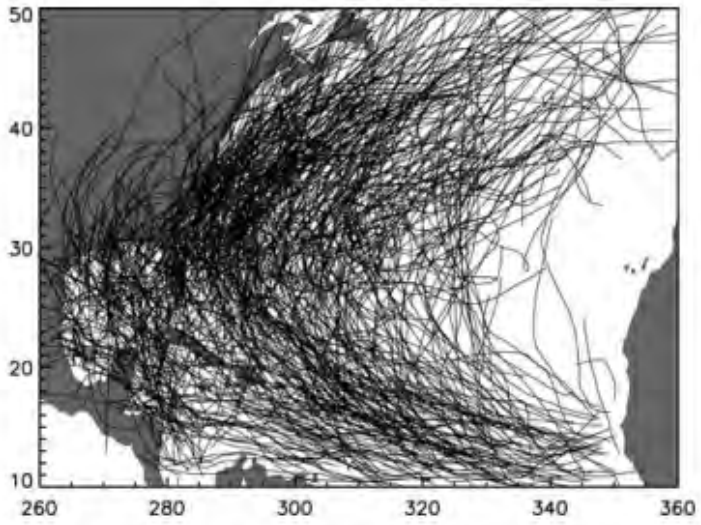

Fig. 1. The 524 HURDAT historical tropical cyclone tracks from 1950 to 2003.

(viii) Compute the magnitudes s_u and s_v of noise forcing using $s^2 = 1 - \phi^2$. (This is the statement that the total variance is equal to the variance correlated with the previous step plus the variance of the noise.)

(xi) Compute the parallel anomalies $\tilde{u}_{n+1} = \phi_u \tilde{u}_n + s_u \epsilon_u$ and perpendicular anomalies $\tilde{v}_{n+1} = \phi_v \tilde{v}_n + s_v \epsilon_v$, where tilde indicates a regularized anomaly quantity (zero mean and unit variance).

(x) Multiply anomalies by the rms variance and add the mean: $u_{\text{rms}}\tilde{u} + \overline{u}$ and $v_{\text{rms}}\tilde{v}$.

(xi) Rotate the displacements to the zonal-meridional orientation.

(xii) Update the current point with these displacements.

(xiii) Apply the lysis model, and terminate the TC if lysis occurs.

The mean, variance and autocorrelation coefficients, as well as elements of the genesis and lysis models, are computed from spatial averages of historical data. The form of the averaging is built on the premise that historical TC displacements closer to the current point should carry more weight. Climatological conditions vary spatially, and nearby historical displacements carry information most relevant to the local climate. On the other hand, the more restrictive is the weight about the current point the less historical information is used, and the averages suffer from sampling error. Thus, there is an optimal averaging length scale that balances the requirements of having local information but avoiding sampling error. This optimal length scale is computed using jackkife out-of-sample validation, as described in more detail in the sections below.

4. Model components

We now describe in detail the elements of the TC modelling. In the process analysis of the historical data is presented.

4.1. Means

The x (zonal) and y (meridional) components of the mean 6-h displacement vector are computed by averaging historical displacements:

$$\overline{x}(\mathbf{r}) = \frac{\Sigma_i x_i e^{-d_i^2/2L^2}}{\Sigma_i e^{-d_i^2/2L^2}}, \tag{1}$$

where d_i is the great-circle distance between the location $\mathbf{r}$ of the current point and the location $\mathbf{r}_i$ of the ith historical TC point, and similarly for $\overline{y}$. The length scale L is optimized using an out-of-sample jackknife procedure. Consider a six-hourly point $\mathbf{r}$ of a historical TC in calendar year j. Select a scale L and sweep over all six-hourly displacements over all historical TCs for all years $k \neq j$, forming $\overline{x}$ and $\overline{y}$. The average displacement vector so computed differs from the historical displacement vector emanating from $\mathbf{r}$, and the magnitude of the difference is the forecast error. We compute the average forecast error over all points for all TCs in all years j in the range 1950–2003. The averaged forecast error is minimized in L, within some tolerance.

Figure 2 shows the mean forecast error as a function of L. There is a minimum at 300 ± 10 km. Figure 3 illustrates the impact of the averaging scale on mean tracks. Ten mean tracks of equal duration are shown originating from evenly spaced longitudes along a line of constant latitude. For the case of $L = 100$ km the tracks display irregularities caused by excessive sensitivity to individual TCs. For $L = 1000$ km the tracks have very little structure, as regions of different climatological properties are averaged together. The optimal case, $L = 300$ km, is intermediate.

Typical scatter of the displacement components about their means can be seen in Fig. 4, which shows the historical displacements vectors within 300 km of two sample locations. Also shown are the pdfs of zonal displacements. The pdfs look rea-

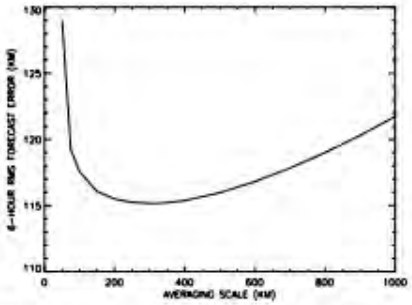

Fig. 2. Mean-track average forecast error versus averaging length-scale.

sonably normal, encouraging the use of a normal distribution to compute variances and their likelihoods, as described next.

4.2. *Variance*

The next step of the TC model construction is the computation of the variance of 6-h displacements about the mean. The pdf of the general multivariate normal distribution can be written

$$f(z) = \frac{1}{(2\pi)^{p/2}\sqrt{D}} \exp\left[-\frac{1}{2}(z-\mu)^T \Sigma^{-1}(z-\mu)\right], \quad (2)$$

where p is the dimensionality, Σ is the $p \times p$ covariance matrix, D is the determinant of Σ, superscript T indicates transpose and z and μ are p-length vectors, with μ being the mean. Here, $p = 2$ and $\mu = (0, 0)$ because the means are removed before modelling the variances of the two-component vector, z.

We have found that an anisotropic model, in which the variances in the u and v directions are distinct, has higher likelihood than an isotropic model. We consider $z = (u, v)$, where u and v are deviations from the mean in directions parallel and perpendicular to the mean. The covariance matrix is

$$\Sigma = \begin{pmatrix} \sigma_u^2 & 0 \\ 0 & \sigma_v^2 \end{pmatrix}, \quad (3)$$

so that (2) becomes

$$f = \frac{1}{2\pi\sigma_u\sigma_v} \exp\left(-\frac{u^2\sigma_v^2 + v^2\sigma_u^2}{2\sigma_u^2\sigma_v^2}\right). \quad (4)$$

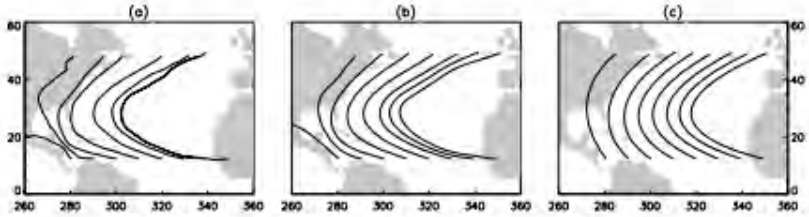

Fig. 3. Eight mean tracks originating from evenly spaced longitudes and having equal durations. The averaging scales are 100 km (left), 300 km (centre), and 1000 km (right). The optimal scale is 300 km (centre).

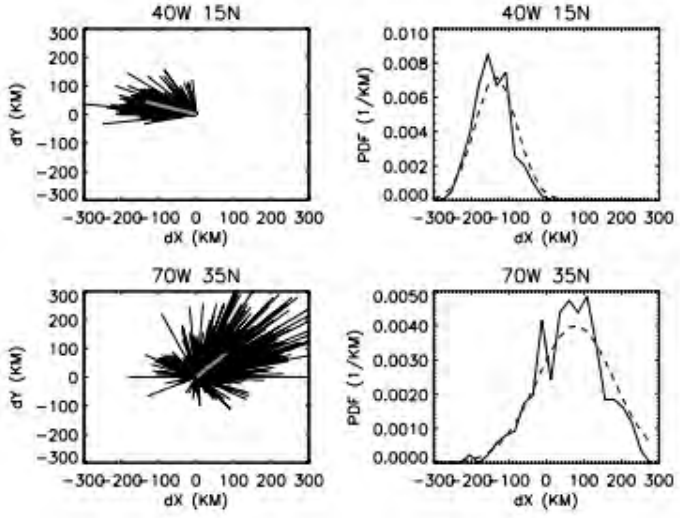

Fig. 4. Distribution of historical longitude (X) and latitude (Y) displacements at two locations, as labeled (left column, black line segments). Also shown are the mean displacements (thick grey). Shown in the right column are the corresponding distributions of longitude displacements (solid) and a fitted normal distribution (dash).

We have also examined an anisotropic correlated variance model, which, turns out to have a higher likelihood than the uncorrelated model. However, for simplicity of analysis of autocorrelation (next section) we retain the uncorrelated model for all subsequent analysis.

The coefficients σ_u and σ_v must be computed. This is done using weighted averages of deviations of historical TC displacements about the optimal mean displacement. That is, at location $\mathbf{r}$

$$\sigma_u(\mathbf{r}) = \left(\frac{\Sigma_i u_i^2 e^{-d_i^2/2L^2}}{\Sigma_i e^{-d_i^2/2L^2}} \right)^{1/2} \tag{5}$$

and similarly for $\sigma_v(\mathbf{r})$, where L is the length scale to be optimized, d_i is the great-circle distance between $\mathbf{r}$ and $\mathbf{r}_i$, and the summations are over historical storm points.

The scale L is optimized in a similar fashion similar to the mean-displacement averaging scale, but now by maximizing the likelihood rather than minimizing the forecast error. The likelihood of a historical deviation (u_i, v_i) in year j at position $\mathbf{r}$ is the distribution f evaluated at u_i and v_i. The summation in the coefficients (5) is taken over all storm points in years $k \neq j$. The log-likelihoods are summed over all historical points $\mathbf{r}$ in all years j, forming the total log-likelihood for a particular scale L for the variance model. Figure 5 shows the total log-likelihood as a function of L, as well as the analogous log-likelihood function for the isotropic variance model. The optimal scales for the anisotropic model is 300 km, identical to the scale for the mean track. Figure 6 shows the spatial distributions of the anisotropic variance components in kilometres. The variances are largest in the northern Atlantic, with values of 100–150 km. This is also the region where the mean-track propagation speed is greatest.

4.3. Autocorrelation

We now turn to the analysis and modelling of the autocorrelation, or 'memory', of the anomalies from the mean track. We first analyse the historical data to determine the nature of the autocorrelations. We then select an autocorrelation model and evaluate it by analysing its residuals.

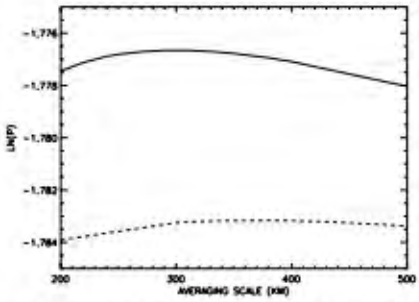

Fig. 5. Log likelihood of the variance versus spatial averaging scale for the isotropic model (dash) and the anisotropic model (solid). Values listed on the vertical axis are divided by 10^5.

4.3.1. Historical autocorrelations. We examine the autocorrelation of historical TC displacement anomalies. First, optimal means are subtracted from the historical track data, and the remainders are divided by optimal variances of the anisotropic variance model, leaving standardized anomalies. Figure 7 shows scatter plots among u and v anomalies (denoted $\bar{u}$ and $\bar{v}$) and their values at the previous 6-h step. The anomalies $\bar{u}$ and $\bar{v}$ are each strongly correlated with their values at the previous time step. On the other hand, no structure is apparent between contemporaneous $\bar{u}$ and $\bar{v}$, or between $\bar{u}$ and $\bar{v}$ with either lagged, suggesting that independent modelling of the $\bar{u}$ and $\bar{v}$ anomalies is appropriate. A similar conclusion was reached about Coral Sea TCs by James and Mason (2005), although these authors considered correlations among raw track increments, rather than regularized anomalies.

Our variance model assumes that the deviations about the mean are normally distributed. The 'quantile–quantile' (QQ) plot of Fig. 8 reveals the degree to which normality is maintained by the anomalies. Both $\bar{u}$ and $\bar{v}$ are normal within ± 2 standard deviations, while outside this range they exhibit 'fat tails;' that is, anomalies greater than ± 2 standard deviations are more common than would be expected normally.

In order to decide how many 6-h lags to consider in the autocorrelation modelling we regress all $\bar{u}$ and $\bar{v}$ against a range of lagged values. Figure 9 shows the resulting regression coefficients for 10 lags. The lag-one coefficients are 0.75–0.8 for $\bar{u}$ and $\bar{v}$, while the coefficients for all greater lags have magnitudes less than 0.05. This indicates that consideration of just one lag is sufficient to model the anomalies.

A lag-one autocorrelation function has the form $f(t) = e^{-t/\tau}$, where t is the lag and τ is the decorrelation time scale. The $\bar{u}$ and $\bar{v}$ time scales τ are plotted spatially in Fig. 10, using an averaging length scale of 900 km to compute the autocorrelation coefficients (justified below). There is spatial structure, with τ for $\bar{u}$ peaking at about 2.25 d in mid-latitudes and τ for $\bar{v}$ peaking at about 1.75 d in the subtropics.

4.3.2. Autocorrelation model. The analysis of the autocorrelations suggests the modelling of the u and v anomalies as independent lag-one autoregressive processes, denoted AR(1). Given anomalies at step $n-1$, the anomalies at step n are

$$\begin{aligned} \bar{u}_n &= \phi_n^u \bar{u}_n + s_n^u \epsilon^u \\ \bar{v}_n &= \phi_n^v \bar{v}_n + s_n^v \epsilon^v, \end{aligned} \tag{6}$$

where ϕ are the autocorrelation coefficients, s the magnitude of the innovations, and ϵ the innovation, drawn from a normal distribution of zero mean and unit variance (and, subsequently, from model residuals). Autoregressive models are also used by Vickery et al. (2000) and James and Mason (2005), though applied to the raw track increments, rather than the anomalies. Note that in (6) s and ϕ are not independent. Squaring and averaging both

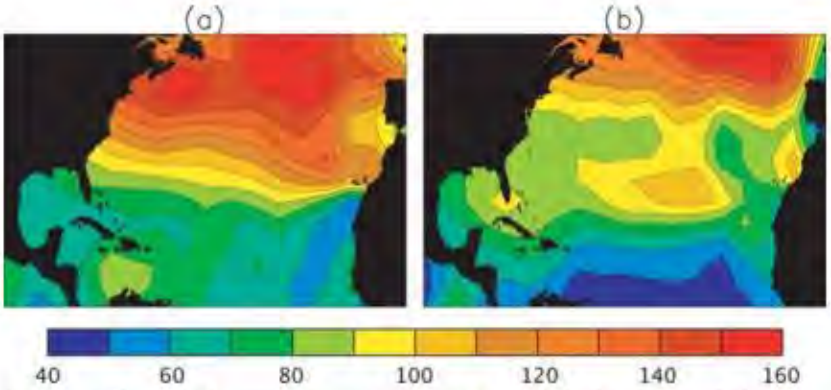

Fig. 6. The spatial distributions of the rms displacement variances parallel (a) and perpendicular (b) to the mean displacement vector. Units are kilometres. The averaging scale is the optimal value of 300 km.

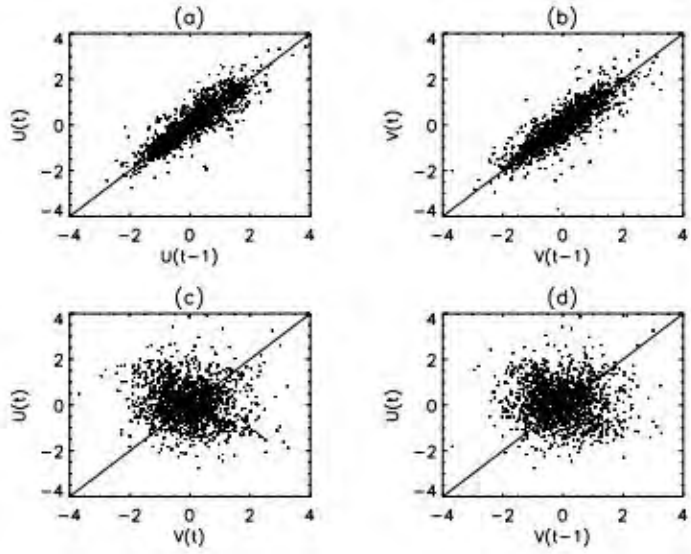

Fig. 7. Scatter plots of anomalies. u refers to direction parallel to mean displacements and v to direction perpendicular to mean displacement. (a) $u(t)$ versus $u(t-\Delta t)$, where Δt is one 6-h time step; (b) $v(t)$ versus $v(t-\Delta t)$; (c) $u(t)$ versus $v(t)$; and (d) $u(t)$ versus $v(t-\Delta t)$. Points are a random subset of the historical data set. One-to-one line is plotted for reference.

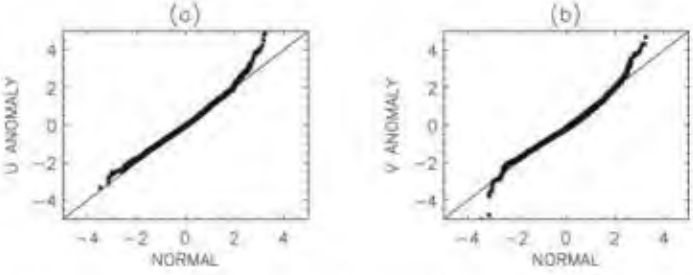

Fig. 8. Quantile–quantile plots of (a) displacement anomalies parallel and (b) perpendicular to mean displacement vectors. The anomalies would be distributed normally if the scatter fell on the straight lines. This is the case within ±2 standard deviations. Outside this, the anomalies exhibit 'fat tails.' That is, large anomalies are more probable than normal.

sides of eq. (6) and using the fact that the regularized anomalies have unit variance, one finds that $s^2 = 1 - \phi^2$.

The coefficients ϕ_u and ϕ_v at a current point $\mathbf{r}$ are computed by weighted spatial averaging of historical autocorrelations. We regress all $\bar{u}_n$ against all $\bar{u}_{n-1}$ anomalies ($n > 1$), using a weight $e^{-d_i^2}/2L^2$ for each historical $(\bar{u}_n, \bar{u}_{n-1})$ pair, where d_i is the great-circle distance between $\mathbf{r}$ and the position $\mathbf{r}_i$ of the historical pair. (An identical calculation is performed for v.) Once again the optimal averaging scale, $L = 900$ km, is obtained by maximizing the jackknife out-of-sample likelihood. To compute the likelihood, the multivariate normal distribution (2) is used to represent the probability of the entire series of $\bar{u}$ or $\bar{v}$ along a TC

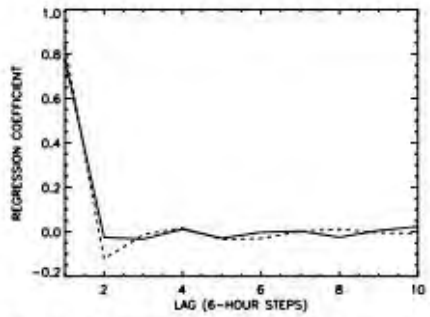

Fig. 9. Coefficients obtained regressing anomalies against themselves at 10 successive six-hourly lags in the direction parallel (solid) and perpendicular (dash) to mean displacements. In this case all historical data are used with equal weight. Only lag one is significantly different than zero, supporting the use of the AR(1) model.

track. The symmetric covariance matrix has dimensions $m \times m$, where m is the number of steps in the track. It can be written

$$\Sigma = \begin{pmatrix} 1 & \phi_1 & \phi_1\phi_2 & \phi_1\phi_2\phi_3 & \dots \\ . & 1 & \phi_1 & \phi_1\phi_2 & \dots \\ . & . & 1 & \phi_1 & \dots \\ . & . & . & 1 & \dots \\ . & . & . & . & 1 \end{pmatrix}, \tag{7}$$

where the subscripts on ϕ refer to the step number along the track. (The diagonal elements are all 1, because the anomalies have been standardized to unit variance.)

4.3.3. Residuals. To evaluate how well AR(1) models the anomalies we examine the residuals; that is, the difference of an AR(1) predicted anomaly from a historical TC point and the

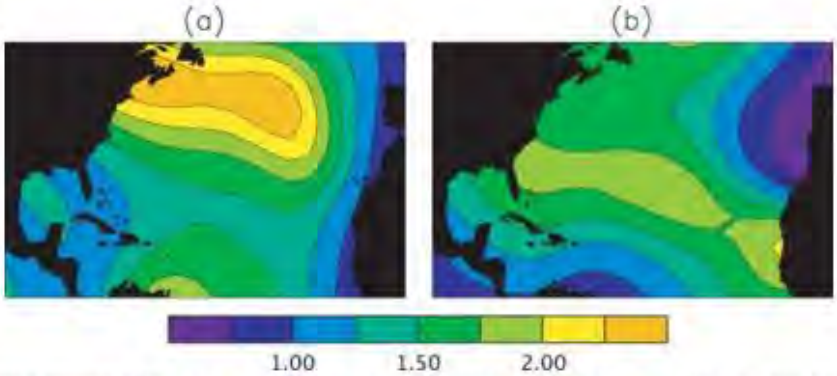

Fig. 10. Autocorrelation timescale τ for anomalies parallel (a) and perpendicular (b) to mean displacements. Units are days. For a perfect AR(1) model the autocorrelation function (ACF) is $f(t) = e^{-t/\tau}$. The timescales plotted here are $\tau = 0.25\ \text{day}/\ln[f(0.25\ \text{day})]$, where $f(t)$ is the empirical ACF computed locally from the historical data using the optimal averaging scale of 900 km.

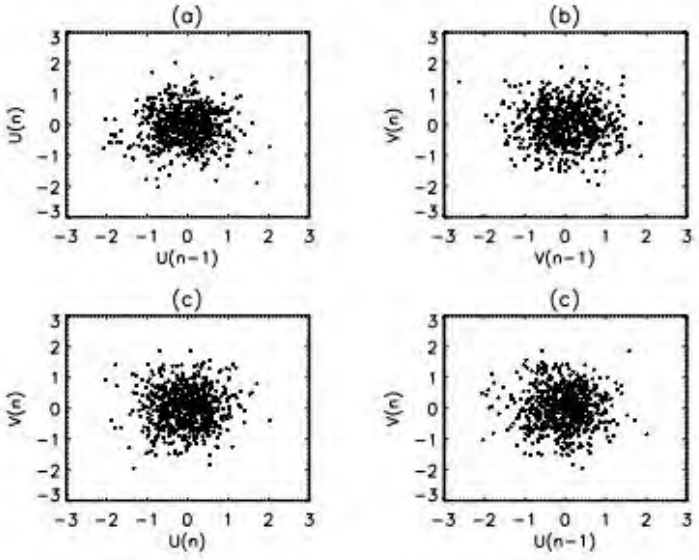

Fig. 11. As in Fig. 7, but now for the residuals of the lag-one autocorrelation model. No structure is apparent, indicating that the lag-one model captures well the u and v correlations and autocorrelations.

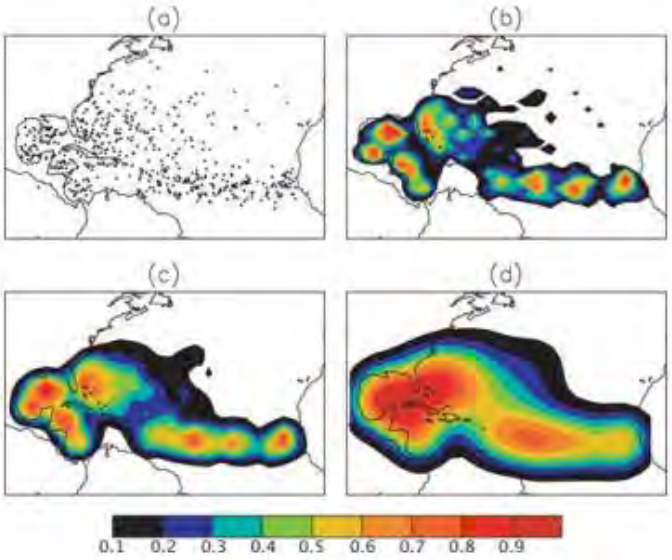

Fig. 12. (a) Historical genesis sites from 1950 to 2003. (b) Kernel genesis pdf with length-scale 100 km, (c) 210 km and (d) 500 km. The case of 210 km is optimal. The pdfs are each normalized to unit maximum.

actual historical anomaly. Figure 11 contains scatter plots analogous to Fig. 7, but now for the residuals. The residual scatter displays no structure, indicating that the relationships have been captured well by the AR(1) model. A QQ analysis of the residuals (not shown) shows behaviour similar to the QQ analysis of the anomalies (Fig. 8): normal behaviour within ±2 standard deviations, and 'fat tails' outside.

To accommodate the effects of the fat tails in track simulations we proceed as follows: At each historical TC point we simulate the $\tilde{u}$ and $\tilde{v}$ using the optimized AR(1) model with standard normal innovations. The residuals of these simulations are stored in a table. In all subsequent TC simulations the innovations consist of sampling randomly from the residual table. In this way anomalies in simulations will have larger than normal magnitude outside ±2 standard deviations. Using residuals for innovations turns out to provide a small increase in the realism of the simulated tracks, as diagnosed by the model-observation comparisons shown in Section 5, below.

4.4. *Genesis.*

The TC genesis model consists of two separate components: (1) simulating the number of TCs in a year, and (2) simulating the geographical sites of these TCs. Substantial effort has been spent developing forecasts for TC number at seasonal and longer leads (e.g. Gray et al., 1992), with much interest generated by increased Atlantic hurricane frequency and intensity in recent years (Webster et al., 2005). These issues are not addressed here for TC number, and we have chosen a simple expedient: random sampling from the historical number of TCs per year in the 1950–2003 period. For comparison, Vickery et al. (2000) sample a fitted negative binomial distribution. Whether or not annual TC number simulation is necessary depends on the nature of model evaluation against historical TCs. Some studies do not simulate TC number, simply generating an large arbitrary number of TCs for comparisons to historical TCs (e.g. James and Mason, 2005; Emanuel et al., 2006).

Given the number of TCs in a year, we model the genesis sites using a two-dimensional (latitude, longitude) pdf comprised of sums of kernels about out-of-sample historical genesis sites. The kernels are Gaussian, with isotropic variance length scale L, which is referred to as the bandwidth of the genesis pdf. (By contrast, Rumpf et al., 2007 use Epanichnikov kernels.) Thus, the pdf for genesis at position $\mathbf{r}$ is

$$f(\mathbf{r}) = \frac{1}{2\pi N\sigma^2} \sum_{i=1}^{N} e^{-d_i^2/2L^2}, \tag{8}$$

where d_i is great-circle distance between $\mathbf{r}$ and the location of the ith genesis site. The optimal bandwidth $L = 210$ km is obtained from the jackknife out-of-sample likelihood maximization. Figure 12 shows the 524 historical genesis sites, along with the pdf $f(\mathbf{r})$ computed using values $L = 100$ km, 210 km (optimal) and 500 km. For $L = 100$ km the pdf has detailed structure and many local maxima. For $L = 500$ km the pdf is much smoother and has just three maxima. The optimal case, $L = 210$ km, is intermediate.

To simulate genesis the pdf is normalized to unit maximum. A random value of $\mathbf{r}$ is chosen from a uniform distribution over a region that encompasses the entire domain. Genesis occurs at $\mathbf{r}$ randomly with a probability given by the normalized f. The procedure is continued until the desired number of genesis events is realized. Fig.13 shows the historical genesis sites from 1950 to 2003 (524 events) and three simulations of genesis sites over the

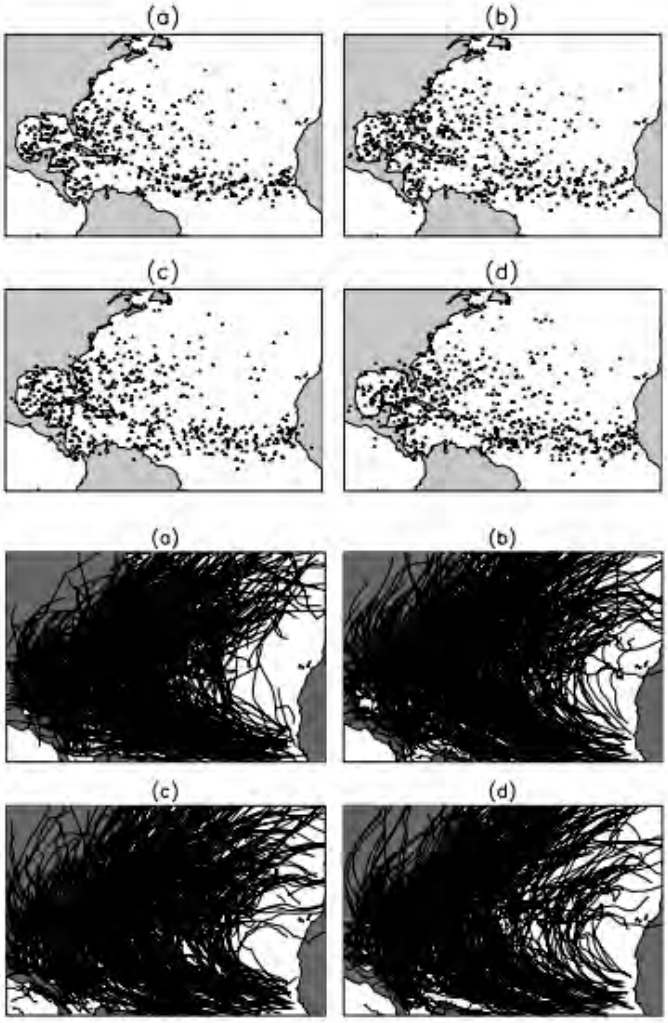

Fig. 13. (a) The 524 historical genesis sites from 1950 to 2003 used in this analysis, as in Fig. 12a. (b), (c) and (d) Three simulations of genesis for the same period. The number of simulated TCs are 516, 510 and 554, respectively.

Fig. 14. (a) Historical TC tracks from 1950 to 2003 (as in Fig. 1). (b), (c) and (d) Three simulations of TC tracks over the same period.

same period (516, 510 and 554 events). The simulations capture the historical genesis pattern well. The simulated genesis events scatter over a latitude band in the eastern subtropical Atlantic that is somewhat broader than the historical distribution.

4.5. *Lysis.*

Ultimately the lysis of a TC should be linked to the simulated evolution of its intensity. A stochastic intensity model is currently being developed. In the meantime, we construct a lysis model from historical lysis rates. The probability $p_L(\mathbf{r})$ of suffering lysis at a current point $\mathbf{r}$ is modelled as

$$p_L(\mathbf{r}) = \frac{\Sigma_i \Theta_i e^{-d_i^2/2L^2}}{\Sigma_i e^{-d_i^2/2L^2}}, \tag{9}$$

and the probability of not suffering lysis is $p_{NL} = 1 - p_L(\mathbf{r})$, where $\Theta_i = 1$ if the storm point i is the last point of a TC, and $\Theta_i = 0$ otherwise. The optimal averaging scale is $L_L = 360$ km, obtained again by jackknife out-of-sample likelihood maximization.

5. Simulations and diagnostics

We now present simulated TCs and compare diagnostics of the simulations to analysis of historical TCs. Figure 14 shows the historical track from 1950 to 2003 and three sets of simulations of this period. The general features of the historical storms are well captured by the model, including the northwestward motion at low latitudes, the northeastward motion at mid-latitudes, the degree of penetration into the continent, and the degree of ran-

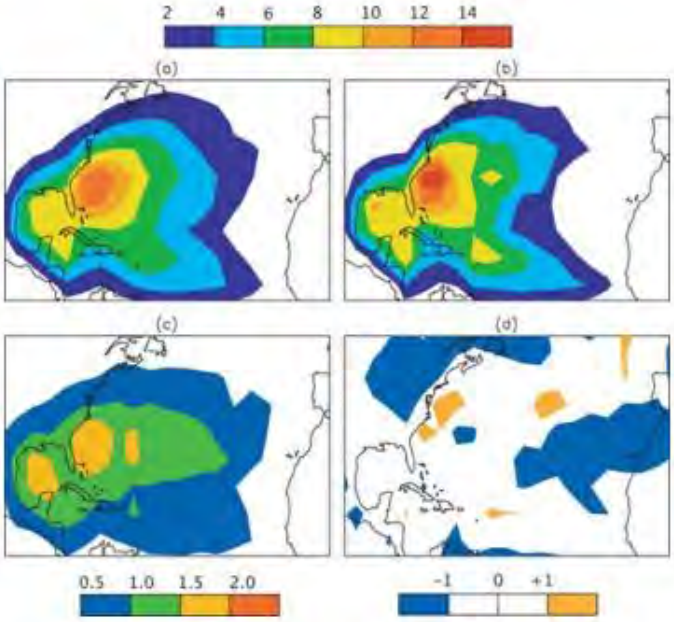

Fig. 15. TC track-point density, defined as the number of six-hourly TC positions ('points') per area accumulated over the period 1950–2003. (a) Mean density over 50-member ensemble of simulations of the 1950–2003 period. (b) Historical density over same period. (c) Root-mean-squared variance of density over 50-member ensemble. (d) 'Z score;' that is, historical minus simulated ensemble mean divided by historical. Units in (a), (b) and (c) are track points per 100 × 100 km box, while the Z-score in (d) is dimensionless.

domness in the tracks. However, there is a higher historical track concentration off the mid Atlantic coast than is simulated, and the simulated TCs tend to sweep too far east at mid-latitudes. Emanuel et al. (2006) also show examples of simulated tracks, which have features qualitatively similar to ours. However, they report no further large-scale diagnostics, making quantitative comparison difficult. Vickery et al. (2000) do not show their simulated tracks, although they evaluate the landfall characteristics of the simulated TCs.

5.1. *Density.*

In order to evaluate the model performance quantitatively we have devised several diagnostics. The first is the spatial density of 'storm points' (six-hourly longitude–latitude positions) computed over the 54-yr 1950–2003 period. We have simulated 50 such periods, forming an ensemble, whose average density is shown in Fig. 15a. Figure 15b shows the density for the historical TCs. Figure 15c shows the distribution of rms variance of density, computed across the ensemble. Finally, Fig. 15d shows the model's 'Z score,' the historical distribution minus the ensemble mean divided by the rms variance. The Z score is a simple test of the statistical significance of the historical-model differences. If the model were unbiased then the historical TC tracks would simply be one sample of the distribution of the simulated ensemble, and the Z score magnitude would surpass unity only infrequently. More sophisticated significance tests would be worthwhile, such as asymptotic distribution-free goodness of fit, which do not depend on normality assumptions in certain limits (e.g. Bishop and Chakraborti, 1989), but we do not pursue them here.

The basic features of the historical density are replicated by the simulations. The largest difference occurs off the US eastern seaboard just south of Cape Hatteras, where the historical density reaches a sharp maximum. The simulated TCs also have a maximum here, but it is not quite as sharp and is located further off shore. Figure 15d shows this difference to be above one standard deviation (about 1.6). Apparently, the simulations do not sufficiently 'focus' TC trajectories into the region adjacent to the mid-Atlantic eastern US coast, a discrepancy that can be seen in the tracks themselves (Fig. 14). By contrast, the simulated density is too high by more than one standard deviation in the eastern subtropical Atlantic and the American interior northeast, although both these regions have few historical or simulated TCs.

5.2. *Latitude and longitude crossing.*

Our second diagnostic is the number of storms crossing various latitude and longitude lines. Figure 16 shows the count of TCs crossing five latitude lines as a function of longitude. Northward and southward crossings are tallied separately. The general northward sweep of TCs can be seen, with the maximum northward penetration occurring at 30°N and about 75°E. Very few storms cross north to south. The simulated crossings are shown as the ensemble-mean rate ± one standard deviation. The spread in simulated crossing rates bounds the historical rates in most places.

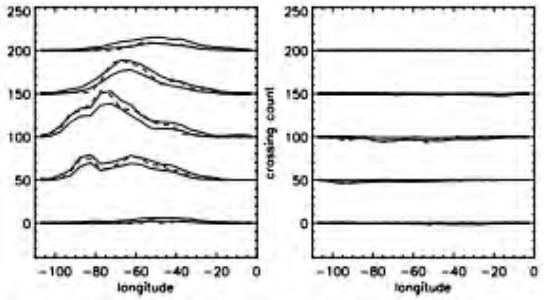

Fig. 16. Number of historical (dash) and simulated (solid) TCs over 1950–2003 period crossing latitude lines as a function of longitude. Counts are made in 5° longitude bins. The latitudes are 10°, 20°, 30°, 40° and 50°N. Northward crossings (left column) and southward crossings (right column) are tallied separately. Simulated crossings are shown as the 50-member ensemble mean ±1 standard deviation. In most regions the historical crossings fall within the variability of the simulations. Units on the vertical axis are 10-count increments, and should be taken to start at zero for each latitude.

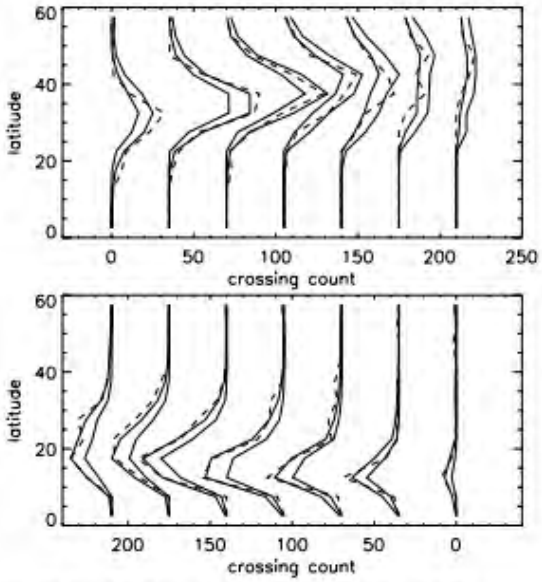

Fig. 17. Number of historical (dash) and simulated (solid) TCs over 1950–2003 period crossing longitude lines as a function of latitude. Counts are made in 5° latitude bins. The longitudes are 280°, 290°, 300°, 310°, 320°, 330° and 340°. Westward crossings (bottom) and eastward crossings (top) are tallied separately. Simulated crossings are shown as the 50-member ensemble mean ±1 standard deviation. The simulations slightly underestimate the westward crossing rate in the subtropics. Units on the horizontal axis are 10-count increments, and should be taken to start at zero for each longitude.

Figure 17 shows the westward and eastward longitude crossings. The westward penetration of TCs occurs primarily 5°N–25°N, while the eastward penetration occurs 25°–50°. In most places the simulation spread encompasses the historical crossings. In the western Atlantic, however, the simulations underestimate the westward penetration at 15°N–20°N and 25°N–30°N. This is consistent with the underestimate in TC-point density off the southern part of the US eastern seaboard (Fig. 15).

5.3. *Landfall.*

Landfall rates are of major interest for risk assessment. To be useful in this regard a TC model needs an intensity component, which we have not yet developed, to separate potentially catastrophic storms from minor storms. Nonetheless, for evaluating our track model, landfall rates for all named TCs taken together, is still a valuable diagnostic. Figure 18 shows historical and simulated landfall rates along the North American east coast and Gulf coast. A coarse model of the coastline is constructed using 39 line segments ('gates') of various lengths, and the number of TC displacement vectors crossing the segments from ocean to land is counted. For this tallying we treat displacement vectors independently; a single TC can make multiple landfalls. The landfall rates are plotted as a function of distance along the coarse-grained coastline from northeast to southwest. The rates are stated in units of TC crossings per year per 100 km of coastline. Shown in Fig. 18 are the coastline map and its gates, the historical landfall rate, the simulated landfall rates for the 50 ensemble members, the mean simulated rate across the ensemble and its standard deviation, and the Z score.

The historical coastal landfall-rate profile is highly structured. It is highest just south of Cape Hatteras, where it reaches 0.2 per 100 km per year, but there are several other local maxima. The landfall rate on a particular coast segment is highly sensitive to the segment's orientation, with a maximum rate occurring when the segment's normal vector is parallel to the local mean track and a minimum occurring when it is perpendicular to the mean track. Thus, the landfall-rate profile depends sensitively on the definition of the coastline gates, which are somewhat arbitrary. Nonetheless, historical regional landfall rates along the US coast shown Vickery et al. (2006) for intense hurricanes display similarly located minimums and maximums.

The simulated TC landfall rates capture much of the structure of the historical rates. The simulated peak occurs near Cape Hatteras, and the locations of the other maxima and minima match the historical profile. Because simulations are stochastic the landfall-rate profile of one 54-yr simulation differs from another. In this light, the historical profile can be viewed as only one possibility among many. The 54-yr periods prior to and following the 1950–2003 period would exhibit different landfall profiles, even in the absence of climate variability or secular change. Taken together the simulated profiles provide a sense of the range of possible landfall rates. Were the simulations unbiased, the range of simulated profiles would bound the historical

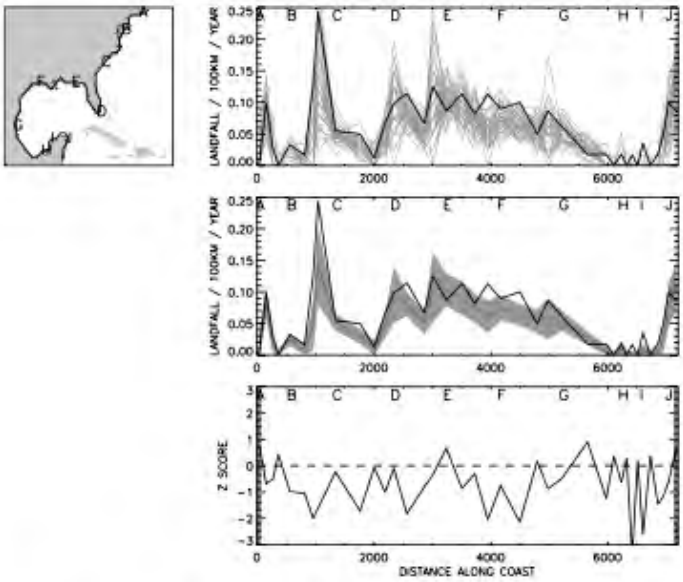

Fig. 18. Top: historical landfall rate over 1950–2003 period (thick black) and 50 simulations over same period (thin grey), both plotted as a function of distance along the coast from northeast to southwest. Rates are expressed as counts per year per 100 km of coastline, as computed over the 39 gates shown at left. Letters are shown for reference. Middle: Historical rates (thick black) and mean over 50-member simulation ensemble (thin black). The grey region represents ±1 standard deviation about the ensemble mean. Bottom: 'Z score,' that is, the simulation mean minus historical rate divided by historical rate.

profile. However, while the simulation profiles of Fig. 18 have shapes very similar to the historical, there is a negative bias in many places, which is most pronounced near Cape Hatteras, the west coast of Florida and the north Gulf Coast ($Z \approx -2$).

These landfall rates are not categorized by TC intensity, as intensity has not been simulated, and no intensity information has gone into the tracks beyond inclusion in HURDAT. Consequently, the successes and limitations of our track model to simulate landfall realistically cannot, at this point, be taken as a complete evaluation of a TC risk assessment model. When we have finished development of an intensity model (including TC wind speed) to complement the track model we will re-evaluate landfall rates at different intensity thresholds.

6. Summary

We have developed a basin-wide statistical model of North Atlantic TC tracks. The model is non-parametric, using near-neighbour historical information to propagate TCs from one 6-h time step to the next and to simulate their genesis and lysis. 'Near' is defined optimally, by maximizing the likelihood in an out-of-sample jack-knife procedure. The propagation consists of computing mean 6-h displacement increments, variances about the mean, and lag-one autocorrelations. Innovations are drawn from model residuals. The genesis model consists of sampling a kernel pdf build from historical genesis whose bandwidth (210 km) is selected to optimize the likelihood of the historical genesis. Ultimately the lysis of the simulated TCs should be based on intensity, the modelling of which is under development. At present the probability of lysis is determined from local historical lysis events.

We have used the statistical model to perform multiple simulations of the 54-yr historical period on which the model is based (1950–2003). Because the processes are stochastic, one simulation differs in detail from another. The ensemble-mean simulation exhibits large-scale features, such as track-point density, crossing rates of lines of constant latitude and longitude, and landfall rates, that match their historical counterparts reasonably well. For most diagnostics in most regions the historical quantity falls within one standard deviation of the ensemble-mean simulation, indicating that the simulations are statistically indistinguishable from the historical record. There are, however, regions of bias in the model, such as an underestimate in the track density and landfall rate in the central mid-Atlantic US coast.

There are several approaches that could be taken to further improve the realism of the tracks. We have neglected a weak correlation between anomalies perpendicular and parallel to the mean TC displacements. More generally, one should use a vector-autoregressive model to relate $(\tilde{u}, \tilde{v})$ anomaly vectors at steps n and $n-1$ by a 2×2 matrix. We have neglected any time-of-year dependence. The genesis and the track formation could be conditioned on date, for example, forming averages with a weight that declines from the date of the current point. Genesis kernels could be made one sided near coastlines to reduce negative bias from inland regions where no genesis occurs.

Finally, we emphasize that at present we have neither modelled TC intensity, nor included any track dependence on intensity. The model evaluation described here should not be considered as an evaluation of a TC risk assessment model, since risk assessments clearly require TC wind speed. Development of a statistical TC model is presently underway using non-parametric techniques similar to those described here. Our strategy is to develop

components individually, thoroughly documenting and testing each separately. We have reported on the track component in this paper.

7. Acknowledgments

This work was supported in part by NASA. The HURDAT data was obtained online courtesy of the Hurricane Research Division of NOAA's Atlantic Oceanographic and Meteorological Laboratory. We thank an anonymous reviewer for comments.

References

Bishop, J. A., Chakraborti, S. and Thistle, P. D. 1989. Asymptotically distribution-free statistical inference for generalized Lorenz curves. *Rev. Econ. Stat.* **71**, 725–727.

Casson, E. and Coles, S. 2000. Simulation and extremal analysis of hurricane events. *Appl. Stat.* **49**, 227–245.

Chu, P. and Wang, J. 1998. Modeling return periods of tropical cyclone intensities in the vicinity of Hawaii. *J. Appl. Meteorol.* **37**, 951–960.

Darling, R. 1991. Estimating probabilities of hurricane wind speeds using a large-scale empirical model. *J. Clim.* **4**, 1035–1046.

Emanuel, K. A., Ravela, S., Vivant, E. and Risi, C. 2006. A statistical-deterministic approach to hurricane risk assessment. *Bull. Amer. Meteor. Soc.* **87**, 299–312.

Gray, W. M., Landsea, C. W., Mielke, P. W. and Berry, K. J. 1992. Predicting Atlantic seasonal hurricane activity 6–11 months in advance. *Wea. Forecasting* **7**, 440–455.

Jagger, T., Elsner, J. B. and Niu, X. 2001. A dynamic probability model of hurricane winds in coastal counties of the United States. *Appl. Stat.* **40**, 853–863.

James, M. K. and Mason, L. B. 2005. Synthetic tropical cyclone database. *J. Wtrwy., Port, Coastal, and Oc. Engrg.* **131**, 181–192.

Jarvinen, B. R., Neumann, JC. J. and Davis, M. A. S. 1984. A tropical cyclone data tape for the North Atlantic Basin, 1886–1983, contents, limitations, and uses. *NOAA Tech. Memo., NWS NHC 22*.

Rumpf, J., Weindl, H., Höppe, P., Rauch, E. and Schmidt, V. 2007. Stochastic modelling of tropical cyclone tracks. *Math. Meth. Oper. Res.* **65**, in press.

Vickery, P. J., Lin, J., Skerlj, P. F., Twisdale, L. A. and Huang, K. 2006. HAZUS-MH hurricane model methodology. I: hurricane hazard, terrain, and wind load modeling. *Natural Hazards Rev.* **7**, 82–93.

Vickery, P. J., Skerlj, P. F. and Twisdale, L. A. 2000. Simulation of hurricane risk in the US using an empirical track model. *J. Struct. Engin.* **126**, 1222–1237.

Webster, P. J., Holland, G. J., Curry, J. A. and Chang, H.-R. 2005. Changes in tropical cyclone number, duration, and intensity in a warming environment. *Science* **309**, 1844–1846.

56. Assignment 2, Module 13: Stochastic Modeling of Storm Tracks: http://www.mathematik.uni-ulm.de/stochastik/aktuelles/sh06/sh_rumpf.pdf

Stochastic Modeling of Tropical Cyclone Track Data

Jonas Rumpf

Universität Ulm, Abteilung Stochastik

Söllerhaus-Workshop 2006

Contents I

Contents II

Basic Concept

- Analyze historical cyclone tracks to extract important characteristics
- Create a stochastic model to simulate these characteristics

Basic Concept

- Analyze historical cyclone tracks to extract important characteristics
- Create a stochastic model to simulate these characteristics
- Simulate a large number of synthetic storm tracks
- Estimate striking probabilities and possible damages from the synthetic storm tracks

Introduction
Classification
Cyclone Tracks
Simulation and Examples
Outlook
Approach to the Problem

Basic Concept

- Analyze historical cyclone tracks to extract important characteristics
- Create a stochastic model to simulate these characteristics
- Simulate a large number of synthetic storm tracks
- Estimate striking probabilities and possible damages from the synthetic storm tracks
- Not intended: weather forecasting

Available Data

- Historical cyclone track data from the western North Pacific
- Location and maximum wind speed of every known tropical cyclone from 1945–2004
- Recorded at intervals of 6 hours; compiled by Munich Reinsurance Company

Introduction
Classification
Cyclone Tracks
Simulation and Examples
Outlook
Approach to the Problem

Available Data

- Historical cyclone track data from the western North Pacific
- Location and maximum wind speed of every known tropical cyclone from 1945–2004
- Recorded at intervals of 6 hours; compiled by Munich Reinsurance Company
- Total: 1,519 storms; 37,377 locations

$\Rightarrow$ Cyclone tracks are given as polygonal trajectories

Example Tracks

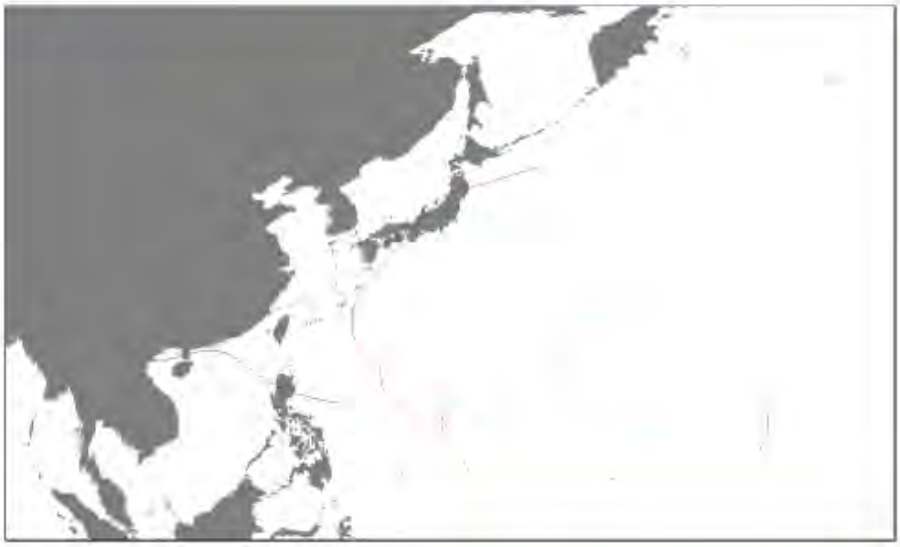

All Tracks

Problem: Strong inhomogeneities in the data

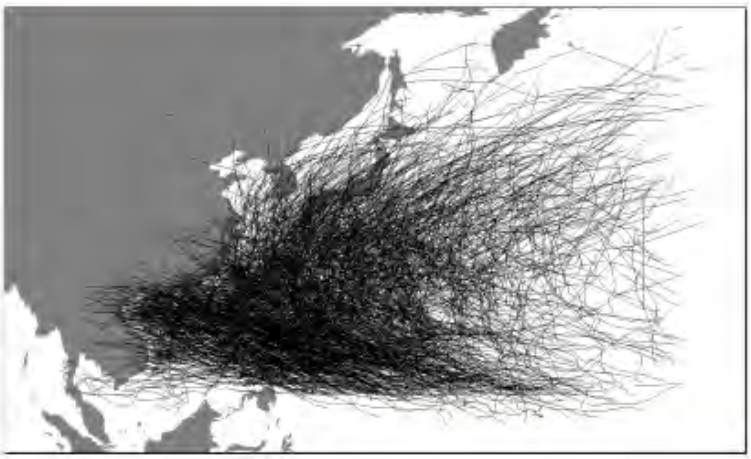

Criteria for Classification

- Idea: Splitting the storms into more homogeneous classes

Criteria for Classification

- Idea: Splitting the storms into more homogeneous classes
- Tracks are assigned to classes according to the areas of the observation window they move across

Storm Tracks, Class 0

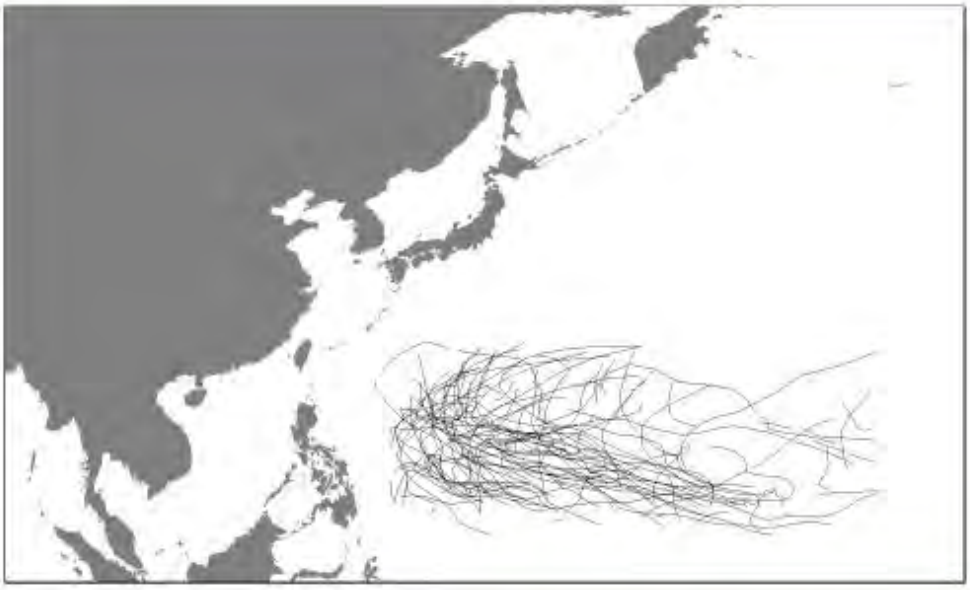

Storm Tracks, Class 1

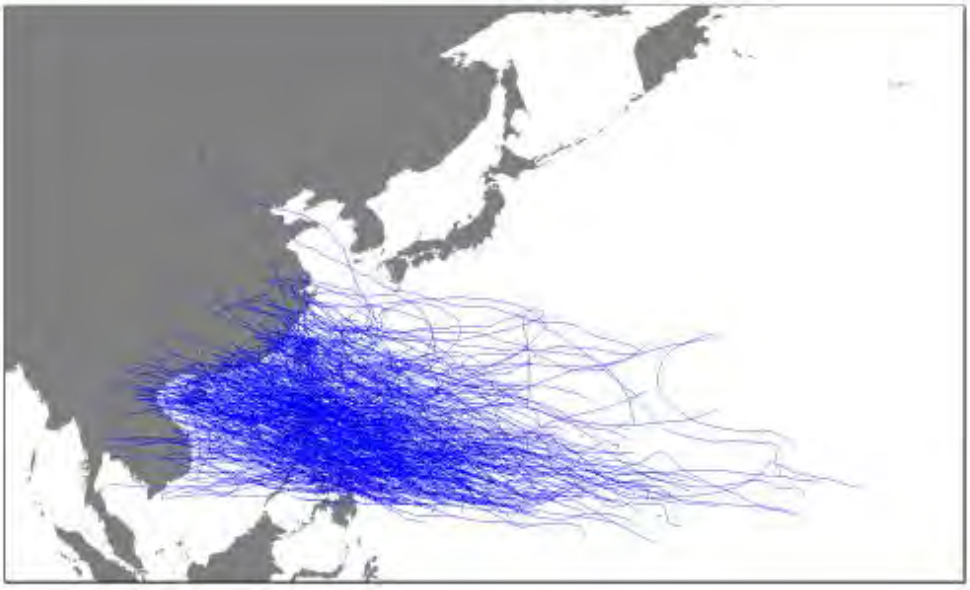

Storm Tracks, Class 2

Storm Tracks, Class 3

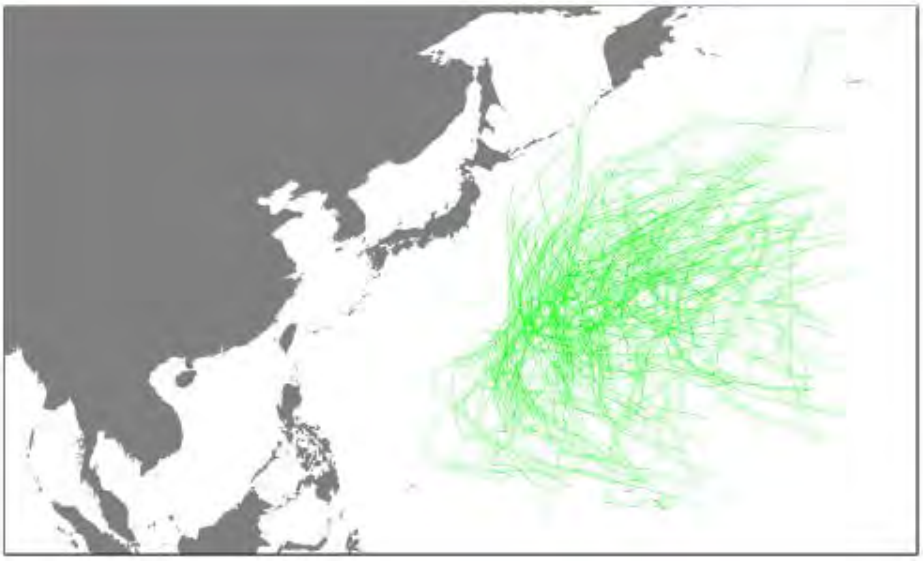

Storm Tracks, Class 4

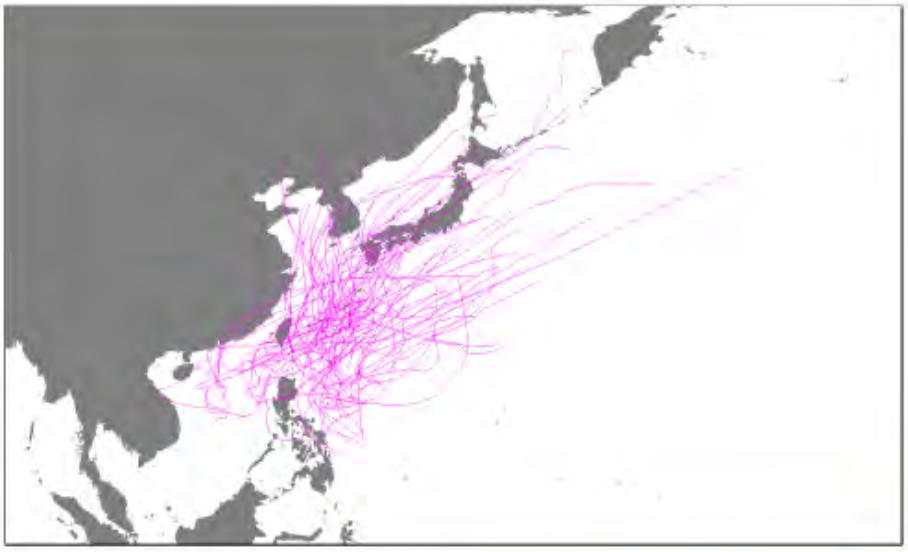

Storm Tracks, Class 5

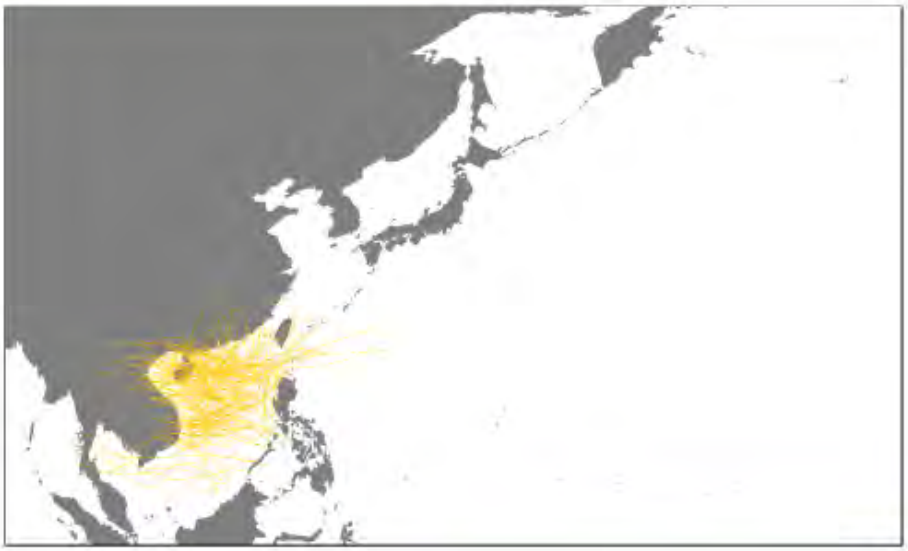

Modeling the tracks

An appropriate model needs to include the following characteristics:

Modeling the tracks

An appropriate model needs to include the following characteristics:

- Points of genesis of storms
- Direction of storm movement
- Translation speeds

Modeling the tracks

An appropriate model needs to include the following characteristics:

- Points of genesis of storms
- Direction of storm movement
- Translation speeds
- Also of interest: Maximum wind speeds along the tracks

Example: Points of Cyclone Genesis, Class 1

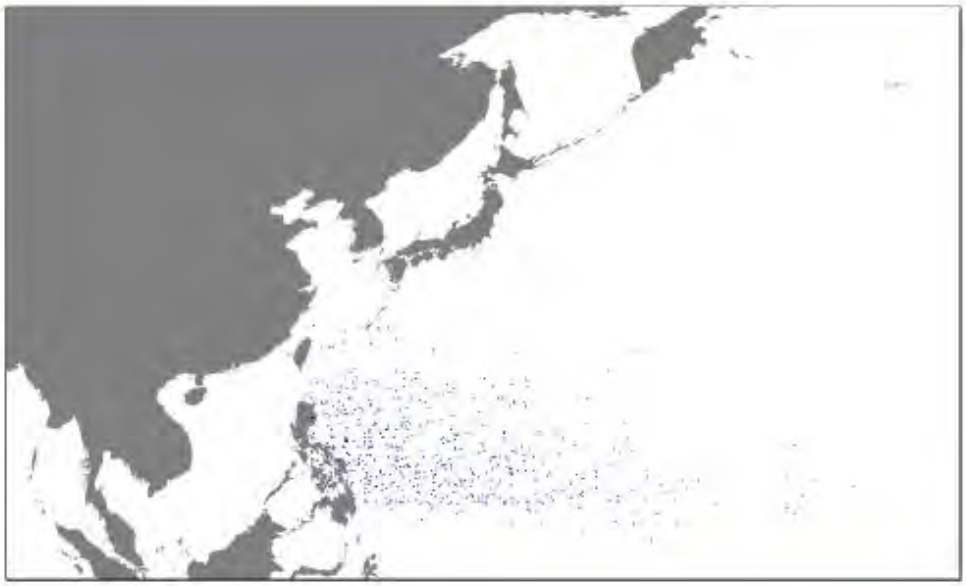

Modeling approach

- Intuitive approach: modeling points of cyclone genesis as a spatial point process
- From meteorology, no interactions between points of genesis are known

$\Rightarrow$ Poisson point process seems appropriate

Modeling approach

- Intuitive approach: modeling points of cyclone genesis as a spatial point process
- From meteorology, no interactions between points of genesis are known

$\Rightarrow$ Poisson point process seems appropriate

- The locations of the points of genesis within the observation window are distributed inhomogenously

$\Rightarrow$ Estimation for the intensity field $f(\mathbf{t})$ of the inhomogeneous Poisson process is needed

Modeling approach

- Intuitive approach: modeling points of cyclone genesis as a spatial point process
- From meteorology, no interactions between points of genesis are known

⇒ Poisson point process seems appropriate

- The locations of the points of genesis within the observation window are distributed inhomogenously

⇒ Estimation for the intensity field $f(\mathbf{t})$ of the inhomogeneous Poisson process is needed

- No parametric distribution immediately comes to mind

⇒ non-parametric estimation technique is needed

Intensity Field Estimation

Generalized nearest neighbor estimator for the intensity field $f(\mathbf{t})$:

$$\widehat{f}(\mathbf{t}) = n^{-1} r_k(\mathbf{t})^{-2} \sum_{i=1}^{n} K_e \left\{ r_k(\mathbf{t})^{-1} (\mathbf{t} - \mathbf{X}_i) \right\} , \qquad (1)$$

where $r_k(\mathbf{t})$ is the distance of the k-th nearest neighbor of $\mathbf{t}$ from the point $\mathbf{t}$, $\mathbf{X}_i$ the i-th observation and K_e the Epanechnikov-Kernel:

$$K_e(\mathbf{x}) = \begin{cases} \frac{2}{\pi}(1 - \mathbf{x}^\top \mathbf{x}) & \text{if } \mathbf{x}^\top \mathbf{x} < 1, \\ 0 & \text{otherwise,} \end{cases} \qquad (2)$$

For details, see [Silverman, 1986].

Points of Cyclone Genesis, Class 0

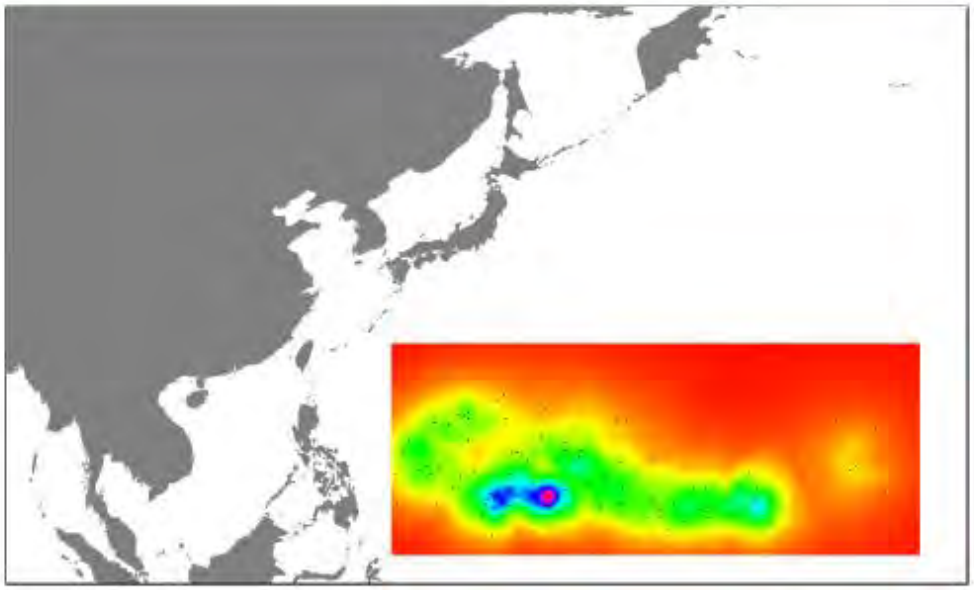

Points of Cyclone Genesis, Class 1

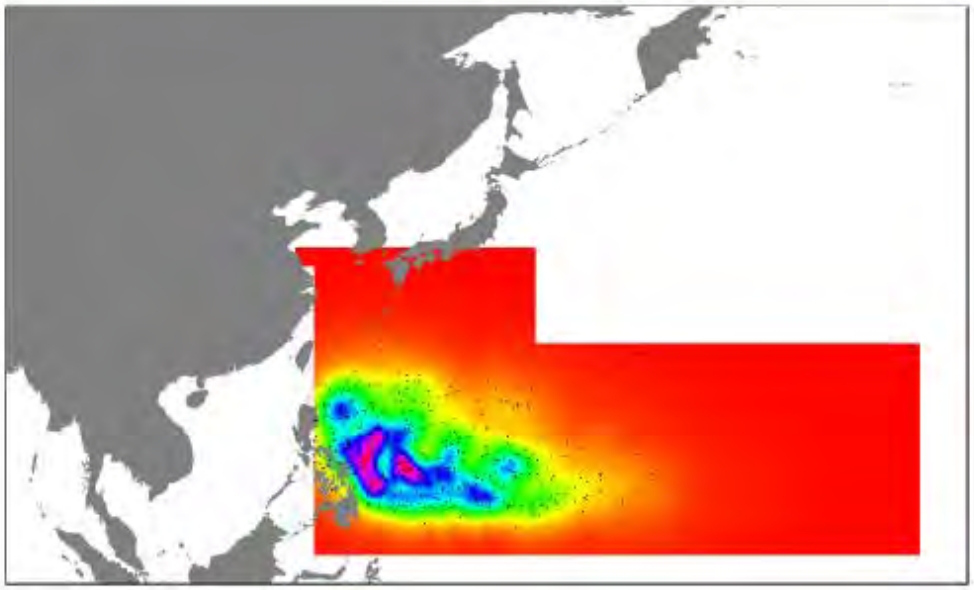

Points of Cyclone Genesis, Class 2

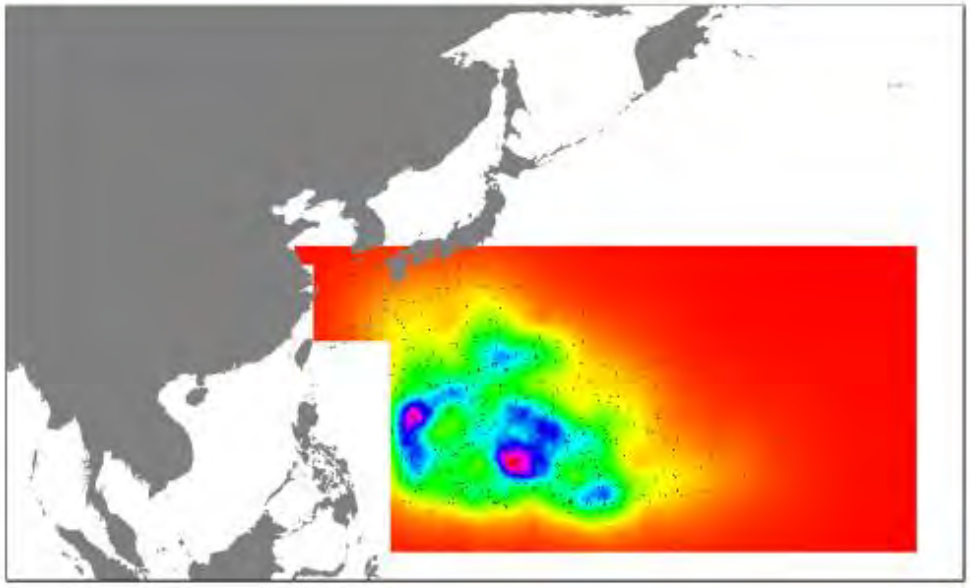

Points of Cyclone Genesis, Class 3

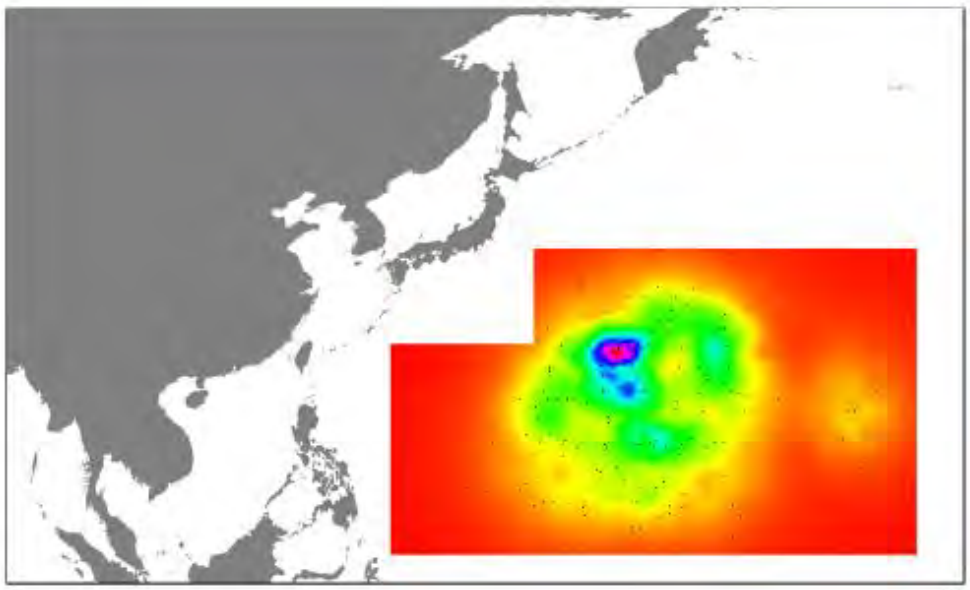

Points of Cyclone Genesis, Class 4

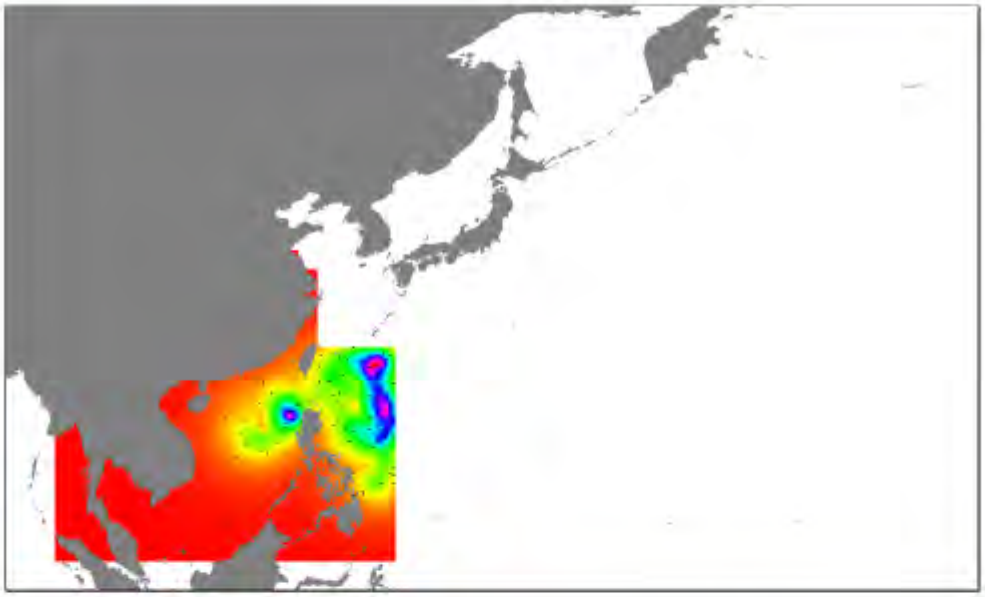

Points of Cyclone Genesis, Class 5

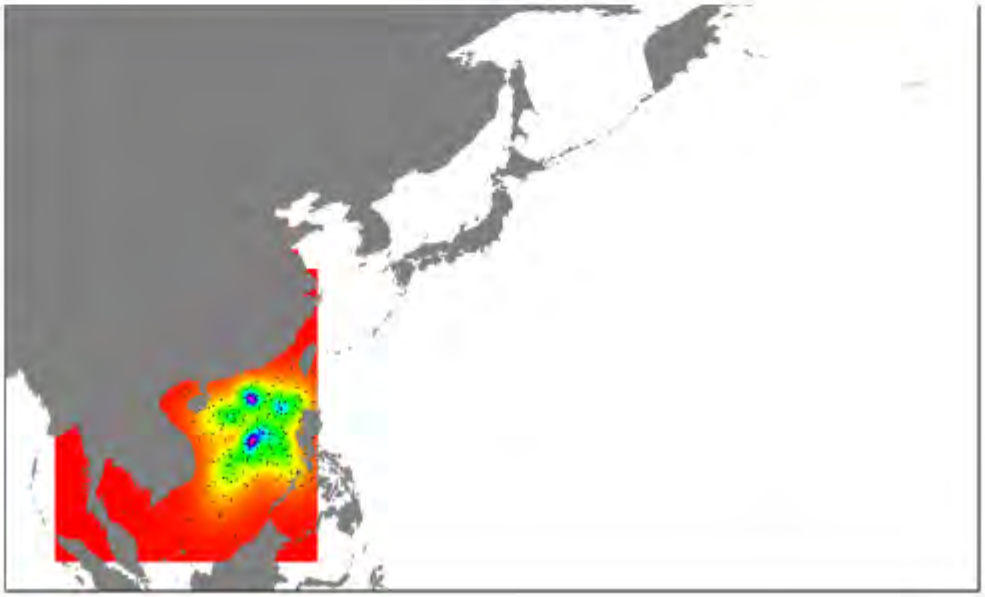

Modeling Approach: Direction

- Consider the direction of movement X as the sum of an initial direction X_0 and i.i.d. changes in direction X_i :

$$X = (X_0 + \sum_{i=1}^{n} X_i) \mod 360^\circ \qquad (3)$$

$\Rightarrow$ Direction of movement can be modeled as a generalized random walk

Modeling Approach: Direction

- Consider the direction of movement X as the sum of an initial direction X_0 and i.i.d. changes in direction X_i :

$$X = (X_0 + \sum_{i=1}^{n} X_i) \mod 360^\circ \qquad (3)$$

$\Rightarrow$ Direction of movement can be modeled as a generalized random walk

- Densities of X_0 and X_i need to be estimated from the historical data

$\Rightarrow$ Kernel techniques similar to those in the estimation of intensity fields can be used

Example Densities

- Density estimation: initial direction, class 1

Example Densities

- Density estimation: initial direction, class 1

- Density estimation: change in direction, class 1

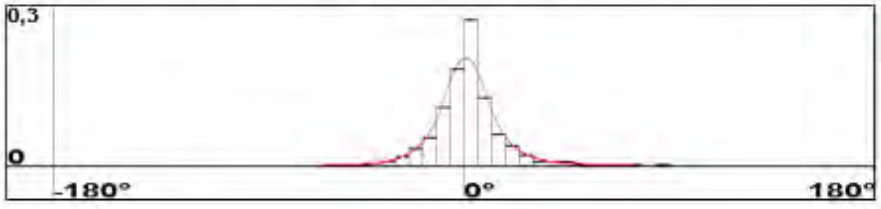

Modeling Approach: Translation Speed

- Consider the translation speed Y as the sum of an initial translation speed Y_0 and i.i.d. changes in translation speed Y_i :

$$Y = Y_0 + \sum_{i=1}^{n} Y_i \tag{4}$$

- Similar approach as for the direction, but certain boundary conditions have to be considered (e. g. $Y \geq 0$)

$\Rightarrow$ Translation speed can be modeled as a generalized random walk

- Densities of Y_0 and Y_i need to be estimated from the historical data

$\Rightarrow$ Kernel techniques similar to those in the estimation of intensity fields can be used

Example Densities

- Density estimation: initial translation speed, class 2

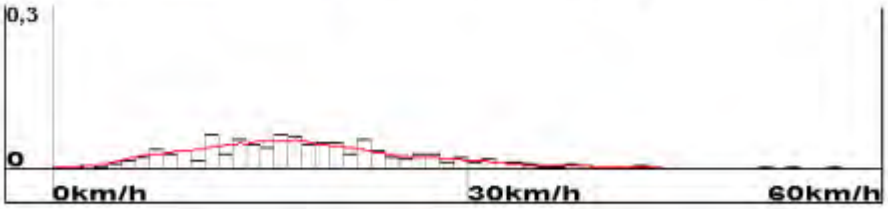

- Density estimation: change in translation speed, class 2

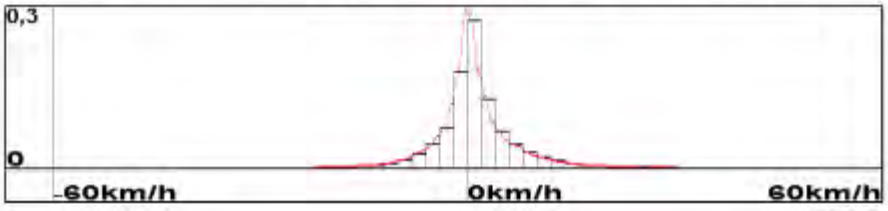

Modeling Approach: Wind Speed

- Consider the wind speed Z as the sum of an initial wind speed Z_0 and i.i.d. changes in wind speed Z_i :

$$Z = Z_0 + \sum_{i=1}^{n} Z_i \tag{5}$$

- Similar approach as for the direction, but certain boundary conditions have to be considered (e. g. $Z \geq 0$)

$\Rightarrow$ Translation speed can be modeled as a generalized random walk

- Densities of Z_0 and Z_i need to be estimated from the historical data

$\Rightarrow$ Kernel techniques similar to those used in the estimation of intensity fields can be used

Example Densities

- Density estimation: initial wind speed, class 5

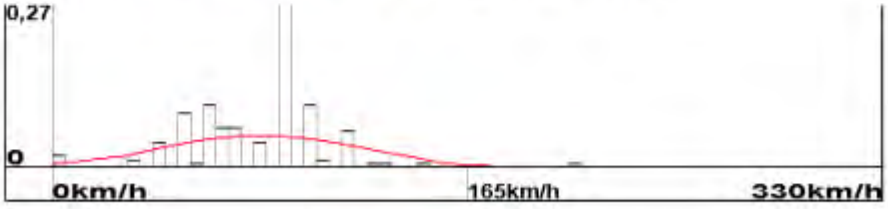

- Density estimation: change in wind speed, class 5

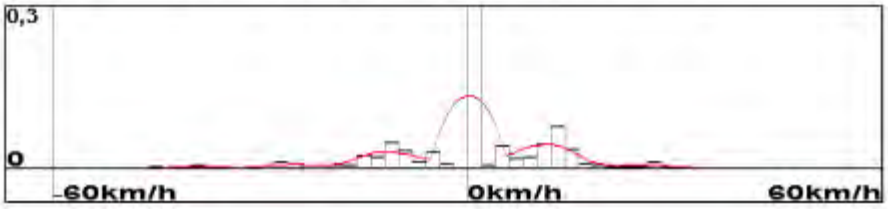

Stopping Probability

- Basic meteorological knowledge: Storms will get weaker and end . . .
  - . . . when moving over land or
  - . . . when moving over cold water or
  - . . . when moving too close to the equator

Stopping Probability

- Basic meteorological knowledge: Storms will get weaker and end . . .
  - . . . when moving over land or
  - . . . when moving over cold water or
  - . . . when moving too close to the equator
- For every location in the observation window, the stopping probability of a storm is estimated depending on . . .
  - . . . geographical circumstances
  - . . . meteorological circumstances

Model Algorithm (I)

1. Generate one realization of an inhomogeneous Poisson process according to the estimated intensity field
   ⇒ points of genesis for a set of storms

Model Algorithm (I)

1. Generate one realization of an inhomogeneous Poisson process according to the estimated intensity field
   ⇒ points of genesis for a set of storms
2. Generate realizations of the random variables *initial direction*, *initial translation speed*, and *initial wind speed* according to the estimated densities
   ⇒ initial segment for a storm

Model Algorithm (I)

1. Generate one realization of an inhomogeneous Poisson process according to the estimated intensity field
   ⇒ points of genesis for a set of storms
2. Generate realizations of the random variables *initial direction*, *initial translation speed*, and *initial wind speed* according to the estimated densities
   ⇒ initial segment for a storm
3. Determine the stopping probability of the storm according to the storm's current position
   ⇒ decision whether the storm ends or not

Model Algorithm (II)

4. Generate realizations of the random variables *change in direction*, *change in translation speed*, and *change in wind speed* according to the estimated densities
   ⇒ next track segment for a storm

Model Algorithm (II)

4. Generate realizations of the random variables *change in direction*, *change in translation speed*, and *change in wind speed* according to the estimated densities
   ⇒ next track segment for a storm
5. Repeat steps 3 and 4 until the track ends
   ⇒ complete storm track

Model Algorithm (II)

4. Generate realizations of the random variables *change in direction*, *change in translation speed*, and *change in wind speed* according to the estimated densities
   ⇒ next track segment for a storm
5. Repeat steps 3 and 4 until the track ends
   ⇒ complete storm track
6. Determine, if the class of the storm track created in step 5 matches the class of the storm according to step 1
   ⇒ accept or reject the storm

Model Algorithm (II)

4. Generate realizations of the random variables *change in direction*, *change in translation speed*, and *change in wind speed* according to the estimated densities
   ⇒ next track segment for a storm
5. Repeat steps 3 and 4 until the track ends
   ⇒ complete storm track
6. Determine, if the class of the storm track created in step 5 matches the class of the storm according to step 1
   ⇒ accept or reject the storm
7. Repeat steps 2 through 6 for every point generated in step 1 until for each point, an accepted track is generated
   ⇒ complete set of storm tracks

Synthetic Storm Tracks, Class 0

Synthetic Storm Tracks, Class 1

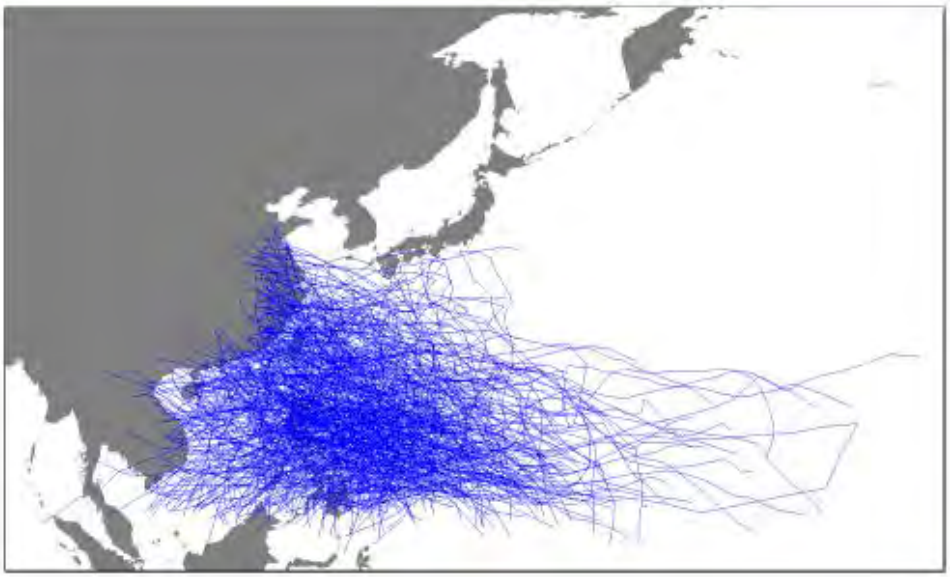

Synthetic Storm Tracks, Class 2

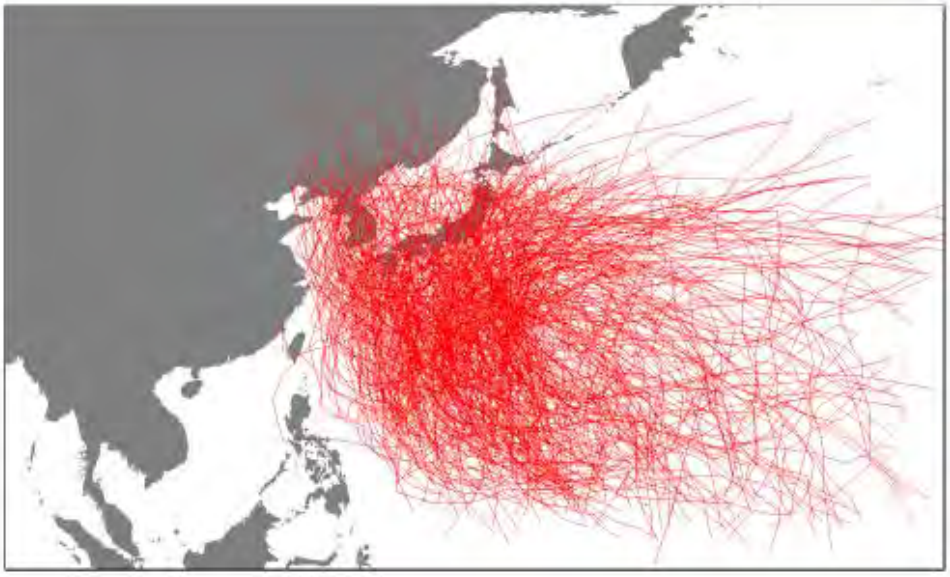

Synthetic Storm Tracks, Class 3

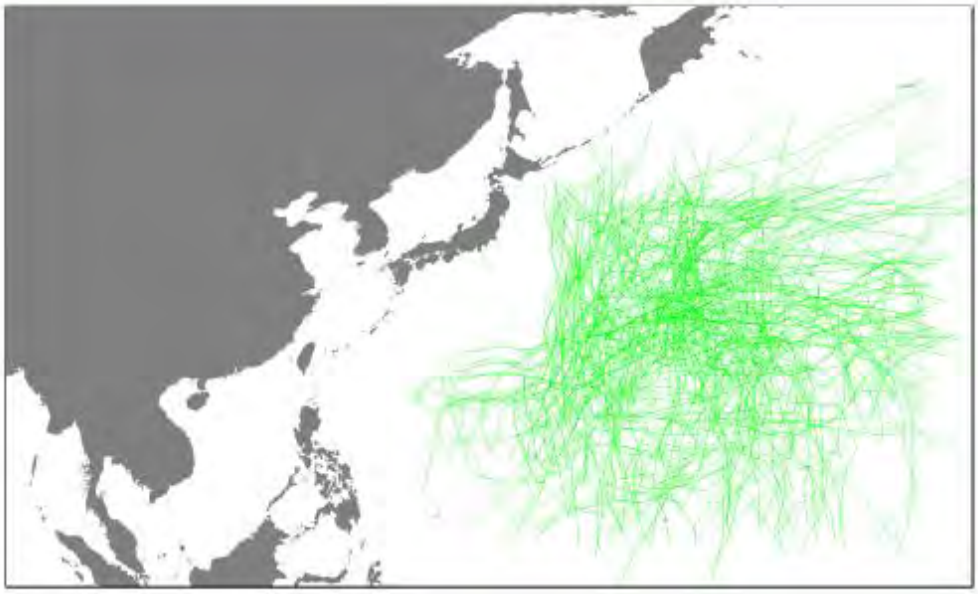

Synthetic Storm Tracks, Class 4

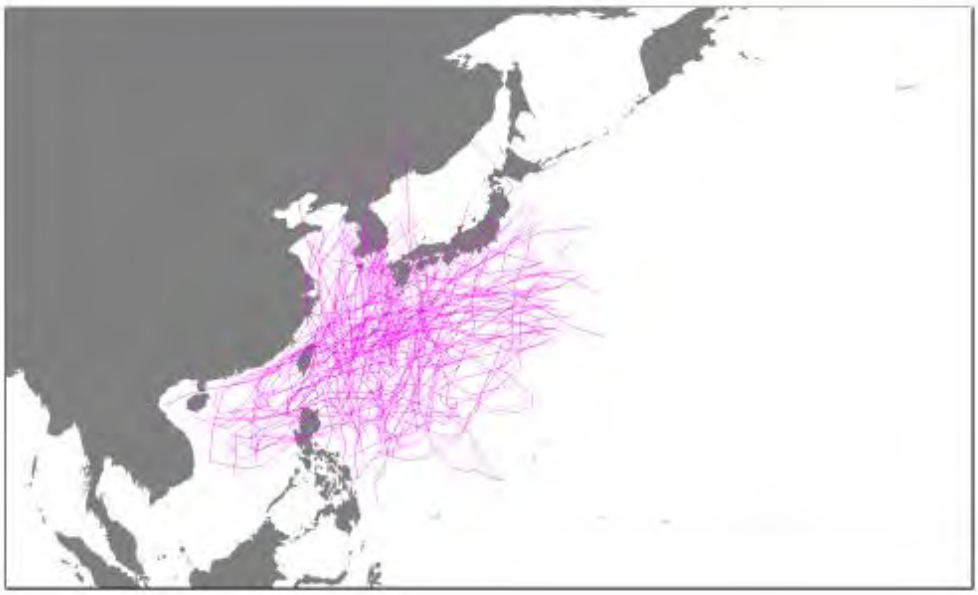

Synthetic Storm Tracks, Class 5

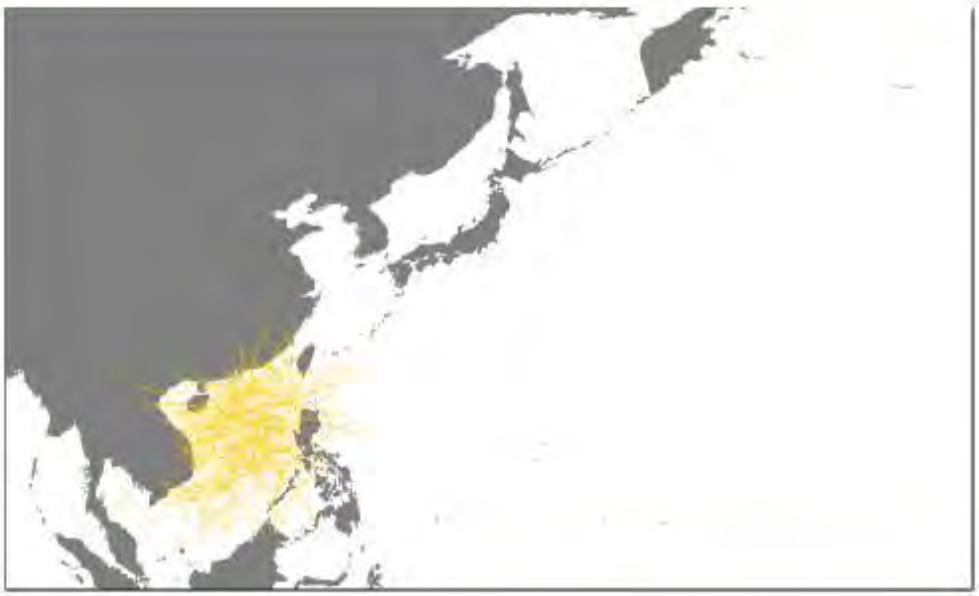

Evaluation (I)

Comparison: Historical and Synthetic Cyclone Tracks, Class 1

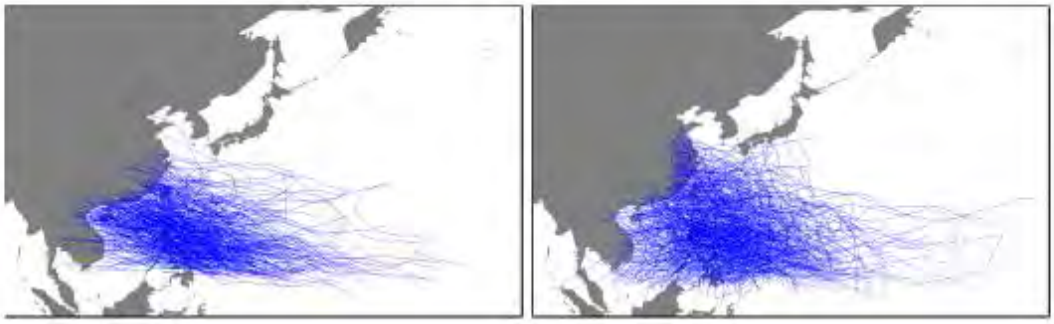

Evaluation (II)

Comparison: Historical and Synthetic Cyclone Tracks, Class 2

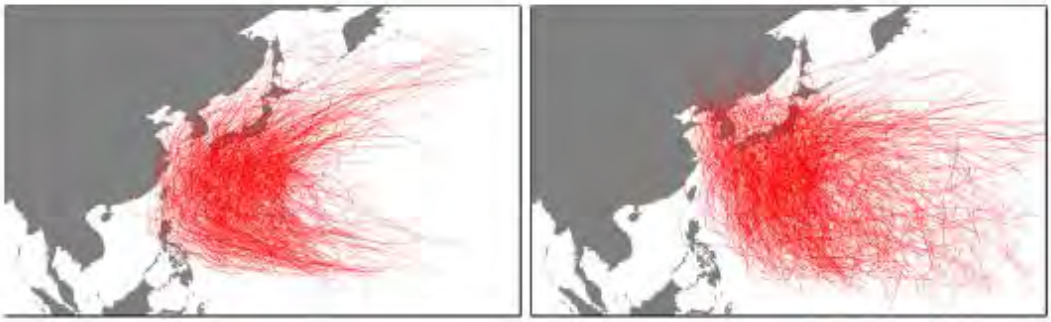

Continued Research

- Project will be expanded with the continuing support of Munich Reinsurance Company
- Current Focus:
  - Making the distributions of X_i, Y_i, Z_i location-dependent
  - Making the distribution of Z_i (wind speed) dependent on Z_{i-1}
  - Readjusting the rules for calculating the stopping probability

Continued Research

- Project will be expanded with the continuing support of Munich Reinsurance Company
- Current Focus:
  - Making the distributions of X_i, Y_i, Z_i location-dependent
  - Making the distribution of Z_i (wind speed) dependent on Z_{i-1}
  - Readjusting the rules for calculating the stopping probability
- Plans for future model enhancements:
  - Modeling the points of cyclone genesis as more general point processes, e. g. Gibbs Processes
  - Modeling possible autocorrelation in X_i, Y_i, Z_i
  - Transfering the model to other ocean basins, e. g. the North Atlantic

Literature

B. W. Silverman (1986)
Density Estimation for Statistics and Data Analysis
Chapman & Hall, New York

K. Emanuel, S. Ravela, E. Vivant, C. Risi (2005)
A combined statistical–deterministic approach to hurricane risk assessment
To appear in: Bulletin of the American Meteorological Society

T. Hall, S. Jewson (2005)
Statistical modelling of tropical cyclone tracks, part 1-6
arXiv:physics/0503231, 0505103, 0509024, 0510203, 0512091, 0512135

57. Assignment 2, Module 13: Using Statistical Models: https://serc.carleton.edu/introgeo/mathstatmodels/why.html

Why Use Mathematical and Statistical Models

This material is replicated on a number of sites as part of the SERC Pedagogic Service Project
Initial Publication Date: December 21, 2006

Mathematical Models

There are several situations in which mathematical models can be used very effectively in introductory education.

- Mathematical models can help students understand and explore the meaning of equations or functional relationships.
- Mathematical modeling software such as Excel, Stella II , or on-line JAVA /Macromedia type programs make it relatively easy to create a learning environment in which introductory students can be interactively engaged in guided inquiry, heads-on and hands-on activities.
- After developing a conceptual model of a physical system it is natural to develop a mathematical model that will allow one to estimate the quantitative behavior of the system.
- Quantitative results from mathematical models can easily be compared with observational data to identify a model's strengths and weaknesses.
- Mathematical models are an important component of the final "complete model" of a system which is actually a collection of conceptual, physical, mathematical, visualization, and possibly statistical sub-models.

Statistical Models

A solid statistical background is very important in the sciences. But the extent to which statistical ideas are appropriate in an introductory course depends on specific course objectives and the degree or institutional structure. Here we list several examples showing why and when statistical models are useful.

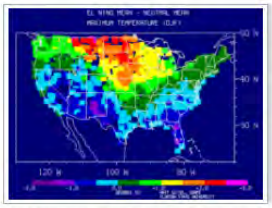

NOAA PMEL predictions for winter El Nino climate changes based on a statistical analysis of data.

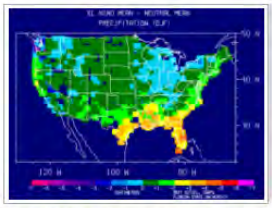

From NOAA PMEL (Regional US Impacts of El Nino). (more info)

Statistical models or basic statistics can be used:

- To characterize numerical data to help one to concisely describe the measurements and to help in the development of conceptual models of a system or process;
- To help estimate uncertainties in observational data and uncertainties in calculation based on observational data;
- To characterize numerical output from mathematical models to help understand the model behavior and to assess the model's ability to simulate important features of the natural system(model validation). Feeding this information back into the model development process will enhance model performance;
- To estimate probabilistic future behavior of a system based on past statistical information, a **statistical prediction model**. This is often a method use in climate prediction. A statement like 'Southern California will be wet this winter because of a strong El Nino' is based on a statistical prediction model.
- To extrapolation or interpolation of data based on a linear fit (or some other mathematical fit) are also good examples of statistical prediction models.
- To estimate input parameters for more complex mathematical models.
- To obtain frequency spectra of observations and model output.

58. Assignment 2, Module 13: Commission Standards Section M-2 Question 1: https://fchlpm.sbafla.com/media/t33jpnml/fchlpm_corelogic2017_12march2019.pdf

M-2 Hurricane Parameters and Characteristics

Methods for depicting all modeled hurricane parameters and characteristics, including but not limited to windspeed, radial distributions of wind and pressure, minimum central pressure, radius of maximum winds, landfall frequency, tracks, spatial and time variant windfields, and conversion factors, shall be based on information documented in current scientific and technical literature.

The modeling of hurricane parameters and characteristics is based on information documented by currently accepted scientific and technical literature or on CoreLogic analyses of meteorological data.

Disclosures

1. *Identify the hurricane parameters (e.g., central pressure, radius of maximum winds) that are used in the hurricane model.*

   The following parameter descriptions all pertain specifically to the Florida Hurricane Model probabilistic analysis. Use of the Florida Hurricane Model in a 'user storm' scenario mode may allow much greater flexibility in some parameters (i.e., landfall location, track direction, etc.) than the discrete, categorized values used in the probabilistic database.

Hurricane Parameters in the Model:

1. Landfall Location: Landfall segments of 10 nautical miles in length run along the coastline from south of the Texas-Mexico border through Maine. There are 310 discrete landfall segments used to develop the probabilistic hurricane data set. The Florida coast runs from landfall segment #84 (Escambia county, FL-Alabama border), through segment #180 (Nassau county, FL-Georgia border). That is, from coastal milepost 840 through 1800. The historical data used is the National Hurricane Center HURDAT2 starting at 1900 as of May 1, 2018.

2. Track Direction: Distributions for storm direction vary geographically and are based on smoothed historical data. The historical data used is the portion of the National Hurricane Center HURDAT2 from 1900 through 2017 as of May 1, 2018. All hurricanes in HURDAT2 from 1900 through 2017 were used.

3. Maximum One-Minute Sustained Wind Speed: The maximum one-minute sustained wind speed is the main parameter used to define hurricane intensity, and is one of the most critical items when considering loss sensitivity. The possible range in landfall values is from 74 mph to 192 mph, although the model will run at lower values (weaker storms) to

accommodate inland filling. The storm intensity is driven directly from the coastline-dependent smoothed wind speed distributions generated from the information in the National Hurricane Center HURDAT2 starting at 1900 as of May 1, 2018. All hurricanes in this data set were used.

4. Radius of Maximum Winds: This is the distance from the geometric center of the storm to the region of highest winds, typically within the eye wall of a well-developed hurricane. This parameter, after landfall location and maximum sustained wind speed, is the next most critical in terms of loss sensitivity. The parameter is statistically dependent on coastline location and landfall intensity. The historical data used is information contained in Hurricane Research Division's HURDAT Reanalysis Project (1900-1960), NOAA Technical Report NWS 38 (1961-1984), National Hurricane Center's Tropical Cyclone Reports and Advisories (1985-1987), and DeMaria's Extended Best Track (1988-2017) updated through the 2017 hurricane season. All hurricanes in HURDAT2 from 1900 through 2017 were used.

5. Translational Speed: This is the speed of the movement of the entire storm system itself. It is generally responsible for the asymmetry of a hurricane's wind field. It also has an effect on the distance which the highest winds are carried inland as the time-dependent filling weakens the storm. The parameter is statistically dependent on coastline location and storm strength, and in Florida, averages about 12-14 mph. The historical data used is information contained in HURDAT2 (1900-1960 and 1983-2017) and NOAA Technical Report NWS 38 (1961-1982), updated through the 2017 hurricane season. All hurricanes in the Official Hurricane Set were used. All hurricanes in HURDAT2 from 1900 through 2017 were used.

6. Filling Rate (inland decay rate): Overland attenuation (filling) is described by exponential decay of the hurricane central pressure deficit (difference between the background pressure and the storm central pressure). The filling rate is the parameter specifying the rate of this exponential decay. The historical data used is the National Hurricane Center HURDAT starting at 1900 as of June 1, 2007.

7. Profile Factor: This is a dimensionless shape parameter that varies the drop-off of winds outward from the hurricane's eye. Since an individual hurricane's profile may differ from the average, this parameter allows the user to best fit an actual storm's profile when modeling the specific event. In the probabilistic hurricane database, the profile factor is based on the profile factors of historical storms that have made landfall near the location of the probabilistic storm subject to a maximum that is dependent on the radius of maximum winds. The historical data used is the National Hurricane Center Marine Exposure from the Advisory Archives (1963-

1967), DeMaria's Extended Best Track (1988-2003), and HURDAT2 (2004-2017).

8. Inflow Angle: This is the angle between purely circular (tangential) motion and the actual direction of air flowing in towards the center of the hurricane. Modeling of the Inflow Angle is based on Kwon and Cheong (2010).

9. The model also considers air density and the Coriolis parameter, among other variables.

59. Assignment 2, Module 14: Human Influence and Harvey: https://www.science.org/content/article/human-influence-may-prolong-ocean-cycle-gave-birth-harvey

Human influence may prolong ocean cycle that gave birth to Harvey

Atlantic Multidecadal Oscillation remains warm and stormy

29 AUG 2017 • BY JULIA ROSEN

Hurricane Harvey on 24 August, a day before it made landfall in Texas as a Category-4 storm. NASA/NOAA GOES PROJECT

Last weekend, Hurricane Harvey put an end to a lucky streak: It became the first major hurricane to make landfall in the United States since 2005. The Category-4 storm barreled into Texas on 25 August, lashing the coast with 200-kilometer-per-hour winds, and deluging Houston with more than a meter of rain. As the third hurricane of the season, Harvey also gave weight to predictions from the National Oceanic and Atmospheric Administration (NOAA) that 2017 will be an above-average year for Atlantic storms. For decades now, storms have been getting a boost from a powerful but still mysterious long-term cycle in North Atlantic sea surface temperatures, which appears to be holding steady in its warm, storm-spawning phase.

This cycle, called the Atlantic Multidecadal Oscillation (AMO), swings between warm and cool phases every 20 to 60 years, shifting North Atlantic temperatures by a degree or so and setting the backdrop for hurricane season. Since about 1995, the AMO has been in a warm state, but researchers aren't sure where it's headed next. The AMO has traditionally been attributed to natural shifts in ocean currents, and some think it's on the cusp of shifting back toward a cool, quiescent phase. But others propose that human activities—a combination of declining air pollution and greenhouse warming—might prolong the current warm period, keeping hurricane activity high.

"It's important to understand the mechanism," says Rong Zhang, an oceanographer at NOAA's Geophysical Fluid Dynamics Laboratory in Princeton, New Jersey. "The projections are opposite."

Researchers first detected the AMO in ocean temperature measurements spanning the past 150 years. But tree rings and other climate records from places strongly influenced by the AMO show evidence of temperature variations going back centuries.

Shifts in the AMO reverberate through the climate system, affecting rainfall in Europe, drought in the Amazon, and Atlantic hurricanes. The warm phase fuels storms by warming the tropical Atlantic and intensifying the West African monsoon. A stronger monsoon, like La Niña (a cooling of the eastern tropical Pacific), reduces wind shear, vertical changes in wind direction that tend to break up embryonic storms. The monsoon also spins up low-pressure systems that enter the hurricane nursery of the tropical Atlantic. "This wind pattern allows these storms to very quickly develop rotation and energize," says Gerry Bell, lead hurricane forecaster at NOAA's Climate Prediction Center in College Park, Maryland.

By NOAA's metrics, the AMO remained in a warm phase this year, but some see hints of a change. "The waters in the far North Atlantic, up by Greenland, have been really cold—much colder than normal," says Phil Klotzbach, a meteorologist at Colorado State University in Fort Collins. The pattern potentially upset tropical conditions from afar, causing quieter than average hurricane seasons in recent years, he says.

The cold anomaly may herald a transition toward a cool phase, especially if the AMO is mainly driven by natural variations in a "conveyor belt" of Atlantic Ocean currents. This circulation draws warm surface water northeast along the Gulf Stream until it cools and sinks in the seas surrounding Greenland, returning south in the deep Atlantic. Stronger circulation brings more warm water north and leads to a positive AMO; when the circulation flags, cooling begins in the far North Atlantic and moves south, culminating in a negative AMO, Zhang says. According to her estimates, the AMO is now close to neutral. Klotzbach's approach, which factors in high-latitude temperatures, suggests that the AMO has already shifted negative.

However, recent research indicates that factors outside the ocean may also trigger changes in the AMO. Natural climate records suggest that, for centuries, volcanic eruptions and small changes in the sun's output warmed and cooled the ocean, helping pace the AMO. In past decades, humans have added their own influences, such as aerosol particles from burning coal, which reflect sunlight back to space and cool the ocean, says Ben Booth, a climate scientist at the Met Office Hadley Centre in Exeter, U.K. Booth thinks skyrocketing aerosol emissions in the second half of the 20th century were the primary cause of the most recent cold phase of the AMO, which lasted from 1970 to 1994. A subsequent drop—thanks to clean air regulations in the United States and Europe—may have instigated the current warm phase.

The role of greenhouse gas emissions is another story. Hotter oceans are generally thought to boost the intensity of storms, but not necessarily their frequency, and researchers subtract out this long-term warming when calculating the AMO. However, research by Lisa Murphy Goes, an atmospheric scientist at the University of Miami in Florida, suggests that greenhouse emissions may still help trigger swings in the AMO. As greenhouse gases keep rising and aerosols fall, Murphy Goes says the AMO should remain slightly positive for at least the next decade.

Understanding what lies ahead depends on whether natural variability or human influences win out. Most likely, both play a role; Booth suggests that their impacts could vary by region. Changes in ocean circulation might matter most in the northern Atlantic—where the cold anomaly has hunkered down—whereas external factors, such as aerosols, might impact the tropics most. These forces might also play off of one another over many decades in unexpected ways, or evolve under the long-term effects of climate change. "We hold many of the pieces," Booth says, "but we don't yet have a holistic picture." Harvey could be a tragic culmination to the current hurricane era—or a sign that it's not over yet.

**Correction, 30 August, 3 p.m.:* *An earlier version of the story gave the incorrect location for the Climate Prediction Center.*

60. Assignment 2, Module 14: Negative AMO Index: https://www.nature.com/articles/s41598-017-11046-x

SCIENTIFIC REPORTS

OPEN

Emerging negative Atlantic Multidecadal Oscillation index in spite of warm subtropics

Received: 16 March 2017
Accepted: 8 August 2017
Published online: 11 September 2017

Eleanor Frajka-Williams[1], Claudie Beaulieu[1] & Aurelie Duchez[2]

Sea surface temperatures in the northern North Atlantic have shown a marked decrease over the past several years. The sea surface in the subpolar gyre is now as cold as it was during the last cold phase of the Atlantic Multidecadal Oscillation index in the 1990s. This climate index is associated with shifts in hurricane activity, rainfall patterns and intensity, and changes in fish populations. However, unlike the last cold period in the Atlantic, the spatial pattern of sea surface temperature anomalies in the Atlantic is not uniformly cool, but instead has anomalously cold temperatures in the subpolar gyre, warm temperatures in the subtropics and cool anomalies over the tropics. The tripole pattern of anomalies has increased the subpolar to subtropical meridional gradient in SSTs, which are not represented by the AMO index value, but which may lead to increased atmospheric baroclinicity and storminess. Here we show that the recent Atlantic cooling is likely to persist, as predicted by a statistical forecast of subsurface ocean temperatures and consistent with the irreversible nature of watermass changes involved in the recent cooling of the subpolar gyre.

The Atlantic Multidecadal Oscillation (AMO, Fig. 1a) is an index of decadal variability in the Atlantic based on sea surface temperatures (SSTs). Though the AMO is constructed from SSTs, which respond quickly to atmospheric forcing, the AMO time series is dominated by low frequency–multi-decadal–variations (Fig. 1a). On these timescales, the AMO and Atlantic SSTs co-vary with the strength of the Atlantic meridional overturning circulation (MOC)[1] where a positive value (anomalously warm Atlantic) of the AMO corresponds to stronger overturning and a negative value (anomalously cool Atlantic) to a weaker MOC. Here, we do not discuss the physical causes of the multidecadal variations in the AMO index, which are debated in the literature[2–7]. Instead, we assess recent tendencies in the AMO index and its relationship to patterns of ocean temperature change.

The last time the AMO was in a cold state was in the 1990s. In the 1990s, the Atlantic shifted from a cold to a warm phase, driven by a strengthening of the MOC and North Atlantic Current[8] and accompanied by a contraction, warming and slowdown of the subpolar gyre. Over the recent two decades, the AMO has been in a warm phase, corresponding to intensified hurricane activity[9, 10], decreased rainfall over the US[11], increased rainfall over India and the Sahel[10], and a shift in fish stocks in the North Atlantic[12]. A return to a cold phase of the AMO could be accompanied by a reversal of these climate impacts.

Over the recent few years, striking changes in Atlantic SSTs have occurred in the subpolar gyre, where the cold anomaly that developed from 2013–2015 was termed the 'cold blob' in the press[13]. This cold anomaly resulted from extremely harsh winters of 2013–2015, characterised by strong surface heat loss[14] which resulted in persistent cooling of the upper ocean[15] and drove deep ocean convection[16, 17]. Here, we assess the impact of this cooling on the AMO index, and evaluate the observed changes over the past 3 years relative to the cold AMO period of the 1990s. The AMO index, however, masks any spatial distributions in SST changes, and while the AMO index is negative, the subpolar cold anomaly is accompanied by a warm anomaly in the subtropics. We investigate whether the cold subpolar anomaly is likely to persist and consider how the present cold state of the AMO may evolve.

Results

Negative AMO anomaly? In the recent 3 years, the AMO has become marginally negative, with an average SST anomaly of about −0.1 °C (Fig. 1a). The AMO index reflects variability in the North Atlantic and is typically intended to separate internally forced variations from anthropogenic climate change. Varying definitions

[1]University of Southampton, Ocean and Earth Science, Southampton, SO14 3ZH, United Kingdom. [2]National Oceanography Centre Southampton, Southampton, SO14 3ZH, United Kingdom. Correspondence and requests for materials should be addressed to E.F.-W. (email: e.frajka-williams@soton.ac.uk)

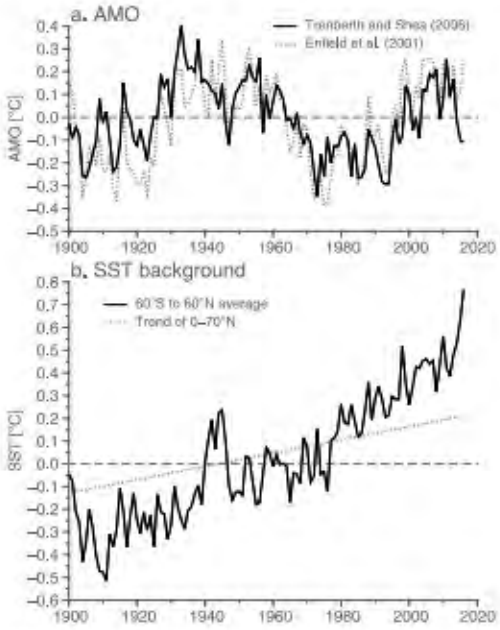

Figure 1. Atlantic sea surface temperature indices and reference field. (**a**) AMO indices following Trenberth and Shea[19] (black) and Enfield *et al.*[11] (grey dashed). For the Trenberth and Shea definition, the 60°S–60°N SSTs are subtracted from the North Atlantic SSTs. For the Enfield defintion, the North Atlantic SSTs (0–70°N) are simply detrended. (**b**) The trend that was removed from the North Atlantic SST averages to construct the AMO[11], and the 60°S–60°N SST that was removed from the 0–60°N, 80–0°W SST[19].

of the AMO exist[18], however, which may highlight different aspects of the basin- or sub-basinscale variability. During the recent reduction of the AMO, both the magnitude and sign of the AMO depend on the definition used to calculate it. The AMO is typically constructed by averaging North Atlantic SSTs and then subtracting a background time series to remove the anthropogenic changes. The Enfield *et al.*[11] definition removes as the background field a linear trend fit to the Atlantic SST average (Fig. 1b), while the Trenberth and Shea[19] (hereafter TS06) removes a global SST average as the background field, where the region 60°S–60°N is used to calculate the global temperatures.

In the past 3 years, the global SST average has increased dramatically (Fig. 1b) with the 2015 year being the warmest on record. In contrast, the linear trend used in the Enfield *et al.* definition does not capture nonlinear variations in its background field, so that the background time series shows a steady increase over the recent few years. When this steady increase is removed from the North Atlantic SST average, the values remain positive (a positive AMO index). Due to the inability of the Enfield definition to capture nonlinear changes, and the likelihood of values changing as the trend-endpoints change, we use the TS06 definition here, where the removal of the large global increase in SST from the Atlantic average results in a negative AMO value.

Temperatures are warming globally (Fig. 1b) and also in the Atlantic, but confined to the subtropics. Over the 2014–2016 period, the temperature anomalies show an intensely cold subpolar region, in spite of the relatively warm subtropics (Fig. 2a). The cold anomaly is centred over the eastern subpolar gyre, between Iceland and Cape Farewell (the southern tip of Greenland) at 50°N. In the subtropics, the warm anomaly is concentrated in the western half of the basin around 55°W (Fig. 2a). On longer timescales, the existence of a cooling tendency in the subpolar North Atlantic, while the rest of the Atlantic is warming, has been termed a "warming hole" and is used to diagnose a longer-term slowdown of the MOC[20]. On interannual timescales, an SST tripole (cold subpolar region, warm subtropics, cold tropics) is associated with positive North Atlantic Oscillation forcing[21]. We find that the subpolar cold anomaly is intense enough to swing the entire AMO to a negative index value (depending on the definition used), though the marginal intensity of the negative AMO is due to compensation by the warm subtropics.

To further investigate the time-variability of the meridional pattern of SST anomalies, we consider the evolution of the zonally-averaged SST anomalies. Over the recent 3 years (2013/14, 2014/15 and 2015/16) the cold subpolar gyre has reached the intensity of the anomaly observed in the latter part of the last cold AMO period (early 1990s) (Fig. 2b). In both periods, the subpolar temperature anomalies were intense, while the subtropics were less cold (1990s) or warm (2013–2016). The details of the meridional position and magnitude of the recent cold anomaly are more readily visible in a line plot (Fig. 2c). The line plot highlights a tripole pattern of temperature anomalies, where the magnitude of the subpolar cooling (around 52°N) and subtropical warming (around 31°N) are similar to the late stages of the AMO cold period (1982–1996). A tripole pattern of SST anomalies in the Atlantic is characteristic of SST anomalies under positive NAO conditions and are primarily attributed to

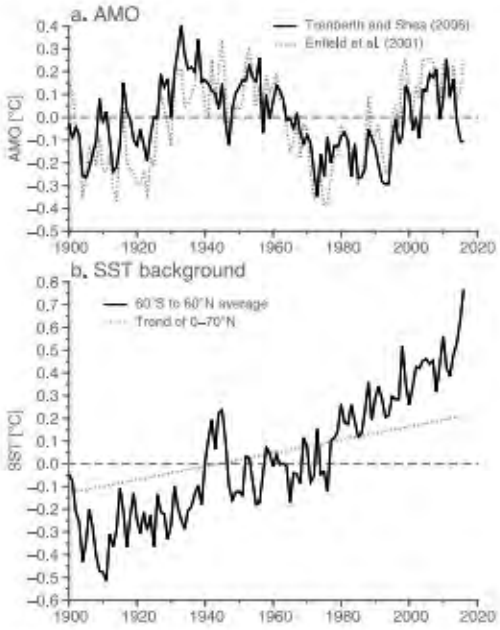

Figure 1. Atlantic sea surface temperature indices and reference field. (**a**) AMO indices following Trenberth and Shea[19] (black) and Enfield *et al.*[11] (grey dashed). For the Trenberth and Shea definition, the 60°S–60°N SSTs are subtracted from the North Atlantic SSTs. For the Enfield defintion, the North Atlantic SSTs (0–70°N) are simply detrended. (**b**) The trend that was removed from the North Atlantic SST averages to construct the AMO[11], and the 60°S–60°N SST that was removed from the 0–60°N, 80–0°W SST[19].

of the AMO exist[18], however, which may highlight different aspects of the basin- or sub-basinscale variability. During the recent reduction of the AMO, both the magnitude and sign of the AMO depend on the definition used to calculate it. The AMO is typically constructed by averaging North Atlantic SSTs and then subtracting a background time series to remove the anthropogenic changes. The Enfield *et al.*[11] definition removes as the background field a linear trend fit to the Atlantic SST average (Fig. 1b), while the Trenberth and Shea[19] (hereafter TS06) removes a global SST average as the background field, where the region 60°S–60°N is used to calculate the global temperatures.

In the past 3 years, the global SST average has increased dramatically (Fig. 1b) with the 2015 year being the warmest on record. In contrast, the linear trend used in the Enfield *et al.* definition does not capture nonlinear variations in its background field, so that the background time series shows a steady increase over the recent few years. When this steady increase is removed from the North Atlantic SST average, the values remain positive (a positive AMO index). Due to the inability of the Enfield definition to capture nonlinear changes, and the likelihood of values changing as the trend-endpoints change, we use the TS06 definition here, where the removal of the large global increase in SST from the Atlantic average results in a negative AMO value.

Temperatures are warming globally (Fig. 1b) and also in the Atlantic, but confined to the subtropics. Over the 2014–2016 period, the temperature anomalies show an intensely cold subpolar region, in spite of the relatively warm subtropics (Fig. 2a). The cold anomaly is centred over the eastern subpolar gyre, between Iceland and Cape Farewell (the southern tip of Greenland) at 50°N. In the subtropics, the warm anomaly is concentrated in the western half of the basin around 55°W (Fig. 2a). On longer timescales, the existence of a cooling tendency in the subpolar North Atlantic, while the rest of the Atlantic is warming, has been termed a "warming hole" and is used to diagnose a longer-term slowdown of the MOC[20]. On interannual timescales, an SST tripole (cold subpolar region, warm subtropics, cold tropics) is associated with positive North Atlantic Oscillation forcing[21]. We find that the subpolar cold anomaly is intense enough to swing the entire AMO to a negative index value (depending on the definition used), though the marginal intensity of the negative AMO is due to compensation by the warm subtropics.

To further investigate the time-variability of the meridional pattern of SST anomalies, we consider the evolution of the zonally-averaged SST anomalies. Over the recent 3 years (2013/14, 2014/15 and 2015/16) the cold subpolar gyre has reached the intensity of the anomaly observed in the latter part of the last cold AMO period (early 1990s) (Fig. 2b). In both periods, the subpolar temperature anomalies were intense, while the subtropics were less cold (1990s) or warm (2013–2016). The details of the meridional position and magnitude of the recent cold anomaly are more readily visible in a line plot (Fig. 2c). The line plot highlights a tripole pattern of temperature anomalies, where the magnitude of the subpolar cooling (around 52°N) and subtropical warming (around 31°N) are similar to the late stages of the AMO cold period (1982–1996). A tripole pattern of SST anomalies in the Atlantic is characteristic of SST anomalies under positive NAO conditions and are primarily attributed to

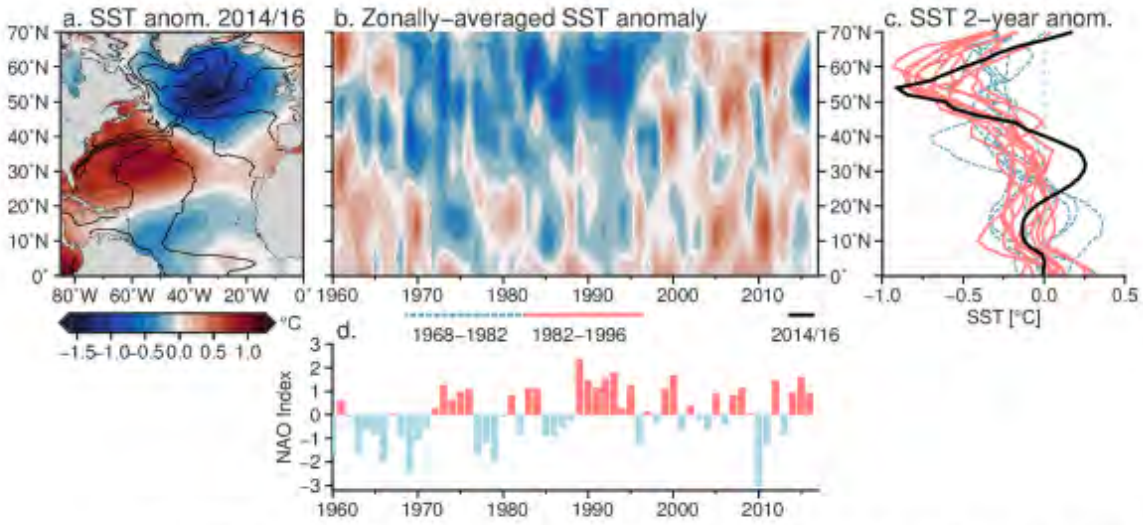

Figure 2. Sea surface temperature anomalies and evolution. (**a**) SST (°C) from the ERSST dataset for the period July 2014–June 2016 are plotted relative to the average over July 2004–June 2012. The map was created using Generic Mapping Toolbox v5.2.1 (gmt.soest.hawaii.edu/). (**b**) Temporal evolution of the zonally-averaged SST as a function of latitude. Both panels show that the recent period has a cold anomaly in the subpolar gyre, but also a warm anomaly in the subtropics. (**c**) Line plots of the zonally-averaged SSTs, where each line represents an average of 2-years. The periods included are the early part of the last cold AMO period (1963–1973, blue) and the late part (1973–1996, red). Black shows the profile for the 2 year period: July 2014–June 2016. (**d**) NAO index where the bar for 2015 represents the December 2015–February 2016 period.

anomalous air-sea heat fluxes[21]. While the NAO was positive through several successive winters in both the early 1990s and 2013–2016 (Fig. 2d), the meridional gradient in SST is more pronounced in the 2014/16 period, in association with the warm anomaly in the subtropical gyre.

While the AMO index is marginally negative in the 2014/16 period (compared to more strongly negative in the 1982–1990s), the AMO index does not capture the spatial pattern of SST anomalies. The persistent meridional gradients in SST over the past few years are likely to influence the atmospheric circulation. The gradients were particularly strong over the North Atlantic Drift region (not shown). In a numerical model, an imposed meridional gradient in SSTs in this region generated variations in sea level pressure, intensifying atmospheric baroclinicity and leading to downstream storminess[22]. In this way, though the patterns of SST anomalies may be set by atmospheric conditions, they can feedback on the atmosphere[23].

Changes in Ocean Heat Content. SSTs respond rapidly to atmospheric forcing in addition to subsurface processes and the large scale ocean circulation. The AMO, however, is associated with longer term variations (multi-decadal) in the Atlantic conditions. In this and the next section, we consider evidence for whether the recent changes (cooling in the subpolar regions and warming in the subtropics) and the negative anomaly in the AMO are likely to persist. In contrast with SSTs, subsurface temperature anomalies can persist for months or years, leaving a longer-term impact on the overlying ocean surface, and so here we focus on upper ocean heat content (OHC).

The subpolar gyre is typified by cooler water temperatures than the subtropics, with the coldest temperatures in the western subpolar region. The gyre has doming isopycnals, which means that in the centre of the gyre, layers of water are elevated through Ekman transport divergence, supporting the large-scale cyclonic circulation (Fig. 3b,c). The subtropics, in contrast, are significantly warmer, with isotherms tilting strongly in the meridional direction between the subtropics and subpolar gyre around 38°N (Fig. 3b). This strong tilt supports the intense eastward flow of the Gulf Stream. During the 2013/14 winter, the cooling by the atmosphere was strongest over the Irminger Sea[14] with the subsequent winter further reducing the OHC[15] (Fig. 3a). A cooling of this magnitude over such a short time scale can be mostly explained by the strong surface heat losses over the combined 2013/14 and 2014/15 winters, with only a secondary role for the weakening of the Atlantic MOC[15].

During the 2014/15 winter, deep convection penetrated down to 1500 m depth in both the western subpolar gyre (Labrador Sea[17]) and the eastern subpolar gyre (Irminger Sea[16]). Convection to these depths was last observed in the early 1990s[24]. Meridional sections of temperature anomalies from objectively analysed hydrographic observations show the deep penetration of the cold anomaly in the subpolar region (Fig. 3d,e). Remarkably, some of the strongest cooling was observed in the intergyre-gyre region (east of 40°W and around 45°N), over the North Atlantic Current, rather than in the centre of the subpolar gyre. The coldest temperatures were found in the Labrador Sea. In-depth analysis of the temperature changes from 2013–15 found that the cold anomalies were consistent with air-sea flux driven watermass transformation, which is an irreversible process[15].

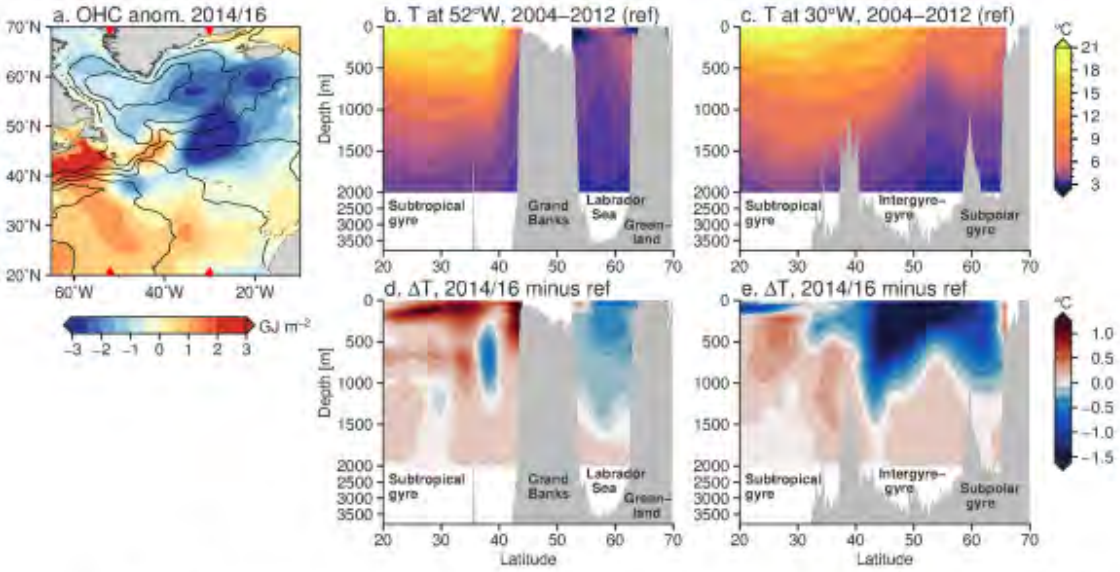

Figure 3. Spatial distribution of ocean temperatures and anomalies. (**a**) Ocean heat content, 0–700 m, for the period July 2014–June 2016 minus the reference period (July 2004–June 2012). Black contours show the mean dynamic ocean topography, while the red triangles indicate the longitudes (52°W and 30°W) for the panels to the right. The map was created using Generic Mapping Toolbox v5.2.1 (gmt.soest.hawaii.edu/). Temperature section from EN4 objectively analysed data at (**b**) 52°W and (**c**) 30°W in the Atlantic, for the reference period. (**d**,**e**) As for (**b**) and (**c**), but showing the difference between the 2014/16 period and the reference period. Positive (negative) values indicate warming (cooling) since the reference period.

In the subtropics the warming is largely confined to the top 300 m in the western half of the subtropical gyre (Fig. 3d). The map further shows some enhanced warming on the North American shelf from Cape Hatteras (around 35°N) to the Grand Banks (around 45°N, Fig. 3a). The subsurface cold anomalies around the latitude of the Gulf Stream (38°N, Fig. 3d) may be associated with a shift in the meridional position of the Gulf Stream, but may also result from the inability of objectively analysed sparse ocean data to capture changes in the sharp temperature gradients in the Gulf Stream region. Unlike changes in the subpolar region, which are typically associated with irreversible, diabatic watermass transformation[25], the OHC changes in the subtropics are often associated with adiabatic heave (the temporary upwards or downwards movement of water layers) driven by wind anomalies[25,26]. Heaving water upwards (downwards) through vertical gradients in temperature results in a cold (warm) anomaly at depth. This process can be reversed through a reversal of the wind pattern.

Persistence of a negative AMO. Here we show that the AMO index tends to covary with OHC anomalies in the subpolar gyre. Due to the expectation that subpolar watermass transformation is an irreversible process, compared to the adiabatic processes in the subtropics, we examine the subpolar OHC for its persistence and potential impact on the lower frequency variations of the AMO index. It is notable that the cold blob disappeared from SSTs during the summer, while the OHC anomaly persisted all year[15].

A pointwise covariance between the AMO (TS06 definition) and upper OHC shows that the relationship between the two is particularly strong in the Labrador Sea (western subpolar gyre) and in the eastern subpolar gyre, north of the North Atlantic Current (Fig. 4, around 40–50°N, 35–45°W). The time series of subpolar OHC (0–700 m, 45–70°N, 10–65°W) tracks the time series of AMO over the recent half-century, including identifying the shift from cold to warm phase in the mid-1990s. In the recent 3 years, the OHC in the subpolar region has reached a low not seen since the 1990s. While we expect OHC anomalies to persist more than SST anomalies[27] we can also show persistence of OHC anomalies using a statistical forecast. Fitting an autoregressive integrated moving average to the subpolar OHC time series indicates that OHC tends to carry memory from year to year (Fig. 4b). The forecast suggests that the cold anomaly will likely persist over the next 2 years with a probability of 0.8. The persistence of subpolar OHC anomalies, and the dominance of subpolar OHC anomalies on the AMO (Fig. 4a) is consistent with the expectation that OHC, rather than SST, carries the memory of the ocean. In the subpolar region, we further expect that subpolar anomalies are generated by irreversible (diabatic) processes and that once formed, take several years for the anomaly to advect or mix away.

Considering the subpolar OHC changes to be diabatic, we can estimate what forcing would be needed to remove the subpolar cold anomaly over the next few years. An anomaly of -0.5 GJ m^{-2} would require a positive heat flux of 10 W m^{-2} sustained over 2 years to remove, or a northward heat flux anomaly of 0.1 PW sustained over 2 years, or some combination of the above. At 26°N, where the mean northward heat transport is about 1.3 PW[28], an increase in the northward heat transport of 0.1 PW would equate to a sustained recovery in the overturning transport of 5% over the mean value. These values are not outside the realm of normal variability, but as

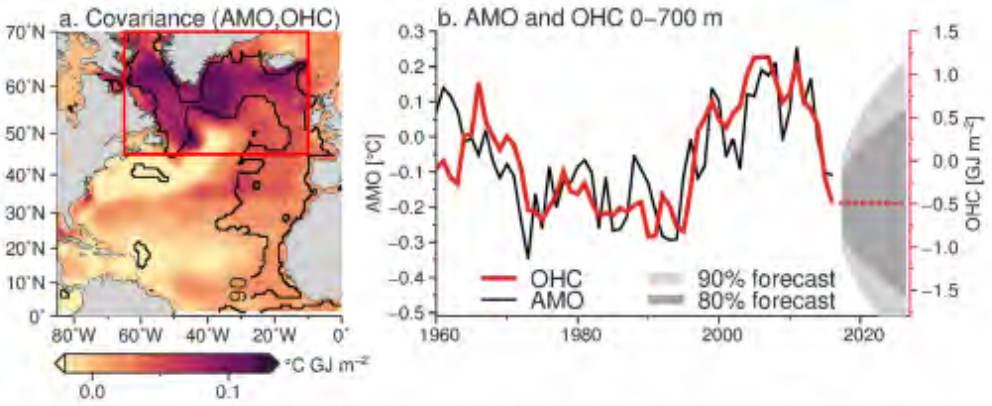

Figure 4. Covariance between OHC and AMO and statistical forecast of subpolar OHC. (**a**) Pointwise covariance between the AMO and OHC over the period 1955–2013 (shading). Significant correlations are contoured at the 90% (black) level, where significance is calculated using the number of degrees of freedom determined by the integral timescale of decorrelation. The red box indicates the subpolar region used in the text. The map was created using Generic Mapping Toolbox v5.2.1 (gmt.soest.hawaii.edu/). (**b**) Time series of the AMO (black) and OHC anomaly (red) from the subpolar North Atlantic (red box in a). The AMO is the Trenberth and Shea[19] definition, with 0–60°N Atlantic surface temperature minus the 60°S to 60°N average. The OHC anomaly is the NODC 0–700 m average for the subpolar region 45–70°N and 10–65°W.

the overturning transport is presently declining at a rate of 0.5 Sv/yr (3%/year)[29], the MOC strength would need to recover several Sverdrups of intensity. If the subtropical warm anomaly is a transient feature due to adiabatic heave, it can reduce immediately with a change in the wind stress curl over the Atlantic. If this were to reverse, while the subpolar cold anomaly persists, then the AMO may develop into a more negative state with a basin wide cold anomaly.

Discussion

The AMO index is designed to capture the multdecadal variability in the Atlantic and is constructed as a large-scale (0–70°N) average of SSTs in the Atlantic, minus a reference time series. However, the choice of reference time series is critical to determining the value of the AMO due to the recent acceleration in global temperature rise. In the recent few years, the magnitude and even the sign of this index can vary depending on the definition used. In one definition, the reference period is the linear trend fit to the Atlantic SSTs[11], while another uses the globally-averaged SSTs (60°S–60°N)[19]. Globally, the 2015 year was the warmest year on record and represented a sharp uptick in global temperatures. What this means is that when the globally-averaged SST time series is removed from the Atlantic SSTs, the AMO index is negative; a linear trend fit to the Atlantic SSTs is not as strongly positive in the past few years, so when using the Enfield *et al.*[11] definition, the AMO index is still positive. As the record grows longer, the linear trend may change (or if a linear model is not a good fit to the tendency of the Atlantic SSTs) then the past values of the AMO will change. For this reason, we have used the TS06 definition.

The recent reduction in the AMO index may lead on to further oceanic change. A weak AMO is typically associated with a weak Atlantic MOC in climate models and proxies[20], and the decreasing trend in the observed Atlantic MOC and meridional heat transport at 26°N[28,30] should result in a cooling to the north of 26°N[31]. However, these effects are too slow to explain the rapid cooling that was observed in the subpolar North Atlantic[15]. Instead, we expect that the intense cooling in the subpolar gyre of 2014/16 and intensification of deep convection across the subpolar gyre will lead to an increase in the strength of the Atlantic MOC[1,32–34]. A direct relationship between convection intensity and the strength of the southward flowing waters of the MOC is elusive in observations[35], but numerical models suggest that strong convection and their accompanying increases in the density of middepth waters (1000–2500 m) in the Labrador Sea are indeed a precursor to a strengthening of the MOC[32]. In the coming decade, the MOC and associated northward heat transport should intensify, following the increase in subpolar convection[34]), and may reverse the present declining trend of the MOC[29,30].

Conclusions

The AMO index is a convenient measure of the decadal and longer timescale variability in the Atlantic. However, it is a simple proxy built on the large-scale Atlantic SST anomalies and should be used with caution when trying to understand physical processes in the Atlantic or overlying atmosphere. In particular, in the recent few years, the AMO index has become negative, associated with the strong cold anomaly in the subpolar North Atlantic. This cold anomaly is strikingly cold, and reaches deep into the oceans (as seen in ocean heat content), but the magnitude of the AMO index does not reflect the stark cooling that occurred in the past few years. Instead, a warm subtropical anomaly has partially compensated for the cool subpolar regions, resulting in a marginally negative AMO. The direct influence of the oceanic SSTs on the atmosphere will likely differ between the recent cool anomaly and that in the 1980s and 90 s, when the Atlantic had a cool anomaly over much of its expanse (Fig. 2). This is

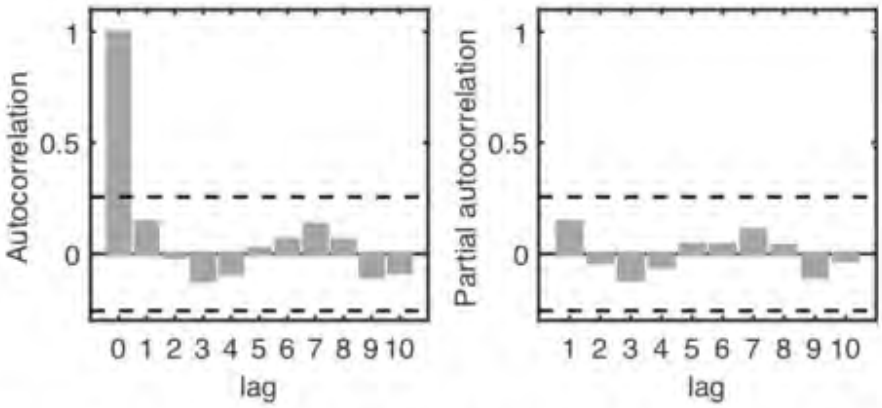

Figure 5. (**a**) Autocorrelation function (grey bars) for the residuals as a function of lag in years. (**b**) Partial autocorrelation function (grey bars). In both (**a**) and (**b**), the black dashed line indicates the 95% confidence interval.

because the atmosphere responds differently to a cool SST anomaly than to an enhanced meridional SST gradient, the latter of which can increase atmospheric baroclinicity and storminess[22].

While the AMO index is only marginally negative, we use spatial information about the distribution of temperature anomalies (both surface and subsurface) to predict that it will persist. Subpolar OHC variations were driven by anomalous air-sea fluxes[14,15] forcing deep convection across the subpolar gyre[16,36]. Subpolar OHC variations are typically driven by such irreversible processes, which contributes to the persistent nature of OHC variations, as captured by a statistical forecast (Fig. 4). We show that subpolar OHC anomalies in particular are correlated with the AMO, suggesting that the negative AMO will persist. Subtropical changes are typically adiabatic, and reverse with a reversal of the wind-driven heave. Our findings suggest that the negative AMO index will persist and, if the subtropical anomaly reverses, will intensify.

Methods

Note that an alternate name for the AMO is the AMV (Atlantic Multidecadal Variability) which removes the implicit expectation of an oscillation in the variability. Two time series of the AMO index are used. One was provided by NOAA Earth System Research Laboratory[11] and derived from monthly 5° resolution Kaplan SST dataset averaged over the Atlantic from 0–70°N and then detrended. The second was calculated from ERSST (Extended Reconstructed Sea Surface Temperature v4) following Trenberth and Shea[19]. According to this defintion, the North Atlantic SST values were averaged, and then the average from them the 60°S–60°N was removed from the North Atlantic time series. For the remainder of the SST calculations, we use the ERSST product since 1854 at 2° resolution.

Ocean heat content (OHC) in the 0–700 m layer was provided by the National Oceanographic Data Center for the period Jan 1950 to Jun 2016[37]. Time series are provided as 3-month averages at 1° resolution. Source data include Argo float profiles, hydrographic data and expendable bathythermograph data as contained in the World Ocean Database. Prior to the Argo period (2004-present), data were relatively sparse, though the North Atlantic remains one of the best sampled regions.

Ocean temperatures for the sections in Fig. 3 are from the UK Met Office EN4 climatology[38]. In the climatology, hydrographic data from ships, probes and Argo float data are gridded at 1° degree spatial resolution and a monthly time interval. Since the Argo array was complete since about 2004, we use a reference period of July 2004–June 2012 in constructing anomalies. Anomalies are typically computed as the data minus the reference period averages, so that a positive anomaly represents a relatively cold area and a negative anomaly represents a relatively warm area.

Data are averaged to annual averages, where the data plotted for 2015 in a time series represents the July 2014–June 2015 average. In the text, the year 2014/15 represents the annual average of monthly values from July 2014–June 2015, while the period 2014/16 represents the 2-year average from July 2014–June 2016. For the NAO index, we used the principal component-based time series from Hurrell (National Center for Atmospheric Research Staff, Hurrell North Atlantic Oscillation Index (PC-Based)). For the NAO, annual values used in Fig. 2 are the December–February averages, so that the value in 2015 represents the average of the value from December 2015–February 2016.

Relationship between AMO and OHC. A pointwise covariance between the AMO and OHC annual time series over the period 1955–2013 was calculated, where the coefficient of covariance is shown in Fig. 4a. The covariance shows a strong relationship between the OHC and AMO, particularly in the subpolar gyre. The area-weighted subpolar OHC and AMO have a correlation coefficient of 0.7, significant at the 90% level. From this, we conclude that OHC in the subpolar North Atlantic covaries with the AMO, while also having substantial temperature fluctuations.

Forecasting OHC. An autoregressive integrated moving average (ARIMA) model was fitted on the subpolar OHC annually averaged values over the region 45–70°N and 10–65°W. The parameters of the ARIMA model were selected using a stepwise procedure fitting all possible ARIMA models from the less complicated ARIMA (0,0,0), which is equivalent to white-noise and does not hold any forecast skills, to an ARIMA(5,2,5). The Akaike information criterion is used to identify the model providing the best likelihood penalized by the number of parameters fitted, thus guards against overfitting. The selected model, an ARIMA(0,1,0), corresponds to a random walk, where each year closely follows the previous year. As measures of model validation, the autocorrelation function and partial autocorrelation function of the residuals are shown in Fig. 5, and indicate that the residuals are independent. Therefore, although very simple the chosen model captures the structure in the OHC time series. To evaluate the forecasting accuracy of the model, we calculate the errors using cross-calibration, i.e. we calculate errors with data that were not used when fitting the model. We use a moving window of ten consecutive observations to fit the model and produce the forecast for the next one. The cross-calibrated root-mean-squared-error (RMSE) is 0.269, showing a high forecast accuracy. As a mean of comparison, the cross-calibrated RMSE for different ARIMA models with the same number of parameters, ARIMA(1,0,0) and ARIMA(0,0,1), are 0.323 and 0.384 respectively. Changing the size of the moving window for the cross-calibration does not have much effect on the accuracy measures. The forecasting was done using the 'forecast' R package[39].

Data availability. The 0–700 m ocean heat content data are available from the National Oceanographic Data Center (NODC) at https://www.nodc.noaa.gov/OC5/3M_HEAT_CONTENT/. The ERSST sea surface temperature data are available from the NOAA Earth System Research Laboratory (https://www.esrl.noaa.gov/psd/data/gridded/data.noaa.ersst.html). The Met Office EN4 objectively analysed hydrographic data, Gouretski version 4.1.1, are available from http://www.metoffice.gov.uk/hadobs/en4/.

References

1. Zhang, R. Coherent surface-subsurface fingerprint of the Atlantic meridional overturning circulation. *Geophysical Research Letters* **35**, L20705, doi:10.1029/2008GL035463 (2008).
2. Delworth, T. L. & Mann, M. E. Observed and simulated multidecadal variability in the Northern Hemisphere. *Climate Dynamics* **16**, 661–676 (2000).
3. Clement, A. *et al.* The Atlantic Multidecadal Oscillation without a role for ocean circulation. *Science* **350**, 320–324, doi:10.1126/science.aab3980 (2015).
4. Zhang, R. *et al.* Comment on "The Atlantic Multidecadal Oscillation without a role for ocean circulation". *Science* **352**, 1527–1527, doi:10.1126/science.aaf1660 (2016).
5. O'Reilly, C. H., Huber, M., Woollings, T. & Zanna, L. The signature of low-frequency oceanic forcing in the Atlantic Multidecadal Oscillation. *Geophysical Research Letters* **43**, 2810–2818, doi:10.1002/2016GL067925 (2016).
6. Booth, B. B. B., Dunstone, N. J., Halloran, P. R., Andrews, T. & Bellouin, N. Aerosols implicated as a prime driver of twentieth-century North Atlantic climate variability. *Nature* **484**, 228–232, doi:10.1038/nature10946 (2012).
7. Zhang, R. *et al.* Have Aerosols Caused the Observed Atlantic Multidecadal Variability? *Journal of the Atmospheric Sciences* **70**, 1135–1144, doi:10.1175/JAS-D-12-0331.1 (2013).
8. Msadek, R. *et al.* Predicting a decadal shift in North Atlantic climate variability using the GFDL forecast system. *Journal of Climate* **27**, 6472–6496, doi:10.1175/JCLI-D-13-00476.1 (2014).
9. Goldenberg, S. B., Landsea, C. W., Mestas-Nuñez, A. M. & Gray, W. M. The recent increase in Atlantic hurricane activity: Causes and implications. *Science* **293**, 474–479, doi:10.1126/science.1060040 (2001).
10. Zhang & Delworth. Impact of Atlantic Multidecadal Oscillations on India/Sahel rainfall and Atlantic hurricanes. *Geophysical Research Letters* **33**, L17712, doi:10.1029/2006GL026267 (2006).
11. Enfield, D. B., Mestas-Nunez, A. M. & Trimble, P. J. The Atlantic Multidecadal Oscillation and its relationship to rainfall and river flows in the continental U.S. *Geophysical Research Letters* **28**, 2077–2080 (2001).
12. Alheit, J. *et al.* Atlantic Multidecadal Oscillation (AMO) modulates dynamics of small pelagic fishes and ecosystem regime shifts in the eastern North and Central Atlantic. *Journal of Marine Systems* **131**, 21–35, doi:10.1016/j.jmarsys.2013.11.002 (2014).
13. Mooney, C. Why some scientists are worried about a cold 'blob' in the North Atlantic ocean. Washington Post https://www.washingtonpost.com/news/energy-environment/wp/2015/09/24/why-some-scientists-are-worried-about-a-cold-blob-in-the-north-atlantic-ocean/?utm_term=.24388ab9c1ec (2015).
14. Grist, J. P. *et al.* Extreme air–sea interaction over the North Atlantic subpolar gyre during the winter of 2013–2014 and its subsurface legacy. *Climate Dynamics* **46**, 4207, doi:10.1007/s00382-015-2819-3 (2015).
15. Duchez, A. *et al.* Drivers of exceptionally cold North Atlantic ocean temperatures and their link to the 2015 European heat wave. *Environmental Research Letters* **11**, 074004, doi:10.1088/1748-9326/11/7/074004 (2016).
16. de Jong, M. F. & de Steur, L. Strong winter cooling over the Irminger Sea in winter 2014-2015, exceptional deep convection, and the emergence of anomalously low SST. *Geophysical Research Letters* **43**, 7106–7113, doi:10.1002/2016GL069596 (2016).
17. Yashayaev, I. & Loder, J. W. Further intensification of deep convection in the Labrador Sea in 2016. *Geophysical Research Letters* (2016). doi 10.1002/2016GL071668.
18. Zanchettin, D., Bothe, O., Müller, W., Bader, J. & Jungclaus, J. H. Different flavors of the Atlantic Multidecadal Variability. *Climate Dynamics* **42**, 381–399, doi:10.1007/s00382-013-1669-0 (2014).
19. Trenberth, K. E. & Shea, D. J. Atlantic hurricanes and natural variability in 2005. *Geophysical Research Letters* **33**, L12704, doi:10.1029/2006GL026894 (2006).
20. Rahmstorf, S. *et al.* Exceptional twentieth-century slowdown in Atlantic Ocean overturning circulation. *Nature Climate Change* **5**, 475–480, doi:10.1038/nclimate2554 (2015).
21. Deser, C., Alexander, M. A., Xie, S.-P. & Phillips, A. S. Sea surface temperature variability: Patterns and mechanisms. *Annual Reviews of Marine Science* **2**, 115–143, doi:10.1146/annurev-marine-120408-151453 (2010).
22. Bradshaw, D. J., Hoskins, B. & Blackburn, M. The basic ingredients of the North Atlantic storm track. Part I: Land-sea contrast and orography. *J. Atmos. Sci.* **68**, 1784–1805 (2011).
23. Czaja, A. & Frankignoul, C. Observed impact of Atlantic SST anomalies on the North Atlantic Oscillation. *Journal of Climate* **15**, 606–623, doi:10.1175/1520-0442(2002)015 (2002).
24. Lazier, J., Hendry, R., Clarke, A., Yashayaev, I. & Rhines, P. Convection and restratification in the Labrador Sea, 1990-2000. *Deep Sea Research I* **49**, 1819–1835 (2002).
25. Lozier, M. S. Deconstructing the conveyor belt. *Science* **328**, 1507–11 (2010).
26. Evans, D. G. *et al.* Recent wind-driven variability in Atlantic water mass distribution and meridional overturning circulation. *Journal of Physical Oceanography*, doi:10.1175/JPO-D-16-0089.1 (2017).

27. Hasselmann, K. Stochastic climate models. Part 1: Theory. *Tellus* **28**, 473–485, doi:10.3402/tellusa.v28i6.11316 (1976).
28. Johns, W. E. *et al.* Continuous, array-based estimates of Atlantic Ocean heat transport at 26.5°N. *Journal of Climate* **24**, 2429–2449, doi:10.1175/2010JCLI3997.1 (2011).
29. Frajka-Williams, E. *et al.* Compensation between meridional flow components of the Atlantic MOC at 26.5°N. *Ocean Science* **12**, 481–493, doi:10.5194/os-12-481-2016 (2016).
30. Smeed, D. A. *et al.* Observed decline of the Atlantic meridional overturning circulation 2004 to 2012. *Ocean Science* **10**, 29–38, doi:10.5194/os-10-29-2014 (2014).
31. Cunningham, S. A. *et al.* Atlantic MOC slowdown cooled the subtropical ocean. *Geophysical Research Letters* **40**, 6202–6207, doi:10.1002/2013GL058464 (2014).
32. Robson, J., Hodson, D., Hawkins, E. & Sutton, R. Atlantic overturning in decline? *Nature Geoscience* **7**, 2–3, doi:10.1038/ngeo2050 (2014).
33. Pillar, H., Heimbach, P., Johnson, H. & Marshall, D. Dynamical attribution of recent variability in Atlantic overturning. *Journal of Climate* **29**, 3339–3352, doi:10.1175/JCLI-D-15-0727.1 (2016).
34. Frajka-Williams, E., Bamber, J. & Vage, K. Greenland melt and the Atlantic meridional overturning circulation. *Oceanography* (2016).
35. Lozier, M. S. Overturning in the North Atlantic. *Annual Reviews of Marine Science* **4**, 291–315 (2012).
36. Piron, A., Thierry, V., Mercier, H. & Caniaux, G. Gyre-scale deep convection in the subpolar North Atlantic Ocean during winter 2014–2015. *Geophysical Research Letters* **44**, 1439–1447, doi:10.1002/2016GL071895 (2017).
37. Levitus, S. *et al.* World ocean heat content and thermosteric sea level change (0–2000 m), 1955–2010. *Geophysical Research Letters* **39**, L10603, doi:10.1029/2012GL051106 (2012).
38. Good, S. A., Martin, M. J. & Rayner, N. A. EN4: quality controlled ocean temperature and salinity profiles and monthly objective analyses with uncertainty estimates. *Journal of Geophysical Research* **118**, 6704–6716, doi:10.1002/2013JC009067 (2013).
39. Hyndman, R. J. & Khandakar, Y. Automatic time series forecasting: The forecast package for R. *Journal of Statistical Software* **26**, 1–22, doi:10.18637/jss.v027.i03 (2008).

Acknowledgements

EFW was funded by a Leverhulme Trust Research Fellowship. AD is beneficiary of an AXA Research Fund postdoctoral grant and is supported by the UK Natural Environment Research Council (NERC) National Capability funding and partly funded by the UK-China Research and Innovation Partnership Fund through the Met Office Climate Science for Service Partnership (CSSP) China as part of the Newton Fund. CB was supported by a Marie Curie FP7 Reintegration Grants within the Seventh European Community Framework (project 631466 - TROPHYZ).

Author Contributions

E.F.W. and C.B. analysed the data. All authors contributed to the writing. All authors reviewed the manuscript.

Additional Information

Competing Interests: The authors declare that they have no competing interests.

Publisher's note: Springer Nature remains neutral with regard to jurisdictional claims in published maps and institutional affiliations.

61. Assignment 2, Module 14: ENSO Teleconnections:
https://www.weather.gov/fwd/teleconnections

ENSO Teleconnections

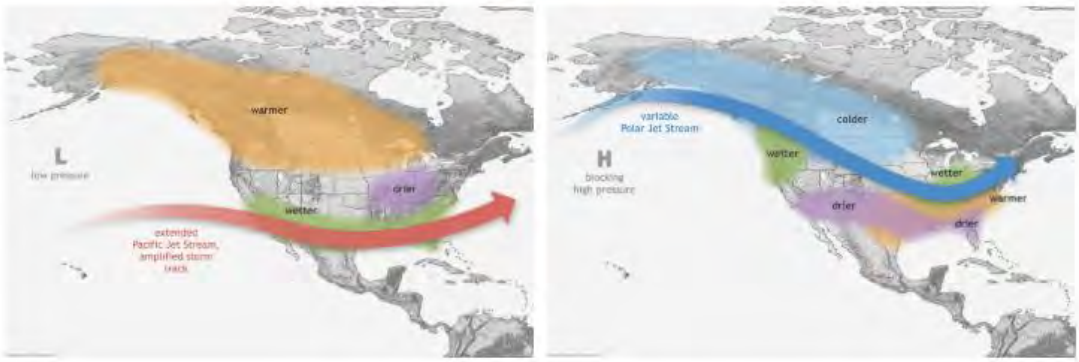

What Are the Impacts of El Niño/La Niña?

- **Global Precipitation Impacts During El Niño and La Niña**

The effects of ENSO are often called teleconnections, emphasizing that changing conditions in one part of the world can affect areas far from the source.

El Niño and Rainfall

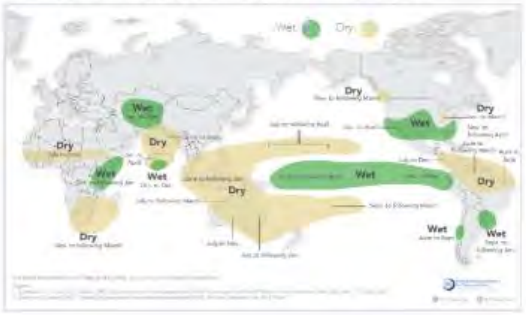

La Niña and Rainfall

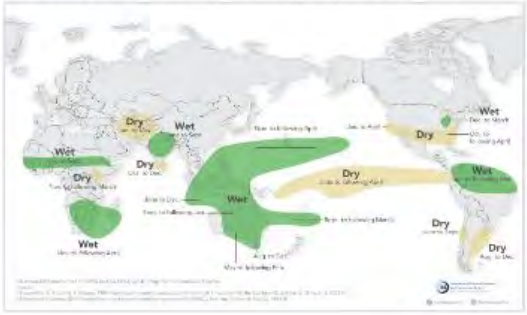

- **Impacts on the United States**

The impacts of ENSO on the United States are most noticeable in the cold season.

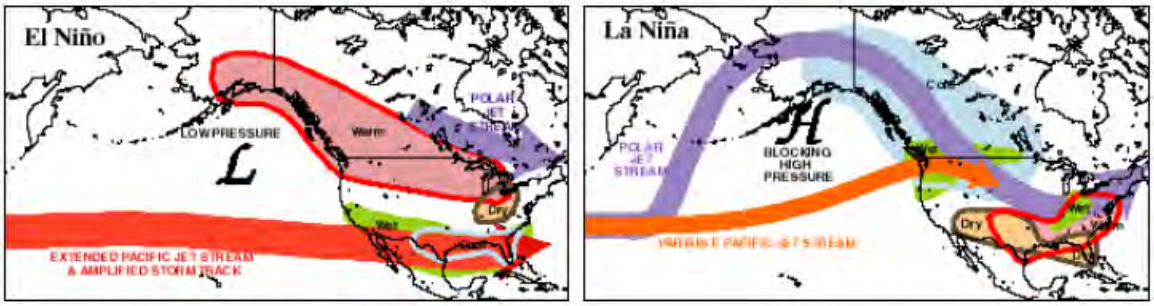

- **Narratives About El Niño and La Niña Impacts (from CPC)**

The Climate Prediction Center discusses how weather patterns are affected by ENSO.

- **Risk of Seasonal Climate Extremes (from PSL)**

Will your area have an increased or decreased risk of temperature or precipitation extremes?

El Niño and Rainfall

El Niño conditions in the tropical Pacific are known to shift rainfall patterns in many different parts of the world. The regions and seasons shown on the map below indicate typical but not guaranteed impacts of La Niña. For further information, consult the probabilistic information* that the map is based on.

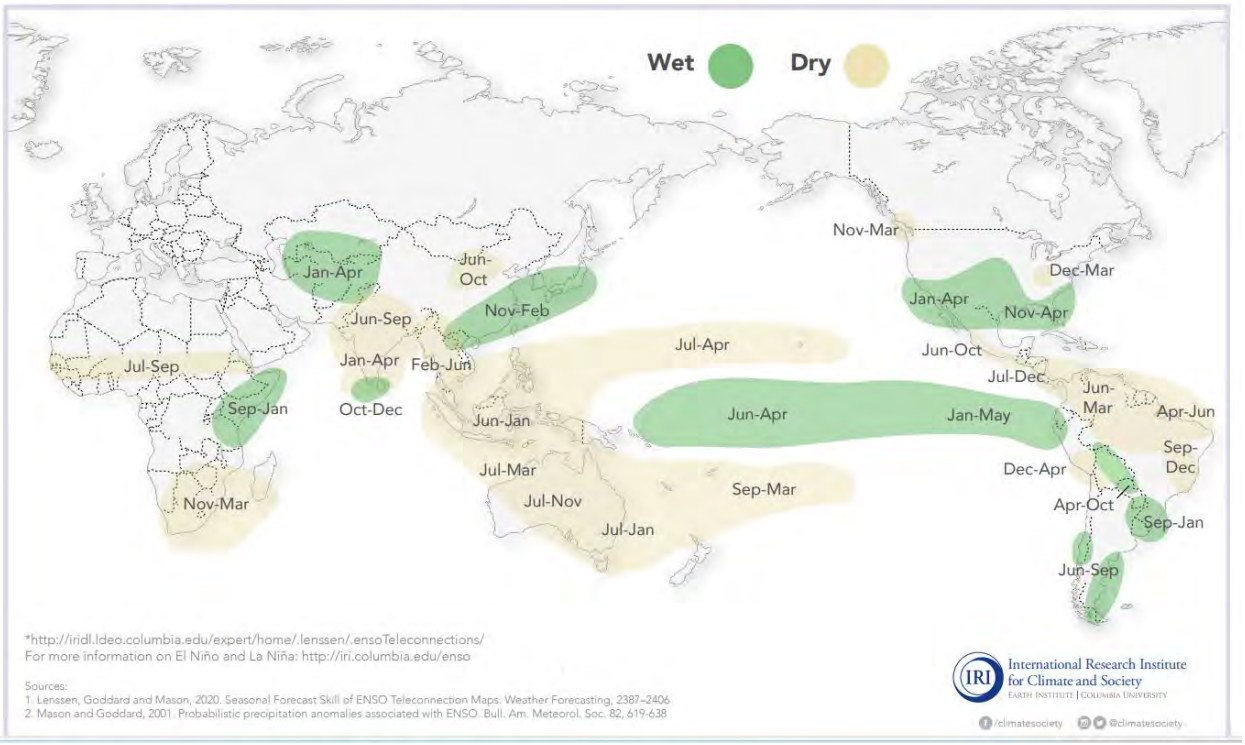

*http://iridl.ldeo.columbia.edu/expert/home/.lenssen/.ensoTeleconnections/
For more information on El Niño and La Niña: http://iri.columbia.edu/enso

Sources:
1. Lenssen, Goddard and Mason, 2020. Seasonal Forecast Skill of ENSO Teleconnection Maps. Weather Forecasting, 2387–2406
2. Mason and Goddard, 2001. Probabilistic precipitation anomalies associated with ENSO. Bull. Am. Meteorol. Soc. 82, 619-638

International Research Institute for Climate and Society
EARTH INSTITUTE | COLUMBIA UNIVERSITY
/climatesociety @climatesociety

La Niña and Rainfall

La Niña conditions in the tropical Pacific are known to shift rainfall patterns in many different parts of the world. The regions and seasons shown on the map below indicate typical but not guaranteed impacts of La Niña. For further information, consult the probabilistic information* that the map is based on.

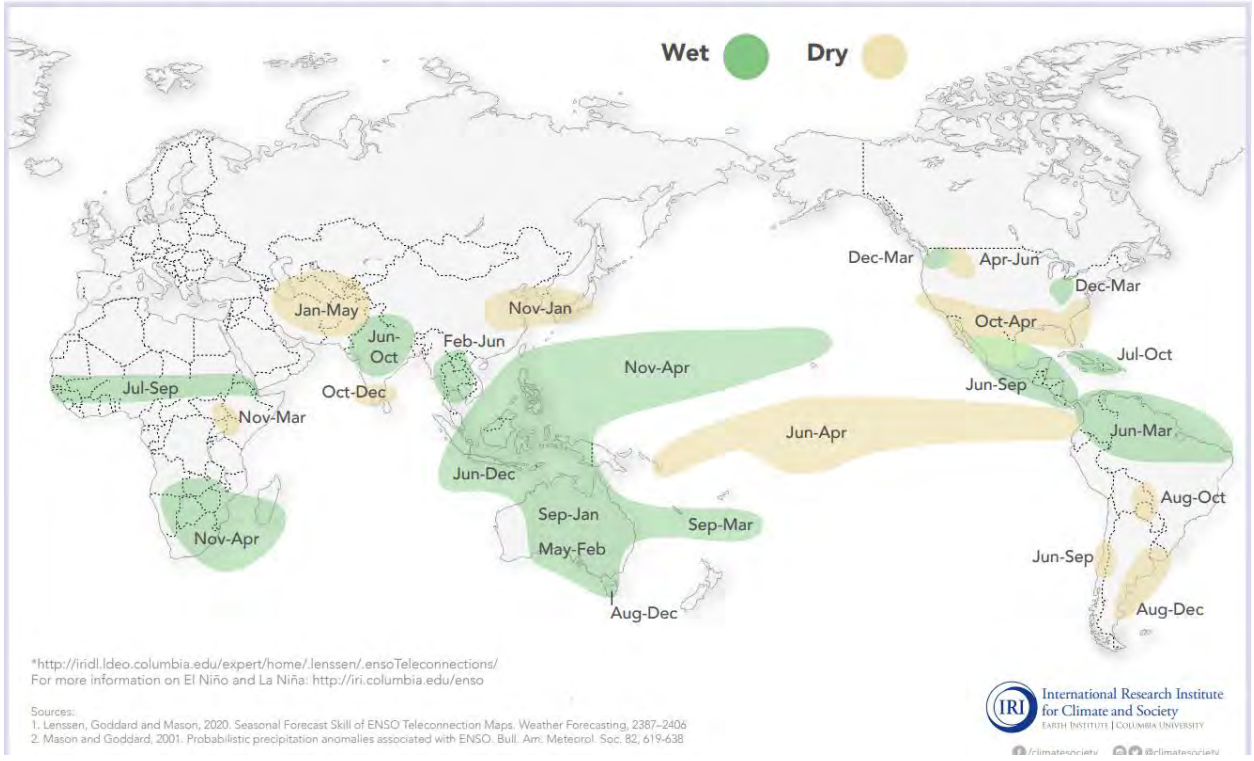

*http://iridl.ldeo.columbia.edu/expert/home/.lenssen/.ensoTeleconnections/
For more information on El Niño and La Niña: http://iri.columbia.edu/enso

Sources:
1. Lenssen, Goddard and Mason, 2020. Seasonal Forecast Skill of ENSO Teleconnection Maps. Weather Forecasting, 2387–2406
2. Mason and Goddard, 2001. Probabilistic precipitation anomalies associated with ENSO. Bull. Am. Meteorol. Soc. 82, 619-638

International Research Institute for Climate and Society
EARTH INSTITUTE | COLUMBIA UNIVERSITY

Warm (El Niño/Southern Oscillation - ENSO) Episodes in the Tropical Pacific

Near the end of each calendar year ocean surface temperatures warm along the coasts of Ecuador and northern Peru. Local residents referred to this seasonal warming as "El Ni&#65533;o", meaning The Child, due to its appearance around the Christmas season. Every two to seven years a much stronger warming appears, which is often accompanied by beneficial rainfall in the arid coastal regions of these two countries. Over time the term "El Ni&#65533;o" began to be used in reference to these major warm episodes.

El Ni&#65533;o is closely related to a global atmospheric oscillation known as the Southern Oscillation (SO). During El Ni&#65533;o episodes lower than normal pressure is observed over the eastern tropical Pacific and higher than normal pressure is found over Indonesia and northern Australia. This pattern of pressure is associated with weaker than normal near-surface equatorial easterly (east-to-west) winds. These features characterize the warm phase of the SO, which is often referred to as an El Ni&#65533;o/Southern Oscillation (ENSO) episode.

During warm (ENSO) episodes the normal patterns of tropical precipitation and atmospheric circulation become disrupted. The abnormally warm waters in the equatorial central and eastern Pacific give rise to enhanced cloudiness and rainfall in that region, especially during the boreal winter and spring seasons. At the same time, rainfall is reduced over Indonesia, Malaysia and northern Australia. Thus, the normal Walker Circulation during winter and spring, which features rising air, cloudiness and rainfall over the region of Indonesia and the western Pacific, and sinking air over the equatorial eastern Pacific, becomes weaker than normal, and for strong warm episodes it may actually reverse.

The increased heating of the tropical atmosphere over the central and eastern Pacific during warm episodes, affects atmospheric circulation features, such as the jet streams in the subtropics and in the temperate latitudes of the winter hemisphere. The jet streams over the eastern Pacific Ocean are stronger than normal during warm episodes (see seasonal atmospheric circulation features). Also, during warm episodes extratropical storms and frontal systems follow paths that are significantly different from normal, resulting in persistent temperature and precipitation anomalies in many regions.

By studying past warm episodes scientists have discovered precipitation and temperature anomaly patterns that are highly consistent from one episode to another. Significant departures from normal are shown in the accompanying figures for the Northern Hemisphere winter and summer seasons. Within the tropics, the eastward shift of thunderstorm activity from Indonesia into the central Pacific during warm episodes results in abnormally dry conditions over northern Australia, Indonesia and the Philippines in both seasons. Drier than normal conditions are also observed over southeastern Africa and northern Brazil, during the northern winter season. During the northern summer season, Indian monsoon rainfall tends to be less than normal, especially in northwest India where crops are adversely affected. Wetter than normal conditions during warm episodes are observed along the west coast of tropical South America, and at subtropical latitudes of North America (Gulf Coast) and South America (southern Brazil to central Argentina).

During a warm episode winter, mid-latitude low pressure systems tend to be more vigorous than normal in the region of the eastern North Pacific. These systems pump abnormally warm air into western Canada, Alaska and the extreme northern portion of the contiguous United States. Storms also tend to be more vigorous in the Gulf of Mexico and along the southeast coast of the United States resulting in wetter than normal conditions in that region.

Since anomaly patterns during warm episodes tend to persist for several months, accurate long-range forecasts (1 to 3 seasons) are possible for the regions shown in the accompanying figures. For the latest information on the status of El Ni&#65533;o, go to ENSO Advisory (issued when appropriate) or the latest monthly Climate Diagnostics Bulletin.

More technical information on the global patterns of abnormal precipitation and temperature related to warm episodes in the tropical Pacific can be found in Ropelewski and Halpert (1987, *Mon. Wea. Rev.*, **115**, 1606-1626), and Halpert and Ropelewski (1992, *J. Climate*, **5**, 577-593). A general description of a warm (ENSO) episode and its composite evolution can be found in Rasmusson and Carpenter (1982, *Mon. Wea. Rev.*, **110**, 517-528). Upper-tropospheric circulation features that accompany extreme phases of the Southern Oscillation are discussed in a paper by Arkin (1982, *Mon. Wea. Rev.*, **110**, 1393-1404).

Cold (La Niña) Episodes in the Tropical Pacific

At times ocean surface temperatures in the equatorial Pacific are colder than normal. These cold episodes, sometimes referred to as La Niña episodes, are characterized by lower than normal pressure over Indonesia and northern Australia and higher than normal pressure over the eastern tropical Pacific. This pressure pattern is associated with enhanced near-surface equatorial easterly winds over the central and eastern equatorial Pacific.

During cold (La Niña) episodes the normal patterns of tropical precipitation and atmospheric circulation become disrupted. The abnormally cold waters in the equatorial central give rise to suppressed cloudiness and rainfall in that region, especially during the Northern Hemispherel **winter** and **spring** seasons. At the same time, rainfall is enhanced over Indonesia, Malaysia and northern Australia. Thus, the normal Walker Circulation during **winter** and **spring**, which features rising air, cloudiness and rainfall over the region of Indonesia and the western Pacific, and sinking air over the equatorial eastern Pacific, becomes stronger than normal.

By studying past cold episodes scientists have discovered precipitation and temperature anomaly patterns that are highly consistent from one episode to another. Significant departures from normal are shown in the accompanying figures for the Northern Hemisphere winter and summer seasons. During **cold episodes**, the colder than normal ocean temperatures in the equatorial central Pacific act to inhibit the formation of rain-producing clouds over that region. Wetter than normal conditions develop farther west over northern Australia, Indonesia and Malaysia, during the northern winter, and over the Philippines during the northern summer. Wetter than normal conditions are also observed over southeastern Africa and northern Brazil, during the northern winter season. During the northern summer season, the Indian monsoon rainfall tends to be greater than normal, especially in northwest India. Drier than normal conditions during **cold episodes** are observed along the west coast of tropical South America, and at subtropical latitudes of North America (Gulf Coast) and South America (southern Brazil to central Argentina) during their respective winter seasons.

Mid-latitude low pressure systems tend to be weaker than normal in the region of the Gulf of Alaska, during a **cold episode** winter. This favors the build-up of colder than normal air over Alaska and western Canada, which often penetrates into the northern Great Plains and the western United States. The southeastern United States, on the other hand, becomes warmer and drier than normal.

Since anomaly patterns during cold episodes tend to persist for several months, accurate long-range forecasts (1 to 3 seasons) are possible for the regions shown in the accompanying figures. For the latest information on the status of La Niña, go to ENSO Advisory (issued when appropriate) or the latest monthly Climate Diagnostics Bulletin.

More technical information on the global patterns of abnormal precipitation and temperature related to cold episodes in the tropical Pacific can be found in Ropelewski and Halpert (1989, *J. Climate*, **2**, 268-284), and Halpert and Ropelewski (1992, *J. Climate*, **5**, 577-593).

62. Assignment 2, Module 14: ENSO and AMO Impact on Atlantic Hurricanes: https://journals.ametsoc.org/view/journals/clim/27/14/jcli-d-13-00687.1.xml#:~:text=The%20impact%20of%20concurrent%20strong%20phases%20of%20the,TCs%20is%20evaluated%20with%20a%20genesis%20potential%20index.

The Impact of the El Niño–Southern Oscillation and Atlantic Meridional Mode on Seasonal Atlantic Tropical Cyclone Activity

CHRISTINA M. PATRICOLA AND R. SARAVANAN

Department of Atmospheric Sciences, Texas A&M University, College Station, Texas

PING CHANG

Department of Oceanography, and Department of Atmospheric Sciences, Texas A&M University, College Station, Texas, and Physical Oceanography Laboratory/Qingdao Collaborative Innovation Center of Marine Science and Technology, Ocean University of China, Qingdao, China

(Manuscript received 11 November 2013, in final form 13 March 2014)

ABSTRACT

Atlantic tropical cyclone (TC) activity is influenced by interannual tropical Pacific sea surface temperature (SST) variability characterized by the El Niño–Southern Oscillation (ENSO), as well as interannual-to-decadal variability in the interhemispheric gradient in tropical Atlantic SST characterized by the Atlantic meridional mode (AMM). Individually, the negative AMM phase (cool northern and warm southern tropical Atlantic SST anomalies) and El Niño each inhibit Atlantic TCs, and vice versa. The impact of concurrent strong phases of the ENSO and AMM on Atlantic TC activity is investigated. The response of the atmospheric environment relevant for TCs is evaluated with a genesis potential index.

Composites of observed accumulated cyclone energy (ACE) suggest that ENSO and AMM can amplify or dampen the influence of one another on Atlantic TCs. To support the observational analysis, numerical simulations are performed using a 27-km resolution regional climate model. The control simulation uses observed SST and lateral boundary conditions (LBCs) of 1980–2000, and perturbed experiments are forced with ENSO phases through LBCs and eastern tropical Pacific SST and AMM phases through Atlantic SST.

Simultaneous strong El Niño and strongly positive AMM, as well as strong concurrent La Niña and negative AMM, produce near-average Atlantic ACE suggesting compensation between the two influences, consistent with the observational analysis. Strong La Niña and strongly positive AMM together produce extremely intense Atlantic TC activity, supported largely by above average midtropospheric humidity, while strong El Niño and negative AMM together are not necessary conditions for significantly reduced Atlantic tropical cyclone activity.

1. Introduction

Interannual variability in tropical Pacific sea surface temperature (SST) characterized by the El Niño–Southern Oscillation (ENSO) strongly influences Atlantic tropical cyclone (TC) activity by inducing changes in tropospheric vertical wind shear (Gray 1984; Goldenberg and Shapiro 1996) and upper tropospheric temperatures (Tang and Neelin 2004) in the tropical Atlantic. Atlantic TC activity is also influenced by modes of Atlantic climate variability, including the interannual-to-decadal Atlantic meridional mode (AMM) (Vimont and Kossin 2007; Kossin and Vimont 2007), which describes the meridional gradient between northern and southern tropical Atlantic SST (Chang et al. 1997; Servain et al. 1999; Chiang and Vimont 2004), and the Atlantic multidecadal oscillation (AMO) (Landsea et al. 1999; Goldenberg et al. 2001; Vitart and Anderson 2001), which describes North Atlantic SST variability.

Different phases of the AMO can dampen or amplify the effect of ENSO on Atlantic TC activity on multi-decadal time scales (Bell and Chelliah 2006). Similarly ENSO and AMO together provide a more complete

Corresponding author address: Christina M. Patricola, Department of Atmospheric Sciences, Texas A&M University, 3150 TAMU, College Station, TX 77843.
E-mail: cmd58@cornell.edu

explanation of TC variability in the Caribbean region than the individual climate modes do (Klotzbach 2011). On interannual to decadal time scales, the AMM exhibits strong correlations with Atlantic TC activity and explains twice as much variance compared with local SST in the TC development region (Vimont and Kossin 2007). This work focuses on how interferences between interannual tropical Pacific (ENSO) and Atlantic (AMM) climate modes influence tropical cyclone variability in the Atlantic basin.

The objective of this study is to address the following questions. What is the impact of concurrent extreme phases of ENSO and AMM on seasonal Atlantic TC activity, and how do various phases of ENSO and AMM together shape the atmospheric environment for Atlantic TCs? In the next section we review observed relationships between ENSO and Atlantic TC activity, and AMM and Atlantic TC activity, followed by a description of the data and methodology used in this study. The questions posed above are then investigated by analyzing composites of observed Atlantic TC activity according to ENSO and AMM phases. We also evaluate Atlantic TC activity during rare extreme events that are conceivably absent from the data record due to its brevity by forcing a regional climate model with constructed pairs of strong ENSO and AMM phases.

2. Background

Proper guidance for informed seasonal and climate change projections of Atlantic tropical cyclone activity relies on a solid understanding of how prominent modes of climate variability influence TC activity; one such dominant interannual mode in the tropical Pacific, the El Niño–Southern Oscillation, has been widely studied in the context of Atlantic TC variability. Tropical Pacific SST variations associated with ENSO drive changes in the upper tropospheric circulation of the tropical Atlantic through the Walker circulation (Arkin 1982). During El Niño, warmer than average eastern tropical Pacific SST suppresses Atlantic TCs by shifting convection in the tropical Pacific eastward and enhancing upper tropospheric westerly winds and vertical wind shear over the tropical Atlantic (Gray 1984; Goldenberg and Shapiro 1996; Zhu et al. 2012). High values of tropospheric vertical wind shear suppress tropical cyclones (Tuleya and Kurihara 1981; Frank and Ritchie 2001; Wong and Chan 2004), with a threshold of about 7.5–10 $m\,s^{-1}$ above which TCs are largely inhibited (Zehr 1992; DeMaria et al. 1993). El Niño also inhibits Atlantic TC activity through warm upper tropospheric temperature anomalies (Tang and Neelin 2004). Likewise, cool eastern tropical Pacific SST anomalies during La Niña support strong Atlantic TC activity through reduced vertical wind shear and cooler than average upper tropospheric temperatures in the tropical Atlantic.

ENSO has a profound influence on Atlantic TC landfall over the United States, with a probability of one or more major hurricanes striking the U.S. coast of 23% during El Niño compared to 63% during La Niña, based on the 1900–97 period (Bove et al. 1998). Similarly, U.S. hurricane damage is 20 times greater during La Niña than El Niño years (Pielke and Landsea 1999), and during the 1900–2005 period La Niña significantly increased the probability of hurricanes making landfall on the U.S. East Coast, with minimal changes in landfall frequency along the Gulf of Mexico or Florida (Smith et al. 2007). Owing to the relatively small sample size (about a century) of the data, it is possible for these estimates to change as the record of ENSO and TC activity grows.

Along with interannual variations in tropical Pacific SST, interannual-to-multidecadal Atlantic SST variability strongly affects Atlantic TCs, with warmer North Atlantic SST supporting enhanced TC activity (Emanuel 2005; Webster et al. 2005; Vimont and Kossin 2007; Klotzbach and Gray 2008) through changes in the local boundary layer and tropospheric vertical wind shear in the Atlantic main development region (MDR) (Landsea et al. 1999; Goldenberg et al. 2001; Vitart and Anderson 2001). Two prominent modes of climate variability expressed through Atlantic SST include 1) the Atlantic multidecadal oscillation, which describes multidecadal North Atlantic SST variations and 2) the Atlantic meridional mode (Chiang and Vimont 2004), or the "dipole mode" (Chang et al. 1997; Servain et al. 1999), which characterizes interannual to decadal variations in the cross-equatorial gradient between Northern and Southern Hemisphere tropical Atlantic SST. Both the AMO and AMM encompass the Atlantic main development region; in addition, the AMO includes the remote subtropical and midlatitude North Atlantic, while the AMM includes the remote southern tropical Atlantic. The AMM is a coupled ocean–atmosphere mode that can be generated by external forcings such as ENSO and the North Atlantic Oscillation and is supported by a positive wind–evaporation–SST (WES) feedback (Curtis and Hastenrath 1995; Nobre and Shukla 1996; Chang et al. 1997; Xie and Tanimoto 1998; Giannini et al. 2000).

Recently, Vimont and Kossin (2007) demonstrated a strong positive relationship on both the interannual and decadal time scales between Atlantic TC activity and tropical Atlantic SST characterized by the AMM. Several conclusions arise from that study with significant bearing on the way we think about Atlantic TC variability: 1) Atlantic TC activity is correlated more

strongly with the AMM than with the AMO, 2) the AMM explains twice as much variance in Atlantic TC activity compared with local SST in the MDR/northern tropical Atlantic, and 3) the AMM influences several environmental factors that cooperate in their impact on Atlantic TCs, including thermodynamic (static stability) and dynamic (vertical wind shear and low-level vorticity) variables. Modeling experiments with prescribed SST forcings provide evidence that the vertical wind shear and air temperature and moisture anomalies correlated with the AMM in observations are indeed caused by the AMM (Smirnov and Vimont 2011). The AMM is also positively correlated with the frequency of African easterly waves (Belanger et al. 2014), which may further contribute to its influence on Atlantic TC activity through the number of TC "seeds" (Avila 1991; Landsea 1993). These studies suggest that the conventional perspective of considering North Atlantic SST and/or local SST in the northern tropical Atlantic (i.e., the MDR) should be refined to focus on the cross-equatorial SST gradient, which depends on both northern and southern tropical Atlantic SST, and that the AMM may be more useful than the AMO in understanding the Atlantic's influence on tropical cyclones on both interannual to decadal time scales; for these reasons we focus on the AMM, rather than the AMO, in this study.

The importance of both tropical Atlantic and Pacific SST variability in controlling Atlantic TC activity spurs the questions: what is the impact of concurrent phases of ENSO and AMM on seasonal Atlantic TC activity, and how do ENSO and AMM together shape the atmospheric environment for Atlantic TCs? Bell and Chelliah (2006) demonstrated that the AMO can dampen or amplify ENSO's influence during hurricane seasons and suggest that both modes together offer a more comprehensive understanding of seasonal Atlantic TC variability compared to considering only ENSO. Similarly, ENSO and AMO in combination provide a more complete explanation of Caribbean TC variability, with La Niña and positive AMO together producing 14 times more major hurricanes than El Niño with negative AMO during the 1900–2008 period (Klotzbach 2011). Both aforementioned studies motivate applying this perspective to understanding seasonal TC activity in the entire North Atlantic.

Of additional interest is how Atlantic tropical cyclone activity responds to *extreme* AMM and ENSO phases, cases which may be missing from the short observational record simply because they are relatively rare. The importance of this question is highlighted by the most active Atlantic hurricane season on record, the destructive season of 2005, which occurred during an extremely positive AMM and neutral ENSO. Although predictions released in August 2005 by both the National Oceanic and Atmospheric Administration (Bell et al. 2005) and the team of W. M. Gray at Colorado State University (Gray and Klotzbach 2005) called for one of the most active hurricane seasons on record, both underpredicted the number of tropical storms and hurricanes. In addition, the midseason forecast by NOAA predicted a seasonal accumulated cyclone energy (ACE) (Bell et al. 2000), which is defined as the sum of the squares of the 6-hourly maximum sustained wind speed throughout the life of a tropical cyclone, of 158–236 ($\times 10^4$ kt^2) (180%–270% of the median), noting that the primary uncertainty was not whether the season would be above normal, but by how much; the observed ACE exceeded the upper range of the prediction at 250 ($\times 10^4$ kt^2). Understanding how Atlantic TC activity responds to extreme tropical climate variability by using model simulations to fill gaps in the data record, as discussed in section 6, can help improve challenging forecasts like that of the 2005 Atlantic hurricane season for which there are few, if any, similar observed cases.

While this study focuses on the influence of phases of AMM and ENSO on Atlantic TC activity, we emphasize the significance of factors other than Atlantic and Pacific SST variability in shaping Atlantic hurricane seasons. For example, despite similar favorable tropical Pacific and Atlantic SST conditions (positive AMM and neutral ENSO) during the 2005 and 2013 Atlantic hurricane seasons, there was a stark difference in the TC activity between the two, with an extremely high ACE of 250 in 2005, but a well below average ACE of about 35 in 2013. The inactive 2013 Atlantic hurricane season, having been linked to anomalously dry conditions in the midtroposphere, midtropospheric subsidence, and a stronger-than-normal trade wind inversion (Klotzbach and Gray 2013), highlights the importance of factors besides AMM and ENSO.

3. Data and methodology

The following subsections describe the observational datasets, climate indices, regional model and simulations, and diagnostic tools that are used in this study.

a. Observational data and climate indices

Observations of seasonal Atlantic accumulated cyclone energy and tropical cyclone, hurricane, and major hurricane frequency are from the revised Hurricane Database (HURDAT2) (Landsea and Franklin 2013), which is updated from HURDAT (Landsea et al. 2004). The HURDAT2 contains information from the "best tracks" of the National Hurricane Center (NHC),

a component of the National Centers for Environmental Prediction (NCEP), including 6-hourly tropical and subtropical cyclone intensity, central pressure, position, and size from 1851 to present for the Atlantic and eastern North Pacific basins. Data are available from the Atlantic Oceanographic and Meteorological Laboratory (AOML)/National Oceanic and Atmospheric Administration (NOAA) Hurricane Research Division (HRD) and from the NHC.

The Atlantic meridional mode is defined as the leading mode of the maximum covariance analysis (MCA) applied to SST and the 10-m wind vector in the tropical Atlantic (21°S–32°N, 74°W–15°E) with a measure of ENSO variability removed as in Chiang and Vimont (2004). For a detailed description of the procedure by which the AMM is calculated, we refer the reader to Chiang and Vimont (2004). The AMM index used in this study is the time series produced by projecting SST from the NCEP–National Center for Atmospheric Research (NCAR) reanalysis (Kalnay et al. 1996) onto the spatial structure of the MCA mode 1, and is calculated by D. J. Vimont at the University of Wisconsin–Madison and provided by the NOAA Earth System Research Laboratory (ESRL).

ENSO variability is represented by the Niño-3.4 index of the NOAA Climate Prediction Center (CPC), calculated as the area average of eastern-central equatorial Pacific (5°S–5°N, 170°–120°W) monthly SST from the Extended Reconstructed Sea Surface Temperature (ERSST.v3b) dataset (Smith et al. 2008). We express the Niño-3.4 index in terms of anomalies by subtracting the 1950–79 monthly climatology from the Niño-3.4 index. The results here are insensitive to the chosen base period since our focus is primarily on percentiles of the index.

b. Regional climate model and simulations

Numerical experiments designed to augment the observational analysis are conducted with the Weather Research and Forecasting Model (WRF) (Skamarock et al. 2008) version 3.3, which is developed and maintained by NCAR. WRF is a nonhydrostatic terrain-following model, and the following physical parameterizations [described in chapter 8 of Skamarock et al. (2008)] are used: the Kain–Fritsch cumulus, Lin et al. microphysics, the Rapid Radiative Transfer Model for general circulation models (RRTMG) longwave radiation, Goddard shortwave radiation, Yonsei University (YSU) planetary boundary layer using a Monin–Obukhov surface scheme, and the Noah land surface model. WRF is configured with a horizontal resolution of 27 km and 28 levels in the vertical reaching to 50 hPa on a domain (Fig. 1) covering the Atlantic sector. The model time step is 90 s, and output is saved every 6 h.

Initial and lateral boundary conditions are prescribed from the 6-hourly 2.5° × 2.5° NCEP–U.S. Department of Energy (DOE) Atmospheric Model Intercomparison Project II (AMIP-II) Reanalysis (NCEP-2) (Kanamitsu et al. 2002). SST and sea ice are based on the monthly 1.0° × 1.0° Hadley Centre Global Sea Ice and Sea Surface Temperature dataset (HadISST) (Rayner et al. 2003).

The 21-yr control integration (Table 1) is initialized on 15 January 1980 and run through 31 December 2000, and is named "year"-e1 corresponding to each of 21 years. Additional simulations for the 1987 (1987-e2 and 1987-e3) and 1999 (1999-e2 and 1999-e3) Atlantic hurricane seasons are run by initializing the model with NCEP-2 during March of the corresponding year (Table 1). For example, the initial conditions of the 1987-e2 and 1987-e3 simulations are taken from NCEP-2 on 29 and 30 March 1987, respectively. The first month of each simulation is disregarded as model spinup.

Much of the control simulation setup follows the protocol of the coordinated experiments of the U.S. Climate Variability and Predictability Program (CLIVAR) Hurricane Working Group, specifically the "interannual" experiment (U.S. CLIVAR 2011). This includes the SST and sea ice forcings, annually updating observed greenhouse gas forcings (e.g., CO_2, CH_4, N_2O, CFC-11, and CFC-12), and integration period.

Four perturbed sets of experiments (Table 1) are conducted to investigate the role of extreme ENSO and AMM phases on Atlantic TC activity. ENSO forcing is prescribed through Pacific SST and, since the western domain edge transects the eastern Pacific (Fig. 1), the lateral boundary conditions (LBCs), while prescribed Atlantic SST represents the AMM forcing. The forcings for each strong climate mode phase are based on an observed case when the August–October (ASO) averaged index representing that phase was less than the 15th or exceeded the 85th percentile over the ASO averaged 1950–2012 period. ENSO is represented by the Niño-3.4 index and AMM by the AMM index as described in section 3a. The ASO average is chosen since it is the peak of the Atlantic hurricane season.

By designing the experiments this way, Pacific SST and LBCs of 1987 and 1999 are chosen to represent a strong El Niño and La Niña, respectively, while strongly positive, moderately positive, neutral, and strongly negative AMM are represented by Atlantic SST of 2005, 1999, 1987, and 1984, respectively. Experiments are named by the following convention: "[year of ENSO case]_[year of AMM case]Atl-e[ensemble number]." For example, the first ensemble member of the strong La Niña and strongly positive AMM experiment is called "1999_2005Atl-e1." Initial conditions for each

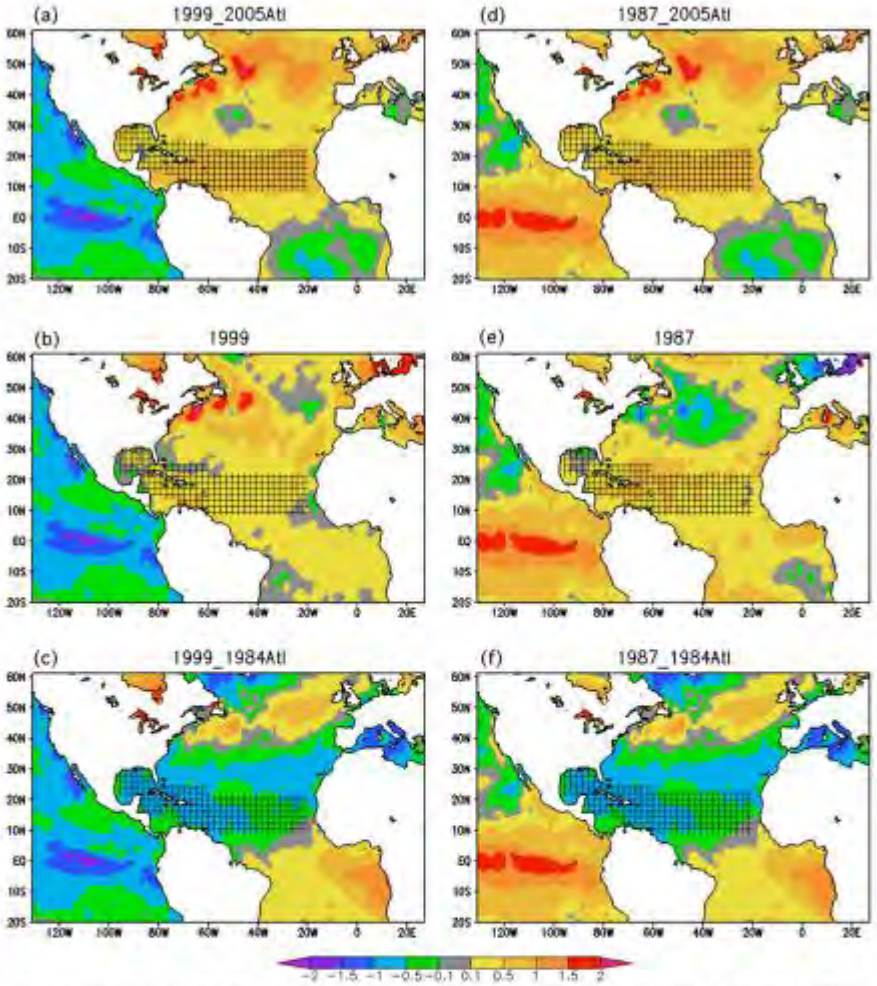

FIG. 1. Prescribed SST (K) forcing averaged over August–October (ASO), as a departure from the ASO 1980–2000 mean, for the (a) 1999_2005Atl, (b) 1999, (c) 1999_1984Atl, (d) 1987_2005Atl, (e) 1987, and (f) 1987_1984Atl simulations on the regional model domain. Land is white, and the main development region and Gulf of Mexico are in black hatching.

experiment are taken from either the model state of the control simulation or reanalysis, as in Table 1, and experiments are run through one hurricane season, terminating on 1 December. Throughout the analysis, when an ensemble-averaged quantity is shown, that quantity is similar among the individual ensemble members unless otherwise noted.

The SST forcings prescribed in the regional climate model (RCM) simulations are shown in Fig. 1, averaged over ASO. The relatively cool eastern tropical Pacific SST of 1999 is prescribed in simulations forced with strong La Niña conditions (Figs. 1a–c), while the warmer than average eastern tropical Pacific SST of 1987 is prescribed in simulations forced with a strong El Niño (Figs. 1d–f). A strongly positive AMM is represented by the above average northern and below average southern tropical Atlantic SST of 2005 (Figs. 1a,d), and a strongly negative AMM is forced through the below average northern and above average southern tropical Atlantic SST of 1984 (Figs. 1c,f).

TABLE 1. Regional climate model simulations designed to investigate the response in Atlantic tropical cyclone activity to forcing characteristic of ENSO (column 2) and AMM (column 3).

Simulation	Pacific SST and LBC (ENSO forcing)	Atlantic SST (AMM forcing)	Initial condition (NCEP-2, unless otherwise stated)
"year"-e1, for years 1980–2000	1980–2000/ variable	1980–2000/ variable	15 Jan 1980
1987_1984Atl-e1 through -e3	1987/ El Niño (strong)	1984/ negative (strong)	29 Mar 1987 (model state of 1987-e1), 29 Mar 1987, 30 Mar 1987
1987-e2 and -e3 (control simulation includes 1987-e1)	1987/ El Niño (strong)	1987/ neutral	29 Mar 1987, 30 Mar 1987
1987_2005Atl-e1 through -e3	1987/ El Niño (strong)	2005/ positive (strong)	29 Mar 1987 (model state of 1987-e1), 29 Mar 1987, 30 Mar 1987
1999_1984Atl-e1 through -e3	1999/ La Niña (strong)	1984/ negative (strong)	26 Mar 1999 (model state of 1999-e1), 26 Mar 1999, 27 Mar 1999
1999-e2 and -e3 (control simulation includes 1999-e1)	1999/ La Niña (strong)	1999/ positive (moderate)	26 Mar 1999, 27 Mar 1999
1999_2005Atl-e1 through -e4	1999/ La Niña (strong)	2005/ positive (strong)	26 Mar 1999 (model state of 1999-e1), 26 Mar 1999, 27Mar 1999, 28 Mar 1999

We note that an inconsistency between LBCs and SST is imposed in the model experiments that use prescribed SST forcings characteristic of the AMM. This prevents the atmospheric response to the SST forcing from propagating globally; however, the local response in Atlantic TCs is captured by the experimental design. As discussed in the following sections, the response in TC activity to AMM and ENSO in the model simulations is similar to that in observations, supporting the validity of the experimental design.

The observational record of Atlantic tropical cyclone activity is relatively short, so it is conceivable that the data record does not include rare extreme events that have yet to be observed. Forcing the model with constructed pairs of extreme phases of ENSO and AMM allows us to evaluate potential gaps in the data record. As we force the model with these extreme combinations of ENSO and AMM, we note that central-eastern tropical Pacific SST can be influenced by North Atlantic SST (Wang et al. 2011); in addition, Atlantic SST is not independent of the Pacific and is influenced by ENSO, particularly in the spring (Enfield and Mayer 1997; Klein et al. 1999; Saravanan and Chang 2000; Mo and Häkkinen 2001; Chang et al. 2006). Northern tropical Atlantic SST may also be affected by the North Atlantic Oscillation (Mo and Häkkinen 2001; Czaja et al. 2002), the AMO (Vimont and Kossin 2007), anthropogenic warming, and sulfate and volcanic aerosols (Mann and Emanuel 2006; Dunstone et al. 2013). Therefore, while this may lead to some tendency for preferred ENSO–AMM combinations, it does not preclude the occurrence of each combination. In fact, each ENSO–AMM pair was observed during at least three Atlantic hurricane seasons from 1950 to 2012. This demonstrates that our proposed question is not contrived and further supports the validity of testing each ENSO–AMM combination.

c. *Genesis potential index*

The response in environmental conditions relevant for Atlantic TC activity in association with phases of ENSO and AMM is assessed using the tropical cyclone genesis potential index (GPI) developed by Emanuel and Nolan (2004). The GPI, which builds upon the TC genesis index of Gray (1979), is defined as

$$\mathrm{GPI} = |10^5\eta|^{3/2}\left(\frac{H}{50}\right)^3\left(\frac{V_{\mathrm{pot}}}{70}\right)^3(1+0.1V_{\mathrm{shear}})^{-2}, \qquad (1)$$

where η (s^{-1}) is absolute vorticity at 850 hPa; H (%) is relative humidity at 600 hPa; V_{pot} ($\mathrm{m\,s}^{-1}$) is potential intensity (Emanuel 1995; Bister and Emanuel 1998; Bister and Emanuel 2002), which is a function of SST, sea level pressure, and vertical profiles of atmospheric temperature and specific humidity; and V_{shear} ($\mathrm{m\,s}^{-1}$) is the magnitude of vertical wind shear between 850 and 200 hPa. The GPI is computed from monthly averaged quantities.

To assess the utility of the GPI in understanding environmental conditions important for TC activity, we compare the correlation between various measures of observed seasonal Atlantic TC activity from HURDAT2 and reanalyzed GPI for the 1950–2011 period. GPI is computed from the NCEP–NCAR reanalysis (Kalnay et al. 1996) and averaged over ASO and the MDR (9°–21.5°N, 80°–20°W). The correlations (R) between seasonal reanalyzed GPI and observed number of TCs, number of hurricanes, and ACE are 0.38, 0.56, and 0.60, respectively. These correlations suggest that the GPI is a reasonable measure to better understand several

of the atmospheric conditions that support TC activity as measured by ACE. (We note that, as expected with any diagnostic, GPI does not provide a full explanation of ACE variability.)

4. Influence of ENSO and AMM on Atlantic tropical cyclone activity: Observations

Investigation of the influence of concurrent phases of ENSO and AMM on Atlantic TC activity begins with an analysis of observed seasonal Atlantic accumulated cyclone energy from HURDAT2 (Landsea and Franklin 2013). Figure 2a shows the deviation from the 1950–2012 mean in observed seasonal Atlantic ACE as a function of the percentile of the corresponding observed ASO averaged AMM and Niño-3.4 indices. The ASO average is chosen for the AMM and Niño-3.4 indices since it is the peak of the Atlantic hurricane season. It is clear from Fig. 2a that a large portion of interannual variability in Atlantic tropical cyclone activity is explained by each AMM and ENSO individually, as has been demonstrated in previous studies (e.g., Gray 1984; Goldenberg and Shapiro 1996; Vimont and Kossin 2007); in addition, it is apparent that considering both AMM and ENSO together provides a more complete explanation of seasonal Atlantic ACE than considering the role of either climate mode alone, with the most active seasons tending to occur during La Niña and/or positive AMM, and the least active seasons tending to occur during El Niño and/or negative AMM. Therefore, we create composites of Atlantic ACE according to the ASO averaged AMM and Niño-3.4 indices (Fig. 2b), with the negative and positive phase defined by the 0th–25th and 75th–100th percentiles, respectively, of the ASO average of those indices as denoted by the dashed black lines in Fig. 2a. (The 25th and 75th percentiles of the ASO averaged Niño-3.4 index for the 1950–2012 period are −0.37 and 0.81, respectively. The 25th and 75th percentiles of the ASO averaged AMM index for the 1950–2012 period are −0.96 and 1.49, respectively.) While we focus on the influence of the AMM and ENSO, we note that a portion of variability in seasonal Atlantic ACE is related to other factors [e.g., upper tropospheric temperature variations unrelated to ENSO or AMM, African easterly waves, Saharan dust (Evan et al. 2006), and internal variability], as evident in Fig. 2a.

The composites of observed Atlantic ACE show that there is vital information to be gained by accounting for both ENSO and AMM together (Fig. 2b). On average, the most active Atlantic TC seasons occur during a positive AMM and La Niña together, with ACE of 181, which is 73% more than the 1950–2012 mean of 105. The observed mean ACE during positive AMM and La Niña

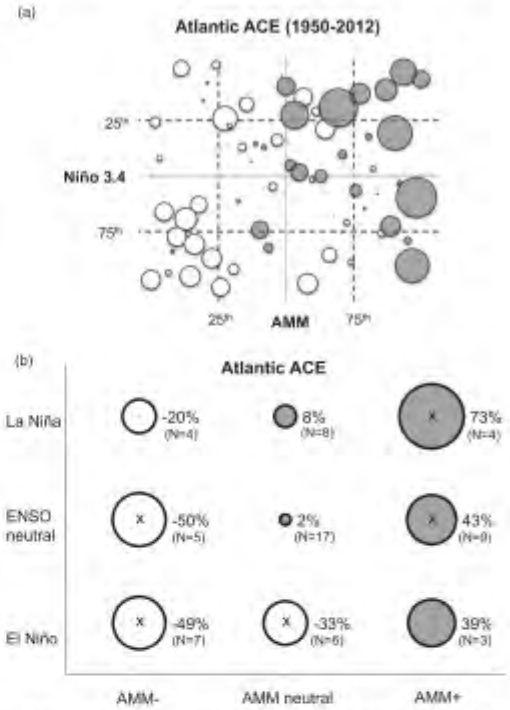

FIG. 2. (a) Deviation from the 1950–2012 mean in observed seasonal Atlantic accumulated cyclone energy (ACE) (10^4 kt^2) from HURDAT2, with the percentile of the observed ASO averaged AMM and Niño-3.4 indices. Deviation in ACE is proportional to the diameter of the circle, with positive shaded gray and negative shaded white. The gray axes represent the 50th percentiles, and the black dashed lines represent the 25th and 75th percentiles, of the ASO averaged AMM and Niño-3.4 indices from 1950 to 2012. (b) Average deviation from the 1950–2012 mean (105×10^4 kt^2) in observed seasonal Atlantic ACE (percent) from HURDAT2 for composites according to the ASO averaged AMM and Niño-3.4 indices. A negative and positive phase is defined by the 0–25th and 75th–100th percentiles, respectively, of the ASO averaged AMM and Niño-3.4 indices during the 1950–2012 period (denoted by the black dashed lines in Fig. 2a). Deviation in ACE is proportional to the diameter of the circle (positive shaded gray) and listed to its right, and the number of occurrences (N) for each ENSO–AMM pair is in parentheses. A mark inside the circle denotes the mean ACE for the given AMM–ENSO pair that is significantly (10% level) different from the mean ACE for the set of all cases not characterized by that AMM–ENSO pair according to a Student's t test. The t test is one-tailed, except for AMM–ENSO pairs with destructive influences on Atlantic tropical cyclones (i.e., positive AMM with positive ENSO, or negative AMM with negative ENSO).

together is significantly (10% level) greater than the mean ACE during the set of all other cases. In addition, concurrent positive AMM and La Niña generally support the greatest number of Atlantic hurricanes (Fig. 3a) and major hurricanes (Fig. 3b) per season. There were

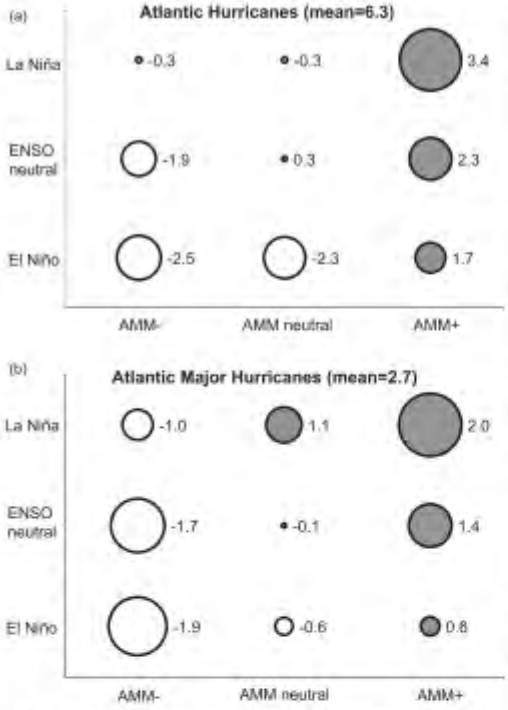

FIG. 3. Average deviation from the 1950–2012 mean in observed number of Atlantic (a) hurricanes and (b) major (category 3, 4, and 5) hurricanes from HURDAT2 for composites according to ASO averaged AMM and Niño-3.4 indices, defined as in Fig. 2b. Deviation is proportional to the diameter of the circle (positive shaded gray) and listed to its right. The 1950–2012 mean is in parentheses.

over 5.5 times more major Atlantic hurricanes per season observed during positive AMM with La Niña compared to concurrent negative AMM and El Niño in the 1950–2012 period, a result that is analogous to the relationship between the number of major hurricanes impacting the Caribbean with AMO and ENSO (Klotzbach 2011). The number of hurricanes that made landfall in the United States during 1950–2012 is also above average during positive AMM with La Niña, although the greatest anomaly occurs during positive AMM with El Niño (not shown). This may be due to the small sample size of a relatively rare event (in comparison to number of Atlantic hurricanes), or differences in preferred TC tracks due to large-scale circulation patterns associated with ENSO and AMM.

The composites of Atlantic ACE also reveal that El Niño alone is not a sufficient condition for weaker than average Atlantic tropical cyclone activity: in fact, when paired with a positive AMM the seasonal activity is on average 39% greater than the mean (Fig. 2b), and the number of Atlantic hurricanes and major hurricanes is greater than the mean (Fig. 3). (We note that the sample sizes for the observationally based composites are generally small, with as few as three observed cases for an AMM and ENSO pair, which motivates the modeling experiments discussed in section 6.) Similarly, La Niña and a negative AMM together support marginally below average (20% less than the mean) Atlantic ACE, suggesting that phases of ENSO and AMM that individually oppose each other in their influence on Atlantic TCs together have a compensating effect. The mean Atlantic ACE during concurrent El Niño and positive AMM, as well as during concurrent La Niña and negative AMM, is not significantly different from the mean ACE during the set of all other ENSO and AMM cases (Fig. 2b). The observational analysis indicates that AMM and ENSO are both primary influences on Atlantic TCs; that is, the AMM does not act as a secondary influence to modulate the impact of ENSO.

Another interesting result from the composites of observed Atlantic ACE is that the weakest Atlantic TC seasons generally do not require the most TC-inhibiting ENSO and AMM conditions together, that is, concurrent El Niño and negative AMM. Atlantic ACE is nearly the same (50% less than the mean) for both negative AMM with El Niño and negative AMM with neutral ENSO (Fig. 2b), and the Atlantic ACE during each of these ENSO and AMM pairs is significantly (10% level) less than the ACE during the set of all cases not characterized by that ENSO and AMM pair. The response in number of Atlantic hurricanes and major hurricanes is similar (Fig. 3), with relatively little difference during negative AMM with either El Niño or neutral ENSO. This suggests that the environmental conditions for TCs are sufficiently poor during concurrent negative AMM and neutral ENSO to effectively reduce Atlantic TC activity.

Although many of the results based on observed Atlantic TC activity presented in this section are statistically significant, the relatively small sample size of 63 seasons and scarcity of observed extreme cases warrant additional investigation using model simulations. The following sections present an evaluation of modeled TCs and an analysis of the influence of extreme AMM and ENSO pairs on simulated Atlantic tropical cyclone activity.

5. Atlantic tropical cyclones in the regional climate model

In this section we examine the ability of the regional climate model to represent the observed climatology

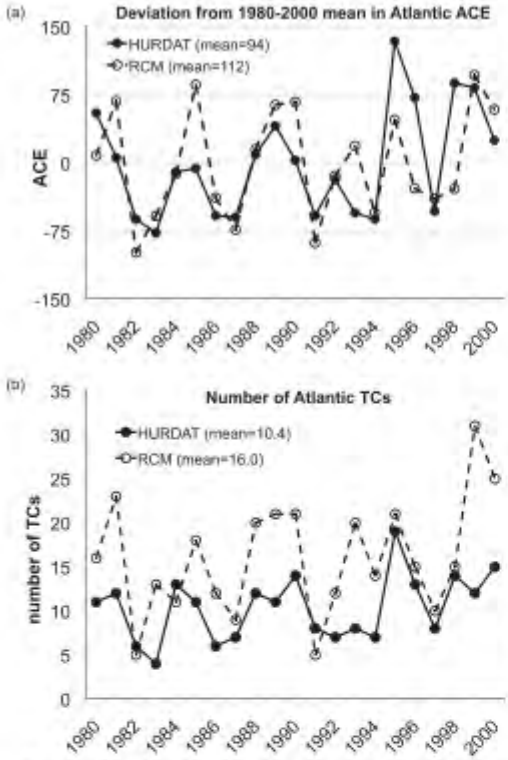

FIG. 4. Time series of (a) deviations from the corresponding 1980–2000 mean (in parentheses) in seasonal ACE (10^4 kt^2) of Atlantic tropical cyclones and (b) seasonal number of Atlantic tropical cyclones, with 1980–2000 mean (in parentheses), from HURDAT2 observations (solid line, closed mark) and the regional climate model control simulation (dashed line, open mark).

and interannual variability of Atlantic tropical cyclones, as well as observed relationships between Atlantic TCs and modes of Atlantic and Pacific climate variability. This is done to demonstrate the model's suitability to study the impacts of ENSO and AMM on Atlantic TC activity.

Tropical cyclones in the RCM are identified according to the tracking algorithm of Walsh (1997), which includes criteria for a minimum 10-m wind speed of 17.5 m s^{-1}, a closed minimum in surface pressure, a minimum 850-hPa vorticity threshold over a 5° by 5° region over the TC center, and a warm core. Additional criteria include a duration threshold of at least 2 days and an origin south of 30°N. We refer to tropical cyclones as including tropical storms and hurricanes.

The RCM reproduces the observed interannual variability of 1980–2000 Atlantic ACE (Fig. 4a, correlation $R = 0.58$) and number of Atlantic TCs (Fig. 4b, correlation $R = 0.59$) fairly well. Two simulations using the Geophysical Fluid Dynamics Laboratory (GFDL) regional model at 18-km resolution produce correlations between observed and simulated ACE ($R = 0.72$ and $R = 0.66$, Knutson et al. 2007) comparable to those from the RCM control simulation. In the context of the GFDL simulations, which employ spectral nudging to reanalysis on the domain interior, the performance of the RCM, which does not use nudging in the domain interior, is relatively good.

TABLE 2. Statistics of Atlantic tropical cyclone seasons over the 1980–2000 period from HURDAT2 observations and the RCM control simulation. Unit of ACE is 10^4 kt^2.

	Observations	RCM	Model control simulation bias
ACE mean	94	112	19%
ACE minimum	17	13	−4 (10^4 kt^2)
ACE 25th percentile	36	73	37 (10^4 kt^2)
ACE median	88	100	12 (10^4 kt^2)
ACE 75th percentile	135	171	36 (10^4 kt^2)
ACE maximum	228	209	−19 (10^4 kt^2)
ACE standard deviation	61	59	−2%
No. of tropical cyclones	10.4	16.0	55%

Tropical cyclone activity is quantified by the seasonal (May–November) total of ACE (Bell et al. 2000, 10^4 kt^2), which is preferentially used for the remainder of the study since it is an integrated measure that accounts for storm strength, number, and duration. Although the classical definition of the Atlantic hurricane season is June–November, we perform the analysis for May–November since the model produces a nonnegligible, but still relatively small, number of tropical cyclones in May.

Statistics of Atlantic ACE and number of Atlantic TCs from the control simulation are compared with observations (Table 2). The RCM simulates a 1980–2000 mean seasonal Atlantic ACE of 112, which is 19% greater than the observed mean of 94; in addition, the simulated median of seasonal ACE also exceeds the observed. While the Atlantic ACE during the most active and inactive seasons is fairly similar between the RCM and observations, there is a positive shift in the simulated distribution of ACE relative to observations, with the 25th and 75th percentiles in the control simulation exceeding those of the observations. Despite the bias in the simulated distribution of seasonal Atlantic TC activity, the simulated standard deviation of ACE is nearly identical to the observed, indicating the RCM reproduces variability in seasonal ACE about the mean well.

TABLE 3. Correlations (R) between seasonal Atlantic ACE of HURDAT2 observations and of the RCM control simulation with climate indices over the 1980–2000 period. All climate indices are averaged over August–October. Correlations that are not statistically significant (10% level) are in parentheses. For quantities prescribed in the model (i.e., the Niño-3.4 index, MDR SST, AMO index, and AMM index), the simulated and observed ACE are correlated with the observed quantities. For variables that are calculated by the model (i.e., wind shear) simulated ACE is correlated with the RCM simulated quantities, and observed ACE is correlated with the reanalyzed (NCEP-2) quantities. The MDR includes 9°–21.5°N, 80°–20°W.

	HURDAT2 Atlantic ACE	RCM Atlantic ACE
Niño-3.4 index	−0.63	−0.59
MDR SST	0.59	0.29
AMO index	0.57	(0.21)
AMM index	0.77	0.44
NCEP-2 or RCM MDR vertical wind shear between 850 and 200 hPa	−0.67	−0.71

The RCM simulates too many Atlantic tropical cyclones, 16.0 per season, compared to the observed 10.4 per season (Table 2). This positive bias in number of TCs contributes to the positive ACE bias; however, the ACE bias (19%) is smaller than expected from the bias in number of TCs (55%) because the model produces too few category 3–5 hurricanes (not shown). This weak bias in TC intensity is expected given that the model horizontal resolution is only 27 km—sufficient to represent general TC dynamics but too coarse to fully resolve complete tropical cyclone dynamics. The spatial distribution of TCs in the control simulation compares fairly well with observations; one exception is an underrepresentation of TCs in "cluster 1" (Fig. 2c of Daloz et al. (2014, manuscript submitted to *J. Climate*), which represents storms that tend to draw energy from a baroclinic environment (Kossin et al. 2010). In association with the underrepresentation of "cluster 1" TCs, there fewer than observed TC landfalls along the east coast of the United States in the control simulation (Fig. 4c of Daloz et al. 2014, manuscript submitted to *J. Climate*).

The RCM reasonably represents observed relationships between Atlantic tropical cyclone activity and Pacific and Atlantic modes of climate variability. The observed correlation between seasonal Atlantic ACE and ASO averaged eastern tropical Pacific SST, represented by the Niño-3.4 index, is $R = -0.63$ during 1980–2000, and the RCM reproduces this well with $R = -0.59$ (Table 3). Observed seasonal Atlantic ACE is positively and significantly correlated with measures of Atlantic SST variability including MDR SST and the AMO and AMM indices (Table 3), with Atlantic ACE most strongly correlated with the AMM index ($R = 0.77$) as in Vimont and Kossin (2007). The RCM simulates positive, but weaker, correlations between Atlantic ACE and these measures of Atlantic SST and, like observations, produces a relationship between Atlantic ACE and the AMM that is stronger than the relationship between ACE and either AMO or MDR SST (Table 3).

Observed relationships between Atlantic tropical cyclone activity and environmental variables important for TCs are also simulated reasonably well in the RCM control simulation (Table 3). Large values of tropospheric vertical wind shear inhibit tropical cyclones (Tuleya and Kurihara 1981; Zehr 1992; DeMaria et al. 1993; Frank and Ritchie 2001; Wong and Chan 2004), and the RCM captures this inverse relationship between ACE and tropospheric vertical wind shear in the MDR, with R of −0.67 in observations and −0.71 in the control simulation.

Based on the evaluation above, we conclude that the RCM is a suitable tool for this study.

6. Influence of ENSO and AMM on Atlantic tropical cyclone activity: RCM simulations

The response in Atlantic ACE to the prescribed ENSO and AMM forcings in the RCM experiments supports the observational analysis, demonstrating that the tropical Pacific and Atlantic climate modes together have a pronounced influence on Atlantic TC activity. This is discussed in detail below, with support from Fig. 5a, which shows seasonal Atlantic ACE from the RCM experiments (Table 1) with the 1980–2000 RCM control mean (112×10^4 kt^2) for reference, and from Fig. 5b, which shows the ensemble average of seasonal Atlantic ACE from the RCM simulations as a percent of the 1980–2000 mean and in terms of the percentile over the 1950–2012 period of the ASO averaged AMM and Niño-3.4 indices that correspond to the prescribed AMM and ENSO forcings.

The response in environmental conditions relevant for Atlantic TC activity due to the ENSO and AMM forcings prescribed in the RCM simulations is also presented below and diagnosed with the GPI (Emanuel and Nolan 2004) described in section 3c. Figure 6 shows the ensemble and ASO averaged GPI as percent deviation from the 1980–2000 ASO mean from the RCM simulations, together with composites according to ENSO and AMM of the ASO averaged GPI as percent deviation from the 1950–2012 ASO mean computed from the NCEP–NCAR reanalysis (Kalnay et al. 1996), averaged over the MDR and Gulf of Mexico (Fig. 1). The GPI computed from reanalysis is composited using the same

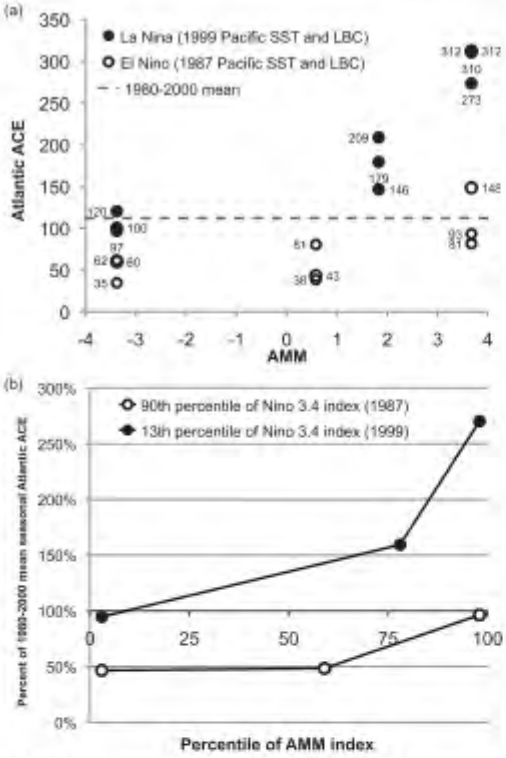

FIG. 5. (a) Seasonal ACE (10^4 kt^2, denoted next to mark) of Atlantic tropical cyclones from RCM simulations forced by the LBCs and Pacific SST of the 1999 La Niña (filled circle) and 1987 El Niño (open circle) and Atlantic SST (corresponding ASO averaged AMM index on the *x* axis), with the RCM 1980–2000 mean Atlantic ACE (dashes). Each mark represents one season-long integration. (b) As in (a), except ACE is expressed as percent of the 1980–2000 mean, the ASO averaged AMM and Niño-3.4 indices are expressed in terms of percentile over the ASO averaged 1950–2012 period, and each mark corresponds to the RCM experiment ensemble average.

procedure as for the HURDAT2 Atlantic ACE (Fig. 2b). The reanalyzed GPI deviations are generally qualitatively similar in the Gulf of Mexico versus the MDR for ENSO/AMM cases that have a relatively strong deviation in GPI; an exception is the El Niño and neutral AMM case, which is characterized by negative GPI anomalies in the MDR and mixed GPI anomalies in the Gulf of Mexico (not shown). We note caution when comparing the GPI between the RCM simulations and reanalysis, since the RCM simulations represent extreme phases of AMM and ENSO, while the composites from reanalysis include all strengths of AMM and ENSO passing a percentile-based threshold.

To estimate the contribution of each atmospheric factor in supporting the response in GPI, the GPI is also calculated by varying each term while keeping the others fixed at their climatological values (Fig. 6), as in Camargo et al. (2007). Note that since the GPI is nonlinear, the sum of the estimated contribution from individual factors does not equal the GPI. This approach is used to provide an estimate of the primary factors that support simulated changes in the GPI.

a. TC limiting conditions: El Niño with neutral or negative AMM

Consistent with the observational analysis, strong El Niño conditions paired with a strongly negative AMM effectively inhibit Atlantic TC activity, with simulated seasonal Atlantic ACE of 35, 60, and 62, compared with the 1980–2000 mean of 112 (Fig. 5a). Under the same El Niño conditions together with a near-neutral AMM, the Atlantic TC activity remains well below average, with seasonal Atlantic ACE of 38, 43, and 81. The ensemble-mean response in Atlantic ACE is nearly equal during the strong (90th percentile) El Niño case paired with Atlantic conditions characterized by an AMM index in both the 0th and 60th percentile (Fig. 5b), supporting the observationally based finding that both unfavorable ENSO and AMM conditions are not required to significantly reduce Atlantic TC activity.

In response to the strong El Niño and near-neutral AMM forcings, the GPI is below average (−13%), with increased vertical wind shear as the largest contributing factor, while the GPI is strongly below average (−55%) due to the strong El Niño and negative AMM forcings, in association with considerable increases in vertical wind shear and decreases in relative humidity and potential intensity (Fig. 6a). It is interesting that although the simulated response in Atlantic ACE is similar due to the concurrent strong El Niño and neutral AMM, and the concurrent strong El Niño and strongly negative AMM forcings (Fig. 5), the reduction in GPI is much larger for the latter than the former. The observational record/reanalysis shows a similar discrepancy between the ACE and GPI, with below average ACE of a similar magnitude for composites according to concurrent El Niño and neutral AMM, as well as El Niño with negative AMM (Fig. 2b), but a negative anomaly in GPI that is much larger for the latter than for the former (Fig. 6b).

This discrepancy between the ACE and GPI may be explained by the threshold response in Atlantic TCs to tropospheric vertical wind shear, with tropical cyclones limited over wind shear of approximately 7.5–10 m s^{-1} (Zehr 1992; DeMaria et al. 1993). While the simulated vertical wind shear between 850 and 200 hPa in the main

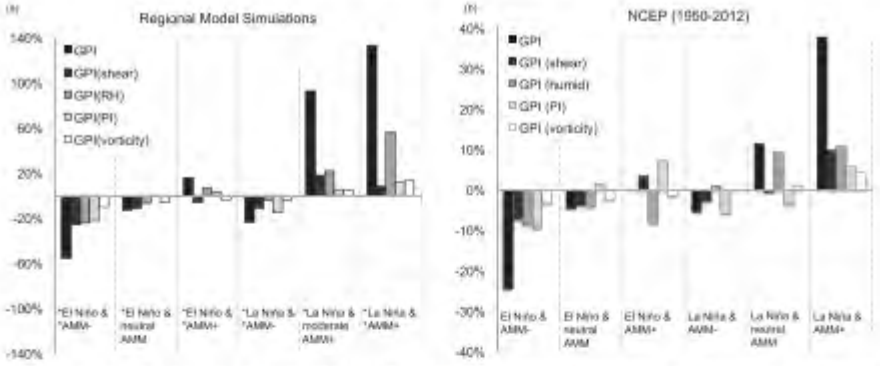

FIG. 6. (a) Percent deviation from the ASO 1980–2000 mean in the ASO averaged GPI index (black) from the ensemble average of the (left to right) 1987_1984Atl, 1987, 1987_2005Atl, 1999_1984Atl, 1999, and 1999_2005Atl RCM simulations. A strong climate mode phase is denoted by an asterisk (*). (b) Composites of percent deviation from the ASO 1950–2012 mean in the ASO averaged GPI index (black) computed from the NCEP–NCAR reanalysis for observed cases of concurrent (left to right) El Niño with negative, neutral, and positive AMM, and La Niña with negative, neutral, and positive AMM. Composites are defined as in Fig. 2b. Also shown are the same values as above, but calculated by varying each term while setting the others fixed at their climatological values, for 850–200-hPa vertical wind shear (dark gray), 600-hPa relative humidity (medium gray), potential intensity (light gray), and 850-hPa vorticity (white). GPI deviations are averaged over the main development region and Gulf of Mexico (hatching in Fig. 1), and positive indicates conditions for tropical cyclones that are more favorable than average.

development region and Gulf of Mexico is stronger than average due to imposed strong El Niño and neutral AMM conditions (Fig. 7a), and much stronger than average in response to strong El Niño and negative AMM (Fig. 7b), the absolute vertical wind shear exceeds $10\,m\,s^{-1}$ over most of the Atlantic TC development region in response to both sets of conditions (Figs. 7d,e). This suggests that concurrent strong El Niño and neutral AMM are sufficiently limiting for Atlantic tropical cyclone development due to the threshold response in TCs to vertical wind shear; this threshold dependence on vertical wind shear is not included in the GPI, which explains the discrepancy between the ACE and GPI in both the simulations and observations/reanalysis. For comparison, the vertical wind shear is below the $10\,m\,s^{-1}$ threshold over most of the Atlantic TC development region in response to strong La Niña and moderately positive AMM forcings (Fig. 7f) in association with below average vertical wind shear (Fig. 7c); this permits active tropical cyclone seasons that are also strongly influenced by midtropospheric moisture, as discussed in section 6c.

Reductions in GPI in response to the strong concurrent El Niño and negative AMM forcings are strongest in the western portion of the northern tropical Atlantic, as shown in Fig. 8a, which displays the deviation from the ASO 1980–2000 mean in ASO averaged GPI from the ensemble average of the 1987_1984Atl experiments. In addition, the simulated reduction in GPI is accompanied by a vast reduction in the region of favorable development for Atlantic tropical cyclones, as shown by the contours of Fig. 8a, which denote the ASO averaged GPI value of 0.5 from the 1980–2000 mean and experiment. The value 0.5 is chosen as an example to demonstrate how the spatial pattern of favorable conditions for TCs changes in response to the AMM and ENSO forcings, with regions east of the 0.5 contour relatively unfavorable and west of the 0.5 contour relatively favorable. The relatively favorable environment for TCs is confined to the Gulf of Mexico and northwestern portion of the tropical Atlantic (Fig. 8a), similar to the observed northwest shift in TC genesis during the negative AMM phase relative to the positive phase (Kossin and Vimont 2007).

b. *Destructive interferences: El Niño with positive AMM, La Niña with negative AMM*

In response to strong simultaneous El Niño and positive AMM, the RCM produces a near-average ensemble mean Atlantic ACE of 107 (ACE of 81, 93, and 148 in individual seasons) compared to the simulated control mean of 112 (Fig. 5a). Atlantic TC activity is also near average (ACE of 97, 100, and 120) in response to strong La Niña with strongly negative AMM (Fig. 5a). These RCM experiments support the observational analysis, which indicates that modes of tropical Atlantic and

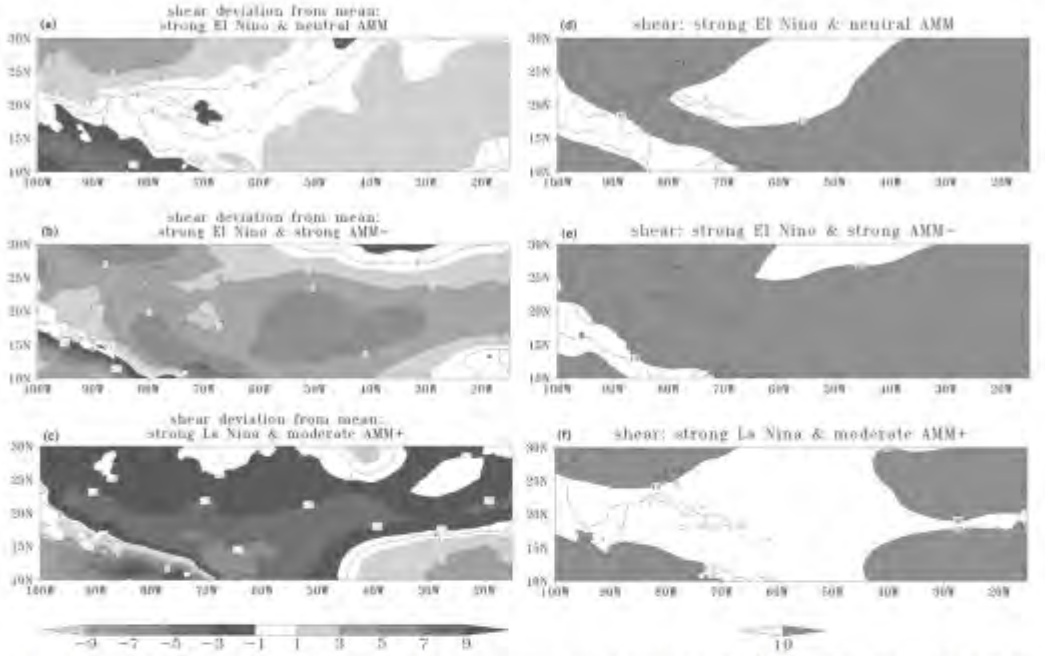

FIG. 7. Deviation from the ASO 1980–2000 mean in the ASO averaged vertical wind shear ($m\,s^{-1}$) between 850 and 200 hPa from the ensemble average of the (a) 1987, (b) 1987_1984atl, and (c) 1999 simulations; bold contour is $0\,m\,s^{-1}$. Magnitude of the vertical wind shear ($m\,s^{-1}$) between 850 and 200 hPa from the ensemble average of the (d) 1987, (e) 1987_1984atl, and (f) 1999 simulations; contour is $10\,m\,s^{-1}$ and white denotes favorable vertical wind shear for tropical cyclones.

Pacific SST variability individually opposing each other in their influence on Atlantic TCs together produce compensating effects, resulting in insignificant deviations from the mean in Atlantic TC activity.

The idea that the influences on the atmospheric environment of simultaneous La Niña and negative AMM, and simultaneous El Niño and positive AMM, compensate each other is supported by the simulated and reanalyzed GPI. In both the 1999_1984Atl and 1987_2005Atl RCM experiments, the GPI is near average or weakly deviates from the mean (±20%) in association with near-average contributions from each of tropospheric vertical wind shear, 600-hPa relative humidity, potential intensity, and 850-hPa vorticity (Fig. 6a). The reanalysis-based composites produce a similar weak GPI response to La Niña with negative AMM, and to El Niño with positive AMM (Fig. 6b).

While the compensation (in terms of influence on Atlantic TC activity) between competing ENSO and AMM influences is a robust response in both observations and the RCM simulations, it is not clear if there is a dominant influence of AMM, ENSO, or neither. Atlantic ACE in the RCM simulations forced with combinations of strongly opposing ENSO and AMM phases does not show a clear dominating influence of ENSO or AMM (Fig. 5a), with nearly identical ensemble averages in the two RCM experiments (Fig. 5b). In addition, the observed mean ACE during each competing ENSO and AMM pair (i.e., positive AMM with El Niño; negative AMM with Niña) is insignificantly different (10% level) from the mean ACE during the set of all other ENSO and AMM pairs (Fig. 2b).

c. *Constructive interferences: La Niña with positive AMM*

The RCM experiments support the observational analysis in section 4 by producing the most active Atlantic TC seasons in response to both positive AMM and La Niña together. Above average Atlantic tropical cyclone activity is simulated in response to concurrent strong La Niña and moderately positive AMM conditions, and concurrent strong La Niña and *strongly* positive AMM work together constructively to sustain *extremely* active Atlantic TC seasons. Forced by the strong La Niña conditions of 1999, the RCM simulates above average Atlantic ACE of 146, 176, and 209 under a coincident

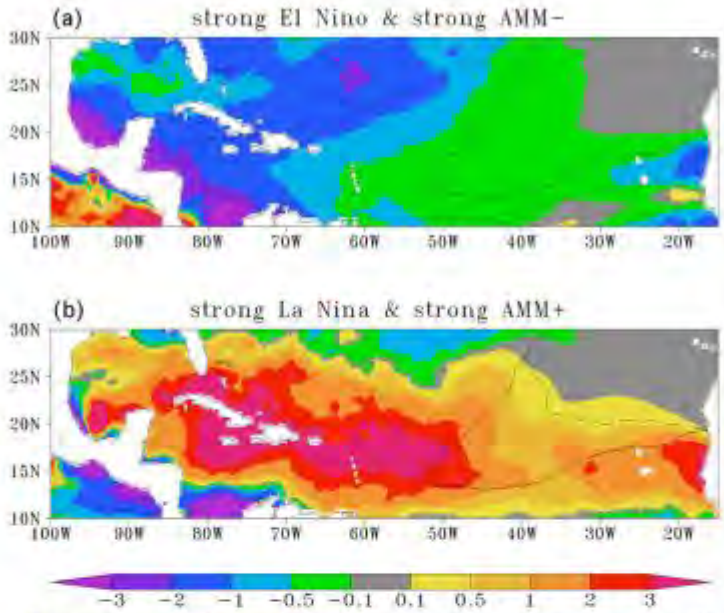

FIG. 8. Deviation from the ASO 1980–2000 mean of the RCM control simulation in the ASO averaged GPI index (unitless; shaded) from the ensemble average of the (a) 1987_1984Atl and (b) 1999_2005Atl RCM experiments, with the ASO average GPI value of 0.5 from the 1980–2000 mean (solid contour) and corresponding RCM experiment (dashed contour). The value 0.5 is chosen as an example to demonstrate how the spatial pattern of favorable environmental conditions for tropical cyclones changes in response to the AMM and ENSO forcings; regions east of the 0.5 contour are relatively unfavorable, and regions west of the 0.5 contour are relatively favorable. Land is white.

moderately positive AMM, and extremely above average Atlantic ACE of 273, 310, 312, and 312 under a coincident strongly positive AMM (Fig. 5a). During strong La Niña conditions there is a nonlinear response in ACE to Atlantic SST conditions described by the AMM, with Atlantic ACE fairly greater for prescribed Atlantic conditions corresponding to an AMM index in the 80th percentile compared to the 0th percentile, but dramatic ACE increases for an AMM index in the 100th percentile (Fig. 5b).

The simulated response in Atlantic ACE to concurrent strong La Niña and strongly positive AMM in each of the four ensemble members exceeds the ACE of the most active observed Atlantic hurricane season, which occurred in 2005 and produced an ACE of 250. Even if we consider the bias in mean Atlantic ACE in the control simulation (Table 2) and scale the ACE of the model experiments accordingly, the "adjusted" ACE values for the concurrent strong La Niña and strongly positive AMM simulations (229, 260, 262, and 262) exceed that observed in the 2005 season in three of four ensemble members. This suggests that the Atlantic may experience hurricane seasons that are more active than the season of 2005 if "prime" conditions in the tropical Atlantic and Pacific occur simultaneously.

The Atlantic ACE of the RCM simulations, which are designed to isolate the influence of ENSO and AMM from other factors, suggests that both strong La Niña and strongly positive AMM are required to support the upper limit of seasonal Atlantic tropical cyclone activity, assuming other factors are equal. This is in rough agreement with the observations, which show that concurrent La Niña and positive AMM support the most above average Atlantic ACE on average (Fig. 2b). We note that, while concurrent La Niña and positive AMM always produced relatively active tropical cyclone seasons, both La Niña and positive AMM were not necessary during some cases of the strongest Atlantic ACE in the observational record (Fig. 2a), including the most active observed season of 2005, which occurred during neutral ENSO conditions; we suspect that, during these cases, variability in factors aside from ENSO and AMM significantly controlled tropical cyclone activity as well.

Comparing the GPI of the RCM simulation forced with a moderately positive AMM and strong La Niña to that derived from reanalysis as the composite including all observed positive AMM and La Niña TC seasons reveals that in both cases, which represent similar but not equal AMM and ENSO conditions, increased midtropospheric relative humidity and decreased tropospheric vertical wind shear support the positive deviations in GPI and ACE (Figs. 6a,b). Similar to the observationally based findings of Vimont and Kossin (2007), multiple atmospheric factors change in ways that cooperate in their influence on Atlantic TCs in response to the AMM forcing in the model simulations (Fig. 6a). In addition, reanalyzed vertical wind shear is positively correlated with the AMM index over the MDR, and negatively correlated with the Niño-3.4 index over the Gulf of Mexico and Caribbean Sea (Fig. 6 of Kossin and Vimont 2007); the reduction in vertical wind shear is located over the MDR, Gulf of Mexico, and Caribbean Sea in response to concurrent moderately positive AMM and strong La Niña forcings in the RCM simulations (Fig. 7c), supporting the idea that positive AMM and La Niña work together constructively in their influence on the atmospheric environment.

We rely on the RCM simulations to understand the influence of strong La Niña and strongly positive AMM on environmental conditions since this extreme case is not represented in the observational record. The GPI indicates that above normal midtropospheric relative humidity is an essential driver for the prime conditions for tropical cyclones during strong La Niña and strongly positive AMM (Fig. 6a). While the strong La Niña and moderately positive AMM produce moderately above average relative humidity and below average vertical wind shear, strongly above normal midtropospheric relative humidity is the main factor supporting the exceedingly favorable conditions for TCs during concurrent strong La Niña and positive AMM (Fig. 6a). The physical mechanism for this response in midtropospheric relative humidity to the AMM SST forcing may be linked to the northward shift of the Atlantic intertropical convergence zone (ITCZ) in association with the positive AMM and to the weakened vertical wind shear in the northern tropical Atlantic associated with La Niña, both conditions that favor deep convection. The enhanced GPI during strong simultaneous La Niña and positive AMM is associated with an eastward expansion of the region favorable for tropical cyclone development relative to the mean (Fig. 8b), similar to Atlantic TC genesis that occurs throughout the tropical Atlantic during the AMM positive phase and is located farther east in comparison with the AMM negative phase (Kossin and Vimont 2007).

We note that the results presented in this section are based on atmosphere-only model simulations forced with prescribed SST, and thus do not take into full account atmosphere–ocean feedbacks in the development of the AMM and ENSO. Future studies are needed to examine how air–sea feedbacks, such as the WES, can affect the influence of the AMM on TCs.

7. Conclusions

The influence of eastern tropical Pacific SST variability during the El Niño–Southern Oscillation on seasonal Atlantic tropical cyclone activity is well documented, with warmer than average SST during El Niño inhibiting Atlantic TCs (e.g., Gray 1984; Goldenberg and Shapiro 1996; Tang and Neelin 2004). Atlantic SST variability also significantly influences Atlantic tropical cyclone activity; the relationship between Atlantic TC activity and the meridional gradient between northern and southern tropical Atlantic SST, which is characterized by the Atlantic meridional mode, is strong on both interannual and decadal time scales (Vimont and Kossin 2007). In this study, we quantify the impact of concurrent extreme phases of ENSO and AMM on seasonal Atlantic TC activity and the atmospheric environment using observations and regional climate model experiments.

Composites of observed Atlantic accumulated cyclone energy (ACE) reveal that individually ENSO or AMM alone provides an incomplete explanation of seasonal Atlantic tropical cyclone variability and that both are primary influences on Atlantic TC activity (i.e., the AMM does not act as a secondary influence to modulate the impact of ENSO). On average, the upper limit of seasonal Atlantic tropical cyclone activity requires a positive AMM and La Niña together, while significantly reduced seasonal Atlantic TC activity does not require both unfavorable ENSO and AMM conditions. In addition, a warm ENSO phase is generally not a sufficient condition for below average Atlantic TC activity since a positive AMM phase exerts a compensating influence.

Regional climate model simulations are used to augment the observational analysis, which is based on a relatively small sample size of 63 seasons, and potentially lacks rare occurrences of concurrent extreme ENSO and AMM phases. Simulations at 27-km resolution are performed with WRF. The control simulation uses observed SST and lateral boundary conditions of 1980–2000, and experiments are forced with ENSO phases through LBCs and eastern tropical Pacific SST and AMM phases through Atlantic SST. Each prescribed ENSO and AMM phase is based on an observed case.

The RCM simulations produce relationships between Atlantic tropical cyclone activity and concurrent AMM

and ENSO phases that are consistent with the observational analysis and improve our understanding of the influence of extreme phases of Atlantic and Pacific climate modes on Atlantic TCs:

- Strong concurrent La Niña and positive AMM work together constructively to sustain extremely active Atlantic TC seasons primarily through above average midtropospheric relative humidity with below average tropospheric vertical wind shear, which produce an extensive region of conditions favorable for TCs. Under strong La Niña conditions, Atlantic TC activity responds nonlinearly to AMM, with dramatic increases for extremely warm Atlantic SST conditions. This combination of "prime" Atlantic and Pacific conditions supports simulated Atlantic hurricane seasons that are more active than the most active season currently on record, 2005.
- Strong phases of ENSO and AMM that individually oppose each other in their influence on Atlantic TCs together produce compensating effects and support near-average Atlantic tropical cyclone activity and environmental conditions relevant for TCs in the Atlantic development region.
- Strong concurrent El Niño and negative AMM are not required to effectively inhibit Atlantic TC activity because the threshold in tropospheric vertical wind shear that suppresses TCs can be achieved without this combination of the most unfavorable Pacific and Atlantic conditions.

This work emphasizes that understanding Atlantic tropical cyclone activity relies critically on considering both ENSO and AMM, with the implication that future predictions of Atlantic TC activity require knowledge of the distribution of seasonal tropical Atlantic and Pacific SST, not just climatological mean SST changes. Although this study does not address seasonal TC prediction directly, it may be applied to guide predictions of Atlantic TC activity, especially for seasons occurring during extreme AMM and ENSO phases, remembering that other factors including upper tropospheric temperature variability, African easterly wave activity, and Saharan dust also play an important role and are not to be neglected.

Acknowledgments. This research is supported by U.S. National Science Foundation Grants AGS-1067937 and AGS-1347808, Department of Energy Grants DE-SC0004966 and DE-SC0006824, and National Oceanic and Atmospheric Administration Grant NA11OAR4310154. PC acknowledges the support from the National Science Foundation of China (41028005, 40921004, and 40930844) and the Chinese Ministry of Education's 111 project (B07036). CP acknowledges support from the University Corporation for Atmospheric Research (UCAR) Joint Office for Science Support (JOSS). The Texas Advanced Computing Center (TACC) at The University of Texas at Austin and the Texas A&M Supercomputing Facility provided high-performance computing resources that contributed to the research results reported in this paper. CP wishes to thank Jen-Shan Hsieh for sharing his TC tracking routine. The Fortran subroutine to calculate potential intensity was written by Kerry Emanuel and is available at http://eaps4.mit.edu/faculty/Emanuel/products. HURDAT2 available from the Atlantic Oceanographic and Meteorological Laboratory/National Oceanic and Atmospheric Administration (AOML/NOAA) Hurricane Research Division (HRD) website at http://www.aoml.noaa.gov/hrd/hurdat/Data_Storm.html. The AMM index is calculated by Daniel J. Vimont at the University of Wisconsin–Madison and provided by the NOAA Earth System Research Laboratory (ESRL). The Niño-3.4 index is provided by the NOAA Climate Prediction Center (CPC). AMM and Niño-3.4 data are obtained from http://www.esrl.noaa.gov/psd/data/climateindices/list/. NCEP-2 and NCEP CFSR data are obtained from the NOAA National Operational Model Archive & Distribution System (NOMADS). We thank the members of the CLIVAR Hurricane WG for helpful discussions and are grateful to Philip J. Klotzbach and two anonymous reviewers for their insightful comments, which improved this paper significantly.

REFERENCES

Arkin, P. A., 1982: The relationship between interannual variability in the 200-mb tropical wind field and the Southern Oscillation. *Mon. Wea. Rev.*, **110,** 1393–1404, doi:10.1175/1520-0493(1982)110<1393:TRBIVI>2.0.CO;2.

Avila, L. A., 1991: Atlantic tropical systems of 1990. *Mon. Wea. Rev.*, **119,** 2027–2033, doi:10.1175/1520-0493(1991)119<2027:ATSO>2.0.CO;2.

Belanger, J. I., V. T. Toma, J. A. Curry, P. J. Webster, and M. T. Jelinek, 2014: Climate dynamics of easterly waves in the North Atlantic and east Pacific. *31st Conf. on Hurricanes and Tropical Meteorology,* San Diego, CA, Amer. Meteor. Soc., 1A.6. [Available online at https://ams.confex.com/ams/31Hurr/webprogram/Paper245355.html.]

Bell, G. D., and M. Chelliah, 2006: Leading tropical modes associated with interannual and multidecadal fluctuations in North Atlantic hurricane activity. *J. Climate,* **19,** 590–612, doi:10.1175/JCLI3659.1.

——, and Coauthors, 2000: Climate assessment for 1999. *Bull. Amer. Meteor. Soc.,* **81,** s1–s50, doi:10.1175/1520-0477(2000)81[s1:CAF]2.0.CO;2.

——, M. Chelliah, K. Mo, S. B. Goldenberg, C. W. Landsea, E. Blake, and R. Pasch, 2005: NOAA: August 2005 update to Atlantic hurricane season outlook. [Available online at http://www.cpc.ncep.noaa.gov/products/outlooks/hurricane2005/August/hurricane.html.]

63. Assignment 2, Module 14: El Nino and La Nina: https://www.climate.gov/news-features/understanding-climate/el-ni%C3%B1o-and-la-ni%C3%B1a-frequently-asked-questions

What are El Niño and La Niña?

El Niño and La Niña are opposite phases of a natural climate pattern across the tropical Pacific Ocean that swings back and forth every 3-7 years on average. Together, they are called ENSO (pronounced "en-so"), which is short for **El** **N**iño-**S**outhern **O**scillation.

The ENSO pattern in the tropical Pacific can be in one of three states: El Niño, Neutral, or La Niña. El Niño (the warm phase) and La Niña (the cool phase) lead to significant differences from the average ocean temperatures, winds, surface pressure, and rainfall across parts of the tropical Pacific. Neutral indicates that conditions are near their long-term average.

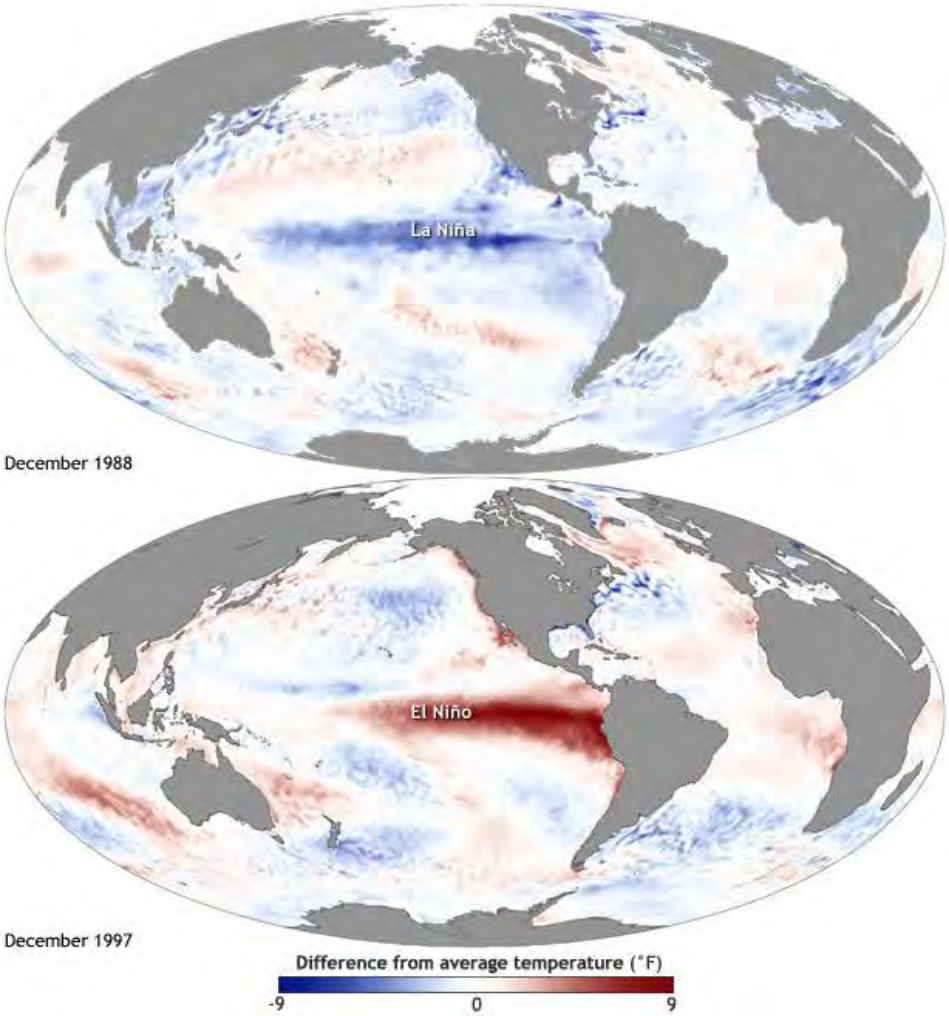

Maps of sea surface temperature anomaly in the Pacific Ocean during a strong La Niña (top, December 1988) and El Niño (bottom, December 1997). Maps by NOAA Climate.gov, based on data provided by NOAA View. **large versions** La Niña | El Niño

What happens during El Niño and La Niña?

During El Niño, the surface winds across the entire tropical Pacific are weaker than usual. Ocean temperatures in the central and eastern tropical Pacific Ocean are warmer than average, and rainfall is below average over Indonesia and above average over the central or eastern Pacific.

Rising air motion (which is linked to storms and rainfall) increases over the central or eastern Pacific, and surface pressure there tends to be lower than average. Meanwhile, an increase in sinking air motion over Indonesia leads to higher surface pressure and dryness.

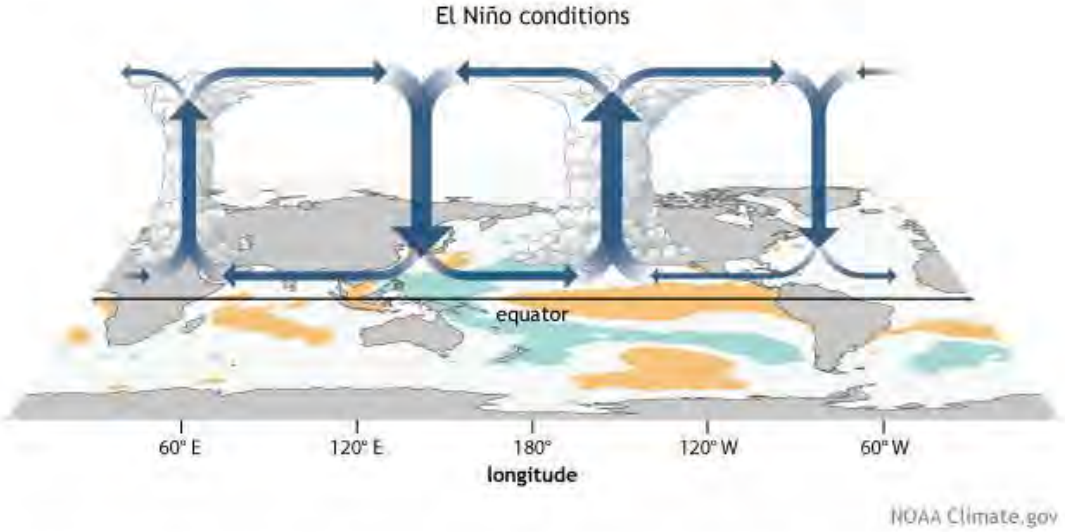

Generalized Walker Circulation (December-February) anomaly during El Niño events, overlaid on map of average sea surface temperature anomalies. Anomalous ocean warming in the central and eastern Pacific (orange) help to shift a rising branch of the Walker Circulation to east of 180°, while sinking branches shift to over the Maritime continent and northern South America. NOAA Climate.gov drawing by Fiona Martin.

During La Niña, it's the opposite. The surface winds across the entire tropical Pacific are stronger than usual, and most of the tropical Pacific Ocean is cooler than average. Rainfall increases over Indonesia (where waters remain warm) and decreases over the central tropical Pacific (which is cool). Over Indonesia, there is more rising air motion and lower surface pressure. There is more sinking air motion over the cooler waters of the central and eastern Pacific.

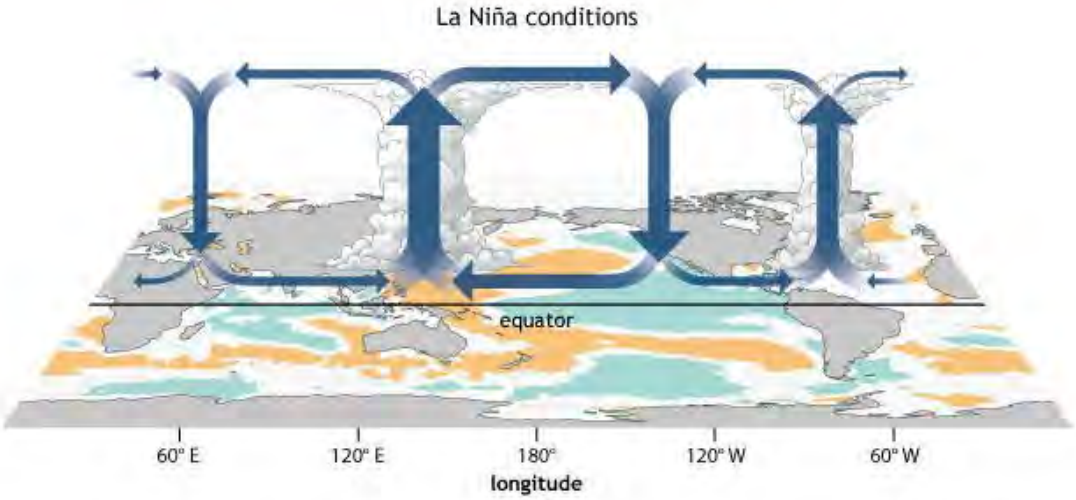

Generalized Walker Circulation (December-February) anomaly during La Niña events, overlaid on map of average sea surface temperature anomalies. Anomalous ocean cooling (blue-green) in the central and eastern Pacific Ocean and warming over the western Pacific Ocean enhance the rising branch of the Walker circulation over the Maritime Continent and the sinking branch over the eastern Pacific Ocean. Enhanced rising motion is also observed over northern South America, while anomalous sinking motion is found over eastern Africa. NOAA Climate.gov drawing by Fiona Martin.

Between the warm phase (El Niño) and cool phase (La Niña), scientists describe conditions as "ENSO-neutral." Neutral means that the temperatures, winds, convection (rising air), and rainfall across the tropical Pacific are near their long-term averages.

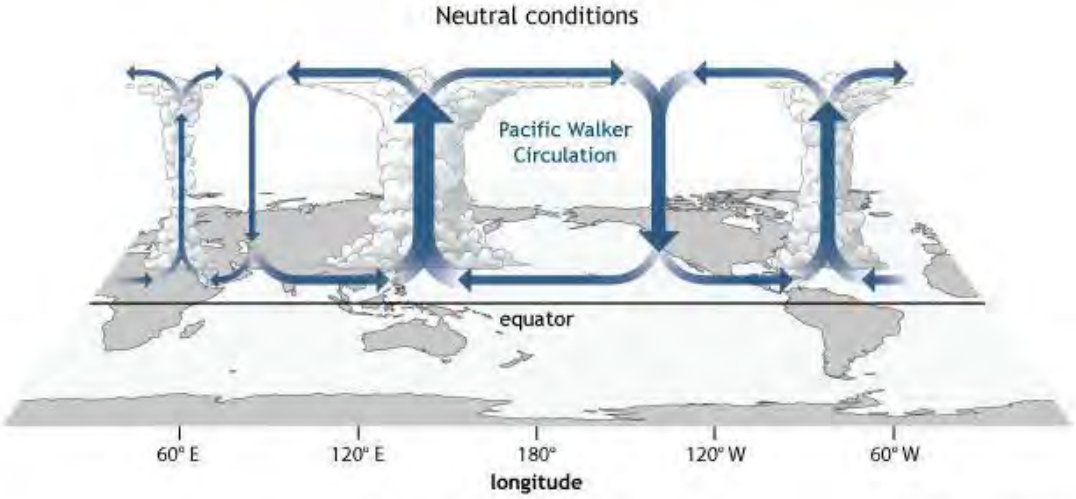

Generalized Walker Circulation (December-February) during ENSO-neutral conditions. Convection associated with rising branches of the Walker Circulation is found over the Maritime continent, northern South America, and eastern Africa. NOAA Climate.gov drawing by Fiona Martin.

Is El Niño a kind of storm that will hit the U.S.?

No, El Niño isn't a storm that will hit a specific area at a specific time. Instead, the warmer tropical Pacific waters cause changes to the global atmospheric circulation, resulting in a wide range of changes to global weather. Think of how a big construction project across town can change the flow of traffic near your house, with people being re-routed, side roads taking more traffic, and normal exits and on-ramps closed. Different neighborhoods will be affected most at different times of the day. You would feel the effects of the construction project through its changes to normal patterns, but you wouldn't expect the construction project to "hit" your house.

Was that big storm we just had due to El Niño?

That isn't an answerable question. El Niño does increase the chances for a wet and stormy winter and early spring overall across the southern tier of the United States, but it's impossible to say that any single storm was solely caused by El Niño and wouldn't have happened otherwise.

Think of it this way: Suppose that in an average year, your state experiences 10 winter storms. During this El Niño winter, perhaps you get 13. It's impossible to say which 10 were your "normal" ones and which 3 were the "extra" ones.

However, for any specific storm, scientists *can* try to estimate if and how much El Niño contributed to making the event especially extreme, for example, by increasing the amount of water vapor available "in the background," or by shifting the position or strength of the jet stream.

This sort of analysis is called an *attribution study*. It requires comprehensive observations—both current and historical—as well as highly detailed climate recreations of the weather patterns that gave rise to the storm. It may take scientists several months to conduct this kind of analysis.

How do El Niño and La Niña affect weather patterns?

El Niño and La Niña alternately warm and cool large areas of the tropical Pacific—the world's largest ocean—which significantly influences where and how much it rains there. The primary location of moist, rising air (over the basin's warmest water) is centered over the central or eastern Pacific during El Niño and over Indonesia and the western Pacific during La Niña.

This shift disrupts the atmospheric circulation patterns that connect the tropics with the middle latitudes, which in turn modifies the mid-latitude jet streams. By modifying the jet streams, ENSO can affect temperature and precipitation across the United States and other parts of the world. The influence on the U.S. is strongest during the winter (January-March), but it lingers into the early spring.

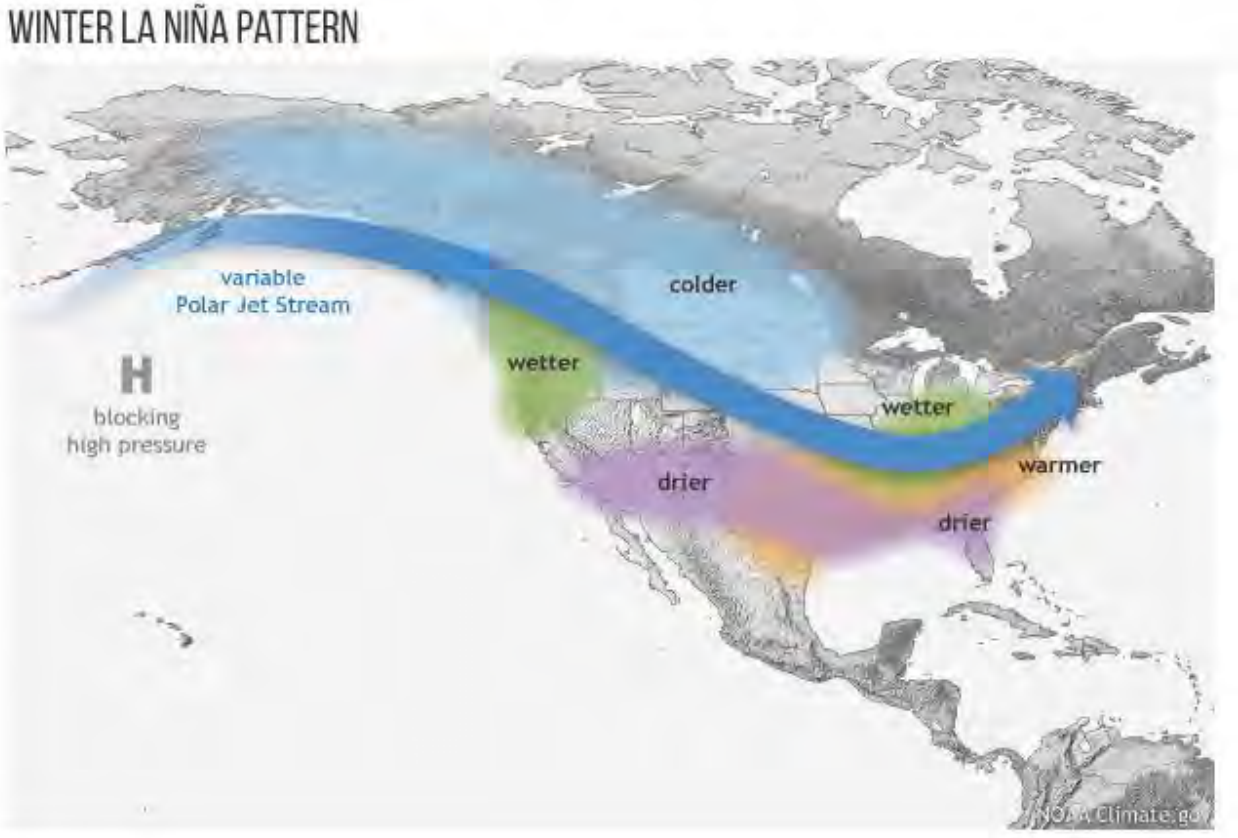

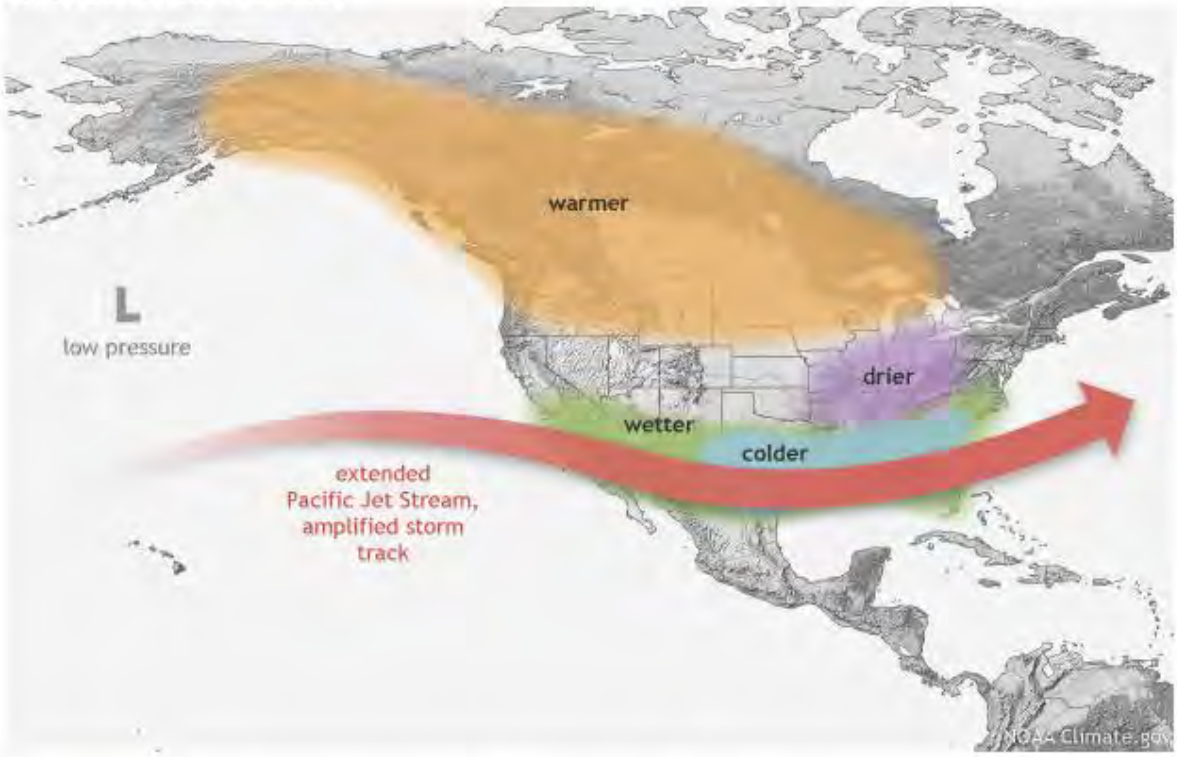

These maps illustrate the typical impacts of El Niño and La Niña on U.S. winter weather. *Typical* means "common," but not guaranteed because each event is unique. NOAA Climate.gov drawings, adapted from originals by the Climate Prediction Center.

During El Niño, the southern tier of Alaska and the U.S. Pacific Northwest tend to be warmer than average, whereas the U.S. southern tier of state—from California to the Carolinas—tends to be cooler and wetter than average. During La Niña, these deviations from the average are approximately (but not exactly) reversed.

The influence of El Niño and La Niña in some parts of the United States and the rest of the world can be so strong that they increase the odds of "extreme weather events"—phenomena that rank in the highest or lowest 10% compared to historical observations. (Click to view a historical perspective on El Niño impacts in the U.S.)

However, not all of these influences are negative. For example, because the northern tier of the U.S. tends to be warmer than average during El Niño winters, heating costs there may be appreciably reduced.

How does ENSO affect global average temperature?

Within any given decade, the warmest years are usually El Niño ones, and the coldest are usually La Niña ones. That's because the Pacific Ocean is a big place. If you walked around the planet along the equator, you'd be spending over 40% of your time attempting to walk on the water in the Pacific Ocean. This vast size means that warming or cooling in the Pacific due to El Niño and La Niña can leave an imprint on the global average surface temperature.

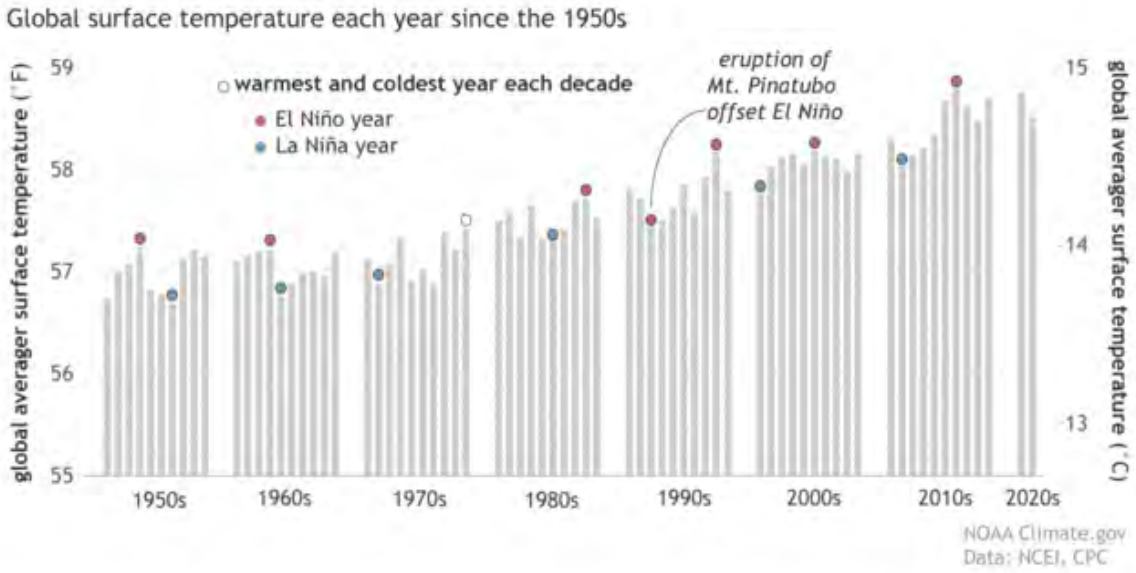

In general, the warmest year of any decade will be an El Niño year, the coldest a La Niña one. This graph shows annual average surface temperatures (gray bars), grouped by decade, from 1950 to 2021. The warmest and coldest years of each decade are topped with circles: **red** for El Niño-influenced years and **blue** for La Niña years. We considered a year El Niño or La Niña "influenced" if the December-February was labelled as part of a historical episode by NOAA's Climate Prediction Center or if more than half of the months in that year were. By our definition, 1979 did not qualify as El Niño year because El Niño conditions were present for only 3 months late in the year. 1992 was the coldest year of the 1990s despite being an El Niño year because of the cooling influence of the eruption of Mount Pinatubo in 1991. NOAA Climate.gov graph based on data from NOAA National Centers for Environmental Information.

But the surface warming and cooling during El Niño and La Niña don't involve more or less heat energy entering or escaping the climate system as a whole. In other words, the whole climate system isn't ***really*** cooling or warming. Heat energy that's already present in the climate system is simply shifting back and forth between the atmosphere (where it shows up in the global surface temperature value) and the deeper layers of the ocean (where it doesn't).

The changes in sea surface temperatures during El Niño and La Niña are caused and helped along by changes in the trade winds, which normally blow from east to west across the tropical Pacific Ocean. When the trade winds are stronger than normal during La Niña, the winds push more surface water to the western half of the Pacific basin. The pool of warm water grows deeper, storing excess heat at depth, and allowing for colder, deeper water to rise to the surface in the eastern half of the Pacific basin.

This wind-driven disturbance creates a large area along the equator where the ocean surface temperatures are below normal. Over the span of months to seasons, heat from the atmosphere then goes ***into*** the ocean, leading to cooler air temperatures over a region broad enough to cool down the global average temperature.

During El Niño, when the trade winds are weak or even occasionally reverse themselves, the amount of cold water that comes to the surface is reduced. Warm waters in the west Pacific Ocean slosh to the east. Now there is a large area along the equator where ocean temperatures are above normal. Heat from the ocean then goes ***out*** into the atmosphere, leading to warmer air temperatures in the Pacific and subsequently, to warmer global air temperatures (plus a cascade of other impacts).

All of this amounts to a shuffling of heat from one place (ocean) to another (the atmosphere) without affecting the Earth's overall energy budget—the balance between incoming and outgoing energy across the entire planet. So unlike volcanic eruptions, which actually block energy from the Sun from reaching the surface, or solar minimums, which reduce the total amount of energy the Sun emits, the phases of ENSO are not creating or removing energy from the climate system. La Niña hides some of Earth's existing heat below the surface, while El Niño reveals it. Climate scientists call this kind of re-shuffling ***internal*** *climate variability.*

Will El Niño affect my town/state/region this winter?

Maybe. Probably. Probably not. The answer depends on many factors, including where you live, how strong the event continues to be, and other climate patterns that develop and influence the seasonal outcome.

Scientists have identified a set of typical U.S. impacts that have been associated with past El Niño events. (See How do El Niño and La Niña affect weather patterns?) But "associated with" doesn't mean that **all** of these impacts happen during **every** El Niño episode. They may happen as often as 80 percent of the time, or as infrequently as 40 percent of the time.

In other words, the influence of El Niño on U.S. winter climate is a matter of *probability*, not certainty. The Climate Prediction Center takes El Niño into consideration in their monthly and seasonal outlooks, which describe the likelihood that temperature and precipitation will be well-above or well- below average.

How does NOAA decide when El Niño is happening?

NOAA uses a 5-category alert system for tracking ENSO that is based on a combination of observed conditions, computer model forecasts, and expert scientific judgment. For El Niño, the eastern tropical Pacific Ocean has to be 0.5°C or more warmer than average, and winds, surface pressure, and rainfall must have begun to show changes consistent with El Niño. (See What happens during El Niño and La Niña?) These changes in average conditions must persist for at least five overlapping three-month periods in order to be count as a full-blown episode in the historical record.

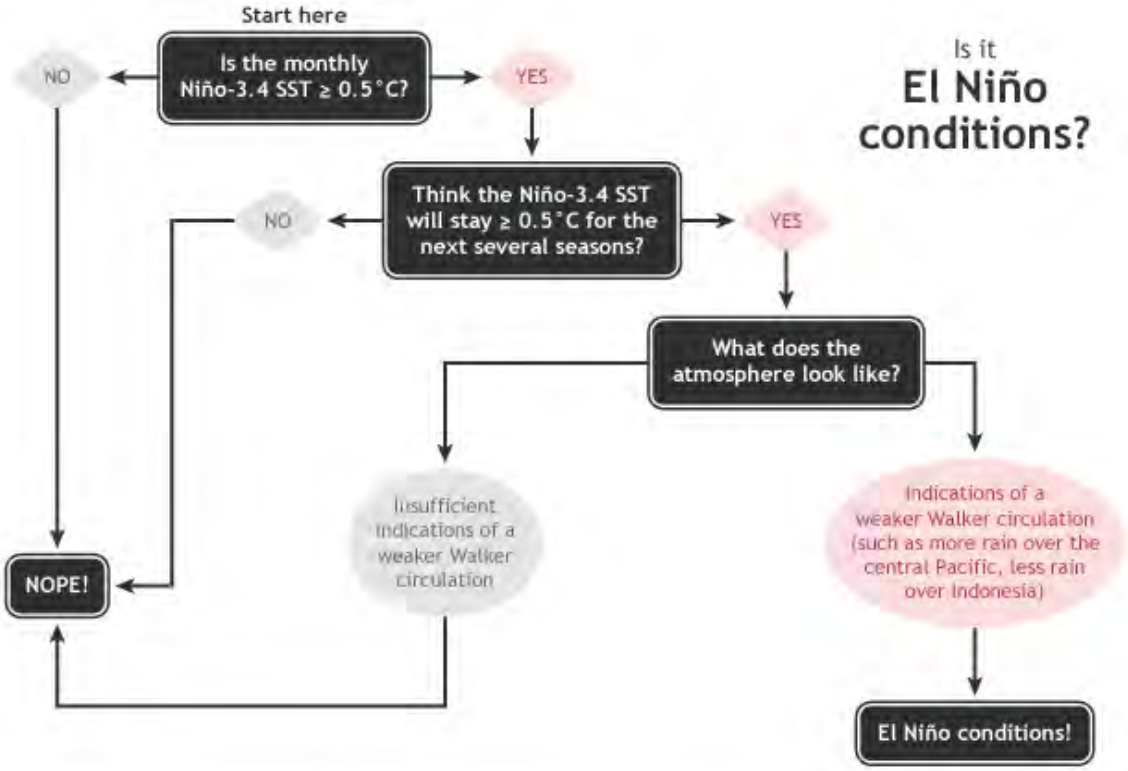

Summary of NOAA decision process in determining El Niño conditions. NOAA Climate.gov drawing by Glen Becker and Fiona Martin.

What causes El Niño and La Niña to occur?

The winds near the surface in the tropical Pacific usually blow from east to west. For reasons scientists don't yet fully understand, these relatively steady winds sometimes weaken or strengthen for weeks or months in a row.

Weak winds allow warm surface waters to build up in the eastern Pacific. Sometimes, but not always, the atmosphere responds to this warming with increased rising air motion and above-average rainfall in the eastern Pacific. This coordinated change in both ocean temperatures and the atmosphere begins an El Niño event. As the event develops, the warmed waters cause the winds to weaken even further, which can cause the waters to warm even more.

El Niño is often (but not always) followed by La Niña the following year, particularly if the El Niño is strong. During La Niña conditions, the easterly trade winds near the equator get even stronger than they usually are. Stronger winds push surface water into the western Pacific. Meanwhile, cool water from deeper in the ocean rises up in the eastern Pacific. If the cooling persists, it can inhibit rising air movement and rainfall in the eastern Pacific, beginning a La Niña event. As the event develops, the cooled waters cause the winds to strengthen even further, which can cause the waters to cool even more.

How long do El Niño and La Niña typically last?

El Niño and La Niña episodes typically last 9-12 months. They both tend to develop during the spring (March-June), reach peak intensity during the late autumn or winter (November-February), and then weaken during the spring or early summer (March-June).

Both El Niño and La Niña can last more than a year, but it is rare for El Niño events to last longer than a year or so, while it is common for La Niña to last for two years or more. The longest El Nino in the modern record lasted 18 months, while the longest la Niña lasted 33 months. Scientists aren't sure why the duration of the two types of events can be so different.

Can we predict El Niño and La Niña before they occur?

Yes, scientists can often predict the onset of El Niño and La Niña several months to a year in advance, thanks to modern climate models (such as those used by NOAA's National Centers for Environmental Prediction) and observation data from the Tropical Pacific Observing System (which includes sensors on satellites, ocean buoys, and radiosondes), which constantly monitors changing conditions in the ocean and atmosphere. Without these tools we wouldn't be able to detect or predict the onset of El Niño or La Niña.

Why is predicting El Niño and La Niña so important?

El Niño and La Niña can make extreme weather events more likely in certain regions. If we can predict El Niño and La Niña, we can predict a greater chance of the associated extreme events. Better predictions of where and when extreme weather events are likely to happen (e.g., floods and droughts) could save the United States billions of dollars in damage costs.

Predicting the life cycle and strength of El Niño and La Niña is critical for helping people plan for, avoid, or mitigate potential damages in every sector of society, including agriculture, fisheries, energy, water, transportation, and health care). Advances in scientists' ability to predict future ENSO states could significantly improve U.S. economic opportunities in these vital sectors.

Can we prevent El Niño and La Niña from occurring?

No, El Niño and La Niña are naturally occurring climate patterns and humans have no direct ability to influence their onset, intensity, or duration.

Does global warming affect El Niño and La Niña?

There are many ways in which global warming could affect the frequency and intensity of El Niño / La Niña (see this ENSO blog post, for example), but scientists currently have low confidence in their ability to predict exactly how a warmer world affect the ENSO. Scientists have high confidence, however, that ENSO itself has been occurring for thousands of years, and will continue into the future. Global warming is likely to affect the *impacts* related to El Niño and La Niña, including extreme weather events.

Do El Niño and La Niña influence the Atlantic and Pacific hurricane seasons?

Yes, the continental United States and Caribbean Islands have a substantially decreased chance of experiencing a hurricane during El Niño and an increased chance of experiencing a hurricane during La Niña.

Typical El Niño influence

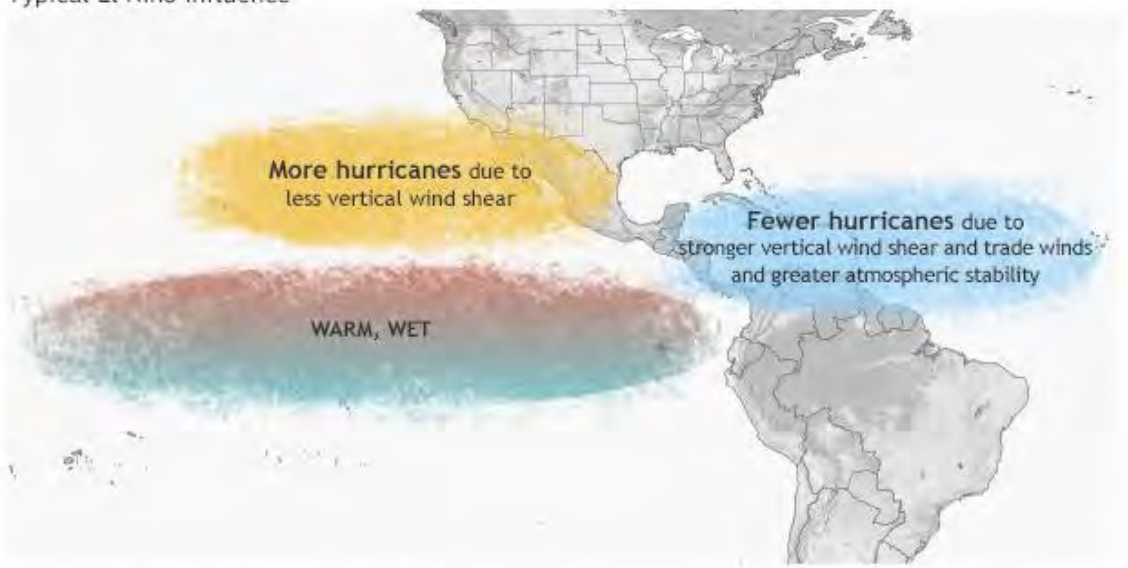

Typical influence of El Niño on Pacific and Atlantic seasonal hurricane activity. Map by NOAA Climate.gov, based on originals by Gerry Bell.

Both El Niño and La Niña influence where Atlantic hurricanes tend to form. During El Niño, fewer hurricanes develop in the deep tropics from African easterly waves. Conversely, during La Niña, more hurricanes form in the deep tropics from African easterly waves and, therefore, have a greater likelihood of becoming major hurricanes that may eventually threaten the Caribbean Islands and the United States.

Typical La Niña influence

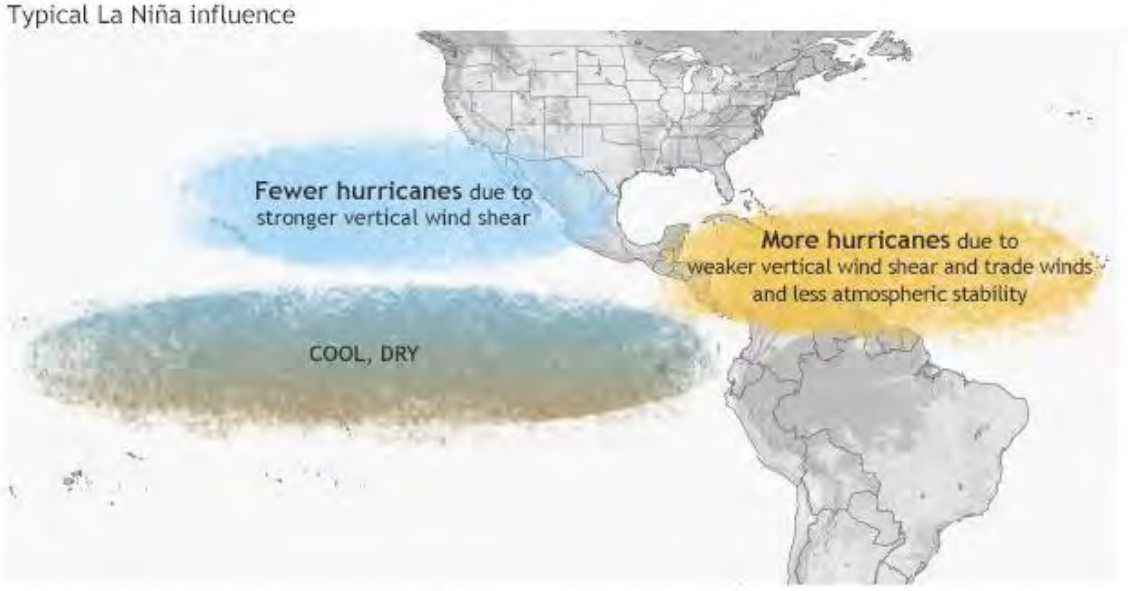

Typical influence of La Niña on Pacific and Atlantic seasonal hurricane activity. Map by NOAA Climate.gov, based on originals by Gerry Bell.

Overall, El Niño contributes to more eastern and central Pacific hurricanes and fewer Atlantic hurricanes while, conversely, La Niña contributes to fewer eastern and central Pacific hurricanes and more Atlantic hurricanes..

Do El Niño and La Niña influence tornado activity in the U.S.?

Yes, El Niño and La Niña appear to have an effect on tornado activity. Since a strong jet stream is an important ingredient for severe weather, the position of the jet stream helps to determine the regions more likely to experience tornadoes.

The jet stream over the United States is typically considerably different during El Niño winters as compared to La Niña winters. During El Niño, the jet stream is oriented from west to east across the southern portion of the United States. Thus, this region becomes more susceptible to severe weather outbreaks during the winter. Conversely, during La Niña, the jet stream and severe weather are likely to be farther north.

Why are these climate patterns called "El Niño" and "La Niña"?

Centuries before it was a focus of scientific study, South American fishermen noticed warmer-than-normal coastal Pacific Ocean waters and dramatic decreases in fish catch occurring periodically around Christmas time. They nicknamed the phenomenon "El Niño" (Spanish for little boy) in connection with the celebration of the Christian holiday marking the birth of Jesus. In the 1980s, when the opposite phase of El Niño was discovered (i.e., cooler-than-normal ocean temperatures), scientists called it "La Niña" (Spanish for little girl).

Where can I find more information about El Niño and La Niña?

NOAA's primary point-of-entry for online information about ENSO is available at http://www.climate.gov/enso.

NOAA Climate.gov publishes a frequently updated "ENSO blog," written by climate scientists in language easy to understand by non-scientists.

ENSO forecasts, outlooks, and diagnostic discussion information is available from NOAA's Climate Prediction Center, at: http://www.cpc.ncep.noaa.gov.

Maps showing El Niño and La Niña historical impacts on weather patterns in the United States are available from NOAA's National Center for Environmental Information (here) and NOAA's Earth System Research Laboratory (here).

64. Assignment 2, Module 14: ENSO Impact around the globe: http://www.aoml.noaa.gov/hrd/tcfaq/G2.html

G2) How Does El Niño-Southern Oscillation Affect Tropical Cyclone Activity Around the Globe?

The El Niño/Southern Oscillation (ENSO) resolves into a warm phase (El Niño), a cold phase (La Niña), and a neutral phase. During El Niño events (ENSO warm phase), tropospheric vertical shear is increased inhibiting tropical cyclone genesis and intensification, primarily by causing the 200 mb (12 km or 8 mi) westerly winds to be stronger (Gray 1984). La Niña events (ENSO cold phase) enhances activity. Recently, Tang and Neelin (2004) also identified that changes to the moist static stability can also contribute toward hurricane changes due to ENSO, with a drier, more stable environment present during El Niño events.

The Australian/Southwest Pacific shows a pronounced shift back and forth of tropical cyclone activity with fewer tropical cyclones between 145° and 165°E and more from 165°E eastward across the South Pacific during El Niño (warm ENSO) events. There is also a smaller tendency to have the tropical cyclones originate a bit closer to the equator. The opposite would be true in La Niña (cold ENSO) events. See papers by Nicholls (1979), Revell and Goulter (1986), Dong (1988), and Nicholls (1992). The western portion of the Northeast Pacific basin (140°W to the dateline) has been suggested to experience more tropical cyclone genesis during the El Niño year and more tropical cyclones tracking into the sub-region in the year following an El Niño (Schroeder and Yu 1995), but this has not been completely documented yet.

The Northwest Pacific basin, similar to the Australian/Southwest Pacific basin, experiences a change in location of tropical cyclones without a total change in frequency. Pan (1981), Chan (1985), and Lander (1994) detailed that west of 160°E there were reduced numbers of tropical cyclone genesis with increased formations from 160E to the dateline during El Niño events. The opposite occurred during La Niña events. Again there is also the tendency for the tropical cyclones to also form closer to the equator during El Niño events than average.

The eastern portion of the Northeast Pacific, the Southwest Indian, the Southeast Indian/Australian, and the North Indian basins have either shown little or a conflicting ENSO relationship and/or have not been looked at yet in sufficient detail.

Reference: Tang, B. H., and J. D. Neelin, 2004: "ENSO Influence on Atlantic hurricanes via tropospheric warming." Geophys. Res. Lett.: Vol 31, L24204.

65. Assignment 2, Module 14: Impacts of ENSO on Hurricane Season: https://www.climate.gov/news-features/blogs/enso/impacts-el-ni%C3%B1o-and-la-ni%C3%B1a-hurricane-season

Impacts of El Niño and La Niña on the hurricane season

BY GERRY BELL
PUBLISHED MAY 30, 2014
20 COMMENTS

With the approach of the 2014 hurricane season and the strong potential for El Niño to develop during the next few months, the effect that El Niño has on both the Atlantic and Pacific hurricanes seasons is worth exploring. The hurricane impacts of El Niño and its counterpart La Niña are like a see-saw between the Pacific and Atlantic oceans, strengthening hurricane activity in one region while weakening it in the other.

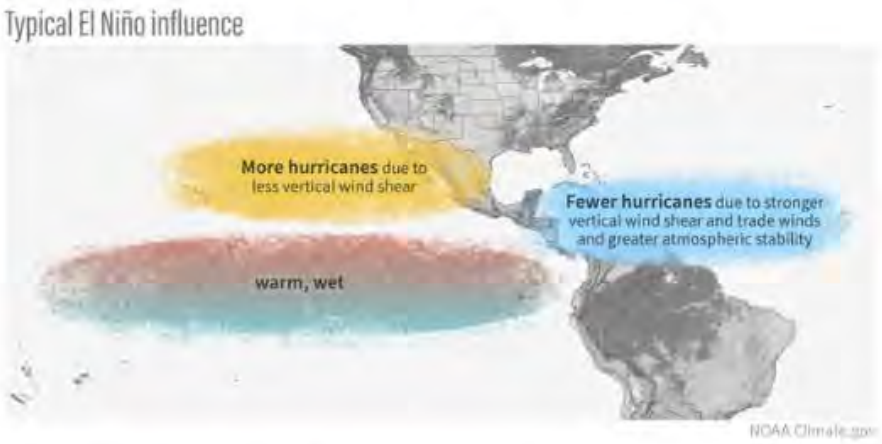

Typical influence of El Niño on Pacific and Atlantic seasonal hurricane activity. Map by NOAA Climate.gov, based on originals by Gerry Bell.

Simply put, El Niño favors stronger hurricane activity in the central and eastern Pacific basins, and suppresses it in the Atlantic basin (Figure 1). Conversely, La Niña suppresses hurricane activity in the central and eastern Pacific basins, and enhances it in the Atlantic basin (Figure 2).

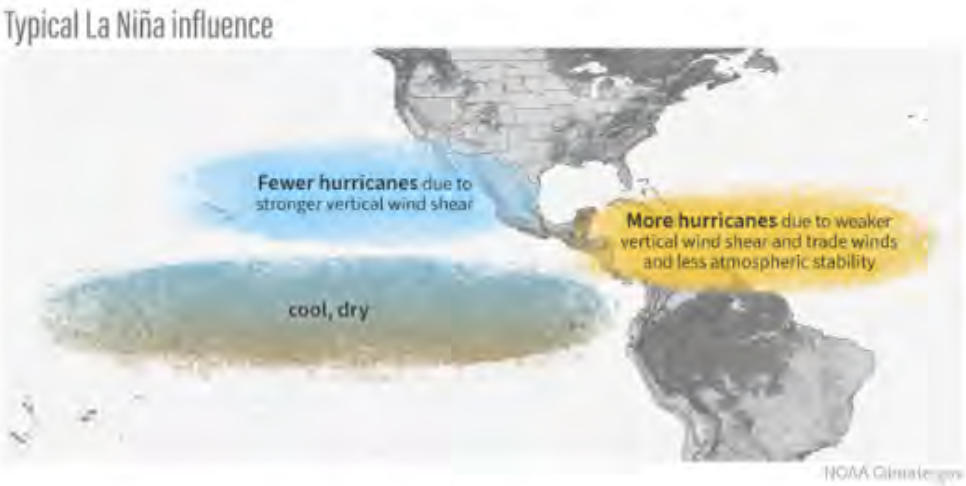

Typical influence of La Niña on Pacific and Atlantic seasonal hurricane activity. Map by NOAA Climate.gov, based on originals by Gerry Bell.

These impacts are primarily caused by changes in the vertical wind shear, which refers to the change in wind speed and direction between roughly 5,000-35,000 ft. above the ground. Strong vertical wind shear can rip a developing hurricane apart, or even prevent it from forming.

ENSO perturbs tropical and subtropical atmospheric circulation

During El Niño, the area of tropical Pacific convection and its associated Hadley circulation expand eastward from the western Pacific, sometimes extending to the west coast of South America. (A tutorial on El Niño and La Niña can be found at the NOAA Climate Prediction Center website.) At the same time, the equatorial Walker circulation is weaker than average.

These conditions produce an anomalous upper-level, ridge-trough pattern in the subtropics, with an amplified ridge over the subtropical Pacific in the area north of the enhanced convection, and a downstream trough over the Caribbean Sea and western tropical Atlantic. Over the central and eastern Pacific, the enhanced subtropical ridge is associated with weaker upper-level winds and reduced vertical wind shear, which favors more hurricane activity.

Over the Atlantic basin, the amplified trough is associated with stronger upper-level westerly winds and stronger lower-level easterly trade winds, both of which increase the vertical wind shear and suppress hurricane activity. In addition to enhanced vertical wind shear, El Niño suppresses Atlantic hurricane activity by increasing the amount of sinking motion and increasing the atmospheric stability.

La Niña has opposite impacts across the Pacific and Atlantic basins. During La Niña, the area of tropical convection and its Hadley circulation is retracted westward to the western Pacific and Indonesia, and the equatorial Walker circulation is enhanced. Convection is typically absent across the eastern half of the equatorial Pacific.

In the upper atmosphere, these conditions produce an amplified trough over the subtropical Pacific in the area north of the suppressed convection, and a downstream ridge over the Caribbean Sea and western tropical Atlantic. Over the central and eastern subtropical Pacific, the enhanced trough is associated with stronger upper-level winds and stronger vertical wind shear, which suppress hurricane activity. Over the Atlantic basin, the anomalous upper-level ridge is associated with weaker upper- and lower-level winds, both of which reduce the vertical wind shear and increased hurricane activity. La Niña also favors increased Atlantic hurricane activity by decreasing the amount of sinking motion and decreasing the atmospheric stability.

ENSO phases interact with other climate patterns that influence hurricanes

Another prominent climate factor to influence Atlantic hurricane activity is the Atlantic Multi-Decadal Oscillation (AMO) (Goldenberg et al. 2001, Bell and Chelliah 2006). The warm phase of the AMO is associated with high-activity eras for Atlantic hurricanes, such as has been in place since 1995. Conversely, the cold phase of the AMO is associated with low-activity eras (such as the period 1971-1994).

The warm phase of the AMO reflects warmer SSTs across the Atlantic hurricane Main Development Region (MDR, Figure 3). A key atmospheric feature of this pattern is a stronger West African monsoon, which produces a westward extension of the upper-level easterly winds (near 35,000 ft), along with weaker easterly trade winds in the lower atmosphere (near 5,000 ft).

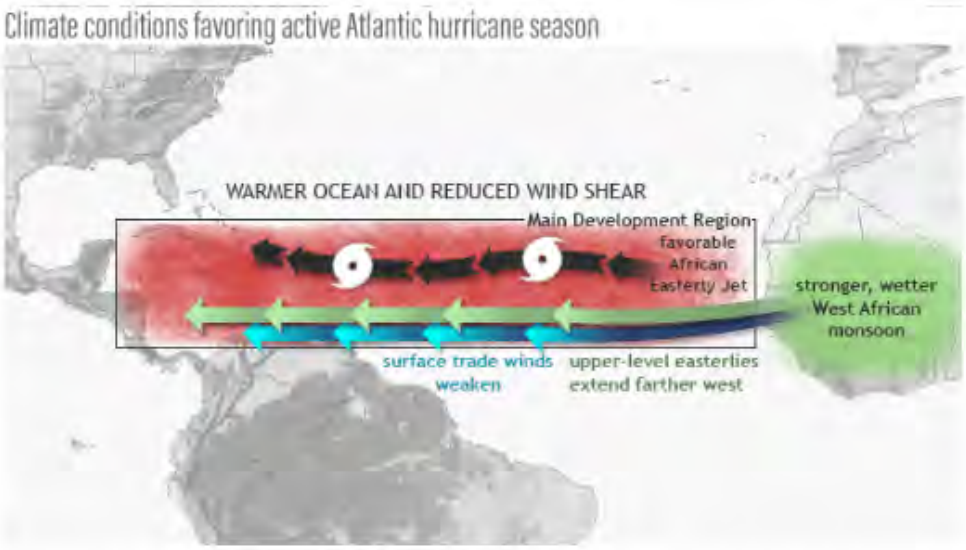

Seasonal climate patterns associated with active hurricane seasons. La Niña contributes to reduced vertical wind shear in the Main Development Region for hurricanes in this basin. Map by NOAA Climate.gov, based on originals by Gerry Bell.

This wind pattern is very conducive to increased Atlantic hurricane activity, partly because it results in weaker vertical wind shear. The weaker trade winds also contribute to a more conducive structure (i.e. increased cyclonic shear) of the mid-level (near 10,000 ft) African Easterly Jet (AEJ), favoring hurricane development from tropical cloud systems (i.e. easterly waves) moving westward from Africa. At the same time, these wind patterns are associated with a more northward push into the MDR of deep tropical moisture and unstable air, each of which also favors stronger hurricanes.

The hurricane activity in a given season often reflects a combination of the multi-decadal signals and ENSO. During an Atlantic high-activity era, El Niño typically results in a near-normal season, and La Niña produces an above-normal season. During an Atlantic low-activity era, El Niño typically results in a below-normal season and La Niña results in a near-normal season (Bell and Chelliah 2006).

Similarly for the central and eastern Pacific basins, the combination of a low-activity era and El Niño often produces a near-normal season, while La Niña produces a below-normal season. For a Pacific high-activity era, El Niño often produces an above-normal season, while La Niña produces a near-normal season.

This year the expectation that El Niño will develop, combined with the multi-decadal climate signals results in a forecast for a near- or below-normal season in the Atlantic, and a near- or above-normal season in both the central and eastern Pacific. For more detail, check out NOAA's 2014 Hurricane Season Outlook.

66. Assignment 2, Module 14: ENSO Impact on Regional Hurricane Activity: https://journals.ametsoc.org/view/journals/clim/20/7/jcli4063.1.xml

ENSO's Impact on Regional U.S. Hurricane Activity

SHAWN R. SMITH, JUSTIN BROLLEY, JAMES J. O'BRIEN, AND CARISSA A. TARTAGLIONE

Center for Ocean–Atmospheric Prediction Studies, The Florida State University, Tallahassee, Florida

(Manuscript received 5 December 2005, in final form 19 June 2006)

ABSTRACT

Regional variations in North Atlantic hurricane landfall frequency along the U.S. coastline are examined in relation to the phase of El Niño–Southern Oscillation (ENSO). ENSO warm (cold) phases are known to reduce (increase) hurricane activity in the North Atlantic basin as a whole. Using best-track data from the U.S. National Hurricane Center, regional analysis reveals that ENSO cold-phase landfall frequencies are only slightly larger than neutral-phase landfall frequencies along the Florida and Gulf coasts. However, for the East Coast, from Georgia to Maine, a significant decrease in landfall frequency occurs during the neutral ENSO phase as compared to the cold phase. Along the East Coast, two or more major (category 3 or above) hurricanes never made landfall in the observational record (1900–2004) during a single hurricane season classified as an ENSO neutral or warm phase.

1. Introduction

Atlantic basin hurricane landfall frequency, categorized by phases of El Niño–Southern Oscillation (ENSO), is examined for regional variations along the U.S. coastline. The work is motivated by a need to better understand regional variations in hurricane landfalls in an era of increasing hurricane activity and growing coastal population (Pielke and Landsea 1998; Changnon et al. 2000). Goldenberg et al. (2001) noted that hurricane activity across the Atlantic basin between 1995 and 2000 was nearly double the activity during the preceding 24 yr (1971–94). Above-normal hurricane numbers in 2004 and 2005 reflect a continuation of active Atlantic hurricane seasons. Clearly, regional landfall probabilities would be useful to many government agencies [e.g., the Federal Emergency Management Agency (FEMA) and local governments] as they plan for potential hurricane emergencies. To achieve maximum benefit, the results of the presented research must be combined with a 3–6-month lead time forecast of the ENSO phase that will onset during the Atlantic hurricane season.

Corresponding author address: Mr. Shawn R. Smith, Center for Ocean–Atmospheric Prediction Studies, The Florida State University, Tallahassee, FL 32306-2840.
E-mail: smith@coaps.fsu.edu

DOI: 10.1175/JCLI4063.1

The presented results expand upon the data and results contained in the master's thesis of Tartaglione (2002). The authors focus on differences in landfall frequency, landfall probability distributions, and the location where U.S. landfalling hurricanes are first classified as tropical storms only for the three phases of ENSO. The authors acknowledge that other climate modes, including the Atlantic Multidecadal Oscillation (AMO; e.g., Goldenberg et al. 2001; Sutton and Hodson 2005) and the North Atlantic Oscillation (NAO; Xie et al. 2005), likely play a role in hurricane frequency in the Atlantic, but these modes will not be explicitly treated in this analysis. Separating hurricane landfalls by ENSO phase and landfall region already limits the sample size for statistical testing. Further simultaneous separation using the AMO or NAO would further limit the ability to test for significant variability in regional landfalls. The primary update to Tartaglione (2002) is the use of the reanalyzed Atlantic hurricane best-track data for 1900–2004 (Landsea et al. 2004). The authors specifically limit discussion of cause and effect relationships, noting up front that this manuscript focuses on statistical relationships and that additional research is required.

The impact of ENSO on basin-wide North Atlantic hurricane activity has been well documented. ENSO warm-phase (El Niño) conditions reduce hurricane ac-

tivity in the North Atlantic basin (Gray 1984). The main factor Gray (1984) credited for the suppression of tropical cyclone development in the North Atlantic during El Niño is a strengthening of the upper-level westerlies over the equatorial Atlantic and Caribbean Sea. These westerly anomalies, estimated at 2–7 m s^{-1} during El Niño years, result in increased vertical wind shear, which is known to suppress tropical cyclone formation and growth (Gray 1968). Recently, Tang and Neelin (2004) have correlated the reduction in hurricanes during ENSO warm phases to changes in column static stability over the Atlantic. Conversely, ENSO cold-phase (La Niña) conditions tend to increase hurricane activity primarily due to weaker upper-level westerlies and reduced vertical wind shear.

Bove et al. (1998) also showed a decrease (increase) in hurricane landfall probabilities in the United States during El Niño (La Niña) events. For the period of record 1900–97, the mean number of hurricanes to make landfall in the United States annually was 1.04 during El Niño years, 1.61 during neutral years, and 2.23 during La Niña years (Bove et al. 1998). For the same period, Bove et al. (1998) found the probability of two or more North Atlantic hurricanes making landfall anywhere along the U.S. coastline to be 28% during El Niño, 48% during the neutral phase, and 66% during La Niña.

The previous studies do not analyze hurricane landfall probabilities for the United States on a regional scale. Regional differences in the effects of ENSO on hurricane landfalls in the Caribbean have been observed (Tartaglione et al. 2003; Landsea et al. 1999). El Niño (La Niña) decreases (increases) hurricane landfall activity relative to the neutral phase for the entire Caribbean region. Regionally, no differences were observed in hurricane landfall probabilities between the El Niño and neutral phases in the eastern and western Caribbean, while more landfalls occurred during the neutral versus warm phases in the northern Caribbean (Tartaglione et al. 2003). More recently, Klotzbach and Gray (2006) have begun providing forecast landfall probabilities for regions along the U.S. coastline; however, the role of ENSO is not directly included in their probability calculation but indirectly through their forecasts of net tropical cyclone activity.

As a follow-up to Tartaglione et al. (2003), hurricane landfall probabilities for the period 1900–2004 are calculated separately for Florida, the Gulf Coast, and the East Coast to assess the regional impact of ENSO on U.S. landfalls. The East Coast was defined as extending from the Florida–Georgia border northward to the Maine–Canada border. The Florida coastline extends from the Florida–Alabama border around Florida to the Florida–Georgia border, and the Gulf Coast spans from the Texas–Mexico border eastward to the Florida–Alabama border.

The analysis reveals a significant increase in the probability of hurricane landfalls along the East Coast during ENSO cold versus neutral phases. Surprisingly, there is virtually no difference in the probability of hurricane landfalls in Florida or along the Gulf Coast during ENSO cold versus neutral years. The probability of an East Coast landfall during ENSO neutral phases is nearly identical to the landfall probability for ENSO warm phases. Along the Gulf Coast and in Florida the landfall probabilities are reduced for warm versus neutral ENSO phases.

2. Methods

The Atlantic basin best-track hurricane dataset (HURDAT; Jarvinen et al. 1984; Neumann et al. 1993; Landsea et al. 2004) is used to identify hurricanes making landfall in the United States. The authors use all hurricanes (winds $\geq$ 64 kt) noted by HURDAT as making at least one landfall along the Florida, Gulf of Mexico, or East coasts. Only hurricanes (storms with winds $\geq$ 64 kt) defined by HURDAT as having a U.S. landfall are considered. The authors note that the list of U.S. landfalls derived from HURDAT includes a few hurricanes whose center never crossed the coastline (termed hurricane strikes) but were included as landfalls because 1-min wind speeds of at least hurricane force (64 kt) impacted the coast (C. Landsea 2006, personal communication). The term landfall in this paper is used to encompass both hurricane strikes and hurricanes whose center (eye) crossed the coastline. The record of landfalling hurricanes is more accurate than the record of all hurricanes because, prior to the deployment of satellites in the 1960s, open-ocean hurricanes may not have been identified if they failed to hit land. It is unlikely that any U.S. hurricane landfall was missed during the twentieth century. In addition, landfalling hurricanes are of more interest to the general public because they directly impact lives and property. The authors also use the Saffir–Simpson hurricane intensity scale listed in HURDAT to identify major (category 3–5) hurricanes.

Each landfalling storm is categorized following the method of Bove et al. (1998) as occurring during the onset summer of a warm, cold, or neutral ENSO phase. The phases of ENSO are defined using the Japan Meteorological Agency (JMA) index of equatorial Pacific sea surface temperatures (SST). Warm and cold phases classified by the JMA index compare favorably with many modern ENSO studies (Trenberth 1997;

TABLE 1. ENSO phases for hurricane seasons (June–November) based on the JMA index and the method of Bove et al. (1998). Row indicates decade, and column indicates year. W = warm, N = neutral, and C = cold ENSO phase.

	0	1	2	3	4	5	6	7	8	9
190	N	N	W	C	W	W	C	N	C	C
191	C	W	N	W	N	N	C	N	W	N
192	N	N	C	N	C	W	N	N	N	W
193	W	N	N	N	N	N	N	N	C	N
194	W	N	C	N	C	N	N	N	N	C
195	N	W	N	N	C	C	C	W	N	N
196	N	N	N	W	C	W	N	C	N	W
197	C	C	W	C	C	C	W	N	N	N
198	N	N	W	N	N	N	W	W	C	N
199	N	W	N	N	N	N	N	W	C	C
200	N	N	W	N	N					

Hanley et al. 2003). The JMA defines the 12-month period October through September as a warm (cold) phase when the 5-month running average SST anomaly over the tropical Pacific, from 4°S–4°N, 150°W–90°, is greater than 0.5°C (less than −0.5°C) for at least 6 consecutive months including October–December (JMA 1991). As an example, the hurricane season of June–November 1997 is split across the 1996 ENSO neutral event (June–September) and the onset of the 1997 ENSO warm event (October–November). By the criteria of Bove et al. (1998), the hurricane season of June–November 1997 is classified as occurring during the onset of an ENSO warm phase. All hurricane seasons that are not categorized as occurring during the onset of an ENSO warm or cold phase are classified as neutral seasons. Using this method, 25 of the hurricane seasons in the 105-yr period are classified as cold phases, 23 are designated warm phases, and 57 are categorized as neutral (Table 1).

The number of landfalls and landfall probabilities are determined for each ENSO phase and coastal region. Landfall counts are made for all hurricanes and for major hurricanes. If a hurricane makes landfall in Florida and then along the Gulf Coast, it is counted as a landfall in each of the two regions; however, the same hurricane is counted only once when considering all regions as a whole. In addition to counts of landfalls in each region, hurricane landfall probabilities for the 105-yr period of record are calculated using inverse cumulative frequency distributions (ICFDs).

The count of hurricane landfalls during a hurricane season is a discrete random variable; therefore, differences in the landfall frequency between ENSO phases can be tested in terms of two Poisson populations. Following the method used by Patten et al. (2003) and Tartaglione et al. (2003), a Z test based on a joint Poisson distribution (Lehmann 1986) is formulated to test the null hypothesis that the two rates of occurrence of hurricane landfalls between two ENSO phases are statistically similar. The alternative hypothesis assumes that the landfall rates of occurrence are significantly different. The Z-test statistic, with a continuity correction, is

$$Z = \left| \frac{x - 0.5 - \left(\frac{tn_x}{n_x + n_y} \right)}{\sqrt{t\left(\frac{n_x}{n_x + n_y} \right)\left(\frac{n_y}{n_x + n_y} \right)}} \right|. \quad (1)$$

Considering the comparison of ENSO cold versus neutral phases, x = the number of landfalls occurring in n_x cold-phase years, y = the number of landfalls in n_y neutral-phase years, and $t = x + y$. The Z test is valid when $t > 25$ and is evaluated for significance levels of 90% or higher.

ENSO phase shifts in the mean and median location where hurricanes making landfall in the United States are first classified within the HURDAT as a tropical storm or stronger (winds $\geq$ 34 kt) are identified for each coastal region. Standard error bars ($s/\sqrt{n}$) are applied to the mean latitude and longitude of tropical storm classification. Box plots of the tropical storm classification latitude and longitude reveal these distributions to be asymmetric (see Fig. 7); therefore, a nonparametric statistical test is used to reveal significant shifts in the median classification location. The test method is based on a 2 × 2 contingency table (Bhattacharyya and Johnson 1977). The null hypothesis tested states that median tropical storm classification latitude and longitude between two ENSO phases are statistically equal versus the alternate hypothesis that the medians are different. Mean and median locations of tropical storm classification are also provided for major hurricanes; however, the small sample size precludes the application of significance tests.

3. Results

The number of hurricane landfalls in the three coastal regions shows a clear pattern of interannual variability (Fig. 1). A total of 53 hurricanes made landfall along the East Coast between 1900 and 2004, with 18 making landfall during the 25 ENSO cold events, 10 during the 23 warm events, and 25 during the 57 neutral events (Fig. 1a). Landfalls along the East Coast show clear active and inactive periods, with only two landfalls from 1917 to 1932 and only one from 1961 to 1970. During the same time period, 67 hurricanes made landfall in Florida (Fig. 1b). There were 20, 7, and 40 land-

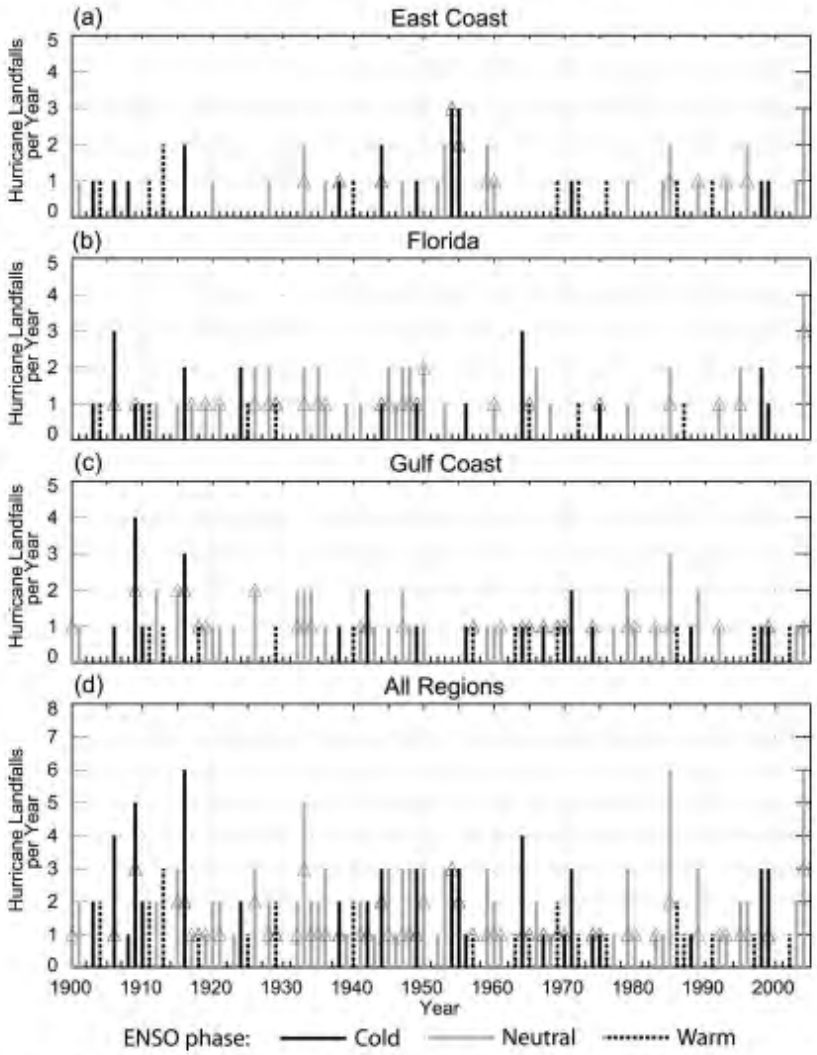

FIG. 1. The number of hurricanes that made landfall along the (a) East Coast (except Florida), (b) Florida coast, (c) Gulf Coast (except Florida), and (d) the entire U.S. coastline during each year between 1900 and 2004. ENSO cold, neutral, and warm phases are indicated by black, gray, and black dashed bars, respectively. Triangles indicate the number of category 3, 4, and 5 hurricanes while bars indicate the total of all hurricane categories.

falls during the cold, warm, and neutral ENSO phases, respectively. The record in Florida shows nearly twice the landfalls (41) from 1900 to 1950 that occurred from 1951 to 2001 (22 landfalls). The Gulf Coast experienced the most landfalls (77) from 1900 to 2004 (Fig. 1c), with 23, 12, and 42 landfalls during the cold, warm, and neutral ENSO phases, respectively. Gulf Coast landfalls are distributed fairly evenly through the 105-yr period record. The totals for all regions combined (57 cold-, 94 neutral-, and 26 warm-phase landfalls) show a drop in landfalls from 1960 to 1995 (Fig. 1d), which coincides with the decrease in Atlantic major hurricanes from the mid-1960s to 1994 noted by Goldenberg et al. (2001).

Landfall frequency per year for the entire U.S. coastline from 1900 to 2004 (Fig. 2d) compares favorably with the results of Bove et al. (1998). Regionally, the highest frequencies occur during ENSO cold phases for each of the three coastal regions (Figs. 2a–c). The landfall counts result in an average of 0.72, 0.80, and 0.92 hurricane landfalls per season, respectively, for the East Coast, Florida, and the Gulf Coast during ENSO cold phases. Comparing landfall frequencies during ENSO

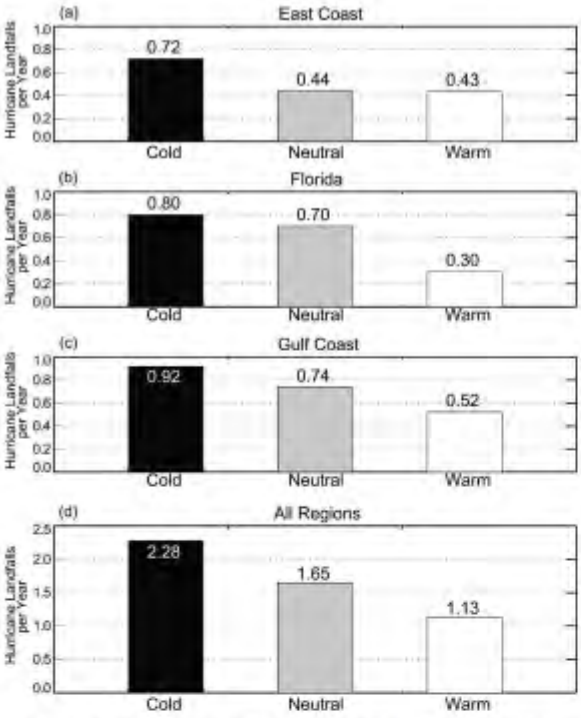

FIG. 2. Average number of hurricane landfalls per year (a) on the East Coast (except Florida), (b) in Florida, (c) along the Gulf Coast (except Florida), and (d) along the entire U.S. coastline from 1900 to 2004 during years classified as cold, neutral, or warm ENSO phases. As an example of how to interpret these averages, approximately one (0.92) landfall occurs per ENSO cold phase vs one landfall for every two ENSO warm phases (0.52) along the Gulf Coast.

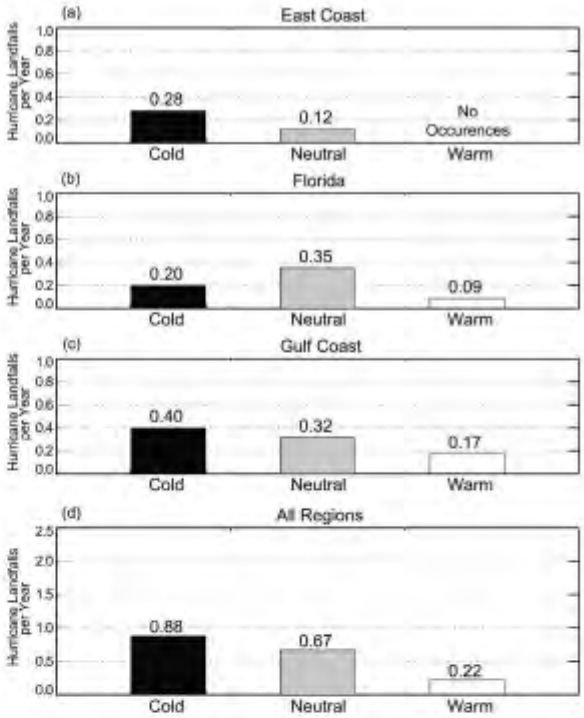

FIG. 3. Average number of major (category 3, 4, or 5) hurricane landfalls per year (a) on the East Coast (except Florida), (b) in Florida, (c) along the Gulf Coast (except Florida), and (d) along the entire U.S. coastline from 1900 to 2004 during years classified as cold, neutral, or warm ENSO phases. Within the 1900–2004 period, there were no occurrences of major hurricane landfalls along the East Coast during ENSO warm phases.

cold versus neutral phases reveals a significant decrease only for hurricanes making landfall along the East Coast. Applying the Z test from (1) allows rejection of the hypothesis that East Coast landfall frequencies are equal during ENSO cold and neutral phases at a significance level of greater than 90%. During a neutral phase along the East Coast (Fig. 2a), only 0.44 hurricane landfalls occur per season, which can be interpreted as approximately four landfalls for every 10 neutral phases. This compares to seven landfalls for every 10 ENSO cold phases along the East Coast. Differences in ENSO cold versus neutral landfall probabilities are notably smaller for Florida and the Gulf Coast (Figs. 2b,c). These results suggest that there is a significant change in formation location and/or steering patterns during neutral years that limits East Coast landfalls.

The probability of hurricane landfalls within each of the three coastal regions is lowest for ENSO warm phases (Fig. 2). The authors expected this result based on previous work, but clear regional variations also exist for the warm versus neutral ENSO phases. First, the probability of hurricane landfall along the East Coast is nearly identical for warm and neutral ENSO phases (Fig. 2a). In addition, the difference in landfall probabilities in Florida between warm (0.30) and neutral (0.70) phases is significant at the 99% level (based on the Z test).

Limiting the analysis to major hurricane landfalls again reveals the Gulf Coast to have the most landfalls (32) as compared to Florida (27) and the East Coast (14). Major hurricane landfall frequency for the combined U.S. coast from 1900 to 2004 mirrors the results for all hurricanes, with more (less) landfalls during cold (warm) phases relative to neutral. Regionally, the highest landfall frequencies occur during the cold ENSO phase for the East and Gulf Coasts (Figs. 3a,c); however, the neutral phase dominates major hurricane landfalls in Florida (Fig. 3b). The number of landfalls represents a summary of rare events during the 1900–2004 period of record and the totals are too small to allow the application of the Z test for major hurricanes. Clearly the warm-phase sample is too small to draw any

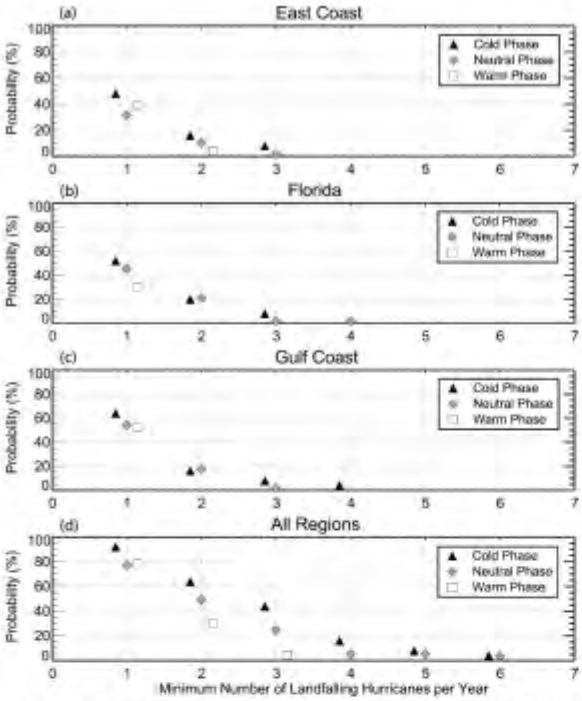

FIG. 4. ICFD of hurricanes making landfall (a) on the East Coast (except Florida), (b) in Florida, (c) on the Gulf Coast (except Florida), and (d) along the entire U.S. coastline for ENSO cold, neutral, and warm phases from 1900 to 2004. ICFD shows the probability of x or more hurricanes making landfall within 1 yr, where x is the abscissa on the plot. For all cases, the probability of zero or more hurricanes is 100% by definition and is not plotted.

regional conclusions beyond the fact that the rare event of a major hurricane landfall is even more infrequent during ENSO warm phases based on the 1900–2004 period of record. Based on the small sample available, the authors note that the only years between 1900 and 2004 with two or more major hurricane landfalls along the East Coast (1954 and 1955) are classified as ENSO cold phases (Fig. 1a). In Florida from 1900 to 2004, only two ENSO neutral years have had multiple major hurricane landfalls (1950 and 2004), while two ENSO cold and two ENSO neutral years (1909 and 1916; 1915 and 1926, respectively) had two major hurricane landfalls on the Gulf Coast (Fig. 1).

The ICFDs from the 1900–2004 period confirm a higher probability of hurricanes making landfall during cold versus neutral ENSO phases along the East Coast. During a cold phase, the probability of two or more hurricanes hitting the East Coast is 16% versus only 10% during a neutral phase (Fig. 4a). In Florida, the probability of two or more hurricanes making landfall is nearly identical for the cold (20%) and neutral (21%) phases (Fig. 4b). Probabilities of two or more landfalls along the Gulf Coast are also similar during a cold (16%) and neutral (17%) phase. The authors note that no ENSO warm-phase season during the 1900–2004 record has produced more than one hurricane landfall in Florida or along the Gulf Coast (Fig. 4). In addition, when considering the combined coastline, only cold and neutral phases have exhibited four, five, or six hurricane landfalls in a single year.

The analysis above clearly shows regional differences in landfall frequencies during ENSO phases. The differences led the authors to question whether there are variations in the location where landfalling hurricanes first reach tropical storm status during the three ENSO phases. Identifying variations in tropical storm classification location will help focus future research into the variability of physical processes (e.g., air–sea fluxes of heat and moisture) that enhance or suppress hurricane activity.

Plotting the location where each U.S. landfalling hurricane was first classified as a tropical storm or stronger in the HURDAT reveals differences by ENSO phase (Fig. 5). Most striking is the expected reduction in the number of tropical cyclones forming during ENSO warm phases (Fig. 5c). The overall mean (Fig. 6) and median (Fig. 7) position of first classification as a tropical storm is shifted to the north and west for hurricanes making landfall along the entire U.S. coastline during a warm phase, relative to cold or neutral phases. Nonparametric tests reject the hypothesis that the all-regions warm-phase median latitude is equal to the neutral (and cold)-phase median with a confidence of greater than 90%. For the East Coast, the northward shift (relative to neutral phase) in median latitude and the westward shift (relative to neutral and cold phases) in median longitude during a warm phase reject the hypothesis of equal medians at the 99% and 95% level, respectively (Table 2; Fig. 7). Similar significance can be expected for the East Coast mean latitude and longitude where the range of 2 times the standard error on the mean for the cold and neutral phases falls outside the same range for the warm phase (Fig. 6). The authors also note that no hurricane making landfall in the United States during ENSO warm phases was first classified as a tropical storm east of 50°W from 1900 to 2004 (Fig. 5c).

Overall, the difference in median tropical storm classification position for cold- versus neutral-phase landfalling hurricanes is small (only 1.0° latitude and 1.5° longitude); however, significant regional variations are present (Table 2; Fig. 7). Hurricanes making landfall in Florida exhibit a 12.8° westward shift in median tropical storm classification location during ENSO cold versus neutral phases (Table 2). This significant westward shift

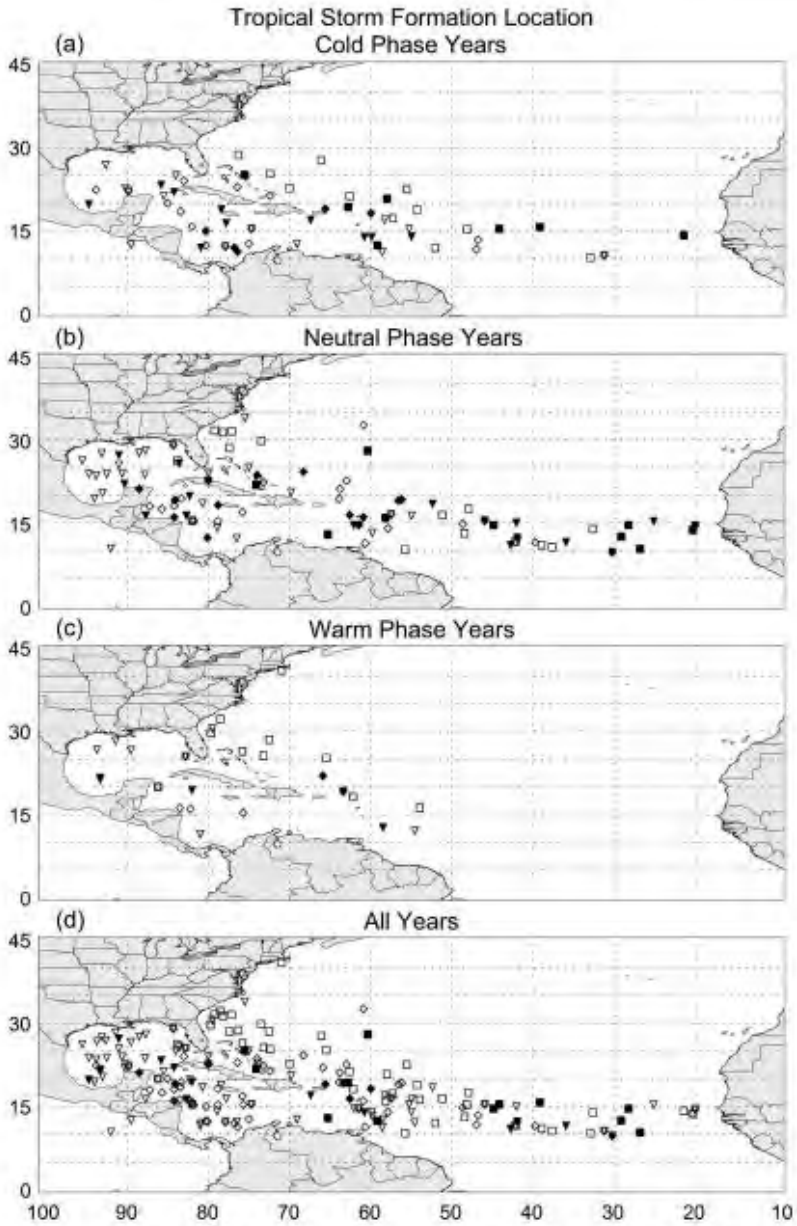

FIG. 5. Location at which hurricanes making landfall in the United States are first designated as a tropical storm (or stronger) within the HURDAT for ENSO (a) cold, (b) neutral, and (c) warm phases and (d) all years combined. Landfall location is separated into East Coast (square), Florida (diamond), and Gulf Coast (inverted triangle). Open symbols are hurricanes that made landfall as a category-1 or -2 storm, and closed symbols are hurricanes that made landfall as a category-3, -4, or -5 storm. Note that storms may move across land as a tropical storm and make landfall in a different region as a hurricane.

(90% level) brings developing tropical storms closer to the Florida coast and increases the probability of these storms making landfall as hurricanes in Florida during ENSO cold phases.

East Coast landfalling hurricanes, except those forming during a warm phase, typically form farther east than those that strike Florida or the Gulf Coast (Figs. 5–7). In fact, the median longitude of tropical storm

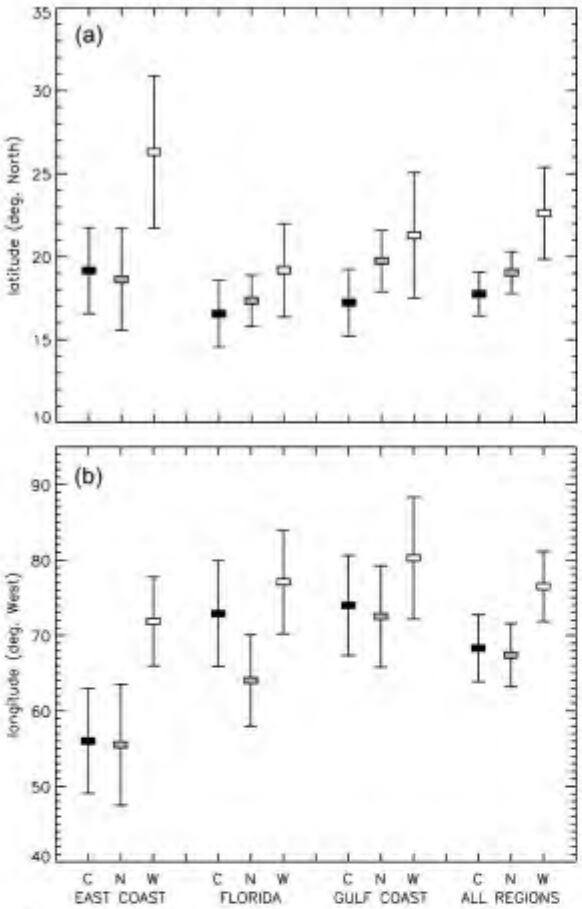

FIG. 6. Mean (a) latitude and (b) longitude at which hurricanes making landfall in the United States are first classified in HURDAT as a tropical storm. Means are separated into cold (C, black), neutral (N, gray), and warm (W, white) ENSO phases and are grouped by landfall region. Error bars represent 2 times the standard error of the mean ($s/\sqrt{n}$).

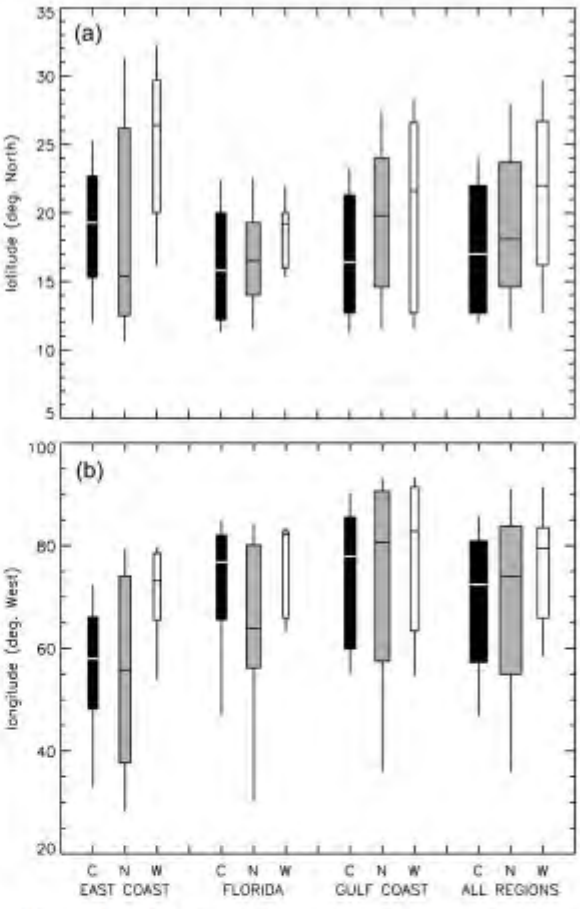

FIG. 7. Box plots showing the median and interquartile range for the (a) latitude and (b) longitude at which hurricanes making landfall in the United States are first classified in HURDAT as a tropical storm. Box plots are separated into cold (C, black), neutral (N, gray), and warm (W, white) ENSO phases and are grouped by landfall region. Upper (lower) whiskers extend to the 90th (10th) percentile value and the box width is proportional to the $\sqrt{n}$.

classification during cold and neutral ENSO phases is near or less than the 25th percentile longitude for both Florida and Gulf Coast landfalling hurricanes (Fig. 7). Tropical cyclones that form in the far eastern Atlantic have more time to be influenced by upper-level troughs as they travel across the Atlantic, thereby increasing the likelihood that they will reach a more northern latitude and impact the East Coast. During the ENSO cold phase, the 19.0° difference in median longitude of tropical storm classification between hurricanes making East Coast versus Florida landfall is significant at the 99% level. During the neutral phase, the East Coast versus Florida median longitude difference is only 8.0°, but this difference grows to 17.1° when considering only major hurricanes. Major hurricanes making landfall during the neutral phase in Florida have a median tropical storm classification longitude of 62.0° versus 44.9°W for East Coast major hurricanes during the neutral phase (Table 2). A classification location closer to the United States may partially explain Florida having the highest probability (35%) of a major hurricane landfall during ENSO neutral phases (Fig. 3b) over the 1900–2004 period of record.

Along the East Coast, the reduction in hurricane landfalls during ENSO neutral phases may be related to variations in the number of hurricanes that are first classified as tropical storms in the eastern tropical North Atlantic Ocean. When considering all hurricanes that make landfall in the United States over the 105-yr period of record there is a 16% probability per year that hurricanes first classified as a tropical storm east of

TABLE 2. Mean, standard error ($s/\sqrt{n}$), and median of the latitude (°N) and longitude (°W) at which U.S. landfalling hurricanes first achieve tropical storm (or stronger) status according to the best-track data. The number of hurricane landfalls (n) is determined by separating landfalls by coastal region (e.g., East Coast, Florida, and Gulf of Mexico) and ENSO phase. Summary statistics for all regions are also presented, but note that the totals are not cumulative due to the method of counting only one landfall for the combined region even if a hurricane makes landfall in multiple subregions. The statistics are shown for (top) all and (bottom) major hurricanes when n ≥ 5.

All landfalling hurricanes

ENSO phase		Cold		Neutral		Warm	
		Lat	Lon	Lat	Lon	Lat	Lon
East Coast	Mean	19.1	56.0	18.6	55.5	26.3	71.9
	Std error	1.3	3.5	1.5	4.0	2.3	2.9
	Median	19.1	57.6	15.4	55.8	26.0	72.8
	n	18	18	25	25	10	10
Florida	Mean	16.6	72.9	17.3	64.0	19.2	77.1
	Std error	1.0	3.5	0.8	3.0	1.4	3.4
	Median	15.6	76.6	16.4	63.8	19.2	82.2
	n	20	20	40	40	7	7
Gulf Coast	Mean	17.2	74.0	19.7	72.5	21.3	80.2
	Std error	1.0	3.3	0.9	3.4	1.9	4.0
	Median	16.4	77.9	19.6	80.3	21.4	82.4
	n	23	23	42	42	12	12
All regions	Mean	17.8	68.3	19.0	67.4	22.6	76.5
	Std error	0.7	2.2	0.6	2.1	1.4	2.3
	Median	17.0	72.4	18.0	73.9	21.8	79.0
	n	57	57	94	94	26	26

Major landfalling hurricanes

ENSO phase		Cold		Neutral		Warm	
		Lat	Lon	Lat	Lon	Lat	Lon
East Coast	Mean	17.6	51.5	16.8	46.0	—	—
	Std error	1.7	6.7	2.3	7.1	—	—
	Median	15.7	58.0	14.6	44.9	—	—
	n	7	7	7	7	0	0
Florida	Mean	15.1	71.8	16.6	59.3	—	—
	Std error	1.6	3.8	0.9	4.9	—	—
	Median	15.0	76.4	16.0	62.0	—	—
	n	5	5	20	20	2	2
Gulf Coast	Mean	17.1	74.5	16.8	58.8	—	—
	Std error	1.2	4.1	1.2	5.7	—	—
	Median	16.7	78.1	15.3	56.9	—	—
	n	10	10	18	18	4	4
All regions	Mean	16.8	66.6	17.1	59.5	19.0	72.6
	Std error	0.8	3.6	0.8	3.6	1.7	6.5
	Median	16.0	66.5	16.0	61.2	19.4	65.9
	n	22	22	38	38	5	5

50°W will make landfall on the East Coast regardless of ENSO phase. The probability drops to 13% for Florida and 9% for Gulf Coast landfalls, respectively. In other words, one hurricane reaching tropical storm status east of 50°W makes landfall on the East Coast every 6 yr versus one in every 10 yr along the Gulf Coast. When we consider the actual number of landfalling hurricanes first classified as tropical storms east of 50°W, we find that 5 (11), 3 (9), and 1 (8) made landfall along the East Coast, in Florida, and along the Gulf Coast during ENSO cold (neutral) phases (Fig. 5). Based on there being only 2.4 times as many neutral-phase years as cold-phase years from 1900 to 2004, it is surprising that 8 times as many hurricanes classified as tropical storms east of 50°W during a neutral phase make landfall on the Gulf Coast. The increase during neutral phases (relative to cold phases) in landfalls along the Florida and Gulf coasts for hurricanes classified as tropical storms east of 50°W allows the authors to hypothesize that a variation in the steering flow exists during neutral phases. The hypothetical variation in the steering flow seems to keep tropical cyclones forming in the eastern tropical North Atlantic on a more southerly track during a neutral ENSO phase, thereby decreasing the probability of East Coast landfalls.

Recent work by Xie et al. (2005) reveals that hurricanes favor tracks moving more to the southwest (northeast) during ENSO cold (warm) phases. This pattern favors landfalls along the East Coast during ENSO cold phases. Xie et al. (2005) do not comment on tracks during ENSO neutral phases; however, separating hurricane landfall locations along the East Coast by state boundaries reveal that hurricanes tend to hit farther south during an ENSO neutral phase than during cold phases. For the 1900–2004 period, both Georgia and South Carolina have more landfalls during ENSO neutral versus cold phases. Georgia averages one landfall for every 20 neutral-phase years while there are no occurrences, from 1900 to 2004, of a hurricane landfall in Georgia during a cold phase. In South Carolina, an average of one hurricane makes landfall for every six (eight) ENSO neutral (cold) phase years. From North Carolina through Massachusetts there are more landfalls during ENSO cold versus neutral phases, excluding Delaware and New Jersey, which recorded no landfalls. The more southerly landfall location on the East Coast during ENSO neutral phases combined with the result that 8 times as many hurricanes reaching tropical storm status east of 50°W during a neutral phase make landfall on the Gulf Coast versus the East Coast imply that a more southerly track for hurricanes is favored during ENSO neutral phases, thus decreasing the likelihood of an East Coast landfall.

4. A look at 2005

The authors' primary analysis was completed during the extremely active 2005 hurricane season, so 2005 data are not included in the results above. We now compare the 2005 hurricane season to the 1900–2004

TABLE 3. Statistics for hurricanes making landfall along the U.S. coastline during the 2005 hurricane season. Note that Katrina made landfall in two regions: category 1 in Florida and category 3 along the Gulf Coast. (Source: HURDAT 2005 update.)

Name	Landfall region	Saffir–Simpson category at landfall	Location at tropical storm classification
Cindy	Gulf Coast	1	25.1°N, 90.2°W
Dennis	Florida	3	13.0°N, 65.9°W
Katrina	Florida	1	24.5°N, 76.5°W
	Gulf Coast	3	
Ophelia	East Coast	1	27.9°N, 78.8°W
Rita	Gulf Coast	3	22.2°N, 72.3°W
Wilma	Florida	3	16.9°N, 79.6°W

results. The JMA index and the method of Bove et al. (1998) classify the 2005 hurricane season as a neutral ENSO phase. A recent update of the HURDAT data to include the 2005 season reveals that six hurricanes made landfall along the U.S. coastline (Table 3). The 2005 hurricane season marks only the fourth time since 1900 that six hurricanes made U.S. landfall (other years are 1916, 1985, and 2004). The 2005 season also marks the first occurrence since 1900 of four hurricanes classified as major at landfall.

By region, one, three, and three hurricane landfalls occurred along the East Coast, in Florida, and along the Gulf Coast, respectively. The fact that only one of the seven landfalls occurred along the East Coast is consistent with the authors' findings of reduced East Coast landfall probabilities during ENSO neutral phases (Fig. 2). The location at which each of these five hurricanes reached tropical storm strength, clustered between 60° and 80°W longitude, also contributed to the reduced probability that they would make landfall along the East Coast (none of these cyclones first reached tropical storm strength in the favored East Coast landfall region east of 50°W). Finally, the authors note that the only occurrences from 1900 to 2005 of multiple major hurricane landfalls in Florida (Fig. 1b; Table 3) are during ENSO neutral years (1950, 2004, and 2005). Multiple major hurricane landfalls along the Gulf Coast (Fig. 1c; Table 3) are almost equally likely during the cold (1909 and 1916) and neutral (1915, 1926, and 2005) phases.

5. Conclusions

The regional differences in Atlantic hurricane landfall probabilities along the U.S. coast are identified with respect to the warm, neutral, and cold phases of ENSO. Combining forecasts of the ENSO phase that will onset during a hurricane season with the landfall frequencies from 1900 to 2004, one can determine whether the probability of a hurricane landfall is the highest along the East Coast, in Florida, or along the Gulf Coast. Local, state, and federal emergency management agencies, particularly with respect to coastal areas, should benefit from the results of this study.

Residents of the East Coast are most likely to see a landfalling hurricane during a season that precedes a La Niña winter. The landfall probability during ENSO cold phases (0.72) drops to 0.44 during neutral phases for East Coast landfalls. In Florida and along the Gulf Coast, there is little difference observed in the frequency of hurricane landfalls between cold and neutral events. As expected from previous works, landfall probabilities are smallest during ENSO warm phases in all regions.

Exploring the possible physical mechanisms that may explain the decrease in hurricane landfalls along the East Coast during neutral years are beyond the scope of this work. Variations in the landfall location of hurricanes first reaching tropical storm status in the eastern tropical North Atlantic Ocean are revealed between ENSO cold and neutral phases. Overall hurricanes reaching tropical storm strength in the eastern tropical Atlantic are more likely to strike the East Coast; however, hurricanes reaching tropical storm strength in this region during ENSO neutral phases have a higher than expected probability of striking Florida or the Gulf Coast. Clearly variations in location where landfalling hurricanes first reach tropical storm strength alone cannot account for variations in regional U.S. landfalls and future research must investigate changes in steering flow during ENSO phases. The strength, position, and shape of the subtropical Atlantic surface anticyclone and its relationship to phases of the North Atlantic Oscillation and Atlantic multidecadal oscillation should be considered. Further investigation is needed to gain a better understanding of the mechanisms suppressing East Coast hurricane landfalls during ENSO neutral years.

Acknowledgments. Funding for this research was provided by the National Oceanic and Atmospheric Administration (NOAA) Office of Global Programs through an Applied Research Center. Additional funding for this work was provided by NASA and the USDA. The authors thank Mark Bourassa for his insight into statistical methods, Melissa Griffin for her helpful suggestions, and Shane Prorok for his contribution to the 2005 hurricane analysis. The authors also express their gratitude to Christopher Landsea and the two anonymous reviewers for their constructive comments on this manuscript.

67. Assignment 2, Module 14: AMO and AMV: https://climatedataguide.ucar.edu/climate-data/atlantic-multi-decadal-oscillation-amo

Atlantic Multi-decadal Oscillation (AMO) and Atlantic Multidecadal Variability (AMV)

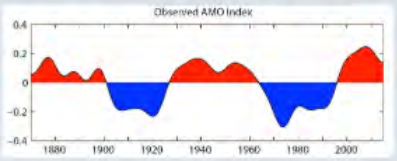

The Atlantic Multi-decadal Oscillation (AMO) has been identified as a coherent mode of natural variability occurring in the North Atlantic Ocean with an estimated period of 60-80 years. It is based upon the average anomalies of sea surface temperatures (SST) in the North Atlantic basin, typically over 0-80N.

To remove the signal of long-term change from the AMO index, users typically detrend the SST data at each gridpoint or detrend the spatially averaged timeseries. Trenberth and Shea (2006) recommend that this be done by subtracting the global-mean SST anomaly timeseries from the spatially averaged timeseries. See the Expert Guidance by Dr. Kevin Trenberth for the rationale for the global-mean detrending approach.

A recent paper, Deser and Phillips (2021), has a more extensive discussion of how to define the unforced AMO/AMV in a changing climate.

The Expert Guidance by Dr. Rong Zhang discusses the impacts and mechanisms of the AMO.

Key Strengths

- The SST-based AMO index provides a simple, concise way to describe multidecadal climate variability in the North Atlantic
- Associated with important climate impacts, such as the multidecadal variability of Atlantic Hurricane activity, North American and European summer climate, northern hemispheric mean surface temperature, and Arctic sea ice anomalies
- The AMO pattern is robust across different datasets (i.e. HadISST, ERSST, Kapan SST)

Key Limitations

- Instrumental SST data are short in length compared to the multidecadal timescale of the AMO
- The SST-based AMO index does not directly capture aspects of the AMO related to coherent variations in salinity, subsurface temperature and ocean-driven turbulent heat fluxes
- Quantifying the relative importance of large scale ocean circulation (especially AMOC) vs. external radiative forcing in causing the AMO is challenging

Data Access

Expert User Guidance

The following was contributed by **Dr. Rong Zhang**, March, 2016:

The observed large-scale multidecadal fluctuations in the Atlantic sea surface temperature (SST), has been referred to as the Atlantic Multidecadal Oscillation (AMO) (Kerr, 2000) to emphasize the "multidecadal" character of this oceanic phenomenon and to distinguish it from the inter-annual variability associated with the atmospheric North Atlantic Oscillation (NAO) (Enfield et al. 2001). The AMO index is defined as an area average of detrended low-pass filtered North Atlantic SST anomalies to reflect the Atlantic low frequency variability at time scales longer than a decade (Enfield et al., 2001; Sutton and Hodson, 2005; Knight et al 2005; Ruiz-Barradas et al., 2013).

The AMO pattern (Figure 2a) is derived by regressing detrended SST anomalies on the AMO index (Figure 1) (Sutton and Hodson, 2005; Knight et al., 2005; Ruiz-Barradas et al., 2013). The positive AMO phase corresponds with positive SST anomalies over most of the North Atlantic, with stronger anomalies in the subpolar region and weaker anomalies in the tropics (Figure 2a). The warm AMO phases occurred during the middle of the 20th century and the recent decades since 1995, and cold phases occurred during the early 20th century and during 1964-1995 (Figure 1). The monopolar AMO pattern associated with this multidecadal variability should be distinguished from the tripolar SST pattern induced by the NAO at the inter-annual time scale (Figure 2b), and hence the AMO pattern should not be derived by regressing on the detrended "unfiltered" North Atlantic basin averaged SST index (see Figure 2).

The AMO has significant regional and hemispheric climate impacts, such as modulating multidecadal variations in U.S. rainfall and drought frequency (Enfield et al., 2001; McCabe et al. 2004), summer climate over North America and Europe (Sutton and Hodson, 2005, 2007; Sutton and Dong, 2012), Atlantic Hurricane activity and India/Sahel summer rainfall (Folland et al., 1986; Goldenberg et al. 2001; Knight et al., 2006; Zhang and Delworth, 2006; Latif et al., 2007), northern hemispheric mean surface temperature (Zhang et al. 2007; Semenov et al., 2010), and Arctic sea ice (Mahajan et al. 2011; Day et al. 2012; Miles et al. 2014; Zhang, 2015; Yeager et al. 2015). Zhang and

Delworth (2007) found that the AMO can contribute to the Pacific Decadal Oscillation (PDO) and the associated Pacific/North America (PNA) pattern at the multidecadal time scale, and suggested that a North Pacific regime shift (opposite to the 1976–77 shift) might occur several years after the mid 90's shift in the observed AMO. The AMO is also found to have had a substantial influence on the equatorial Pacific decadal variability (Kucharski et al. 2015) and have modulated the El Niño Southern Oscillation (ENSO) variability at low frequency (Dong and Sutton, 2007; Kang et al. 2014). Observational and modeling studies suggest that multidecadal variations of the atmospheric NAO are modulated by the AMO, with the positive AMO phase leading the negative winter NAO phase by a few years (Gastineau and Frankignoul, 2012; Hodson et al. 2014). Recent modeling studies show that the simulated multidecadal winter NAO response to the AMO can be significantly improved by resolving the stratosphere and enhancing stratosphere/troposphere coupling (Omrani et al., 2014, 2016).

The AMO is often thought to be driven by the variability of the Atlantic Meridional Overturning Circulation (AMOC) (Kushnir, 1994; Delworth and Mann, 2000; Knight et al., 2005; Latif et al., 2006), although some have suggested that the AMO is mainly driven by changes in anthropogenic radiative forcing (Mann and Emanuel, 2006). Various approaches have been proposed for the quantitative attribution of the AMO to an anthropogenic radiatively forced part and a part arising from natural variability (Trenberth and Shea, 2006; Kravtsov and Spannagle, 2008; Ting et al. 2009; DelSole et al. 2011; Wu et al. 2011). Recently it has been suggested that anthropogenic aerosols are a prime driver of the AMO using climate model simulations incorporating aerosol indirect effects (Booth et al., 2012). However, there are major discrepancies between the simulations in Booth et al. (2012) and observations in the North Atlantic upper-ocean heat content, in the spatial pattern of multidecadal SST changes within and outside the North Atlantic, and in the subpolar North Atlantic sea surface salinity (SSS), due to overestimated aerosol indirect effects (Zhang et al. 2013). Besides, the aerosol effects cannot account for the observed anticorrelation between detrended multidecadal surface and subsurface temperature variations in the tropical North Atlantic. These discrepancies cast considerable doubt on the claim that aerosols drive the bulk of the AMO. On the other hand, independent AMOC fingerprints derived from the observed subsurface ocean temperature indicate that the past AMOC variations are coherent with the observed AMO (Zhang, 2007, 2008; Wang and Zhang, 2013), bringing more evidence that the observed AMO is linked to AMOC variations rather than merely a 20th century artifact of changes in radiative forcing.

The SST-based definition of the AMO index often leads to the incomplete understanding of the AMO only in terms of North Atlantic SST anomalies. In contrast, the AMO actually reflects coherent multivariate low frequency variability observed in the Atlantic, including correlated variations in the subpolar North Atlantic heat content, salt content, and ocean-driven surface turbulent heat fluxes, as well as anticorrelated variations in the tropical North Atlantic subsurface temperature (Zhang 2007, 2008; Wang et al. 2010, Robson et al. 2012; Zhang et al. 2013; Gulev et al. 2013; Wang and Zhang, 2013). Mechanisms proposed for the AMO have to account for the observed coherent multivariate low frequency variability in the Atlantic, in addition to the low frequency North Atlantic SST variations. It is crucial to use multivariate metrics to understand the mechanisms causing the AMO.##

Key Figures

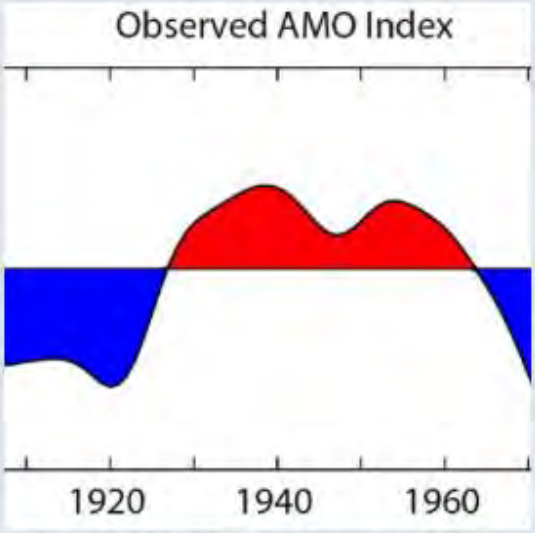

Observed AMO index, defined as detrended 10-year low-pass filtered annual mean area-averaged SST anomalies over the North Atlantic basin (0N-65N, 80W-0E), using HadISST dataset (Rayner et al. 2003) for the period 1870-2015. (Created by Dennis Shea and Dr Rhong Zhang for the Climate Data Guide)

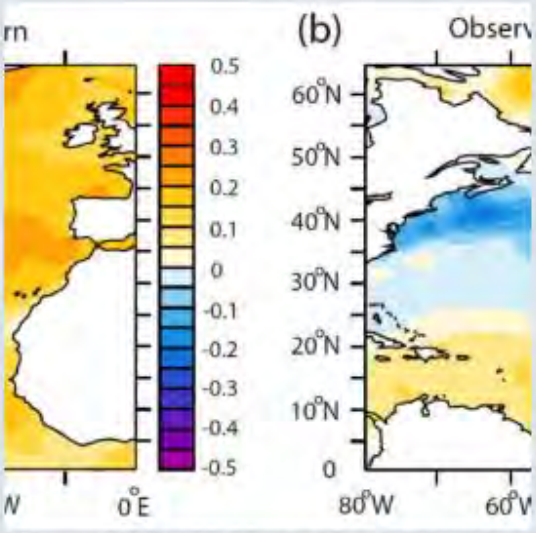

(a) Observed AMO SST pattern, derived by regressing detrended North Atlantic annual mean SST anomalies on the observed AMO index (Figure 1), using HadISST dataset (Rayner et al. 2003) for the period 1870-2015. The regression corresponds to 1 standard deviation of the observed AMO index. (b) Observed NAO SST pattern (inverted), derived by regressing detrended North Atlantic annual mean SST anomalies (HadISST dataset) on the inverted detrended observed winter NAO index (Hurrell Station-Based DJFM NAO Index) for the period 1870-2016. The regression corresponds to 1 standard deviation of the inverted observed NAO index. (Created by Dr Rhong Zhang for the Climate Data Guide)

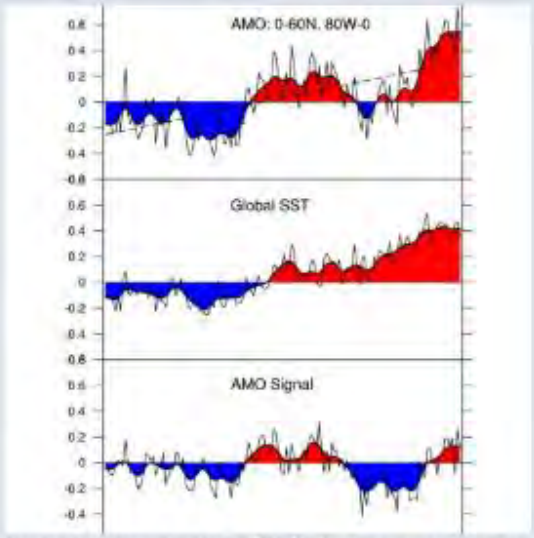

Atlantic Multi-decadal Oscillation (AMO) 1870-2011 derived from HadISST and using the Trenberth and Shea (2006) definition. [Climate Data Guide; D. Shea]

68. Assignment 2, Module 14: NAO: https://www.metoffice.gov.uk/research/climate/seasonal-to-decadal/gpc-outlooks/ens-mean/nao-description

The North Atlantic Oscillation

The term 'North Atlantic Oscillation' is used by meteorologists to refer to variations in the large-scale surface pressure gradient in the North Atlantic region.

In the average state of the atmosphere, the North Atlantic surface pressure is relatively high in the subtropics at latitudes 20°N to 40°N ('the Azores High'), and lower further North at latitudes 50°N to 70°N (the 'Icelandic Low'). The North-South pressure difference determines the strength of the westerly winds across the Atlantic and is known as the North Atlantic Oscillation (NAO).

When the pressure difference is large, the NAO is positive and the westerly winds are strong and storms tend to be stronger, more frequent and travel across northwestern Europe. When the pressure difference is small, they travel across southern Europe. The NAO is also associated with changes in temperature and rainfall in Europe and North America.

The fluctuations in the NAO occur on a wide range of time-scales. There are day-to-day changes associated with weather systems, and slower changes associated with seasonal and longer term variability, which is predictable from November for the coming winter.

NAO impacts

Winter (December-January-February) conditions

When the NAO index is well above normal, there is an increased chance that seasonal temperatures will be higher than normal in northern Europe, northern Asia and South-East North America, and lower than normal in North Africa, North-East Canada and southern Greenland. The patterns for precipitation (rainfall, snowfall) are more localised, with an increased chance of higher rainfall in northwest Europe and lower rainfall in southern Europe. When the NAO index is well below normal, the tendencies are generally opposite. The figures below show where seasonally-averaged temperatures and rainfall are likely to be in the top or bottom one third of observed values, given that the seasonal NAO index is in the top or bottom quarter of observed values.

when the winter NAO index is well above zero

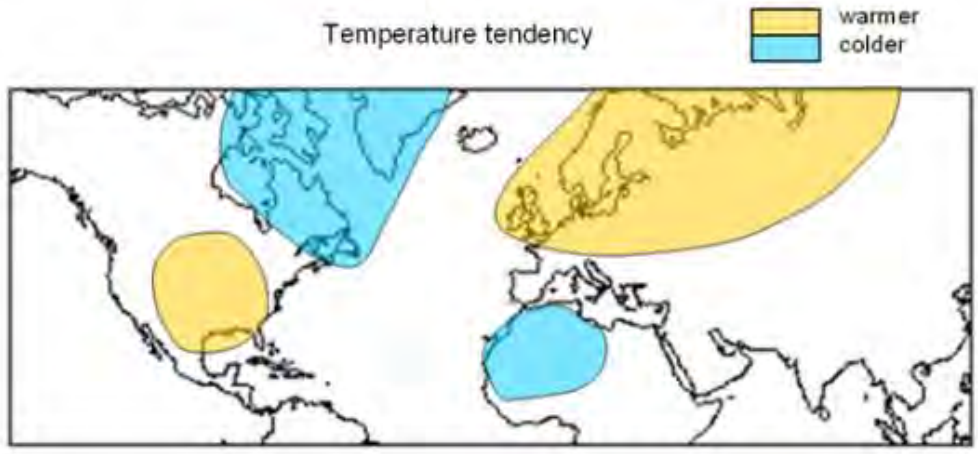

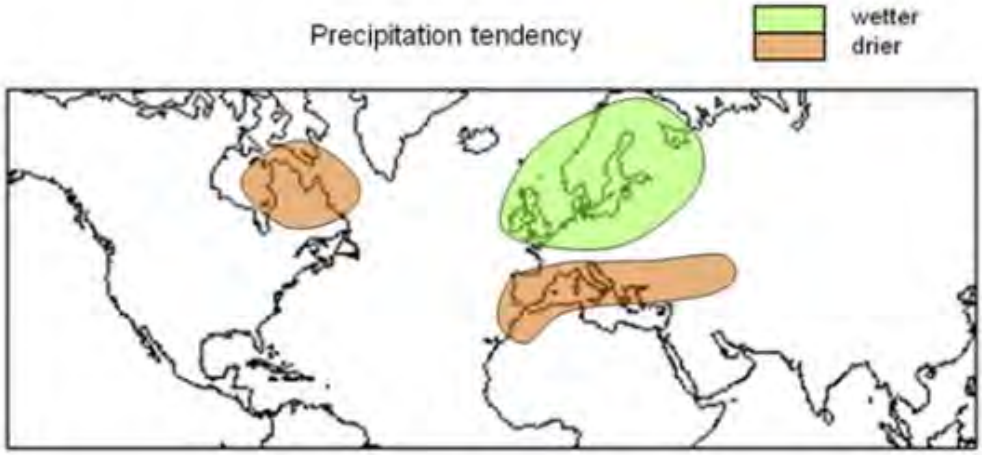

when the winter NAO index is well below zero

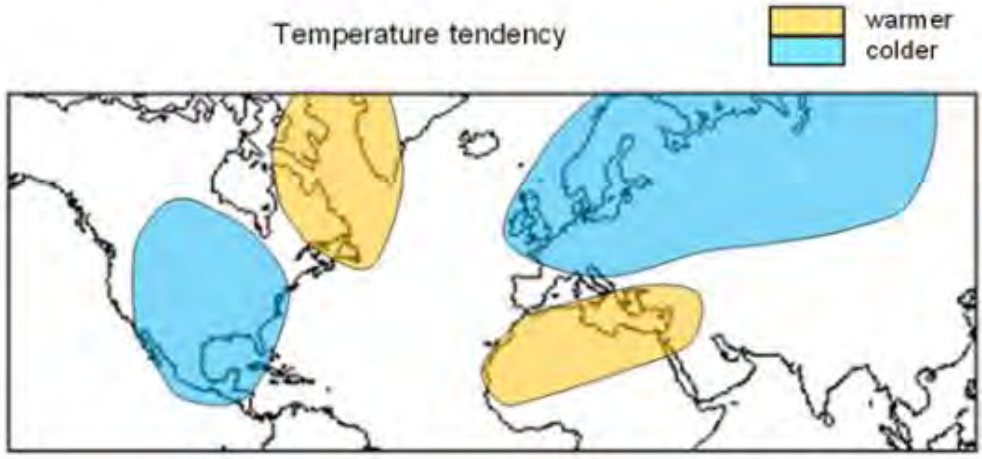

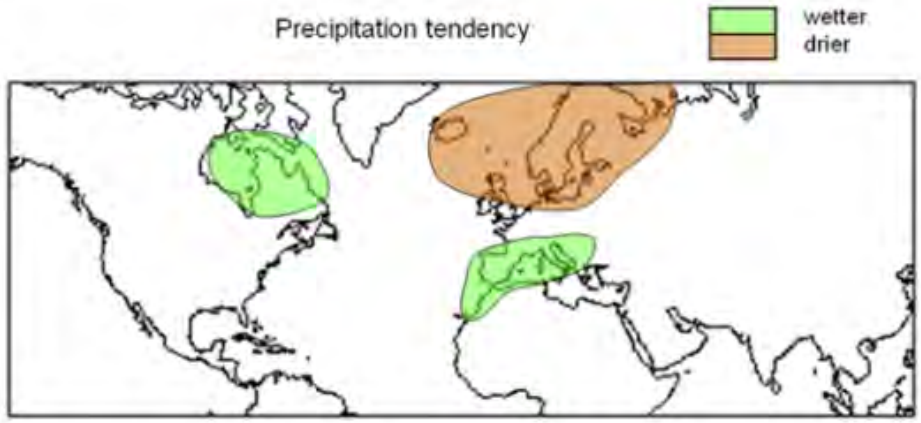

Summer (July-August) NAO conditions

The long-term-average pressure patterns vary with season, the Summer North Atlantic Oscillation index (SNAO) used here represents the strength of a spatial pattern of pressure variability in July-August whose main feature is located over northern Europe and the northern North Atlantic ocean.

When the summer NAO index is well above normal there is an increased chance that temperatures will be higher than normal over North-West Europe, central Canada, North Central USA, and parts of North Africa, and lower than normal over the Mediterranean region, southern USA, North Mexico, and the Greenland region. For precipitation this increased chance is for lower rainfall in North-West Europe, North-East Canada, and the Sahel region of Africa, and higher rainfall in the Mediterranean, and parts of southern Greenland and Iceland. When the SNAO index is well below normal, conditions are mainly opposite in the European sector, with an increased likelihood of north-west Europe being cooler and wetter.

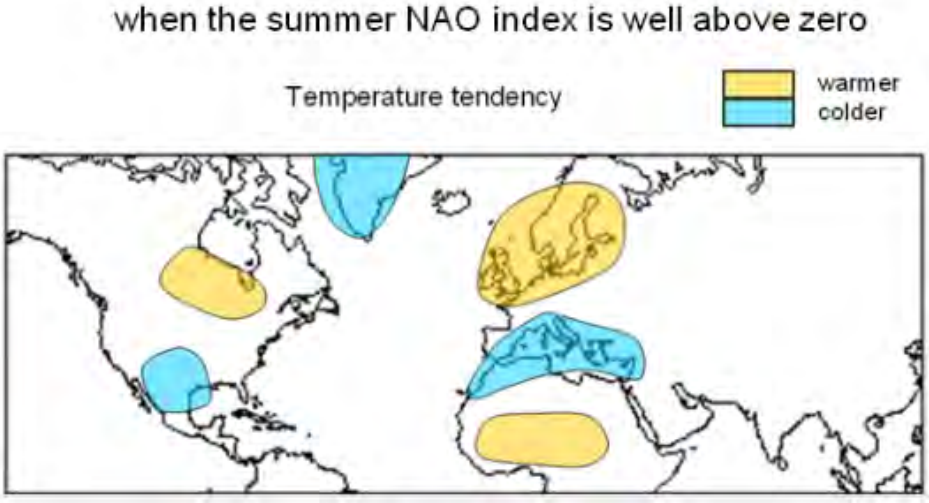

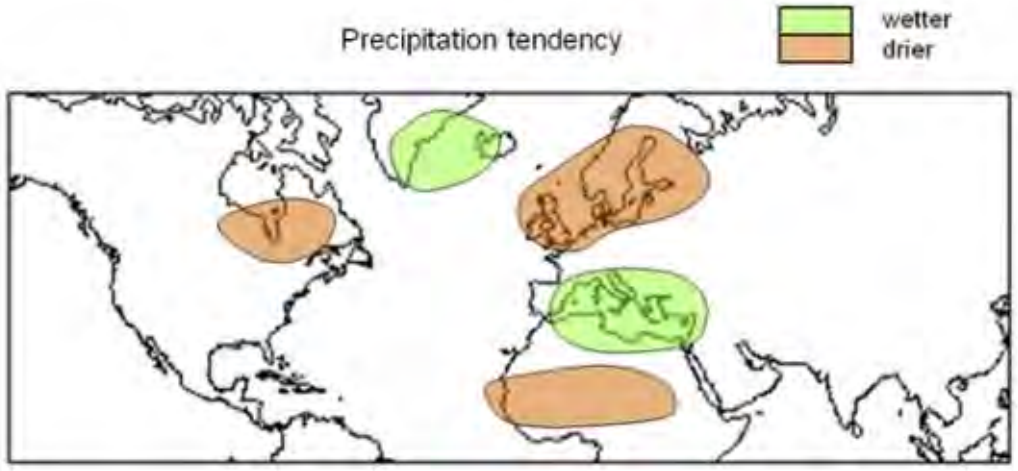

when the summer NAO index is well below zero

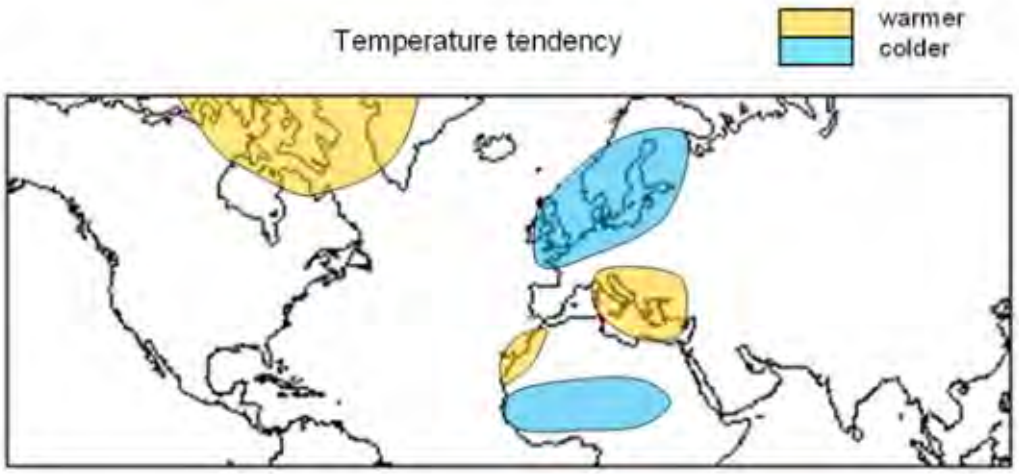

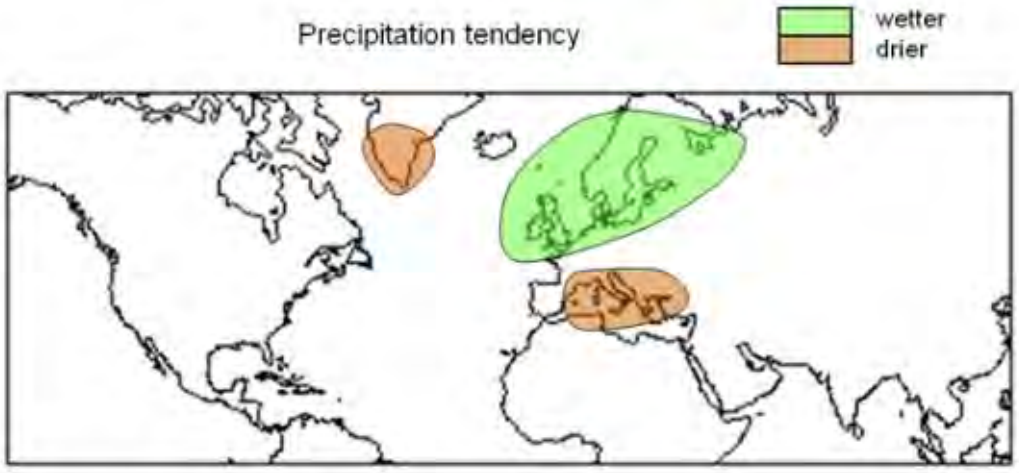

Please note:

- The maps are schematic and the areas marked are not geographically precise.
- These summary maps do not indicate the severity of impacts and the probabilities and magnitudes vary from place to place.
- The maps are based on categorised information. Maps produced using different criteria will have somewhat different features.

Data sources:

For winter the NAO data are from the Hurrell station-based index (monthly values) provided by the Climate Analysis Section, National Center for Atmospheric Research, USA.

The summer NAO index data are provided by the Met Office.

The analyses of temperature and precipitation impacts made use of gridded monthly-average data: temperature and precipitation from CRU TS (Harris et al., 2014) , temperature from the National Centers for Environmental Prediction atmospheric re-analysis, and precipitation from the Global Precipitation Climatology Project.

69. Assignment 2, Module 14: NAO and Climate Variability: https://www.climate.gov/news-features/understanding-climate/climate-variability-north-atlantic-oscillation

Climate Variability: North Atlantic Oscillation

BY REBECCA LINDSEY AND LUANN DAHLMAN | REVIEWED BY TOM DI LIBERTO
PUBLISHED AUGUST 30, 2009

HIGHLIGHTS

- The North Atlantic Oscillation (NAO) index describes changes in the strength of two recurring pressure patterns in the atmosphere over the North Atlantic: a low near Iceland, and a high near the Azores Islands.
- Positive NAO index values indicate these features are strong, creating a big pressure difference between them. Strongly positive values are linked to warm conditions across the U.S. East and Northern Europe, and cold conditions across southern Europe.
- Negative NAO index values indicate these features are relatively weak, and the pressure difference between them is smaller. Strongly negative values are linked to cold conditions in the U.S. East and Northern Europe, and warm conditions in Southern Europe.

Related Content

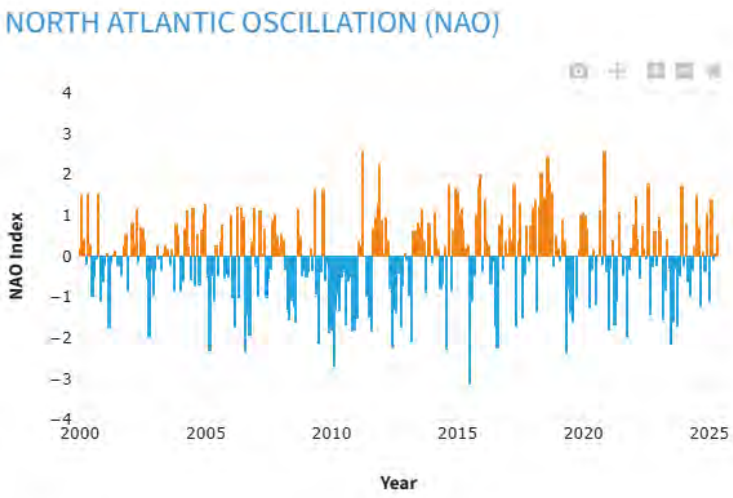

Monthly average of the North Atlantic Oscillation (NAO), which compares the relative strength of semi-permanent high and low pressure patterns in the North Atlantic Ocean. A positive NAO index favors mild winters in the U.S. East. Negative values favor stronger cold-air outbreaks and increased storminess in the eastern U.S. NOAA Climate.gov image, based on data from the Climate Prediction Center.

Late in the 18th century, a missionary who had traveled back and forth across the Atlantic Ocean for several years noted that mild winter conditions in Greenland often coincided with severe winter conditions in Denmark, and vice versa. The severe-versus-mild phenomenon he described is now recognized as an impact of the **North Atlantic Oscillation** or **NAO**.

NAO TEMPERATURE PATTERNS

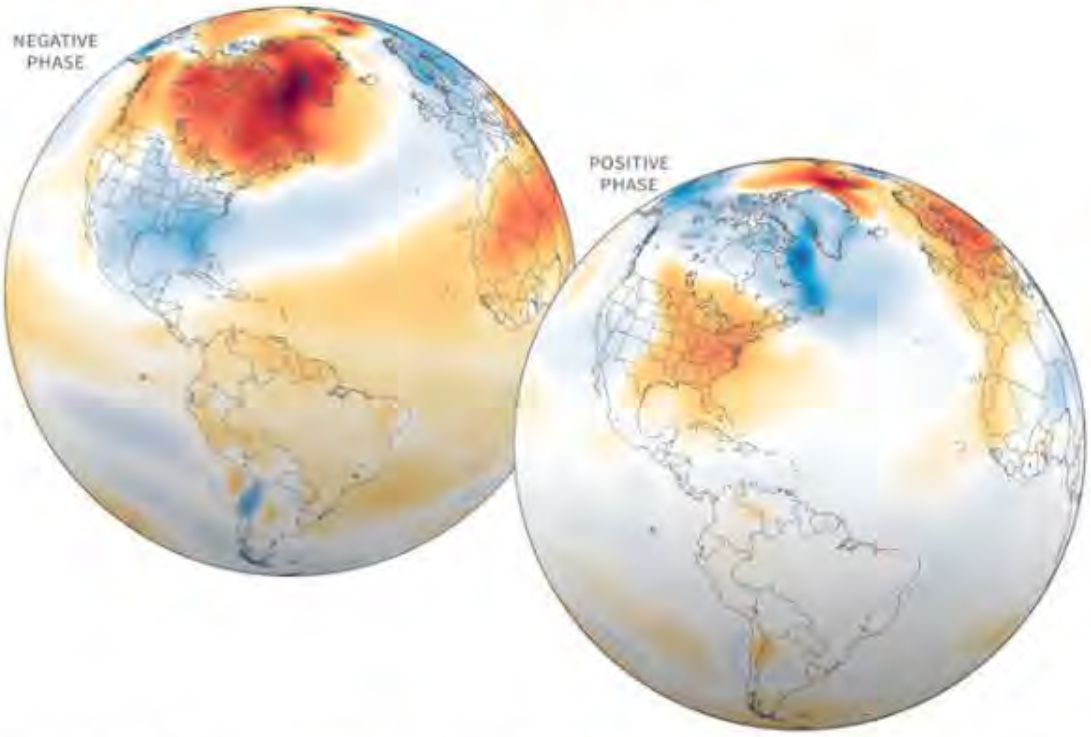

Late winter temperatures compared to the 1981-2010 average when the North Atlantic Oscillation (NAO) was strongly negative (top, Jan-March 2010) and when it was strongly positive (bottom, January-March 1990). Winters are often cooler than average across the mid-latitudes when the NAO is negative, and warmer than average when it is positive. NOAA Climate.gov image, based on data from the Physical Sciences Lab.

Air pressure over two regions drive this oscillation:

- The high latitudes of the North Atlantic Ocean near Greenland and Iceland generally experience lower air pressure than surrounding regions. This zone of low pressure is called the sub-polar low, or sometimes the Icelandic Low.
- Farther to the south, air pressure over the central North Atlantic Ocean is generally higher than surrounding regions. This atmospheric feature is called the subtropical high, or the Azores High.

The NAO is in a positive phase when both the sub-polar low and the subtropical high are stronger than average. During positive NAO phases, the increased difference in pressure between the two regions results in a stronger Atlantic jet stream and a northward shift of the storm track. Consequently, northern Europe experiences increased storminess and precipitation, and warmer-than-average temperatures that are associated with the air masses that arrive from lower latitudes. At the same time, southern Europe experiences decreased storminess and below-average precipitation. In eastern North America, the positive phase of the NAO generally brings higher air pressure, a condition associated with fewer cold-air outbreaks and decreased storminess.

The NAO is in a negative phase when both the sub-polar low and the subtropical high are weaker than average. During negative NAO phases, the Atlantic jet stream and storm track have a more west-to-east orientation, and this brings decreased storminess, below-average precipitation, and lower-than-average temperatures to northern Europe. Conversely, southern Europe experiences increased storminess, above-average precipitation, and warmer-than-average temperatures. In eastern North America, the negative phase of NAO generally brings lower air pressure, a condition associated with stronger cold-air outbreaks and increased storminess.

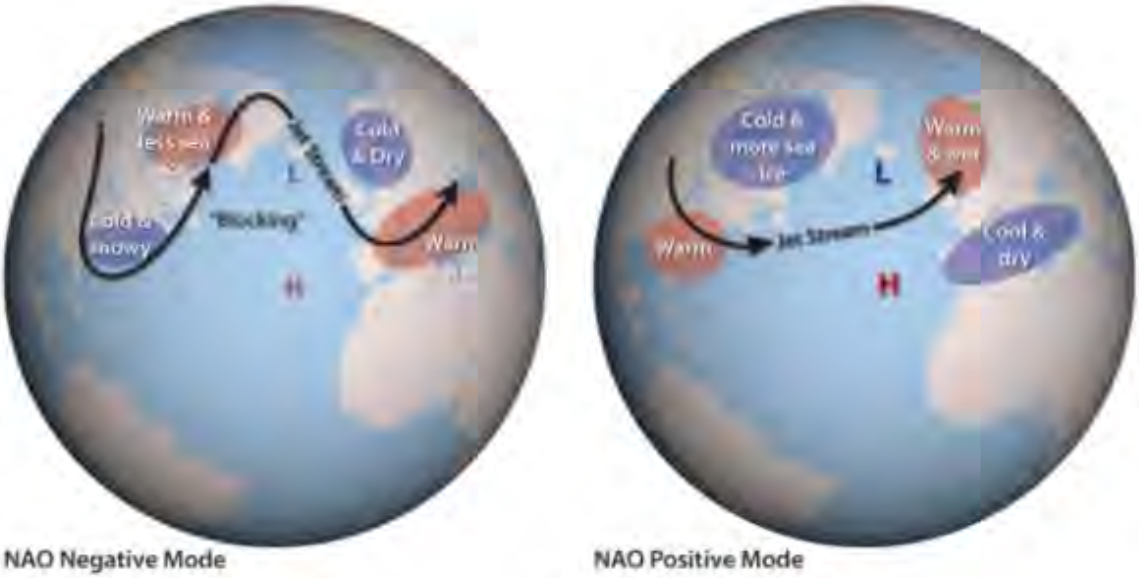

NAO Negative Mode **NAO Positive Mode**

On average, the surface pressure near Iceland is relatively low (L), while the pressure near the Azores Island is relatively high (H). During a negative phase (left), this pressure difference weakens. During a positive phase (right), the difference becomes even stronger than usual. The variation in pressure patterns influences the strength and location of the jet stream and the path of storms across the North Atlantic. Schematic adapted from AIRMAP by Ned Gardiner and David Herring, NOAA.

The North Atlantic Oscillation is often strongly correlated with the Arctic Oscillation, which describes hemisphere-wide shifts in atmospheric pressure between the Arctic and the mid-latitudes of both the North Pacific and North Atlantic. In fact, atmospheric scientists continue to debate whether the two are separate phenomena or whether the North Atlantic Oscillation is simply the Atlantic half of the Arctic Oscillation. Regardless, the NAO is the most prominent pattern of climate variability in the mid and high Northern latitudes, and it has a strong influence on weather over northeastern North America, Greenland, and Europe.

Conditions associated with the two phases of the NAO directly affect human demand for energy, quality of crop yields, and productivity of fisheries. Unlike like the El Niño-Southern Oscillation, the North Atlantic Oscillation is not currently predictable more than a week or two in advance.

Data

A record of NAO phases for 1950 through the present is available from NOAA's Climate Prediction Center.

References

North Atlantic Oscillation page at Lamont-Doherty Earth Institute, Columbia University, by Ian Bell and Martin Visbeck. Accessed December 8, 2023.

North Atlantic Oscillation, NOAA's Climate Prediction Center. Accessed December 8, 2023.

Wallace, J. M., and D. S. Gutzler, 1981: Teleconnections in the geopotential height field during the Northern Hemisphere Winter. *Mon. Wea. Rev.*, 109, 784-812.

70. Assignment 2, Module 14: NAO Impacts: https://hogback.atmos.colostate.edu/cmmap/research/docs/aug10/poster-ChrisAlston-final.pdf

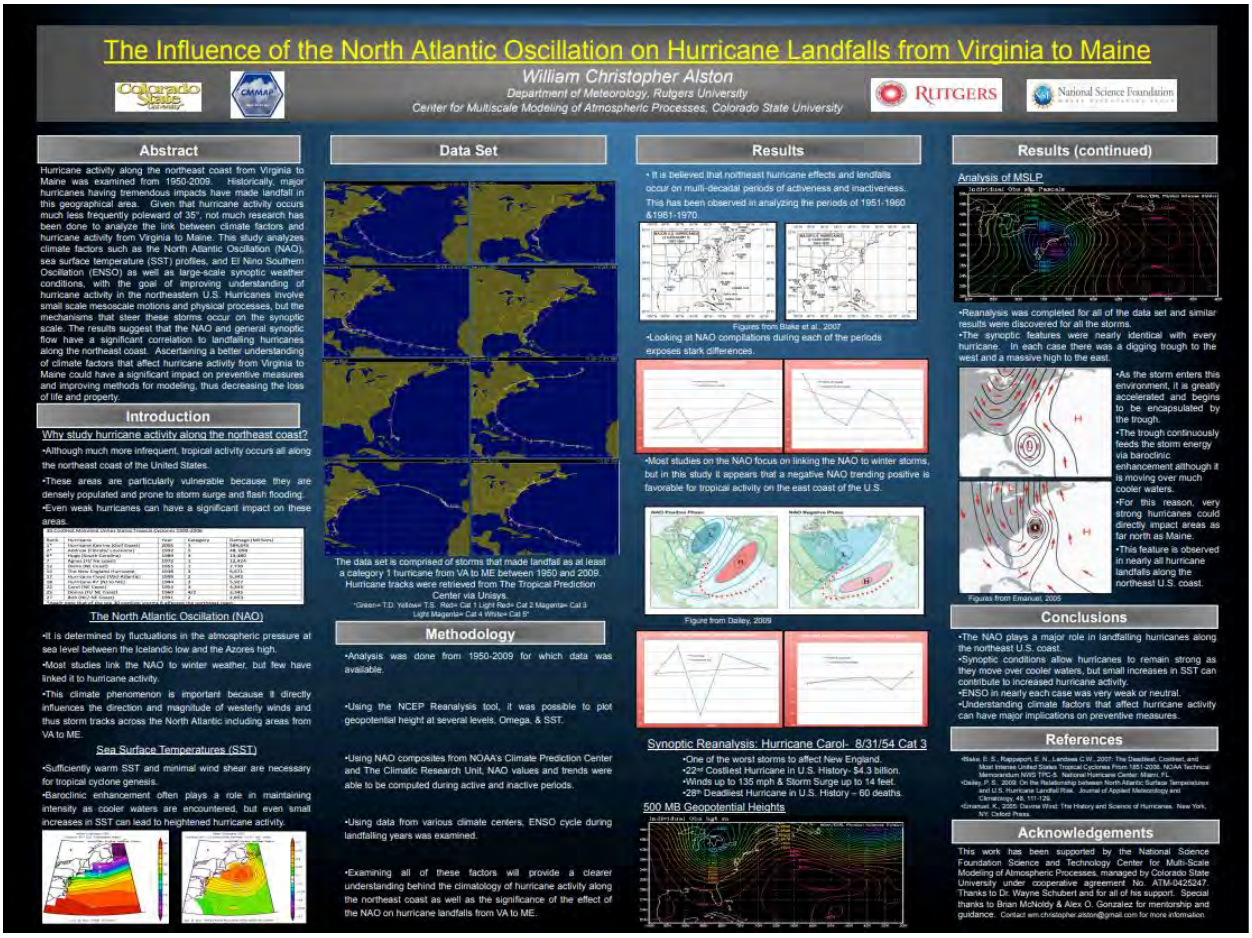

71. Assignment 2, Module 15: Wind Profile: https://www.nhc.noaa.gov/aboutwindprofile.shtml

Eyewall Wind Profiles in Hurricanes Determined By GPS Dropwindsondes

James L. Franklin[1], Michael L. Black[2], and Krystal Valde[1]

[1]NOAA/NWS/TPC/National Hurricane Center, Miami, Florida
[2]NOAA/AOML/Hurricane Research Division, Miami, Florida

April 2000

1. Introduction

One of the more difficult problems for operational tropical cyclone forecasters is the assessment of the cyclone's maximum sustained surface wind. Even when aircraft reconnaissance data are available, these are typically obtained from the 700 mb (10,000 ft) level; from these flight-level observations, the forecaster is left to estimate the surface winds. Based on comparisons of flight-level and buoy data, Powell and Black (1990) recommended that a ratio of 63%-73% be used to reduce reconnaissance flight-level wind observations. While operational practices at the National Hurricane Center (NHC) have varied over time, in recent years surface winds have typically been taken to be 80%-90% of the flight-level wind. In view of studies such as Powell and Black, use of these relatively high ratios has periodically resulted in criticism of NHC intensity estimates.

In 1997, the National Oceanic and Atmospheric Administration (NOAA) and Air Force Reserve Command (AFRC) hurricane reconnaissance aircraft began to deploy Global Positioning System (GPS)-based dropwindsondes (Hock and Franklin 1999) in the hurricane eyewall. These instruments provide for the first time, detailed, accurate profiles (15 ft vertical resolution, with 1-4 mph accuracy) of the inner core of a hurricane from flight level (typically 700 mb) down to the surface. More than 350 such profiles have been obtained through the 1999 hurricane season.

For this report we use the dropsonde data to document the mean structure of the lowest 10,000 ft of the hurricane eyewall, and discuss the implications for operational reductions of reconnaissance observations.

2. Data and Methodology

This study is based on a sample of 357 quality-controlled eyewall profiles from the following hurricanes: Guillermo and Erika in 1997; Bonnie, Danielle, Georges, Mitch, Lester, and Madeline in 1998; and Bret, Dennis, Floyd, Gert, Irene, Jose, Lenny, Dora and Eugene in 1999. A majority of these dropsonde releases were made from the 700 mb level. For sondes released from NOAA aircraft, airborne radar was used to determine whether a particular sonde was released in the eyewall; for AFRC sondes we relied on the comments of the operational air-crews, as well as examination of flight-level wind profiles.

The individual soundings have been used to construct a mean eyewall profile for the data set. Prior to the averaging, the wind at each level in the drop profile is normalized by the wind speed at 700 mb (10,000 ft).

3. Results

Figure 1 shows the mean eyewall wind speed profile, where the wind at each level has been normalized by the wind speed at 700 mb (taken from the dropsonde profile, if available, or from the aircraft 700 mb flight-level wind at the time of launch, if not). The strongest winds in the eyewall are found near 500 m (1600 ft) elevation; these are about 20% higher than the 700 mb wind, owing to the warm-core nature of the tropical cyclone. For comparison, the mean profile for non-eyewall sondes within 200 miles of the cyclone center is also shown. In the outer part of the vortex, the low-level wind maximum is found at a somewhat higher elevation and is not as pronounced as in the eyewall. The ratio of the surface to 700 mb wind (R_{700}) is 0.78 in the outer vortex and 0.91 in the eyewall. Note that the former figure is not far from Powell and Black's (1990) estimate of 0.73. This is not surprising given that their sample was comprised almost exclusively of outer vortex observations.

The outward slope of the radius of maximum wind (RMW) in the hurricane eyewall with height causes the value R_{700} = 0.91 given above to be biased slightly high, since many sondes are released inward of the flight-level RMW in an attempt to measure the maximum surface winds. When R_{700} is evaluated only from sondes at the RMW a value of 0.88 is obtained. This value should represent a lower bound on R_{700}, placing the true value of R_{700} between 0.88 and 0.91. ***Thus at least in the mean, the dropsonde data confirm NHC's operational practice for the reduction of aircraft reconnaissance data.***

While a reduction factor of about 0.9 may be appropriate in the mean, individual eyewall profiles illustrate how difficult it can be to estimate a hurricane's maximum surface winds from flight-level reconnaissance data. Figure 2 show an example from 1998's Hurricane Mitch. Over a period of several hours, the NOAA Hurricane Hunter aircraft could find flight-level winds no higher than 150 mph, yet this and several other dropsondes indicated much higher wind speeds near the surface. In this case, Mitch appeared to be weakening from the "top-down"; the circulation at flight-levels was decreasing but this trend had not yet begun at the surface. On the other hand, several storms (including Bonnie) have shown surface winds much lower than the flight-level wind.

4. Operational Recommendations

Based on these and similar analyses for other normalization altitudes, the following reduction factors are recommended for reducing flight-level winds in the inner core of a tropical cyclone to the surface (33 ft) level: for the 700 mb level, R = 0.90; for the 850 mb level (commonly flown in tropical storms), R = 0.80. For investigative flights at 1,000 ft, R = 0.85. As significant variations from these means have been noted in individual storms; these guidelines can be modified as conditions warrant. Storm-to-storm variability will primarily be influenced by wind speed, cyclone convective intensity, and sea-surface temperature.

The mean eyewall profile (Fig. 1) has implications for high-rise buildings and elevated terrain. Table 1 gives the wind at various altitudes as a percentage of the surface wind. ***Winds at the top of a 30-story building will average about 20 mph (one Saffir-Simpson category) higher than at the surface.*** This can be seen in an example from Hurricane Georges (Fig. 3). In this case, the surface winds are near the lower end of Category Three; yet at an altitude of 300 ft the winds are now in the middle of Category Four.

5. References

Powell, M. D. and P. G. Black, 1990: The relationship of hurricane reconnaissance flight-level wind measurements to winds measured by NOAA's oceanic platforms. *J. Wind Engineering and Industrial Aerodynamics*, 36, 381-392.

Hock, T. F., and J. L. Franklin, 1999: The NCAR GPS dropwindsonde. *Bull. Amer. Meteor. Soc.*, 80, 407-420.

Table 1. Mean Hurricane Eyewall Wind Variation With Elevation

Height (ft)	# Storys	Wind (% surface)	Pressure Force (% surface)
33 (sfc)	3	100	100
50	5	103	106
100	10	108	117
150	15	111	123
200	20	115	132
250	25	117	137
300	30	119	142
400	40	121	146
500	50	123	151
600	60	125	156
750	75	128	164
1000	100	131	172

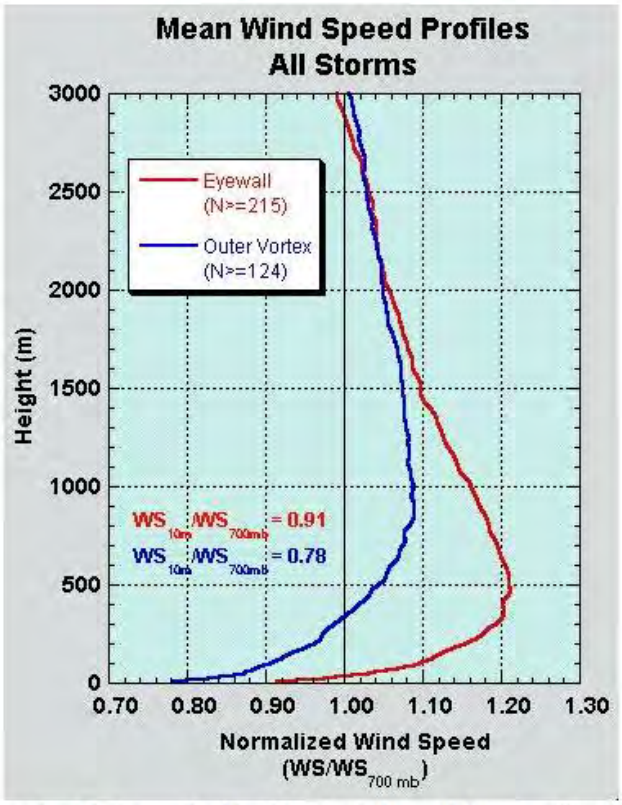

Figure 1. Mean wind speed profile (normalized by 700 mb wind speed) for eyewall and outer vortex soundings.

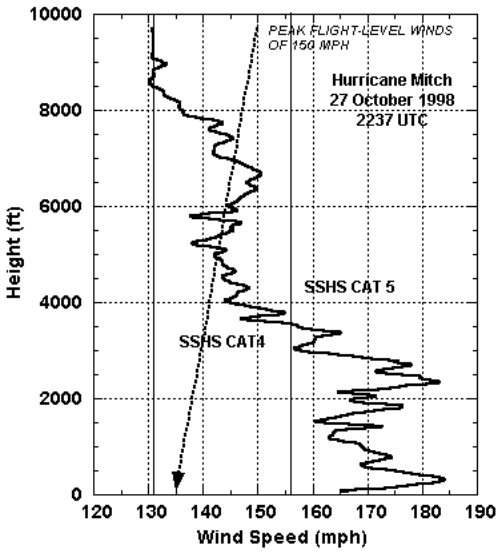

Figure 2. Wind speed profile from the eyewall of Hurricane Mitch at 2337 UTC 27 October 1998. Vertical lines indicate the boundaries of Saffir-Simpson Hurricane Scale categories. Sloping dashed line indicates the peak flight-level wind found during the reconnaissance flight, and its conversion to an assumed surface wind using a 0.9 reduction factor.

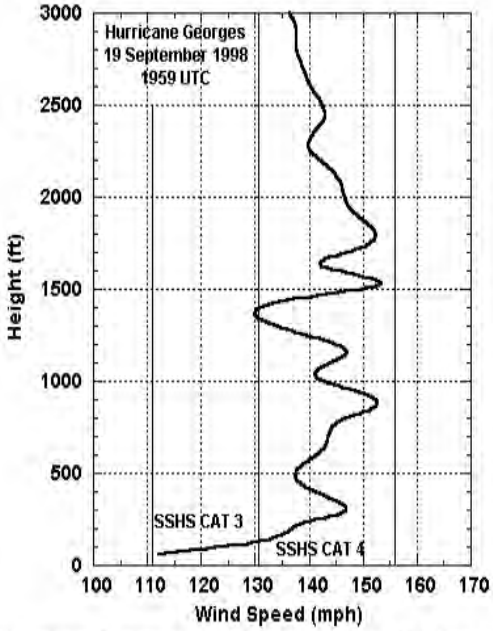

Figure 3. Wind speed profile from the eyewall of Hurricane Georges at 1959 UTC 19 September 1998. Vertical lines indicate the boundaries of Saffir-Simpson Hurricane Scale categories.

72. Assignment 2, Module 16: Extra-tropical Cyclones: https://www.aoml.noaa.gov/hrd-faq/#tc-types

What Is the Difference Between a Sub-tropical Cyclone, an Extra-tropical Cyclone, and a Post-tropical Cyclone?

The "**sub-tropical**" in sub-tropical cyclone refers to the latitudes 25°N to 35°N (or °S). However, the term refers to cyclones whose characteristics are neither fully tropical nor extratropical. They are either asymmetrical with a warm core or symmetrical with a cold core. Sub-tropical cyclones can transform into tropical or extra-tropical storms depending on conditions.

The "**extra-tropical**" in extra-tropical cyclone refers to the latitudes 35°N to 65°N (or °S). However, the term refers to cyclones that get their energy from the horizontal temperature contrasts that exist in the atmosphere. Extra-tropical cyclones are low-pressure systems generally associated with cold fronts, warm fronts, and occluded fronts. They are asymmetrical and have a cold core.

A **post-tropical cyclone** is a former tropical cyclone that no longer possesses sufficient characteristics to be considered a tropical cyclone, such as convection at its center. Post-tropical cyclones can continue producing heavy rains and high winds. Former tropical cyclones that have become fully **extra-tropical, sub-tropical, or remnant lows**, are three classes of post-tropical cyclones.

Neutercane is a term no longer in use. It referred to small (<100 miles in diameter) sub-tropical low-pressure systems that are short-lived.

73. Assignment 2, Module 16: Difference between Hurricane and Typhoon: https://oceanservice.noaa.gov/facts/cyclone.html

What is the difference between a hurricane and a typhoon?

The **only difference** between a hurricane and a typhoon is the **location where the storm occurs**.

A close-up satellite image of Hurricane Isabel taken on Sept. 15, 2003.

A close-up satellite image of Hurricane Isabel taken on Sept. 15, 2003. The National Ocean Service helps coastal communities prepare for and recover from major coastal storms such as hurricanes.

Hurricanes and typhoons are the same weather phenomenon: tropical cyclones. A tropical cyclone is a generic term used by meteorologists to describe a rotating, organized system of clouds and thunderstorms that originates over tropical or subtropical waters and has closed, low-level circulation.

The weakest tropical cyclones are called *tropical depressions* . If a depression intensifies such that its maximum sustained winds reach 39 miles per hour, the tropical cyclone becomes a *tropical storm.* Once a tropical cyclone reaches maximum sustained winds of 74 miles per hour or higher, it is then classified as a hurricane, typhoon, or tropical cyclone, depending upon where the storm originates in the world. In the North Atlantic, central North Pacific, and eastern North Pacific, the term *hurricane* is used. The same type of disturbance in the Northwest Pacific is called a *typhoon* . Meanwhile, in the South Pacific and Indian Ocean, the generic term *tropical cyclone* is used, regardless of the strength of the wind associated with the weather system.

The ingredients for tropical cyclones include a pre-existing weather disturbance, warm tropical oceans, moisture, and relatively light winds. If the right conditions persist long enough, they can combine to produce the violent winds, large waves, torrential rains, and floods we associate with this phenomenon. At times, when a weather system does not meet all of these conditions, but is forecast to bring tropical storm or hurricane force winds to land in the next day or two, it is called a *potential tropical cyclone* in the Atlantic basin and the central and eastern North Pacific basins.

In the Atlantic, hurricane season officially runs from June 1 to November 30. Ninety-seven percent of tropical cyclone activity occurs during this time period. However, there is nothing magical about these dates. Hurricanes can and do occur outside of this six month period.

Get **Social**

More **Information**

- What is a hurricane?
- Tropical Cyclone Climatology
- National Hurricane Center
- What is the difference between a hurricane watch and a warning?
- Why do we name tropical storms?

Did you know?

The main parts of a tropical cyclone are the rainbands, the eye, and the eyewall. Air spirals in toward the center in a counter-clockwise pattern in the northern hemisphere (clockwise in the southern hemisphere), and out the top in the opposite direction. In the very center of the storm, air sinks, forming an "eye" that is mostly cloud-free.

Last updated: 06/16/24
Author: NOAA
How to cite this article

Contact Us

74. Assignment 2, Module 16: Hurricane and Typhoon:
    https://gpm.nasa.gov/resources/faq/what-difference-between-typhoon-cyclone-and-hurricane

What is the difference between a typhoon, cyclone, and hurricane?

The terms "hurricane" and "typhoon" are regional names for tropical cyclones. All tropical cyclones are alike in that they draw heat from warm water at the ocean's surface to power horizontal, rotating wind. Although similar in size, tropical cyclones have a different energy source than synoptic cyclones, which are storm systems that draw their energy from weather fronts and jet streams.

Over the Atlantic and East Pacific, tropical cyclones are commonly called "hurricanes." The common term is "typhoon" for a tropical cyclone that forms in the West Pacific. Tropical cyclones are called just "cyclones" in the Indian Ocean and near Australia.

75. Assignment 2, Module 16: Extratropical Transition: https://journals.ametsoc.org/view/journals/mwre/145/11/mwr-d-17-0027.1.xml

REVIEW

The Extratropical Transition of Tropical Cyclones. Part I: Cyclone Evolution and Direct Impacts

CLARK EVANS,[a] KIMBERLY M. WOOD,[b] SIM D. ABERSON,[c] HEATHER M. ARCHAMBAULT,[d] SHAWN M. MILRAD,[e] LANCE F. BOSART,[f] KRISTEN L. CORBOSIERO,[f] CHRISTOPHER A. DAVIS,[g] JOÃO R. DIAS PINTO,[h] JAMES DOYLE,[i] CHRIS FOGARTY,[j] THOMAS J. GALARNEAU JR.,[k] CHRISTIAN M. GRAMS,[l] KYLE S. GRIFFIN,[m] JOHN GYAKUM,[n] ROBERT E. HART,[o] NAOKO KITABATAKE,[p] HILKE S. LENTINK,[q] RON MCTAGGART-COWAN,[r] WILLIAM PERRIE,[s] JULIAN F. D. QUINTING,[t] CAROLYN A. REYNOLDS,[i] MICHAEL RIEMER,[u] ELIZABETH A. RITCHIE,[v] YUJUAN SUN,[s] AND FUQING ZHANG[w]

[a] *University of Wisconsin–Milwaukee, Milwaukee, Wisconsin*
[b] *Mississippi State University, Mississippi State, Mississippi*
[c] *NOAA/Atlantic Oceanographic and Meteorological Laboratory/Hurricane Research Division, Miami, Florida*
[d] *NOAA/Climate Program Office, Silver Spring, Maryland*
[e] *Embry-Riddle Aeronautical University, Daytona Beach, Florida*
[f] *University at Albany, State University of New York, Albany, New York*
[g] *National Center for Atmospheric Research, Boulder, Colorado*
[h] *University of São Paulo, São Paulo, Brazil*
[i] *Naval Research Laboratory, Monterey, California*
[j] *Canadian Hurricane Center, Dartmouth, Nova Scotia, Canada*
[k] *The University of Arizona, Tucson, Arizona*
[l] *Institute for Atmospheric and Climate Science, ETH Zurich, Zurich, Switzerland*
[m] *RiskPulse, Madison, Wisconsin*
[n] *McGill University, Montreal, Quebec, Canada*
[o] *Florida State University, Tallahassee, Florida*
[p] *Meteorological College, Kashiwa, Chiba, Japan*
[q] *Karlsruhe Institute of Technology, Karlsruhe, Germany*
[r] *Environment and Climate Change Canada, Dorval, Quebec, Canada*
[s] *Bedford Institute of Oceanography, Dartmouth, Nova Scotia, Canada*
[t] *School of Earth, Atmosphere and Environment, and ARC Centre of Excellence for Climate System Science, Monash University, Clayton, Victoria, Australia*
[u] *Johannes Gutenberg-Universität Mainz, Mainz, Germany*
[v] *University of New South Wales, Canberra, Australia*
[w] *The Pennsylvania State University, University Park, Pennsylvania*

(Manuscript received 7 February 2017, in final form 8 August 2017)

ABSTRACT

Extratropical transition (ET) is the process by which a tropical cyclone, upon encountering a baroclinic environment and reduced sea surface temperature at higher latitudes, transforms into an extratropical cyclone. This process is influenced by, and influences, phenomena from the tropics to the midlatitudes and from the meso- to the planetary scales to extents that vary between individual events. Motivated in part by recent high-impact and/or extensively observed events such as North Atlantic Hurricane Sandy in 2012 and western North Pacific Typhoon Sinlaku in 2008, this review details advances in understanding and predicting ET since the publication of an earlier review in 2003. Methods for diagnosing ET in reanalysis, observational, and model-forecast datasets are discussed. New climatologies for the eastern North Pacific and southwest Indian Oceans are presented alongside updates to western North Pacific and North Atlantic Ocean climatologies. Advances in understanding and, in some cases, modeling the direct impacts of ET-related wind, waves, and precipitation are noted. Improved understanding of structural evolution throughout the transformation stage of ET fostered in large part by novel aircraft observations collected in several recent ET events is highlighted. Predictive skill for operational and numerical model ET-related forecasts is discussed along with environmental factors influencing posttransition cyclone structure and evolution. Operational ET forecast and analysis practices and challenges are detailed. In particular, some

DOI: 10.1175/MWR-D-17-0027.1

challenges of effective hazard communication for the evolving threats posed by a tropical cyclone during and after transition are introduced. This review concludes with recommendations for future work to further improve understanding, forecasts, and hazard communication.

1. Introduction

In October 2012, Hurricane Sandy drove a devastating storm surge in excess of 2 m into the northeastern U.S. coastline, tore down trees and power lines that left millions without electricity, and dumped over 900 mm of snow (Blake et al. 2013). As Sandy approached the coast, it acquired structural characteristics consistent with both tropical and extratropical cyclones, with an intact inner–tropical cyclone (TC) warm core embedded within an expansive outer-core wind field (Blake et al. 2013). Contributions from both tropical and baroclinic energy sources caused Sandy to reintensify as it approached the coastline (Galarneau et al. 2013; Shin and Zhang 2017). The TC followed an atypical track northwestward toward the Northeast United States, rather than out to sea, fostered by interaction with an upstream trough (Barnes et al. 2013; Qian et al. 2016) of the type identified by Fujiwhara (1931), the practical predictability of which depended on the modeling system (Bassill 2014; Magnusson et al. 2014; Torn et al. 2015). Sandy tested existing infrastructure for hazard communication (NOAA 2013; Blake et al. 2013) and posed challenges related to risk perception (Meyer et al. 2014) due to its atypical track and forecast structure (Munsell and Zhang 2014) near landfall. Few TCs produce such a broad range of impacts, but Sandy was not ordinary. Rather, Sandy is a dramatic example of the direct impacts, structural evolution, and forecast challenges associated with TCs that become extratropical cyclones, a process known as extratropical transition (ET; Jones et al. 2003).

Tropical cyclones gain energy from warm ocean waters through evaporation and subsequent latent heat release by deep, moist convection. The storm develops a warm core as a result, with the strongest winds near the surface that decrease in strength with height. The wind, precipitation, and temperature fields become more axisymmetric as the TC matures. Conversely, extratropical cyclones are driven by comparatively large temperature and moisture gradients. Within these baroclinic environments, frontal boundaries separate warm, moist air from cool, dry air, resulting in highly asymmetric energy distributions to drive wind and rainfall. In addition, wind speed increases with height due to the cold-core structure of these systems. During ET, the deep warm core associated with the TC becomes shallow and is often replaced by a cold-core, asymmetric structure (e.g., Evans and Hart 2003; Hart et al. 2006), including the development of surface fronts (Klein et al. 2000). This evolution occurs as the TC moves poleward into a baroclinic environment characterized by the aforementioned temperature and moisture gradients as well as increased vertical wind shear, reduced sea surface temperature (SST), and an increasing Coriolis parameter (Fig. 1). Only a subset of TCs complete ET and become fully extratropical, yet even a cyclone that only begins ET can directly produce hazards (such as Hurricane Sandy) and/or generate hazards downstream [e.g., Hurricane Katia in 2011 as described by Grams and Blumer (2015); Typhoon Nabi in 2005 as described by Harr et al. (2008)].

An earlier review (Jones et al. 2003) provided a then-current synthesis of the fundamental understanding of ET and its direct impacts. The paper also outlined significant ET-related forecast challenges and research needs that had yet to be addressed. Focusing on ET itself and the direct impacts of transitioning cyclones, the present review documents the extensive research that addresses how those needs have been met in the most recent decade and a half. This review also identifies questions that remain unanswered as well as potential avenues for future research that have been motivated by recent investigations. Section 2 discusses efforts toward a universal definition of, and classifiers for, ET. Section 3 documents the development of, and additions to, new and existing ET climatologies and looks to how ET climatology may change in the future. Section 4 describes the updated understanding of direct impacts associated with wind, waves, and precipitation. Jones et al. (2003) stressed the necessity of improving use of existing observations and exploiting new capabilities for understanding ET itself, as well as forecasting the phenomenon, and section 5 summarizes progress in and ongoing needs for both. Section 6 documents advances in the forecasting and analysis of ET. Finally, this review concludes with recommendations for future research. As noted above, this review focuses on ET and its direct impacts. A companion article (Keller et al. 2018, manuscript submitted to *Mon. Wea. Rev.*, hereafter Part II)

Denotes content that is immediately available upon publication as open access.

Corresponding author: Dr. Clark Evans, evans36@uwm.edu

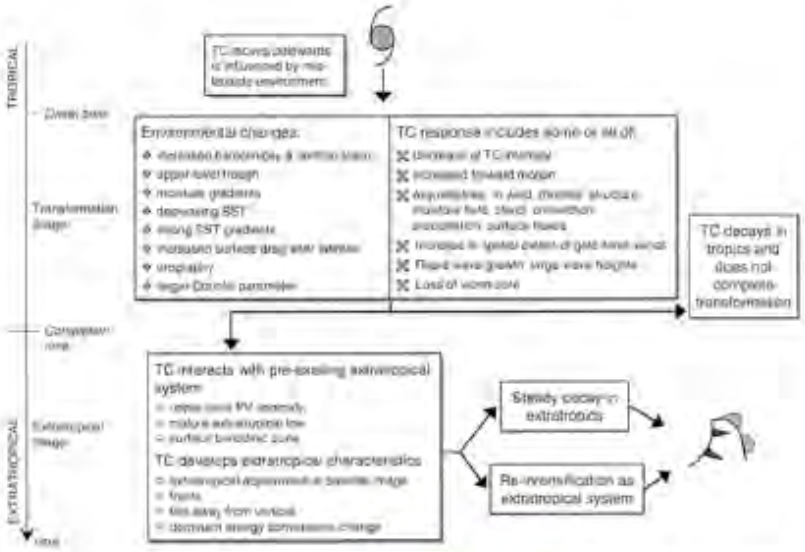

FIG. 1. A two-stage ET classification based on Klein et al. (2000). The onset and completion times correspond to the definitions of Evans and Hart (2003). The "tropical" and "extratropical" labels indicate approximately how the system would be regarded by an operational forecast center. Figure reproduced from Jones et al. (2003, their Fig. 11).

covers research progress related to ET's downstream impacts, including downstream cyclogenesis, cyclone evolution after becoming extratropical, effects on the midlatitude flow and predictability, and phenomena such as predecessor rain events.

geopotential height gradient with height. Tropical cyclones are warm-core systems characterized by a positive geopotential thickness anomaly near the center, resulting in a positive value of $-V_T^L$. Extratropical cyclones are generally cold-core systems characterized by a negative

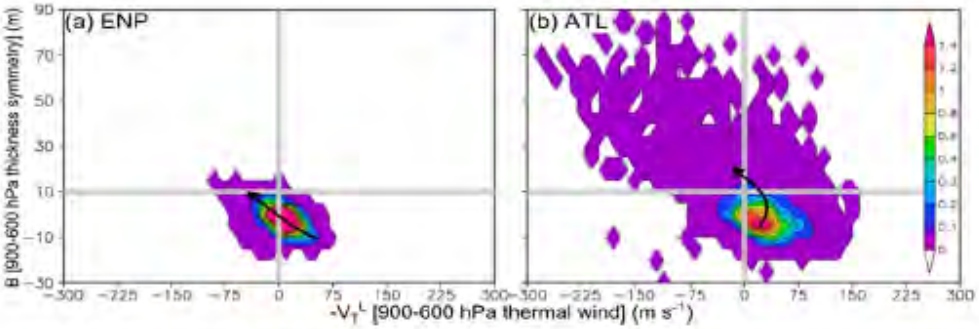

FIG. 5. Average JRA-55 CPS frequency (e.g., number of times during its life span that a given TC is located at a given location within the CPS, $-V_T^L$ and B only; shaded) per TC during 2001–10 in the (a) ENP (150 TCs) and (b) North Atlantic (here, ATL; 174 TCs). The arrows in each panel indicate the general trajectories that TCs in each basin follow through the CPS. Figure reproduced from Wood and Ritchie (2014a, their Figs. 10a,b).

poleward-directed steering winds (Walsh and Katzfey 2000). Conversely, WNP ET likelihood may decrease as the magnitude of the meridional temperature gradient decreases (Ito et al. 2016). In the NATL, ET frequency increased over the period 1970–2012 (Mokhov et al. 2014), and several studies (Semmler et al. 2008; Haarsma et al. 2013; Baatsen et al. 2015; Liu et al. 2017) suggest further increases in NATL ET frequency in the future, particularly in the eastern portion of the basin. These projected increases were attributed to a poleward expansion of the conditions that support TCs (viz., sufficiently high SST and low deep-layer vertical wind shear) toward latitudes supportive of extratropical cyclone maintenance or intensification. Vortex interactions such as what occurred with Sandy (2012) may become less frequent if midlatitude blocking and cyclonic wave breaking frequencies decrease (Barnes et al. 2013), although there is disagreement on whether midlatitude blocking frequency will decrease in future climates (e.g., Coumou et al. 2014; Francis and Vavrus 2015).

4. Direct impacts

Though climatological studies can help explain the overall characteristics of ET for a given basin, whether in the past, present, or future, the impacts of an individual ET event on lives and property are directly tied to the hazards of strong winds, large waves, and heavy precipitation. During ET, the TC wind field expands and becomes increasingly asymmetric, shifting the coverage and location of maximum wind speeds and thus the regions at risk. The evolving wind field affects the distribution of large waves, and these large waves can directly impact marine interests and coastlines. In addition, extreme inland precipitation can occur within ET systems, sometimes far removed from the cyclone center. Like the wind field, the precipitation distribution tends to shift during the ET process. Jones et al. (2003) emphasized the importance of better understanding the evolution and prediction of these hazards to mitigate the societal impacts of a given ET event. Many studies have responded to these research needs since Jones et al. (2003) was published, and the following subsections

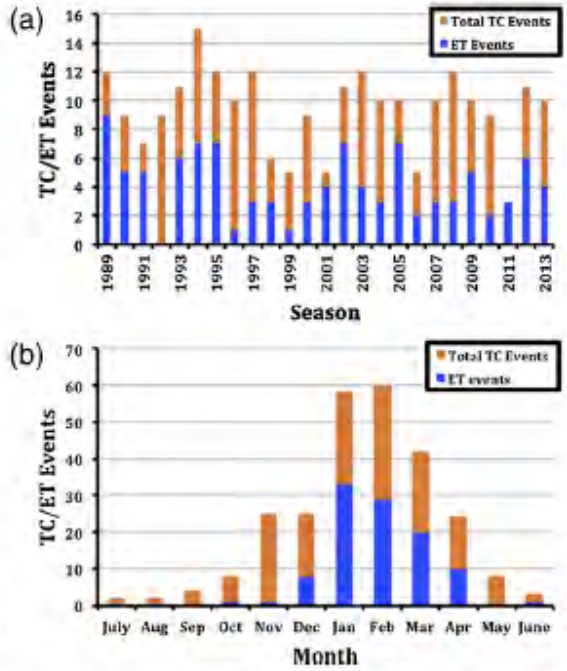

FIG. 6. Summary of TC and ET events in the SWIO west of 90°E by (a) TC season and (b) month for the period 1989–2013. The full height of the bar represents TC events, while the bottom (blue) portion of the bar represents the number of ET events. In (a), the year on the chart refers to the year the TC season ended. In (b), events that occur in two months are included in the month in which the TC dissipated or underwent ET. Figure reproduced from Griffin and Bosart (2014, their Fig. 1).

examine research progress on each of the three major direct ET hazards.

a. Wind

As the TC near-surface wind field becomes increasingly asymmetric during ET (e.g., Powell 1982; Merrill 1993), with the strongest winds preferentially found to the right of track (e.g., aligned with its motion), the radius of maximum wind (RMW; the distance from the cyclone's center at which the fastest tangential wind speeds are found) moves away from the center. At the same time, winds outside the RMW increase, flattening the azimuthally averaged tangential wind profile of the cyclone and increasing the cyclone's integrated kinetic energy (Kozar and Misra 2014). As a result, the wind field expands, as illustrated by Evans and Hart (2008) through numerical simulations of NATL Hurricane Bonnie (1998). The wind field expansion has been ascribed to the following: 1) the import of absolute angular momentum into the cyclone as asymmetry increases, accelerating the wind field beyond the RMW; and 2) temporally and vertically integrated cooling maximized inside the RMW, weakening the radial geopotential height gradient near the center and causing the RMW to move radially outward (Evans and Hart 2008; Fig. 7). The diabatically driven expansion of cyclonic PV associated with TC wind field growth (Hill and Lackmann 2009) or sting jet development along the trailing end of a bent-back front (e.g., Browning 2004) may also contribute to the wind field evolution during ET, although further research is necessary to test these hypotheses.

Though the wind field expansion is generally associated with strong near-surface winds becoming isolated equatorward (or, for the Northern Hemisphere, right) of the TC's track during ET (e.g., Fujibe and Kitabatake 2007), in some cases strong winds can also be observed poleward (or, for the Northern Hemisphere, left) of the TC's track during ET (e.g., Fig. 8; Fujibe et al. 2006; Fujibe and Kitabatake 2007; Kitabatake and Fujibe 2009; Loridan et al. 2014). There exists disagreement, however, as to the frequency of such occurrences, with estimates ranging from 11.4% (Fujibe and Kitabatake 2007; Kitabatake and Fujibe 2009) to 66.7% (Loridan et al. 2014) of WNP TCs near Japan. Potential causes of strong left-of-track winds during ET include frontogenesis along a warm front rearward of the TC (e.g., Riemer et al. 2006), terrain-induced flow channeling (e.g., Mashiko 2008), and the vortex response to sufficiently large vertical wind shear (e.g., Uhlhorn et al. 2014).

Knowledge of the diverse wind field structures that may arise during ET, even if only incomplete understanding exists of how and why they arise, is necessary to improve parametric wind models that can be used as input for

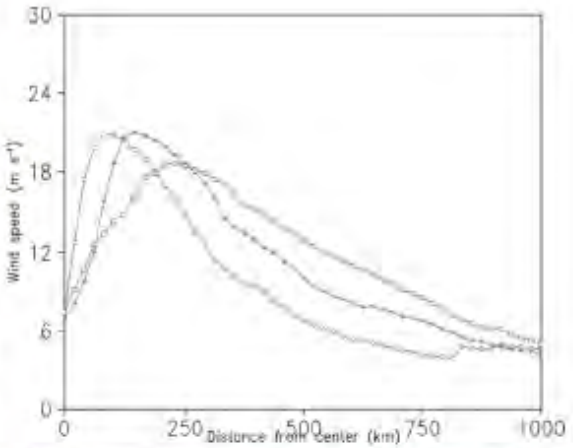

FIG. 7. Azimuthally averaged 10-m wind speed ($m s^{-1}$) as a function of radius at 0400 UTC 29 Aug (open circles; before ET), 1000 UTC 30 Aug (closed circles; during ET), and 1000 UTC 31 Aug (open squares; after ET) 1998, as obtained from the 12-km fifth-generation Pennsylvania State University–NCAR Mesoscale Model (Dudhia 1993), simulation of NATL TC Bonnie (1998). Figure reproduced from Evans and Hart (2008, their Fig. 5).

trapped-fetch wave models (MacAfee and Pearson 2006; Bruneau et al. 2017) and catastrophe models (e.g., Loridan et al. 2014, 2015). Parametric wind models typically assume strongest winds right of track, whereas there is a diverse range of near-surface wind fields that are observed during ET. Thus, to improve model skill, adjustments must be made to better represent the diversity of wind field structures observed during ET. This has been done by applying size, shape, storm motion, static stability, and/or bias-correction factors to parametric wind models commonly used at low latitudes (MacAfee and Pearson 2006; Loridan et al. 2015). In the Loridan et al. (2015) formulation, specific term values vary between transitioning TCs with a right-of-track surface wind speed maximum, left-of-track surface wind speed maximum, and right-of-track surface wind speed maximum with small cross-track asymmetry. Applying the Loridan et al. (2015) parametric wind model to storm surge prediction for idealized ET events near Japan resulted in improved storm surge and wave predictions relative to those derived using winds from a purely TC wind model (Bruneau et al. 2017).

b. Waves

The evolving TC wind field during ET has a direct influence upon the cyclone's ocean-wave field. Large ocean waves in TCs and extratropical cyclones alike pose hazards to marine activities including oil and gas extraction, fisheries, recreation, and transport. Generally, ocean wave growth is tied to cyclone characteristics such as translation speed, wind speed, and trapped-fetch length (Bowyer and MacAfee 2005; MacAfee and

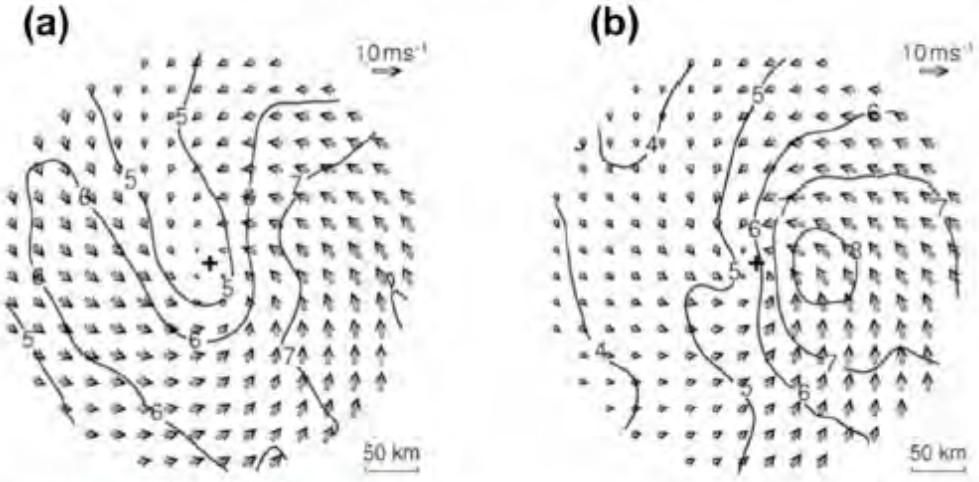

FIG. 8. Composite surface wind vectors (arrows, reference vector in the top right of each panel) and surface wind speed (isotachs, m s^{-1}) for (a) the subset of TCs ($n = 13$) with wind maxima both left and right of track that made landfall in Japan from 1979 to 2004 and (b) all TCs ($n = 70$) that made landfall in Japan from 1979 to 2004. The y axis is taken in the direction of the storm motion. The cross in the center of each panel indicates the storm center. Figure reproduced from Fujibe and Kitabatake (2007, their Figs. 3d,f).

Bowyer 2005). Strongly enhanced waves are more likely for strong storms moving quickly with relatively small trapped-fetch lengths, with transitioning TCs having the greatest potential for these enhanced waves (Bowyer and MacAfee 2005).

Waves are small-scale phenomena, however, and their impacts tend to be parameterized in mesoscale models (if represented at all), complicating our ability to analyze and predict these features for ET events. Consequently, in addition to requiring improved inputs from meteorological forecasts, improved wave forecasts require state-of-the-art wave physics that include accurate parameterizations of the physical links between the atmosphere and ocean that govern wave behavior.

One such physical link is the generation of sea spray, which is known to contribute to TC intensification by enhancing surface latent heat flux through evaporation (e.g., Ma et al. 2015). Simulations of two TCs after ET and one of an intense extratropical cyclone demonstrated that including a sea spray parameterization increased extratropical cyclone intensity by 5–10 kt (1 kt = 0.5144 m s^{-1}), depending on the storm, by increasing latent and sensible heat flux at the ocean surface (Perrie et al. 2005). The parameterization improved forecast wind speed estimates compared to those estimated from numerical model outputs and satellite observations. Wind speed, storm size, SST, and cyclone translation speed all affected the impacts of sea spray. Further research is necessary, however, to understand how sea spray generation evolves during ET (i.e., not just for TCs and extratropical cyclones separately).

Another physical link is wave drag, or the amount of friction generated by the production of ocean waves by the wind field. Using a coupled atmosphere–wave–sea spray model to investigate the combined effects of wave generation and sea spray on extratropical cyclone development, Zhang et al. (2006) found that simulated cyclone intensities better resembled their observed counterparts when including wave drag and sea spray compared to simulations without either. The influence of sea spray decreased due to decreasing SSTs as storms moved poleward, which coincided with an increasing influence of wave drag. As with sea spray, however, further research is necessary to understand how wave drag evolves during, and not just after, ET.

c. *Precipitation*

Although distinct from a transitioning TC's wind and wave field evolutions, precipitation is perhaps the most notable ET impact to inland locations. Indeed, precipitation from TCs that undergo ET is a partial contributor to the overall precipitation climatologies of locations such as the southeastern United States (Brun and Barros 2014; Mahoney et al. 2016) and northwestern Australia (Ng et al. 2015). Rainfall associated with transitioning TCs can be directly associated with the cyclone itself or well removed (e.g., by >1000 km) from the cyclone. Although these latter events, known as predecessor rain events (e.g., Galarneau et al. 2010), can result in damaging flash floods, they are considered an indirect impact of ET and are discussed in more detail in Part II. Several heavy-precipitation events associated

with transitioning TCs have caused historic flash floods in the United States well inland from the Atlantic coast, including Hazel in 1954 (Palmén 1958; Matano 1958), Agnes in 1972 (e.g., Carr and Bosart 1978; Bosart and Dean 1991), and Irene in 2011 (e.g., Milrad et al. 2013; Smith et al. 2016).

Because heavy precipitation associated with ET can occur well inland, as the cases cited above indicate, it is crucial to understand where heavy precipitation occurs during ET and the conditions that cause ET-related heavy-precipitation events to inform timely warnings. During ET, precipitation shifts radially outward and has maximum intensity downshear (Matyas 2010a,b,c). Precipitation coverage grows in areal extent as ET begins, but decreases in areal extent later in the process (Matyas 2013). Whereas TCs are typically characterized by heaviest precipitation to the left of the vertical wind shear (e.g., Lonfat et al. 2004; Chen et al. 2006), which is often right of track in the NATL, the heaviest precipitation during ET may be found either left or right of track (Atallah and Bosart 2003; Atallah et al. 2007; Milrad et al. 2009; Chen 2011; Zhou and Matyas 2017). Left-of-track precipitation is more common under atmospheric conditions resembling those favoring reintensification after becoming extratropical (section 5b), notably a negative-tilted upstream trough near to, and of similar scale as, the TC, with amplified mid- to upper-tropospheric ridging atop and downstream of the TC (Atallah et al. 2007; Milrad et al. 2009). Conversely, cases with right-of-track precipitation maxima generally never completed ET or decayed shortly after becoming extratropical. Despite advanced understanding of precipitation field evolution during ET, however, the extent to which precipitation asymmetries evolve and/or are in phase with the wind, wave, and thermal asymmetries warrants further study.

Though orography has long been known to affect TC precipitation rates, particularly in Taiwan (e.g., Lin et al. 2001; Yu and Cheng 2008, 2013), it may also focus extreme precipitation during ET. For example, Vermont was heavily impacted by flash flooding from NATL TC Irene (2011), largely due to orographic precipitation enhancement in the complex terrain of the Green Mountains (Liu and Smith 2016; Smith et al. 2016). Similarly, as precipitation with NATL TC Sandy (2012) shifted to the left of track during and after ET, upslope flow induced by the cyclone within a highly anomalous antecedent cold air mass along the western slopes of the Appalachian Mountains of North Carolina, Virginia, and West Virginia resulted in up to 900 mm of snowfall (Keighton et al. 2016). Only three prior NATL TCs are known to have produced accumulating snow in the United States, all of which occurred in New England in fall or winter in the presence of elevated terrain and an antecedent cold air mass (Keighton et al. 2016). Orography can also modulate a transitioning TC's rainfall distribution, as has been seen with systems in the St. Lawrence River valley of Canada (Milrad et al. 2009, 2013). Here, ageostrophic frontogenesis focused by the local topography, rather than the synoptic-scale pattern, has been found to exert primary control on where the heaviest precipitation occurs with transitioning TCs in this region (Milrad et al. 2013).

5. Structural evolution

The potential impacts of winds, waves, and precipitation are tied to the evolving structure of the transitioning cyclone. Historically, numerical model simulations and model-derived observation syntheses have been the primary means of obtaining insight into cyclone structure evolution during ET (Jones et al. 2003). This prompted Jones et al. (2003) to stress the critical need for increased in situ observations and targeted field experiments of ET events to validate the insights gleaned from numerical simulations and to improve our knowledge of the ET process.

In recent years, several field experiments with partial ET foci have been conducted. NOAA's Intensity Forecasting Experiment (IFEX; Rogers et al. 2006, 2013) included flights into NATL TC Ophelia (2005) that provided novel observations of a transitioning TC's structural evolution using airborne Doppler radar and dropsondes (Fogarty 2006; Rogers et al. 2006). Later IFEX missions sampled Earl (2010), Sandy (2012), Arthur (2014), Kate (2015), and Karl (2016) before and during ET, including Sandy's interrupted transition east of Florida (Blake et al. 2013). Additionally, three separate programs investigated WNP ET during 2008: The Observing System Research and Predictability Experiment (THORPEX)-Pacific Asian Regional Campaign (T-PARC; Elsberry and Harr 2008; Waliser et al. 2012), the Dropsonde Observations for Typhoon Surveillance near the Taiwan Region (DOTSTAR; Wu et al. 2005) experiment, and the Tropical Cyclone Structure (TCS-08; Elsberry and Harr 2008) experiment.

Together, observation- and numerical model–based studies have advanced understanding of structural evolution both during and after ET. In particular, observations have provided validation of previously developed conceptual models, and numerical model–based studies have increased our knowledge of variation and environmental sensitivities in structural evolution during and after ET. Organized around the two-stage ET conceptual model highlighted in Fig. 1 and the three-step conceptualization of the transformation stage of Klein et al. (2000;

76. Assignment 2, Module 16: Extratropical Hermine: https://weather.com/storms/hurricane/news/hurricane-hermine-transition-impacts-forecast-post-tropical

Tropical vs. Non-Tropical ; What's The Difference?

Does a tropical cyclone's transition to a non-tropical cyclone make any difference in its overall impacts ?

By Tom Moore • September 6, 2016

Start the conversation | Share

Watches Issued In Caribbean For Future Ernesto

Tropical cyclones can undergo a transition to a non-tropical or "post tropical" cyclone. So, what does that actually mean and does that really change anything as far as weather impacts are concerned?

In William Shakespeare's Romeo and Juliet, Juliet poses a question and follows with the remark, "What's in a name? That which we call a rose by any other name would smell as sweet."

In the world of weather, meteorologists have names for all kinds of phenomenon, but information must be communicated to the public and all of these names and the terminology can be very confusing. To be honest, sometimes they are even confusing to the meteorologists.

(MORE: Florida's Record-Smashing Hurricane Drought Has Ended)

Tropical vs. Non-Tropical Cyclones

A tropical (or warm core) cyclone (area of low pressure) usually forms over warm waters in the tropics. Air rises rapidly around the edges of the center of the storm. Sinking air in the center of the storm heats up the air, so the storm has warm temperatures from the surface all the way up to high levels of the atmosphere. Hurricanes and tropical storms are (warm core) tropical cyclones.

At the surface, stronger winds are usually proximate to the storm's location and they diminish quickly when you move away from the storm.

A non-tropical (or cold core) storm has the coldest temperatures in the center of the storm. Temperatures cool as you move higher in the atmosphere and there is a trough at the highest levels. Unlike tropical (warm core) storms, winds are not as concentrated near the center of the storm, but can spread out for hundreds of miles from it.

Precipitation in a cold core (non-tropical cyclone) can also spread far away from the center of the storm. Most mid-latitude storms are cold core including nor'easters.

Tropical cyclones are nearly symmetric in shape and are without fronts. Mid-latitude (cold core) cyclones are comma shaped and have fronts associated with them.

Hurricanes and tropical storms often transition to cold core cyclones. When the National Hurricane Center concludes that a tropical storm has transitioned to a (cold core) mid-latitude storm it will designate it as "post-tropical" meaning that it has transitioned to a non-tropical storm.

The transition often occurs when a tropical cyclone moves to higher latitudes and interacts with atmospheric features that are more common there. An example of this is the transition that Tropical Storm Hermine went though, in early September of 2016, as it emerged off of the North Carolina coast and into the Atlantic.

The main point is that the designation "post-tropical" is NOT a downgrade from a tropical storm. It merely means that the tropical storm has undergone a transition. It can remain as a high impact storm but those impacts can be similar to or, in some cases, vary from when it was a tropical storm.

So, the storm could feature a different structure and have a different look, but it still can threaten lives and property.

Non/Post - Tropical ? What's the Difference?

Tropical cyclones can transitions to non-tropical or "post-tropical" cyclones, meaning that it has technically lost many of its tropical characteristics and is more closely related to a mid-latitude (non-tropical) storm. As indicated earlier, this is NOT a downgrade!

One reason for a tropical cyclone's transition is when it interacts with mid-latitude features such as an upper-level trough (dip in the jet stream) and a frontal boundary at the surface. These features create physical changes in the storm's structure.

Although a tropical storm's physical structure changes, it can remain an extremely dangerous storm. Impacts that are associated with tropical cyclones such as dangerous storm surge, flooding rain and strong winds can continue.

In fact, winds in a storm that transitions to non-tropical can actually increase in strength.

Although a tropical storm can be designated non tropical or "post-tropical," the National Hurricane Center can issue tropical storm warnings for areas that are about to feel impacts from the "transitioned" storm.

Why Can Tropical Advisories Be Issued For Non-Tropical Storms: The "Sandy" Rule

In October 2012, Hurricane Sandy was a powerful storm that was barreling westward toward the coast of New Jersey. The National Hurricane Center forecast was for Hurricane Sandy to transition to a "post-tropical" cyclone before making landfall.

On October 29, 2012 in the late afternoon, Sandy remained a hurricane but a special advisory issued by the National Hurricane Center indicated that the storm had lost its tropical characteristics and was designated a "post-tropical" cyclone.

Back then, when a transition occurred, the responsibility of communication with the public switched to the local National Weather Service offices that would receive impacts from the storm.

This all happened only a few hours before landfall. In addition, there were no tropical advisories such as a hurricane warning in effect for coastal areas of New Jersey and farther north to New York.

This created much confusion as many public officials and emergency management staff believed that Sandy was "downgraded" and no longer posed a great threat. The results proved that this was far from true. It also created much confusion for the public, who were eager to receive the latest information.

After a complete review, the National Weather Service allowed the National Hurricane Center to issue tropical advisories, even after a tropical cyclone or hurricane transitions to post-tropical if it poses a significant threat to life and property.

For example, the National Hurricane Center issued tropical storm warnings from the mid-Atlantic region to New England for Hermine after it had transitioned to a "post" tropical storm.

So, even though a storm transitions from a tropical to "post" tropical, it can continue to threaten life and property.

Regardless of what meteorologists call these storms, their impacts can still be significant.

78. Assignment 3, Module 17: FEMA 454, Section 2.2.1:
https://www.wbdg.org/FFC/DHS/fema454.pdf

2.2.1 Plate Tectonics and Seismicity

A coherent global explanation of the occurrence of the majority of earthquakes is provided by the geological model known as Plate Tectonics. The basic concept is that the Earth's outermost part (called the lithosphere) consists of several large and fairly stable rock slabs called plates. The ten largest plates are mapped in Figure 2-2. Each plate extends to a depth of about 100-200 km and includes the Earth's outermost rigid rocky layer, called the crust.

The moving tectonic plates of the Earth's surface also provide an explanation of the various mechanisms of most significant earthquakes. Straining and fracturing of the regional crustal rocks result from collisions between adjacent lithospheric plates, from destruction of rocky slab-like plate as it descends or **subducts** into a dipping zone beneath island arcs, and from spreading out of the crust along mid-oceanic ridges. In the United States, the most significant subduction zone is the Cascadia Zone in western Washington state, where the Juan de Fuca Plate slides (or subducts) under the America Plate (Figure 2-2). Research indicates that ruptures along this zone have resulted in very large magnitude earthquakes about every 500-600 years . The 1964 Alaska earthquake was in a subduction zone and was responsible for the greatest recorded United States earthquake. The earthquakes in these tectonically active boundary regions are called **interplate earthquakes**. The very hazardous shallow earthquakes of Chile, Peru, the eastern Caribbean, Central America, Southern Mexico, California, Southern Alaska, the Aleutians the Kuriles, Japan, Taiwan, the Philippines, Indonesia, New

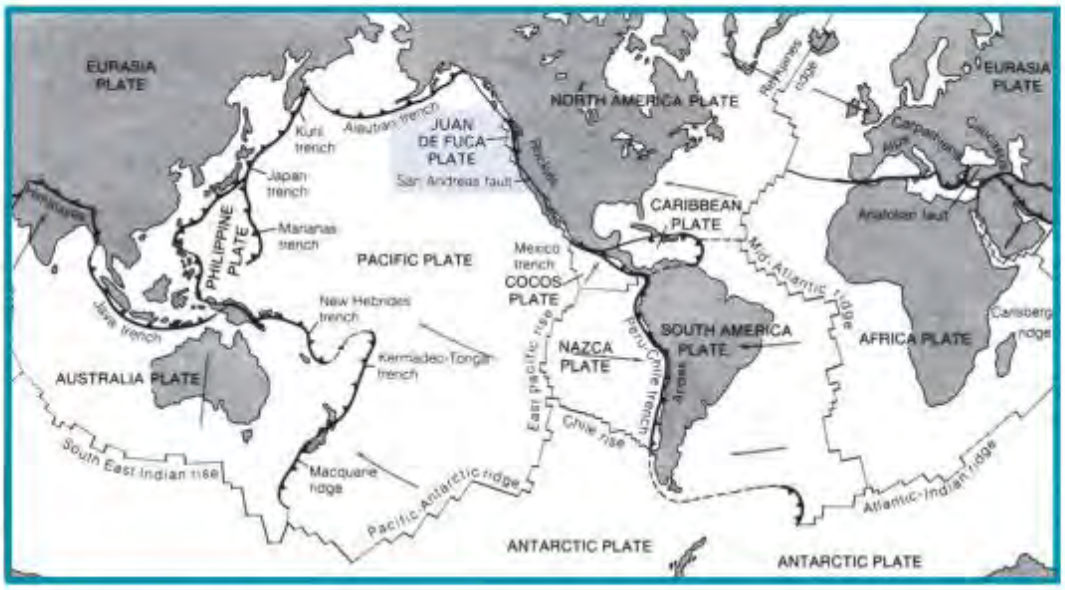

Figure 2-2: The major tectonic plates, midoceanic ridges, trenches and transform faults.

SOURCE: BRUCE A. BOLT, *NUCLEAR EXPLOSIONS AND EARTHQUAKES: THE PARTED VEIL* (SAN FRANCISCO: W. H. FREEMAN AND COMPANY. COPYRIGHT 1976.

Zealand, the Alpine-Caucasian-Himalayan belt are of plate-edge type. Earthquakes generated at depths down to 700 km also occur along plate edges by a mechanism yet unclear.

As the mechanics of the lithospheric plates have become better understood, long-term predictions of the place and size of interplate earthquakes become possible. For example, many plates spread toward the subduction zones at long-term geologic rates of from 2 to 5 cm (about one to two inches) per year. Therefore, in active arcs like the Aleutian and Japanese islands and subduction zones like Chile and western Mexico, the history of large earthquake occurrence can identify areas that currently lag in earthquake activity.

There is a type of large earthquake that is produced by slip along faults connecting the ends of offsets in the spreading oceanic ridges and the ends of island arcs or arc-ridge chains (see Figure 2-2). In these regions, plates slide past each other along what are called **strike–slip**, or **transform faults**. Considerable work has been done on the estimation of strong ground motion parameters for the design of critical structures in earthquake-prone countries with either transform faults or ocean-plate subduction tectonics, such as Japan, Alaska, Chile, Mexico, and the United States. Similar hazard studies have been published for the Himalaya, the Zagros (Iran), and Alpine regions all examples of mountain ranges formed by **continent-to-continent collisions**. Such collision zones are regions where very damaging earthquakes sometimes occur.

While simple plate-tectonic theory provides a general understanding of earthquakes and volcanoes, it does not explain all seismicity in detail, for within continental regions, away from boundaries, there are also large devastating earthquakes. These **intraplate** earthquakes can be found on nearly every continent (Yeats et al., 1997). The disastrous Bhuj (M = 7.7) earthquake in northeast India in the seismically active Kutch province was a recent example of such an intraplate earthquake (see Section 2.3.3 for an explanation of earthquake magnitude (M). In the United States, the most famous intraplate earthquakes occurred in 1811-1812 in the New Madrid area of Missouri, along the Mississippi River; another is the damaging 1886 Charleston, South Carolina, earthquake. The Nisqually earthquake of 2001 that took place in Washington was a deep focus earthquake with a moment magnitude of 6.8. However, because of its depth of focus (32 miles), structural damage to buildings was not widespread and modern buildings and those recently upgraded performed well.

Shallow-focus earthquakes (focus depth less than 70 km) wreak the most devastation, and they contribute about three-quarters of the total energy released in earthquakes throughout the world. In California, for example, all of the known damaging earthquakes to date have been shallow-focus. In fact, it has been shown that the great majority of earthquakes occurring in California originate from foci in the upper ten kilometers of the Earth's crust, and only a few are as deep as 15-20 km, excepting those associated with subduction north of Cape Mendocino.

All types of tectonic earthquakes defined above are caused by the sudden release of elastic energy when a fault ruptures; i.e. opposite sides rapidly

slip in opposite directions. This slip does work in the form of heat and wave radiation and allows the rock to rebound to a position of less strain.

Most moderate to large shallow earthquakes are followed, in the ensuing hours and even in the next several months, by numerous, usually smaller, earthquakes in the same vicinity. These earthquakes are called **aftershocks**, and large earthquakes are sometimes followed by very large numbers of them. The great Rat Island earthquake caused by subduction under the Aleutian Islands on 4 February 1965 was, within the next 24 days, followed by more than 750 aftershocks large enough to be recorded by distant seismographs. Aftershocks are sometimes energetic enough to cause additional damage to already weakened structures. This happened, for example, a week after the Northridge earthquake of 17 January 1994 in the San Fernando Valley, when some weakened structures sustained additional cracking from magnitude 5.5-6.0 aftershocks. A few earthquakes are preceded by smaller **foreshocks** from the source area, and it has been suggested that these can be used to predict the main shock, but attempts along this line have not proven statistically successful.

Volcanoes and earthquakes often occur together along the margins of plates around the world that are shown in Figure 2-2. Like earthquakes, there are also intraplate volcanic regions, such as the Hawaiian volcanoes in which earthquakes and volcanic activity are clearly physically related.

79. Assignment 3, Module 17: Plate Tectonics:
https://pubs.usgs.gov/gip/dynamic/dynamic.html

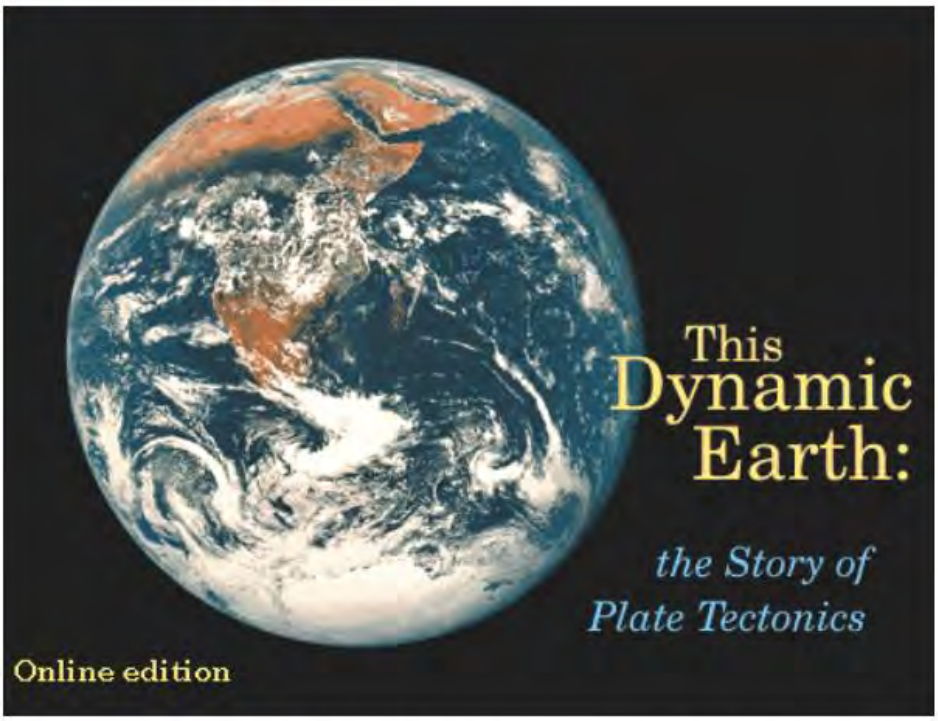

View of the planet Earth from the *Apollo* spacecraft. The Red Sea, which separates Saudi Arabia from the continent of Africa, is clearly visible at the top. (Photograph courtesy of NASA.)

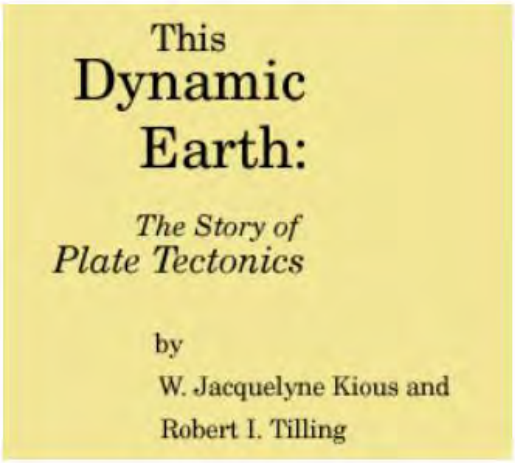

Preface

In the early 1960s, the emergence of the *theory of plate tectonics* started a revolution in the earth sciences. Since then, scientists have verified and refined this theory, and now have a much better understanding of how our planet has been shaped by plate-tectonic processes. We now know that, directly or indirectly, plate tectonics influences nearly all geologic processes, past and present. Indeed, the notion that the entire Earth's surface is continually shifting has profoundly changed the way we view our world.

People benefit from, and are at the mercy of, the forces and consequences of plate tectonics. With little or no warning, an earthquake or volcanic eruption can unleash bursts of energy far more powerful than anything we can generate. While we have no control over plate-tectonic processes, we now have the knowledge to learn from them. The more we know about plate tectonics, the better we can appreciate the grandeur and beauty of the land upon which we live, as well as the occasional violent displays of the Earth's awesome power.

This booklet gives a brief introduction to the concept of plate tectonics and complements the visual and written information in *This Dynamic Planet* (see **Further reading**), a map published in 1994 by the U.S. Geological Survey (USGS) and the Smithsonian Institution. The booklet highlights some of the people and discoveries that advanced the development of the theory and traces its progress since its proposal. Although the general idea of plate tectonics is now widely accepted, many aspects still continue to confound and challenge scientists. The earth-science revolution launched by the theory of plate tectonics is not finished.

Oldoinyo Lengai, an active volcano in the East African Rift Zone, where Africa is being pulled apart by plate-tectonic processes. (Photograph by Jorg Keller, Albert-Ludwigs-Universität Freiburg, Germany.)

Historical perspective

In geologic terms, a *plate* is a large, rigid slab of solid rock. The word *tectonics* comes from the Greek root "to build." Putting these two words together, we get the term *plate tectonics*, which refers to how the Earth's surface is built of plates. The *theory of plate tectonics* states that the Earth's outermost layer is fragmented into a dozen or more large and small plates that are moving relative to one another as they ride atop hotter, more mobile material. Before the advent of plate tectonics, however, some people already believed that the present-day continents were the fragmented pieces of preexisting larger landmasses ("supercontinents"). The diagrams below show the break-up of the supercontinent *Pangaea* (meaning "all lands" in Greek), which figured prominently in the *theory of continental drift* -- the forerunner to the theory of plate tectonics.

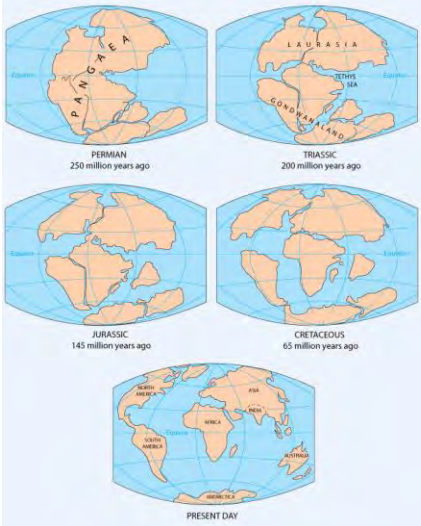

According to the continental drift theory, the supercontinent Pangaea *began to break up about 225-200 million years ago, eventually fragmenting into the continents as we know them today.*

Plate tectonics is a relatively new scientific concept, introduced some 30 years ago, but it has revolutionized our understanding of the dynamic planet upon which we live. The theory has unified the study of the Earth by drawing together many branches of the earth sciences, from *paleontology* (the study of fossils) to *seismology* (the study of earthquakes). It has provided explanations to questions that scientists had speculated upon for centuries -- such as why earthquakes and volcanic eruptions occur in very specific areas around the world, and how and why great mountain ranges like the Alps and Himalayas formed.

Why is the Earth so restless? What causes the ground to shake violently, volcanoes to erupt with explosive force, and great mountain ranges to rise to incredible heights? Scientists, philosophers, and theologians have wrestled with questions such as these for centuries. Until the 1700s, most Europeans thought that a Biblical Flood played a major role in shaping the Earth's surface. This way of thinking was known as "catastrophism," and *geology* (the study of the Earth) was based on the belief that all earthly changes were sudden and caused by a series of catastrophes. However, by the mid-19th century, catastrophism gave way to "uniformitarianism," a new way of thinking centered around the "Uniformitarian Principle" proposed in 1785 by James Hutton, a Scottish geologist. This principle is commonly stated as follows: *The present is the key to the past.* Those holding this viewpoint assume that the geologic forces and processes -- gradual as well as catastrophic -- acting on the Earth today are the same as those that have acted in the geologic past.

Tectonic plates [115 k]

The belief that continents have not always been fixed in their present positions was suspected long before the 20th century; this notion was first suggested as early as 1596 by the Dutch map maker Abraham Ortelius in his work *Thesaurus Geographicus*. Ortelius suggested that the Americas were "torn away from Europe and Africa . . . by earthquakes and floods" and went on to say: "The vestiges of the rupture reveal themselves, if someone brings forward a map of the world and considers carefully the coasts of the three [continents]." Ortelius' idea surfaced again in the 19th century. However, it was not until 1912 that the idea of moving continents was seriously considered as a full-blown scientific theory -- called *Continental Drift* -- introduced in two articles published by a 32-year-old German meteorologist named Alfred Lothar Wegener. He contended that, around 200 million years ago, the supercontinent Pangaea began to split apart. Alexander Du Toit, Professor of Geology at Witwatersrand University and one of Wegener's staunchest supporters, proposed that Pangaea first broke into two large continental landmasses, *Laurasia* in the northern hemisphere and *Gondwanaland* in the southern hemisphere. Laurasia and Gondwanaland then continued to break apart into the various smaller continents that exist today.

In 1858, geographer Antonio Snider-Pellegrini made these two maps showing his version of how the American and African continents may once have fit together, then later separated. Left: The formerly joined continents before (avant) their separation. Right: The continents after (après) the separation. (Reproductions of the original maps courtesy of University of California, Berkeley.)

Wegener's theory was based in part on what appeared to him to be the remarkable fit of the South American and African continents, first noted by Abraham Ortelius three centuries earlier. Wegener was also intrigued by the occurrences of unusual geologic structures and of plant and animal fossils found on the matching coastlines of South America and Africa, which are now widely separated by the Atlantic Ocean. He reasoned that it was physically impossible for most of these organisms to have swum or have been transported across the vast oceans. To him, the presence of identical fossil species along the coastal parts of Africa and South America was the most compelling evidence that the two continents were once joined.

In Wegener's mind, the drifting of continents after the break-up of Pangaea explained not only the matching fossil occurrences but also the evidence of dramatic climate changes on some continents. For example, the discovery of fossils of tropical plants (in the form of coal deposits) in Antarctica led to the conclusion that this frozen land previously must have been situated closer to the equator, in a more temperate climate where lush, swampy vegetation could grow. Other mismatches of geology and climate included distinctive fossil ferns *(Glossopteris)* discovered in now-polar regions, and the occurrence of glacial deposits in present-day arid Africa, such as the Vaal River valley of South Africa.

The *theory of continental drift* would become the spark that ignited a new way of viewing the Earth. But at the time Wegener introduced his theory, the scientific community firmly believed the continents and oceans to be permanent features on the Earth's surface. Not surprisingly, his proposal was not well received, even though it seemed to agree with the scientific information available at the time. A fatal weakness in Wegener's theory was that it could not satisfactorily answer the most fundamental question raised by his critics: What kind of forces could be strong enough to move such large masses of solid rock over such great distances? Wegener suggested that the continents simply plowed through the ocean floor, but Harold Jeffreys, a noted English geophysicist, argued correctly that it was physically impossible for a large mass of solid rock to plow through the ocean floor without breaking up.

Rejoined continents [48 k]

Undaunted by rejection, Wegener devoted the rest of his life to doggedly pursuing additional evidence to defend his theory. He froze to death in 1930 during an expedition crossing the Greenland ice cap, but the controversy he spawned raged on. However, after his death, new evidence from ocean floor exploration and other studies rekindled interest in Wegener's theory, ultimately leading to the development of the *theory of plate tectonics.*

Plate tectonics has proven to be as important to the earth sciences as the discovery of the structure of the atom was to physics and chemistry and the theory of evolution was to the life sciences. Even though the theory of plate tectonics is now widely accepted by the scientific community, aspects of the theory are still being debated today. Ironically, one of the chief outstanding questions is the one Wegener failed to resolve: What is the nature of the forces propelling the plates? Scientists also debate how plate tectonics may have operated (if at all) earlier in the Earth's history and whether similar processes operate, or have ever operated, on other planets in our solar system.

USGS

Developing the theory

Continental drift was hotly debated off and on for decades following Wegener's death before it was largely dismissed as being eccentric, preposterous, and improbable. However, beginning in the 1950s, a wealth of new evidence emerged to revive the debate about Wegener's provocative ideas and their implications. In particular, four major scientific developments spurred the formulation of the plate-tectonics theory: (1) demonstration of the ruggedness and youth of the ocean floor; (2) confirmation of repeated reversals of the Earth magnetic field in the geologic past; (3) emergence of the seafloor-spreading hypothesis and associated recycling of oceanic crust; and (4) precise documentation that the world's earthquake and volcanic activity is concentrated along oceanic trenches and submarine mountain ranges.

Ocean floor mapping

About two thirds of the Earth's surface lies beneath the oceans. Before the 19th century, the depths of the open ocean were largely a matter of speculation, and most people thought that the ocean floor was relatively flat and featureless. However, as early as the 16th century, a few intrepid navigators, by taking soundings with hand lines, found that the open ocean can differ considerably in depth, showing that the ocean floor was not as flat as generally believed. Oceanic exploration during the next centuries dramatically improved our knowledge of the ocean floor. We now know that most of the geologic processes occurring on land are linked, directly or indirectly, to the dynamics of the ocean floor.

"Modern" measurements of ocean depths greatly increased in the 19th century, when deep-sea line soundings (*bathymetric* surveys) were routinely made in the Atlantic and Caribbean. In 1855, a bathymetric chart published by U.S. Navy Lieutenant Matthew Maury revealed the first evidence of underwater mountains in the central Atlantic (which he called "Middle Ground"). This was later confirmed by survey ships laying the trans-Atlantic telegraph cable. Our picture of the ocean floor greatly sharpened after World War I (1914-18), when echo-sounding devices -- primitive sonar systems -- began to measure ocean depth by recording the time it took for a sound signal (commonly an electrically generated "pung") from the ship to bounce off the ocean floor and return. Time graphs of the returned signals revealed that the ocean floor was much more rugged than previously thought. Such echo-sounding measurements clearly demonstrated the continuity and roughness of the submarine mountain chain in the central Atlantic (later called the *Mid-Atlantic Ridge*) suggested by the earlier bathymetric measurements.

The Mid-Ocean Ridge [70 k]

In 1947, seismologists on the U.S. research ship *Atlantis* found that the sediment layer on the floor of the Atlantic was much thinner than originally thought. Scientists had previously believed that the oceans have existed for at least 4 billion years, so therefore the sediment layer should have been very thick. Why then was there so little accumulation of sedimentary rock and debris on the ocean floor? The answer to this question, which came after further exploration, would prove to be vital to advancing the concept of plate tectonics.

Computer-generated topographic map of the Mid-Ocean Ridge [55 k]

In the 1950s, oceanic exploration greatly expanded. Data gathered by oceanographic surveys conducted by many nations led to the discovery that a great mountain range on the ocean floor virtually encircled the Earth. Called the *global mid-ocean ridge*, this immense submarine mountain chain -- more than 50,000 kilometers (km) long and, in places, more than 800 km across -- zig-zags between the continents, winding its way around the globe like the seam on a baseball. Rising an average of about 4,500 meters(m) above the sea floor, the mid-ocean ridge overshadows all the mountains in the United States except for Mount McKinley (Denali) in Alaska (6,194 m). Though hidden beneath the ocean surface, the global mid-ocean ridge system is the most prominent topographic feature on the surface of our planet.

Magnetic striping and polar reversals

Beginning in the 1950s, scientists, using magnetic instruments *(magnetometers)* adapted from airborne devices developed during World War II to detect submarines, began recognizing odd magnetic variations across the ocean floor. This finding, though unexpected, was not entirely surprising because it was known that *basalt* -- the iron-rich, volcanic rock making up the ocean floor-- contains a strongly magnetic mineral *(magnetite)* and can locally distort compass readings. This distortion was recognized by Icelandic mariners as early as the late 18th century. More important, because the presence of magnetite gives the basalt measurable magnetic properties, these newly discovered magnetic variations provided another means to study the deep ocean floor.

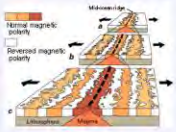

*A theoretical model of the formation of magnetic striping. New oceanic crust forming continuously at the crest of the mid-ocean ridge cools and becomes increasingly older as it moves away from the ridge crest with seafloor spreading (see text): **a**, the spreading ridge about 5 million years ago; **b**, about 2 to 3 million years ago; and **c**, present-day.*

Early in the 20th century, *paleomagnetists* (those who study the Earth's ancient magnetic field) -- such as Bernard Brunhes in France (in 1906) and Motonari Matuyama in Japan (in the 1920s) -- recognized that rocks generally belong to two groups according to their magnetic properties. One group has so-called *normal polarity*, characterized by the magnetic minerals in the rock having the same polarity as that of the Earth's present magnetic field. This would result in the **north** end of the rock's "compass needle" pointing toward magnetic **north**. The other group, however, has *reversed polarity*, indicated by a polarity alignment opposite to that of the Earth's present magnetic field. In this case, the **north** end of the rock's compass needle would point **south**. How could this be? This answer lies in the magnetite in volcanic rock. Grains of magnetite -- behaving like little magnets -- can align themselves with the orientation of the Earth's magnetic field. When *magma* (molten rock containing minerals and gases) cools to form solid volcanic rock, the alignment of the magnetite grains is "locked in," recording the Earth's magnetic orientation or polarity (normal or reversed) at the time of cooling.


Magnetic striping in the Pacific Northwest [70 k]

As more and more of the seafloor was mapped during the 1950s, the magnetic variations turned out not to be random or isolated occurrences, but instead revealed recognizable patterns. When these magnetic patterns were mapped over a wide region, the ocean floor showed a zebra-like pattern. Alternating stripes of magnetically different rock were laid out in rows on either side of the mid-ocean ridge: one stripe with normal polarity and the adjoining stripe with reversed polarity. The overall pattern, defined by these alternating bands of normally and reversely polarized rock, became known as magnetic striping.

Seafloor spreading and recycling of oceanic crust

The discovery of magnetic striping naturally prompted more questions: How does the magnetic striping pattern form? And why are the stripes symmetrical around the crests of the mid-ocean ridges? These questions could not be answered without also knowing the significance of these ridges. In 1961, scientists began to theorize that mid-ocean ridges mark structurally weak zones where the ocean floor was being ripped in two lengthwise along the ridge crest. New magma from deep within the Earth rises easily through these weak zones and eventually erupts along the crest of the ridges to create new oceanic crust. This process, later called *seafloor spreading*, operating over many millions of years has built the 50,000 km-long system of mid-ocean ridges. This hypothesis was supported by several lines of evidence: (1) at or near the crest of the ridge, the rocks are very young, and they become progressively older away from the ridge crest; (2) the youngest rocks at the ridge crest always have present-day (normal) polarity; and (3) stripes of rock parallel to the ridge crest alternated in magnetic polarity (normal-reversed-normal, etc.), suggesting that the Earth's magnetic field has flip-flopped many times. By explaining both the zebralike magnetic striping and the construction of the mid-ocean ridge system, the seafloor spreading hypothesis quickly gained converts and represented another major advance in the development of the plate-tectonics theory. Furthermore, the oceanic crust now came to be appreciated as a natural "tape recording" of the history of the reversals in the Earth's magnetic field.

Additional evidence of seafloor spreading came from an unexpected source: petroleum exploration. In the years following World War II, continental oil reserves were being depleted rapidly and the search for offshore oil was on. To conduct offshore exploration, oil companies built ships equipped with a special drilling rig and the capacity to carry many kilometers of drill pipe. This basic idea later was adapted in constructing a research vessel, named the *Glomar Challenger*, designed specifically for marine geology studies, including the collection of drill-core samples from the deep ocean floor. In 1968, the vessel embarked on a year-long scientific expedition, criss-crossing the Mid-Atlantic Ridge between South America and Africa and drilling core samples at specific locations. When the ages of the samples were determined by paleontologic and isotopic dating studies, they provided the clinching evidence that proved the seafloor spreading hypothesis.

A profound consequence of seafloor spreading is that new crust was, and is now, being continually created along the oceanic ridges. This idea found great favor with some scientists who claimed that the shifting of the continents can be simply explained by a large increase in size of the Earth since its formation. However, this so-called "expanding Earth" hypothesis was unsatisfactory because its supporters could offer no convincing geologic mechanism to produce such a huge, sudden expansion. Most geologists believe that the Earth has changed little, if at all, in size since its formation 4.6 billion years ago, raising a key question: how can new crust be continuously added along the oceanic ridges without increasing the size of the Earth?

This question particularly intrigued Harry H. Hess, a Princeton University geologist and a Naval Reserve Rear Admiral, and Robert S. Dietz, a scientist with the U.S. Coast and Geodetic Survey who first coined the term *seafloor spreading*. Dietz and Hess were among the small handful who really understood the broad implications of sea floor spreading. If the Earth's crust was expanding along the oceanic ridges, Hess reasoned, it must be shrinking elsewhere. He suggested that new oceanic crust continuously spread away from the ridges in a conveyor belt-like motion. Many millions of years later, the oceanic crust eventually descends into the oceanic *trenches* -- very deep, narrow canyons along the rim of the Pacific Ocean basin. According to Hess, the Atlantic Ocean was expanding while the Pacific Ocean was shrinking. As old oceanic crust was consumed in the trenches, new magma rose and erupted along the spreading ridges to form new crust. In effect, the ocean basins were perpetually being "recycled," with the creation of new crust and the destruction of old oceanic lithosphere occurring simultaneously. Thus, Hess' ideas neatly explained why the Earth does not get bigger with sea floor spreading, why there is so little sediment accumulation on the ocean floor, and why oceanic rocks are much younger than continental rocks.

Concentration of earthquakes

During the 20th century, improvements in seismic instrumentation and greater use of earthquake-recording instruments *(seismographs)* worldwide enabled scientists to learn that earthquakes tend to be concentrated in certain areas, most notably along the oceanic trenches and spreading ridges. By the late 1920s, seismologists were beginning to identify several prominent earthquake zones parallel to the trenches that typically were inclined 40-60° from the horizontal and extended several hundred kilometers into the Earth. These zones later became known as *Wadati-Benioff zones*, or simply *Benioff zones*, in honor of the seismologists who first recognized them, Kiyoo Wadati of Japan and Hugo Benioff of the United States. The study of global seismicity greatly advanced in the 1960s with the establishment of the Worldwide Standardized Seismograph Network (WWSSN) to monitor the compliance of the 1963 treaty banning above-ground testing of nuclear weapons. The much-improved data from the WWSSN instruments allowed seismologists to map precisely the zones of earthquake concentration worldwide.


Earthquake zones [175 k]

But what was the significance of the connection between earthquakes and oceanic trenches and ridges? The recognition of such a connection helped confirm the seafloor-spreading hypothesis by pin-pointing the zones where Hess had predicted oceanic crust is being generated (along the ridges) and the zones where oceanic lithosphere sinks back into the mantle (beneath the trenches).

USGS

Understanding plate motions

Scientists now have a fairly good understanding of how the plates move and how such movements relate to earthquake activity. Most movement occurs along narrow zones between plates where the results of plate-tectonic forces are most evident.

There are four types of plate boundaries:

- Divergent boundaries -- where new crust is generated as the plates pull away from each other.
- Convergent boundaries -- where crust is destroyed as one plate dives under another.
- Transform boundaries -- where crust is neither produced nor destroyed as the plates slide horizontally past each other.
- Plate boundary zones -- broad belts in which boundaries are not well defined and the effects of plate interaction are unclear.


Illustration of the Main Types of Plate Boundaries [55 k]

Divergent boundaries

Divergent boundaries occur along spreading centers where plates are moving apart and new crust is created by magma pushing up from the mantle. Picture two giant conveyor belts, facing each other but slowly moving in opposite directions as they transport newly formed oceanic crust away from the ridge crest.

Perhaps the best known of the divergent boundaries is the Mid-Atlantic Ridge. This submerged mountain range, which extends from the Arctic Ocean to beyond the southern tip of Africa, is but one segment of the global mid-ocean ridge system that encircles the Earth. The rate of spreading along the Mid-Atlantic Ridge averages about 2.5 centimeters per year (cm/yr), or 25 km in a million years. This rate may seem slow by human standards, but because this process has been going on for millions of years, it has resulted in plate movement of thousands of kilometers. Seafloor spreading over the past 100 to 200 million years has caused the Atlantic Ocean to grow from a tiny inlet of water between the continents of Europe, Africa, and the Americas into the vast ocean that exists today.


Mid-Atlantic Ridge [26 k]

The volcanic country of Iceland, which straddles the Mid-Atlantic Ridge, offers scientists a natural laboratory for studying on land the processes also occurring along the submerged parts of a spreading ridge. Iceland is splitting along the spreading center between the North American and Eurasian Plates, as North America moves westward relative to Eurasia.

Map showing the Mid-Atlantic Ridge splitting Iceland and separating the North American and Eurasian Plates. The map also shows Reykjavik, the capital of Iceland, the Thingvellir area, and the locations of some of Iceland's active volcanoes (red triangles), including Krafla.

The consequences of plate movement are easy to see around Krafla Volcano, in the northeastern part of Iceland. Here, existing ground cracks have widened and new ones appear every few months. From 1975 to 1984, numerous episodes of *rifting* (surface cracking) took place along the Krafla fissure zone. Some of these rifting events were accompanied by volcanic activity; the ground would gradually rise 1-2 m before abruptly dropping, signalling an impending eruption. Between 1975 and 1984, the displacements caused by rifting totalled about 7 m.


Lava Fountains, Krafla Volcano [35 k]


Thingvellir Fissure Zone, Iceland [80 k]

In East Africa, spreading processes have already torn Saudi Arabia away from the rest of the African continent, forming the Red Sea. The actively splitting African Plate and the Arabian Plate meet in what geologists call a *triple junction*, where the Red Sea meets the Gulf of Aden. A new spreading center may be developing under Africa along the East African Rift Zone. When the continental crust stretches beyond its limits, tension cracks begin to appear on the Earth's surface. Magma rises and squeezes through the widening cracks, sometimes to erupt and form volcanoes. The rising magma, whether or not it erupts, puts more pressure on the crust to produce additional fractures and, ultimately, the rift zone.


Historically Active Volcanoes, East Africa [38 k]

East Africa may be the site of the Earth's next major ocean. Plate interactions in the region provide scientists an opportunity to study first hand how the Atlantic may have begun to form about 200 million years ago. Geologists believe that, if spreading continues, the three plates that meet at the edge of the present-day African continent will separate completely, allowing the Indian Ocean to flood the area and making the easternmost corner of Africa (the Horn of Africa) a large island.


Summit Crater of 'Erta 'Ale [55 k]


Oldoinyo Lengai, East African Rift Zone [38 k]

Convergent boundaries

The size of the Earth has not changed significantly during the past 600 million years, and very likely not since shortly after its formation 4.6 billion years ago. The Earth's unchanging size implies that the crust must be destroyed at about the same rate as it is being created, as Harry Hess surmised. Such destruction (recycling) of crust takes place along convergent boundaries where plates are moving toward each other, and sometimes one plate sinks (is *subducted*) under another. The location where sinking of a plate occurs is called a *subduction zone*.

The type of convergence -- called by some a very slow "collision" -- that takes place between plates depends on the kind of lithosphere involved. Convergence can occur between an oceanic and a largely continental plate, or between two largely oceanic plates, or between two largely continental plates.

Oceanic-continental convergence

If by magic we could pull a plug and drain the Pacific Ocean, we would see a most amazing sight -- a number of long narrow, curving *trenches* thousands of kilometers long and 8 to 10 km deep cutting into the ocean floor. Trenches are the deepest parts of the ocean floor and are created by subduction.

Oceanic-continental convergence

Off the coast of South America along the Peru-Chile trench, the oceanic Nazca Plate is pushing into and being subducted under the continental part of the South American Plate. In turn, the overriding South American Plate is being lifted up, creating the towering Andes mountains, the backbone of the continent. Strong, destructive earthquakes and the rapid uplift of mountain ranges are common in this region. Even though the Nazca Plate as a whole is sinking smoothly and continuously into the trench, the deepest part of the subducting plate breaks into smaller pieces that become locked in place for long periods of time before suddenly moving to generate large earthquakes. Such earthquakes are often accompanied by uplift of the land by as much as a few meters.


Convergence of the Nazca and South American Plates [65 k]

On 9 June 1994, a magnitude-8.3 earthquake struck about 320 km northeast of La Paz, Bolivia, at a depth of 636 km. This earthquake, within the subduction zone between the Nazca Plate and the South American Plate, was one of deepest and largest subduction earthquakes recorded in South America. Fortunately, even though this powerful earthquake was felt as far away as Minnesota and Toronto, Canada, it caused no major damage because of its great depth.

Ring of Fire [76 k]

Oceanic-continental convergence also sustains many of the Earth's active volcanoes, such as those in the Andes and the Cascade Range in the Pacific Northwest. The eruptive activity is clearly associated with subduction, but scientists vigorously debate the possible sources of magma: Is magma generated by the partial melting of the subducted oceanic slab, or the overlying continental lithosphere, or both?

Oceanic-oceanic convergence

As with oceanic-continental convergence, when two oceanic plates converge, one is usually subducted under the other, and in the process a trench is formed. The Marianas Trench (paralleling the Mariana Islands), for example, marks where the fast-moving Pacific Plate converges against the slower moving Philippine Plate. The Challenger Deep, at the southern end of the Marianas Trench, plunges deeper into the Earth's interior (nearly 11,000 m) than Mount Everest, the world's tallest mountain, rises above sea level (about 8,854 m).

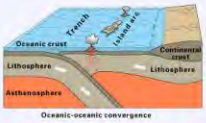

Oceanic-oceanic convergence

Subduction processes in oceanic-oceanic plate convergence also result in the formation of volcanoes. Over millions of years, the erupted lava and volcanic debris pile up on the ocean floor until a submarine volcano rises above sea level to form an island volcano. Such volcanoes are typically strung out in chains called *island arcs*. As the name implies, volcanic island arcs, which closely parallel the trenches, are generally curved. The trenches are the key to understanding how island arcs such as the Marianas and the Aleutian Islands have formed and why they experience numerous strong earthquakes. Magmas that form island arcs are produced by the partial melting of the descending plate and/or the overlying oceanic lithosphere. The descending plate also provides a source of stress as the two plates interact, leading to frequent moderate to strong earthquakes.

Continental-continental convergence

The Himalayan mountain range dramatically demonstrates one of the most visible and spectacular consequences of plate tectonics. When two continents meet head-on, neither is subducted because the continental rocks are relatively light and, like two colliding icebergs, resist downward motion. Instead, the crust tends to buckle and be pushed upward or sideways. The collision of India into Asia 50 million years ago caused the Indian and Eurasian Plates to crumple up along the collision zone. After the collision, the slow continuous convergence of these two plates over millions of years pushed up the Himalayas and the Tibetan Plateau to their present heights. Most of this growth occurred during the past 10 million years. The Himalayas, towering as high as 8,854 m above sea level, form the highest continental mountains in the world. Moreover, the neighboring Tibetan Plateau, at an average elevation of about 4,600 m, is higher than all the peaks in the Alps except for Mont Blanc and Monte Rosa, and is well above the summits of most mountains in the United States.

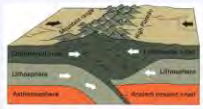

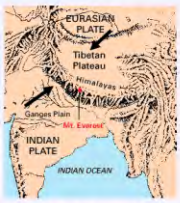

Above: The collision between the Indian and Eurasian plates has pushed up the Himalayas and the Tibetan Plateau. Below: Cartoon cross sections showing the meeting of these two plates before and after their collision. The reference points (small squares) show the amount of uplift of an imaginary point in the Earth's crust during this mountain-building process.

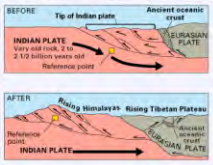

Transform boundaries

The zone between two plates sliding horizontally past one another is called a *transform-fault boundary*, or simply a *transform boundary*. The concept of transform faults originated with Canadian geophysicist J. Tuzo Wilson, who proposed that these large faults or *fracture zones* connect two spreading centers (divergent plate boundaries) or, less commonly, trenches (convergent plate boundaries). Most transform faults are found on the ocean floor. They commonly offset the active spreading ridges, producing zig-zag plate margins, and are generally defined by shallow earthquakes. However, a few occur on land, for example the San Andreas fault zone in California. This transform fault connects the East Pacific Rise, a divergent boundary to the south, with the South Gorda -- Juan de Fuca -- Explorer Ridge, another divergent boundary to the north.

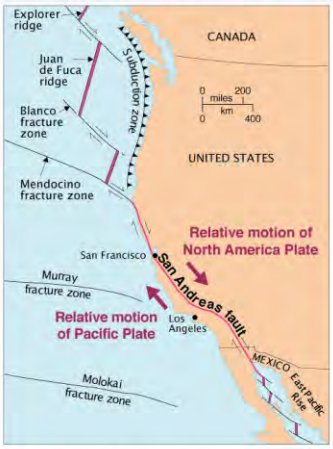

The Blanco, Mendocino, Murray, and Molokai fracture zones are some of the many fracture zones (transform faults) that scar the ocean floor and offset ridges (see text). The San Andreas is one of the few transform faults exposed on land.

The San Andreas fault zone, which is about 1,300 km long and in places tens of kilometers wide, slices through two thirds of the length of California. Along it, the Pacific Plate has been grinding horizontally past the North American Plate for 10 million years, at an average rate of about 5 cm/yr. Land on the west side of the fault zone (on the Pacific Plate) is moving in a northwesterly direction relative to the land on the east side of the fault zone (on the North American Plate).


San Andreas fault [52 k]

Oceanic fracture zones are ocean-floor valleys that horizontally offset spreading ridges; some of these zones are hundreds to thousands of kilometers long and as much as 8 km deep. Examples of these large scars include the Clarion, Molokai, and Pioneer fracture zones in the Northeast Pacific off the coast of California and Mexico. These zones are presently inactive, but the offsets of the patterns of magnetic striping provide evidence of their previous transform-fault activity.

Plate-boundary zones

Not all plate boundaries are as simple as the main types discussed above. In some regions, the boundaries are not well defined because the plate-movement deformation occurring there extends over a broad belt (called a *plate-boundary zone*). One of these zones marks the Mediterranean-Alpine region between the Eurasian and African Plates, within which several smaller fragments of plates *(microplates)* have been recognized. Because plate-boundary zones involve at least two large plates and one or more microplates caught up between them, they tend to have complicated geological structures and earthquake patterns.

Rates of motion

We can measure how fast tectonic plates are moving today, but how do scientists know what the rates of plate movement have been over geologic time? The oceans hold one of the key pieces to the puzzle. Because the ocean-floor magnetic striping records the flip-flops in the Earth's magnetic field, scientists, knowing the approximate duration of the reversal, can calculate the average rate of plate movement during a given time span. These average rates of plate separations can range widely. The Arctic Ridge has the slowest rate (less than 2.5 cm/yr), and the East Pacific Rise near Easter Island, in the South Pacific about 3,400 km west of Chile, has the fastest rate (more than 15 cm/yr).


Easter Island monolith [80 k]

Evidence of past rates of plate movement also can be obtained from geologic mapping studies. If a rock formation of known age -- with distinctive composition, structure, or fossils -- mapped on one side of a plate boundary can be matched with the same formation on the other side of the boundary, then measuring the distance that the formation has been offset can give an estimate of the average rate of plate motion. This simple but effective technique has been used to determine the rates of plate motion at divergent boundaries, for example the Mid-Atlantic Ridge, and transform boundaries, such as the San Andreas Fault.


GPS Satellite and Ground Receiver [63 k]

Current plate movement can be tracked directly by means of ground-based or space-based *geodetic* measurements; *geodesy* is the science of the size and shape of the Earth. Ground-based measurements are taken with conventional but very precise ground-surveying techniques, using laser-electronic instruments. However, because plate motions are global in scale, they are best measured by satellite-based methods. The late 1970s witnessed the rapid growth of *space geodesy*, a term applied to space-based techniques for taking precise, repeated measurements of carefully chosen points on the Earth's surface separated by hundreds to thousands of kilometers. The three most commonly used space-geodetic techniques -- very long baseline interferometry (VLBI), satellite laser ranging (SLR), and the Global Positioning System (GPS) -- are based on technologies developed for military and aerospace research, notably radio astronomy and satellite tracking.

Among the three techniques, to date the GPS has been the most useful for studying the Earth's crustal movements. Twenty-one satellites are currently in orbit 20,000 km above the Earth as part of the NavStar system of the U.S. Department of Defense. These satellites continuously transmit radio signals back to Earth. To determine its precise position on Earth (longitude, latitude, elevation), each GPS ground site must simultaneously receive signals from at least four satellites, recording the exact time and location of each satellite when its signal was received. By repeatedly measuring distances between specific points, geologists can determine if there has been active movement along faults or between plates. The separations between GPS sites are already being measured regularly around the Pacific basin. By monitoring the interaction between the Pacific Plate and the surrounding, largely continental plates, scientists hope to learn more about the events building up to earthquakes and volcanic eruptions in the circum-Pacific Ring of Fire. Space-geodetic data have already confirmed that the rates and direction of plate movement, averaged over several years, compare well with rates and direction of plate movement averaged over millions of years.

USGS

"Hotspots": Mantle thermal plumes

The vast majority of earthquakes and volcanic eruptions occur near plate boundaries, but there are some exceptions. For example, the Hawaiian Islands, which are entirely of volcanic origin, have formed in the middle of the Pacific Ocean more than 3,200 km from the nearest plate boundary. How do the Hawaiian Islands and other volcanoes that form in the interior of plates fit into the plate-tectonics picture?

Space Shuttle photograph of the Hawaiian Islands, the southernmost part of the long volcanic trail of the "Hawaiian hotspot" (see text). Kauai is in the lower right corner (edge) and the Big Island of Hawaii in the upper left corner. Note the curvature of the Earth (top edge). (Photograph courtesy of NASA.)

In 1963, J. Tuzo Wilson, the Canadian geophysicist who discovered transform faults, came up with an ingenious idea that became known as the "hotspot" theory. Wilson noted that in certain locations around the world, such as Hawaii, volcanism has been active for very long periods of time. This could only happen, he reasoned, if relatively small, long-lasting, and exceptionally hot regions -- called *hotspots* -- existed below the plates that would provide localized sources of high heat energy *(thermal plumes)* to sustain volcanism. Specifically, Wilson hypothesized that the distinctive linear shape of the Hawaiian Island-Emperor Seamounts chain resulted from the Pacific Plate moving over a deep, stationary hotspot in the mantle, located beneath the present-day position of the Island of Hawaii. Heat from this hotspot produced a persistent source of magma by partly melting the overriding Pacific Plate. The magma, which is lighter than the surrounding solid rock, then rises through the mantle and crust to erupt onto the seafloor, forming an active seamount. Over time, countless eruptions cause the seamount to grow until it finally emerges above sea level to form an island volcano. Wilson suggested that continuing plate movement eventually carries the island beyond the hotspot, cutting it off from the magma source, and volcanism ceases. As one island volcano becomes extinct, another develops over the hotspot, and the cycle is repeated. This process of volcano growth and death, over many millions of years, has left a long trail of volcanic islands and seamounts across the Pacific Ocean floor.

According to Wilson's hotspot theory, the volcanoes of the Hawaiian chain should get progressively older and become more eroded the farther they travel beyond the hotspot. The oldest volcanic rocks on Kauai, the northwesternmost inhabited Hawaiian island, are about 5.5 million years old and are deeply eroded. By comparison, on the "Big Island" of Hawaii -- southeasternmost in the chain and presumably still positioned over the hotspot -- the oldest exposed rocks are less than 0.7 million years old and new volcanic rock is continually being formed.

Above: *Artist's conception of the movement of the Pacific Plate over the fixed Hawaiian "Hot Spot," illustrating the formation of the Hawaiian Ridge-Emperor Seamount Chain. (Modified from a drawing provided by Maurice Krafft, Centre de Volcanologie, France).* Below: *J. Tuzo Wilson's original diagram (slightly modified), published in 1963, to show his proposed origin of the Hawaiian Islands. (Reproduced with permission of the* Canadian Journal of Physics.*)*

The possibility that the Hawaiian Islands become younger to the southeast was suspected by the ancient Hawaiians, long before any scientific studies were done. During their voyages, sea-faring Hawaiians noticed the differences in erosion, soil formation, and vegetation and recognized that the islands to the northwest (Niihau and Kauai) were older than those to the southeast (Maui and Hawaii). This idea was handed down from generation to generation in the legends of Pele, the fiery Goddess of Volcanoes. Pele originally lived on Kauai. When her older sister Namakaokahai, the Goddess of the Sea, attacked her, Pele fled to the Island of Oahu. When she was forced by Namakaokahai to flee again, Pele moved southeast to Maui and finally to Hawaii, where she now lives in the Halemaumau Crater at the summit of Kilauea Volcano. The mythical flight of Pele from Kauai to Hawaii, which alludes to the eternal struggle between the growth of volcanic islands from eruptions and their later erosion by ocean waves, is consistent with geologic evidence obtained centuries later that clearly shows the islands becoming younger from northwest to southeast.

Prominent world hotspots [54 k]

Although Hawaii is perhaps the best known hotspot, others are thought to exist beneath the oceans and continents. More than a hundred hotspots beneath the Earth's crust have been active during the past 10 million years. Most of these are located under plate interiors (for example, the African Plate), but some occur near diverging plate boundaries. Some are concentrated near the mid-oceanic ridge system, such as beneath Iceland, the Azores, and the Galapagos Islands.

A few hotspots are thought to exist below the North American Plate. Perhaps the best known is the hotspot presumed to exist under the continental crust in the region of Yellowstone National Park in northwestern Wyoming. Here are several *calderas* (large craters formed by the ground collapse accompanying explosive volcanism) that were produced by three gigantic eruptions during the past two million years, the most recent of which occurred about 600,000 years ago. Ash deposits from these powerful eruptions have been mapped as far away as Iowa, Missouri, Texas, and even northern Mexico. The thermal energy of the presumed Yellowstone hotspot fuels more than 10,000 hot pools and springs, geysers (like Old Faithful), and bubbling *mudpots* (pools of boiling mud). A large body of magma, capped by a *hydrothermal system* (a zone of pressurized steam and hot water), still exists beneath the caldera. Recent surveys demonstrate that parts of the Yellowstone region rise and fall by as much as 1 cm each year, indicating the area is still geologically restless. However, these measurable ground movements, which most likely reflect hydrothermal pressure changes, do not necessarily signal renewed volcanic activity in the area.

Authors' Note: Since this booklet's publication in 1996, vigorous scientific debate has ensued regarding volcanism at "hotspots." New studies suggest that hotspots are neither deep phenomena nor "fixed" in position over geologic time, as assumed in the popular plume model. See http://www.mantleplumes.org/."

Mauna Loa Volcano [36 k]

USGS

Some unanswered questions

The tectonic plates do not randomly drift or wander about the Earth's surface; they are driven by definite yet unseen forces. Although scientists can neither precisely describe nor fully understand the forces, most believe that the relatively shallow forces driving the lithospheric plates are coupled with forces originating much deeper in the Earth.

What drives the plates?

From seismic and other geophysical evidence and laboratory experiments, scientists generally agree with Harry Hess' theory that the plate-driving force is the slow movement of hot, softened mantle that lies below the rigid plates. This idea was first considered in the 1930s by Arthur Holmes, the English geologist who later influenced Harry Hess' thinking about seafloor spreading. Holmes speculated that the circular motion of the mantle carried the continents along in much the same way as a conveyor belt. However, at the time that Wegener proposed his theory of continental drift, most scientists still believed the Earth was a solid, motionless body. We now know better. As J. Tuzo Wilson eloquently stated in 1968, "The earth, instead of appearing as an inert statue, is a living, mobile thing." Both the Earth's surface **and** its interior are in motion. Below the lithospheric plates, at some depth the mantle is partially molten and can flow, albeit slowly, in response to steady forces applied for long periods of time. Just as a solid metal like steel, when exposed to heat and pressure, can be softened and take different shapes, so too can solid rock in the mantle when subjected to heat and pressure in the Earth's interior over millions of years.

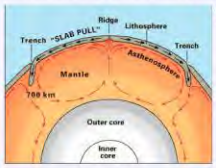

Left: *Conceptual drawing of assumed convection cells in the mantle (see text). Below a depth of about 700 km, the descending slab begins to soften and flow, losing its form.* Below: *Sketch showing convection cells commonly seen in boiling water or soup. This analogy, however, does not take into account the huge differences in the size and the flow rates of these cells.*

The mobile rock beneath the rigid plates is believed to be moving in a circular manner somewhat like a pot of thick soup when heated to boiling. The heated soup rises to the surface, spreads and begins to cool, and then sinks back to the bottom of the pot where it is reheated and rises again. This cycle is repeated over and over to generate what scientists call a *convection cell* or *convective flow*. While convective flow can be observed easily in a pot of boiling soup, the idea of such a process stirring up the Earth's interior is much more difficult to grasp. While we know that convective motion in the Earth is much, much slower than that of boiling soup, many unanswered questions remain: How many convection cells exist? Where and how do they originate? What is their structure?

Convection cannot take place without a source of heat. Heat within the Earth comes from two main sources: *radioactive decay* and *residual heat*. Radioactive decay, a spontaneous process that is the basis of "isotopic clocks" used to date rocks, involves the loss of particles from the nucleus of an isotope (the *parent*) to form an isotope of a new element (the *daughter*). The radioactive decay of naturally occurring chemical elements -- most notably uranium, thorium, and potassium -- releases energy in the form of heat, which slowly migrates toward the Earth's surface. Residual heat is gravitational energy left over from the formation of the Earth -- 4.6 billion years ago -- by the "falling together" and compression of cosmic debris. How and why the escape of interior heat becomes concentrated in certain regions to form convection cells remains a mystery.

Until the 1990s, prevailing explanations about what drives plate tectonics have emphasized mantle convection, and most earth scientists believed that seafloor spreading was the primary mechanism. Cold, denser material convects downward and hotter, lighter material rises because of gravity; this movement of material is an essential part of convection. In addition to the convective forces, some geologists argue that the intrusion of magma into the spreading ridge provides an additional force (called "ridge push") to propel and maintain plate movement. Thus, subduction processes are considered to be secondary, a logical but largely passive consequence of seafloor spreading. In recent years however, the tide has turned. Most scientists now favor the notion that forces associated with subduction are more important than seafloor spreading. Professor Seiya Uyeda (Tokai University, Japan), a world-renowned expert in plate tectonics, concluded in his keynote address at a major scientific conference on subduction processes in June 1994 that "subduction . . . plays a more fundamental role than seafloor spreading in shaping the earth's surface features" and "running the plate tectonic machinery." The gravity-controlled sinking of a cold, denser oceanic slab into the subduction zone (called "slab pull") -- dragging the rest of the plate along with it -- is now considered to be the driving force of plate tectonics.

We know that forces at work deep within the Earth's interior drive plate motion, but we may never fully understand the details. At present, none of the proposed mechanisms can explain all the facets of plate movement; because these forces are buried so deeply, no mechanism can be tested directly and proven beyond reasonable doubt. The fact that the tectonic plates have moved in the past and are still moving today is beyond dispute, but the details of why and how they move will continue to challenge scientists far into the future.

Extraterrestrial plate tectonics?

The Earth may be unique in our solar system because it appears to be the only planet that is still volcanically and tectonically active; our planet therefore remains very much alive, while the others apparently have long ceased activity. Volcanic activity requires a source of internal heat, and it is the escape of this heat that fuels plate tectonics. While volcanism played a major role in the early history of Mars, the Moon, and probably Mercury, their small sizes relative to Earth resulted in the loss of internal heat at a much faster rate. They have been inactive globes for the last billion years or so.

Venus may still be active, though the evidence is questionable. In 1979, the Pioneer-Venus spacecraft measured a high amount of sulfur in the upper atmosphere of the planet; the sulfur amount then decreased over the next few years. This observation suggested that the high sulfur concentration measured in 1979 may have resulted from a catastrophic event, perhaps a volcanic eruption. Beginning in 1990, radar images made by the Magellan spacecraft revealed dramatic volcanic features and long, deep valleys similar in size and shape to oceanic trenches on Earth.

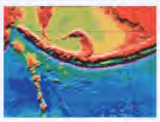

Left: *A computer-generated image of the Aleutian Trench (in violet); "warm" colors (yellow to red) indicate topographic highs, and "cool" colors (green to blue) represent lower elevations.* Below: *The topography of Artemis Corona, a trench-like feature on Venus, shown at the same vertical and horizontal scale as the Aleutian Trench. (Imagery courtesy of David T. Sandwell, Scripps Institution of Oceanography.)*

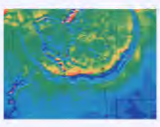

The Voyager spacecraft discovered several volcanic plumes rising many hundreds of kilometers above the surface of Io, one of the moons of Jupiter and about the size of our Moon. Scientists speculate that large pools of liquid sulfur may exist on Io, possibly heated by tidal forces resulting from gravitational attraction between Io and Jupiter. The thermal energy generated by such tidal forces may be enough to produce convection in Io's interior, although no one has clearly recognized any surface feature that may have formed from such convection.

The surface of Ganymede, another moon of Jupiter and about the size of Mercury, is broken into many plate-like blocks, with long narrow depressions between some of them. Whether these surface features represent ancient "fossil" plate tectonics, or are actively forming, remains to be answered. Crucial to determining whether plate tectonics is occurring on Ganymede is the search for evidence of a deep ocean beneath its icy surface. Such a body of water, if it exists, might contribute to internal convection.

The surface of Ganymede, another moon of Jupiter and about the size of Mercury, is broken into many plate-like blocks, with long narrow depressions between some of them. Whether these surface features represent ancient "fossil" plate tectonics, or are actively forming, remains to be answered. Crucial to determining whether plate tectonics is occurring on Ganymede is the search for evidence of a deep ocean beneath its icy surface. Such a body of water, if it exists, might contribute to internal convection.

A volcanic plume of sulfur dioxide (SO_2) gas rising about 150 km above the surface of Io. This computer-enhanced image was captured "live" by the Voyager 2 spacecraft on 4 March 1979. (Imagery courtesy of NASA.)

The rate of heat loss is critical to a planet's tectonic activity. Size is one determining factor: larger bodies lose heat more slowly and will therefore remain active longer. Another factor is composition, which influences the ability of a body to convect. For example, a liquid interior, such as may exist within Ganymede, is more likely to convect and drive plate tectonics than the "stony" interiors of the Moon, Mercury, Venus, and Mars. The amount of radioactive elements present in the planet's composition also affects the likelihood of internal convection, because the decay of these elements produces heat. Apparently, the interiors of the Moon, Mercury, and Mars are either too rigid or have lost too much of their internal heat to convect and drive plate tectonics.

Eventually the Earth, too, will lose so much heat that its interior will stop convecting. Earthquake and volcanic activity will then cease. No new mountains will form, and the geologic cycle of mountain building, erosion, sedimentation, and soil formation will be disrupted and also will cease. Exactly how a cooled-down Earth will change surface conditions -- and whether our planet will still be habitable -- nobody knows. Fortunately, these changes will not happen for many billions of years!

USGS

Plate tectonics and people

Over geologic time, plate movements in concert with other geologic processes, such as glacial and stream erosion, have created some of nature's most magnificent scenery. The Himalayas, the Swiss Alps, and the Andes are some spectacular examples. Yet violent earthquakes related to plate tectonics have caused terrible catastrophes -- such as the magnitude-7.7 earthquake that struck the Chinese province of Hebei in 1976 and killed as many as 800,000 people.

Natural hazards

Most earthquakes and volcanic eruptions do not strike randomly but occur in specific areas, such as along plate boundaries. One such area is the circum-Pacific *Ring of Fire*, where the Pacific Plate meets many surrounding plates. The Ring of Fire is the most seismically and volcanically active zone in the world.

Earthquakes

Because many major population centers are located near active fault zones, such as the San Andreas, millions of people have suffered personal and economic losses as a result of destructive earthquakes, and even more have experienced earthquake motions. Not surprisingly, some people believe that, when the "Big One" hits, California will suddenly "break off" and "fall into the Pacific," or that the Earth will "open up" along the fault and "swallow" people, cars, and houses. Such beliefs have no scientific basis whatsoever. Although ground slippage commonly takes place in a large earthquake, the Earth will not open up. Nor will California fall into the sea, because the fault zone only extends about 15 km deep, which is only about a quarter of the thickness of the continental crust. Furthermore, California is composed of continental crust, whose relatively low density keeps it riding high, like an iceberg above the ocean.

Aerial view, looking north toward San Francisco, of Crystal Springs Reservoir, which follows the San Andreas fault zone. (Photograph by Robert E. Wallace, USGS.)

Like all transform plate boundaries, the San Andreas is a *strike-slip* fault, movement along which is dominantly horizontal. Specifically, the San Andreas fault zone separates the Pacific and North American Plates, which are slowly grinding past each other in a roughly north-south direction. The Pacific Plate (western side of the fault) is moving horizontally in a northerly direction relative to the North American Plate (eastern side of the fault). Evidence of the sideways shift of these two landmasses can be found all along the fault zone, as seen from the differences in topography, geologic structures, and, sometimes, vegetation of the terrain from one side of the fault to the other. For example, the San Andreas runs directly along Crystal Springs Reservoir on the San Francisco Peninsula. Topographically, this reservoir fills a long, straight, narrow valley that was formed by erosion of the easily erodible rocks mashed within the fault zone.

Movement along the San Andreas can occur either in sudden jolts or in a slow, steady motion called *creep*. Fault segments that are actively creeping experience many small to moderate earthquakes that cause little or no damage. These creeping segments are separated by segments of infrequent earthquake activity (called *seismic gaps*), areas that are stuck or locked in place within the fault zone. Locked segments of the fault store a tremendous amount of energy that can build up for decades, or even centuries, before being unleashed in devastating earthquakes. For example, the Great San Francisco Earthquake (8.3-magnitude) in 1906 ruptured along a previously locked 430 km-long segment of the San Andreas, extending from Cape Men-docino south to San Juan Bautista.

Map of the San Andreas and a few of the other faults in California, segments of which display different behavior: locked or creeping (see text). (Simplified from USGS Professional Paper 1515.)

The stresses that accumulate along a locked segment of the fault and the sudden release can be visualized by bending a stick until it breaks. The stick will bend fairly easily, up to a certain point, until the stress becomes too great and it snaps. The vibrations felt when the stick breaks represent the sudden release of the stored-up energy. Similarly, the seismic vibrations produced when the ground suddenly ruptures radiate out through the Earth's interior from the rupture point, called the *earthquake focus*. The geographic point directly above the focus is called the *earthquake epicenter*. In a major earthquake, the energy released can cause damage hundreds to thousands of kilometers away from the epicenter.

A dramatic photograph of horses killed by falling debris during the Great San Francisco Earthquake of 1906, when a locked segment of the San Andreas fault suddenly lurched, causing a devastating magnitude-8.3 earthquake. (Photograph by Edith Irvine, courtesy of Brigham Young University Library), Provo, Utah.)

The magnitude-7.1 Loma Prieta earthquake of October 1989 occurred along a segment of the San Andreas Fault which had been locked since the great 1906 San Francisco earthquake. Even though the earthquake's focus (approximately 80 km south of San Francisco) was centered in a sparsely populated part of the Santa Cruz Mountains, the earthquake still caused 62 deaths and nearly $6 billion in damage. Following the Loma Prieta earthquake, the fault remains locked from Pt. Arena, where it enters California from the ocean, south through San Francisco and the peninsula west of San Francisco Bay, thus posing the threat of a potential destructive earthquake occurring in a much more densely populated area.

The lesser known Hayward Fault running east of San Francisco Bay, however, may pose a potential threat as great as, or perhaps even greater than, the San Andreas. From the televised scenes of the damage caused by the 7.2-magnitude earthquake that struck Kobe, Japan, on 16 January 1995, Bay Area residents saw the possible devastation that could occur if a comparable size earthquake were to strike along the Hayward Fault. This is because the Hayward and the Nojima fault that produced the Kobe earthquake are quite similar in several ways. Not only are they of the same type (strike-slip), they are also about the same length (60p;80 km) and both cut through densely populated urban areas, with many buildings, freeways, and other structures built on unstable bay landfill.

On 17 January 1994, one of the costliest natural disasters in United States history struck southern California. A magnitude-6.6 earthquake hit near Northridge, a community located in the populous San Fernando Valley within the City of Los Angeles, California. This disaster, which killed more than 60 people, caused an estimated $30 billion in damage, nearly five times that resulting from the Loma Prieta earthquake. The Northridge earthquake did not directly involve movement along one of the strands of the San Andreas Fault system. It instead occurred along the Santa Monica Mountains Thrust Fault, one of several smaller, concealed faults (called *blind thrust faults*) south of the San Andreas Fault zone where it bends to the east, roughly paralleling the Transverse Mountain Range. With a *thrust fault*, whose plane is inclined to the Earth's surface, one side moves upward over the other. Movement along a blind thrust fault does not break the ground surface, thus making it difficult or impossible to map these hidden but potentially dangerous faults. Although scientists have found measurable uplift at several places in the Transverse Range, they have not found any conclusive evidence of ground rupture from the 1994 Northridge earthquake. Similar earthquakes struck the region in 1971 and 1987; the San Fernando earthquake (1971) caused substantial damage, including the collapse of a hospital and several freeway overpasses.

Not all fault movement is as violent and destructive. Near the city of Hollister in central California, the Calaveras Fault bends toward the San Andreas. Here, the Calaveras fault creeps at a slow, steady pace, posing little danger. Much of the Calaveras fault creeps at an average rate of 5 to 6 mm/yr. On average, Hollister has some 20,000 earthquakes a year, most of which are too small to be felt by residents. It is rare for an area undergoing creep to experience an earthquake with a magnitude greater than 6.0 because stress is continually being relieved and, therefore, does not accumulate. Fault-creep movement generally is non-threatening, resulting only in gradual offset of roads, fences, sidewalks, pipelines, and other structures that cross the fault. However, the persistence of fault creep does pose a costly nuisance in terms of maintenance and repair.

Mid-plate earthquakes -- those occurring in the interiors of plates -- are much less frequent than those along plate boundaries and more difficult to explain. Earthquakes along the Atlantic seaboard of the United States are most likely related in some way to the westward movement of the North American Plate away from the Mid-Atlantic Ridge, a continuing process begun with the break-up of Pangaea. However, the causes of these infrequent earthquakes are still not understood.

East Coast earthquakes, such as the one that struck Charleston, South Carolina, in 1886 are felt over a much larger area than earthquakes occurring on the West Coast, because the eastern half of the country is mainly composed of older rock that has not been fractured and cracked by frequent earthquake activity in the recent geologic past. Rock that is highly fractured and crushed absorbs more seismic energy than rock that is less fractured. The Charleston earthquake, with an estimated magnitude of about 7.0, was felt as far away as Chicago, more than 1,300 km to the northwest, whereas the 7.1-magnitude Loma Prieta earthquakes was felt no farther than Los Angeles, about 500 km south. The most widely felt earthquakes ever to strike the United States were centered near the town of New Madrid, Missouri, in 1811 and 1812. Three earthquakes, felt as far away as Washington D.C., were each estimated to be above 8.0 in magnitude. Most of us do not associate earthquakes with New York City, but beneath Manhattan is a network of intersecting faults, a few of which are capable of causing earthquakes. The most recent earthquake to strike New York City occurred in 1985 and measured 4.0 in magnitude, and a pair of earthquakes (magnitude 4.0 and 4.5) shook Reading, Pennsylvania, in January 1994 causing minor damage.


Left: *Creeping along the Calaveras fault has bent the retaining wall and offset the sidewalk along 5th Street in Hollister, California (about 75 km south-southeast of San Jose).* Right: *Close-up of the offset of the curb. (Photographs by W. Jacquelyne Kious.)*

We know in general how most earthquakes occur, but can we predict when they will strike? This question has challenged and frustrated scientists studying likely precursors to moderate and large earthquakes. Since the early 1980s, geologists and seismologists have been intensively studying a segment of the San Andreas near the small town of Parkfield, located about halfway between San Francisco and Los Angeles, to try to detect the physical and chemical changes that might take place -- both above and below ground -- before an earthquake strikes. The USGS and State and local agencies have blanketed Parkfield and the surrounding countryside with seismographs, creep meters, stress meters, and other ground-motion measurement devices.


Ground-motion measurement system **[40 k]**

The Parkfield segment has experienced earthquakes measuring magnitude 6.0 about every 22 years on average since 1881. During the most recent two earthquakes (1934, 1966), the same section of the fault slipped and the amount of slippage was about the same. In 1983, this evidence, in addition to the earlier recorded history of earthquake activity, led the USGS to predict that there was a 95 percent chance of a 6.0 earthquake striking Parkfield before 1993. But the anticipated earthquake of magnitude 6.0 or greater did not materialize. The Parkfield experiment is continuing, and its primary goals remain unchanged: to issue a short-term prediction; to monitor and analyze geophysical and geochemical effects before, during, and after the anticipated earthquake; and to develop effective communications between scientists, emergency-management officials, and the public in responding to earthquake hazards.

While scientists are studying and identifying possible precursors leading to the next Parkfield earthquake, they also are looking at these same precursors to see if they may be occurring along other segments of the fault. Studies of past earthquakes, together with data and experience gained from the Parkfield experiment, have been used by geoscientists to estimate the probabilities of major earthquakes occurring along the entire San Andreas Fault system. In 1988, the USGS identified six segments of the San Andreas as most likely to be hit by a magnitude 6.5 or larger earthquake within the next thirty years (1988-2018). The Loma Prieta earthquake in 1989 occurred along one of these six segments. The Parkfield experiment and other studies carried out by the USGS as part of the National Earthquake Hazards Reduction Program have led to an increased official and public awareness of the inevitability of future earthquake activity in California. Consequently, residents and State and local officials have become more diligent in planning and preparing for the next big earthquake.

Volcanic eruptions

As with earthquakes, volcanic activity is linked to plate-tectonic processes. Most of the world's active above-sea volcanoes are located near convergent plate boundaries where subduction is occurring, particularly around the Pacific basin. However, much more volcanism -- producing about three quarters of all lava erupted on Earth -- takes place unseen beneath the ocean, mostly along the oceanic spreading centers, such as the Mid-Atlantic Ridge and the East Pacific Rise.

Subduction-zone volcanoes like Mount St. Helens (in Washington State) and Mount Pinatubo (Luzon, Philippines), are called *composite cones* and typically erupt with explosive force, because the magma is too stiff to allow easy escape of volcanic gases. As a consequence, tremendous internal pressures mount as the trapped gases expand during ascent, before the pent-up pressure is suddenly released in a violent eruption. Such an explosive process can be compared to putting your thumb over an opened bottle of a carbonated drink, shaking it vigorously, and then quickly removing the thumb. The shaking action separates the gases from the liquid to form bubbles, increasing the internal pressure. Quick release of the thumb allows the gases and liquid to gush out with explosive speed and force.

In 1991, two volcanoes on the western edge of the Philippine Plate produced major eruptions. On June 15, Mount Pinatubo spewed ash 40 km into the air and produced huge ash flows (also called *pyroclastic flows*) and mudflows that devastated a large area around the volcano. Pinatubo, located 90 km from Manila, had been dormant for 600 years before the 1991 eruption, which ranks as one of the largest eruptions in this century. Also in 1991, Japan's Unzen Volcano, located on the Island of Kyushu about 40 km east of Nagasaki, awakened from its 200-year slumber to produce a new lava dome at its summit. Beginning in June, repeated collapses of this active dome generated destructive ash flows that swept down its slopes at speeds as high as 200 km per hour. Unzen is one of more than 75 active volcanoes in Japan; its eruption in 1792 killed more than 15,000 people--the worst volcanic disaster in the country's history.


Mount Pinatubo plume **[85 k]**

While the Unzen eruptions have caused deaths and considerable local damage, the impact of the June 1991 eruption of Mount Pinatubo was global. Slightly cooler than usual temperatures recorded worldwide and the brilliant sunsets and sunrises have been attributed to this eruption that sent fine ash and gases high into the stratosphere, forming a large volcanic cloud that drifted around the world. The sulfur dioxide (SO_2) in this cloud -- about 22 million tons -- combined with water to form droplets of sulfuric acid, blocking some of the sunlight from reaching the Earth and thereby cooling temperatures in some regions by as much as 0.5 °C. An eruption the size of Mount Pinatubo could affect the weather for a few years. A similar phenomenon occurred in April of 1815 with the cataclysmic eruption of Tambora Volcano in Indonesia, the most powerful eruption in recorded history. Tambora's volcanic cloud lowered global temperatures by as much as 3 °C. Even a year after the eruption, most of the northern hemisphere experienced sharply cooler temperatures during the summer months. In part of Europe and in North America, 1816 was known as "the year without a summer."

Apart from possibly affecting climate, volcanic clouds from explosive eruptions also pose a hazard to aviation safety. During the past two decades, more than 60 airplanes, mostly commercial jetliners, have been damaged by in-flight encounters with volcanic ash. Some of these encounters have resulted in the power loss of all engines, necessitating emergency landings. Luckily, to date no crashes have happened be-cause of jet aircraft flying into volcanic ash.

Diagram showing the lower two layers of the atmosphere: the troposphere and the stratosphere. The tropopause--the boundary between these two layers--varies in altitude from 8 to 18 km (dashed white lines), depending on Earth latitude and season of the year. The summit of Mt. Everest (inset photograph) and the altitudes commonly flown by commercial jetliners are given for reference. (Photograph by David G. Howell, USGS.)

Since the year A.D. 1600, nearly 300,000 people have been killed by volcanic eruptions. Most deaths were caused by *pyroclastic flows* and *mudflows*, deadly hazards which often accompany explosive eruptions of subduction-zone volcanoes. Pyroclastic flows, also called *nuées ardentes* ("glowing clouds" in French), are fast-moving, avalanche-like, ground-hugging incandescent mixtures of hot volcanic debris, ash, and gases that can travel at speeds in excess of 150 km per hour. Approximately 30,000 people were killed by pyroclastic flows during the 1902 eruption of Mont Pelée on the Island of Martinique in the Caribbean. In March-April 1982, three explosive eruptions of El Chichón Volcano in the State of Chiapas, southeastern Mexico, caused the worst volcanic disaster in that country's history. Villages within 8 km of the volcano were destroyed by pyroclastic flows, killing more than 2,000 people.

Mudflows (also called *debris flows* or *lahars*, an Indonesian term for volcanic mudflows) are mixtures of volcanic debris and water. The water usually comes from two sources: rainfall or the melting of snow and ice by hot volcanic debris. Depending on the proportion of water to volcanic material, mudflows can range from soupy floods to thick flows that have the consistency of wet cement. As mudflows sweep down the steep sides of composite volcanoes, they have the strength and speed to flatten or bury everything in their paths. Hot ash and pyroclastic flows from the eruption of the Nevado del Ruiz Volcano in Colombia, South America, melted snow and ice atop the 5,390-m-high Andean peak; the ensuing mudflows buried the city of Armero, killing 25,000 people.


Armero, Colombia [88 k]

Eruptions of Hawaiian and most other mid-plate volcanoes differ greatly from those of composite cones. Mauna Loa and Kilauea, on the island of Hawaii, are known as *shield volcanoes*, because they resemble the wide, rounded shape of an ancient warrior's shield. Shield volcanoes tend to erupt non-explosively, mainly pouring out huge volumes of fluid lava. Hawaiian-type eruptions are rarely life threatening because the lava advances slowly enough to allow safe evacuation of people, but large lava flows can cause considerable economic loss by destroying property and agricultural lands. For example, lava from the ongoing eruption of Kilauea, which began in January 1983, has destroyed more than 200 structures, buried kilometers of highways, and disrupted the daily lives of local residents. Because Hawaiian volcanoes erupt frequently and pose little danger to humans, they provide an ideal natural laboratory to safely study volcanic phenomena at close range. The USGS Hawaiian Volcano Observatory, on the rim of Kilauea, was among the world's first modern volcano observatories, established early in this century.


Wahaula Visitor Center, Hawaii [40 k]

In recorded history, explosive eruptions at subduction-zone (convergent-boundary) volcanoes have posed the greatest hazard to civilizations. Yet scientists have estimated that about three quarters of the material erupted on Earth each year originates at spreading mid-ocean ridges. However, no deep submarine eruption has yet been observed "live" by scientists. Because the great water depths preclude easy observation, few detailed studies have been made of the numerous possible eruption sites along the tremendous length (50,000 km) of the global mid-oceanic ridge system. Recently however, repeated surveys of specific sites along the Juan de Fuca Ridge, off the coast of the Oregon and Washington, have mapped deposits of fresh lava, which must have been erupted sometime between the surveys. In June 1993, seismic signals typically associated with submarine eruptions -- called *T-phases* -- were detected along part of the spreading Juan de Fuca Ridge and interpreted as being caused by eruptive activity.

Iceland, where the Mid-Atlantic Ridge is exposed on land, is a different story. It is easy to see many Icelandic volcanoes erupt non-explosively from fissure vents, in similar fashion to typical Hawaiian eruptions; others, like Hekla Volcano, erupt explosively. (After Hekla's catastrophic eruption in 1104, it was thought in the Christian world to be the "Mouth to Hell.") The voluminous, but mostly non-explosive, eruption at Lakagigar (Laki), Iceland, in 1783, resulted in one of the world's worst volcanic disasters. About 9,000 people -- almost 20% of the country's population at the time -- died of starvation *after* the eruption, because their livestock had perished from grazing on grass contaminated by fluorine-rich gases emitted during this eight month-long eruption.

Tsunamis

Major earthquakes occurring along subduction zones are especially hazardous, because they can trigger tsunamis (from the Japanese word *tsunami* meaning "harbor wave") and pose a potential danger to coastal communities and islands that dot the Pacific. Tsunamis are often mistakenly called "tidal waves" when, in fact, they have nothing to do with tidal action. Rather, tsunamis are seismic sea waves caused by earthquakes, submarine landslides, and, infrequently, by eruptions of island volcanoes. During a major earthquake, the seafloor can move by several meters and an enormous amount of water is suddenly set into motion, sloshing back and forth for several hours. The result is a series of waves that race across the ocean at speeds of more than 800 km per hour, comparable to those of commercial jetliners. The energy and momentum of these transoceanic waves can take them thousands of kilometers from their origin before slamming into far-distant islands or coastal areas.

A giant wave engulfs the pier at Hilo, Hawaii, during the 1946 tsunami, which killed 159 people. The arrow points to a man who was swept away seconds later. (Retouched photograph courtesy of NOAA/EDIS.)

To someone on a ship in the open ocean, the passage of a tsunami wave would barely elevate the water surface. However, when it reaches shallower water near the coastline and "touches bottom," the tsunami wave increases in height, piling up into an enormous wall of water. As a tsunami approaches the shore, the water near shore commonly recedes for several minutes -- long enough for someone to be lured out to collect exposed sea shells, fish, etc. -- before suddenly rushing back toward land with frightening speed and height.

The 1883 eruption of Krakatau Volcano, located in the Sunda Straits between the islands of Sumatra and Java, Indonesia, provides an excellent example of an eruption-caused tsunami. A series of tsunamis washed away 165 coastal villages on Java and Sumatra, killing 36,000 people. The larger tsunamis were recorded by tide gauges as far away as the southern coast of the Arabian Peninsula-more than 7,000 km from Krakatau!

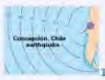

Travel times for tsunamis [55 k]

Because of past killer tsunamis, which have caused hundreds of deaths on the Island of Hawaii and elsewhere, the International Tsunami Information Center was created in 1965. This center issues tsunami warnings based on earthquake and wave-height information gathered from seismic and tide-gauge stations located around the Pacific Ocean basin and on Hawaii.

Natural resources

Many of the Earth's natural resources of energy, minerals, and soil are concentrated near past or present plate boundaries. The utilization of these readily available resources have sustained human civilizations, both now and in the past.

Fertile soils

Volcanoes can clearly cause much damage and destruction, but in the long term they also have benefited people. Over thousands to millions of years, the physical breakdown and chemical weathering of volcanic rocks have formed some of the most fertile soils on Earth. In tropical, rainy regions, such as the windward (northeastern) side of the Island of Hawaii, the formation of fertile soil and growth of lush vegetation following an eruption can be as fast as a few hundred years. Some of the earliest civilizations (for example, Greek, Etruscan, and Roman) settled on the rich, fertile volcanic soils in the Mediterranean-Aegean region. Some of the best rice-growing regions of Indonesia are in the shadow of active volcanoes. Similarly, many prime agricultural regions in the western United States have fertile soils wholly or largely of volcanic origin.

Ore deposits

Most of the metallic minerals mined in the world, such as copper, gold, silver, lead, and zinc, are associated with magmas found deep within the roots of extinct volcanoes located above subduction zones. Rising magma does not always reach the surface to erupt; instead it may slowly cool and harden beneath the volcano to form a wide variety of crystalline rocks (generally called *plutonic* or *granitic* rocks). Some of the best examples of such deep-seated granitic rocks, later exposed by erosion, are magnificently displayed in California's Yosemite National Park. Ore deposits commonly form around the magma bodies that feed volcanoes because there is a ready supply of heat, which convectively moves and circulates ore-bearing fluids. The metals, originally scattered in trace amounts in magma or surrounding solid rocks, become concentrated by circulating hot fluids and can be redeposited, under favorable temperature and pressure conditions, to form rich mineral veins.

The active volcanic vents along the spreading mid-ocean ridges create ideal environments for the circulation of fluids rich in minerals and for ore deposition. Water as hot as 380 °C gushes out of geothermal springs along the spreading centers. The water has been heated during circulation by contact with the hot volcanic rocks forming the ridge. Deep-sea hot springs containing an abundance of dark-colored ore minerals (sulfides) of iron, copper, zinc, nickel, and other metals are called "black smokers." On rare occasions, such deep-sea ore deposits are later exposed in remnants of ancient oceanic crust that have been scraped off and left ("beached") on top of continental crust during past subduction processes. The Troodos Massif on the Island of Cyprus is perhaps the best known example of such ancient oceanic crust. Cyprus was an important source of copper in the ancient world, and Romans called copper the "Cyprian metal"; the Latin word for copper is cyprium.

Fossil fuels

Oil and natural gas are the products of the deep burial and decomposition of accumulated organic material in geologic basins that flank mountain ranges formed by plate-tectonic processes. Heat and pressure at depth transform the decomposed organic material into tiny pockets of gas and liquid petroleum, which then migrate through the pore spaces and larger openings in the surrounding rocks and collect in reservoirs, generally within 5 km of the Earth's surface. Coal is also a product of accumulated decomposed plant debris, later buried and compacted beneath overlying sediments. Most coal originated as peat in ancient swamps created many millions of years ago, associated with the draining and flooding of landmasses caused by changes in sea level related to plate tectonics and other geologic processes. For example, the Appalachian coal deposits formed about 300 million years ago in a low-lying basin that was alternately flooded and drained.


Half Dome, Yosemite National Park [148 k]

Geothermal energy

Geothermal energy can be harnessed from the Earth's natural heat associated with active volcanoes or geologically young inactive volcanoes still giving off heat at depth. Steam from high-temperature geothermal fluids can be used to drive turbines and generate electrical power, while lower temperature fluids provide hot water for space-heating purposes, heat for greenhouses and industrial uses, and hot or warm springs at resort spas. For example, geothermal heat warms more than 70 percent of the homes in Iceland, and The Geysers geothermal field in Northern California produces enough electricity to meet the power demands of San Francisco. In addition to being an energy resource, some geo-thermal waters also contain sulfur, gold, silver, and mercury that can be recovered as a byproduct of energy production.


Geothermal powerplant, The Geysers [60 k]

A formidable challenge

As global population increases and more countries become industrialized, the world demand for mineral and energy resources will continue to grow. Because people have been using natural resources for millennia, most of the easily located mineral, fossil-fuel, and geothermal resources have already been tapped. By necessity, the world's focus has turned to the more remote and inaccessible regions of the world, such as the ocean floor, the polar continents, and the resources that lie deeper in the Earth's crust. Finding and developing such resources without damage to the environment will present a formidable challenge in the coming decades. An improved knowledge of the relationship between plate tectonics and natural resources is essential to meeting this challenge.

Farmer plowing a lush rice paddy in central Java, Indonesia; Sundoro Volcano looms in the background. The most highly prized rice-growing areas have fertile soils formed from the breakdown of young volcanic deposits. (Photograph by Robert I. Tilling, USGS.)

The long-term benefits of plate tectonics should serve as a constant reminder to us that the planet Earth occupies a unique niche in our solar system. Appreciation of the concept of plate tectonics and its consequences has reinforced the notion that the Earth is an integrated whole, not a random collection of isolated parts. The global effort to better understand this revolutionary concept has helped to unite the earth-sciences community and to underscore the linkages between the many different scientific disciplines. As we enter the 21st century, when the Earth's finite resources will be further strained by explosive population growth, earth scientists must strive to better understand our dynamic planet. We must become more resourceful in reaping the long-term benefits of plate tectonics, while coping with its short-term adverse impacts, such as earthquakes and volcanic eruptions.

81. Assignment 3, Module 17: Understanding Earthquakes: https://www.jishin.go.jp/main/pamphlet/brochures2014en/understanding_earthquakes.pdf

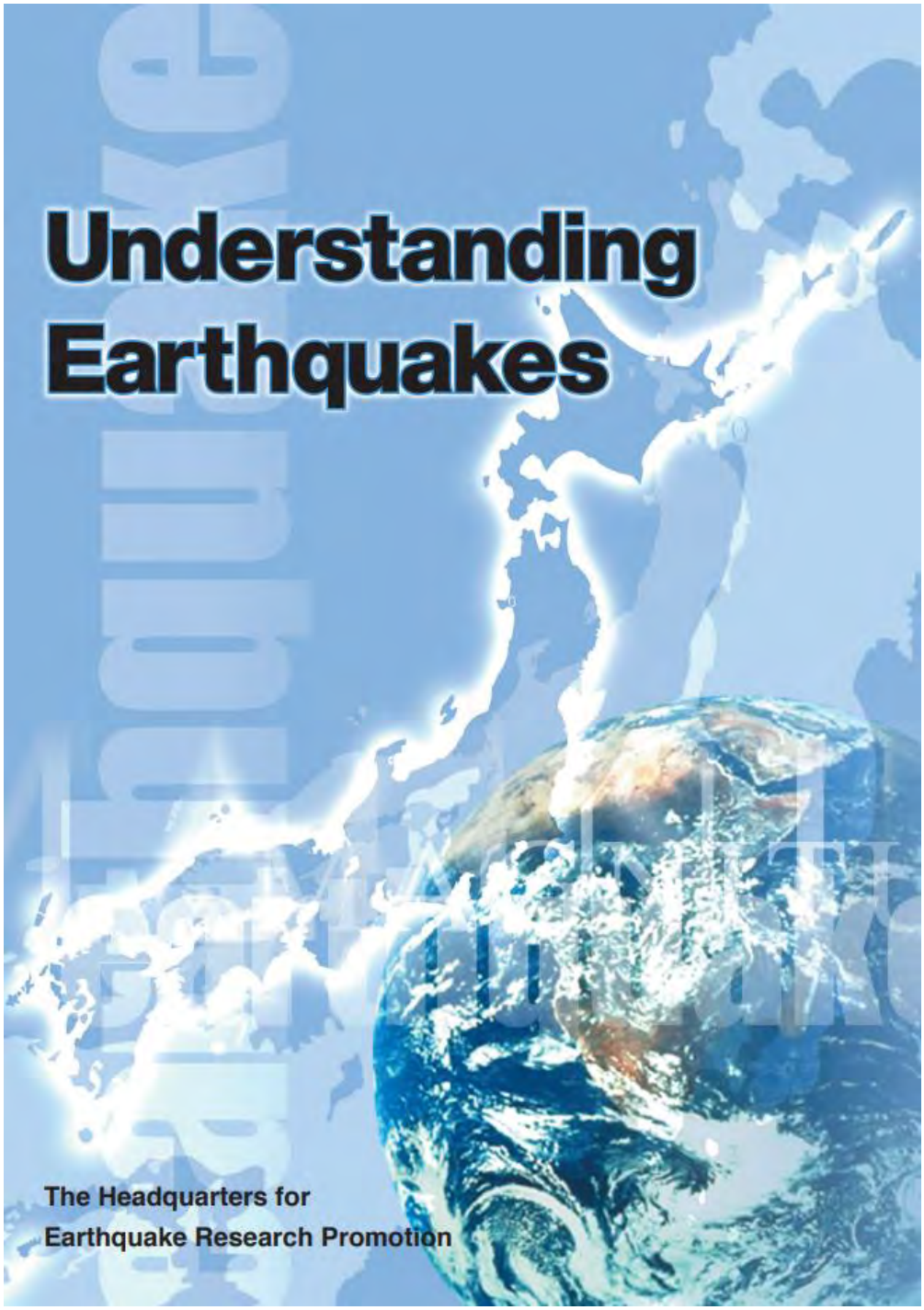

Introduction

This booklet is written to help people better understand earthquakes. In preparing this booklet a great deal of data and information has been provided by many institutions and researchers. We are extremely grateful to them.

Q & A

Supporting Section

Supplementary Material Section

Recent earthquakes in Japan and around the world

Understanding Earthquakes

The huge earthquake that occurred off Sumatra Island, Indonesia in 2004 caused an enormous tsunami. The tsunami caused tremendous damages to the countries facing the Indian Ocean. Large earthquakes like this that inflict serious damage occur repeatedly around the world. Living in Japan, one of the world's most earthquake-prone countries, we should never forget that we have also suffered severe damage from many earthquakes. These include the Hyogoken-nanbu Earthquake (The Great Hanshin-Awaji Earthquake Disaster) in 1995 and the off the Pacific Coast of Tohoku Earthquake (The Great East Japan Earthquake Disaster) in 2011.

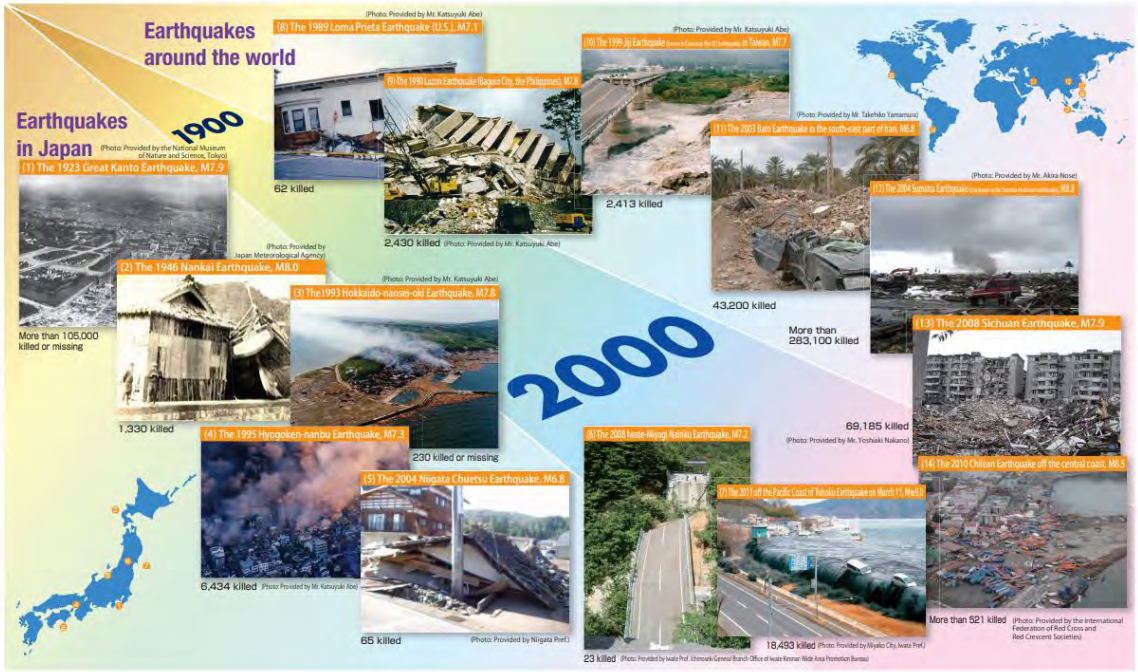

Q1 Why do we have so many earthquakes in Japan?

That is because Japan is situated on the plate boundaries, an area where large strains are accumulated.

The surface of the earth is covered with more than a dozen huge plates (plate-like masses of rock). The plates move in different directions at a speed of several centimeters per year (plate motion). Looking at things on a large scale, most earthquakes occur in the belt-like zones along the plate boundaries. It is said that Japan has been struck by approximately ten percent of the world's earthquakes. This is despite its small area, being less than one percent of the world's total land area.

Tremendous forces are applied by plate motion to the inside of the underground rock masses near the plate boundaries. Over many years a vast amount of energy builds up inside the rock masses as a strain and accordingly stress is accumulated. If a rock mass fractures due to the accumulated stress, an earthquake occurs. Japan is situated along the boundaries of four plates. The large strain energy accumulated in the rock masses therefore cause many earthquakes to be generated. However this doesn't only apply to the type of earthquakes that occur near the plate boundaries. Earthquakes that occur inland are also thought to be the result of accumulated strain in continental plates.

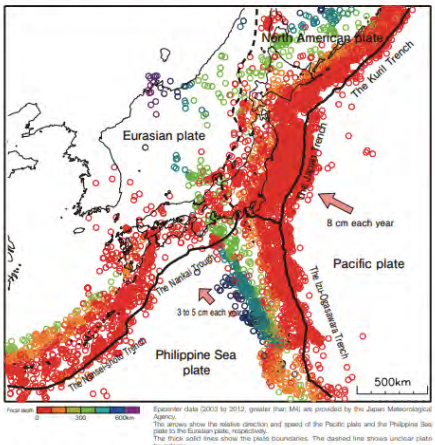

Epicenter data (2003 to 2012, greater than M4) are provided by the Japan Meteorological Agency.
The arrows show the relative direction and speed of the Pacific plate and the Philippine Sea plate to the Eurasian plate, respectively.
The thick solid lines show the plate boundaries. The dashed line shows unclear plate boundaries.

○ shows the locations of epicenters. The color shows the depth of each hypocenter. You can see that the earthquakes are concentrated along the areas near plate boundaries.

Q2 How do earthquakes occur?

Earthquakes occur when stressed underground rock masses rapidly move in opposite directions to each other along a certain plane (a fault plane). This movement is called fault movement (or faulting).

Along the Japan Trench and the Nankai Trough on the Pacific side of Japan, oceanic plates are continuously moving under the continental plates (subduction). At the same time, the continental plates are being dragged inland.

The subduction of an oceanic plate stresses rock masses around the plate boundary. When the accumulated stress exceeds its limit, a fault movement occurs. This leads the continental plate to rapidly jump up. This movement is a type of earthquake called an inter-plate earthquake.

On the other hand, earthquakes can occur in oceanic plates. The stress accumulated inside the oceanic plate generates a fault movement in the plate; this also causes an earthquake. This type of earthquake is called an intra-oceanic plate earthquake.

In continental plates, indirect forces from plate motion accumulate strain energy. Fault movements occur to release this strain energy in the continental plate. They occur at depths of up to 20 km from the ground surface. When a large-scale fault movement occurs in a continental plate, a fault displacement may develop on or near the ground surface.

The Headquarters for Earthquake Research Promotion calls earthquakes that occur along or around a plate boundary related to a trench or trough a "subduction zone (trench type) earthquake". It also calls earthquakes that occur at the shallow section of a continental plate a "shallow inland earthquake."

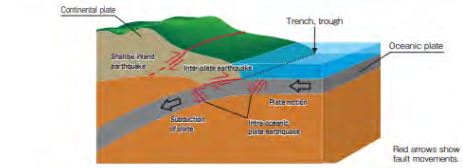

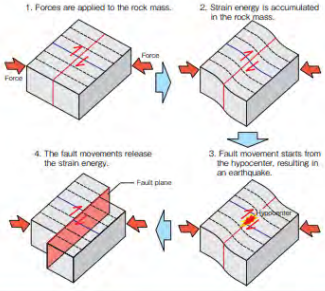

Earthquakes occur as fault movements. A fault movement is a phenomenon that involves two adjacent rock masses moving in opposite directions to each other along a certain plane (a fault plane). The energy of strain accumulated by plate motion in the rock mass is released in the form of a seismic wave. This is due to abrupt faulting.

Q3 What is an active fault?

An active fault is a fault that has repeatedly experienced fault movements in the past and is still deemed to be a source fault of future earthquakes.

If a large earthquake occurs inside a continental plate, the fault displacement can reach the ground surface and deform geological layers and geographical features. The deformations caused by repetitive fault movements such as these form characteristic geographies. These can include dislocations along mountain ridges, dislocations along valley faults, and continuous cliff formations. By surveying these characteristic geographies through aerial photography, it is presumed that approximately 2,000 active faults currently exist in Japan. Excavating active faults is useful for estimating the probability of fault activity in the future. By undertaking the excavations, we can find out the scale and interval of earthquakes in the past.

The fault cliff that was formed as a result of the fault movements that occurred during the Nobi Earthquake in 1891 (shown by the arrows). In this earthquake, a total of 80 km of surface fault rupture emerged along the Nobi Fault. Active faults show that earthquakes that form such a characteristic geography have occurred repeatedly in the past.

Dislocation of geological layers generated by the Nobi Earthquake (the Neodani Fault).
A vertical displacement of approximately 6 m can be observed. Past fault activities can be clarified by examining the dislocation of layers such as this one.

(Photo: Provided by the Education Committee of Motosu City)

Q4 Do earthquakes not happen in places where there are no active faults?

Earthquakes can occur where no active faults have been recognized.

If the magnitude of the earthquake is small, the displacement of the causal fault does not always show up on the ground surface. Even if the fault displacement reaches the ground surface, sometimes such evidence of the fault activity is removed by erosion or sedimentation over a long period of time. Therefore, even in places where no apparent active faults have been presently found, active faults may still exist and cause earthquakes in the future.

Detailed investigations of underground areas and geography may lead to detection of such underground faults.

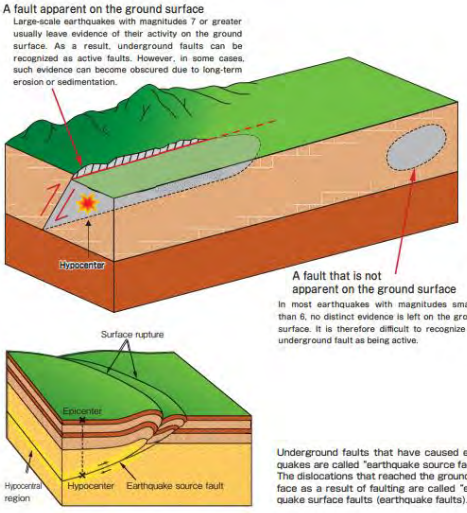

Underground faults that have caused earthquakes are called "earthquake source faults." The dislocations that reached the ground surface as a result of faulting are called "earthquake surface faults (earthquake faults)."

Q5 Do earthquakes occur repeatedly at the same places?

Large-scale earthquakes tend to occur repeatedly at the same place over a long period of time.

In Japan, it is well known that there are many active faults and places where large-scale subduction zone earthquakes repeat all over the country.

Large-scale earthquakes have a tendency of "happening repeatedly at the same place as in the past." For example, records show that at the Nankai Trough, where subduction zone earthquakes occur, large-scale earthquakes have been happening repeatedly. The investigation of active faults shows that large-scale inland earthquakes also have repeated at the same fault as in the past.

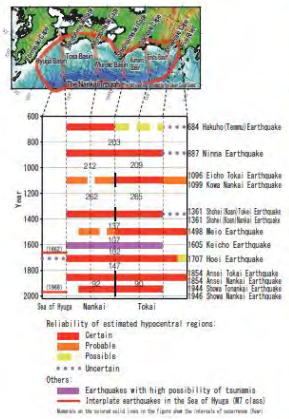

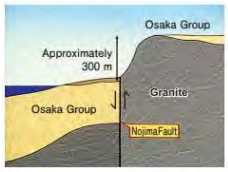

During the Hyogoken-nanbu earthquake, which caused the Great Hanshin-Awaji Earthquake Disaster, the Nojima Fault in Awaji Island moved. The Osaka Group, which had accumulated several million years ago, was displaced along the Nojima fault by more than 300 m.

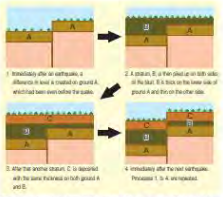

Such geological formations are found by excavating active faults. They reveal that the faults moved repeatedly in the past.

Q6 How often do large earthquakes occur?

The intervals of subduction zone earthquakes, which occur near plate boundaries, range from several decades to several hundreds of years. On the other hand, the intervals of active fault earthquakes, which occur at inland active faults, range from a thousand to tens of thousands of years.

Subduction zone earthquakes, which occur near plate boundaries, occur at intervals ranging from decades to several hundreds of years on average. This is a relatively short period. Inland active fault earthquakes, on the other hand, occur at intervals ranging from a thousand to tens of thousands of years. This is quite a long period compared with the human life-span. These intervals differ from fault to fault, because they depend on the speed of strain that is accumulated in the rock mass by plate motion. They also depend on the strength of the rock mass against strain. However, earthquakes that are caused by individual active faults have almost the same size and recurrence intervals.

Taking all the earthquakes in Japan that inflicted major damage over the past 200 years, the average recurrence interval is 20 years for subduction zone earthquakes and 10 years for shallow inland earthquakes.

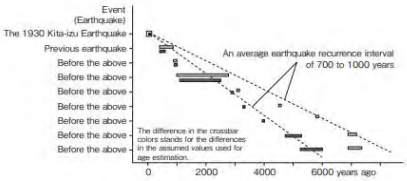

The trench excavation survey at the Tanna Fault indicates that the Tanna Fault moved nine times in the past, with an average interval of 700 of 1000 years. (The history of the fault activity was obtained by the Tanna Fault Excavation Survey and Research Group in 1983.)

Q7 How do seismic waves travel?

Part of the earthquake energy travels in the form of waves (seismic waves).

When the underground rock mass is broken and a fault moves, part of the energy propagates in all directions as seismic waves. Typical seismic waves contain two different types of waves: P waves and S waves. P waves are the propagation of density change. The direction of P waves' shake is the same as the direction of their propagation. S waves are the propagation of shear deformation. The direction of S waves' shake is perpendicular to the direction of their propagation. According to the direction of their shake, P waves and S waves are called "longitudinal waves" and "transverse waves," respectively. P waves travel faster than S waves. That is why when an earthquake occurs first the ground rattles due to the arrival of P waves. After this the ground slowly sways a little bit due to the arrival of S waves. Additionally, if an earthquake occurs in a distant place (especially if the hypocenter is shallow) large and slow swaying can occur after the ground shake by P waves and S waves. Those waves are called surface waves and travel only on or near the surface of the ground. They are able to reach distant places.

P waves stand for primary waves, which means they come first. S waves stand for secondary waves, which means they come second.

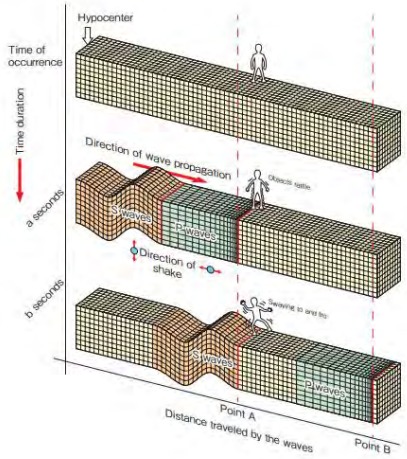

Q8 In what place does the ground shake the strongest?

The softer the ground is, the stronger the ground shakes.

How strongly the ground shakes at the surface depends largely on the structure of deep ground near the surface. Generally, the ground shakes more strongly at surfaces where the soil near the surface is soft, compared to ground where the soil near the surface is hard. Furthermore, sometime deep portions of ground also make the ground shake more strongly. This happens because seismic waves increase their strength when they propagate from hard rock mass to soft soil. They also increase their strength when the deflected waves and reflected waves overlap.

The underground structures near the surface can be estimated from geographical features to some extent. The deep ground structures can also be known through boring investigations or studies using artificial earthquakes.

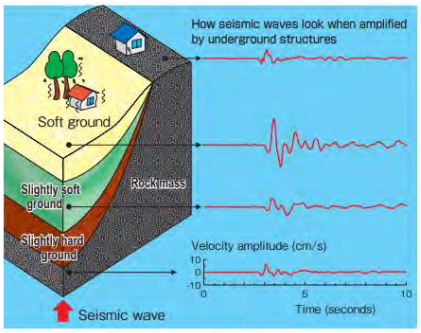

Earthquake near Hakone on Aug. 5, 1990 (M5.1)
In the figure, underground structures such as rock mass and soft ground are simply illustrated. The earthquake data (waveforms) shown in the figure are actual records. The ground shakes approximately three times as strongly on the soft ground than it does on the hard rock. The ground shakes for a longer amount of time on the soft ground than it does on the hard ground. (This figure based on a figure by Mr. Kazuyoshi Kudo)

Q9 How long does the ground shake for?

The duration of large shakes in the large-scale earthquakes that occur near Japan is thought to be generally one minute at the longest. The intensity of shake depends on the scale of the earthquake, the location of hypocenter, and the condition of the ground.

Generally, the larger that the earthquake source fault is, the duration of large shakes in the earthquakes that occur near Japan generally becomes longer. For example, in the 1995 Hyogoken-nanbu Earthquake the length and breadth of the earthquake source fault was several dozen kilometers. Subsequently, the duration of strong shakes lasted more than a dozen seconds.

On the other hand, during the 2011 off the Pacific Coast of Tohoku Earthquake both the length and breadth of the earthquake source fault were as large as several hundred kilometers. Subsequently, strong shakes lasted more than 3 minutes in some areas. On the other hand, for example, during the 2003 Tokachi-oki Earthquake shakes have lasted for long periods of time, even if the earthquake source fault is not so large. In cases involving long periods of ground motion, slow swaying motions may continue even after large shakes.

The magnitude of shake (seismic intensity) at a given location depends on the scale of the earthquake itself (earthquake magnitude), it also relies on its position relative to the hypocenter and the underground soil structure. In the case of shallow inland earthquakes, strong shakes can come in the vicinity of the hypocenter and inflict severe damages even if the scale of the earthquake is relatively small.

The 1995 Hyogoken-nanbu Earthquake (Chuo-Ku, Kobe City)

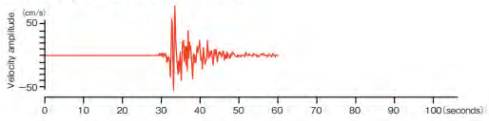

The 1995 Hyogoken-nanbu Earthquake: a large shake lasted for more than a dozen seconds in Kobe City. During this time an extremely large shake lasted for 4 or 5 seconds.

(Data taken from the Japan Meteorological Agency website)

The 2003 Tokachi-oki Earthquake (Tomakomai City)

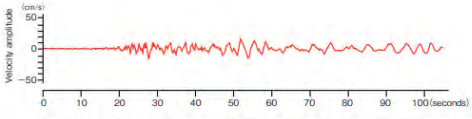

The 2003 Tokachi-oki Earthquake: long-period ground motions were observed in Tomakomai City, where the sway continued for nearly 3 minutes.
*In the figure, a part exceeding 100 seconds is cut off.
(Data taken from the Japan Meteorological Agency website)

Q10 What is "long-period ground motion"?

It means a relatively slow swaying motion during earthquake shake.

When a relatively large-scale earthquake occurs, unlike ordinary earthquakes that have short shake periods, they occasionally cause slow swaying ground motions that last for a long period of time. The period can range from several seconds to more than a dozen seconds. Such ground motions are called "long-period ground motions". Long-period ground motion can travel to places very distant from the hypocenter. Strong swaying motions can even be observed in places that are quite far from the hypocenter. This is one of the features of long-period ground motion.

(Photo provided by the Fire and Disaster Management Agency)

In this earthquake at Tomakomai Harbor, which was 200 km or more away from the hypocenter, a long-period ground motion caused the oil in storage tanks to slosh about. This caused the tanks to rupture, leading to fire.

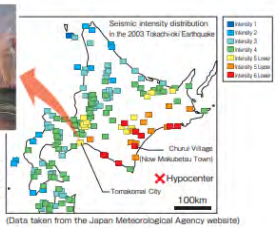

(Data taken from the Japan Meteorological Agency website)

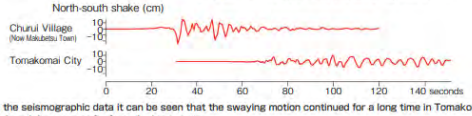

From the seismographic data it can be seen that the swaying motion continued for a long time in Tomakomai, even though it was very far from the hypocenter.

Large structures tend to resonate with long-period ground motions. It is now known that during the 1923 Great Kanto Earthquake, there were large tremors with periods of more than 5 seconds. However these long-period ground motions did not attract much attention at the time. This was because back then there were not many large structures in Tokyo. However, nowadays ultra-high-rise buildings and large-scale bridges have been constructed in various part of Japan. Structures like these tend to resonate with ground motions that have periods exceeding several seconds. There are therefore fears that long-period ground motions will affect those structures. On the other hand, low-rise buildings tend resonate with short-period ground motions.

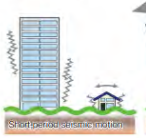

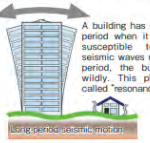

A building has its own unique period when it is particularly susceptible to shake. If seismic waves occur near that period, the building shakes wildly. This phenomenon is called "resonance."

Q11 What are the hypocenter, epicenter and hypocentral areas?

The point where the fracture started is called the hypocenter. An epicenter is the point on the ground surface directly above the hypocenter. Hypocentral regions are regions where fractures have spread due to faulting.

Enormous forces are acting on the underground rock masses. When the forces become too great for the rock masses to bear, they fracture. This induces an earthquake. A hypocenter is the point where the fracturing has started. An epicenter is the point on the ground surface directly above the hypocenter. The fracture, which started at the hypocenter, spreads to the surrounding region and stops at a certain distance. This expanded region is called the hypocentral region. It is in this region that the vast energy of earthquakes is generated.

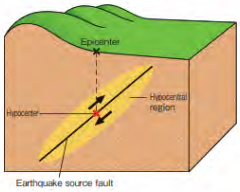

Pattern diagram showing the relation between hypocenters, epicenters and hypocentral regions

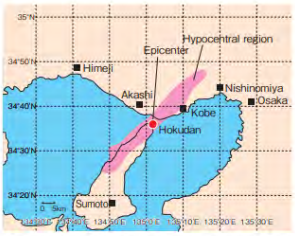

Epicenter of the 1995 Hyogoken-nanbu Earthquake (M7.3) and ground surface projection of its hypocentral region

Q12 Are seismic intensity and earthquake magnitude different?

Intensity is the greatness of the shake observed at the location and earthquake magnitude is the greatness of the earthquake itself.

Intensity is a measure of the shake at a particular location. When an earthquake occurs, the seismic waves propagate in every direction. Since the behavior of the wave propagation differs depending on the distance from the hypocenter and ground condition, the strength of shake differs with location. The strength is measured at various locations to define the intensity at each place.

Earthquake magnitude, on the other hand, is a measure of how great the actual fault movement that occurred at a hypocentral region is. The scale of an earthquake (earthquake magnitude) depends on the size of the fault plane and amount of displacement. By using the maximum amplitude on equipment such as a seismograph, earthquake magnitude can be seen as an indirect expression of the energy unleashed by seismic waves caused as a result of faulting.

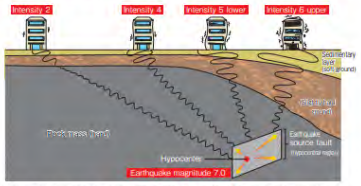

Earthquake magnitude, which represents the scale of faulting, only provides one reading for earthquakes. However, the intensity, which represents the strength of shake at different locations, varies with the location. The figure shows that shake movements are larger when the hypocenter is nearer and the ground is softer.

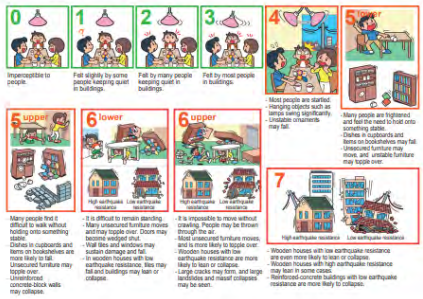

Q13 What are"main shocks"and"aftershocks"?

A main shock is the largest earthquake in a sequence. Smaller earthquakes that repeatedly occur afterward are aftershocks.

When large earthquakes occur, many small earthquakes often occur afterward. The largest earthquake is called the main shock and the subsequent smaller earthquakes are called aftershocks.

The magnitude of aftershocks varies but the largest of them is called the largest aftershock. Generally the magnitude of the largest aftershock is smaller by 1 or more than the main shock. It is known that aftershocks frequently occur immediately after the main shock. However, their rate declines as time elapses. It is also known that if the magnitude of the main shock is large, it takes a longer amount of time for the aftershocks to die down.

Example of "main shock – aftershock" type earthquake activity
(the Iwate-Miyagi Nairiku Earthquake on June 14, 2008)

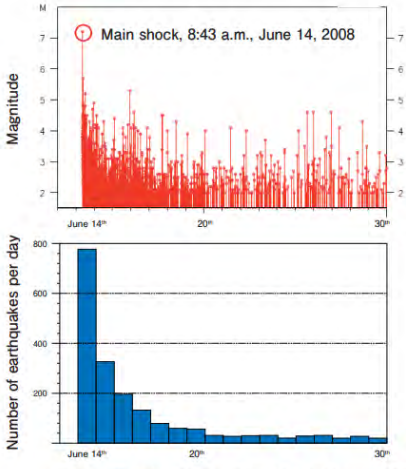

(Hypocenters with magnitudes of 2.0 or greater, provided by the Japan Meteorological Agency)

Q14 What are "earthquake swarms"?

Earthquake swarms are sequences of earthquakes in which similar size earthquakes occur in a relatively small area in a concentrated manner.

Sometimes similar size earthquakes occur in a concentrated manner in a relatively small area. This happens for a certain period of time and then they calm down. Such earthquakes are called earthquake swarms. What makes earthquake swarms distinctive is that they occur many times, their hypocenters are shallow, and they are quite small. However, sometimes medium-sized earthquake swarms with magnitudes of 5 to 6 occur.

The 1965 Matsushiro Earthquake Swarm, the 1978 Izu Hanto Toho-oki Earthquake Swarm, and the 2000 Izu Shoto Earthquake Swarm are famous in Japan. It is assumed that earthquake swarms are somehow related to the underground movement of fluids, such as magma. It is assumed from crustal deformation data that the 2000 Izu Shoto Earthquake Swarm occurred when plate-shaped magma intruded into the rock mass.

Example of "swarm type" earthquake activities
(The 2000 Izu Shoto Earthquake Swarm)

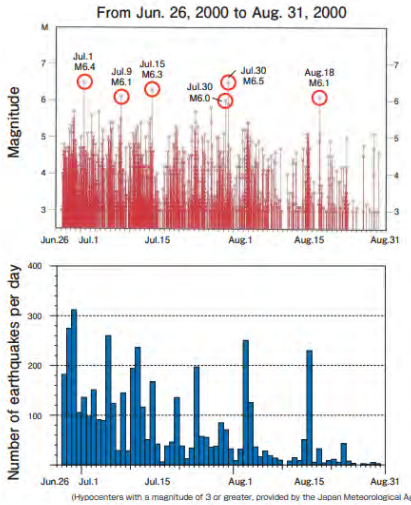

(Hypocenters with a magnitude of 3 or greater, provided by the Japan Meteorological Agency)

Q15 How are tsunamis generated?

If large crustal deformation occurs under the sea as a result of an earthquake, it moves the overlying mass of seawater and generates a tsunami.

When large earthquakes occur in the ocean, large crustal deformation occurs on the seafloor. Due to the crustal deformation, the overlying seawater rises and falls. This fluctuation of seawater creates a tsunami. Tsunamis are generated not only by earthquakes under the ocean, but also by submarine volcanic eruptions, seafloor landslides, or large collapses near the shore.

Tsunamis characteristically decrease their velocity and increase their height rapidly as they approach land and the depth of the sea decreases. The velocity, although it may be slower near land, is still nearly 40 km/h in areas where water depth is approximately 10 m. The height of a tsunami doesn't only depend on how great the earthquake was, but also on the topography of the seabed and the geographical shape of the coastline. Tsunamis can become much higher due to the shape of a particular bay or cape.

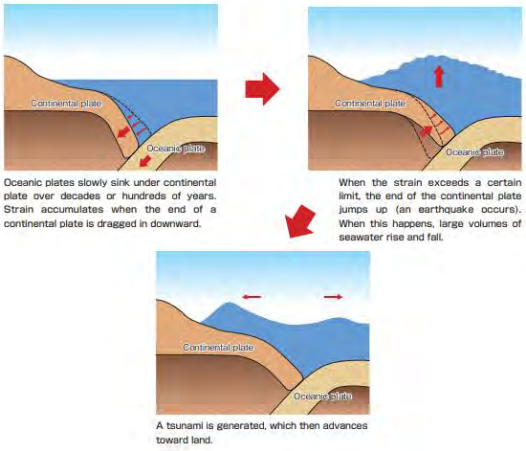

Oceanic plates slowly sink under continental plate over decades or hundreds of years. Strain accumulates when the end of a continental plate is dragged in downward.

When the strain exceeds a certain limit, the end of the continental plate jumps up (an earthquake occurs). When this happens, large volumes of seawater rise and fall.

A tsunami is generated, which then advances toward land.

Q16 What is "liquefaction"?

Liquefaction is a phenomenon where, due to the shaking of an earthquake, soil with high water content becomes like liquid.

Soil on low land or reclaimed land contains a lot of water (pore water). In soil such as this, sandy particles are holding each other together. With their water-filled pores, they stay stable. When a strong shake is applied by an earthquake, this system is destroyed. When this happens, the water pressure between the sandy particles increases. This turns the ground into a muddy, water-like state. The muddy water tries to support the load from above. However, if there are fissures or weak parts in the ground surface, the water becomes unable to support the load. This causes muddy water to erupt to the surface. Liquefaction can cause various types of damage. In addition to ground subsidence, it can cause ground-based tanks or manholes to float, and buildings and other structures to lean or collapse.

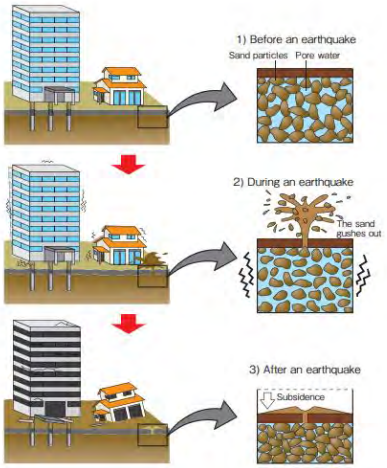

Q17 Is it possible to predict earthquakes?

Generally speaking, it is difficult to predict the occurrence of earthquakes.

Earthquake prediction means to predict "when, where an earthquake will occur, as well as how big it will be, before its occurrence based on scientific grounds." Earthquake prediction is generally considered to be difficult with present science and technology, even if limited to large-scale earthquakes.

It is thought that a large-scale earthquake could occur at any time in Tokai. This is a conclusion drawn from the history of repeated large earthquakes. About half of the hypocentral regions of past earthquakes were underground and inland. Therefore, it is thought that earthquake prediction might be possible by developing highly accurate observation networks for capturing earthquake precursors and monitoring the obtained data. Arrangements for monitoring and information sharing are now in place.

However, there are still many unknown factors when it comes to the occurrence processes of an earthquake in Tokai. In some cases, earthquake precursors are too obscure to detect, or even if they are detected there is sometimes no time to release the information before the earthquake occurs. Therefore, preparing measures for disaster prevention is also a necessary step that must be taken to guard against sudden earthquake strikes.

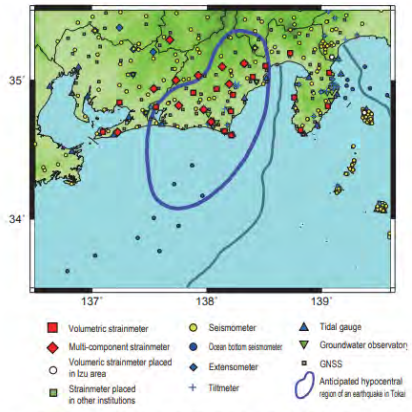

Anticipated hypocentral region of an earthquake in Tokai and the crustal deformation observation network (Figure from the Japan Meteorological Agency website)

Q18 What is an "earthquake early warning"?

An earthquake early warning is an information announcement about the occurrence of an earthquake before the actual main shake arrives. The information is obtained from the characteristic seismic waves.

Seismic waves have P waves (preliminary tremors), which have a large propagating velocity, and S waves (main tremors), which are slower. Damage due to earthquake shaking is mainly caused by the S waves. Real-time analysis of the hypocenter location and strength of the earthquake (magnitude) are now possible immediately after the occurrence of an earthquake, thanks to the progress in seismology and information processing technology. This can be done with just the arrival data of P waves near the hypocenter. Once the hypocenter and the magnitude of the earthquake are determined, it is possible to estimate the seismic intensity at a given location.

This is the system that is currently maintained all over the country to transfer information regarding analyzed and predicted hypocenters, earthquake magnitudes and seismic intensity before the arrival of S waves. It is known as the "earthquake early warning" system and the information is provided by the Japan Meteorological Agency through formats such as TV. It is expected that disaster prevention organizations, transportation facilities, public facilities, and others will be able to respond to the warning and prevent or minimize the earthquake damages before the S waves arrive. However, if the hypocenter is close, it becomes impossible to cope with the S waves before they arrive. It is therefore important to keep the differences between P waves and S waves in mind.

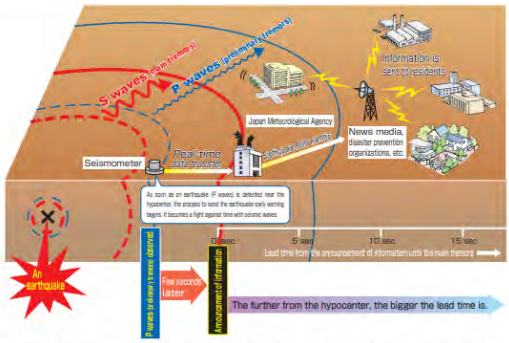

- The earthquake early warning system catches earthquakes (P waves and preliminary tremors) near their hypocenter and automatically calculates their location, magnitude, and estimated seismic intensity. The result is notified swiftly, ranging from several seconds to several dozen seconds, before the strong shaking (S waves and main tremors) arrives.
- However, for locations near the hypocenter, sometimes there is no warning time to prepare for strong shaking.

(Taken from a leaflet published by the Japan Meteorological Agency)

Supporting Section Part 1 Government Efforts

Ⅰ. General Overview of the Headquarters for Earthquake Research Promotion

The Great Hanshin-Awaji Earthquake Disaster on January 17, 1995 killed 6,434 people and destroyed over 100,000 buildings. This was the worst damage that Japan had suffered since the end of World War II. It also brought to light a number of problems in the national earthquake disaster prevention measures at the time.

Based on these problems, the Special Measure Law on Earthquake Disaster Prevention was enacted by legislators in July 1995. It was designed to promote a comprehensive national policy on earthquake disaster prevention.

The law recognized that the national system had failed to sufficiently communicate and apply the results of earthquake research to general public and disaster prevention organizations. As a result, the Headquarters for Earthquake Research Promotion was established in accordance with this law as a special governmental organization attached to the Prime Minister's Office (it now belongs to the Ministry of Education, Culture, Sports, Science and Technology). It was established in order to clarify the systems of responsibility regarding earthquake research that is directly connected to government policy. It manages this in an integrated fashion with a governmental capacity.

1. The basic objectives and roles of the Headquarters for Earthquake Research Promotion

Basic objectives

To promote research of earthquakes in order to strengthen earthquake disaster prevention measures, especially for the reduction of damages from earthquake.

Roles

1. Planning of comprehensive and basic policies
2. Coordination of budgets and other administrative work with related governmental organizations
3. Establishment of comprehensive survey and observation plans
4. Collection, arrangement, analyses, and comprehensive evaluation of survey results by related governmental organizations, universities, etc.
5. Publication based on the above evaluations

2. Composition of the Headquarters for Earthquake Research Promotion

The Headquarters for Earthquake Research Promotion consists of a director (the Minister of Education, Culture, Sports, Science and Technology) and staff members (such as the vice ministers of related ministries and agencies). Underneath them are the "Policy Committee" and the "Earthquake Research Committee," composed of staff from related government offices and academia.

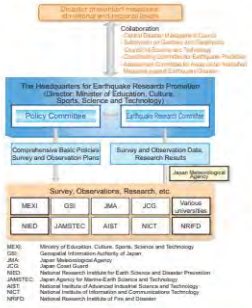

MEXT: Ministry of Education, Culture, Sports, Science and Technology
GSI: Geospatial Information Authority of Japan
JMA: Japan Meteorological Agency
JCG: Japan Coast Guard
NIED: National Research Institute for Earth Science and Disaster Prevention
JAMSTEC: Japan Agency for Marine-Earth Science and Technology
AIST: National Institute of Advanced Industrial Science and Technology
NICT: National Institute of Information and Communications Technology
NRIFD: National Research Institute of Fire and Disaster

The "Policy Committee" implements the planning of basic policy concerning the promotion of earthquake research. It also coordinates budgets and other administrative work and deals with matters such as evaluation-based publications.

The "Earthquake Research Committee" holds regular meetings on a monthly basis and classifies and analyzes research and observation results, as well as study outcomes. It does this in order to evaluate seismic activity in a comprehensive manner and to publish evaluation results. In addition, ad hoc meetings are held in response to damaging earthquakes or marked seismic activity. The meeting seeks to assess the current activity and the probability of aftershocks.

The Headquarters for Earthquake Research Promotion formulated its new policy, which was titled: "New Promotion of Earthquake Research - Comprehensive Basic Policies for the Promotion of Seismic Research through the Observation, Measurement, and Survey -." This policy is a guideline of earthquake research for the next 10 years, and was released in 2009 (revised in September 2012).

Supporting Section Part 2

Applying the Outcome of Investigative Earthquake Research for Disaster Prevention

Ⅰ. Long-term Evaluation

The Headquarters for Earthquake Research Promotion is evaluating earthquakes along the main active faults of Japan, as well as and subduction zone earthquakes. It is doing this to estimate the magnitudes of possible earthquakes and the probabilities of them occurring in given periods. The Headquarters refers to this practice as "long-term evaluation."

In long-term evaluation, you can see the "places" where large-scale earthquakes might occur, as well as their their specific "scale (earthquake magnitude)" and "probability" of occurrence.

■ The results of long-term evaluation along the main active fault zones

As of Jan.15, 2014

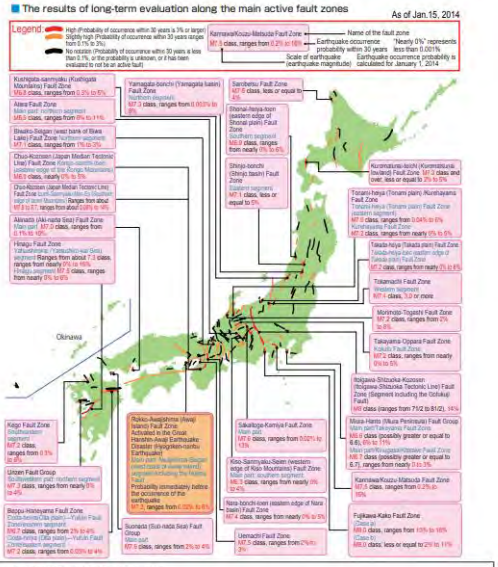

"Occurrence probability" of earthquake

Earthquakes are generated by dislocation on a fault. It is thought that individual faults have their own individual recurrence intervals. If the recurrence interval and the time of the previous earthquake are known, the time of the next earthquake can be estimated to a certain extent. However, since the actual recurrence interval can vary and is sometimes uncertain, the time of the next earthquake is expressed as a probability.

The probability of earthquake occurrence and the probability of other accidents or disastrous events

The probability of earthquake occurrence given in the figure is usually only a few percent. This might seem small, but this value does not mean that we are free from earthquakes and are safe.

For example, the probability of getting killed in a traffic accident within 30 years is approximately 0.2%*1. If you compare this value with that of an earthquake, you can see that the probability of earthquake occurrence is not so small. Furthermore, an earthquake can, even if the occurrence probability is low, inflict enormous damages once it occurs. It is important to consider its possible extent of damages when accepting this probability.

*1 Calculated based on the statistics from the White Paper published by the Fire and Disaster Management Agency, using a specific assumption.

Results of long-term evaluations of Subduction zone earthquakes

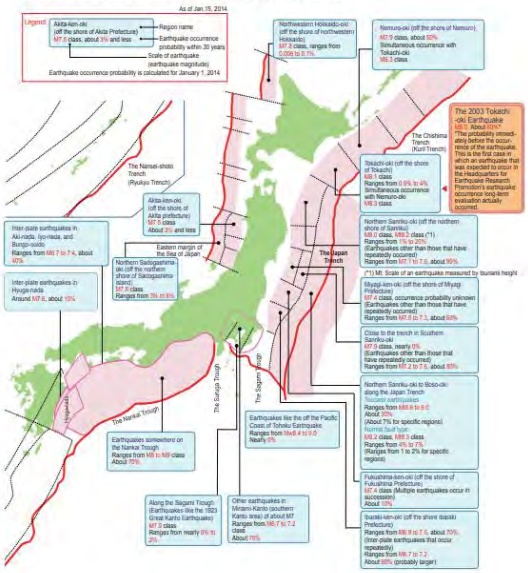

II. Seismic Hazard Maps

The Headquarters for Earthquake Research Promotion made the "National Seismic Hazard Maps for Japan" public in 2005. Since then it has been publishing seismic hazard maps that reflect the latest information.

There are two types of seismic hazard maps, which have different perspectives. The first of these is the "Probabilistic Seismic Hazard Maps," which shows the probability of strong shakes occurring at given areas over designated periods. The second is the "Seismic Hazard Maps for Specified Seismic Source Faults," which shows specified faults and how strongly certain areas near the faults can shake if an earthquake were to occur at those faults. Seismic hazard maps are prepared based on long-term evaluations. These are predictions of earthquake magnitudes and the probability of earthquake occurrence in a given period. They target earthquakes that occur at main active faults, as well as subduction-zone earthquakes. Seismic hazard maps are also based on seismic ground motion prediction methods, which specify earthquake source faults.

Since these two maps have different perspectives, you must properly choose which should be used depending on your purpose or interest in preparing for future earthquakes.

Basic use of seismic hazard maps

○ Probabilistic Seismic Hazard Maps

With this map you can find out how high and how regionally different the probability of strong shaking occurrences are over a certain period. You can also consider all the possible earthquakes that will influence a particular area of interest.

○ Seismic Hazard Maps for Specified Seismic Source Faults

With this map you can see how severe the ground motion would be in particular areas around a particular seismic source fault if an earthquake occurred.

■ A diagram showing the probability distribution of a shaking with intensity 6 or greater hitting within 30 years (Base date: Jan.1, 2013)

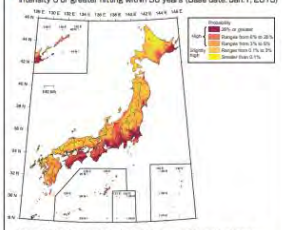

Revisions for the seismic hazard map are currently being undertaken. Please keep in mind that the seismic hazard map in this material, including the above diagram, is in the process of revision.

■ Evaluation of a strong ground motion, assuming that an earthquake occurs along an active fault

Evaluation of a strong ground motion, assuming that the earthquake occurs along the Kego Fault Zone (south-eastern segment) (made public in April 2008)

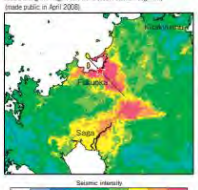

Utilization of the "Seismic Hazard Map"

The "Probabilistic Seismic Hazard Map" and "Seismic Hazard Maps for Specified Seismic Source Faults" are prepared by the Earthquake Research Committee. They are not only used to raise awareness about seismic disaster prevention; they also fulfil the following roles:

Earthquake-related survey and observation

Basic materials for selecting areas to be highlighted for earthquake-related survey and observation.

Regional inhabitants

Raising of awareness of the local residents concerning earthquake disaster prevention.

Earthquake disaster prevention measures

Basic materials for drawing up land utilization plans, seismic designs for facilities or structures. Basic materials for the planning of regional disaster prevention schemes.

Risk evaluation

Basic materials for risk evaluation, such as locating important facilities, deciding new business locations, or evaluating of insurance rates.

Probabilistic Seismic Hazard Maps

The Probabilistic Seismic Hazard Maps indicate the "possibilities of strong shaking within a certain period at every location on the map."

In preparing this map, all earthquakes that might influence a particular area have been considered. The considered earthquakes in these maps consist of not only earthquakes that have already been through long-term evaluation, but also earthquakes that are difficult to find source faults for before they occur. This includes earthquakes that occur in an area where no active fault has yet been found.

For the probabilistic seismic hazard maps, three quantities are used. These are the "time span," "intensity of shakes," and "probability." To present the maps, a convention was adopted so that two of the quantities were fixed to show the distribution of the remaining quantity. For example, below is a distribution map of "probability," that is shown with the "time period" and "intensity of ground motion" fixed. Reports on the Probabilistic Seismic Hazard Map are publicly available on the Headquarters for Earthquake Research Promotion's website.

Seismic hazard maps can also be seen on the website of the National Research Institute for Earth Science and Disaster Prevention (NIED), "Japan Seismic Hazard Information Station (J-SHIS)." You can zoom-in on the map, find out "the probability of ground motion equal to or larger than seismic intensities of 6 lower, occurring within 30 years from the present," or the "ground susceptibility to shaking." You can also check the main active faults or the hypocentral regions of subduction zone earthquakes. Seismic hazard maps are revised every year.

Probabilistic Seismic Hazard Maps

A distribution map with of the probability of ground motions equal to or larger than seismic intensity of 6 lower, occurring within 30 years into the future (Base date: January 1, 2013)

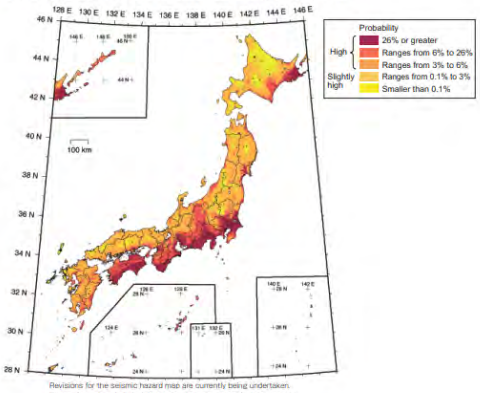

Revisions for the seismic hazard map are currently being undertaken. Please keep in mind that the seismic hazard map in this material, including the above diagram, is in the process of revision.

Seismic Hazard Maps for Specified Seismic Source Faults

The Seismic Hazard Maps for Specified Seismic Source Faults focuses on specific earthquake source faults. They show the shaking intensity of the areas around the faults when the earthquakes occur. For example, they are useful for checking how strong the shaking will be if an earthquake occur at a fault near you. These kinds of maps have been provided and widely utilized for estimating damages and drawing up national or regional disaster mitigation plans. To ensure that any user can obtain the same predicted results, the Earthquake Research Committee has been working toward standardization of the strong ground motion prediction method and has formulated the "Recipe for Predicting Strong Ground Motion for Specified Seismic Source Faults". At the same time, the committee has been conducting estimations of how strong shaking would be and has been making a series of seismic hazard maps publics for specified seismic source faults. For the evaluation, the committee has been selecting earthquakes that may have large impacts on their surrounding areas, out of those that may occur at active faults or subduction-zones. Seismic hazard maps for specified seismic source faults are openly available on the Headquarters for Earthquake Research Promotion's website.

Seismic Hazard Maps for Specified Seismic Source Faults

Strong ground motion evaluation, assuming the earthquake occurs along the Kego Fault Zone (southeastern segment)

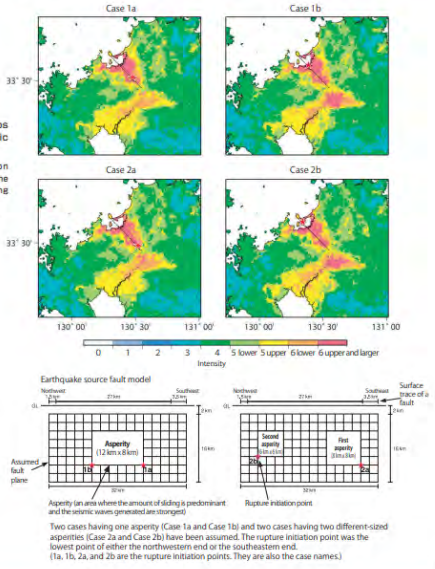

Two cases having one asperity (Case 1a and Case 1b) and two cases having two different-sized asperities (Case 2a and Case 2b) have been assumed. The rupture initiation point was the lowest point of either the northwestern end or the southeastern end.
(1a, 1b, 2a, and 2b are the rupture initiation points. They are also the case names.)

Supplementary Material Section

Measures you can take to stay safe from earthquakes

Ⅰ. Before an earthquake occurs:

Earthquakes can hit suddenly. It is important to always be as prepared as you possibly can.

(Provided by the Tokyo Fire Department)

Ⅱ. If an earthquake occurs:

In order to stay safe from earthquakes, it is important to know and think about what to do in advance. If there is ever a tsunami threat, evacuate at once. When doing so, keep the preparations shown on the following page in mind.

(Provided by the Tokyo Fire Department)

82. Assignment 3, Module 17: Australia Earthquakes:
https://www.ga.gov.au/education/natural-hazards/earthquake

What is an earthquake?

Earthquakes occur when rocks deep within the earth suddenly break and slip past one another. What we feel as earthquake vibrations and shaking (seismic waves) is the energy that propagates through the earth when the rocks break. The rocks break along pre-existing fractures, or zones of weakness known as a fault, or a fault plane.

The focus, or **hypocentre**, of an earthquake is the point where it originated within the Earth. The point on the Earth's surface directly above the hypocentre is called the earthquake **epicentre**.

The size or magnitude of earthquakes is a measure of the energy released by the earthquake and is determined by measuring the amplitude of the seismic waves recorded on a seismometer, together with the distance of that seismometer from the earthquake. These parameters are used in a formula which converts them to a magnitude. For every one unit increase in magnitude, there is roughly a thirty-fold increase in the energy released. For instance, a magnitude 6.0 earthquake releases approximately 30 times more energy than a magnitude 5.0 earthquake, while a magnitude 7.0 earthquake releases approximately 900 times (30×30) more energy than a magnitude 5.0.

Earthquake magnitude was traditionally measured on the Richter scale. It is often now reported as **moment magnitude**, which is calculated from seismic moment. The seismic moment of an earthquake is calculated using the area of the fault that ruptured, the strength of the rocks that slipped (the shear modulus), and the amount of slip along the fault during the earthquake.

Where do earthquakes occur?

No part of Earth's surface is immune from earthquakes, but some regions experience them more frequently than others. They are most frequent and largest at tectonic plate boundaries. They particularly occur around the margins of the Pacific Plate; for example in New Zealand, Vanuatu, the Solomon Islands, Papua New Guinea, Japan and the Americas, and also along the Indonesian islands arc, where the Australian Plate collides with the Eurasian Plate. Earthquake hypocentre depths in these collision zones can range from the surface to 700 km in depth.

Away from plate boundaries in **intraplate** regions, earthquakes are less frequent and do not follow easily recognisable patterns. **Intraplate** areas can be defined as either **active intraplate** closer to plate boundaries, or **stable continental regions** far from plate boundaries. Australia is considered a stable continental region, though the offshore of northern Western Australia is considered active intraplate as it is closer to the Indonesia – Australia plate collision zone.

Intraplate earthquakes generally originate at shallow depths (i.e. less than 20 km), but can still be of large magnitude. In 1811-1812 four earthquakes of estimated magnitude >7 occurred in the New Madrid region of the eastern United States (a stable continental region). More recently, the magnitude 7.7 2001 Bhuj earthquake in intraplate India killed more than 20,000 people (and active intraplate region).

Why do we get earthquakes in Australia?

The Australian plate is the fastest moving continental land mass on Earth and is colliding into the Pacific plate to Australia's north and east, and the Eurasian Plate to the northwest. This generates mainly compressive stress in the interior of the Australian continent, which is slowly building up across the plate as it moves northeast about 7 cm per year. Australia's earthquakes are caused by the sudden release of this stress when rocks deep underground break and move along a fault line. While some parts of the country are more likely to experience earthquakes than others, large earthquakes can occur anywhere across the continent, and without warning.

On average 100 earthquakes of magnitude 3 or more are recorded in Australia each year. Earthquakes above magnitude 5.0, such as the destructive 1989 Newcastle earthquake, occur on average every one-to-two years. About every ten years Australia experiences a potentially damaging earthquake of magnitude 6.0 or more.

Australia's largest recorded earthquake was in 1988 at Tennant Creek in the Northern Territory, with an estimated moment magnitude of 6.6. It occurred in a sparsely populated area and resulted in damage to a major gas pipeline. A magnitude 6.5 earthquake at Meckering in 1968 caused extensive damage to buildings and was felt over most of southern Western Australia. These earthquakes are two of the eleven Australian earthquakes that created **surface ruptures** or **fault scarps**. These occur when the earthquake ruptures along a fault from depth all the way to the ground surface.

Over 400 **fault scarps** are mapped across Australia, these are termed **neotectonic features**. Most faults mapped by geologists in Australia are very old and non-active. However, **neotectonic features** are those with landscape evidence for large, often repeating, earthquakes over the last 5 to 10 million years and might therefore host large earthquakes into the future.

Field photograph of part of the fault scarp produced by the 14th October 1968 MW6.5 Meckering earthquake (photo credit Ian Everingham)

What is Geoscience Australia's role in reducing risk to Australians from earthquakes?

We provide earthquake data and scientific information to help Australians understand the consequences of earthquakes, which contributes to more resilient communities now and in the future. Our capability spans the earthquake value chain from maintenance of a national-scale monitoring network, to 24-hour monitoring and alerting, to national earthquake hazard and risk assessments.

We collaborate with a range of stakeholders in Australia and through Australia's overseas aid program to apply this value chain to develop actionable earthquake risk information to support evidence-based decisions for disaster risk reduction.

We do this by:

- developing nationally consistent data, information and advice to enable informed decisions on preparedness and response to the impact of earthquakes
- advancing our understanding of Australia's earthquake hazard through data collection and scientific research
- advancing our understanding of the earthquake vulnerability of Australia's built environment to support mitigation and reduce the cost of disasters
- providing ongoing real-time monitoring, analysis and advice on significant earthquakes and potentially tsunamigenic earthquakes to help safeguard Australian and Indian Ocean communities.

To learn more about our work, access our latest data or hazard assessment tools, visit the Community Safety page.

How do we record earthquakes?

We monitor, analyse and report on significant earthquakes to alert the Australian Government, State and Territory Governments and the public about earthquakes in Australia and overseas.

Earthquakes are detected by scientific instruments called seismometers. The word *seismo* originates from the Greek word *seismos* which means to shake or move violently and was later applied to the science and equipment associated with earthquakes. Old paper seismometers relied on a mechanical system to record the seismic energy in the Earth onto rotating paper drums. In contrast, modern seismometers detect and convert any small movement in the Earth into an electrical signal for use in computer systems, as shown in the digital seismogram image of seven seismic sensors which detected the magnitude 7.2 earthquake in the Banda Sea, north of Australia on 24th June 2019.

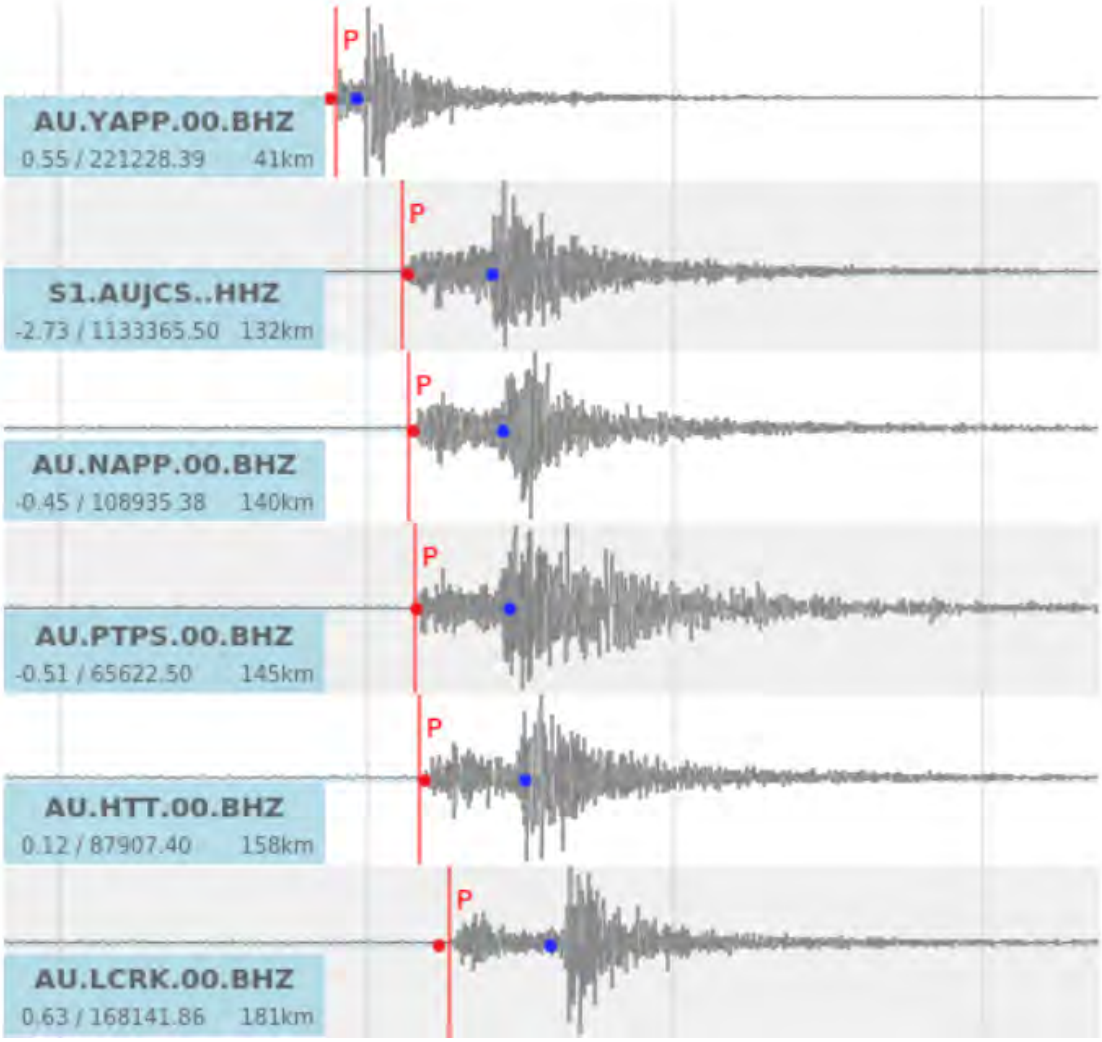

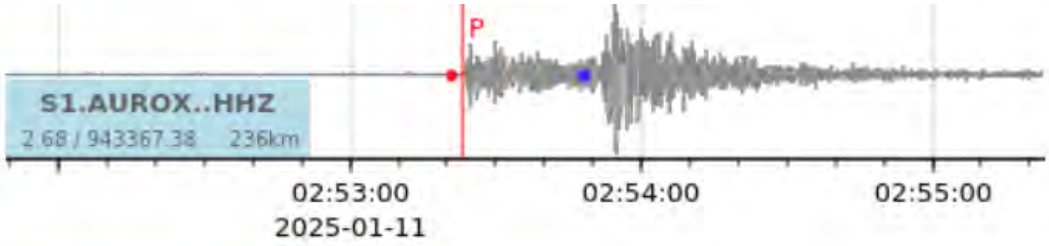

Digital seismogram image of seven seismic sensors which detected the magnitude 4.5 earthquake near Hawker in the Flinders Ranges of South Australia on 11th January 2025. The tremors from this earthquake were felt in Adelaide.

Determining the location of an earthquake

The arrival times of the seismic waves at the seismometers, together with the locations of the seismometers and the speed at which the seismic waves travel to the seismometers are all used to “triangulate” the location of the earthquake. The location relies on models that estimate the speed at which seismic waves generated by earthquakes travel through the Earth. This location is also known as its focus or hypocentre which is represented by the latitude, longitude and depth below the surface.

How does Geoscience Australia monitor earthquakes?

We monitor seismic data from more than 150 locations in Australia and in excess of 500 stations worldwide in near real-time, 24 hours a day, seven days a week. Data are delivered within 30 seconds of being recorded at the seismometer to our central processing facility in Canberra through various digital satellite and broadband communication systems.

Seismic data are also provided by overseas Governments which have national seismic networks. We use data provided by the Governments of New Zealand, Indonesia, Malaysia, Singapore and China and have access to data from global seismic networks provided by the USA, Japan, Germany and France. These networks, together with the Comprehensive Nuclear Test Ban Treaty Organisation’s ↗ International Monitoring System, also provide seismic data for tsunami warning purposes.

The seismic data are collected and analysed automatically and immediately reviewed by our Duty Seismologists.

As part of the Joint Australian Tsunami Warning Centre (JATWC), Duty Seismologists are also responsible for analysing and reporting within 10 minutes of the origin time of significant Australian earthquakes, or earthquakes which have the potential to generate a tsunami. An earthquake alert is then sent to our partner in the JATWC, the Australian Bureau of Meteorology, to determine tsunami advice and publish tsunami bulletins.

The parameters of all other earthquakes with a magnitude greater than 3.5 are generally computed within 20 minutes. The analysis includes an earthquake's magnitude, origin time and date of the earthquake and the location of its hypocentre. Smaller earthquakes that are not detected by many seismometers are difficult to locate in real-time and, consequently, are located by Seismic Analysts during normal business hours.

Geoscience Australia's National Earthquake Alerts Centre

What are the impacts of earthquakes?

The size and intensity of the shaking caused by an earthquake depends on many factors, such as the magnitude, distance from the epicentre, depth, topography, and the local ground conditions.

In Australia, earthquakes with magnitudes of less than 3.5 seldom cause damage, and the smallest magnitude earthquake known to have caused fatalities is the magnitude M_w 5.4 (M_L5.6) Newcastle earthquake in 1989. However, magnitude 4.0 earthquakes occasionally topple chimneys or result in other damage which could potentially cause injuries or fatalities.

Apart from causing shaking, earthquakes of magnitude 4.0 or greater can also trigger landslides, which can impact communities and infrastructure. The larger the magnitude of the earthquake, the bigger the area over which landslides may occur.

In areas underlain by water-saturated loosely packed sediments, large earthquakes, usually magnitude 6.0 or greater, may cause **liquefaction**. The strong ground shaking causes the sediment to lose its strength and stiffness. Subsidence from liquefaction can affect the foundations of structures and cause buildings to topple, allow sub-surface infrastructure to become buoyant and float to the surface, and the sediment might erupt at the surface from craters and fountains.

Undersea earthquakes can cause a tsunami, or a series of waves which can cross an ocean and cause extensive damage to coastal regions.

The destruction from strong earthquake shaking can be worsened in some parts of the world by fires caused by downed power lines and ruptured gas mains.

Large earthquakes are often followed by aftershocks, which can themselves be large enough to cause damage. The size and number of aftershocks generally decreases quickly with time after an earthquake, though in Australia aftershocks can continue for days, years, or even decades.

Some earthquakes, such as the 1968 Meckering earthquake in Western Australia, rupture along a fault from depth to the ground surface. This can cause significant damage, particularly to linear infrastructure which may cross the rupturing fault such as roads, pipes, power lines, trainlines, and large infrastructure such as dams, powerplants, and mines.

Earthquake effects, based on human observation, are rated using the Modified Mercalli (MM) intensity scale, which ranges from I (imperceptible) up to XII (total destruction) (see table below).

The Modified Mercalli Intensity (MMI) scale

Intensity	Shaking	Description/Damage
I	Not felt	Not felt except by a very few under especially favorable conditions.
II	Weak	Felt only by a few persons at rest,especially on upper floors of buildings.
III	Weak	Felt quite noticeably by persons indoors, especially on upper floors of buildings. Many people do not recognize it as an earthquake. Standing motor cars may rock slightly. Vibrations similar to the passing of a truck. Duration estimated.
IV	Light	Felt indoors by many, outdoors by few during the day. At night, some awakened. Dishes, windows, doors disturbed; walls make cracking sound. Sensation like heavy truck striking building. Standing motor cars rocked noticeably.
V	Moderate	Felt by nearly everyone; many awakened. Some dishes, windows broken. Unstable objects overturned. Pendulum clocks may stop.
VI	Strong	Felt by all, many frightened. Some heavy furniture moved; a few instances of fallen plaster. Damage slight.
VII	Very strong	Damage negligible in buildings of good design and construction; slight to moderate in well-built ordinary structures; considerable damage in poorly built or badly designed structures; some chimneys broken.
VIII	Severe	Damage slight in specially designed structures; considerable damage in ordinary substantial buildings with partial collapse. Damage great in poorly built structures. Fall of chimneys, factory stacks, columns, monuments, walls. Heavy furniture overturned.
IX	Violent	Damage considerable in specially designed structures; well-designed frame structures thrown out of plumb. Damage great in substantial buildings, with partial collapse. Buildings shifted off foundations.
X	Extreme	Some well-built wooden structures destroyed; most masonry and frame structures destroyed with foundations. Rails bent.

Source: Replicated from the USGS ↗

Magnitude vs Intensity

- Earthquake ***magnitude*** is related to the energy released over its ruptured fault area
- The ***intensity*** of an earthquake refers to the level of ground-shaking ***at a given location***
- Earthquake intensity typically ***decreases*** with ***increasing distance away*** from an earthquake
- The Modified Mercalli Intensity (MMI) scale is commonly used to describe the damage and felt effects of an earthquake at a given location
- MMI is a ***qualitative*** assessment of earthquake effects on structures and people
- Earthquake magnitude is a ***quantitative*** measure based on physical recordings made on seismometers

Australia's largest historical earthquakes

The Australian continent has experienced many large earthquakes in the historical past. The 10 largest recorded earthquakes are listed in the table below. However, evidence preserved in the Australian landscape demonstrates that the continent has experienced much larger earthquakes in its pre-historical past. Some of these earthquakes are even represented in First Nations Dreaming stories (link to: https://www.abc.net.au/news/2021-09-25/ancient-earthquakes-cadell-fault-diverted-murray-river/100489426).

Magnitude post-2016 revisions	Magnitude pre-2016 revisions	Location	Date
6.6	6.7	Tennant Creek, NT	1988
6.5	6.9	Meckering, WA	1968
6.4	5.6	Simpson Desert, NT	1941
6.3	6.4	Tennant Creek, NT	1988
6.3	7.2	Meeberrie, WA	1941
6.2	6.3	Collier Bay, WA.	1997
6.2	6.3	Tennant Creek, NT	1988
6.1	6.2	Cadoux, WA	1979
6.1	N/A	Petermann Ranges, NT	2016
6.0	6.0	West of Lake Mackay, WA	1970

** The earthquakes listed above have epicentres on the Australian mainland or adjacent to the Australian coast.*

83. Assignment 3, Module 1: Plate Boundaries: https://www.gns.cri.nz/our-science/natural-hazards-and-risks/earthquakes/

By understanding earthquakes and the hazards they cause, we can work to build a more earthquake-resilient society.

Land of the long complex plate boundary

Aotearoa New Zealand straddles the Pacific and Australian tectonic plates. These plates are colliding with huge force, causing one to slowly grind over, under or alongside the other. As the brittle crust gives way under the pressure, a fault ruptures and an earthquake is unleashed. Every year, GNS Science records over 20,000 earthquakes in New Zealand. About 100-150 of these quakes are large enough to be felt – the others we only know about because they are recorded by seismographs.

The team at GNS Science leads and contributes to a variety of research efforts to understand our earthquakes and the associated hazards and risks they pose to New Zealand. Our research ensures our communities are prepared and resilient.

Earthquakes in Aotearoa New Zealand – On average, we locate over 20,000 earthquakes a year in and around Aotearoa New Zealand. So why do we get so many earthquakes? Discover the cause, and what is happening beneath our feet.

View transcript +

Earthquake monitoring and response

Nationwide, there are hundreds of seismographs and strong motion sensors monitoring thousands of small shakes and many large quakes per year. Continuous GPS is being used to monitor "slow" earthquakes, recording land movement down to a few millimetres. These data are acquired, collected, stored and made available for research and monitoring by the GeoNet programme.

GeoNet is a collaboration between GNS, the Natural Hazards Commission Toka Tū Ake and Toitū Te Whenua LINZ and includes the National Geohazards Monitoring Centre (NGMC), which contributes significantly to the analysis of seismic data and monitors seismic activity around the country. Earthquake monitoring feeds into applications such as emergency response and the rapid analysis of possible tsunami. Through a number of programmes, GNS works to develop and maintain scientific capability to rapidly assess and analyse earthquakes, ensure timely and accurate advice is provided to emergency management and stakeholders and inform the public about the event.

Earthquake readiness

One of the goals of natural hazard research is to help communities build resilience. We work to deliver earthquake research that supports the aspirations of communities to increase their resilience. Specifically, we contribute earthquake-specific knowledge and data to hazard and risk modelling so that communities can predict and respond to multi-hazard scenarios. We also partner with research groups and communities to inspire, educate and facilitate a deeper understanding of our hazard-prone nation.

Our research

We incorporate several fields of study in our research to best understand earthquakes in the context of our complex plate boundary. Our research involves models of earthquakes and their ground motions (seismology), earthquake geology, geodynamics and geodesy.

We contribute our expertise in these fields to a variety of projects, drawing on our wide range of disciplines. Recent projects and programmes we have led and supported include Resilience to Nature's Challenges, Rapid Characterisation of Earthquakes and Tsunami (RCET), National Seismic Hazard Model (NSHM) and It's Our Fault.

84. Assignment 3, Module 1: New Zealand Faults: https://www.gns.cri.nz/our-science/land-and-marine-geoscience/earth-dynamics/

Earth Dynamics

Aotearoa New Zealand is positioned astride the active Pacific-Australian plate boundary.

Our continent's position provides an ideal natural laboratory for a global community of researchers to better understand processes that control natural hazards.

GNS Science drives our work in this area through our Te Riu-a-Māui Zealandia SSIF programme. This research investigates the geological processes that formed and evolved the continent beneath our feet. It covers all work on the plate boundary with a focus on the Hikurangi Subduction Zone, which is characterised by high and unknown risk.

Our research

We investigate and model the crustal structure, deformation mechanisms and processes in and near the modern Pacific-Australian plate boundary that transects Te Riu-a-Māui Zealandia.

Our main emphasis is on the Hikurangi subduction zone where we find a spectrum of plate boundary slip processes, including steady creep, episodic slow slip events, and seismic (stick-slip) behaviour. We focus our research on:

- Understanding the transition from subduction to collision
- Understanding the role of the Alpine Fault in New Zealand tectonics and earthquake occurrence
- Using exhumed, ancient analogues to better understand modern plate boundary processes

We also focus our research on how volcanism and geothermal properties have been shaped by our continent's unique movement due to the plate boundary processes happening underneath.

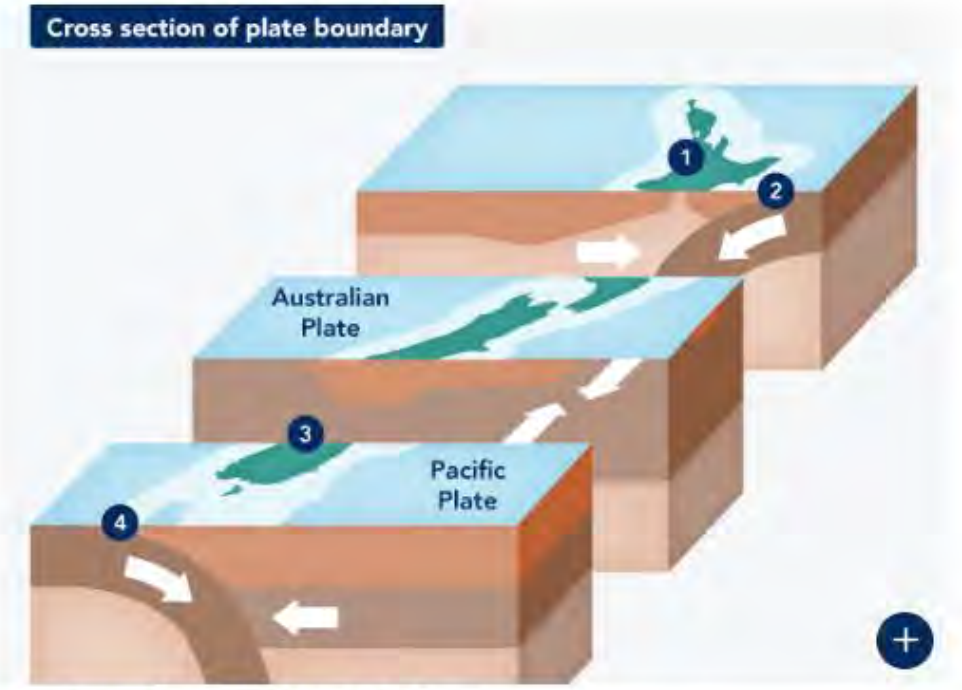

Cross Section of Aotearoa New Zealand's Plate Boundary.

Key questions driving our research

- Why, when and where do large plate boundary earthquakes happen?
- How are stress and strain distributed across the plate boundary?
- How do volcanism and geothermal systems in Aotearoa New Zealand link to magma, heat production and crustal fluid circulation?
- How do we develop model-informed monitoring and future-focused data acquisition networks across all our hazards, environments and energy risks?
- How can we better detect and provide warnings for tsunami generated from all sources including earthquakes, submarine landslides, tsunami earthquakes and volcanic edifice collapse?
- What role do Earth's surface and sea floor processes play in defining the changing dynamics of Aotearoa New Zealand's landmass?

85. Assignment 3, Module 2: FEMA 454, Section 2.2.2:
https://www.wbdg.org/FFC/DHS/fema454.pdf

2.2.2 Earthquake Fault Types

The mechanical aspects of geological faults are the key factors in understanding the generation of strong seismic motions and modeling their different characteristics. Some knowledge of the fault type to be encountered at a site is useful to the architect because of the different types and intensities of motion that each fault type may generate.

First, the geometry of fault-slip is important (see Figure 2-3). The **dip** of a fault is the angle that the fault surface makes with a horizontal plane, and the **strike** is the direction of the fault line exposed or projected at the ground surface relative to the north. A **strike-slip** or **transform** fault involves displacements of rock laterally, parallel to the strike. If, when we stand on one side of a fault and see that the motion on the other side is from left to right, the fault is **right-lateral** strike-slip. If the motion on the other side of the fault is from right to left, the fault is termed a left-lateral strike slip. Events of strike-slip type include the 1857 and 1906 San

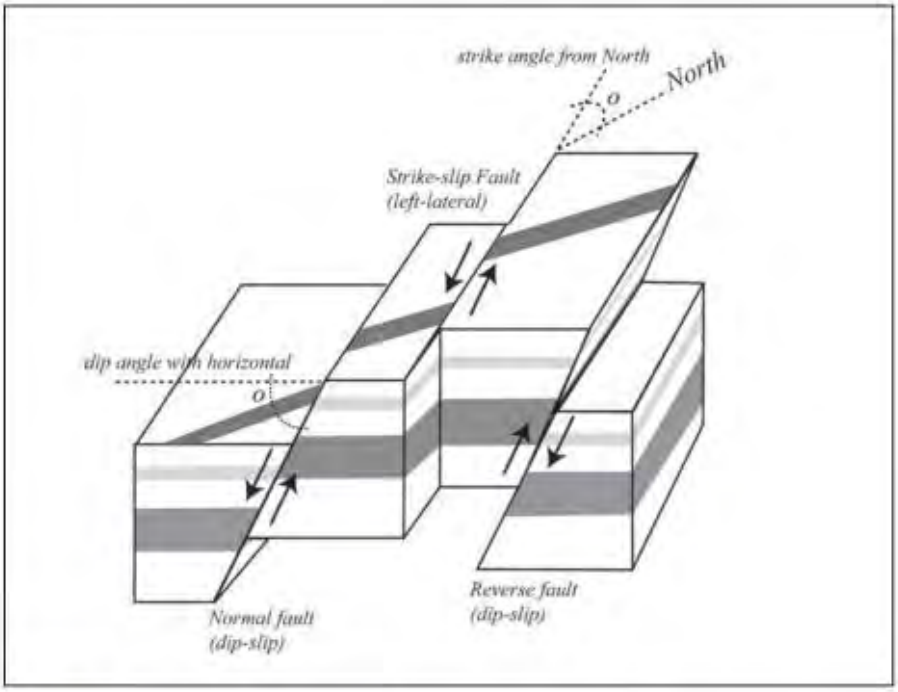

Figure 2-3: The three primary fault types.

The strike is the angle the surface trace of the fault makes with respect to geographic north. The dip is the angle the fault plane makes in the vertical with respect to the horizintal.

SOURCE: Bruce A. Bolt, *Earthquakes*, 2003

Andreas fault, California, earthquakes and more recently the 1996 Kobe, Japan ($M_W = 6.9$), 1999 Izmit, Turkey ($M_W = 7.6$, Figure 2-4), and 2002 Denali, Alaska ($M_W = 7.9$), earthquakes.

The **right-lateral** displacement of the North Anatolian fault in Turkey from the 1999 event is shown in Figure 2-4. Catastrophic damage to multi-story buildings both near and across the fault resulted from the fault motions. A lone standing building in the foreground demonstrates that variation in building construction is also a factor in the survivability of a structure.

A **dip-slip** fault is one in which the motion is largely parallel to the dip of the fault and thus has vertical components of displacement. There are two types of dip-slip faults: the normal and the **reverse** fault.

Figure 2-4: Izmit, Turkey, 1999.

The right-lateral strike-slip fault motion (depicted by white arrows and evidenced by the offset masonry wall) pass through a collapsed structure. Note that collapsed and standing structures adjacent to the fault demonstrate both the severity of ground shaking and variation in the quality of construction.

A normal fault is one of dip-slip type in which the rock above the inclined fault surface moves downward relative to the underlying crust. Faults with almost vertical slip are also included in this category. The Borah Peak (M_W = 7.3) earthquake in Idaho in 1983 is an example of a normal-type event that produced a scarp six feet high.

In a reverse fault, the crust above the inclined fault surface moves upward relative to the block below the fault. **Thrust** faults belong to this category but are generally restricted to cases when the dip angle is small. In **blind thrust faults**, the slip surface does not penetrate to the ground surface (for example, in the 1994 Northridge earthquake).

For the common shallow crustal earthquakes, seismic ground motions differ systematically when generated by strike-slip, thrust, or normal mechanisms. Given the same earthquake magnitude, distance to the site, and site condition, the ground motions from thrust earthquakes tend to be (about 20-30 percent) larger than the ground motions from strike-slip earthquakes, and the ground motions from normal faulting earthquakes tend to be smaller (about 20 percent) than the ground motions from strike-slip earthquakes. For subduction earthquakes such as the 1964 Alaska (M_W = 9.2) event, the ground motions systematically differ from those generated by interface or intra-plate earthquakes. Again, for the same magnitude, distance, and site condition, the ground motions from intra-plate earthquakes tend to be about 40 percent larger than the ground motions from inter-plate earthquakes.

Reverse-fault slips have the greatest range of size, because they can grow both in the strike and dip directions. In subduction zones, the largest reverse events occur in the depth range from 0-100 km, with lengths on the order of 1,000 km. The 1960 Chile and 1964 Alaska mega-earthquakes ($M_W = 9.5$ and $M_W = 9.2$, respectively) are examples of this type. The 1994 Northridge, California, earthquake, despite its moderate size ($M_W = 6.7$), inflicted considerable damage and casualties because of its location on a blind thrust beneath a heavily populated region. In most cases however, fault slip is a mixture of strike-slip and dip-slip and is called **oblique** faulting, such as occurred in the 1989 Loma Prieta ($M_W = 6.9$) earthquake in central California. In the latter case also, the fault slip was not visible at the surface of the ground but was inferred from seismological recordings. Large scale thrusting of the ground surface was very evident along the Chelungpu fault in the 1999 Chi Chi earthquake ($M_W = 7.6$) in Taiwan (see Figure 2-5).

It is at once obvious that any description of seismicity requires a measure of earthquake size, for comparison between earthquakes and between seismic hazard zones. As in classical mechanics, a suitable quantity to characterize the mechanical work done by the fault rupture that generates the seismic waves is the mechanical moment. In these terms we can

Figure 2-5: This building near Juahan, in Taiwan, was lifted several feet by the fault. Fault rupture runs just near the side of the building, down the alley. The white lines highlight the offset ground surface. There was no apparent damage to the building.

SOURCE: PHOTO BY JACK MOEHLE FROM THE NATIONAL INFORMATION SERVICE FOR EARTHQUAKE ENGINEERING (NISEE) AT THE UNIVERSITY OF CALIFORNIA, BERKELEY.

consider the seismic moment that is, as might be expected, proportional to the area of fault slip A multiplied by the slip distance D.

Fault offset a poses high risk for certain types of structures. When such structures, including dams and embankments, must be built across active faults, the design usually incorporates joints or flexible sections in the fault zone. The maximum horizontal offset in the 1906 San Francisco earthquake was about 18 feet.

86. Assignment 3, Module 2: USGS Fault Types: https://www.usgs.gov/faqs/what-a-fault-and-what-are-different-types

What is a fault and what are the different types?

A fault is a fracture or zone of fractures between two blocks of rock. Faults allow the blocks to move relative to each other. This movement may occur rapidly, in the form of an earthquake - or may occur slowly, in the form of creep. Faults may range in length from a few millimeters to thousands of kilometers. Most faults produce repeated displacements over geologic time. During an earthquake, the rock on one side of the fault suddenly slips with respect to the other. The fault surface can be horizontal or vertical or some arbitrary angle in between.

Earth scientists use the **angle of the fault** with respect to the surface (known as the dip) and the **direction of slip** along the fault to classify faults. Faults which move along the direction of the dip plane are dip-slip faults and described as either normal or reverse (thrust), depending on their motion. Faults which move horizontally are known as strike-slip faults and are classified as either right-lateral or left-lateral. Faults which show both dip-slip and strike-slip motion are known as oblique-slip faults.

The following definitions are adapted from *The Earth* by Press and Siever.

normal fault - a dip-slip fault in which the block above the fault has moved downward relative to the block below. This type of faulting occurs in response to extension and is often observed in the Western United States Basin and Range Province and along oceanic ridge systems.

Normal Fault Animation

reverse (thrust) fault - a dip-slip fault in which the upper block, above the fault plane, moves up and over the lower block. This type of faulting is common in areas of compression, such as regions where one plate is being subducted under another as in Japan. When the dip angle is shallow, a reverse fault is often described as a thrust fault.

Thrust Fault Animation

Blind Thrust Fault Animation

strike-slip fault - a fault on which the two blocks slide past one another. The San Andreas Fault is an example of a right lateral fault.

Strike-slip Fault Animation

A **left-lateral strike-slip fault** is one on which the displacement of the far block is to the left when viewed from either side.

A **right-lateral strike-slip fault** is one on which the displacement of the far block is to the right when viewed from either side.

87. Assignment 3, Module 2: Normal Fault:
https://www.iris.edu/hq/inclass/animation/fault_normal

Fault: Normal

11s | Novice | Spanish | Chinese | Greek

How does a normal fault move?

In a normal fault, the block above the fault moves down relative to the block below the fault. This fault motion is caused by tensional forces and results in extension. Other names: normal-slip fault, tensional fault or gravity fault. Examples: Sierra Nevada/Owens Valley; Basin & Range faults.

Objectives:

- The block above the fault moves down relative to the block below the fault
- Fault motion is caused by tensional forces that result in extension.

Keypoints:

- The block above the fault moves down relative to the block below the fault
- Fault motion is caused by tensional forces that result in extension.

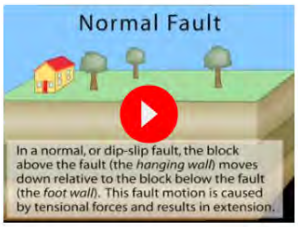

Resource Files

Download All 624KB

Optional Files 2

- BACKGROUND earthquake faults
- GIF Normal fault (excerpt from animation)

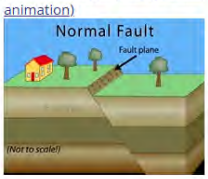

88. Assignment 3, Module 2: Reverse Fault:
https://www.iris.edu/hq/inclass/animation/fault_reverse_

Fault: Reverse

15s | Novice | Spanish | Chinese | Greek

How does a reverse fault move?

In a reverse fault, the block above the fault moves up relative to the block below the fault. This fault motion is caused by compressional forces and results in shortening. A reverse fault is called a thrust fault if the dip of the fault plane is small. Other names: thrust fault, reverse-slip fault or compressional fault. Examples: Rocky Mountains, Himalayas.

Objectives:

- The block above the fault moves up relative to the block below the fault.
- Fault motion is caused by compressional forces and results in shortening.

Keypoints:

- The block above the fault moves up relative to the block below the fault.
- Fault motion is caused by compressional forces and results in shortening.

Resource Files

Download Animation 297KB

Optional Files 2

- Background about faults
- GIF Reverse Fault (Excerpt from animation)

89. Assignment 3, Module 2: Strike Slip Fault:
    https://www.iris.edu/hq/inclass/animation/fault_strikeslip

Fault: Strike-slip

18s | Novice | Spanish | Chinese | Greek

How does a horizontal fault move?

Strike-slip faults are vertical (or nearly vertical) fractures where the blocks have mostly moved horizontally. The fault motion of a strike-slip fault is caused by shearing forces. If the block on the far side of the fault moves to the left, as shown in this animation, the fault is called left-lateral. If the block on the far side moves to the right, the fault is called right-lateral Other names: transform, transcurrent fault, lateral fault, tear fault or wrench fault. Examples: San Andreas Fault, California; Anatolian Fault, Turkey.

Objectives:

- Strike-slip motion is horizontal
- The fault is vertical, or nearly vertical

Keypoints:

- Strike-slip motion is horizontal
- The fault is vertical, or nearly vertical
- It can be right lateral or left lateral

Resource Files

Download Animation 282KB

Optional Files 1

- GIF Fault—Strike slip fast (Excerpt from animation)

90. Assignment 3, Module 2: Oblique:
https://www.iris.edu/hq/inclass/animation/fault_oblique_

Fault: Oblique

Novice | Spanish | Chinese | Greek

What is the motion that is halfway between a normal fault and a strike-slip fault?

This left-lateral oblique-slip fault suggests both normal faulting and strike-slip faulting.

This is caused by a combination of shearing and tension or compressional forces. Nearly all faults will have some component of both dip-slip (normal or reverse) and strike-slip, so defining a fault as oblique requires both dip and strike components to be *measurable* and *significant*.

Objectives:

- Oblique faults can be normal or reverse
- Oblique faults have a strike slip component also
- Most faults have an oblique component

Keypoints:

- Normal and reverse faults move vertically
- Strike-slip faults move horizontally
- Most faults have either a dominant vertical or horizontal component but also possess variations between pure vertical or pure horizontal.

Resource Files

Download Animation 224KB

Optional Files 1

- GIF Oblique (Excerpt from animation)

91. Assignment 3, Module 2, Pacific Northwest EQs: https://www.iris.edu/hq/inclass/animation/pacific_northwest_three_types_of_tectonic_earthquakes

Pacific Northwest: Three types of tectonic earthquakes

4min 13s | Novice

Subduction-zone earthquakes aren't the only ones...

The Pacific Northwest is host to more than the anticipated megathrust earthquake that will happen off the Cascadia coast in the future. That earthquake will be due to the stress building between the Juan de Fuca and North American plates as the oceanic Juan de Fuca plate dives deep beneath the Pacific Northwest. However, there are also deep earthquakes within the subducting plate, and shallow earthquakes in the overlying continental crust. This is because of additional forces acting on the region besides subduction-zone processes.

CLOSED CAPTIONING: A **.srt** file is included with the download. Use an appropriate media player to utilize captioning.

Keypoints:

The Pacific Northwest is host to three kinds of tectonic earthquakes :

- *Magnitude nine Cascadia megathrust quakes*
- *Magnitude 6.5 to seven deep earthquakes , and*
- *Shallow crustal-fault earthquakes with magnitudes up to 7.5.*

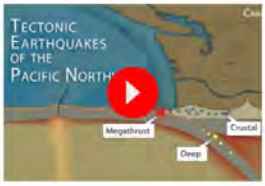

Resource Files

Download All 33MB

Optional Files 7

- Text from the animation—Word doc.
- Quake Scenarios for PNW earthquakes
- GIF Pacific NW—Load & Release (excerpt from animation)

- GIF Pacific NW—Block Rotation (excerpt from animation)

- GIF Pacific NW—Blocks move north (excerpt from animation)

- GIF GIF PNW SeattleVsNisqually 1200

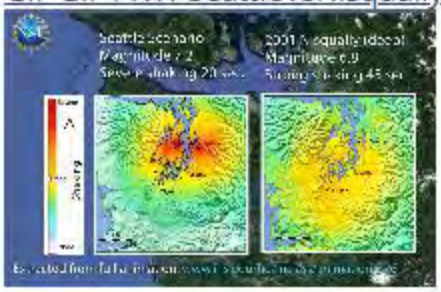

- GIF Pacific NW Seattle Fault vs Nisqually earthquakes

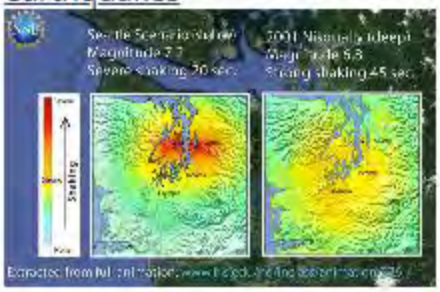

92. Assignment 3, Module 2, Tectonic Boundaries:
https://www.iris.edu/hq/inclass/animation/plate_boundaries_three_types_described

What are the lithospheric plates and how do they interact?

The cool, rigid outer layer of Earth is highly fractured. In most places, huge chunks or pieces of this rigid outer layer, called plates, are in continuous motion. Plates can range from 50 km to 200km thick. Continental plates are thicker and less dense than oceanic plates that are formed at spreading ridges.

Viewers will learn to define a tectonic or lithospheric plate; differentiate between continental and oceanic plates; differentiate between the 3 types of plate boundaries; and learn about the generalized seismicity associated with boundaries.

CLOSED CAPTIONING: A **.srt** file is included with the download. Use an appropriate media player to utilize captioning.

Time codes:
0:00 Intro
0:40 Inside the Earth
1:20 Lithosphere, asthenosphere, crust
2:42 Types of boundaries
5:55 Diffuse boundary

Keypoints:

Discovery

- What forces are acting on the earth that result in different types of plate boundaries?
- Can you name three basic types of faults?
- Is a reverse fault caused by tension, extension or shearing?

CLOSED CAPTIONING: Please use the "**CC**" option on our YouTube version:
https://youtu.be/Xzpk9110Lyw

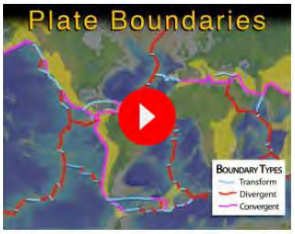

Resource Files

Download All 25MB

Optional Files 4

- Background for Plate Boundaries
- Text from Narration doc
- GIF Plate motion (Excerpt from animation)

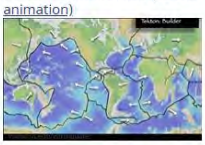

- GIF Convergent boundary (Excerpt from animation)

93. Assignment 3, Module 2, Convergent Boundary:
https://www.iris.edu/hq/inclass/animation/plate_boundary_convergent_margin

Plate Boundary: Convergent margin

1min 16s | Novice | Spanish | Chinese

How do megathrust earthquakes generate a tsunami?

In this animation, we are showing an ocean/continent convergent boundary at the leading edge of the plate. We see the denser oceanic plate diving beneath the continental plate. The down-going oceanic plate eventually warms up to the temperature of the surrounding mantle. Such destruction (recycling) of oceanic plates occurs along convergent boundaries where plates collide and an oceanic plate is subducted. (This animation does not address volcanoes formed inboard of the boundary where water released from the oceanic plate facilities magma production in the mantle wedge beneath the continent.)

CLOSED CAPTIONING: A **.srt** file is included with the download. Use appropriate media player to utilize captioning.

Keypoints:

Denser oceanic plate dives beneath the continental plate. Plates are locked by high friction. Over time, friction is overcome in process called elastic rebound Sudden movement of overlying plate generates a tsunami

Resource Files

Download All 8MB

Optional Files 3

- Subduction animation text
- PlateBoundaries Background
- GIF Convergent FAST (Excerpt from animation)

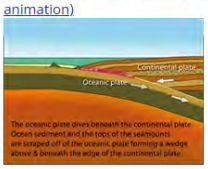

94. Assignment 3, Module 2: Divergent Fast-Spreading Ridge:
https://www.iris.edu/hq/inclass/animation/plate_boundary_divergent_fastspreading_ridge

Plate Boundary: Divergent (Fast-spreading Ridge)

1min 10s | Novice | Spanish | Chinese

How do mid-ocean ridges form new crust?

Spreading mid-ocean ridges form the longest mountain ranges in the world. New oceanic crust is created at this boundary when basalt magma, formed in the mantle, rises into fractures in the crust and solidifies. Spreading ridges are high elevation because the young oceanic plate at the ridge crest is hot and less dense than the older, colder and more dense plate on the flanks of the ridge. As the plates move away from the boundary, they thicken because underlying mantle rocks cool and add to the bottom of the plate.

CLOSED CAPTIONING: A **.srt** file is included with the download. Use appropriate media player to utilize captioning.

Keypoints:

- Hot mantle rock rises beneath mid-ocean ridges
- Melt forms beneath the lithosphere
- Magma rises into magma chambers
- Lava erupts onto ocean floor building new crust
- Plates move apart

Resource Files

Download All 8MB

Optional Files 2

- Divergent margin animation text
- GIF Divergent FAST (Excerpt from animation)

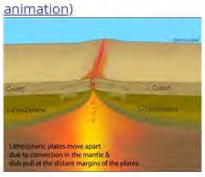

95. Assignment 3, Module 2: Transform:
https://www.iris.edu/hq/inclass/animation/fault_transform

Fault: Transform

Novice Spanish

How do the plates accommodate motion near spreading ridges?

A transform fault is a type of strike-slip fault wherein the relative horizontal slip is accommodating the movement between two ocean ridges or other tectonic boundaries. They are connected on both ends to other faults. A transform fault or transform boundary, also known as conservative plate boundary since these faults neither create nor destroy lithosphere, is a type of fault whose relative motion is predominantly horizontal. Additional animations on seafloor spreading and transform faults are available from Tanya Atwater (http://emvc.geol.ucsb.edu/2_infopgs/IP1GTect/eSoAtlantic_CutGlobe.html).

Objectives:

- A transform fault accommodates relative horizontal slip between other tectonic elements, such as oceanic plates
- A transform fault has strike-slip motion
- It is connected on both ends to other faults

Keypoints:

- A transform fault accommodates relative horizontal slip between other tectonic elements, such as oceanic plates
- A transform fault has strike-slip motion

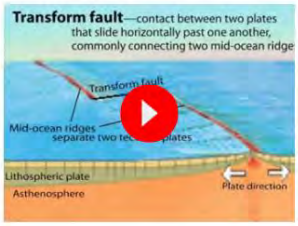

Resource Files

Download Animation 1MB

Optional Files 1

- GIF Transform fault connects other faults (excerpt from animation)

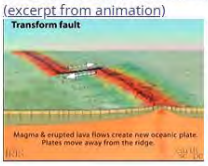

96. Assignment 3, Module 3: FEMA 454, Section 2.4.1:
https://www.wbdg.org/FFC/DHS/fema454.pdf

2.4.1 Earthquake Magnitude

The original instrumental measure of earthquake size has been significantly extended and improved in recent years. First, because the fundamental period of the now superseded Wood-Anderson seismograph is about 0.8 sec., it selectively amplifies those seismic waves with periods ranging from 0.5 to 1.5 sec. It follows that because the natural periods of many building structures are within this range, the first commonly used parameter, called the **Richter magnitude** (M_L) based on this seismograph, remains of value to architects. Generally, shallow earthquakes have to attain Richter magnitudes of more than 5.5 before significant damage occurs, even near the source of the waves. It should be remembered that a one unit increase in magnitude indicates a tenfold increase in the amplitude of the earthquake waves.

The definition of all magnitude scales entails that they have no theoretical upper or lower limits. However, the size (i.e., the seismic moment) of an earthquake is practically limited at the upper end by the strength of the rocks of the earth's crust and by the area of the crucially strained fault source. Since 1935, only a few earthquakes have been recorded on seismographs that have had a magnitude over 8.0 (see Table 2-1). At the lower extreme, highly sensitive seismographs can record earthquakes with a magnitude of less than minus two.

For reference, an architect may still encounter the following magnitude scales.

- **Surface Wave Magnitude** (M_S) is based on measuring the amplitude of surface waves with a period of 20 sec. Surface waves with a period around 20 sec are often dominant on the seismograph records of distant earthquakes (epicentral distances of more than 1,000 km).
- **Body Wave Magnitude** (M_b) Because deep focus earthquakes have no trains of surface waves, only the amplitude of the recorded P wave is used.

Nowadays, because of the shortcomings of M_L, M_b, and to a lesser degree M_S in distinguishing between the size of the biggest earthquakes, the **Moment Magnitude** scale, M_W, has replaced earlier definitions.

Studies have shown that the Richter Magnitude (M_L) scale progressively underestimates the strength of earthquakes produced by large fault ruptures. The upper-bound value for this scale is about $M_L = 7$. The body wave magnitude (M_b) saturates at about the same point. In contrast, the surface-wave magnitude (M_S) that uses the amplitude of waves with periods of 20 seconds saturates at about $M_S = 8$. Its inadequacy in measuring the size of great earthquakes can be illustrated by comparing values for the San Francisco earthquake of 1906 and the great Chilean

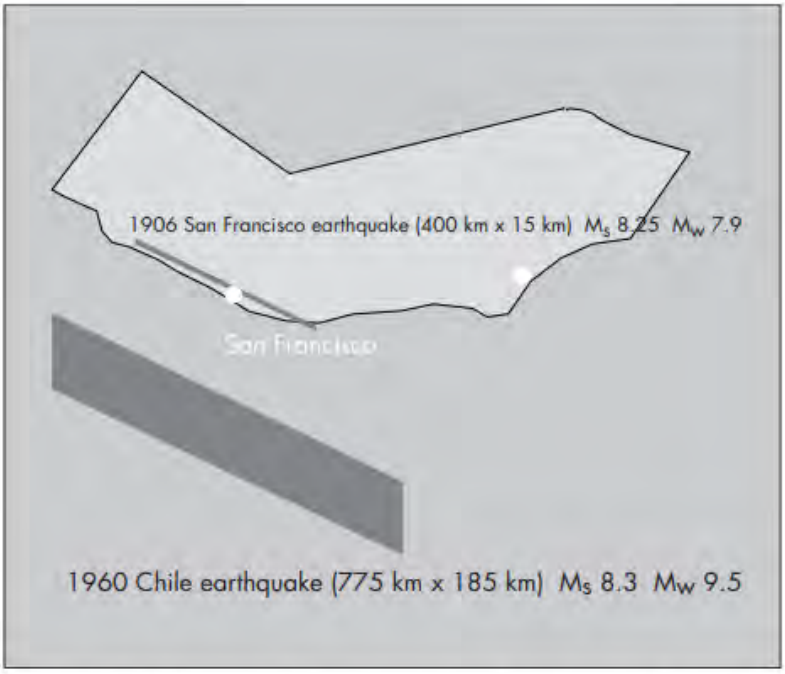

Figure 2-10: Two earthquakes may have equal magnitudes but be distinctly unequal in other respects.

The 1906 San Francisco, California, earthquake ruptured rock over a shorter length and shallower depth - only about 1/25 the area - as the 1960 Chilean earthquake. Although the surface wave magnitudes are the same, the moment magnitude for these two earthquakes (Table 2-1) are distinctly different. A sketch of the outline of California is shown for scale.

earthquake of 1960. Both earthquakes had a surface wave magnitude (M_S) of 8.3. However, the area that ruptured in the San Francisco earthquake was approximately 15 km deep and 400 km long, whereas the length that ruptured in the Chilean earthquake was equal to about half of the state of California. Clearly the Chilean earthquake was a much "larger" event (Figure 2-10).

The moment-magnitude scale (M_W) does not suffer from saturation for great earthquakes. The reason is that it is directly based on the forces that work over the area of the fault rupture to produce the earthquake and not on the amplitude and limited frequencies of specific types of seismic waves. Hence, as can be expected, when moment magnitudes were assigned to the 1906 San Francisco earthquake and the 1960 Chilean earthquake, the magnitude of the San Francisco earthquake dropped to 7.9, whereas the magnitude of the Chilean earthquake rose to 9.5. M_S and M_W for some great earthquakes are compared in Table 2-1.

97. Assignment 3, Module 3: Magnitude: https://www.usgs.gov/glossary/earthquake-hazards-program#S

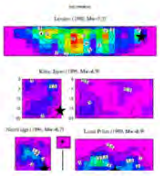

Magnitude

A number that characterizes the relative size of an earthquake. Magnitude is based on measurement of the maximum motion recorded by a seismograph. Several scales have been defined, but the most commonly used are (1) local magnitude (ML), commonly referred to as "Richter magnitude", (2) surface-wave magnitude (Ms), (3) body-wave magnitude (Mb), and (4) moment magnitude (Mw). Scales 1-3 have limited range and applicability and do not satisfactorily measure the size of the largest earthquakes. The moment magnitude (Mw) scale, based on the concept of seismic moment, is uniformly applicable to all sizes of earthquakes but is more difficult to compute than the other types. All magnitude scales should yield approximately the same value for any given earthquake.

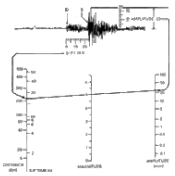

Richter scale

The Richter magnitude scale was developed in 1935 by Charles F. Richter of the California Institute of Technology as a mathematical device to compare the size of earthquakes. The magnitude of an earthquake is determined from the logarithm of the amplitude of waves recorded by seismographs. Adjustments are included for the variation in the distance between the various seismographs and the epicenter of the earthquakes. On the Richter Scale, magnitude is expressed in whole numbers and decimal fractions. For example, a magnitude 5.3 might be computed for a moderate earthquake, and a strong earthquake might be rated as magnitude 6.3. Because of the logarithmic basis of the scale, each whole number increase in magnitude represents a tenfold increase in measured amplitude; as an estimate of energy, each whole number step in the magnitude scale corresponds to the release of about 31 times more energy than the amount associated with the preceding whole number value.

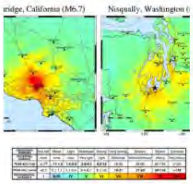

Intensity/Modified Mercalli Intensity Scale (MMI)

A number (written as a Roman numeral) describing the severity of an earthquake in terms of its effects on the earth's surface and on humans and their structures. Several scales exist, but the ones most commonly used in the United States are the Modified Mercalli scale and the Rossi-Forel scale. There are many intensities for an earthquake, depending on where you are, unlike the magnitude, which is one number for each earthquake.

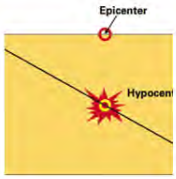

Hypocenter/focus

The point within the earth where an earthquake rupture starts. The epicenter is the point directly above it at the surface of the Earth. Also commonly termed the focus.

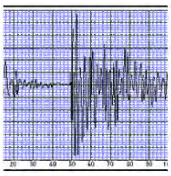

Ground motion

The movement of the earth's surface from earthquakes or explosions. Ground motion is produced by waves that are generated by sudden slip on a fault or sudden pressure at the explosive source and travel through the earth and along its surface.

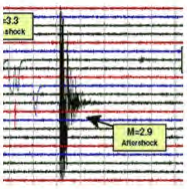

Foreshocks

Relatively smaller earthquakes that precede the largest earthquake in a series, which is termed the mainshock. Not all mainshocks have foreshocks.

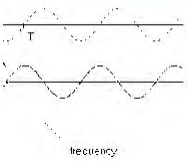

Frequency

The number of times something happens in a certain period of time, such as the ground shaking up and down or back and forth during an earthquake.

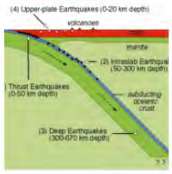

Focal depth

The depth of an earthquake hypocenter.

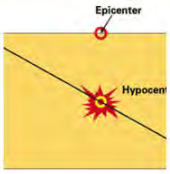

Epicenter

The point on the earth's surface vertically above the hypocenter (or focus), point in the crust where a seismic rupture begins.

Attenuation

When you throw a pebble in a pond, it makes waves on the surface that move out from the place where the pebble entered the water. The waves are largest where they are formed and gradually get smaller as they move away. This decrease in size, or amplitude, of the waves is called attenuation. Seismic waves also become attenuated as they move away from the earthquake source.

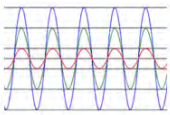

Amplitude

The size of the wiggles on an earthquake recording.

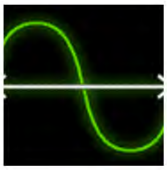

Period

The time interval required for one full cycle of a wave.

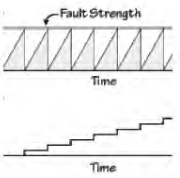

Recurrence interval/return period

The recurrence interval, or return period, is the average time span between earthquake occurrences on a fault or in a source zone.

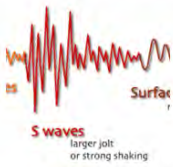

Seismic wave

An elastic wave generated by an impulse such as an earthquake or an explosion. Seismic waves may travel either along or near the earth's surface (Rayleigh and Love waves) or through the earth's interior (P and S waves).

Seismogram

A record written by a seismograph in response to ground motions produced by an earthquake, explosion, or other ground-motion sources.

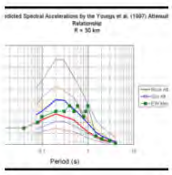

Spectral acceleration (SA)

PGA (peak acceleration) is what is experienced by a particle on the ground. SA (spectral acceleration) is approximately what is experienced by a building, as modeled by a particle on a massless vertical rod having the same natural period of vibration as the building.

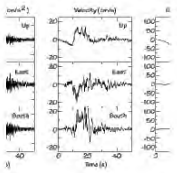

Velocity

How fast a point on the ground is shaking as a result of an earthquake.

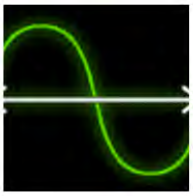

Wavelength

The distance between successive points of equal amplitude and phase on a wave (for example, crest to crest or trough to trough).

98. Assignment 3, Module 3: EQ Intensity:
https://www.iris.edu/hq/inclass/animation/earthquake_intensity

Earthquake Intensity

8min 15s | Novice | Spanish | Greek

What controls the shaking you feel during an earthquake?

We compare a light bulb to an earthquake to clarify the difference between magnitude and intensity, two concepts that are often used interchangably, but in error. Though both are related to a measured earthquake, intensity reflects what is felt during an earthquake at many locations, and the magnitude is a single measured value. Intensity was originally calculated by gathering personal, anecdotal reports during an earthquake. intensity can be estimated by instrumentally, but the definitive intensity is assigned either via *Did You Feel It* (DYFI), or via expert judgement, as was done historically. (An IRIS/USGS collaboration)

CLOSED CAPTIONING: A **.srt** file is included with the download. Use an appropriate media player to utilize captioning.

Keypoints:

Earthquake shaking is controlled by:

- Magnitude: how big was the earthquake?
- Distance from the hypocenter: Intensity varies from place to place
- Local rock and soil conditions: Soft sediment shakes more than hard bedrock.

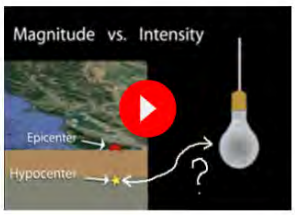

Resource Files

Download All 35MB

Optional Files 5

- Earthquake Related Glossary
- Narration for Earthquake Intensity
- GIF Intensity-Light Bulb analog (excerpt from animation)

99. Assignment 3, Module 3: Moment Magnitude:
https://www.iris.edu/hq/inclass/animation/magnitudes_moment_magnitude_explained

Magnitude Explained: Moment Magnitude vs. Richter Scale

Novice Spanish

What happened to the Richter Scale?

Scientists have developed far-more sensitive seismometers that, with faster computers, have enabled them to record & interpret a broader spectrum of seismic signals than was possible in the 1930's, when the Richter magnitude was developed. The moment magnitude uses seismograms plus what physically occurs during an earthquake (which can also be derived from seismograms), known as the "seismic moment". The seismic moment defines how much force is needed to generate the recorded waves. That information is plugged into the moment magnitude scale to give us the amount of energy that is released during an earthquake.

CLOSED CAPTIONING: A **.srt** file is included with the downloaid. Use appropriate media player to utilize captioning.

Keypoints:

- Richter Scale is mostly effective for regional earthquakes no greater than M5
- Moment Magnitude is more effective for large earthquakes Moment Magnitude uses more variables to calculate the energy released using seismic moment
- Seismic moment combines the seismic energy with offset on the fault and rigidity of rock
- Noodles can be used to teach relative magnitude

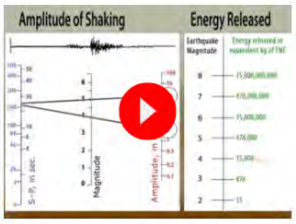

Resource Files

Download All 35MB

Optional Files 4

- Text for the animation
- GIF Magnitude: Seismic Moment (Excerpt from animation)

100. Assignment 3, Module 3: Energy Release: https://www.iris.edu/hq/inclass/animation/magnitude_graphical_comparison_of_earthquake_energy_release

Magnitude Perspective: Graphical comparison of earthquake energy release (NOAA)

1min 52s | Novice

From the NOAA site: Tsunami warning center scientists usually measure an earthquake's "size" with the moment magnitude scale rather than the older but more famous Richter magnitude scale. The moment magnitude scale is better suited for measuring the "sizes" of very large earthquakes and its values are proportional to an earthquake's total energy release, making this measurement more useful for tsunami forecasting. Moment magnitude numbers scale such that that energy release increases by a factor of about 32 for each whole magnitude number. For example, magnitude 6 releases about 32 times as much energy as magnitude 5, magnitude 7 about 32 times as much as magnitude 6, and so on. This animation graphically compares the relative "sizes" of some 20th and 21st century earthquakes by their moment magnitudes. Each circle's area represents its relative energy release, and its label lists its moment magnitude, its location, and the year it happened

Watch YouTube/Vimeo

The Pacific Tsunami Warning Center (PTWC) is one of the United States' two tsunami warning centers operated by its National Weather Service to monitor the world's oceans 24/7 for tsunami hazards, respond to tsunamis with appropriate alerts, develop new tsunami hazard detection techniques, and inform emergency managers and the public about their operations and tsunami science. PTWC is primarily responsible for protecting Hawaii, U.S. Pacific territories, and nations participating in the Pacific and Caribbean tsunami warning systems. For more information about PTWC please see our official site at http://ptwc.weather.gov/

101. Assignment 3, Module 4: FEMA 454, Sections 2.3.1 and 2.3.2: https://www.wbdg.org/FFC/DHS/fema454.pdf

2.3 SEISMIC WAVES AND STRONG MOTION

2.3.1 Seismic Instrumental Recordings and Systems

Seismographs are instruments that are designed to record ground motions such as accelerations and displacements in earthquakes. Nowadays, technological developments in electronics have given rise to high-precision pendulum seismometers and sensors of both weak and strong ground motion. In these instruments, the electronic voltages produced by motions of a pendulum or the equivalent are passed through electronic circuitry to amplify the ground motion and digitize the signals for more exact measurements.

When seismic waves close to their source are to be recorded, special design criteria are needed. Instrument sensitivity must ensure that the relatively large amplitude waves remain on scale. For most seismological and engineering purposes, the wave frequency is high (1 to 10 Hz, i.e., cycles per second), so the pendulum or its equivalent can be small. For comparison, displacement meters need a pendulum with a long free period (many seconds).

Because many strong-motion instruments need to be placed at unattended sites for periods of months or years before a strong earthquake occurs, they usually record only when a trigger mechanism is actuated with the onset of seismic motion. Solid-state memories are now used with digital recording instruments, making it possible to preserve the first few seconds before the trigger starts the permanent recording. In the past, recordings were usually made on film strips, providing duration of up to a few minutes.

In present-day equipment, digitized signals are stored directly on a memory chip, and are often telemetered to central recording sites in near real-time (several to tens of seconds). In the past, absolute timing was not provided on strong-motion records but only accurate relative time marks; the present trend, however, is to provide Universal (Greenwich Mean) Time - the local mean time of the prime meridian by means of special radio receivers or Global Positioning Satellite (GPS) receivers.

The prediction of strong ground motion and response of engineered structures in earthquakes depends critically on measurements of the lo-

cational variation of earthquake intensities near the fault. In an effort to secure such measurements, special arrays of strong-motion seismographs have been installed in areas of high seismicity around the world, both away from structures **(free field)** and on them (Figure 2-7). The seismic instrumentation of various types of buildings is clearly to be encouraged by architects, both for post-earthquake performance evaluation, future design modification and improved emergency response.

It is helpful for the user of strong-motion **seismograms** (called "**time histories**") to realize that the familiar "wiggly line" graphic records are not the actual motion of the ground, but have been filtered in some way by both the recording instrument and by the agency providing the data (see Section 2.6). In most cases, however, for practical applications the architect or engineer need not be concerned about the difference.

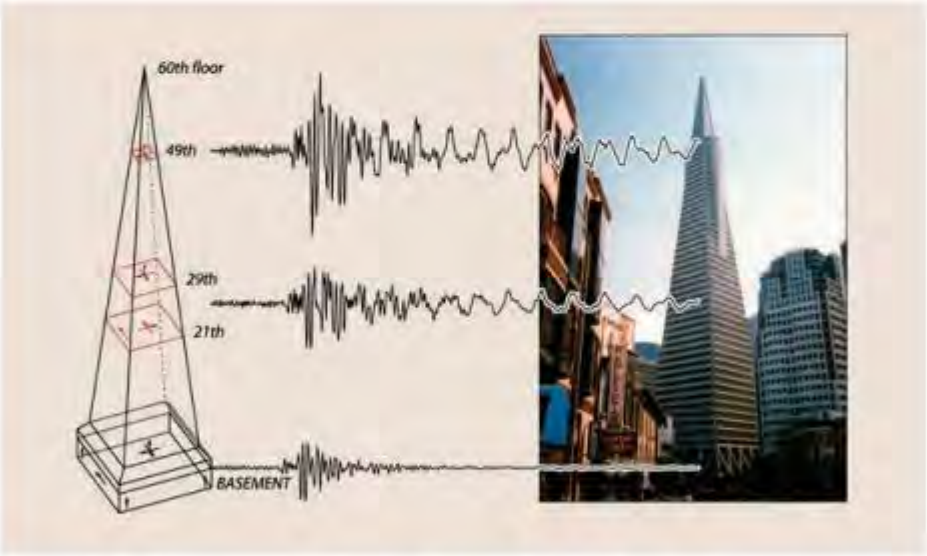

Figure 2-7: Transamerica "Pyramid" building in downtown San Francisco.

Modern instruments capable of recording large motions strategically placed in structures provide information on the structural response. In this case it is evident that there is amplification of both short-period and long-period motions in the upper floors. Also the duration of shaking at periods corresponding to characteristic vibrations of the structure become quite long towards the top.

SOURCE: USGS FACT SHEET 017-03.

2.3.2 Types of Earthquake Waves

In most instances of seismic ground motions in solid rock or soil, the waves involved are made up of four basic types of elastic waves that create the shaking that people feel and that causes damage in an earthquake. These waves are similar in many important ways to the waves observed in air, water, and elastic solids.

The first two types of waves travel through the body of the earth before arriving at the surface. The faster of these "body" waves is appropriately called the **primary** or P wave (Figure 2-8a). Its motion is the same as that of a sound wave in that, as it spreads out, it alternately pushes (compresses) and pulls (dilates) the rock. These **P** waves, just like acoustic waves, are able to travel through solid rock, such as granite and alluvium, through soils, and through liquids, such as volcanic magma or the water of lakes and oceans.

The second and slower seismic body wave through the earth is called the **secondary** or **S** wave or sometimes the **shear wave** (Figure 2-8b). As an S wave propagates, it shears the rocks sideways at right angles to the direction of travel. At the ground surface, the upward emerging S waves also produce both vertical and horizontal motions. Because they depend on elastic shear resistance, S waves cannot propagate in liquid parts of the earth, such as lakes. As expected from this property, their size is significantly weakened in partially liquefied soil. The speed of both P and S seismic waves depends on the density and elastic properties of the rocks and soil through which they pass. In earthquakes, P waves move faster than S waves and are felt first. The effect is similar to a sonic boom that bumps and rattles windows. Some seconds later, S waves arrive with their significant component of side-to-side shearing motion. As can be deduced from Figure 2-8, for upward wave incidence, the ground shaking in the S waves becomes both vertical and horizontal, which is the reason that the S wave motion is so effective in damaging structures.

The other two types of earthquake waves are called **surface waves** because their motion is restricted to near the earth's surface. Such waves are analogous to waves in the ocean that do not disturb the water at depth. In a similar way, as the depth below the ground surface increases, the ground displacements of seismic surface waves decrease.

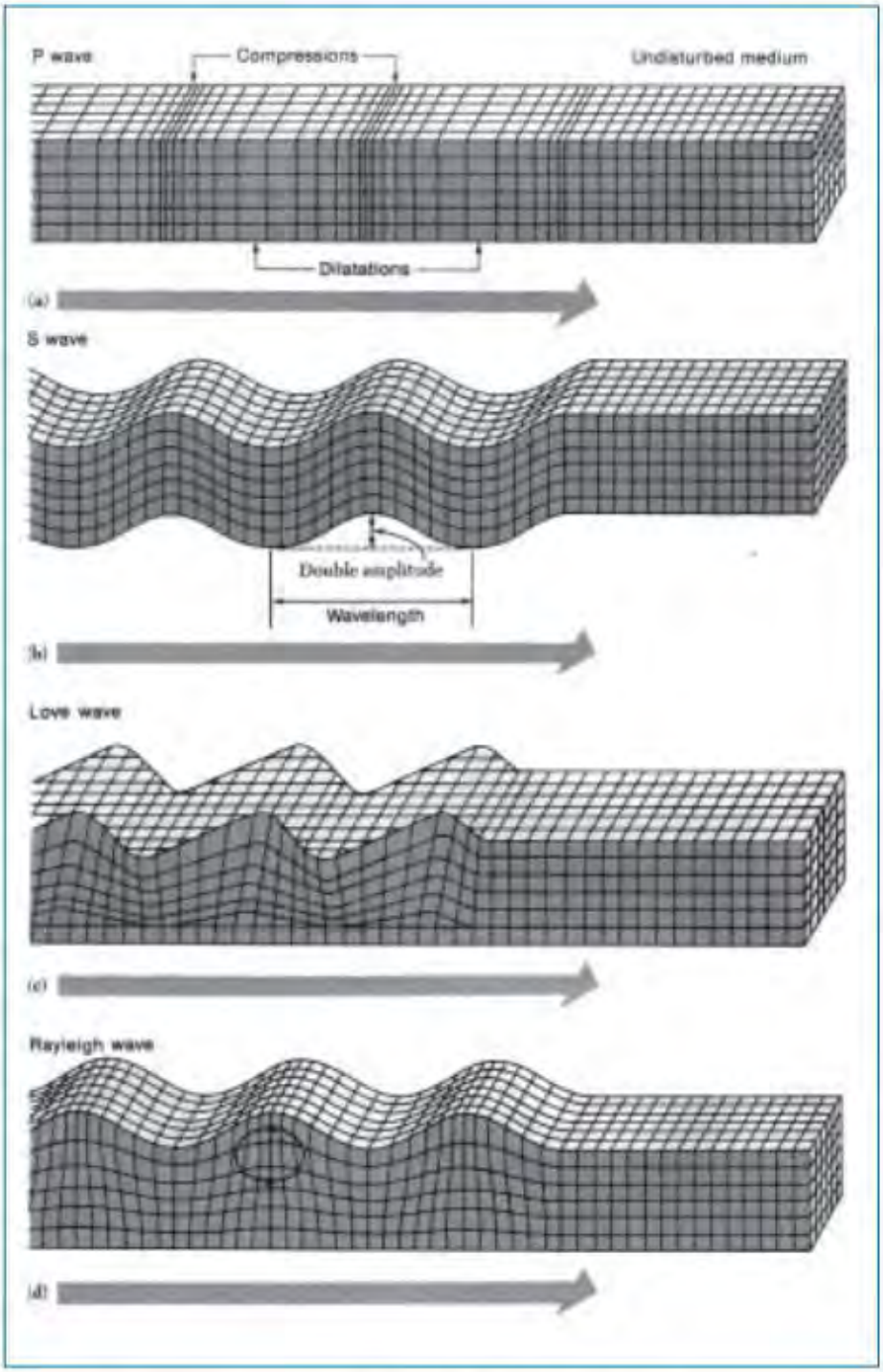

Figure 2-8: Diagram illustrating the forms of ground motion near the ground surface in four types of earthquake waves.

SOURCE: BRUCE A. BOLT, *NUCLEAR EXPLOSIONS AND EARTHQUAKES: THE PARTED VEIL* [SAN FRANCISCO: W. H. FREEMAN AND COMPANY. COPYRIGHT 1976)]

The first type of surface wave is called a **Love wave** (Figure 2-8c) Its motion is the same as that of S waves that have no vertical displacement; it moves the ground side to side in a horizontal plane parallel to the earth's surface, but at right angles to the direction of propagation. The second type of surface wave is called a **Rayleigh wave** (Figure 2-8d). Like ocean waves, the particles of rock displaced by a Rayleigh wave move both vertically and horizontally in a vertical plane oriented in the direction in which the waves are traveling. The motions are usually in a retrograde sense, as shown by the arrows in Figure 2-8. Each point in the rock moves in an ellipse as the wave passes.

Surface waves travel more slowly than P and S waves and Love waves travel faster than Rayleigh waves in the same geological formation. It follows that as the seismic waves radiate outwards from the rupturing fault into the surrounding rocks, the different types of waves separate out from one another in a predictable pattern. However, because large earthquake fault sources have significantly extended slip surfaces (i.e., many tens of kilometers), the separation is often obscured by overlapping waves of different wave types at sites close to the fault. Examples of near-fault large amplitude time histories are shown in Figure 2-9.

As seismic body waves (the P and S waves), move through layers of rock or soil, they are reflected or refracted at the layer interfaces. To complicate matters further, whenever either one is reflected or refracted, some of the energy of one type is converted to waves of the other type. When the material stiffnesses differ from one layer to another, the layers act as wave filters that amplify the waves at some frequencies and deamplify them at others.

It is important to note that when P and S waves reach the surface of the ground, most of their energy is reflected back into the crust, so that the surface is affected almost simultaneously by upward and downward moving waves. For this reason, considerable amplification of shaking typically occurs near the surface, sometimes doubling the amplitude of the upcoming waves. This surface amplification enhances the input shaking to structures and is responsible for much of the damage produced at the surface of the earth. In contrast, in many earthquakes, mineworkers below ground report less shaking than people on the surface. Nowadays, it is routine for soil engineers to make allowance for the wave amplification effect as the input seismic waves pass upwards through the soil layer to the ground surface.

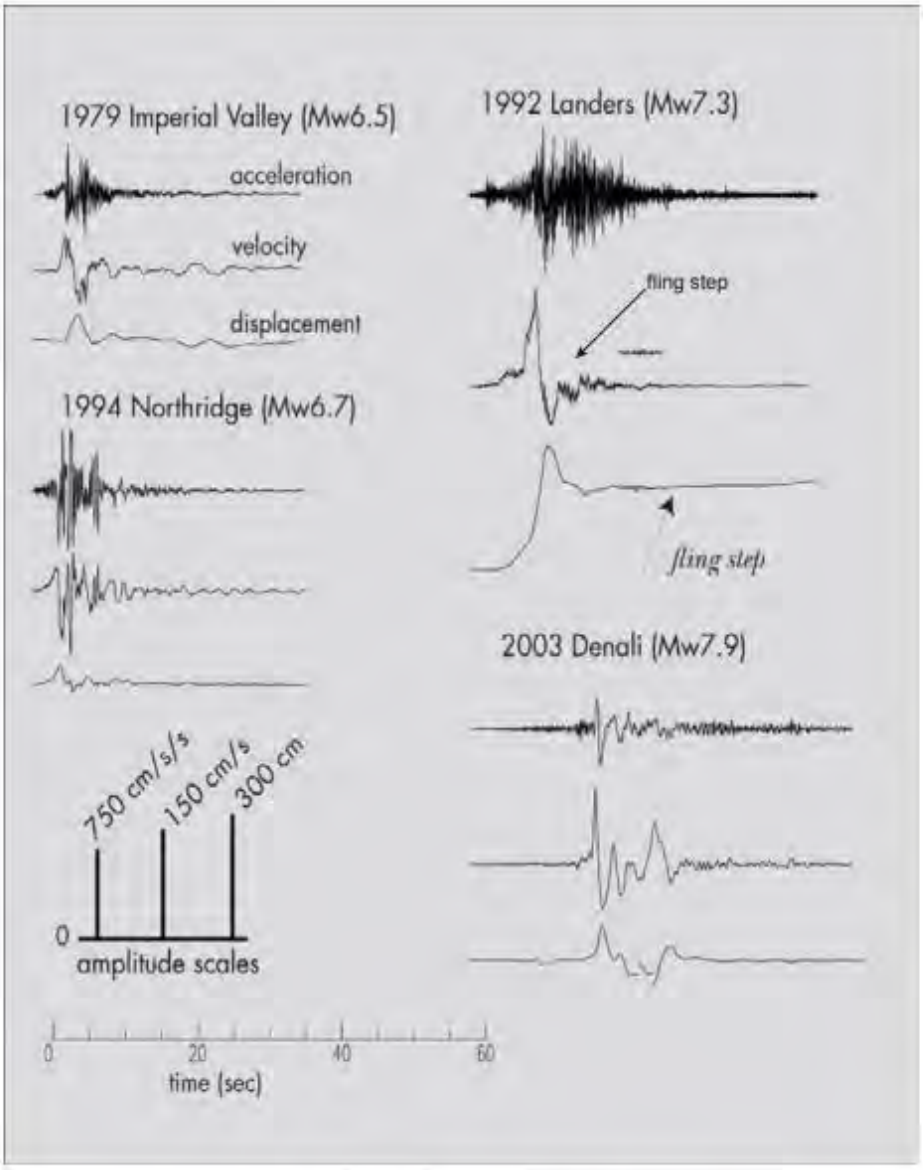

Figure 2-9: Examples of near-fault, large amplitude seismograms (time-histories).

The figure includes records from Imperial Valley, Landers (Lucerne), Northridge (Newhall) and Denali (Trans-Alaska Pipeline). Note the permanent offset in displacement of the Landers record. This is due to fault ground rebound or fling, shown by the arrows. The bars (lower left) give the common amplitude scales for the displacement, velocity and acceleration records.

It should be noted that seismic S waves travel through the rocks and soils of the earth with both a shearing and a rotational component. The latter components of ground motion have important effects on the response of certain types of structures, and some building codes now take rotational ground motion into consideration.

Seismic waves of all types progressively decrease in amplitude with distance from the source. This attenuation of waves varies with different regions in the United States. The attenuation of S waves is greater than that of P waves, but for both types attenuation increases as wave frequency increases. Ground motion attenuation can flatten and even reverse its downward trend due to strong reflected arrivals from rock interfaces. It has been shown that such reflections led to elevated ground motions in the 60-80 km distance range from the 1989 Loma Prieta, California, earthquake (i.e., in Oakland and San Francisco). Deposits of low velocity sediments in geological basins can also cause elevated levels of ground motions.

For a more detailed discussion of seismic wave attenuation and theoretical wave amplitude, see Section 2.6.1.

The physical characteristics of seismic waves have been verified by many recordings at moderate (15-30 km) to larger distances from the wave source called the **far-field**, but are not adequate to explain important details of the heavy shaking near the source of an energetic earthquake called the **near-field**. As explained above, near a rupturing fault, the strong ground shaking consists of mixtures of seismic wave types that have not separated distinctly. Although this complication makes identification of P, S, and surface waves on strong motion records obtained near the rupturing fault difficult, there has been recent progress in this skill, based on correlations between actual recordings and theoretical modelling. This advance has made possible the computation of realistic ground motions at specified sites for engineering design purposes.

Three final points about seismic waves are worth emphasizing here:

- Earthquake waves are much affected by soil elastic properties. For example, in weathered surface rocks, alluvium and water-saturated soil, the relative sizes of P, S, and surface waves can vary significantly, depending on wave frequency, as they propagate through the

surficial non-homogenous geological structures. Under extreme conditions of large wave amplitude and special geotechnical properties, the linear elastic behavior breaks down and nonlinear effects occur.

- Patterns of incoming seismic waves are modified by the three-dimensional nature of the underground geological structures. As mentioned above, instrumental evidence on this effect was obtained from recordings of the 1989 Loma Prieta, California, earthquake. In this case, strong-motion recordings indicated that there were reflections of high-frequency S-waves from the base of the earth's crust at a depth of about 25 km under the southern San Francisco Bay. Also, in this earthquake, large differences in the rock structure from one side of the San Andreas fault to the other produced variations in ground motion by lateral refraction of S waves. The effect produced significant S wave amplitude variation as a function of azimuth from the seismic source, in a period range of about 1 to 2 seconds. In addition, there was measurable scattering of S waves by separate alluvial basins in the south part of San Francisco Bay. Overall, the seismic intensity was enhanced in a region between San Francisco and Oakland, about 10 km wide by 15 km long. The observed damage and seismic intensity are well explained by these seismological results.

- It is important to explain the special seismic intensity enhancement in the near field of the earthquake source. Because of special features of engineering importance, this discussion of seismic wave patterns near to the fault source is given in the separate Section 2.4. As may be seen in Figure 2-10, time histories of the seismic waves contain pulse-like patterns of motion of crucial importance to earthquake response of larger structures.

102. Assignment 3, Module 4: Seismogram: https://www.iris.edu/hq/inclass/animation/3component_seismogram_records_seismicwave_motion

3-Component Seismogram Records Seismic-wave Motion

2min 55s | Novice | Spanish | Greek

How do we capture the motion of an earthquake?

Modern seismometers include three (3) elements to determine the simultaneous movement in three (3) directions: up-down, north-south, and east-west. Each direction of movement gives information about the earthquake. This animation shows both the movement of the three (3) basic waves (P, S, and surface) and the effect of the waves on a building. The three (3) seismograms produced by a modern seismograph station show that the *P* wave is more visible on the vertical component and the *S* wave amplitude is larger on the horizontal components.

We emphasize that seismic waves traveling away from an earthquake occur everywhere, not just at seismic stations.

CLOSED CAPTIONING: A **.srt** file is included with the download. Use an appropriate media player to utilize captioning.

Keypoints:

Following an earthquake:

- the ground responds to P, S, and surface waves by moving in all directions
- the motion can't be captured by a single seismometer in one direction
- three signals are received by the three components to reflect N-S, E-W, and up-down motion.

Resource Files

Download All 5MB

Optional Files 3

- 3-component Seismograms: Background
- GIF Simple seismograms

- GIF 3-component seismograms

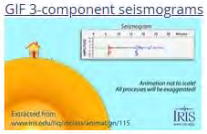

103. Assignment 3, Module 4: Seismic Waves:
https://www.geometrics.com/community/general-seismograph/what-are-the-different-types-of-seismic-waves/

Question What are the different types of seismic waves?

GENERAL SEISMOGRAPH INFO
Last Post by Gretchen Schmauder 2 years ago
1 Posts 1 Users 0 Reactions 10.7 K Views

RSS

Gretchen Schmauder
(@gschmauder)
Member
Admin
Joined: 7 years ago
Posts: 122

Topic starter 30/08/2023 12:56 pm

A seismic wave front emanates from an energy source like ripples on a pond, but in three dimensions. **It is the surface connecting points of equal travel time from the source.** In a homogeneous medium, a surface drawn through points of equal travel time is spherical, as depicted in the animation below.

The seismic trace, which is what is recorded by the seismograph, represents particle motion vs. time. In a homogeneous medium, the wave front can also be described as a **surface of constant phase**.

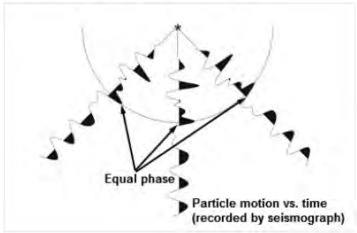

There are four main types of seismic waves, each characterized by its specific particle motion:

- **Compressional Waves** ("p" waves) are identical to sound waves – the particle motion is parallel to the propagation direction:

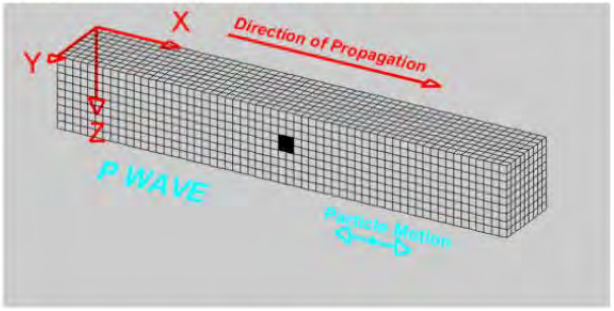

p-wave animation by L.W. Braille, Purdue University.

- **Shear Waves** ("s" waves) are characterized by particle motion that is perpendicular to the propagation direction:

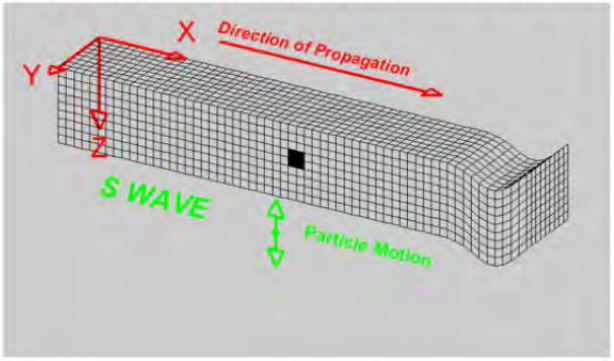

Taken collectively, p- and s-waves are known as "body" waves. The velocities of both can be measured via seismic refraction.

Surface Waves, as the name implies, travel primarily along the ground surface; amplitudes decrease rapidly with depth. There are two types of surface waves. Like body waves, they are characterized by particle motion.

- **Rayleigh waves** are characterized by elliptical motion perpendicular to the surface:

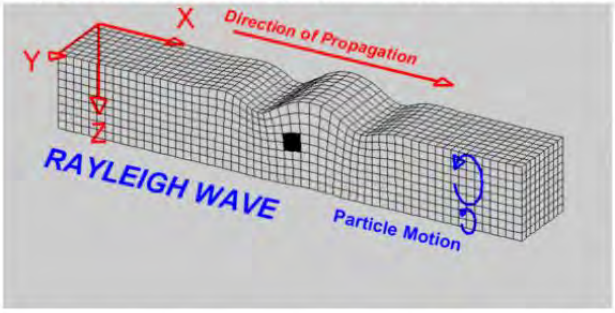

In the near surface, this motion is "retrograde", meaning that it is counter-clockwise when the propagation is left-to-right. At depth, the motion can reverse to prograde.

- **Love Waves** are created when particles vibrate perpendicular to the propagation direction:

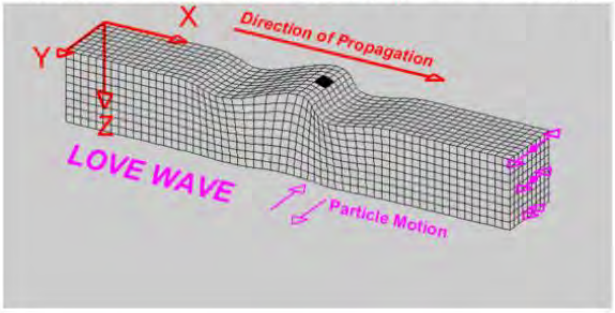

While the particle motion is similar to that of shear waves, Love wave amplitude is much higher and decreases rapidly with depth. Love waves are the most destructive waves in earthquakes because of their high amplitude and transverse particle motion.

While the various wave types shown above have been isolated for illustration purposes, all are present to some degree whenever seismic energy is traveling through a solid medium. Hence actual particle motion is extremely complex.

104. Assignment 3, Module 5: FEMA 454, Section 2.2.3:
https://www.wbdg.org/FFC/DHS/fema454.pdf

2.2.3 Earthquake Effects

There are many earthquake effects related to the geology and form of the earth that are of significance for architects. In the most intensely damaged regions, the effects of severe earthquakes are usually complicated. The most drastic effects occur chiefly near he causative fault, where there is often appreciable ground displacement as well as strong ground shaking (e.g. Figure 2-4); at greater distance, noticeable earthquake effects often depend on the topography and nature of the soils, and are often more severe in soft alluvium and unconsolidated sediment basins. Some remarkable effects are produced in bodies of water such as lakes, reservoirs, and the sea.

● Ground Shaking Intensity

Efforts to measure the size of an earthquake by rating microseismic data in the affected area go back to the 19th century. Before the invention of instrumentally based seismic magnitude, the most common historical scale rated the relative "intensity" of an earthquake. This measure is not capable of strict quantitative definition because seismic intensity at a particular point of the Earth's surface depends on many factors, including the source moment M0, area of the rupture fault, the fault mechanism, the frequency-spectrum of wave energy released, the geological conditions, and the soils at a given site.

The most widely used scale historically was originated by Rossi and Forell in 1878. A later modification developed by Mercalli in Italy, now termed the **Modified Mercalli Intensity (MMI)** scale, is suitable for conditions in the United States. Bolt (2003) describes the details of the various intensity measures.

The geographical distribution of intensity is summarized by constructing isoseismal curves, or contour lines, which separate areas of equal inten-

sity. The most probable position of the epicenter and the causative fault rupture is inside the area of highest intensity. An example of MMI curves for two moderate events is given in Figure 2-6. Clearly there can be large regional differences in MMI. Such variations in seismic wave attenuation are discussed in Section 2.6.1.

Correlations have been worked out between measured characteristics of the seismic waves and the reported Modified Mercalli intensity. A common one is that between the maximum ("peak") ground acceleration, A (centimeters per second squared), and the MM intensity, I. Such correlations are only broadly successful, particularly at the higher intensities. The description of the seismic waves for architectural and engineering purposes depends on a mixture of parameters, many of which are dependent on the frequency of the seismic waves. Nevertheless, because in many parts of the world instrumental measurements of ground

motion are not available, rough seismic intensity remains popular as a descriptor as well as for great historical earthquakes. Peak Ground Acceleration is employed as a measure in the current USGS **Shake-Maps** program, for example: these are maps showing ground shaking intensities that are available on the internet within a few minutes of an earthquake occurrence (see Section 2.6).

A number of other hazards of a geological nature may be triggered by an earthquake occurrence. These may at times cause severe damage and loss of life.

Landslides

Landslides, ground settlement, and avalanches occur widely with and without earthquakes as a cause. All require special architectural treatment. Landslides and avalanches occur on slopes of a variety of geological materials. For engineering works, the speed at which a landslide develops and moves is a most important feature. Few defenses are available against rapid unexpected movements, but those that move slowly over periods of months to years lend themselves to some precautionary measures. Zoning regulations based on localized geological studies are the most effective mitigation measures.

During an earthquake, a series of seismic waves shakes the ground in all directions, so that under the critical conditions of water saturation, slope, and soil type, even relatively low levels of ground acceleration can cause a landslide. Even if these dynamic accelerations last for only a short time, widespread sliding can occur on marginally stable slopes. During and following the 1971 San Fernando, California, earthquake, for example, thousands of landslides and rockfalls occurred in the San Gabriel Mountains and caused a prominent dust-cloud over the strongly shaken area for days. This was repeated during the nearby 1994 Northridge earthquake.

Another human catastrophe caused by an earthquake-triggered debris avalanche occurred in Peru on May 31, 1970. The earthquake of magnitude 7.7 stimulated a rock avalanche amounting to some 50 million cubic meters of rock, snow, ice, and soil that travelled 15 km from the north peak of Huascarn Mountain, buried the towns around Ranraharca and most of Yungay, and killed at least 18,000 people.

In many instances, smaller landslides and avalanches can be detected in advance by suitable instrumentation installed on the slope with the readings monitored at regular intervals. Means of control can then be applied in appropriate circumstances: for example, removing small volumes of material to relieve the load at the head of the slope and adding material to the toe can be accomplished by earth-moving equipment. For cuts that are man-made, local regulations or ordinances may need to be developed and enforced during construction in a vulnerable area. Slopes made of fill, for example, may be required to be no steeper than 1 vertical to 1-1/2 horizontal, and the fraction of the soil covering the slope must be carefully controlled. Drainage of water away from such slopes is usually specified.

Tsunamis and Seiches

The occurrence of an earthquake and a sudden offset along a major fault under the ocean floor, or a large submarine landslide, displaces the water like a giant paddle, thus producing powerful water waves at the ocean surface. When they reach a coastline, they may run up on land to many hundreds of meters. The elevation above the tide level (at the time of the tsunami) reached by the water is called the **run-up height**. This vertical distance is not the same as the tsunami water wave height offshore or the horizontal distance of water run-up from the normal water edge.

There have been tsunamis in most oceans of the world, but most notably in the Pacific Ocean. The coastline of Hilo, Hawaii, has seen inundation several times, and the giant earthquake in Alaska in 1964 had a run-up height of six meters in Crescent City, California, killing several people. Near the fault motion, 119 people drowned in Alaska.

A seismic sea wave warning system was set up in the Pacific after the devastating Aleutian tsunami of April 1, 1946. The tsunami warning center in Honolulu provides tsunami alerts and alerts local jurisdictions to issue warnings.

The best disaster prevention measures for a tsunami-prone coast involve zoning that controls the types and sizes of buildings that, if any, are permitted. If a site has a high possibility of tsunami incursion, the designer should consider some of the design provisions against flood, such as elevating the building above an estimated waterline. Of course in the case

of locally generated tsunami, provisions must also be made for the severe strong shaking.

Long-period movements of water can also be produced in lakes and reservoirs by large earthquakes. These oscillations of lake levels are termed **seiches**. The November 2003 Denali earthquake in Alaska generated seismic seiches in wells and lakes of the south central United States. In the 1971 San Fernando, California, earthquake water sloshed out of swimming pools, producing some risk.

Liquefaction

A notable hazard from moderate to large earthquakes is the liquefaction of water-saturated soil and sand produced by the ground shaking. In an earthquake, the fine-grained soil below the ground surface is subjected to alternations of shear and stress. In cases of low-permeability soils and sand, the water does not drain out during the vibration, building up pore pressure that reduces the strength of the soil.

Because earthquake shaking of significant amplitude can extend over large areas, and fine-grained soils in a saturated state are so widespread in their distribution, liquefaction has frequently been observed in earthquakes. In some cases, it is a major cause of damage and therefore is a factor in the assessment of seismic risk. Liquefaction in the 1964 Alaskan earthquake caused major disruptions of services and utilities and led to substantial building settlements and displacements. In the 1971 San Fernando, California, earthquake, liquefaction of soils in the San Fernando Dam caused a landslide in the upstream portion of the dam structure that almost resulted in a catastrophic dam failure. Widespread liquefaction resulted in severe damage after the 1811-1812 New Madrid and 1886 Charleston, South Carolina, earthquakes.

Many seismic regions have available liquefaction maps so that the risk of liquefaction at building sites can be assessed. Soil engineers have developed various technical methods of controlling liquefaction, the description of which goes beyond this chapter (see Chapter 3).

105. Assignment 3, Module 5: MMI: https://www.usgs.gov/programs/earthquake-hazards/modified-mercalli-intensity-scale

The effect of an **earthquake** on the Earth's surface is called the intensity. The intensity scale consists of a series of certain key responses such as people awakening, movement of furniture, damage to chimneys, and finally - total destruction. Although numerous*intensity scales* have been developed over the last several hundred years to evaluate the effects of earthquakes, the one currently used in the United States is the Modified Mercalli (MM) Intensity Scale. It was developed in 1931 by the American seismologists Harry Wood and Frank Neumann. This scale, composed of increasing levels of intensity that range from imperceptible shaking to catastrophic destruction, is designated by Roman numerals. It does not have a mathematical basis; instead it is an arbitrary ranking based on observed effects.

The Modified Mercalli Intensity value assigned to a specific site after an earthquake has a more meaningful measure of severity to the nonscientist than the **magnitude** because intensity refers to the effects actually experienced at that place.

The **lower** numbers of the intensity scale generally deal with the manner in which the earthquake is felt by people. The **higher** numbers of the scale are based on observed structural damage. Structural engineers usually contribute information for assigning intensity values of VIII or above.

Intensity	Shaking	Description/Damage
I	Not felt	Not felt except by a very few under especially favorable conditions.
II	Weak	Felt only by a few persons at rest,especially on upper floors of buildings.
III	Weak	Felt quite noticeably by persons indoors, especially on upper floors of buildings. Many people do not recognize it as an earthquake. Standing motor cars may rock slightly. Vibrations similar to the passing of a truck. Duration estimated.
IV	Light	Felt indoors by many, outdoors by few during the day. At night, some awakened. Dishes, windows, doors disturbed; walls make cracking sound. Sensation like heavy truck striking building. Standing motor cars rocked noticeably.
V	Moderate	Felt by nearly everyone; many awakened. Some dishes, windows broken. Unstable objects overturned. Pendulum clocks may stop.
VI	Strong	Felt by all, many frightened. Some heavy furniture moved; a few instances of fallen plaster. Damage slight.
VII	Very strong	Damage negligible in buildings of good design and construction; slight to moderate in well-built ordinary structures; considerable damage in poorly built or badly designed structures; some chimneys broken.
VIII	Severe	Damage slight in specially designed structures; considerable damage in ordinary substantial buildings with partial collapse. Damage great in poorly built structures. Fall of chimneys, factory stacks, columns, monuments, walls. Heavy furniture overturned.
IX	Violent	Damage considerable in specially designed structures; well-designed frame structures thrown out of plumb. Damage great in substantial buildings, with partial collapse. Buildings shifted off foundations.
X	Extreme	Some well-built wooden structures destroyed; most masonry and frame structures destroyed with foundations. Rails bent.

Sources/Usage: Public Domain. *View Media Details*

Abbreviated description of the levels of Modified Mercalli intensity. (Public domain.)

History and Details of MMI

The following is an excerpt from Intensity Distribution and Isoseismal Maps for the Northridge, California, Earthquake of January 17,1994.

The intensity of an earthquake at a location is a number that characterizes the severity of ground shaking at that location by considering the effects ofthe shaking on people, on manmade structures, and on the landscape.

Intensities assigned by the U. S. Geological Survey and (prior to 1973) by agencies in the U. S. Department of Commerce have for many decades been based on the Modified Mercalli Intensity Scale of 1931 (Wood and Neumann, 1931), which we usually refer to simply as the "Modified Mercalli" or "MM" scale. The scale lists criteria that permit the seismologist to represent the severity of ground shaking in a community or part of a community by a number. Experience with the MM scale in the decades since 1931 has shown that some criteria are more reliable than others as indicators of the level of ground shaking. Moreover, construction methods have changed appreciably since the scale was introduced. Assigning of MM intensity values therefore involves use of the original criteria of Wood and Neumann (1931) with amendments and modifications that have been developed in the decades since 1931.

...

The Modified Mercalli scale is given as originally abridged by Wood and Neumann (1931) ... the unabridged scale is reproduced in Stover and Coffman (1993). ... Since 1931 ithas become clear that many phenomena that Wood and Neumann (1931) originally used as criteria to define the highest Modified Mercalli intensities (X and above) are related less to the level of ground shaking than to the presence of ground conditions susceptible to spectacular failure or to the ease with which seismic faulting of different style and depth can propagate to the ground surface. Criteria based on such phenomena are downweighted now in assigning of USGS intensities (Stover and Coffman, 1993).

106. Assignment 3, Module 5: EQ Hazards Q&A: https://www.usgs.gov/programs/earthquake-hazards/science/earthquake-hazards-201-technical-qa

What is spectral acceleration (SA)?

PGA (peak acceleration) is what is experienced by a particle on the ground, and SA is approximately what is experienced by a building, as modeled by a particle mass on a massless vertical rod having the same natural **period** of vibration as the building.

The mass on the rod behaves about like a simple harmonic oscillator (SHO). If one "drives" the mass-rod system at its base, using the seismic record, and assuming a certain damping to the mass-rod system, one will get a record of the particle motion which basically "feels" only the components of **ground motion** with periods near the natural period of this SHO. If we look at this particle seismic record we can identify the maximum **displacement**. If we take the derivative (rate of change) of the displacement record with respect to time we can get the **velocity** record. The maximum velocity can likewise be determined. Similarly for response acceleration (rate of change of velocity) also called response spectral acceleration, or simply spectral acceleration, SA (or Sa).

PGA is a good index to hazard for short buildings, up to about 7 stories. To be a good index, means that if you plot some measure of demand placed on a building, like inter story displacement or base shear, against PGA, for a number of different buildings for a number of different earthquakes, you will get a strong correlation.

PGA is a natural simple design parameter since it can be related to a force and for simple design one can design a building to resist a certain horizontal force.PGV, peak ground velocity, is a good index to hazard to taller buildings. However, it is not clear how to relate velocity to force in order to design a taller building.

SA would also be a good index to hazard to buildings, but ought to be more closely related to the building behavior than peak ground motion parameters. Design might also be easier, but the relation to design force is likely to be more complicated than with PGA, because the value of the period comes into the picture.

PGA, PGV, or SA are only approximately related to building demand/design because the building is not a simple oscillator, but has overtones of vibration, each of which imparts maximum demand to different parts of the structure, each part of which may have its own weaknesses. Duration also plays a role in damage, and some argue that duration-related damage is not well-represented by response parameters.

On the other hand, some authors have shown that non-linear response of a certain structure is only weakly dependent on the **magnitude** and distance of the causative earthquake, so that non-linear response is related to linear response (SA) by a simple scalar (multiplying factor). This is not so for peak ground parameters, and this fact argues that SA ought to be significantly better as an index to demand/design than peak ground motion parameters.

There is no particular significance to the relative size of PGA, SA (0.2), and SA (1.0). On the average, these roughly correlate, with a factor that depends on period.While PGA may reflect what a person might feel standing on the ground in an earthquake, I don't believe it is correct to state that SA reflects what one might "feel" if one is in a building. In taller buildings, short period ground motions are felt only weakly, and long-period motions tend not to be felt as forces, but rather disorientation and dizziness.

What is probability of exceedence (PE)?

For any given site on the map, the computer calculates the ground motion effect (peak acceleration) at the site for all the earthquake locations and magnitudes believed possible in the vicinity of the site. Each of these magnitude-location pairs is believed to happen at some average probability per year. Small ground motions are relatively likely, large ground motions are very unlikely.Beginning with the largest ground motions and proceeding to smaller, we add up probabilities until we arrive at a total probability corresponding to a given probability, P, in a particular period of time, T.

The probability P comes from ground motions larger than the ground motion at which we stopped adding. The corresponding ground motion (peak acceleration) is said to have a P probability of exceedance (PE) in T years.The map contours the ground motions corresponding to this probability at all the sites in a grid covering the U.S. Thus the maps are not actually probability maps, but rather ground motion hazard maps at a given level of probability.In the future we are likely to post maps which are probability maps. They will show the probability of exceedance for some constant ground motion. For instance, one such map may show the probability of a ground motion exceeding 0.20 g in 50 years.

What is the relationship between peak ground acceleration (PGA) and "effective peak acceleration" (Aa), or between peak ground velocity (PGV) and "effective peak velocity" (Av) as these parameters appear on building code maps?

Aa and Av have no clear physical definition, as such. Rather, they are building code constructs, adopted by the staff that produced the Applied Technology Council (1978) (ATC-3) seismic provisions. Maps for Aa and Av were derived by ATC project staff from a draft of the Algermissen and Perkins (1976) probabilistic peak acceleration map (and other maps) in order to provide for design ground motions for use in model building codes. Many aspects of that ATC-3 report have been adopted by the current (in use in 1997) national model building codes, except for the new NEHRP provisions.

This process is explained in the ATC-3 document referenced below, (p 297-302). Here are some excerpts from that document:

- p. 297. "At the present time, the best workable tool for describing the design ground shaking is a smoothed elastic response **spectrum** for single degree-of-freedom systems...
- p. 298. "In developing the design provisions, two parameters were used to characterize the intensity of design ground shaking. These parameters are called the Effective Peak Acceleration (EPA), Aa, and the Effective Peak Velocity (EPV), Av. These parameters do not at present have precise definitions in physical terms but their significance may be understood from the following paragraphs.
- "To best understand the meaning of EPA and EPV, they should be considered as normalizing factors for construction of smoothed elastic response spectra for ground motions of normal duration. The EPA is proportional to spectral ordinates for periods in the range of 0.1 to 0.5 seconds, while the EPV is proportional to spectral ordinates at a period of about 1 second . . . The constant of proportionality (for a 5 percent damping spectrum) is set at a standard value of 2.5 in both cases.
- "...The EPA and EPV thus obtained are related to peak ground acceleration and peak ground velocity but are not necessarily the same as or even proportional to peak acceleration and velocity. When very high frequencies are present in the ground motion, the EPA may be significantly less than the peak acceleration. This is consistent with the observation that chopping off the spectrum computed from that motion, except at periods much shorter than those of interest in ordinary building practice has very little effect upon the response spectrum computed from that motion, except at periods much shorter than those of interest in ordinary building practice. . . On the other hand, the EPV will generally be greater than the peak velocity at large distances from a major earthquake..."

- p. 299. "Thus the EPA and EPV for a motion may be either greater or smaller than the peak acceleration and velocity, although generally the EPA will be smaller than peak acceleration while the EPV will be larger than the peak velocity.
- ". . .For purposes of computing the lateral force coefficient in Sec. 4.2, EPA and EPV are replaced by dimensionless coefficients Aa and Av respectively. Aa is numerically equal to EPA when EPA is expressed as a decimal fraction of the acceleration of **gravity**..."

Now, examination of the tripartite diagram of the response spectrum for the 1940 El Centro earthquake (p. 274, Newmark and Rosenblueth, Fundamentals of Earthquake Engineering) verifies that taking response acceleration at .05 percent damping, at periods between 0.1 and 0.5 sec, and dividing by a number between 2 and 3 would approximate peak acceleration for that earthquake. Thus, in this case, effective peak acceleration in this period range is nearly numerically equal to actual peak acceleration.

However, since the response acceleration spectrum is asymptotic to peak acceleration for very short periods, some people have assumed that effective peak acceleration is 2.5 times less than true peak acceleration. This would only be true if one continued to divide response accelerations by 2.5 for periods much shorter than 0.1 sec. But EPA is only defined for periods longer than 0.1 sec.

Effective peak acceleration could be some factor lower than peak acceleration for those earthquakes for which the peak accelerations occur as short-period spikes. This is precisely what effective peak acceleration is designed to do.

On the other hand, the ATC-3 report map limits EPA to 0.4 g even where probabilistic peak accelerations may go to 1.0 g, or larger. THUS EPA IN THE ATC-3 REPORT MAP may be a factor of 2.5 less than than probabilistic peak acceleration for locations where the probabilistic peak acceleration is around 1.0 g.

The following paragraphs describe how the Aa, and Av maps in the ATC code were constructed.

The USGS 1976 probabilistic ground motion map was considered. Thirteen seismologists were invited to smooth the probabilistic peak acceleration map, taking into account other regional maps and their own regional knowledge. A final map was drawn based upon those smoothing's. Ground motions were truncated at 40 % g in areas where probabilistic values could run from 40 to greater than 80 % g. This resulted in an Aa map, representing a design basis for buildings having short natural periods. Aa was called "Effective Peak Acceleration."

An **attenuation** function for peak velocity was "draped" over the Aa map in order to produce a spatial broadening of the lower values of Aa. The broadened areas were denominated Av for "Effective Peak Velocity-Related Acceleration" for design for longer-period buildings, and a separate map drawn for this parameter.

Note that, in practice, the Aa and Av maps were obtained from a PGA map and NOT by applying the 2.5 factors to response spectra.

Note also, that if one examines the ratio of the SA(0.2) value to the PGA value at individual locations in the new USGS national probabilistic hazard maps, the value of the ratio is generally less than 2.5.

107. Assignment 3, Module 5: Spectral Acceleration:
https://www.sciencedirect.com/topics/earth-and-planetary-sciences/spectral-acceleration

Spectral Acceleration

In subject area: Earth and Planetary Sciences

Spectral acceleration (S_a) is defined as a measure of the 'strength' of seismic ground motion that impacts structures at specific frequencies, describing seismic motion based on the response of elastic single degree of freedom oscillators with a given damping percentage and natural periods. It is primarily used to assess the inertial response of above-ground structures during seismic events.

108. Assignment 3, Module 5: Seismic Waves on Buildings: https://www.usgs.gov/programs/earthquake-hazards/how-seismic-waves-affect-different-size-buildings#:~:text=Large%20structures%20or%20high%20rise,short%20waves%20in%20quick%20succession.

Effect of seismic waves on different size buildings. (Public domain.)

Small Buildings:

Small buildings are more affected, or shaken, by high **frequency** waves (short and frequent).

For example, a small boat sailing in the ocean will not be greatly affected by a large swell. On the other hand several small waves in quick succession can overturn, or capsize, the boat.

In much the same way, a small building experiences more shaking by high frequency **earthquake** waves.

Tall High Rises:

Large structures or high rise buildings are more affected by long **period**, or slow shaking.

For instance, an ocean liner will experience little disturbance by short waves in quick succession. However, a large swell will significantly affect the ship.

Similarly, a skyscraper will sustain greater shaking by long period earthquake waves, than by the shorter waves.

109. Assignment 3, Module 5: JMA Intensity:

https://www.jma.go.jp/jma/en/Activities/inttable.html

Notes

1. As a rule, seismic intensities announced by JMA are values observed using seismic intensity meters installed on the ground or on the first floor of low-rise buildings. This document describes the phenomena and damage that may be observed for individual seismic intensity levels. Seismic intensities are not determined from the observed phenomena described here.
2. Seismic ground motion is significantly influenced by underground conditions and topography. Seismic intensity is the value observed at a site where a seismic intensity meter is installed, and may vary even within the same city. In addition, the amplitude of seismic motion generally differs by floor and location within the same building, as shaking on upper floors may be considerably amplified.
3. Sites with the same level of seismic intensity will not necessarily suffer the same degree of damage, as the effect of tremors depends on the nature of the seismic motion (such as amplitude, period and duration), the type of construction and underground conditions.
4. This document describes typical phenomena that may be seen at individual levels of seismic intensity. In some cases, the level of damage may be greater or less than specified. Not all phenomena described for each intensity level may necessarily occur.
5. The information outlined here is regularly checked at intervals of about five years, and is updated in line with actual phenomena observed in new cases or improvements in the earthquake resistance of buildings and structures.

Human perception and reaction, indoor situation, outdoor situation

Seismic intensity	Human perception and reaction	Indoor situation	Outdoor situation
0	Imperceptible to people, but recorded by seismometers.	-	-
1	Felt slightly by some people keeping quiet in buildings.	-	-
2	Felt by many people keeping quiet in buildings. Some people may be awoken.	Hanging objects such as lamps swing slightly.	-
3	Felt by most people in buildings. Felt by some people walking. Many people are awoken.	Dishes in cupboards may rattle.	Electric wires swing slightly.
4	Most people are startled. Felt by most people walking. Most people are awoken.	Hanging objects such as lamps swing significantly, and dishes in cupboards rattle. Unstable ornaments may fall.	Electric wires swing significantly. Those driving vehicles may notice the tremor.
5 Lower	Many people are frightened and feel the need to hold onto something stable.	Hanging objects such as lamps swing violently. Dishes in cupboards and items on bookshelves may fall. Many unstable ornaments fall. Unsecured furniture may move, and unstable furniture may topple over.	In some cases, windows may break and fall. People notice electricity poles moving. Roads may sustain damage.
5 Upper	Many people find it hard to move; walking is difficult without holding onto something stable.	Dishes in cupboards and items on bookshelves are more likely to fall. TVs may fall from their stands, and unsecured furniture may topple over.	Windows may break and fall, unreinforced concrete-block walls may collapse, poorly installed vending machines may topple over, automobiles may stop due to the difficulty of continued movement.
6 Lower	It is difficult to remain standing.	Many unsecured furniture moves and may topple over. Doors may become wedged shut.	Wall tiles and windows may sustain damage and fall.
6 Upper	It is impossible to remain standing or move without crawling. People may be thrown through the air.	Most unsecured furniture moves, and is more likely to topple over.	Wall tiles and windows are more likely to break and fall. Most unreinforced concrete-block walls collapse.
7		Most unsecured furniture moves and topples over, or may even be thrown through the air.	Wall tiles and windows are even more likely to break and fall. Reinforced concrete-block walls may collapse.

Wooden houses

Seismic intensity	Wooden houses	
	High earthquake resistance	Low earthquake resistance
5 Lower	-	Slight cracks may form in walls.
5 Upper	-	Cracks may form in walls.
6 Lower	Slight cracks may form in walls.	Cracks are more likely to form in walls. Large cracks may form in walls. Tiles may fall, and buildings may lean or collapse.
6 Upper	Cracks may form in walls.	Large cracks are more likely to form in walls. Buildings are more likely to lean or collapse.
7	Cracks are more likely to form in walls. Buildings may lean in some cases.	Buildings are even more likely to lean or collapse.

(Note 1) Wooden houses are classified into two categories according to their earthquake resistance, which tends to be higher for newer foundations. Earthquake resistance tends to be low for structures built up to 1981, and high for those built since 1982. However, to maintain a certain range of earthquake resistance according to differences in structure and wall arrangement, resistance is not necessarily determined only by foundation age. The earthquake resistance of existing buildings can be ascertained through quakeproofing diagnosis.
(Note 2) The walls in this table are assumed to be made of mud and/or mortar. Mortar in a wall with a weak base can easily break off and fall, even under conditions of low deformation.
(Note 3) Damage to wooden houses depends on the period and duration of seismic waves. In some cases (such as the Iwate-Miyagi Nairiku Earthquake of 2008), few buildings sustain damage in relation to the level of seismic intensity observed.

Reinforced-concrete buildings

Seismic intensity	Reinforced-concrete buildings	
	High earthquake resistance	Low earthquake resistance
5 Upper	-	Cracks may form in walls, crossbeams and pillars.
6 Lower	Cracks may form in walls, crossbeams and pillars.	Cracks are more likely to form in walls, crossbeams and pillars.
6 Upper	Cracks are more likely to form in walls, crossbeams and pillars.	Slippage and X-shaped cracks may be seen in walls, crossbeams and pillars. Pillars at ground level or on intermediate floors may disintegrate, and buildings may collapse.
7	Cracks are even more likely to form in walls, crossbeams and pillars. Ground level or intermediate floors may sustain significant damage. Buildings may lean in some cases.	Slippage and X-shaped cracks are more likely to be seen in walls, crossbeams and pillars. Pillars at ground level or on intermediate floors are more likely to disintegrate, and buildings are more likely to collapse.

(Note 1) Earthquake resistance tends to be higher for newer foundations. The value tends to be low for structures built up to 1981, and high for those built since 1982. However, to maintain a certain range of earthquake resistance according to differences in structure and 2D/3D arrangement of reinforced walls, resistance is not necessarily determined only by foundation age. The earthquake resistance of existing buildings can be ascertained through quakeproofing diagnosis.
(Note 2) Slight cracks may form in reinforced-concrete buildings without their core structure being affected.

Situation of ground and slopes, etc.

Seismic intensity	Situation of ground	Situation of slopes, etc.
5 Lower	Small cracks may form and liquefaction*1may occur.	Rock falls and landslips may occur.
5 Upper		
6 Lower	Cracks may form.	Landslips and landslides may occur.
6 Upper	Large cracks may form.	Landslips are more likely to occur; large landslides and massif collapses may be seen*2.
7		

*1 Liquefaction may be seen in areas with a high groundwater level and loose sand deposits. Damage observed as a result of liquefaction includes spouts of muddy water from the ground, outbreaks of subsidence in riverbanks and quays, elevation of sewage pipes and manholes, and leaning or destruction of building foundations.
*2 When large landslides and massif collapses occur, dams may form depending on geographical features, and debris flow may occur due to the large quantities of sediment produced.

Influence on utilities and infrastructure, etc.

Suspension of gas supply	In the event of shaking with a seismic intensity of about 5 Lower or more, gas meter with safety devices are tripped, stopping the supply of gas. In the event of stronger shaking, the gas supply may stop for entire local blocks*.
Suspension of water supply, electrical blackouts	Suspension of water supply and electrical blackouts may occur in regions experiencing shaking with a seismic intensity of about 5 Lower or more*.
Suspension of railroad services, regulation of highways, etc.	In the event of shaking with a seismic intensity of about 4 or more, services on railroads or highways may be stopped for safety confirmation. Speed control and traffic regulations are performed according the judgment of the relevant bodies. (Standards for safety confirmation differ by organization and area.)
Disruption to lines of communication such as telephones	In the event of an earthquake, telephone line congestion may occur as a result of increased use related to safety confirmation around regions of strong shaking. To combat this, telecommunications providers offer message boards and message dial services for use in disasters resulting from earthquakes with a seismic intensity of about 6 Lower or more.
Suspension of elevator services	In the event of shaking with a seismic intensity of about 5 Lower or more, elevators with earthquake control devices will stop automatically for safety reasons. Resumption of service may be delayed until safety is confirmed.

*In the event of shaking with a seismic intensity of 6 Upper or more, gas, water and electric supplies may stop over wide areas.

Effects on large-scale structures

Shaking of skyscrapers from long-period ground motion*	Due to their longer characteristic period, skyscrapers react less to earthquakes than general reinforced-concrete buildings, which have a shorter characteristic period. However, they exhibit slow shaking over a long time in response to long-period ground motion. If motion is strong, poorly fixed office appliances may move significantly, and people may have to hold onto stable objects to maintain their position.
Sloshing of oil tanks	Sloshing of oil tanks occurs in response to long-period ground motion. As a result, oil outflows or fires may occur.
Damage or collapse of ceilings etc. at institutions covering large spaces	In institutions covering large spaces such as gymnasiums or indoor pools, ceilings may shake significantly and sustain damage or collapse, even in cases where ground motion is not severe enough to cause other structural damage.

*Occasionally, when a large earthquake occurs, long-period seismic waves reach locations far from the hypocenter; such waves may be amplified over plains depending on the characteristic period of the ground, thus extending their duration.

110. Assignment 3, Module 5: Macroseismic Intensity:
https://www.guycarp.com/insights/2024/09/revolutionizing-seismic-data-international-macroseismic-scale-reinsurance-implications.html

The International Macroseismic Scale (IMS) provides a common language for describing earthquake shaking intensities across the globe, facilitating effective communication among scientists, engineers, emergency managers, insurers and the public. Read on to learn about the evolution of ground-shaking intensity scales, the need for a unified international scale, and the role of the (re)insurance industry's collaboration in supporting this effort.

Macroseismic Intensity Scales: Past, Present and Future

Introduction to shaking intensities

A macroseismic or seismic intensity scale is a qualitative measure of shaking from earthquakes, based on the resulting damage to structures and eyewitness observations. The nature of these scales allows scientists to leverage historical sources to extend the record of observed ground motions further back in time, before the advent of seismometers, which instrumentally record ground motions. Even today, people vastly outnumber seismometers, hence crowd-sourced shaking information illuminates the distribution of ground motions in more detail than the seismic network can alone. Intensity scales typically range from 1 (shaking not felt) to 10 (total destruction).

Past

Previously, independent macroseismic intensity scales were used around the world, such as Modified Mercalli Intensity Scale (MMI), European Macroseismic Scale (EMS), Mercalli Cancani Seiberg scale (MCS), and Japan Meteorological Agency (JMA) Seismic Intensity Scale. These scales assigned intensity values per structure or observation (Figure 1).

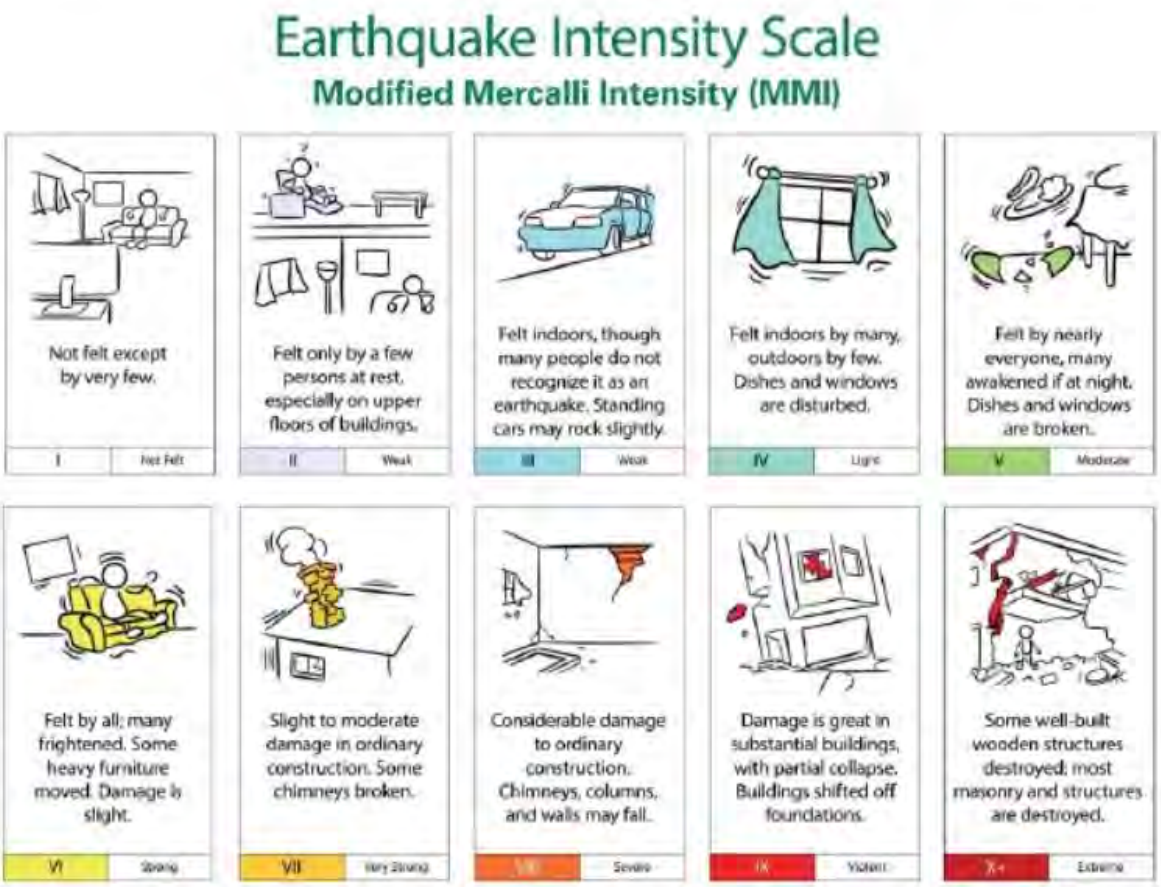

Figure 1: A sample illustration of MMI indicators. Source: US Geological Survey, public domain image

Present

With the advent of internet crowd-sourced and aggregated data, shaking measures have become more representative. Platforms like the US Geological Survey's "Did You Feel It?" allow for the rapid collection of data from citizen scientists, leading to improved intensity assessments (Figure 2).

Figure 2: Overview of USGS' "Did You Feel It?" Platform. Courtesy of D. Wald at the US Geological Survey

The online questionnaires correspond to the same shaking indicators in past scales, most closely following MMI, but have more precision due to the increased number of reports gathered.

International Macroseismic Scale

Future

The development of a unified international scale is crucial, especially for high intensities (7+) that contribute most to seismic risk. This unified scale would eliminate the need for conversion between different macroseismic scales, making risk assessments more efficient and accurate.

Countries would contribute appendices based on their typical building stock, describing their vulnerabilities and damage grades, thus creating a globally comprehensive and standardized measure (Figure 3).

Classification of damage to masonry buildings	
	**Grade 1: Negligible to slight damage** **(no structural damage, slight non-structural damage)** Hair-line cracks in very few walls. Fall of small pieces of plaster only. Fall of loose stones from upper parts of buildings in very few cases.
	**Grade 2: Moderate damage** **(slight structural damage, moderate non-structural damage)** Cracks in many walls. Fall of fairly large pieces of plaster. Partial collapse of chimneys.
	**Grade 3: Substantial to heavy damage** **(moderate structural damage, heavy non-structural damage)** Large and extensive cracks in most walls. Roof tiles detach. Chimneys fracture at the roof line; failure of individual non-structural elements (partitions, gable walls).
	**Grade 4: Very heavy damage** **(heavy structural damage, very heavy non-structural damage)** Serious failure of walls; partial structural failure of roofs and floors.
	**Grade 5: Destruction** **(very heavy structural damage)** Total or near total collapse.

Figure 3: Overview of USGS' "Did You Feel It?" Platform. Courtesy of D. Wald at the US Geological Survey

- **Improved Communication**: The IMS provides a common language for describing earthquake intensities, facilitating effective communication among scientists, engineers, emergency managers and the general public. This standardized scale ensures that information about earthquake impacts is consistent and easily understood across different regions and countries.
- **Enhanced Risk Assessment:** The IMS can support more accurate and reliable assessment of earthquake risks. A standardized measure of intensity can enable better estimation of potential damage to buildings, infrastructure and communities immediately following an earthquake. This timely information is crucial for (re)insurers, policymakers and urban planners.
- **Global Comparison:** The IMS enables global comparison of earthquake events, allowing for enhanced understanding of seismic activity patterns and trends. It facilitates sharing of best practices and lessons learned from regions with different levels of seismic risk, potentially leading to more effective risk reduction strategies worldwide.

Current Challenges and Opportunities for Industry Support

- **Data Availability and Quality:** Successful implementation of the IMS relies on the availability and quality of data. Thus, data collection systems should be robust, standardized and accessible. Collaboration between national and international agencies, academic institutions, and industry stakeholders is essential to address data gaps and improve data quality.
- **Regional Variations:** Different regions may have unique characteristics that need to be considered and require flexibility in the framework when implementing the IMS. Supplements specific to each region can provide additional information on local building practices, geological conditions, and societal factors that influence earthquake impacts.
- **Public Awareness and Education:** The successful adoption of the IMS requires public awareness and education initiatives. Efforts should be made to educate the general public about the scale, its meaning, and its implications for personal safety and preparedness. This can be achieved through public outreach campaigns, educational programs in schools, collaboration with media outlets, and by insurance carriers facilitating policyholder education.

The IMS represents a significant advancement in earthquake hazard and risk assessment. By transitioning from independent scales to a unified international scale, the IMS can improve the accuracy and efficiency of risk assessments. Industry collaboration, particularly from the (re)insurance sector, is vital in supporting the development and implementation of the IMS. By actively participating in this effort, (re)insurers can contribute to the improvement of catastrophe risk assessment and ensure the relevance of the IMS for the industry as a whole.

How Can the (Re)Insurance Industry Contribute and Collaborate?

Industry-Level: As the (re)insurance industry has a long track record of managing diverse global portfolios exposed to seismic risk, it has invested in research and development on large scales due to the global and infrequent nature of the peril. The (re)insurance industry has been a major sponsor of global earthquake hazard and risk estimation efforts over decades. Collaborative initiatives like the Global Earthquake Model (GEM) demonstrate the industry's commitment to coordination and cooperation. Collaboration and supporting IMS initiatives would be a natural extension of on-going work and can build up the global earthquake hazard risk estimation.

Company-Level: Contributing to the development, adoption and application of the IMS would be a natural next step in the ongoing collaboration between science and the (re)insurance industry. By actively participating in this effort and building capabilities that bring the IMS to the industry, there is potential for enhancing risk management activities. From a catastrophe modeling lens, globally consistent frameworks and metrics help with evaluation and management of a complex and infrequent peril.

Small Group to Individual Level: Information from post-event reconnaissance and damage assessments are crucial for implementing the IMS. This information can be integrated into the claims adjustment process, which could then be aggregated for portfolio risk management; there are similar practices in emergency management. Opportunities for (re)insurers to aggregate and share exposure characteristics and performance data, including the data collected from building or equipment sensors, would contribute to IMS development. As explained earlier, crowd-sourcing intensity data is tremendously valuable, but does require participation from the public. This can be the first step in contributing to the larger effort.

111. Assignment 3, Module 6: FEMA 454, Sections 2.6.1 and 2.6.2: https://www.wbdg.org/FFC/DHS/fema454.pdf

2.6.1 Empirical Attenuation Curves

As has been outlined in the previous sections, the estimation of the earthquake hazard in a region or at a site requires the prediction of ground motions. The empirical estimation of seismic hazard curves is a necessary step. It follows that hazard calculations involve a number of assumptions and extrapolations. The common initial difficulty is ignorance of the actual seismic wave attenuation for the site in question, despite the recent publication of a variety of average curves for certain regions. The importance of attenuation factors in calculation of predicted ground motion at arbitrary distances has led to competing empirical attenuation forms based on available intensity measurements and geological knowledge.

Usually wave attenuation changes significantly from one geological province to another, and local regional studies are advisable to calibrate the parameters involved.

As mentioned in Section 2.4, although different measures of earthquake magnitude are still used, particularly with historical data, the moment magnitude (M_W) is now usually adopted as a standard measure of size in attenuation statistics. Also, nowadays, some form of "closest" distance to the rupture is used as the distance parameter rather than epicentral or hypocentral distance. It is important to use the appropriate distance measure for a given attenuation relation. The most common source, ray path, and site parameters are magnitude, distance, style-of-fault, directivity, and site classification. Rupture directivity is defined in detail in Section 2.4.3 and is not discussed here. In some studies, additional parameters are used: hanging-wall flag, rupture directivity parameters, focal depth, and soil depth classification.

Table 2-2: Examples of near-fault strong-motion recordings from crustal earthquakes with large peak horizontal ground motions

Earthquake	Magnitude M_W	Source Mechanism	Distance km*	Acceleration (g)	Velocity (cm/sec)	Displace (cm)
1940 Imperial Valley (El Centro, 270)	7.0	Strike-Slip	8	0.22	30	24
1971 San Fernando (Pacoima 164)	6.7	Thrust	3	1.23	113	36
1979 Imperial Valley (EC #8, 140)	6.5	Strike-Slip	8	0.60	54	32
Erzican (Erzican, 1992)	6.9	Strike-Slip	2	0.52	84	27
1989 Loma Prieta (Los Gatos, 000)	6.9	Oblique	5	0.56	95	41
1992 Lander (Lucerne, 260)	7.3	Strike-Slip	1	0.73	147	63
1992 Cape Mendocino (Cape Mendocino, 000)	7.1	Thrust	9	1.50	127	4
1994 Northridge (Rinaldi, 228)	6.7	Thrust	3	0.84	166	29
1995 Kobe (Takatori, 000)	6.9	Strike-Slip	1	0.61	127	36
1999 Kocaeli (SKR, 090)	7.4	Strike-Slip	3	0.41	80	205
1999 Chi-Chi (TCU068, 000)	7.6	Thrust	1	0.38	306	940

* distence km shows surface distance from fault

There are also differences in site classification schemes in different regions that make comparison of estimates of ground motions from alternative estimates difficult. Broad site categories such as "rock," "stiff-soil," and "soft-soil" are common and affect ground motions (Figure 2-12), but more quantitative site classifications based on the S-wave velocity, such as the average S-wave speed in the top 30 m, are now preferred. Most attenuation relations simply use a site category such as "deep soil"; however, this general category covers a wide range of soil depths from less than 100 m to several kilometers of sediments. Some attenuation relations use an additional site parameter to describe the depth of the sediment.

For thrust faults, high-frequency ground motions on the upthrown block (hanging-wall side of a thrust fault) are much larger than on the downdropped block (footwall). This increase in ground motions on the hanging wall side is in part an artifact of using a rupture distance measure, but may also be due to the dynamics of waves interacting with the dipping fault plane and the surface of the earth. If a site on the hanging wall and footwall are at the same rupture distance, the site on the hanging wall side is closer to more of the fault than the site on the footwall side. Such difference was marked in damage patterns to houses and other structures in the 1999 Chi Chi, Taiwan, earthquake ($M_W = 7.6$).

In the eastern U.S., incorporation of a variation in the distance slope of the attenuation relation to accommodate the increase in ground motions due to supercritical reflections from the base of the crust has been suggested. Typically, this result leads to a flattening of the attenuation curve at distances of about 100 km). This is most significant for regions in which the high activity sources are at a large distance from the site.

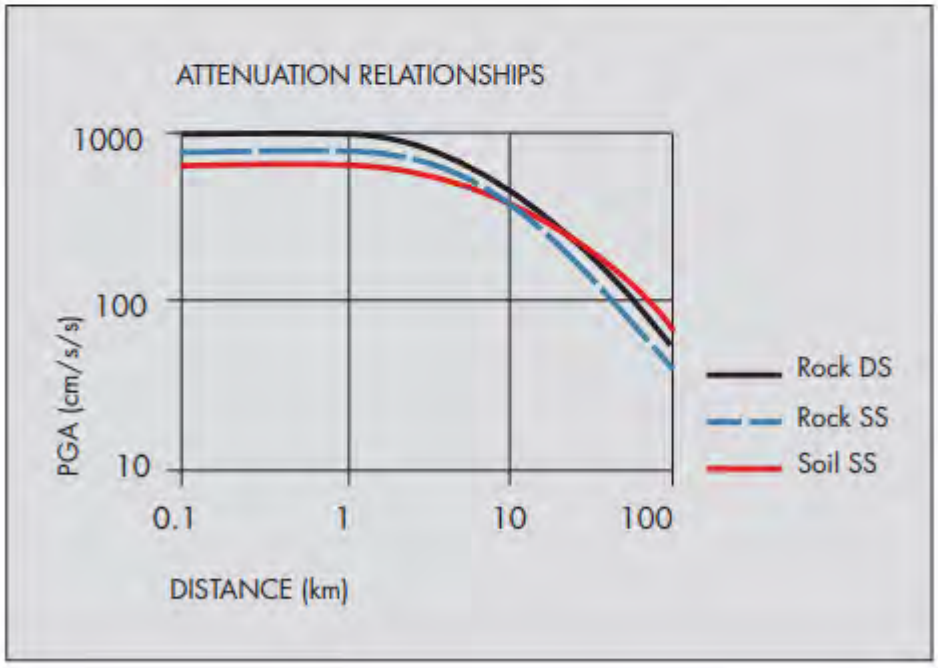

Figure 2-12: Examples of attenuation curves for a M_W7 earthquake obtained by data regression, illustrating the effects of a **site** type: rock (blue dashed) vs. deep soil (red), and **event** type: strike-slip fault (blue dashed) vs. reverse fault (black)

SOURCE: ABRAHAMSON AND SILVA, 1997

An important statistical issue in developing attenuation relations is the uneven sampling of the data from different earthquakes. For example, in some cases, an earthquake may have only one or two recordings (e.g., the 1940 El Centro event), whereas, some of the recent earthquakes have hundreds of recordings (e.g., the 1999 Chi Chi earthquake). The use of statistical weights can reduce this uneven sampling problem. There are two extremes: give equal weight to each data point or give equal weight to each earthquake. The random-effects model seems best. It uses a weighting scheme that varies between giving equal weight to each earthquake and equal weight to each data point, depending on the distribution of the data.

In addition to the median measure of ground motion, the standard deviation of the measured ground motion parameters is also important for either deterministic or probabilistic hazard analyses. Worldwide, it is common to use a constant standard deviation, but recently, several attenuation relations have attributed magnitude or amplitude dependence to the standard deviation.

2.6.2 Probabilistic Seismic Hazard Analysis (PSHA) and Building Codes

Probabilistic Seismic Hazard Analysis provides an estimate of the likelihood of hazard from earthquakes based on geological and seismological studies. It is probabilistic in the sense that the analysis takes into consideration the uncertainties in the size and location of earthquakes and the resulting ground motions that could affect a particular site. Seismic hazard is sometimes described as the probability of occurrence of some particular earthquake characteristic (such as peak ground acceleration) For statistical reasons, these probabilities cover a range of values, and because risk involves values being greater than expected, the word "exceedance" has been coined as explained below.

Probabilistic analysis uses four basic steps in order to characterize the probable seismic hazard:

- Identification of the seismic source or faults.

This often includes the identification of surface faulting features that can be recognized as active. Seismic sources may be specified as site specific, for an active source region or, when geologic information is poor,

for random occurrence of active faults in the study region. Once the faulting hazard is identified, earthquake occurrence statistics are compiled, which might be in the form of annual rates of seismic events or, in an active regions of known faults, more specific information provided by paleoseismic studies such as dating episodes of fault offsets. (Paleoseismology involves digging to expose the underground face of a fault, so that historic offsets can be made visible and material suitable for radiocarbon age dating can be obtained). The objective is to obtain a measure of the frequency of earthquakes within a given time period as a function of magnitude that may be expressed as a probabilistic statement (or mathematical likelihood) of the earthquake occurrence.

- Characterization of annual rates of seismic events.

As an example, if there is one magnitude 7 earthquake in a given region every 50 years, then the annual rate of occurrence is 0.5. Commonly used maps to express probability are cast in terms of a 50-year return period, and are used to determine the ground motion values to be specified in building codes and used in seismic design.

Since damaging ground motions can result from nearby moderate earthquakes as well as large distant earthquakes, the recurrence rates for each magnitude range must be determined.

- Development of attenuation relationships

Attenuation relationships and their uncertainty due to limited information must be developed so that the ground motion parameters for each of the sources developed in the first step can be related to the distance of the study site from them.

- Combining factors

The annual recurrence and the attenuation are combined to determine the site-specific hazard.

Until the 1990s, seismic building codes used a single map of the United States that divided the country into numbered seismic zones (0,1,2,3,4) in which each zone was assigned a single acceleration value in % g which was used to determine seismic loads on the structure.

Starting in the 1970s, new hazard maps began to be developed on a probabilistic basis. In the 1994 *NEHRP Recommended Provisions* (FEMA 222A), two maps of the US were provided in an appendix for comment. They showed effective peak acceleration coefficients and effective peak velocity–related coefficients by use of contour lines that designated regions of equal value. The ground motions were based on estimated probabilities of 10% of exceedance in various exposure times (50, 100 and 250 years). The 1997 *Recommended Provisions* (FEMA 302) provided the first spectral response maps to pass consensus ballot. This lead to the current maps which, with some revisions, are now used in the 2003 *NEHRP Provisions* (FEMA 450), the ASCE *Prestandard and Commentary for the Seismic Rehabilitation of Buildings* (FEMA 356), and the *International Building Code.*

The probabilistic analysis is typically represented in maps in the form of a percentage probability of exceedance in a specified number of years. For example, commonly used probabilities are a 10% probability of exceedance in 50 years (a return period of about 475 years) and a 2% probability of exceedance in 50 years (a return period of about 2,500 years). These maps show ground motions that may be equaled but are not expected to be exceeded in the next 50 years: the odds that they will not be exceeded are 90% and 98%, respectively.

Seismic hazard probability maps are produced by the United States Geological Survey (USGS) as part of the National Seismic Hazard Mapping Project in Golden, Colorado. The latest sets of USGS of maps provide a variety of maps for Peak Ground Acceleration and Spectral Acceleration, with explanatory material, and are available on the USGS web site

The USGS map shown in Figure 2-13 is a probabilistic representation of hazard for the coterminous United States. This shows the spectral acceleration in %g with a 2% probability of exceedance in 50 years: this degree of probability is the basis of the maps used in the building codes.

The return period of 1 in 2,500 years may seem very infrequent, but this is a statistical value, not a prediction, so some earthquakes will occur much sooner and some much later. The design dilemma is that if a more frequent earthquake - for example, the return period of 475 years - were used in the lower seismic regions, the difference between the high and low-probability earthquakes is a ratio of between 2 and 5. Design for

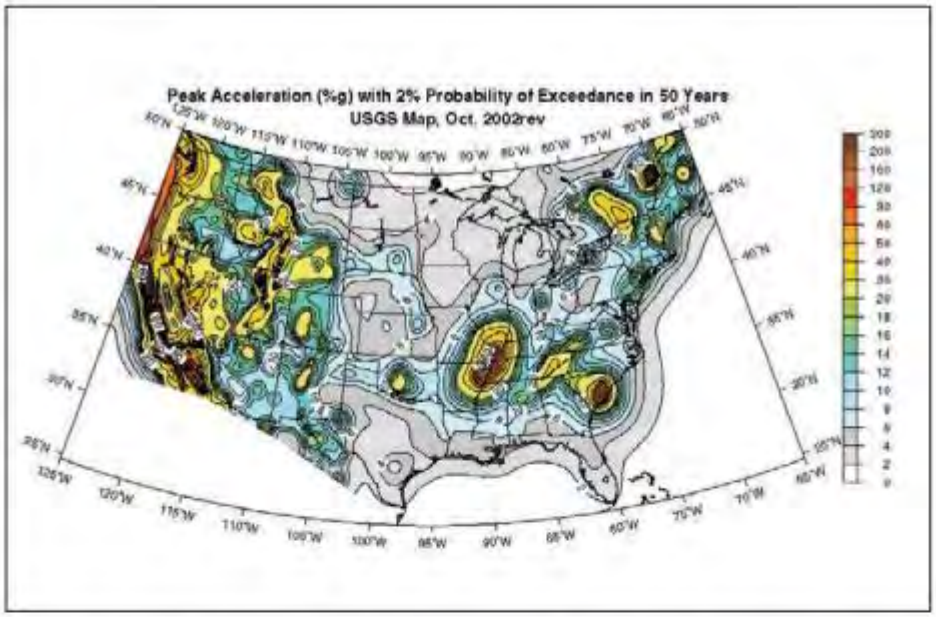

Figure 2-13: Spectral Acceleration values in %g with a 2% Probability of Exceedance in 50 years for the coterminous United States. The color scale to the right relates to the %g values.

SOURCE: USGS NATIONAL SEISMIC HAZARD MAPPING PROJECT

the high-probability earthquake would be largely ineffective when the low-probability event occurred

In practical terms, the building designer must assume that the large earthquake may occur at any time. Thus, use of the 2,500 return period earthquake in the lower seismic regions ensures protection against rare earthquakes, such as the recurrence of the 1811-1812 earthquake sequence in New Madrid, Missouri, or the 1898 Charleston, South Carolina, earthquake. It was judged that the selection of 2 per cent in 50 years likelihood as the maximum considered earthquake ground motion would result in acceptable levels of seismic safety for the nation.

The acceleration experienced by a building will vary depending on the period of the building, and in general short-period buildings will experience more accelerations than long-period buildings, as shown in the response spectrum discussed in section 4.5.3. The USGS maps recognize this phenomenon by providing acceleration values for periods

of 0.2 seconds (short) and 1.0 seconds (long). These are referred to as spectral acceleration (SA), and the values are approximately what are experienced by a building (as distinct from the peak acceleration which is experienced at the ground). The spectral acceleration is usually considerably more than the peak ground accelerations, for reasons explained in Section 4.7.

Figure 2-14 shows 2%/50 year probability maps for the central and southern United States for 0.2 seconds, and Figure 2-15 shows a similar map for 1.0 second spectral acceleration.

These USGS probability maps provide the basis for USGS maps used in building codes that provide design values for spectral acceleration used by structural engineers to calculate the seismic forces on a structure. These design value maps differ by use of a maximum considered earthquake (MCE) for the regions. For most regions of the country the maximum considered earthquake is defined as ground motion with a uniform likelihood of exceedance of 2% in 50 years (a return period of about 2,500 years) and is identical to the USGS probability maps. However, in regions of high seismicity, such as coastal California, the seismic hazard is typically controlled by large-magnitude events occurring on a limited number of well-defined fault systems. For these regions, rather than using the 2% in 50-year likelihood, it is considered more appropriate to directly determine the MCE ground motions based on the characteristic earthquakes of those defined faults.

The 2000 *NEHRP Provisions* and the 2003 *IBC* provide maps that show the MCE for the Coterminous United States, California and Hawaii, the Utah region, Alaska, the Puerto Rico region and Guam. These maps are produced in black and white line with no color coding. A CD-ROM is available from FEMA, USGS, ACSF and IBC that includes a software package that can provide map values based on latitude/longitute or postal zip code.

Finally, the acceleration values shown on the maps are not used directly for design. Instead, they are reduced by 1/3; this value is termed the Design Earthquake (DE) and is the value used by engineers for design. The reason for this is that engineers believe that the design provisions contain at least a margin of 1.5 against structural failure. MCE is inferred to

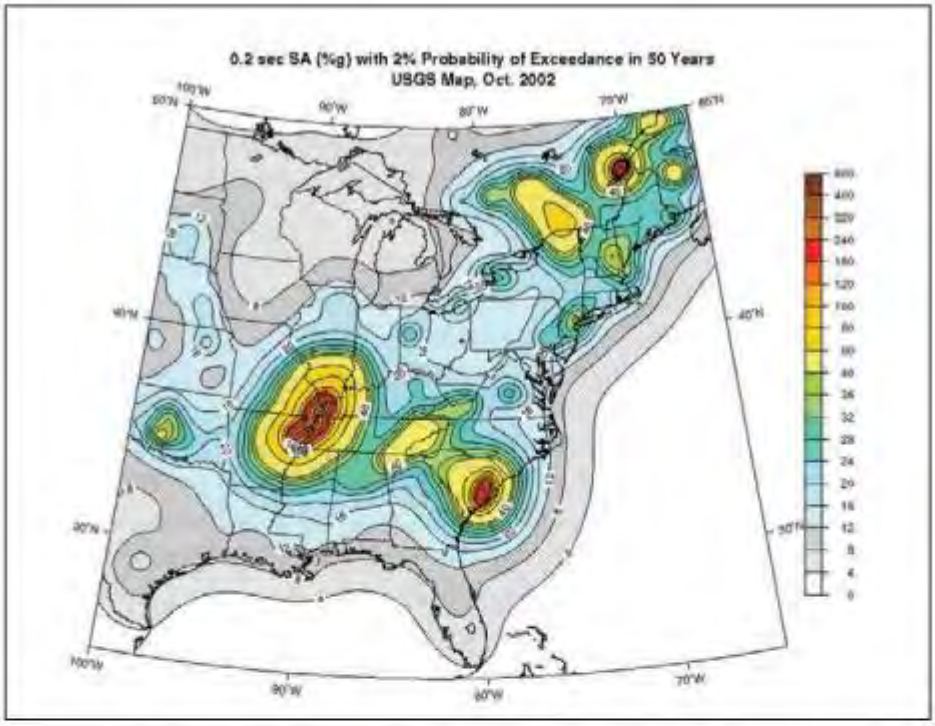

Figure 2-14: 0.2 second (short) period Spectral Acceleration values in %g with a 2% Probability of Exceedance in 50 years for Central and Southern United States.

SOURCE: USGS NATIONAL SEISMIC HAZARD MAPPING PROJECT

provide collapse prevention level, while the actual design is done using the design earthquake (DE), which is 2/3 MCE for code-level life-safety protection-level. This belief is the result of the study of the performance of many types of buildings in earthquakes, mostly in California.

There have been numerous comments that the level of seismic hazard being used in the central and eastern United States results in design values that are unreasonably high. As a result, a review and re-verification of the 2% in 50 years ground-shaking probability for use as the MCE will be implimented. This study is being done as part of the 2008 *NEHRP Recommended Provisions* update process.

112. Assignment 3, Module 6: Seismic Hazard Maps: https://www.usgs.gov/faqs/what-seismic-hazard-what-a-seismic-hazard-map-how-are-they-made-how-are-they-used-why-are#:~:text=Hazard%20maps%20can%20be%20used,problems%20in%20the%20western%20US.

What is seismic hazard? What is a seismic hazard map and how are they used?

Seismic hazard is the hazard associated with potential earthquakes in a particular area, and a seismic hazard map shows the relative hazards in different areas. The maps are made by considering what we currently know about:

1. Past faults and earthquakes
2. The behavior of seismic waves as they travel through different parts of the U.S. crust
3. The near-surface site conditions at specific locations of interest

Hazard maps can be used for land-use planning, mitigation, and emergency response.

The different maps show different probabilities that are selected to provide an idea of the relative range of hazard across the US. The larger probabilities indicate the level of ground motion likely to cause problems in the western US. The smaller probabilities show how unlikely damaging ground motions are in many places of the eastern US. However, basically the values chosen reflect the more recent history in earthquake engineering.

How does an individual person select a map? Technical users probably have to follow predefined rules. A non-technical person may be interested in avoiding living in a location where significant shaking will cause worry, deciding on whether to carry earthquake insurance, or deciding whether to do some rehabilitation for an existing dwelling. The probability level chosen should reflect how anxious one is to avoid earthquake shaking.

Learn more:

- Introduction to the National Seismic Hazard Maps
- Earthquake Hazards 101: The Basics provides more details on all of these questions.
- Unified Hazard Tool - For advanced users: earthquake hazard and probability maps, hazard curves, and deaggregation

Explore Search

Natural Hazards

earthquakes

earthquake probabilities

Earthquake Hazards

Natural Hazards

113. Assignment 3, Module 6: Earthquake Hazards: https://www.usgs.gov/natural-hazards/earthquake-hazards/science/earthquake-hazards-101-basics?qt-science_center_objects=0#qtscience_center_objects

What is earthquake hazard?

Earthquake ground shaking varies from place to place and the hazard mapping in this project will show this variability. The mapped hazard refers to an estimate of the probability of exceeding a certain amount of ground shaking, or ground motion, in 50 years. The hazard depends on the magnitudes and locations of likely earthquakes, how often they occur, and the properties of the rocks and sediments that earthquake waves travel through.

What are hazard maps?

The National Seismic Hazard Model (NSHM) develops maps to show the distribution of earthquake shaking levels that have a certain probability of occurring in the United States and the U.S. Territories. These maps are created to provide the most accurate and detailed information possible to assist engineers in designing buildings, bridges, highways, and utilities that will withstand shaking from earthquakes. Additionally, the datasets, models, and maps are used to create and update the building codes that are now used by more than 20,000 cities, counties, and local governments to help establish construction requirements necessary to preserve public safety.

Applications of the Hazard Maps:

1. Building Codes (NEHRP, IBC, ASCE 7) About building codes? (FEMA)
2. Highway bridge design nationwide (AASHTO)
3. Insurance rates
4. Business and land-use planning
5. Estimations of stability and landslide potentials of hillsides
6. Construction standards for waste-disposal facilities (EPA)
7. Retrofit priorities
8. Allocation planning of assistance funds for education and preparedness (FEMA)
9. Concerned general public

How to read a hazard map

Suppose the figure on the right is a hazard map for the area of Nowhere City developed for a 50-year time span and a 5% chance of exceedance.

We would read the shaking hazards for Nowhere City as:
The earthquake peak ground acceleration (PGA) that has a 5% chance of being exceeded in 50 years has a value between 4 and 8% g (percent of gravity, g).

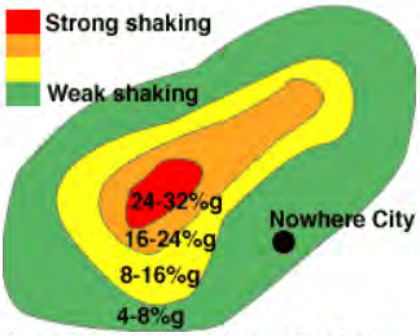

Sources/Usage: Public Domain. View Media Details

Example hazard map for Nowhere City. (Public domain.)

What is probabilistic ground motion, and why use it for hazard determination?

Probabilistic ground motion maps depict earthquake hazard by showing, by contour values, the earthquake ground motions (of a particular frequency) that have a common given probability of being exceeded in 50 years (and other time periods).The ground motions being considered at a given location are those from all future possible earthquake magnitudes at all possible distances from that location. The ground motion coming from a particular magnitude and distance is assigned an annual probability.

So the goal of a hazard map is to depict the potential shaking hazard from future earthquakes. The following sequence explains why probabilistic ground motion is the best way to accomplish this goal:

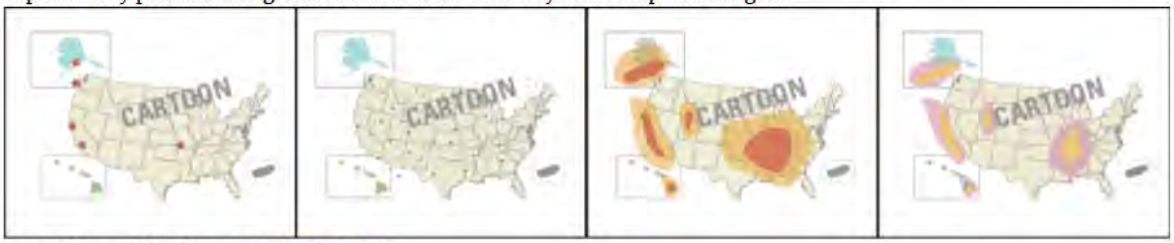

Sources/Usage: Public Domain. View Media Details

The sequence depicts steps 1-4 that follow below, respectively. This sequence shows why probabilistic ground motion is used for hazard determination. (Public domain.)

Step 1

We can use a map showing the location and date of significant damaging earthquakes in the United States, *but* a map like that would not generalize from seismic history to indicate where other damaging earthquakes might be expected to occur in the future. To add this missing information...

Step 2

We can add to the map all the smaller earthquakes that have occurred in the past, and then we can use that seismic history information to assume that damaging earthquakes can also occur in the future in the same locations as the smaller earthquakes, *but* we can't tell what the size of the expected ground motion hazard is. To add this missing information...

Step 3

We can make a map of the historical maximum seismic intensities (amount of shaking) to estimate the size of the hazard, *but* we are ignoring the fact that earthquakes occur at a much lower rate in some parts of the U.S. than in others. To add this missing information...

Step 4

We can incorporate **seismicity** rates in different parts of the country into the map using the methods of probabilistic ground motion hazard, *but* now the historical seismicity information is overemphasized compared to the evidence of seismic potential determined from geologic data. To add this missing information...

Sources/Usage: Public Domain. *View Media Details*

Example model of future seismicity in the U.S. (Public domain.)

Step 5

Finally, we add a model of future seismicity based on the prehistoric geologic information. In this way we arrive at the final hazard map.

The method assumes a reasonable future catalog of earthquakes, based upon historical earthquake locations and geological information on the recurrence rate of fault ruptures. When all the possible earthquakes and magnitudes have been considered, one can find a ground motion value such that the annual rate of its being exceeded has a certain value. Hence, on a given map, for a given probability of exceedance, PE, locations shaken more frequently, will have larger ground motions.

For a LARGE exceedance probability, the map will show the relatively likely ground motions, which are LOW ground motions, because small magnitude earthquakes are much more likely to occur than are large magnitude earthquakes.

For a SMALL exceedance probability, the map will emphasize the effect of less likely events: larger-magnitude and/or closer-distance events, producing overall LARGE ground motions on the map. The maps have this format, because they are designed to be useful in building codes, in which we assume that, for the most part, all buildings would be built to the same level of safety. For other applications, maps of another format might be more useful. For instance, many buildings across the US are built more or less the same, regardless of earthquake hazard. If we knew that a particular type of building was likely to fail at a particular ground motion level, we could make a map showing contours of the likelihood of that ground motion value being exceeded, due to earthquakes.

Why are there different probability maps, and which one do I use?

The different probabilities are selected to provide an idea of the relative range of hazard across the US. The larger probabilities indicate the level of ground motion likely to cause problems in the western US. The smaller probabilities show how unlikely damaging ground motions are in many places of the eastern US. However, basically the values chosen reflect the more recent history in earthquake engineering.

Probability from the engineering point of view

Rather than start with the idea of probability, consider approaching the issue from this direction: A structure is designed to resist earthquake ground motion having a particular value. Given this design resistance, one might ask several questions:

- Under what ground motion will the building sway so much that it is uncomfortable to the persons working inside, and disrupts their work for the day? (This could occur with winds as well as with earthquakes.)
- Under what ground motion will the building bend so much that interior partitions crack and wall or ceiling fixtures drop?
- Under what ground motion will the building become permanently deformed and require expensive rehabilitation or abandonment.
- Under what ground motion will the building collapse during the shaking?

Using a hazard curve, one could determine the annual probability of occurrence of each of these ground motions. Then one could decide whether that corresponding probability is acceptable. If one of the probabilities is unacceptably high, the design would have to be revised.

The different probability values reflect probabilities sometimes considered for design. The value 10 percent in 50 years seemed to provide values similar to those already used in design in the 1970s in California. On the other hand, this level of probability in the eastern US produced values too low for the seismic design then under consideration to provide residual toughness in the event of possible earthquakes (unlikely in any one location, but likely in some locations). The probabilities more likely to produce useful design ground motions would be near 5 percent in 50 years.

The ground motions given by probabilistic maps span a range of probabilities considered interesting to earthquake engineers and a range of ground motions which have some intuitive understanding for the consequences. There have been requests for maps of larger probabilities for purposes having to do with investment, insurance, and banking.

How do I know what map to choose then?

How does an individual person select a map? Technical users probably have to follow predefined rules. A non-technical person may be interested in avoiding living in a location where significant shaking will cause worry, deciding on whether to carry earthquake insurance, or deciding whether to do some rehabilitation for an existing dwelling. The probability level chosen should reflect how anxious a person is to avoid earthquake shaking.

Here is some perspective on the 10 percent in 50 year map:
If a person lives in a 100-year floodplain, there is about 1 chance in 100 of experiencing the flood in any given year. In 50 years, one would expect 0.5 floods, and there is a 1 - exp(-0.5) = 39 percent chance of experiencing such a flood in 50 years. This is a higher likelihood than that of experiencing a damaging ground motion in an area where that ground motion has only a 10 percent chance of being exceeded in 50 years. In a 200-year floodplain the chance would be 22 percent, still larger than the chance for the damaging ground motion. People who are not comfortable with probabilities as large as 10 percent in 50 years for damaging earthquake ground motion should use maps with smaller probabilities. But they should also be aware that many other hazards are higher than earthquake hazards, even in California.

How is a hazard map made? What is a hazard curve and how is it made?

How probabilistic ground motion is calculated:

Calculating the probability of a ground motion being exceeded

We demonstrate how to get the probability that a ground motion is exceeded for an individual earthquake - the "probability of exceedance".

1. Show a curve of ground motion vs distance for a given magnitude, given a particular **attenuation** relation.
2. At a given distance show distribution of ground motion.
3. Intercept the distribution with a horizontal line at a given ground motion.
4. The area of the distribution above the horizontal line is divided by the total area of the distribution. The result is "Probability of Exceedance" of the given ground motion given that earthquake having that magnitude experienced at that distance, given that particular attenuation relation.

Annual rate of exceedance

How to get the expected number of exceedances in 1 year owing to that earthquake.

1. Multiply the annual occurrence rate of the earthquake times the probability of exceedance of the ground motion, given that earthquake.
2. Expected number of exceedances in 1 year = Annual rate of exceedance

Annual rate of exceedance, given several earthquakes

Expected number of exceedances for several earthquakes. "Adding exceedances"

1. The expected number of exceedances for several earthquakes is calculated by merely adding the annual rate of exceedance owing to each earthquake.

Calculating a hazard curve.

A hazard curve is calculated by plotting annual rate of exceedance vs ground motion:

1. Perform the above calculation for 18 other ground motion levels.
2. Plot the results.
3. Make a smooth curve.

Now, for any ground motion we can find the annual rate of exceedance. Likewise, for any annual rate of exceedance we can find the corresponding ground motion.

Exceedance probability in *Y* years.

(This part is mathematical)

The expected number, n of exceedances in Y years is n = Y times r, the annual rate of exceedance. **Assumption:** The rate of earthquake occurrence in time is governed by the Poisson Law. **Application:** Under the Poisson Law, if you expect over some **period** of time n occurrences of "something", the probability of 0 occurrences is e^{-n}. If the "something" is exceedance of some ground motion, the probability of getting an exceedance is 1 – P(0). So, one can work backwards to find the annual rate of exceedance corresponding to "the probability of exceedance is 5% in 50 years."

$1 - P(0) = \frac{5}{100}$ (5%)
$P(0) = 1 - 0.05 = 0.95 = e^{-n}$

Take the log to the base e of both sides of the last equality.

$n = -ln(0.95) = 0.05129 = Yr = 50r$
$r = \frac{0.05129}{50} = 0.0010258 = \frac{1}{974.8}$

The last result tells us that at low exceedance probabilities (less than 10%) r is approximately PE / (100 Y). Now one can use the hazard curve to find the corresponding ground motion. The hazard maps are just the contoured version of the corresponding ground motion plotted on a geographic grid.

There are 3 types of maps:

- Peak Ground Acceleration (PGA)
- 0.2 second Spectral Acceleration (SA)
- 1.0 second Spectral Acceleration (SA)

Units for all 3 maps are %g (percent of gravity). This can also be expressed in decimal form, example 10%g = 0.1g. The ground motion values apply to ground motion expected for future individual earthquakes. The probabilistic ground motion calculation takes into account all possible future ground motions from all modeled earthquake magnitudes at all possible distances from the map site. The spatial distribution of probabilistic ground motion values is shown with contours on the map, like a topo map shows different elevations, with each color representing a different range of levels of shaking.

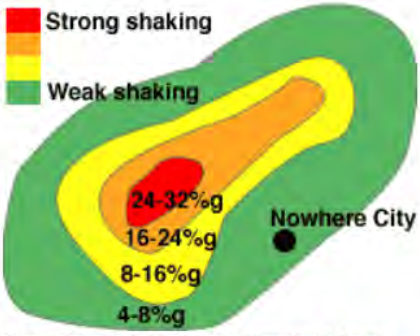

Sources/Usage: Public Domain. *View Media Details*

Hazard map showing chance of exceedance in a 50-year time interval for Nowhere City. (Public domain.)

Sources/Usage: Public Domain. View Media Details

TIME INTERVAL (X). A time interval during which all possible earthquakes may occur is set in order to determine the shaking hazard. The time interval is typically set to 50 years. The 50-year period can be ANY 50 years, not just the NEXT 50 years; the red bar above can span any 50-year period. (Public domain.)

What data are used to make hazard maps?

Three basic pieces of information are needed to produce probabilistic ground motion maps:

1. **Model of Future Earthquakes**

   Using information about past historical earthquakes, **Quaternary** faults (prehistoric earthquakes), and present crustal **deformation** (geodetic data), USGS analysts make a model of the potential for future earthquakes. This model includes *areal sources* and *fault sources*. For each **source** the relative rate for earthquakes of different magnitudes is given, and the absolute rate for magnitudes larger than some minimum magnitude.

2. **Attenuation Relations**

   An attenuation relation is an equation or a table that describes how earthquake ground motion decreases as the distance to the earthquake increases. Because earthquake ground motion increases with magnitude, the attenuation relation also depends on magnitude. **Strong motion** data (recordings close to the earthquake) and geophysical attenuation models are used to establish the attenuation relations.

relations.

3. **Geologic Site Condition**

   Earthquake ground motion waves travel rapidly in the earth's crust and mantle. That part of the earth's solid crust closest to the surface is called bed rock. The size of the ground motion experienced at the earth's surface is affected by the geology of the material between bed rock and the surface. Because the earthquake waves move more slowly in this material than in rock, the size of the ground motion increases.

   This material, often called alluvium or "the soil column," increases the ground motion in such a way that "softer" soils, soils with less density, have lower seismic velocity, and hence experience larger increases in ground motion. It is necessary to know the geologic site condition in order to estimate the surface ground motion.

   Maps are usually made for a common widespread site condition, and then rules are given for the user to adjust to other site conditions.

Who uses hazard maps?

Hazard maps can be used by public and private groups for land-use planning, mitigation, and emergency response. The scale of the maps does not allow them to be used in a site-specific manner (such as a house-by-house assessment), but it does show a neighborhood overview to guide where more detailed studies are needed.

Why do the hazard maps keep changing and getting updated?

The maps are updated as additional data becomes available from scientific analysis of earthquake-related data, such as:

1. new fault data
2. new attenuation relations
3. new geodetic data
4. more seismic data

I just want to know what faults are near me; how will these maps help?

Knowing where the faults are is not the most relevant information when trying to learn what your risks are of being affected by an earthquake. Since a large earthquake can affect distant locations, you can be affected by a fault tens-of-miles away from where you are, because of the prolonged shaking that can occur.

Nearby faults can represent a hazard from ground rupture accompanying an earthquake. Faults, both near and far, provide a source for hazard from shaking. Furthermore, in the Eastern US there are earthquakes for which the actual location or extent of faulting is poorly known. In this case, historical seismicity is the source for understanding the shaking hazard.

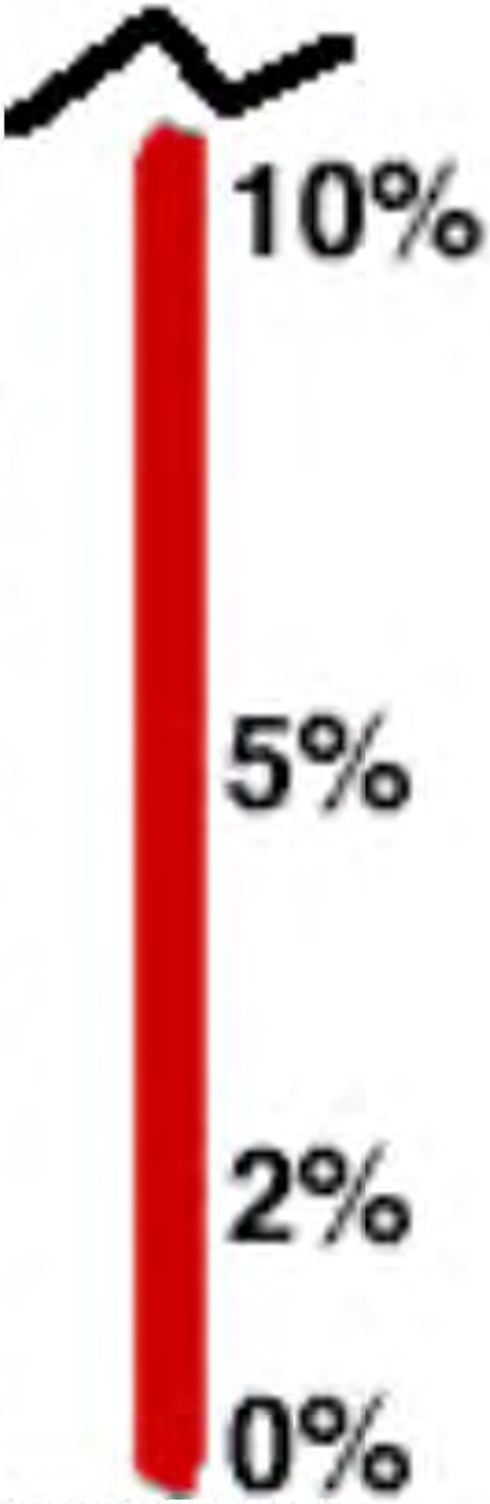

Sources/Usage: Public Domain. View Media Details

% CHANCE of EXCEEDANCE (Y) The percent (%) chance that a certain amount of mapped shaking distribution will occur over the time period being considered. Typically the values of 2%, 5% and 10% are used. Keep in mind that a 5% chance of exceedance means there is a 95% chance that the shaking will NOT exceed the value. (Public domain.)

The models and maps developed by the NSHM integrate all the faulting and seismicity information into an indication of shaking hazard. The actual values of the shaking hazards depend upon the ground motion parameter of interest and degree of safety which one wants. This is why the maps are different for different ground motions and different probabilities. The ground motion hazard values can be compared with the capacity of a structure to withstand shaking, and thus give an indication of safety.

114. Assignment 3, Module 6: Earthquake Scenarios: https://earthquake.usgs.gov/scenarios/

Earthquake Scenarios

A scenario represents one realization of a potential future earthquake by assuming a particular magnitude, location, and fault-rupture geometry and estimating shaking using a variety of strategies.

In planning and coordinating emergency response, utilities, local government, and other organizations are best served by conducting training exercises based on realistic earthquake situations—ones similar to those they are most likely to face. ShakeMap Scenario earthquakes can fill this role. They can also be used to examine exposure of structures, lifelines, utilities, and transportation corridors to specified potential earthquakes.

A ShakeMap earthquake scenario is a predictive ShakeMap with an assumed magnitude and location, and, optionally, specified fault geometry.

Scenario for Cascadia Rising Exercise

Scenario Catalogs

Map and list of scenarios determined using the 2014 National Seismic Hazard fault database.

Related Scenarios and Exercises

Related scenario efforts include ongoing and past ShakeOut exercises, drills, and 3-D simulations.

115. Assignment 3, Module 6: Earthquake Recurrence: https://www.iris.edu/hq/inclass/fact-sheet/how_often_do_earthquakes_occur

How Often Do Earthquakes Occur?

Date: April 15, 2025 | Novice | Spanish

Earth is an active place and earthquakes are always happening somewhere. In fact, the National Earthquake Information Center locates about 12,000-14,000 earthquakes each year! This fact sheet illustrates information on the frequency of earthquakes of various magnitudes, along with details on the effects of earthquakes and the equivalent energy release. This figure, also provided separately, provides energy comparisons for earthquakes of different magnitudes—like historical explosions, volcanic eruptions, and asteroid impacts.

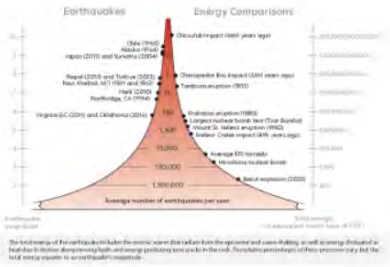

Keypoints:

- Earthquakes are always happening somewhere.
- For each step up in magnitude the annual number of earthquakes decreases (roughly) by a factor of 10.
- For each step up in magnitude an earthquake releases 30 times more energy.
- While the number of earthquakes that can be detected and located each year has been increasing, this doesn't mean that the annual average number of earthquakes has increased.

Resource Files

Download All 751KB

Optional Files 2

- Figure for Fact Sheet #3
- ¿Cuán frecuente los terremotos ocurren?

116. Assignment 3, Module 6: Global Earthquake Model:
https://www.globalquakemodel.org/product/global-seismic-hazard-map

Global Seismic Hazard Map

Openly accessible global datasets and plots for peak ground acceleration with a return period of 475 years on rock

Description

The Global Earthquake Model (GEM) Global Seismic Hazard Map (version 2023.1) depicts the geographic distribution of the Peak Ground Acceleration (PGA) with a 10% probability of being exceeded in 50 years, computed for reference rock conditions (shear wave velocity, Vs30, of 760-800 m/s).

The map was created by collating maps computed using national and regional probabilistic seismic hazard models developed by various institutions and projects, in collaboration with GEM Foundation scientists. This version represents an update from the previous release from 2018 and features improvements in most regions of the world, as well as a higher spatial definition (approx. 2.5X) compared to the previous version.

For the first time, it is now openly available in raster format as a direct download under a CC BY-NC-SA 4.0 license. An interactive online viewer (CC BY-NC-SA 4.0) is available, as well as a PDF poster and a high-resolution PNG (CC BY-SA 4.0) through the links on this page.

A set of comprehensive maps is also available that features up to 20 layers with global coverage, considering PGA and spectral acceleration (SA) for four periods of vibration (0.2s, 0.3s, 0.6s and 1.0s), calculated for reference rock and spatially variable soil conditions, for 2% and 10% probability of exceedance in 50 years. By clicking the "License Request" button, the full set or individual layers can be requested freely for research and public-good applications, or for a licensing fee in the case of commercial applications.

Available Versions

The base layer of PGA on rock for 10% exceedance in 50 years is available for direct download as a raster file, under a CC BY-SA-NC 4.0 license. Users interested in this version can click the "Open Version Download" button in the right panel to access the information. A PDF poster, as well as a high-resolution PNG, is available for direct download under a CC BY-SA 4.0 license. If your use case does not meet the open license requirement, or if you are interested in obtaining the full set of layers, please submit a request in our system by clicking on the "License Request", where a specific license will be provided, depending on the use case. Additionally, users interested in the previous version of the Global Map (v2018) can access the previous poster on this link.

117. Assignment 3, Module 7: FEMA 454, Section 3.6.3:
https://www.wbdg.org/FFC/DHS/fema454.pdf

3.6.3 Areas of Intensified Ground Motions

Local geology, proximity to faults and soil conditions play significant roles in how earthquake forces impact a structure. The Loma Prieta earthquake (1989) provided a striking example of how local soils and regional geology can determine damage. Sixty miles from the earthquake's epicenter in the Santa Cruz Mountains, the soils determined the pattern of damage to the Cypress Viaduct in Oakland. As illustrated below, the damage corresponded to the quality of the ground. On bedrock materials in the East Bay hills of Oakland, ground motions were small and there was little damage. On sandy and gravel soils between the East Bay hills and the San Francisco Bay, the amplitude of ground motions increased, but there were few collapsed structures. However, on the soft mud adjacent to the Bay, the amplitude of the ground motions and the duration of strong shaking increased. The Cypress Structure, where it passed from "sand and gravel" to "soft mud" collapsed (Figure 3-14).

A similar condition existed in the Marina District of San Francisco where soft soils liquefied, amplified motions and extended the duration of shaking until several structures collapsed, while elsewhere in San Francisco, on firmer ground, there was little or no damage.

Figure 3-15 was developed by the USGS and predicts amplification of ground motions based on soil types adjacent to San Francisco Bay. According to the USGS, "this map shows the capability of the ground to amplify earthquake shaking in the communities of Alameda, Berkeley, Emeryville, Oakland, and Piedmont. The National Earthquake Hazards Reduction Program recognizes five categories of soil types and assigns amplification factors to each. Type E soils in general have the greatest

Figure 3-14

Comparison of ground motions under the Cypress Viaduct, Loma Prieta Earthquake 1989.

SOURCE: GRAPHIC FROM THE USGS

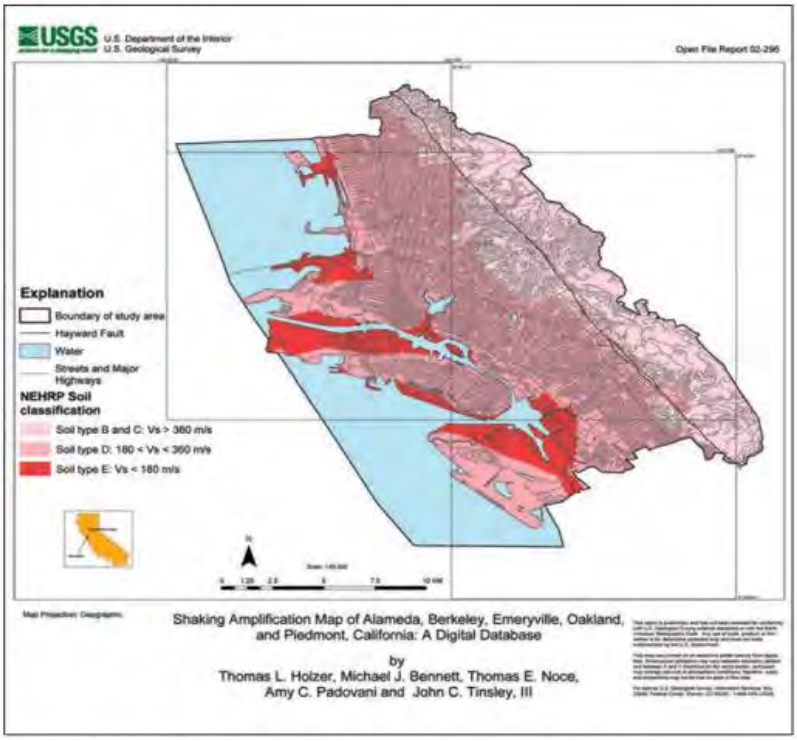

Figure 3-15: USGS Shaking Amplification Map of Alameda, Berkeley, Emeryville, Oakland and Piedmont, California. SOURCE: USGS (HOLZER ET AL.)

potential for amplification, and type A soils have the least. These soil types are recognized in many local building codes. Records from many earthquakes show that ground conditions immediately beneath a structure affect how hard the structure shakes. For example, sites underlain by soft clayey soils tend to shake more violently than those underlain by rock. The map depicts the amplification potential at a regional scale, and it should not be used for site-specific design. Subsurface conditions can vary abruptly, and borings are required to estimate amplification at a given location."

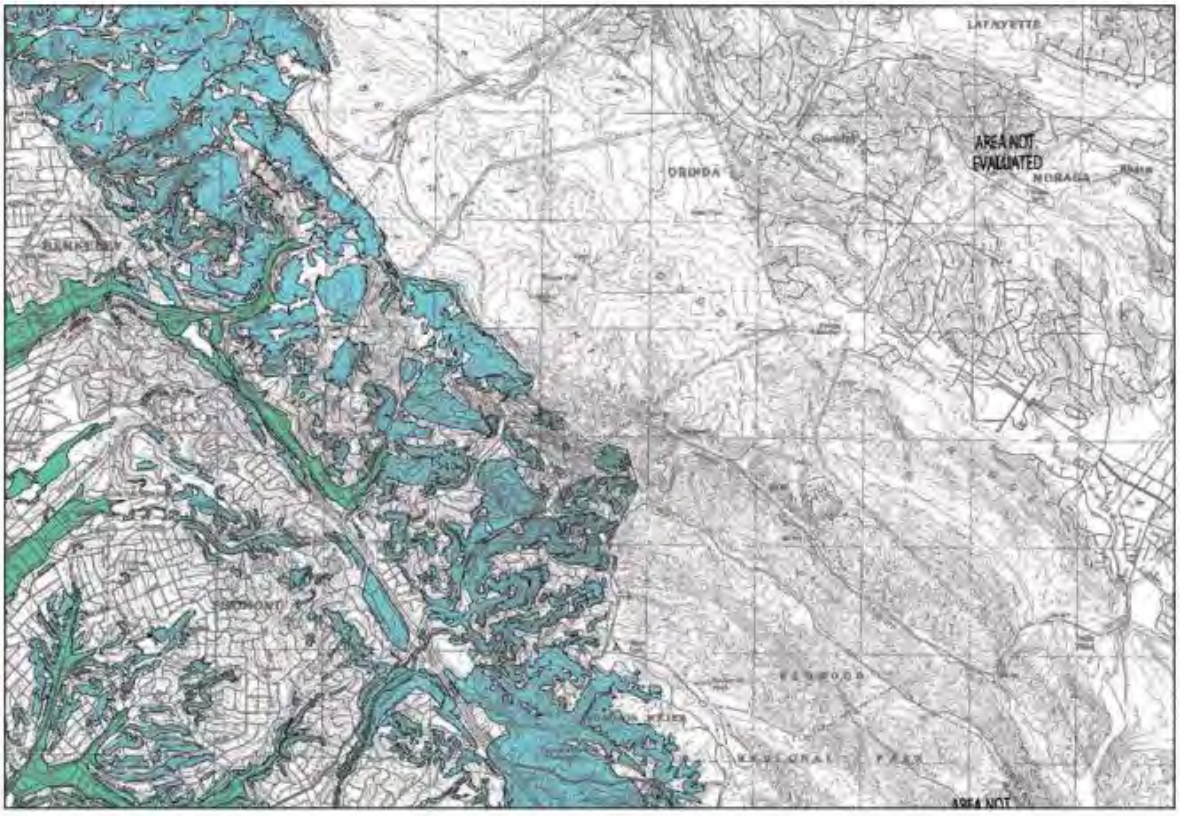

Figure 3-16: Landside Hazard Zones for Berkeley and Oakland, California.
Blue areas are those that are susceptible to earthquake-caused landslides.

SOURCE: CGS

118. Assignment 3, Module 7: San Francisco Liquefaction Maps: https://www.usgs.gov/programs/earthquake-hazards/science/san-francisco-bay-area-liquefaction-hazard-maps

San Francisco Bay Area Liquefaction Hazard Maps

By Earthquake Hazards Program June 8, 2023

Overview Publications

These maps are designed to give the general public as well as land-use planners, utilities and lifeline owners, and emergency response officials, new and better tools to assess their risk from earthquake damage. The maps also contribute to the California Geological Survey's Seismic Hazard Zone maps.

The California Geological Survey has zoned the greater San Francisco area for liquefaction hazard in their seismic hazard maps and liquefaction-related regulatory maps.

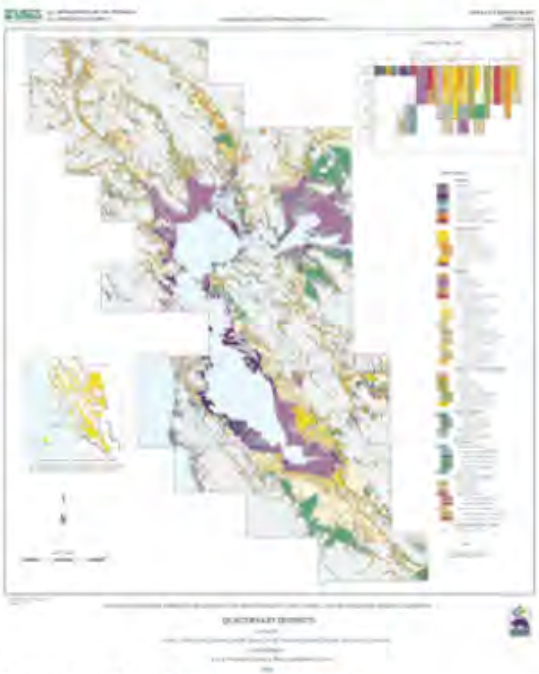

Sources/Usage: Public Domain. View Media Details

Figure 1. Quaternary Deposits from Maps of Quaternary Deposits and Liquefaction Susceptibility in the Central San Francisco Bay region, California, 2006

Figure 1 is a map of the young geologic deposits in the low-lying sections of the Bay Area. It is important to map these deposits because so much of our infrastructure resides on them, and because they may host liquefaction, the phenomenon of saturated soils losing their stiffness and strength during shaking. Some of the young deposits strongly affect the strength of earthquake shaking that is transmitted through the deposits.

affect the strength of earthquake shaking that is transmitted through the deposits.

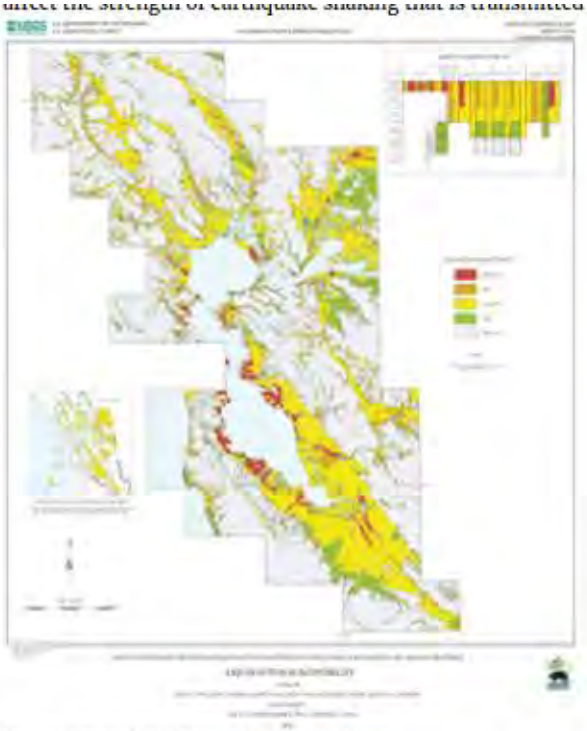

Sources/Usage: Public Domain. View Media Details

Figure 2. Liquefaction Susceptibility from Maps of Quaternary Deposits and Liquefaction Susceptibility in the Central San Francisco Bay region, California, 2006

Figure 2 shows the likelihood that these young deposits will liquefy, or turn into a sandy liquid due to the strong shaking a big earthquake will produce. When the ground liquefies, it may lose its ability to support buildings and other structures. Liquefaction during large earthquakes commonly disrupts pipelines and road networks and also may cause buildings to settle and move downslope or toward stream banks.

Sources/Usage: Public Domain. View Media Details

Figure 3. Recordings of the shaking levels in three different areas in the San Francisco Bay from the Loma Prieta Earthquake show that the shaking experienced depends very strongly on the type of deposits found near the surface. Soft muds shake much harder than bedrock.

Figure 3 shows that the shaking experienced in a region depends very strongly on the type of deposits found near the surface. Soft muds shake much harder than bedrock. Figure 4 shows part of the Cypress structure, the freeway approach to the Bay Bridge from Oakland, which collapsed during the Loma Prieta earthquake, killing 42 people. Soft muds on which it was constructed shook much more strongly than surrounding regions on stronger ground. Detailed mapping is needed to forecast where shaking will be strongest during future earthquakes.

We can expect history to repeat itself in the next big Bay Area earthquake.

The highest hazard areas shown by the liquefaction

hazard maps are concentrated in regions of man-made landfill, especially fill that was placed many decades ago in areas that were once submerged bay floor. Such areas along the Bay margins are found in San Francisco, Oakland and Alameda Island, as well as other places around San Francisco Bay. Other potentially hazardous areas include those along some of the larger streams, which produce the loose young soils that are particularly susceptible to liquefaction.

These maps show a lower likelihood of liquefaction than previously thought in regions underlain by Bay mud that fringes many parts of San Francisco Bay. Bay mud remains a seismic hazard because on the basis of its past performance in earthquakes it will produce stronger levels of shaking than other geologic units.

The maps show in unprecedented detail the nature of the materials that underlie areas of densest urban development and highlight areas that may be prone to shaking-related damage during future earthquakes.

Sources/Usage: Public Domain. View Media Details

Figure 4. Side view of support-column failure and collapsed upper deck, Cypress viaduct.

Sources/Usage: Public Domain. View Media Details

Figure 5. 1906 earthquake damage to home on Howard and 17th Streets in San Francisco. Liquefaction, the phenomenon of saturated soils losing their stiffness and strength during shaking, caused structures to tilt and collapse.

These maps are the result of over a decade of work and collaboration between geologists from the consulting firm William Lettis & Associates, the U.S. Geological Survey, and the California Geological Survey.

Many of the region's utilities and lifeline owners have made use of an earlier version of these maps in vulnerability assessments of their systems.

These new maps cover the San Francisco Bay region (outlined in red). A previous USGS map, published in 2000, covers a larger region (outlined in black).

Northern San Francisco and the Marin peninsula are not included in the new maps because geologic field mapping in these regions is incomplete. Please use the older map for areas not covered by the new map. The older map also shows locations of liquefaction observed in historical earthquakes, particularly the Great 1906 earthquake and the 1989 Loma Prieta quake.

Sources/Usage: Public Domain. View Media Details

Figure 6. An automobile lies crushed under the third story of this apartment building in the Marina District. The ground levels are no longer visible because of structural failure and sinking due to liquefaction.

Sources/Usage: Public Domain. View Media Details

Figure 7. New vs Old Map Boundaries for Liquefaction Maps of San Francisco Bay Area (2006 versus 2000)

120. Assignment 3, Module 8: FEMA 454, Sections 2.2.3 and 3.6.2: https://www.wbdg.org/FFC/DHS/fema454.pdf

2.2.3 Earthquake Effects

There are many earthquake effects related to the geology and form of the earth that are of significance for architects. In the most intensely damaged regions, the effects of severe earthquakes are usually complicated. The most drastic effects occur chiefly near he causative fault, where there is often appreciable ground displacement as well as strong ground shaking (e.g. Figure 2-4); at greater distance, noticeable earthquake effects often depend on the topography and nature of the soils, and are often more severe in soft alluvium and unconsolidated sediment basins. Some remarkable effects are produced in bodies of water such as lakes, reservoirs, and the sea.

● Ground Shaking Intensity

Efforts to measure the size of an earthquake by rating microseismic data in the affected area go back to the 19th century. Before the invention of instrumentally based seismic magnitude, the most common historical scale rated the relative "intensity" of an earthquake. This measure is not capable of strict quantitative definition because seismic intensity at a particular point of the Earth's surface depends on many factors, including the source moment M0, area of the rupture fault, the fault mechanism, the frequency-spectrum of wave energy released, the geological conditions, and the soils at a given site.

The most widely used scale historically was originated by Rossi and Forell in 1878. A later modification developed by Mercalli in Italy, now termed the **Modified Mercalli Intensity (MMI)** scale, is suitable for conditions in the United States. Bolt (2003) describes the details of the various intensity measures.

The geographical distribution of intensity is summarized by constructing isoseismal curves, or contour lines, which separate areas of equal inten-

sity. The most probable position of the epicenter and the causative fault rupture is inside the area of highest intensity. An example of MMI curves for two moderate events is given in Figure 2-6. Clearly there can be large regional differences in MMI. Such variations in seismic wave attenuation are discussed in Section 2.6.1.

Correlations have been worked out between measured characteristics of the seismic waves and the reported Modified Mercalli intensity. A common one is that between the maximum ("peak") ground acceleration, A (centimeters per second squared), and the MM intensity, I. Such correlations are only broadly successful, particularly at the higher intensities. The description of the seismic waves for architectural and engineering purposes depends on a mixture of parameters, many of which are dependent on the frequency of the seismic waves. Nevertheless, because in many parts of the world instrumental measurements of ground

motion are not available, rough seismic intensity remains popular as a descriptor as well as for great historical earthquakes. Peak Ground Acceleration is employed as a measure in the current USGS **Shake-Maps** program, for example: these are maps showing ground shaking intensities that are available on the internet within a few minutes of an earthquake occurrence (see Section 2.6).

A number of other hazards of a geological nature may be triggered by an earthquake occurrence. These may at times cause severe damage and loss of life.

Landslides

Landslides, ground settlement, and avalanches occur widely with and without earthquakes as a cause. All require special architectural treatment. Landslides and avalanches occur on slopes of a variety of geological materials. For engineering works, the speed at which a landslide develops and moves is a most important feature. Few defenses are available against rapid unexpected movements, but those that move slowly over periods of months to years lend themselves to some precautionary measures. Zoning regulations based on localized geological studies are the most effective mitigation measures.

During an earthquake, a series of seismic waves shakes the ground in all directions, so that under the critical conditions of water saturation, slope, and soil type, even relatively low levels of ground acceleration can cause a landslide. Even if these dynamic accelerations last for only a short time, widespread sliding can occur on marginally stable slopes. During and following the 1971 San Fernando, California, earthquake, for example, thousands of landslides and rockfalls occurred in the San Gabriel Mountains and caused a prominent dust-cloud over the strongly shaken area for days. This was repeated during the nearby 1994 Northridge earthquake.

Another human catastrophe caused by an earthquake-triggered debris avalanche occurred in Peru on May 31, 1970. The earthquake of magnitude 7.7 stimulated a rock avalanche amounting to some 50 million cubic meters of rock, snow, ice, and soil that travelled 15 km from the north peak of Huascarn Mountain, buried the towns around Ranraharca and most of Yungay, and killed at least 18,000 people.

In many instances, smaller landslides and avalanches can be detected in advance by suitable instrumentation installed on the slope with the readings monitored at regular intervals. Means of control can then be applied in appropriate circumstances: for example, removing small volumes of material to relieve the load at the head of the slope and adding material to the toe can be accomplished by earth-moving equipment. For cuts that are man-made, local regulations or ordinances may need to be developed and enforced during construction in a vulnerable area. Slopes made of fill, for example, may be required to be no steeper than 1 vertical to 1-1/2 horizontal, and the fraction of the soil covering the slope must be carefully controlled. Drainage of water away from such slopes is usually specified.

Tsunamis and Seiches

The occurrence of an earthquake and a sudden offset along a major fault under the ocean floor, or a large submarine landslide, displaces the water like a giant paddle, thus producing powerful water waves at the ocean surface. When they reach a coastline, they may run up on land to many hundreds of meters. The elevation above the tide level (at the time of the tsunami) reached by the water is called the **run-up height**. This vertical distance is not the same as the tsunami water wave height offshore or the horizontal distance of water run-up from the normal water edge.

There have been tsunamis in most oceans of the world, but most notably in the Pacific Ocean. The coastline of Hilo, Hawaii, has seen inundation several times, and the giant earthquake in Alaska in 1964 had a run-up height of six meters in Crescent City, California, killing several people. Near the fault motion, 119 people drowned in Alaska.

A seismic sea wave warning system was set up in the Pacific after the devastating Aleutian tsunami of April 1, 1946. The tsunami warning center in Honolulu provides tsunami alerts and alerts local jurisdictions to issue warnings.

The best disaster prevention measures for a tsunami-prone coast involve zoning that controls the types and sizes of buildings that, if any, are permitted. If a site has a high possibility of tsunami incursion, the designer should consider some of the design provisions against flood, such as elevating the building above an estimated waterline. Of course in the case

of locally generated tsunami, provisions must also be made for the severe strong shaking.

Long-period movements of water can also be produced in lakes and reservoirs by large earthquakes. These oscillations of lake levels are termed **seiches**. The November 2003 Denali earthquake in Alaska generated seismic seiches in wells and lakes of the south central United States. In the 1971 San Fernando, California, earthquake water sloshed out of swimming pools, producing some risk.

Liquefaction

A notable hazard from moderate to large earthquakes is the liquefaction of water-saturated soil and sand produced by the ground shaking. In an earthquake, the fine-grained soil below the ground surface is subjected to alternations of shear and stress. In cases of low-permeability soils and sand, the water does not drain out during the vibration, building up pore pressure that reduces the strength of the soil.

Because earthquake shaking of significant amplitude can extend over large areas, and fine-grained soils in a saturated state are so widespread in their distribution, liquefaction has frequently been observed in earthquakes. In some cases, it is a major cause of damage and therefore is a factor in the assessment of seismic risk. Liquefaction in the 1964 Alaskan earthquake caused major disruptions of services and utilities and led to substantial building settlements and displacements. In the 1971 San Fernando, California, earthquake, liquefaction of soils in the San Fernando Dam caused a landslide in the upstream portion of the dam structure that almost resulted in a catastrophic dam failure. Widespread liquefaction resulted in severe damage after the 1811-1812 New Madrid and 1886 Charleston, South Carolina, earthquakes.

Many seismic regions have available liquefaction maps so that the risk of liquefaction at building sites can be assessed. Soil engineers have developed various technical methods of controlling liquefaction, the description of which goes beyond this chapter (see Chapter 3).

3.6.2 Ground Failure Due to Liquefaction

Liquefaction occurs when water-saturated soils, sands, or gravels flow laterally or vertically like a liquid. This occurs when earthquake ground motions shake the material until the water pressure increases to the point that friction between particles is lost, and the ground flows, losing its strength (Figure 3-9). Liquefaction is most likely to occur where the soils are not consolidated (near rivers and streams, in basins, near coastlines and in areas of unconsolidated alluvium) and where ground water is within three to four meters of the surface. Liquefaction can occur at greater depths, resulting in large-scale ground failure that can destroy pavement, underground utilities, and building foundations (Figure 3-10). The subsidence of Turnagain Heights in Anchorage during the 1964 earthquake is an example of deep-seated liquefaction and ground failure. When a soil liquefies, it can flow laterally, eject vertically as a sand boil, or result in subsidence and ground failure (Figure 3-11).

Figure 3-10

Liquefaction in San Francisco's Marina District (1989)

SOURCE: USGS

Sand boils and flows on the surface can displace and damage structures and utilities. Lateral liquefaction flows will result in subsidence, loss of foundation integrity, disruption of underground utilities and damage to structures resting on the soil surface, including roadways and utility structures. Liquefaction susceptibility and potential should be identified in the site geotechnical investigation, as explained in Section 3.3.3.

Liquefaction Hazard Zones

Liquefaction susceptibility can be determined from site geologic investigations and from a review of geologic and soil maps and water well and bore hole logs. In California, liquefaction potential mapping is part of

Figure 3-11: Sand Boil.

the CGS's Earthquake Hazard Mapping Program. Liquefaction hazard zone maps have been completed for sections of the Los Angeles and San Francisco Bay Regions (Figures 3-12 and 3-13).

Within an identified liquefaction hazard zone, maps of liquefiable soils, prepared by a geotechnical engineer, should identify the location and extent of "cohesionless silt, sand, and fine-grained gravel in areas where the ground water is within 50 feet of the surface." Procedures for testing and criteria for determining liquefaction susceptibility are contained in *Recommended Procedures for Implementation of DMG Special Publication 117: Guidelines for Analyzing and Mitigating Liquefaction in California.*[13]

Mitigation Options for Liquefiable Sites

There are structural solutions for mitigating liquefaction potential that address the design of foundation systems that penetrate the liquefiable layers. It should be noted that while it is frequently cost effective to design structures to withstand liquefaction, making access and egress routes, parking and storage facilities and above and underground utilities "liquefaction-resistant" is prohibitively expensive. "A whole-site solution" may be more practical when site choice is limited and susceptibility is significant. See the mitigation approaches below.

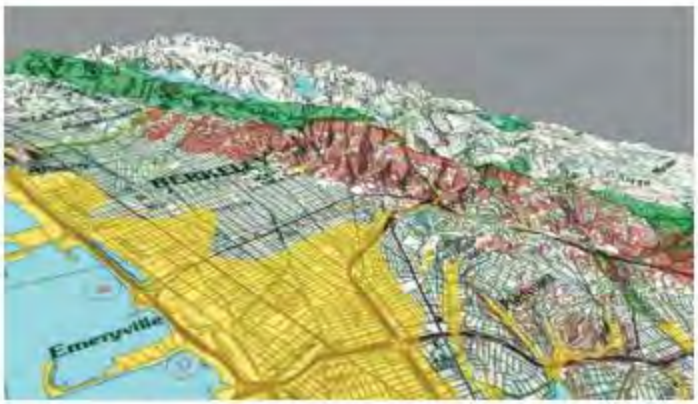

Figure 3-12: 3-D image of Liquefaction and Landslide Hazard Zone Map for Berkeley and Emeryville. Yellow indicates liquefaction, which is related to soil type and proximity to ground water.

SOURCE: CGS

Figure 3-13: Liquefaction Hazard Zone Map for West Oakland and Emeryville.

SOURCE: CGS EARTHQUAKE HAZARD MAPPING PROGRAM

Location of the Structure

The simplest way to mitigate the potential of liquefaction is to avoid those locations in a region or on a site where the potential for ground failure is identified in the geotechnical investigation. Locate structures where ground water is low, where soils are compacted, and where soils are not homogeneous sands or gravels.

Intervention on the Site

While avoidance is the optimum solution, it is not always possible. Mitigating liquefaction potential involves changing the characteristics of the site. The following options are all costly and vary in extent of risk mitigation. Seek advice from geotechnical and civil engineering consultants about the most cost-effective intervention.

- Site Compaction

  On sites with unconsolidated soils, the response of the site can be improved by compacting the soil, compressing it so that soil particles are forced together, reducing water-filled voids and increasing the friction between soil particles.

- Change Soil

  The performance of the site can also be improved by excavation of the liquefiable soils and replacement with compacted heterogeneous fill. By changing the soil, the susceptibility of the site to liquefaction will be significantly reduced. However, for both this approach and the compaction alternative, site performance is improved by construction of barriers to the infiltration of water so that the groundwater level of the site is lowered.

- Dewatering the Site

  An alternative to "reconstituting the site" by replacing the soil is to dewater the site. This approach requires constructing wells to pump out and lower the ground water level to reduce liquefaction susceptibility. To reduce the demand for continuous pumping, dewatering should be combined with the construction of infiltration barriers. A back-up power source to ensure post-disaster pump operations should be provided.

Special Design Considerations

As noted above, the potential for liquefaction of a site poses severe problems for maintenance of access and egress and performance of lifelines including power, telecommunications, water sewer and roadways. For facilities that are expected to be in continuous operation after disasters, redundant access to utility networks, multiple access and egress paths, and back-up power and communication systems should be provided. Liquefaction potential may be difficult to assess, so a conservative approach to the design of continuous operation facilities is essential.

121. Assignment 3, Module 8: 1906 Liquefaction:
https://www.iris.edu/hq/inclass/animation/liquefaction_during_the_1906_san_francisco_earthquake

Liquefaction during the 1906 San Francisco Earthquake

43s Novice

Why did buildings tip over during this earthquake?

Liquefaction is a process by which water-saturated sediment temporarily loses strength and acts as a fluid. This effect can be caused by earthquake shaking. This cutaway (cross section) animation shows how liquefaction of compacted sediment in the San Francisco area led to the tilting of houses during the 1906 earthquake. Tilted Victorian home at Howard and 17th Streets in the Mission District of San Francisco showing liquefaction-related damage from the 1906 earthquake. This area is underlain by marsh deposits that were covered by artificial fill in the middle to late 1800s. The earthquake shaking caused the artificial fill to liquefy and lose its ability to support the house. (Photograph by G.K. Gilbert of the U.S. Geological Survey; description from USGS).

Resource Files

Download Animation 3MB

122. Assignment 3, Module 8: Sand Boils, Loma Prieta: https://www.iris.edu/hq/inclass/animation/sand_boil_forms_example_from_1989_loma_prieta_earthquake

Sand Boil Forms: Example from 1989 Loma Prieta earthquake

24s Novice

What is a sand volcano??

Sand Boil: sand-laden water can be ejected from a buried liquefied layer and erupt at the surface to form sand volcanoes; the surrounding ground often fractures and settles. Definition & photo from USGS.

Resource Files

Download Animation 1MB

123. Assignment 3, Module 8: Liquefaction:
https://www.scienceworld.ca/resource/liquefaction/

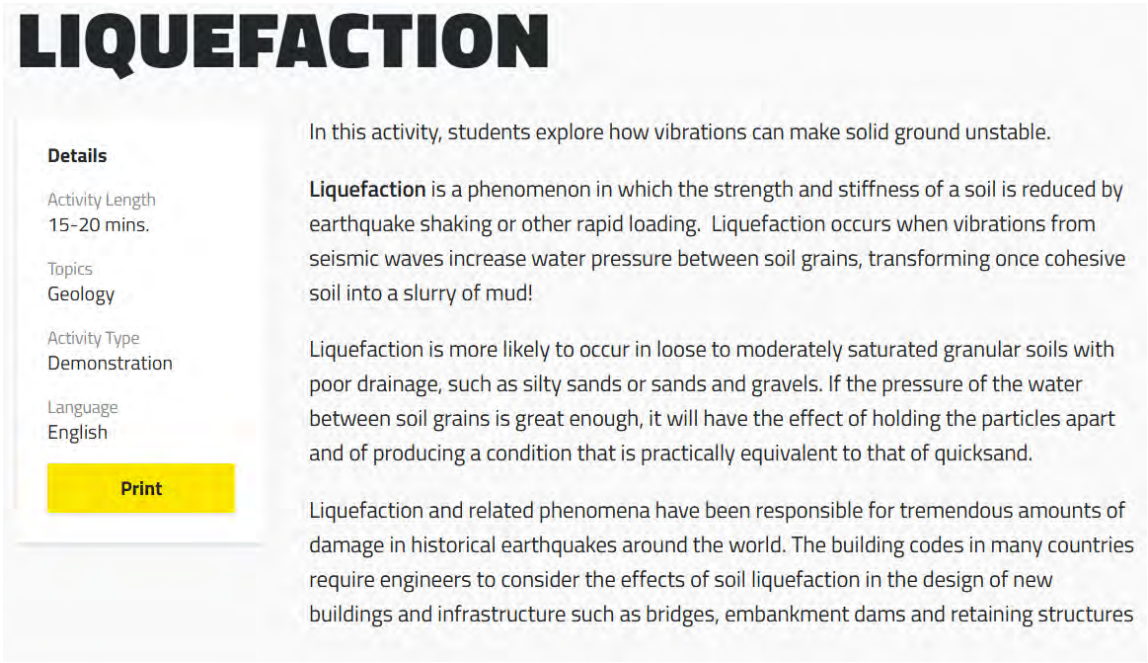

LIQUEFACTION

Details

Activity Length
15-20 mins.

Topics
Geology

Activity Type
Demonstration

Language
English

Print

In this activity, students explore how vibrations can make solid ground unstable.

Liquefaction is a phenomenon in which the strength and stiffness of a soil is reduced by earthquake shaking or other rapid loading. Liquefaction occurs when vibrations from seismic waves increase water pressure between soil grains, transforming once cohesive soil into a slurry of mud!

Liquefaction is more likely to occur in loose to moderately saturated granular soils with poor drainage, such as silty sands or sands and gravels. If the pressure of the water between soil grains is great enough, it will have the effect of holding the particles apart and of producing a condition that is practically equivalent to that of quicksand.

Liquefaction and related phenomena have been responsible for tremendous amounts of damage in historical earthquakes around the world. The building codes in many countries require engineers to consider the effects of soil liquefaction in the design of new buildings and infrastructure such as bridges, embankment dams and retaining structures

Objectives

- Describe the effect of earthquakes on mud and sand

Materials

- **Per Demo or Group:**
  metal cake pan
  sand
  water
  smooth brick
  rubber mallet
  ping pong ball or cork (optional)

Key Questions

- What happens to the sand and brick?
- Was this the same as your predictions?

What To Do

1. Fill the pan with sand. The deeper the sand, the better.
2. Put the pan on the table.
3. Pour water into the pan so it reaches just below the surface of the sand.
4. Wiggle the skinny end of the brick down into the wet sand so it stands up like a building would.

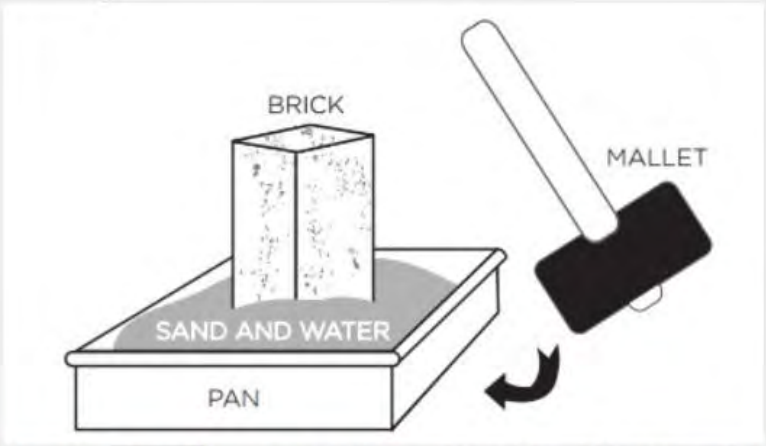

5. Now very gently, repeatedly tap the side of the pan with a mallet.
6. 

Extensions

- Submerge a buoyant object (ping pong ball) in the sand before starting the demo and watch the result on that object: Why is it able to float to the surface?

124. Assignment 3, Module 8: FEMA 454, Section 3.6.4:
https://www.wbdg.org/FFC/DHS/fema454.pdf

3.6.4 Ground Failure, Debris Flows, and Land Slides

Potential for ground failure and landslides is determined by soil type, water content (degree of saturation), gradient (slope angle) and triggering events (an earthquake, excavation that upsets the site equilibrium, increase in water content resulting from irrigation or storm run-off). Geotechnical investigations of the site and surrounding terrain are critical in determining site vulnerability.

● Landslide Hazard Maps

The USGS and CGS have prepared Landslide Hazard Zone Maps for parts of northern and southern California (Figure 3-16). The map de-

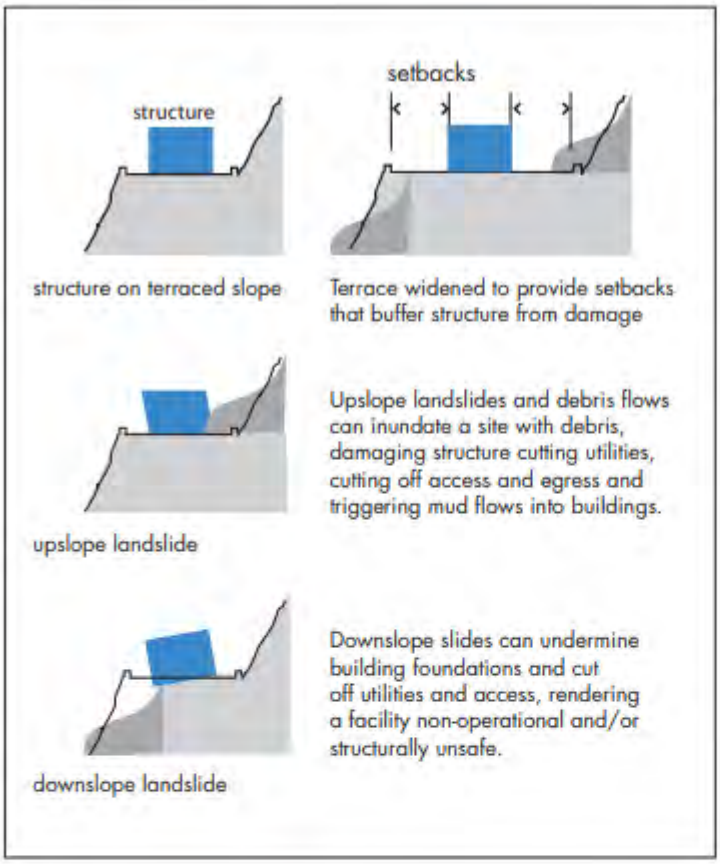

Figure 3-17

The effect of upslope and downslope landslides.

picts a section of the Oakland-Berkeley East Bay Hills, indicating areas where slope, soil type and seismic risk could trigger landslides. Construction in the Landslide Hazard Zone requires an assessment by a geotechnical engineer.

Downslope slides can undermine building foundations and cut off utilities and access, rendering a facility non-operational and/or structurally unsafe (Figure 3-17). The USGS's *National Landslide Hazards Mitigation Strategy*[14] and the California Geological Survey's *Recommended Procedures for Implementation of DMG Special Publication 117: Guidelines for Analyzing and Mitigating Landslide Hazards in California*[15] offer guidance in determining landslide vulnerability and mitigation options.

● Mitigation Options

Foundation systems and structures can be designed to reduce damage from ground failure. The geotechnical engineer can provide recommendations for appropriate foundation design.

❍ Set-Back

The most failsafe option for mitigation is to locate structures and lifelines in parts of the site that are not at risk to slide damage. Set back structures from both the toe of an upslope and from the lip of a down slope. Allow separation to accommodate catch basins, debris diverters and barriers. Parking lots or storage areas can be designed and located to "buffer" structures from debris.

❍ Drainage

Since water acts as a lubricant on slope-failure surfaces, it is critical that the site and its surroundings be well drained, that irrigation is limited, and that dewatering systems reduce subsurface hydrostatic (water pressure) pressures. Dewatering systems can either be passive (drains into slopes, "French drains," top-of-slope catch basins) or active, providing pumping of subsurface water from sumps into a drain system. In both cases, continuous maintenance is essential to ensure reliable operation of the system. Emergency power may also be required for active drainage systems. Where storm water runoff must be managed on site, design of parking and landscaped areas should accommodate storage. Facility access procedures will need to address displacement of parking and limitations on access during periods the site is flooded.

❍ Redundant Infrastructure

Ground failure can severely disrupt utility and lifeline connections to a site. Where continued operations are essential to a client, connections to utility and transportation networks should be redundant, providing more than one means of connection, access, and egress. For telecommunications, redundancy would include dedicated connections to two different switching offices, planned to follow two different routes to the site. Multiple access and egress paths should also be provided. For facilities dependent on electrical power, multiple, dispersed connections to the grid, co-generation and/or emergency back-up power generation should be planned.

Where continuous operation is not essential, emergency back-up power should be provided to ensure safety, security and operation of environmental protection systems (such as heating and ventilating systems [HVAC], water pumps, security systems, evacuation and lighting systems, computer operations and data security. Emergency power generation capacity should exceed minimum requirements to ensure adequate power for projected needs of essential systems. For facilities where a consistent quality-controlled supply of water is essential for operations, on-site storage and purification should be provided to meet operational needs until alternative sources can be secured.

125. Assignment 3, Module 8: Landslides: https://www.usgs.gov/natural-hazards/landslide-hazards/science/landslides-101

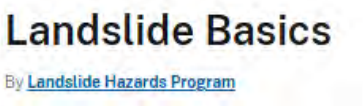

Landslides occur in all 50 states and territories and they affect lives, property, infrastructure, and the environment. Understanding when, where, and how landslides occur can help to reduce the risk of living with these natural hazards.

What is a landslide?

Sources/Usage: Public Domain. View Media Details

Landslides are the downslope movement of earth materials (rock, debris, and soil) at rates that range from inches per year to tens of miles per hour. Some landslides can move faster than a person can run. Landslides can happen with no notice or can take place over a period of days, weeks, or longer.

Where do landslides occur?

Landslides occur in every state and U.S. territory including the Appalachian Mountains, the Rocky Mountains, the Pacific Coastal Ranges, and some parts of Alaska and Hawaii. Any area composed of very weak or fractured materials resting on a steep slope can and will likely experience landslides.

Sources/Usage: Public Domain. View Media Details

Sources/Usage: Public Domain. View Media Details

What are the signs of landslide development/movement?

Landslides are dangerous and very difficult to predict. Some landslides may provide clues that they are about to happen; others may happen suddenly without any warning signs.

Authors

Stephen L. Slaughter

Associate Program Coordinator

Landslide Hazards Program
Email: sslaughter@usgs.gov
Phone: 303-273-8482

Contacts

Emily C Bedinger (Former Employee)

Hydrologist

Landslide Hazards Program

How do I prepare for a landslide?

If you live on or below a slope, here are some simple steps you can take to identify a landslide hazard and reduce your landslide risk.

Sources/Usage: Some content may have restrictions. View Media Details

The University of Puerto Rico Mayagüez, the Natural Hazards Center at the University of Colorado Boulder, and the USGS Landslide Hazards Program collaborated to create educational materials for residents of Puerto Rico to learn about how to prepare for, mitigate, respond to, and recover from landslides. Pages from "Landslide Guide for Residents of Puerto Rico " are shown in this figure.

What do I do after a landslide has occurred?

Depending on the severity of the landslide, you may not be able to return home right away. If authorities say it is safe to return to your home, continue to be prepared to leave the area immediately if you observe unusual activity.

Sources/Usage: Public Domain. View Media Details

126. Assignment 3, Module 8: Coseismic Landslide: https://www.usgs.gov/data/coseismic-landslide-runout-and-mobility-ratio-data-publicly-available-mapped-landslide

Coseismic landslide runout and mobility ratio data from publicly available mapped landslide inventories

December 17, 2024

View Data Release

Earthquake-triggered landslides can significantly contribute to human and economic losses during and immediately following earthquakes, but data on the runout behavior of such ground failures is limited. Hazard assessment of coseismic landslide risk can vary dramatically depending on landslide mobility and runout extent, which makes modeling of such behavior imperative. Predictive and empirical models require comprehensive datasets with diverse climatic, topographic, and geologic factors. We present an openly accessible global dataset of coseismic landslide runout lengths, produced from an automated method for estimating runout length from existing landslide inventories. This tool was developed and validated using manually measured runout lengths of 1,726 landslides from five global earthquake-induced landslide inventories spanning a variety of terrains and geologic settings. The resultant database contains 73,665 measured and estimated runout lengths of coseismic landslides from 23 global earthquakes derived from the USGS's open repository of earthquake-triggered ground-failure inventories on ScienceBase (https://doi.org/10.5066/F7H70DB4, v4.0, Schmitt et al., 2022). We present separate data files for each inventory, reporting area and predicted or measured runout lengths of individual landslides.

Citation Information

Publication Year	2024
Title	Coseismic landslide runout and mobility ratio data from publicly available mapped landslide inventories
DOI	10.5066/P9QUPO2P
Authors	Natalie K Culhane, Alex R Grant
Product Type	Data Release
Record Source	USGS Asset Identifier Service (AIS)
USGS Organization	Earthquake Science Center
Rights	This work is marked with CC0 1.0 Universal

Study Area

Contact

Earthquake Science Center
350 N. Akron Road
Moffett Field, CA 94035
United States

Explore Search

Seismology
Remote Sensing
Geomorphology
Earthquake
hazard
View All ↓

127. Assignment 3, Module 8: Landslide Handbook Parts A and D: https://pubs.usgs.gov/circ/1325/pdf/Sections/Section1.pdf

Part A. What is a Landslide?

Geologists, engineers, and other professionals often rely on unique and slightly differing definitions of landslides. This diversity in definitions reflects the complex nature of the many disciplines associated with studying landslide phenomena. For our purposes, landslide is a general term used to describe the downslope movement of soil, rock, and organic materials under the effects of gravity and also the landform that results from such movement (please see figure 1 for an example of one type of landslide).

Varying classifications of landslides are associated with specific mechanics of slope failure and the properties and characteristics of failure types; these will be discussed briefly herein.

There are a number of other phrases/terms that are used interchangeably with the term "landslide" including mass movement, slope failure, and so on. One commonly hears such terms applied to all types and sizes of landslides.

Regardless of the exact definition used or the type of landslide under discussion, understanding the basic parts of a typical landslide is helpful. Figure 2 shows the position and the most common terms used to describe the unique parts of a landslide. These terms and other relevant words are defined in the Glossary of Landslide Terms included in Appendix A.

Figure 1. This landslide occurred at La Conchita, California, USA, in 2005. Ten people were killed. (Photograph by Mark Reid, U.S. Geological Survey.)

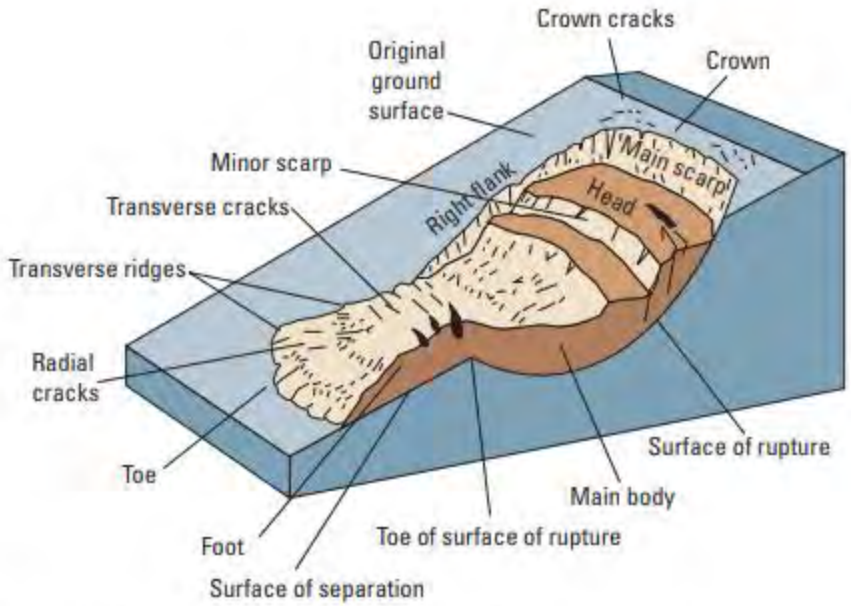

Figure 2. A simple illustration of a rotational landslide that has evolved into an earthflow. Image illustrates commonly used labels for the parts of a landslide (from Varnes, 1978, Reference 43).

Part D. What Causes Landslides?

There are two primary categories of causes of landslides: natural and human-caused. Sometimes, landslides are caused, or made worse, by a combination of the two factors.

Natural Occurrences

This category has three major triggering mechanisms that can occur either singly or in combination —(1) water, (2) seismic activity, and (3) volcanic activity. Effects of all of these causes vary widely and depend on factors such as steepness of slope, morphology or shape of terrain, soil type, underlying geology, and whether there are people or structures on the affected areas. Effects of landslides will be discussed in more detail in Part E.

Landslides and Water

Slope saturation by water is a primary cause of landslides. Saturation can occur in the form of intense rainfall, snowmelt, changes in ground-water levels, and surface-water level changes along coastlines, earth dams, and in the banks of lakes, reservoirs, canals, and rivers. Landslides and flooding are closely associated because both are related to precipitation, runoff, and the saturation of ground by water. Flooding may cause landslides by undercutting banks of streams and rivers and by saturation of slopes by surface water (overland flow). In addition, debris flows and mudflows usually occur in small, steep stream channels and commonly are mistaken for floods; in fact, these two events often occur simultaneously in the same area. Conversely, landslides also can cause flooding when sliding rock and debris block stream channels and other waterways, allowing large volumes of water to back up behind such dams. This causes backwater flooding and, if the dam fails, subsequent downstream flooding. Moreover, solid landslide debris can "bulk" or add volume and density to otherwise normal streamflow or cause channel blockages and diversions, creating flood conditions or localized erosion. Landslides also can cause tsunamis (seiches), overtopping of reservoirs, and (or) reduced capacity of reservoirs to store water. Steep wildfire-burned slopes often are landslide-prone due to a combination of the burning and resultant denudation of vegetation on slopes, a change in soil chemistry due to burning, and a subsequent saturation of slopes by water from various sources, such as rainfall. Debris flows are the most common type of landslide on burned slopes (for a description and images of a debris flow, see "*Part B.* Basic Landslide Types" in Section I). Wildfires, of course, may be the result of natural or human causes. Figure 26 shows a devastating landslide caused by rainfall, and possibly made worse by a leaking water pipe, which added even more water to the soil.

Figure 26. The Mameyes, Puerto Rico, landslide, 1985. This landslide destroyed 120 houses and killed at least 129 people. The catastrophic slide was triggered by a tropical storm that produced extremely heavy rainfall. Contributing factors could also have included sewage saturating the ground in the densely populated area, and a leaking water pipe at the top of the landslide. (Photograph by Randall Jibson, U.S. Geological Survey.)

Landslides and Seismic Activity

Many mountainous areas that are vulnerable to landslides have also experienced at least moderate rates of earthquake activity in recorded times. Earthquakes in steep landslide-prone areas greatly increase the likelihood that landslides will occur, due to ground shaking alone, liquefaction of susceptible sediments, or shaking-caused dilation of soil materials, which allows rapid infiltration of water. For instance, the 1964 Great Alaska earthquake in the United States caused widespread landsliding and other ground failure, which led to most of the monetary loss attributed to the earthquake. Other areas in North America, such as the State of California, the Puget Sound region in Washington, and the St. Lawrence lowlands of eastern Canada, have experienced landslides, lateral spreading, and other types of ground failure classified as landslides, due to moderate to large earthquakes. Rockfalls and rock topples can also be caused by loosening of rocks or rocky formations as a result of earthquake ground shaking. Figure 27 shows damage from a landslide that was triggered by an earthquake. There is also a great danger of landslide dams forming in streams and rivers below steep slopes, a result of rock and earth being shaken down by the earthquake. These landslide dams often completely or partially block the flow of water, causing water to back up behind the landslide dam, flooding areas upriver. As these dams are often unstable, they may erode either quickly or over a period of time and fail catastrophically, unleashing the backed up water as a rapid deluge below the dam. This deluge is capable of causing a great deal of damage downriver.

Figures 32, 42, C53, C54, and C55 show examples of large landslide dams that still exist

Figure 27. Earthquake-induced landslide damage to a house built on artificial fill, after the 2004 Niigata Prefecture earthquake in Japan. (Photograph by Professor Kamai, Kyoto University, Japan.)

Landslides and Volcanic Activity

Landslides due to volcanic activity represent some of the most devastating types of failures. Volcanic lava may melt snow rapidly, which can form a deluge of rock, soil, ash, and water that accelerates rapidly on the steep slopes of volcanoes, devastating anything in its path. These volcanic debris flows (also known as lahars, an Indonesian term) can reach great distances after they leave the flanks of the volcano and can damage structures in flat areas surrounding the volcanoes. Volcanic edifices are young, unconsolidated, and geologically weak structures that in many cases can collapse and cause rockslides, landslides, and debris avalanches. Many islands of volcanic origin experience periodic failure of their perimeter areas (due to the weak volcanic surface deposits), and masses of soil and rock slide into the ocean or other water bodies, such as inlets. Such collapses may create massive sub-marine landslides that may also rapidly displace water, subsequently creating deadly tsunamis that can travel and do damage at great distances, as well as locally. Figure 28 shows a collapse of the side of a volcano and the resulting devastation.

Figure 28. The side of Casita Volcano in Nicaragua, Central America, collapsed on October 30, 1998, the day of peak rainfall as Hurricane Mitch moved across Central America. This lahar killed more than 2,000 people as it swept over the towns of El Porvenir and Rolando Rodriguez. (Photograph by K.M. Smith, U.S. Geological Survey.)

Human Activities

Populations expanding onto new land and creating neighborhoods, towns, and cities is the primary means by which humans contribute to the occurrence of landslides. Disturbing or changing drainage patterns, destabilizing slopes, and removing vegetation are common human-induced factors that may initiate landslides. Other examples include oversteepening of slopes by undercutting the bottom and loading the top of a slope to exceed the bearing strength of the soil or other component material. However, landslides may also occur in once-stable areas due to other human activities such as irrigation, lawn watering, draining of reservoirs (or creating them), leaking pipes, and improper excavating or grading on slopes. New construction on landslide-prone land can be improved through proper engineering (for example, grading, excavating) by first identifying the site's susceptibility to slope failures and by creating appropriate landslide zoning.

See Appendix A for an expanded, detailed list of causes/triggering mechanisms of landslides.

128. Assignment 3, Module 8: Tsunami Basics: https://walrus.wr.usgs.gov/tsunami/basics.html

Life of a Tsunami

By Pacific Coastal and Marine Science Center

Panel 1 — Initiation

Earthquakes are commonly associated with ground shaking that is a result of elastic waves traveling through the solid earth.

Sources/Usage: Public Domain. View Media Details

However, near the source of submarine earthquakes, the seafloor is "permanently" uplifted and down-dropped, pushing the entire water column up and down. The potential energy that results from pushing water above mean sea level is then transferred to horizontal propagation of the tsunami wave (kinetic energy). For the case shown above, the earthquake rupture occurred at the base of the continental slope in relatively deep water. Situations can also arise where the earthquake rupture occurs beneath the continental shelf in much shallower water.

Note: In the figure, the waves are greatly exaggerated compared to water depth. In the open ocean, the waves are at most several meters high spread over many tens to hundreds of kilometers in length.

Panel 2 — Split

Within several minutes of the earthquake, the initial tsunami (Panel 1) is split into a tsunami that travels out to the deep ocean (distant tsunami) and another tsunami that travels towards the nearby coast (local tsunami). The height above mean sea level of the two oppositely traveling tsunamis is approximately half that of the original tsunami (Panel 1). (This is somewhat modified in three dimensions, but the same idea holds.) The speed at which both tsunamis travel varies as the square root of the water depth. Therefore, the deep-ocean tsunami travels faster than the local tsunami near shore.

Sources/Usage: Public Domain. View Media Details

Panel 3 — Amplification

Several things happen as the local tsunami travels over the continental slope. Most obvious is that the amplitude increases. In addition, the wavelength decreases. This results in steepening of the leading wave--an important control of wave runup at the coast (next panel). Note that the first part of the wave reaching the local shore is a trough, which will appear as the sea receeding far from shore. This is a common natural warning sign for tsunamis. Note also that the deep ocean tsunami has traveled much farther than the local tsunami because of the higher propagation speed. As the deep ocean tsunami approaches a distant shore, amplification and shortening of the wave will occur, just as with the local tsunami shown above.

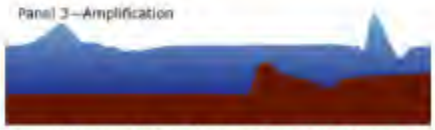

Sources/Usage: Public Domain. View Media Details

Panel 4 — Runup

Tsunami runup occurs when a peak in the tsunami wave travels from the near-shore region onto shore. Runup is a measurement of the height of the water onshore observed above a reference sea level.

Sources/Usage: Public Domain. View Media Details

Except for the largest tsunamis, such as the 2004 Indian Ocean event, most tsunamis do not result in giant breaking waves (like normal surf waves at the beach that curl over as they approach shore). Rather, they come in much like very strong and fast-moving tides (i.e., strong surges and rapid changes in sea level). Much of the damage inflicted by tsunamis is caused by strong currents and floating debris. The small number of tsunamis that do break often form vertical walls of turbulent water called bores. Tsunamis will often travel much farther inland than normal waves.

Persistence of Tsunami Waves

Do tsunamis stop once on land? No! After runup, part of the tsunami energy is reflected back to the open ocean and scattered by sharp variations in the coastline. In addition, a tsunami can generate a particular type of coastal trapped wave called an edge wave. Edge waves travel back-and forth, parallel to shore. This results in many arrivals of the tsunami at a particular point on the coast rather than an arrival as a single wave. Because of the complicated behavior of tsunami waves near the coast, the first amplitude and surge (runup) of a tsunami is often not the largest, emphasizing the importance of not returning to a beach many hours after a tsunami initially hits.

Northern California

To illustrate this phenomenon, the simulations below show tsunami wave behavior along the northern California coastline. For visualization purposes, tsunami wave amplitudes are exaggerated and 2.5 hours of elapse time has been compressed into 30 seconds of animation time.

Resonance within harbors and estuaries is not shown in these simulations, but it is another important aspect that contributes to the persistence of tsunami waves.

Note: these animations might take a moment to load, depending on your internet speed. If they do not play immediately upon clicking the play button, please give them some time to load.

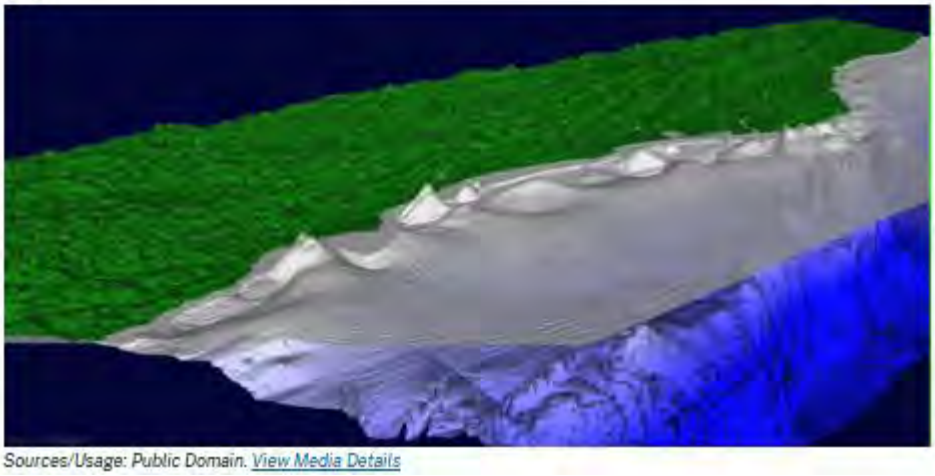
Sources/Usage: Public Domain. View Media Details

View to the southeast.

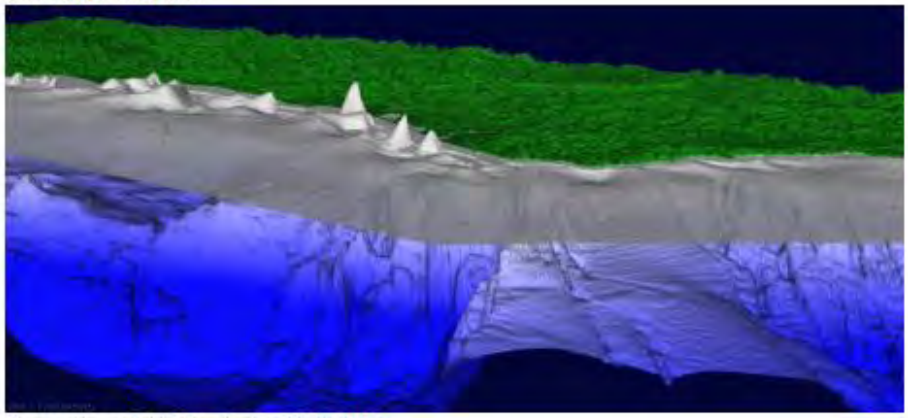

Sources/Usage: Public Domain. View Media Details

View to the northeast.

Central California

The simulations below show tsunami wave behavior long the central California coastline. For visualization purposes, tsunami wave amplitudes are exaggerated and 70 minutes of elapse time has been compressed into 20 seconds of animation time.

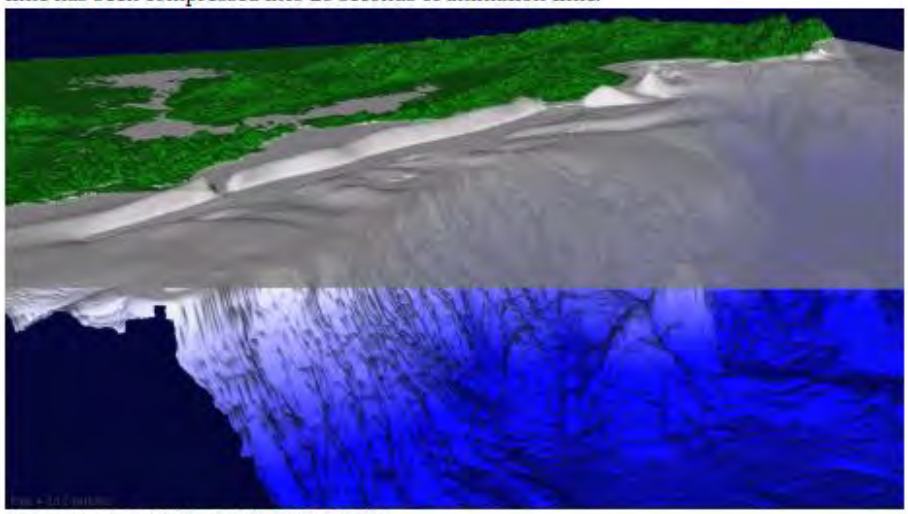

Sources/Usage: Public Domain. View Media Details

View to the southeast.

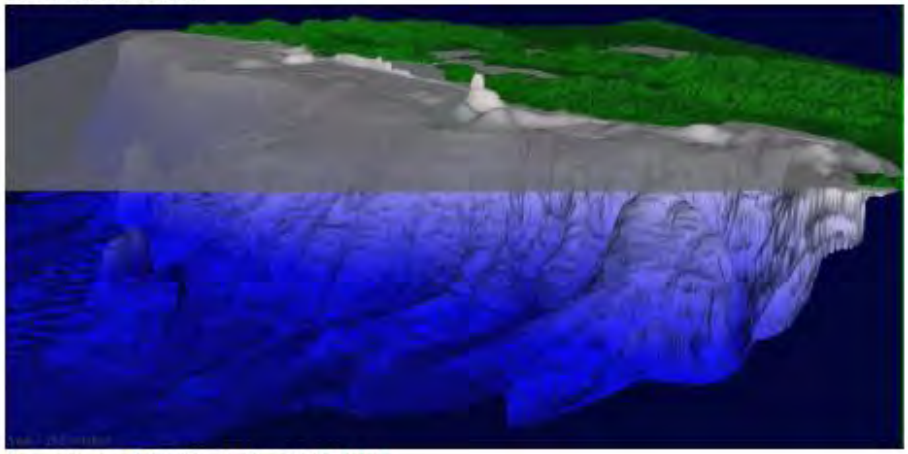

Sources/Usage: Public Domain. View Media Details

View to the northeast.

129. Assignment 3, Module 8: Megathrust Tsunamis: https://www.iris.edu/hq/inclass/animation/subduction_zone_tsunamis_generated_by_megathrust_earthquakes

Subduction Zone: Tsunamis Generated by Megathrust Earthquakes

5min 43s | Novice | Spanish

What is a megathrust earthquake?

Subduction zone megathrust earthquakes, the most powerful earthquakes in the world, can produce tsunamis through a variety of structures that are missed by simple models. These include fault boundary rupture, deformation of overlying plate, splay faults and landslides. In this animation, we explore the three different tsunami-producing mechanisms by examining three famous earthquakes: Japan 2011, Chile 2010, and Alaska 2014. From a hazards viewpoint, it is critical to remember that tsunamis are multiple waves that often arrive on shore for many hours after the initial wave. The above mentioned quakes, as well as the catastrophic 2004 Sumatra subduction-zone megathrust earthquake, have delivered powerful lessons that rapid evacuation of tsunami inundation zones is a life-saving emergency response.

CLOSED CAPTIONING: A **.srt** file is included with the download. Use appropriate media player to utilize captioning.

Keypoints:

Megathrust earthquakes :

- are the most powerful earthquakes in the world
- occur where two plates converge, particularly in subduction zones
- reveal several different tsunami-producing behaviors
- can generate large tsunamis

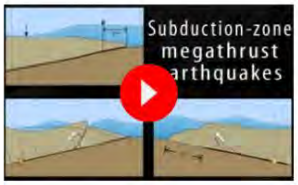

Resource Files

Download All 16MB

Optional Files 4

- Megathrust animation text
- Megathrust Type 1 (excerpt from animation)
- GIF Megathrust Type 3 (excerpt from animation)

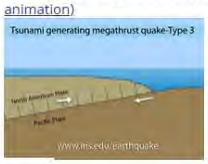

- GIF Megathrust Type 2 (excerpt from animation)

130. Assignment 3, Module 8: Tsunami: https://www.ga.gov.au/education/natural-hazards/tsunami

What is a tsunami?

Tsunami (pron: 'soo-nar-me') is a Japanese word: 'tsu' meaning harbour and 'nami' meaning wave. Tsunami are waves caused by sudden movement of the ocean surface due to earthquakes, landslides on the sea floor, land slumping into the ocean, large volcanic eruptions or meteorite impact in the ocean.

Until recently, tsunami were called tidal waves, but this term is generally discouraged because tsunami generation has nothing to do with tides (which are driven by the gravity of the Earth, Moon and Sun). Although some tsunami may appear like a rapidly rising or falling tide at the coast, in other situations they can also feature one or more turbulent breaking waves.

The Great Wave off Kanagawa, by Katsushika Hokusai.

How do tsunami differ from regular waves?

A tsunami is different from a wind-generated surface wave on the ocean. While wind-generated waves in the deep ocean only cause water movement near the surface, a tsunami involves the movement of water from the surface to the seafloor. Interestingly this causes the speed of a tsunami to be controlled by the water depth, with faster speeds in deeper water. Consequently, a tsunami slows as it approaches land and reaches increasingly shallow water, which causes the distance between successive wave peaks to decrease as well. Because the total energy within the wave does not change, the energy is transferred to increasing the wave height (or amplitude). This is called wave shoaling.

A tsunami is often a series of waves and the first may not necessarily have the greatest amplitude. In the open ocean, even the largest tsunami are relatively small, with wave heights typically tens of centimetres or less away from the initial tsunami generation zone. Higher oceanic wave heights often occur very close to the tsunami generation zone and are sometimes observed (e.g., deep oceanic waves near two metres were measured close to the source of the 2011 Japan tsunami). In any case, the shoaling effect can greatly increase open ocean wave heights upon reaching the coast, with some tsunami reaching an onshore height more than ten metres above sea level. Such extreme inundation is more likely to occur nearer to the tsunami generation location (where oceanic wave heights are larger), and at locations where the coastline shape is particularly favourable to tsunami amplification. Most tsunami do not cause such extreme coastal inundation, and the effect of small events may not be noticeable to without careful analysis of tide gauge measurements.

What causes tsunami?

Earthquakes

75% of tsunami have been caused by large earthquakes on the sea floor when slabs of rock move past each other suddenly, causing the overlying water to move. The resulting waves move away from the source of the earthquake event.

Landslides

Landslides can happen on the seafloor, just like on land. Areas of the seafloor that are steep and loaded with sediment, such as the edge of the continental slope, are more prone to undersea landslides.

When an undersea landslide occurs (perhaps after a nearby earthquake) a large mass of sand, mud and gravel can move down the slope. This movement will draw the water down and may cause a tsunami that will travel across the ocean.

Volcanic eruptions

Tsunami initiated by volcanic eruptions are less common. They occur in several ways:

- destructive collapse of coastal, island and underwater volcanoes which result in massive landslides
- pyroclastic flows, which are dense mixtures of hot blocks, pumice, ash and gas, plunging down volcanic slopes into the ocean and pushing water outwards
- a caldera volcano collapsing after an eruption causing overlying water to drop suddenly.
- Resonance of the ocean and atmospheric pressure waves caused by a large volcanic explosion

Where do tsunami occur in Australia?

There is evidence that the Australian coast may have experienced large tsunami during the past few thousand years. This evidence is revealed through anomalous sedimentary deposits (such as those containing shell or coral) or other geomorphic features (Dominey Howes, 2007 ↗, Goff and Chauge-Goff, 2014 ↗). More recently, tsunami continue to be recorded in Australia with most presenting little threat to coastal communities. The significant tsunamis recorded in recent times have all been recorded at tide gauges around the country with some causing damage in the marine environment ↗.

The tsunami hazard faced by Australia ranges from relatively low along the southern coasts of Australia to moderate along the west coast of Western Australia. This area is more susceptible because of its proximity to large subduction zones along the south-coast of Indonesia, which is a region of significant earthquake and volcanic activity.

Several significant tsunami have impacted Australia's north west coast region. The largest run-up (measured as elevation above sea level) was recorded as 7.9m (Australian Height Datum (AHD)) at Steep Point in Western Australia from the July 2006 Java tsunami ↗. The largest reported offshore wave height was six metres near Cape Leveque from the August 1977 Sunda tsunami.

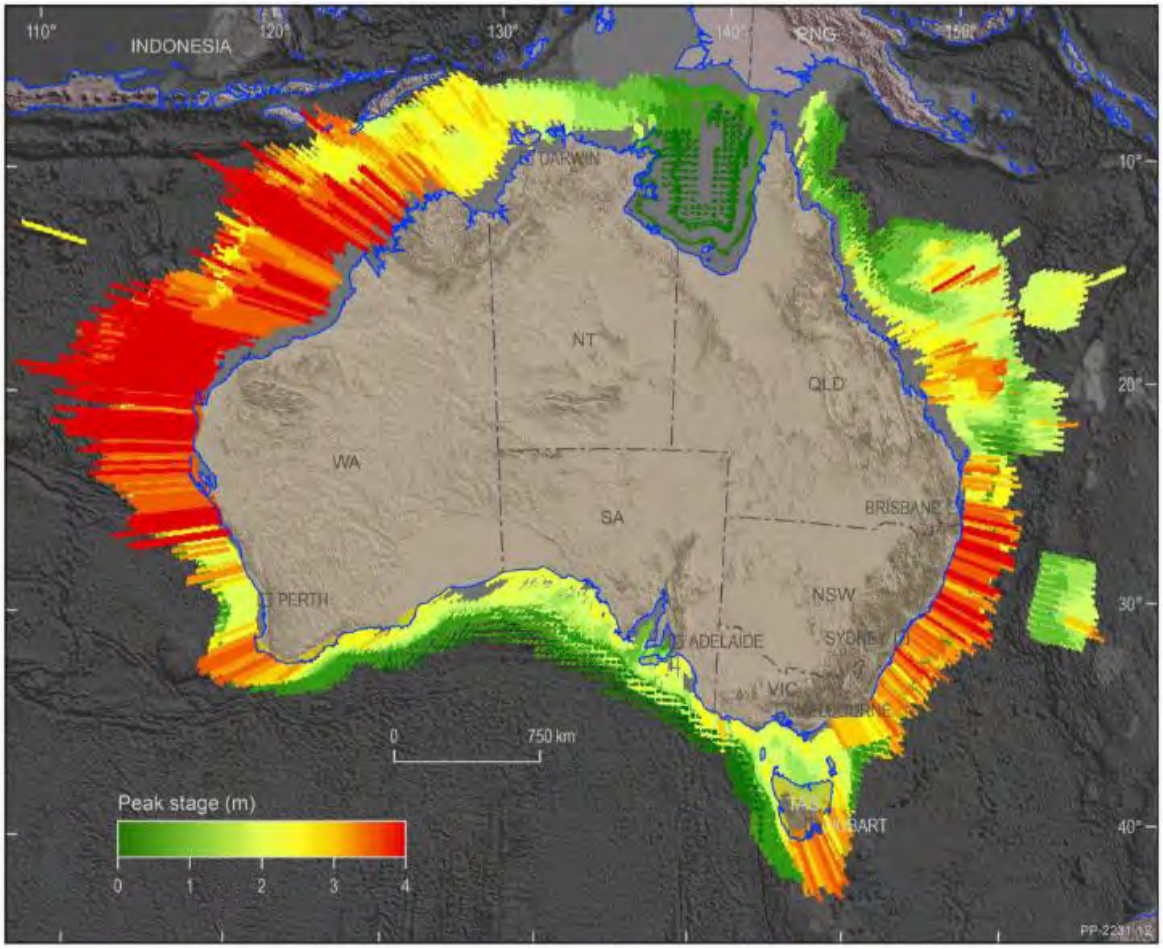

Probabilistic Tsunami Hazard Assessment (PTHA), from Geoscience Australia.

131. Assignment 3, Module 8: Tsunami Ultimate Guide: https://knowledge.aidr.org.au/resources/the-ultimate-guide-tsunami/#/

Earth's Structure

Our planet is made of many layers, like an onion. On the outside is the hard crust sitting on top of the mantle. On the inside is the solid core, which is surrounded by the liquid outer core.

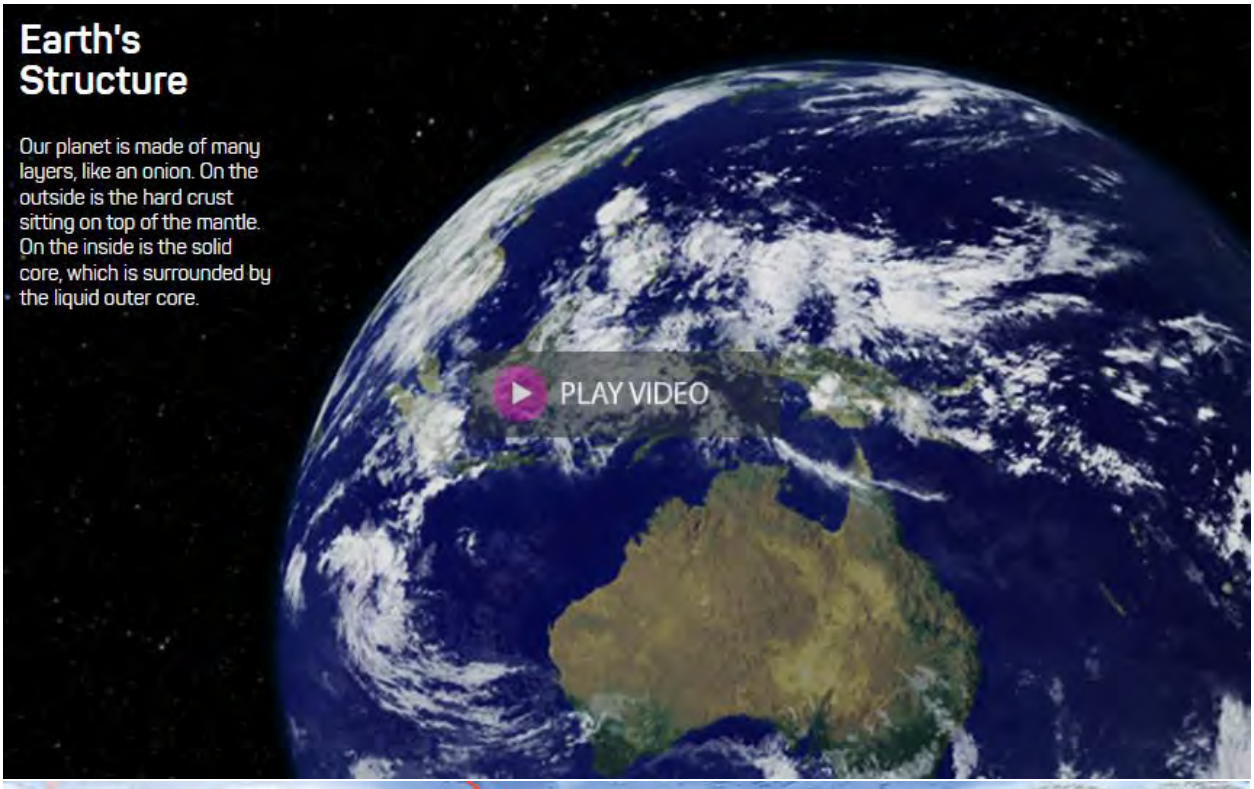

Plate Boundaries

Earth's crust is divided into several pieces called tectonic plates, which are about 20 km thick. They are constantly moving towards, away from or past each other.

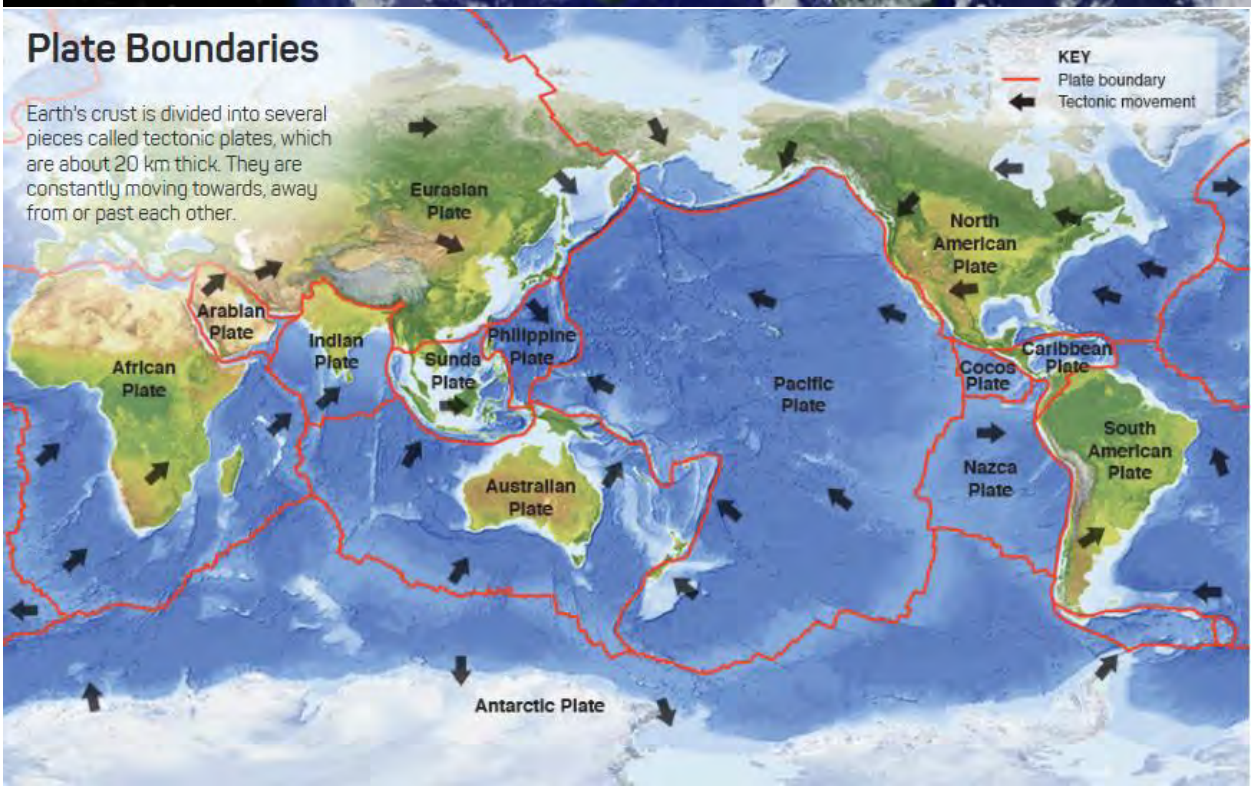

Earthquakes

An earthquake occurs as a result of a sudden release of stress in Earth's crust caused by plate movements. Seismic waves created by this energy make rocks in the crust break and move. During an earthquake the ground may shake and sometimes move permanently.

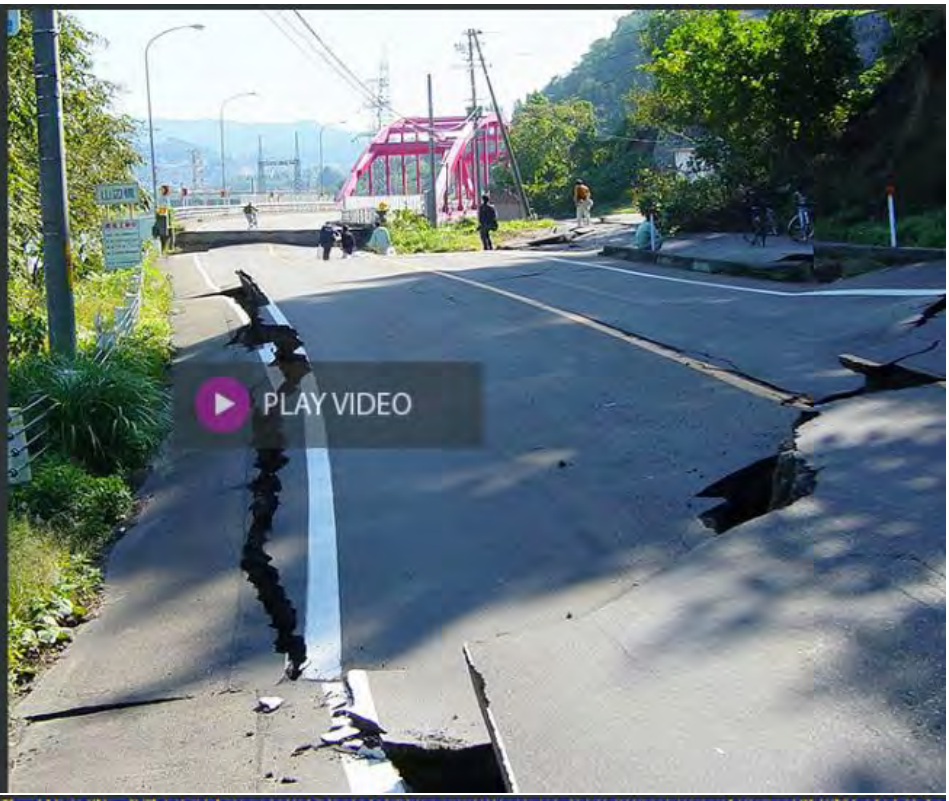

Measuring Earthquakes

Earthquakes produce seismic waves that travel through Earth. The size (or magnitude) of an earthquake is measured by devices called seismometers, which record movement of the ground, including seismic waves. Earthquakes greater than magnitude 6.5 can potentially cause a tsunami.

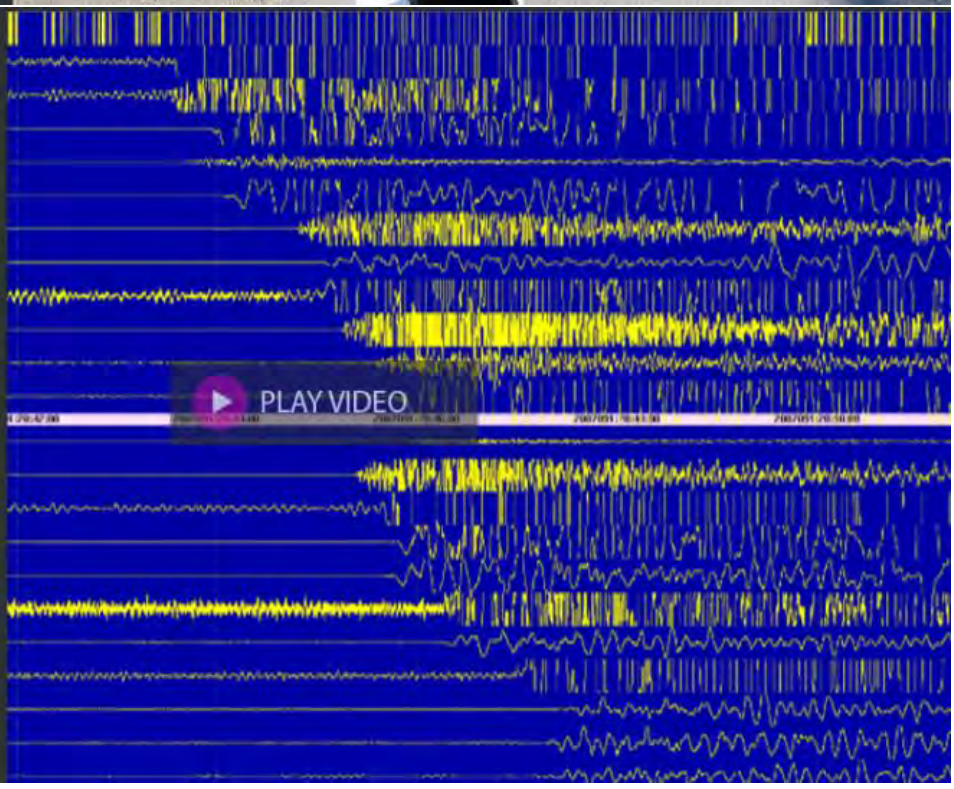

Subduction

Subduction occurs on Earth's crust where two tectonic plates meet. When one plate moves under the other plate it sinks into the mantle and forces the other plate upwards causing an earthquake. Typically, large tsunami waves are created by underwater earthquakes that occur along subduction zones.

How Earthquakes Feel

Have you ever wondered how an earthquake feels? These spheres show the relative energy of earthquake magnitudes 4 to 10. The release of energy from an earthquake increases by 32 for every unit of magnitude. Examples of actual events are also shown.

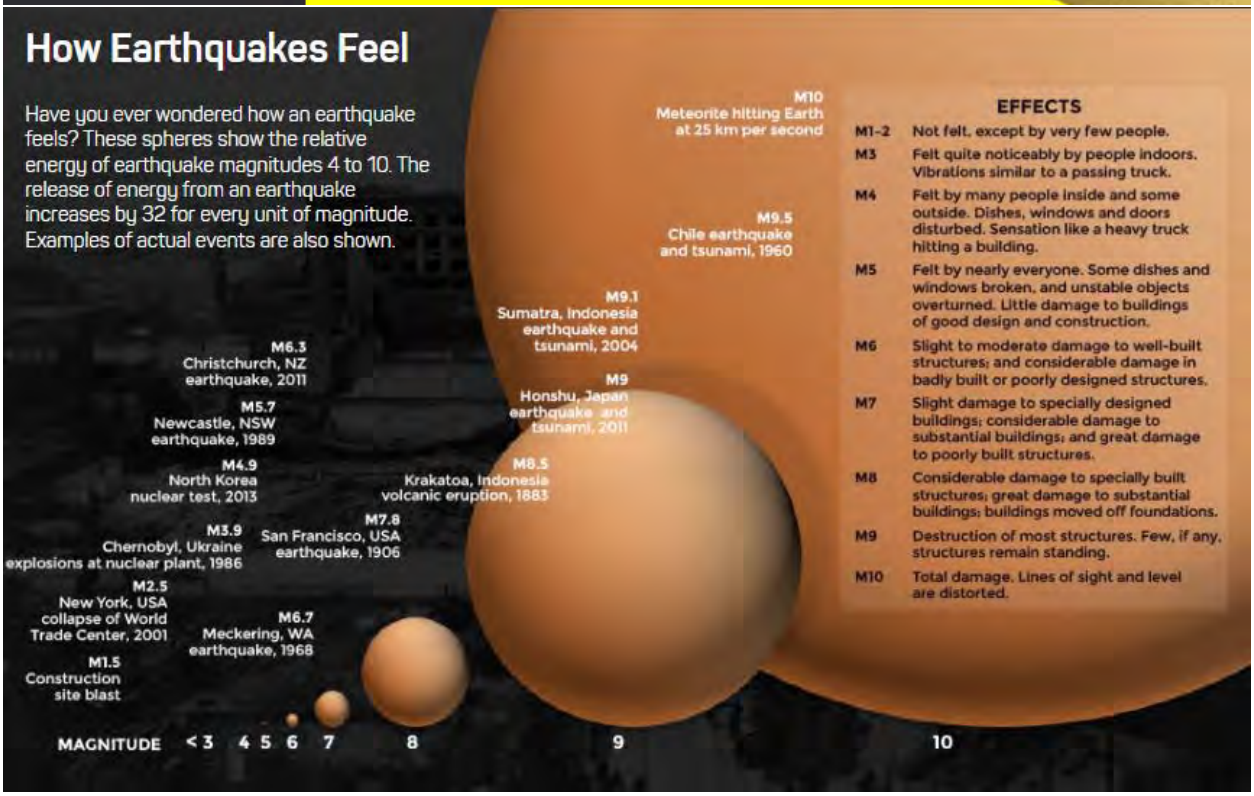

EFFECTS	
M1-2	Not felt, except by very few people.
M3	Felt quite noticeably by people indoors. Vibrations similar to a passing truck.
M4	Felt by many people inside and some outside. Dishes, windows and doors disturbed. Sensation like a heavy truck hitting a building.
M5	Felt by nearly everyone. Some dishes and windows broken, and unstable objects overturned. Little damage to buildings of good design and construction.
M6	Slight to moderate damage to well-built structures; and considerable damage in badly built or poorly designed structures.
M7	Slight damage to specially designed buildings; considerable damage to substantial buildings; and great damage to poorly built structures.
M8	Considerable damage to specially built structures; great damage to substantial buildings; buildings moved off foundations.
M9	Destruction of most structures. Few, if any, structures remain standing.
M10	Total damage. Lines of sight and level are distorted.

Ring of Fire

Around the Pacific Ocean is a region called the Ring of Fire. The edges of the tectonic plates interact to form highly active seismic belts. The ring contains about 90 per cent of the world's volcanoes, and most of the world's tsunami events originate in the area.

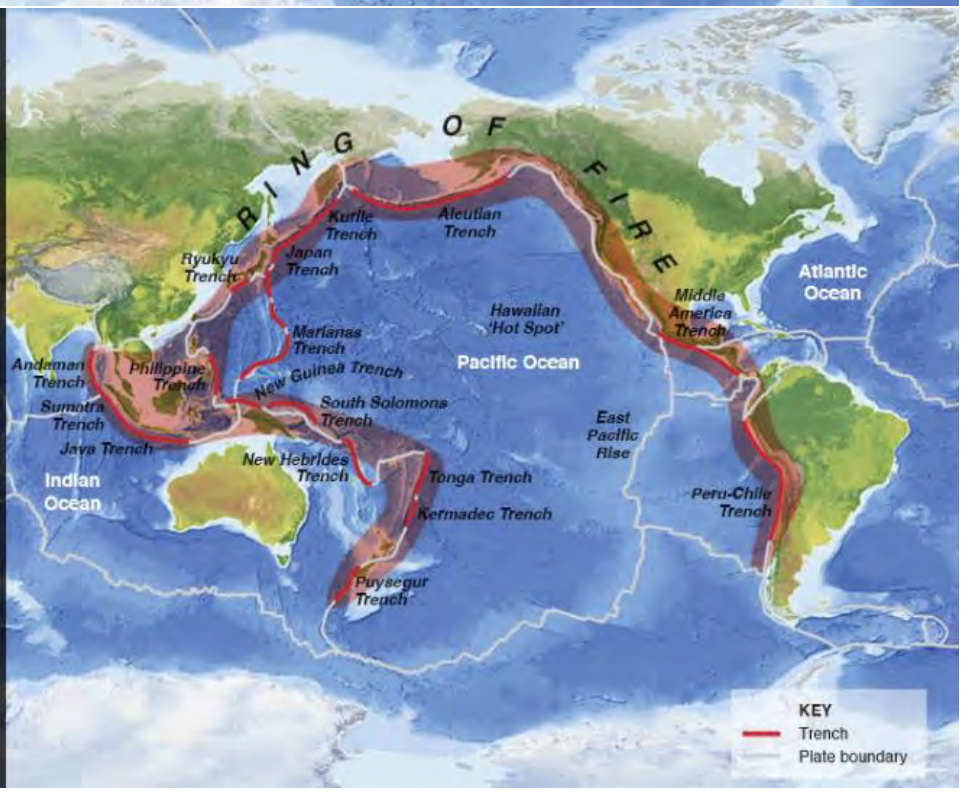

2011 World Earthquakes

In 2011, there were more than 9,300 earthquakes of magnitude 4.5 or higher. A large series of earthquakes preceded and followed the M9.0 earthquake that caused the Japanese tsunami on 11 March. This video shows the location of each of these earthquakes, and the yellow line (at the bottom left) keeps count of the quakes.

Tsunami Causes

Most tsunami waves are started by earthquakes, usually on the ocean floor. Other causes include landslides, volcanic eruptions, weather events and meteors hitting Earth. Scientists do not know the cause of about 10 per cent of all tsunami events.

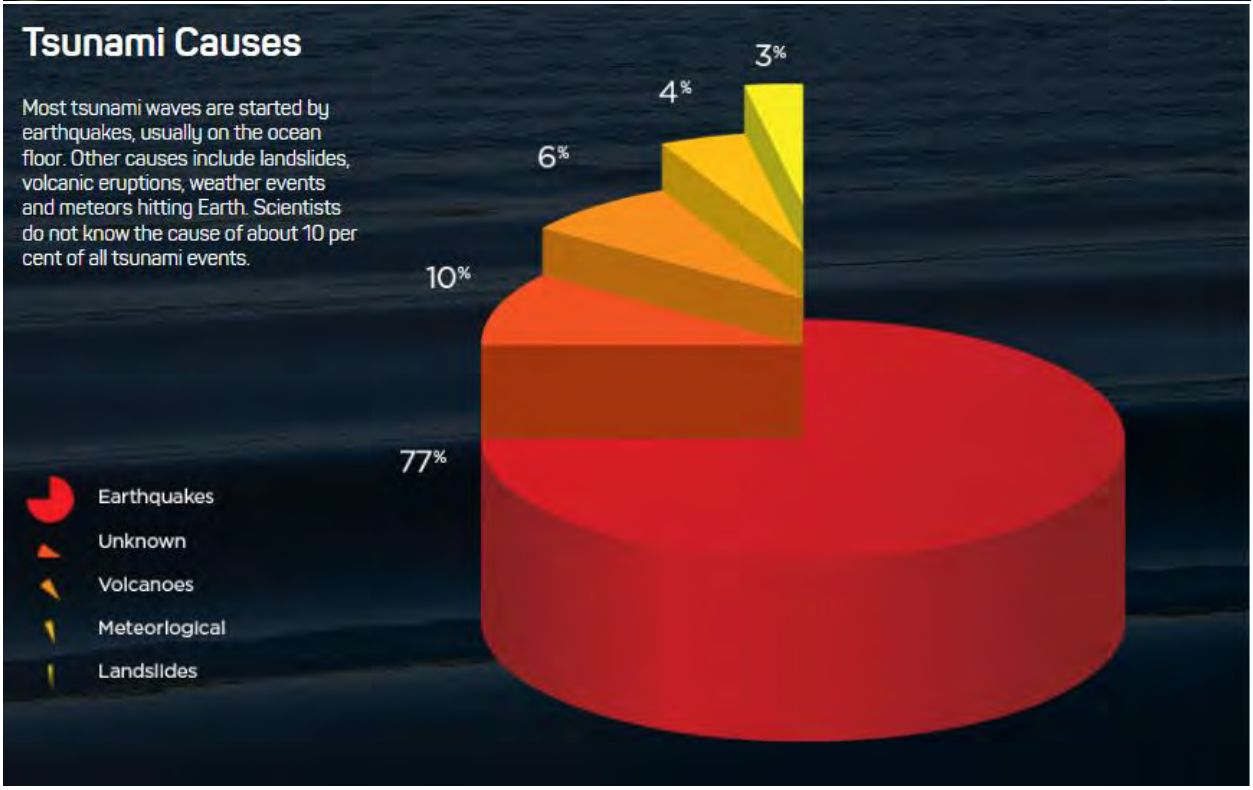

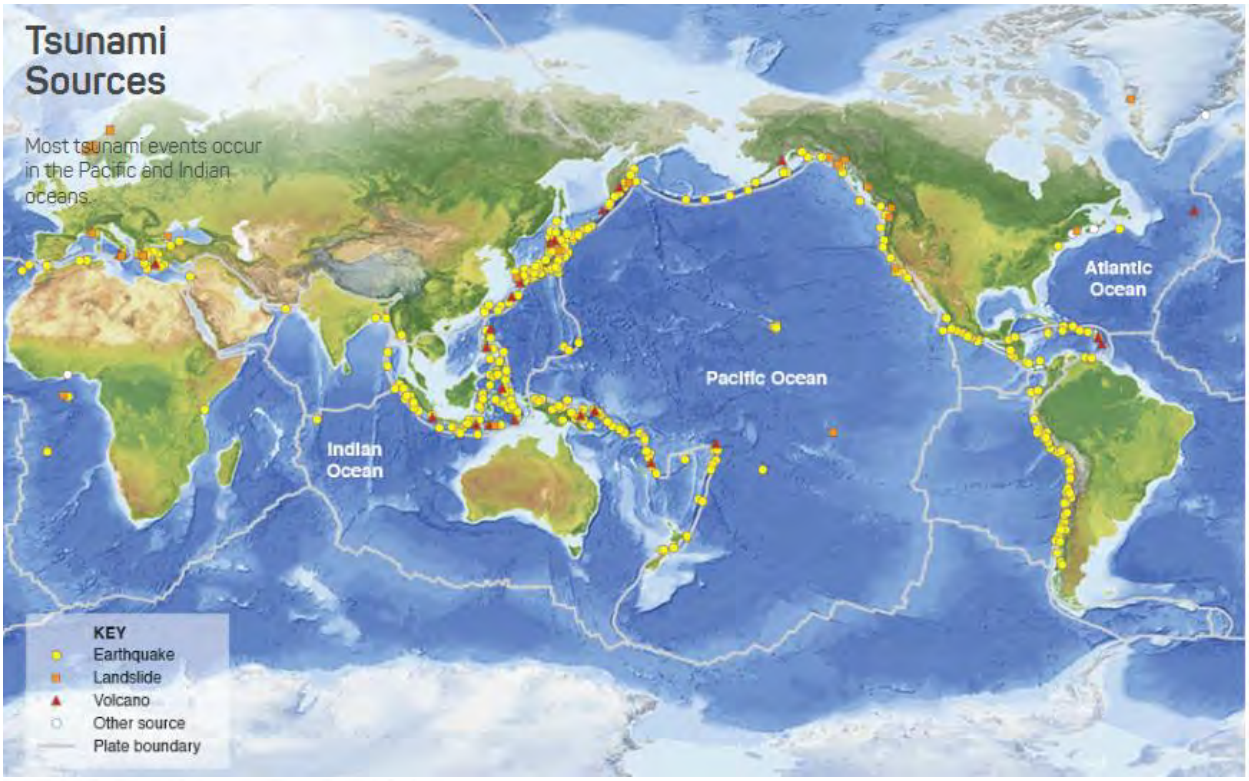

Undersea Earthquakes

An earthquake on the ocean floor can result in a sudden rise or fall of Earth's crust. This movement can cause the water above to rise or fall, creating tsunami waves.

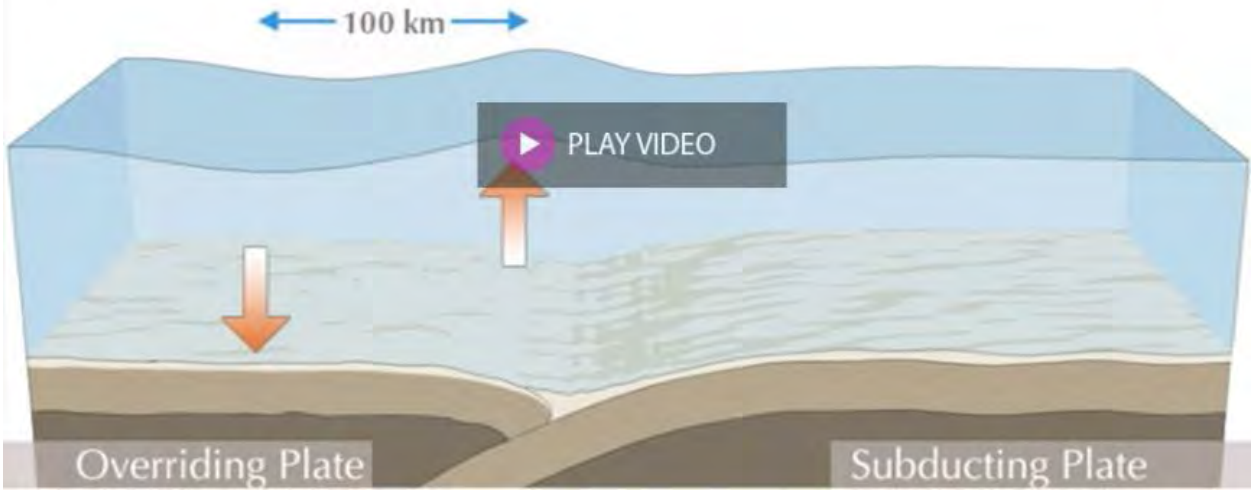

Landslides

An undersea landslide, or one that happens on land and moves into the ocean, can disturb the overlying water and create a tsunami. Landslides are produced when slopes become unstable and fail because of gravity. Australia's east coast could experience a tsunami generated from a landslide on its continental shelf, which is the world's steepest.

Volcanic Activity

The collapse of a coastal or underwater volcano can cause a landslide leading to a tsunami. Underwater eruptions where hot magma and cold sea water meet can create a steam explosion resulting in a tsunami.

Likely Tsunami Risk Zones

Subduction zones are often the source of earthquakes that create tsunami. The waves can travel thousands of kilometres across the ocean.

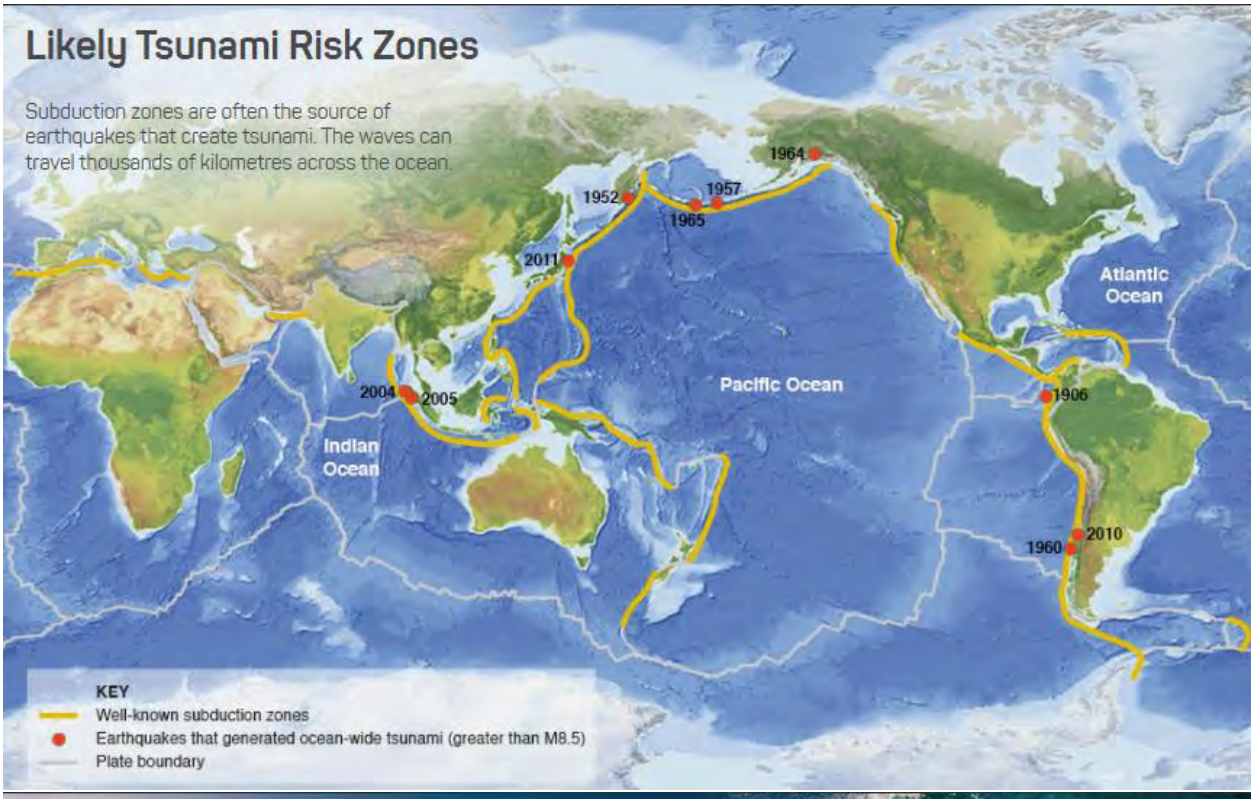

Tsunami and Wind Waves

Tsunami waves move an entire column of water from the ocean floor to its surface and can be hundreds of kilometres apart. Waves generated by wind only move across the surface of the ocean and are usually just a few metres apart.

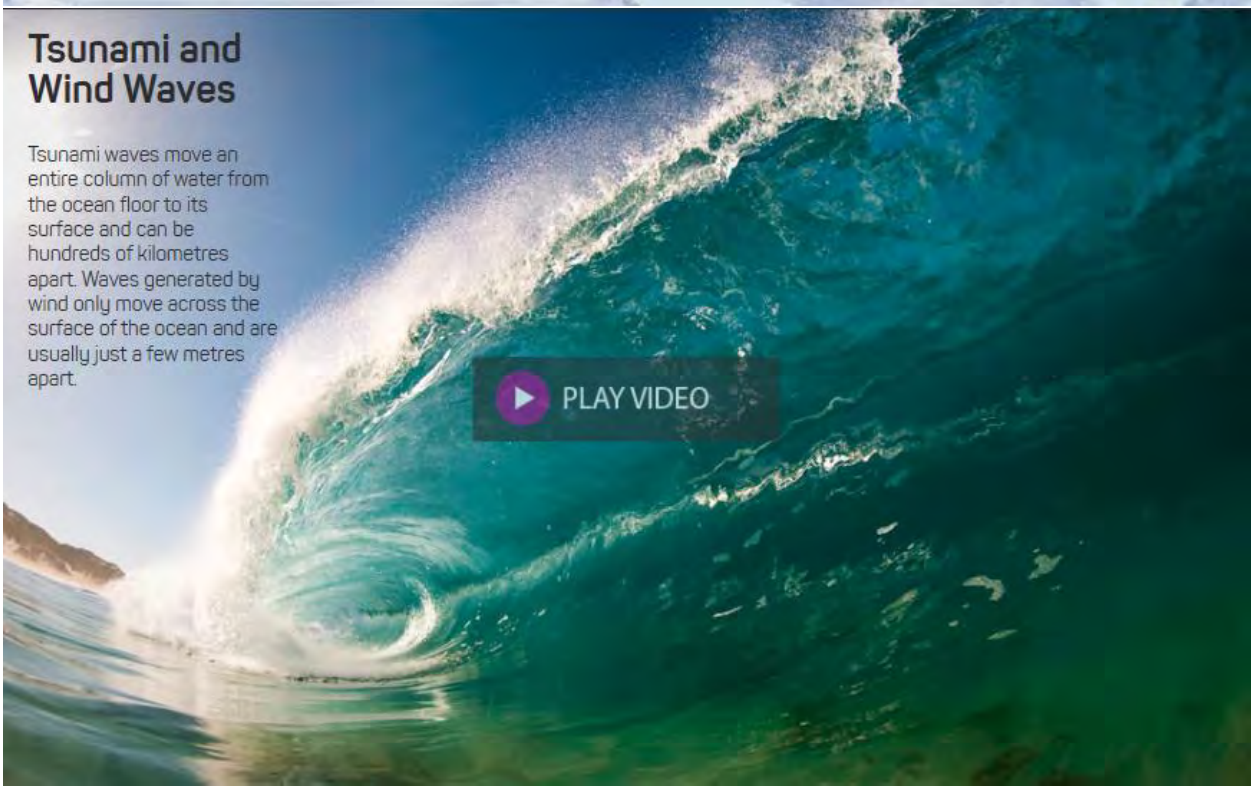

Tsunami in Motion

From their point of origin, tsunami waves travel in many directions. As the waves move through the ocean they change shape and direction when they encounter land and variations in the sea floor. This video shows the generation of the 2011 Japanese tsunami and its waves in motion.

PLAY VIDEO

Tsunami Travel Time

In the open ocean, tsunami waves can travel as fast as a jet plane (640-960 km per hour). Tsunami waves can travel thousands of kilometres from their point of origin, affecting large areas of ocean. This map shows how rapidly (in hours) waves from the 2011 Japanese tsunami spread across the Pacific Ocean.

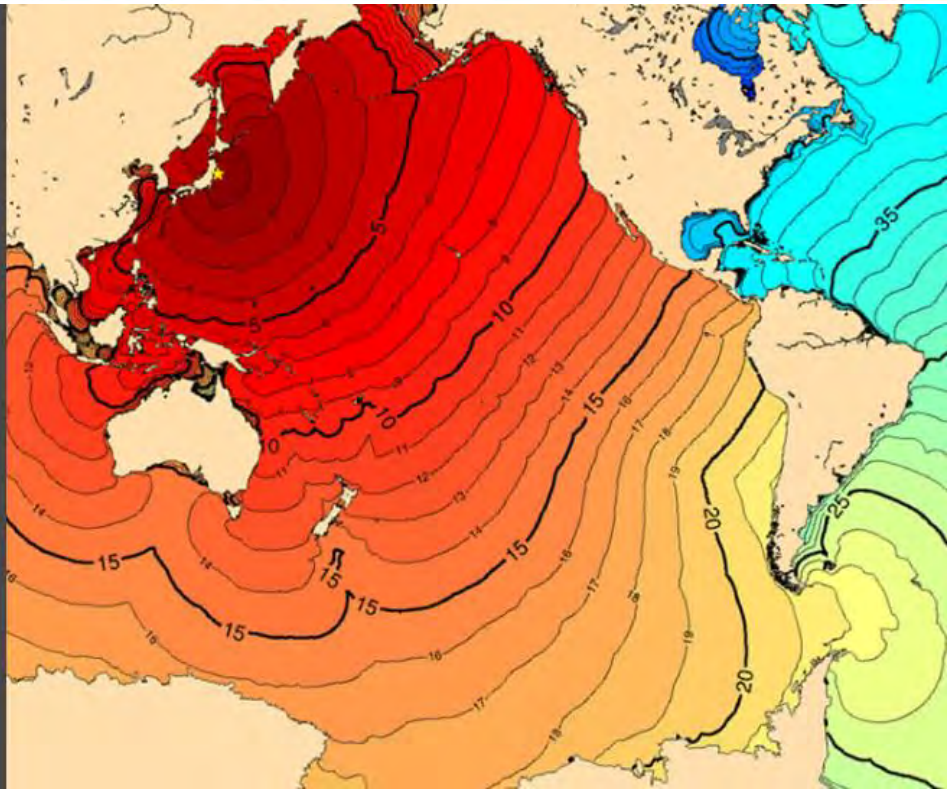

132. Assignment 3, Module 9: EQ ShakeMaps: https://earthquake.usgs.gov/data/shakemap/

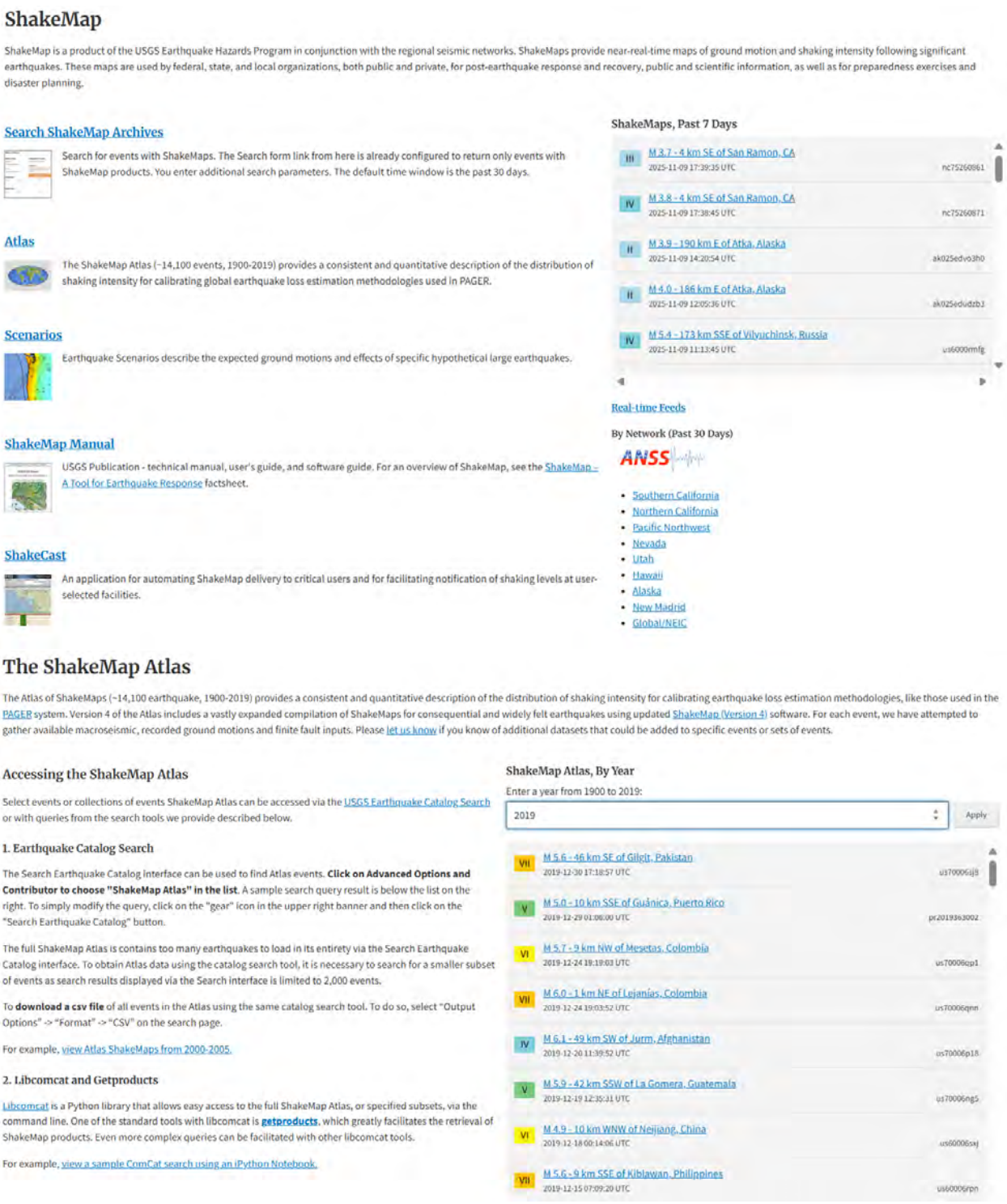

ShakeMap

ShakeMap is a product of the USGS Earthquake Hazards Program in conjunction with the regional seismic networks. ShakeMaps provide near-real-time maps of ground motion and shaking intensity following significant earthquakes. These maps are used by federal, state, and local organizations, both public and private, for post-earthquake response and recovery, public and scientific information, as well as for preparedness exercises and disaster planning.

Search ShakeMap Archives

Search for events with ShakeMaps. The Search form link from here is already configured to return only events with ShakeMap products. You enter additional search parameters. The default time window is the past 30 days.

Atlas

The ShakeMap Atlas (~14,100 events, 1900-2019) provides a consistent and quantitative description of the distribution of shaking intensity for calibrating global earthquake loss estimation methodologies used in PAGER.

Scenarios

Earthquake Scenarios describe the expected ground motions and effects of specific hypothetical large earthquakes.

ShakeMap Manual

USGS Publication - technical manual, user's guide, and software guide. For an overview of ShakeMap, see the ShakeMap - A Tool for Earthquake Response factsheet.

ShakeCast

An application for automating ShakeMap delivery to critical users and for facilitating notification of shaking levels at user-selected facilities.

ShakeMaps, Past 7 Days

- III M 3.7 - 4 km SE of San Ramon, CA — 2025-11-09 17:39:35 UTC — nc75260861
- IV M 3.8 - 4 km SE of San Ramon, CA — 2025-11-09 17:38:45 UTC — nc75260871
- II M 3.9 - 190 km E of Atka, Alaska — 2025-11-09 14:20:54 UTC — ak025edvo3h0
- II M 4.0 - 186 km E of Atka, Alaska — 2025-11-09 12:05:36 UTC — ak025edudzbJ
- IV M 5.4 - 173 km SSE of Vilyuchinsk, Russia — 2025-11-09 11:13:45 UTC — us6000mnfg

Real-time Feeds

By Network (Past 30 Days)

ANSS

- Southern California
- Northern California
- Pacific Northwest
- Nevada
- Utah
- Hawaii
- Alaska
- New Madrid
- Global/NEIC

The ShakeMap Atlas

The Atlas of ShakeMaps (~14,100 earthquake, 1900-2019) provides a consistent and quantitative description of the distribution of shaking intensity for calibrating earthquake loss estimation methodologies, like those used in the PAGER system. Version 4 of the Atlas includes a vastly expanded compilation of ShakeMaps for consequential and widely felt earthquakes using updated ShakeMap (Version 4) software. For each event, we have attempted to gather available macroseismic, recorded ground motions and finite fault inputs. Please let us know if you know of additional datasets that could be added to specific events or sets of events.

Accessing the ShakeMap Atlas

Select events or collections of events ShakeMap Atlas can be accessed via the USGS Earthquake Catalog Search or with queries from the search tools we provide described below.

1. Earthquake Catalog Search

The Search Earthquake Catalog interface can be used to find Atlas events. **Click on Advanced Options and Contributor to choose "ShakeMap Atlas" in the list.** A sample search query result is below the list on the right. To simply modify the query, click on the "gear" icon in the upper right banner and then click on the "Search Earthquake Catalog" button.

The full ShakeMap Atlas is contains too many earthquakes to load in its entirety via the Search Earthquake Catalog interface. To obtain Atlas data using the catalog search tool, it is necessary to search for a smaller subset of events as search results displayed via the Search interface is limited to 2,000 events.

To **download a csv file** of all events in the Atlas using the same catalog search tool. To do so, select "Output Options" -> "Format" -> "CSV" on the search page.

For example, view Atlas ShakeMaps from 2000-2005.

2. Libcomcat and Getproducts

Libcomcat is a Python library that allows easy access to the full ShakeMap Atlas, or specified subsets, via the command line. One of the standard tools with libcomcat is **getproducts**, which greatly facilitates the retrieval of ShakeMap products. Even more complex queries can be facilitated with other libcomcat tools.

For example, view a sample ComCat search using an iPython Notebook.

ShakeMap Atlas, By Year

Enter a year from 1900 to 2019:

2019 — Apply

- VII M 5.6 - 46 km SE of Gilgit, Pakistan — 2019-12-30 17:18:57 UTC — us70006ij3
- V M 5.0 - 10 km SSE of Guánica, Puerto Rico — 2019-12-29 01:08:00 UTC — pr2019363002
- VI M 5.7 - 9 km NW of Mesetas, Colombia — 2019-12-24 19:19:03 UTC — us70006cp1
- VII M 6.0 - 1 km NE of Lejanías, Colombia — 2019-12-24 19:03:52 UTC — us70006qnn
- IV M 6.1 - 49 km SW of Jurm, Afghanistan — 2019-12-20 11:39:52 UTC — us70006p18
- V M 5.9 - 42 km SSW of La Gomera, Guatemala — 2019-12-19 12:35:31 UTC — us70006ng5
- VI M 4.9 - 10 km WNW of Neijiang, China — 2019-12-18 00:14:06 UTC — us60006sxj
- VII M 5.6 - 9 km SSE of Kiblawan, Philippines — 2019-12-15 07:09:20 UTC — us60006rpn

Earthquake Scenarios

September 27, 2022

Access Scenario Catalogs

In planning and coordinating emergency response, utilities, local government, and other organizations are best served by conducting training exercises based on realistic earthquake situations—ones similar to those they are most likely to face. ShakeMap Scenario earthquakes can fill this role. They can also be used to examine exposure of structures, lifelines, utilities, and transportation corridors to specified potential earthquakes.

A ShakeMap earthquake scenario is a predictive ShakeMap with an assumed magnitude and location, and, optionally, specified fault geometry.

This 2017 collection of nearly 800 ShakeMap earthquake scenarios is the authoritative U.S.G.S. collection for the continental U.S. The **scenario fault ruptures are derived from the latest National Seismic Hazard Model for the U.S. (Petersen et al, 2014); the collection of events is known as the 2014 Building Seismic Safety Council (BSSC) catalog.** For this BSSC ShakeMap catalog, we leverage ArcGIS Server and ArcGIS Online to display locations, ruptures, and maximum shaking intensities. Each ShakeMap can be selected and any format of each can downloaded.

Sources/Usage: Public Domain. View Media Details

Scenario for Cascadia Rising Exercise.

U.S. Map and List of Scenarios for Building Seismic Safety Council 2014 Event Set

See **bssc2014** catalog link below for more detailed information about this scenario collection. Legacy scenario catalogs are included for archival purposes.

ShakeMap Scenario Documentation

Explore Search

Natural Hazards

Earthquake

Natural Hazards Mission Area

Earthquake Hazards Program

Earthquakes

View All ↓

ShakeMap 4 Manual

written by: C. Bruce Worden, Eric M. Thompson, Michael G. Hearne, and David J. Wald

This online ShakeMap Manual (Worden et al., 2020), is for ShakeMap version 4. Version 4 is the official, supported version of ShakeMap and all earlier versions are now deprecated. This manual supersedes all other versions of the ShakeMap Manual, including the ShakeMap 3.5 Manual (both printed and online) and the USGS Techniques and Methods document (508)12-A1.

ShakeMap®, developed by the U.S. Geological Survey (USGS), facilitates communication of earthquake information beyond just magnitude and location. By rapidly mapping out earthquake ground motions, ShakeMap portrays the distribution and severity of shaking. This information is critical for gauging the extent of the areas affected, determining which areas are potentially hardest hit, and allowing for rapid estimation of losses. Key to ShakeMap's success, algorithms were developed that take advantage of any high-quality recorded ground motions—and any available macroseismic intensity data—to provide ground-truth constraints on shaking. Yet ShakeMap also utilizes best practices for both interpolating recordings and—critically—providing event-specific estimates of shaking in areas where observations are sparse or nonexistent. Thus, ShakeMap portrays the best possible description of shaking by employing a combination of recorded and estimated shaking values.

This Manual provides background on technical aspects of ShakeMap including: 1) information on the wide range of products and formats ShakeMap produces, 2) the uses of these products, and 3) guidance for ShakeMap developers and operators.

Readers interested in understanding the way ShakeMaps works can navigate to the Technical Guide. Those who want to use ShakeMap products and understand their varied forms can jump to the User's Guide. The Software Guide provides information on the software architecture, installation and configuration, and operational considerations for those wishing to run a regional ShakeMap system.

ShakeCast

Last edited by **Kuo-Wan Lin** Mar 28, 2023

Summary

ShakeCast®, short for ShakeMap Broadcast, is a freely available, post-earthquake situational awareness software application. The application aims to help users (e.g., transportation agencies, utility managers, businesses) automatically retrieve earthquake shaking data at their facilities from U.S. Geological Survey (USGS) earthquake products such as the ShakeMap. Users can set thresholds for triggering established post-earthquake response protocols at their facilities. In the event of an earthquake, ShakeCast automatically sends notifications to emergency managers and responders about potential impacts, inspection priorities, and other web-based products.

In general, users could develop their own strategies and tools for utilizing ShakeMap given their unique facilities and communication paths. However, such efforts can be costly and complex. The USGS facilitated this process with the development of ShakeCast, which accomplishes most of the users' critical needs. ShakeCast is particularly useful when an organization manages a significant portfolio of facilities that may be affected by earthquakes and must prioritize with limited resources. Additional user needs include obtaining detailed site-specific information such as licensing basis, response protocol, loss estimate, or ground failure potential.

Suggested citation: Lin, Kw., Wald, D.J., Slosky, D. (2020). Earthquakes, ShakeCast. In: Gupta, H. (eds) Encyclopedia of Solid Earth Geophysics. Encyclopedia of Earth Sciences Series. Springer, Cham. DOI: 10.1007/978-3-030-10475-7_255-1.

Who should use ShakeCast

Businesses, utility managers, emergency responders, and others who have an urgent need for information about the post-earthquake impact on their own facilities so that they can make informed decisions and act quickly to ensure safety, restore system functionality, and minimize losses.

Who should probably not use ShakeCast

Individual users without a significant number of facilities and knowledge of their inventory. ShakeCast requires significant commitment of time, involving expertise in both earthquake engineering and information technology.

Service model

As a distributed software application, ShakeCast can be used in two ways: (1) by running an instance of it in a cloud-hosted service, or (2) by installing it on-premise within a user's network and operating systems.

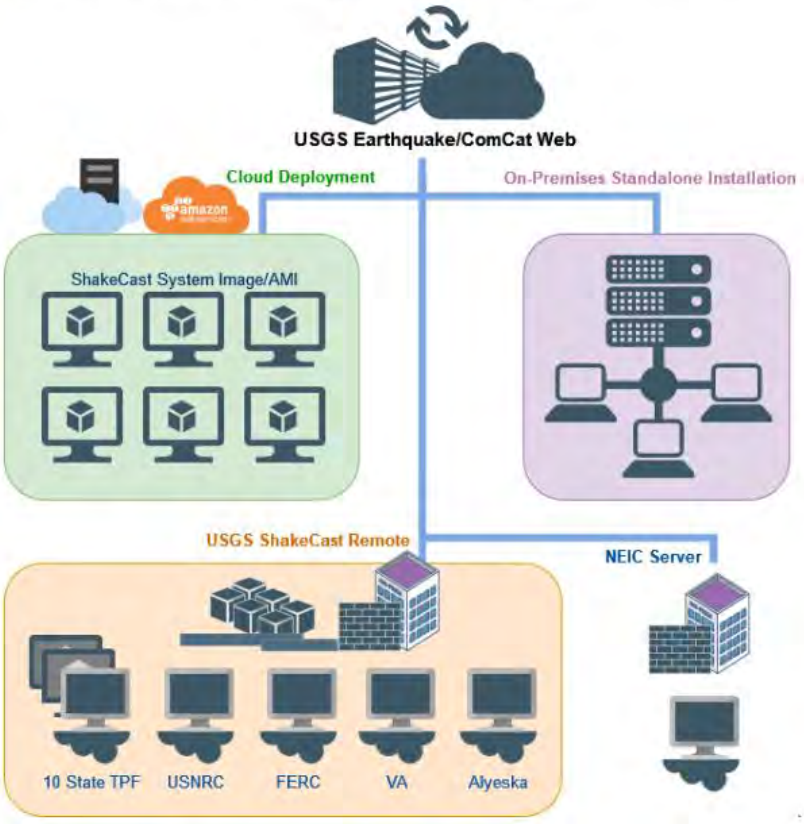

User story: State Departments of Transportation (DOTs)

Caltrans has been collaborating with the USGS since 2005 to develop and continuously improve a robust and operational platform. ShakeCast is particularly suitable for earthquake planning and response purposes by Caltrans and other State DOTs, since they can utilize existing NBI databases, which they are required to keep up-to-date, to assess potential impacts and implement shaking-based inspection priorities. Since 2017, USGS has partnered with Caltrans and nine other State DOTs under a Transportation Pooled Fund (TPF) to fully implement ShakeCast for these departments, adding customized configurations for each department and functions that are pertinent across all departments. An additional goal of this TPF solicitation was to "connect the DOTs" by bringing ShakeCast to all states with seismic hazards, which is important as impacts from major earthquakes could cross state borders (Turner et al., 2018).

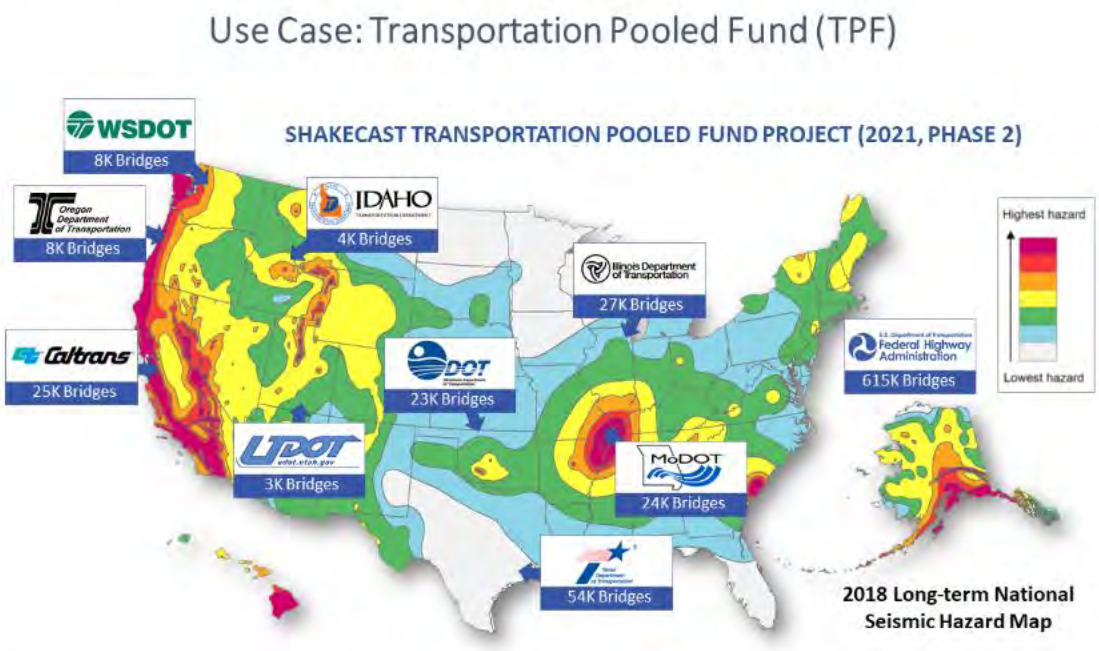

Software history

The current version of ShakeCast, V4 released in 2019, is a complete re-design of the application aimed at alleviating the pain points of its consumer base, while improving functionality. Newer versions of ShakeCast, ShakeMap, "Did You Feel It?", and PAGER systems have been developed in Python due to its functionality and near-ubiquity in computer science courses and in academia. ShakeCast aims to be more intuitive and include features that both general users and administrators will find helpful. Many of the modifications are based on direct feedback from many ShakeCast users, feature requests, best practices in software development, and culling of vestigial functions. For example, developing and incorporating advanced fragility assignments into the ShakeCast Workbook required extensive software modifications and database improvements (Wald et al., 2017).

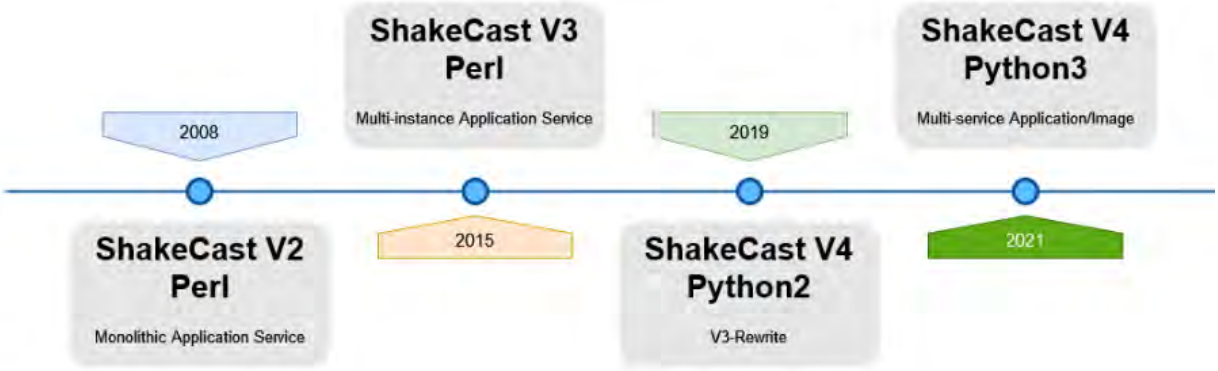

Licensing

133. Assignment 3, Module 9: Induced Seismicity: https://www.usgs.gov/programs/earthquake-hazards/myths-and-misconceptions-about-induced-earthquakes

Myths and Misconceptions About Induced Earthquakes

By Earthquake Hazards Program

Fact 1: Fracking is not directly causing most of the induced earthquakes. Disposal of waste fluids that are a byproduct of oil production is the primary cause of the recent increase in earthquakes in the central United States.

Wastewater disposal wells typically operate for longer durations and inject much more fluid than hydraulic fracturing, making them more likely to induce earthquakes. In Oklahoma, which has the most induced earthquakes in US, only 1–2% of the earthquakes can be linked to hydraulic fracturing operations. The remaining earthquakes are induced by wastewater disposal.

Fact 2: Not all wastewater injection wells induce earthquakes.

Most injection wells are not associated with felt earthquakes. A combination of many factors is necessary for injection to induce felt earthquakes. These include: the injection rate and total volume injected; the presence of faults that are large enough to produce felt earthquakes; stresses that are large enough to produce earthquakes; and the presence of pathways for the fluid pressure to travel from the injection point to faults.

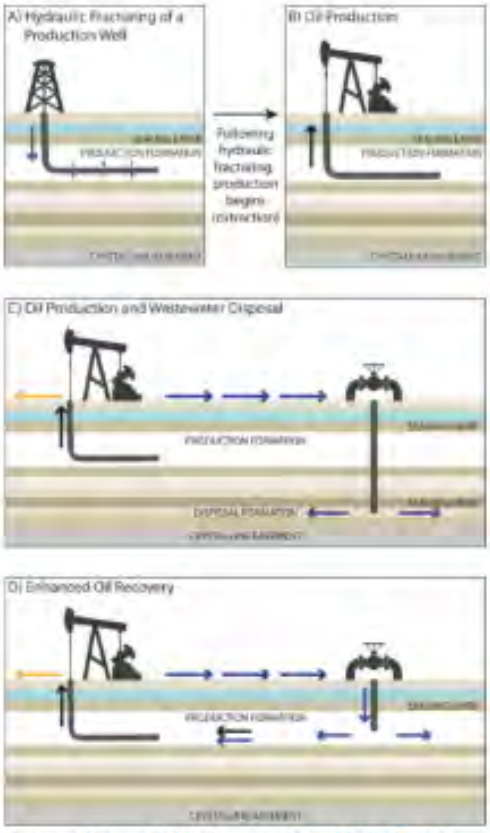

Sources/Usage: Public Domain. View Media Details

Cartoon illustration showing hydraulic fracturing, oil production, wastewater disposal, and enhanced oil production. (Public domain.)

Fact 3: Wastewater is produced at all oil wells, not just hydraulic fracturing sites.

Most wastewater currently disposed of across the nation is generated and produced in the process of oil and gas extraction. As discussed above, saltwater is produced as a byproduct during the extraction process. This wastewater is found at nearly every oil and gas extraction well.

The other main constituent of wastewater is leftover hydraulic fracturing fluid. Once hydraulic fracturing is completed, drilling engineers extract the fluids that are remaining in the well. Some of this recovered hydraulic fracturing fluid is used in subsequent fracking operations, while some of it is disposed of in deep wells.

Fact 4: The content of the wastewater injected in disposal wells is highly variable.

In many locations, wastewater has little or nothing to do with hydraulic fracturing. In Oklahoma, less than 10% of the water injected into wastewater disposal wells is used hydraulic fracturing fluid. Most of the wastewater in Oklahoma is saltwater that comes up along with oil during the extraction process.

In contrast, the fluid disposed of near earthquake sequences that occurred in Youngstown, Ohio, and Guy, Arkansas, consisted largely of spent hydraulic fracturing fluid.

Fact 5: Induced seismicity can occur at significant distances from injection wells and at different depths.

Seismicity can be induced at distances of 10 miles or more away from the injection point and at significantly greater depths than the injection point.

Fact 6: Wells not requiring surface pressure to inject wastewater can still induce earthquakes.

Wells where you can pour fluid down the well without added pressure at the wellhead still increase the fluid pressure within the formation and thus can induce earthquakes.

134. Assignment 3, Module 9: EQ Early Warning Basics:
https://www.usgs.gov/media/images/earthquake-early-warning-basics-0

Earthquake Early Warning Basics

By Earthquake Hazards Program

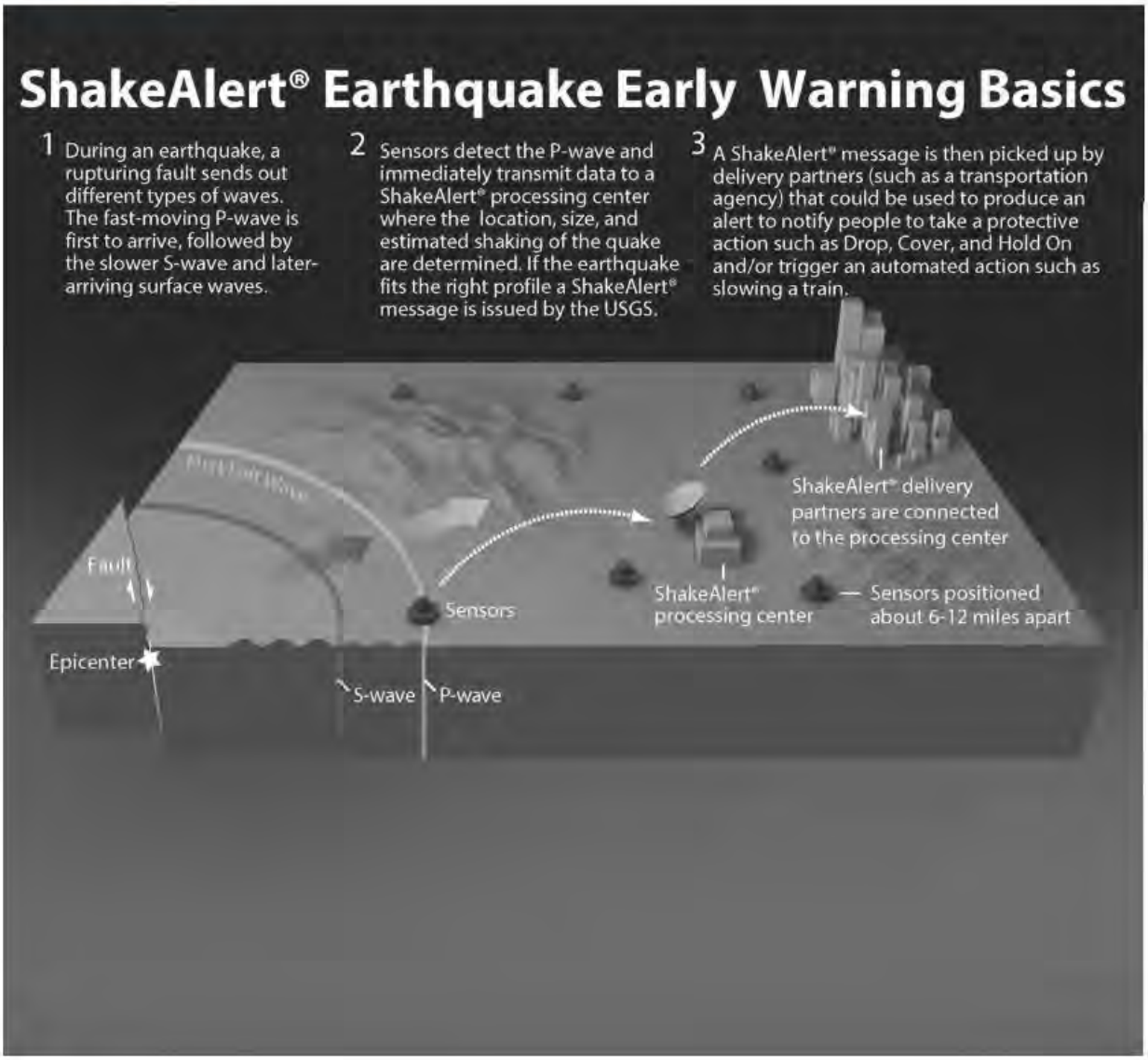

Detailed Description

Earthquake early warning systems like ShakeAlert® work because an alert can be transmitted almost instantaneously, whereas the shaking waves from the earthquake travel through the shallow layers of the Earth at speeds of one to a few kilometers per second (0.5 to 3 miles per second). This diagram shows how such a system would operate. When an earthquake occurs, both compressional (P) waves and transverse (S) waves radiate outward from the epicenter. The P wave, which travels fastest, trips sensors placed in the landscape, transmitting data to a ShakeAlert® processing center where the location, size, and estimated shaking of the earthquake are determined. If the earthquake fits the right profile a ShakeAlert® message is issued by the USGS. The message is picked up by ShakeAlert® partners which could be used to produce an alert to notify people to take a protective action such as Drop, Cover, and Hold On and/or trigger an automated action. USGS image created by Erin Burkett (USGS) and Jeff Goertzen (Orange County Register) and updated by Robert de Groot (USGS).

135. Assignment 3, Module 9: EQ Early Warning USGS:
https://www.usgs.gov/programs/earthquake-hazards/science/early-warning

How the ShakeAlert® System Works

DETECT, DELIVER, PROTECT: ShakeAlert® is not earthquake prediction. Rather, the USGS-operated ShakeAlert Earthquake Early Warning system detects an earthquake that has already started and estimates its location, magnitude and shaking intensity. If an earthquake becomes large enough to meet USGS alert thresholds, a ShakeAlert Message is issued. Then, technical partners, which have entered into a license agreement with the USGS, use this information produce and deliver an alert that prompts people to take a protective action, such as DROP, COVER, AND HOLD ON, and/or to trigger an automated action that can protect vital systems, equipment, facilities, and infrastructure. These automated actions could include slowing a train, closing valves, issuing a public announcement, and many others.

The ShakeAlert system takes a network approach to earthquake detection and alerting. This network uses sensors distributed over a wide area where earthquakes are likely to occur on the West Coast of the United States (with nearly 1,700 anticipated on network build-out). Data from individual sensors across large regions are combined to maximize accuracy and alerting time during moderate-to-large earthquakes.

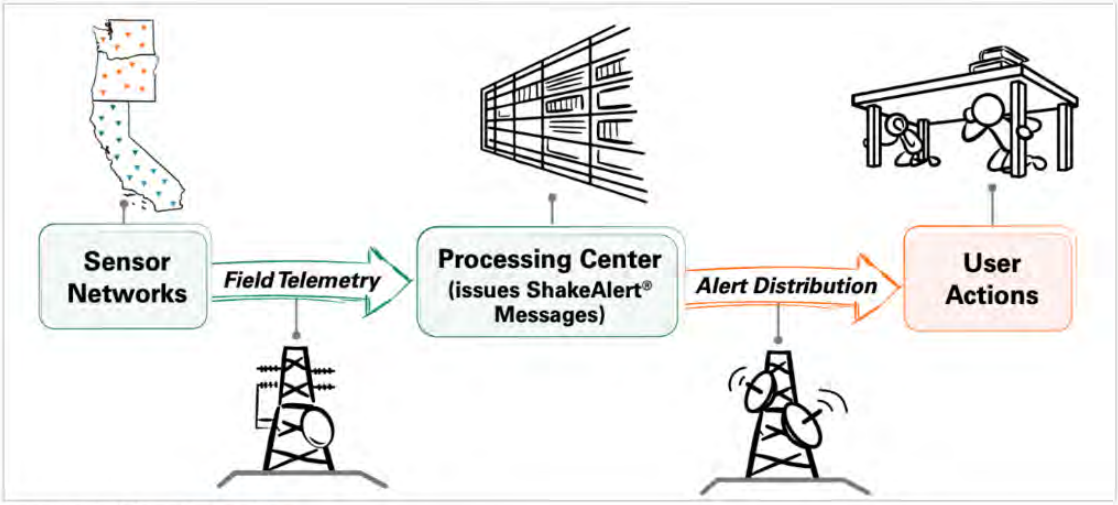

Sources/Usage: Public Domain. View Media Details

ShakeAlert 3 Basic Steps: Sensor Networks to processing center to users.

During an earthquake, a rupturing fault produces several different kinds of waves that carry energy away

from the epicenter like ripples from a rock thrown into a pond. The fastest-moving seismic waves (primary or P-waves) travel about 3.7 miles per second and generally do not produce strong shaking. P-waves are followed by slower moving, and generally more damaging waves (secondary or S-waves) and surface waves that travel about 2.5 miles per second. The ShakeAlert sensor network detects earthquakes quickly, and immediately transmits data to a ShakeAlert Processing Center, where estimates of the location, size, and shaking intensity of the earthquake are determined in a matter of seconds.

Technical Partners are integral to the ShakeAlert System because they are responsible for producing and delivering ShakeAlert-powered alerts to people and critical systems. Technical Partners span multiple industries and sectors, and include private for-profit companies, public entities, and nonprofits that can benefit from becoming part of the ShakeAlert System.

ShakeAlert works because:

- P-waves travel almost twice as fast as the damaging S-waves and surface waves; and
- The speeds of today's data telecommunications systems are many times faster than seismic waves. Both of these factors make it possible for ShakeAlert-powered alerts to reach people before shaking arrives. Because of the speed difference between P-waves, S-waves, and surface waves, someone who is farther from the earthquake's origin has more time to potentially receive an alert before shaking arrives.

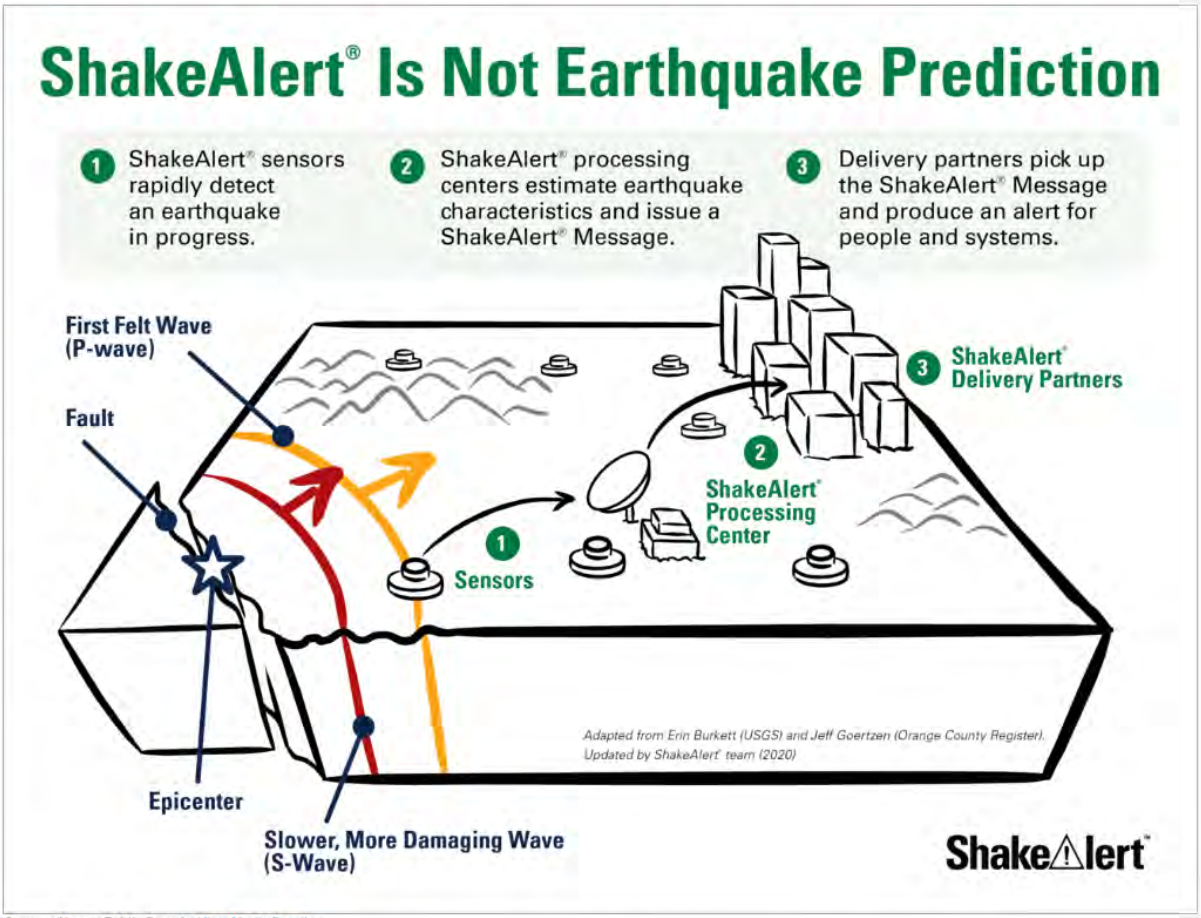

Sources/Usage: Public Domain. *View Media Details*

ShakeAlert Is Not Earthquake Prediction. Cartoon showing that the earthquake has already started when the ShakeAlert message is distributed.

ShakeAlert®-Powered Alert Delivery Levels

If an earthquake becomes large enough to meet USGS alert thresholds, a ShakeAlert Message is issued. ShakeAlert technical partners use this information to produce and deliver alerts that rapidly prompts people to take a protective action, such as DROP, COVER, AND HOLD ON, and/or to trigge an automated action that can protect vital systems, equipment, facilities, and infrastructure. These automated actions could include slowing a train, closing valves, issuing a public announcement, and many others.

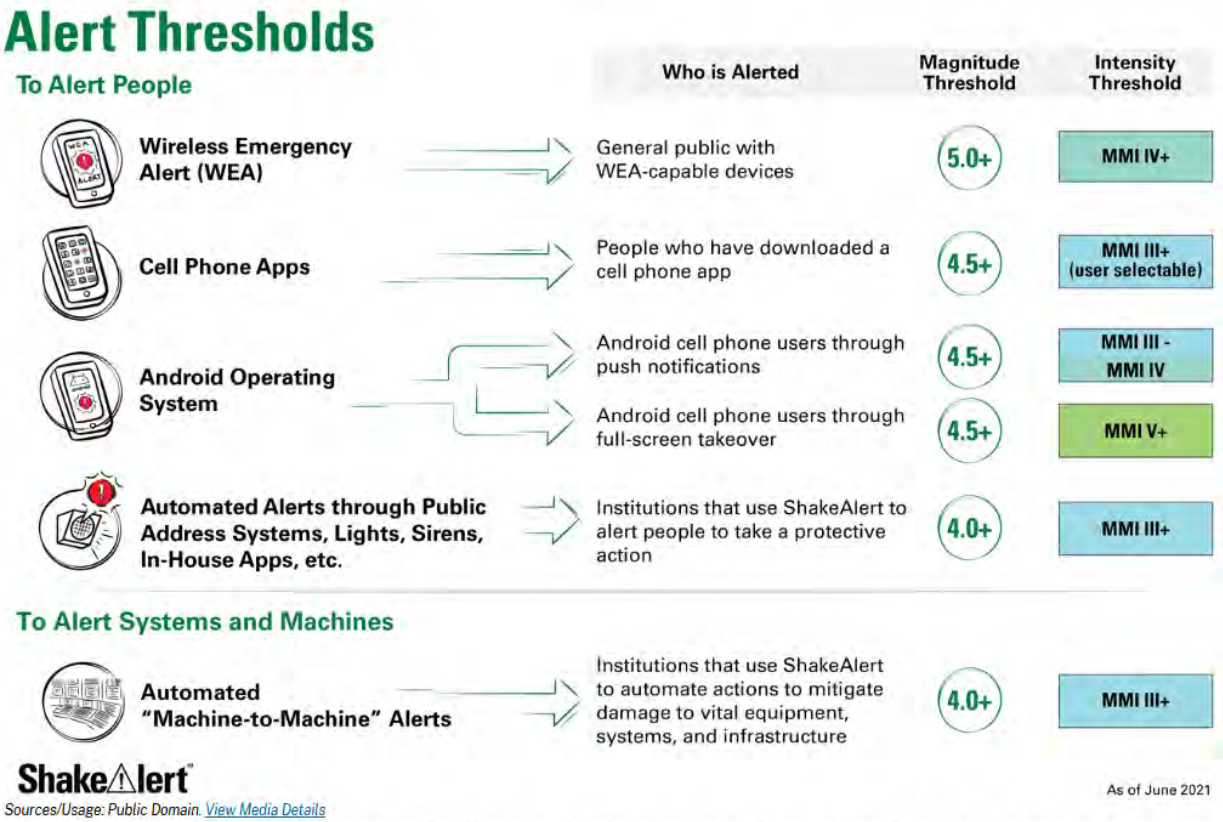

Sources/Usage: Public Domain. View Media Details

Alert Delivery Thresholds used by ShakeAlert partners - The USGS issues ShakeAlert Messages but delivery of alerts will come by other public and private means (internet, radio, television, cellular), including Wireless Emergency Alerts (WEA) delivered by FEMA's Integrated Public Alert and Warning System (IPAWS).

For example, cell phone app providers and Android can deliver ShakeAlert-powered alerts to people who could feel weak shaking (Modified Mercalli Intensity - MMI III) or greater for earthquakes M4.5 and larger. For people who could feel moderate shaking (MMI V) or greater Android delivers alerts with more urgent language.

The Modified Mercalli Intensity (MMI) Scale is composed of increasing levels of intensity that range from imperceptible shaking to catastrophic destruction; levels of intensity are designated by Roman numerals. The MMI Scale does not have a mathematical basis; instead, it is a holistic ranking based on observed effects. The lower range of the MMI scale generally deals with the manner in which the earthquake is felt by people. The higher range considers observed structural damage.

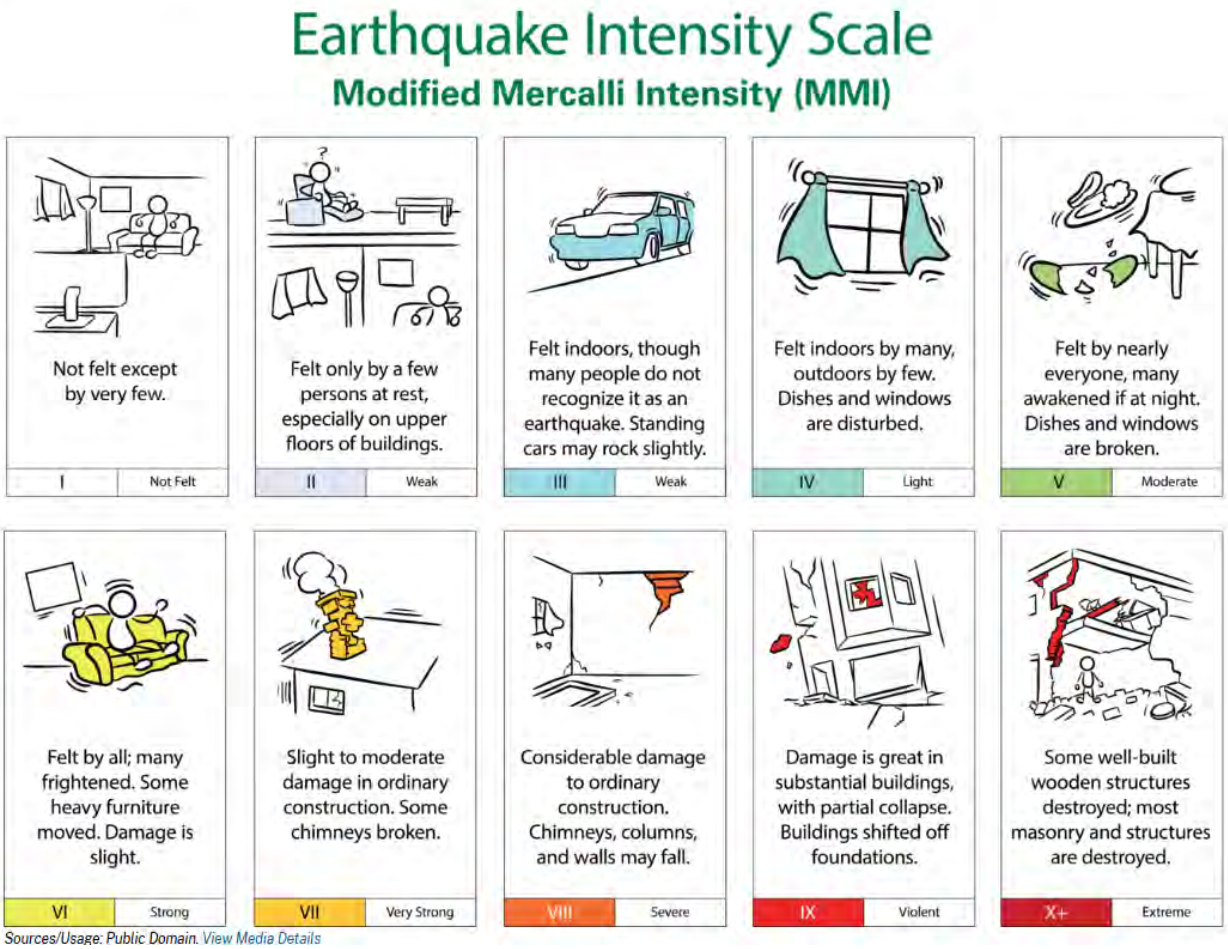

Sources/Usage: Public Domain. View Media Details

Earthquake Intensity Scale (Abridged). The Modified Mercalli Intensity (MMI) Scale is composed of increasing levels of intensity that range from imperceptible shaking to catastrophic destruction; levels of intensity are designated by Roman numerals. The MMI Scale does not have a mathematical basis; instead, it is a holistic ranking based on observed effects. The lower range of the MMI scale generally deals with the manner in which the earthquake is felt by people. The higher range considers observed structural damage.

136. Assignment 3, Module 9: Tsunami Warnings: https://www.bom.gov.au/resources/learn-and-explore/tsunami-knowledge-centre/about-tsunami-warnings

About tsunami warnings

Discover how we issue tsunami watches and warnings on behalf of the Joint Australian Tsunami Warning Centre

On this page

Stage one: tsunami watch

Seismologists first identify an undersea earthquake that could cause a tsunami threat to Australia. The Joint Australian Tsunami Warning Centre (JATWC) issues a National Tsunami Watch if there is a potential threat, notifying those affected that they should be on standby and await further updates. If no threat is detected, the Centre issues a National Tsunami No Threat Bulletin.

The JATWC may reissue a National Tsunami Watch if the tsunami remains unconfirmed and more than 90 minutes away.

Stage two: tsunami warning

The JATWC will issue a tsunami warning if:

- sea level observations or trusted reports confirm a tsunami threat, or
- the potential first impact time is less than 90 minutes away, even if a tsunami threat isn't yet confirmed.

Warnings are issued individually for each affected state or territory. A National Tsunami Warning Summary is also issued to give a national overview of all warnings and observations.

The Joint Australian Tsunami Warning Centre will show any current tsunami warnings affecting Australian regions. It includes offshore islands and Australian Antarctic Stations.

Types of tsunami warnings

Tsunami threats are categorised into three levels:

1. **No threat** – we've detected an undersea earthquake but it hasn't generated a tsunami, or the tsunami poses no threat to Australia.
   No action is required.
2. **Marine and immediate foreshore threat** – there could be dangerous rips, waves and strong ocean currents in coastal waters. Seawater may overflow onto immediate foreshore.
   Action: although no evacuation is required, people should get out of the water and stay away from the beach and immediate water's edge.
3. **Land inundation threat** – low-lying coastal areas could be inundated or flooded, in addition to dangerous rips, waves and strong ocean currents in coastal waters.
   Action: get out of the water and move inland at least 1 km away from the coast or go to higher ground at least 10 m above sea level.

Cancelling a tsunami warning

We'll issue a Tsunami Watch Cancellation or Tsunami Warning Cancellation if a tsunami didn't occur or when the main threat has passed.

The relevant state or territory emergency authority will inform the public when it is safe to return to the affected area.

Distributing tsunami bulletins and warnings

We publish all tsunami bulletins and warnings on our website and audio warnings service – 1300 878 626.

We work with media organisations across Australia to inform the public. We also send these tsunami bulletins and warnings directly to:

- state and territory emergency services
- local councils
- port authorities
- police

so they can take immediate response action.

For emergency assistance during a tsunami, call your state or territory emergency services on 132 500.

For information to help you prepare, respond and recover from a disaster, visit the National Emergency Management Agency.

137. Assignment 3, Module 10: FEMA 454, Section 2.10:
https://www.wbdg.org/FFC/DHS/fema454.pdf

2.10 WEB RESOURCES

Consortium of Organizations for Strong-Motion Observational Systems
COSMOS http://www.cosmos-eq.org

European Strong-Motion Database (ISESD)
http://www.isesd.cv.ic.ac.uk/

National Seismic Hazard Mapping Project, Golden, Colorado
http://geohazards.cr.usgs.gov/eq/

ShakeMaps www.trinet.org/shake

Tsunami Warning Centers http://www.prh.noaa.gov/pr/ptwc/
http://wcatwc.gov/

USGS Earthquake Hazards Program http://earthquake.usgs.gov/

138. Assignment 3, Module 10: HERP: https://www.hp1039.jishin.go.jp/eqchreng/eqchrfrm.htm

1 Introduction

The Southern Hyogo Prefecture Earthquake (Hyogo-ken Nanbu Earthquake) of January 17, 1995 left behind an immense trail of destruction: by December 26, 1996 of the following year, the earthquake had claimed 6,427 lives with more than 40,000 people sustaining serious injury. After the earthquake, many people in the area said that they had no idea such a large earthquake could occur in Kobe, which has revealed the importance of acquiring basic knowledge about earthquakes. In response, the Earthquake Research Committee of the Headquarters for Earthquake Research Promotion compiled this report on earthquakes. The objective is to provide accurate information on earthquakes in an easy-to-understand manner.

After the Southern Hyogo Prefecture Earthquake, a Special Measures Law on Earthquake Disaster Prevention was enacted to shore up existing measures against earthquake damage. The Headquarters for Earthquake Research Promotion was established based on this legislation, and a new organization was launched to promote surveys and research on earthquakes. Within this organization, the Earthquake Research Committee is responsible for collecting and organizing the results of seismic surveys, conducting research earthquakes, and analyzing and evaluating this information. One of this committee's objectives is to gain a better understanding of the characteristics of seismic activity in Japan, a second is to evaluate the possibility of earthquakes occurring over the long term. Accordingly, the Subcommittee for Long-Term Evaluation was formed in December 1995. This subcommittee divided Japan into three regions, and established special panels to compile the characteristics of seismic activity in each region.

Chapter 2 of the present report provides an overview of seismic activity throughout Japan, along with some basic information on earthquakes. In Chapters 3 to 9, Japan is divided into the Hokkaido, Tohoku, Kanto, Chubu, Kinki, Chugoku-Shikoku, and Kyushu-Okinawa regions. Each chapter begins with an overview of seismic activity in each region. This is followed by a description of the type of destructive earthquakes that have occurred in each region, an overview of the primary destructive earthquakes that have occurred in each region, and a description of the characteristics of each prefecture (as for Hokkaido, of each district). We also have provided an explanation of technical terms, and appended diagrams for the reader's reference.

One salient feature of this report is that we have described destructive earthquakes from the perspective of each prefecture, or each area in Hokkaido's case. * In addition, we have attempted to provide a comprehensive account of the subject by correlating information obtained from separate fields of earthquake study, including the history of past earthquakes, active faults, and crustal movements. A chart and explanation of terms is provided to make this technical material as easy to understand as possible. Please note that although the information in this report is all up to date, we provide several differing explanations for those points that have yet to be conclusively evaluated.

We expect that future long-term progress in earthquake research will result from the new technology and observational systems now in place. The results of these investigations will be incorporated into this report as soon as they become available.

With improvements in seismological survey and observation under way, progress is anticipated in seismology and other related sciences. This report will be reviewed and revised whenever such occasion arises.

We hope this report will be used widely, and not only by members of local government responsible for dealing with disasters.

* The English edition of this report does not include a description of the characteristics of each prefecture.

1-1 Explanation of methods used to create figures and tables

Figures showing Japan's primary destructive earthquakes

The destructive earthquakes listed in the "Chronological Scientific Tables (Rika Nenpyo)" and those described in this report are shown (those with the largest magnitude in the case of earthquake swarms) in the figure on the primary destructive earthquakes in each region and surrounding areas. In some cases, earthquake swarms are shown even if they were not destructive.

For earthquakes of a certain magnitude -- M 7.3 or greater for earthquakes at sea and M 6.7 for inland earthquakes -- we have shown the source region whenever known. As a rule, we have used the wave source region from Hatori's papers on earthquakes at sea, and the fault models from the "The Parameter Handbook about the Earthquake Fault in Japan" for inland earthquakes.

For those earthquakes occurring since 1980 for which no fault model exists, we have estimated the source region based on the aftershock distributions observed by research organizations and universities.

We used the "Chronological Scientific Tables" for the location of the hypocenter of earthquakes occurring before 1884; Utsu's papers for earthquakes occurring from 1885 to 1925; and data from the Japan Meteorological Agency (JMA) for earthquakes occurring after 1926.

Generally, we use the figures from the Chronological Scientific Tables for the magnitude (M) of the earthquake. For those earthquakes not listed, we use data for locations of the hypocenter. Estimates are sometimes used for the magnitude of earthquakes known from historical data, i.e., M 7.9 - 8.2. In these cases, the values of the magnitude shown in the figures were obtained from the average value for the interval rounded off from the second decimal place. Also, for the values of magnitudes in which fractions are used, such as M 6 1/4, we rounded off from the second decimal place after conversion to decimal fractions. Finally, we used the lower limit for magnitudes expressed by the phrase, "M 7.5 or greater".

The active faults are those shown in the book "Active Faults in Japan (Revised Edition)" with a degree of certainty of I or II. Please note that some faults have been removed or their degree of certainty modified due to the current information (See the text)

The topographical information is based on the "Digital Map 250m Grid (Elevation)".

The location of volcano is based on the "National Catalogue of the Active Volcanoes in Japan" (Second Edition)

For more details, refer to the references (Appendix 3).

Figures showing topography and active faults

The figures showing the topography and active faults are taken from those included in a degree of certainty I or II in the book "Active Faults in Japan (Revised Edition)". Please note that some faults have been removed or their degree of certainty modified due to the availability of new information (See the text).

The topography is based on the "Digital Map 250m Grid (Elevation)".

For more details, refer to the references (Appendix 3).

Figures showing extension and compression

Each region has a figure that indicates extension and compression over a roughly 100-year period and a 10-year period. The extension and compression for the most recent 100-year period were determined by obtaining the difference between the survey taken in the late 19th century (Meiji era) and the most recent measurements. It requires several years to survey an entire region, so the measurement period of each region differs. Strictly speaking, there are also differences in the survey period for points within the same region. Therefore, we use the descriptive expression, "roughly 100-year period". These same conditions apply for extension and compression for the roughly 10-year period.

Figures showing seismic intensity distribution

We show the seismic intensity distribution in each region for those earthquakes cited as destructive. The data for seismic intensity is generally taken from the Japan Meteorological Agency (JMA). For older earthquakes, we have also used such data as the "Materials for Comprehensive List of Destructive Earthquakes in Japan (Revised and Enlarged Edition)". We use those figures showing seismic intensity distribution in the original text where these are available. Where these figures do not exist, we have quoted contours based on seismic intensity data.

Graphs showing aftershock frequency

We provide graphs showing trends in aftershock frequency for those earthquakes cited as examples of destructive earthquakes. In some instances, the frequency of aftershocks shown is that observed at an observation point (or the frequency of sensing aftershocks in the case of felt earthquakes). Also, in some instances, the number of earthquakes indicated is that detected by the seismological observation network of JMA. For the observations by the JMA's network, the numbers indicate the frequency of the aftershocks that can be felt at any observation station.

2-1 Seismic activity in the Japanese archipelago and surrounding areas

Where do earthquakes occur? Fig.2-1 shows the distribution of recent earthquakes of M 4 or above and a depth of 100 km or less. (Magnitude is a scale of an earthquake source size, and hereafter will be expressed as "M"). Fig.2-1 shows that earthquakes do not occur uniformly across the planet, but rather within a narrow band. The Japanese archipelago is one zone within that band.

In this section, we will examine the location and distribution of recent earthquakes in and around the Japanese archipelago.

Fig.2-2 shows the distribution of earthquakes that have occurred in and around the Japanese archipelago over the past 70 years or so with M 5 or greater and a depth of 100 km or less. Fig.2-3 shows the distribution of earthquakes that have occurred in the past 110 years or so with M 6 or greater and a depth of 100 km or less. Most of the earthquakes shown are ranked as either M 5 or M 6. At a minimum, this indicates that earthquakes of this magnitude have occurred throughout Japan over the past about 100 years. It is also apparent that several areas have an extremely high rate of occurrence of earthquakes, particularly the area in the offshore area of the Pacific Ocean of the Tohoku region. We can also see that on land in the Japanese archipelago, earthquakes occur at depths of 20 km or less. Further earthquakes that occur in these shallow locations-even M 5 or M 6 earthquakes-sometimes cause extensive damage locally. Finally, when viewed from a nationwide perspective, earthquakes of M 6 or greater occur at a generally uniform frequency over the long term (Fig.2-4).

Earthquakes off the Pacific coast occur at increasingly deeper locations the closer they come to the Japanese archipelago. The tendency continues to the land area and areas deep under the Sea of Japan (Japan Sea). Using the earthquakes in Japan's Tohoku region as an example, the depth of these earthquakes extends from 0-50 km in the open sea, 50-200 km in the area from the coastal area to land, and 400-600 km in the area from the western part of the Sea of Japan to the coast of Russia (Fig.2-5).

Next, we'll look at the distribution of larger earthquakes. Fig.2-6 shows the distribution of earthquakes of M 7 or greater that have occurred in the past 110 years or so and at a depth of 100 km or less. A comparison with Fig.2-2 and Fig.2-3 shows that the frequency of occurrence significantly declines as the magnitude increases, and the areas of occurrence are rather limited. In such case, a rule has been found that the frequency of earthquake occurrence drops to about 1/10 with each increase of one degree in magnitude. Fig.2-6 shows there is an extremely high rate of occurrence of earthquakes with M 7 or greater in the open sea of the Pacific Ocean from Hokkaido to the Kanto region. There is also a high frequency of earthquakes in the belts ranging from the open sea off the Boso Peninsula (Boso Hanto) to Sagami Bay (Sagami Wan), and the area in the open sea in the Pacific Ocean from Kyushu to the Nansei Islands (Nansei Syoto). Deep ocean trenches known as "troughs" run parallel to these zones (Fig.2-7). In this region, few earthquakes occur along the Nankai Trough, which extends from Suruga Bay (Suruga Wan) to the open sea off Shikoku, as shown in Fig.2-6. It is known, however, that a series of great M 8-level earthquakes occurred here in the past. There is also a zone running from north to south in the Sea of Japan from Hokkaido to the Tohoku region in which earthquakes of M 7 or greater frequently occur. While there are comparatively fewer earthquakes in the land area than in the sea regions, particularly in the areas where there are active faults (which are described later), earthquakes of M 7 or greater do occur in shallow locations on land.

Many destructive earthquakes are known based on report contained in historical documents. Fig.2-8 shows the locations of the primary destructive earthquakes of the past that are known based on historical documents. There are periods in the past in which a concentration of earthquakes of M 7 or greater occurred. For example, there were many M7 - M8 destructive earthquakes in the 1850s during the Ansei Era (*1).

Thus, we can estimate the location and scale of earthquakes that occurred before 1884, when modern earthquake observation began, from the conditions and extent of the damage described in these historical accounts. Therefore, there are larger errors for the earlier earthquakes than for those for which modern observation equipment was available. Also, the precision with which the location and the scale of earthquakes is determined by observation equipment improves every year due to advances in observation equipment, greater numbers of monitoring areas, and improved methods for determining the hypocenter of an earthquake.

---

*1

The 1853 Odawara Earthquake (M 6.7), the 1854 Iga-Ueno Earthquake (M 7 1/4), the 1854 Ansei Tokai Earthquake (M 8.4), the 1854 Ansei Nankai Earthquake (M 8.4), the 1854 earthquake near Ehime and Oita Prefectures (M 7.3-7.5), the 1855 Ansei Edo Earthquake (M 6.9), the 1856 earthquake off the east coast of Aomori Prefecture (M 7.5), the 1857 Earthquake at Aki-nada Sea (M 7 1/4), the 1858 Hietsu Earthquake (M 7.0-7.1), and the 1858 earthquake off the east coast of Aomori Prefecture (M 7-7.5)

2-2 What are earthquakes?

Before providing a more detailed explanation of the characteristics of seismic activities nationwide, we will examine the fundamental question, "What are earthquakes?"

The word "earthquake" in daily use usually refers to a perceptible shaking of the earth. When used in the term "earthquake distribution", however, the word has a different meaning. "Earthquake" in the latter sense means the source of the shaking of the earth, and refers to an event that occurs underground. In this report, the term "earthquake" will be used in the latter sense. We will use the term "seismic ground motion" in the sense of a general shaking of the earth.

The shaking of the earth (ground motion) results when a seismic wave is transmitted from the site where the earthquake occurs, and this wave shakes the earth. The source that causes this wave, or the essence of the earthquake itself, has been accurately identified only recently, during the 1960s. This essence is the fault movement that releases the strain energy accumulated in the bedrock (rock mass) underground.

Let's review the process in the order in which this happens. First, a strong force is exerted on the rock mass underground for some reason. This rock mass gradually becomes deformed. At the same time, energy accumulates in the form of strain in the rock mass. To visualize this, think of a rock being compressed by a giant press. When, the rock mass can no longer withstand the continually mounting pressure, a rupture occurs. The strain energy that has built up is violently released in the form of a seismic wave. Earthquakes are what happen when this phenomenon occurs underground. If it had no support, the rock under stress would crumble and fly apart at the instant of rupture. The rupture of rock mass underground, however, is considerably different from this sort of situation and will generally occur as slip along a certain plane. This may be more difficult to visualize than the more ordinary conception of rupture, but the rupture that occurs underground and causes an earthquake consists of a rapid slipping movement along a plane between giant slabs of rock mass. Planes of this type within the rock mass are thought to be existing weak planes (fault planes) that caused slipping in the past. Hereafter, we will refer to the portion of the rock mass slabs in the weak plane that slip as the "area of rupture". Also, the slipping movement of the rock mass on both sides of this plane will be termed "fault movement". A fault refers to a condition in which the fault movement on the originally continuous strata and rock mass results in the slipping with a certain plane as a boundary. The basic types of faults are classified by the type of slip, and are known as "normal faults", "reverse faults", and "lateral faults".

The velocity of rupture propagation - the speed of the expansion of the rupture zone - is extremely fast. In locations that are not deep underground (in the earth's crust), this speed is about 2 or 3 km per second. (In fact, seismic waves are transmitted at an even faster speed.) The speed at which both sides of the rock mass slip against each other is slow, between 10-100 cm per second (Fig.2-9). We will refer to the range of maximum expansion of the rupture zone - the entire range over which fault movement occurs - as the "focal region".

From the proceeding, we can see that earthquakes do not occur at a single point, but spread along a plane. It is easy to picture in the mind's eye that an earthquake's magnitude will increase as the extent of the fault movement grows (and the extent of the rupture grows) where rock mass is alike. The amount of slipping volume and the breadth of the area over which the fault movement occurs determine the extent of the fault movement. If the fault is viewed as a rectangle, this breadth can be expressed by the length in a horizontal direction (fault length) and the length in an angular direction (width) (Fig.2-10).

Next, we'll use an example to examine fault movement. The 1995 Hyogo-ken Nanbu Earthquake (Southern Hyogo Prefecture Earthquake) (M 7.2) that caused the Great Hanshin-Awaji Earthquake Disaster was an earthquake of M 7 class. An analysis of all the data shows that the fault length of this earthquake was about 40-50 km, and the width was about 15 km. The value of the slip was about 1 to 2 m. Recent research has enabled us to make a rather specific estimate of the distribution of slip on the fault plane, as shown in Fig.2-11. A look at these figures shows areas with substantial slip, and areas with very little slip. Also, the Kanto Earthquake of 1923 (M 7.9) that caused the Great Kanto Earthquake Disaster was nearly M 8. The fault length of this earthquake was about 100 km, and the width was about 50 km. The slip is estimated to have been about 5 to 7 m.

The hypocenter announced by the Japan Meteorological Agency (JMA) immediately after the earthquake occurred is the location where slip first occurred, i.e., the point where the rupture started (Fig.2-9). The hypocenter of an earthquake is determined by the time required for the first earthquake waves (P waves and S waves) to reach a set of observation points. The hypocentral region of a large earthquake is very large, so points at a distance from the hypocenter will be subject to strong ground motion if the fault movement has extended to a nearby location.

Fig.2-1, Fig.2-2, Fig.2-3, Fig.2-5, and Fig.2-6 show the location of earthquakes using the hypocenter. We are convinced that for large earthquakes, however, fault movement occurs over a rather large area, including the hypocenter. Fig.2-12 uses current observations to show the focal regions for the primary destructive earthquakes of the past 100 years. Fig.2-12 shows the fault model for earthquakes that occurred on land and the source area of tsunami for earthquakes that occurred at sea. Most of the faults in the focal region of the earthquakes that occurred on land are roughly vertical. Therefore, as the figures shows, the actual focal region appears smaller than it actually is, when projected at ground level. In contrast, the source area of tsunami indicates the range in which a tsunami is generated, and tends to appear larger than the actual underground focal region.

Generally, when a large earthquake (main shock) occurs, many somewhat smaller earthquakes follow. These are known as aftershocks. Most of these aftershocks occur in the focal region of the main shock. The distribution of aftershocks - in particular those that occur immediately after the main shock (from several hours to one day later) - indicate very clearly the location of the focal region of the main shock. Therefore, the focal region of the main shock (the area in which the fault movement occurred) can be determined by the aftershock distribution (Fig.2-13). Many aftershocks immediately follow the main shock, but these decrease with time. It is now understood that the manner of this decrease is quite regular. Most aftershocks are of a magnitude of 1 or smaller than the main shock - even aftershocks of the largest magnitude. However, sometimes there are aftershocks of a magnitude approaching that of the main shock.

2-3 Plate tectonics

In the previous section, we described how pressure builds up underground, resulting in an accumulation of strain in the rock mass. An earthquake occurs when this strain reaches its limit. How much pressure is building up beneath the Japanese archipelago and the surrounding areas? This pressure is extremely difficult to measure directly. Therefore, the method used is to observe the extent of the strain and deformation of the earth as a result of the pressure and then to work backwards, estimating the extent of the pressure built up underground over a wide area.

Recent advances in space technology have enabled us to accurately, efficiently, and continuously measure deformation in the earth over a wide area. Typical of these technological advances is a measurement technology using satellites, the Global Positioning System (GPS) for continuous observation. Fig.2-14 shows the extent and direction of the movement of the land throughout the entire the Japanese archipelago for the past year as determined by the use of this technology. This movement is in relation to an observation point in Suwon, Republic of Korea. No large earthquakes occurred in the Japanese archipelago during this period. Therefore, we believe this figure shows the stationary movement of each area of the Japanese archipelago in relation to the Continent. Fig.2-15 shows a calculation of the deformation in the Japanese archipelago during the measurement year based on the results of these measurements. There is compression from a northwest-southeast to a north-northwest south-southeast direction in the area from the Pacific Ocean side of Hokkaido and the southern Kanto area to the Kii Peninsula (Kii Hanto) and Shikoku. In other areas, there are deformations indicating compression in an east-west direction.

Thus, we can assume that strong compression is now occurring in an east-west direction underneath the Japanese archipelago. Depending on the location, this compression sometimes occurs in a northwest-southeast direction. A similar conclusion can be obtained from an analysis of seismic observation data. The results of various topographical and geological surveys are form the basis for the hypothesis that a similar force has been exerted underground for quite some time - at least several hundred thousand years.

Is it possible to present a uniform explanation of earthquake distribution, as described in Section 2-1, and the forces at work in the Japanese archipelago described in this section? In the zone that is part of the belt off the Pacific coast of the Japanese archipelago, the frequent occurrence of large earthquakes indicates that prominent weak planes (fault planes) exist along this zone, in other words, fault movement frequently occurs along the planes. This leads us to believe that the underground structure of the zone in this Pacific Ocean belt is discontinuous and that there must be some sort of boundaries present. Meanwhile, the pressure applied in an east-west direction over a wide area throughout the Japanese archipelago is being applied to the archipelago from the east. It can be conjectured that the Continent is applying pressure from the west. Plate tectonics, a new earth science that emerged at the end of the 1960s, explains this clearly.

Here is the basic idea behind plate tectonic.

The entire surface of the earth is completely covered by dozens of slabs of rock mass of several-tens-km thick. These slabs are called "plates", and drift in different directions at a speed of several centimeters per year. At their boundaries, these plates move in a divergent direction, convergent each other, or passing each other (Fig.2-16).

Next, we will consider the plates in the Japanese archipelago and the surrounding areas. The results of different types of research show that several plates are converging each other in the Japanese archipelago and the surrounding areas. At the boundary of these converging plates, both plates are pushing against each other. As a result, a huge mountain range similar to the Himalayas is being formed, as one plates subducts the other. Along the site of this subduction, large trench-like terrain is being formed, including trenches. This type of submarine topography can actually be seen in areas close to the Japanese archipelago (Fig.2-7).

There are at least three plates in the Japanese archipelago and the surrounding areas: the Pacific Plate, the Philippine Sea Plate, and a plate on land (Fig.2-17). The Pacific Plate approaches the Japanese archipelago from the east-southeast at a speed of 8 cm annually, and subducts under the land plate from the Japan Trench (Nihon Kaiko) and other areas. Observation of earthquake distribution at a deeper location from a profile that cuts across the Japanese archipelago (northeast Japan) from east to west clearly shows that the Pacific Plate is subducting under the archipelago (Fig.2-5). The Philippine Sea Plate is approaching the archipelago from the southeast at a speed of roughly 3-7 cm per year, and is subducting under the land plate at the site of the Nankai Trough. The boundaries between the land plate and the subducting plates are large (weak boundaries). There is a powerful compression force operating between the plates that are approaching each other. It is easy to imagine that many large earthquakes (fault movements) are generated here. One theory postulates that a plate boundary exists off the Sea of Japan (Japan Sea) coast of northeast Japan (the eastern margin of the Sea of Japan) (Fig.2-12, broken line). A series of earthquakes has occurred here in recent years.

Thus, the occurrence of earthquakes along trenches is believed to have a direct relationship with the subducting plates. Moreover, earthquakes in shallow land areas occur a slight distance from the boundary of the subducting plates. These earthquakes are thought to occur due to the pressure exerted on the surrounding area with the subducting plate.

In the next section, we will provide a more detailed classification of the types of earthquakes that occur in the Japanese archipelago, and describe their characteristics.

With the development of new observation and research techniques for studying plates in the Japanese archipelago and the surrounding areas, a more detailed understanding of the positions and movements of the plates can be exported in the future.

2-4 Types of earthquakes in the Japanese archipelago

In the preceding section, we described how earthquakes in the Japanese archipelago and the surrounding areas could be roughly divided into two types. The first type comprises those earthquakes at or extremely close to plate boundaries in trenches and other locations. The second type comprises those earthquakes that occur some distance away, in shallow locations on land. Today, earthquakes are classified not only based on their distribution, but also on the geological characteristics at the site of the earthquake.

A breakdown follows of the types of large earthquakes that occur in the Japanese archipelago and the surrounding areas (Fig.2-18).

(1)Earthquakes near the plate boundary

In the following we will provide an explanation of earthquakes that occur near plate boundaries, broken down into interplate earthquakes caused by the subducting Pacific Plate, interplate earthquakes caused by the subducting Philippine Sea Plate, and intraplate earthquakes within a subducting plate.

1) Interplate earthquakes caused by the subducting Pacific Plate

Large earthquakes of M 7-8 sometimes occur near the Chishima (Kuril) Trench, Japan Trench, and the Izu-Ogasawara Trench, where the Pacific Plate is subducting. Large earthquakes such as these are generated by fault movement in which the edge of the plate on land is dragged along as the Pacific Plate subducts, and the plate on land finally pushes up when the stress has reached its limit (Fig.2-19). Examples of this type of earthquake are the 1968 Tokachi-Oki Earthquake (Earthquake off the Coast of Tokachi) (M 7.9) and the more recent 1994 Sanriku Haruka-Oki Earthquake (Earthquake far off the Coast of Sanriku) (M 7.5). This type of earthquake is called an "interplate earthquake" or a "plate boundary earthquake". When the fault length reaches 100 km or longer, the earthquake's magnitude climbs to roughly 8. Also, the crustal movement (upheaval and subsidence) at sea floor accompanying this type of large earthquake causes the seawater to either rise or fall, and tsunami tend to occur as a result. Therefore, coastal areas facing plate boundaries, particularly areas near their hypocenter, often experience strong ground motion caused by interplate earthquakes and tsunami that arrive immediately after the earthquake. The tsunami sometimes arrives and causes damage in coastal areas far away from the hypocenter, even when the ground motion is weak. Fig.2-20 shows the source area of tsunami caused by earthquakes occurring near plate boundaries.

The crustal movement (upheaval and subsidence) at the sea floor also can generate tsunami when the slip along the fault plane occurs gradually at one section of the plate boundary. In this instance, the slip occurs gradually, so the seismic waves - or more accurately, the perceptible seismic waves over a short period - are comparatively small. Therefore, we feel only a slight ground motion. The extent of the crustal movement at the sea floor that creates tsunami, however, does not depend on the speed of the slip. Rather, it depends on the size of the fault movement (the area and extent of the slip). Therefore, even if the perceived ground motion is relatively weak, a large tsunami may occur if there is extensive fault movement. Thus, the earthquakes that generate large tsunami even when human perception ground motion is weak are called "tsunami earthquakes" , "slow earthquakes" or "low-frequency earthquakes". One such earthquake was the Meiji Sanriku Earthquake of 1896. This earthquake is estimated at roughly M 7 from the strength of the short-period ground motion. Actually, however, it is determined to have been M 8 1/2 based on the scale of the estimated fault movement.

Tsunami scale depends on the scale of the fault movement as well as the inclination of the fault plane and the direction of slip. The closer the fault plane inclination is to the vertical, or the greater the dip-slip components, the more efficiently the sea water is raised or lowered and the larger the tsunami becomes.

2) Interplate earthquakes caused by the subducting Philippine Sea Plate

Large earthquakes occur from the Sagami Trough and Suruga Trough to the Nankai Trough and the vicinity of the Nansei Islands Trench, where the Philippine Sea Plate is subducting. Frequently, great earthquakes on the order of M 8 occur here. Typical examples of these earthquakes are the 1923 Kanto Earthquake (M 7.9) which caused the Great Kanto Earthquake Disaster, the 1944 Tonankai Earthquake (M 7.9), and the 1946 Nankai Earthquake (M 8.0). All of these were interplate earthquakes that occurred at the boundary of the Philippine Sea Plate and the land plate. Historical data makes clear that great earthquakes of M 8 frequently occur in the Suruga Trough and the Nankai Trough. It is also known that a series of earthquakes with adjoining source regions tend to occur here within several-year periods. If a series of earthquakes is considered as one event, historical accounts show that this type of event has taken place nine times. [For details, refer to 8-1 (1).1)]

These M 7 - 8 earthquakes are generally accompanied by tsunami caused by crustal movement of the sea floor(upheaval and subsidence). Therefore, the occurrence of earthquakes of this type results in strong ground motion and the immediate arrival of a tsunami, in the coastal areas facing the plate boundaries or especially in sites close to the hypocenter. Even coastal regions far away from the hypocenter sometimes suffer damage from tsunami, even when the ground motion is weak.

Sometimes, there is gradual fault movement (tsunami earthquake, slow earthquake, or low-frequency earthquake) that only creates tsunami without strong ground motion, even with the subducting Philippine Sea Plate.

3) Earthquakes within subducting plates

Extensive collapse can occur within subducting plates from sea trenches or elsewhere, and this sometimes causes large earthquakes. When large earthquakes of this type occur in relatively shallow underground areas, they are accompanied by tsunami. For example, the 1933 Sanriku Earthquake (M 8.1) and the 1994 Hokkaido Toho-Oki Earthquake (Earthquake off the East Coast of Hokkaido) (M 8.1) were earthquakes of this type, and both were accompanied by tsunami.

A deep earthquake will be generated when rupture occurs within a subducting plate. Even earthquakes with a deep hypocenter of 100-200 km will generate strong ground motion at the earth's surface if the earthquake is large enough. For example, with the 1993 Kushiro-Oki Earthquake (Earthquake off the Coast of Kushiro) (M 7.8), a seismic intensity of 6 (JMA scale) was observed at Kushiro, and significant damage was sustained even though the earthquake occurred in the Pacific Plate at a depth of about 100 km.

(2)Shallow inland earthquakes

Sometimes, large earthquakes occur on land in the Japanese archipelago, such as the 1995 Southern Hyogo Prefecture Earthquake (M 7.2) that caused the Great Hanshin-Awaji Earthquake Disaster. In the underground area of the Japanese archipelago, there are generally powerful forces of compression exerted in an east-west or northwest-southeast direction which cause earthquakes of this type to occur. Past research has shown that with earthquakes occurring on land, rock mass with hardness sufficient to cause earthquakes extends to about 15-20 km underground. Temperatures are high at depths lower than that, so it is thought that the rock mass will not suddenly break up when pressure is exerted on it. Rather, fluid distortion will occur. Therefore, the hypocenter of large earthquakes that occur on land will be located less than 20 km below the surface. Most of these earthquakes will be at the M 7 level, and earthquakes at the M 8 level seldom occur, with an example being the 1891 Nobi Earthquake (M 8.0).

Because these earthquakes have a shallow hypocenter, in many cases, fault movement reaches the surface during large earthquakes of M 7 or greater. We have learned from topographical and geological surveys that slip caused by fault movement accumulate for at least several hundred thousand years on faults that have slipped the earth's surface. This signifies repeated slipping on an existing, roughly uniform weak plane (fault plane), in other words, several large earthquakes must have occurred. It also signifies that a roughly equivalent force has been exerted in the subterranean area of the Japanese archipelago for at least last several hundred thousand years. Therefore, it is believed that large earthquakes will continue to occur at faults such as these in the future as long as this force is applied. Faults at which this activity has repeatedly occurred in the past and at where it is likely to occur in the future are known as "active faults".

Active faults form characteristic topographical conditions through the accumulation of slip that accompanied earthquakes in the past (Fig.2-21, Fig.2-22). One such condition is the formation of topographical discontinuities at locations that had been uniform. These conditions can be used as clues to discover active faults and estimate their extent of activity. Surveys to locate active faults often make use of aerial photography to reveal the topographical conditions such as those seen in Fig.2-21. A look at the distribution of the primary active faults in and around the Japanese archipelago in Fig.2-23 shows there is a close relation between topography and the distribution of active faults. For example, active faults are often found at the boundary between mountains and lowlands.

A detailed survey of active faults reveals sharp differences in the proportion of accumulated slip among active faults. That is, the extent of activity for active faults differs greatly with each fault. There are three categories for this activity, termed A, B, and C class, ranging from the greatest to the least. The categories are based on the average volume of slip per 1,000 years. This is called the "mean slip rate". For the A class, which has the greatest activity, the average amount of slip over 1,000 years will be from 1-10 m. The activity is an important indicator when considering the interval between earthquakes on each active fault and the characteristics of regional seismic activity. For example, regions with many other active faults in the A class of activity have a higher incidence of large earthquakes than other regions.

Scientists also study the history of this activity by excavating these active faults (trenching) (Fig.2-24). These studies enable an evaluation to a certain degree of the next period and the magnitude of activity if the history of previous activity is clarified. This history includes such factors as the intervals of activity, the most recent period of activity, and the size of the fault where the activity occurred. It also may include reactions to earthquakes that are known of from historical accounts. The intervals between activity on active faults stretch to about 1,000 years at the shortest. Further, there is a certain degree of variations, so the accuracy of evaluating the next period of activity can only be in the range of several hundred years. Also, slip does not occur on the earth's surface during M 6 earthquakes, which sometimes can cause significant local destruction. Therefore it is difficult to understand earthquakes of this size through ordinary active fault surveys.

Repeated active fault movement in the Japanese archipelago creates plains and basins, where many cities have developed. Hence, large earthquakes sometimes occur directly below or very close to these areas. In addition, in some parts in these plains and basins, deposit carried by rivers can accumulate rapidly. However, visual examination alone of the topography in these areas is insufficient to determine the existence of active faults.

Strong ground motion immediately followed by tsunami occurs with earthquakes on active faults at the sea floor near coastal areas.

Earthquakes, which occur at deeper locations (50-200 km) in land areas, are classified as earthquakes that occur within the subducting Pacific Plate and the Philippine Sea Plate. [Refer to 2-4(1) 3)].

(3)Earthquakes in the eastern margin of the Sea of Japan

Several large earthquakes have recently occurred extending north and south along the Sea of Japan coast of the Tohoku region. These include the 1983 Central Sea of Japan Earthquake (Nihonkai Chubu Earthquake) (M 7.7) and the 1993 Earthquake off the Southwest Coast of Hokkaido (Hokkaido Nansei-Oki Earthquake) (M 7.8). Some seismologists have advanced the theory that a plate boundary exists along the eastern margin of the Sea of Japan (Fig.2-17, broken line). Therefore, we will classify and describe earthquakes in this area as earthquakes in the eastern margin of the Sea of Japan.

Large earthquakes in this area occur in relatively shallow locations. Therefore, the crustal movement at the sea floor (upheaval and subsidence) often results in tsunami. The hypocenter in these cases is near land, so coastal areas near the earthquake source experience strong ground motion and the arrival of a tsunami several minutes later. Further, tsunami sometimes occur at coastal regions far from the hypocenter. The Sea of Japan is surrounded by land, so the transmission of the tsunami has a very complex process. In some cases, the tsunami reaches its maximum height several hours after the earthquake.

(4)Other earthquakes

Forces operate locally in the shallow sections of rock mass on the periphery of a volcano. Small and medium size earthquakes frequently accompany volcanic activity. On rare occasions, large earthquake on the order of M 7 occur. One example was the 1914 earthquake at Sakurajima (M 7.1) that accompanied large eruptions on Sakurajima Volcano.

Earthquake swarms are sometimes seen on the periphery of volcanoes. For example, the swarm activity in the open sea east of the Izu Peninsula is thought to be related to volcanic activity.

2-5 Earthquakes and the damage they cause

In addition, there are several factors that contribute to the nature of earthquake damage beyond the size of the earthquake itself and its distance from the focal region. These factors include natural characteristics, such as the area's geological, topographical, and underground structures, the time and season of the earthquake, and social factors in the area itself. Also, the extent and nature of such secondary disaster caused by the earthquake, including fires and floods, depend on many factors. In the following section, we will describe the primary or direct disaster caused by earthquakes, including tsunami.

(1)Damage related to ground motion

Damage resulting from seismic ground motion is tied to many factors. This damage varies greatly in extent and characteristics.

The strength of the seismic ground motion ordinarily decreases with the greater the distance from the focal region. In some locations, however, distance from the hypocenter alone does not determine the strength of the ground motion. The ground near the earth's surface is also a major influence. Generally, structures on ground with a thick alluvium or on weaker ground, such as land created by landfills, undergo more violent motion and suffer greater damage. Therefore, ground of this type is suspected to be a factor when unexpected destruction occurs in locations some distance from the hypocenter. The strength of the ground motion depends on the direction of the progression of the fault movement, the distribution of the slip, and other factors. The region's underground structure is also a factor. For example, strong ground motion is sometimes generated in the direction of rupture propagation due to the interaction of the rapid progression of the rupture and the diffusion of the seismic waves. In the 1994 Earthquake far off the Coast of Sanriku (M 7.5), the fault movement began directly west of the Japan Trench. It moved in a westerly direction and reached off the east coast of Hachinohe (Hatinohe) City (Fig.2-13A). It seems likely that the fault movement progressing in the general direction of the city was one factor behind the strong ground motion at Hachinohe (seismic intensity 6 in JMA scale). In the 1995 Southern Hyogo Prefecture Earthquake, fault movement progressed from the vicinity of the Akashi Channel (Akasi Kaikyo) to both the Awaji Island (Awazisima) and toward Kobe City (Fig.2-13B). Factors believed to account for the extensive destruction in the outskirts of Kobe City are the progression of the fault movement in the direction of the city and the local amplification of the earthquake wave by the underground structure.

The circumstances of the destruction become more complex when we consider how the effects of ground motion combine with other natural factors.

For example, the phenomenon of liquefaction frequently occurs due to strong ground motion in soft ground with a sandy stratum and substantial water content. Liquefaction tends to occur when strong motion loosens the bonds between the grains of sand all at once, and the entire stratum becomes fluid. At this time, the fluid soil sometimes rises to the earth's surface (see Fig.2-25, Sand Blow Phenomenon). As a result, the ground loses the ability to support structures. Buildings and bridges with a high specific gravity sink, and buoyancy causes underground embedded pipes, manholes, and other objects with a low specific gravity to float to the surface, resulting in serious damage. When liquefaction occurs, the ground does not merely lose the capacity to support structures; the liquefied stratum also shifts extensively in a lateral direction as if in a landslide. This results in damage when embankments collapse.

Seismic ground motion also causes slope failures and landslides. This destroys buildings on sloping surfaces and causes destruction in surrounding areas. Sometimes, debris flow occurs as a result of a large slope failure. In the 1984 Western Nagano Prefecture Earthquake (Nagano-ken Seibu Earthquake) (M 6.8), a large slope failure took place south of the summit of Mt. Ontake (Ontakesan). In addition, the large volume of dirt that collapsed started an avalanche and flowed about 10 km downstream, leading a wide path of destruction. When slope failures and debris flows occur, rivers are blocked and secondary disaster results from collapsing embankments. Smaller collapses also occur frequently, such as the caving in of dirt and rock from ground motion. This results in small pockets of localized destruction. Sometimes, ground motion triggers slow landslides over a wide area on gently sloping land. During the 1995 Southern Hyogo Prefecture Earthquake, localized damage was sustained in the hilly area of Kobe due to the cracking that accompanies landslides.

Ground motion and rainfall are some of the factors that cause slope failures and landslides. Underlying these phenomena, however, are natural factors as the local geology, topography, and ground water. Slope failures and landslides also occur due to aftershocks after a main shock and rainfall.

(2)Tsunami damage

When a tsunami strikes, the extent of the damage will depend on prior awareness of the tsunami and the prompt and accurate transmission of information on emergency measures.

For example, during the 1896 Meiji Sanriku Earthquake (M 8 1/2), the perceptible ground motion was slight despite extremely large fault movement. Moreover, the earthquake occurred on the evening of the Boy's Festival Day (Tango-no-sekku) on the lunar calendar, and many people had gathered indoors for parties. This delayed evacuation, and is the reason cited for the drowning deaths of more than 20,000 people. In contrast, about 3,000 died from the tsunami during the 1933 Sanriku Earthquake (M 8.1), because the lessons learned from the tsunami of 1896 were applied and evacuation was conducted efficiently.

Following knowledge about tsunami can be instrumental in preventing the large-scale loss of life - tsunami may accompany earthquakes of M 6 or greater that take place offshore, the size of the tsunami that hits shore cannot be determined based on the perceptible ground motion, large tsunami may hit shore that are caused by earthquakes far away; finally, the initial tsunami may be followed by even larger succeeding tsunami.

The damage that can be caused by tsunami includes the destruction of buildings caused by flowing water or flotsam, the loss of fishing vessels, damage to the maritime hatchery industry and maritime facilities, and flood damage to farmland. Houses and fishing vessels washed away by tsunami sometimes result in the outbreak of fire. Finally, damage sometimes occurs by tsunami that move upstream.

(3)Other damage

Shallow earthquakes sometimes cause direct damage to roads and buildings when the slip of the fault reaches the earth's surface. In the Southern Hyogo Prefecture Earthquake, slipping of the Nojima fault(Nozima fault) occurred on Awaji Island, resulting in the destruction of buildings and roads. The manifestation of this slip on the earth's surface differed depending on the local ground conditions, particularly the thickness of the weak stratum. The nature of the damage thus varied from place to place.

Damage also occurs due to wide-ranging crustal movement (upheaval and subsidence) that accompanies the earthquakes. For example, the ground near Kochi (Koti) City subsided about 1 meter during the 1854 Ansei Nankai Earthquake (M 8.4) and the 1946 Nankai Earthquake (M 8.0). This caused an influx of sea water, resulting in damage due to the flooding of farmland. Also, the uplift of the earth that accompanies earthquakes makes harbors shallower, preventing their use.

(4)Changes in social conditions and earthquake damage

The nature of earthquake damage changes as conditions in society change, particularly with respect to urbanization and the development of large housing areas. For example, the 1936 earthquake (M 7.5) and 1978 earthquake (M 7.4 Miyagi-ken-Oki Earthquake) that occurred in the Pacific Ocean off the coast of Miyagi Prefecture had nearly identical hypocenters and were of nearly the same magnitude. The extent and nature of the damage, however, were quite different. The damage in Miyagi Prefecture by the 1936 earthquake resulted in the injury of 4 people, the complete collapse of 3 houses, the partial collapse of 2 houses, and the fissuring of roads. The damage in Miyagi Prefecture by the 1978 earthquake was more severe, however. A total of 28 people died, 1,325 people were injured, and 1,183 houses were completely destroyed. The damage was particularly severe in those areas with new housing. The basic infrastructure urban area that are indispensable for daily life, including gas, water, and electrical supply, were also damaged, essentially bringing daily life to a halt in Sendai City (For details refer to 4-2 (3)). It has been surmised that the degree of urbanization and the development of large housing areas were key differences in the extent of the damage sustained.

3 Characteristics of seismic activity in the Hokkaido region

Destructive earthquakes in the Hokkaido region frequently occur at sea, as with the 1952 Earthquake off the Coast of Tokachi (Tokachi-Oki Earthquake) (M 8.2) and the 1993 Earthquake off the Southwest Coast of Hokkaido (Hokkaido Nansei-Oki Earthquake) (M 7.8). The damage caused by these earthquakes resulted both from ground motion and tsunami. The Earthquake off the Southwest Coast of Hokkaido was particularly devastating. Damage due to the tsunami and other factors resulted in 230 dead or missing. Many inland earthquakes have also caused local destruction, though the earthquakes themselves were not as severe. Earthquakes and tsunami have also caused damage in the areas surrounding Hokkaido. Examples are the 1968 Earthquake off the Coast of Tokachi (M7.9), which occurred off the east coast of Aomori Prefecture, and the 1983 Central Sea of Japan (Japan Sea) Earthquake (Nihonkai Chubu Earthquake) (M 7.7), which occurred off the west coast of Aomori and Akita Prefectures. The latter was accompanied by a tsunami that caused additional destruction. Further, tsunami caused by earthquakes in foreign countries have also resulted in tsunami disaster, such as the 1960 Chile Earthquake Tsunami. Historical accounts on earthquakes in Hokkaido before the Meiji period (the late 19th century) is scanty compared to that available for other regions in Japan. Therefore, it is not as easy to acquire details on the characteristics of seismic activity here as it is for other regions. Fig.3-1 shows the known primary destructive earthquakes in Hokkaido.

Seismic activity in Hokkaido can be roughly divided into three types: first, earthquakes that occur in the Pacific Ocean near the plate boundary subducting toward land from the Chishima(Kuril) Trench and the Japan Trench; second, earthquakes that occur in shallow locations on land less than 20 km underground; third, those earthquakes that occur on the eastern margin of the Sea of Japan (Japan Sea). Among the earthquakes that occur on land, there are also M 7 earthquakes that occur in deeper locations from 20-40 km underground, particularly in the southern Hidaka Mountains (Hidaka Sanmyaku) and the offshore area of Urakawa.

The Pacific Plate is approaching Hokkaido from the east-southeast at a rate of about 8 cm a year. This plate is subducting toward Hokkaido from the Chishima Trench and the Japan Trench. The seismic activity that accompanies this subducting force can be observed to a depth of 400-500 km underground near southern Sakhalin (Fig.3-2). The Pacific Plate almost directly faces the land at the Japan Trench, and is subducting at a rather steep angle at the Chishima Trench. The earthquakes in the southern Hidaka Mountains are thought to be related to this angular subducting force. Some have theorized that the plate has begun to subduct in the area along the eastern margin of the Sea of Japan (Japan Sea).

Crustal deformation can be observed accompanying the subducting Pacific Plate in the eastern part of Hokkaido facing the Chishima Trench. The ground tends to extend in a southwestern Hokkaido, while the earth is compressing in other regions, generally from a west-northwest and east-southeast direction to an east-west direction (Fig.3-4).

The central area of Hokkaido includes the Hidaka Mountains, which are surrounded by two broad plains, the Ishikari and Tokachi Plains (Isikari and Tokati Heiya). The primary active faults lie from north to south along the edge of these plains, but there are fewer active faults here than in other areas. There are many volcanoes in the areas southwest of Sapporo and Tomakomai, where earthquake swarms are known to occur. Active faults in this area lie in a north-south direction. Many volcanoes are also found from the area near Mt. Taisetsu in central Hokkaido to Shiretoko Peninsula (Siretoko Hanto) in the east, and earthquake swarms also occur here. The active faults in this region are found near the Shiretoko Peninsula. There have been several M 6 earthquakes with slipping of the ground in the area surrounding Lake Kussharo (Kussyaro Ko) near Teshikaga. In the area north of Asahikawa, the mountainous areas have gentler slopes, such as Teshio Mountains (Tesio Santi) and Soya Hills (Soya Kyuryo). There are few active faults here. Fig.3-3 provides bird's eye views of the topography and distribution of the active faults in the Hokkaido region from the southeast and the northwest.

After the 1973 Earthquake off the Coast of Nemuro Peninsula (Nemuro-hanto-Oki Earthquake) (M 7.4), there were few destructive earthquakes in the Pacific Ocean off the coast of Hokkaido and the surrounding areas. This changed with the 1993 Earthquake off the Coast of Kushiro (M 7.8), followed by the 1994 Earthquake off the East Coast of Hokkaido (Hokkaido Toho-Oki Earthquake) (M 8.1). These earthquakes caused damage near the eastern part of Hokkaido. After the 1967 Earthquake near Teshikaga (M 6.5), no destructive earthquakes occurred for some time in shallow land areas. In the area of the Sorachi branch administrative office, both the 1986 earthquake near Numata (M 5.3) and the 1995 earthquake east of Mt. Shokanbetsu (M 5.7) did cause some slight damage, and destructive earthquakes have occurred in somewhat deeper locations near the southern Hidaka Mountains. One such was the 1982 Earthquake off the Coast of Urakawa (Urakawa-Oki Earthquake) (M 7.1), which caused damage primarily in the area of the Hidaka branch administrative office. In the eastern margin of the Sea of Japan (Japan Sea), the 1993 Earthquake off the Southwest Coast of Hokkaido (M 7.8) caused the most fatalities in Hokkaido since the start of the Meiji period in 1868. The tsunami resulting from the 1983 Central Sea of Japan (Japan Sea) Earthquake (M 7.7) also caused a number of fatalities and destroyed several buildings. Finally, earthquake swarms began in the area off the coast of Matsumae in October 1995, with the largest earthquake in the swarm having a magnitude of 4.4.

(1)Earthquakes near the plate boundary off the Coast of Pacific Ocean

The Pacific Plate is subducting beneath the Hokkaido region from the Chishima (Kuril) Trench and the Japan Trench in the Pacific Ocean off the coast of Hokkaido (Fig.3-2).

Two types of earthquakes occur near plate boundaries in the offshore area of the Pacific Ocean and other locations: first, the interplate earthquakes caused by slipping at the boundary of the subducting Pacific Plate and the plate on land; and second, those earthquakes that occur within the subducting Pacific Plate.

1) Interplate earthquakes caused by the subducting Pacific Plate

Great interplate earthquakes caused by the subducting Pacific Plate have occurred along the Chishima Trench and other locations. This ground motion has caused damage to areas located on the Pacific Ocean side of Hokkaido, and sent earthquake-generated tsunami crashing onto the Pacific Ocean coast.

Examples of this type of earthquake in the 19th century include the 1843 Earthquake off the Coast of Kushiro (M 7.5), the 1856 Earthquake off the east Coast of Aomori Prefecture (M 7.5), and the 1894 Earthquake off the Coast of Nemuro (M7.9). More recent earthquakes include the 1952 Earthquake off the Coast of Tokachi (Tokachi-Oki Earthquake) (M 8.2), the 1968 Earthquake off the East of Aomori Prefecture (Tokachi-Oki Earthquake) (M 7.9), and the 1973 Earthquake off the Coast of Nemuro Peninsula (M 7.4). These earthquakes occurred within a relatively short period of time, and their source regions did not overlap. A series of large earthquakes of this type are thought to occur repeatedly in the sea along the Chishima Trench in the Pacific Ocean at intervals ranging from several decades to 100 years.

These earthquakes can be explained in the following way. Strain accumulates over a period of several decades to 100 years in the area adjoining the Chishima Trench due to the subducting Pacific Plate. As the area in eastern Hokkaido facing the Chishima Trench compresses in a northwest-southeast direction, crustal movement is observed, with subducting of the coastal area in a stationary condition. This phenomenon is thought to be related to the accumulation of strain (Fig.3-4, Fig.3-5). After this strain has approached its limit, it is released by a series of interplate earthquakes. As a result, a series of large earthquakes occurs along the trench in a short time with no overlapping of focal regions. When the series of interplate earthquakes has finished, large earthquakes do not occur again until sufficient strain has reaccumulated. This cycle is expected to continue in the future. Great earthquakes within subducting Pacific Plate also occur in this area, such as the 1994 Earthquake off the East Coast of Hokkaido (M 8.1). It is difficult to forecast the occurrence of large earthquakes using only the interval between large earthquake series.

So-called "tsunami earthquakes" ("slow earthquakes" or "low-frequency earthquakes") also occur in this region. The characteristics of these earthquakes include fault movement less intense than that of ordinary earthquakes, and tsunami larger in comparison to the ground motion felt on land. Measured by ground motion, the 1975 Earthquake off the East Coast of Hokkaido registered M 7.0. However, estimated by the size of the tsunami, which is thought to roughly express the extent of fault movement, the magnitude of this earthquake is greater than 7.5.

2) Earthquakes within the subducting Pacific Plate

Large earthquakes occur inside the subducting Pacific Plate underneath the Hokkaido region. The 1993 Earthquake off the Coast of Kushiro (Kushiro-Oki Earthquake) (M7.8) occurred in a somewhat deeper area of roughly 100 km, and was caused by fault movement on a roughly horizontal fault. Also, the 1994 Earthquake off the East Coast of Hokkaido (M 8.1) was in a somewhat shallower area of about 20 km. This was caused by fault movement on a reversed fault at a large inclination. Further, an earthquake (M 7.7) occurred inside the Pacific Plate directly beneath the Kunashiri Channel at a depth of about 150 km. Of the earthquakes that occurred in the area adjoining the Hokkaido region, the 1933 Sanriku Earthquake (M 8.1) on a normal fault occurred in a very shallow location (about 20 km) near a trench. This earthquake was in the Pacific Plate as it was beginning to subduct. [For details, refer to 4-2 (1).] This earthquakes was accompanied by large tsunami and caused damage to areas along the Pacific Ocean coast of Hokkaido.

(2)Shallow inland earthquakes (Depths of 20 km or less)

A look at the topography of Hokkaido shows various mountainous regions lying from north to south in locations south of Asahikawa. These include the Hidaka Mountains, Yubari Mountains (Yubari Santi) and Mashike Mountains (Masike Santi). Also, there are broad plains adjoining these mountains, including the Tokachi Plain and the Ishikari Plain. The primary active faults in Hokkaido lie adjacent to the edge of these plains. They have activity classifications of B and C class, and are located in the Tokachi-plain (Tokachi-heiya) fault zone, the eastern margin of the Mashike Mountains (Mashike-sanchi-toen) fault zone, and the eastern margin of the Ishikari-lowlands (Ishikari-teichi-toen) fault zone. Most of these faults run in a north-south direction, and are classed as reverse faults. This indicates that the central area of Hokkaido is being compressed in an east-west direction. Observation of crustal movements shows that the ground is being compressed in a roughly west-northwest to east-southeast direction. These factors have led to speculation that the central area of Hokkaido is being compressed in an east-west direction by a force resulting from the subducting Pacific Plate.

The area near the Oshima Peninsula (Osima Hanto) in southwest Hokkaido is believed to be a topographical and geological extension of the Ou Mountains (Ou Sanmyaku) in the Tohoku District. There are active faults at the western margin of the Hakodate Plain (Hakodate-heiya-seien) fault zone in Hakodate Plain, and at the Kuromatsunai lowlands (Kuromatsunai-teichi) fault zone in the Kuromatsunai lowlands extending, from Suttsu (Suttu) on the Sea of Japan (Japan Sea) coast through to Uchiura Bay (Uturа Wan). These are believed to be reverse faults with activity of B or C class. An active fault is also known to exist in the area near the Shiretoko Peninsula (Siretoko Hanto).

While almost no active faults have been observed in the Sarobetsu Plain in the northern part of Hokkaido, pronounced deformations on terrace surfaces and in strata have been observed. There is significant crustal movement that indicates compression from a west-northwest to an east-southeast direction, but the reasons for this movement are not yet understood.

There is no record of large M 7-level earthquakes having their focal regions in shallow inland taking place in Hokkaido. This can be attributed to the scarcity of information on Hokkaido earthquakes before 1868. Also, there are no known examples of direct action of existing active faults. Since the interval of activity for most active faults is 1,000 years or more, this does not mean that earthquakes have not occurred here. Of the destructive earthquakes in the past, there is the 1938 earthquake at Lake Kussharo near Teshikaga (M 6.1), during which slip occurred at the surface. Earthquakes of M 5-6 have also struck here. Historical accounts indicate that the 1834 earthquake near the mouth of the Ishikari River (Isikari Gawa) (M 6.4) known as the Ishikari Earthquake, was of this type. In present-day Sapporo, many traces remain of the ground liquefaction thought to have been caused by this earthquake. Other events include the 1995 earthquake east of Mt. Shokanbetsu (M 5.7) in the area of the Sorachi branch administrative office, and the 1956 earthquake off the coast of Abashiri (M 6.3) that caused slight damage on the Okhotsk Sea coast of Hokkaido.

Earthquake swarms are known to occur in eastern and southwestern Hokkaido. Most of these earthquakes occur near volcanoes. The magnitude of individual earthquakes in the swarms is usually less than M 5. Individual earthquakes with M larger than 5 rarely occur and cause damage usually restricted to near the hypocenter. The earthquake swarms usually occur within a short period lasting one to three months, but some have been known to last for more than one year. Examples of recent primary earthquake swarms include the 1964 swarm at Rausu, where the largest earthquake was M 4.6; the swarm that have continued since 1989 in the northern part of the area of the Tokachi branch administrative office, whose largest earthquake was M 4.8; the swarm off the coast of Hakodate that occurred from 1978 to 1980, and whose largest earthquake was M 4.2; and the swarm off the coast of Matsumae that started in 1995 and are continuing, the largest of which had a magnitude of 4.4.

(3)Earthquakes in the eastern margin of the Sea of Japan (Japan Sea)

The coastal area of the Sea of Japan from Hokkaido to the Tohoku Region is referred to as the "eastern margin of the Sea of Japan (Japan Sea)". Several large earthquakes have occurred here recently, and significant damage has resulted due to tsunami, seismic ground motion, and ground liquefaction. Because the focal regions of these earthquakes have been near land, in some cases tsunami have hit shore immediately after or, in some case, several minutes after an earthquake has occurred.

One of these earthquakes was the 1993 Earthquake off the Southwest Coast of Hokkaido (M 7.8). The 1983 Central Sea of Japan Earthquake (M 7.7) was located south of the 1993 earthquake, while the 1940 earthquake off the coast of Cape Kamui (Kamui Misaki), (M 7.5) occurred just north of here, off the coast of Shakotan Peninsula (Syakotan Hanto). Off the coast of Rumoi located in the northeast of Cape Kamui, earthquakes occurred in 1947 (M 6.7) and in 1959 (M 6.2). Most of these earthquakes were accompanied by tsunami. Further north, an earthquake occurred off the southwest coast of Sakhalin (M 6.9) in 1971.

Since the mechanisms of these earthquakes were reversed faults compressed in an east-west direction. This is the basis for recent speculation that a plate boundary exists in the "eastern margin of the Sea of Japan (Japan Sea)". Some hold that the phenomenon can be explained even if no plate boundary exists, but no firm conclusions have been reached [See 4-1 (3)]. Existing data indicates that no large earthquakes have taken place in the open sea to the west of Hokkaido from Teuri Island and Yagishiri Island to Rishiri Island and Rebun Island, which lie between the source regions for the previously-mentioned earthquake in the open sea off the coast of Rumoi and the earthquake off the southwest coast of Sakhalin. Some believe that this area is a seismic gap.

(4)Earthquakes in the southern Hidaka Mountains

In the Pacific Ocean off the southern part of the Hidaka Mountains, the trench bends from a roughly north-south direction (Japan Trench) to a northeast-southwest direction (Chishima Trench). This bend in the trench also causes a bend in the subducting Pacific Plate, and the subterranean area is thought to be greatly distorted. In the Chishima Trench, the Pacific Plate is subducting obliquely, dragging the earth's crust on land in a westward direction. This earth's crust is thought to be colliding with the earth's crust in the southwestern part of Hokkaido in the southern part of the Hidaka Mountains. Thus, a great deal of strain has built up from the southern Hidaka Mountains to the area off the coast of Urakawa due to the large distortion and unique underground structure caused by the bend in the plate, as well as to the collision with the earth's crust resulting from the obliquely subducting plate. As a result the seismic activity in this area is quite active.

Several large earthquakes have occurred here, including the 1982 Earthquake off the Coast of Urakawa (M 7.1) and the 1970 earthquake in the Hidaka Mountains (M 6.7). These earthquakes occurred at somewhat deeper locations (20-40 km) than those that normally occur on land (depths of 20 km or less). Therefore, the damage tends to be alleviated somewhat. In addition, many earthquakes occur in deeper areas that are directly related to the subducting of the Pacific Plate.

4 Characteristics of seismic activity in the Tohoku region

One well-known destructive earthquake in the Tohoku region was the 1896 Meiji Sanriku Earthquake (M 8 1/2) that occurred off the coast of Sanriku. The combined earthquake and tsunami resulted in more than 20,000 fatalities. Other earthquakes occurring at sea since the Meiji period (1868) include the 1933 Sanriku Earthquake (M 8.1) and the 1983 Central Sea of Japan (Japan Sea) Earthquake (Nihonkai Chubu Earthquake) (M 7.7), and those occurring inland include the 1894 Shonai Earthquake (M 7.0) and the 1896 Rikuu Earthquake (M 7.2). They caused damage both from seismic ground motion and tsunami. There are fewer historical accounts of older earthquakes in the Tohoku region than there are for the Kinki and other regions. Many destructive earthquakes have occurred in this region both on land and at sea, however. The oldest known earthquake here was the 830 earthquake at Dewa (M 7 - 7.5). Damage is known to have been caused in the Tohoku region by earthquakes and tsunami in surrounding areas. One destructive earthquake that occurred in this surrounding area was the 1993 Earthquake off the Southwest Coast of Hokkaido (Hokkaido Nansei-Oki Earthquake) (M 7.8) Tsunami generated by earthquakes in foreign countries have also caused damage, such as the 1960 Chile Earthquake Tsunami. Fig.4-1 and Fig.4-2 show the known primary destructive earthquakes in the Tohoku region.

Seismic activity in the Tohoku region can be roughly divided into three types: first, earthquakes that occur in the Pacific Ocean near the plate boundary that subducts from the Japan Trench to the land; second, earthquakes that occur on land in shallow locations less than 20 km underground, and third, earthquakes in the eastern margin of the Sea of Japan (Japan Sea). Of these three types, the earthquakes that are large and strike with great frequency are those in the Pacific Ocean.

The Pacific Plate approaches the Tohoku region from the east-southeast at a rate of about 8 cm a year. This plate subducts toward Tohoku from the Japan Trench. The seismic activity that accompanies this subduction occurs at a depth of about 150-200 km underground on the Sea of Japan side of the Tohoku region. This activity can be detected as far underground as 600 km below the area near the southern edge of the maritime region of Russia (Fig.4-3, Fig.2-5). The land is being compressed in an east-west direction in the eastern margin of the Sea of Japan. Some have theorized that the plate has begun subducting along a row of earthquakes, running in a north-south direction in this region.

The topography of the Tohoku region is characterized by alternating mountain ranges and lowlands running in a north-south direction, particularly the Ou Mountains (Ou Sanmyaku) and the Dewa Mountains (Dewa Santi) area. The primary active faults of the Tohoku region lie at the boundaries of the mountains and the lowlands, and most of these run in a north-south direction. Most are reverse faults, indicating that the area is uniformly being compressed in an east-west direction. Observations of crustal movement, however, show that many more areas are being extended than compressed. The manner and extent of crustal movement have local characteristics, however, and overall the Tohoku region is not uniformly being compressed in an east-west direction (Fig.4-5). Most of the large destructive inland earthquakes occur on identified active faults, but some earthquakes occur in areas where no active faults are known. Earthquake swarms are known to occur in some locations. Fig.4-4 provides bird's eye views of the topography and distribution of the active faults in the Tohoku region from the northeast and the northwest.

There has not been any destructive earthquake in the Pacific Ocean near the Tohoku region and surrounding areas since the 1978 Earthquake off the Coast of Miyagi Prefecture (Miyagi-ken-Oki Earthquake) (M 7.4). The Earthquake far off the Coast of Sanriku (Sanriku Haruka-Oki Earthquake) occurred in 1994 (M 7.5), however, and caused damage primarily in Aomori Prefecture. There have not been any recent destructive earthquakes of note on land, but some damage was caused by seismic activity (maximum M 5.9) in 1996 near the border of Miyagi and Akita Prefectures. On the eastern margin of the Sea of Japan, the 1983 Central Sea of Japan Earthquake (M 7.7) and the 1993 Earthquake off the Southwest Coast of Hokkaido (M 7.8) caused substantial damage, primarily on the Sea of Japan coast.

(1)Earthquakes near the plate boundary off the Coast of Pacific Ocean

The Pacific Plate is subducting toward the Tohoku region from the Japan Trench off the east coast of the Tohoku region (Fig.4-3).

There are two types of earthquakes that occur near the plate boundaries off the Pacific Coast: first, the interplate earthquakes that are caused by the slipping movement at the boundary of the subducting Pacific Plate and the plate on land; second, earthquakes that occur within the subducting Pacific Plate. Most known destructive earthquakes have been interplate earthquakes.

1) Interplate earthquakes caused by the subducting Pacific Plate

Many destructive earthquakes of this type are known, including the 1896 Meiji Sanriku Earthquake (M 8 1/2), the 1968 Earthquake off the Coast of Tokachi (Tokachi-Oki Earthquake) (M7.9), the 1978 Earthquake off the Coast of Miyagi Prefecture (M 7.4), and the 1994 Earthquake far off the Coast of Sanriku (M 7.5). Many of these earthquakes occur at relatively shallow locations underneath the sea floor. In most cases, the crustal movement on the sea floor caused by fault movement accompanies a tsunami. The tsunami height grows larger in proportion to the shallowness of the water, and therefore becomes generally high when it reaches the coast. The tsunami height is also determined by the shape of a bay and other factors. The hypocenter will be slightly deeper for earthquakes of this type which occur closer to shore because the Pacific Plate inclines and subducts in the direction of land. Therefore, tsunami occurring with this type of earthquake are not usually high. The ground motion can cause substantial damage on land, however, because the focal region is close to land. This happened during the Earthquake off the Coast of Miygai Prefecture and the Earthquake far off the Coast of Sanriku.

The area off the Pacific coast of the Tohoku region is one of the most seismically active regions around Japan. The characteristics of how earthquakes occur here differ depending on the location. For example, great earthquakes of M 8 sometimes occur in the sea off the coast of Aomori and Miyagi Prefectures. These include the 1896 Meiji Sanriku Earthquake (M 8 1/2) and the 1968 Earthquake off the Coast of Tokachi (M 7.9). The type of seismic activity that occurs in the open sea off Fukushima is of a different nature, however. While there have been several earthquakes with M 7 or so , such as the 1938 Earthquake off the East Coast of Fukushima Prefecture (Fukushima-ken Toho-Oki Earthquake) (M7.5), no earthquakes with M 8 or so are known to have occurred. Also, earthquakes of roughly the same magnitude have occurred every about 40 years since 1855 near the same sea location, the most recent one was the 1978 Earthquake off the Coast of Miyagi Prefecture (M 7.4).

So-called "tsunami earthquakes" ("slow earthquakes" or "low-frequency earthquakes") also occur in this region. The characteristics of these earthquakes are relatively slow fault movement. In this case, tsunami is large, although people do not feel strong ground motion. Typical example was the 1896 Meiji Sanriku Earthquake (M 8 1/2). The fault movement during that earthquake was clearly much greater than that estimated from the ground motion. Thus, there are some earthquakes for which it is difficult to ascertain the existence of a tsunami or to assess its size from perceptible ground motion only.

2) Earthquakes within the subducting Pacific Plate

The 1933 Sanriku Earthquake (M 8.1) is a destructive earthquake of this type known to have occurred in this region. This earthquake occurred on a normal fault in a shallow location near the Japan Trench, from which the Pacific Plate is beginning to subduct directly under the land plate. The tsunami caused upward of 3,000 fatalities. Among earthquakes which occur within subducting plates, there are also destructive earthquakes other than those occurring in shallow locations on normal faults. In the Chishima Trench (Tisima Trench), the 1993 Earthquake off the Coast of Kushiro (Kushiro-Oki Earthquake) (M 7.8) occurred in a somewhat deeper area of roughly 100 km, and was caused by the fault movement on a roughly horizontal fault. Also, the 1994 Earthquake off the East Coast of Hokkaido (Hokkaido Toho-Oki Earthquake) (M 8.1) was in a somewhat shallower area of about 20 km deep. This was caused by the fault movement of a reverse fault at a high inclination. Therefore, the hypocentral depth and the nature of the fault movement vary for earthquakes that occur within subducting plates.

Recently, the 1987 earthquake (M 6.6, depth about 70 km) caused slight damage in northern Iwate Prefecture.

(2)Shallow inland earthquakes (Depths of 20 km or less)

There is a close connection between the topography of the Tohoku region and the distribution of active faults. The topography of the Tohoku region can be divided into several areas, each running in a north-south direction. On the Pacific Ocean side, the gently sloping Kitakami highlands (Kitakami Koti) and the Abukuma highlands (Abukuma Koti) extend from north to south. On the western side of these highlands, the Kitakami and Abukuma Rivers flank a lowland area, and the steep Ou Mountains cut through the central part of the Tohoku region from north to south. The Ou Mountains contain many volcanoes, including Mt. Iwate, Mt. Kurikoma, and Mt. Zao. In addition, there is a mountainous area that includes Dewa, running north to south in the western part of the area adjoining the Sea of Japan. This mountainous area flanks several basins, including the Yokote and Yamagata Basins (Yokote and Yamagata Bonti). Several plains run roughly north to south along the Sea of Japan coast, including the Akita Plain (Akita Heiya) and the Shonai Plain (Syonai Heiya).

The primary active faults in the Tohoku region are distributed in a roughly north to south direction, and lie at the boundaries of mountainous areas and basins, plains, and lowlands, as well as along the Sea of Japan coast. Most of these active faults are reverse faults with an activity of B class. So far, the fault movement has been in a direction that makes the mountainside higher. This characteristic indicates that compression is being applied to the active faults in an east-west direction. Crustal movement in this area, however, indicates that locations with prominent extension outnumber those with compression. Also, there are local differences in the characteristics and extent of this movement. The subducting Pacific Plate is not believed simply to be causing compression in an east-west direction (Fig.4-5). Old rock is widely distributed in the Kitakami and Abukuma highlands, and the geologic characteristics of this area are relatively stable. There is slight crustal movement in this area, and a few active faults.

Many earthquakes are known to have occurred in shallow locations on land, mostly 15-20 km deep. Destructive earthquakes of this type after the Meiji Period (1868) include the 1894 Shonai Earthquake (M 7.0), the 1896 Rikuu Earthquake (M 7.2), the 1900 earthquake in northern Miyagi Prefecture (M 7.0), and the 1914 Akita Senboku Earthquake (M 7.1, also known as the Kowakubi Earthquake). The 1896 Rikuu Earthquake is thought to have occurred on the eastern margin of the Yokote-Basin (Yokote-bonchi-toen) fault zone and the 1894 Shonai Earthquake is thought to have occurred on the eastern margin of Shonai Plain (Shonai-heiya-toen) fault zone. In contrast, the active faults corresponding to the 1900 earthquake in northern Miyagi Prefecture and the 1914 Akita Senboku Earthquake are not yet discovered. Thus large earthquakes have occurred even in locations where active faults are not known to exist. Destructive earthquakes from an older period include those that occurred in the coastal area of Akita Prefecture, such as the 1694 earthquake near Noshiro (M 7.0) and the 1804 Kisakata Earthquake (M 7.0), and those in the interior, such as the 1611 earthquake at Aizu (M 6.9) and the 1766 earthquake at Tsugaru (M 7 1/4). Earthquakes of M 6 or so, smaller than those previously described, also occur even in locations other than active fault zones, and sometimes cause damage locally. In addition, the intervals of activity for most active faults are 1,000 years or longer. Therefore, even if none are known today, this does not indicate that no earthquakes occur here however.

Earthquake swarms are known to occur in several places in the Tohoku region. Most of these earthquakes occur near volcanoes. The magnitudes of the individual earthquakes that comprise the earthquake swarms are usually M 4 or less; an individual earthquake of M 5 or stronger rarely occurs, and damage occurs locally. The duration of earthquake swarm activity is usually short, from one to three months. However, there are cases of this activity lasting longer than one year.

(3)Earthquakes in the eastern margin of the Sea of Japan (Japan Sea)

The sea area off the Sea of Japan coast of Hokkaido and the Tohoku region is called the eastern margin of the Sea of Japan. One well-known destructive earthquake that occurred in the open sea off the coast of Akita and Aomori Prefectures was the 1983 Central Sea of Japan Earthquake (M 7.7). This caused significant damage due to a tsunami, ground motion, and ground liquefaction. As with earthquakes in the Pacific Ocean, most earthquakes in the eastern margin of the Sea of Japan are caused by crustal movement (upheavals and subsidence) on the sea floor from fault movement, and consequently generate tsunami. The focal regions of these earthquakes have been close to land, thus in some cases tsunami has reached shore several minutes after the earthquake occurred.

Historical data and research into tsunami show that several earthquakes have occurred along a north-south direction in this area. The 1940 Earthquake off the Coast of Shakotan Peninsula (Syakotan Hanto) (M 7.5) and the 1964 Niigata Earthquake (M 7.5) were earthquakes that occurred on reverse faults with compression in an east-west direction. In addition, compression is being exerted in an east-west direction over a wide area extending from Hokkaido to the Chubu region. This led to the formulation of a theory in the early 1980s that the eastern margin of the Sea of Japan was a convergent plate boundary. Two large earthquakes later occurred in this area: the 1983 Central Sea of Japan Earthquake (M 7.7), and the 1993 Earthquake off the Southwest Coast of Hokkaido (M 7.8). Research into the nature and causes of these earthquakes is currently under way. Some hold that the pattern of earthquakes here can be explained even if the eastern margin of the Sea of Japan is not a plate boundary; however, no firm conclusions have drawn as yet.

There is less seismic activity in this area than occurs offshore in the Pacific Ocean. If we limit the time of seismic activity to the period of the recent several decades, we find that a succession of large earthquakes has occurred in the open sea from Hokkaido to Niigata Prefecture. The southern third of the stretch of sea off the coast of Akita and Yamagata Prefectures between the source region of the 1983 Central Sea of Japan Earthquake and the 1964 Niigata Earthquake encompassed part of the source region of the 1833 Earthquake off the Coast of Shonai (Shonai-Oki Earthquake) (M 7 1/2). No earthquakes are known to have occurred in the northern most two-thirds of this area, however. Therefore, some have advanced the theory that this area is a seismic gap.

5 Characteristics of seismic activity in the Kanto region

The destructive earthquakes of the Kanto region are well known, including as they do the 1923 Kanto Earthquake (M 7.9, also known as the Great Kanto Earthquake) that occurred near Sagami Bay (Sagami Wan). This earthquake resulted in more than 140,000 dead or missing. Many other destructive earthquakes have occurred in this region in the sea and on land, causing damage from ground motion or the tsunami. The oldest known of these is the 818 earthquake in Kanto Shokoku (Provinces) (larger than M 7.5). Others include the 1703 Genroku Earthquake (M 7.9-8.2), the 1855 Ansei Edo (former name of Tokyo) Earthquake (M 6.9), the 1894 Meiji Tokyo Earthquake (M 7.0), and the 1931 West Saitama Earthquake (Nishi-Saitama Earthquake) (M 6.9). Most of these earthquakes caused destruction primarily in the southern Kanto region, but destructive earthquakes have also occurred in the northern Kanto region, including the 1949 Imaichi Earthquakes (M 6.2 and M 6.4). In addition, earthquakes in surrounding areas have indirectly caused damage in the Kanto region, such as those occurring near the Izu Peninsula (Izu Hanto) or off the coast of Tokai District. Also, tsunami generated by earthquakes overseas has caused damage, such as the 1960 Chile Earthquake Tsunami. The primary destructive earthquakes known to have taken place in the Kanto region are shown in Fig.5-1, Fig.5-2, and Fig.5-3.

Seismic activity in the Kanto region is roughly divided into three types. First are earthquakes that occur near the Pacific Plate boundary which inclines toward land from the Japan Trench in the open sea east of the Kanto region. Second are earthquakes that occur near the Philippine Sea Plate boundary which inclines toward land from the Sagami Trough in the area from Sagami Bay to the open sea off the coast of the Boso Peninsula (Boso Hanto). Third are earthquakes that occur in shallow locations on land. As we will explain later, the plate boundaries underneath the Kanto region have a complex structure. Earthquakes that occur near plate boundaries are often of the same type that occur in deep locations on land. Therefore, the Kanto region is one of those in Japan with an extreme amount of seismic activity. Both earthquakes that occur in shallow land locations due to active faults and earthquakes that occur due to subducting plates can occur directly beneath urban areas (Fig.5-9).

The Pacific Plate is approaching the Kanto region from the east-southeast at a rate of about 8 cm a year. This plate is subducting in the direction of the Kanto region from the Japan Trench. The seismic activity in this area accompanying the subduction of the plate has been observed to a depth of about 200 km. This activity continues into the area beneath the Chubu and Kinki regions (Fig.5-5, Fig.6-4). Meanwhile, the Philippine Sea Plate is approaching the Kanto region from the southeast at a rate of about 3 to 4 cm a year. It is subducting toward the northwest as if to wedge between the land plate extending from the Sagami Trough and the Pacific Plate. The seismic activity accompanying the subduction of the Philippine Sea Plate can be observed to a depth of about 100 km in the northern Kanto region (Fig.5-6). The subduction of these two plates creates a complex structure, in which the plates abut beneath the southern Kanto region. Also, the Izu Peninsula located on the Philippine Sea Plate is colliding with the Japanese archipelago. Hence, the boundary between the Philippine Sea Plate and the plate on land is just 10-30 km below the surface of the earth in the southern Kanto region. As a result, the southern Kanto region, like the Tokai region, has the potential to become the source region of great interplate earthquakes extending to relatively shallow areas directly beneath urban districts (Fig.5-9).

The topography of the Kanto region is characterized by the broad Kanto Plain (Kanto Heiya) surrounded by mountainous and hilly areas, including the Kanto Mountains (Kanto Santi). There are many active faults in the southern part of the Kanto region, particularly in the southern Boso Peninsula, the southern tip of the Miura Peninsula (Miura Hanto), and western Kanagawa Prefecture. Several active faults are also known to exist in the central part of the Kanto Plain. Many of these have been covered by sediment in relatively recent times, so their topography in many cases is not yet clear. Fig.5-7 provides bird's eye views of the topography and distribution of the active faults in the Kanto region from the south and the southeast. The southern part of the Kanto region is known to have more crustal movement than the northern part. This movement is thought to be related primarily to the subducting Philippine Sea Plate (Fig.5-8).

Recent seismic activities in the Kanto region and surrounding area include frequent earthquake swarms in areas from the Izu Islands to the Izu Peninsula, and many others such as the 1978 Earthquake near the Coast of Izu Oshima (Izu Oshima Kinkai Earthquake) (M 7.0), the 1980 Earthquake off the East Coast of Izu Peninsula (Izu-hanto Toho-Oki Earthauake) (M 6.7), and the 1990 Earthquake near the Coast of Izu Oshima (Izu Oshima Kinkai Earthquake) (M 6.5). Seismic activity in the area surrounding the Boso Peninsula has included the 1987 Earthquake off the East Coast of Chiba Prefecture (Chiba-ken Toho-Oki Eartquake) (M 6.7) and the 1996 earthquake off the Coast of Choshi (Tyosi) (M6.4). Brisk seismic activity regularly occurs once every few years in southwest Ibaraki Prefecture. This occurs at somewhat deeper locations of roughly 50 km, and generates earthquakes of M 5-6. Other activity includes the 1988 Earthquake in the eastern Tokyo Metropolitan District (M 6.0, a depth of 96 km), and the 1992 Earthquake in the southern Tokyo Bay near the Uraga Channel (M 5.9, a depth of 92 km). No large earthquakes of M 7 or greater have occurred in the past several decades near the Sagami Trough, from the interior of the Kanto region and Sagami Bay to an area off the southeast of the Boso Peninsula. Fig.5-4 shows recent seismic activity on land in locations deeper than 30 km.

(1)Earthquakes near the plate boundary from Sagami Bay to off the southeast Coast of the Boso Peninsula

The Philippine Sea Plate is subducting under the Kanto region from the Sagami Trough, which extends from Sagami Bay to an area off the southeast of the Boso Peninsula (Fig.5-6).

There are two types of earthquakes that occur near the plate boundary from Sagami Bay to this area southeast of the Boso Peninsula: first, interplate earthquakes occurring due to the slipping movement at the boundary of the subducting Philippine Sea Plate and the plate on land; and second, earthquakes that occur within the subducting Philippine Sea Plate.

Earthquakes related to the subducting Philippine Sea Plate occur even in somewhat deeper areas on land in the Kanto region. There is an explanation of these earthquakes in 5-1 (3).

1) Interplate earthquakes caused by the subducting Philippine Sea Plate

Known examples of this type of earthquake with M 8 or so include the 1923 Kanto Earthquake (M 7.9, also known as the Great Kanto Earthquake) and the 1703 Genroku Earthquake (M 7.9-8.2). These earthquakes occur in locations close to land, and part of the source region of these earthquakes may actually lie inland. These large earthquakes generate extremely strong ground motion, primarily in the southern Kanto region. They have caused significant damage, collapsing houses and causing fires. This type of earthquake occurs in relatively shallow locations underneath the sea floor. As a result, fault movement causes crustal deformation (upheaval and subsidence) on the sea floor and generates large tsunami, that can seriously damage coastal areas. Also, the source region of these earthquakes is near land, so it is possible that the tsunami will strike land immediately after the earthquake.

2) Earthquakes within the subducting Philippine Sea Plate

The Philippine Sea Plate is subducting from the Sagami Trough toward the Kanto region, but destructive earthquakes are not known to occur within plates in relatively shallow locations. An explanation of earthquakes that occur in relatively deeper locations that are extensions of the landmass is found in 5-1 (3).

The Izu Peninsula located on the Philippine Sea Plate has similar characteristics to the land plate. Therefore, it can not be subducting under the plate and appears to collide with the Japanese archipelago. Thus, the force is rather complex in such areas as the Izu Peninsula and western Kanagawa Prefecture, and there is substantial seismic activity. (For details on earthquakes in western Kanagawa Prefecture, refer to 5-1 (3) and 5-3 (7); for details on the earthquakes in the Izu Peninsula, refer to 6-1 (2) and 6-2 (6)).

(2)Earthquakes occurring near the plate boundary off the east Coast of the Kanto region

The Pacific Plate is subducting toward the Kanto region from the Japan Trench and the Izu-Ogasawara Trench, which extend north to south along an offshore area east of the Kanto region (Fig.5-5).

There are two types of earthquakes that occur near the plate boundary off the open sea east of the Kanto region. First are interplate earthquakes occurring from the slipping movement at the boundary of the subducting Pacific Plate and the plate on land. Second are earthquakes that occur within the subducting Pacific Plate.

Earthquakes related to the subducting Pacific Plate occur even in somewhat deeper areas on land in the Kanto region. There is an explanation of these earthquakes in 5-1 (3).

1) Interplate earthquakes caused by the subductng Pacific Plate

Known cases of interplate earthquakes caused by the subducting Pacific Plate from the open sea east of the Kanto region to an area in the open sea off Fukushima Prefecture since the Meiji period (1868) include the 1909 (M 7.5) and 1916 (M 7.0) earthquakes in the open sea southeast of the Boso Peninsula and the 1938 Earthquake off the East Coast of Fukushima Prefecture (Fukushima-ken Toho-Oki Earthquake) (M 7.5). Many of these earthquakes occur in relatively shallow locations under the sea floor. Most cause crustal deformation (upheaval and subsidence) on the sea floor due to fault movement, and are accompanied by tsunami. While great earthquakes of M 8 or so sometimes occur in the Japan Trench in the open sea off the coast of Sanriku, no earthquakes of this magnitude have occurred in the open sea off the coast of Fukushima and Ibaraki Prefectures or further south since the Meiji period (1868), though both earthquakes were caused by the subducting Pacific Plate. An examination of historical accounts, however, shows that extensive damage was caused by a tsunami from Fukushima Prefecture to the coast of the Boso Peninsula and Hachijojima Island (Hatuzyo Jima) due to an M 8 earthquake in 1677 that is thought to have occurred in the open sea east of the Boso Peninsula. Details of the source region of this earthquake are unknown, however. This is the only destructive earthquake known from historical data that occurred in the open sea east of the Kanto region. Large M 7 earthquakes are known to occur further south along the Izu-Ogasawara Trench, including, for example, the 1972 Earthquake off the East Coast of Hachijojima Island (Hachijojima Toho-Oki Earthquake) (M 7.2). Great M 8 or so earthquakes are unknown to have occurred here.

2) Earthquakes within the subducting Pacific Plate

One destructive earthquake of this type was the 1953 Earthquake off the Coast of Boso (Boso-Oki Earthquake) (M 7.4). This earthquake is thought to have occurred on a normal fault in a shallow location near a spot where three ocean trenches meet (the Japan Trench, the Izu-Ogasawara Trench, and the Sagami Trough) and was accompanied by a tsunami. Few earthquakes of this type are known, and the mechanism for the old earthquakes classified as interplate earthquakes in the preceding paragraph 1) is not well known. Therefore, it is possible that some of them could be classified as earthquakes occurring within a subducting plate.

(3)Inland earthquakes

There are three types of earthquakes that occur on land in the Kanto region: first, shallow earthquakes (depths of 0-20 km) that occur on active faults; second, somewhat deeper earthquakes (depths of 20-50 km) that occur on the surface of or inside the subducting Philippine Sea Plate; third, deep earthquakes (depths of 50-100 km) that occur on the surface of or inside the subducting Pacific Plate. Thus, a characteristic of the Kanto region is that it has several seismically active areas under the landmass (Fig.5-9). Also, the area from western Kanagawa Prefecture to eastern Yamanashi Prefecture corresponds to an extension of the Sagami Trough on land that is the boundary between the Philippine Sea Plate and the plate on land. Earthquakes here are generated by complicated forces that accompany the collision with the Izu Peninsula.

1) Shallow inland earthquakes (Depths of 20 km or less)

The topography of the Kanto region is characterized by the broad Kanto Plain surrounded by mountainous and hilly areas, including the Kanto Mountains (Fig.5-7).

The primary active faults in the Kanto region are located primarily in the south. In particular, many highly active faults (A-B classes) are located in the southern part of the Boso Peninsula, the southern tip of the Miura Peninsula, and western Kanagawa Prefecture. These active faults are thought to be closely related to the Philippine Sea Plate that is subducting from the Sagami Trough. It is possible that their activity occurs together with the interplate earthquakes along the Sagami Trough. The most active fault is the Kannawa/Kouzu-Matsuda fault zone that lies from the northwest to the southeast in western Kanagawa Prefecture. It has an A class activity. This fault zone extends as a continuation of the submarine active fault in the Sagami Bay. The active fault zone in the southern Boso Peninsula and the southern tip of the Miura Peninsula also probably extend to sea.

Several active faults lying from northwest to southeast whose activity is classified as B and C classes are known to exist at the border of the Kanto Mountains and the Kanto Plain. These include the northwestern margin of the Kanto-Plain (Kanto-heiya-hokuseien) fault zone and the Tachikawa fault zone. Some areas in the Kanto Plain have been covered with thick sediment from a relatively recent period known as the Quaternary Period (starting about 2 million years ago). Underneath this sediment is an older stratum of bedrock that continues from the surrounding mountainous area. The surface of this bedrock forms a large valley whose depth reaches 4,000 m in places. This subterranean valley extends in a northwest-southeast direction to pass through the Kanto Mountains and the Ashio Mountains (Asio Santi). It is assumed that several active faults classified as B and C class activity exist as an extension of this valley, stretching in a northwest to southeast direction from the central Kanto Plain to the coast of Tokyo Bay. These faults include the Arakawa fault and the northern margin of the Tokyo Bay (Tokyo Wan-hokuen) fault . These active faults are covered by sediment from a relatively recent period, and their shape will be better understood through surveys of the underground structure. It is possible that undiscovered active faults lie under the Kanto Plain. From the extent of topographical deformation in the surface, however, it is unlikely that any of these faults would have an activity of an A class. While there are few active faults in the northern Kanto Plain, the Sekiya fault with an A class activity is in northern Tochigi Prefecture.

Considering the direction and type of activity of the active faults in the Kanto region, the direction of the force exerted on these active faults differs depending on the location. This is believed to result from the complex forces coming from different directions under the Kanto region due to the influence of the subducting Philippine Sea Plate and the Pacific Plate.

Several destructive earthquakes are known to have occurred at shallow locations on land. Since the Meiji period (1868), these have included the 1931 West Saitama Earthquake (M 6.9) and the 1949 Imaichi earthquakes (M 6.2 and M 6.4). Previously there have been the 818 earthquake in Kanto Provinces (larger than M 7.5), the 878 Sagami-Musashi Earthquake (M 7.4), and the 1683 earthquake near Nikko (M 7.0). The possibility exists that the 878 Sagami-Musashi earthquake took place on the Isehara fault, and the 1683 earthquake near Nikko on the Sekiya fault. All of these earthquakes, however, do not correspond to known active faults. Further, earthquakes of M 6 or so that cause local damage sometimes occur even outside the active fault zone. Also, the intervals of activity for most active faults are 1,000 years or more. This does not indicate, however, that no earthquakes can occur here even if none are known at present.

Regarding the 1855 Ansei Edo Earthquake (M 6.9), there are two ideas: first, it has been caused by active fault movement close to the surface; second, it has occurred on the upper surface of the Philippine Sea Plate.

Frequent seismic activity regularly occurs in the Nikko and Ashio areas of Tochigi Prefecture, as well as the area surrounding the Izu Islands. This seismic activity sometimes causes damage locally.

2) Intermediate-depth inland earthquakes (Depths of 20-50 km)

One of the earthquakes that occurred on the surface of the subducting Philippine Sea Plate was the 1968 earthquake in central Saitama Prefecture (M 6.1, roughly 50 km deep). Brisk seismic activity at a depth of roughly 50 km is also known to occur regularly in the western part of the two seismically active areas in southwest Ibaraki Prefecture (part a of Fig.5-4 and Fig.5-5). Earthquakes also occur in the interior of the Philippine Sea Plate. Examples include the 1987 earthquake near Kujukuri Beach (Kujukuri-hama) on the Boso Peninsula (M 6.7; depth of roughly 50 km: This is also referred to as the Earthquake of the East Coast of Chiba Prefecture.)

Regarding the 1855 Ansei Edo Earthquake (M 6.9), there are two ideas: first, it has been caused by active fault movement close to the surface; second, it has occurred on the upper surface of the Philippine Sea Plate.

3) Deep inland earthquakes (Depths of 50-100 km)

Brisk seismic activity at a depth of roughly 70 km is known to occur regularly as earthquakes on the surface of the subducting Pacific Plate in the eastern part of the two seismically active areas in southwest Ibaraki Prefecture (Fig.5-4 and Fig.5-5). Brisk seismic activity from the surface to the interior of the Pacific Plate is also known to occur at a depth of roughly 80 km in northwest Chiba (Tiba) Prefecture (Fig.5-4 and Fig.5-5). Recent earthquakes known to have occurred within the Pacific Plate are the 1985 earthquake in southern Ibaraki Prefecture (M 6.1; depth of roughly 78 km), the 1988 earthquake in the eastern part of the Tokyo Metropolitan District (M 6.0; depth roughly 96 km), and the 1992 earthquake in the southern part of Tokyo Bay (near the Uraga Channel; M 5.9; depth roughly 92 km). The depth of the 1894 earthquake known as the Meiji Tokyo Earthquake (M 7.0) has not been determined, but it is thought to have occurred within the subducting Pacific Plate under the Kanto region.

4) Earthquakes in western Kanagawa Prefecture

There has been a series of destructive earthquakes with M 7 or so in the area from western Kanagawa Prefecture to eastern Yamanashi Prefecture. These include the 1633 Sagami-Suruga-Izu Earthquake (M7 0), the 1782 Sagami-Musashi-Kai Earthquake (M 7), and the 1853 earthquake near Odawara (M6.7). The plate structure in this area is complex, and it is not possible to determine in a general way if these earthquakes occurred between plates or within plates. Also, the Kannawa/Kouzu-Matsuda fault zone with an A class activity is located at the surface here. Its relationship to the boundary of the subterranean plate has already been pointed out.

A look at recent seismic activity shows that brisk activity occurs regularly at a depth of 10-30 km from the Tanzawa Mountains (Tanzawa Santi) to eastern Yamanashi Prefecture. There are frequent earthquakes in the M 5-6 range that cause some damage. It is also possible for a tsunami to accompany these earthquakes when the source region extends into the sea.

6 Characteristics of seismic activity in the Chubu region

The destructive earthquakes in the Chubu region include great earthquakes of M 8 or so that have occurred repeatedly in the past in the Pacific Ocean and large earthquakes of M 7 to 8 that have occurred on land. The great earthquakes that have occurred in the Pacific Ocean have been characterized by strong seismic ground motion over a broad area and a large tsunami, and have caused significant damage. Since the Meiji period (1868), these have included the 1944 Tonankai Earthquake (M 7.9) and the 1946 Nankai Earthquake (M 8.0). Those that have occurred in shallow locations on land include the 1891 Nobi Earthquake (M 8.0), which caused more than 7,000 fatalities, and the 1948 Fukui Earthquake (M 7.1) that occurred directly underneath an urban area. On the Sea of Japan (Japan Sea) side of the region, the 1964 Niigata Earthquake (M 7.5) caused damage both from seismic ground motion and the accompanying tsunami. Damage is also known to have been caused by earthquakes in surrounding areas, such as the Great Kanto Earthquake (M 7 9) that occurred along the Sagami Trough in 1923, and by tsunami that originate overseas, such as the 1960 Chile Earthquake Tsunami. Fig.6-1 and Fig.6-2 show the primary destructive earthquakes known to have occurred in the Chubu region. (Refer to Fig.5-3 for earthquakes in the Izu area.)

Generally, there are three types of earthquakes in the Chubu region. The first type occurs near the plate boundary that is subducting toward land from the Suruga Trough and the Nankai Trough in the Pacific Ocean. The second type occurs at relatively shallow locations on land, at depths less than about 20 km. The third type occurs in the eastern margin of the Sea of Japan, near the area off Niigata Prefecture. The area from the Chubu region to the Kinki region relatively active for large earthquakes occurring in shallow locations on land in the Japanese archipelago.

The Philippine Sea Plate is approaching the Chubu region from the southeast at a speed of about 4 - 5 cm per year. The Philippine Sea Plate is subducting underneath the Chubu region from the Suruga Trough and Nankai Trough. Seismic activity from this subduction is observed down to a depth of few tens of kilometers (Fig.6-3). Also, the Izu Peninsula (Izu Hanto) on the Philippine Sea Plate is colliding with the Japanese archipelago at the eastern side of the Suruga Trough. The Pacific Plate, which is subducting at the Japan Trench east off the Kanto region, extends to a location deep under the Chubu region. The depth of the upper surface of this plate ranges from 150-400 km (Fig.6-4). One theory holds that there is a plate boundary that links the Suruga Trough and the Sagami Trough from the eastern margin of the Sea of Japan (near a location in the sea off the coast of Niigata Prefecture in the Chubu region) and passes through a location close to the Itoigawa-Shizuoka tectonic line(Itoigawa Shizuoka-Kozosen), a large boundary in terms of geological structure (details to follow).

The Chubu region has some extremely steep mountains, including the Hida, Kiso, and Akaishi Mountains. These mountains lie on the western side of the Itoigawa-Shizuoka tectonic line. There are many active faults in this area, at the boundary between mountains and basins, or mountains and hilly areas or plains (Fig.6-5). The Chubu region also has some of the largest crustal movement in the Japanese archipelago, and there is a pronounced contraction that generally ranges from an east-west to a northwest-southeast direction (Fig.6-6).

Relatively large earthquakes occur at shallow locations on these active faults in the Chubu region. The Nobi Earthquake (M 8.0), for example, occurred in the Nobi fault zone, which includes the Neodani fault. This was an extremely large earthquake of the type that occurs at shallow locations on land. Many M 7 or so earthquakes are known from historical documents. There are also cases, however, in which large destructive earthquakes have occurred in areas where there is no known active fault.

There are active earthquake swarms in the eastern Izu Peninsula and surrounding area, as well as in western Nagano Prefecture. Active swarms were also observed in the past in Matsushiro (Matusiro), Nagano City.

No destructive earthquakes have occurred along the Nankai Trough in the Pacific Ocean since the 1946 Nankai Earthquake (M 8.0). On land, the 1984 Western Nagano Prefecture Earthquake (Nagano-ken Seibu Earthquake) (M 6.8) near Mt. Ontake caused substantial damage. Frequent seismic activity is observed in this area. On the Izu Peninsula and surrounding area, there have been M 6-7 earthquakes as well as repeating swarm activity since the latter half of the 1970s. More recently, there was frequent swarm activities off the east coast of the Izu Peninsula (Ito City) from May to June 1993 and September to October 1995, as well as in October 1996 and March 1997. An earthquake of M 6.6 occurred in 1993 off the coast of Noto Peninsula (Noto Hanto), which caused injuries and damaged houses. In the eastern margin of the Sea of Japan, the 1983 Central Sea of Japan Earthquake (Nihonkai Chubu Earthquake) (M 7.7) and the 1993 Earthquake off the Southwest Coast of Hokkaido (Hokkaido Nansei-Oki Earthquake) (M 7.8) generated a tsunami that caused damage on the Sea of Japan coast.

(1)Earthquakes near the plate boundary off the coast of Pacific Ocean

The Philippine Sea Plate is subducting toward the Chubu region from the Suruga Trough and the Nankai Trough, which lie in the Pacific Ocean off Suruga Bay (Suruga Wan) and the Chubu region (Fig.6-3). The Pacific Plate is subducting toward the Chubu region from the Japan Trench off the east coast of the Kanto region (Fig.6-4).

The earthquakes that occur near the plate boundaries off the coast of Pacific Ocean are classified as either interplate earthquakes caused by the subduction of the Philippine Sea Plate, or earthquakes that occur within the Philippine Sea Plate.

1) Interplate earthquakes caused by the subduction of the Philippine Sea Plate

Great earthquakes caused by the subduction of the Philippine Sea Plate have occurred along the Suruga Trough and the Nankai Trough.

This type of earthquake has caused damage from seismic ground motion over wide areas, including the Chubu region, and has caused the tsunami disasters on the Pacific Ocean coast from the Boso and Izu Peninsulas to Kyushu. Extensive damage has been caused in the Chubu region from these earthquakes, whose source region lie off the coast of the Ku Peninsula (Ku Hanto) and the Tokai region. Great earthquakes can occur whose source region ranges over a wide area from the Suruga Bay to western Shikoku, as with the 1707 Hoei Earthquake (M 8.4). This type of earthquakes cause severe damage over a wide area in the Chubu region. Such earthquakes have recurred in the past from the Suruga Trough to the Nankai Trough, and records of many those earthquakes exist in historical accounts. See 8-1 (1) for a detailed explanation of recurrence of this type of earthquake.

The forthcoming Tokai Earthquake, which has caused much concern, is an earthquake of this type. The hypothesized source region of this earthquake would be limited to the area along the western side of the Suruga Trough. In the Tokai region, crustal movement such as the subsidence of the west coast of Suruga Bay, has been confirmed to occur with the subduction of the Philippine Sea Plate (Fig.6-7).

2) Earthquakes within the subducting Philippine Sea Plate

Earthquakes occur within the Pacific Plate and the Philippine Sea Plate that are subducting under the Chubu region. These occur in deep locations, and are not thought to cause significant damage. The 1952 Yoshino Earthquake (M 6.8) occurred within the subducting Philippine Sea Plate at a depth of about 60 km in central Nara Prefecture. In the Chubu region, it caused slight damage in Aichi, Gifu (Gihu), and Ishikawa Prefectures. In addition, the March 1997 earthquake in eastern Aichi Prefecture (M 5.8) also occurred within the subducting Philippine Sea Plate, and a seismic intensity of 5 upper in JMA scale was observed in Toyohashi.

(2)Shallow inland earthquakes (Depths of 20 km or less)

Characteristics of the topography of the Chubu region are the plains on the one hand, including the Niigata Plain (Niigata Heiya) and Nobi Plain (Nobi Heiya), and the precipitous mountains on the other, including the Hida, Kiso, and Akaishi Mountains. Close observation of this topography shows that it can change very abruptly. The boundary is the Itoigawa-Shizuoka tectonic line that runs roughly north and south through Nagano Prefecture from Itoigawa in Niigata Prefecture to Fuji in Shizuoka Prefecture. In other words, the steep mountains rapidly descend into plateaus, and then become basins. The geological features change greatly on either side of this tectonic line. West of this line is a series of old geological formations, but east of line the new formations and volcanoes are particularly noticeable.

Next, we will examine the distribution of active faults (Fig.6-5). The Itoigawa-Shizuoka tectonic line is both a large tectonic boundary, as previously mentioned, and a highly active fault that lies in Nagano and Yamanashi Prefectures. The active fault along the Shinanogawa River is the only large active fault known to exist on the eastern side of this tectonic line in the Chubu region. However, there are many active faults with high activity (A and B classes) on the western side of this tectonic line such as the Atotsugawa fault, the Adera fault zone, the Inadani fault zone, the Nobi fault zone including the Neodani fault and the Yoro-Kuwana-Yokkaichi fault zone. These active faults lie at the boundary between mountainous areas and basins or between mountainous areas and hilly areas or plains. Most of these faults run in either northeast-southwest or northwest-southeast directions. Accumulated fault movements are reflection of compression in an east-west direction in that area. It is known from historical accounts that the 1858 Hietsu Earthquake (M 7.0-7.1) occurred on the Atotsugawa fault, and the 1586 Tensho Earthquake (M 7.8) is thought to have occurred in the area extending from the Shokawa River (Syokawa) fault zone to the Adera fault zone. Most of the active faults in this area are strike-slip faults or strike-slip faults with reverse-fault components. The area surrounding the Izu Peninsula corresponds to the boundary between the Philippine Sea Plate and the land plate. Active faults with an A class activity are known to exist here, including the Fujikawa River-mouth (Fujikawa-kako) fault zone and the Kannawa-Kouzu-Matsuda fault zone.

The Chubu region experiences the greatest crustal movement of any region in the Japanese archipelago. There is distinct compression from northwest-southeast to west-northwest-east-southeast in the Kiso and Akaishi Mountains just west of the Itoigawa-Shizuoka tectonic line. Moving further west to the Hida highlands (Hida Koti) and the Ryohaku Mountains (Ryohaku Santi), the compression is in a nearly east-west direction (Fig.6-6).

The presence of steep mountains and many active faults and the extensive crustal movement are all interrelated, suggesting that a strong compression beneath this region is working in a northwest-southeast to east-west direction. The factors behind this force are thought to be the result of complex interrelated activity between the Philippine Sea Plate, the Pacific Plate, and the inland plate. However, the details of this activity are not well understood.

Other than those in the area surrounding the Izu Peninsula, the major destructive earthquakes occurring in shallow locations on land since the Meiji Period (1868) include the 1891 Nobi Earthquake (M 8.0), the 1945 Mikawa Earthquake (M 6.8), the 1948 Fukui Earthquake (M 7.1), and the 1984 Western Nagano Prefecture Earthquake (M 6.8). The Nobi Earthquake occurred on the Nobi fault zone and the Gifu-Ichinomiya fault zone. During the Mikawa Earthquake, there appeared offset at the surface on the Fukozu fault. Visible fault offset on the earth's surface was not present during the Fukui Earthquake or the Western Nagano Prefecture Earthquake, however. Also, the 1952 Earthquake off the Coast of Daishoji (Daishoji-Oki Earthquake) (M 6.5), the 1963 Earthquake off the Coast of Cape Echizen (Echizen-misaki-Oki Earthquake) (M 6.9), and the 1993 Earthquake off the Coast of Noto Peninsula (Noto-hanto-Oki Earthquake) (M 6.6) occurred in the area from the Noto Peninsula (Noto Hanto) to the west in the Sea of Japan. They are thought to be of a type identical to those occurring in shallow locations on land. There are active faults with a B class activity in the Noto Peninsula and other areas close to the coast in the Hokuriku region. These include the Ouchigata fault zone, the Tonami Plain (Tonami-heiya) fault zone, and the Morimoto-Togashi fault zone. Many of these faults are reverse faults.

The Itoigawa-Shizuoka tectonic line is a highly active fault from the vicinity of Hakuba in Nagano Prefecture to near the western margin of the Kofu Basin (Kohu Bonti), it also referred to as the Itoigawa-Shizuoka tectonic line fault zone. A comprehensive evaluation conducted by the Headquarters for Earthquake Research Promotion based on the results of active fault survey shows it is quite likely that an M 8 earthquake with a source region from Hakuba to the vicinity of Kobuchizawa within this fault zone occurred about 1,200 years ago. Based on the history of fault activity, it also is thought likely that an M 8 level (M 7 1/2-8 1/2) earthquake could occur at any time in the next several hundred years in this fault zone, an area that includes the Gofukuji fault near Matsumoto. The Median Tectonic Line (Chuo-kozosen) is an important tectonic boundary from a viewpoint of geological structure [for details, refer to 8-1 (2)]. One section of this tectonic line in the Chubu region is not a highly active fault.

East of the Itoigawa-Shizuoka tectonic line, the Shinano-gawa fault zone and others stretch from north of Nagano City to the Echigo Plain (Etigo Heiya). The activity for these faults are A or B classes. The 1847 Zenkoji (Zenkoji Temple) Earthquake (M 7.4) occurred in the Shinano-gawa fault zone in Nagano Prefecture, producing fault offset on the earth's surface that extended for about 40 km. On the northern side of the Shinano-gawa fault zone, an active fold zone, in which the stratum gradually curves due to east-west compression, runs north and south. The active fold zone is related to earthquakes that occur in extremely shallow locations here.

Earthquakes in the M 6 to M 7 range, swarm activity, and submarine volcanic eruptions have occurred since the 1970s in the area surrounding Izu Peninsula. There are relatively new volcanoes on this peninsula, and the stratum has not undergone significant deformation. Therefore, the geological characteristics differ substantially from those of surrounding areas, including the Tanzawa Mountains (Tanzawa Santi) and the Fujikawa River basin. Izu Peninsula is considered part of the Philippine Sea Plate, but the earthquakes that occur here are the same type as those that occur in shallow locations on land. Destructive earthquakes have occurred here fairly recently. Examples are the 1974 Earthquake off the Coast of Izu Peninsula (Izu-hanto-Oki Earthquake) (M 6.9) and the 1978 Earthquake Near the Coast of Izu Oshima (Izu Oshima Kinkai Earthquake) (M 7.0). A survey of crustal movements in the area around Ito in the northeastern Izu Peninsula indicates extension of the crustal movement in a northeast-southwest direction believed to accompany volcanic activity. There has been an upheaval of the land here by about 50 cm over the past 20 years. In July 1989, severe swarm activity occurred with submarine eruptions 3 km off the coast of Ito City. After that brisk swarm activity here has been recurring. Previously, the 1930 North Izu Earthquake (Kita-Izu Earthquake) (M 7.3) occurred in the Kitaizu (North Izu) fault zone on the northern Izu Peninsula. Violent swarm activity (Maximum M 5.9) occurred here from February to May 1930, followed by the 1930 North Izu Earthquake in November.

The intervals of seismic activity for most active faults are 1,000 years or more; however, this does not indicate that no earthquake can occur even if no earthquake has occurred here since the beginning of history.

Swarm activity frequently occurs in the vicinity of volcanoes. Some activity of this type includes that in the open sea east of the Izu Peninsula, as well as near the Hakone volcano, the southern base of Mt. Ontake, and the southwestern base of Mt. Norikura. There were large eruptions of water during the latter period of swarm activity in Matsushiro in Nagano Prefecture that occurred from 1965 to 1968.

(3)Earthquakes in the eastern margin of the Sea of Japan

A series of large earthquakes has occurred recently in the eastern margin of the Sea of Japan, north of Niigata Prefecture. These earthquakes have caused the damage by seismic ground motion and tsunami. The tsunami reaches the coast in an extremely short time since the source region of the earthquakes is close to land. [For details refer to 4-1(3)] One example of this type of earthquake in the Chubu region was the 1964 Niigata Earthquake (M 7.5).

A theory has recently been advanced that the eastern margin of the Sea of Japan is a plate boundary. [Refer to 2-4 (3) and 4-1 (3)] According to this theory, the extension of this plate boundary is thought to emerge somewhere in the area from the central to southern Niigata Prefecture to the vicinity of Toyama Bay (Toyama Wan) and then turns south. The plate boundary then crosses Honshu in a roughly north-south direction along the Itoigawa-Shizuoka tectonic line, and links the Suruga Trough and the Sagami Trough. Further, there is another idea that plate boundaries of this type have a width of a certain dimension.

There are no specific records of large earthquakes occurring off the coast of Itoigawa to the vicinity of Toyama Bay. However, one theory holds that this phenomenon can be explained even if the eastern margin of the Sea of Japan is not a plate boundary. However a firm conclusion has yet to be reached.

7 Characteristics of seismic activity in the Kinki region

One recent destructive earthquake in the Kinki region was the well-known 1995 Southern Hyogo Prefecture Earthquake (Hyogo-ken Nanbu Earthquake) (M 7.2) that caused more than 6,000 fatalities. Other destructive earthquakes have occurred here since the Meiji period (1868) both on land and sea, including the 1925 North Tajima Earthquake (Kita -Tajima Earthquake) (M 6.8), the 1927 North Tango Earthquake (Kita-Tango Earthquake) (M 7.3), the 1944 Tonankai Earthquake (M 7.9), and the 1946 Nankai Earthquake (M 8.0). The destruction by these earthquakes was caused by seismic ground motion, a tsunami, and other factors. Thanks to historical accounts stretching back almost 1,500 years, earthquakes in the Kinki region have been documented over a longer period than any region in Japan. A long-term perspective shows that many destructive earthquakes have occurred in this region. Historical accounts record many instances of destruction, starting with the Yamato-Kawachi Earthquake in the year 416. However the location of the hypocenter is not well understood for most of these old earthquakes. It is also known that earthquakes in surrounding areas have caused damage in the Kinki region with one example being the 1891 Nobi Earthquake (M 8.0). Further, it is known that damage here has been caused by earthquakes occurring in the eastern margin of the Sea of Japan (Japan Sea), such as the 1983 Central Sea of Japan Earthquake (Nihonkai Chubu Earthquake) (M 7.7). Also, tsunami generated by earthquakes in foreign countries are known to have caused damage, such as the 1960 Chile Earthquake Tsunami. Fig.7-1 and Fig.7-2 show the primary destructive earthquakes known to have occurred in the Kinki region. Fig.7-1 shows that several destructive earthquakes are overlapped in the northeastern region of the Kyoto Basin (Kyoto Bonti). These are old earthquakes, and the reason all of them were described as occurring in that location is that damage was recorded only in Kyoto.

Seismic activity in the Kinki region can be roughly divided into two types: first, earthquakes that occur in shallow locations on land at 20 km or less; and second, those that occur near a plate boundary subducting toward land from the Nankai Trough in the Pacific Ocean. Also, earthquakes here sometimes occur in somewhat deeper locations on land. These are thought to be within the subducted Philippine Sea Plate.

The Philippine Sea Plate is approaching the Kinki region from the southeast at a speed of about 5 cm a year. This plate is subducting from the Nankai Trough in the Pacific Ocean toward the Kinki region. Seismic activity that accompanies the subduction of this plate is observed to depths of about 70-80 km in the central part of the region (Fig.7-3 and Fig.7-4). Historical data indicates that interplate earthquakes of M 8 or so recur along the Nankai Trough in roughly 100-150 year intervals. Historical accounts further indicate that seismic activity on land increases for several decades before and after great earthquakes along the Nankai Trough. Seismic activity in the Kinki region is thought to be closely related to the subduction of the Philippine Sea Plate.

A look at the topography of the Kinki region shows the Median Tectonic Line (Chuo-kozosen)running east to west across the Ku Peninsula (Ku Hanto). The topographical characteristics of the region differ to the north and south of this line. The area to the north of the Median Tectonic Line has large plains and basins ringed by mountains. Most of the active faults of the Kinki region are in this area, and many run along the boundary between the plains and basins on one side and the mountainous area on the other. There are many active faults known to exist in this area, which has one of the highest concentrations of active faults of any area in Japan. In contrast, vast mountainous areas characterize the area to the south of the Median Tectonic Line, where there are almost no active faults. Destructive earthquakes in shallow locations on land have occurred in areas with known active faults and areas with no known active faults. The 1995 Southern Hyogo Prefecture Earthquake (M 7.2) occurred on a known active fault, while the 1925 North Tajima Earthquake (M 6.8) occurred in an area with no known active faults. Fig.7-5 gives a bird's eye view of the topography of the Kinki region and the distribution of active faults from the southeast and the northwest.

A look at the crustal deformation in the Kinki region shows that the earth's surface is being compressed in a roughly east-west direction in the area north of the Median Tectonic Line. This deformation is harmonized with the distribution of active faults and the direction of the activity. In the area south of the Median Tectonic Line, extension in a northwest-southeast direction is occurring due to the 1944 Tonankai Earthquake and the 1946 Nankai Earthquake (Fig.7-6A). Ordinarily, however, this area experiences compression (Fig.7-6B). [Refer to 7-1 (1) 1)]

A look at recent seismic activity in the Kinki region and surrounding areas shows that destructive earthquakes have not occurred in the Pacific Ocean since the 1944 Tonankai Earthquake (M 7.9) and the 1946 Nankai Earthquake (M 8.0). The 1995 Southern Hyogo Prefecture Earthquake (M 7.2) occurred in shallow land and caused devastation concentrated in the Kobe, Osaka, and Awaji areas. Further, damage was caused by a tsunami on the coast of Wakasa Bay (Wakasa Wan) accompanying the earthquakes in the eastern margin of the Sea of Japan, including the 1983 Central Sea of Japan Earthquake (M 7.7), and the 1993 Earthquake off the Southwest Coast of Hokkaido (Hokkaido Nanset-Oki Earthquake) (M 7.8).

(1)Earthquakes near the plate boundary off the coast of Pacific Ocean

The Philippine Sea Plate is subducting from the Nankai Trough toward the Kinki region (Fig.7-3).

There are two types of earthquakes that occur near the plate boundary off the coast of Pacific Ocean. First are the interplate earthquakes caused by the slipping movement at the boundary of the subducting Philippine Sea Plate and the land plate. The other type covers those that occur within the subducting Philippine Sea Plate.

There are also earthquakes that occur at deeper locations of 200-400 km and which are related to the subducting Pacific Plate from the Japan Trench underneath the Japanese archipelago. These are considered unlikely to cause any significant damage in the Kinki region.

1) Interplate earthquakes caused by the subducting Philippine Sea Plate

Great earthquakes at the M 8 level are known to have recurred along the Nankai Trough from historical accounts. The source region for many of these earthquakes covers a wide area from the vicinity of the Nankai Trough in the Pacific Ocean to areas that incorporate parts of land. Therefore, in many cases, there is both damage caused by seismic ground motion over a wide area and damage by a tsunami along the Pacific Ocean coast. This tsunami damage has not been limited to the coastal areas of Mie or Wakayama Prefectures, and has even extended to the interior of Osaka Bay (Osaka Wan).

Historical accounts indicate that great earthquakes have occurred along the Nankai Trough from an area off the coast of Tokai to an area off the coast of Shikoku in roughly 100-150 year intervals.

The area in which these great earthquakes occur is somewhat defined. Those earthquakes whose source region lies only in the open sea from Shikoku to the Kii Peninsula are called "Nankai Earthquakes". Earthquakes whose source region lies further east are called "Tokai Earthquakes". The forthcoming Tokai Earthquakes, the occurrence of which cause great concern, are those with a source region along the Suruga Trough. Compared to the Tokai Earthquakes of the past, this source region is much smaller.

Great earthquakes along the Nankai Trough have occurred either simultaneously or in a series in adjoining source regions. Many of those that have continued in a series have started off the coast of Tokai area and later moved west to off the coast of Nankai area. For example, these great earthquakes can occur over a period of several months or years, such as the 1944 Tonankai Earthquake (M 7.9) followed two years later by the 1946 Nankai Earthquake (M 8.0). In other cases, this series can occur over a very short time, such as the Ansei Tokai Earthquake (M 8.4) of December 23, 1854, followed 32 hours later on December 24 by the Ansei Nankai Earthquake (M 8.4). In addition, two earthquakes have occurred almost simultaneously off the coast of Tokai and Nankai. Examples are the 1605 Keicho Earthquake (M 7.9) and the 1707 Hoei Earthquake (M 8.4), which are thought to have occurred over the entire Tokai and Nankai sea areas.

Compared to earthquakes in other regions of Japan, these earthquakes occur at well-understood intervals. The seismic ground motion and size of the tsunami differ greatly with each occurrence, however. For example, the 1605 Keicho Earthquake generated a tsunami that struck the Pacific Ocean coast from the Kanto region to Kyushu. Yet, there was almost no recorded damage from seismic ground motion. Therefore, it seems that this was a "tsunami earthquake" ("slow earthquake" or "low-frequency earthquake") whose fault slipped more slowly than that of a normal earthquake.

A look at the crustal movement in the Kinki region shows that there was northwest-southeast extension in the southern Kii Peninsula during the period in which the 1946 Nankai Earthquake occurred (Fig.7-6A). It is also known that vertical movement, including uplifts of 50 cm, accompanied this earthquake in Cape Shionomisaki (Stono Misaki) and other locations. These phenomena suggest that this earthquake caused substantial uplift on the Pacific Ocean side (southeast side) of the land plate on which the Kii Peninsula is located. There is flat terraced topography (coastal terraces) on the coast at southern Wakayama Prefecture, which was formed by upheavals caused by great earthquakes occurring along the Nankai Trough for more than 100,000 years. About 125,000 years ago, the coastline is known to have been near Kushimoto, but this site has now been lifted to a height of about 60 m above sea level.

For more details on great earthquakes occurring along the Nankai Trough, refer to 8-1 (1).

2) Earthquakes within the subducting Philippine Sea Plate

The Philippine Sea Plate is subducting under the Kinki region from the Nankai Trough. No destructive earthquakes are known to have occurred in shallow locations within the plate recently subducted near the Nankai Trough. Somewhat larger earthquakes occur at depths deeper than 30 km on land. Destructive earthquakes of the past include the 1952 Yoshino Earthquake (M 6 8, a depth of 60 km), which produced damage centering on Nara Prefecture. The hypocenter for this type of earthquake is somewhat deep, so the destruction can spread across a wide area. The 1899 earthquake in the southeastern Kii Peninsula (M 7 0, also known as the Kii Yamato Earthquake) may have been of this type.

(2)Shallow inland earthquakes (Depths of 20 km or less)

A look at the topography of the Kinki region shows the Median Tectonic Line running east to west across the central part of the Kii Peninsula. The topographical characteristics of the region differ to the north and south of this line. The area to the north of the Median Tectonic Line has large plains and basins, including the Osaka Plain (Osaka Heiya), the Kyoto Basin, and Lake Biwa (Biwa Ko). This area is ringed by mountainous areas, including the Suzuka Mountains (Suzuka Sanmyaku), and the Hira, Kokko, Ikoma, and Kongo Mountains (Kongo Santi). Most of the active faults of the Kinki region are in this area, and many run along the boundary between the plains and basins on one side and the mountains on the other. The large plains and basins of the Kinki region mentioned above are thought to have developed due to the accumulation of slip on the active faults at the edge of these areas. In contrast, vast mountainous areas and almost no active faults characterize the area to the south of the Median Tectonic Line.

A look at the active faults in the Kinki region shows one active fault zone with Tsuruga Bay (Tsuruga Wan) as the summit extending to Ise Bay (Ise Wan), and another with Tsuruga Bay as the summit extending to the Awaji Island (Awaji Sima) after passing through Kyoto and Kobe. The active faults are concentrated in the triangular area bounded by these two fault zones and the Median Tectonic Line. This has one of the highest densities of active faults of any area in Japan. Except for the Kizugawa fault zone, the active faults lying in this triangular area have a predominantly dip-slip component. The fault zones that comprise the boundary of this triangular area and the fault zones outside this area have a predominantly strike-slip component.

Most of the active faults in the Kinki region have a B class activity, and their movements repeated correspond to compression in an east-west direction. Part of the Median Tectonic Line fault zone lies west of the central area of the Kii Peninsula, however, and its activity is an A class. Their movements repeated correspond to compression in a northwest-southeast direction. Observation of the crustal movement shows significant compression in an east-west direction north of the Median Tectonic Line, in keeping with the activity of the active fault (Fig.7-6 A, Fig.7-6 B). South of the Median Tectonic Line, there is usually compression in the northwest-southeast direction as a result of the strong effect of the subducting Philippine Sea Plate (Fig.7-6B). Extension in a northwest-southeast direction is created during great earthquakes along the Nankai Trough, however (Fig.7-6 A). The activity of the Median Tectonic Line is also thought to be strongly affected by the subducting Philippine Sea Plate.

One example of a destructive earthquake in this region is the 1596 earthquake (M 7 1/2, Keicho Fushimi Earthquake), which caused damage primarily in Kyoto, Osaka, and Nara. A recent survey of active faults has shown that this earthquake may have occurred on the Arima-Takatsuki fault zone, which stretches east to west from southern Hyogo Prefecture to the southern Kyoto and Rokko-Awajishima fault zone. Two other examples can be cited. The first is the 1662 earthquake (M 7 1/4 - 7.6) that caused substantial destruction primarily on the west side of Lake Biwa, and is thought to have occurred in the northern section of the West Coast of Lake Biwa (Biwako-seigan) fault zone and the Mikata Hanaore fault zone. The second is the 1854 earthquake (M 7 1/4, the Iga-Ueno Earthquake) that caused extensive damage primarily in Iga, and is thought to have occurred on the Kizugawa fault zone. Major destructive earthquakes that occurred after 1868 (the start of the Meiji period) include the 1925 North Tajima Earthquake (M 6.8) in northern Hyogo Prefecture, the 1927 North Tango Earthquake (M 7.3) that occurred on the Tango Peninsula (Tango Hanto) in Kyoto, and the 1995 Southern Hyogo Prefecture Earthquake (M 7.2). Research into these earthquakes indicates that the North Tango Earthquake and the Southern Hyogo Prefecture Earthquake occurred on previously known faults. [For details, refer to 7-2 (2), (3)] It is not known, however, on which fault the North Tajima Earthquake occurred, though it caused slip at the earth's surface. Therefore, it is possible for earthquakes to occur in areas where there are no known active faults. In addition, shallow earthquakes M 6 or so can cause damage locally, and are not necessarily limited to active fault zones. Since the interval of activity for most active faults is 1,000 years or longer, this does not indicate that no earthquakes can occur where there are no historical records.

There is stationary seismic activity in Wakayama City. Most of these are earthquakes of M 5 or less, but 35 of them can be felt here in an average every year. This area is one of the highest active area of felt earthquakes in Japan. [Refer to 7-3(7)]

8 Characteristics of seismic activity in the Chugoku-Shikoku region

The destructive earthquakes in the Chugoku-Shikoku region include the great M 8 level earthquakes that have recurred in the Pacific Ocean, and the large M 7 level earthquakes that have occurred on land. Of these, the great earthquakes that occur in the Pacific Ocean cause strong seismic ground motion over a wide area and large tsunami, which cause extensive damage. Since the Meiji period beginning in 1868, there has been the 1946 Nankai Earthquake (M 8.0) that occurred primarily in the Shikoku area and caused more than 1,000 fatalities. Destructive earthquakes that have occurred in shallow locations on land include the 1872 Hamada Earthquake (M 7.1) and the 1943 Tottori Earthquake (M 7.2). The Tottori Earthquake was a large earthquake that occurred directly beneath an urban area and caused extensive damage. Destructive earthquakes of M 7 or so have also occurred in the area near the Akinada Sea (Akinada) and the Iyonada Sea (Iyonada). Damage is also known to be caused in this region by earthquakes in surrounding areas, such as the Hyuganada Sea , by tsunami generated by earthquakes occurring in the eastern margin of the Sea of Japan (Japan Sea), and by tsunami generated by earthquakes occurring overseas, such as the 1960 Chile Earthquake Tsunami. Fig.8-1 and Fig.8-2 show the known primary destructive earthquakes in the Chugoku-Shikoku region.

Seismic activity in the Chugoku-Shikoku region can be roughly divided into two types. First are earthquakes that occur near the plate boundary subducting toward land from the Nankai Trough. Second are those occurring in shallow locations on land at depths of 20 km or less. Earthquakes also occur in somewhat deeper locations, such as the Akinada Sea and Iyonada Sea earthquakes from the western part of the Seto Inland Sea to the area near the Bungo Channel.

The Philippine Sea Plate is approaching the Chugoku-Shikoku region from the southeast at a speed of about 5 cm a year. This plate is subducting from the Nankai Trough in the Pacific Ocean toward the Chugoku-Shikoku region. Seismic activity accompanied the subduction of this plate occurs to depths of about 40 km on the north coast of central Shikoku (Fig.8-3A), but it is observed to occur in deeper locations to the west on the southern coast of the western Chugoku area (Fig.8-3B). Earthquakes in the somewhat deeper locations in the western part of the Seto Inland Sea are believed to occur because the subduction of the Philippine Sea Plate has reached this area.

One of the most prominent topological features of the Chugoku region is the Chugoku mountainous area stretching from east to west. These are generally gently sloping mountains. There are few active faults in this region, and records indicate few large earthquakes have occurred in shallow land areas here. This region is also characterized by slight crustal movement compared with the rest of the Japanese archipelago (Fig.8-5). However, two large earthquakes have occurred here since the Meiji period (beginning in 1868): the Hamada Earthquake and the Tottori Earthquake. There are some mountainous areas on Shikoku with extremely steep slopes, such as Mt. Ishizuchi and Mt. Tsurugi. At the northern edge of these mountains, the Median Tectonic Line(Chuo-kozosen), which is a major boundary in terms of geological structure, runs roughly east to west. These mountainous areas directly adjoin plains, such as the Nuhama Plain (Nihama Heiya), with the Median Tectonic Line as the boundary. Also, narrow sections of plains (the Tokushima Plain(Tokusima Heiya)) generally enter the mountainous areas along this tectonic line. Thus, in the Shikoku region the Median Tectonic Line forms very pronounced topographical features, and is also an active fault with an extremely high level of activity. No other active faults of high activity are known to exist in Shikoku in addition to this one. Fig.8-4 provides a bird's eye view from the southeast and the northwest of the topography of the Chugoku-Shikoku region and the distribution of active faults.

A look at recent seismic activity in the Chugoku-Shikoku region and surrounding area shows that no destructive earthquakes have occurred along the Nankai Trough in the Pacific Ocean since the 1946 Nankai Earthquake. Several M 5 or 6 earthquakes have occurred at shallow locations on land in the Chugoku region, and resulted in local damage. Examples include the M 5 to 6 earthquakes that occurred in central Shimane Prefecture in 1977 and 1978 near Mt. Sanbe, the M 5 to 6 earthquakes that occurred near the border of Tottori and Shimane Prefectures in 1989 and 1991, the 1987 earthquake in central Yamaguchi Prefecture (M 5.2), the 1991 earthquake at the Suonada Sea (Suonada) (M 6 0), and the 1997 earthquake near the border of Yamaguchi and Shimane Prefectures (M 6.1). Since the 1955 earthquake in southern Tokushima Prefecture (M 6.4), no destructive earthquakes have occurred in shallow locations in the Shikoku region. In the areas surrounding Chugoku and Shikoku regions, there was the 1995 Southern Hyogo Prefecture Earthquake (Hyogo-ken-Nanbu Earthquake) (M 7.2), causing slight damage in Tokushima and Kagawa Prefectures. Earthquakes occurred in 1968 and 1979 at somewhat deeper locations in the western part of the Seto Inland Sea. These were M 6 level earthquakes, causing slight damage. Also, the 1968 earthquake at the Hyuganada Sea (M 7.5) resulted in damage in Kochi and Ehime Prefectures.

(1)Earthquakes near the plate boundary off the coast of Pacific Ocean

The Philippine Sea Plate is subducting toward the Chugoku-Shikoku region from the Nankai Trough, which lies in the Pacific Ocean off the coast of Shikoku (Fig.8-3).

The earthquakes that occur near the plate boundary off the coast of Shikoku are classified as (a) interplate earthquakes that occur due to the slipping movement at the boundary between the subducting Philippine Sea Plate and the land plate and (b) earthquakes that occur in somewhat deeper areas within the subducting Philippine Sea Plate.

1) Interplate earthquakes caused by the subduction of the Philippine Sea Plate

Great earthquakes of this type have occurred along the Nankai Trough. The seismic ground motion from these earthquakes creates damage over a wide area, and generates tsunami that cause damage on the Pacific Ocean coast from the Kanto region to the Kyushu-Okinawa region. Some of the largest earthquakes in Japan have been of this type. An example is the 1707 Hoei earthquake (M 8.4), with a broad source region from the western part of Suruga Bay to western Shikoku. These earthquakes have recurred in the past, and there are many accounts of them in historical records.

One of these older earthquakes occurred in 684. In addition to damage caused by the seismic ground motion throughout the region, records indicate that many ships were sunk by the tsunami at Tosa, and that fields were submerged due to the crustal deformation. Later earthquakes occurred in 887, 1096 and 1099, 1361, 1498, 1605, 1707, 1854, 1944 and 1946. Therefore, great earthquakes of M 8 or so have recurred at intervals of 100-150 years along the Nankai Trough.

The area in which these great earthquakes occur is somewhat defined. Those earthquakes whose source region extends from off the coast of Shikoku to off the coast of the Kii Peninsula are called Nankai Earthquakes. Earthquakes whose source region is further east than that of Nankai Earthquakes are called Tokai earthquakes. The forthcoming Tokai Earthquake, which are the cause of great concern has a source region along the Suruga Trough. Compared to the Tokai earthquakes of the past, this source region is much smaller.

The great earthquakes along the Nankai Trough have occurred either simultaneously or in a series in adjoining source regions. Many of those that have continued in a series have started on the east side (Tokai Earthquake) and later moved to the west side (Nankai Earthquake). For example, these great earthquakes can occur over several months or years, such as the 1944 Tonankai Earthquake (M 7.9) followed two years later by the 1946 Nankai Earthquake (M 8.0). In other cases, this series can occur over a very short time, such as the December 23, 1854 Ansei Tokai Earthquake (M 8.4), followed 32 hours later, on December 24, by the Ansei Nankai Earthquake (M 8.4). In addition, two earthquakes have occurred almost simultaneously in the Tokai area and the Nankai area. An example is the 1605 Keicho Earthquake (M 7.9) and the 1707 Hoei Earthquake (M 8.4), which are thought to have occurred over the entire sea area from Tokai to Nankai.

Compared to earthquakes in other regions in Japan, these earthquakes occur at well-understood intervals. The seismic ground motion and size of the tsunami differ considerably with each occurrence, however. For example, the 1605 Keicho Earthquake generated a tsunami that struck the Pacific Ocean coast from the Kanto region to Kyushu, however, there was almost no recorded damage from seismic ground motion. Therefore, it is suggested that this was a "tsunami earthquake" ("slow earthquake" or "low-frequency earthquake") whose fault slipped more slowly than that of a normal earthquake.

A look at the crustal movement in the Shikoku region shows that the area near Cape Muroto extended in a northwest-southeast direction during the period in which the 1946 Nankai Earthquake occurred. In addition, Cape Muroto, which ordinarily subsides, uplifted about 1 meter during the earthquake. These phenomena indicate that the earthquake caused the Shikoku-side crust to greatly ride over the Pacific Ocean side one. This type of crustal movement near Cape Muroto and Cape Ashizuri accompanied by great earthquakes has occurred repeatedly along the Nankai Trough for at least the past 100 thousand years. Near Cape Muroto, in particular, there is flat terraced land (coastal terraces) where upheavals of the shallow seabed have occurred in the past. This was known to have been coastline about 125 thousand years ago, but this site has now been lifted to a height of about 200 m above sea level. In addition, the outskirts of Kochi City at the rear of Cape Muroto on the northwest side subsided about 1 meter at the maximum during the 1946 Nankai Earthquake. Damage was caused by an influx of seawater.

Since the 1946 Nankai Earthquake, compression has been observed throughout Shikoku in a northwest-southeast direction. This indicates that the accumulation of strain has begun, preparing the next Nankai earthquake, caused by the subduction of the Philippine Sea Plate.

2) Earthquakes within the subducting Philippine Sea Plate

The depth of earthquakes within the subducting Philippine Sea Plate is about 30 km near the Pacific Ocean coast in central Shikoku. To the north, for example, near the Median Tectonic Line, this depth extends to about 40 km. The depth is unclear further north. Small earthquakes periodically occur within the subducting Philippine Sea Plate beneath the Shikoku region, but large destructive earthquakes are unknown. One theory, however, holds that the 1789 earthquake in southern Tokushima Prefecture (M 7.0) occurred within the subducted Philippine Sea Plate.

In contrast, the earthquakes that occur periodically from the western part of the Seto Inland Sea to the area near the Bungo Channel appear to be related to the area of occurrence for deep earthquakes that occur below Kyushu (earthquakes within the subducted Philippine Sea Plate below Kyushu). Several earthquakes are known to have caused damage to the surrounding coastline from the western part of the Seto Inland Sea to the area near the Bungo Channel. Historical accounts indicate that destructive earthquakes of the M 7 or so occurred in 1649 (M 7.0), 1686 (M 7-7.4), and 1854 (M 7.3-7.5). An earthquake that occurred after 1868 (the beginning of Meiji era) was the 1905 Geiyo Earthquake (M 7 1/4). These earthquakes are also thought to have occurred in somewhat deeper locations within the subducted plate, though the locations have not been defined. Additionally, the 1968 earthquake at Bungo Channel (M 6.6) and the 1979 earthquake at the western part of the Seto Inland Sea (M 6.1), were events within the subducted plate at somewhat deeper locations.

(2)Shallow inland earthquakes (Depths of 20 km or less)

The Chugoku and Shikoku Mountainous run in a roughly east to west direction in the Chugoku and the Shikoku regions, respectively. The Chugoku Mountains show extremely gentle figures, while the Shikoku Mountains are extremely steep. Other than the Okayama Plain (Okayama Heiya), the plains in the Chugoku region are generally small. Plains such as the Hiroshima Plain (Hirosima Heiya), consisting of deltas formed at the mouth of a large river, are scattered throughout the region. Shikoku also has few plains. Other than the Sanuki Plain, this region has small scattered plains consisting of deltas identical to those of the Chugoku region (Fig.8-4).

The Chugoku region has few active faults, and their activity is a B- class or lower. The primary active faults include the Itsukaichi fault and the Iwakuni fault zone, which run from Hiroshima City to a location near Iwakuni, the Kikukawa fault in northern Shimonoseki, and the Yamasaki fault zone stretching from Hyogo Prefecture to Okayama Prefecture. These active faults run in a northeast-southwest or northwest-southeast direction, and their movement is consistent with compression in an east-west direction. The crustal movement in Chugoku region is smaller than in other regions of the Japanese archipelago. In the central and eastern sections, the surface of the earth tends to be compressed in a roughly east-west direction in continuation from the Chubu and Kinki regions. Compression occurs in this area, but to a lesser extent than in the Chubu and Kinki regions (Fig.8-5). Many linear valleys called "lineaments" run in a northeast-southwest direction in western Hiroshima Prefecture. These are viewed as having appeared through erosion along the faults in an older age. These faults are unlikely to be active.

One large earthquake that has occurred in a shallow location on land in the Chugoku region since the Meiji period (beginning in 1868) is the 1943 Tottori Earthquake (M 7.2). The source region of the 1872 Hamada Earthquake (M 7.1) was partly at sea, but the mechanism for the earthquake occurrence is thought to be identical to those that occur in shallow locations on land. Over the past several decades, large earthquakes have occurred in shallow locations on land along the Sea of Japan coast, from the Hokuriku region through the Kinki region to the Chugoku region. In addition to the Tottori Earthquake, these include the 1948 Fukui Earthquake (M 7.1) and the 1927 North Tango Earthquake (Kita-Tango Earthquake) (M 7.3). These large earthquakes have caused particularly severe damage locally because they occurred in shallow locations on land. The source regions of the Tottori and Fukui earthquakes in particular were very close to urban areas with a thick accumulation of weak strata, causing widespread damage. The earthquake occurring in the year of 868 at Harima-Yamashiro (larger than M 7) is thought to have occurred on the Yamasaki fault zone, and recent M 6 level earthquakes (1984, M 5.6, etc.) are known to have occurred there. Shallow earthquakes sometimes occur on reverse faults in the southwestern Sea of Japan (Japan Sea), such as the 1940 earthquake (M 6 6). Damage caused by tsunami have occurred on the Korean Peninsula, so it is possible they could also occur along the Sea of Japan coast.

One of the characteristics of the Shikoku region is a series of right-lateral active faults (Median Tectonic Line fault zone) along the Median Tectonic Line. There are almost no active faults in the south. The Median Tectonic Line fault zone in the Shikoku region has mostly right-lateral strike-slip faults with an A class activity. The vertical slip harmonizes with the distribution of the mountainous areas. In the southern Sanuki Mountains it rises to the north, rises to the south in the northern Ishizuchi Mountains, rises to the north on the Takanawa Peninsula, and rises to the south from Matsuyama westward. Active faults with a low activity have been found on the Muroto Peninsula and near Cape Ashizuri, and it is considered that they are closely related to the great earthquakes along the Nankai Trough. In the Shikoku region, damage from shallow inland earthquakes is almost unknown, even in historical accounts.

The interval of activity for most active faults is 1,000 years or longer, but this does not indicate that no earthquakes can occur here even if no earthquake occurrence has been reported so far.

9 Characteristics of seismic activity in the Kyushu-Okinawa region

There are various types of destructive earthquakes in the Kyushu region. These include the earthquakes that occur at sea, such as the Hyuganada Sea , and earthquakes that occur at shallow locations on land. Earthquakes with M 7 or so frequently occur in the area near Hyuganada Sea. In addition to damage from seismic ground motion, damage is also caused by accompanying tsunami on the Pacific coast of Kyushu. Great M 8 or so earthquakes also occur in the area near the Nansei Shoto Islands (Nansei Syoto). One example was the 1911 earthquake (M 8.0) near Amami Oshima (Amami Osima). Many destructive M 6 to 7 earthquakes have occurred in shallow locations on land. Since the Meiji period (beginning in 1868) alone, these have included the 1889 earthquake at Kumamoto (M 6.3), the 1914 earthquake at Sakurajima Island (Sakurajima) (M 7.1), the 1922 earthquake on the Shimabara Peninsula (Simabara Hanto) (M 6.9), and the 1968 Ebino Earthquake (M 6.1). Damage is also known to be caused here by earthquakes in surrounding areas, such as the 1946 Nankai Earthquake (M 8.0). Additionally, tsunami generated by earthquakes in foreign countries have caused damage, such as the 1960 Chile Earthquake Tsunami.

The destructive earthquakes in the Okinawa region include those that occur in the open sea off the Pacific coast. The 1771 Yaeyama Earthquake Tsunami (M 7.4) reportedly killed nearly 12,000 people in the Sakishima Islands (Sakisima Syoto). Few records exist of destructive earthquakes occurring before the end of the 19th century on Okinawa Island (Okinawa To) and the Kerama Islands, but damage was caused by the 1911 earthquake near Amami Oshima (M 8.0). Also, damage has been known to occur in the Okinawa region from a tsunami caused by earthquakes overseas, such as the 1960 Chile Earthquake Tsunami. Fig.9-1, Fig.9-2 and Fig.9-3 show the known primary destructive earthquakes in the Kyushu-Okinawa region.

Seismic activity in the Kyushu-Okinawa region is roughly divided into two types. First are earthquakes that occur in the Pacific Ocean near the plate boundary subducting toward land from the Nankai Trough and the Nansei Islands Trench (Nansei Syoto Trench). Second are shallow earthquakes occurring on land at a depth of 20 km or less.

The Philippine Sea Plate is approaching the Kyushu-Okinawa region from the southeast at a rate of about 5 to 7 cm a year. This plate is subducting beneath the Kyushu-Okinawa region from the Nankai Trough and the Nansei Islands Trench. The seismic activity in the Kyushu region that accompanies this subduction occurs at a depth of about 60 km near the coastline from Miyazaki Prefecture to Kagoshima (Kagosima) Prefecture. This activity can be observed at a depth of almost 200 km in the western land areas (Fig.9-4). In the Okinawa region, the seismic activity that accompanies this subduction of the Philippine Sea Plate occurs at depths below 200 km.

The topography of the Kyushu region is characterized by volcanoes that bisect the island almost horizontally from east to west from Beppu Bay (Beppu Wan) to the Shimabara Peninsula. These volcanoes include Mt. Kuju, Mt. Aso, and Mt. Unzen. Many short active faults also lie in an east-west direction. These active faults are normal faults that consistent with extension in a north-south direction there, and move in a direction that causes the surface to subside. This is a unique zone in Japan, where force is usually exerted to cause compression (reverse faults and strike-slip faults). The crustal movement also extends in a north-south direction (Fig.9-7). This zone is called the Beppu-Shimabara rift valley. Shallow earthquakes on land frequently occur in this zone or in the surrounding area. The Okinawa Trough runs parallel to the Nansei Shoto Islands at the sea floor on the northwest side (East China Sea side) of the islands, which correspond to an extension of the Beppu-Shimabara rift valley to the southwest. Seabed surveys show that this zone has many normal faults. Many of the earthquakes that occur in the Okinawa Trough are shallow earthquakes on normal faults, as are those in the Beppu-Shimabara rift valley. There are volcanoes in the southern part of the Kyushu region, including Kirishima and Sakurajima. Seismic activity is also seen in this area. Active faults can be found on the Tanegashima Island, the Yakushima Island and at the southern part of Okinawa Islands, and on the Ishigaki Island (Isigakijima), but no earthquakes are known to occur on these active faults. Fig.9-5 and Fig.9-6 provide bird's eye views of the topography and distribution of the active faults in the Kyushu-Okinawa region from the southeast and the northwest.

A look at the recent seismic activity in the Kyushu-Okinawa region shows that a destructive earthquake (M 7.1) occurred in 1984 in the Hyuganada Sea area. In 1987, another earthquake (M 6.6) in the Hyuganada Sea resulted in one fatality, while others in October and December 1996 (both M 6.6) caused slight damage. Earthquakes of M 6.6 and M 6.5 occurred in October 1995 near Amami Oshima, causing slight damage on Kikaijima Island and other locations. Tsunami accompanied these earthquakes. Several destructive earthquakes occurred in shallow locations on land. These include the 1975 earthquakes at the north edge of Mt. Aso (Maximum M 6.1), the earthquake in central Oita Prefecture in the same year (M 6.4), the 1984 earthquake swarm on the western area of the Shimabara Peninsula (Maximum M 5.7), the 1994 earthquake in northern Kagoshima Prefecture (M 5.7) and the 1997 earthquakes in northwestern Kagoshima Prefecture (M 6.3, M 6.2). Earthquake swarms began in September 1992, primarily in northwestern Iriomotejima Island (Iriomote Jima). An earthquake of M 5.0 in October of that year caused slight damage.

(1)Earthquakes near the plate boundary off the coast of Pacific Ocean

The Philippine Sea Plate is subducting underneath the Kyushu-Okinawa region from the Nankai Trough and Nansei Islands Trench in the Pacific Ocean off the coast of Kyushu and Okinawa region (Fig.9-4).

There are two types of earthquakes that occur near the plate boundary from the Pacific Ocean to the coastal areas. First are interplate earthquakes caused by the slipping at the boundary of the subducting Philippine Sea Plate and the land plate. Second are those that occur in somewhat deep locations within the subducted Philippine Sea Plate.

1) Interplate earthquakes caused by the subduction of the Philippine Sea Plate

Many of the M 7 or so earthquakes that occur near Hyuganada Sea are interplate earthquakes caused by the subducting Philippine Sea Plate. Examples of these earthquakes are those occurring in 1961 (M 7.0), in 1968 (M 7.5), and in 1984 (M 7.1). Earthquakes in the M 7 or so occur in this area once every 10 years to several decades. There are no records of great M 8 or larger earthquakes, however. The earthquakes that occur near Hyuganada Sea result in damage caused by the ground motion on the coastline in this area. A tsunami also causes damage when the source region of the earthquake is shallow.

There are many remarkable examples of destructive earthquakes occurring near the Nansei Islands Trench. The 1771 Yaeyama Earthquake Tsunami (M 7.4) and the 1911 earthquake near Amami Oshima (M 8.0) occurred either when there was no network of seismic stations or the network was inadequate. It is unknown whether or not these were interplate earthquakes. At any rate, the large earthquakes that occur here are frequently accompanied by tsunami. Also, one theory holds that the tsunami accompanying the 1771 Yaeyama Earthquake was caused by a great landslide on the sea floor.

2) Earthquakes within the subducting Philippine Sea Plate

The two earthquakes near Amami Oshima in October 1995 (M 6.6, M 6.5) occurred in somewhat deep locations near a trench (20-40 km). These were earthquakes within the subducted Philippine Sea Plate. They occurred due to fault movement on a normal fault in which the subducted Philippine Sea Plate can break. They were accompanied by tsunami. It also has been suggested regarding the destructive earthquakes occurring near the Nansei Islands Trench in the past, that the 1911 earthquake near Amami Oshima (M 8.0) and others could have been of this type.

While rare, large earthquakes sometimes occur within subducted plates deep on land. Many of these earthquakes cause damage in a broad area. For example, the 1909 earthquake that occurred at a depth of about 150 km in western Miyazaki Prefecture (M 7.6) is known to have caused damage in distant Okayama and Hiroshima Prefectures.

(2)Shallow inland earthquakes

Based on topographical characteristics, the Kyushu region can roughly be divided into three areas: the northern, central, and southern areas. The central area contains the previously described Beppu-Shimabara rift valley and surrounding area. Specifically, it incorporates central Oita Prefecture, southern Fukuoka Prefecture, central and northern Kumamoto Prefecture, and the Shimabara Peninsula of Nagasaki Prefecture.

There are no volcanoes and a few active faults in the northern area, which incorporates Saga and Fukuoka Prefectures and the central part of Nagasaki Prefecture to the north. The Nishiyama fault zones and the other primary active faults run from northwest - southeast to north - south , and are either strike-slip faults or reverse faults with activity of B or C class. No destructive earthquakes are known to have been associated with these active faults. The only large destructive earthquakes in the northern area described by historical accounts are the 1700 Earthquake at Iki and Tsushima (M 7) and the 1898 Itoshima Earthquake (M 6.0).

There are many volcanoes and active faults in the central area, including Mt. Aso and Mt. Unzen. The Minoo fault zone runs roughly east to west along the northern edge of the central area, while the Futagawa/Hinagu fault zone is at the southern edge. The active faults in the central area are normal faults that run in a roughly east-west direction and sometimes have right lateral strike-slip components. Numerous active faults have been discovered by seismic profiling in Beppu Bay, the Yatsushiro Sea, Chijiwa Bay, and near Koshikijima Island (Kosikijima). The crustal movement extends throughout the land area of Kyushu. Pronounced extension has been observed running in a roughly north-south direction, particularly in the central area (Fig.9-7). It is presumed from the distribution of the active faults, the crustal movement, and other factors that a force is acting to cause extension in the earth's surface in a north-south direction, primarily in the central area.

Most of the destructive earthquakes in shallow locations on land in the Kyushu region occur in the central area. More than 15 destructive M6-level earthquakes are known to have occurred in the nearly 400 years since 1600. No active faults are known, however, for which slip has clearly been identified as a factor in these earthquakes. There are records of earthquakes estimated at M 7 or so occurring before 1600, including the earthquake occurring in the Tsukushi province (Tsukushi-no-kuni) in the year of 679 (M 6.5-7.5) and the 1596 earthquake at Beppu Bay (M 7.0). Recent research on active faults has shown that the 679 earthquake is likely to have occurred on the Minoo fault. Also, sea floor research indicates that the 1596 earthquake occurred on an active fault in Beppu Bay.

The southern area incorporates more than half of the land area of Kyushu, including the Kyushu Mountains (Kyusyu Santi), the Miyazaki Plain (Miyazaki Heiya), the Osumi Peninsula (Osumi Hanto) and Satsuma Peninsula (Satsuma Hanto). There are volcanoes in the southern area, including Sakurajima Island and Mt. Kirishima, but few active faults. The primary active fault is the Izumi fault zone in the vicinity of Izumi, near the Yatsushiro Sea. The primary destructive earthquakes here include the 1914 earthquake accompanying the eruption of Volcano Sakurajima (M 7.1), the 1968 Ebino Earthquake (M 6.1), and the earthquakes in northwestern Kagoshima Prefecture in March and May 1997 (M 6.3, M 6.2).

The earthquakes that occur in shallow areas around the Nansei Shoto Islands, which have a small land area, are thought to be of the type similar to those that occur at shallow locations on land, even when the hypocenter is in the sea. Destructive earthquakes of this type include the 1909 earthquake near the coast of the southern part of Okinawa Island (M 6.2) and the 1898 Earthquake off the East Coast of Ishigakijima Island (M 7). Also, earthquake swarms in the M 4 to 5 range frequently occur in the sea near the Tokara Islands (Tokara Retto).

The Okinawa Trough runs parallel to the Nansei Shoto Islands at the sea floor on the northwest side of the islands in the East China Sea. Research on the sea floor shows there are many normal faults here. The Beppu-Shimabara rift valley , which also has many normal faults, is located as an extension of the Okinawa Trough in roughly a northeast direction. The 1938 earthquake north off Miyakojima Island (Miyako Jima) (M 6.7), which occurred in the Okinawa Trough, was accompanied by a tsunami of about 1.5 m high that struck the island about 10 minutes after the earthquake occurred.

The interval of activity for most active faults is 1,000 years or longer. This does not indicate that no earthquake can occur here even if there is no record of past events.

139. Assignment 3, Module 10: EQ Hazard Basics: https://www.usgs.gov/programs/earthquake-hazards/science/earthquake-hazards-101-basics

Earthquake Hazards 101 - the Basics

ACTIVE

By Earthquake Hazards Program August 6, 2019

Overview

What is earthquake hazard?

Earthquake ground shaking varies from place to place and the hazard mapping in this project will show this variability. The mapped hazard refers to an estimate of the probability of exceeding a certain amount of ground shaking, or ground motion, in 50 years. The hazard depends on the magnitudes and locations of likely earthquakes, how often they occur, and the properties of the rocks and sediments that earthquake waves travel through.

What are hazard maps?

The National Seismic Hazard Model (NSHM) develops maps to show the distribution of earthquake shaking levels that have a certain probability of occurring in the United States and the U.S. Territories. These maps are created to provide the most accurate and detailed information possible to assist engineers in designing buildings, bridges, highways, and utilities that will withstand shaking from earthquakes. Additionally, the datasets, models, and maps are used to create and update the building codes that are now used by more than 20,000 cities, counties, and local governments to help establish construction requirements necessary to preserve public safety.

Applications of the Hazard Maps:

1. Building Codes (NEHRP, IBC, ASCE 7) About building codes? (FEMA)
2. Highway bridge design nationwide (AASHTO)
3. Insurance rates
4. Business and land-use planning
5. Estimations of stability and landslide potentials of hillsides
6. Construction standards for waste-disposal facilities (EPA)
7. Retrofit priorities
8. Allocation planning of assistance funds for education and preparedness (FEMA)
9. Concerned general public

How to read a hazard map

Suppose the figure on the right is a hazard map for the area of Nowhere City developed for a 50-year time span and a 5% chance of exceedance.

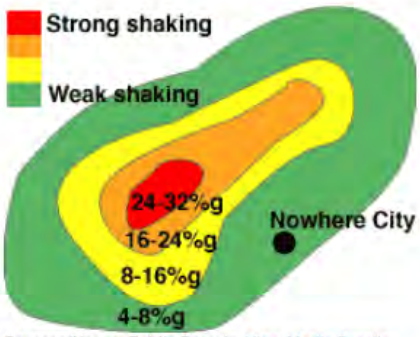

Sources/Usage: Public Domain. View Media Details

Example hazard map for Nowhere City. (Public domain.)

We would read the shaking hazards for Nowhere City as:
The earthquake peak ground acceleration (PGA) that has a 5% chance of being exceeded in 50 years has a value between 4 and 8% g (percent of gravity, g).

What is probabilistic ground motion, and why use it for hazard determination?

Probabilistic ground motion maps depict earthquake hazard by showing, by contour values, the earthquake ground motions (of a particular frequency) that have a common given probability of being exceeded in 50 years (and other time periods).The ground motions being considered at a given location are those from all future possible earthquake magnitudes at all possible distances from that location. The ground motion coming from a particular magnitude and distance is assigned an annual probability.

So the goal of a hazard map is to depict the potential shaking hazard from future earthquakes. The following sequence explains why probabilistic ground motion is the best way to accomplish this goal:

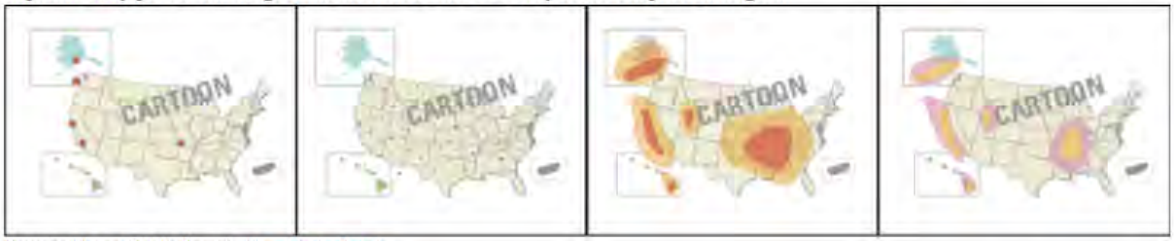

Sources/Usage: Public Domain. View Media Details

The sequence depicts steps 1-4 that follow below, respectively. This sequence shows why probabilistic ground motion is used for hazard determination. (Public domain.)

Step 1

We can use a map showing the location and date of significant damaging earthquakes in the United States, *but* a map like that would not generalize from seismic history to indicate where other damaging earthquakes might be expected to occur in the future. To add this missing information...

Step 2

We can add to the map all the smaller earthquakes that have occurred in the past, and then we can use that seismic history information to assume that damaging earthquakes can also occur in the future in the same locations as the smaller earthquakes, *but* we can't tell what the size of the expected ground motion hazard is. To add this missing information...

Step 3

We can make a map of the historical maximum seismic intensities (amount of shaking) to estimate the size of the hazard, *but* we are ignoring the fact that earthquakes occur at a much lower rate in some parts of the U.S. than in others. To add this missing information...

Step 4

We can incorporate **seismicity** rates in different parts of the country into the map using the methods of probabilistic ground motion hazard, *but* now the historical seismicity information is overemphasized compared to the evidence of seismic potential determined from geologic data. To add this missing information...

Sources/Usage: Public Domain. View Media Details

Example model of future seismicity in the U.S. (Public domain.)

Step 5

Finally, we add a model of future seismicity based on the prehistoric geologic information. In this way we arrive at the final hazard map.

The method assumes a reasonable future catalog of earthquakes, based upon historical earthquake locations and geological information on the recurrence rate of **fault** ruptures. When all the possible earthquakes and magnitudes have been considered, one can find a ground motion value such that the annual rate of its being exceeded has a certain value. Hence, on a given map, for a given probability of exceedance, PE, locations shaken more frequently, will have larger ground motions.

For a LARGE exceedance probability, the map will show the relatively likely ground motions, which are LOW ground motions, because small magnitude earthquakes are much more likely to occur than are large magnitude earthquakes.

For a SMALL exceedance probability, the map will emphasize the effect of less likely events: larger-magnitude and/or closer-distance events, producing overall LARGE ground motions on the map. The maps have this format, because they are designed to be useful in building codes, in which we assume that, for the most part, all buildings would be built to the same level of safety. For other applications, maps of another format might be more useful. For instance, many buildings across the US are built more or less the same, regardless of earthquake hazard. If we knew that a particular type of building was likely to fail at a particular ground motion level, we could make a map showing contours of the likelihood of that ground motion value being exceeded, due to earthquakes.

Why are there different probability maps, and which one do I use?

The different probabilities are selected to provide an idea of the relative range of hazard across the US. The larger probabilities indicate the level of ground motion likely to cause problems in the western US. The smaller probabilities show how unlikely damaging ground motions are in many places of the eastern US. However, basically the values chosen reflect the more recent history in earthquake engineering.

Probability from the engineering point of view

Rather than start with the idea of probability, consider approaching the issue from this direction: A structure is designed to resist earthquake ground motion having a particular value. Given this design resistance, one might ask several questions:

- Under what ground motion will the building sway so much that it is uncomfortable to the persons working inside, and disrupts their work for the day? (This could occur with winds as well as with earthquakes.)
- Under what ground motion will the building bend so much that interior partitions crack and wall or ceiling fixtures drop?
- Under what ground motion will the building become permanently deformed and require expensive rehabilitation or abandonment.
- Under what ground motion will the building collapse during the shaking?

Using a hazard curve, one could determine the annual probability of occurrence of each of these ground motions. Then one could decide whether that corresponding probability is acceptable. If one of the probabilities is unacceptably high, the design would have to be revised.

The different probability values reflect probabilities sometimes considered for design. The value 10 percent in 50 years seemed to provide values similar to those already used in design in the 1970s in California. On the other hand, this level of probability in the eastern US produced values too low for the seismic design then under consideration to provide residual toughness in the event of possible earthquakes (unlikely in any one location, but likely in some locations). The probabilities more likely to produce useful design ground motions would be near 5 percent in 50 years.

The ground motions given by probabilistic maps span a range of probabilities considered interesting to earthquake engineers and a range of ground motions which have some intuitive understanding for the consequences. There have been requests for maps of larger probabilities for purposes having to do with investment, insurance, and banking.

How do I know what map to choose then?

How does an individual person select a map? Technical users probably have to follow predefined rules. A non-technical person may be interested in avoiding living in a location where significant shaking will cause worry, deciding on whether to carry earthquake insurance, or deciding whether to do some rehabilitation for an existing dwelling. The probability level chosen should reflect how anxious a person is to avoid earthquake shaking.

Here is some perspective on the 10 percent in 50 year map:
If a person lives in a 100-year floodplain, there is about 1 chance in 100 of experiencing the flood in any given year. In 50 years, one would expect 0.5 floods, and there is a 1 - exp(-0.5) = 39 percent chance of experiencing such a flood in 50 years. This is a higher likelihood than that of experiencing a damaging ground motion in an area where that ground motion has only a 10 percent chance of being exceeded in 50 years. In a 200-year floodplain the chance would be 22 percent, still larger than the chance for the damaging ground motion. People who are not comfortable with probabilities as large as 10 percent in 50 years for damaging earthquake ground motion should use maps with smaller probabilities. But they should also be aware that many other hazards are higher than earthquake hazards, even in California.

How is a hazard map made? What is a hazard curve and how is it made?

How probabilistic ground motion is calculated:

Calculating the probability of a ground motion being exceeded

We demonstrate how to get the probability that a ground motion is exceeded for an individual earthquake - the "probability of exceedance".

1. Show a curve of ground motion vs distance for a given magnitude, given a particular attenuation relation.
2. At a given distance show distribution of ground motion.
3. Intercept the distribution with a horizontal line at a given ground motion.
4. The area of the distribution above the horizontal line is divided by the total area of the distribution. The result is "Probability of Exceedance" of the given ground motion given that earthquake having that magnitude experienced at that distance, given that particular attenuation relation.

Annual rate of exceedance

How to get the expected number of exceedances in 1 year owing to that earthquake.

1. Multiply the annual occurrence rate of the earthquake times the probability of exceedance of the ground motion, given that earthquake.
2. Expected number of exceedances in 1 year = Annual rate of exceedance

Annual rate of exceedance, given several earthquakes

Expected number of exceedances for several earthquakes. "Adding exceedances"

1. The expected number of exceedances for several earthquakes is calculated by merely adding the annual rate of exceedance owing to each earthquake.

Calculating a hazard curve.

A hazard curve is calculated by plotting annual rate of exceedance vs ground motion:

1. Perform the above calculation for 18 other ground motion levels.
2. Plot the results.
3. Make a smooth curve.

Now, for any ground motion we can find the annual rate of exceedance. Likewise, for any annual rate of exceedance we can find the corresponding ground motion.

Exceedance probability in Y years.

(This part is mathematical)

The expected number, n of exceedances in Y years is n = Y times r, the annual rate of exceedance. **Assumption:** The rate of earthquake occurrence in time is governed by the Poisson Law. **Application:** Under the Poisson Law, if you expect over some period of time n occurrences of "something", the probability of 0 occurrences is e^{-n}. If the "something" is exceedance of some ground motion, the probability of getting an exceedance is 1 − P(0). So, one can work backwards to find the annual rate of exceedance corresponding to "the probability of exceedance is 5% in 50 years."

$1 - P(0) = \frac{5}{100}$ (5%)
$P(0) = 1 - 0.05 = 0.95 = e^{-n}$

Take the log to the base e of both sides of the last equality.

$n = -ln(0.95) = 0.05129 = Yr = 50r$
$r = \frac{0.05129}{50} = 0.0010258 = \frac{1}{974.8}$

The last result tells us that at low exceedance probabilities (less than 10%) r is approximately PE / (100 Y). Now one can use the hazard curve to find the corresponding ground motion. The hazard maps are just the contoured version of the corresponding ground motion plotted on a geographic grid.

There are 3 types of maps:

- Peak Ground Acceleration (PGA)
- 0.2 second Spectral Acceleration (SA)
- 1.0 second Spectral Acceleration (SA)

Units for all 3 maps are %g (percent of gravity). This can also be expressed in decimal form, example 10%g = 0.1g. The ground motion values apply to ground motion expected for future individual earthquakes. The probabilistic ground motion calculation takes into account all possible future ground motions from all modeled earthquake magnitudes at all possible distances from the map site. The spatial distribution of probabilistic ground motion values is shown with contours on the map, like a topo map shows different elevations, with each color representing a different range of levels of shaking.

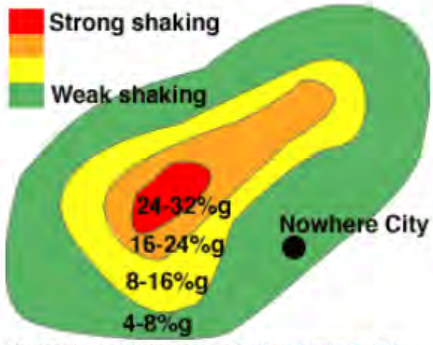

Sources/Usage: Public Domain. View Media Details

Hazard map showing chance of exceedance in a 50-year time interval for Nowhere City. (Public domain.)

Sources/Usage: Public Domain. View Media Details

TIME INTERVAL (X). A time interval during which all possible earthquakes may occur is set in order to determine the shaking hazard. The time interval is typically set to 50 years. The 50-year period can be ANY 50 years, not just the NEXT 50 years; the red bar above can span any 50-year period. (Public domain.)

What data are used to make hazard maps?

Three basic pieces of information are needed to produce probabilistic ground motion maps:

1. **Model of Future Earthquakes**

   Using information about past historical earthquakes, Quaternary faults (prehistoric earthquakes), and present crustal deformation (geodetic data), USGS analysts make a model of the potential for future earthquakes. This model includes *areal sources* and *fault sources*. For each source the relative rate for earthquakes of different magnitudes is given, and the absolute rate for magnitudes larger than some minimum magnitude.

2. **Attenuation Relations**

   An attenuation relation is an equation or a table that describes how earthquake ground motion decreases as the distance to the earthquake increases. Because earthquake ground motion increases with magnitude, the attenuation relation also depends on magnitude. Strong motion data (recordings close to the earthquake) and geophysical attenuation models are used to establish the attenuation relations.

3. **Geologic Site Condition**

   Earthquake ground motion waves travel rapidly in the earth's crust and mantle. That part of the earth's solid crust closest to the surface is called bed rock. The size of the ground motion experienced at the earth's surface is affected by the geology of the material between bed rock and the surface. Because the earthquake waves move more slowly in this material than in rock, the size of the ground motion increases.

   This material, often called alluvium or "the soil column," increases the ground motion in such a way that "softer" soils, soils with less density, have lower seismic velocity, and hence experience larger increases in ground motion. It is necessary to know the geologic site condition in order to estimate the surface ground motion.

   Maps are usually made for a common widespread site condition, and then rules are given for the user to adjust to other site conditions.

Who uses hazard maps?

Hazard maps can be used by public and private groups for land-use planning, mitigation, and emergency response. The scale of the maps does not allow them to be used in a site-specific manner (such as a house-by-house assessment), but it does show a neighborhood overview to guide where more detailed studies are needed.

Why do the hazard maps keep changing and getting updated?

The maps are updated as additional data becomes available from scientific analysis of earthquake-related data, such as:

1. new fault data
2. new attenuation relations
3. new geodetic data
4. more seismic data

I just want to know what faults are near me; how will these maps help?

Knowing where the faults are is not the most relevant information when trying to learn what your risks are of being affected by an earthquake. Since a large earthquake can affect distant locations, you can be affected by a fault tens-of-miles away from where you are, because of the prolonged shaking that can occur.

Nearby faults can represent a hazard from ground rupture accompanying an earthquake. Faults, both near and far, provide a source for hazard from shaking. Furthermore, in the Eastern US there are earthquakes for which the actual location or extent of faulting is poorly known. In this case, historical seismicity is the source for understanding the shaking hazard.

Source/Usage: Public Domain. View Media Details

% CHANCE of EXCEEDANCE (Y) The percent (%) chance that a certain amount of mapped shaking distribution will occur over the time period being considered. Typically the values of 2%, 5% and 10% are used. Keep in mind that a 5% chance of exceedance means there is a 95% chance that the shaking will NOT exceed the value. (Public domain.)

The models and maps developed by the NSHM integrate all the faulting and seismicity information into an indication of shaking hazard. The actual values of the shaking hazards depend upon the ground motion parameter of interest and degree of safety which one wants. This is why the maps are different for different ground motions and different probabilities. The ground motion hazard values can be compared with the capacity of a structure to withstand shaking, and thus give an indication of safety.

140. Assignment 3, Module 10: EQ Hazard Education:
https://www.usgs.gov/programs/earthquake-hazards/education

What is an earthquake?

An **earthquake** is what happens when two blocks of the earth suddenly slip past one another. The surface where they slip is called the **fault** or **fault plane**. The location below the earth's surface where the earthquake starts is called the **hypocenter**, and the location directly above it on the surface of the earth is called the **epicenter**.

Sometimes an earthquake has **foreshocks**. These are smaller earthquakes that happen in the same place as the larger earthquake that follows. Scientists can't tell that an earthquake is a foreshock until the larger earthquake happens. The largest, main earthquake is called the **mainshock**. Mainshocks always have **aftershocks** that follow. These are smaller earthquakes that occur afterwards in the same place as the mainshock. Depending on the size of the mainshock, aftershocks can continue for weeks, months, and even years after the mainshock!

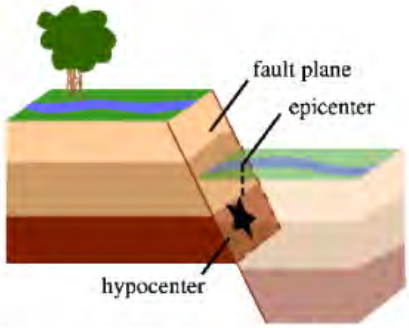

Sources/Usage: Public Domain. View Media Details

A normal (dip-slip) fault is an inclined fracture where the rock mass above an inclined fault moves down (Public domain.)

What causes earthquakes and where do they happen?

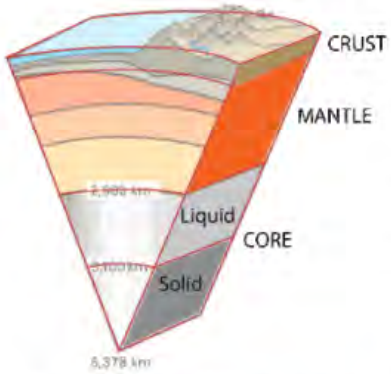

Sources/Usage: Public Domain. View Media Details

A simplified cartoon of the crust (brown), mantle (orange), and core (liquid in light gray, solid in dark gray) of the earth. (Public domain.)

The earth has four major layers: the inner core, outer core, mantle and crust. The crust and the top of the mantle make up a thin skin on the surface of our planet.

But this skin is not all in one piece – it is made up of many pieces like a puzzle covering the surface of the earth. Not only that, but these puzzle pieces keep slowly moving around, sliding past one another and bumping into each other. We call these puzzle pieces **tectonic plates**, and the edges of the plates are called the **plate boundaries**. The plate boundaries are made up of many faults, and most of the earthquakes around the world occur on these faults. Since the edges of the plates are rough, they get stuck while the rest of the plate keeps moving. Finally, when the plate has moved far enough, the edges unstick on one of the faults and there is an earthquake.

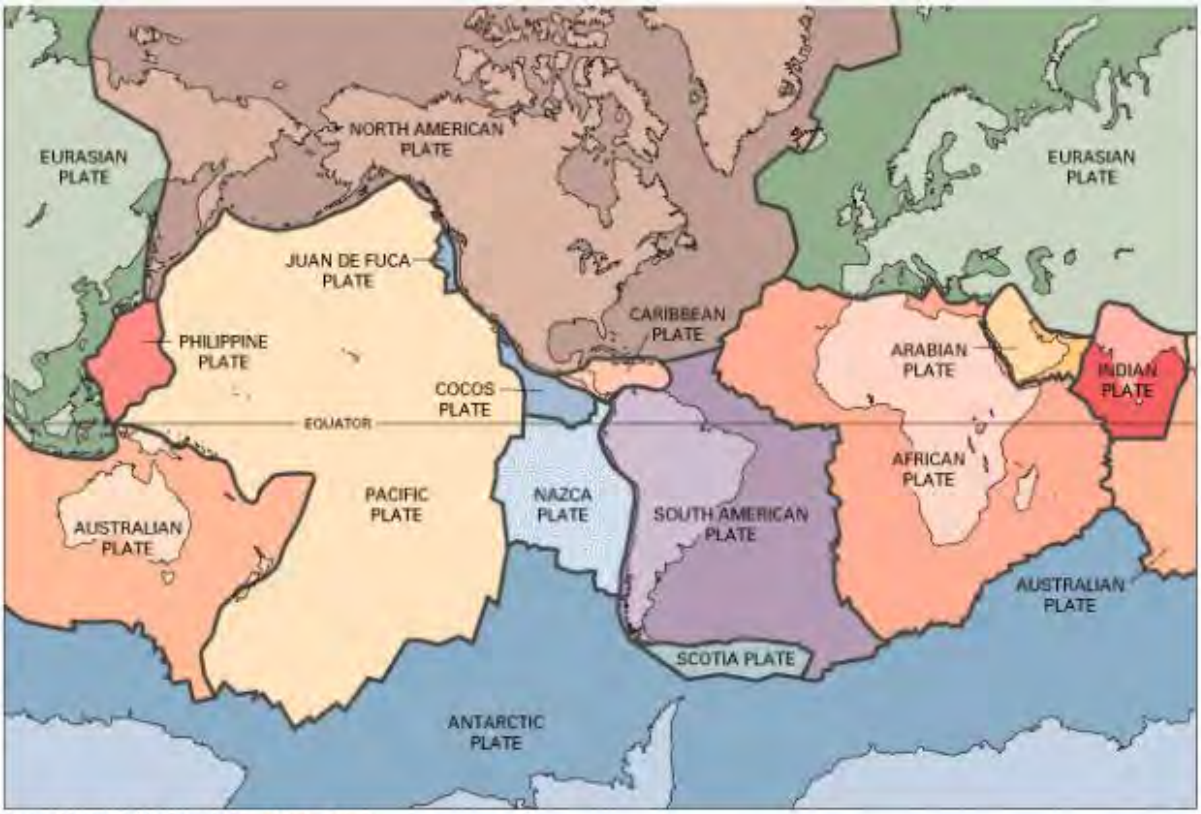

Sources/Usage: Public Domain. View Media Details

The tectonic plates divide the Earth's crust into distinct "plates" that are always slowly moving. Earthquakes are concentrated along these plate boundaries. (Public domain.)

Why does the earth shake when there is an earthquake?

While the edges of faults are stuck together, and the rest of the block is moving, the energy that would normally cause the blocks to slide past one another is being stored up. When the force of the moving blocks finally overcomes the **friction** of the jagged edges of the fault and it unsticks, all that stored up energy is released. The energy radiates outward from the fault in all directions in the form of **seismic waves** like ripples on a pond. The seismic waves shake the earth as they move through it, and when the waves reach the earth's surface, they shake the ground and anything on it, like our houses and us!

How are earthquakes recorded?

Earthquakes are recorded by instruments called **seismographs**. The recording they make is called a **seismogram**. The seismograph has a base that sets firmly in the ground, and a heavy weight that hangs free. When an earthquake causes the ground to shake, the base of the seismograph shakes too, but the hanging weight does not. Instead the spring or string that it is hanging from absorbs all the movement. The difference in position between the shaking part of the seismograph and the motionless part is what is recorded.

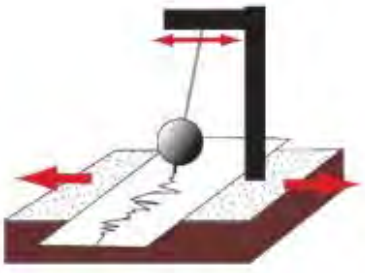

Sources/Usage: Public Domain. View Media Details

The cartoon sketch of the seismograph shows how the insrument shakes with the earth below it, but the recording device remains stationary (instead of the other way around). (Public domain.)

How do scientists measure the size of earthquakes?

The size of an earthquake depends on the size of the fault and the amount of slip on the fault, but that's not something scientists can simply measure with a measuring tape since faults are many kilometers deep beneath the earth's surface. So how do they measure an earthquake? They use the **seismogram** recordings made on the **seismographs** at the surface of the earth to determine how large the earthquake was (figure 5). A short wiggly line that doesn't wiggle very much means a small earthquake, and a long wiggly line that wiggles a lot means a large earthquake. The length of the wiggle depends on the size of the fault, and the size of the wiggle depends on the amount of slip.

Sources/Usage: Public Domain. View Media Details

An example of a seismic wave with the P wave and S wave labeled. (Public domain.)

The size of the earthquake is called its **magnitude**. There is one magnitude for each earthquake. Scientists also talk about the*intensity* of shaking from an earthquake, and this varies depending on where you are during the earthquake.

How can scientists tell where the earthquake happened?

Seismograms come in handy for locating earthquakes too, and being able to see the **P wave** and the **S wave** is important. You learned how P & S waves each shake the ground in different ways as they travel through it. P waves are also faster than S waves, and this fact is what allows us to tell where an earthquake was. To understand how this works, let's compare P and S waves to lightning and thunder. Light travels faster than sound, so during a thunderstorm you will first see the lightning and then you will hear the thunder. If you are close to the lightning, the thunder will boom right after the lightning, but if you are far away from the lightning, you can count several seconds before you hear the thunder. The further you are from the storm, the longer it will take between the lightning and the thunder.

P waves are like the lightning, and S waves are like the thunder. The P waves travel faster and shake the ground where you are first. Then the S waves follow and shake the ground also. If you are close to the earthquake, the P and S wave will come one right after the other, but if you are far away, there will be more time between the two.

By looking at the amount of time between the P and S wave on a seismogram recorded on a seismograph, scientists can tell how far away the earthquake was from that location. However, they can't tell in what direction from the seismograph the earthquake was, only how far away it was. If they draw a circle on a map around the station where the **radius** of the circle is the determined distance to the earthquake, they know the earthquake lies somewhere on the circle. But where?

Scientists then use a method called **triangulation** to determine exactly where the earthquake was (see image below). It is called triangulation because a triangle has three sides, and it takes three seismographs to locate an earthquake. If you draw a circle on a map around three different seismographs where the **radius** of each is the distance from that station to the earthquake, the intersection of those three circles is the **epicenter**!

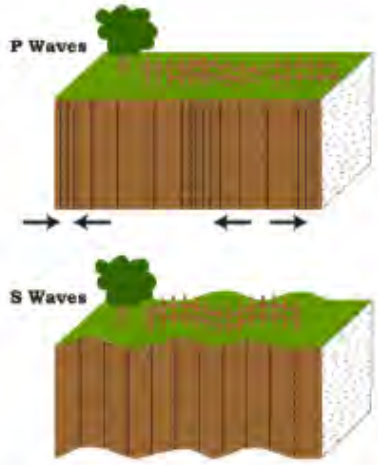

Sources/Usage: Public Domain. View Media Details

P Waves alternately compress and stretch the crustal material parallel to the direction they are propagating. S Waves cause the crustal material to move back and forth perpendicular to the direction they are travelling. (Public domain.)

Can scientists predict earthquakes?

No, and it is unlikely they will ever be able to predict them. Scientists have tried many different ways of predicting earthquakes, but none have been successful. On any particular fault, scientists know there will be another earthquake sometime in the future, but they have no way of telling when it will happen.

Is there such a thing as earthquake weather? Can some animals or people tell when an earthquake is about to hit?

These are two questions that do not yet have definite answers. If weather does affect earthquake occurrence, or if some animals or people can tell when an earthquake is coming, we do not yet understand how it works.

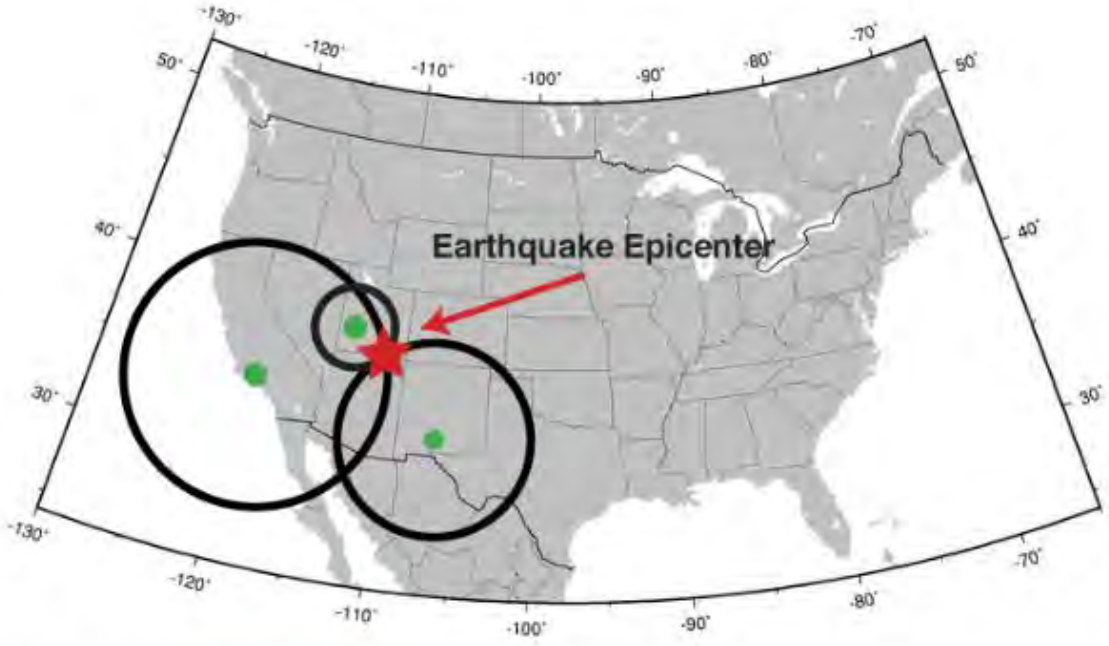

Sources/Usage: Public Domain. View Media Details

Triangulation can be used to locate an earthquake. The seismometers are shown as green dots. The calculated distance from each seismometer to the earthquake is shown as a circle. The location where all the circles intersect is the location of the earthquake epicenter. (Public domain.)

- The **largest recorded earthquake in the United States** was a magnitude 9.2 that struck Prince William Sound, Alaska on Good Friday, March 28, 1964 UTC.

Sources/Usage: Public Domain. View Media Details

Damage from the 1964 Alaskan Earthquake. Credit: USGS (Public domain.)

- The **largest recorded earthquake in the world** was a magnitude 9.5 (Mw) in Chile on May 22, 1960.
- The **earliest reported earthquake in California** was felt in 1769 by the exploring expedition of Gaspar de Portola while the group was camping about 48 kilometers (30 miles) southeast of Los Angeles.
- Before electronics allowed recordings of large earthquakes, scientists built large **spring-pendulum seismometers** in an attempt to record the long-period motion produced by such quakes. The largest one weighed about 15 tons. There is a medium-sized one three stories high in Mexico City that is still in operation.
- The **fastest wave**, and therefore the first to arrive at a given location, is called the P wave. The P wave, or compressional wave, alternately compresses and expands material in the same direction it is traveling.

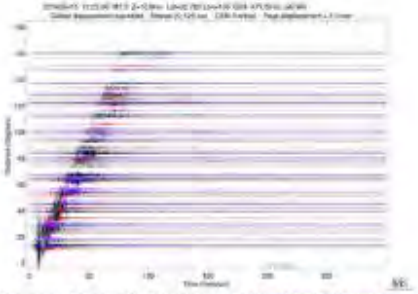

Sources/Usage: Public Domain. View Media Details

waveform stack (Public domain.)

- The **average rate of motion across the San Andreas Fault Zone** during the past 3 million years is 56 mm/yr (2 in/yr). This is about the same rate at which your fingernails grow. Assuming this rate continues, scientists project that Los Angeles and San Francisco will be adjacent to one another in approximately 15 million years.
- The **East African Rift System** is a 50-60 km (31-37 miles) wide zone of active volcanics and faulting that extends north-south in eastern Africa for more than 3000 km (1864 miles) from Ethiopia in the north to Zambezi in the south. It is a rare example of an active continental rift zone, where a continental plate is attempting to split into two plates which are moving away from one another.

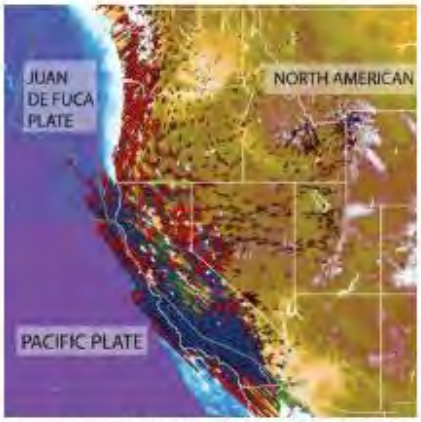

Sources/Usage: Public Domain. View Media Details

Relief map of the western United States with the background velocity field (relative to a fixed North American plate) determined from two decades of GPS observations. Measurements have been made by numerous academic and government organizations, including the Plate Boundary Observatory and the USGS. (Public domain.)

- The **first "pendulum seismoscope"** to measure the shaking of the ground during an earthquake was developed in 1751, and it wasn't until 1855 that faults were recognized as the source of earthquakes.
- **Moonquakes** ("earthquakes" on the moon) do occur, but they happen less frequently and have smaller magnitudes than earthquakes on the Earth. It appears they are related to the tidal stresses associated with the varying distance between the Earth and Moon. They also occur at great depth, about halfway between the surface and the center of the moon.

- Although both are sea waves, a **tsunami and a tidal wave** are two different unrelated phenomenona. A tidal wave is a shallow water wave caused by the gravitational interactions between the Sun, Moon, and Earth. A tsunami is a sea wave caused by an underwater earthquake or landslide (usually triggered by an earthquake) displacing the ocean water.

- The **hypocenter** of an earthquake is the location beneath the earth's surface where the rupture of the fault begins.

- The **epicenter** of an earthquake is the location directly above the hypocenter on the surface of the earth.

- The **"Ring of Fire"** also called the Circum-Pacific belt, is the zone of earthquakes surrounding the Pacific Ocean — about 90% of the world's earthquakes occur there. The next most seismic region (5-6% of earthquakes) is the Alpide belt (extends from Mediterranean region, eastward through Turkey, Iran, and northern India.

- It is estimated that there are **500,000 detectable earthquakes** in the world each year. 100,000 of those can be felt, and 100 of them cause damage.

- It is thought that more damage was done by the resulting fire after the **1906 San Francisco earthquake** than by the earthquake itself.

- A **seiche** (pronounced SAYSH) is what happens in the swimming pools of Californians during and after an earthquake. It is "an internal wave oscillating in a body of water" or, in other words, it is the sloshing of the water in your swimming pool, or any body of water, caused by the ground shaking in an earthquake. It may continue for a few moments or hours, long after the generating force is gone. A seiche can also be caused by wind or tides.

Sources/Usage: Public Domain. *View Media Details*

Volcanic arcs and oceanic trenches partly encircling the Pacific Basin form the so-called Ring of Fire, a zone of frequent earthquakes and volcanic eruptions. The trenches are shown in blue-green. The volcanic island arcs, although not labelled, are parallel to, and always landward of, the trenches. For example, the island arc associated with the Aleutian Trench is represented by the long chain of volcanoes that make up the Aleutian Islands. (Public domain.)

- Each year the **southern California area has about 10,000 earthquakes**. Most of them are so small that they are not felt. Only several hundred are greater than magnitude 3.0, and only about 15-20 are greater than magnitude 4.0. If there is a large earthquake, however, the aftershock sequence will produce many more earthquakes of all magnitudes for many months.

- The **magnitude** of an earthquake is a measured value of the earthquake size. The magnitude is the same no matter where you are, or how strong or weak the shaking was in various locations. The **intensity** of an earthquake is a measure of the shaking created by the earthquake, and this value does vary with location.

- The **Wasatch Range**, with its outstanding ski areas, runs North-South through Utah, and like all mountain ranges it was produced by a series of earthquakes. The 386 km (240-mile)-long Wasatch Fault is made up of several segments, each capable of producing up to a M7.5 earthquake. During the past 6,000 years, there has been a M6.5+ about once every 350 years, and it has been about 350 years since the last powerful earthquake, which was on the Nephi segment.

- The world's **greatest land mountain range** is the Himalaya-Karakoram. It countains 96 of the world's 109 peaks of over 7,317m (24,000 ft). The longest range is the Andes of South America which is 7,564km (4700 mi) in length. Both were created by the movement of tectonic plates.

- The longest mountain range in the world, though, is the **mid-ocean ridge**, extending 64,374 km (40,000 mi) from the Arctic Ocean to the Atlantic Ocean, around Africa, Asia, and Australia, and under the Pacific Ocean to the west coast of North America.

- As far as we know, there is no such thing as **"earthquake weather"**. Statistically, there is an equal distribution of earthquakes in cold weather, hot weather, rainy weather, etc. If weather does affect earthquake occurrence, we do not yet understand how it works.

- From 1975-1995 there were only **four states that did not have any earthquakes**. They were: Florida, Iowa, North Dakota, and Wisconsin.

- The **core of the earth** was the first internal structural element to be identified. In 1906 R.D. Oldham discovered it from his studies of earthquake records. The inner core is solid, and the outer core is liquid and so does not transmit the shear wave energy released during an earthquake.

- The swimming pool at the University of Arizona in Tucson lost water from sloshing (seiche) caused by the **1985 M8.1 Michoacan, Mexico earthquake** 2000 km (1240 miles) away.

- Earthquakes occur in the central portion of the United States too! Some very powerful earthquakes occurred along the New Madrid fault in the **Mississippi Valley in 1811-1812**. Because of the crustal structure in the Central US which efficiently propagates seismic energy, shaking from earthquakes in this part of the country are felt at a much greater distance from the epicenters than similar size quakes in the Western US.

Sources/Usage: Public Domain. View Media Details

Active faults of the segmented Wasatch fault zone are next to the largest and growing population centers of central Utah. Structural fault segment boundaries play an unknown role in limiting large earthquakes.

- Most earthquakes occur at depths of **less than 80 km (50 miles)** from the Earth's surface.

- The **San Andreas fault is NOT a single, continuous fault**, but rather is actually a fault zone made up of many segments. Movement may occur along any of the many fault segments along the zone at any time. The San Andreas fault system is more that 1300 km (800 miles) long, and in some spots is as much as 16 km (10 miles) deep.

- The **origin of the name of the San Andreas Fault** is often cited as the San Andreas Lake. However, based on some 1895 and 1908 reports by geologist A.C. Lawson, who named the fault, the name was actually taken from the San Andreas Valley. He likely did not realize at the time that the fault ran almost the entire length of California!

- The **world's deadliest recorded earthquake** occurred in 1556 in central China. It struck a region where most people lived in caves carved from soft rock. These dwellings collapsed during the earthquake, killing an estimated 830,000 people. In 1976 another deadly earthquake struck in Tangshan, China, where more than 250,000 people were killed.

- Florida and North Dakota have the **smallest number of earthquakes** in the United States.

- The **deepest earthquakes** typically occur at plate boundaries where the Earth"s crust is being subducted into the Earth's mantle. These occur as deep as 750 km (400 miles) below the surface.

- Alaska is the **most earthquake-prone state** and one of the most seismically active regions in the world. Alaska experiences a magnitude 7 earthquake almost every year, and a magnitude 8 or greater earthquake on average every 14 years.

- The **majority of the earthquakes and volcanic eruptions** occur along plate boundaries such as the boundary between the Pacific Plate and the North American plate. One of the most active plate boundaries where earthquakes and eruptions are frequent, for example, is around the massive Pacific Plate commonly referred to as the Pacific Ring of Fire.

Sources/Usage: Public Domain. View Media Details

Peter Haeussler prepares to measure the offset of a crevasse on the Canwell Glacier, Alaska, USA. Photo by Peter Haeussler, USGS, November 9, 2002 (Public domain.)

- The **earliest recorded evidence of an earthquake** has been traced back to 1831 BC in the Shandong province of China, but there is a fairly complete record starting in 780 BC during the Zhou Dynasty in China.

- It was recognized as early as 350 BC by the Greek scientist Aristotle that **soft ground shakes more than hard rock** in an earthquake.

- The **cause of earthquakes was stated correctly in 1760** by British engineer John Michell, one of the first fathers of seismology, in a memoir where he wrote that earthquakes and the waves of energy that they make are caused by "shifting masses of rock miles below the surface".

- **Subduction** is the process of the oceanic lithosphere colliding with and descending beneath the continental lithosphere.

- In 1663 the European settlers experienced their **first earthquake in America**.

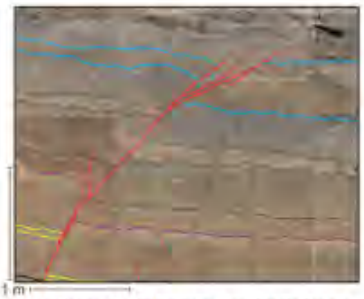

Sources/Usage: Public Domain. View Media Details

Exposure of the San Andreas Fault in a trench. The horizontal colored lines highlight different layers of sediment. The red line is traced on a fault that offsets the layers. (Public domain.)

- Human beings can detect sounds in the frequency range 20-20,000 Hertz. If a P wave refracts out of the rock surface into the air, and it has a frequency in the audible range, it will be heard as a rumble. **Most earthquake waves have a frequency of less than 20 Hz**, so the waves themselves are usually not heard. Most of the rumbling noise heard during an earthquake is from buildings and their contents moving.

- When the Chilean earthquake occurred in 1960, **seismographs recorded seismic waves that traveled all around the Earth**. These seismic waves shook the entire earth for many days! This phenomenon is called the free oscillation of the Earth.

- The **interior of Antarctica has icequakes** which, although they are much smaller, are perhaps more frequent than earthquakes in Antarctica. The icequakes are similar to earthquakes, but occur within the ice sheet itself instead of the land underneath the ice. Some of our polar observers have told us they can hear the icequakes and see them on the South Pole seismograph station, but they are much too small to be seen on enough stations to obtain a location.

- On January 26, 1700 at about 9 PM Pacific time, the **largest known earthquake in the continental U.S.** occurred. We know the time so precisely because Japan has been recording tsunamis at least as far back as 684 CE, and this large Cascadia earthquake caused a tsunami that Japan recorded. We can work backwards from the time the tsunami arrived in Japan to determine when the earthquake happened.

- The present-day location of **The Pinnacles** is 195 mi (314 km) northwest from the volcano that the San Andreas sliced it from. We know these volcanic rocks are 23 million years old. That means the San Andreas fault has moved 0.59 in/yr (1.5 cm/yr) over the last 23 million years.

Sources/Usage: Public Domain. View Media Details

Pinnacles, California Offset by San Andreas Fault. The present-day location of The Pinnacles is 195 mi (314 km) from the volcano that the San Andreas sliced it from. We know these volcanic rocks are 23 million years old. That means the San Andreas fault has moved 0.59 in/yr (1.5 cm/yr) over the last 23 million years. (Public domain.)

141. Assignment 3, Module 10: EQ Hazards Animation: https://earthquake.usgs.gov/earthquakes/feed/v1.0/kml.php#:~:text=To%20view%20earthquake%20animations%20in%20Google%20Earth%20follow,Select%20the%20earthquake%20feed%2C%20in%20the%20left%20navigation.

Google Earth™ KML

Description

KML is Google's Keyhole Markup Language. The KML feeds offer a variety of options, you can view earthquakes colored by age or depth and an animated feed allows you to animate the series of earthquakes.

This feed adheres to the USGS Earthquakes Feed Life Cycle Policy.

Usage

You will need to download and install Google Earth to view KML files.

Automatic Feeds
These feeds will automatically update every 5 or 15 minutes when downloaded and installed into Google Earth.

Feeds
Download a normal KML feed to view earthquake data in Google Earth. You will have to re-download the KML file to access updated earthquake information.

Earthquake Animations

To view earthquake animations in Google Earth follow the directions below:

1. Download an animated USGS Earthquakes KML Feed.
2. Open the KML using Google Earth.
3. Select the earthquake feed, in the left navigation.
4. Use the time slider, in the upper left hand corner of the map, to animate the series of earthquakes. You may also click through the animation one frame at a time. 

   For more information on how to use the time slider, click here.

Output

Screenshot of “Past 7 Days, M1+ Earthquakes, Colored by Age” KML in Google Earth.

142. Assignment 3, Module 10: Design Maps: https://www.usgs.gov/programs/earthquake-hazards/design-ground-motions

The USGS collaborates with organizations that develop building codes (for buildings, bridges, and other structures) to make seismic design parameter values available to engineers. The design code developers first decide how USGS earthquake hazard information should be applied in design practice. Then, the USGS calculates values of seismic design parameters based on USGS hazard values and in accordance with design code procedures.

U.S. Seismic Design Maps Web Services

Due to insufficient resources and the recent development of similar web tools by third parties, the USGS has replaced its former U.S. Seismic Design Maps web applications with web services that can be used through third-party tools. Your options for using the replacement USGS web services, which still provide seismic design parameter values from numerous design code editions, are:

Third-party Graphical User Interfaces (GUIs)

Most users obtain seismic design parameter values from the USGS web services through third-party GUIs like the following:

- ASCE 7 Hazard Tool
- SEAOC/OSHPD Seismic Design Maps Tool

USGS U.S. Seismic Design Maps Web Services

It is possible, but less convenient, to obtain seismic design parameter values directly from the USGS web services:

- Documentation for all design code editions
- Step-by-step Instructions for *AASHTO Guide Specifications*
- Step-by-step instructions for *ASCE/SEI 7-16 Standard*

Risk-Targeted Ground Motion Calculator

This web tool calculates risk-targeted ground motion values from probabilistic seismic hazard curves in accordance with the site-specific ground motion procedures defined in "Method 2" (Section 21.2.1.2) of the *ASCE/SEI 7-10, and 7-16* and *7-22* standards for new buildings, and the *AASHTO Guide Specifications for LRFD Seismic Bridge Design (3rd Edition, October 2023)*. A Risk-Targeted Ground Motion interactive web tool is available for performing these calculations for a single intensity measure hazard curve. For bulk calculations for a larger number of hazard curves, please refer to the underlying USGS Web-Services or the USGS Python source code. The vast majority of engineering projects in the U.S. will require use of the *U.S. Seismic Design Maps Web Services* (see above) rather than this *Risk-Targeted Ground Motion Calculator*.

Seismic Design Data

For underlying datasets, please see the design ground motions portal. For the most up-to-date information on available data, please email nluco@usgs.gov, srezaeian@usgs.gov, amakdisi@usgs.gov, and zkortum@usgs.gov.

143. Assignment 3, Module 10: Earthquake Risk: https://www.fema.gov/emergency-managers/risk-management/earthquake

Earthquake Risk

English

On July 25, 2025, FEMA published the Fiscal Year 2025 funding opportunity for the National Earthquake Hazards Reduction Program Individual State Earthquake Assistance. Learn more on Grants.gov.

The National Earthquake Hazards Reduction Program (NEHRP) leads the federal government's efforts to reduce the fatalities, injuries and property losses caused by earthquakes. Congress established NEHRP in 1977, directing that four federal agencies coordinate their complementary activities to implement and maintain the program. These agencies are:

- Federal Emergency Management Agency (FEMA)
- National Institute of Standards and Technology (NIST)
- National Science Foundation (NSF)
- U.S. Geological Survey (USGS)

NEHRP also partners with state and local governments, universities, research centers, professional societies and trade associations and businesses.

Learn more about the National Earthquake Hazards Reduction Program (NEHRP).

Earthquake Hazard Maps

English

The maps displayed below show how earthquake hazards vary across the United States. Hazards are measured as the likelihood of experiencing earthquake shaking of various intensities.

How To Read The Maps

The colors in the maps denote “seismic design categories” (SDCs), which reflect the likelihood of experiencing earthquake shaking of various intensities. (Building design and construction professionals use SDCs specified in building codes to determine the level of seismic resistance required for new buildings.)

The following table describes the hazard level associated with each SDC and the associated levels of shaking. Although stronger shaking is possible in each SDC, it is less probable than the shaking described.

SDC/Map Color	Earthquake Hazard	Potential Effects of Shaking
A/White	Very small probability of experiencing damaging earth-quake effects.	
B/Gray	Could experience shaking of moderate intensity.	Moderate shaking—Felt by all, many frightened. Some heavy furniture moved; a few instances of fallen plaster. Damage slight.
C/Yellow	Could experience strong shaking.	Strong shaking—Damage negligible in buildings of good design and construction; slight to moderate in well-built ordinary structures; considerable damage in poorly built structures.
D/Light Brown D1/Darker Brown D2/Darkest Brown	Could experience very strong shaking (the darker the color, the stronger the shaking).	Very strong shaking—Damage slight in specially designed structures; considerable damage in ordinary substantial buildings with partial collapse. Damage great in poorly built structures.
E/Red	Near major active faults capable of producing the most intense shaking.	Strongest shaking—Damage considerable in specially designed structures; frame structures thrown out of plumb. Damage great in substantial buildings, with partial collapse. Buildings shifted off foundations. Shaking intense enough to completely destroy buildings.

*Abbreviated descriptions from The Modified Mercalli Intensity (MMI) Scale.

SDCs take into account the type of soil at the site, as poor soils can significantly increase earthquake shaking. These maps have simplified this by assuming normal Site Class "D" soils, which are the most commonly found.

When viewing the maps, it is important to remember that areas with high earthquake hazards do not necessarily face high seismic risks. Defined as the losses that are likely to result from exposure to earthquake hazards, seismic risks are determined not only by hazard levels but also by the amount of people and property that are exposed to the hazards and by how vulnerable people and property are to the hazards.

Maps

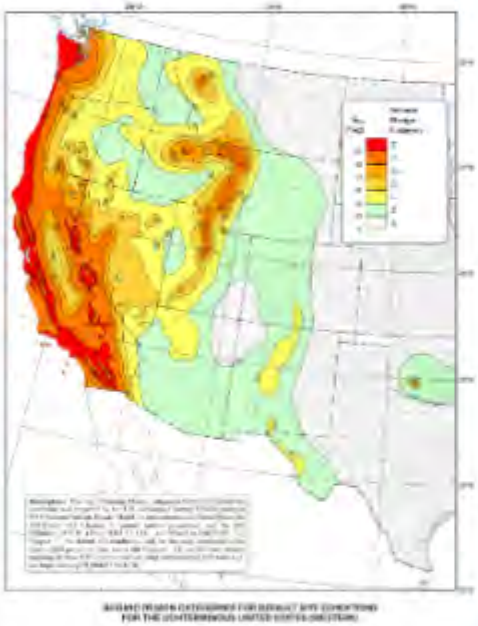

View earthquake hazards from across the United States.

- Eastern United States
- Western United States
- Alaska
- Hawaii
- Puerto Rico
- Guam and the Northern Mariana Islands (CNMI)

Data For Building Design Professionals

The U.S. Geological Survey, in cooperation with FEMA and the Building Seismic Safety Council (BSSC), has developed a web-based seismic design application for building designers. This program can be used to obtain the earthquake ground motion parameters needed to design structures for specific geographic locations in accordance with the latest building code reference documents.

To access this application, as well as the seismic design maps on which it is based, go to U.S. Seismic Design Maps.

144. Assignment 3, Module 10: Exploring Natural Hazards:
https://www.sciencelearn.org.nz/resources/2624-exploring-natural-hazards

Exploring natural hazards

In this recorded professional learning session, Lyn Rogers and guest Aliki Weststrate from GNS Science explore some of the science involved in building our understandings of natural hazards, including volcanoes, earthquakes, tsunamis and lahars. They introduce some readily available resources and activities and delve into some of the exciting research happening in this field in New Zealand. They discuss how engaging students in 'real' science stories can support them in developing their own skills for science inquiry.

> *Great from a geography perspective! Thanks*
>
> *Teacher*

This content connects easily to other learning across the curriculum and can be adapted to any level.

Includes webinar with following timestamps (webinar not included in this document):

Topic	PowerPoint slide number(s)	Video timecode
Introducing the Science Learning Hub and presenters	1	00:00
Index	2–3	00:12
Webinar purpose	4	00:42
Curriculum connections	5	02:05
What are natural hazards?	6–8	04:35
Pacific Rim of Fire	9	05:37
Plate boundaries	10–13	07:09
Planning pathway – earthquakes	14	17:42
Planning pathway – volcanoes	15	18:37
Associated hazards – tsunamis and landslides	16	19:10
JOIDES Resolution – researching natural hazards	17	21:35
Expedition #375 – Hikurangi subduction zone	18–20	22:28
What are slow slips?	21	26:49
What did you find out?	22	30:21
What were the challenges?	23	33:09
What next – for science?	24	39:37
What next – in the classroom?	25	42:09
SLH links, keep in touch and thanks	26	43:58

145. Assignment 5, Module 1: Occupancy Study Note: https://www.catriskcredentials.org/wp-content/uploads/2020/05/Exam-3c-Study-Note-Occupancy-Class.pdf

Exam 3: Cat Risk Management Insurance Fundamentals
Part C – Module Title: Occupancy Class
Study Note

Learning Objective:

Describe how occupancy class can influence damage to different coverages.

This document contains original content.

Occupancy class is the most commonly reported primary risk characteristic and is one of the four main primary risk characteristics used to differentiate vulnerability in a catastrophe model. When occupancy class is unknown, a general occupancy class can often be derived or assumed based on the general line of business (Residential, Commercial, Industrial or Agricultural).

There are separate vulnerability curves for each coverage type:

- **Building coverage:** Provides insurance coverage for damage associated with the structural and non-structural elements of the building. This includes things like beams, columns, walls, drywall, carpet and ceiling tiles.
- **Contents coverage:** Provides insurance coverage for damage associated with contents on the property. This includes things like furniture, appliances, electronics, equipment and inventory.
- **Loss of use coverage:** Provides insurance coverage for damage associated with additional living expenses incurred or business interruption associated with things like relocation, loss of income, storage and utility interruptions while the physical structure is repaired.

The vulnerability curve associated with building coverage is a function of the hazard of the peril. For hurricane, this is generally wind speed and for earthquake, this is generally spectral acceleration. The vulnerability curves associated with contents and loss of use are typically a function of the building damage. In addition, the occupancy class is used to further differentiate vulnerability.

Occupancy Class to Differentiate Building Vulnerability

Occupancy Classes with Varying Design Standards

Building codes generally require higher design standards for occupancies like large entertainment centers and shopping malls that contain a high number of occupants to protect the life safety of the occupants. Additionally, an occupancy such as a hospital, is also designed to a higher standard to ensure the structure can remain operable during a major catastrophic event. On the other hand, storage facilities or agricultural risks may be designed to a lower design standard where the structure does not house humans on a regular basis.

Some catastrophe models acknowledge the varying design standards for these occupancy classes by differentiating building vulnerability across occupancy classes. Consider a hospital, an office building and a barn and hypothetically built with the same construction materials. Building codes might require the hospital to have larger beams and columns and stronger connections when compared to the office building or the barn. Thus, when the three occupancies are exposed to the same hazard, it is expected the hospital will result in less building damage.

Exam 3: Cat Risk Management Insurance Fundamentals
Part C – Module Title: Occupancy Class
Study Note

Occupancy Classes with Similar Structural or Non-Structural Features

Claims data is often used to inform vulnerability curves in a catastrophe model. Claims data is much more available and easy to work with for residential risks. For commercial risks, claims data is less available so model vendors employ engineering judgement along with claims data to differentiate commercial vulnerability. Model vendors study the structural and non-structural features of different occupancy classes to help inform how to differentiate occupancy classes built with the same construction materials.

For example, occupancies such as gas stations and strip malls often have large storefront windows that make these types of structures more vulnerable to wind damage from wind-borne debris. Other occupancy classes, such as a warehouse or an auto repair shop, might have large garage door bays that are highly vulnerable to damage from high wind pressure.

Occupancy Class to Differentiate Contents Vulnerability

The contents within a structure vary greatly between occupancy classes. As a result, two occupancy classes can result in the same level of building damage but have different levels of contents damage. Consider a hospital a hospital and an auto repair shop. The hospital has very sensitive equipment that can be easily damaged during an earthquake when subject to high levels of ground motion, or easily damaged during a hurricane when subject to rain and wind. The auto repair shop contains heavy tools, workbenches, etc. that may be able to better survive the elements of a hurricane or earthquake. Assuming both occupancies are subject to the same level of building damage, we might expect more damage to the contents of the hospital than the auto repair shop.

Occupancy Class to Differentiate Loss of Use Vulnerability

Occupancy class heavily influences the additional living expenses or business interruption costs (collectively defined as loss of use). The downtime that results while a home or business is addressing the associated building and contents-related damages will vary by occupancy class. Some occupancy classes, such as a church or a school, may be able to more relocate into temporary facilities to resume operations while repairs are made to the damaged structure. Other occupancy classes, such as a hotel, rely on their location and cannot easily relocate. As a result, these occupancy classes might result in higher loss of use damage for the same level of building damage as other occupancy classes.

Not all event result in significant building repairs. The less severe events might result in limited physical damage but loss of use damage can still be incurred due to utility damage and power outages. A restaurant or a grocery store can result in significant business interruption loss during a power outage, while an office building may only have limited business interruption costs.

146. Assignment 5, Module 1: FEMA 454, Sections 4.5.2, 4.9, and 5.2: https://www.wbdg.org/FFC/DHS/fema454.pdf

4.5.2 Ground Motion, Building Resonance, and Response Spectrum

When a vibrating or swinging object is given further pushes that are also at its natural period, its vibrations increase dramatically in response to even rather small pushes and, in fact, its accelerations may increase as much as four or five times. This phenomenon is called resonance.

The ground obeys the same physical law and also vibrates at its natural period, if set in motion by an earthquake. The natural period of ground varies from about 0.4 seconds to 2 seconds, depending on the nature of the ground. Hard ground or rock will experience short period vibration. Very soft ground may have a period of up to 2 seconds but, unlike a structure, it cannot sustain longer period motions except under certain unusual conditions. Since this range is well within the range of common building periods, it is quite possible that the pushes that earthquake ground motion imparts to the building will be at the natural period of the building. This may create resonance, causing the structure to encounter accelerations of perhaps 1g when the ground is only vibrating with accelerations of 0.2g. Because of this, buildings suffer the greatest damage from ground motion at a frequency close or equal to their own natural frequency.

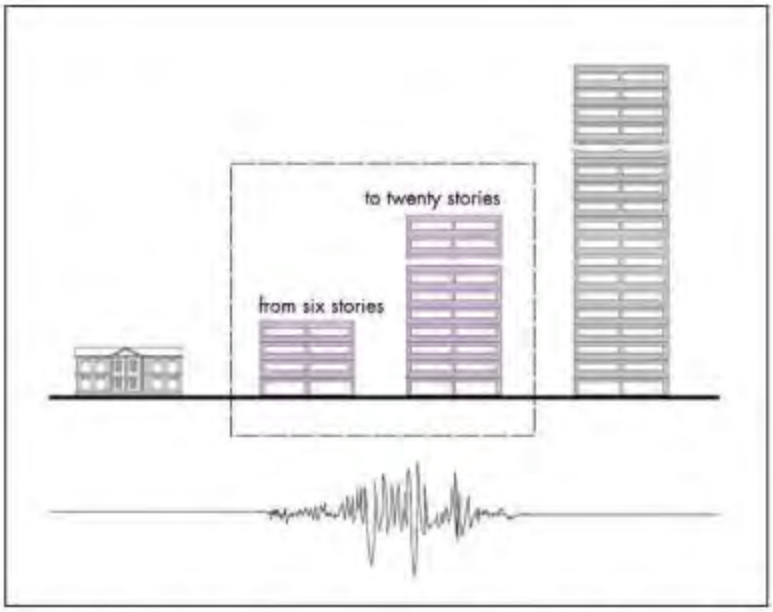

Figure 4-5: The vulnerable group: Mexico City, 1985. The periods of buildings in the 6 to 20 story range resonated with the frequency content of the earthquake.

The terrible destruction in Mexico City in the earthquake of 1985 was primarily the result of response amplification caused by coincidence of building and ground motion periods (Figure 4-5). Mexico City was some 250 miles from the earthquake focus, and the earthquake caused the soft ground in margins of the old lake bed under the downtown buildings to vibrate for over 90 seconds at its long natural period of around 2 seconds. This caused buildings that were between about 6 and 20 stories in height to resonate at a similar period, greatly increasing the accelerations within them. Taller buildings suffered little damage. This amplification in building vibration is very undesirable. The possibility of it happening can be reduced by trying to ensure that the building period will not coincide with that of the ground. Thus, on soft (long-period) ground, it would be best to design a short, stiff (short-period) building.

Taller buildings also will undergo several modes of vibration so that the building will wiggle back and forth like a snake (Figure 4-6).

However, later modes of vibration are generally less critical than the natural period, although they may be significant in a high-rise building. For low-rise buildings, the natural period (which, for common structures, will always be relatively short) is the most significant. Note, however, that the low-period, low- to mid-rise building is more likely to experience resonance from the more common short-period ground motion.

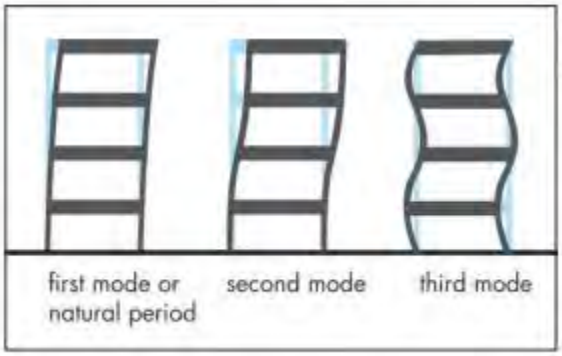

Figure 4-6
Modes of vibration.

4.9 DUCTILITY

The gap between design capacity (the theoretical ability of a building to withstand calculated forces) and possible actual forces is, finally, largely dealt with by relying on the material property of ductility. This is the property of certain materials (steel in particular) to fail only after considerable inelastic deformation has taken place, meaning that the material does not return to its original shape after distortion. This deformation, or distortion, dissipates the energy of the earthquake.

This is why it is much more difficult to break a metal spoon by bending it than one made of plastic. The metal object will remain intact, though distorted, after successive bending to and fro while the plastic spoon will snap suddenly after a few bends. The metal is far more ductile than the plastic (Figure 4-11).

The deformation of the metal (even in the spoon) absorbs energy and defers absolute failure of the structure. The material bends but does not break and so continues to resist forces and support loads, although with diminished effectiveness. The effect of earthquake motion on a building

Figure 4-11: Ductility

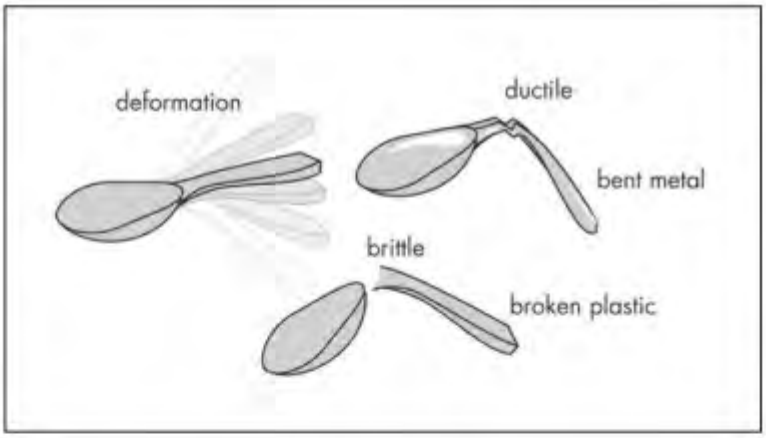

is rather like that of bending a spoon rapidly back and forth: the heavy structure is pushed back and forth in a similar way several times a second (depending on its period of vibration).

Brittle materials, such as unreinforced masonry or inadequately reinforced concrete, fail suddenly, with a minimum of prior distortion. The steel bars embedded in reinforced concrete can give this material considerable ductility, but heavier and more closely spaced reinforcing bars and special detailing of their placement are necessary.

Ductility and reserve capacity are closely related: past the elastic limit (the point at which forces cause permanent deformation), ductile materials can take further loading before complete failure. In addition, the member proportions, end conditions, and connection details will also affect ductility. Reserve capacity is the ability of a complete structure to resist overload, and is dependent on the ductility of its individual members. The only reason for not requiring ductility is to provide so much resistance that members would never exceed elastic limits.

Thus, buildings are designed in such a way that in the rare case when they are subjected to forces higher than those required by a code, the materials and connections will distort but not break. In so doing, they will safely absorb the energy of the earthquake vibrations, and the building, although distorted and possibly unusable, is at least still standing.

5.2 THE BASIC SEISMIC STRUCTURAL SYSTEMS

A building's structural system is directly related to its architectural configuration, which largely determines the size and location of structural elements such as walls, columns, horizontal beams, floors, and roof structure. Here, the term **structural/architectural configuration** is used to represent this relationship.

5.2.1 The Vertical Lateral Resistance Systems

Seismic designers have the choice of three basic alternative types of vertical lateral force–resisting systems, and as discussed later, the system must be selected at the outset of the architectural design process. Here, the intent is to demonstrate an optimum architectural/structural configuration for each of the three basic systems. The three alternatives are illustrated in Figure 5-1.

These basic systems have a number of variations, mainly related to the structural materials used and the ways in which the members are connected. Many of these are shown in Chapter 7: Figures 7-2, 7-3, 7-11A and 7-11b show their comparative seismic performance characteristics.

- Shear walls

  Shear walls are designed to receive lateral forces from diaphragms and transmit them to the ground. The forces in these walls are predominantly shear forces in which the material fibers within the wall try to slide past one another. To be effective, shear walls must run from the top of the building to the foundation with no offsets and a minimum of openings.

- Braced frames

  Braced frames act in the same way as shear walls; however, they generally provide less resistance but better ductility depending on their detailed design. They provide more architectural design freedom than shear walls.

  There are two general types of braced frame: conventional concentric and eccentric. In the concentric frame, the center lines of the bracing members meet the horizontal beam at a single point.

  In the eccentric braced frame, the braces are deliberately designed to meet the beam some distance apart from one another: the short piece of beam between the ends of the braces is called a link beam. The purpose of the link beam is to provide ductility to the system: under heavy seismic forces, the link beam will distort and dissipate the energy of the earthquake in a controlled way, thus protecting the remainder of the structure (Figure 5-2).

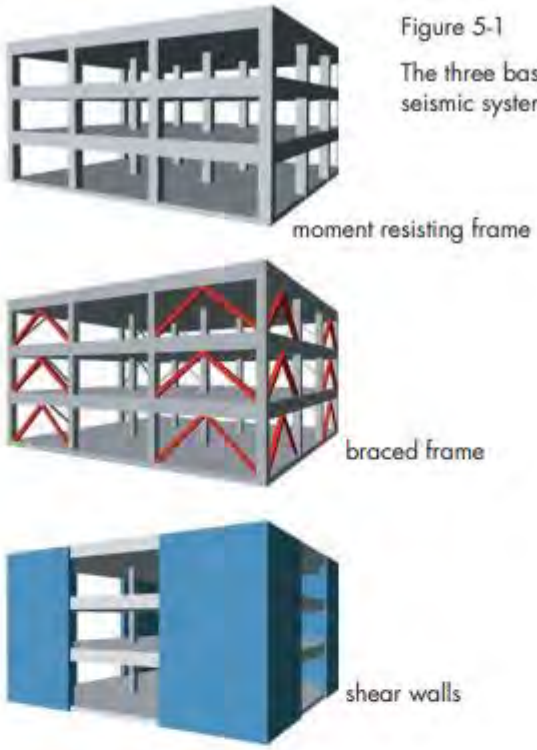

Figure 5-1

The three basic vertical seismic system alternatives.

❍ Moment-resistant frames

A moment resistant frame is the engineering term for a frame structure with no diagonal bracing in which the lateral forces are resisted primarily by bending in the beams and columns mobilized by strong joints between columns and beams. Moment-resistant frames provide the most architectural design freedom.

These systems are, to some extent, alternatives, although designers sometimes mix systems, using one type in one direction and another type in the other. This must be done with care, however, mainly because the different systems are of varying stiffness (shear-wall systems are much stiffer than moment-resisting frame systems, and braced systems fall in between), and it is difficult to obtain balanced resistance when they are mixed. However, for high-performance structures,) there is now increasing use of dual systems, as described in section 7.7.6. Examples of effective mixed systems are the use of a shear-wall core together with a perimeter moment-resistant frame or a perimeter steel-moment frame

Figure 5-2
Types of braced frames.

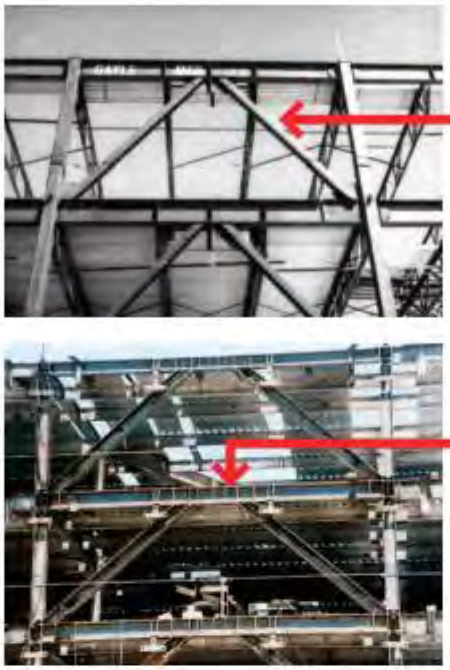

with interior eccentric-braced frames. Another variation is the use of shear walls combined with a moment-resistant frame in which the frames are designed to act as a fail-safe back-up in case of shear-wall failure.

The framing system must be chosen at an early stage in the design because the different system characteristics have a considerable effect on the architectural design, both functionally and aesthetically, and because the seismic system plays the major role in determining the seismic performance of the building. For example, if shear walls are chosen as the seismic force-resisting system, the building planning must be able to accept a pattern of permanent structural walls with limited openings that run uninterrupted through every floor from roof to foundation.

5.2.2 Diaphragms—the Horizontal Resistance System

The term "diaphragm" is used to identify horizontal-resistance members that transfer lateral forces between vertical-resistance elements (shear walls or frames). The diaphragms are generally provided by the floor and roof elements of the building; sometimes, however, horizontal bracing systems independent of the roof or floor structure serve as dia-

phragms. The diaphragm is an important element in the entire seismic resistance system (Figure 5-3).

The diaphragm can be visualized as a wide horizontal beam with components at its edges, termed **chords**, designed to resist tension and compression: chords are similar to the flanges of a vertical beam (Figure 5-3A)

A diaphragm that forms part of a resistant system may act either in a **flexible** or **rigid** manner, depending partly on its size (the area between enclosing resistance elements or stiffening beams) and also on its material. The flexibility of the diaphragm, relative to the shear walls whose

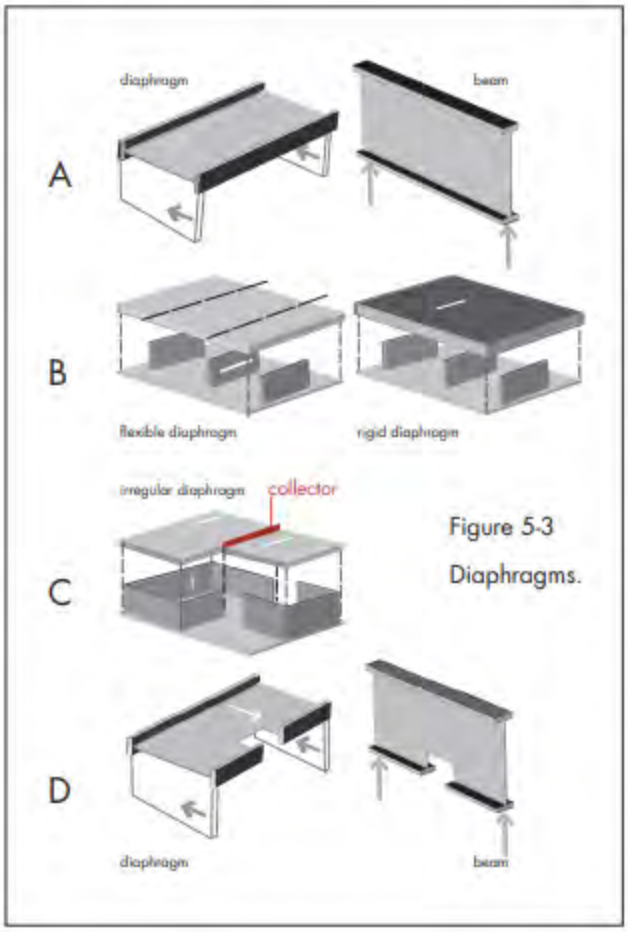

Figure 5-3
Diaphragms.

forces it is transmitting, also has a major influence on the nature and magnitude of those forces. With flexible diaphragms made of wood or steel decking without concrete, walls take loads according to tributary areas (if mass is evenly distributed). With rigid diaphragms (usually concrete slabs), walls share the loads in proportion to their stiffness (figure 5-3B).

Collectors, also called **drag struts** or **ties**, are diaphragm framing members that "collect" or "drag" diaphragm shear forces from laterally unsupported areas to vertical resisting elements (Figure 5-3C).

Floors and roofs have to be penetrated by staircases, elevator and duct shafts, skylights, and atria. The size and location of these penetrations are critical to the effectiveness of the diaphragm. The reason for this is not hard to see when the diaphragm is visualized as a beam. For example, it can be seen that openings cut in the tension flange of a beam will seriously weaken its load carrying capacity. In a vertical load-bearing situation, a penetration through a beam flange would occur in either a tensile or compressive region. In a lateral load system, the hole would be in a region of both tension and compression, since the loading alternates rapidly in direction (Figure 5-3D).

5.2.3 Optimizing the Structural/Architectural Configuration

Figure 5-4 shows the application of the three basic seismic systems to a model structural/architectural configuration that has been designed for near optimum seismic performance. The figure also explains the particular characteristics that are seismically desirable.

Building attributes:

- **Continuous load path.**
  Uniform loading of structural elements and no stress concentrations.
- **Low height-to base ratio**
  Minimizes tendency to overturn.
- **Equal floor heights**
  Equalizes column or wall stiffness, no stress concentrations.
- **Symmetrical plan shape**
  Minimizes torsion.

moment resisting frame

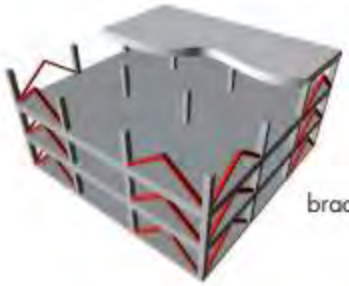

braced frame

shear walls

Figure 5-4

The optimized structural/ architectural configuration.

- **Identical resistance on both axes**
  Eliminates eccentricity between the centers of mass and resistance and provides balanced resistance in all directions, thus minimizing torsion.

- **Identical vertical resistance**
  No concentrations of strength or weakness.

- **Uniform section and elevations**
  Minimizes stress concentrations.

- **Seismic resisting elements at perimeter**
  Maximum torsional resistance.

- **Short spans**
  Low unit stress in members, multiple columns provide redundancy -loads can be redistributed if some columns are lost.

- **No cantilevers**
  Reduced vulnerability to vertical accelerations.

- **No openings in diaphragms(floors and roof)**
  Ensures direct transfer of lateral forces to the resistant elements.

In the model design shown in Figure 5-4, the lateral force resisting elements are placed on the perimeter of the building, which is the most effective location; the reasons for this are noted in the text. This location also provides the maximum freedom for interior space planning. In a large building, resistant elements may also be required in the interior.

Since ground motion is essentially random in direction, the resistance system must protect against shaking in all directions. In a rectilinear plan building such as this, the resistance elements are most effective when placed on the two major axes of the building in a symmetrical arrangement that provides balanced resistance. A square plan, as shown here, provides for a near perfectly balanced system.

Considered purely as architecture, this little building is quite acceptable, and would be simple and economical to construct. Depending on its exterior treatment - its materials, and the care and refinement with which they are disposed- - it could range from a very economical functional building to an elegant architectural jewel. It is not a complete building, of course, because stairs, elevators, etc., must be added, and the building is not spatially interesting. However, its interior could be configured with nonstructural components to provide almost any quality of room that was desired, with the exception of unusual spatial volumes such as spaces more than one story in height.

In seismic terms, engineers refer to this design as a **regular** building. As the building characteristics deviate from this model, the building becomes increasingly **irregular**. It is these irregularities, for the most part created by the architectural design, that affect the building's seismic performance. **Indeed many engineers believe that it is these architectural irregularities that contribute primarily to poor seismic performance and occasional failure.**

147. Assignment 5, Module 1: Building Height Study Note: https://www.catriskcredentials.org/wp-content/uploads/2020/07/Exam-3c-Study-Note-Building-Height.pdf

Exam 3: Cat Risk Management Insurance Fundamentals
Part C – Module Title: Number of Stories (Building Height)
Study Note

Learning Objective:

Explain why number of stories is an important indicator of hurricane damage.

This document contains original content.

Number of stories is one of the primary risk characteristics that model vendors use to differentiate hurricane vulnerability. Model vendors group the number of stories together into bands to differentiate the vulnerability of a low-rise structure from a mid-rise or high-rise structure.

Wind speed increases with altitude. Winds near the earth's surface are reduced due to surface friction, as winds interact with the terrain, landscape and infrastructure. At higher altitudes, wind speeds increase due to the lack of surface friction.

Despite the higher wind speeds at higher altitudes, a mid-rise or high-rise structure will generally result in less hurricane damage than a low-rise structure. The main reason for this is that mid-rise and high-rise structures are engineered, while some low-rise structures may be permitted to be constructed without direct oversight from an engineer.

Under certain guidelines, low-rise structures may be permitted to be constructed with a series of prescriptive standards. Prescriptive standards provide a set of building requirements that a contractor must follow. Examples include the nailing pattern in a roof deck or the type of connections used for attaching the roof to the wall frame. These are acceptable standards, but do not require the direct involvement of an engineer in the design and construction process.

Mid-rise and high-rise structures are too large to meet the guidelines of prescriptive standards and are required to be designed and constructed with direct involvement from a licensed professional engineer. The engineer will provide detailed building plans for the contractor that are specific to the structure that will be constructed. The engineer is often directly involved in the inspection of the building once it has been constructed to ensure it was built according to his or her plans.

Due to the direct involvement of the engineer during the design and construction process, mid-rise and high-rise structures often result in less hurricane damage, when compared to low-rise structures. Even though the taller structures are subject to higher wind loads, these structures are specifically designed to resist these loads. Non-engineered low-rise construction standards are much less rigorous, and therefore more likely to sustain damage when exposed to the same hazard.

148. Assignment 5, Module 1: Building Codes Study Note: https://www.catriskcredentials.org/wp-content/uploads/2020/07/Exam-3c-Study-Note-Building-Codes.pdf

Exam 3: Cat Risk Management Insurance Fundamentals
Part C – Module Title: Year Built (Building Codes)
Study Note

Learning Objectives:

- Describe the use of the year built to indicate the age of the building, and what code(s) may have been in place at the time of construction
- Identify key hurricane and earthquake events that influenced changes in building codes.

This document contains original content.

Year built is one of the primary risk characteristics that model vendors use to differentiate hurricane vulnerability. It is used to infer what codes may have been in place at the time of construction. Key catastrophic events resulted in lessons learned that have influenced changes in building codes over time. These building code changes are generally improvements and therefore a newer year built typically results in less damage than an older year built when exposed to the same hazard. Below is a summary of the key building code changes over time and the catastrophic events that influenced the building code change.

Hurricane

Pre-1995

Prior to 1995, three separate building code organizations existed for building code adoption and enforcement:

- Building Officials and Code Administrators International, Inc (BOCA)
- International Conference of Building Officials (ICBO)
- Southern Building Code Congress International, Inc. (SBCCI)

The three organizations maintained separate building codes with a regional focus – BOCA along the East Coast and Midwest, ICBO in the Western States and SBCCI in the Southeast. Standards were not always consistent between the three organizations and code adoption and enforcement did not always occur at the state level.

Hurricane Andrew made landfall just south of Miami as a Category 5 hurricane in 1992. It became the costliest event at the time, surpassing the records left behind from Hurricane Hugo's Category 4 landfall in South Carolina in 1989.

Hurricane Andrew, along with the recent memory of Hurricane Hugo, drew attention to the lack of consistent building code and adoption and enforcement at the state level. It also highlighted the need for additional emphasis on better protection of the building envelope components (roof covering, windows, doors, etc.). Existing building codes in place at the time primarily focused on the design of the Main Wind-Force Resisting System (the beams, walls and columns that support the structure). The devastation from these events showed that failure of the building envelope while the Main Wind-Force Resisting System remains intact can still results in significant damage.

In 1994, the three regional building code organizations combined into a single building code organization known as the International Code Council (ICC), with the goal of creating a single building code standard, updated every three years, and enforced at the state-level.

1995 to 2001

As the ICC worked towards their goals, more immediate efforts to improve building codes were taking place:

149. Assignment 6, Module 1: FEMA 454, Sections 1.4.1 – note the below contains all of section 1.4 (there are no sub-sections): https://www.wbdg.org/FFC/DHS/fema454.pdf

1.4 THE BOTTOM LINE

This publication is an introduction to its subject, and deals more with principles than with the many detailed tasks that go into ensuring the seismic safety of a building. These tasks require a team approach in which all the participants in the building design and construction process must participate in a timely manner. Understanding the principles discussed in this publication will assist the design team as they search for affordable solutions that will provide building safety without compromising building function, amenity and delight.

In the confines of a document that contains a huge scope, the authors must necessarily be very selective. Seismic hazard is now clearly recognized as a national problem, and analytical and experimental research is being pursued in a number of regional centers and universities. However, there are great regional variations in seismic hazard levels. California, in particular, has had extensive experience with damaging earthquakes that have significantly influenced building design. Seismic codes, design practices and related land use and rehabilitation provisions originated in California and have been refined there for decades. Most of the material in this publication, developed by authors with first-hand experience, draws on that readily available wealth of knowledge and lessons learned.

Each chapter includes references to other readily available publications and other sources that will enable the interested reader to dig deeper into the subject matter.

150. Assignment 6, Module 1: ARA Mitigation Study, Sections 5.2 and 5.3: https://enclosurenews.com/PDFs/ARA_Loss_Mitigation_Study.pdf

5.2 Group I Buildings

The analysis of Group I MF residential buildings is divided into two major building code eras: pre-FBC and post-FBC. Pre-FBC construction refers to all site-built MF buildings built before the implementation of the 2001 Florida Building Code (permitted prior to March 1, 2002). Post-FBC construction refers to any Florida building permitted on or after March 1, 2002 and includes two eras (FBC 2001 and FBC 2006). This separation recognizes the changes brought about by the FBC and the fact that the methods used to verify the construction features may be different for existing and new construction.

5.2.1 Pre-FBC Construction

The development of loss relativities for Group I MF residential buildings built prior to the FBC follows the same approach used in Section 4.2 for pre-FBC single-family homes. For Group I buildings, the determination of the presence or absence of wind mitigation features for houses built prior to the FBC is made from an inspection/verification process. That is, since Group I buildings permitted before March 1, 2002 were built to different standards in different parts of the state, it was concluded that the determination of wind mitigation features should be accomplished though visual inspection on a building-by-building basis. In other words, it was not practical to evaluate and develop loss relativities for all the possible year-built construction eras on a statewide basis. Hence, the concept of verifiable wind mitigation features through an inspection process has driven the development of rate differentials for Group I buildings permitted prior to March 1, 2002.

The mitigation features for Group I construction follow from the single family residence features discussed in Section 4. New features include: roof cover type, roof slope, and soffits. We also include a flat roof shape for Group I. Group I construction is based on modeled 2 story buildings and we do not consider number of stories as a factor for Group I.

5.2.1.1 Loss Relativity Tables Normalized to Typical Construction

Table 5-2 through Table 5-5 are the loss relativity tables, normalized to typical construction. These tables are analogous to Table 4-5 through Table 4-8. The typical building corresponds to the low-slope other roof shape, non-tile and non-FBC roof cover, clips, Deck B, no shutters and wood soffits. This is the same typical building used to normalize the single family tables, except that for Group I, the building is two stories instead of one.

The range of relativities is less that the same range for the single family houses. For example, in Terrain B, the strongest building has a relativity that is 2.27 lower than the typical building, whereas the weakest building has a relativity that is 1.86 time larger than the typical building. The overall range is 4.2 vs. 7.5 for Terrain B single family.

In Terrain C, the strongest building has a relativity that is 3.75 times lower than the typical building and the weakest building has a relativity that is 1.58 times larger than the typical building. The overall range is 5.9, which is less than the overall Terrain C single family range of 10.3.

Table 5-2. Group I Terrain B Non-FBC, Normalized to Typical Building

Group I Terrain B-Normalized toTypical					Flat		Low Roof Slope (≤ 5:12)								Other Roof slope (> 5:12)							
					Built-Up		Non-tile				Tile				Non-tile				Tile			
							Other		Hip		Other		Hip		Other		Hip		Other		Hip	
Roof Cover	Roof Deck	Roof-Wall	Opening Prot.	Soffits	No SWR	SWR	No SWR	SWR	No SWR	SWR	No SWR	SWR	No SWR	SWR	No SWR	SWR	No SWR	SWR	No SWR	SWR	No SWR	SWR
Non-FBC	A	Toe Nails	None	Other			1.6106	1.3132	1.2365	1.0815	1.7966	1.5881	1.4680	1.3634	1.6198	1.3535	1.2347	1.0988	1.6786	1.4976	1.3578	1.2716
				Wood	1.8579	1.8330	1.3421	1.0943	1.0304	0.9012	1.4972	1.3234	1.2231	1.1362	1.3498	1.1279	1.0289	0.9157	1.3988	1.2480	1.1315	1.0597
			Hurricane	Other			1.2856	0.9533	0.9025	0.7162	1.5570	1.3278	1.2268	1.0935	1.1889	0.8752	0.8424	0.6822	1.4306	1.2348	1.1506	1.0464
				Wood	1.5021	1.3477	1.0713	0.7944	0.7521	0.5969	1.2975	1.1065	1.0224	0.9163	0.9908	0.7293	0.7020	0.5685	1.1922	1.0290	0.9588	0.8720
		Clips	None	Other			1.4724	1.1728	1.1053	0.9488	1.6697	1.4667	1.3579	1.2521	1.4011	1.1226	1.0267	0.8840	1.5105	1.3329	1.2201	1.1276
				Wood	1.7771	1.7128	1.2693	1.0110	0.9528	0.8179	1.4394	1.2644	1.1706	1.0794	1.2078	0.9678	0.8851	0.7621	1.3022	1.1491	1.0518	0.9721
			Hurricane	Other			1.2292	0.9001	0.8685	0.6790	1.5006	1.2762	1.1805	1.0553	1.1318	0.8194	0.8020	0.6432	1.3743	1.1816	1.1019	1.0044
				Wood	1.4896	1.3198	1.0597	0.7759	0.7487	0.5854	1.2936	1.1028	1.0206	0.9148	0.9757	0.7064	0.6914	0.5545	1.1847	1.0186	0.9499	0.8659
		Wraps	None	Other			1.3560	1.0633	1.0205	0.8650	1.5778	1.3836	1.2963	1.1966	1.2418	0.9614	0.9054	0.7580	1.4303	1.2504	1.1544	1.0655
				Wood	1.7363	1.6474	1.2107	0.9494	0.9111	0.7723	1.4087	1.2353	1.1574	1.0684	1.1087	0.8584	0.8084	0.6768	1.2771	1.1165	1.0307	0.9513
			Hurricane	Other			1.1800	0.8633	0.8337	0.6528	1.4482	1.2324	1.1412	1.0199	1.0833	0.7819	0.7688	0.6130	1.3243	1.1399	1.0626	0.9689
				Wood	1.4866	1.3161	1.0535	0.7708	0.7444	0.5829	1.2930	1.1004	1.0189	0.9106	0.9672	0.6981	0.6864	0.5473	1.1824	1.0177	0.9487	0.8651
	B	Toe Nails	None	Other			1.3304	1.0913	1.1453	1.0121	1.5578	1.3714	1.3725	1.2728	1.4659	1.2337	1.1883	1.0749	1.5193	1.3458	1.3140	1.2315
				Wood	1.2793	1.2697	1.1087	0.9044	0.9544	0.8434	1.2981	1.1429	1.1438	1.0607	1.2215	1.0281	0.9902	0.8958	1.2661	1.1215	1.0950	1.0262
			Hurricane	Other			0.9749	0.7121	0.8034	0.6509	1.2988	1.0930	1.1445	1.0317	0.9860	0.7120	0.7930	0.6469	1.2998	1.0679	1.1068	1.0064
				Wood	0.8672	0.7664	0.8124	0.5934	0.6895	0.5425	1.0823	0.9109	0.9538	0.8597	0.8217	0.5933	0.6609	0.5391	1.0498	0.8899	0.9224	0.8387
		Clips	None	Other			1.1600	0.9130	0.9802	0.8420	1.4108	1.2264	1.2349	1.1327	1.1990	0.9492	0.9590	0.8351	1.3402	1.1609	1.1401	1.0530
				Wood	1.1237	1.0701	1.0000	0.7870	0.8450	0.7259	1.2162	1.0573	1.0646	0.9765	1.0336	0.8183	0.8267	0.7199	1.1553	1.0008	0.9829	0.9077
			Hurricane	Other			0.9008	0.6299	0.7577	0.6015	1.2471	1.0448	1.1004	0.9909	0.9117	0.6337	0.7467	0.6032	1.2093	1.0224	1.0610	0.9685
				Wood	0.8262	0.6991	0.7765	0.5430	0.6532	0.5185	1.0750	0.9007	0.9486	0.8542	0.7860	0.5463	0.6437	0.5200	1.0425	0.8814	0.9147	0.8349
		Wraps	None	Other			1.0326	0.7831	0.8551	0.7168	1.3037	1.1132	1.1343	1.0298	1.0127	0.7548	0.7958	0.6628	1.2121	1.0313	1.0453	0.9554
				Wood	1.0314	0.9465	0.9220	0.6892	0.7635	0.6400	1.1640	0.9940	1.0128	0.9195	0.9042	0.6739	0.7105	0.5918	1.0823	0.9208	0.9333	0.8510
			Hurricane	Other			0.8616	0.5972	0.7236	0.5747	1.1979	1.0034	1.0561	0.9487	0.8695	0.5955	0.7095	0.5704	1.1612	0.9781	1.0213	0.9310
				Wood	0.8156	0.6841	0.7693	0.5332	0.6461	0.5131	1.0696	0.8959	0.9429	0.8471	0.7763	0.5317	0.6315	0.5093	1.0386	0.8793	0.9129	0.8312
	C	Toe Nails	None	Other			1.3256	1.0952	1.1409	1.0110	1.5413	1.3625	1.3810	1.2809	1.4632	1.2214	1.1943	1.0774	1.5118	1.3388	1.3083	1.2247
				Wood	1.2617	1.2213	1.1046	0.9127	0.9508	0.8425	1.2861	1.1354	1.1508	1.0674	1.2110	1.0178	0.9953	0.8978	1.2998	1.1157	1.0903	1.0206
			Hurricane	Other			0.9573	0.7090	0.8022	0.6511	1.2861	1.0888	1.1483	1.0310	0.9858	0.7120	0.7921	0.6471	1.2588	1.0657	1.1090	1.0131
				Wood	0.8292	0.7431	0.7978	0.5909	0.6685	0.5426	1.0717	0.9073	0.9569	0.8583	0.8215	0.5934	0.6601	0.5393	1.0490	0.8881	0.9242	0.8442
		Clips	None	Other			1.1470	0.9089	0.9745	0.8416	1.4036	1.2236	1.2316	1.1307	1.1981	0.9506	0.9531	0.8283	1.3308	1.1538	1.1451	1.0592
				Wood	1.0937	1.0487	0.9888	0.7835	0.8401	0.7256	1.2100	1.0548	1.0618	0.9748	1.0329	0.8195	0.8216	0.7140	1.1473	0.9947	0.9871	0.9131
			Hurricane	Other			0.8818	0.6280	0.7543	0.6015	1.2304	1.0375	1.0997	0.9878	0.9054	0.6300	0.7450	0.6029	1.2070	1.0175	1.0585	0.9680
				Wood	0.7833	0.6750	0.7601	0.5414	0.6503	0.5185	1.0607	0.8944	0.9480	0.8515	0.7805	0.5431	0.6423	0.5197	1.0405	0.8772	0.9125	0.8345
		Wraps	None	Other			1.0210	0.7844	0.8510	0.7114	1.2894	1.1067	1.1327	1.0294	1.0061	0.7539	0.7953	0.6620	1.2064	1.0265	1.0475	0.9576
				Wood	0.9824	0.9132	0.9116	0.7003	0.7598	0.6152	1.1513	0.9881	1.0113	0.9191	0.8983	0.6731	0.7101	0.5911	1.0772	0.9165	0.9353	0.8550
			Hurricane	Other			0.8472	0.5958	0.7192	0.5743	1.1802	0.9940	1.0533	0.9479	0.8597	0.5933	0.7065	0.5667	1.1568	0.9748	1.0182	0.9275
				Wood	0.7713	0.6562	0.7565	0.5319	0.6421	0.5127	1.0538	0.8875	0.9405	0.8464	0.7676	0.5297	0.6308	0.5060	1.0328	0.8704	0.9091	0.8282

Table 5-3. Group I Terrain B FBC, Normalized to Typical Building

Group I Terrain B-Normalized to Typical					Flat		Low Roof Slope (< 5:12)								Other Roof slope (≥ 6:12)							
					Built-Up		Non-tile				Tile				Non-tile				Tile			
							Other		Hip		Other		Hip		Other		Hip		Other		Hip	
Roof Cover	Roof Deck	Roof-Wall	Opening Prot.	Soffits	No SWR	SWR	No SWR	SWR	No SWR	SWR	No SWR	SWR	No SWR	SWR	No SWR	SWR	No SWR	SWR	No SWR	SWR	No SWR	SWR
FBC	A	Toe Nails	None	Other			1.2448	1.2053	1.0155	0.9851	1.2234	1.1934	1.0307	1.0167	1.2625	1.2500	1.0220	1.0192	1.1267	1.1153	0.9414	0.9364
				Wood	1.3927	1.3231	1.0373	1.0044	0.8463	0.8293	1.0195	0.9945	0.8589	0.8472	1.0521	1.0416	0.8517	0.8493	0.9389	0.9294	0.7845	0.7803
			Hurricane	Other			0.8756	0.8426	0.6314	0.6191	0.9494	0.9236	0.7539	0.7414	0.7881	0.7709	0.6005	0.5927	0.8621	0.8474	0.7154	0.7081
				Wood	0.9675	0.9503	0.7297	0.7021	0.5262	0.5159	0.7911	0.7697	0.6282	0.6178	0.6567	0.6424	0.5004	0.4939	0.7184	0.7062	0.5962	0.5901
		Clips	None	Other			1.1064	1.0715	0.8678	0.8531	1.1052	1.0812	0.9250	0.9129	1.0329	1.0182	0.8028	0.7954	0.9815	0.9677	0.7987	0.7939
				Wood	1.2798	1.2211	0.9538	0.9237	0.7481	0.7355	0.9527	0.9321	0.7974	0.7870	0.8904	0.8778	0.6921	0.6857	0.8461	0.8342	0.6885	0.6844
			Hurricane	Other			0.8234	0.7902	0.6000	0.5876	0.9161	0.8878	0.7209	0.7112	0.7346	0.7145	0.5683	0.5581	0.8220	0.8095	0.6811	0.6744
				Wood	0.9545	0.9419	0.7099	0.6812	0.5173	0.5066	0.7897	0.7654	0.6214	0.6131	0.6333	0.6159	0.4900	0.4812	0.7086	0.6979	0.5872	0.5814
		Wraps	None	Other			0.9878	0.9564	0.7861	0.7734	1.0294	1.0064	0.8724	0.8630	0.8741	0.8586	0.6996	0.6629	0.8919	0.8808	0.7422	0.7372
				Wood	1.2246	1.1633	0.8820	0.8539	0.7019	0.6905	0.9191	0.8986	0.7789	0.7705	0.7805	0.7666	0.5978	0.5918	0.7964	0.7865	0.6626	0.6583
			Hurricane	Other			0.7902	0.7567	0.5776	0.5631	0.8805	0.8544	0.6955	0.6862	0.7067	0.6856	0.5384	0.5268	0.7921	0.7802	0.6544	0.6500
				Wood	0.9506	0.9083	0.7056	0.6757	0.5157	0.5027	0.7862	0.7628	0.6210	0.6127	0.6310	0.6121	0.4807	0.4721	0.7072	0.6966	0.5843	0.5804
	B	Toe Nails	None	Other			1.0461	1.0109	0.9523	0.9335	1.0408	1.0143	0.9602	0.9467	1.1521	1.1392	0.9983	0.9941	1.0238	1.0101	0.9096	0.9048
				Wood	1.1667	1.1084	0.8718	0.8419	0.7936	0.7779	0.8673	0.8453	0.8002	0.7890	0.9601	0.9494	0.8319	0.8284	0.8532	0.8418	0.7580	0.7540
			Hurricane	Other			0.6538	0.6246	0.5758	0.5644	0.7628	0.7393	0.7008	0.6951	0.6476	0.6258	0.5714	0.5612	0.7446	0.7267	0.6896	0.6807
				Wood	0.7159	0.6801	0.5448	0.5205	0.4799	0.4703	0.6357	0.6161	0.5840	0.5792	0.5397	0.5215	0.4762	0.4676	0.6205	0.6056	0.5746	0.5673
		Clips	None	Other			0.8667	0.8326	0.7718	0.7575	0.9089	0.8853	0.8245	0.8142	0.8880	0.8675	0.7565	0.7496	0.8486	0.8318	0.7449	0.7392
				Wood	0.9924	0.9480	0.7472	0.7177	0.6653	0.6530	0.7835	0.7632	0.7108	0.7019	0.7655	0.7479	0.6522	0.6462	0.7316	0.7171	0.6421	0.6372
			Hurricane	Other			0.5790	0.5443	0.5330	0.5212	0.7265	0.7019	0.6708	0.6614	0.5794	0.5521	0.5314	0.5230	0.7061	0.6860	0.6524	0.6453
				Wood	0.6621	0.6290	0.4991	0.4692	0.4595	0.4493	0.6263	0.6051	0.5782	0.5701	0.4995	0.4759	0.4581	0.4509	0.6087	0.5913	0.5624	0.5563
		Wraps	None	Other			0.7377	0.7064	0.6431	0.6320	0.8073	0.7867	0.7220	0.7159	0.7083	0.6823	0.5887	0.5814	0.7278	0.7104	0.6563	0.6513
				Wood	0.8784	0.8345	0.6587	0.6307	0.5742	0.5643	0.7208	0.7024	0.6446	0.6392	0.6324	0.6092	0.5256	0.5191	0.6499	0.6343	0.5860	0.5815
			Hurricane	Other			0.5489	0.5138	0.5059	0.4924	0.6927	0.6724	0.6454	0.6347	0.5448	0.5177	0.4894	0.4817	0.6708	0.6563	0.6251	0.6171
				Wood	0.6489	0.6165	0.4901	0.4618	0.4517	0.4443	0.6185	0.6004	0.5762	0.5667	0.4864	0.4622	0.4500	0.4432	0.5989	0.5860	0.5604	0.5550
	C	Toe Nails	None	Other			1.0416	1.0095	0.9494	0.9290	1.0410	1.0189	0.9593	0.9462	1.1555	1.1427	1.0057	0.9996	1.0237	1.0094	0.9104	0.9057
				Wood	1.1639	1.1057	0.8680	0.8412	0.7912	0.7742	0.8675	0.8491	0.7994	0.7885	0.9629	0.9522	0.8381	0.8310	0.8530	0.8412	0.7586	0.7548
			Hurricane	Other			0.6443	0.6189	0.5753	0.5646	0.7523	0.7307	0.7020	0.6926	0.6453	0.6276	0.5664	0.5578	0.7404	0.7226	0.6851	0.6815
				Wood	0.7120	0.6764	0.5369	0.5141	0.4794	0.4705	0.6269	0.6089	0.5850	0.5773	0.5378	0.5230	0.4720	0.4649	0.6170	0.6021	0.5709	0.5679
		Clips	None	Other			0.8553	0.8223	0.7694	0.7561	0.9075	0.8842	0.8185	0.8111	0.8914	0.8710	0.7998	0.7919	0.8470	0.8309	0.7402	0.7357
				Wood	0.9875	0.9381	0.7373	0.7088	0.6633	0.6518	0.7823	0.7622	0.7056	0.6992	0.7684	0.7509	0.6550	0.6499	0.7301	0.7163	0.6181	0.6142
			Hurricane	Other			0.5697	0.5414	0.5304	0.5188	0.7177	0.6930	0.6703	0.6609	0.5748	0.5484	0.5304	0.5167	0.7011	0.6826	0.6527	0.6469
				Wood	0.6539	0.6212	0.4911	0.4667	0.4572	0.4473	0.6187	0.5974	0.5778	0.5697	0.4955	0.4727	0.4572	0.4455	0.6044	0.5885	0.5627	0.5577
		Wraps	None	Other			0.7286	0.6987	0.6431	0.6330	0.7990	0.7796	0.7209	0.7142	0.6958	0.6736	0.5880	0.5797	0.7277	0.7117	0.6557	0.6503
				Wood	0.8742	0.8358	0.6505	0.6238	0.5742	0.5652	0.7134	0.6961	0.6437	0.6377	0.6213	0.6014	0.5250	0.5176	0.6497	0.6355	0.5855	0.5806
			Hurricane	Other			0.5412	0.5110	0.5055	0.4942	0.6869	0.6632	0.6427	0.6344	0.5400	0.5126	0.5019	0.4932	0.6707	0.6542	0.6253	0.6189
				Wood	0.6422	0.6101	0.4832	0.4563	0.4513	0.4412	0.6133	0.5922	0.5738	0.5665	0.4821	0.4577	0.4481	0.4404	0.5989	0.5841	0.5583	0.5526

Table 5-4. Group I Terrain C Non-FBC, Normalized to Typical Building

Group I Terrain C-Normaillized to Typical					Flat		Low Roof Slope (≤ 5:12)								Other Roof slope (> 5:12)							
					Built-Up		Non-tile				Tile				Non-tile				Tile			
							Other		Hip		Other		Hip		Other		Hip		Other		Hip	
Roof Cover	Roof Deck	Roof-Wall	Opening Prot.	Soffits	No SWR	SWR	No SWR	SWR	No SWR	SWR	No SWR	SWR	No SWR	SWR	No SWR	SWR	No SWR	SWR	No SWR	SWR	No SWR	SWR
Non-FBC	A	Toe Nails	None	Other			1.3430	1.1894	1.1531	1.0636	1.4068	1.2912	1.2480	1.1801	1.4533	1.3060	1.2162	1.1342	1.3512	1.2403	1.1421	1.0801
				Wood	1.5841	1.3347	1.2406	1.0997	1.0664	0.9843	1.2991	1.1911	1.1534	1.0912	1.3418	1.2067	1.1243	1.0490	1.2482	1.1464	1.0563	0.9995
			Hurricane	Other			0.8071	0.5877	0.5694	0.4181	0.9031	0.7431	0.7022	0.5966	0.7699	0.5431	0.5300	0.3924	0.8393	0.6947	0.6554	0.5677
				Wood	0.9632	0.6187	0.7490	0.5477	0.5309	0.3921	0.8370	0.6902	0.6527	0.5559	0.7093	0.5068	0.4947	0.3685	0.7785	0.6459	0.6098	0.5293
		Clips	None	Other			1.2732	1.1106	1.0901	0.9940	1.3408	1.2252	1.1670	1.1015	1.2878	1.1185	1.0354	0.9312	1.2015	1.0854	0.9564	0.8833
				Wood	1.5359	1.2616	1.1865	1.0959	1.0170	0.9280	1.2491	1.1421	1.0882	1.0275	1.2000	1.0433	0.9663	0.8699	1.1201	1.0126	0.8932	0.8255
			Hurricane	Other			0.7861	0.5597	0.5617	0.4050	0.8941	0.7343	0.6951	0.5887	0.7505	0.5217	0.5200	0.3813	0.8301	0.6852	0.6455	0.5585
				Wood	0.9542	0.6076	0.7355	0.5258	0.5277	0.3827	0.8355	0.6882	0.6516	0.5533	0.7026	0.4907	0.4891	0.3606	0.7762	0.6420	0.6061	0.5247
		Wraps	None	Other			1.2230	1.0600	1.0186	0.9220	1.2599	1.1435	1.1137	1.0499	1.1477	0.9627	0.8485	0.7307	1.0774	0.9555	0.8704	0.7945
				Wood	1.5012	1.2198	1.1498	0.9974	0.9587	0.8684	1.1842	1.0755	1.0476	0.9879	1.0794	0.9065	0.7997	0.6896	1.0136	0.8998	0.8202	0.7492
			Hurricane	Other			0.7786	0.5521	0.5537	0.3982	0.8865	0.7289	0.6897	0.5846	0.7350	0.5107	0.5124	0.3734	0.8213	0.6786	0.6412	0.5531
				Wood	0.9501	0.6031	0.7344	0.5227	0.5242	0.3789	0.8352	0.6880	0.6514	0.5531	0.6937	0.4840	0.4857	0.3557	0.7743	0.6409	0.6060	0.5237
	B	Toe Nails	None	Other			1.1743	1.0483	1.0733	0.9946	1.2466	1.1359	1.1572	1.0908	1.3463	1.2218	1.1699	1.0997	1.2272	1.1189	1.0923	1.0161
				Wood	1.2601	1.1781	1.0858	0.9703	0.9932	0.9210	1.1522	1.0506	1.0701	1.0092	1.2436	1.1294	1.0818	1.0174	1.1344	1.0350	1.0106	0.9590
			Hurricane	Other			0.5795	0.4082	0.4740	0.3579	0.7042	0.5558	0.6266	0.5357	0.5983	0.4059	0.4731	0.3559	0.6931	0.5464	0.6076	0.5266
				Wood	0.5328	0.4079	0.5401	0.3830	0.4433	0.3368	0.6546	0.5184	0.5833	0.4999	0.5574	0.3809	0.4426	0.3351	0.6444	0.5098	0.5660	0.4916
		Clips	None	Other			1.0718	0.9294	0.9754	0.8868	1.1592	1.0433	1.0384	0.9703	1.1417	0.9917	0.9691	0.8809	1.0306	0.9091	0.8615	0.7938
				Wood	1.1420	1.0448	1.0000	0.8682	0.9108	0.8287	1.0809	0.9736	0.9692	0.9060	1.0648	0.9259	0.9049	0.8233	0.9619	0.8494	0.8053	0.7426
			Hurricane	Other			0.5358	0.3483	0.4529	0.3311	0.6889	0.5418	0.6144	0.5232	0.5556	0.3511	0.4552	0.3322	0.6786	0.5315	0.5986	0.5144
				Wood	0.4940	0.3535	0.5037	0.3301	0.4270	0.3142	0.6455	0.5093	0.5765	0.4921	0.5221	0.3327	0.4291	0.3152	0.6360	0.4998	0.5618	0.4840
		Wraps	None	Other			1.0021	0.8537	0.8509	0.7568	1.0293	0.9071	0.8845	0.8071	0.9436	0.7747	0.7136	0.6066	0.8380	0.7020	0.6834	0.6022
				Wood	1.0605	0.9518	0.9412	0.8046	0.8019	0.7140	0.9687	0.8545	0.8134	0.7610	0.8886	0.7307	0.6737	0.5736	0.7899	0.6628	0.6454	0.5696
			Hurricane	Other			0.5252	0.3361	0.4469	0.3230	0.6810	0.5348	0.6093	0.5169	0.5426	0.3352	0.4449	0.3217	0.6683	0.5196	0.5870	0.5045
				Wood	0.4902	0.3446	0.4975	0.3208	0.4244	0.3086	0.6432	0.5065	0.5762	0.4898	0.5139	0.3200	0.4225	0.3074	0.6313	0.4923	0.5554	0.4782
	C	Toe Nails	None	Other			1.1683	1.0465	1.0719	0.9925	1.2415	1.1318	1.1564	1.0910	1.3472	1.2254	1.1785	1.1091	1.2254	1.1203	1.0970	1.0422
				Wood	1.2449	1.1755	1.0803	0.9686	0.9919	0.9191	1.1475	1.0468	1.0694	1.0094	1.2445	1.1327	1.0897	1.0260	1.1327	1.0363	1.0150	0.9647
			Hurricane	Other			0.5663	0.4048	0.4757	0.3588	0.6886	0.5513	0.6257	0.5359	0.5965	0.4063	0.4735	0.3553	0.6846	0.5430	0.6081	0.5275
				Wood	0.5024	0.4040	0.5280	0.3799	0.4449	0.3377	0.6403	0.5143	0.5825	0.5002	0.5557	0.3812	0.4429	0.3345	0.6366	0.5067	0.5664	0.4924
		Clips	None	Other			1.0632	0.9250	0.9686	0.8793	1.1525	1.0409	1.0366	0.9692	1.1313	0.9847	0.9759	0.8882	1.0253	0.9065	0.8661	0.7970
				Wood	1.1191	1.0417	0.9921	0.8641	0.9045	0.8218	1.0748	0.9714	0.9674	0.9090	1.0552	0.9194	0.9113	0.8300	0.9569	0.8470	0.8096	0.7455
			Hurricane	Other			0.5151	0.3420	0.4514	0.3303	0.6764	0.5355	0.6144	0.5234	0.5525	0.3480	0.4539	0.3328	0.6720	0.5265	0.5950	0.5141
				Wood	0.4563	0.3469	0.4846	0.3243	0.4256	0.3134	0.6339	0.5035	0.5765	0.4922	0.5192	0.3299	0.4279	0.3157	0.6298	0.4951	0.5586	0.4837
		Wraps	None	Other			0.9900	0.8440	0.8505	0.7570	1.0220	0.9026	0.8800	0.8018	0.9459	0.7787	0.7137	0.6081	0.8341	0.6997	0.6814	0.6036
				Wood	1.0317	0.9465	0.9320	0.7955	0.8016	0.7142	0.9619	0.8503	0.8292	0.7561	0.8908	0.7345	0.6737	0.5750	0.7863	0.6607	0.6436	0.5709
			Hurricane	Other			0.5022	0.3289	0.4436	0.3216	0.6674	0.5269	0.6067	0.5161	0.5362	0.3316	0.4416	0.3200	0.6613	0.5165	0.5864	0.5043
				Wood	0.4477	0.3360	0.4761	0.3141	0.4213	0.3073	0.6304	0.4992	0.5738	0.4890	0.5079	0.3166	0.4194	0.3058	0.6247	0.4894	0.5547	0.4780

Table 5-5. Group I Terrain C FBC, Normalized to Typical Building

Group I Terrain C-Normalized to Typical					Flat		Low Roof Slope (≤ 5:12)								Other Roof slope (> 5:12)							
					Built-Up		Non-tile				Tile				Non-tile				Tile			
							Other		Hip		Other		Hip		Other		Hip		Other		Hip	
Roof Cover	Roof Deck	Roof-Wall	Opening Prot	Soffits	No SWR	SWR	No SWR	SWR	No SWR	SWR	No SWR	SWR	No SWR	SWR	No SWR	SWR	No SWR	SWR	No SWR	SWR	No SWR	SWR
FBC	A	Toe Nails	None	Other			1.1748	1.1405	1.0409	1.0173	1.1471	1.1199	1.0519	1.0314	1.2716	1.2628	1.0973	1.0936	1.0754	1.0675	0.9305	0.9270
				Wood	1.3471	1.3131	1.0863	1.0548	0.9635	0.9418	1.0609	1.0360	0.9735	0.9547	1.1751	1.1670	1.0152	1.0118	0.9951	0.9878	0.8622	0.8590
			Hurricane	Other			0.5611	0.5305	0.3819	0.3689	0.5819	0.5567	0.4421	0.4301	0.5076	0.4894	0.3558	0.3456	0.5263	0.5121	0.4114	0.4050
				Wood	0.6110	0.5929	0.5233	0.4952	0.3589	0.3470	0.5423	0.5192	0.4141	0.4031	0.4742	0.4575	0.3349	0.3256	0.4913	0.4783	0.3859	0.3801
		Clips	None	Other			1.0961	1.0637	0.9728	0.9498	1.0795	1.0543	0.9603	0.9447	1.0715	1.0602	0.8938	0.8886	0.9037	0.8939	0.7246	0.7197
				Wood	1.2674	1.2347	1.0225	0.9926	0.9084	0.8871	1.0072	0.9838	0.8968	0.8824	0.9998	0.9893	0.8352	0.8304	0.8444	0.8353	0.6786	0.6740
			Hurricane	Other			0.5361	0.5033	0.3695	0.3542	0.5730	0.5475	0.4346	0.4226	0.4841	0.4649	0.3442	0.3342	0.5180	0.5037	0.4044	0.3978
				Wood	0.5993	0.5821	0.5041	0.4736	0.3497	0.3356	0.5382	0.5146	0.4100	0.3997	0.4561	0.4381	0.3264	0.3171	0.4873	0.4740	0.3820	0.3759
		Wraps	None	Other			1.0434	1.0128	0.8988	0.8799	0.9944	0.9725	0.8988	0.8876	0.9185	0.9060	0.6828	0.6769	0.7695	0.7601	0.6224	0.6179
				Wood	1.2348	1.2031	0.9819	0.9513	0.8467	0.8290	0.9361	0.9156	0.8467	0.8363	0.8652	0.8535	0.6449	0.6394	0.7259	0.7171	0.5884	0.5842
			Hurricane	Other			0.5286	0.4956	0.3652	0.3492	0.5663	0.5423	0.4313	0.4202	0.4756	0.4556	0.3374	0.3265	0.5092	0.4959	0.3996	0.3936
				Wood	0.5969	0.5805	0.5008	0.4699	0.3481	0.3331	0.5360	0.5135	0.4098	0.3995	0.4512	0.4325	0.3220	0.3119	0.4827	0.4702	0.3802	0.3746
	B	Toe Nails	None	Other			1.0366	1.0069	0.9721	0.9494	1.0187	0.9938	0.9636	0.9458	1.1926	1.1832	1.0761	1.0736	0.9848	0.9748	0.9031	0.8997
				Wood	1.2007	1.1723	0.9595	0.9323	0.9004	0.8795	0.9431	0.9203	0.8925	0.8762	1.1027	1.0940	0.9957	0.9935	0.9120	0.9028	0.8371	0.8319
			Hurricane	Other			0.3930	0.3654	0.3269	0.3157	0.4268	0.4090	0.3924	0.3822	0.3858	0.3662	0.3202	0.3124	0.4138	0.3974	0.3818	0.3753
				Wood	0.4150	0.4015	0.3690	0.3437	0.3084	0.2982	0.4000	0.3800	0.3685	0.3591	0.3625	0.3445	0.3023	0.2951	0.3882	0.3731	0.3588	0.3528
		Clips	None	Other			0.9255	0.8932	0.8589	0.8404	0.9215	0.8995	0.8412	0.8282	0.9649	0.9491	0.8467	0.8424	0.7887	0.7763	0.6512	0.6460
				Wood	1.0644	1.0416	0.8645	0.8347	0.8029	0.7858	0.8609	0.8405	0.7866	0.7745	0.9011	0.8864	0.7916	0.7826	0.7379	0.7264	0.6106	0.6057
			Hurricane	Other			0.3407	0.3064	0.3025	0.2896	0.4155	0.3925	0.3829	0.3732	0.3367	0.3085	0.3008	0.2909	0.4003	0.3821	0.3699	0.3624
				Wood	0.3616	0.3462	0.3231	0.2914	0.2877	0.2758	0.3924	0.3711	0.3622	0.3532	0.3194	0.2932	0.2861	0.2770	0.3783	0.3615	0.3502	0.3432
		Wraps	None	Other			0.8454	0.8148	0.7362	0.7222	0.7825	0.7634	0.6674	0.6586	0.7620	0.7405	0.5757	0.5676	0.5718	0.5551	0.4602	0.4532
				Wood	0.9739	0.9291	0.7968	0.7683	0.6948	0.6817	0.7380	0.7202	0.6305	0.6223	0.7188	0.6988	0.5448	0.5372	0.5411	0.5255	0.4368	0.4303
			Hurricane	Other			0.3311	0.2950	0.2945	0.2809	0.4097	0.3862	0.3776	0.3681	0.3251	0.2945	0.2904	0.2791	0.3918	0.3728	0.3632	0.3548
				Wood	0.3536	0.3371	0.3162	0.2824	0.2820	0.2693	0.3896	0.3677	0.3596	0.3508	0.3106	0.2819	0.2782	0.2676	0.3729	0.3551	0.3462	0.3383
	C	Toe Nails	None	Other			1.0406	1.0099	0.9704	0.9488	1.0146	0.9901	0.9653	0.9481	1.1934	1.1844	1.0719	1.0692	0.9889	0.9792	0.9011	0.8979
				Wood	1.1962	1.1683	0.9632	0.9350	0.8988	0.8789	0.9393	0.9168	0.8941	0.8784	1.1033	1.0951	0.9919	0.9894	0.9158	0.9069	0.8352	0.8322
			Hurricane	Other			0.3875	0.3646	0.3273	0.3166	0.4200	0.4011	0.3922	0.3825	0.3836	0.3653	0.3217	0.3139	0.4115	0.3963	0.3817	0.3750
				Wood	0.4105	0.4003	0.3640	0.3430	0.3088	0.2990	0.3938	0.3764	0.3683	0.3594	0.3605	0.3436	0.3036	0.2965	0.3860	0.3721	0.3587	0.3525
		Clips	None	Other			0.9189	0.8906	0.8614	0.8428	0.9246	0.9019	0.8357	0.8239	0.9588	0.9444	0.8485	0.8438	0.7797	0.7672	0.6905	0.6851
				Wood	1.0543	1.0324	0.8585	0.8322	0.8052	0.7880	0.8637	0.8427	0.7814	0.7705	0.8954	0.8821	0.7933	0.7890	0.7295	0.7180	0.6099	0.6049
			Hurricane	Other			0.3287	0.3001	0.3008	0.2884	0.4069	0.3861	0.3810	0.3708	0.3348	0.3093	0.3001	0.2902	0.3981	0.3814	0.3691	0.3623
				Wood	0.3520	0.3407	0.3120	0.2855	0.2861	0.2746	0.3844	0.3652	0.3604	0.3509	0.3177	0.2940	0.2855	0.2763	0.3763	0.3608	0.3494	0.3431
		Wraps	None	Other			0.8352	0.8074	0.7352	0.7212	0.7774	0.7578	0.6626	0.6537	0.7611	0.7420	0.5780	0.5701	0.5681	0.5534	0.4596	0.4529
				Wood	0.9709	0.9242	0.7873	0.7613	0.6938	0.6807	0.7333	0.7149	0.6260	0.6176	0.7181	0.7002	0.5469	0.5395	0.5372	0.5239	0.4363	0.4300
			Hurricane	Other			0.3191	0.2899	0.2929	0.2799	0.3996	0.3797	0.3747	0.3643	0.3199	0.2920	0.2892	0.2779	0.3884	0.3712	0.3624	0.3556
				Wood	0.3420	0.3298	0.3050	0.2777	0.2805	0.2683	0.3802	0.3616	0.3570	0.3472	0.3057	0.2797	0.2770	0.2665	0.3698	0.3536	0.3454	0.3391

The differences in typical and strong and weak buildings indicate that the modeled reductions in loss are reasonable when compared to a typical building. These ranges are reduced over those obtained in Section 4 for single family houses due to the fact that the number of stories is not a factor for Group I buildings and the buildings are larger than single family houses. Larger buildings have a smaller percentage of the envelope that is near a corner or eave, where the negative pressure coefficients are the most severe. The introduction of the flat roof shape tends to increase the range, but does not make up the difference due to the consideration of only one model building height. Another consideration is that the loads have been updated and improved in the modeling of roof shape and these updates are reflected in the model results for sloped and flat roofs considered in Group I.

5.2.1.2 Loss Relativities Normalized to Weakest Construction

Table 5-6 through Table 5-9 provide the loss relativities for Group I construction normalized to the weakest building, which is the flat roof building for both Terrain B and C. The strongest building in both Terrain B and Terrain C corresponds to:

- Other Roof Slope ($\geq$ 6:12)
- Non-tile
- Hip
- SWR
- FBC Roof Cover
- Roof Deck C
- Wrap Roof-to Wall
- Hurricane Opening Protection
- Wood Soffits

The relativities of these buildings are 0.2370 in Terrain B and 0.1682 in Terrain C.

Similar to the analysis in Section 4 for single family residences, we see that tile roof coverings and roof slope can have both positive and negative impacts. In general, non-tile roof coverings produce lower relativities and high slope roofs are generally better than low-slope roofs.

5.2.1.3 Group I Secondary Factors

The secondary factors for Group I incorporate those in Table 4-15 for single family residences with the following exception:

- Reinforced concrete roof deck does not apply. Group I buildings must have wood roof decks. A group I building that has a reinforced concrete roof deck is treated as a Group II multifamily residence.

Two new secondary factors are considered for Group I buildings with a flat roof shape. These factors are parapets and rooftop equipment (RTE). Parapets of sufficient height can dramatically reduce the wind loads on a flat roof. Inadequately-restrained RTE is highly vulnerable to wind damage. If the restraints for the RTE fail, total replacement (vs. repair) of the RTE is generally required. These two features are rare for Group I buildings with wooden roof decks, but we have analyzed both parapets and RTE for Group I buildings.

Table 5-6. Group I Terrain B Non-FBC, Normalized to Weakest

Group I Terrain B-Normalized to Weakest					Flat		Low Roof Slope (≤ 5:12)								Other Roof slope (> 5:12)							
					Built-Up		Non-tile				Tile				Non-tile				Tile			
							Other		Hip		Other		Hip		Other		Hip		Other		Hip	
Roof Cover	Roof Deck	Roof-Wall	Opening Prot.	Soffits	No SWR	SWR	No SWR	SWR	No SWR	SWR	No SWR	SWR	No SWR	SWR	No SWR	SWR	No SWR	SWR	No SWR	SWR	No SWR	SWR
Non-FBC	A	Toe Nails	None	Other			0.8669	0.7068	0.6655	0.5821	0.9670	0.8548	0.7901	0.7338	0.8718	0.7285	0.6646	0.5914	0.9085	0.8060	0.7308	0.6844
				Wood	1.0000	0.9866	0.7224	0.5890	0.5546	0.4851	0.8058	0.7123	0.6584	0.6115	0.7265	0.6071	0.5538	0.4929	0.7529	0.6717	0.6090	0.5704
			Hurricane	Other			0.6920	0.5131	0.4858	0.3855	0.8380	0.7147	0.6603	0.5918	0.6399	0.4711	0.4534	0.3672	0.7700	0.6646	0.6193	0.5632
				Wood	0.8085	0.7254	0.5766	0.4276	0.4048	0.3213	0.6984	0.5956	0.5503	0.4932	0.5333	0.3926	0.3779	0.3060	0.6417	0.5539	0.5161	0.4693
		Clips	None	Other			0.7925	0.6312	0.5949	0.5107	0.8987	0.7894	0.7309	0.6739	0.7541	0.6042	0.5526	0.4758	0.8130	0.7174	0.6567	0.6069
				Wood	0.9565	0.9219	0.6832	0.5442	0.5128	0.4402	0.7747	0.6805	0.6301	0.5810	0.6501	0.5209	0.4764	0.4102	0.7009	0.6185	0.5661	0.5232
			Hurricane	Other			0.6616	0.4844	0.4674	0.3655	0.8077	0.6869	0.6354	0.5680	0.6092	0.4410	0.4317	0.3462	0.7397	0.6360	0.5931	0.5406
				Wood	0.8068	0.7103	0.5704	0.4176	0.4030	0.3151	0.6961	0.5936	0.5493	0.4924	0.5252	0.3802	0.3721	0.2985	0.6377	0.5482	0.5113	0.4660
		Wraps	None	Other			0.7298	0.5723	0.5492	0.4656	0.8492	0.7447	0.6977	0.6441	0.6684	0.5175	0.4873	0.4080	0.7698	0.6730	0.6213	0.5715
				Wood	0.9345	0.8867	0.6516	0.5110	0.4904	0.4157	0.7582	0.6649	0.6230	0.5751	0.5968	0.4620	0.4351	0.3643	0.6874	0.6009	0.5547	0.5120
			Hurricane	Other			0.6351	0.4647	0.4487	0.3514	0.7795	0.6633	0.6142	0.5490	0.5831	0.4208	0.4138	0.3299	0.7128	0.6135	0.5719	0.5215
				Wood	0.8001	0.7084	0.5671	0.4149	0.4007	0.3137	0.6960	0.5923	0.5484	0.4901	0.5206	0.3757	0.3694	0.2946	0.6364	0.5478	0.5106	0.4656
	B	Toe Nails	None	Other			0.7161	0.5874	0.6164	0.5447	0.8384	0.7382	0.7387	0.6851	0.7890	0.6640	0.6396	0.5786	0.8177	0.7244	0.7072	0.6628
				Wood	0.6886	0.6834	0.5967	0.4895	0.5137	0.4539	0.6987	0.6151	0.6156	0.5709	0.6575	0.5533	0.5330	0.4821	0.6814	0.6036	0.5894	0.5524
			Hurricane	Other			0.5247	0.3833	0.4324	0.3504	0.6991	0.5883	0.6160	0.5553	0.5307	0.3832	0.4268	0.3482	0.6781	0.5748	0.5957	0.5417
				Wood	0.4667	0.4125	0.4373	0.3194	0.3603	0.2920	0.5825	0.4903	0.5134	0.4627	0.4422	0.3193	0.3557	0.2901	0.5650	0.4790	0.4964	0.4514
		Clips	None	Other			0.6244	0.4914	0.5276	0.4532	0.7594	0.6601	0.6647	0.6097	0.6453	0.5109	0.5162	0.4495	0.7213	0.6249	0.6136	0.5667
				Wood	0.6048	0.5760	0.5382	0.4236	0.4548	0.3907	0.6546	0.5691	0.5730	0.5256	0.5563	0.4404	0.4450	0.3875	0.6218	0.5387	0.5290	0.4886
			Hurricane	Other			0.4848	0.3390	0.4078	0.3237	0.6712	0.5624	0.5923	0.5333	0.4907	0.3411	0.4019	0.3247	0.6509	0.5903	0.5711	0.5213
				Wood	0.4447	0.3763	0.4180	0.2923	0.3516	0.2791	0.5786	0.4848	0.5106	0.4598	0.4230	0.2940	0.3465	0.2799	0.5611	0.4744	0.4923	0.4494
		Wraps	None	Other			0.5558	0.4215	0.4602	0.3858	0.7017	0.5992	0.6105	0.5543	0.5451	0.4063	0.4283	0.3567	0.6524	0.5551	0.5626	0.5142
				Wood	0.5551	0.5094	0.4962	0.3768	0.4109	0.3445	0.6265	0.5350	0.5451	0.4949	0.4867	0.3627	0.3824	0.3185	0.5825	0.4956	0.5023	0.4591
			Hurricane	Other			0.4647	0.3214	0.3895	0.3093	0.6448	0.5401	0.5684	0.5106	0.4680	0.3205	0.3819	0.3070	0.6261	0.5264	0.5497	0.5011
				Wood	0.4390	0.3682	0.4141	0.2870	0.3477	0.2762	0.5757	0.4822	0.5075	0.4559	0.4178	0.2862	0.3410	0.2741	0.5590	0.4700	0.4908	0.4474
	C	Toe Nails	None	Other			0.7135	0.5895	0.6141	0.5441	0.8107	0.7314	0.7433	0.6894	0.7821	0.6574	0.6428	0.5799	0.8137	0.7206	0.7042	0.6592
				Wood	0.6791	0.6573	0.5946	0.4912	0.5117	0.4535	0.6922	0.6111	0.6194	0.5745	0.6518	0.5478	0.5357	0.4832	0.6781	0.6005	0.5868	0.5493
			Hurricane	Other			0.5153	0.3816	0.4318	0.3505	0.6922	0.5860	0.6181	0.5544	0.5306	0.3832	0.4263	0.3483	0.6776	0.5736	0.5969	0.5453
				Wood	0.4463	0.4000	0.4294	0.3180	0.3598	0.2921	0.5768	0.4884	0.5150	0.4620	0.4422	0.3194	0.3553	0.2903	0.5646	0.4780	0.4974	0.4544
		Clips	None	Other			0.6173	0.4892	0.5245	0.4530	0.7555	0.6586	0.6629	0.6086	0.6449	0.5116	0.5130	0.4458	0.7163	0.6210	0.6163	0.5701
				Wood	0.5887	0.5645	0.5322	0.4217	0.4521	0.3905	0.6513	0.5677	0.5715	0.5247	0.5559	0.4411	0.4422	0.3843	0.6175	0.5354	0.5313	0.4914
			Hurricane	Other			0.4746	0.3380	0.4060	0.3237	0.6623	0.5584	0.5919	0.5317	0.4873	0.3391	0.4010	0.3245	0.6497	0.5477	0.5697	0.5210
				Wood	0.4216	0.3633	0.4091	0.2914	0.3500	0.2791	0.5709	0.4814	0.5102	0.4583	0.4201	0.2923	0.3457	0.2797	0.5601	0.4721	0.4911	0.4491
		Wraps	None	Other			0.5495	0.4222	0.4580	0.3829	0.6940	0.5956	0.6096	0.5541	0.5415	0.4057	0.4281	0.3563	0.6493	0.5525	0.5638	0.5154
				Wood	0.5288	0.4915	0.4906	0.3769	0.4090	0.3419	0.6197	0.5318	0.5443	0.4947	0.4835	0.3623	0.3822	0.3181	0.5798	0.4933	0.5034	0.4602
			Hurricane	Other			0.4560	0.3207	0.3871	0.3091	0.6352	0.5350	0.5669	0.5102	0.4627	0.3193	0.3803	0.3050	0.6226	0.5247	0.5480	0.4992
				Wood	0.4151	0.3532	0.4072	0.2863	0.3496	0.2760	0.5672	0.4777	0.5062	0.4555	0.4131	0.2851	0.3395	0.2724	0.5559	0.4685	0.4893	0.4457

Table 5-7. Terrain B FBC, Normalized to Weakest

Group I Terrain B-Normalized to Weakest					Flat		Low Roof Slope (≤ 5:12)								Other Roof Slope (> 6:12)							
					Built-Up		Non-tile				Tile				Non-tile				Tile			
							Other		Hip		Other		Hip		Other		Hip		Other		Hip	
Roof Cover	Roof Deck	Roof-Wall	Opening Prot.	Soffits	No SWR	SWR	No SWR	SWR	No SWR	SWR	No SWR	SWR	No SWR	SWR	No SWR	SWR	No SWR	SWR	No SWR	SWR	No SWR	SWR
FBC	A	Toe Nails	None	Other			0.6700	0.6487	0.5466	0.5356	0.6585	0.6423	0.5548	0.5472	0.6795	0.6728	0.5901	0.5486	0.6064	0.6003	0.5067	0.5040
				Wood	0.7496	0.7121	0.5583	0.5406	0.4555	0.4463	0.5488	0.5353	0.4623	0.4560	0.5663	0.5606	0.4584	0.4571	0.5054	0.5002	0.4223	0.4200
			Hurricane	Other			0.4713	0.4535	0.3899	0.3832	0.5110	0.4971	0.4058	0.3990	0.4242	0.4149	0.3232	0.3190	0.4640	0.4561	0.3851	0.3811
				Wood	0.5207	0.5115	0.3927	0.3779	0.2832	0.2777	0.4258	0.4143	0.3381	0.3325	0.3535	0.3458	0.2694	0.2658	0.3867	0.3801	0.3209	0.3176
		Clips	None	Other			0.5955	0.5767	0.4671	0.4592	0.5949	0.5820	0.4978	0.4914	0.5559	0.5480	0.4321	0.4281	0.5283	0.5209	0.4299	0.4273
				Wood	0.6888	0.6572	0.5134	0.4972	0.4027	0.3959	0.5128	0.5017	0.4292	0.4236	0.4793	0.4725	0.3725	0.3691	0.4554	0.4490	0.3706	0.3684
			Hurricane	Other			0.4432	0.4253	0.3229	0.3163	0.4931	0.4778	0.3880	0.3828	0.3954	0.3846	0.3059	0.3004	0.4424	0.4357	0.3666	0.3630
				Wood	0.5137	0.5069	0.3821	0.3667	0.2784	0.2727	0.4251	0.4119	0.3345	0.3300	0.3409	0.3315	0.2637	0.2590	0.3814	0.3756	0.3160	0.3129
		Wraps	None	Other			0.5317	0.5148	0.4231	0.4163	0.5541	0.5417	0.4696	0.4645	0.4705	0.4621	0.3604	0.3568	0.4801	0.4741	0.3995	0.3968
				Wood	0.6591	0.6261	0.4742	0.4596	0.3778	0.3717	0.4947	0.4837	0.4193	0.4147	0.4201	0.4126	0.3218	0.3185	0.4286	0.4233	0.3567	0.3543
			Hurricane	Other			0.4253	0.4073	0.3109	0.3031	0.4739	0.4598	0.3744	0.3693	0.3804	0.3690	0.2898	0.2846	0.4263	0.4199	0.3522	0.3499
				Wood	0.5117	0.4889	0.3798	0.3637	0.2776	0.2706	0.4231	0.4106	0.3342	0.3298	0.3396	0.3295	0.2587	0.2541	0.3807	0.3749	0.3145	0.3124
	B	Toe Nails	None	Other			0.5631	0.5438	0.5126	0.5024	0.5602	0.5459	0.5168	0.5096	0.6201	0.6132	0.5373	0.5351	0.5511	0.5437	0.4896	0.4870
				Wood	0.6280	0.5966	0.4692	0.4532	0.4272	0.4187	0.4668	0.4550	0.4107	0.4246	0.5168	0.5110	0.4478	0.4459	0.4592	0.4531	0.4080	0.4058
			Hurricane	Other			0.3519	0.3362	0.3099	0.3038	0.4106	0.3979	0.3772	0.3741	0.3486	0.3368	0.3075	0.3020	0.4008	0.3911	0.3712	0.3664
				Wood	0.3853	0.3661	0.2932	0.2801	0.2583	0.2531	0.3421	0.3316	0.3141	0.3118	0.2905	0.2807	0.2563	0.2517	0.3340	0.3259	0.3093	0.3053
		Clips	None	Other			0.4665	0.4481	0.4154	0.4077	0.4892	0.4765	0.4438	0.4382	0.4280	0.4669	0.4072	0.4034	0.4567	0.4477	0.4009	0.3979
				Wood	0.5342	0.5103	0.4022	0.3863	0.3581	0.3515	0.4217	0.4108	0.3825	0.3778	0.4120	0.4025	0.3510	0.3478	0.3937	0.3860	0.3456	0.3430
			Hurricane	Other			0.3116	0.2930	0.2869	0.2805	0.3910	0.3778	0.3610	0.3560	0.3138	0.2972	0.2860	0.2815	0.3800	0.3692	0.3511	0.3473
				Wood	0.3563	0.3385	0.2687	0.2526	0.2473	0.2418	0.3371	0.3257	0.3112	0.3069	0.2688	0.2562	0.2466	0.2427	0.3276	0.3183	0.3027	0.2994
		Wraps	None	Other			0.3971	0.3802	0.3462	0.3402	0.4345	0.4234	0.3886	0.3853	0.3812	0.3672	0.3169	0.3130	0.3918	0.3824	0.3533	0.3505
				Wood	0.4728	0.4491	0.3545	0.3395	0.3091	0.3037	0.3880	0.3781	0.3470	0.3440	0.3404	0.3279	0.2829	0.2794	0.3498	0.3414	0.3154	0.3130
			Hurricane	Other			0.2954	0.2766	0.2723	0.2650	0.3728	0.3619	0.3474	0.3416	0.2932	0.2786	0.2688	0.2646	0.3611	0.3532	0.3364	0.3322
				Wood	0.3493	0.3318	0.2638	0.2485	0.2431	0.2391	0.3329	0.3232	0.3101	0.3050	0.2618	0.2488	0.2422	0.2386	0.3224	0.3154	0.3016	0.2987
	C	Toe Nails	None	Other			0.5606	0.5433	0.5110	0.5000	0.5603	0.5484	0.5163	0.5093	0.6219	0.6150	0.5413	0.5380	0.5510	0.5433	0.4900	0.4875
				Wood	0.6265	0.5951	0.4672	0.4528	0.4258	0.4167	0.4669	0.4570	0.4303	0.4244	0.5183	0.5125	0.4511	0.4483	0.4591	0.4527	0.4083	0.4062
			Hurricane	Other			0.3468	0.3320	0.3096	0.3039	0.4049	0.3933	0.3778	0.3729	0.3473	0.3378	0.3049	0.3002	0.3985	0.3889	0.3687	0.3668
				Wood	0.3832	0.3641	0.2890	0.2767	0.2580	0.2532	0.3374	0.3278	0.3149	0.3107	0.2894	0.2815	0.2541	0.2502	0.3321	0.3241	0.3073	0.3057
		Clips	None	Other			0.4604	0.4426	0.4141	0.4070	0.4884	0.4759	0.4406	0.4366	0.4798	0.4688	0.4089	0.4058	0.4559	0.4472	0.3984	0.3960
				Wood	0.5315	0.5049	0.3969	0.3815	0.3570	0.3508	0.4211	0.4103	0.3798	0.3763	0.4136	0.4042	0.3525	0.3498	0.3930	0.3855	0.3435	0.3414
			Hurricane	Other			0.3066	0.2914	0.2855	0.2793	0.3863	0.3730	0.3608	0.3557	0.3094	0.2951	0.2855	0.2781	0.3773	0.3674	0.3513	0.3482
				Wood	0.3520	0.3344	0.2643	0.2512	0.2461	0.2407	0.3330	0.3215	0.3110	0.3066	0.2667	0.2544	0.2461	0.2398	0.3253	0.3167	0.3029	0.3002
		Wraps	None	Other			0.3922	0.3760	0.3461	0.3407	0.4301	0.4196	0.3880	0.3844	0.3745	0.3626	0.3165	0.3120	0.3917	0.3831	0.3529	0.3500
				Wood	0.4706	0.4498	0.3501	0.3358	0.3091	0.3042	0.3840	0.3747	0.3465	0.3432	0.3344	0.3237	0.2826	0.2786	0.3497	0.3420	0.3151	0.3125
			Hurricane	Other			0.2913	0.2750	0.2721	0.2690	0.3697	0.3570	0.3459	0.3415	0.2906	0.2759	0.2701	0.2655	0.3610	0.3521	0.3365	0.3331
				Wood	0.3457	0.3284	0.2601	0.2456	0.2429	0.2375	0.3301	0.3187	0.3089	0.3049	0.2595	0.2464	0.2412	0.2370	0.3223	0.3144	0.3005	0.2974

Table 5-8. Group I Terrain C Non-FBC, Normalized to Weakest

Group I Terrain C- Normalized to Weakest					Flat		Low Roof Slope (≤ 5:12)								Other Roof Slope (≥ 6:12)							
					Built-Up		Non-tile				Tile				Non-tile				Tile			
							Other		Hip		Other		Hip		Other		Hip		Other		Hip	
Roof Cover	Roof Deck	Roof-Wall	Opening Prot.	Soffits	No SWR	SWR	No SWR	SWR	No SWR	SWR	No SWR	SWR	No SWR	SWR	No SWR	SWR	No SWR	SWR	No SWR	SWR	No SWR	SWR
Non-FBC	A	Toe Nails	None	Other			0.8478	0.7509	0.7279	0.6714	0.8881	0.8151	0.7878	0.7450	0.9175	0.8244	0.7678	0.7160	0.8530	0.7830	0.7210	0.6819
				Wood	1.0000	0.8426	0.7832	0.6942	0.6732	0.6214	0.8201	0.7532	0.7281	0.6888	0.8471	0.7617	0.7097	0.6622	0.7879	0.7237	0.6668	0.6309
			Hurricane	Other			0.5095	0.3710	0.3595	0.2640	0.5701	0.4691	0.4433	0.3766	0.4822	0.3429	0.3346	0.2477	0.5298	0.4386	0.4137	0.3584
				Wood	0.6080	0.3906	0.4728	0.3457	0.3351	0.2475	0.5284	0.4357	0.4120	0.3509	0.4478	0.3199	0.3123	0.2326	0.4914	0.4077	0.3849	0.3342
		Clips	None	Other			0.8037	0.7011	0.6882	0.6275	0.8464	0.7735	0.7367	0.6953	0.8129	0.7061	0.6536	0.5879	0.7585	0.6852	0.6038	0.5576
				Wood	0.9696	0.7964	0.7490	0.6540	0.6420	0.5858	0.7886	0.7210	0.6870	0.6486	0.7575	0.6586	0.6100	0.5491	0.7071	0.6392	0.5639	0.5211
			Hurricane	Other			0.4963	0.3533	0.3546	0.2557	0.5644	0.4635	0.4388	0.3716	0.4738	0.3293	0.3283	0.2407	0.5240	0.4325	0.4075	0.3526
				Wood	0.6024	0.3836	0.4643	0.3320	0.3331	0.2416	0.5274	0.4345	0.4113	0.3493	0.4435	0.3098	0.3088	0.2277	0.4900	0.4053	0.3826	0.3313
		Wraps	None	Other			0.7721	0.6692	0.6430	0.5820	0.7954	0.7219	0.7031	0.6628	0.7245	0.6077	0.5356	0.4613	0.6801	0.6032	0.5495	0.5015
				Wood	0.9477	0.7700	0.7258	0.6296	0.6052	0.5482	0.7476	0.6789	0.6613	0.6237	0.6814	0.5722	0.5048	0.4353	0.6399	0.5680	0.5178	0.4730
			Hurricane	Other			0.4915	0.3485	0.3495	0.2514	0.5596	0.4602	0.4354	0.3691	0.4640	0.3224	0.3235	0.2357	0.5185	0.4284	0.4048	0.3492
				Wood	0.5998	0.3807	0.4636	0.3300	0.3309	0.2392	0.5273	0.4343	0.4112	0.3492	0.4379	0.3056	0.3066	0.2246	0.4868	0.4046	0.3825	0.3306
	B	Toe Nails	None	Other			0.7413	0.6618	0.6776	0.6279	0.7869	0.7171	0.7105	0.6816	0.8499	0.7713	0.7386	0.6942	0.7747	0.7063	0.6895	0.6540
				Wood	0.7955	0.7437	0.6865	0.6125	0.6270	0.5814	0.7273	0.6632	0.6755	0.6371	0.7851	0.7130	0.6829	0.6423	0.7161	0.6534	0.6380	0.6054
			Hurricane	Other			0.3658	0.2577	0.2992	0.2259	0.4446	0.3509	0.3955	0.3381	0.3777	0.2562	0.2987	0.2247	0.4376	0.3449	0.3836	0.3324
				Wood	0.3363	0.2575	0.3410	0.2418	0.2799	0.2126	0.4132	0.3273	0.3682	0.3156	0.3519	0.2404	0.2794	0.2115	0.4068	0.3218	0.3573	0.3103
		Clips	None	Other			0.6766	0.5867	0.6158	0.5598	0.7318	0.6586	0.6556	0.6125	0.7207	0.6261	0.6117	0.5561	0.6506	0.5739	0.5439	0.5011
				Wood	0.7209	0.6596	0.6313	0.5481	0.5750	0.5232	0.6824	0.6146	0.6118	0.5720	0.6722	0.5845	0.5712	0.5197	0.6072	0.5362	0.5084	0.4688
			Hurricane	Other			0.3382	0.2199	0.2859	0.2090	0.4349	0.3420	0.3878	0.3303	0.3507	0.2216	0.2873	0.2097	0.4284	0.3356	0.3779	0.3247
				Wood	0.3118	0.2231	0.3180	0.2084	0.2695	0.1983	0.4075	0.3215	0.3639	0.3106	0.3296	0.2100	0.2709	0.1990	0.4085	0.3155	0.3547	0.3055
		Wraps	None	Other			0.6326	0.5389	0.5371	0.4778	0.6498	0.5727	0.5584	0.5095	0.5957	0.4890	0.4505	0.3829	0.5290	0.4432	0.4314	0.3802
				Wood	0.6695	0.6009	0.5955	0.5079	0.5062	0.4508	0.6115	0.5394	0.5261	0.4804	0.5610	0.4613	0.4253	0.3621	0.4986	0.4184	0.4074	0.3596
			Hurricane	Other			0.3315	0.2122	0.2821	0.2039	0.4299	0.3376	0.3846	0.3263	0.3425	0.2116	0.2808	0.2031	0.4219	0.3280	0.3706	0.3185
				Wood	0.3095	0.2175	0.3141	0.2025	0.2679	0.1948	0.4060	0.3198	0.3637	0.3092	0.3244	0.2020	0.2667	0.1941	0.3985	0.3108	0.3506	0.3019
	C	Toe Nails	None	Other			0.7375	0.6607	0.6767	0.6265	0.7837	0.7145	0.7300	0.6887	0.8505	0.7735	0.7440	0.7001	0.7736	0.7072	0.6925	0.6579
				Wood	0.7858	0.7421	0.6820	0.6115	0.6262	0.5802	0.7244	0.6608	0.6751	0.6372	0.7856	0.7150	0.6879	0.6477	0.7151	0.6542	0.6407	0.6090
			Hurricane	Other			0.3575	0.2556	0.3003	0.2265	0.4347	0.3481	0.3950	0.3383	0.3765	0.2565	0.2989	0.2241	0.4322	0.3428	0.3839	0.3310
				Wood	0.3171	0.2590	0.3333	0.2398	0.2808	0.2132	0.4042	0.3247	0.3677	0.3157	0.3508	0.2407	0.2796	0.2112	0.4019	0.3199	0.3576	0.3108
		Clips	None	Other			0.6712	0.5839	0.6115	0.5551	0.7276	0.6571	0.6544	0.6118	0.7142	0.6216	0.6161	0.5607	0.6472	0.5723	0.5468	0.5031
				Wood	0.7065	0.6576	0.6263	0.5455	0.5710	0.5188	0.6785	0.6132	0.6107	0.5713	0.6661	0.5804	0.5753	0.5240	0.6041	0.5347	0.5111	0.4706
			Hurricane	Other			0.3252	0.2159	0.2850	0.2085	0.4270	0.3381	0.3879	0.3304	0.3488	0.2197	0.2865	0.2101	0.4242	0.3324	0.3756	0.3246
				Wood	0.2880	0.2190	0.3059	0.2047	0.2687	0.1979	0.4002	0.3178	0.3640	0.3107	0.3277	0.2082	0.2701	0.1993	0.3976	0.3126	0.3526	0.3053
		Wraps	None	Other			0.6250	0.5328	0.5369	0.4779	0.6452	0.5698	0.5555	0.5062	0.5971	0.4916	0.4505	0.3839	0.5266	0.4417	0.4302	0.3810
				Wood	0.6513	0.5975	0.5883	0.5022	0.5060	0.4509	0.6072	0.5368	0.5234	0.4773	0.5623	0.4637	0.4253	0.3630	0.4964	0.4171	0.4063	0.3604
			Hurricane	Other			0.3170	0.2076	0.2800	0.2030	0.4213	0.3326	0.3830	0.3258	0.3385	0.2093	0.2788	0.2020	0.4174	0.3260	0.3702	0.3183
				Wood	0.2826	0.2121	0.3005	0.1983	0.2659	0.1940	0.3980	0.3151	0.3622	0.3087	0.3206	0.1999	0.2648	0.1930	0.3944	0.3090	0.3502	0.3018

Table 5-9. Group I Terrain C FBC, Normalized to Weakest

Group I Terrain C- Normalized to Weakest					Flat		Low Roof Slope (≤ 5:12)								Other Roof slope (> 5:12)							
					Built-Up		Non-tile				Tile				Non-tile				Tile			
							Other		Hip		Other		Hip		Other		Hip		Other		Hip	
Roof Cover	Roof Deck	Roof-Wall	Opening Prot.	Soffits	No SWR	SWR	No SWR	SWR	No SWR	SWR	No SWR	SWR	No SWR	SWR	No SWR	SWR	No SWR	SWR	No SWR	SWR	No SWR	SWR
FBC	A	Toe Nails	None	Other			0.7416	0.7200	0.6571	0.6422	0.7241	0.7070	0.6640	0.6511	0.8027	0.7972	0.6927	0.6904	0.6789	0.6739	0.5874	0.5852
				Wood	0.8504	0.8290	0.6857	0.6659	0.6082	0.5945	0.6997	0.6540	0.6146	0.6027	0.7418	0.7367	0.6409	0.6388	0.6282	0.6236	0.5443	0.5422
			Hurricane	Other			0.3542	0.3349	0.2411	0.2329	0.3673	0.3514	0.2791	0.2715	0.3204	0.3090	0.2246	0.2182	0.3322	0.3233	0.2597	0.2557
				Wood	0.3857	0.3743	0.3303	0.3126	0.2265	0.2190	0.3423	0.3278	0.2614	0.2545	0.2993	0.2888	0.2134	0.2055	0.3101	0.3019	0.2436	0.2399
		Clips	None	Other			0.6919	0.6715	0.6141	0.5996	0.6815	0.6656	0.6062	0.5964	0.6764	0.6693	0.5642	0.5610	0.5705	0.5643	0.4575	0.4543
				Wood	0.8001	0.7795	0.6455	0.6266	0.5734	0.5600	0.6358	0.6211	0.5661	0.5570	0.6311	0.6245	0.5272	0.5242	0.5330	0.5273	0.4284	0.4255
			Hurricane	Other			0.3385	0.3177	0.2332	0.2236	0.3617	0.3456	0.2743	0.2668	0.3058	0.2935	0.2173	0.2110	0.3270	0.3180	0.2553	0.2511
				Wood	0.3783	0.3674	0.3182	0.2990	0.2208	0.2118	0.3397	0.3248	0.2588	0.2523	0.2879	0.2769	0.2060	0.2002	0.3076	0.2992	0.2412	0.2373
		Wraps	None	Other			0.6587	0.6394	0.5674	0.5554	0.6277	0.6139	0.5674	0.5603	0.5798	0.5720	0.4411	0.4273	0.4857	0.4798	0.3929	0.3900
				Wood	0.7795	0.7595	0.6199	0.6018	0.5345	0.5234	0.5909	0.5780	0.5345	0.5279	0.5462	0.5188	0.4071	0.4036	0.4582	0.4527	0.3714	0.3688
			Hurricane	Other			0.3337	0.3129	0.2306	0.2205	0.3575	0.3423	0.2723	0.2653	0.3002	0.2876	0.2130	0.2061	0.3215	0.3130	0.2523	0.2485
				Wood	0.3768	0.3665	0.3161	0.2967	0.2197	0.2103	0.3384	0.3242	0.2587	0.2522	0.2848	0.2731	0.2033	0.1969	0.3047	0.2968	0.2400	0.2365
	B	Toe Nails	None	Other			0.6544	0.6357	0.6137	0.5993	0.6431	0.6274	0.6083	0.5970	0.7529	0.7469	0.6793	0.6778	0.6217	0.6153	0.5701	0.5679
				Wood	0.7580	0.7400	0.6057	0.5885	0.5684	0.5552	0.5953	0.5809	0.5634	0.5531	0.6961	0.6906	0.6286	0.6272	0.5757	0.5699	0.5284	0.5264
			Hurricane	Other			0.2481	0.2307	0.2064	0.1993	0.2694	0.2556	0.2477	0.2412	0.2436	0.2312	0.2022	0.1972	0.2612	0.2508	0.2411	0.2369
				Wood	0.2620	0.2535	0.2330	0.2170	0.1947	0.1882	0.2525	0.2399	0.2326	0.2267	0.2288	0.2175	0.1908	0.1863	0.2490	0.2355	0.2265	0.2227
		Clips	None	Other			0.5842	0.5639	0.5422	0.5305	0.5817	0.5678	0.5311	0.5228	0.6091	0.5991	0.5345	0.5318	0.4979	0.4900	0.4111	0.4078
				Wood	0.6719	0.6576	0.5458	0.5269	0.5068	0.4961	0.5434	0.5306	0.4965	0.4889	0.5688	0.5596	0.4997	0.4972	0.4658	0.4585	0.3855	0.3824
			Hurricane	Other			0.2151	0.1934	0.1910	0.1828	0.2623	0.2478	0.2417	0.2356	0.2126	0.1947	0.1899	0.1836	0.2527	0.2412	0.2335	0.2288
				Wood	0.2283	0.2185	0.2039	0.1839	0.1816	0.1741	0.2477	0.2342	0.2286	0.2229	0.2016	0.1851	0.1806	0.1748	0.2388	0.2282	0.2211	0.2166
		Wraps	None	Other			0.5337	0.5144	0.4648	0.4559	0.4940	0.4819	0.4213	0.4158	0.4810	0.4675	0.3634	0.3583	0.3610	0.3504	0.2905	0.2861
				Wood	0.6148	0.5865	0.5030	0.4850	0.4386	0.4303	0.4659	0.4547	0.3980	0.3928	0.4518	0.4412	0.3439	0.3391	0.3416	0.3318	0.2757	0.2716
			Hurricane	Other			0.2090	0.1862	0.1859	0.1773	0.2586	0.2438	0.2384	0.2324	0.2052	0.1859	0.1834	0.1762	0.2473	0.2353	0.2293	0.2240
				Wood	0.2233	0.2128	0.1996	0.1783	0.1780	0.1700	0.2460	0.2321	0.2270	0.2214	0.1961	0.1780	0.1756	0.1689	0.2354	0.2242	0.2185	0.2136
	C	Toe Nails	None	Other			0.6569	0.6375	0.6126	0.5989	0.6405	0.6250	0.6094	0.5985	0.7534	0.7477	0.6767	0.6750	0.6243	0.6182	0.5688	0.5668
				Wood	0.7551	0.7375	0.6080	0.5902	0.5674	0.5548	0.5930	0.5788	0.5644	0.5545	0.6965	0.6913	0.6262	0.6246	0.5781	0.5725	0.5272	0.5254
			Hurricane	Other			0.2446	0.2301	0.2066	0.1999	0.2651	0.2532	0.2476	0.2415	0.2422	0.2306	0.2031	0.1981	0.2598	0.2502	0.2410	0.2367
				Wood	0.2591	0.2527	0.2298	0.2165	0.1949	0.1887	0.2486	0.2376	0.2325	0.2269	0.2275	0.2169	0.1917	0.1871	0.2437	0.2349	0.2264	0.2225
		Clips	None	Other			0.5801	0.5622	0.5438	0.5321	0.5837	0.5693	0.5275	0.5201	0.6052	0.5962	0.5357	0.5327	0.4922	0.4843	0.4106	0.4072
				Wood	0.6656	0.6517	0.5420	0.5254	0.5083	0.4975	0.5452	0.5320	0.4933	0.4864	0.5652	0.5569	0.5008	0.4981	0.4605	0.4533	0.3850	0.3819
			Hurricane	Other			0.2075	0.1894	0.1899	0.1820	0.2569	0.2438	0.2405	0.2341	0.2114	0.1953	0.1895	0.1812	0.2513	0.2408	0.2330	0.2287
				Wood	0.2222	0.2151	0.1970	0.1802	0.1806	0.1734	0.2427	0.2305	0.2275	0.2215	0.2005	0.1856	0.1802	0.1744	0.2375	0.2278	0.2206	0.2166
		Wraps	None	Other			0.5273	0.5097	0.4641	0.4553	0.4908	0.4784	0.4183	0.4126	0.4805	0.4684	0.3649	0.3599	0.3586	0.3493	0.2902	0.2859
				Wood	0.6129	0.5835	0.4970	0.4806	0.4380	0.4297	0.4629	0.4513	0.3952	0.3899	0.4533	0.4420	0.3453	0.3406	0.3394	0.3307	0.2754	0.2714
			Hurricane	Other			0.2015	0.1830	0.1849	0.1767	0.2522	0.2397	0.2366	0.2300	0.2019	0.1844	0.1826	0.1754	0.2452	0.2343	0.2288	0.2245
				Wood	0.2159	0.2082	0.1925	0.1753	0.1771	0.1694	0.2400	0.2282	0.2253	0.2192	0.1930	0.1765	0.1749	0.1682	0.2334	0.2232	0.2181	0.2141

Parapets and Rooftop Equipment. The results in Table 5-2 through Table 5-9 are for the case of no parapet and no RTE. Parapets can have a significant effect on reducing the extent and magnitude of negative pressures on a flat roof. As discussed in Section 3.6.1, wind tunnel test data have been used to model this effect. The parapets must be at least 6 feet in height to achieve the full benefit of the pressure reduction. Rooftop equipment (RTE) is vulnerable to wind damage, which adds to the losses for a building. RTE failures can also result in holes in the flat roof cover, thereby producing another path for water to enter the building.

We analyzed flat roof shape Group I buildings for 4 cases that cover the possibilities for the presence of parapets and inadequately-restrained rooftop equipment. We performed 72 simulations for each case. Table 5-10 summarizes the results of these simulations. Figure 5-1 also shows the resulting K_i factors for the possible cases of parapets and RTE for Group I buildings. Adequately-restrained RTE should be tested as "No" RTE in Table 5-10.

Table 5-10. Flat Roof Group I Parapet and RTE Secondary Factor K_i Values

Parapet and RTE Cases		*K_i Value*	
Parapet	*Inadequately-Restrained Rooftop Equipment*	*No SWR*	*SWR*
No	No	1.00	1.00
No	Yes	1.04	1.04
Yes	No	0.86	0.93
Yes	Yes	0.90	0.97

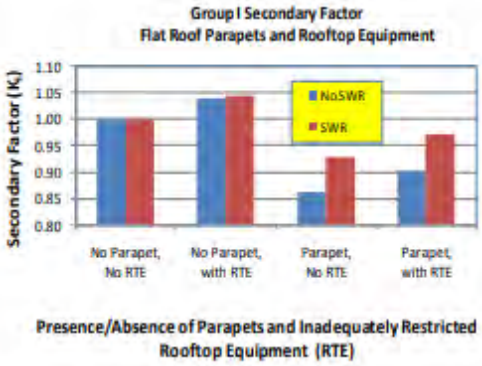

Figure 5-1. Effect of Parapets and Inadequately-Restrained RTE on Group I Buildings.

The Group I multi-family secondary factors are summarized in Table 5-11. This table is a similar to Table 4-15, except for the addition of parapets and RTE. The secondary factors are applied in the same manner as for single family houses using Equations (4-1), (4-2), and (4-3).

5.2.2 Post-FBC Construction

Wind loading provisions of the Florida Building Code (FBC) and effective dates of FBC code changes were summarized in Section 2.2.3. Two FBC construction eras were identified for the purposes of developing loss relativities for wind mitigation features:

1. FBC 2001 includes permit application dates of March 1, 2002 through December 7, 2006.
2. FBC 2006 includes permit applications on or after December 8, 2006.

There are several methods by which the FBC era can be determined and these are discussed in Section 2.2.4.8. There are many code amendments between these dates. The FBC 2006 date is significant since ring-shank nails, and soffit loads, and an option for 150 mph shingles were all introduced at that time. We designed buildings to the 2006 FBC and used our previous designs from the 2002 loss relativity study for the FBC 2001 designs.

Section 5.2.2.1 contains the Group I 2006 FBC loss relativities and Section 1 contains the 2001 FBC loss relativities.

Table 5-11. Multi-Family Group I Secondary Factors (K_3).

No.	*Secondary Factor Description*	*Can Apply to post-FBC era*	*Loss Relativity Multiplier (K_3)*	*Comments*
1	Dimensional Lumber Deck	Yes	0.96	Based on 2002 study. Applies to Deck C.
2	Unreinforced Masonry Walls	No	0.98	Based on 2002 study.
3	Reinforced Masonry Walls	Yes	0.95	Based on 2002 study; Secondary Factors 2 and 3 are mutually exclusive.
4	Opening Coverage - All Openings[1]	Yes Except not in HVHZ	0.98 Hurricane Only.	Based on 2002 study. Applies to Hurricane Protection Level; does not apply to other protection levels.
5	Unbraced Gable End	No	1.02	Based on 2002 study.
6	Foundation Restraint	No	Ter B: 1.38; Ter C: 1.54	Based on 2002 study.
7	Reinforced Concrete Roof Deck Integrate with Concrete or Reinforced Masonry Walls	Yes	DOES NOT APPLY.	Group 1 Buildings with reinforced concrete roof decks should be treated as Group II Buildings.
8	Enhanced Wood Panel Roof Deck (≥ 5/8 " plywood)	Yes	0.99	HSRS (Secondary Factor 1 and 8 are mutually exclusive.) Applies to Deck C.
9	Shutter Interpolation Between None and Hurricane	Yes	Ordinary: Terrain B S = 0.72, Terrain C S = 0.56 OSB: Terrain B S = 0.72, Terrain C S = 0.56 Plywood: Terrain B S = 0.48, Terrain C S = 0.46 Basic: Terrain B S = 0.23, Terrain C S = 0.19	Based on 2003-2004 DCA Shutter Impact Tests for OSB and Plywood. Values given are shutter interpolation factors (S).
10	Vinyl Siding	Yes	1.02	Based on HSRS study.
11	Window, Door, and Skylight Water Leak Potential[2] Total Number of Openings a. Casement and Fixed 0 1 to 10 11 to 20 21 to 30 ≥ 31 b. All Other Window/Door Types 0 1 to 10 11 to 20 21 to 30 ≥ 31	Yes	Other / Non-Porous Shutters 1.00 / 1.00 1.03 / 1.01 1.05 / 1.03 1.08 / 1.06 1.11 / 1.09 1.00 / 1.00 1.04 / 1.02 1.07 / 1.04 1.11 / 1.08 1.14 / 1.11	Based on new sensitivity study. Count the number of openings in each category. All doors are counted as other type. Determine the appropriate factor for each type and multiply the factors together.
12	Double Wrap Roof-to-Wall Connector	No	Other: Terrain B 0.98, Terrain C 0.93 Basic, Hurricane: Terrain B 0.99, Terrain C 0.97	Based on new sensitivity study. Does not apply to post-FBC.
13	Roof Cover Age Interpolation	Yes	Tile, Cement, Slate, Metal: A(yrs) 40 Other: A(yrs) 25	Use Equation (4-3a) to interpolate from FBC to non-FBC Roof Cover. (N=Age of roof cover in years.)
14	Partially Enclosed Designs	Yes	0.98	Applies to post-FBC era, partially enclosed designs in WBD region. Apply to "Opening Protection = None."
15	Parapets and Roof Top Equipment		Use Table 5-10	Based on new sensitivity study.

[1] All openings protected factor shall only be used when all openings (including non-glazed) are protected to "Hurricane."

[2] Each sliding glass door is counted as 4 openings in determining the total number of openings. All other openings (doors, windows and skylights) are counted as one each.

5.2.2.1 2006 FBC Group I Construction

We developed new designs for the Group I buildings for each Florida wind zone (100 mph to 150 mph). Similar to the single family approach, we performed consistency checks with the Group I pre-FBC relativities. These consistency checks controlled the mapping of the post-FBC construction into the pre-FBC tables. Hence, similar to the single family post-FBC relativities, there are errors in the post-FBC Group I construction relativities resulting from the use of a single pre-FBC table for Group I buildings.

FBC 2006 Group I Loss Relativities. The loss relativities for Group I Buildings constructed to the 2006 FBC are given in Table 5-12 and Table 5-13 for Terrains B and C, respectively. These relativities reflect the consistency constraint of mapping the building features into the pre-FBC Group I statewide relativities. These relativities match the strongest features of the pre-FBC tables and the lowest relativities are slightly lower than the lowest relativity in Table 5-6 through Table 5-9.

Secondary Factors Regarding secondary factors for Group I FBC 2006 construction, the following notes apply:

1. Factor 1 or Factor 8 can be applied if the wood deck is dimensional lumber or enhanced (See Appendix A).
2. Factor 3 applies to Group I Residences with reinforced masonry walls.
3. The HVHZ relativities reflect the fact that all openings are protected and, hence, there is no need to apply Secondary Factor 4 to the HVHZ results. Secondary Factor 4 can be applied to non-HVHZ locations if all openings are protected to "Hurricane" level.
4. If the opening protection is provided by wood panel shutters, use the interpolation approach given by Equation (4-2) and the factors (Secondary Factor 9) in Table 5-11.
5. If the building has vinyl siding, apply Secondary Factor 10 in Table 5-11.
6. The leak potential factor (Secondary Factor 11 in Table 5-11) for windows, doors, and skylights should be applied to FBC 2006 buildings.
7. Double-wrap factor does not apply to post-FBC Group I.
8. Roof cover age interpolation is appropriate for post-FBC.
9. If the building has a reinforced concrete roof deck, use the Group II relativity tables.
10. If the building has Secondary Water Resistance (SWR), which meets the requirements in Appendix A, apply the appropriate factor from Table 5-14 or Table 5-15. We note that few FBC buildings are built with self adhering SWR and hence, this factor will rarely be applied to post-FBC residences.

5.2.2.2 2001 FBC Group I Construction

The FBC 2001 Group I loss relativities were developed by simulating the FBC 2001 designs developed in the 2002 loss relativity study to the updated hurricane wind hazard model results summarized in Section 2.3.6.

Table 5-16 (Terrain B) and Table 5-17 (Terrain C) contain the loss relativities for Group I buildings built to the FBC 2001. Table 5-18 and Table 5-19 contain the SWR secondary factors for these buildings. The application of these factors and other secondary factors follows the same approach as illustrated previously. Since the FBC 2001 did not include requirements for soffit design pressures, the Group I FBC 2001 tables include wood and other soffits.

We note that the FBC tables and the SWR tables contain all the information needed for mitigation factors (for designs beyond the FBC minimal requirements) for opening protection and applying SWR.

Table 5-12. Terrain B FBC 2006 Multifamily Group I Buildings

Terrain B Group I 2006 FBC[1,2]			Flat	Low Roof Slope (≤ 5:12)				Other Roof slope (≥ 6:12)			
			Built-Up	Non-Tile		Tile		Non-Tile		Tile	
Roof Cover	FBC Windspeed (mph)	Opening Protection		Other	Hip	Other	Hip	Other	Hip	Other	Hip
FBC[3]	100	None	0.4658	0.3466	0.3060	0.3801	0.3430	0.3310	0.2797	0.3462	0.3120
		Hurricane[5]	0.3422	0.2575	0.2405	0.3268	0.3058	0.2569	0.2388	0.3191	0.2975
	110	None	0.4564	0.3396	0.2998	0.3725	0.3361	0.3244	0.2741	0.3392	0.3057
		Hurricane[6]	0.3353	0.2523	0.2356	0.3202	0.2996	0.2517	0.2339	0.3127	0.2915
	≥ 120	None[7]	0.4519	0.3362	0.2968	0.3687	0.3327	0.3211	0.2714	0.3358	0.3026
		Hurricane	0.3319	0.2497	0.2333	0.3170	0.2966	0.2492	0.2316	0.3095	0.2885
Non-FBC[4]	100	None	0.8308	0.6113	0.5307	0.6209	0.5517	0.5505	0.4463	0.5387	0.4775
		Hurricane	0.6499	0.4835	0.4349	0.5492	0.4992	0.4528	0.3965	0.5066	0.4657
	110	None	0.8140	0.5990	0.5200	0.6084	0.5406	0.5393	0.4372	0.5278	0.4678
		Hurricane	0.6367	0.4738	0.4261	0.5381	0.4891	0.4436	0.3885	0.4963	0.4563
	≥ 120	None	0.8059	0.5930	0.5148	0.6023	0.5352	0.5340	0.4329	0.5226	0.4631
		Hurricane	0.6303	0.4690	0.4218	0.5327	0.4842	0.4391	0.3846	0.4913	0.4516

[1] Refer to discussion in Section 2.2.4.8 and Figure 4-7 to determine whether or not FBC 2001 or FBC 2006 relativity tables should be used for FBC 2006 construction.

[2] Use Table 5-20 for FBC 2006 Group I Buildings with reinforced concrete roof deck.

[3] FBC Roof Covers (apply this part of the table with no roof cover age interpolation for 2006 FBC roof covers less than or equal to 5 years old).

[4] Non FBC Roof Covers (this part of the table is used with FBC Roof Covers to interpolate for 2006 FBC construction with roof covers 6 years old or more). See Section 4.2.5.

[5] Opening Protection is not required by the 2006 FBC for 100 mph design windspeeds. Hence, this row only applies to 2006 FBC Group I Buildings that are further mitigated with opening protection.

[6] Opening protection is required within 1 mile of coast for 110 mph design windspeeds. For most locations in Florida in the 110 mph windzone, this row only applies to 2006 FBC Group I Buildings mitigated with opening protection.

[7] This row is included only for interpolation of shutters less than "Hurricane" level of protection per Table 5-11.

Table 5-13. Terrain C 2006 FBC Multifamily Group I Buildings

Terrain C Group I FBC 2006[1,2]			Flat	Low Roof Slope (≤ 5:12)				Other Roof slope (≥ 6:12)			
			Built-Up	Non-Tile		Tile		Non-Tile		Tile	
Roof Cover	FBC Windspeed (mph)	Opening Protection		Other	Hip	Other	Hip	Other	Hip	Other	Hip
FBC[3]	100	None	0.6129	0.4970	0.4380	0.4629	0.3952	0.4533	0.3453	0.3394	0.2754
		Hurricane[5]	0.2159	0.1925	0.1771	0.2400	0.2253	0.1930	0.1749	0.2334	0.2181
	110	None	0.5947	0.4822	0.4250	0.4491	0.3834	0.4398	0.3350	0.3293	0.2672
		Hurricane[6]	0.2095	0.1868	0.1718	0.2328	0.2186	0.1872	0.1697	0.2265	0.2116
	≥ 120	None[7]	0.5881	0.4769	0.4203	0.4442	0.3792	0.4350	0.3313	0.3257	0.2643
		Hurricane	0.2095	0.1868	0.1718	0.2328	0.2186	0.1872	0.1697	0.2265	0.2116
	HVHZ[8]	Hurricane	0.2011	0.1793	0.1649	0.2235	0.2099	0.1797	0.1629	0.2174	0.2031
Non-FBC[4]	100	None	0.9039	0.7397	0.7152	0.6980	0.6192	0.6448	0.5165	0.4889	0.4074
		Hurricane	0.3928	0.3534	0.3185	0.3997	0.3741	0.3261	0.2853	0.3706	0.3462
	110	None	0.8770	0.7176	0.6939	0.6772	0.6008	0.6256	0.5011	0.4743	0.3953
		Hurricane	0.3811	0.3429	0.3090	0.3878	0.3630	0.3164	0.2768	0.3596	0.3359
	≥ 120	None	0.8674	0.7097	0.6863	0.6697	0.5942	0.6187	0.4956	0.4691	0.3909
		Hurricane	0.3811	0.3429	0.3090	0.3878	0.3630	0.3164	0.2768	0.3596	0.3359
	HVHZ	Hurricane	0.3658	0.3292	0.2966	0.3723	0.3485	0.3038	0.2657	0.3452	0.3225

[1] Refer to discussion in Section 2.2.4.8 and Figure 4-7 to determine whether or not FBC 2001 or FBC 2006 relativity tables should be used for FBC 2006 construction.

[2] Use Table 5-21 for FBC 2006 Group I Buildings with reinforced concrete roof deck.

[3] FBC Roof Covers (apply this part of the table with no roof cover age interpolation for 2006 FBC roof covers less than or equal to 5 years old).

[4] Non FBC Roof Covers (this part of the table is used with FBC Roof Covers to interpolate for 2006 FBC construction with roof covers 6 years old or more). See Section 4.2.5.

[5] Opening Protection is not required by the 2006 FBC for 100 mph design windspeeds. Hence, this row only applies to 2006 FBC Group I Buildings that are further mitigated with opening protection.

[6] Opening protection is required within 1 mile of coast for 110 mph design windspeeds. For most locations in Florida in the 110 mph windzone, this row only applies to 2006 FBC Group I Buildings mitigated with opening protection.

[7] This row is included only for interpolation of shutters less than "Hurricane" level of protection per Table 5-11.

[8] Secondary Factor 4 (All Openings Protected) has already been considered for HVHZ.

FBC 2001 Partially Enclosed Designs. The 2001 FBC allowed for partially-enclosed designs in the WBD region. Partially enclosed designs do not provide opening protection for wind-borne debris. Although the building is designed for internal pressures, it still has unprotected glazing and hence is subject to higher losses than a building with opening protection.

The relativities for partially-enclosed designs are determined by using the no opening protection values in Table 5-16 and Table 5-17. With a secondary factor of 0.98. This factor accounts for the

increased pressure resistance of the windows, doors, and other components due to the internal pressure design requirement.

Table 5-14. Terrain B Secondary Water Resistance Factors for Group I 2006 FBC

Terrain B Group I FBC 2006 SWR[1]			Flat	Low Roof Slope (≤ 5:12)				Other Roof slope (≥ 6:12)			
			Built-Up	Non-tile		Tile		Non-tile		Tile	
Roof Cover	FBC Windspeed (mph)	Opening Protection		Other	Hip	Other	Hip	Other	Hip	Other	Hip
FBC[2]	100, 110	None	0.956	0.959	0.984	0.984	0.991	0.968	0.986	0.978	0.992
	≥120	Hurricane	0.950	0.944	0.978	0.978	0.987	0.949	0.983	0.975	0.990
Non-FBC[3]	100, 110	None	0.748	0.751	0.792	0.855	0.888	0.780	0.840	0.875	0.928
	≥120	Hurricane	0.741	0.736	0.797	0.854	0.901	0.773	0.858	0.881	0.934

[1] These SWR factors must be determined by separate inspection or affadavit. SWR is not required by the FBC and is not typical of new construction.
[2] FBC roof covers (apply this part of the table with no roof cover age interpolation for 2001 FBC roof covers less than or equal to 5 years old). The SWR factor must be applied as part of the FBC roof cover age interpolation (Eq. 4-3) and not as a separate factor per Eq. 4-1(b).
[3] Non-FBC roof covers (this part of the table is used with FBC to interpolate for 2001 FBC construction with roof covers 6 years old or more). The SWR factor must be applied as part of the FBC roof cover age interpolation (Eq. 4-3) and not as a separate factor per Eq. 4-1(b).

Table 5-15. Terrain C Secondary Water Resistance Factors for Group I 2006 FBC

Terrain C Group I FBC 2006 SWR[1]			Flat	Low Roof Slope (≤ 5:12)				Other Roof slope (≥ 6:12)			
			Built-Up	Non-tile		Tile		Non-tile		Tile	
Roof Cover	FBC Windspeed (mph)	Opening Protection		Other	Hip	Other	Hip	Other	Hip	Other	Hip
FBC[2]	100, 110	None	0.952	0.967	0.981	0.975	0.987	0.975	0.987	0.974	0.986
	≥120[4]	Hurricane	0.964	0.911	0.956	0.951	0.973	0.915	0.962	0.956	0.982
Non-FBC[3]	100, 110	None	0.771	0.757	0.735	0.825	0.837	0.799	0.796	0.856	0.881
	≥120	Hurricane	0.777	0.668	0.735	0.810	0.854	0.724	0.806	0.849	0.903

[1] These SWR factors must be determined by separate inspection or affadavit. SWR is not required by the FBC and is not typical of new construction.
[2] FBC roof covers (apply this part of the table with no roof cover age interpolation for 2001 FBC roof covers less than or equal to 5 years old). The SWR factor must be applied as part of the FBC roof cover age interpolation (Eq. 4-3) and not as a separate factor per Eq. 4-1(b).
[3] Non-FBC roof covers (this part of the table is used with FBC to interpolate for 2001 FBC construction with roof covers 6 years old or more). The SWR factor must be applied as part of the FBC roof cover age interpolation (Eq. 4-3) and not as a separate factor per Eq. 4-1(b).
[4] Use this row also for HVHZ

Table 5-16. Terrain B FBC 2001 Multifamily Group I Buildings

Terrain B Group I FBC 2001[1]				Flat	Low Roof Slope (≤ 5:12)				Other Roof slope (≥ 6:12)			
					Non-Tile		Tile		Non-Tile		Tile	
Roof Cover	FBC Windspeed (mph)	Opening Protection	Soffits[7]	Built-Up	Other	Hip	Other	Hip	Other	Hip	Other	Hip
FBC[2]	100, 110	None	Other		0.3971	0.3462	0.4345	0.3886	0.3812	0.3169	0.3918	0.3533
			Wood	0.4728	0.3545	0.3091	0.3880	0.3470	0.3404	0.2829	0.3498	0.3154
		Hurricane[4,5]	Other		0.2954	0.2723	0.3728	0.3474	0.2932	0.2688	0.3611	0.3364
			Wood	0.3493	0.2638	0.2431	0.3329	0.3101	0.2618	0.2422	0.3224	0.3016
	≥120	None[6]	Other		0.3931	0.3427	0.4302	0.3847	0.3774	0.3137	0.3878	0.3497
			Wood	0.4680	0.3510	0.3060	0.3841	0.3435	0.3370	0.2801	0.3463	0.3123
		Hurricane	Other		0.2925	0.2696	0.3691	0.3439	0.2903	0.2661	0.3574	0.3331
			Wood	0.3458	0.2612	0.2407	0.3296	0.3070	0.2592	0.2398	0.3191	0.2986
Non-FBC[3]	100, 110	None	Other		0.6893	0.5878	0.7032	0.6209	0.6101	0.4907	0.5979	0.5352
			Wood	0.8384	0.6338	0.5425	0.6421	0.5672	0.5760	0.4556	0.5529	0.4912
		Hurricane	Other		0.5502	0.4927	0.6325	0.5733	0.5109	0.4473	0.5776	0.5313
			Wood	0.6549	0.4986	0.4447	0.5697	0.5163	0.4697	0.4111	0.5226	0.4821
	≥120	None	Other		0.6824	0.5819	0.6962	0.6147	0.6040	0.4858	0.5919	0.5298
			Wood	0.8300	0.6275	0.5371	0.6357	0.5616	0.5702	0.4510	0.5474	0.4863
		Hurricane	Other		0.5447	0.4877	0.6262	0.5676	0.5058	0.4428	0.5718	0.5259
			Wood	0.6483	0.4936	0.4403	0.5640	0.5112	0.4650	0.4070	0.5174	0.4773

[1] Use Table 5-20 for FBC 2001 Group I Buildings with reinforced concrete roof deck.

[2] FBC Roof Covers (apply this part of the table with no roof cover age interpolation for 2001 FBC roof covers less than or equal to 5 years old).

[3] Non FBC Roof Covers (this part of the table is used with FBC Roof Covers to interpolate for 2001 FBC construction with roof covers 6 years old or more). See Section 4.2.5.

[4] Opening Protection is not required by the 2001 FBC for 100 mph design windspeeds. Hence, this row only applies to 2001 FBC Group I Buildings that are further mitigated with opening protection.

[5] Opening protection is required within 1 mile of coast for 110 mph design windspeeds. For most locations in Florida in the 110 mph windzone, this row only applies to 2001 FBC Group I Buildings mitigated with opening protection.

[6] This row included for: (a) Panhandle WBD exception; (b) interpolation of shutters less than "Hurricane" per Table 5-11; and (c) partially enclosed designs in the WBDR. Apply a factor of 0.98 to the row for partially enclosed designs, per Table 4-15.

[7] Use wood soffit row for the use of this table for any FBC 2006 construction.

Table 5-17. Terrain C FBC 2001 Multifamily Group I Buildings

Terrain B Group I FBC 2001[1]				Flat	Low Roof Slope (≤ 5:12)				Other Roof slope (≥ 6:12)			
					Non-Tile		Tile		Non-Tile		Tile	
Roof Cover	FBC Windspeed (mph)	Opening Protection	Soffits[7]	Built-Up	Other	Hip	Other	Hip	Other	Hip	Other	Hip
FBC[2]	100, 110	None	Other		0.5337	0.4648	0.4940	0.4213	0.4810	0.3634	0.3610	0.2905
			Wood	0.6148	0.5030	0.4386	0.4659	0.3980	0.4538	0.3439	0.3416	0.2757
		Hurricane[4,5]	Other		0.2090	0.1859	0.2586	0.2384	0.2052	0.1834	0.2473	0.2293
			Wood	0.2233	0.1996	0.1780	0.2460	0.2270	0.1961	0.1756	0.2354	0.2185
	≥120	None[6]	Other		0.5220	0.4595	0.4859	0.4141	0.4757	0.3612	0.3551	0.2872
			Wood	0.6068	0.4921	0.4336	0.4583	0.3912	0.4488	0.3418	0.3360	0.2727
		Hurricane	Other		0.1994	0.1831	0.2497	0.2342	0.1999	0.1807	0.2428	0.2265
			Wood	0.2137	0.1906	0.1753	0.2376	0.2231	0.1910	0.1731	0.2311	0.2159
	HVHZ[8]	Hurricane	Other		0.1955	0.1794	0.2447	0.2295	0.1959	0.1771	0.2379	0.2220
			Wood	0.2095	0.1868	0.1718	0.2328	0.2186	0.1872	0.1697	0.2265	0.2116
Non-FBC[3]	100, 110	None	Other		0.7710	0.7106	0.7112	0.6258	0.6560	0.5083	0.4971	0.4077
			Wood	0.8947	0.7395	0.7034	0.6924	0.6141	0.6419	0.5119	0.4920	0.4052
		Hurricane	Other		0.3546	0.3171	0.4131	0.3797	0.3225	0.2788	0.3716	0.3447
			Wood	0.4005	0.3616	0.3184	0.4131	0.3757	0.3315	0.2881	0.3742	0.3470
	≥120	None	Other		0.7673	0.7156	0.7119	0.6239	0.6507	0.5059	0.4900	0.4051
			Wood	0.8940	0.7323	0.7081	0.6910	0.6130	0.6384	0.5113	0.4840	0.4033
		Hurricane	Other		0.3488	0.3137	0.4036	0.3757	0.3141	0.2755	0.3646	0.3403
			Wood	0.3884	0.3499	0.3153	0.3957	0.3704	0.3229	0.2825	0.3669	0.3428
	HVHZ	Hurricane	Other		0.3418	0.3074	0.3956	0.3682	0.3078	0.2700	0.3574	0.3335
			Wood	0.3807	0.3429	0.3090	0.3878	0.3630	0.3164	0.2768	0.3596	0.3359

[1] Use Table 5-21 for FBC 2001 Group I Buildings with reinforced concrete roof deck.

[2] FBC Roof Covers (apply this part of the table with no roof cover age interpolation for 2001 FBC roof covers less than or equal to 5 years old).

[3] Non FBC Roof Covers (this part of the table is used with FBC Roof Covers to interpolate for 2001 FBC construction with roof covers 6 years old or more). See Section 4.2.5.

[4] Opening Protection is not required by the 2001 FBC for 100 mph design windspeeds. Hence, this row only applies to 2001 FBC Group I Buildings that are further mitigated with opening protection.

[5] Opening protection is required within 1 mile of coast for 110 mph design windspeeds. For most locations in Florida in the 110 mph windzone, this row only applies to 2001 FBC Group I Buildings mitigated with opening protection.

[6] This row included for: (a) Panhandle WBD exception; (b) interpolation of shutters less than "Hurricane" per Table 5-11; and (c) partially enclosed designs in the WBDR. Apply a factor of 0.98 to the row for partially enclosed designs, per Table 4-15.

[7] Use wood soffit row for the use of this table for any FBC 2006 construction.

[8] Secondary Factor 4 (All openins protected) have already been considered in the HVHZ.

Table 5-18. Terrain B Secondary Water Resistance Factors for Group I 2001 FBC

Terrain B Group I FBC 2001 SWR[1]				Flat	Low Roof Slope (≤ 5:12)				Other Roof slope (≥ 6:12)			
					Non-tile		Tile		Non-tile		Tile	
Roof Cover	FBC Windspeed (mph)	Opening Protection	Soffit	Built-Up	Other	Hip	Other	Hip	Other	Hip	Other	Hip
FBC[2]	100, 110	None	Other		0.947	0.978	0.973	0.988	0.957	0.986	0.977	0.990
			Wood	0.950	0.950	0.983	0.973	0.988	0.957	0.986	0.977	0.991
	≥120	Hurricane	Other		0.936	0.973	0.971	0.983	0.950	0.985	0.978	0.987
			Wood	0.950	0.942	0.984	0.971	0.983	0.950	0.985	0.978	0.990
Non-FBC[3]	100, 110	None	Other		0.724	0.787	0.845	0.886	0.774	0.838	0.875	0.924
			Wood	0.724	0.731	0.794	0.851	0.885	0.774	0.840	0.876	0.924
	≥120	Hurricane	Other		0.715	0.789	0.841	0.892	0.765	0.844	0.878	0.926
			Wood	0.727	0.728	0.806	0.845	0.897	0.777	0.857	0.885	0.934

[1] These SWR factors must be determined by separate inspection or affidavit. SWR is not required by the FBC and is not typical of new construction.

[2] FBC roof covers (apply this part of the table with no roof cover age interpolation for 2001 FBC roof covers less than or equal to 5 years old). The SWR factor must be applied as part of the FBC roof cover age interpolation (Eq. 4-1) and not as a separate factor per Eq. 4-1(b).

[3] Non-FBC roof covers (this part of the table is used with FBC to interpolate for 2001 FBC construction with roof covers 6 years old or more). The SWR factor must be applied as part of the FBC roof cover age interpolation (Eq. 4-1) and not as a separate factor per Eq. 4-1(b).

Partially enclosed designs are not allowed in the HVHZ and, hence, these factors do not apply to the HVHZ.

Consideration of 2001 Panhandle WBD Region Exemption. The 2001 FBC had an exemption for the Florida Panhandle for the WBD requirements for the buildings more than one mile from the coast. Therefore, Group I buildings built in the Panhandle to the 2001 FBC more than 1 mile from the coast and in a ≥ 120 mph wind zone may not have WBD protection. The loss relativities for these buildings should be determined by using the no shutter results for buildings built without opening protection under the Panhandle WBD exception.

Table 5-19. Terrain C Secondary Water Resistance Factors for Group I 2001 FBC

Terrain C Group I FBC 2001 SWR[1]				Flat	Low Roof Slope (≤ 5:12)				Other Roof slope (≥ 6:12)			
					Non-tile		Tile		Non-tile		Tile	
Roof Cover	FBC Windspeed (mph)	Opening Protection	Soffit	Built-Up	Other	Hip	Other	Hip	Other	Hip	Other	Hip
FBC[2]	100, 110	None	Other		0.927	0.967	0.959	0.981	0.939	0.973	0.961	0.981
			Wood	0.954	0.929	0.968	0.960	0.981	0.940	0.974	0.962	0.981
	≥120	Hurricane	Other		0.909	0.955	0.950	0.972	0.913	0.961	0.956	0.981
			Wood	0.964	0.911	0.956	0.951	0.973	0.915	0.962	0.956	0.982
Non-FBC[3]	100, 110	None	Other		0.720	0.731	0.813	0.836	0.773	0.802	0.851	0.888
			Wood	0.739	0.727	0.724	0.814	0.833	0.771	0.786	0.846	0.880
	≥120	Hurricane	Other		0.652	0.715	0.789	0.837	0.712	0.789	0.838	0.897
			Wood	0.699	0.667	0.735	0.805	0.854	0.725	0.804	0.849	0.903

[1] These SWR factors must be determined by separate inspection or affidavit. SWR is not required by the FBC and is not typical of new construction.

[2] FBC roof covers (apply this part of the table with no roof cover age interpolation for 2001 FBC roof covers less than or equal to 5 years old). The SWR factor must be applied as part of the FBC roof cover age interpolation (Eq. 4-1) and not as a separate factor per Eq. 4-1(b).

[3] Non-FBC roof covers (this part of the table is used with FBC to interpolate for 2001 FBC construction with roof covers 6 years old or more). The SWR factor must be applied as part of the FBC roof cover age interpolation (Eq. 4-1) and not as a separate factor per Eq. 4-1(b).

5.3 Group II Buildings

Group II MF residential buildings are structures that are 60 feet or less in height with non-wood roof decks. The typical roof deck types for Group II buildings are concrete or metal roof decks. The three construction eras modeled in the analysis of Group II buildings are:

1. 1982 or earlier, for which buildings designed to 1976 Standard Building Code (SBC 1976) are assumed to be typical.
2. 1983 through February 28, 2002, for which buildings designed to the 1988 Standard Building Code (SBC 1988) are assumed to be typical.
3. March 1, 2002 and later, for which buildings designed to the provisions of the 2001 Florida Building Code (FBC 2001) are assumed to be typical.

Both the building code era and visual inspection are required to determine the proper loss relativity.

5.3.1 Group II Loss Relativity Tables

The Group II loss relativity data for a 2% deductible (as a percentage of building replacement value) are given in Table 5-20 and Table 5-21 for Terrains B and C, respectively. To use these tables, one must obtain the following information:

1. The exposure category: Terrain B or Terrain C. Use the definitions given in Section A.1.1.1 of Appendix A. Note that the determination of the terrain type for the purposes of determining loss relativities for Group II buildings does not depend on whether the building is within the High Velocity Hurricane Zone (HVHZ).
2. The basic wind speed zone. Use the 2007 revision to FBC 2004 Figure 1609 or simply the county if the building is located in Broward, Miami-Dade, or Monroe County.
3. The design code era: SBC 1976, SBC 1988, or FBC 2001. If the design code era is FBC 2001 and the building is located in the Wind Borne Debris Region (WBDR), then the FBC 2001 design option is also required (Partially Enclosed or Enclosed). Note that the Partially Enclosed design option was removed from the FBC effective July 1, 2007.

Table 5-20. Group II Relativities for Terrain B

					Metal Roof Deck				Concrete	
					Non-FBC Equivalent Roof Covering		FBC Equivalent Roof Covering		Non-FBC Equiv. Roof Cover	FBC Equiv. Roof Cover
Actual Terrain	FBC Wind Speed	Model Design Code	FBC 2001 Design Option	Protection	No SWR	SWR	No SWR	SWR		
B	< = 100	SBC 1976		None	**1.0000**	0.6902	0.7263	0.6695	0.4862	0.4670
		(Pre 1983)		Hurricane	0.6578	0.3805	0.4069	0.3552	0.3159	0.2945
		SBC 1988		None	0.6281	0.4142	0.4328	0.3875	0.3331	0.3132
		(1983-2001)		Hurricane	0.4876	0.3499	0.3532	0.3225	0.3118	0.2900
		FBC 2001	Enclosed	None			0.4144	0.3774		0.2354
		(2002-present)		Hurricane			0.2373	0.2281		0.1860
	101-110	SBC 1976		None	**1.0000**	0.6324	0.6820	0.6093	0.5001	0.4771
		(Pre 1983)		Hurricane	0.7880	0.4427	0.4852	0.4161	0.3970	0.3710
		SBC 1988		None	0.7244	0.4695	0.5022	0.4465	0.4061	0.3866
		(1983-2001)		Hurricane	0.5971	0.4257	0.4346	0.3964	0.3911	0.3646
		FBC 2001	Enclosed	None			0.4528	0.4062		0.3221
		(2002-present)		Hurricane			0.3463	0.3216		0.2869
	111-120	SBC 1976		None	**1.0000**	0.6580	0.7159	0.6395	0.5030	0.4850
		(Pre 1983)		Hurricane	0.7616	0.4366	0.4914	0.4163	0.3862	0.3657
		SBC 1988		None	0.7168	0.4691	0.5137	0.4515	0.3968	0.3818
		(1983-2001)		Hurricane	0.5837	0.4151	0.4346	0.3920	0.3797	0.3590
		FBC 2001	Partially-Encl.	None			0.4276	0.3771		0.3346
		(2002-present)	Enclosed	Hurricane			0.3830	0.3399		0.3135
	121-130	SBC 1976		None	**1.0000**	0.6457	0.7257	0.6273	0.5163	0.5016
		(Pre 1983)		Hurricane	0.8175	0.4689	0.5526	0.4486	0.4118	0.3957
		SBC 1988		None	0.8882	0.5816	0.6627	0.5685	0.4803	0.4663
		(1983-2001)		Hurricane	0.7071	0.4985	0.5539	0.4813	0.4506	0.4330
		FBC 2001	Partially-Encl.	None			0.5340	0.4560		0.4127
		(2002-present)	Enclosed	Hurricane			0.4815	0.4222		0.3929
	131-140	SBC 1976		None	**1.0000**	0.6590	0.7318	0.6399	0.5675	0.5514
		(Pre 1983)		Hurricane	0.7482	0.5114	0.5622	0.4921	0.4517	0.4382
		SBC 1988		None	0.9696	0.6641	0.7405	0.6553	0.5012	0.4888
		(1983-2001)		Hurricane	0.7560	0.5233	0.5801	0.5099	0.4535	0.4388
		FBC 2001	Partially-Encl.	None			0.5904	0.4980		0.4602
		(2002-present)	Enclosed	Hurricane			0.5336	0.4603		0.4301
	Broward	SBC 1976		None	**1.0000**	0.6520	0.7638	0.6432	0.5621	0.5517
		(Pre 1983)		Hurricane	0.7813	0.5285	0.5985	0.5076	0.4738	0.4571
		SBC 1988		None	0.9460	0.6334	0.7243	0.6207	0.5005	0.4871
		(1983-2001)		Hurricane	0.7441	0.5256	0.5910	0.5105	0.4617	0.4452
		FBC 2001	Enclosed	Hurricane			0.5180	0.4484		0.4287
	Miami-Dade	SBC 1976		None	**1.0000**	0.6577	0.7704	0.6485	0.5606	0.5506
		(Pre 1983)		Hurricane	0.7737	0.5237	0.5978	0.5045	0.4644	0.4485
		SBC 1988		None	0.9441	0.6379	0.7304	0.6261	0.4940	0.4813
		(1983-2001)		Hurricane	0.7382	0.5224	0.5906	0.5080	0.4513	0.4357
		FBC 2001	Enclosed	Hurricane			0.5250	0.4521		0.4263
	Monroe	SBC 1976		None	**1.0000**	0.6861	0.8015	0.6739	0.5541	0.5459
		(Pre 1983)		Hurricane	0.7465	0.5091	0.5947	0.4933	0.4259	0.4128
		SBC 1988		None	0.9374	0.6623	0.7585	0.6518	0.4691	0.4578
		(1983-2001)		Hurricane	0.7150	0.5116	0.5880	0.4999	0.4067	0.3943
		FBC 2001	Partially-Encl.	None			0.6269	0.5041		0.4351
		(2002-present)	Enclosed	Hurricane			0.5471	0.4568		0.3927

Table 5-21. Group II Relativities for Terrain C

					Metal Roof Deck				Concrete	
					Non-FBC Equivalent		FBC Equivalent		Non-FBC Equiv. Roof Cover	FBC Equiv. Roof Cover
Actual Terrain	FBC Wind Speed	Model Design Code	FBC 2001 Design Option	Protection	No SWR	SWR	No SWR	SWR		
C	< = 100	SBC 1976		None	**1.0000**	0.7695	0.8053	0.7482	0.4660	0.4509
		(Pre 1983)		Hurricane	0.4496	0.2949	0.3106	0.2727	0.2183	0.2004
		SBC 1988		None	0.5903	0.4056	0.4351	0.3861	0.2702	0.2548
		(1983-2001)		Hurricane	0.3889	0.2528	0.2659	0.2326	0.2102	0.1934
		FBC 2001	Enclosed	None			0.3126	0.2737		0.1499
		(2002-present)		Hurricane			0.1832	0.1633		0.1202
	101-110	SBC 1976		None	**1.0000**	0.6966	0.7481	0.6749	0.4642	0.4453
		(Pre 1983)		Hurricane	0.5748	0.3643	0.3949	0.3403	0.3032	0.2808
		SBC 1988		None	0.6678	0.4135	0.4559	0.3917	0.3307	0.3100
		(1983-2001)		Hurricane	0.5242	0.3360	0.3622	0.3115	0.2963	0.2741
		FBC 2001	Enclosed	None			0.3843	0.3244		0.2303
		(2002-present)		Hurricane			0.2946	0.2565		0.2104
	111-120	SBC 1976		None	**1.0000**	0.7260	0.7858	0.7107	0.4664	0.4521
		(Pre 1983)		Hurricane	0.5615	0.3595	0.4018	0.3423	0.2900	0.2734
		SBC 1988		None	0.6603	0.4215	0.4747	0.4051	0.3225	0.3070
		(1983-2001)		Hurricane	0.5070	0.3252	0.3624	0.3072	0.2827	0.2657
		FBC 2001	Partially-Encl.	None			0.3312	0.2710		0.2367
		(2002-present)	Enclosed	Hurricane			0.2931	0.2422		0.2278
	121-130	SBC 1976		None	**1.0000**	0.6917	0.7740	0.6738	0.4739	0.4603
		(Pre 1983)		Hurricane	0.6463	0.4133	0.4841	0.3962	0.3346	0.3195
		SBC 1988		None	0.8513	0.5423	0.6335	0.5247	0.4179	0.4023
		(1983-2001)		Hurricane	0.6753	0.4364	0.5137	0.4177	0.3750	0.3603
		FBC 2001	Partially-Encl.	None			0.4520	0.3610		0.3257
		(2002-present)	Enclosed	Hurricane			0.4123	0.3411		0.3149
	131-140	SBC 1976		None	**1.0000**	0.6462	0.7463	0.6286	0.4994	0.4826
		(Pre 1983)		Hurricane	0.7481	0.4619	0.5567	0.4448	0.3896	0.3754
		SBC 1988		None	0.9995	0.7188	0.8040	0.6978	0.5007	0.4844
		(1983-2001)		Hurricane	0.7478	0.4787	0.5668	0.4680	0.3841	0.3711
		FBC 2001	Partially-Encl.	None			0.5150	0.4116		0.3893
		(2002-present)	Enclosed	Hurricane			0.4853	0.3891		0.3635
	Broward	SBC 1976		None	**1.0000**	0.6203	0.7455	0.6030	0.5002	0.4865
		(Pre 1983)		Hurricane	0.7749	0.4743	0.5780	0.4572	0.4082	0.3932
		SBC 1988		None	0.9420	0.6176	0.7216	0.6019	0.4599	0.4450
		(1983-2001)		Hurricane	0.7362	0.4797	0.5717	0.4626	0.3993	0.3856
		FBC 2001	Enclosed	Hurricane			0.4898	0.3956		0.3620
	Miami-Dade	SBC 1976		None	**1.0000**	0.6280	0.7553	0.6121	0.4995	0.4867
		(Pre 1983)		Hurricane	0.7709	0.4738	0.5807	0.4572	0.4020	0.3878
		SBC 1988		None	0.9470	0.6288	0.7349	0.6143	0.4605	0.4464
		(1983-2001)		Hurricane	0.7336	0.4800	0.5752	0.4644	0.3928	0.3797
		FBC 2001	Enclosed	Hurricane			0.4944	0.4024		0.3649
	Monroe	SBC 1976		None	**1.0000**	0.6633	0.7909	0.6504	0.4975	0.4861
		(Pre 1983)		Hurricane	0.7548	0.4739	0.5908	0.4588	0.3751	0.3634
		SBC 1988		None	0.9687	0.6808	0.7885	0.6695	0.4671	0.4546
		(1983-2001)		Hurricane	0.7221	0.4835	0.5868	0.4719	0.3634	0.3524
		FBC 2001	Partially-Encl.	None			0.5451	0.4135		0.3779
		(2002-present)	Enclosed	Hurricane			0.5033	0.3938		0.3481

The data listed in Table 5-20 and Table 5-21 represent the relativities obtained at a representative location within each FBC basic wind speed zone. For each unique combination of terrain category and FBC basic wind speed zone, the loss costs have been normalized to the SBC 1976 building with no opening protection, a non-FBC equivalent roof cover, no secondary water resistance, a non-concrete roof deck, no parapet, and no inadequately restrained rooftop equipment present. This building has been selected arbitrarily and the tables can be easily re-normalized by any other building type. A key point in the use of the tables is that they have been normalized within each terrain category and wind speed zone. The user determines the terrain category and wind speed zone using the one set of definitions, regardless of the year built.

As an example of how to use these tables, consider the case of a four-story condominium building built in 1990 in Terrain B in Orlando. The building is reinforced concrete with a reinforced concrete roof deck and non-FBC equivalent roof cover. The building has no opening protection. Since the building was built in 1990, we use the SBC 1988 relativities. The FBC design windspeed for Orlando is 110 mph. Therefore, we find the loss relativity to be 0.4061. This means that for 2% deductible (as a percentage of building replacement value) that the loss costs are 59% less than that of the reference SBC 1976 non-concrete deck building at that location.

Table 5-20 and Table 5-21 are based on minimal load designs for each building code era. Over design is not considered. The only exceptions are the FBC 2001 relativities given for Terrain B in the High Velocity Hurricane Zone (i.e., Broward and Miami-Dade Counties). Buildings in the HVHZ must be designed for Terrain C, even if the actual terrain meets the requirements of Exposure Category B.

5.3.2 Secondary Factors for Group II Loss Relativities

Table 5-22 provides the secondary factors for parapets and inadequately restrained rooftop equipment for Group II buildings. Three sets of factors are provided: (1) parapets only, (2) rooftop equipment only, and (3) parapets combined with rooftop equipment. Tall parapets (minimum of 6 feet in height) reduce expected losses – particularly for building with metal roof decks, no secondary water resistance, and/or non-FBC equivalent roof coverings. The reduction in loss costs ranges from 24% for buildings with the weakest roofs to 2% for buildings with the strongest roofs. Unrestrained or poorly restrained rooftop equipment increases expected losses. The increase in loss costs ranges from 5% for buildings with the weakest roofs to 9% for buildings with the strongest roofs. The effect of parapets combined with rooftop equipment also varies depending on the types of roof construction and roof covering.

Table 5-22. Group II Secondary Factors for Parapets and Inadequately Restrained RoofTop Equipment

Roof Deck	*SWR*	*Roof Cover*	*Parapets*	*Unrestrained Rooftop Equipment*	*Both*
Metal	No	Non-FBC Equivalent	0.76	1.05	0.80
Metal	No	FBC Equivalent	0.88	1.06	0.94
Metal	Yes	Non-FBC Equivalent	0.92	1.07	0.99
Metal	Yes	FBC Equivalent	0.94	1.07	1.01
Concrete	N/A	Non-FBC Equivalent	0.95	1.09	1.03
Concrete	N/A	FBC Equivalent	0.98	1.09	1.06

In addition to the parapets and rooftop equipment secondary factor, the following Group I secondary factors from Table 5-11 also apply to Group II MF residential buildings:

- Opening coverage – all openings (Table 5-11, Item #4)

- Shutter interpolation between None and Hurricane (Table 5-11, Item #9)
- Wind, door, and skylight leakage potential (Table 5-11, Item #11)
- Roof Cover Age Interpolation (Table 5-11, Item #13)

The application of the secondary factors follows the methodology provided for SF homes in Section 4.2.5. First, the shutter interpolation factor should be applied to the primary relativity using Equation (4-2). Next, the FBC roof cover age interpolation factor should be applied (if applicable) using Equation (4-3). Any other secondary factors should then be combined using Equation (4-1b), and the final relativity should be computed using Equation (4-1a).

5.3.3 Discussion of Group II Loss Relativity Results

As expected, there is a wide range of relativities from the weakest to the strongest buildings. For Terrain B, the ratios of weakest to strongest relativities range between 5.4 in the lowest wind zone to 2.5 in the highest wind zone. For Terrain C, the ratios are larger, ranging from 8.3 in the lowest wind zone to 2.9 in the highest wind zone. The variation in the ratios is due to the fact that opening protection and FBC equivalent roof covers are much less likely to fail in the lower wind speed zones than in the higher wind speed zones. Nonetheless, the dollar savings in losses due to mitigation will be higher in the high wind speed zones because the frequency of severe events is higher and the expected losses for the base building class are higher.